

**ELEVENTH INTERNATIONAL CONFERENCE
ON COMPOSITE MATERIALS**

**Gold Coast, Queensland, Australia
14th - 18th July 1997**

PROCEEDINGS

VOLUME I

**COMPOSITES APPLICATIONS
AND DESIGN, PLENARIES**

**Editor
Murray L. Scott**

**AUSTRALIAN COMPOSITE STRUCTURES SOCIETY
WOODHEAD PUBLISHING LIMITED**

TABLE OF CONTENTS

Plenaries

On the Certification of Bonded Composite Repairs to Primary Aircraft Structure	1
<i>Alan Baker</i>	
Recent Work on Stitching of Laminated Composites - Theoretical Analysis and Experiments	25
<i>Lalit K. Jain, Yiu-Wing Mai</i>	
The First Fair Dinkum Macro-Level Fibrous Composite Failure Criteria	52
<i>L.J. Hart-Smith</i>	
Application of Composite Materials to the Renewal of Twenty-First Century Infrastructure	88
<i>Vistasp M. Karbhari</i>	
The Potential of Knitted Fabrics as a Reinforcement for Composites	108
<i>Ignas Verpoes, Bart Gommers, Gert Huymans, Ian Ivens, Yimen Luo, Surya Pandita, Dirk Phillips</i>	
Aerospace Materials and Structural Research into the Next Millennium	134
<i>Jim C.I. Chang</i>	
Delamination Fracture in the Presence of Through-Thickness Reinforcement	159
<i>Brian Cox, Roberta Massabó, Daniel Mumm, André Turrettini, Keith Kedward</i>	
777 Empennage Certification Approach	178
<i>A. Fawcett, J. Trostle, S. Ward</i>	
Large Composite Fan Blade Development for Modern Aeroengines	200
<i>Keith T. Kedward</i>	
Can Braided Composites Be Used for Crushing Elements in Cars ?	218
<i>Hiroyuki Hamada</i>	

Applications

Development of a Composite Floor Panel to Replace Plywood Flooring in Rail Car Interiors	247
<i>H. Snaith</i>	
Composite Materials at The Crossroads - Transition to Affordability	257
<i>Cecil W. Schneider</i>	
Composite Applications in Sports Equipment: Table Rolling of Composite Tubes	266
<i>Jerome S. Berg, John T. Kanne</i>	
The Need and Requirements Driving the Development of Polymer Composites for Automotive Applications	275
<i>Gilbert B. Chapman, II</i>	
Application of Advanced Carbon-Carbon Composites to a Tip Turbine Structure of the Atrex Engine	283
<i>Hiroshi Hatta, Yasuo Kogo, Muneharu Yoshizawa, Nobuhiro Tanatsugu, Hisaichi Onabe, Masakazu Onozuka, Fumiki Tomioka</i>	

Development of High Performance Carbon/Carbon Brake Disk for an Advanced Aircraft	295
<i>Jinyong Lee, Jong-kyoo Park, Heun-seung Ha, Byung-il Yoon</i>	
The Development of the Composite Horizontal Stabilizer for a Fighter Aircraft	302
<i>C.L. Ong, T.B. Hong, J.S. Chen, J.Y. Huang</i>	
Towards a Composite Civil Aircraft Wing	310
<i>G. Clayton, P. Falzon, S. Georgiadis, X.L. Liu</i>	
Concrete Columns Wrapped by Glass Fibre Composites	320
<i>Shi Zhang, Lin Ye, Yiu-Wing Mai</i>	
Design of Composite (Fiber Reinforced Plastic) Bridges in Hungary	330
<i>László P. Kollár, Ákos Sapkás, Adrián Horváth</i>	
Geosynthetic Applications of Superdrawn Polyoxymethylene Fibers: 1. Reinforcement of Asphalt Concrete	336
<i>Tamikuni Komatsu, Hiroshi Kikuta, Yoshinobu Tuji, Eijiro Muramatsu</i>	
Graphite/Epoxy Composites for Offshore Applications	344
<i>S.T. Mear, H.G. Wheat, H.L. Marcus</i>	
Material and Lamination Design for Dynamic Performance of High Modulus Carbon Fiber Golf Shafts	355
<i>Kazuro Kageyama, Isao Kimpara, Toshio Suzuki, Isamu Ohsawa</i>	
Design and Construction of a High Performance Composite Cricket Bat	365
<i>R. Brooks, S. Knowles, J.S.B. Mather</i>	
Optimization of the Carbon-Composite Wing for the Skua High Speed Target Drone	375
<i>D. Grygier, T.C. Raman</i>	
The High-Speed Civil Transport: A Supersonic Leap in Technology	383
<i>S. Jason Hatakeyama</i>	
Developing of Composite CNG Pressure Vessels	393
<i>B.S. Kim, B.H. Kim, J.B. Kim, E.J. Jun, C.R. Joe</i>	
PWR Composite Materials Use: A Particular Case of Safety-Related Service Water Pipes	402
<i>T. Le Courtois, M.-F. Pays</i>	
Thermoplastic Filament Winding of a Pressure Vessel	411
<i>Kurt Olofsson, R. Långström, Tore Serrander, Roland Scott</i>	
Innovative Applications with Thermoplastic Filament Winding Techniques	419
<i>R. Funck, M. Neitzel, O. Christen</i>	
Development of a Composite Fairing Band Assembly for a Stainless Steel Sonar Dome	426
<i>Tamunoiyala S. Koko, Milton J. Connor, Garry V. Corbett</i>	
Design Optimization of Centrifugal Rotor of Composite Materials	436
<i>Sung Kyu Ha, Jong Kweon Park, Young-Ho Kim, Young-Soo Cho</i>	
<i>Biocomposites</i>	
Modelling Deformation of Filament Wound Arteries	448
<i>Jacqueline Rebecca Postle, Ron Postle</i>	
Development of a Knitted Fabric Reinforced Elastomeric Composite Intervertebral Disc Prosthesis	458
<i>S. Ramakrishna, S. Ramaswamy, S.H. Teoh, C.T. Tan</i>	

Long Term Aging of Implanted Silicone/Silica Composite Breast Implants	467
<i>Clarence J. Wolf, H.J. Brandon, K.L. Jerina, V.L. Young</i>	
A Development of Composite Artificial Leg Shell Using RTM Process	477
<i>Moon-Kwang Um, Byung-Ha Kim, Byung Sun Kim, Eui-Jin Jun</i>	
Hydroxyapatite-Polyethylene Composites for Bone Substitution: Effects of Hydrostatic Extrusion	488
<i>M. Wang, I.M. Ward, W. Bonfield</i>	
A Study of the Mechanical Properties and Bioactivity of Functionally Graded Titanium Matrix Composites Reinforced with Bioactive Particles	496
<i>A.E. Adoba, H.B. McShane, R.D. Rawlings, I.U. Rehman</i>	
Fibre-Reinforced Thermoplastic Composite Osteosynthesis Implants with Variable Mechanical Properties for Better Treatment of Bone Fractures	509
<i>J. Krebs, K. Friedrich, R. Heuwinkel, P. Rieger, P. Kosack</i>	
Tailormade Composite Titanium-Based Biomaterials	518
<i>J. Breme</i>	

Certification and Technology Transfer

C-130 Composite Flap Design Development and Certification	528
<i>Doug McPherson, Scott Reeve, Dewey Meadows, Arun Sibal</i>	
Certification of Structural Composite Components Used on the MD900 Helicopter	535
<i>Stuart E. Dutton, R.A. (Dick) Lofland</i>	
Tech Transfer Mechanisms for Composite Manufacturing from Universities to Industry - a Survey of Successful Models	543
<i>Michael J. Martin</i>	
Damage Tolerance of Composite Aircraft Structures: Analysis and Certification	552
<i>Peter Shyprykevich</i>	
Overview of Composite Projects at the FAA Airworthiness Assurance Validation Center	563
<i>William W. Shurtleff, Dennis P. Roach, Michael T. Valley</i>	
Development of a Composite Axle Housing: A Case Study in Multidisciplinary Technology Transfer Mechanisms	574
<i>A. MacDonald, W.M. Banks, A. Desport</i>	

Computer Aided Engineering

A System for the Design and Automated Lay-Up for the Manufacture of Composite Components	583
<i>Rodney Peck, Israel Herszberg, Sabu John</i>	
Modeling of Laminated Composite Structures for Computer Aided Design and Manufacturing Systems	590
<i>Takeshi Takatoya, Isao Kimpara, Kazuro Kageyama</i>	
The Design and Application of Tailored Fibre Placement	600
<i>P.J. Crothers, K. Drechsler, D. Feltn, I. Herszberg, M. Bannister</i>	

Application of Evolutionary Algorithms to Buckling Design of FRP Laminated Cylindrical Shells	611
<i>Yoshio Aoki, O-IL Byon(Goichi Ben)</i>	

Costing

Materials and Process Selection for Cost-Performance Effective Laminates	621
<i>Michael G. Bader</i>	
A Computer System for Lifecycle Cost Estimation and Manufacturability Assessment of Composites	630
<i>Mengchen Li, Elizabeth Kendall, Jayanthi Kumar</i>	
Cost Estimates of Composite Aerospace Structures Based on Complexity	640
<i>Jayanthi Kumar, Elizabeth Kendall, Amit Satyawadi, Chand Kumar Malu</i>	

Design

Methodology for Designing Composite Laminate Box Beams	652
<i>Aaron S. Blicblau, David Wallace</i>	
Sandwich Plates with 'Fully Potted' Inserts: a High-Order Approach for Analysis and Design	661
<i>Ole Thybo Thomsen</i>	
Thermoelastic and 3D Failure Analyses of Carbon-Carbon Composite Brake Disks	671
<i>Chun-Gon Kim, Jung-Seok Kim, Jae-Seok Yu, Chang-Sun Hong, Byung-Il Yoon</i>	
High Performance Composite Structures for High Precision Particle Detectors	679
<i>Claude Hauviller</i>	
Transverse Shear Effects in Discrete Optimization of Laminated Compressed Plates Under Buckling and FPF Constraints	689
<i>A. Muc, P. Saj</i>	
Thermoelastic Analysis of Foam-Cored Sandwich Construction Tee-Joints	699
<i>J.M. Dulieu-Smith, P.J.C.L. Read, R. A. Shenoi</i>	
Stress Analysis of Upright Composite Flanges	709
<i>James M. Whitney</i>	
Study of the Spring-In Phenomenon	719
<i>Lalit K. Jain, Brian G. Lutton, Yiu-Wing Mai, Rowan Paton</i>	
Finite Difference Method for the Analysis of Filament Wound Composite Shells	730
<i>E.V. Morozov, E.G. Evseev</i>	
Design and Behavior of a Gradient CFRP Beam	738
<i>Patrick Kim, Toshio Tanimoto</i>	
Design of Impact Damage Tolerant Composite Laminates	748
<i>Chen Puhui, Liu Junshi, Shen Zhen, Yang Xu</i>	
Effects of Stacking Sequences on the Hydroelastic Behavior of Composite Propeller Blades	757
<i>H.J. Lin, J.J. Lin</i>	
Plydrops for Tapered Design Optimization of Composite Plates	762
<i>Philippe M. Manne, Stephen W. Tsai</i>	

Stealth Airframe Design Methodology for High Altitude Real-Time Reconnaissance Drones	772
<i>D. Grygier</i>	
Structural Analysis of Cord-reinforced Rubber Composites	781
<i>Ramana M. Pidaparti</i>	
Design of a Roll-Control Suspension Link Using Composite Material	789
<i>Xiao-Jing Gong, Donald Hearn, Shahram Aivazzadeh, Georges Verchery, Frédéric Moll</i>	
Simulation of Thermo-Mechanical Behavior During Quenching Process of Metal Matrix Composites	797
<i>Dong-Ying Ju</i>	
Applications of Advanced Materials to Robotic Design: the FREEDOM-7 Haptic Hand Controller	806
<i>John McDougall, Larry B. Lessard, Vincent Hayward</i>	
A Code to Analyse the Structural-Technological Design of Filament Wound Pressure Vessels	816
<i>G. Di Vita, M. Marchetti, M. Nappi</i>	
Design Considerations for Ply Drops in Composite Structures	827
<i>D.S. Cairns, J.F. Mandell, M.E. Scott, J.Z. Maccagnano</i>	
Integrated Optimum Design of Wing Structure with Composite Skins	840
<i>Xu Yang, Yining Zhang</i>	
The Optimum Design of Functional Composite Materials for Electrical Brushes in DC Machines	851
<i>Yuying Wu, Weijie Tang, Guoding Zhang, Qing Hong</i>	

ON THE CERTIFICATION OF BONDED COMPOSITE REPAIRS TO PRIMARY AIRCRAFT STRUCTURE

Alan Baker

Airframes and Engines Division, Defence Science and Technology Organisation, Aeronautical and Maritime Research Laboratory, Australia.

SUMMARY: Repairs based on adhesively bonded fibre composite patches or reinforcements are standard procedure for repairing mechanical damage in thin-skinned graphite/epoxy and are becoming widely accepted for repairing cracks, corrosion and other defects in aluminium alloy airframe structure. However, bonded composite repairs although often more cost effective and efficient than mechanically fastened patch repairs, and thus a promising technology for extending the life of ageing aircraft, are generally limited to non-primary structure and to non-critical damage in primary structure. Perhaps the major obstacle to the application of bonded composite repairs to critical damage in primary structure is the cost of airworthiness certification.

This paper discusses the critical issues in the certification in bonded repairs to primary structure and suggests a generic approach to minimise costs. Two case histories are described as examples: one a boron/epoxy repair to an F111 aluminium alloy wing skin the other a demonstrator scarf repair to a F/A-18 graphite/epoxy stabilator. Finally, the "Smart Patch" concept is discussed and an early attempt for using this approach to monitor in-service structural integrity of a critical boron/epoxy reinforcement of the F111 wing pivot fitting is described.

KEYWORDS: bonded repairs, certification; ageing aircraft; smart patches

INTRODUCTION

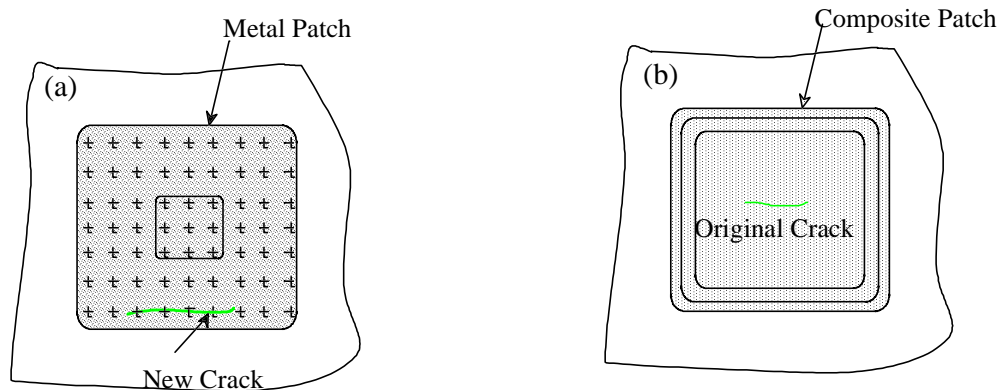
Repairs for graphite/epoxy (gr/ep) or aluminium alloy airframe components based on adhesively bonded composite reinforcements or patches are far more effective in restoring strength than repairs based on mechanically fastened metallic patches [1,2].

However, application of bonded composite repair technology to primary structure, although often highly feasible, is generally acceptable only on the basis that design limit-load (DLL) capability is retained in the loss (total failure) of the repair [3]; DLL is usually the maximum load expected in the life of the airframe. Thus the repair is essentially required to restore the safety margin to design ultimate load (DUL), usually $1.5 \times \text{DLL}$.

Whilst the DLL limitation is obviously safe and minimises certification requirements it will result in the scrapping of many expensive, yet potentially repairable components. Further, the implications of the DLL restriction are potentially far more limiting for repair situations where damage growth is possible [4] even though static strength of the repair is initially above DLL. The implications in this case are that inspection intervals must be based on the predicted rate of damage growth from the unrepaired damage. The related issue of damage tolerance requirements is considered later.

BONDED COMPOSITE REPAIRS TO METALS

Figures 1a) and b) highlight some of the major disadvantages of mechanical repairs to cracks and advantages of bonded repairs based on boron/epoxy (b/ep). The important point is that bonded repairs provide a far more effective reinforcement than mechanical repairs so that “live” (untreated) cracks can be left in the structure. Mechanical repairs require the removal of the cracked region and also the introduction of extra fastener holes. Both of these requirements are costly, highly intrusive, and potentially damaging to the structure and substructure. Swift [5] shows that mechanical patch repairs unless very carefully designed can significantly reduce fatigue life.



- | | |
|---|--|
| <ul style="list-style-type: none"> • Stress concentrations at fastener holes • Difficult to detect cracks under patch • Low patching efficiency, cannot patch cracks • Rapid crack growth on exit from patch • Danger of corrosion under patch | <ul style="list-style-type: none"> • No damage to structure or hidden components • Minimises stress concentrations • Slow crack growth even on exit from patch • High patching efficiency, can repair cracks • Can detect crack growth under patch • No corrosion problems, sealed interface |
|---|--|

Figure 1: a) Some disadvantages of standard mechanically fastened repairs and b) advantages of bonded composite repairs.

Compared to metals, advanced fibre composites such as b/ep and gr/ep have the advantages for making patches or reinforcements of formability, tailorability of stiffness, high specific strength and stiffness, and immunity to corrosion or fatigue. Composite patches or reinforcements can be pre-cured and secondarily bonded (first pre-formed and then bonded) or cocured (cured with the repair adhesive) directly on the structure.

In addition to cracking, critical damage includes pitting or exfoliation corrosion. Bonded composite repairs, based on b/ep or gr/ep patches are very effective for all of these damage types [6]. Bonded composite doublers can also be used very effectively to reduce fatigue strain in regions prone to cracking or simply to replace material lost by corrosion damage.

The scope of bonded composites to repair or reinforce metallic structure can be summarised as follows:

Reduce Stress Intensity

in regions with fatigue cracks

in regions with stress corrosion cracks

to increase damage tolerance (provide slow crack growth characteristics) in safe life structure, this may be cracked or uncracked

Restore Strength and Stiffness

after removal of corrosion damage below allowable limits

after removal of flaws, for example those produced during manufacture

Stiffen Underdesigned Regions to

- reduce strain and increase fatigue life
- remove strain concentrations, including that due to secondary bending
- reduce vibration and acoustic damage

The use of bonded composites (mainly b/ep) to repair cracking and other defects in aluminium airframe structures has been pioneered and extensively developed in Australia. Applications to primary structure (mostly in Royal Australian Air Force aircraft) include:

C130 Wings	- stress-corrosion cracks in wing risers
Mirage III Wings	- fatigue cracks in wing skin
F111-C Wing	- reduce strain in high-strength steel wing pivot fitting
F111-C Wing	- fatigue crack above critical size in wing skin
C141 Wings (USAF)*	- fatigue cracks from fuel weep holes in wing risers
Boeing 767 Keel Beam	- severe corrosion damage (has FAA Type Certification)
F/A-18 Bulkhead	- reduce fatigue strain in wing attachment bulkhead

The repair shown boxed is the only bonded composite repair undertaken in Australia to date where the cracked component would not withstand DLL in the absence of the repair; this is discussed as a case study later.

BONDED COMPOSITE REPAIR OF COMPOSITES

Critical service damage in gr/ep airframe components generally results from mechanical impact, which when severe causes extensive trans-ply cracking, inter-ply delaminations and fibre fractures. Other serious service damage includes major delaminations due to unexpected through-thickness loading and local matrix degradation due to overheating or lightning burn.

Because of the rapid rate of impact damage growth in composites (at high strain levels) the damaged region is generally removed prior to patch repair; however, there is an option to leave some or all of the damage to minimise the removal of sound material. Figure 2a and b shows some typical repairs to composite components.

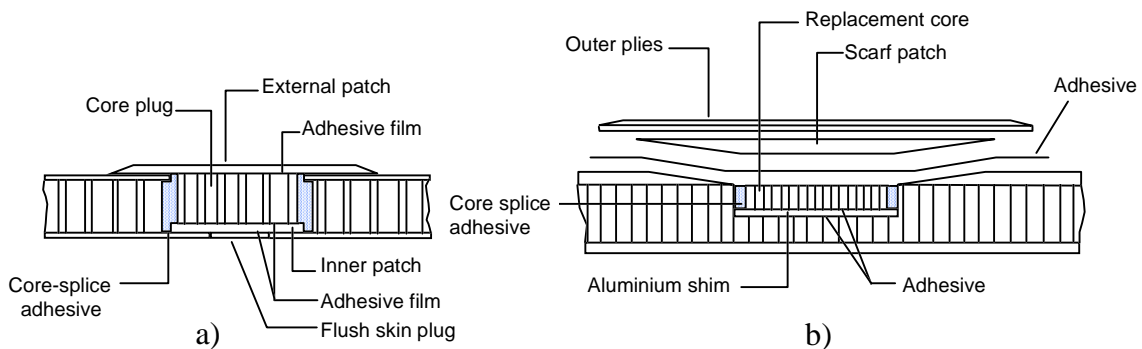


Figure 2: Typical bonded composite airframe repairs to honeycomb sandwich components a) external patch repair of thin-skinned and b) scarf repair of thick-skinned primary structure.

Repairs [7,8] based on external gr/ep composite patches, Figure 2 a) (or thin titanium sheet) are standard for relatively thin gr/ep (generally honeycomb cored) components and pose no

* With licensee companies: Helitech Australia, Composites Technology Inc. USA, and Advanced Repair Technology Inc. (ARTI), USA.

major structural problems. Scarf repairs, Figure 2 b) are an alternative to externally bolted titanium (or sometimes aluminium alloy or composite) patches for repair of highly-loaded thick-skinned gr/ep. Scarf repairs are much more effective in restoring strength than bolted repairs but large areas of skin removal must be made in thick parent structure to develop the required scarf angle, generally about 3° . Generally scarf repairs are made only to thick-skinned honeycomb or integrally stiffened structures, as mechanical repairs provide adequate static and fatigue strength recovery in structure already joined by mechanical fastening. In contrast to the fatigue problems with metals, discussed earlier, the introduction of new fastener holes is not generally a concern with composite structures.

CLASSIFICATION OF AIRCRAFT STRUCTURES FOR INSPECTION AND REPAIR

For the purpose of engineering management, aircraft structures are generally classified as follows:

Primary: Structure critical to the safety of the aircraft;

Secondary: Structure that, if it were to fail, would affect the operation of the aircraft but not lead to its loss;

Tertiary: Structure in which failure would not significantly affect operation of the aircraft.

Inspection, damage assessment, and repair requirements, differ significantly between these classifications. Even within a single component the allowable damage type and size (and consequently acceptable repair actions) will vary according to the criticality of the damaged region. The component is generally zoned by the Original Equipment Manufacturer (OEM) in the Structural Repair Manual (SRM) to indicate these regions. Mainly, the SRM addresses repairs to non-primary structure or non-critical repairs to primary structure. Repairs outside the scope of the SRM, particularly to critical regions of primary structure, require engineering design and approval by the OEM (or its delegate).

Essentially, certification of repairs to primary structure requires demonstration that the repaired structure is as flight worthy as the original structure, possibly allowing for life already consumed. Further, according to the latest regulations, such as FAR 25.571 (for civil aircraft), there is now a need to demonstrate that the repaired structure is damage-tolerant, even if the original structure was designed on a safe life basis.

While it is possible to demonstrate that these requirements are met by testing closely representative repaired structure under simulated service loading and environmental conditions, the challenge is to accomplish it (at least to a large extent) on a generic basis. If this is not possible many technically feasible repairs to primary structure will not be cost effective. Thus it is the purpose of this paper to discuss how a (largely) generic repair approach may be developed for bonded composite repairs to primary structure. The approach proposed here largely follows current procedures for certifying new structure.

CERTIFICATION APPROACHES FOR METALLIC AIRCRAFT STRUCTURE

Typically, certification for new metallic structures requires that the airframe structure (by test and or analysis) must demonstrate the following capabilities:

Static Strength:

DLL no failure or unacceptable deformations

DUL no failure although permanent deformation is acceptable; $DUL = DLL \times 1.5$
(generally)

Fatigue:

Safe life: no cracking which could lead to failure for the life of the airframe.

or

Fail safe: cracking may occur but will not reduce strength below acceptable level before being detected. This approach is generally based on multi-load-path structure.

or

Damage tolerant: cracking may occur but will grow slowly and will not cause failure for the full life of the structure or before detection (safety by inspection). Damage tolerant design is often based on the assumed presence of flaws at critical locations at the start of life.

Damage Tolerance:

The strength will not fall below an acceptable level (typically $1.2 \times DLL$) due to representative damage to the structure, eg caused by fatigue cracking, or corrosion before being detected. Critical damage must be of a size that can be detected with a high degree of probability.

Durability:

For the life of the airframe damage requiring costly repairs will not occur for example, due to fatigue or corrosion.

The requirements for composites (and to some extent for bonded structure) are broadly similar [9] but must account for several differences in behaviour [10] including:

Resistance to fatigue (flat S/N curve) but high scatter and damage growth rate.

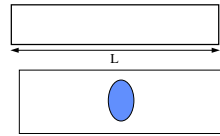
Sensitivity to out-of-plane loads.

Sensitivity to hot/wet environment.

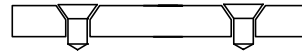
Sensitivity to mechanical (impact) damage.

Design of the airframe involves firstly a detailed structural analysis, usually using a structural finite-element (F-E) model and secondly a test program on specimens of increasing complexity from simple coupons to structural simulations and full-scale structures [11]. Coupon and structural element (also called structural feature) tests are used to obtain material and structural allowables for design and must therefore interrogate all critical loading conditions and potential failure modes; the other tests are essentially for proof of structure. These specimens (shown schematically) fulfil the following requirements:

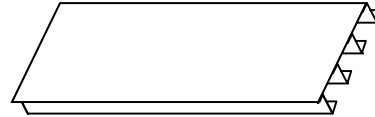
Coupons: $L \approx 0.1\text{m}$; $N \approx (\text{test number}) 400$
 -generate generic materials data base
 eg materials **A** and **B** allowables



Structural Elements: $L \approx 0.2\text{m}$; $N \approx 50$
 Generate generic feature data base
 represent all potential failure modes
 check calculation rules



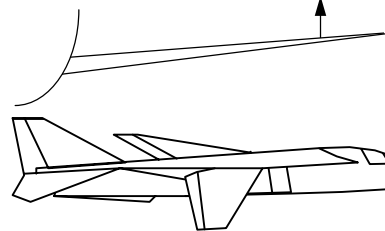
Structural Details: $L \approx 1\text{m}$; $N \approx 10$
 Generate non-generic design values
 check damage tolerance



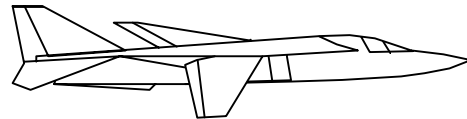
Sub-Component: $L \approx 3\text{m}$; $N \approx 4$
 Check for unexpected failure modes
 compare with detail and element tests



Component: $L \approx 15\text{m}$; $N \approx 2$
 Check strain levels against failure strains
 demonstrate airworthiness compliance



Aircraft: $L \approx 30\text{m}$; $N \approx 1$
 Demonstrate airworthiness compliance



Similar requirements can be stated for repairs which can be considered as new structure. The damage tolerance requirements are particularly significant when damage is allowed to remain in the parent structure.

Before considering in more detail the certification of repairs, which have similar requirements, the issue of the design allowables is discussed in the next section.

DESIGN ALLOWABLES

Strength

The development of design allowables from coupons and structural features is a very important and costly component of the design and certification process. Design allowables will also be needed for design of repairs particularly when made to primary structure. Mil Handbooks 5 and 17 set out, respectively, the statistical requirements and estimating procedures for metals and composites.

Briefly, airframe design is based on coupon and structural element data which allows for statistical variation or scatter in strength. Two allowable values are generally estimated:

A-allowable: value achieved by 99% of the population at the 99% confidence level

B-allowable: value achieved by 90% of the population at the 95% confidence level

To determine these allowables the statistical model which best fits the property distribution is first determined. For metals the distribution is generally normal or (often for fatigue) log normal. When dealing with composites the first model evaluated is the two-parameter Weibull distribution (as it is a physically more realistic model for brittle materials) followed by the normal and then the log normal.

An important economic aspect in testing is the estimation [12] of the minimum number of specimens which need to be tested to obtain acceptable allowables. This depends on the

statistical parameters. Testing can be reduced significantly if the distribution parameters are already known. For example, it has been shown [10] that the shape parameter for the Weibull distribution for strength of composites and metals is generally around 35 and 20 respectively, corresponding to coefficients of variation of 3.5% and 6.5%.

The choice of which allowable to work with depends on the particular application. For materials with a low scatter, such as airframe alloys, the **A**-allowable strength is often used since this obviously offers the greatest margin of safety, but in cases where scatter is large this may impose too great a penalty on useable strength. The **B**-allowable strength is also appropriate for fail-safe or multiple load-path design. For composites the **B**-allowable is generally used because of the relatively high scatter on strength.

Because of the costly specimen testing requirements to obtain **A** or **B** allowables “knockdown factors” can be used to reduce the allowables which would allow for variations in strength properties, for example with metals due to temperature changes. This approach essentially assumes that the coefficient of variation is unchanged by the variable. For composites and bonded structure knockdown factors can be determined for hot/wet conditions. The effect of representative flaws and defects in structural features can also be covered by this approach.

Fatigue Life

The main aim of the component fatigue test is to demonstrate with an acceptable level of probability that failure of the aircraft structure will not occur at the design stress; this stress corresponds with the **B**-allowable fatigue strength found from the coupon and structural element tests and is the allowed maximum stress at DLL, the highest stress in the spectrum. For development of the fatigue allowables (life and residual strength) coupons and structural elements, are tested under spectrum loading, representative of expected service conditions. The affect of representative damage will generally be evaluated on structural elements and structural features. S/N curves of coupons and structural elements may also be determined under constant amplitude cycling to obtain basic data for assessment of spectrum loading behaviour and to establish load discrimination levels.

The main feature of fatigue is that scatter is significantly greater than for most other mechanical properties so many more of these time-consuming tests are required to obtain the allowable values. Fibre composites have an even greater scatter in fatigue lives than metals as they are highly resistant to fatigue [10]. For example the shape coefficients in the Weibull distribution for fatigue of metals and composites are generally 1.25 and 7.5 respectively [13] corresponding with coefficients of variation of around 80% and 15% respectively.

The use of load enhancement to reduce testing times and to minimise the need for hot/wet testing of composite components is discussed in references [13] and [14].

Damage Growth

A knowledge of the critical dimensions of damage for catastrophic growth and rate of growth to critical size are the basic requirements for damage tolerance designs.

Cracking is the main damage of concern for metals and allowables (eg critical crack size and growth rate) are based on linear elastic fracture mechanics approaches. The information on crack growth rate is used to set inspection intervals. Generally for metals the rate of crack

growth $da/dn \propto \Delta G^n$ where ΔG is the range of strain energy release rate and n an empirical exponent, usually between 1.4 and 2.

For composites (and bonded structures) disbonds and delaminations are the main damage types of concern and growth rate can be rapid above the (high) damage initiation threshold. Typically the exponent n for damage growth of fatigue damage is 4 to 5, although it can be lower for loading configurations having low peel stresses.

Thus for composites the approach is to specify as a **B**-allowable the stress at the threshold for damage growth. This is generally determined from coupons with pre-existing visible damage (such as a small indentation [10]); design allowables based on growth of non-visible damage are generally unacceptable. Thus essentially a safe life approach to damage tolerance is taken.

REQUIREMENTS FOR CERTIFICATION OF BONDED COMPOSITE REPAIRS

Repairs to Cracked Metallic Structure (Slow Damage Growth in Parent)

Based, in part, on the recommendations provided in reference 3 (based on FAR 25.571 for damage tolerant repairs, as mentioned earlier) it was proposed [6] that certification should be on the basis of demonstration by analysis and/or test that the repair meets the following requirements [modified further here]:

Residual Strength

Provide a minimum residual strength of $1.5 \times$ DLL or some other acceptable factor (often around 1.2) times DLL under the temperature and environmental conditions in which the aircraft is operated.

Retain this level of residual strength in the repair region through the remaining life of the airframe or for a suitable period - ideally coinciding with the requirements for the undamaged structure.

Minimise strain elevation in adjacent sound structure to avoid life reduction.

Damage Tolerance [15]

Provide zero or very slow (predictable) crack growth from the pre-existing crack. Even if the crack emerges from under the patch (due, for example, to faulty inspection), it must be shown that growth will be slow enough to be detected during the next scheduled inspection.

Allow easy high-reliability detection of the crack by standard NDI ultrasonic or eddy-current procedures (patch should be transparent to NDI of parent structure).

Be insensitive to flaws including disbonds and impact damage.

Durability

Be highly resistant to minor disbonding or other local degradation of the patch system that would require frequent patch maintenance or replacement.

Repairs to Composite Structure (Rapid Damage Growth in Parent)

Similar requirements apply to repairs to composites with one major exception. This is that the damage tolerance requirements for slow damage growth in the parent structure are usually not applicable, since as previously discussed damage growth in composites can be very rapid. Generally, the pre-existing damage will have been removed and the situation is simply that of dealing with the threshold for damage growth from a reinforced cut-out. However, there is the option of leaving some damage, such as minor delaminations if it can be shown that the

rate of damage growth is low. This situation may apply where minor delaminations are left under a relatively stiff doubler able to suppress mode 1 peel stresses. Generally, however, repairs to composites will need to be certified using a safe-life approach on the basis that strains are kept below a damage threshold.

Reinforcement versus Repair

In many bonded composite repair applications to primary structure (including the F111 wing pivot fitting discussed later) the aim is simply to reduce strain before the onset of critical damage. In this application since the structure is essentially unmodified (no damage or cut-outs) the certification requirements are somewhat less stringent since the structure in the absence (failure of) of the reinforcement is still able to carry the design loads.

ISSUES AND PROPOSED APPROACHES FOR CERTIFICATION

Assurance of Bond Environmental Durability - *The Crucial Issue*

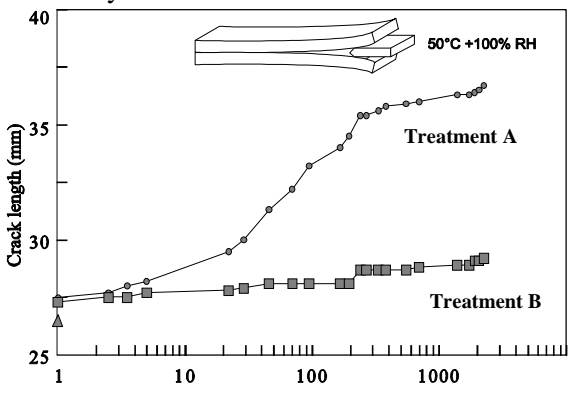
Without doubt the most crucial need for bonded repairs is to establish with a high level of confidence that no catastrophic disbonding of the reinforcement can occur due to environmental degradation or to service loading. In the absence of this assurance all other engineering estimations are meaningless. The use of proven surface treatment and bonding processes (suitable for use in repair situations) together with high-level quality control procedures [16], including technician training, are the only effective means of providing confidence that environmental degradation will not be a concern, since there is currently no effective NDI procedure for assessing bond durability (and unlikely to be in the foreseeable future), all that can be detected are fairly gross voids and disbonds.

Considerable effort has been devoted in Australia to the development of *in-situ* bonding surface treatments for metals and composites which are: simple, versatile to apply, effective, non-specific, low risk (tolerant to adverse environments) and non-hazardous. Simplicity, tolerance and low risk are very important since repairs are often performed in difficult situations and adverse environments.

Fortunately for epoxy-matrix composites, simple ceramic grit blasting is an optimised surface treatment process, even for factory usage; however, for metals more complex chemical treatments are required. While *in-situ* surface treatments specifically for aluminium alloys based on phosphoric acid anodising are the most effective in providing bond durability they lack versatility and tolerance. Australian work [2,17] has concentrated on the use of coupling agents (epoxy-compatible silanes) following grit blasting. This process has the desired attributes (including ability to treat titanium alloys and steel) and provides adequate bond durability, as judged from laboratory tests and confirmed by Australian service experience.

The proposed requirements and approaches to assure a high level of quality control in the environmental durability of bonded repairs (focusing on metals) are provided in Table 1.

Table 1: Bond environmental durability assurance approaches

Requirement	Approach
<p>To ensure high confidence in repair bond durability</p>  <p>The graph plots Crack length (mm) on the y-axis (25 to 40) against Time (Hours) on a logarithmic x-axis (1 to 1000). Treatment A (circles) shows a sharp increase in crack length starting around 10 hours, reaching approximately 37 mm at 1000 hours. Treatment B (squares) shows a much slower, steady increase, reaching about 29 mm at 1000 hours. An inset shows a wedge coupon test setup under 50°C +100% RH.</p>	<p>Undertake Process Evaluation: Evaluate repair treatments (shown inset, based on Boeing wedge test) Benchmark against factory treatment assess process window</p> <p>Develop Quality Procedures [18], including: training and qualifying technicians develop process documentation make/test traveller repair wedge coupons</p>

Development of Generic Patch System Design Allowables

To guard against failure in the patch system due to service loading the design approach is to ensure shear and peel strains in the adhesive and patch, particularly at the ends of the reinforcement, Figure 3, are maintained below the damage initiation threshold since disbond growth in this region can be rapid. This is achieved [19,2] by limiting strains in the critical regions by design (eg appropriate end tapering) and use of appropriate strain allowables.

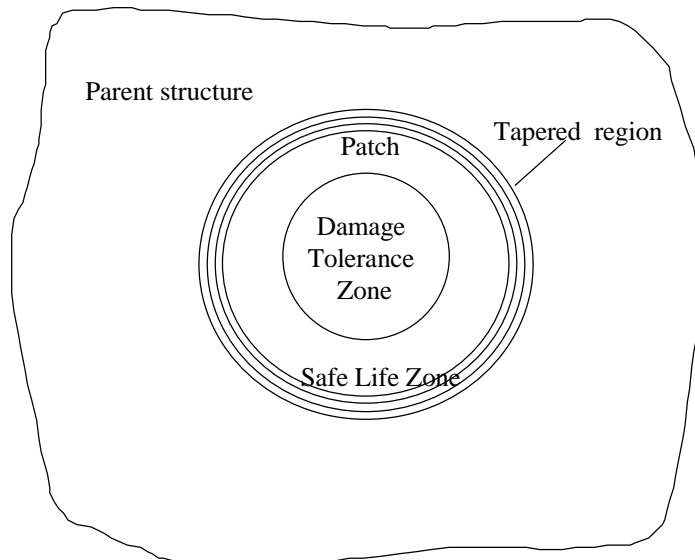


Figure 3: Illustration of an external bonded patch showing safe life zone (no cracking allowed in patch system) and damage tolerance zone (slow crack growth allowed in patch system).

Even slow initial disbond growth in the end region is unacceptable since once the disbond reaches the inner end of the taper region peel and shear strains dramatically increase and

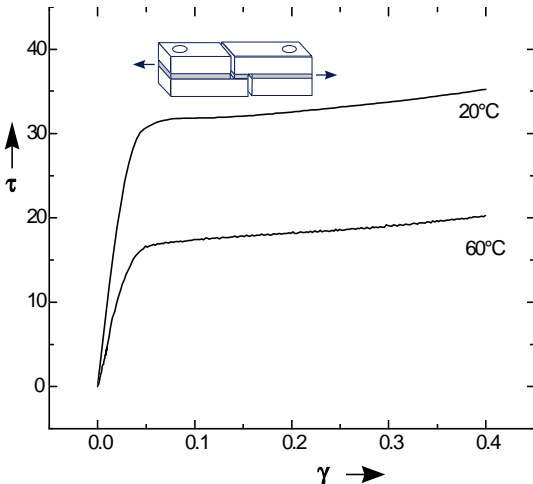
growth will become rapid. Thus the patch system in this region must be designed on a safe life basis.

However, for an external patch, limited disbond growth in the patch system (usually the highest stress region) is acceptable over the damage region in the parent structure, Figure 3, as this is generally slow (peel stresses are low or negative) and has only a small effect on reinforcing efficiency [6].

Following the approach for new structures, repair design allowables are obtained from tests on coupons and generic structural features- in this case generic bonded joints:

Coupon tests, mainly to obtain adhesive and composite static strength/strain (and possibly also fatigue) allowables, as indicated in Table 2.

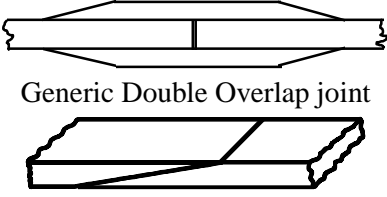
Table 2: Coupon test program for process and quality control

Requirement	Approach
<p>To obtain data base for static strength of repair materials <i>eg for adhesive shear stress/strain:</i></p> 	<p>Undertake adhesive tests (short over-lap shear test shown inset) to obtain:</p> <ul style="list-style-type: none"> B basis allowables for yield and failure shear strains B basis allowable strain range for fatigue damage initiation N cycles, constant amplitude <p>Undertake composite tests to obtain:</p> <ul style="list-style-type: none"> B basis allowables for static failure strain in a simple joint configuration <p>Obtain for both knock-down factors for:</p> <ul style="list-style-type: none"> hot/wet conditions strain rate/creep effects (adhesive) off-optimum cure etc

Generic bonded joints mainly to obtain the reinforcement system fatigue allowables; however, they can also provide effective adhesive properties in place of the coupon tests.

The proposed tests are outlined in Table 3.

Table 3: Generic joint test program to obtain repair system allowables

Requirement	Approach
<p>To find joint static and fatigue strain allowables and confirm validity of failure criteria based on coupon test data.</p> <p><i>The failure criteria must hold for similar geometrical configurations, eg adherend thickness and stiffness and adhesive thickness.</i></p> <div style="text-align: center;">  <p>Generic Double Overlap joint</p> <p>Generic Scarf Joint</p> </div>	<p>Undertake static strength tests to: check strength against predictions based on coupon data</p> <p>Undertake fatigue tests to: obtain B-basis threshold for fatigue disbond growth rate of disbond growth at constant amplitude and spectrum loading</p> <p>Find knockdown factors for: hot/wet conditions non-optimum manufacture representative damage</p>

As an example, tests are in progress to measure the threshold for disbond initiation and growth rate in generic bonded joints representing b/ep patch repairs to aluminium alloy specimen; shown inset in Figure 4.

The approach being evaluated is to use the theoretical or the measured strain range in the adhesive $\Delta\gamma$ as the damage severity criteria and plot this against disbond growth rate db/dN , as shown in Figure 4. The dotted line is arbitrarily defined as the initiation threshold in this case.

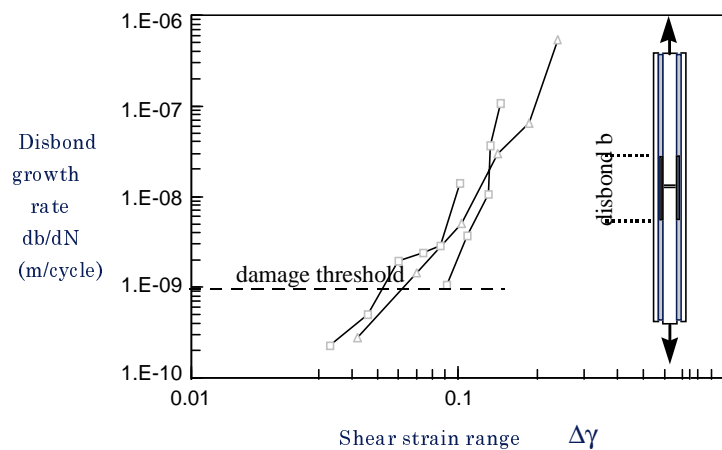
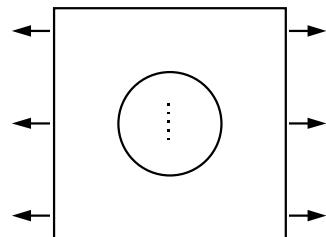
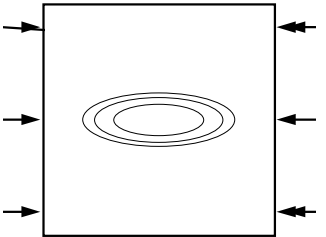


Figure 4: Plot of disbond growth rate in the adhesive versus shear strain range obtained from tests on a double overlap joint, shown inset. The adhesive is FM73, around 0.3mm thick, the inner adherend is 2024T6 aluminium, around 3mm thick, and the outer adherends are b/ep, around 1mm thick.

Generic Structural Detail Tests - Validation of Repair Models

The aim of this program is mainly to validate design approaches for generic repair configurations and to assess damage tolerance. This program is based on tests on a range of generic structural detail specimens, as indicated in Table 4.

Table 4: Validation of design approaches based on generic structural detail program

Requirement	Approach
Validate (F-E ²⁰ /analytical ²²) design procedures and assess repair damage tolerance  Generic External Patch  Generic Scarf Patch	Undertake tests to assess: Static strength under various environments Fatigue strength, threshold for damage initiation in patch system Threshold for growth and rate of growth of residual damage, eg cracks in metals Influence of spectrum loading and environment Assess damage tolerance: Residual strength before and after fatigue damage to patch system and residual damage Influence of impact damage to patch and deliberate disbonds in patch system

Work on generic repair structural detail specimens (patched metallic specimens) has been in progress for some time in Australia [21]. Figure 5 a) depicts the specimen tested and Figure 5 b) plots results which help to validate the analytical patching model [22] used.

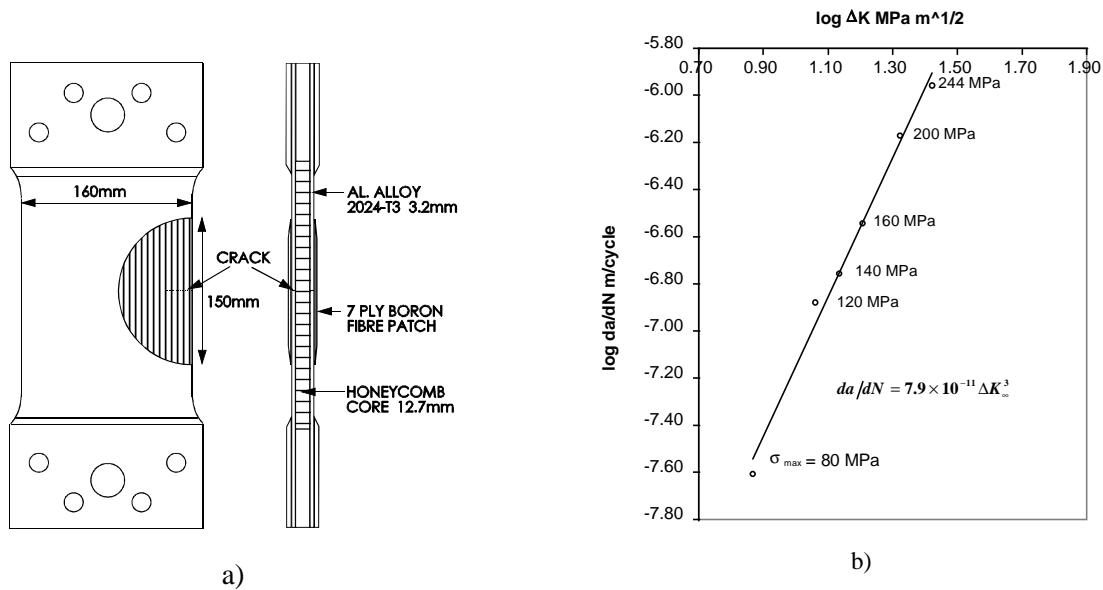



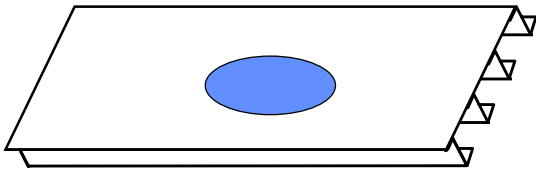
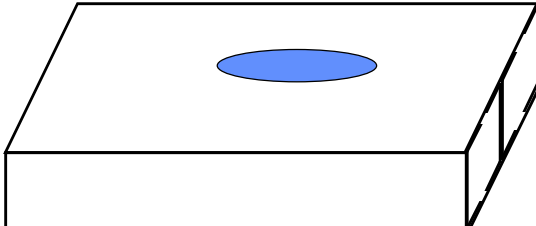
Figure 5: a) Generic structural detail test specimen for patched cracks in metallic structures used to validate the patching model and b) plot of experimental log da/dN versus log ΔK , obtained from the analytical patching model.

PROPOSED REPAIR CERTIFICATION APPROACH

The steps, as set out in Table 5, are i) undertake preliminary design using the data base and validated model from the generic test program, ii) identify by detailed F-E or other analysis how the specific repair differs from the generic case and ii) develop and validate the final design based on tests which interrogate only these differences.

Table 5: Outline of the approach proposed for repair certification

Step	Approach
Qualification of processes and repair materials	Follow prescribed quality procedures
Obtain stress information eg DUL and fatigue spectrum load etc	Obtain OEM design data for DUL etc. Fatigue spectrum (military aircraft) best obtained from instrumented aircraft, if available
Preliminary feasibility assessment and design of repair based on generic data and patching model	Use allowables data from generic coupons and repair joints. Base design on validated model from generic studies
Design representative bonded joint to interrogate differences (if any) with generic repair	Use detailed F-E model of actual repair, to design representative joint specimens
Test representative bonded joints to check safety margin of repair joint 	Test sufficient representative bonded joints to obtain indication of fatigue performance compared with generic joint. Test at constant amplitude up to DLL level

Step	Approach
Finalise design of repair, based on new data, and check performance 	Test representative structural details under spectrum loading, ambient and representative hot/wet conditions. <i>Could use elevated load at a level based on representative bonded joint hot/wet tests</i> <i>May not need to do this test if differences with generic structural detail specimen are not too great</i>
Check for unexpected secondary stresses <i>For example due to neutral axis offset bending or to strain concentration in adjacent structure</i> 	Static strain survey on instrumented sub-component specimen may be adequate to check similarity to structural detail. <i>Could be done on actual repair in some cases</i> <i>Optional additional testing under spectrum loading,</i>

CASE HISTORIES

Two case histories are presented here as (imperfect) examples of the proposed approach. The first is an real repair developed for a critical fatigue crack in the aluminium alloy lower wing skin of an F111 and the second is a demonstrator repair to a gr/ep skin in an F/A-18 horizontal stabilator.

Bonded Composite Repair to F111 Lower Wing Skin [23]

The need for this repair followed the discovery of a 48 mm long fatigue crack in the lower wing skin (aluminium alloy 2024-T851) of an F111 aircraft. Preliminary fracture mechanics calculations indicated that the residual strength had been degraded to 168 MPa, which is considerably less than the Design Ultimate Stress of 358 MPa specified for this region of the wing.

The cracking arises because of the local geometry of the wing skin at the site of cracking which gives rise to a significant stress concentration coupled with secondary bending.

A repair based on a mechanically fastened metallic doubler was initially considered, but this repair option was discarded because of poor fatigue properties, poor inspectability and undesirable aerodynamic implications. Thus, the only viable alternative to a bonded repair would have been scrapping the wing.

This repair has several features which are particularly significant for the certification of critical bonded repairs to primary structure. The most important being that the crack reduced the residual strength below the specified Design Limit Stress of 238 MPa, compromising safety-of-flight. Thus, the implementation and approval of any repair option required very stringent scrutiny. Indeed, from the viewpoint of demonstrating compliance with certification requirements, this repair can claim to be the most technically challenging bonded repair yet undertaken by the RAAF and most likely by any organisation.

An important issue for this repair is that the local geometry (responsible for the cracking) also results in the development of significant peel stresses in the adhesive, in addition to the usual shear stresses resulting from load transfer into the patch. Thus the stressing differs somewhat from the generic repair studied and this was taken into account in the certification program.

The verification program had to be more extensive than desirable because some of the generic information required was not available. However, had this information been available, along the lines discussed, the effort required to substantiate this repair would have been markedly reduced. Generally the approach followed the steps set out in Table 6.

Table 6: Outline of F111 wing skin repair certification program, continued on next page

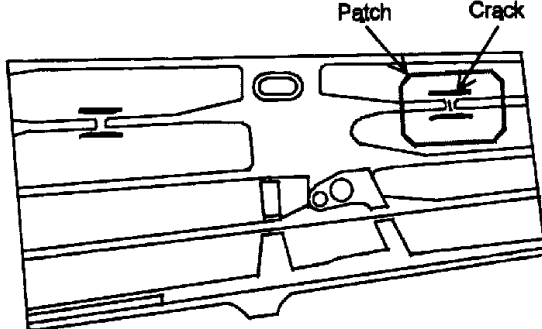
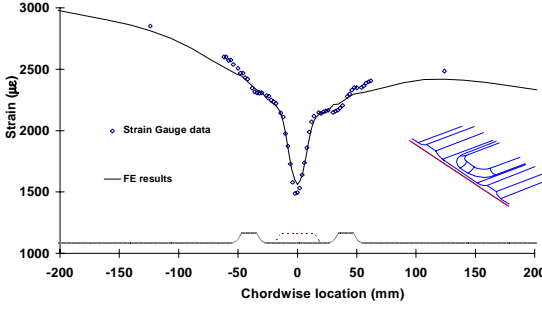
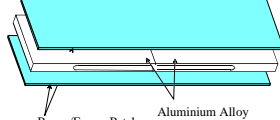
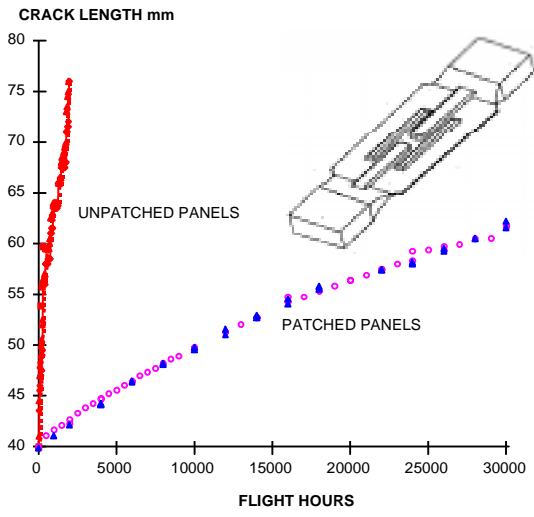
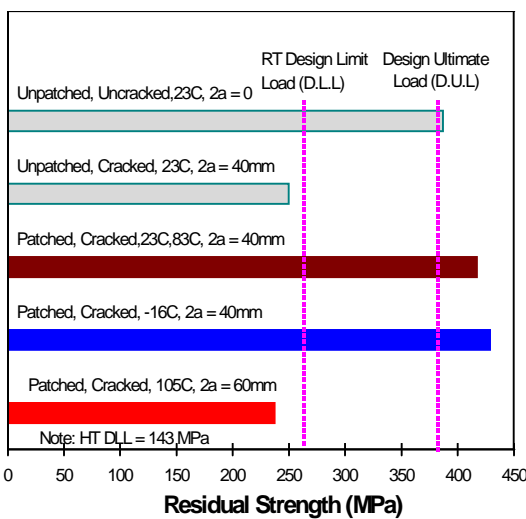
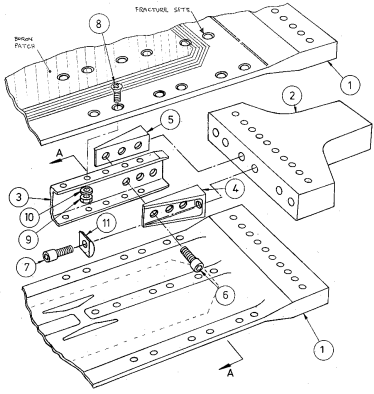
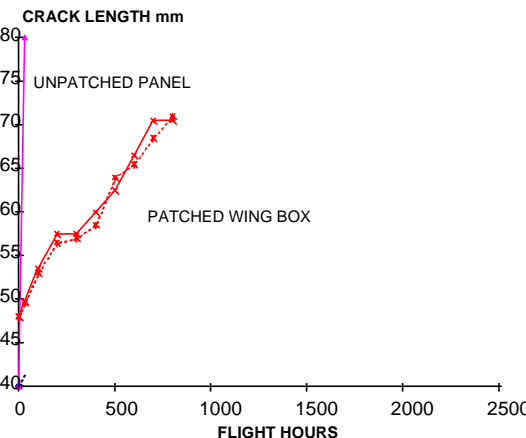
Activity	Approach
Establish critical static load cases and fatigue spectrum	Manufacturer's information indicated a DUL of 358 MPa. Fatigue load spectrum at the wing root was available through the F111 Australian ASIP program
Establish stresses in the cracked region.	Undertook F-E analysis of the region before and after patching and calibrated with experimental strain survey. <i>Noted high peel component in patch</i>
Preliminary design of patch 	Based on patching allowables from generic joint tests and RAAF Engineering Standard [18,24], Tables 4 and 5 <i>Fig shows location of cracking on the F111 lower wing-skin inner surface showing also the outline of the repair patch made of 14 ply b/ep (0₂, ± 45, 0₃)_S bonded with adhesive FM73 around 500 mm spanwise × 350 mm chordwise.</i>
Verify patch design 	Using F-E analysis the design was checked and found to be acceptable, despite complications due to peel Predicted patching performance was checked against the generic model <i>Fig shows predictions of 3D finite-element model of the region compared with strain gauge readings. The strain reduction on the outside surface results from the secondary bending which, correspondingly, causes a marked strain elevation on the inside surface - resulting in the fatigue cracking</i>
Design representative joint and structural detail specimen	Using F-E model to check that stress distribution corresponds with that for repaired structure
Verify patching allowables. 	Test a representative bonded joint under a range of environmental and fatigue conditions [25] <i>To check the influence of the peel component compared with the generic bonded joint</i>

Table 6: Outline of F111 wing skin repair certification program.

Activity	Approach
<p>Assess residual static strength and crack growth rate in the patch system</p> 	<p>Test structural detail specimen (shown inset in graph) under representative F111 spectrum using discrimination levels based on generic structural detail tests</p> <p>Test for static strength post fatigue at various conditions, shown below</p> 
<p>Confirm repair efficiency and influence of patch on strain levels in surrounding structure</p> 	<p>Test a few representative wing box specimens, including taper-lock fastener holes</p> 

F/A-18 HORIZONTAL STABILATOR [26]

An F/A-18 horizontal stabilator (gr/ep skins AS4/3501-6, on a heavy aluminium alloy honeycomb core) suffered impact damage near the spindle attachment point in a high-strain region (from around 7 to 32 plies thick), and was therefore deemed by the OEM to be unreparable. While most of the design ultimate strains in the stabilator are around 3750 microstrain ($\mu\epsilon$) the peak design ultimate strain close to the spindle was stated to be very high, around 5200 $\mu\epsilon$.

To evaluate the effectiveness of scarf repairs to such a highly strained structure, a research program was undertaken based on representative joint tests and the damaged and repaired stabilator. This program was simply a feasibility study for a very challenging repair; however, for the purpose of this discussion it is considered as part of a certification evaluation - with the missing aspects noted. The overall program is as shown in Table 7.

Table 7: Outline of the F/A-18 gr/ep horizontal stabilator repair program, continued on next page

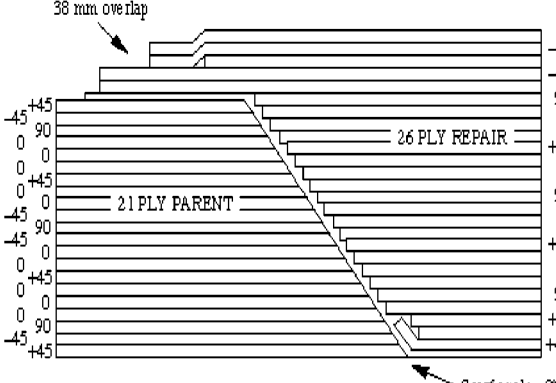
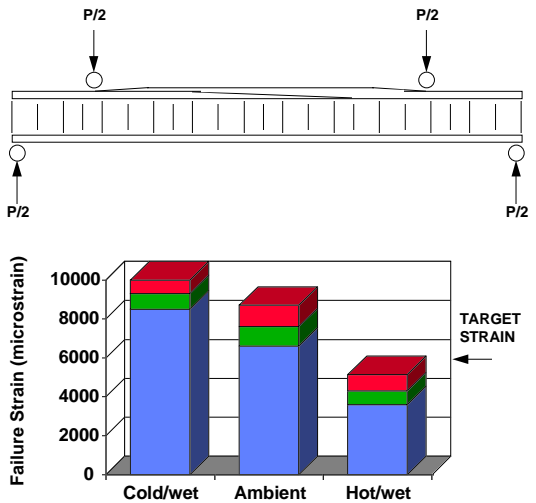
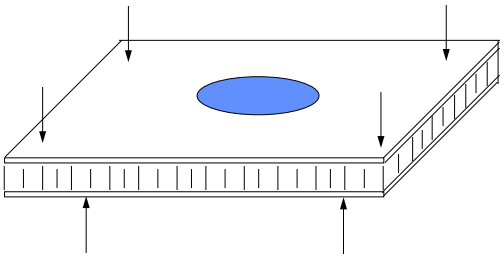
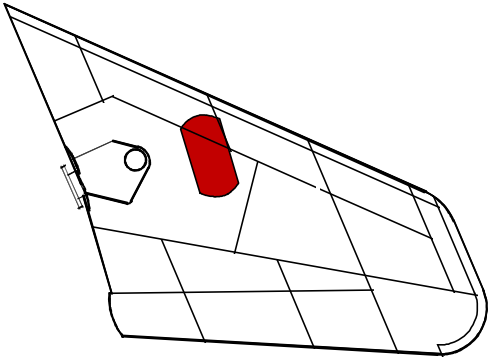
Activity	Approach
<p>Establish critical strains for component test</p> <p>Design representative joint</p> 	<p>Obtained from F-E analysis provided by OEM.</p> <p>Based on Northrop approach using very limited materials allowables data.</p> <p><i>An extensive coupon and generic joint test program was needed to establish B-allowable adhesive strain, particularly fatigue threshold, and knock-down factors for hot/wet environment non-optimum manufacture</i></p>
<p>Establish residual strength of the representative joint.</p> 	<p>Test representative joints, to measure ultimate failure strain in the skin to +104°C, -40°C and to evaluate ultimate failure strain following impact damage and cyclic loading</p> <p><i>Data from generic joints unavailable, would have minimised test program if available</i></p> <p><i>Strength of scarf under hot/wet conditions found to be marginal; critical in the adhesive layer</i></p> <p><i>Found potential adhesive creep problem</i></p> <p><i>Joint tolerant to fatigue at constant amplitude cycling at DLL and under spectrum loading</i></p> <p><i>Preliminary tests suggest impact resistance good</i></p>
<p>Final design and validation testing</p> 	<p>Not undertaken in this program but required</p> <p><i>Only few tests needed on a representative structural detail specimen if a good generic data base had been available</i></p> <p><i>This test may have provided more optimistic result as alternate load path allows load redistribution due to creep, etc and unloads adhesive. Essentially some load can be carried around hole by undamaged material</i></p>

Table 7: Outline of the F/A-18 gr/ep horizontal stabilator repair program.

Activity	Approach
<p>Test fully instrumented component to DLL to establish if allowable strains at design ultimate hot/wet <u>would have been exceeded</u>.</p> <p><i>Repair implemented by US Navy to Northrop specification.</i></p> 	<p>Strains to a maximum of 5200 microstrain found at DUL by extrapolation, as specified by OEM and predicted by our F-E analysis²⁷.</p> <p><i>This confirmed that representative joint results were not sufficiently high, allowing for knock-down factors.</i></p> <p><i>However, structural detail tests if undertaken may have altered this conclusion</i></p>

“SMART PATCH” APPROACH: F111 WING PIVOT B/EP DOUBLER

For the certification and management of critical repairs for very high cost components the “Smart Patch” approach may be acceptable from the airworthiness perspective and be cost effective for the operator and may even allow some relaxation of the certification requirements. In the most elementary application of smart patches, (which could also be called *in situ* NDI) sensors are used as a nerve system to monitor in service the structural condition (health) of the patch system and the status of any remaining damage in the parent structure. The sensors, which may for example be resistance [28] or piezoelectric strain gauges or optical fibres [29,30], are ideally (for robustness) embedded in the composite patch or more simply bonded to its surface.

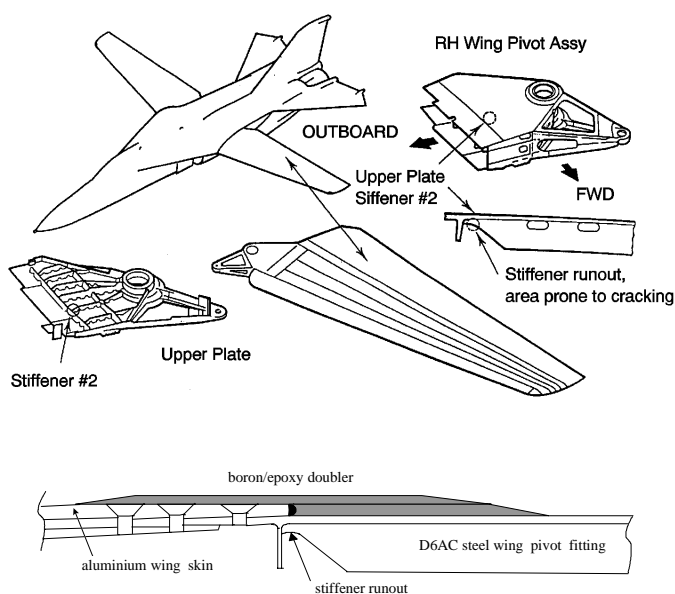


Figure 6: Schematic showing above location of critical area in the F111 wing pivot fitting and below detail of the critical area and b/ep doubler, over 120 plies (16mm) thick.

The specific objectives, referring to Figure 3, are to detect disbond growth in the safe life zone of the patch (which is unacceptable) and monitor damage growth in the parent material (below the damage tolerance zone) - delaminations for composites or cracks for metals. The smart patch approach for detecting disbond growth in a repair system during service operation was planned for in-service management of a large (120+ ply thick) b/ep doubler reinforcement for the wing pivot fitting (WPF) of Australian F111 aircraft.

Fatigue cracks can initiate in the upper-skin of the F111 Wing Pivot Fitting (WPF) stiffener runout region shown in Figure 6. Initiation of cracks in this highly-stressed D6ac steel component can be traced back to plastic yielding in this region which occurs during the (severe) Cold Proof Load Test (CPLT) which the aircraft periodically undergoes to screen for small cracks. Residual tensile stresses developed as a result of the yielding can lead to crack-initiation and catastrophic failure in flight or (more likely) during a subsequent CPLT. A strain reduction of over 30 % is required to avoid plastic yielding in this region [31] and also to increase the in-service inspection interval. The required strain reduction is particularly challenging because of the thick steel structure and high loading. To achieve the required strain reduction without causing damage to the structure, b/ep doublers, as depicted in Figure 6, were designed and developed [28,32].

The approach taken was to apply external resistance strain gauges on the ends of the taper on the b/ep doubler and on the surface of the steel WPF away from the doubler and monitor the ratio (doubler strains) / (strain in the steel fitting) during service life. Any decrease in this ratio is an indication of disbonding of the doubler. It is important to note there is no requirement in this approach for measurement of the loading. A similar approach is being used [33] to monitor the structural integrity of a large (5m × 1m) 6mm thick doubler used to reduce cracking around welds in the aluminium deck of an Royal Australian Navy Frigate.

Figure 7 shows results obtained from tests on an F111 representative bonded joint specimen (representing a section through the doubler) subjected to CPLT loads and the F111 loading spectrum.

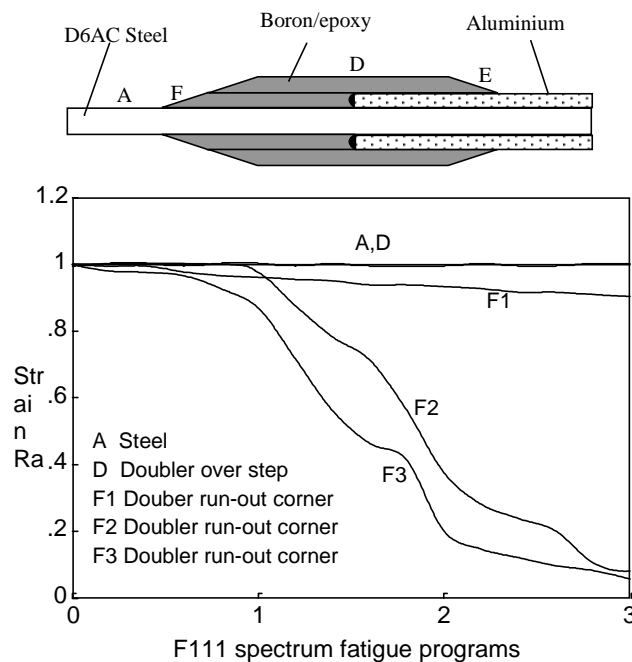


Figure 7: Plot of strain ratio reduction due to disbond growth as a result of fatigue cycling and above representative bonded joint specimen showing strain gauge positions. The F gauge results plotted are on the corners of the doubler.

Disbonding is indicated by the reduction in relative strain, as shown in Figure 7. The disbands initiated and grew mainly from the corners of the doubler at the ends of the taper growth was very much less in the centre. In the aircraft doubler system the sides are tapered normal to the doubler axis, so stress concentrations in these corners will be much less severe; however, the results show the effectiveness of the monitoring approach proposed.

This early attempt at in-service monitoring of the doubler gauges (using strain gauge wiring passing through an over wing fairing which covers the doubler), although highly effective for aircraft undergoing the CPLT, proved too cumbersome to be practical for service use.

Current work is aimed at developing a fully self-contained miniaturised strain gauge bridge and data acquisition system attached to the wing (under the over wing fairing) for storing recent in-flight high-load readings of the strain ratio. The data acquisition data will be read remotely as required using infra-red technology. Alternatively the system could be programmed to provide an early warning when significant changes in strain ratio occur.

A far more sophisticated application of the "Smart Patch" approach is to include both a sensor - nerve system (as just discussed) and a reactive - muscle capability. One application of this technology is for example in the repair of acoustic cracking where the patch can provide both reinforcement (while monitoring its own integrity) and reactive damping. This approach is being evaluated in connection with an acoustic fatigue cracking problem being encountered in the engine inlet case in the F/A-18.

CONCLUDING COMMENTS

An approach for the certification of adhesively bonded composite repairs to primary aircraft structure, metal or composite, is proposed based on the development of a data base from tests on generic structural elements (joints) and generic structural details; the latter being used to validate repair design models. Tests on representative structure is limited mainly to evaluating only those aspects in which the actual repair differs from the generic configuration. This approach requires a very good analytical capability to assess the differences and to design appropriate test specimens. A somewhat similar approach is suggested by Hall [34] et al for repairs to composite primary structure.

The crucial requirements for repair bonding are highlighted: This requires the use of effective bonding processes together with a high level of quality control.

Two case histories are briefly described as examples of the proposed approach: one a b/ep patch repair to an F111 aluminium alloy wing skin and the other a demonstrator scarf repair to an F/A-18 gr/ep stabilator.

The concept of the "Smart Patch," a patch able to monitor its own structural integrity, is described and an early attempt to incorporate this approach on a massive b/ep doubler developed to reinforce the high-strength steel wing pivot fitting on F111 is discussed.

ACKNOWLEDGMENTS

The author would like to thank Dr Steven Galea for his helpful comments on the manuscript and Drs Francis Rose and Richard Chester, AED; WGCDR Eric Wilson and Mr Max Davis, RAAF and Mr Alan Kerr, Advanced Repair Technologies Inc (ARTI) for their contributions and stimulating discussions on the topic of bonded composite repairs to metals.

REFERENCES

1. A.A. Baker, "Repair of Cracked or Defective Metallic Aircraft Components with Advanced Fibre Composites- An Overview of Australian work," *Composite Structures*, 1984, Vol 30, pp. 153-181.
2. A.A. Baker "Crack Patching: Experimental Studies, Practical Applications" in *Bonded Repair of Aircraft Structures*, A.A Baker and R Jones Editors, Martinus Nijhoff, 1988, Chapter 6.
3. C. Torkington "The Regulatory Aspects of the Repair of Civil Aircraft Metallic Structures", *Proceedings of International Conference on Aircraft Damage and Repair*, Australian Institute of Engineers, Melbourne, 1991, pp 1-6.
4. A. Cardrick, "Certification Aspects of the Use of Composite Patches to Enhance Fatigue Performance of Metal Primary Structure" Unpublished RAE Minute, 1987.
5. T. Swift, "Repairs to Damage Tolerant Aircraft," *Proceedings International Symposium on Structural Integrity of Aging Airplanes*, FAA-AIR-01, 1990.
6. A.A Baker, "Bonded Composite Repair of Metallic Aircraft Components", *Paper 1 in AGARD-CP-550 Composite Repair of Military Aircraft Structures*, 1994.
7. A.A. Baker, "Joining and Repair of Aircraft Composite Structures" chapter in *Composite Engineering Handbook*, editor P. K. Mallick, Marcel Dekker, inc 1997.
8. A.A. Baker, "Repair Techniques For Composite Structures," in *Composite Materials in Aircraft Structure*, Middleton D.H. Editor, Longman Scientific and Technical Publishers 1990, Chapter 13.
9. R.S. Whitehead, H.P. Kan, R. Cordero, E.S. Saether, " Certification Testing Methodology for Composite Materials" NADC-87042-60 Report, 1986.
10. R.S. Whitehead , "Certification of Primary Composite Structures," in *New Materials and Fatigue Resistant Aircraft Design*, *Proceedings 14th ICAF Symposium* , 1987.
11. B.C. Hoskin, "Airworthiness Considerations," in *Composite Materials for Aircraft Structures*, B.C. Hoskin and A.A. Baker editors, AIAA Education Series, 1986, Chapter 14.
12. W.J. Park, "On Estimating Sample Size for Testing Composite Materials," *J. Composite Materials* 1979, Vol 13, pp 219-212.

13. Composite J. Lameris, "The Use of Load Enhancement Factors in the Certification of Aircraft Structures," National Aerospace Laboratory, NLR TP 90068 U.
14. Aircraft Structures, J. Rouchon, "Fatigue Damage and Damage Tolerance Aspects for Composite Structures", Korea-France Joint Conference on Advanced Composite Materials, Taejeon Korea, 1995.
15. FAA/NASA and J.W. Lincoln, "Challenges for the Aircraft Structural Integrity Program", Symposium on Advanced Structural Integrity Methods for Airframe Durability and Damage Tolerance, NASA Publication 3274 P1, 1994 pp 409-423.
16. Repairs," M. Davis, "The Development of an Engineering Standard for Composite Structures, 1994. Paper 24 in AGARD-CP-550 Composite Repair of Military Aircraft Structures, 1994.
17. Bonded Repairs," A.A. Baker and R.J. Chester, "Minimum Surface Treatments For Adhesively Repairs," International Journal of Adhesives and Adhesion, 1992, Vol 12, pp. 73-78.
18. Australia. Royal Australian Air Force Engineering Standard for Composite Materials and Adhesive Bonded Repairs, No C5033 Issue 1. Department of Defence, Australia.
19. L.J Hart-Smith, "An Engineers Viewpoint on Design and Analysis of Aircraft Structural Joints", Douglas Paper MDC 91K0067, Proceedings of International Conference on Aircraft Damage Assessment and Repair, Australian Institute of Engineers, Melbourne, Australia, August 1991.
20. Aircraft R. Jones, "Crack Patching: Design Aspects , " Chapter 4 in Bonded Repair of Structures, Editors A.A Baker and R Jones, Martinus Nijhoff, pp 49-76 1988.
21. Patching FAA/NASA USA. A.A. Baker, "Fatigue Studies Related to Certification of Composite Crack for Primary Metallic Structure" to be published in the proceedings of the Symposium on Continued Airworthiness of Aircraft Structures, 1996, Atlanta USA.
22. Repair 107-173 L.R.F. Rose, "Theoretical Analysis of Crack Patching, " Chapter 6 in Bonded of Aircraft Structures, Editors A.A Baker and R Jones, Martinus Nijhoff, pp 1988.
23. Air for a Air A.A. Baker, L.R.F Rose, K.F Walker. and E.S.Wilson, "Repair Substantiation Bonded Composite Repair to a F-111 Lower Wing Skin," Proceedings of the Force 4th Aging Aircraft Conference, Colorado July 1996.

24. Primary M.J. Davis, K.J. Kearns and M.O. Wilkin. Bonded Repair to Cracking in Structure: A Case Study. Proceedings PICAST2-AA6 Institution of Engineers, Melbourne, Australia, 20-23 March 1995, pp 323-330.
25. F-111c Jakarta, L. Mirabella, S. Galea and S. Sanderson, "Validation of a Bonded Repair to an Wing - Coupon Testing Program (Phase 1)," *ISASTI '96 Proceedings* , Indonesia, 23-27 June, 1996.
26. Military A.A Baker, R.J. Chester, G.R Hugo and T.K. Radtke, "Scarf Repairs to Graphite/Epoxy Composites," AGARD-CP-550, Composite Repairs of Aircraft Structures, 1995, Paper 19.
27. Stabilator Note in S.C. Galea, R. Boykett and T. Radtke "Static Test on an F/A-18 Horizontal Incorporating an Adhesively Bonded Scarf Repair", DSTO-TN (Technical preparation 1997)
28. Fitting - A.A. Baker, R.J. Chester, M.J. Davis, J.A. Retchford and J.D. Roberts, "The development of a Boron/Epoxy doubler system for the F111 Wing Pivot Materials Engineering Aspects" *Composites* 1993 Vol 24, pp. 511 - 521.
29. Repair C.C. Chang and J. Sirkis "Multiplexed Optical Fibre Sensors for Air Frame Patch Monitoring," *Experimental Mechanics* 1996, Vol 36, pp 353 to 359.
30. Metallic Coast S.C. Galea "Monitoring Damage in Bonded Composite Repairs of Cracked Components Using Surface Strain Measurements," Proceedings of Eleventh International Conference on Composite Materials (ICCM-11), 1997, Gold Australia.
31. Research A.F. Cox , "Fatigue Cracking in the Upper Plate of Wing Pivot Fittings in F111 Aircraft", Defence Science and Technology Department Aeronautical Laboratory Report ARL-MAT-R-121, 1988.
32. Composite L Molent, R.J.Callinan, and R. Jones, "Design of an all Boron/Epoxy Doubler Reinforcement for the F-111C Wing Pivot Fitting:Structural Aspects", *Structures* 1989 Vol 11, pp. 57-83.
33. I.Grabovac, R.A.Bartholomeusz and A.A.Baker, "Composite Reinforcement of a Ship Superstructure - Project Overview", *Composites* 1993 Vol 24, pp. 501-509.
34. S.R Hall, M.D. Raizenne and D.L Simpson, "A proposed Composite Repair Methodology for Primary Structure," *Composites* 1989, Vol 20, pp 479- 484.

RECENT WORK ON STITCHING OF LAMINATED COMPOSITES - THEORETICAL ANALYSIS AND EXPERIMENTS

Lalit K. Jain¹ and Yiu-Wing Mai²

¹ *Cooperative Research Centre for Advanced Composite Structures (CRC-ACS) Ltd.
361 Milperra Road, Bankstown, New South Wales, 2200, Australia.*

² *Centre for Advanced Materials Technology, Department of Mechanical and Mechatronic Engineering, University of Sydney, Sydney, New South Wales, 2006, Australia.*

SUMMARY: One major problem with resin-based advanced fibre composites is their sensitivity to impact-induced mechanical damage at the interfaces between the laminated plies. Such delamination damage extends under subsequent applications of external load, and causes the laminate to lose much of its original strength. A simple way to combat this problem is to improve delamination crack-growth resistance by means of through-thickness reinforcement in the form of transverse stitching. Although stitching may lead to a significant improvement in the delamination crack-growth resistance, at the same time it may degrade the in-plane mechanical properties due to the creation of resin pockets or the breakage of in-plane fibres. This paper presents the effect of stitching on interlaminar as well as in-plane properties. The sample composite components were fabricated from unidirectional pre-preg tape as well as from dry carbon fabric and resin using resin transfer moulding (RTM) technique. The stitching was performed with the Kevlar thread. The effect of stitching on the degradation of in-plane mechanical properties was found to be negligible. The mode I toughness improved by up to ten times and the mode II toughness three times. The effects of various parameters such as stitch density, stitch-thread diameter were examined. In addition, a comparison with the micromechanics-based models developed by Jain and Mai [1,2] to predict the mode I and mode II delamination toughness is provided and good agreement is found between theoretical predictions and experimental data.

KEYWORDS: through-thickness reinforcement, stitching, delamination, mechanical properties, mode I and mode II fracture toughness, modelling.

INTRODUCTION

Fibre-reinforced composite laminates have a considerable advantage over traditional engineering materials in weight-critical applications. However, due to their low interlaminar fracture toughness, these laminates are susceptible to delamination when subjected to interlaminar stress concentrations. Interlaminar stresses may arise from manufacturing defects such as air entrapment or regions of insufficient resin, low velocity impact or geometric discontinuities such as free edges, notches, ply terminations, and bolted and bonded joints [3]. In some circumstances, this may lead simply to a substantial decrease in the structural integrity whilst in others it may be responsible for the catastrophic failure of the component.

There are two methods by which the damage tolerance of a composite structure can be improved. The first involves material selection and focuses on the use of tougher matrices, better fibre/matrix interfaces, fibre hybridisation and interleaving concepts [4-6]. These techniques, with the exception of interleaving, generally only lead to minor improvements in the delamination resistance [7,8]. The second method utilises existing textile technologies such as stitching, knitting, weaving or braiding to introduce through-thickness fibre reinforcement into the laminate. [7,9-20].

Textile fibre geometries which have through-thickness reinforcement are called three-dimensional (3D) fabrics. The fabrication of a fabric using knitting, weaving or braiding can be done in a one-step process with the z-direction fibres being introduced simultaneously. Damage to the in-plane fibres can therefore be avoided. Stitching, on the other hand, requires at least one additional step with the through-thickness fibres being introduced after the layup of the laminate and the sewing process is responsible for an amount of in-plane fibre damage. However, whilst a considerable improvement in the mode I fracture toughness is possible with weaving, knitting and braiding, these methods create large resin pockets throughout the structure and thus reduce the volume fraction of the in-plane fibres, compared to an analogous two-dimensional (2D) laminate, which results in a large decrease in the in-plane properties. Perhaps the biggest advantage of stitching compared to the other methods of through-thickness reinforcement is its versatility. Stitching utilises traditional materials and fabrication processes and components can be manufactured from either a prepreg or preform layup. In addition stitching can be used in composite joining instead of more traditional mechanical or adhesive techniques [21,22].

In this study, the composite specimens were fabricated from dry fabric and resin using resin transfer moulding (RTM) technique and from unidirectional prepreg tape. The stitching process degrades the in-plane mechanical properties (such as stiffness, strength, etc.) due to the formation of resin-rich pockets near the stitching loops or due to the breakage of in-plane fibres. The in-plane properties of the stitched laminates were determined experimentally and then compared with those of the unstitched laminates. The effect of stitching on mode I interlaminar fracture toughness was determined using the double cantilever beam (DCB) test and on mode II interlaminar fracture toughness using the end-notched flexure (ENF) test (see Figures 1 and 2). During the mode I testing of RTM specimens, the stitched specimens exhibited failure of a cantilever in bending rather than self-similar crack propagation between the plies. Therefore, a new DCB specimen configuration based on the design developed by Guenon et al. [9] was consequently used. This specimen, termed the tabbed DCB (TDCB), utilises long aluminium tabs bonded along the specimen length to prevent failure of the composite cantilevers (Figure 1). These reinforcing tabs may alter the failure mechanisms of the stitching thread and thus may have an effect on the improvement in mode I delamination toughness. Therefore, to examine the effect of the reinforcing tabs on the mode I toughness, the prepreg samples were tested with and without the tabs. The mode I and mode II interlaminar fracture toughnesses of stitched laminates were compared with those of unstitched laminates having similar material system and in-plane stacking sequence.

In addition, the steady state delamination toughness of stitched RTM specimens was compared with that of stitched prepreg specimens. Experimental data were finally compared with theoretical predictions based on micromechanics models developed by Jain and Mai [1,2].

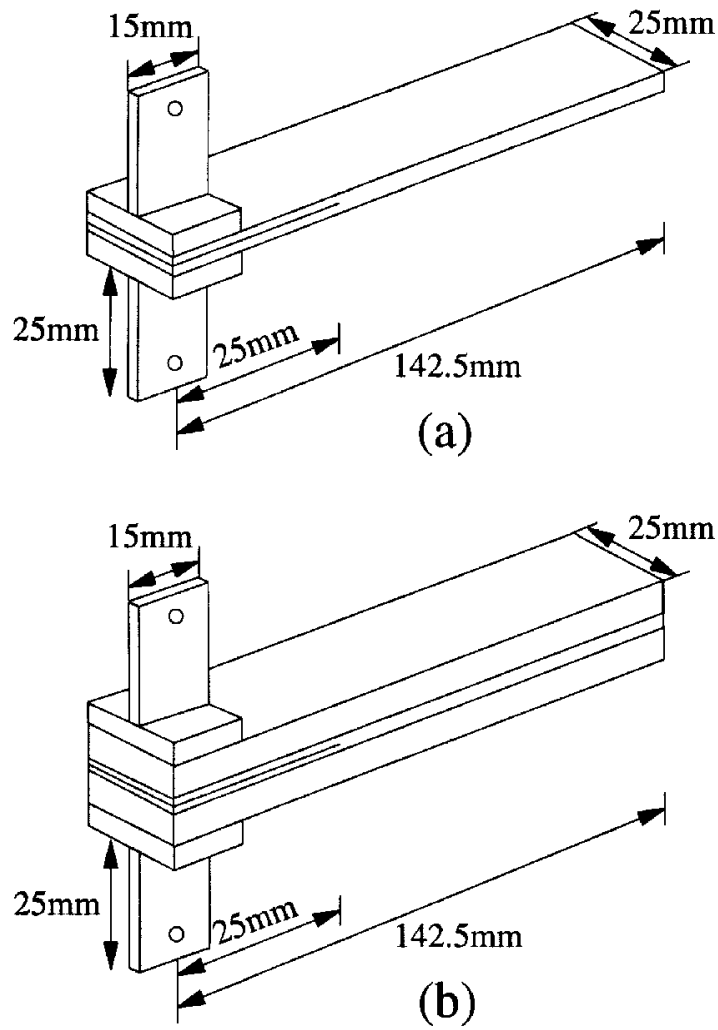


Fig. 1: Schematic representation of (a) untabbed specimen and (b) tabbed specimen for mode I indicating specimen and tab dimensions.

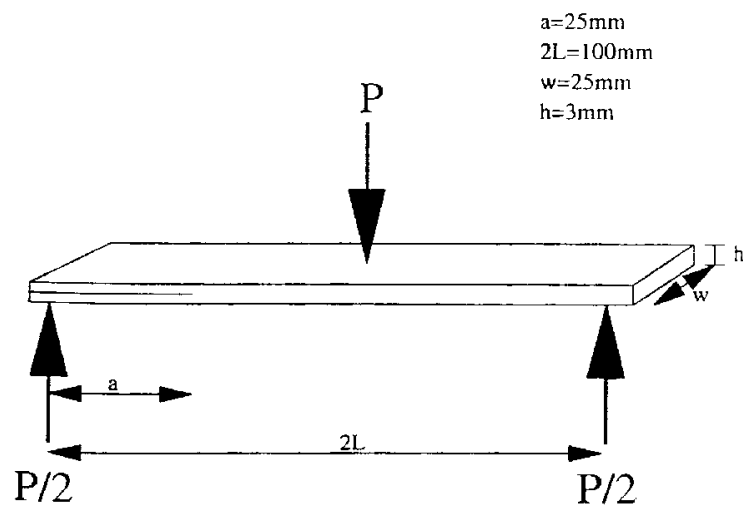


Fig. 2: End-notched flexure specimen geometry.

MATERIAL SYSTEMS

Specimen Manufacture

Carbon/epoxy RTM panels with mid-plane inserts were fabricated from Ciba-Geigy "uniweave" Injectex fabric and GY260 resin. "Uniweave" fabric consists of a large percentage of 3K tow carbon warp yarns (in this case 90% by weight) held together by 1K tow carbon fill yarns in the weft direction. Following the stacking, some of the dry fabric lay-ups were stitched through-the-thickness at 90° to the warp direction. Modified lock stitch was employed to avoid the disruption to the laminate arising from any interior looping process between the bobbin and needle threads. The through-thickness reinforcement penetrated the in-plane yarns hence some fibre breakage and misalignment occurred at each stitching needle penetration. The advent of fibre damage and misalignment resulted in the formation of resin rich pockets around the thread. The ply orientation of both the unstitched and stitched materials were essentially unidirectional. All the dry fibre preforms were infiltrated with the GY260 epoxy resin in conjunction with HY917 hardener and DY070 accelerator with 100, 90 and 1 weight proportions, respectively. The laminates were cured for 4 hours at 80 °C and then postcured for 4 hours at 160 °C.

The prepreg samples were fabricated from Ciba-Geigy aerospace grade 913 prepreg and ICI Fiberite 948 prepreg tapes. To enable direct comparison with RTM specimens, the lay-up was kept unidirectional. Prior to curing the laminates, stitching was performed with a domestic sewing machine. The cure cycles recommended by the manufacturer were employed. For the 948 system, the layup was first heated from room temperature to 80°C at a rate of 2°C/min. This temperature was held for 15 minutes. The temperature was subsequently raised at a rate of 2°C/min to 121°C and this temperature was held for 120 minutes. Cooling at a rate of 2°C/min followed. An external pressure of 7 atmosphere and a vacuum of 1 atmosphere was applied throughout the procedure. For the 913 system, cure cycle consisted of four hours at 120°C with a differential pressure of 4 atmospheres. The differential pressure consisted of 1 atmosphere of vacuum and 3 atmospheres of external pressure.

All test coupons were 14 plies thick. The average specimen thickness for both the stitched and unstitched materials was 2.97 mm. The mid-plane delamination was introduced during the layup by means of a 0.012 mm thick Teflon strip inserted between the 7th and 8th plies. All specimens were milled after the cutting procedure to ensure a consistent cross-section and to eliminate any damage.

Stitching Yarns

The stitching was performed with the commercially available K40, K60 and K80 Kevlar® threads. The terms K40, K60 and K80 represent 40 Tex (2 ply), 60 Tex (3 ply) and 80 Tex (3 ply) sewing threads, respectively. The tensile strength and modulus of the threads were evaluated as per ASTM D2256-81 and D3379-75. Under mode I loading failure of the thread was predominantly at the needle/bobbin thread intersection. Thus the intersection was imitated using a "loop" configuration (ASTM D3217-79) and the thread strength was determined both prior to and after the stitching process. Each result was determined from 16-20 tests using a Weibull data reduction method. The results are presented in Table 1. Further details on the test methods and data reduction method may be found in Ref. [20].

The use of the theoretical models [1] required a knowledge of the thread/matrix interfacial shear stress. The interfacial properties were determined using a novel pull-out test where the

thread was pulled from a composite laminate. The interfacial properties of the thread pull-out test are also presented in Table 1.

A summary of the stitching variables studied and the fibre volume fraction for the various laminates is presented in Table 2. The term discontinuous in this table refers to the laminates where the surface loops are removed by grinding the top and the bottom parts.

IN-PLANE MECHANICAL PROPERTIES

Stitching of preforms or prepregs causes stress concentrations and damage to the in-plane fibres and hence degrades the in-plane mechanical properties. The Young's modulus, flexural modulus, failure strength, and shear strength of stitched laminates were determined experimentally for some of the laminates and are summarised below. In determining these properties, the transverse shear modulus, where required, was assumed to be 5.8 GPa.

The tensile and compressive properties were determined by loading the specimen in uniaxial tension and compression, respectively. These tests were carried out on rectangular coupons of 160 mm in length, 15 mm in width and 3 mm in thickness as per ASTM standard. For the tensile test specimens, at each end, 40 mm of the specimen was held in the grips, leaving a test area of 80 x 15 mm². To prevent failure in the grips, it was also necessary to employ aluminium tabs in the case of longitudinal tension specimens. However, no tabbing was required while performing the test in the transverse direction. The compressive test specimen had a test area of 10 x 15 mm² with 70 mm held in the grips at both ends (in an IITRI test fixture). The measurement of the Young's modulus and failure strain were facilitated by the use of a centrally located strain gauge. The strain gauge data was directly fed into a 486 PC data logger. The load was applied by a screw driven Instron 1195 using a 100KN load cell. The self-tightening wedge action grips were used to introduce the load to the specimen. An increasing load was applied to the specimen at a uniform displacement rate of 1 mm/min until fracture of the specimen occurred. The load, displacement, time and strain were constantly recorded using a 486 PC data logger throughout the test. For each variable four to six specimens were tested. The load-displacement curves were essentially linear until fracture occurred. The strength was determined from the failure load and the Young's modulus was determined from the gradient of the linear (elastic) portion of the stress-strain curve. The results for the longitudinal and transverse tensile properties and compressive properties are summarised in Tables 3-5.

It can be seen from Tables 3 and 5 that the longitudinal Young's modulus and tensile and compressive strengths reduce by up to 15% due to the in-plane fibre damage and stress concentrations caused by the stitches. However, reduction in these properties is quite insignificant compared to the improvements achieved in the delamination toughness. In most cases, the failure of the specimen was caused by crack initiation at the stitch line. To examine the effect of surface in-plane waviness caused by the stitching loops, the top and the bottom surfaces of the CRC-AS K40 4 st/cm² laminate were ground off. These samples are designated as CRC-AS K40 4 st/cm² "discontinuous" stitched samples. These specimens exhibited an apparent increase in strength and a reduction in stiffness in tension. However, in compression, a reduction in strength and an increase in stiffness was found. Table 4 shows that stitching did not affect the transverse tensile properties. It should be noted here that the transverse modulus and strengths of RTM specimens is much larger than that of pre-preg specimens because of 10% carbon fill yarns in the weft direction.

Table 1 Fibre and Thread Tensile Properties [20].

	Single Fibre			Prior to stitching			After stitching			Pull-out shear stress τ (MPa)
	Tensile			Tensile			Tensile			
	σ_m (GPa)	E_f (GPa)	σ_m (GPa)	E_f (GPa)	Loop σ_m (GPa)	σ_m (GPa)	E_f (GPa)	Loop σ_m (GPa)		
2-ply Kevlar	3.20	124	2.82	76.3	2.10	2.05	62.5	1.79	18.2	
3-ply Kevlar	3.20	124	2.65	66.8	2.15	2.09	56.8	1.89	21.4	
4-ply Kevlar	3.20	124	2.59	57.8	2.21	2.14	49.3	1.87	24.7	

Table 2: Materials studied, stitch variables and average fibre volume fraction [20].

Material	Thread Type	Stitch density (stitches/cm ²)	Stitch Pitch	Stitch Line Spacing	Volume Fraction (%)
RTM	-	Unstitched	-	-	58.0
RTM	2 ply Kevlar	4	3.40 mm	7.5 mm	58.6
RTM	2 ply Kevlar	4 (discontinuous stitch)	3.40 mm	7.5 mm	60.5
RTM	2 ply Kevlar	8	3.40 mm	3.35 mm	58.6
RTM	2 ply Kevlar	12	3.25 mm	2.6 mm	57.6
RTM	3 ply Kevlar	4	3.40 mm	7.5 mm	58.8
RTM	4 ply Kevlar	4	3.40 mm	7.5 mm	57.4
RTM	4 ply Kevlar	8	3.40 mm	3.35 mm	58.0
948	-	unstitched	-	-	63.5
948	2 ply Kevlar	4	3.12 mm	6.9 mm	63.4
913	-	unstitched	-	-	64.7
913	2 ply Kevlar	2	3.12 mm	14.0 mm	64.1
913	2 ply Kevlar	4	3.12mm	6.9 mm	64.5
913	2 ply Kevlar	4 (discontinuous stitch)	3.12mm	6.9 mm	66.3

Table 3: Effect of stitching on longitudinal tensile properties.

Material	Thread type and stitch density	Failure strength σ_m (GPa)	Young's Modulus E_{11} (GPa)
RTM	unstitched	1.20 ± 0.01	106.3 ± 0.5
RTM	2-ply K 4 st/cm ²	1.19 ± 0.05	105.3 ± 11
RTM	2-ply K 8 st/cm ²	1.15 ± 0.02	105.8 ± 1.8
RTM	3-ply K 4 st/cm ²	1.02 ± 0.01	103.3 ± 2.3
RTM	2-ply K 4 st/cm ² (1)	1.27 ± 0.06	91.5 ± 2.5
948	unstitched	1.55 ± 0.04	119.3 ± 2.3
948	2-ply K 4 st/cm ²	1.43 ± 0.03	127.6 ± 2.0
913	unstitched	1.39 ± 0.03	126.7 ± 1.0
913	2-ply K 2 st/cm ²	1.16 ± 0.02	121.2 ± 1.3
913	2-ply K 4 st/cm ²	1.18 ± 0.01	122.2 ± 0.7
913	2-ply K 4 st/cm ² (1)	1.38 ± 0.01	110.9 ± 8.5

K - Kevlar, (1) - discontinuous stitch

Table 4: Effect of stitching on transverse tensile properties.

Material	Thread type and stitch density	Failure strength σ_m (MPa)	Young's modulus E_{22} (GPa)
RTM	unstitched	164.2 ± 5.7	36.0 ± 0.8
RTM	2-ply K 4 st/cm ²	157.8 ± 1.1	36.5 ± 0.1
913	unstitched	82.3 ± 2.3	8.7 ± 0.5
913	2-ply K 4 st/cm ²	83.4 ± 3.1	8.5 ± 0.4

K - Kevlar

Table 5: Effect of stitching on compressive properties.

Material	Thread type and stitch density	Failure strength σ_m (MPa)	Young's Modulus E_{11} (GPa)
RTM	unstitched	472.2 ± 10.2	99.8 ± 0.3
RTM	2-ply K 4 st/cm ²	406.2 ± 15.3	113.4 ± 1.6
RTM	2-ply K 8 st/cm ²	403.3 ± 25.8	104.3 ± 3.1
RTM	3-ply K 4 st/cm ²	398.7 ± 12.9	108.7 ± 7.6
RTM	2-ply K 4 st/cm ² (1)	416.2 ± 12.6	107.9 ± 5.3
948	unstitched	708.0 ± 32.6	111.8 ± 3.5
948	2-ply K 4 st/cm ²	614.1 ± 25.4	102.2 ± 4.8
913	unstitched	713.1 ± 18.3	117.8 ± 2.8
913	2-ply K 2 st/cm ²	643.3 ± 15.4	112.1 ± 3.5
913	2-ply K 4 st/cm ²	632.6 ± 30.2	105.3 ± 4.2
913	2-ply K 4 st/cm ² (1)	658.5 ± 12.8	112.4 ± 1.7

K - Kevlar, (1) - discontinuous stitch

The composite interlaminar shear specimens were 33 mm in length, 6.5 mm in width and 3 mm in thickness. The interlaminar shear strength properties were determined using the short beam shear test (ASTM standard D2344). This test utilises a three-point bending fixture of 25 mm gauge length. The compressive load was applied through a servo-hydraulic Instron 4302 material testing machine using a 10KN load cell. A uniform displacement rate of 5 mm/min was used until an interlaminar crack appeared in the specimen. The specimens were very rate sensitive with rates of 1 and 2 mm/min producing compressive failure under the central loading pin rather than interlaminar failure. The load, displacement and time were continuously recorded using a 286 PC data logger. The load increased linearly until the interlaminar crack was observed. This interlaminar crack tended to extend from the central loading pin to the specimen end in the unstitched specimen, and from the central loading pin to the nearest stitch line in the stitched specimen. For each variable six specimens were tested. The interlaminar shear strength was obtained from the following expression:

$$\tau_s = \frac{3P}{8wh_c} \quad (1)$$

where P is the failure load, w is the width of the specimen and h_c is the half-beam thickness. The results are presented in Table 6. It can be seen from this table that the effect of stitching on the interlaminar shear strength is negligible.

Table 6: Effect of stitching on interlaminar shear strength.

Material	Thread type and stitch density	Shear strength τ_s (MPa)
RTM	unstitched	51.64 ± 1.23
RTM	2-ply K 4 st/cm ²	51.02 ± 2.41
RTM	2-ply K 4 st/cm ² (1)	50.92 ± 0.94
RTM	2-ply K 8 st/cm ²	51.52 ± 1.15
RTM	3-ply K 4 st/cm ²	50.40 ± 1.97
948	unstitched	57.3 ± 2.70
948	2-ply K 4 st/cm ²	57.5 ± 4.24
913	unstitched	59.5 ± 2.08
913	2-ply K 2 st/cm ²	57.9 ± 0.87
913	2-ply K 4 st/cm ²	62.0 ± 2.41
913	2-ply K 4 st/cm ² (1)	48.9 ± 1.56

K - Kevlar, (1) - discontinuous stitch

MODE I DELAMINATION TOUGHNESS

Experimental Technique

The standard double-cantilever-beam (DCB) test is ideal to determine the mode I interlaminar fracture toughness. This test utilises specimens of 3 mm thickness, 25 mm width and 150 mm in length. The specimens were manufactured so that the crack length from the loading point to the crack tip was 25 mm.

The load was applied through the use of aluminium T-tabs fixed to the specimen end containing the delamination (Figure 1). This methodology was found to be adequate with the unstitched RTM and both stitched and unstitched prepreg specimens. However, as mentioned earlier, when the stitched RTM specimens were tested, failure of a cantilever in bending rather than self-similar crack propagation between the plies occurred. Therefore, tabbed DCB (TDCB) specimens based on the design developed by Guenon et al. [9] were consequently used. This specimen configuration utilises long aluminium tabs bonded along the specimen length to prevent failure of the composite cantilevers (Figure 1). To prevent the yielding of the long aluminium tabs, a minimum thickness of 6 mm is required for the tabs. However, readily available 10 mm thick aluminium tabs were used. To examine the effect of these reinforcing tabs, stitched prepreg specimens were tested both with and without tabs. To ensure consistency with the results and to help identify failure mechanisms associated with the stitches, unstitched specimens were also tested both with and without the long aluminium tabs.

For load application T-tabs were fixed to the long aluminium tabs using both adhesive and bolts. Following the specimen manufacture, a razor blade was used to wedge open the initial delamination to form a sharp mode I precrack. The sides of the specimen were coated with a thin layer of white correction fluid to aid measurement of the initial crack length and to assist visual observation of the crack propagation during the test. Subsequently, the DCB specimens, both untabbed and tabbed, were pin loaded in tension using Instron grips in a servohydraulic Instron 4302 materials testing machine. A 10 KN load cell was employed to apply the load to the specimen through the fixture and T-tab. Displacement control mode was used with a cross-head speed of 1 mm/min. A data logger was used to continuously record the load, displacement and time. A travelling microscope with a light source enabled visual examination of the specimen throughout the test and measurement of the crack length.

The specimen was loaded until the crack propagated several millimetres. The specimen was then unloaded and the crack tip marked. This process was repeated 10-15 times for each specimen. The crack lengths, defined as the distance from the loading point to the crack tip, were measured using the travelling microscope. For each variable four to six specimens were tested.

Analysis

The interlaminar fracture toughness was determined in terms of the mode I critical energy release rate, G_{IR} (which may be regarded as G_{IC} in the case of unstitched laminates with no R-curve behaviour), using the direct method. This method requires information on the crack propagation load as a function of crack length which was determined using the data logger and the travelling microscope.

The mode I critical energy release rate, G_{IR} , as defined by the Griffith's energetic fracture criterion, is given by [1]

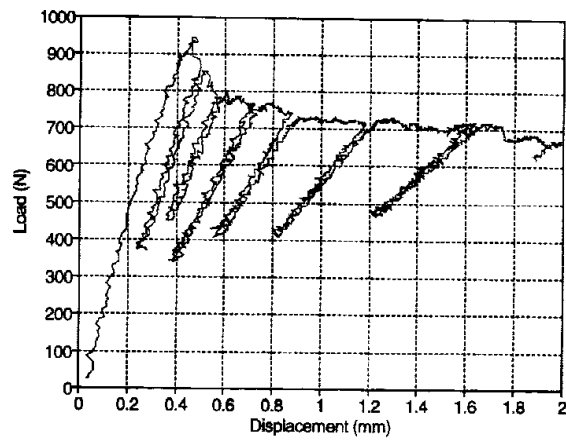
$$G_{IR} = \frac{P^2}{w} \left[\frac{(a + \chi h_c)^2}{E_c I_c} + \frac{6}{5 G_{12c} h_c w} \right] \quad (2)$$

where P is the applied load, a is the crack length, E_c is the flexural modulus of the composite, $E_c I_c$ is the flexural rigidity, w is the beam width, h_c is the beam thickness and G_{12c} is the transverse shear modulus. χ is a correction factor which takes into account the additional

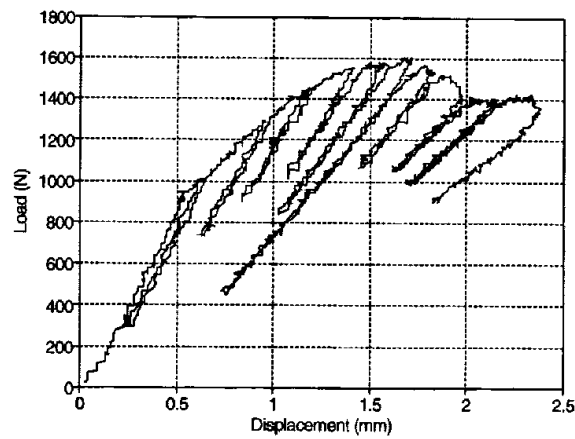
deflection due to rotation of the beams and is equal to 0.6 [23]. The two terms on the right hand side of the equation are the contributions from bending and shear deflections, respectively. From equation (2) it is possible to determine a set of mode I energy release rate values, G_{IR} , as a function of crack growth, Δa , if the crack propagation load is known. To account for the long aluminium tabs required by the stitched RTM DCB specimens, in equation (2), the beam thickness h_c is replaced by $h_c + h_a$ where h_a is the thickness of the aluminium tab. The flexural rigidity $E_c I_c$ is replaced by EI and the shear modulus G_{12c} is replaced by G_{12} for the composite-aluminium beam. The expressions for EI and G_{12} may be found in Ref. [24,25]. In determining flexural rigidity, EI , and the shear modulus, G_{12} , E_a of 6061 aluminium was taken as 68.9 GPa and G_a as 26.9 GPa [26].

Results and Discussion

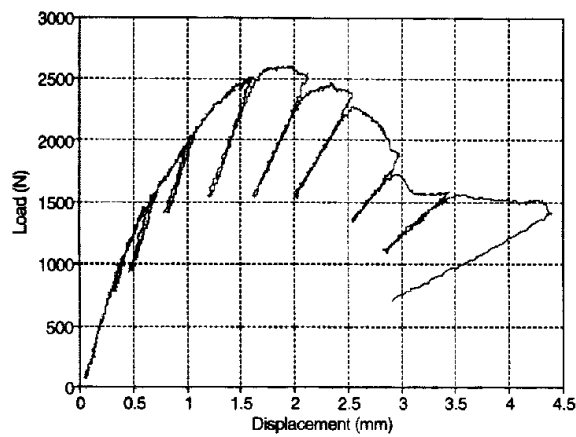
Observation of the load-displacement curves obtained from stitched specimens (Figure 3) shows that initially there is an increase in the crack propagation load as the crack grows. This is caused by the development of the stitch bridging zone. After the bridging zone is fully developed, the steady-state interlaminar fracture toughness is attained and with further crack propagation the stitches start breaking and the crack propagation load decreases with increasing crack length. The crack propagation part of the curve generally exhibited stable crack propagation behaviour consisting of successive load drops followed by crack arrest. This is termed the "stick-slip" behaviour. In the case of the unstitched specimen, there was a continual decrease in the crack propagation load with increasing crack length for both the untabbed and tabbed samples. The load-displacement curves of the stitched specimen also show an appreciable amount of permanent deformation. The crack opening displacement is non-zero after unloading and observation of the crack tip with the travelling microscope revealed that the crack tip had not closed completely. This was due to the fact that most of the stitches did not break in the plane of the crack. Instead, the stitches fractured at the thread intersection at the outer surface of the composite and subsequently pulled out. The pulled-out stitch loops did not return to their original location during unloading and this led to a non-linear unloading behaviour and a permanent deflection of the specimen after unloading was complete. The R-curves for different material variables were determined. The flexural modulus required to determine these curves are given in Table 7 and the out-of-plane shear modulus was estimated to be 5.8 GPa. The R-curves are shown in Figures 4 and 5. It was immediately obvious that the addition of through-thickness reinforcement by stitching produced a significant improvement in the mode I delamination fracture toughness. To determine the major energy absorption mechanisms responsible for the improvement, delamination surfaces of the stitched specimens were examined using scanning electron microscopy (SEM). Evidence of thread breakage and subsequent pull-out was found (Figure 6). Thus it was postulated that several processes were involved in increasing the toughness. Debonding of the thread/matrix interface allowed elastic stretching of the thread. This created fibre bridging of the crack by the stitch lines providing crack closure forces until thread failure and pull-out occurred. The unstitched specimens also exhibited R-curve behaviour (Figures 4-5). This incremental increase in the fracture toughness was due to some fibre bridging effect caused by the in-plane carbon fibres. A study of the fracture surface using a scanning electron microscope (SEM) found some evidence of fibre bridging (Figure 7). The steady-state G_{IRs} values for the unstitched specimens, both tabbed and untabbed, exhibited good agreement for RTM as well as prepreg specimens (see Table 8).



(a)



(b)



(c)

Fig. 3: Typical load versus displacement plots for (a) an unstitched, tabbed specimen (b) a specimen stitched with K40 thread at 4 st/cm² and (c) a specimen stitched with K80 thread at 8 st/cm².

This indicated that for the unstitched specimens, the addition of long aluminium tabs did not alter the failure mechanisms during the crack propagation. However, a considerable increase in the length of the crack bridging or process zone before attaining steady-state behaviour was observed. The reason for this is that addition of the aluminium tabs has produced a stiffer specimen and thus created a longer crack bridging zone. It can clearly be observed from the R-curves (Figure 4-5) that the crack bridging zone of the unstitched specimens increased from 20-25 mm to 37-42 mm for the RTM specimens and from 20-25 mm to 45-55 mm for 948 and 913 prepreg specimens. The unstitched RTM material exhibited higher toughness compared to the prepreg materials. Amongst the prepreg materials, the tougher, aerospace grade 913 prepreg demonstrated 30% higher toughness compared to the 948 prepreg material.

Table 7 Material and Geometric parameters used in the prediction of G_{IR}

Parameter	RTM						948	913	
	2-ply K			3-ply K	4-ply K		2-ply K	2-ply K	
stitch/cm ²	4	8	12	4	4	8	4	4	8
E_c (GPa)	95.5	88.9	87.5	90.7	89.5	85.6	119.3	121.2	122.2
τ (MPa)	18.2			21.4	24.7		18.2	18.2	
E_0 (GPa)	11.4			11.4	11.4		12.3	12.3	
K_{Ic} (MPa \sqrt{m})	2.24			2.24	2.24		1.8	2.04	
a_0 (mm)	25			25	25		25	25	
h_c (mm)	1.5			1.5	1.5		1.5	1.5	
d_f (mm)	0.16			0.200	0.234		0.16	0.16	
L_p (mm)	3.33			3.33	3.33		3.33	3.33	
S_f (mm)	7.5	3.75	2.5	7.5	7.5	3.75	7.5	15.0	7.5
σ_u (GPa)	1.79			1.89	1.87		1.8	1.8	
E_c (GPa)	62.5			56.8	49.3		62.5	62.5	

K-Kevlar®

It is reasonable to hypothesise that a larger stitch bridging zone resulting from stiffening the specimen by the addition of tabs would produce higher G_{IRs} values. However, in the case of all stitched prepreg laminates, although a significant increase in the length of the bridging zone was observed after the application of tabs, a 30% reduction in G_{IRs} was found as compared to untabbed specimens (see Table 8). To ascertain possible explanations for this the role of the surface stitch loop must be considered. The G_{IRs} values of continuously stitched specimens prior to and after removal of the surface loop (discontinuous) displayed a loss of 50% for both the 913 prepreg and RTM specimens. Compared to unstitched specimens, a two to three-fold improvement in delamination toughness with discontinuous stitching was still produced. This eventuated from debonding at the thread/matrix interface and subsequent pull-out of the thread. Therefore it may be deduced that the interfacial shear stress at the thread/matrix interface is considerable to provide the crack closure forces. However, in the case of continuous stitching employing the same thread and stitch density, a five to seven fold improvement in the mode I delamination toughness was found. Thus it was concluded that the major contribution to the improvement in toughness transpired from elastic stretching of the stitches prior to thread failure and pull-out.

Having postulated that the elastic stretching of the thread was the major contributing mechanism involved in the improvement in toughness, the toughness must be dependent on the length of thread available to stretch. To analyse this the delaminated surfaces of the

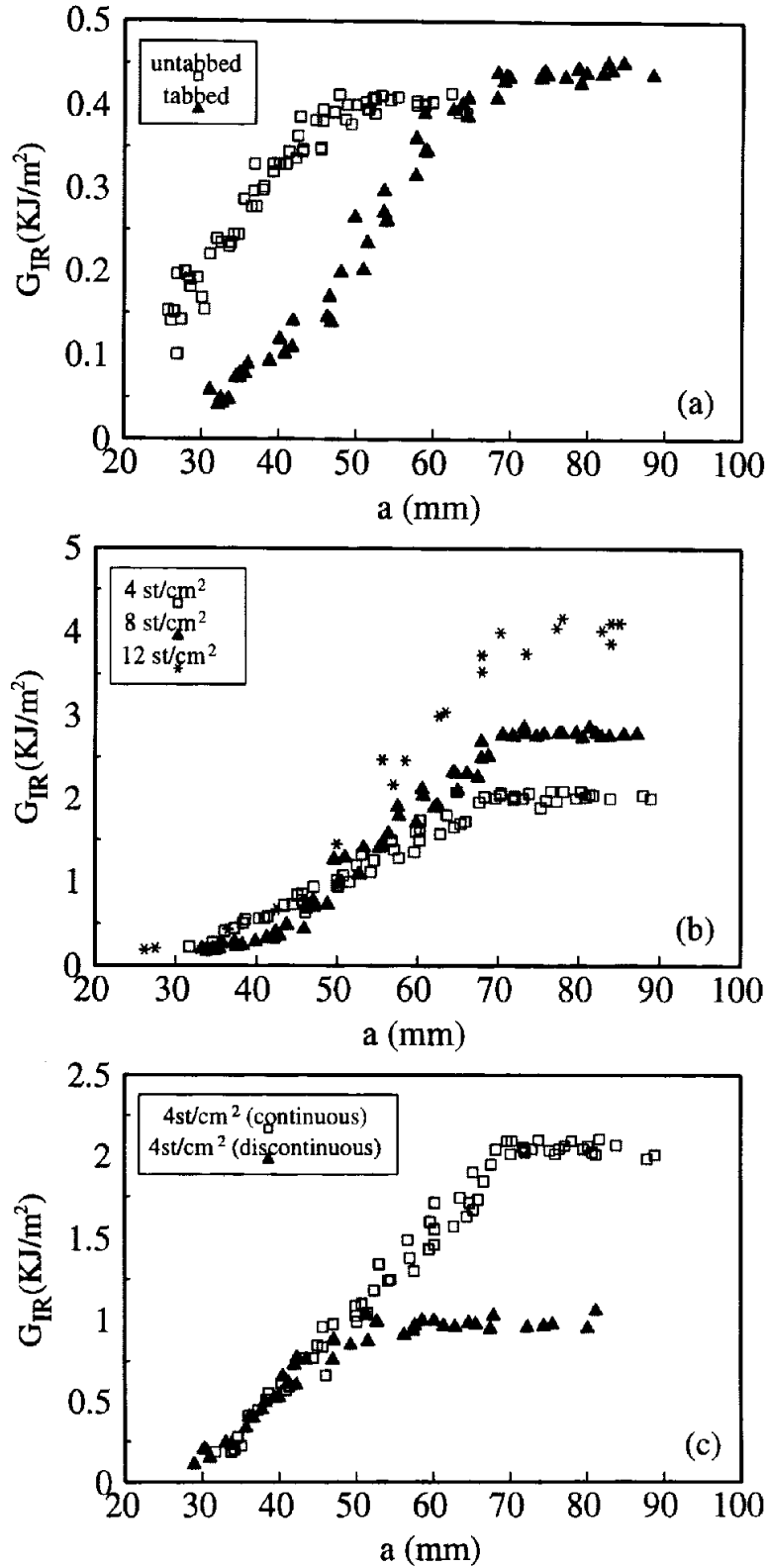


Fig. 4: R-curves for RTM specimens - (a) unstitched, (b) stitched with 2-ply Kevlar thread at 4 st/cm^2 , 8 st/cm^2 , and 12 st/cm^2 and (c) continuous and discontinuous stitches with 2-Ply Kevlar at 4 st/cm^2 . The R-curves for specimens stitched with 3-ply and 4-ply Kevlar threads are similar.

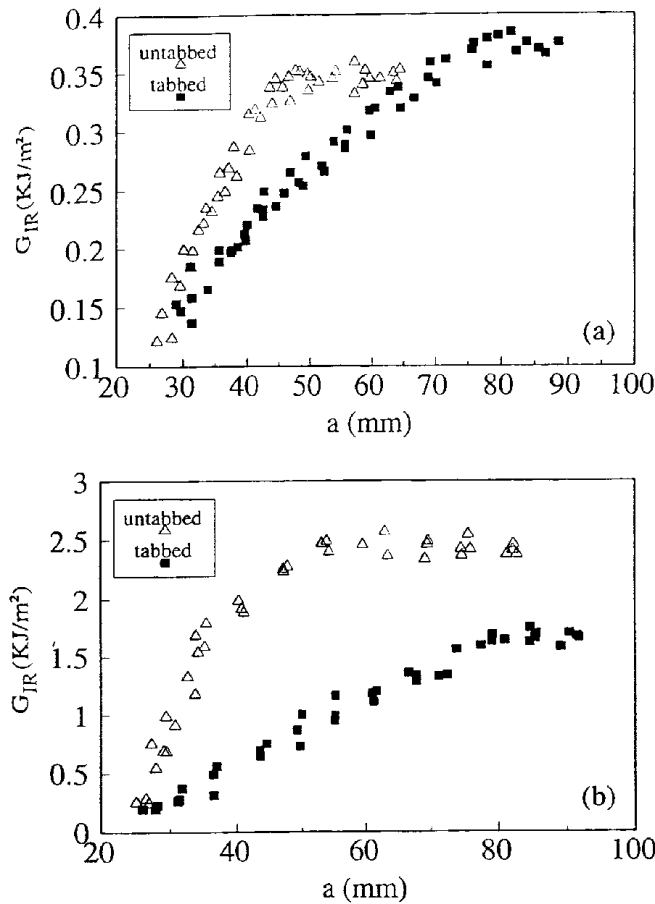


Fig. 5: R-curves for 913 prepreg specimens - (a) unstitched, untabbed and tabbed and (b) stitched with 2-ply Kevlar at 4 st/cm², untabbed and tabbed. The R-curves for 948 prepreg specimens are similar.

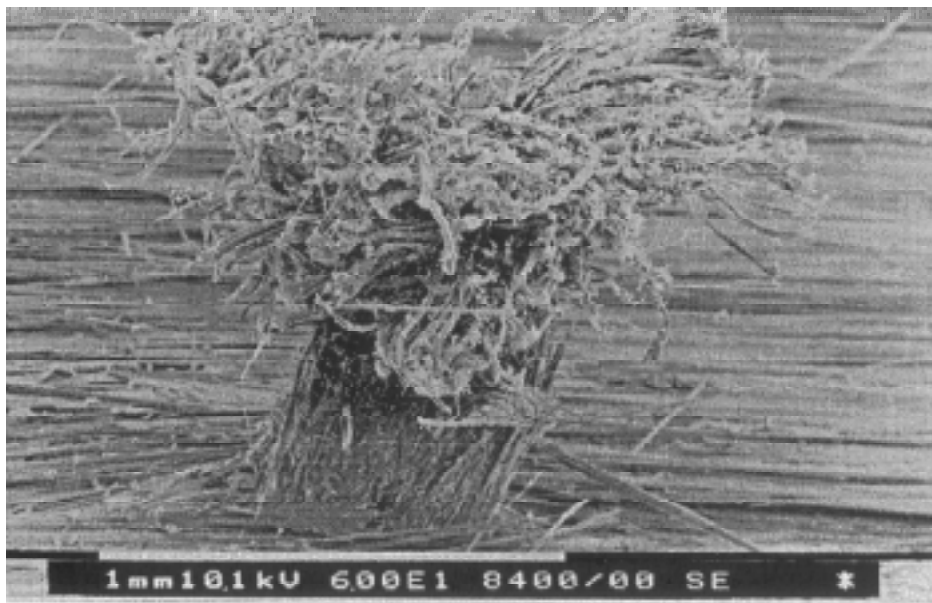


Fig. 6: SEM fractograph displaying the failure behaviour under mode I loading of a Kevlar thread. Evidence of debonding, thread failure and pull out may be seen (After [20]).

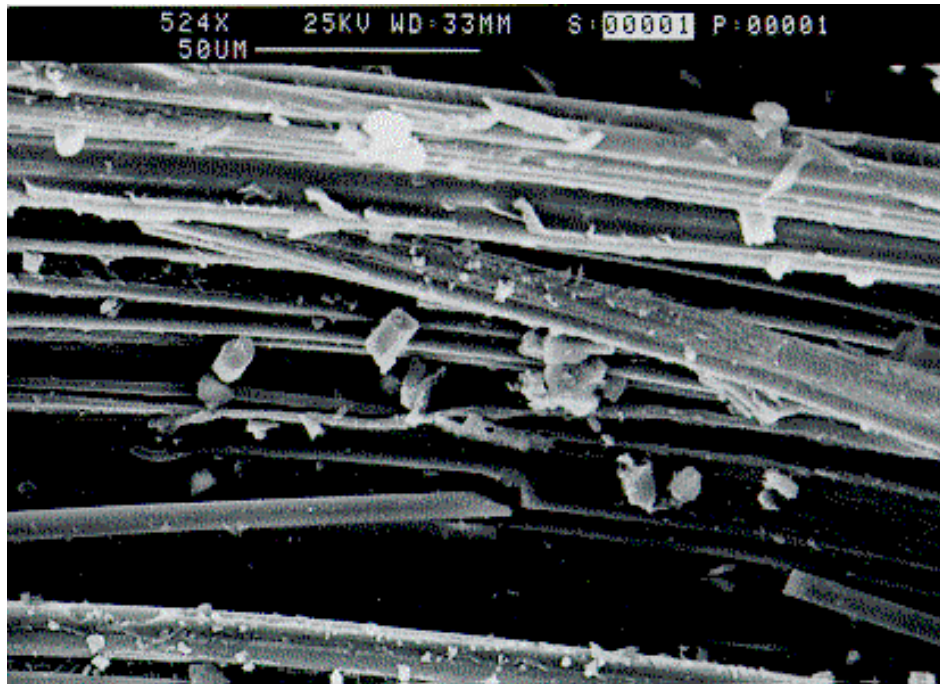


Fig. 7: SEM fractograph showing fibre bridging of in-plane carbon fibres in an unstitched specimen (After [20]).

Table 8 Mode I toughness determined using the direct method

Specimen			G_{TRC} (KJ/m ²)	Improvement Factor
RTM	unstitched	untabbed	0.41 ± 0.02	-
		tabbed	0.44 ± 0.03	-
RTM	K40 4 st/cm ²	tabbed	2.03 ± 0.04	4.6
RTM	K40 4 st/cm ² (1)	tabbed	0.98 ± 0.09	2.2
RTM	K40 8 st/cm ²	tabbed	2.82 ± 0.09	6.4
RTM	K40 12 st/cm ²	tabbed	4.10 ± 0.25	9.3
RTM	K60 4 st/cm ²	tabbed	2.59 ± 0.11	5.9
RTM	K80 4 st/cm ²	tabbed	2.90 ± 0.12	6.6
RTM	K80 8 st/cm ²	tabbed	4.54 ± 0.10	10.3
948	unstitched	untabbed	0.26 ± 0.012	-
		tabbed	0.28 ± 0.010	-
948	4 stitches/cm ²	untabbed	2.19 ± 0.14	8.4
		tabbed	1.48 ± 0.05	5.2
913	unstitched	untabbed	0.34 ± 0.01	-
		tabbed	0.38 ± 0.02	-
913	2 stitches/cm ²	untabbed	1.56 ± 0.09	4.5
913	4 stitches/cm ²	untabbed	2.44 ± 0.07	7.2
		tabbed	1.64 ± 0.10	4.3
913	4 stitches/cm ² (1)	tabbed	1.13 ± 0.08	3.0

(1) Discontinuous stitch

various stitched specimens were examined using SEM. It was determined that the thread fracture processes consisted similar mechanisms in all specimens, namely (i) thread/matrix interfacial debonding, (ii) elastic stretching of the thread and, (iii) thread failure and pull-out. Examination of the delamination surfaces of the tabbed stitched specimens disclosed failure of the thread at the intersection of the stitch loop and the surface thread (Figure 8). In the case of untabbed specimens, although thread failure at the intersection of the stitch loop and the surface thread occurred, it was obvious from the observation of the surfaces of the stitched specimens that the portion of the thread on the surface also underwent significant stretching. Thus it was concluded that the addition of tabs prevented the surface loop from stretching. This reduced the thread length available for stretching and hence resulted in a decrease in the improvement in mode I delamination toughness.

A summary of the improvement in toughness when compared to the relevant unstitched toughness values is also presented in Table 8. From this table it can also be seen that stitched, tabbed RTM specimens exhibited higher delamination toughness as compared to the stitched, tabbed prepreg specimens. This trend is similar to the one observed for the unstitched specimens.



Fig. 8: SEM fractograph displaying thread loop pull-out failure behaviour under mode I loading of a tabbed, Kevlar thread stitched specimen (After [20]).

Micromechanical Model

Two simple micromechanics-based models using a stress intensity factor approach have been developed by Jain and Mai [1] to predict the effect of stitching on the mode I delamination toughness. In the first model each stitch was considered as an independent (discontinuous) through-thickness reinforcement. In this case, the expression for crack closure traction contained terms for frictional slip and thread pull-out. In the second model, the effect of

interconnected stitching was incorporated. This model utilised terms for frictional slip, elastic stretching, and thread rupture in the crack plane. However, as described above, the thread fracture behaviour of the stitched double cantilever beam specimens was found experimentally to consist of (i) thread debonding (ii) elastic stretching of the thread (iii) thread rupture, and (iv) thread pull-out. These models, therefore, have been modified by Jain et al. [24,25] to accurately account for the various failure mechanisms occurring during the delamination crack propagation. It should also be pointed out here that Mourtiz and Jain [27] found that in the case of 6 mm thick stitched glass reinforced polymer composites, the stitches failed in the crack plane and no stitch thread pull-out was observed.

The assumptions involved in the theoretical models may be found in Ref. [1]. To simulate the failure mechanisms observed in the case of tabbed RTM and prepreg specimens, it was assumed that the effective thread length available for elastic stretching was equal to the laminate thickness ($2h_c$) and that available for pull-out was half the laminate thickness, h_c , as the stitch breaks at one end and then pulls out. In the case of untabbed prepreg specimens, the effect of stitch pitch length, L_p , has to be accounted. Therefore, the stitch length available for elastic stretching was estimated to be $2h_c + L_p$ and that available for pull out was h_c .

From the closure traction $P(t)$ provided by the bridging stitches, the crack growth resistance, K_{IR} , as a function of crack growth, Δa , can be obtained as follows [1]

$$K_{IR}(\Delta a) = K_{Ic} + Y \int_{t=0}^{\Delta a} P(t) \frac{1}{\sqrt{h_c}} f\left(\frac{t}{h_c}\right) dt \quad (3)$$

where K_{Ic} is the initiation fracture toughness of the stitched composite which is taken as the steady state value for the unstitched composite. Inclusion of the matrix R-curve (i.e. matrix process zone) in addition to the fibre bridging zone for fibre cements has been analysed by Cotterell and Mai [28]. The parameter Y is an orthotropic correction factor and $f(t/h_c)$ is a geometric factor [1].

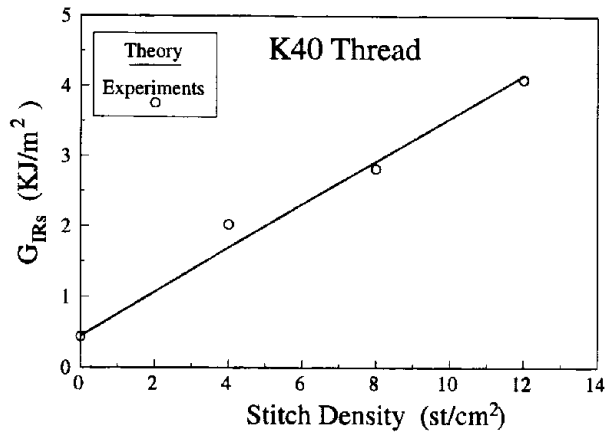
Once the stress intensity $K_{IR}(\Delta a)$ has been determined using equation (3), the fracture toughness in terms of energy release rate, $G_{IR}(\Delta a)$, may be obtained as follows

$$G_{IR}(\Delta a) = \frac{K_{IR}^2(\Delta a)}{E_0} \quad (4)$$

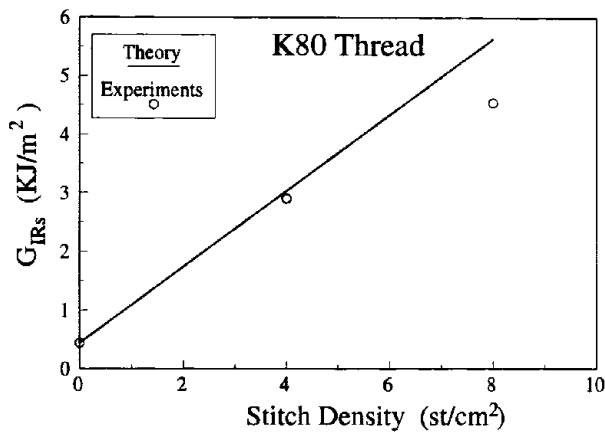
where E_0 is the orthotropic modulus [1].

The material and geometric parametric values of the laminate and thread materials used in the prediction of delamination toughness are given in Table 7. Note that a_0 is the initial crack length and S_L is the stitch line spacing. The value for the initiation fracture toughness of the stitched composite, K_{Ic} , was calculated from the experimentally determined steady-state energy release rate for the unstitched specimens using equation (4).

The theoretical predictions and the experimental results are presented in Figures 9-11. In the case of RTM specimens, comparison between theory and experimental results with increasing stitch density shows good agreement. Likewise for the prepreg materials, the agreement is very good for both tabbed and untabbed specimens.



(a)



(b)

Fig. 9: Comparison of experimental results and theoretical predictions showing trend with stitch density for tabbed, RTM specimens for (a) 2-ply Kevlar thread and (b) 4-ply Kevlar thread.

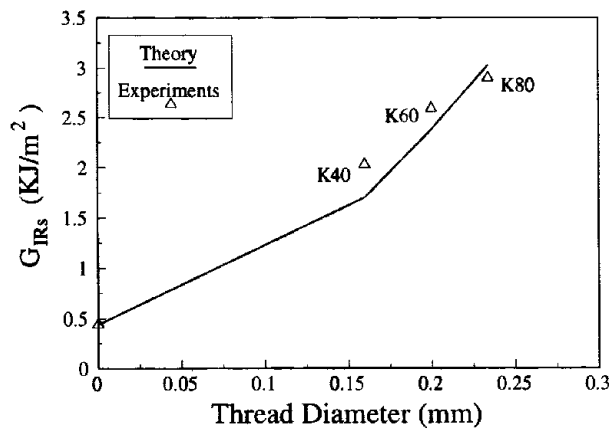
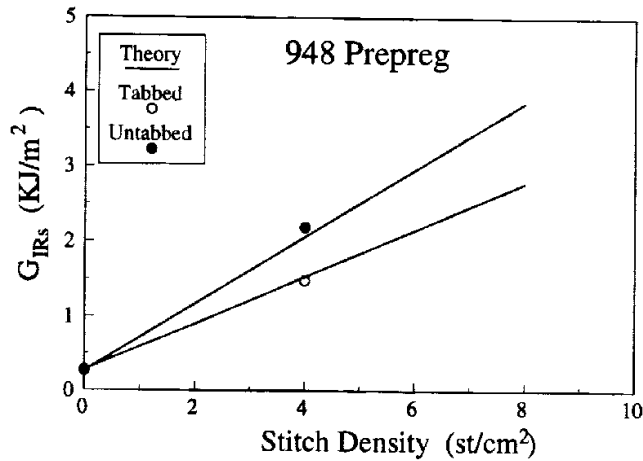
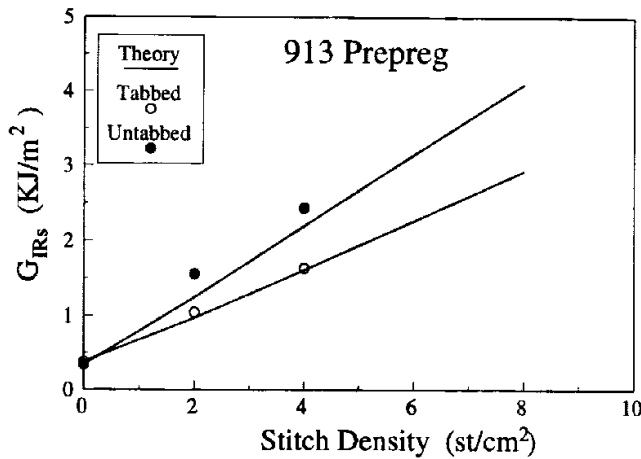


Fig. 10: Comparison of experimental results and theoretical predictions with Kevlar thread diameter for RTM specimens.



(a)



(b)

Fig. 11: Comparison of experimental results and theoretical predictions for (a) 948 and (b) 913 tabbed and untabbed prepreg specimens.

MODE II DELAMINATION TOUGHNESS

Experimental Procedure

All mode II tests were performed on end-notched flexure (ENF) specimens using a three point bend fixture (Figure 2). Prior to testing, a mode I precrack was propagated in the specimen by wedging the initial delamination open with a razor blade. This procedure was performed to transform the blunt resin rich crack tip into a sharp one.

As with mode I testing, following the precracking procedure the specimen edges were coated with a thin layer of water soluble correction fluid to enable accurate measurement of the initial crack length and visual observation of the delamination. The specimens were positioned in the three-point bend fixture with a total span of 100 mm so that an initial crack length of 25 mm was achieved. The load was applied to the specimen via the central loading pin by a servo-hydraulic

Instron 4302 in displacement controlled mode. A 10 KN load cell was employed. The cross-head moved at a constant speed of 1 mm/min. A data logger was used to record the load, displacement and time information continuously. A travelling microscope with a light source was employed to observe delamination. The specimens were loaded until crack propagation occurred. In the case of the unstitched specimens this cracking was unstable and continued to the central loading pin instantaneously. The test was then concluded. Crack propagation in stitched, prepreg samples was also unstable. This resulted from the loosening of the stitches due to the compaction during the autoclave processing. The slackening of the stitches was measured to be close to 0.3 mm for the laminates. Thus over a specimen gauge length of 100 mm, which induced a relative sliding between the top and bottom of the specimen of 0.18 mm at the first stitch line, a load would not yet be applied to the bridging threads. Theoretically, if a large enough specimen was tested, stable crack propagation would result subsequent to the thread slackness being taken up by 0.3 mm of relative sliding in the specimen. However, the crack propagation in the stitched, RTM specimens displayed a stable behaviour. Thus after the crack had propagated several millimetres the specimens were unloaded and the crack tip marked. The specimens were subsequently loaded again. This process was repeated several times until the crack had reached the central loading pin. The crack lengths were measured using the travelling microscope.

Analysis

Since the layup of the laminates under study was essentially unidirectional, the mode II interlaminar fracture toughness in terms of the energy release rate was determined using the following expression:

$$G_{IIR} = \frac{9}{16} \frac{P^2}{w^2 E_c h_c^3} (a + \alpha h_c)^2 \quad (5)$$

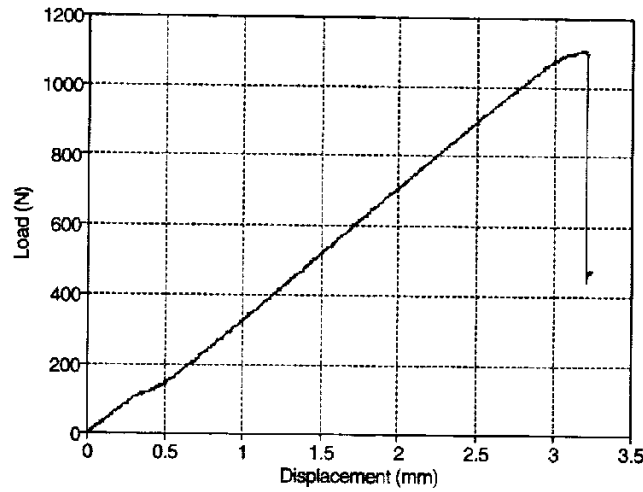
where α is a shear correction factor which depends on the ratio of axial (E_{11}) and out-of-plane shear (G_{12}) stiffnesses of the beam. For unidirectional composites, α can be approximated by [29]

$$\alpha = 0.13 \left(\frac{E_{11}}{G_{12}} \right)^{1/2} \quad (6)$$

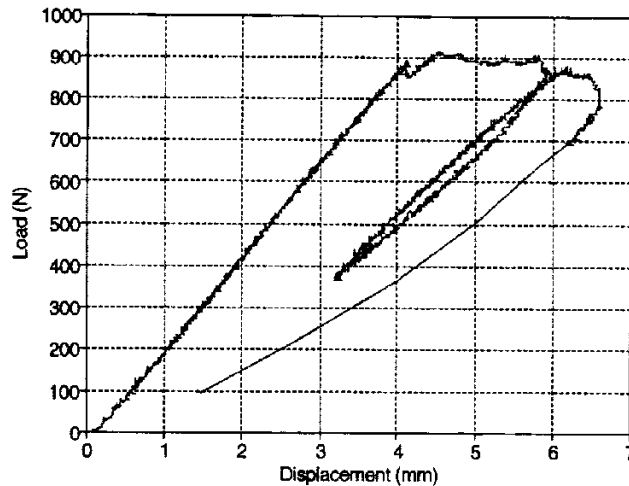
Results and Discussion

Typical load versus deflection curves obtained from testing the stitched and unstitched laminates using the ENF geometry are shown in Figure 12. It can be seen from Figure 12a that the load increases linearly in the case of the unstitched specimen and when the energy release rate exceeds the critical energy release rate, the crack propagates in an unstable manner to the central loading pin, leading to a sudden load drop. In the case of stitched composites, the crack growth was generally stable and initially there was an increase in the crack propagation load with crack growth due to the development of bridging stitch thread zone (see Figure 12b). This leads to an increase in the delamination toughness and hence a rising R-curve. Some unstable crack propagation leading to a sudden load drop and then crack arrest at the next stitch line was also observed. This artifact was probably related to stitch line breakage indicating that steady-state was reached. This behaviour was quite obvious in the

case of low stitch density (4 stitch/cm²). However, in the case of high stitch density (12 stitch/cm²), this was not very obvious as the distance between the stitch lines decreased.



(a)



(b)

Fig. 12: The load versus displacement plot for (a) an unstitched ENF specimen and (b) for an ENF specimen stitched with 2-ply Kevlar thread at 12 st/cm².

After every crack growth step, the specimen was unloaded, the crack length marked, and the specimen was loaded again and the crack propagation load was determined. The complete R-curve was then determined using equation (5) from the load required for the crack to propagate at a known crack length. The out-of-plane shear modulus was estimated to be 5.8 GPa and the axial modulus was assumed to be same as the flexural modulus as the layup was essentially unidirectional. The R-curves are shown in Figure 13 where each specimen tested is marked by a different symbol. The mode II delamination toughness values, G_{IIRs} , are presented in Table 9. All values presented are the averages of 4-6 tests.

A comparison of the critical G_{IIc} values calculated for the unstitched specimens with the initiation G_{IIi} values determined from the respective R-curves established a slight increase in toughness with the advent of stitching (Table 9). Typically, the R-curves (Figure 13) showed the establishment of a steady-state zone. The improvement was in excess of 100% when compared to the G_{IIc} of the unstitched specimens and closer to 200% for some of the higher

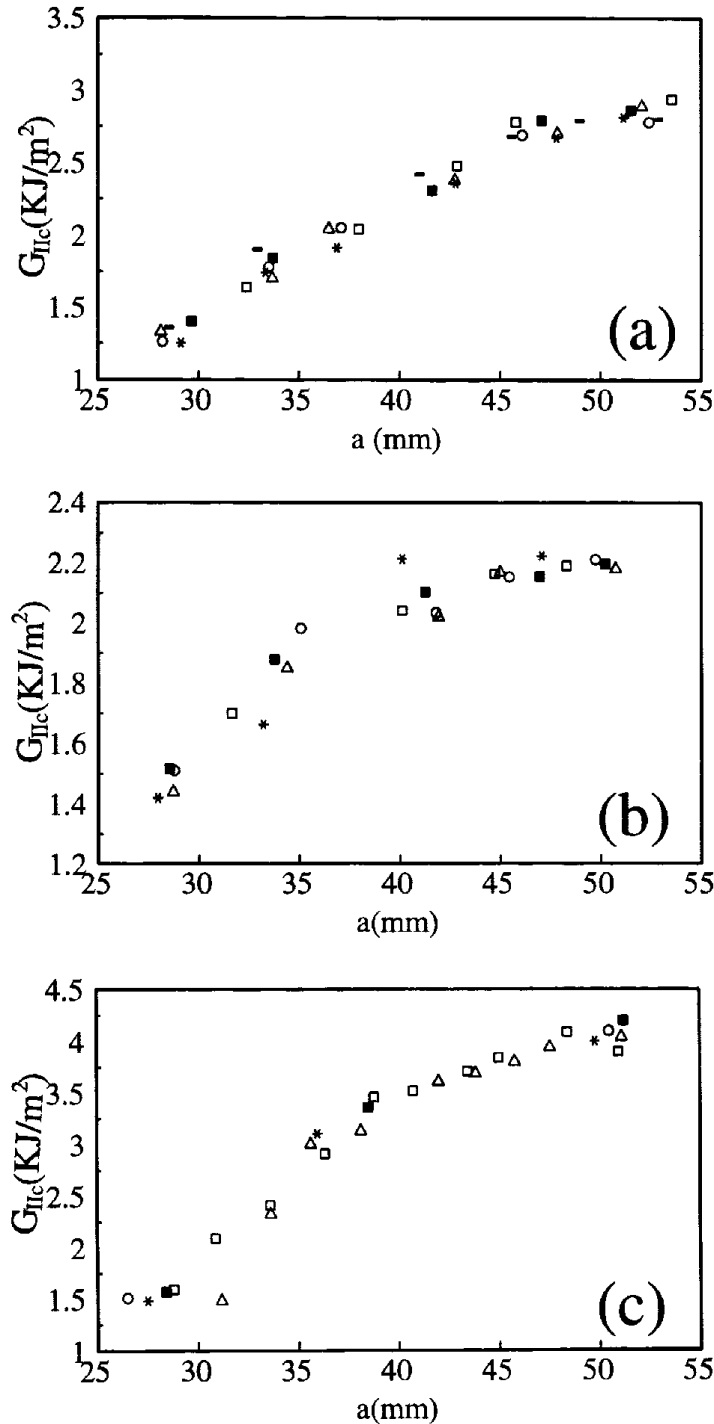


Fig. 13: R-curves determined for RTM specimens stitched with 2-ply Kevlar thread at (a) 4st/cm², (b) 4st/cm², discontinuous and (c) 12st/cm². The R-curves for RTM specimens stitched with 3-ply and 4-ply Kevlar threads were similar.

stitch densities. However, to ensure the steady-state condition has been attained, it may be necessary to employ longer crack propagation lengths. The significant increase in toughness transpired mainly from the development of crack closure traction due to the bridging stitches. Increasing stitch density resulted in considerable improvement in G_{IIRs} . Increasing thread diameter also generated some improvement in G_{IIRs} (Table 9).

Micromechanical Model

The micromechanics-based theoretical model developed by Jain and Mai [2] has been employed to predict the improvement in mode II delamination toughness. The model assumes that the thread failure mechanism, as the crack propagates, consists of the elastic stretching of the stitches followed by rupture in the crack plane. The tensile strength of the stitching thread is assumed to be single-valued. To determine the load carried by the stitches, the frictional shear stress between the thread and the matrix is neglected and the load supported by each stitch is approximated from the elastic elongation of the thread. The energy release rate available for crack propagation is given by [2]:

$$G_{II} = \frac{A^*}{\cosh^2(\lambda\Delta a)} \left\{ \tau \left(\frac{\sinh(\lambda\Delta a)}{\lambda} + a_0 + \alpha h_c \right) - \frac{\lambda}{A^*} \left(\frac{\alpha_1}{\alpha_2} \right) \sinh(\lambda\Delta a) \right\}^2 \quad (7)$$

where τ is the shear stress and is related to the applied load P , α is the correction factor to include shear deformation, α_1 and α_2 are stitching parameters, and λ is related to material properties through A^* and α_1 . The expressions for τ , A^* , α , α_1 , α_2 , and λ may be found in Ref. [2]. Using the crack propagation condition, $G_{II} = G_{IIc}$, where G_{IIc} is the critical energy release rate for the unstitched composite, the shear stress τ required for crack propagation can be determined. Then the energy release rate from the applied load is calculated from:

$$G_{IIR} = A^* \tau^2 (a + \alpha h_c)^2 \quad (8)$$

With an increase in crack length a , the energy release rate increases and steady-state is attained when the stitches start breaking. The condition for steady-state attainment is

$$A^* \tau \left\{ \frac{1}{\lambda^2} - \frac{1}{\lambda^2 \cosh(\lambda\Delta a)} + \frac{a_0}{\lambda} \tanh(\lambda\Delta a) \right\} + \frac{\alpha_1}{\alpha_2} \frac{1}{\cosh(\lambda\Delta a)} \geq \frac{\sigma_{fu} A_f (h_c + 0.5L_p)}{A_f E_f + F_t} \quad (9)$$

where σ_{fu} is the thread rupture strength.

The geometric and material parameters used to determine the effect of stitching on the mode II delamination toughness are given in Table 7. The energy release rate required to initiate the crack propagation in stitched laminates was taken to be that of the unstitched specimen, i.e. $G_{IIc} = 1.3 \text{ KJ/m}^2$. From SEM observation, it was found that breakage of the thread takes place in the crack plane rather than at the stitch loop on the surface. For this reason, the thread tensile strength, σ_{fu} , was taken as the stitched thread strength (Table 1).

Table 9: The mode II delamination toughness values determined experimentally.

RTM SPECIMEN	G_{IRI} (KJ/m ²)	G_{IRS} (KJ/m ²)	Improvement Factor
unstitched	1.29 ±0.10	--	--
2-ply K 4st/cm ²	1.45 ±0.02	2.98 ± 0.05	2.3
2-ply K 4st/cm ² (1)	1.76 ±0.10	2.30 ±0.05	1.8
2-ply K 8st/cm ²	1.50 ±0.05	3.62 ±0.03	2.8
2-ply K 12st/cm ²	1.51 ±0.09	4.10 ±0.05	3.2
3-ply K 4st/cm ²	1.43 ±0.04	3.06 ±0.06	2.4
4-ply K 4st/cm ²	1.52 ±0.03	3.14 ±0.10	2.4
4-ply K 8st/cm ²	1.61 ±0.11	3.70 ±0.09	2.9

K - Kevlar® thread and (1) - Discontinuous stitch

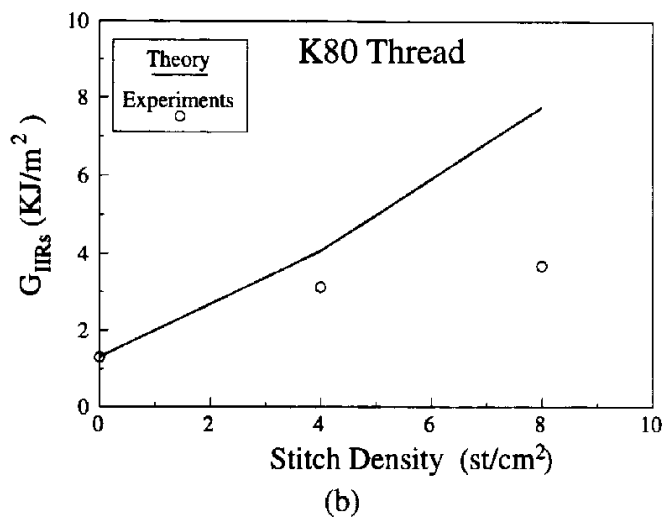
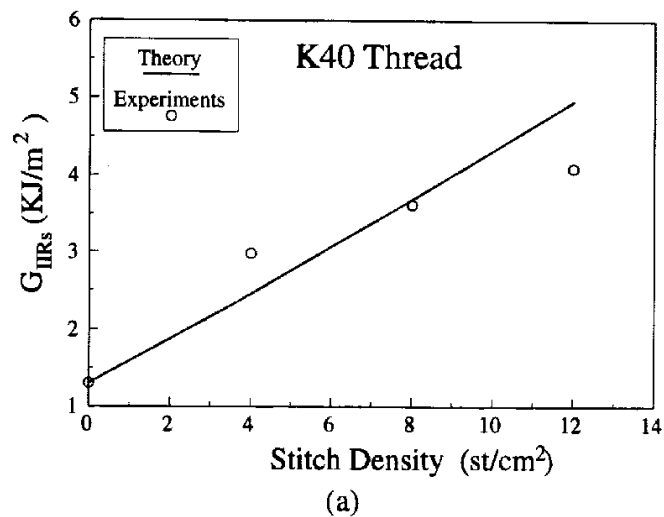


Fig. 14: Comparison of experimental results and theoretical predictions showing trend with stitch density for (a) 2-ply Kevlar thread and (b) 4-ply Kevlar thread.

The comparisons between experimental results and theoretical predictions are presented in Figures 14 and 15. In the case of 2-ply Kevlar (K40) thread, the correlation between theory and experiments was reasonable (see Figure 14a). However, in the case of 4-ply Kevlar (K80) thread, the theoretical predictions are higher than the experimental data. Similar trends were observed when we examined the effect of stitching on mode I delamination toughness. This ensures the accuracy of the model and, therefore, the discrepancies can be attributed to the inaccurate thread properties. The model can be further improved by using a more accurate force-displacement relationship for the thread in the composite instead of using a simple elastic constitutive law and by accounting for the effect of bending of stitches due to the relative slip of the top and bottom parts of the ENF specimen.

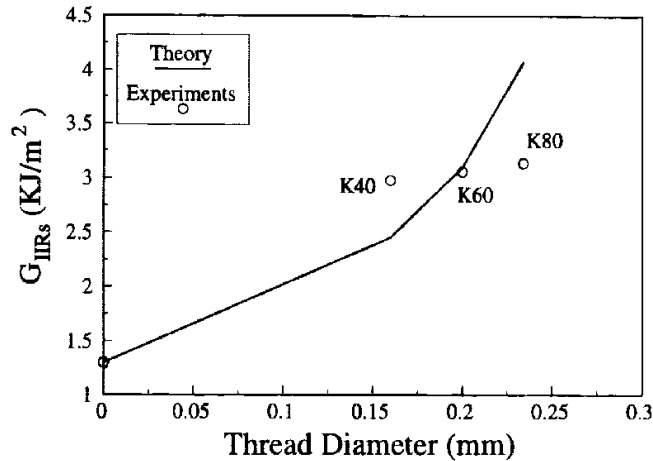


Fig. 15: Comparison of experimental results and theoretical predictions with Kevlar thread diameter at 4st/cm².

CONCLUSIONS

It has been determined that the addition of through-thickness reinforcement in the form of stitches produces significant improvements in both mode I and mode II delamination toughness. The use of long aluminium tabs to prevent cantilever failure results in underestimation of the improvement in mode I delamination toughness. The correlation between theoretical predictions based on the models developed by Jain and Mai [1,2] and experimentally determined toughness was found to be good.

ACKNOWLEDGEMENTS

We wish to thank our past and present colleagues at Sydney University, particularly Kimberley Dransfield and Caroline Baillie, and others at the CRC-ACS for their contributions in the form of original data and useful discussions which have made this keynote lecture possible. Partial support by the Australian Research Council to one of us (YWM) on this project is much appreciated. CRC-ACS also kindly provided the RTM samples for testing.

REFERENCES

- [1] Jain, L.K. and Mai, Y.-W., "On the Effect of Stitching on Mode I Delamination Toughness of Laminated Composites," *Comp. Sci Tech.*, Vol. 51 (1994), pp. 331-345.

- [2] Jain, L.K. and Mai, Y.-W., "Determination of Mode II Delamination Toughness of Stitched Laminated Composites," *Comp. Sci Tech.*, Vol. 55 (1995), pp. 241-253.
- [3] Wilkins, D.J., "The Engineering Significance of Defects in Composite Structures," AGARD Conference Proceedings, No. 355, Elsevier, London, 1983.
- [4] Kim, J.K., Baillie, C., Poh, J. and Mai, Y.-W., "Fracture Toughness of CFRP with Modified Epoxy Matrices," *Comp. Sci and Tech.*, Vol. 43 (1992) pp 283-297.
- [5] Kim, J.K., Mackay, D., and Mai, Y.-W., "Drop-Weight Impact Tolerance of CFRP with Rubber Modified Epoxy Matrices," *Composites*, Vol. 24 (1993) pp 485-494.
- [6] Mai, Y.-W., Cotterell, B. and Lord, R., "On Fibre Composites with Partial Interlaminar Bonding," in *Progress in Science and Engineering of Composite Materials* (T. Hyashi, K. Kawato and S. Umekawa, eds.), Japan Society of Composite Materials, 1 (1982) 271-278.
- [7] Dransfield, K.A., Baillie, C.A. and Mai, Y.-W., "Improving the Delamination Resistance of CFRP by Stitching - A Review", *Comp.Sci and Tech.*, Vol.50 (1994) pp305-317.
- [8] Kim, J.K., Baillie, C.A., Poh, J. and Mai, Y.-W., "Fracture Toughness of CFPR with Modified Epoxy Resin Matrices", *Comp. Sci. and Tech.*, (1992) pp283.
- [9] Guenon, V.A., Chou, T-W. and Gillespie, J.W. Jr, "Toughness Properties of a Three-dimensional Carbon-Epoxy Composite", *J.of Mat.Sci*, Vol.24 (1989) pp4168-4175.
- [10] Ogo, Y., "The Effect of Stitching on In-plane and Interlaminar Properties of Carbon/Epoxy Fabric Laminates", M.Sc. Thesis, Univ. of Delaware (1987).
- [11] Sharma, S.K., and Sankar, B.V., "Effect of Stitching on impact and Interlaminar Properties of Graphite/Epoxy laminates", *Proceedings of the 9th technical conference of the American Society for Composites*, Delaware (1994).
- [12] Morales, A., "Structural Stitching of Textile Preforms", 22nd Int.SAMPE Tech.Conf. (Nov.6-8 1990) pp1217-1230.
- [13] Mignery, L.A., Tan, T.M. and Sun, C.T., "The Use of Stitching to Suppress Delamination in Laminated Composites", *ASTM STP 876* (1985) pp371-385.
- [14] Su, K.B., "Delamination Resistance of Stitched Thermoplastic Matrix Composite Laminates", *ASTM STP 1044* (1989) pp279-300.
- [15] Farley, G.L., Smith, B.T. and Maiden, J., "Compression Response of Thick Layer Composite Laminates with Through-the-Thickness Reinforcement", *J.of Reinf.Plastics and Comp.*, Vol.11 (1992) pp787-811.
- [16] Chung, W.C., Jang, B.Z., Chang, T.C., Hwang, L.R. and Wilcox, R.C., "Fracture Behaviour in Stitched Multidirectional Composites", *Mat.Sci. and Eng.*, A112 (1989) pp157-173.

- [17] Pelstring, R.M. and Madan, R.C., "Stitching to Improve Damage Tolerance of Composites", 34th Int.SAMPE Symp. (May 1989) pp1519-1528.
- [18] Dow, M.B., and Smith, D.L., "Damage Tolerant Composite Materials Produced by Stitching Carbon Fibres", 21st Int.SAMPE Tech.Conf. (Sept 1989) pp595-605.
- [19] Liu, D., "Delamination Resistance in Stitched and Unstitched Composite Plates Subjected to Composite Loading", J.of Reinf.Plastics and Comp. (1990) pp59-69.
- [20] Dransfield, K.A., "*Through-Thickness Reinforcement of Carbon Fibre Composites by Stitching*", PhD Thesis, University of Sydney (September 1995).
- [21] Tong, L. and Jain, L.K., "Analysis of Adhesive Bonded Composite Lap Joints with Transverse Stitching," Journal of Applied Composite Materials, Vol. 2 (1995), pp. 243-365.
- [22] Tong, L., Jain, L.K. and Leong, K.H., "Failure of Transversely Stitched RTM Lap Joints," Submitted for publication to Composites Science and Technology (1996).
- [23] Mostovoy, S., Crosley, P.B. and Ripling, E.J., Journal of Materials Science, 2 (1967), pp. 661.
- [24] Dransfield, K., Jain, L.K. and Mai, Y.-W., "On the Effects of Stitching in CFRPs. Part I: Mode I Delamination Toughness," To be submitted for publication (1997).
- [25] Jain, L.K., Dransfield, K. and Mai, Y.-W., "Effect of Reinforcing Tabs on the Mode I Delamination Toughness of Stitched CFRPs,." To be submitted for publication (1997).
- [26] IMMA Handbook of Metals and Alloys, 1990.
- [27] Mouritz, A. and Jain, L.K., Interlaminar Fracture Properties of Stitched Fibreglass Composites, To appear in the proceedings of the 11th International Conference of Composite Materials, July 14-18, Australia (1997).
- [28] Cotterell, B., and Mai, Y.-W., *Fracture Mechanics of Cementitious Materials*, Published by Blackie Academic and Professional, An Imprint of Chapman and Hall, pp. 294 (1996).
- [29] Chatterjee, S.N., "Analysis of Test Specimen for Interlaminar Mode II Fracture Toughness - Part 1. Elastic Laminates", J. of Comp. Mat., Vol.25 (1991) pp 47

THE FIRST FAIR DINKUM MACRO-LEVEL FIBROUS COMPOSITE FAILURE CRITERIA

L. J. Hart-Smith

Douglas Aircraft Company[©]
McDonnell Douglas Corporation
Long Beach, California

SUMMARY: The strength of fibre-polymer composites is characterized mechanistically, needing separate equations for each mode of failure in each constituent of the so-called composite material. The traditional maximum-shear-stress (Tresca) criterion is generalized to transversely isotropic materials like carbon fibres and a case is made that this is the best representation possible, at the fibre level, for both carbon and glass fibres. In converting this micro-level phenomenon to the macro- (or ply) level, it is found that the original (untruncated) maximum-strain model is more appropriate for glass fibres, but that the truncated maximum-strain model is necessary for carbon fibres. This conversion is accomplished via a formula derived to relate the transverse strains in the fibres to those in the laminae. The work of others, who have mechanistically characterized the strength limits imposed by matrix failures, is cited. This is the dominant failure mechanism for fibreglass-reinforced polymer composites. Well-designed carbon-fibre-reinforced laminates, however, fail consistently in the fibres; this permits far simpler characterizations of matrix failures. In explaining the use of the maximum-shear-stress criterion in the present context, comparisons are drawn with the von Mises/Hencky distortional energy model and it is suggested that both theories are equivalent. The only circumstances under which the maximum-shear-stress theory can be expressed in terms of critical differences between principal stresses is shown to be for isotropic materials. For anisotropic materials, only those stress or strain components which contribute to distortional strain energy should be included in the assessment. Other stress and strain components must be omitted. Possibly new generalizations of both the Tresca and von Mises/Hencky criteria have been provided for totally anisotropic materials.

KEYWORDS: composite failure criteria, composite laminate strengths, analysis methods, mechanistic considerations, fibre failures, matrix failures

INTRODUCTION AND HISTORICAL BACKGROUND

Published analyses of the strength of fibre-polymer composites fall mainly into two categories. The first is micromechanical, where a distinction is drawn between the constituents of so-called composite materials. Separate analyses have been prepared for failures in the fibres, the matrix, and the interface between them. There are many such papers covering one or more aspects of this problem, although the author is unaware of any which have evolved to the state of a *complete* design and analysis procedure for composite aircraft structures. There are also a small number of simple and useful noninteractive failure models at the macromechanical level, such as netting theory and the maximum-strain and maximum-stress failure models. Analysis methods like those developed for plywood have also been

[©] Copyright, 1997, McDonnell Douglas Corporation. All Rights Reserved

effective when applied to fibre-polymer composites at the *laminate* level. (They have been very useful for predicting fibre failures, but have only limited capability in regard to matrix failures.) The second main category is interactive macromechanical analyses where, for the most part, no attempt has been made to relate the predictions to physical phenomena. Indeed, the authors of the most well known such theory assert that it is impossible to do so. Nevertheless, the mathematical elegance and apparent completeness of such theories has led to their widespread teaching. Some of these interactive analyses, for *homogeneous* anisotropic solids, can be applied to real materials, like rolled metallic plates and extrusions (and even to individual isolated carbon fibres), but they do not realistically characterize *heterogeneous* fibre-polymer composites of materials. Other such theories can best be described as awaiting the discovery of materials to which they may be applied.

The author's occupational environment, in the aircraft industry, is one in which many of his counterparts have recognized that there is a need for *reliable* analysis methods which are also simpler to use and understand than micromechanics, even if they were based in part on empirical techniques which might be invalid for the composite materials used in other industries. Unfortunately, no such theory arose when advanced composites were still in their infancy, although the noninteractive maximum-strain model came quite close (see Ref. 1), and many in the aerospace industry have benefited from its use, with and without empirical modifications. Had an entirely suitable method been developed then, it might also have resulted in a better understanding of *how* to characterize composite materials, and of changes in *which* properties justified an expensive new allowables program, while changes in others did *not*. Unfortunately, the tests by which composite laminae are characterized today have been defined more by the need for inputs for interactive failure theories than by what is scientifically the most appropriate set of data. There is still a widespread belief that *any* change in even *one* measured property requires that a "new" composite material be characterized. This is simply not so, and one consequence of failing to acknowledge this is a major burden on the operators of composite aircraft structures whenever repairs are needed. The author's early career was spent on bonded and bolted joints and, by the time he became involved in composite failure criteria, the prevailing analysis methods revolved around computer codes of overly simplistic interactive models. These are so deeply embedded in finite-element analysis procedures that it is now extremely difficult to replace them by other models which relate to the actual mechanical behaviour of the materials, particularly in regard to matrix failures.

The author's work has focussed on fibre failures in well-designed carbon-epoxy laminates and the like, which has until recently spared him the need to also consider what happens when the matrix fails first (as it usually does in fibreglass-reinforced polymer composites). Characterizing the *in-situ* matrix strength of each ply in a composite laminate, or even recognizing that it *wasn't* the same as measured on an isolated unidirectional lamina, has been the only major problem with the widely used, and coded, noninteractive maximum-strain failure model for fibre-polymer composites. This theory has worked well for the aircraft industry, provided that one *disregarded* any and all predictions of matrix failures based on *measured* lamina properties. Most industrial companies (as distinct from academic institutions) have applied selective truncations to this theory, particularly for fibre failures under in-plane-shear loads. However, the inability to reliably predict failures has forced us to resort to testing more and larger components than is customary for metallic structures.

During the past quarter century, the author developed, and piece by piece refined, an extremely simple rule-of-mixtures analysis method, the "Ten-Percent Rule" (Ref.'s 2 and 3)

which was so simple that the coefficients governing the effects of fibre pattern and state of biaxial stress could be evaluated by mere mental arithmetic. The effects of environment and of different reference material properties are covered by mechanical tests of the longitudinal tension and compression strengths of the laminae from which the laminates are made. Significantly, *no* transverse strengths or stiffnesses need be measured. Yet this simple method is without peer in analyzing advanced all-composite structures (and one complete aircraft) which have actually flown. Parallel work, using much the same basic physical model but including measured matrix-dominated stiffnesses, while presenting it in a form suitable for use with large automated finite-element analyses, has taken longer to complete – and even longer to gain acceptance. It has been challenged and rejected by many established experts in the field because, by its nature, it cannot coexist with most older well-established theories. They cannot all be correct. While some such criticism has resulted in detailed improvements to the author's model, a final resolution has been delayed by the lack of valid, or in some cases *any*, test data for discriminating states of stress in selected laminates.

The author has therefore tried to publicize the need for change by using the theories he has challenged to make predictions which contradict other predictions made with the same theories (see Ref. 4). Application of the principle of *reductio ad absurdum* has exposed additional fundamental problems with these theories. The message is beginning to get through, and is firmly accepted by many of the younger generation in academia. Replacing existing computer codes is a greater challenge, however. It can be difficult to match measured and predicted strengths using a new theory which permits only one attempt to do so. Older theories containing adjustable unmeasurable parameters which are not tied to any specific lamina or laminate properties permit multiple attempts at the solution. To be fair, others have accepted a different message – that *not needing* to make such adjustments to matrix-dominated properties is even better.

What distinguishes the author's failure theory for fibre-dominated composite laminates is the use of a generalization of the maximum-shear-stress (Tresca) criterion, from as long ago as 1983, although it was not until 1988 that the author recognized the need to express the criterion on the strain (rather than stress) plane (see Ref. 5). From the outset, the possibility of additional failure mechanisms was recognized – brittle fracture in tension, and some form of instability in compression. Some experts have expressed their conviction that carbon fibres, in particular, *cannot* fail in shear. Yet the fact is that axial tension and compression tests alone could not possibly explain fibre failures under loads which were not aligned *exactly* along the axis of the fibres; they lie on two flat parallel surfaces of a failure envelope, which would be unbounded in the other direction. If fibre shear failures were truly impossible, the *transverse strengths of the fibres* in tension and compression would either *have* to be infinite, or be limited by still more independent failure mechanisms, such as splitting of the fibres under transverse tension. Avoiding this issue by asserting that the matrix was not strong enough to fail the fibres under transverse loads is not at all the same as proving that shear failures *cannot* occur in the fibres. As it transpired, the author was not the first to recognize that carbon fibres could fail by shear when embedded in epoxy matrices (see Ref. 6). However, he does seem to have been the first to formulate an entire failure criterion around this mechanism, permitting it to be truncated *locally* by other mechanisms as need be. (Most of what the author has learned about or contributed to the art of predicting matrix failures cannot be expressed so simply. Nevertheless, an empirical constant-transverse-stress matrix *cracking* cut-off can be added, one laminate at a time. Covering *multiple* fibre patterns for such failure modes would require the use of fracture mechanics, as in Ref. 7.)

Many of the published failure criteria for composite materials are inconsistent with the mechanistic approach followed by the author and by some other researchers. Those failure models with which the author disagrees can be identified by the following characteristics. Each involves one or more equations in which there are reference strengths for *two* constituents (fibre and matrix) in the *same* equation. Each relies on progressive-failure or ply-discounting theories to “modify” unacceptable “first-ply failure” estimates into more acceptable “last-ply failure” estimates, usually by changing the matrix stiffnesses to allow for “cracks” which seem to miraculously heal themselves before the application of the next load condition. (If the healing failed to occur, there would be a need to account for path-dependent strengths of laminates, as a function of the sequence and environments in which each subcritical load was applied.) Somewhere in the text for these theories is a statement that each applies to “anisotropic solids”, with no accompanying concession that fibre-polymer composites of materials are *heterogeneous* and, therefore, *not* governed by strength theories for *homogeneous* materials only. There is also an implicit position adopted that, once a “lamina” has been characterized by test *in isolation*, those *same* properties are retained under all circumstances, no matter in what laminate the lamina may be *embedded*. (This is the key to the ply-by-ply decomposition of laminates when seeking to predict failures.)

The author’s criticism of these interactive theories, both on fundamental grounds and via obviously unacceptable specific predictions, has failed to convince many in America. Nevertheless, it may be noted that, with few if any exceptions, every developer of such a theory has implicitly disassociated himself from it subsequently, by rejecting all first-ply-failure calculations from his *own* theory and calculating a second set of answers, the last-ply-failure predictions, using *someone else’s* theory in the form of a close approximation to netting theory, the maximum-strain theory, or the maximum-stress theory. This is done without drawing any attention to the fact that the theories being used were being changed as fast as the matrix-dominated input properties were. The changes are buried in the computer codes and not explained in texts. Significantly, this change in procedures was firmly established long before the author started publishing in this field; in no way was it a response to his criticisms. Ironically, the only *measured* properties used in these last-ply-failure calculations are the same abbreviated set as used in the author’s Ten-Percent Rule. The Ten-Percent Rule is rightly regarded as a mere approximation, albeit an extremely useful one. The interactive failure theories are regarded by many, with the notable exception of this author, as rigorous scientific theories. But where is the difference?

This background needs to be appreciated in understanding how and why the author developed his generalization of the maximum-shear-stress failure model for analyzing fibre-dominated failures in well-designed advanced composite aircraft structures, made mainly from various carbon-epoxies. In retrospect, it is now apparent that his work on fibre failures *needs* complementing by the best of work by others on mechanistic theories for matrix failures, mainly by micromechanics and particularly for fibreglass-reinforced polymer composites. Perhaps the greatest pioneer in this aspect of the work is Puck, whose first paper on the subject was published in 1969 (see Ref. 8). Ironically, Puck and his students expressed concern about the very same theories the author was later to condemn, but for the opposite reason. They were rightly troubled by interactive failure theories in which the characterization of *matrix* strengths was invalidated by the erroneous inclusion of terms pertaining to fibre failures, in exactly the same way as the author was concerned about the erroneous influence of matrix-stress ratios on the prediction of *fibre* failures. There can be no doubt that Puck and his students have proceeded on the correct path and contributed disproportionately to the understanding of *their* subject. It is now clear to the author, and to

Puck and his colleagues at least, that their use of the simple maximum-strain failure model to characterize the strength of *glass* fibres, at the lamina level, really was the most appropriate. The author may have eventually explained *why* this was so, when the governing mechanism was one of stress, but he has not affected their theories other than to draw attention to the need to include residual intralaminar thermal stresses. Conversely, their work with glass-fibre laminates is shown here *not* to invalidate the author's efforts to develop better failure models for carbon-fibres, with which they concur. In the carbon-epoxy aircraft world in which the author lived, however, quite simple matrix-failure criteria were adequate – provided that one adhered to straightforward design rules to preclude structurally significant matrix cracking.

THE NEED FOR MECHANISTIC FAILURE MODELS FOR FIBRE-POLYMER COMPOSITES

The first point of departure of the author's composite failure theories from classical macromechanics is outright rejection of the old notion that it is possible to formulate such a theory without tying *all* estimates of strength precisely to a related failure mechanism. Fig. 1 summarizes the author's views on this subject, views which are shared by many other researchers, albeit most of whom have not developed a macroscopic failure model themselves.

SEPARATE CHARACTERIZATIONS ARE NEEDED FOR EACH FAILURE MECHANISM IN EACH CONSTITUENT OF THE COMPOSITE OF MATERIALS

INTERACTIONS BETWEEN STRESSES AFFECTING THE SAME FAILURE MODE IN THE SAME CONSTITUENT OF THE COMPOSITE ARE PERMITTED

INTERACTIONS BETWEEN DIFFERENT FAILURE MODES ARE SCIENTIFICALLY INCORRECT

TYPICAL FAILURE MECHANISMS FOR FIBRE-POLYMER COMPOSITES:

	FRACTURE OF FIBRES AT FLAWS AND DEFECTS, UNDER LONGITUDINAL TENSION
	FAILURE OF FIBRES REMOTE FROM ANY FLAWS OR DEFECTS, UNDER TENSILE
LOADS	MICRO-INSTABILITY, OR KINKING, OF FIBRES UNDER COMPRESSIVE LOADS
	SHEAR FAILURE OF WELL-STABILIZED FIBRES UNDER COMPRESSIVE LOADS
	DUCTILE FAILURE OF MATRIX, WITHOUT CRACKING, UNDER IN-PLANE LOADS
	CRACKING OF MATRIX BETWEEN THE FIBRES UNDER TRANSVERSE-TENSION
LOADS,	
	WHICH INVOLVES BOTH A MATERIAL PROPERTY AND A GEOMETRIC PARAMETER
	INTERFACIAL FAILURE BETWEEN THE FIBRES AND THE MATRIX
	INTERLAMINAR FAILURE OF MATRIX AT EDGES AND DISCONTINUITIES
	DELAMINATIONS BETWEEN THE PLYS UNDER IMPACT OR TRANSVERSE SHEAR
LOADS	
	DELAMINATIONS BETWEEN THICK PLYS INITIATING AT THROUGH-THICKNESS
MATRIX	
	CRACKS WITHIN A TRANSVERSE PLY
	FATIGUE FAILURES IN THIN PLYS CAUSED BY THROUGH-THICKNESS TRANSVERSE
	CRACKS IN ADJACENT THICK PLYS

EACH OF THESE POSSIBILITIES REQUIRES ITS OWN EQUATION, EVEN THOUGH NOT EVERY MODE CAN OCCUR FOR EVERY FIBRE-POLYMER COMBINATION AND EVEN THOUGH SOME MODES CAN BE SUPPRESSED BY SKILLFUL SELECTION OF THE STACKING SEQUENCE

Fig. 1 Specification for fibre-polymer composite failure criteria

Selecting *which* of these many possible failure mechanisms might govern in a particular laminate under a particular set of stresses requires a reference system. If the laminate

contains fibres in more than one direction, only one reference system is unique, at least in the interior, away from local edge effects. This is the *lamina strain field*. Therefore, each possible failure mode, be it in the fibres, the matrix, or an interface, must be *reformulated* at the macro level, even if it is *derived* at the micro level. Only then is it possible to *compare* possible alternative failure modes and identify the most likely to occur. The *lamina stress* field will not suffice, in this regard, for any laminate other than a completely unidirectional tape lamina. Stresses in embedded laminae can be computed only *after* compatibility of deformations has been ensured. It is the relative strains which establish the sequence of failures.

The importance of the difference between stress and strain formulations, and between mechanistic and interactive characterizations is not well understood. For instance, two prominent researchers (who share the author's opinion of interactive composite failure models in the form of a *single* equation involving *four* unrelated measured strengths) developed their own theories around sets of *four* equations, as many as two of which involve *two* unrelated measured reference strengths in the same equation – with no apparent awareness that they were thereby perpetuating the very error they claimed to be eliminating.

The full consequences of homogenizing the fibres and resin are not fully appreciated, either. Obviously, it should not even be *possible* to differentiate between fibre and matrix failures thereafter, but it is *necessary* to do so to implement progressive-failure analyses which are used to enhance the predicted ply strengths. The issue of *how* this is accomplished within the various computer codes has not always been explained. Even so, there is a significant quirk in perhaps the most widely distributed such code. For laminates made from layers of unidirectional tape, the theory predicts first-ply failures in the matrix, followed by higher last-ply failures for tensile loads once the matrix properties have been modified (and lower last-ply failures for compressive loads, via use of yet another equation). On the other hand, for laminates made from layers of woven fabric, the first-ply failures are inevitably predicted to occur in the fibres. However, since there is no cue in the input with which to differentiate between tape and fabric plies, the computer code then proceeds to reduce the stiffnesses of the “failed” fibres and compute a much lower last-ply strength based on the “intact” matrix. This is easy to recognize when solving problems one at a time. But how is the appropriate strength selected deep within a large finite-element analysis of a composite structure?

Another overlooked effect concerns the nature of the test specimen on which the transverse strength of a unidirectional lamina is traditionally measured. Some such measurements have been made on tubes, but most are made on flat coupons. Even though in both cases the *final* failure is a matrix crack between the fibres, through the entire cross section of the specimen, the mechanisms which *trigger* the matrix cracking are very different. Failure of the tubular specimens usually initiates at microcracks in the matrix, which form as the resin cools down after cure. Failure of the flat-coupons, however, usually initiates at the *edges* of the panel, as the result of thermal stresses induced as the matrix shrinks (transversely across the coupon) during the cool-down after cure, and the fibres do not. Consequently, this measured “lamina property” is even more unrelated to the other three than is generally recognized.

Satisfying the requirements for the kind of model indicated by Fig. 1 *requires* that each possible mode of failure be characterized at the micro level first, and *then* be reformulated at the macro level for use in actual analysis of complete multidirectional laminates. It may seem to some that the author's works on composite failure theories failed to take this into account, since no distinction was drawn between strains in the constituents of each lamina. Actually,

he was well aware of this situation many years ago and, for better or worse, chose not to mention it at the time out of fear that the mere mention of the word “micromechanics” would discourage acceptance of his theory by those who needed it the most – analysts who were familiar only with *macromechanical* analyses. The distinction, for the author’s theories, always has been numerically trivial for carbon-epoxy type laminates, although the author has only recently become aware that this was not the case for fibreglass-epoxy type laminates (see Ref. 9). However, this difference between the transverse strain in the fibres and the transverse strain in the lamina has been offered as one “proof” that the 45° cut-offs in the author’s theory do not exist at the lamina level. (The longitudinal strains, parallel to the fibres, *must* be common, of course, except in the immediate vicinity of holes, cut-outs, edges, and breaks in the fibre.) Under the circumstances, it is now necessary to acknowledge the difference openly, both to refute the unsubstantiated criticism and to extend the author’s work to fibreglass reinforced laminates which are used extensively *outside* the aerospace industry.

GENERALIZATION OF THE MAXIMUM-SHEAR STRESS CRITERION TO ORTHOTROPIC MATERIALS SUCH AS CARBON FIBRES

The author’s analysis of fibre failures in composite laminates begins with a generalization of the well-known maximum-shear-stress (Tresca) criterion from homogeneous isotropic solids to homogeneous solids which are only transversely isotropic. Fig. 2 depicts this criterion, often thought of as one denoting yielding but not necessarily so restricted, on both the stress plane, on the left, and the strain plane on the right (both for the special case of zero stress in the third direction). Without this limit on the third principal stress, the two parallel lines with a 45° slope would extend to infinity.

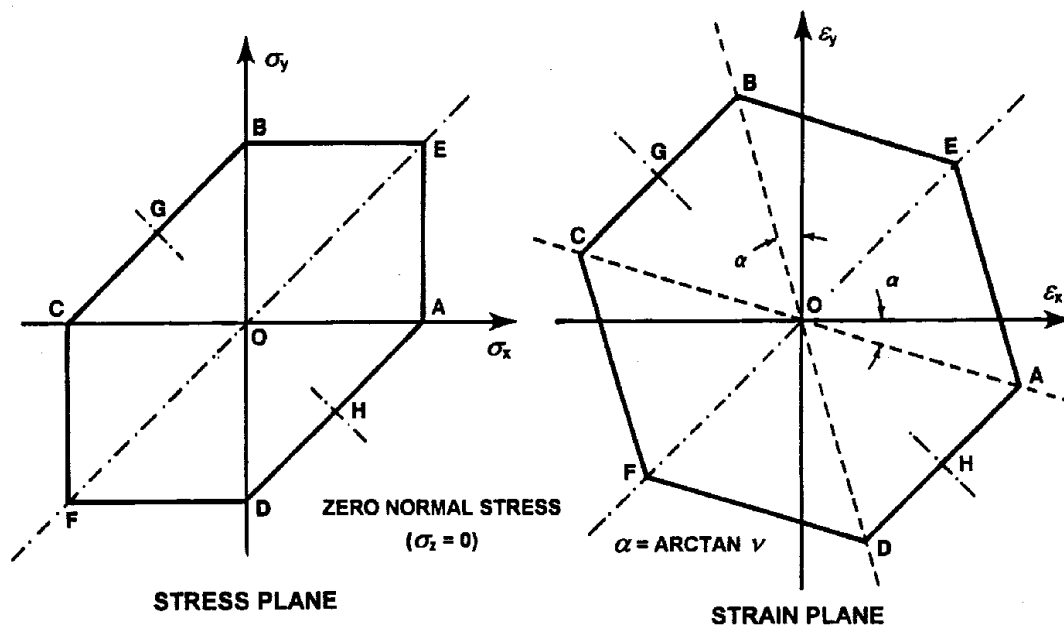


Fig. 2 Maximum-shear-stress (Tresca) condition on the stress and strain planes for isotropic homogeneous materials

What is most significant about Fig. 2 is that it can be constructed *completely* from *only two* elements of data – the strain-to-failure under either unidirectional tension or compression, and

the *single* Poisson's ratio. The tensile and compressive strengths are *necessarily equal*, provided that the failure mechanism is by shear. Since glass fibres are known to be isotropic, *both* versions of Fig. 2 *must* be directly applicable to *all shear failures* of the fibres. Note that this does *NOT* preclude the possibility of alternative failure modes; it only states that the tensile and compressive strengths *must* be equal *IF* the failure mechanism is one of shear.

The diagram *equivalent* to Fig. 2 for transversely isotropic materials, like carbon fibres, can be constructed in exactly the same way, except for the need to distinguish between the *two* Poisson's ratios, as is done in Fig. 3.

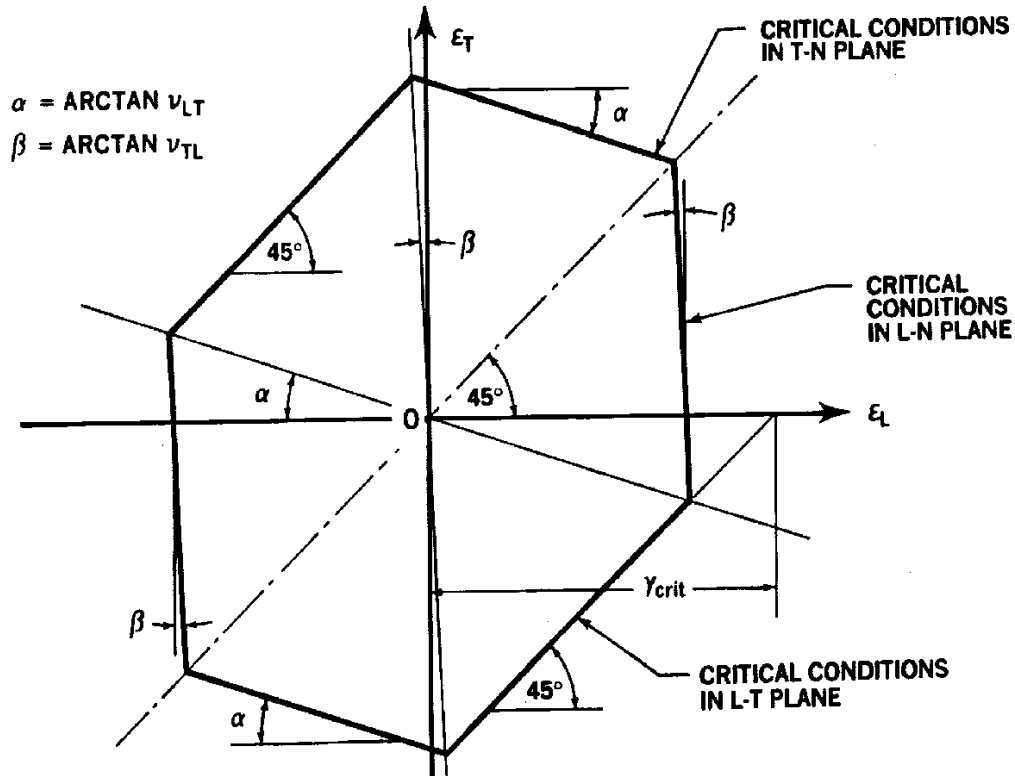


Fig. 3 Shear failure envelope for transversely isotropic materials having equal tension and compression strengths

The mathematical significance of the lines in Fig. 3 is as follows. Along lines AD and CB, there is a constant in-plane *shear strain*;

$$\varepsilon_1 - \varepsilon_2 = (1 + \nu_{LT})\varepsilon_L = \text{CONSTANT} \quad . \quad (1)$$

Along lines AE and CF, the *longitudinal stress* in the fibres is constant;

$$\sigma_L = F_L = \text{CONSTANT} \quad . \quad (2)$$

Along lines BE and DF, the *transverse stress* is constant;

$$\sigma_T = F_T = \text{CONSTANT} \quad . \quad (3)$$

Each corner point in Fig. 3 corresponds with one in Fig. 2. The lines with slopes of α and β are self explanatory, being constant-stress lines. The 45° slope has been a cause for confusion, some believing that it should be drawn at whatever slope would join the failure strains for *measured* longitudinal tension and transverse compression, and vice versa, completely missing the point that doing so would almost certainly violate the presumption of a *COMMON FAILURE MECHANISM* for *every* facet of the failure envelope in Fig. 3. (Other failure mechanisms for some states are stress are very real, and will be addressed later in the derivation. They are simply not germane to the issue under discussion *here*.) Even without being able to measure the transverse fibre strengths in tension and compression, others have challenged the validity of the 45° slope on the basis that, if two of three principal stresses are zero and the transverse stress at failure differs from that in the longitudinal direction, as it undoubtedly does (except for glass fibres which are isotropic), the shear strains at failure cannot possibly be common. This issue was addressed at length in Ref. 10. In a nutshell, the issue is as follows. The maximum-shear-stress failure criterion, in the present context, is really one of *distortional strain energy*, between axes oriented at $\pm 45^\circ$ from the fibre axis. In the case of a homogeneous *isotropic* material, a constant *difference* between longitudinal and transverse stresses- *or* strains-to-failure is a valid assurance that the distortional strain energy does not change. Any relationship for anisotropic materials must *reduce* to this special case for isotropic materials, but it does *not* follow that this special case *restricts* the form of the relationship in more general cases, where there is not a one-to-one relation between overall stresses and strains.

The effect of fibre anisotropy is that the shear stress acting on these planes at $\pm 45^\circ$ to the fibre axes is proportional to the shear strain developed between them, in accordance with some shear modulus *other* than that which could be measured by shearing individual fibres with respect to their 0° and 90° directions. In the case of a transversely isotropic fibre, there are multiple elastic constants but, more importantly, there are stress components which are *NOT* directly proportional to their corresponding strains. Specifically, in the case of planes inclined at $\pm 45^\circ$ from the fibre longitudinal axis, there are now *three* components of the shear stresses. However, only *one* of these components contributes to distortional energy – and only that *one* component can therefore be involved in a failure criterion *for shear*. However, *all three* are involved in a Mohr-circle assessment of the shear stresses, with respect to those axes, as the applied external load varies between one of pure longitudinal load and pure transverse load. *This* is why the longitudinal and transverse strengths of anisotropic materials need *not* be the same, even if failure *is* by shear in both cases. The only requirement that they then be the same is restricted to *isotropic* materials, such as isolated glass fibres. The difference between the mechanically induced longitudinal and transverse strains remains an unambiguous characterization of the shear strain between axes at $\pm 45^\circ$ the fibre axes for both isotropic *and* anisotropic fibres. It should be self evident that the maximum-shear-stress criterion for isotropic materials cannot possibly be directly *generalized* in terms of a constant shear *stress*, per Mohr circles, even when *stress* is known to be the cause of failure, not strain. This is why the author eventually learned to express the generalization in terms of *strains*, instead.

This lack of a one-for-one relation between stress and strain in nonisotropic homogeneous materials is most easily visualized in terms of thermal expansion rather than mechanical distortion. If an unrestrained block of homogeneous isotropic material is uniformly heated, no stresses of *any* kind will be developed. Neither will there be any *shear* strains – only *direct* strains. Consider, next, a large block of homogeneous transversely isotropic material having the properties of carbon fibres, thermally loaded under the same conditions. Again, there can be absolutely *no stresses*, because there are *no restraints*. There are *direct* strains,

as for isotropic materials, but there will necessarily *ALSO* be *shear* strains between planes at $\pm 45^\circ$ from the material axis of symmetry whenever the longitudinal and transverse coefficients of thermal expansion differ. In other words, there would be shear strains in the absence of shear stresses, just as there were components of shear stress with no matching shear strain for the mechanical loads discussed in the previous paragraph. It should be clear that the process of generalizing the maximum-shear-stress criterion (or probably any others for that matter) necessarily *breaks* the traditional one-for-one match between stress and strain with which we have become familiar for isotropic materials.

The construction of Fig. 3 requires *only one* measured strength, just as for Fig. 2. The process is illustrated step by step in Fig. 4.

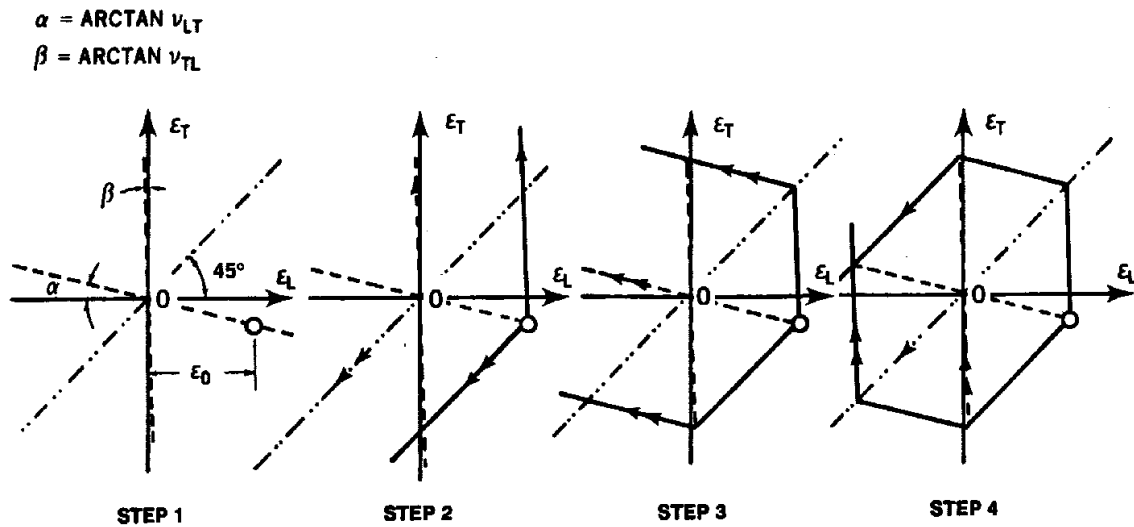


Fig. 4 Construction of complete failure envelope from a single measurement of strength

This process of generating *complete* failure envelopes with only *one* reference strength may be difficult to accept for those who are familiar only with composite failure criteria requiring a *minimum of five* properties (even if only four are actually measured) before they can *begin* to construct the failure envelope. This difficulty can be traced back to a fundamental misinterpretation of Hill's plasticity theory (Ref. 11) by some of the pioneers in the field of composite failure criteria, resulting from a failure to recognize the need for mechanistic failure models. Hill's failure (yield) envelopes can be characterized by *smooth continuous* ellipses *ONLY* because the material he was working with was *homogeneous*, and the situation he was characterizing involved only *ONE* mechanism, yielding! Hill had no need to specify any such restrictions on the validity of *his* theory, because *he* had no intention of ever applying it to any *different* kind of material. The significance of these unstated restrictions was apparently lost on those who sought to adapt his theory to cover distinctly *different* failure mechanisms for every strength it was possible to measure and to apply it to *heterogeneous* fibre-polymer composites. With four *unrelated* strength measurements, only the noninteractive *box* defined by maximum-stress or maximum-strain limits can be justified as a failure envelope. It is true that Hill's theory was formulated in terms of multiple reference strengths, even though they differed very little. But he could equally have formulated it in terms of a *single* reference strength and multiple elastic constants, as in Fig. 5, which is a smooth continuous stress-based ellipse passed through the stresses corresponding with the corner-point strains in Fig. 3. The co-ordinates for the stress-based formulation of

the author's generalization of the maximum-shear-stress criterion are included in Fig. 5, along with the straight lines defining the boundary.

The formula used to plot the ellipse in Fig. 5 is as follows.

$$(\sigma_L)^2 - \left(\frac{1 + \nu_{TL}}{1 + \nu_{LT}} \right) \left(\frac{E_L}{E_T} \right) (\sigma_L \sigma_T) + \left[\left(\frac{1 + \nu_{TL}}{1 + \nu_{LT}} \right) \left(\frac{E_L}{E_T} \right) \right]^2 (\sigma_T)^2 = (F_L)^2 \quad (4)$$

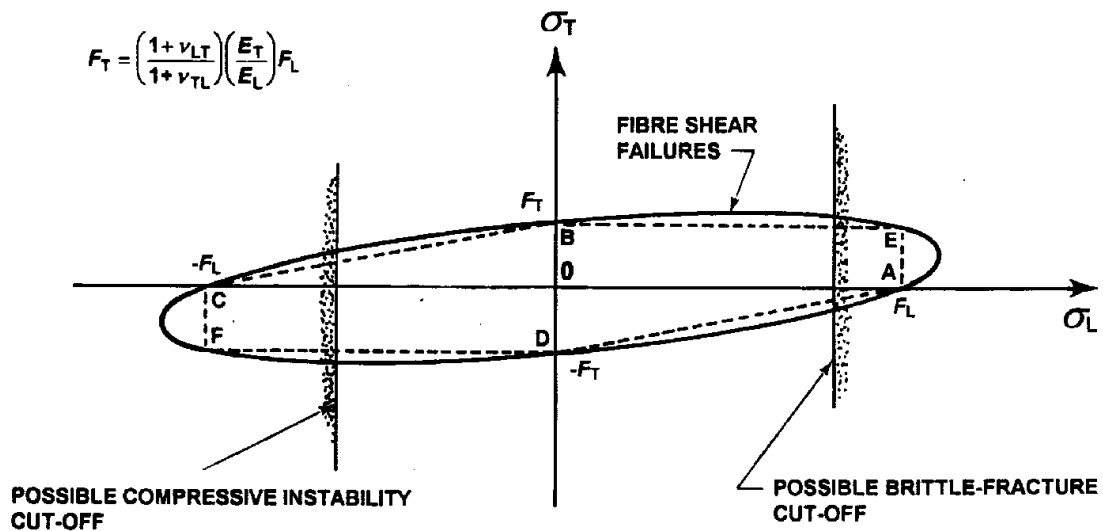


Fig. 5 Equivalent stress-based failure ellipse, also based on a single reference strength

Only *one* reference strength is involved, that for tension (or compression) *along* the length of the fibres, F_L . Yet it is a *complete* failure envelope for this particular mode of failure, and would be the *only* valid one if failure of the fibres by shear were the only possible failure mode. The transverse tension strength of the fibre, in both tension and compression, for *this* mode of failure is

$$F_T = \left(\frac{1 + \nu_{LT}}{1 + \nu_{TL}} \right) \left(\frac{E_T}{E_L} \right) F_L \quad (5)$$

As is shown later, additional failure mechanisms truncate this basic failure envelope *locally* – without affecting it anywhere *else*. (The well publicized concept of a composite failure envelope as akin to a balloon which bulges out somewhere else if it is squeezed locally is not really scientific.) It is most important to comprehend that there is usually absolutely *no interaction* between discrete failure modes when failure criteria are formulated mechanistically. Fig. 5 has all the validity, and all the restrictions of Hill's ellipses, without incurring any of the errors caused by interacting *reference* strengths as is done inappropriately in conventional interactive composite failure criteria. [The equivalence of Eqn (4) to Hill's

plasticity theory for *almost* isotropic materials should be easy enough to establish by relating two of his three reference strengths to the two *independent* elastic constants here.]

A line joining the longitudinal and transverse strengths in Fig. 5 would *not* be inclined at 45° to the stress axes – *unless* the fibres were isotropic. In that case, Eqn (4) would reduce to the well-known von Mises/Hencky relation (Ref. 12). So the generalization proposed by the author *does* revert to what one would expect for isotropic homogeneous materials.

Actually, the issue is a little more complicated than has been portrayed above. Reference to the Appendix in which there is derived an even *more* general version of the maximum-shear-stress criterion will suggest that, for transversely isotropic materials, the lines BE and FD in Fig. 3 should probably be displaced to another pair of lines parallel to these two, but at a different distance from the origin. Since a failure to explain this would undoubtedly be viewed by some as another opportunity to question the validity of his work, the author feels obliged to clarify the issue, even though there is no indication that the associated phenomena have ever been observed in fibre-polymer composites. Doing so also provides an opportunity to expound on the physical significance of *all* of the lines in Fig. 3. Were it not for the restriction to the absence of normal stress, the lines AD and CB in Fig. 3 could be projected indefinitely and *every* point on them would be associated with the *same* critical shear strain (and stress component) on planes at $\pm 45^\circ$ from the fibre axes. The critical conditions on these lines would be developed in the longitudinal-transverse (L-T) plane of the fibres. The line FE could likewise be extended to infinity in both directions, and would signify the locus of points for which this increment of strain energy was zero.

The lines AE and CF can likewise be extended indefinitely, if the normal stress were adjusted to suit. These two lines represent critical conditions in the longitudinal-normal (L-N) plane of the fibre. At points A and C, the critical shear-strain conditions are the same for *both* planes, but only because the fibres have properties which are symmetric about their length. If this were not the case, they too would be displaced to parallel locations, equidistant from the origin, but at a different distance. Consider a purely longitudinal load in a fibre, along the line OA in Fig. 3. As the load is increased, critical in-plane shear conditions are identified as being reached at point A in the L-T plane, at least. If we pretend that the fibre properties were *not* symmetric, we could postulate that it was necessary to continue further along OA until critical conditions were reached for the L-N plane. Having got to this point, the next question is what in-plane stresses, if any, can be added to this uniaxial load without altering the criticality in the L-N plane of the shear strains *and* stresses in the fibre. Only a purely transverse stress, in the T-direction, is capable of doing so, since only it can induce *absolutely zero* stresses in the L-N plane. It would induce *strains* in that plane, of course but, in the absence of any matching stresses, these could neither add to nor subtract from the distortional strain energy in the fibre. Fig. 6 shows these displaced lines AE and CF extending to infinity in both directions, as well as the earlier extended lines AD and BC. These four lines define a parallelogram, with *two* different levels of critical distortional energy, depending on which sides attention is focussed.

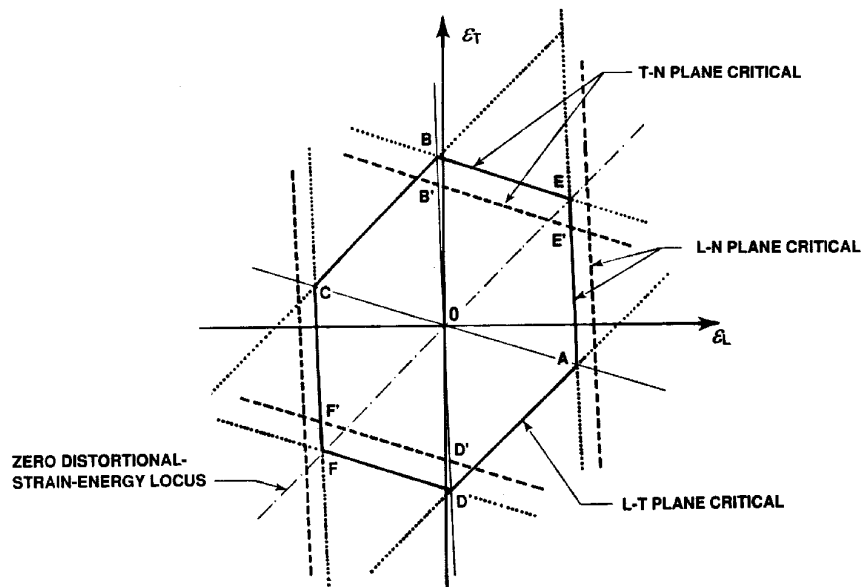


Fig. 6 Strain-based failure envelope for materials lacking transverse isotropy

If, instead of a longitudinal load in the fibres, along the lines OA or OC, a transverse load were applied along lines OB or OD in Fig. 3, the same process would be followed. At points D and B, critical conditions would develop in the L-T plane. At some greater, or probably lesser distance, a *different* critical shear-strain condition would be reached in the T-N plane. Only, in this case, the distinction need not be artificial, since the transverse isotropy of the fibre implies that the critical shear strains *could* differ between these planes. Suppose that these critical conditions in the T-N plane develop at points the B' and D' shown in Fig. 6. The only possible additional stresses which can be applied without changing *these* critical conditions in the T-N plane are tensile or compressive stresses along the length of the fibres, i.e., the L-direction. In other words, they must be parallel to, but displaced from, the lines BE and FD.

An attempt to derive an ellipse equivalent to that in Eqn (4), with the same longitudinal and transverse strengths, at Points A and B in Fig. 5, but with a different biaxial strength at point E, resulted in a surprising finding. It was not *possible* to do so with only the one independent material reference strength F_L . (It *is* possible to do so when the tensile and compressive strengths differ, of course. But this necessarily implies *different* failure mechanisms which should *not* be interacted in a *single* ellipse. Two independent equations are needed.) This uniqueness implies that, if the lines B'E' and F'D' in Fig. 6 did not lie exactly on BE and FD, they must lie on *another* ellipse in Fig. 5, not on a distortion of the one shown. This is explained by the *superposition* of two ellipses in Fig. 7, one for each distinct critical condition. Significantly, that for failures in the T-N plane *must* be longer and narrower than the basic envelope for failures in the L-T and L-N planes, or the measured longitudinal strengths would be undercut. The transverse strengths are undercut but cannot be directly measured in either event; matrix failures would govern.

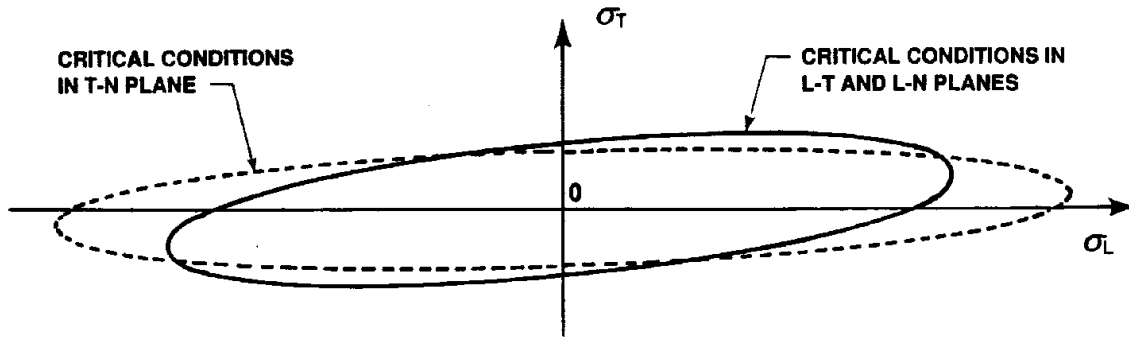


Fig. 7 Characterization, on the lamina stress plane, of distinct fibre-failure mechanisms by multiple ellipses, instead of by a single distorted shape

The fibre failure mechanisms would be quite different. When critical conditions developed in the L-T or L-N planes, the failure surface would be inclined at 45° from the longitudinal axis of the fibre. When they developed in the T-N plane, the failure surface would be *parallel* to this axis, being inclined at 45° from the principal radial load acting on the fibre. These failure mechanisms are quite *unrelated* and should *never* be interacted. On this basis, any doubt about the position of lines B'E' and F'D', in relation to the *present* fibre-failure envelope, is removed. They cannot possibly lie *outside* lines BE and FD. Any possibility that they lie *inside* these two sides of the hexagon in Fig. 3 can be resolved only by *biaxial* testing under predominantly, but not entirely transverse loads. The issue is largely moot for fibre-polymer composites because the matrix would then be expected to fail first. What matters here is that the skewed hexagon in Fig. 3 is, at worst, a true upper bound on failure of the fibres *by shear*, even though there is a good possibility that, theoretically at least, it should be *locally* truncated by straight constant-transverse-stress lines, in exactly the same manner as for actually observed alternative failure modes, as is discussed in the following section.

SUPERPOSITION OF ADDITIONAL FIBRE FAILURE MECHANISMS

Fig.'s 3 and 5 *require* that the longitudinal fibre strengths in tension and compression be the same. This is sometimes the case, but not always, so it is necessary to also provide a means of accounting for fibre failures by different mechanisms. If we *accept* that these figures characterize shear failures when they *do* occur, we can add the other failure mechanisms very simply. If fibres were to fail by brittle fracture, caused by surface flaws on glass fibres or elongated voids in the precursor for carbon fibres, for example, the ellipse in Fig. 5 would obviously be truncated by a vertical line at the measured tension strength. Likewise, if fibres embedded in a polymer matrix were too small in diameter or not sufficiently stiffly supported to develop their intrinsic shear strength under longitudinal compressive loads, there could be a further *constant-stress* cut-off at the other end of the ellipse in Fig. 5. The presence of either such cut-off implies *nothing* about the presence or absence of the other. More importantly, these possible additional failure mechanisms have *absolutely no effect* on the predicted shear-failure envelope *outside* their domain of dominance. They do *NOT* interact. The corresponding constant-longitudinal-stress cut-offs on the strain plane are illustrated in Fig. 8. These are drawn parallel to the pure-transverse-tension/compression line, inclined by the angle β from the vertical (transverse) strain axis. The position of the compressive instability lines is customarily established by macro-level testing, since more than one such failure mechanism is known to be possible. However, this theory can accommodate any such measurement.

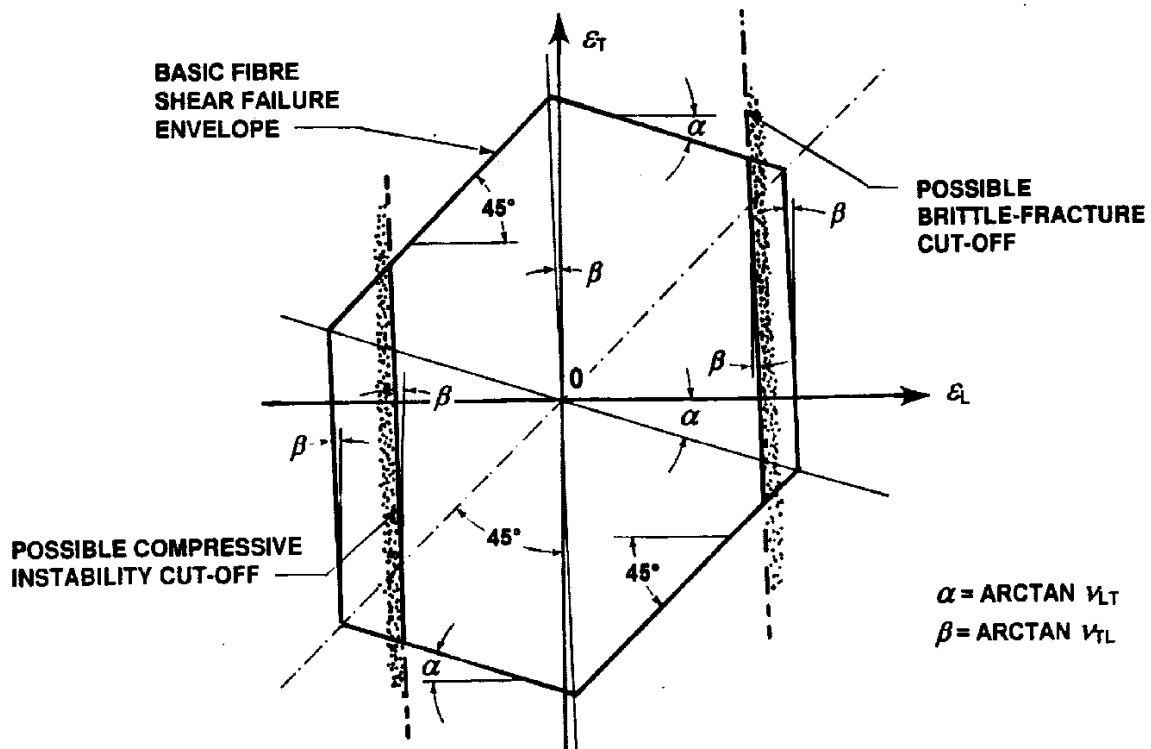


Fig. 8 Superposition of brittle fracture and compressive instability strength limits on basic shear-failure envelope

What is most significant about these two *additional* fibre-failure cut-offs, when expressed on *either* the stress or strain plane, is that the failure envelope would be *unbounded* in regard to transverse loads if these were the *only* possible failure mechanisms included in the model. This makes the reluctance to accept the possibility of shear failures in the fibres by some of the established experts in the field so much more difficult for the author to accept, particularly when it has been confirmed so many times experimentally (as the author has discussed in earlier papers on the subject). Unlike those who developed other failure models, the author has no trouble in accepting that shear failures are not the *only* possible failure mechanism of fibre failure; after all, there are experiments which prove the existence of brittle fracture and compressive instability failures, too. A valid argument that typical polymer matrices are likely to fail *first* in no way implies that the fibres could not fail by shear under transverse loads if only the matrix were strong enough. And, in any case, possible matrix failures belong on a totally *different* failure envelope.

Fig. 8, and its equivalent on the stress plane in Fig. 5, also reveal something which is commonly overlooked. If *both* the brittle-fracture and compressive-instability modes of failure occur for the fibres in some particular unidirectional lamina in which they are being characterized by the traditional longitudinal loads, only a *biaxial test in which the fibres fail before the matrix* is capable of characterizing the location of those portions of the *fibre* failure envelope *not* characterized by either of those mechanisms. If the measured unidirectional lamina strengths in longitudinal tension and compression are equal, one has no possible justification for *not* assuming that shear is the governing mechanism for the rest of the failure envelope – because it is then implausible for it not to be the *only* failure mechanism *anywhere* around its perimeter. This equality of strength has commonly been observed in some of the older high-tension-strength (HTS) carbon fibres, T-300 and AS-1. Indeed, it was on this basis that the authors of Ref. 6 first concluded that the carbon fibres in the laminates they were

testing were failing by shear. (What drove the author to the same conclusion was very different – the customarily predicted fibre-dominated in-plane-shear strengths of $\pm 45^\circ$ laminates were too high by almost a factor of 2.) Shear failures have also been observed in tests with the AS-4 fibres in which better than normal care has been taken to stabilize the fibres in high-quality test coupons, but it clearly is not normally the case for the newer small-diameter high-strain fibres like IM-6 and IM-7. Undeniable shear failures have even been observed in individual carbon fibres stabilized by gluing them, one at a time, to the side of a Plexiglass block which has then been compressed, see Ref. 13, but this does require better stabilization than is achievable in structural laminates. Nevertheless, these results (at compression strains far higher than normally obtained) *should* have removed any lingering doubts about the possibility of carbon fibres failing in shear. *Any* comprehensive failure theory for the fibres in fibre-polymer composites *must* encompass, at a minimum, all three of these failure modes, as stated in Fig. 1. There may also be a transverse-tension splitting mode, for the *fibres*.

If a composite material has been characterized only by measured tensile and compressive strengths, the author recommends basing the 45° shear-failure limit *for the fibres* on the *higher* of the two measurements. This can, at worst, be conservative. Under no circumstances would he recommend setting it any *lower* than this if separate tension, compression, and shear tests were available, and the measured shear-failure limit lay *inside* that for tension or compression, because the fibre-dominated in-plane shear test is even more difficult to execute correctly than tension and compression tests. Indeed, it may be observed that the only thing more unreliable than most composite failure criteria is the bulk of the test data.

The manner in which different failure *mechanisms* locally truncate the basic shear-failure envelope rather than distort it explains well the confusion mentioned earlier about an elliptical failure envelope in the stress plane covering two different levels of distortional strain energy for a transversely isotropic fibre. The existence of different critical conditions in the T-N plane from those in the L-T and L-N planes is plausible. However, if they were regarded as being as different from each other as ductile shear failure and brittle fracture, for example, the temptation to *interact* them in a *single* failure envelope would disappear and, with it, any mystery about why the ellipse in Fig. 5 is completely defined by a *single* reference strength.

THE EQUIVALENT STRAINS AT THE LAMINA LEVEL

The next step in the analysis is to convert the fibre strains into equivalent lamina strains, so that the possibility of matrix failures can be assessed and a determination made as to whether or not they would precede the fibre failures. It is obvious by inspection that the *longitudinal* strains in fibre, matrix, and lamina will be common except for the immediate vicinity of any interruptions or terminations of the fibres. Whether or not the *transverse* strains are common, or nearly so, depends on the relative transverse stiffness of the fibres to the modulus of the matrix. The greatest such difference is found for glass fibres which, being isotropic, are far stiffer in the transverse direction than carbon fibres, which are far stiffer than glass fibres in the longitudinal direction. Using the same model as was applied by Chamis (Ref. 14) in deriving an expression for the ratio of the transverse strains in the matrix between the fibres and that in the overall lamina, the author has derived a relation between the transverse strains in the *fibres* and those in the lamina (see Ref. 9). The following equation refers to a pure

transverse load on a fibre in a unidirectional lamina and expresses the ratio of the transverse strain in the lamina (between the fibres) and the lesser strain across the diameter of the fibres.

$$R_\epsilon = \frac{\epsilon_T}{\epsilon_{fT}} = \sqrt{KV_f} + (1 - \sqrt{KV_f}) \left[(1 - \nu_m^2) \frac{E_{fT}}{E_m} + \nu_m \nu_{fTL} \right] \quad (6)$$

Here, V_f is the fibre volume fraction, K is a coefficient close to unity which varies slightly with the fibre array, as explained in Ref. 9, the subscript f refers to the fibre and m to the matrix. Strains are denoted by ϵ , while E and ν are Young's moduli and Poisson's ratios. The sub-script T denotes the transverse direction, while L signifies the longitudinal (fibre axis) direction.

Typical values of the strain amplification factor R_ϵ are 1.5 for carbon-epoxy composites and 5 for fibreglass-epoxy laminates. These factors correspond with ratios between the peak strain in the matrix between the fibres to the average transverse strain in the lamina of barely 2 and almost 4, respectively, in comparison with a theoretical value of just under 4.5 (for a fibre volume fraction of 0.60), if *all* of the transverse strain were to occur in the matrix. This wide disparity between transverse matrix strains explains why there has been a legitimate need for far more scientific research into matrix cracking in fibreglass-reinforced laminates than for those reinforced by carbon fibres. Not only do glass fibres strain more before they fail, permitting higher overall strains to develop, they are so much stiffer in the transverse direction than either carbon fibres or the resin that virtually all of the transverse strain in a lamina occurs in the resin matrix between the fibres. This is why a small increase in resin content can make laminates so much more resistant to impact damage.

The already small minor Poisson's ratio ν_{fTL} for isolated carbon fibres is effectively further reduced when embedded in a lamina or laminate by the factor R_ϵ , while the initially far larger value for glass fibres is also dramatically reduced, almost to zero, by its far larger value of R_ϵ . This is why a maximum *strain* model proves to be the better representation of a maximum *stress* phenomenon, even for isotropic glass fibres. Fig. 9 shows how the transverse fibre and lamina strains are related throughout the remainder of the strain plane.

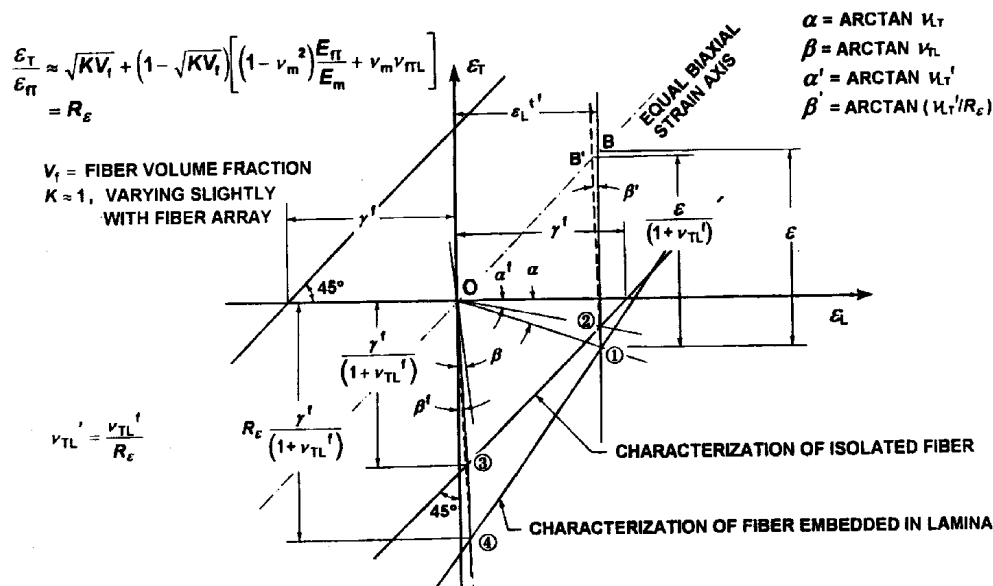


Fig. 9 Differences between transverse strains in the fibres and the lamina, with longitudinal strains common

The construction of Figure 9 may imply to some that it refers only to a unidirectional lamina. It applies equally to what have hitherto wrongly been perceived as bi-directional laminae, and an explanation of this issue is included here, later, in the discussion on matrix failures. In both cases, the analysis needs to be for a fibre embedded in a matrix.

The line ①④, which governs at the lamina level, is established from the line ②③, which governs at the fibre level, in the following manner. Point ② is located from the measured longitudinal strain to failure, point ①, at the same longitudinal strain and with the transverse strain reduced in the ratio v_{LT}/v_{LT} . Point ③ is located by projecting a line from point ② at a slope of 45° , until it intercepts the pure-transverse-stress line from the origin, at a slope established by the fibre minor Poisson's ratio v_{FTL} . Point ④ follows from point ③ at the same longitudinal strain, with the transverse strain amplified by the factor R_ϵ . The same reduction in effective slope, with respect to the vertical axis in Fig. 9, is applied to the transverse-tension strains originating at point ②. Consequently, when equal biaxial strains are developed in a unidirectional lamina embedded in a multidirectional laminate, the transverse strain in the fibre will be less than the longitudinal strain by roughly the factor R_ϵ . (The same is also true for fibres in each individual tow if the "lamina" is a bi-directional woven fabric.) This is a further reason for lack of concern about the precise location of the lines E'B' and F'D' in Fig.6.

FIBRE FAILURES CHARACTERIZED ON THE LAMINA STRAIN PLANE

It is now possible to characterize fibre failures on the lamina strain plane, combining the possible failure mechanisms discussed in relation to isolated fibres with the preceding relationship between the difference in transverse strains arising from the different stiffnesses of the fibres and matrix. Fig. 10 shows, roughly to scale, the *fibre*-failure limits for T-300 carbon and E-glass fibres embedded as unidirectional plies in epoxy matrices, using data supplied by the organizers of the comparison between failure theories referred to in Ref. 9. Significantly, the constant-longitudinal-tension and -compression lines in Fig. 3, AE and CF, are almost vertical for both of these fibres. Points B and D have almost disappeared off the page for the fibreglass-reinforced laminates, and have been significantly displaced further from the origin for the carbon-fibre-reinforced laminates. In the absence of specific test data with which to locate the 45° fibre-failure cut-offs in the 2nd and 4th quadrants, they have been passed through the higher of the uniaxial tension and compression strains-to-failure; in both of these cases the tensile strains govern.

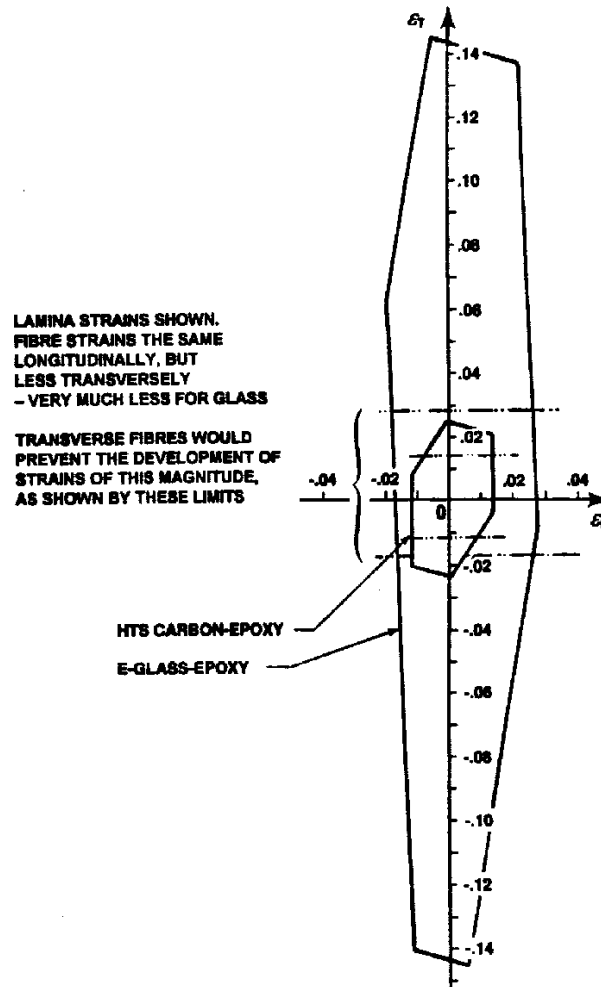


Fig. 10 Fibre-failure envelopes for carbon and glass fibres embedded in epoxy matrix, in terms of lamina strains

It should be immediately apparent that no great error would be introduced by approximating these results for the lines AD and CB, sloping at 45° in Fig. 3, by 45° sloping lines for the carbon fibres in Fig. 10 and vertical (90°) lines for the glass fibres. The desirability of doing so becomes even greater when an entire laminate is assessed, containing fibres in multiple directions.

Fig. 11 shows how the failure envelopes at the lamina level, as in Fig. 10, would be truncated by other truly possible fibre failures – tensile brittle fracture and compressive instability. Since *both* of these mechanisms are associated with constant axial stress *in the fibres*, the corresponding loci in the *lamina* strain plane would be made even closer to vertical in Fig. 11 than in Fig. 3, by the factor R_e , just as for *transverse* loads on the fibres. Even though these are, in reality, constant-stress-phenomena, they *appear* closer to constant-strain cut-offs at the lamina level for fibre-polymer composites.

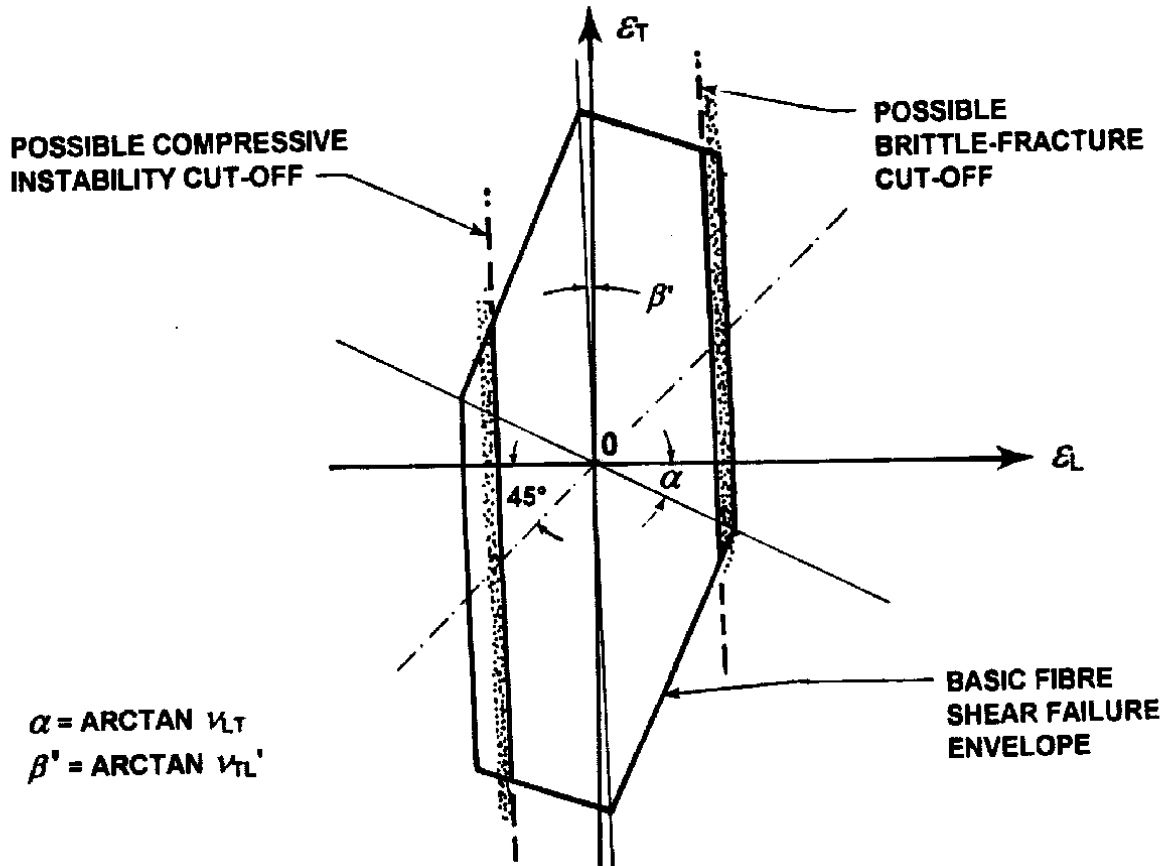


Fig. 11 Fibre-failure envelope for all mechanisms, at lamina level

CHARACTERIZATION OF MATRIX FAILURES AT THE LAMINA STRAIN LEVEL

The most straightforward matrix-failure mechanism to consider is that of in-plane shear *between* the fibres. Within the aerospace industry, it is customarily characterized by measurements of tensile loads on $\pm 45^\circ$ laminates, but in its purest (and more difficult-to-test form), it refers to shear with respect to 0° and 90° axes in any combination of 0° and 90° plies. As a first approximation for the design of multidirectional laminates, it has been customary to assume that the measured shear strength is independent of in-plane direct stresses. The similarity of in-plane shear strengths of both laminae and laminates implies either matrix failure by ductile shear, which would not be affected by residual thermal stresses, or microcracking by a mechanism which does *not* involve any interaction with adjacent plies. Extensive published research into the strength of unidirectional laminae under a combination of in-plane shear and transverse direct loads, however, has shown significant variation in shear strength, particularly when expressed on the *stress* plane which, unfortunately, gives no indication of whether or not the abrupt drops in shear strength *precede* other possible failure modes within a laminate. For a uniform in-plane shear strength, the related failure envelope is represented here as an infinite flat-topped plateau, of the type shown in Fig. 12, with vertical walls established by limits on the strains-to-failure of fibres – provided that there are fibres in a sufficient number of directions to establish a *complete* boundary.

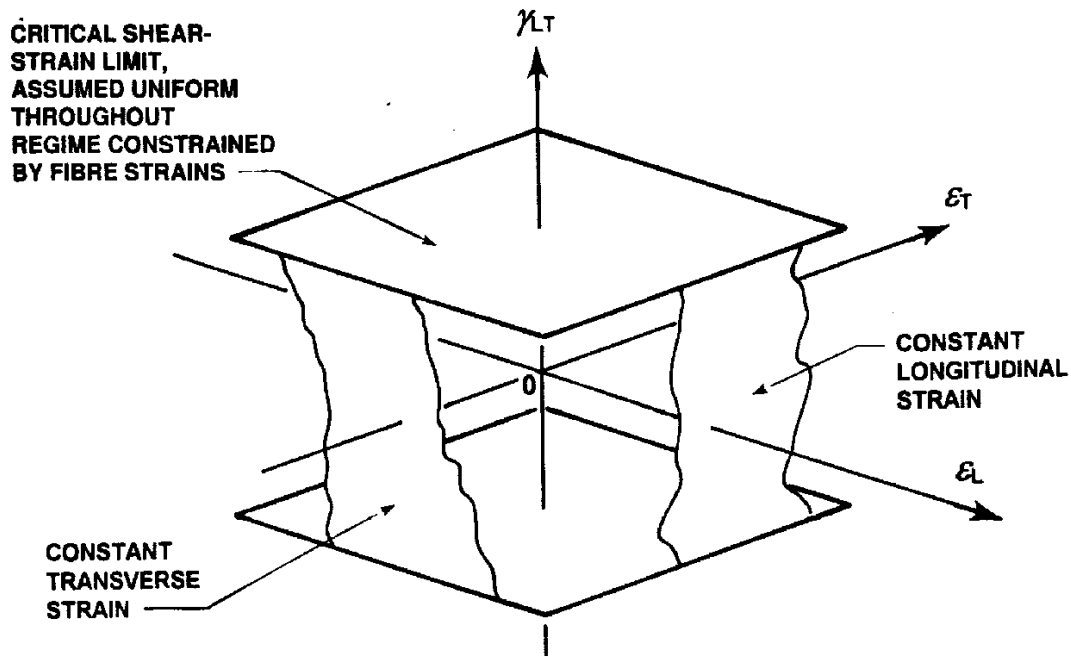


Fig. 12 Matrix shear-failure cut-offs for fibre-polymer composites

The implication of Fig. 12 is that the soft matrix in fibre-polymer composites strains so much more than the fibres before it finally fails that its shear strength is unaffected by those components of matrix stress *parallel* to the fibres, which carry most of the load because of their far greater stiffness. This has proved to be a realistic approximation for carbon-reinforced laminates with some fibres in each of the 0° , $\pm 45^\circ$, and 90° directions, but would be questioned by those engineers and scientists who have worked with glass-fibre-reinforced composites and is in any case even deficient for carbon-reinforced composites with fibres in too few directions to represent a structure rather than a mechanism. Nevertheless, for small in-plane direct strains, even in the transverse direction, this approximation is acceptable for *all* fibre-polymer composites. Its accuracy diminishes as high in-plane stresses are developed in the matrix, particularly for unidirectional laminae. In the extreme, the in-plane shear capacity of the matrix can drop to zero; in reality, failure of orthogonal fibres in a multidirectional laminate often precedes the matrix failures.

By definition, a *unidirectional* lamina can provide such constraints in only *one* direction, so the plateau ceases to be flat for sufficiently high *transverse strains*, with limits established by the matrix-dominated transverse *strengths*. The use of glass rather than carbon fibres allows far more interaction between the shear stress and the in-plane matrix stresses, because any fibre-strain cut-offs are then further removed from the origin in Fig. 12.

The next failure mechanism which is easy to integrate with Fig. 12 is for matrix *cracking* between, and parallel to, the fibres in a ply. Being a fracture-mechanics problem, this is easily recognized as being governed by a constant-transverse-tension stress. The difficulty is in establishing at *what* stress level such a failure would occur. Only micromechanicians and experimentalists can do this. The stress level *cannot* be established by analysis at the *macro* level, because the propagation of any such cracks, traditional ply-by-ply decomposition analyses notwithstanding, *IS* influenced by the nature of adjacent plies, particularly in regard to crack arrest, and by the *thickness* of the reference and adjacent plies. The failure stress for matrix cracking is definitely *NOT* a pure material property, as several micromechanicians have already demonstrated. Any measurement of it as such, rather than as a fracture

toughness, applies *only* to the particular geometry on which it was measured. One of the great mysteries about analyzing composite laminates is why so few people acknowledge that the transverse-tension strength measured on a unidirectional test coupon applies to that lamina *only* in isolation, and *not* when it is *embedded in a laminate* (with fibres in more than one direction). [If there were no ply-to-ply interaction, boron-epoxy patching of cracked metallic structures could not possibly enhance the fatigue life. Yet it does (Ref. 15)!] Nevertheless, leaving aside the issue of *where* such a cut-off should lie, its *form* will be as shown in Fig. 13.

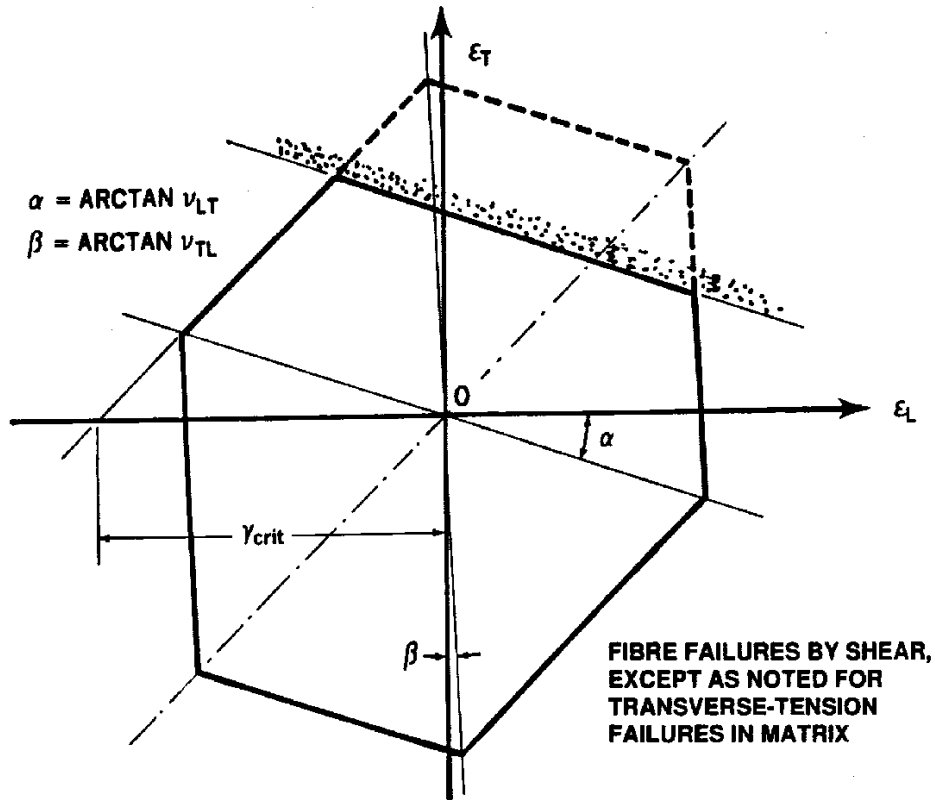


Fig. 13 Characterization of matrix cracking between fibres, on the lamina strain plane

It has been the author's good fortune to work in an industry where the most cost-effective and reliable carbon-epoxy laminates are made from thin plies with fibres in at least four directions, all thoroughly interspersed to ensure that the matrix neither fails because of this mechanism nor because of interlaminar stresses at the edges, (which are covered by quite different equations). Under such circumstances, it is best to *ignore* the possibility of matrix failures, on the basis that any estimate of strength using conventional macro-level analyses will be even more unreliable. Worse, if such failures really did occur (except in the immediate vicinity of bolt holes, where they are unavoidable), the service life of such structures would be so variable as to render them unsaleable. As he has recently learned, however, workers outside the aircraft industry have not been so fortunate, particularly when working with polymer composites reinforced by glass fibres which can strain even more than the matrix before they fail (instead of at most 1/3rd to 1/2 as much for the older carbon fibres, although the newest high-strain carbon fibres are pushing this limit towards 1 to 1). Several researchers have prepared physically realistic failure models for matrix cracking, during the past 20 years or more. Oblivious to this at the time, because so much of the literature contained unsound characterizations of fibre failures in laminates which hindered rather than helped his research, the author focussed attention on the need for better fibre-failure models.

His main contribution to the analysis of matrix failures is to question the wisdom of ignoring consideration of the major residual thermal stresses, those within *isolated* unidirectional laminae, while developing theories which accounted only for the additional thermal stresses associated with laminating plies with fibres in different directions.

While matrix-failure theories have not been his forte, the author cannot refrain from acknowledging the noble efforts of Alfred Puck to place the analysis of matrix failures in fibreglass-reinforced polymer composites on the same sound mechanistic base the author has tried to develop for carbon fibre failures – in a career that dates back to the infancy of fibreglass sailplanes. Puck and his colleagues had the benefit of legitimately using the very simple noninteractive maximum-strain failure model for glass fibres. Most of what the author now knows about matrix failures in fibre-polymer composites he owes to Alfred Puck and to Ralf Cuntze (see Ref. 17). The most significant aspect of their works is that, just as the author has characterized specific failure *mechanisms* in the fibres, these German scientists have formulated their analyses around the concept of “action planes”, by identifying those relatively few planes in the matrix in which failure was *not* inhibited by the fibres and, *for each one*, developing a failure model in terms of the stresses acting on and in that particular plane. The similarity in approach now apparent between these independent studies is amazing, even to the extent that a distinction must often be drawn between the same phenomena in isolated unidirectional plies and when those plies are embedded in multidirectional laminates.

In summary, researchers into matrix failures in fibre-polymer composites have identified three distinct failure mechanisms in the interior of laminates, and particularly unidirectional laminae, under predominantly in-plane loads. (Edge failures are a special case, as noted earlier, and not covered by the level of analysis addressed here.) The first is brittle fracture parallel to the fibres, in the longitudinal-normal (L-N) plane of the lamina, as characterized in Fig. 13. This is governed primarily by the transverse-tension stress alone but, as Cuntze has shown, is influenced by in-plane shear and longitudinal tensile stresses also, since it involves enlarging the randomly distributed microcracks created by residual thermal stresses. (Much of the German testing has been on composite tubes, which eliminate failure initiation from the edge stresses which are unavoidable in flat test coupons.) The stress levels at which matrix cracking occurs between, and parallel to, adjacent fibres is strongly influenced by fibres in adjacent plies, particularly if they are orthogonal to the first. Such adjacent plies have long been known to alter the residual thermal stresses in the matrix of the ply under consideration, and also the tendency of any initial cracks to spread. The second failure mechanism is in-plane shear, in the longitudinal-transverse (L-T) plane, as characterized in Fig. 12, with the matrix apparently shearing between the fibres. (Puck and others are of the opinion that this is actually the result of mini tensile cracks at 45° or so from the fibre axis, with a myriad of short cracks, each arrested by the fibres. This position is supported by their photomicrographs of failed specimens.) This mechanism is affected by in-plane shear loads, longitudinal tension or compression loads, and by transverse compression loads, not being able to occur if the transverse-tension loads are too high. The third distinct matrix failure is associated with predominantly transverse compression, with the matrix splitting between the fibres, but at roughly $\pm 45^\circ$ from the plane of the lamina. The failure surface looks like that left by driving a wedge into the sides of the lamina. This mechanism, also, is influenced by the axial stress in the matrix, parallel to the fibres. (In theory, this same chevron-shaped failure surface could occur under transverse-tension loads, if a matrix were sufficiently ductile.) These three failure mechanisms for the matrix in a unidirectional lamina are depicted in Fig. 14.

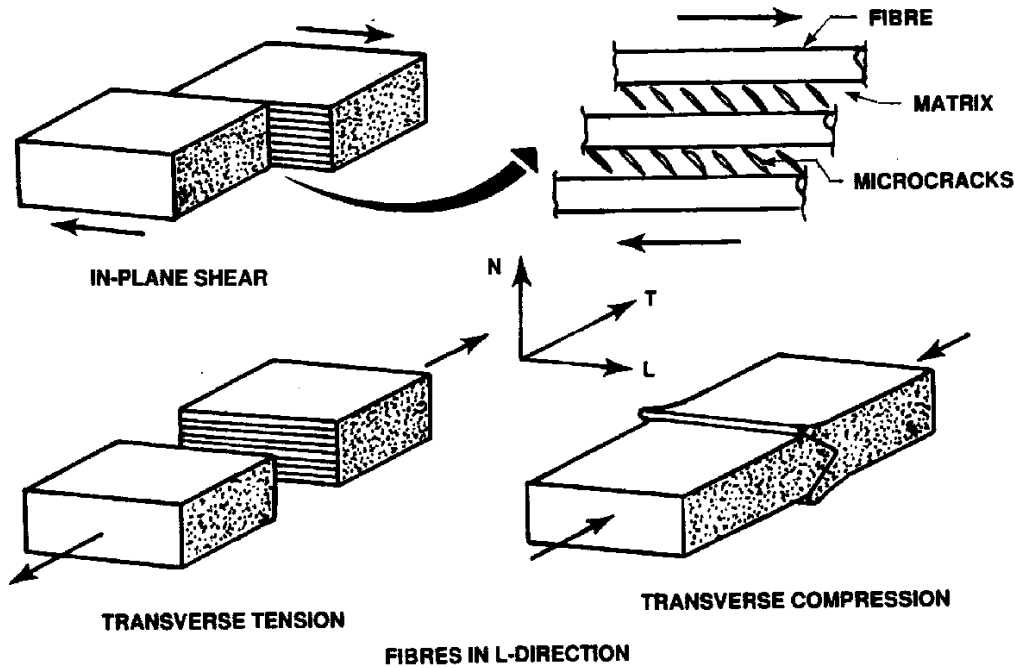


Fig. 14 Matrix-failure modes in fibre-polymer composite laminates

Given that typical resin matrices are conventional isotropic materials, it should not be the least bit surprising to learn that their failure can be predicted in terms of a Mohr-circle assessment of *all* the stresses acting at the micro level. Changes in “ductile” failure mode are associated with changes in which pair of principal stresses are associated with the highest difference between them – taking proper account of residual thermal stresses which are often far too large to ignore. Cuntze and his colleagues believe that it is not the maximum shear stress so calculated which causes the matrix to fail, but the associated maximum tensile stress (oriented roughly half way between the axes associated with the peak shear stress). So even the “ductile” behaviour at the macro level can be brittle at the micromechanical level.

The domains throughout which each of the failure mechanisms shown in Fig. 14 govern for a unidirectional lamina under combined transverse and in-plane-shear loads are identified in Fig. 15. As noted earlier, Fig. 15 is a stress-based characterization, which does not lend itself to easily establishing whether or not one or other end of the this failure envelope would be truncated by failures in orthogonal fibres whenever the unidirectional lamina was embedded within a structural laminate. Only a comparison between *strains* to failure can establish this. To complicate this issue further, the actual *locations* of these truncations on the stress or strain plane can be altered by the nature of adjacent plies, particularly for matrix cracking modes defined by a principal tension stress. Indeed, for all but quasi-isotropic and angle-ply laminates, it is quite possible for the characterization of matrix cracking to vary from ply to ply within the *same* laminate. This is influenced by the fractions of plies in each direction within the laminate, as well as by the effective ply thicknesses resulting from thorough interspersions or blocking together of parallel layers.

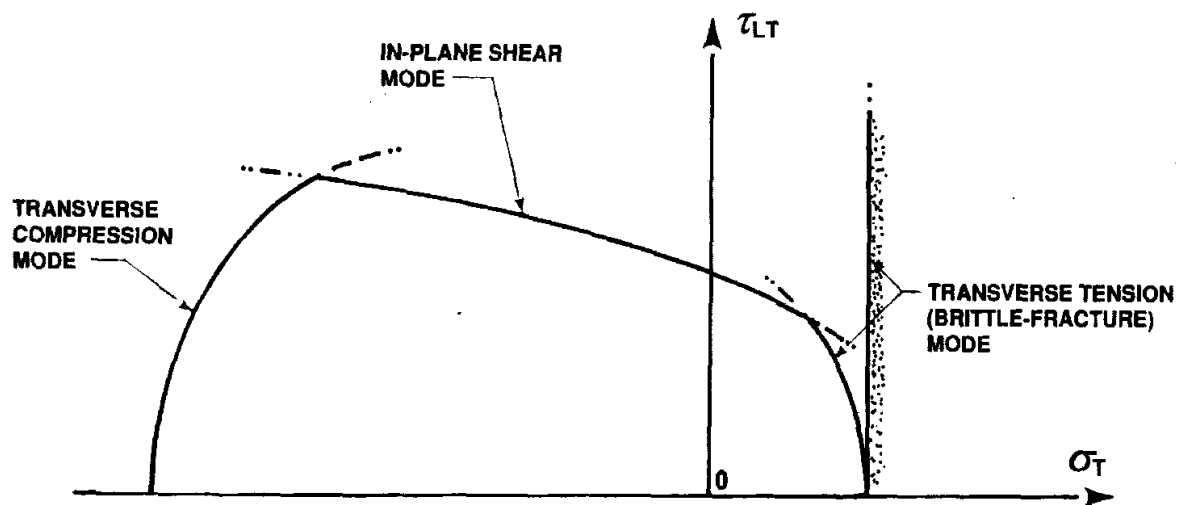


Fig. 15 Strength of unidirectional lamina under transverse and in-plane-shear loads

FIBRE OR MATRIX FAILURES AT THE LAMINATE STRAIN LEVEL

Apart from the influence of adjacent plies on the tendency or otherwise for the matrix to *crack* between fibres under transverse-tension loads, failure by *any* of the other mechanisms discussed here is not affected by the presence or absence of adjacent plies, so exactly the same analysis procedures can be applied to laminae embedded in laminates as when they are tested in isolation. However, failures in some *other* ply will often *precede* those calculated for the ply in question. This is why the use of a common reference level, strains in the lamina (embedded or not), is so critical. It is not at all obvious that a longitudinal stress of, say 150 ksi (1000 MPa) in one ply is more or less critical than a transverse stress of 15 ksi (100 MPa) in a transverse ply. But a common strain level of, say 2 percent, would be quite discriminating, if the fibres were predicted to fail at a strain of 1.5 percent, while the matrix could withstand a strain of 2.5 percent without failure (or vice versa).

The analysis of composite laminates using the author's failure models, or anyone else's *mechanistic* failure models, differs little from the standard techniques other than by replacing a *single* superficial check, of highly questionable physical meaning, against an abstract mathematical failure envelope with *multiple* checks for possible failures by *each* failure mechanism in *each* constituent of the laminate. This process is repeated for each ply, until the most critical condition is identified. In the event that matrix cracking must be considered, either a scientific micromechanical analysis must be used, or a check made against an empirical constant-transverse-stress cut-off appropriate for the circumstances.

A possibly surprising change in procedures, with respect to traditional analyses, concerns the fibres and matrix in what have hitherto erroneously been considered as *biaxially* reinforced (homogeneous) *laminae*, such as woven fabrics. The complete evaluation of such plies by *ANY* mechanistic failure model *requires* that such a ply first be decomposed into *two equivalent unidirectional laminae*, in which the influence on strength and stiffness of any crimping of the fibres caused by the weaving process is properly accounted for. This is accomplished by using lamination theory in reverse. The transverse properties of each equivalent unidirectional lamina may reasonably be considered to be the same as for a truly separate unidirectional lamina. So may the matrix-dominated in-plane shear stiffness.

Measurement of the elastic constants of the bi-directional “lamina”, in combination with these assumed minor lamina properties, then permits the calculation of effective properties *parallel* to the fibres. Two “unidirectional” laminae, with these equivalent longitudinal properties, would replace each bi-directional layer in the laminate. (As a rough rule of thumb, such equivalent unidirectional plies would have an axial stiffness equal to between 1.82 and 1.86 times the stiffness measured on a plain-weave carbon-epoxy cloth laminate, as explained in Ref. 18.) Both laminae would be located at the same height, through the thickness of the laminate, for plain-weave cloth layers, and would be appropriately stacked one on top of the other for asymmetric layers like satin-weave cloths. This same decomposition process would also need to be followed for dry preform-laminates with fibres in two or more directions. The need to be able to separate each layer of composite material into its fibre and matrix constituents derives from the impossibility of writing a meaningful strength, as distinct from stiffness, criterion against an artificially homogenized lamina, whether it be bi-directional or unidirectional.

THE TRUNCATED MAXIMUM-STRAIN FAILURE CRITERION FOR CARBON-FIBRE REINFORCED COMPOSITE LAMINATES

Many laminates contain some fibres in each of the 0°, ±45°, and 90° directions, which is a common basis for design in composite aircraft structures. The reasons for this design philosophy are that it is consistent with the use of woven fabric laminates, even if supplemented by unidirectional tape plies in a predominant load direction, and that without such standardization, the cost of testing for certification of structures would be prohibitive. Such laminates, when made from well interspersed thin carbon-epoxy plies, are essentially totally fibre dominated, so the possibility of matrix failures can then be ignored for well-designed laminates. In this case, the author’s model is simplified greatly by assessing orthogonal pairs of fibre directions, one for 0° and 90° fibres and the other for the ±45° fibres. Since the failure criterion is strain-, rather than stress-based, the *same* analysis is applied, regardless of the fibre pattern. Recommended fibre patterns are shown in Fig. 16, with both lower and upper limits appropriate for bolted primary composite structure.

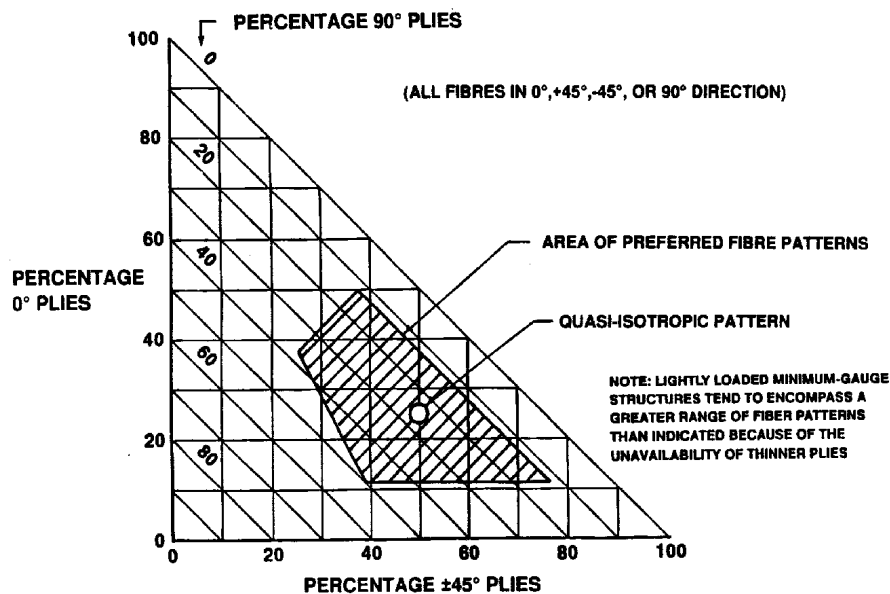


Fig. 16 Preferred fibre patterns for fibre-polymer composite laminates

Fig. 17 shows the superimposed failure envelopes for shear failures in orthogonal layers of carbon fibres, created by rotating the failure envelope for the 0° fibres through 180° around the equal-biaxial-strain axis. The undefined transverse failures of each unidirectional ply are truncated by longitudinal failures in the other ply. The common area is almost identical with the classical maximum-strain failure model, only with the corners truncated in the 2nd and 4th quadrants – by a *universal* amount applying to *all* fibre patterns in the 0° , 90° , $\pm 45^\circ$ family. The cut-off is based on the major Poisson's ratio for a *unidirectional* lamina. It would be quite *wrong* to use that measured on a $0^\circ/90^\circ$ laminate, even if the structure were made from such layers. The corresponding cut-off for glass fibres in typical polymer matrices can be ignored, at least on the lamina strain plane.

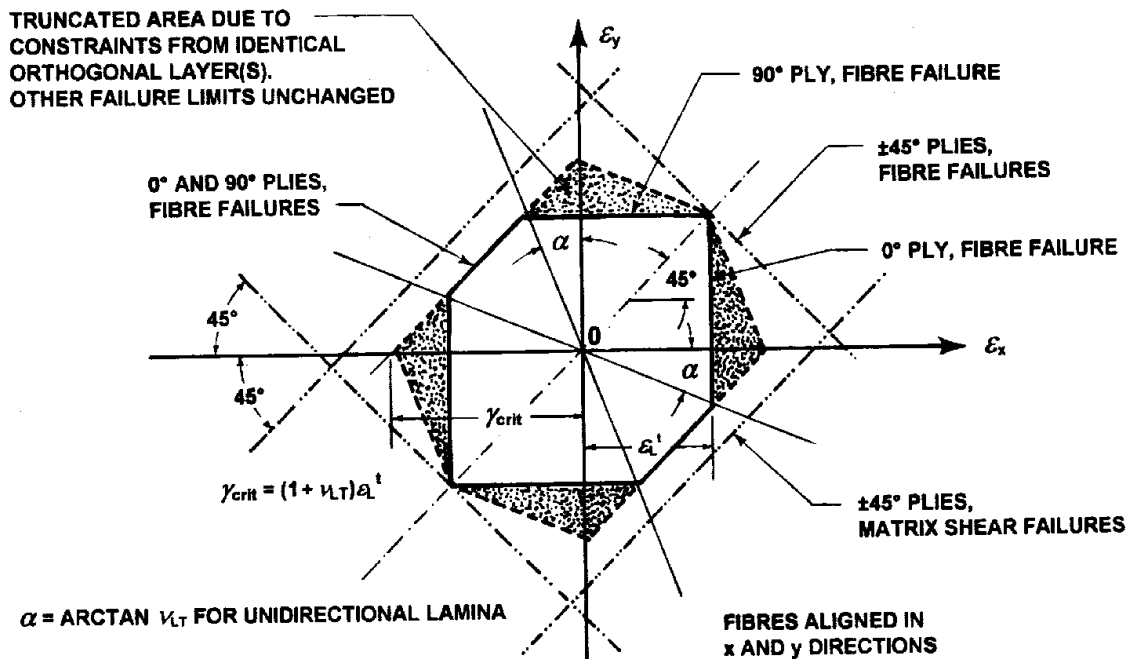


Fig. 17 Superimposed shear-failure envelopes for orthogonal layers of carbon-fibre-reinforced laminates

Fig. 17 also shows the base portion of the failure envelope for $\pm 45^\circ$ layers to the same scale as for the 0° and 90° plies. In the absence of in-plane shear loads with respect to the 0° and 90° axes, the *fibres* in the $\pm 45^\circ$ layers cannot fail *before* those in the 0° and 90° directions. The failure conditions are common only for equal-biaxial-tension or -compression loads. Matrix shear failures for these $\pm 45^\circ$ layers are shown parallel to and slightly outside the 45° cut-off for shear failures of typical 0° and 90° carbon fibres. In such a case, they would be inoperative. However, they could actually truncate fibre failures in glass-epoxy laminates under in-plane-shear loads.

The manner in which the failure strains for $\pm 45^\circ$ fibres lie *outside* the failure envelope defined by 0° and 90° fibres in Fig. is typical of *all* other fibre angles, as demonstrated by analyses in Ref.'s 3 and 9 for $\pm 55^\circ$ and $90^\circ/\pm 30^\circ$ laminates. Of greater significance is the fact that, had the failure envelopes for 0° and 90° plies included inappropriate matrix-cracking cut-offs which did not reflect the in-situ behaviour in laminates, the $0^\circ/90^\circ$ failure envelope on the strain plane would have been even smaller, being truncated by matrix-cracking limits in both plies, with consequential reductions in the size of the corresponding envelope on the stress

plane. In the world of ceramics, this is what actually *does* happen. In the world of carbon-fibre-polymer composites, this usually does *not* happen, but is often *predicted* to happen.

If the nearly vertical and horizontal lines in Fig. 16 are made precisely so, and the slightly kinked cut-offs replaced by a single 45° sloping line, the failure envelope is transformed into the truncated maximum-strain failure model (Ref.'s 19 & 20), the development of which actually preceded the author's justification of why it was such an excellent representation of fibre failures in carbon-epoxy-type laminates. Fig. 18 shows how this model is adjusted to account for the additional failure mechanisms characterized in Fig. 11. The entire failure envelope is governed by fibre failures. As stated earlier, the 45° cut-offs are based on the *higher* of the measured tension and compression strains-to-failure.

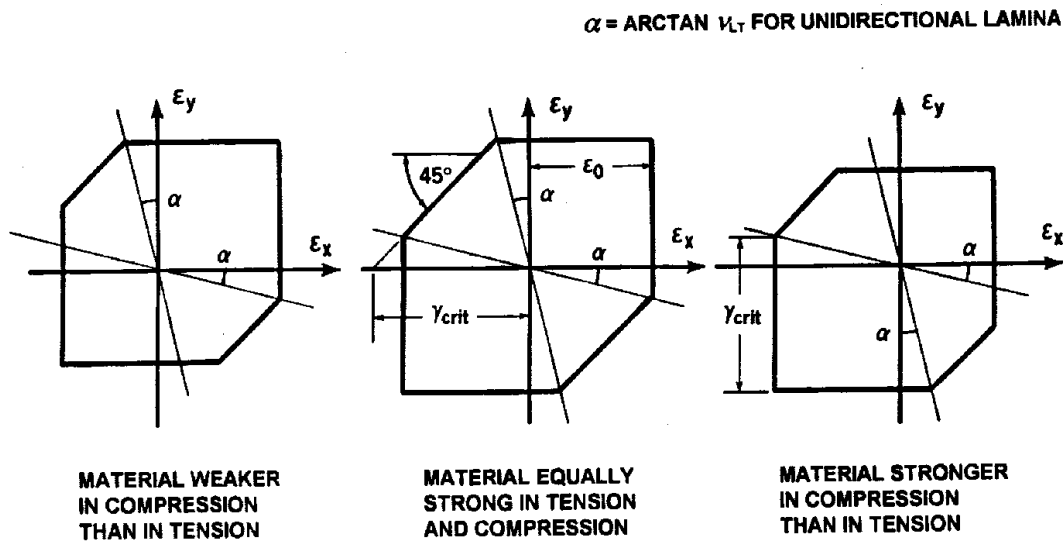


Fig. 18 Truncated maximum-strain failure model for fibre-dominated failures of cross-plyed fibre-polymer composite laminates

When there really are fibres orthogonal to those being assessed, this failure envelope halves the assessment process without introducing any conservatism. For laminates with fibres in so few directions that real matrix failures are a possibility, it makes more sense to delete the horizontal cut-offs and apply the criterion to every fibre direction, in turn. For laminates lacking fibres in sufficient directions to form a structure, rather than a mechanism, portions of the failure envelope will be established by matrix failures, most frequently by in-plane shear. Additional equations are needed for this task.

It is actually possible to produce a universal strain-based failure envelope for *any* fibre-dominated laminate in the 0°, ±45°, 90° family, at least for purely membrane stresses. This is shown in Fig. 19, in which failure envelopes at the lamina and laminate level are compared. There is no equivalent universal solution at the *laminate* level for *stress*-based formulations. Fig. 19 is based on the truncated maximum-strain failure model, which is appropriate for carbon-fibre reinforced polymer composites. Similar diagrams could be prepared for fibreglass-reinforced laminates, without the truncations associated with shear loads. The plateau on top of the right-hand illustration would then be replaced by a horizontal ridge over the -45° (equal and opposite strain) axis. The flat vertical walls in the middle of the front and

back of these surfaces would be replaced by extensions of the vertical walls passing through the equal-biaxial-strain points, increasing the tolerable in-plane shear strains.

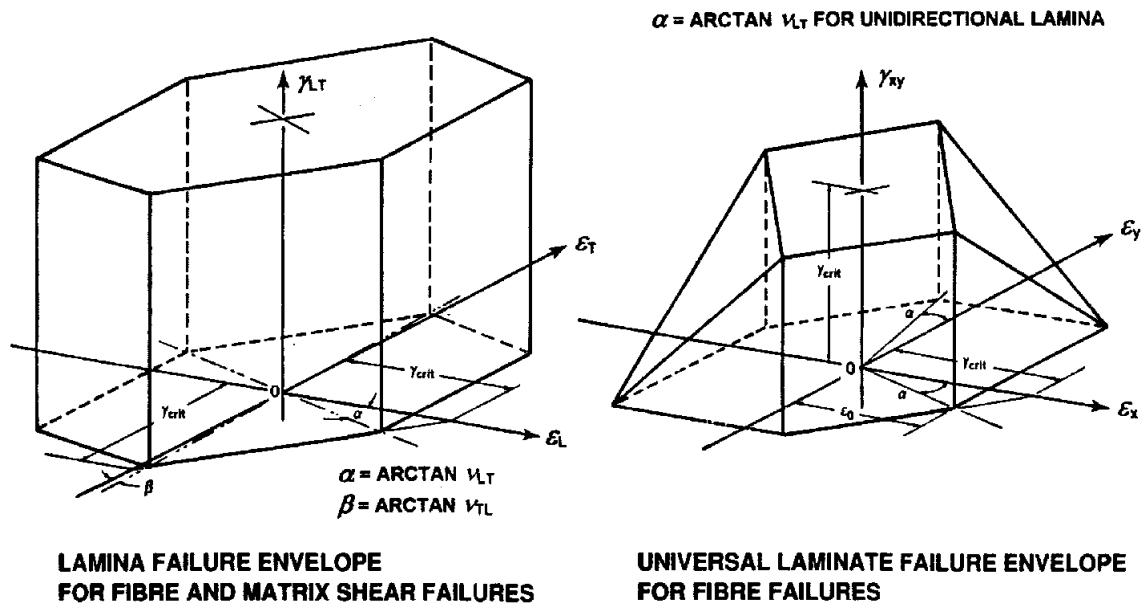


Fig. 19 Lamina and laminate failure envelopes, according to the truncated maximum-strain failure model, for carbon-epoxy composites

What is most significant about Fig. 19 is that the failure envelope is necessarily *pointed* at both ends, even when the additional fibre-failure mechanisms are included, and *rectangular* in cross section. This will be true of *any* mechanistic failure model for fibre failures in fibre-polymer composites made from the $0^\circ, \pm 45^\circ, 90^\circ$ family, with at least some plies in each direction.

As Fig. 10 suggests, the truncated maximum-strain failure model would be significantly conservative for shear loads on glass-fibre-reinforced polymer laminates, while the original (untruncated) maximum-strain model would be only slightly unconservative. The expansions of the failure envelope for fibreglass-polymer composites, of course, provide an opportunity for matrix shear failures, which usually lie beyond the carbon fibre-failure envelope in Fig. 19, to precede fibre failures predicted by the pure maximum-strain failure envelope instead. Fig. 19 omits consideration of matrix *cracking*, characterized in Fig. 13. On the lamina failure envelope in Fig. 19, this would appear as vertical walls, for the 0° and 90° plies, truncating the facets shown connected to the equal-biaxial-tension point, but not parallel to these facets.

RECENT DEVELOPMENTS WITH THE TEN-PERCENT RULE

The author's Ten-Percent Rule (Ref. 2) for predicting the fibre-dominated strengths of laminates in the $0^\circ, \pm 45^\circ, 90^\circ$ family using nothing more elaborate than mental arithmetic has recently been extended to cover arbitrary fibre angles and matrix shear failures. The theory has been applied in the form of a conventional lamina failure envelope as part of the exercise being conducted by *Composites Science and Technology*, to a $0^\circ/\pm 45^\circ/90^\circ$ carbon-epoxy laminate and to $\pm 55^\circ$ and $90^\circ/\pm 30^\circ$ fibreglass epoxy laminates (see Ref. 3). The basis of the expansion in capabilities is that the transverse modulus is still set at one tenth of the longitudinal modulus for unidirectional ply, but that the transverse strains have been increased

in the ratio $(1 + \nu_{LT})$ to suppress the prediction of matrix failures and to thereby generate similar laminate strengths to those predicted by the original formulation. Despite the fact that only fibre-dominated properties are actually measured, the new procedures permit realistic estimates to be made of the matrix-dominated shear strains to failure. As with *all* of the author's theories, however, *cracking* of the resin matrix between the fibres remains a fracture mechanics problem and, in the context of the Ten-Percent Rule, is best resolved by designing laminates not to crack.

CONCLUDING REMARKS

A strong case is made that not only is it *necessary* to formulate composite failure criteria on a *mechanistic* basis, it is possible – and the equations governing fibre failures are quite simple. If only the same could be said of matrix failures

Separate limits are prescribed for fibre failures by shear (the *only* possibility for a *complete* failure envelope), and by brittle fracture (for a limited range of tensile stresses), and compressive instability (for a limited range of compressive stresses). These three mechanisms are *noninteractive*, the latter two locally truncating the first, which is well represented by a generalization of the maximum-shear-stress (Tresca) criterion..

The three fibre-failure mechanisms can, and must, be characterized at the lamina *strain* level for it to be possible to identify whether failure by one mechanism in one ply will precede or follow failure in another ply in the same laminate.

Rational analysis of the strength of composite “materials” requires that *all* governing phenomena be first assessed at the *micro* level and then be characterized at the *macro* level. Only in this way were the appreciable differences between the behaviour of fibreglass-epoxy and carbon-epoxy laminates explained. The analysis of matrix failures is unavoidable for the former but, for the latter, arises only through poor design or inappropriate analysis tools (or extreme environments).

The truncated maximum-strain failure model, at the *lamina* level, is confirmed (by more precise analyses than used hitherto) to be very appropriate for fibre failures in well-designed carbon-epoxy type laminates. However, when the proper distinction is made between transverse strains in fibres and those in the lamina, the original (untruncated) maximum-strain failure model is shown to be more appropriate, at the *lamina* level, for fibre failures in fibreglass-epoxy laminates, and the like. Failure of the individual fibres of *both* kinds is still governed by the *same* generalization of the maximum-shear-stress failure criterion, appropriately truncated for brittle fracture and compressive instability failures. The reason for the need for the two different models *at the lamina level* is that there is a far greater difference between the transverse stiffness of the fibre and the matrix for isotropic glass fibres than for orthotropic carbon fibres.

Reliable micromechanical analyses for predicting cracks in the matrix have been formulated by other authors. They are addressed here only to make the vital point that such failures *cannot* meaningfully be assessed on a ply-by-ply basis, no matter how many interactive macromechanical analyses suggest that it can. There *is* an interaction with adjacent plies, which can act as crack stoppers if the fibres are orthogonal to those in the ply being evaluated. There is also a ply-thickness effect for matrix cracking, as other authors have noted. In

addition, the shape and location of the matrix-failure envelope on either the stress or strain plane can be altered by the nature of the fibres in adjacent plies.

Yet another error in past practices is the omission of *intralaminar* residual thermal stresses, between the fibres and matrix, *within* each individual ply. It is pointless to pretend to be able to predict matrix failures after what are often the largest matrix stress components have been excluded from consideration by artificially homogenizing the fibres and matrix in each ply. Since such “plies” can have fibres in one *or two* directions, why not homogenize the entire laminate at the same time – and remove even more residual thermal stresses from consideration? Significantly, there are some useful but largely neglected composite failure theories, for complete laminates, formulated under just such terms. At least they handle residual thermal stresses *consistently*, and predict many fibre failures quite well. One should now ask whether or not these are any more empirical than other seemingly more rigorous theories which include only those thermal stresses associated with the lamination process – and which are then customarily ignored because including them in nonmechanistic analyses often results in predicted strengths which are even less credible than when they are ignored.

In the process of generalizing the maximum-shear-stress criterion from isotropic to transversely isotropic materials, like carbon fibres, it has become apparent that the name of the original theory may have misled some people trying to understand its generalization. It is, in truth, a distortional energy model, with only those shear stresses and strains with matching components contributing. Stresses and strains with no matching counterpart contribute nothing to energy and must, therefore, be excluded from consideration. No such confusion can arise with isotropic materials, for which energy criteria can be expressed equally uniquely in terms of stresses, strains, and their products (energy).

Possibly new greater generalizations have been developed for the Tresca hexagon and von Mises/Hencky ellipse, to materials having no symmetry of properties at all. These characterizations could be applicable far beyond the realm of fibre-polymer composites.

The use and teaching of interactive macro-level composite failure criteria should cease forthwith. They have no scientific basis for heterogeneous materials such as fibre-polymer composites. By the time an acceptable answer has been produced by alteration of the material input properties, by hand or within a computer code, they are so highly empirical as to be little more than curve fits.

ACKNOWLEDGEMENT

Despite the fact that his work on composite failure theory has obviously been revolutionary, rather than evolutionary, the author gratefully acknowledges the benefit of considerable help and constructive criticism from a great many people and organizations around the world. Without such encouragement, it would not have been possible to persevere in the face of staunch criticism from others, widespread apathy in regard to *any* changes, and, until recently, pressures to divert his attention to other activities with seemingly better short-term profitability.

REFERENCES

1. Waddoups, M. E., "Characterization and Design of Composite Materials," in *Composite Materials Workshop*, edited by S. W. Tsai, J. C. Halpin, and N. J. Pagano, Technomic, Connecticut, 1968, pp. 254-308.
2. Hart-Smith, L. J., "The Ten-Percent Rule for Preliminary Sizing of Fibrous Composite Structures", McDonnell Douglas Paper MDC 92K0024, SAWE Paper No. 2054, presented to 51st SAWE International Conference, Hartford, Connecticut, 18-20 May, 1992; published by *Aerospace Materials*, Vol. 5, No. 2, August-October 1993, pp. 10-16.
3. Hart-Smith, L. J., "Expanding the Capabilities of the Ten-Percent Rule for Predicting the Strength of Fibre-Polymer Composites", McDonnell Douglas Paper MDC 97K0012, prepared for publication in *Composites Science and Technology*.
4. Hart-Smith, L. J., "The Role of Biaxial Stresses in Discriminating Between Meaningful and Illusory Composite Failure Theories", McDonnell Douglas Paper MDC 91K0077, presented to 9th DoD/NASA/FAA Conference on Fibrous Composites in Structural Design, Lake Tahoe, Nevada, November 4-7, 1991, in Proceedings, DOT/FAA/CT-92-25, Part III, pp. 1507-1528; also published in *Composite Structures*, Vol. 25, 1993, pp. 3-20.
5. Hart-Smith, L. J., "A New Approach to Fibrous Composite Laminate Strength Prediction", Douglas Paper 8366, presented to MIL-HDBK-17 Committee Meeting, Singer Island, Palm Beach, Florida, October 3-5, 1989; represented to 8th DoD/NASA/FAA Conference on Fibrous Composites in Structural Design, Norfolk, Virginia, November 28-30, 1989; in Proceedings, NASA CP-3087, Part 2, pp. 663-693.
6. Ewins, P. D. and Potter, R. T., "Some Observations on the Nature of Fibre Reinforced Plastics and the Implications for Structural Design", *Phil. Trans. Roy. Soc. Lond.*, Series A, Vol. 294, pp. 507-517, (1980).
7. McCartney, L. N., "The Generalized Framework for the Prediction of Ply Cracking in Any General Symmetric Laminate", NPL Report CMMT(A) 51, December 1996.
8. Puck, A., '*Festigkeitsanalyse von Faser-Matrix-Laminaten: Modelle für die Praxis*'; Hanser; München, Wien, 1996.
9. Hart-Smith, L. J., "Predictions of a Generalized Maximum-Shear-Stress Failure Criterion for Certain Fibrous Composite Laminates", McDonnell Douglas Paper MDC 97K0011, prepared for publication in *Composites Science and Technology*.
10. Hart-Smith, L. J., "Fibrous Composite Failure Criteria – Fact and Fantasy", McDonnell Douglas Paper MDC 93K 0047, presented to Plenary Session of Seventh International Conference on Composite Structures, Paisley, Scotland, July 5-7, 1993; abridgement to be published in *Composites Part A: Applied Science and Manufacturing*, Vol. 28A, 1997, under the title "A Bona-Fide Fibrous Composite Failure Criterion".

11. Hill, R., ‘*The Mathematical Theory of Plasticity*,’ Oxford University Press, London, UK, (1971), pp. 317-340.
12. von Mises, R., Gottingen Nachrichten, *Math. Phys. Kl.*, 1913, p. 582; Hencky, H., *Zeitschr. f. Angew. Math. u. Mech.*, Vol. 5, 1925, p. 115. (Cited by S. Timoshenko, *Strength of Materials, Part II*, D Van Nostrand, New York, 2nd ed’t’n, (1940).
13. De Teresa, S., “Piezoresistivity and Failure of Carbon Filaments in Axial Compression”, *Carbon*, Vol. 20, No. 3, 1991, pp. 397-409.
14. Chamis, C. C., “Micromechanics Strength Theories”, *Composite Materials, Vol. 5, Fracture and Fatigue*, edited by L. J. Broughtman, Academic Press, New York, (1974) pp. 126-131.
15. Baker, A. A., “Bonded Composite Repair of Metallic Aircraft Components – Overview of Australian Activities”, AGARD-CP-550, pp. 1-1 to 1.14.
16. Li, S., Reid, S. R., and Soden, P. D., “A Continuum Damage Model for Transverse Matrix Cracking in Laminated Fibre Reinforced Composites”, *Proc. Roy. Soc. (London)*, March 1997
17. Cuntze, R. G., “Evaluation of Multiaxial Test Data of UD Laminae by So-Called Fracture-Type Strength Criteria and by Supporting Probabilistic Means”, to be presented to 11th ICCM Conference, Gold Coast, Australia, July 14-18, 1997.
18. Hart-Smith, L. J., “Backing Out Equivalent Unidirectional Lamina Strengths from Tests on Cross-Plied Laminates”, McDonnell Douglas Paper MDC 91K0078, Proc. 37th International SAMPE Symposium and Exhibition, Anaheim, California, March 9-12, 1992; pp. 977-990.
19. Hart-Smith, L. J., “The Truncated Maximum-Strain Composite Failure Model”, *Composites*, Vol. 24, No. 7, 1993, pp. 587-591.
20. Hart-Smith, L. J., “Predictions of the Original and Truncated Maximum-Strain Failure Models for Certain Fibrous Composite Laminates”, McDonnell Douglas Paper MDC 97K0010, prepared for publication in *Composites Science and Technology*.

APPENDIX

COMPLETE GENERALIZATION OF THE MAXIMUM-SHEAR-STRESS CRITERION

The specific analysis of interest here for carbon fibres (reinforcing polymer composites) is for a homogeneous material known to be transversely isotropic because of the method of manufacture. In the more general case, this symmetry around the axis of the fibre would not exist. In this more general case, the maximum-shear-stress criterion, whether it be for failure or yield, can be extended from the classical model for isotropic materials in the following manner. If we consider three mutually orthogonal principal strain axes, 1, 2, and 3, any states of strain for which the *direct* strains in each of these three directions are all equal and of the same sign cannot possibly be associated with any *shear* strain and, therefore, is an axis of zero

distortional energy. This axis, extending to both plus and minus infinity, and inclined equally from each axis, is well known in classical elasticity, being associated with both the circular cylinder of the von Mises/Hencky model and the equi-sided hexagon of the Tresca model (which may have previously been proposed by Coulomb). This axis is shown in Fig. A1.

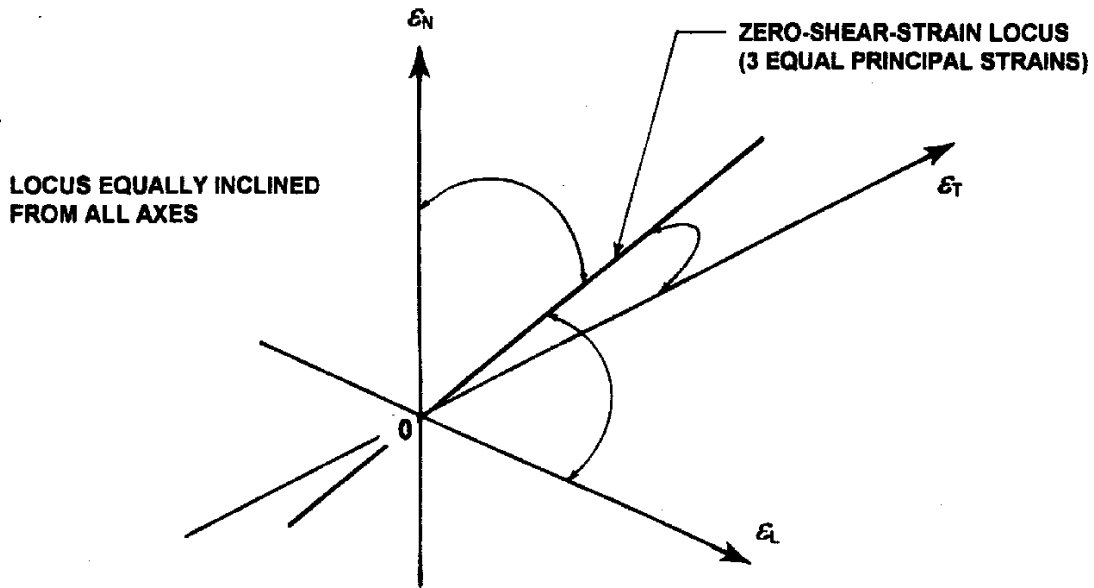


Fig. A1 Zero-shear-strain axis in three-dimensional space

The greater the distance from this axis, the greater can be the shear strains. In other words, the general extension of the maximum-shear-stress criterion, in the context of limits on the distortional strain energy in a material, can be expressed by three *independent* limits on the difference between principal stresses. That is

$$|(\varepsilon_1 - \varepsilon_2)| \leq \gamma_{12 \text{ crit}}, \quad |(\varepsilon_1 - \varepsilon_3)| \leq \gamma_{13 \text{ crit}}, \quad |(\varepsilon_2 - \varepsilon_3)| \leq \gamma_{23 \text{ crit}} \quad \cdot$$

(A.1)

These limits will define a cylinder around the axis in Fig. A1 having a skewed hexagonal cross section in which each pair of sides is parallel and equidistant from the axis, but the three pairs are *not* at the same distance from the axis. (In the case of an isotropic material, they would be.) As with classical theories of elasticity, this cylinder will be unbounded if no limits are imposed on the possible states of stress which can exist in each of the three directions. This cylinder is illustrated in Fig. A2, which includes one arbitrary cross section. The failure surface looks like a flattened hexagonal pencil. (Thanks to Richard Potter, of the DRA at Farnborough for this excellent analogy.)

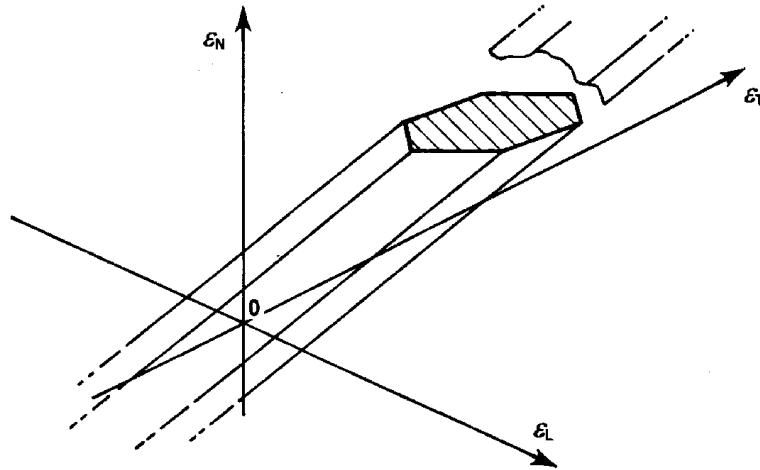


Fig. A2 Generalized maximum-shear-stress cylinder in three-dimensional space

What is usually of interest for thin-shelled laminated construction is the *particular* section cut through this cylinder on which the stress normal to the local plane of the laminate is equal to zero. (This direction is custom-arily associated with the third direction.) Those who work with thick-walled pressure vessels probably have an interest in *more* than this isolated detail of the model, even if it does suffice for most aircraft structures.)

The question obviously arises as to why a maximum-shear-stress criterion is formulated with limits on shear *strains* instead. The obvious answer is that the criterion was *first* formulated for *isotropic* materials, in which case the distinction was irrelevant; the axes coincided. A little reflection, however, might show that the whole issue is one of semantics. Just as the von Mises/Hencky model can be regarded as a *distortional energy* model, so can that of Tresca. It is quite possible that A. E. H. Love could have formulated this criterion in *either* set of reference axes, but this author is not as great a mathematician. His understanding of the failure of homogeneous solids may be summed up as follows. When the stresses (and strains) are all low enough, failure does not occur. Regardless of the mechanism of failure, the stresses acting on and in a body can be characterized by Mohr circles. As one or more of these stresses is increased, the circles expand. Eventually they grow large enough to reach some limit. If that limit is a principal shear stress, failure is by ductile yielding, with no preconditions on how *much* yielding. If, instead, a principal direct-stress limit is reached first, failure is by brittle fracture. (The second possibility can occur only for tensile loads, of course, and the critical stress is not purely a material property; it is affected also by geometry. The true *material* property is the fracture toughness, which can be expressed on the Mohr-circle plane only for *one* geometry at a time.) *Both* of these failure scenarios can be associated with an interaction between the individual stress components within the *homogeneous* material which is being assessed.

If it is accepted that the maximum-shear-stress criterion is really one of distortional energy, it is theoretically possible to express the very same limit(s) in terms of strain-energy, stresses, or strains. This was done centuries ago for isotropic materials. The author knows only how to express the generalization of this criterion to nonisotropic materials in terms of *strains*, omitting those stresses for which there is no associated strain because they cannot contribute to *energy*. The challenges of extending this work further to materials which do *not* have an

axis of symmetry, and of formulating the model in terms of energy or stresses, remain for a more skilled mathematician.

One further interesting point about the failure surface for the general case is the issue of characterizing it in a form which would reduce to the von Mises/Hencky model for isotropic materials. Perhaps surprisingly, the solution is *not necessarily* a cylinder with an elliptical cross section. It would be for a *single* failure mechanism. In the more general case with multiple failure mechanisms, however, it would be the combination of *three* elliptical cylinders with their axes along the line shown in Fig. A1. The aspect ratios, sizes, and orientations of these ellipses would be set by the various critical conditions associated with the presumed independent levels of distortional energy as a function of the anisotropy of the material. In general, the failure envelope would be defined by those portions of these ellipses closest to the central axis, leading to a shape like a hexagon with convex curved facets. If each ellipse had an extremely high aspect ratio, these arcs would reduce to the same flat sides on the hexagon of the Tresca formulation.

APPLICATION OF COMPOSITE MATERIALS TO THE RENEWAL OF TWENTY-FIRST CENTURY INFRASTRUCTURE

Vistasp M. Karbhari

*Division of Structural Engineering, University of California, San Diego
MC-0085, 9500 Gilman Drive, La Jolla, CA 92093-0085, USA*

SUMMARY: Based on their high strength- and stiffness-to-weight ratios, corrosion resistance, environmental durability and inherent tailorability, fiber reinforced polymer composites are being increasingly considered for use in infrastructure renewal. Areas of potential application, besides those involving composite cables and rebar, range from strengthening and seismic retrofit of reinforced concrete columns, decks and girders, to their use for all composite structural elements such as bridge decks. This paper explains the motivation and need for the development of composite systems for such applications and describes a number of such applications. The use of composites for the fabrication of light weight bridge decks that can be deployed in uses ranging from the replacement of deteriorating decks, to the erection of completely new superstructure is also described with test results. Aspects related to materials selection, manufacturing, quality control and standards for the use of composites in civil infrastructure are also discussed.

KEYWORDS: composites, civil infrastructure, renewal, decks, columns, seismic retrofit, durability, manufacturing.

INTRODUCTION

The deterioration of transportation related civil infrastructure represents one of the most significant challenges facing the nations of the world as we move our lifelines into the 21st century. The current impasse is due to the fact that (i) a large number of our bridge inventory are reaching the end of their initial design life, (ii) deterioration rates due to aging and environmental degradation are being accelerated and aggravated by causes ranging from poor initial construction and materials selection to shortcomings in design, workmanship and quality control and even improper use of retrofit and repair measures, and (iii) in addition routine maintenance has often not been conducted on these aging structures. Further, our traffic needs have increased dramatically over the past two decades with transportation of goods and services being conducted on a global, rather than local basis, resulting in a growing need for the widening of our highway system to accommodate more lanes, and for the renewal of existing structures to carry heavier loads at higher speeds. It is increasingly becoming apparent that deteriorating transportation related systems such as roads and bridges have a tremendous impact on society in terms of socio-economic losses resulting from delays and accidents. Anecdotal estimates point out that by 2005, traffic delays caused by an inadequate road system will cost the United States over \$50 billion a year in lost wages and wasted fuel. This will not only have an impact on local economies, but will in fact affect the economic well being of the nation in general.

Conventional materials such as steel, concrete and wood have a number of advantages, not the least among which is the relatively low cost of materials and construction. However, it is clear that conventional materials and technologies, although suitable in many cases and with a history of good applicability, lack in longevity in some cases, and in others are susceptible to rapid deterioration, emphasizing the need for better grades of these materials or newer technologies to supplement the conventional ones used. It should also be noted that in a number of cases, design alternatives are constrained by the current limitations of materials used, e.g. in the length of the clear span of a bridge due to weight constraints, or the size of a column due to restrictions on design and minimum cover needed. In a similar manner, often the use of conventional materials is either not possible in cases of retrofit, or may be deemed as ineffective in terms of functionality. In other case restraints such as dead load, restrict the widening of current structures, or the carriage of higher amounts of traffic over existing lifelines. In all such (and other) cases, there is a critical need for the use of new and emerging materials and technologies, with the end goal of facilitating functionality and efficiency.

Fiber reinforced composite materials, consisting of stiff and strong reinforcing fibers, held together by tough and environmentally durable resin systems show immense potential to add to the current palette of materials being used in civil infrastructure. Due to their high strength-to-weight and stiffness-to-weight ratios, corrosion- and fatigue-resistance, and overall durability, these materials are tailor made for use in infrastructure renewal. Despite the widespread use of fiber reinforced composites in the aerospace and defense related sectors, and the increasing potential for their use in civil infrastructure as showcased through demonstration projects, actual applications in the civil engineering sector have been slow. This is primarily due to three reasons: (i) unfamiliarity with composites, (ii) lack of predictive models, durability data, and design guidelines for their use in civil infrastructure, and (iii) economics related to fabrication. The key advantages of fiber reinforced composites, such as free-form and tailored design characteristics, strength/weight and stiffness/weight ratios which significantly exceed those of conventional civil engineering materials, high fatigue resistance, and a high degree of inertness to chemical and environmental factors, are often lost in high materials and manufacturing costs, particularly in direct comparison with conventional structural materials such as steel and concrete. However, the recent downturn in defense spending and the resulting need for new markets has spurred renewed efforts in reducing the costs of both raw materials and manufacturing processes, making it highly feasible to use composites in civil infrastructure. Within the vast applications area in civil infrastructure, this paper will concentrate on the narrow area of bridges, with focus on both rehabilitation and renewal. However, it should be mentioned that there is immense applicability in other areas such as tunnels, buildings, pipelines etc. We will also focus on the use of composites involving applications other than those using composite rebar, grids or cables.

APPLICATION IN THE REHABILITATION OF STRUCTURES

The use of composites for rehabilitation / retrofit / strengthening of bridge structures can be thought of as akin to the application of a surface layer that either protects and/or improves on the response of the encapsulated element. Within this area, three major structural areas can be identified (i) seismic retrofit of bridge columns, (ii) strengthening of deteriorated columns and piers, and (iii) strengthening of girders and bridge decks. Of these the first area has received perhaps the maximum attention because of the critical need for retrofit in areas of high seismic activity such as California and Japan as evidenced by the recent Northridge and Kobe earthquakes. Since topics in this area have been extensively discussed elsewhere, this section

will make brief note of advances in this area. Further discussion will be conducted in the section entitled "Issues Related to Materials and Manufacturability."

Seismic Retrofit of Bridge Columns

The confinement of concrete through the use of an external jacket has been proven to result in enhanced system ductility and subsequent performance under seismic events. This is because the external jacket provides constraint to the dilation of concrete in the absence of sufficient hoop steel. Amongst other conventional seismic retrofit strategies, steel jackets have been extensively used in both Japan and the United States. However this method of retrofit necessitates the welding of jacket sections in the field which is a concern as related to effectiveness and overall quality control. Further the use of steel in some areas carries with it the potential for rapid corrosion and degradation. The use of composites as wraps/jackets on columns to replace steel jackets in seismic retrofit has achieved a high level of interest both in Japan and the United States, with at least seven different methods being used to achieve the confinement of concrete, with the generic categories being listed below:

- Wet winding of tows,
- Winding of prepreg tow/tape,
- Wet layup of fabric,
- Layup of tape,
- Adhesive bonding of prefabricated shells,
- Insitu resin infusion of jackets, and
- Use of composite cables wrapped around concrete core

As an example of development, tests on 40% scale bridge columns at UCSD have shown that the use of carbon fiber reinforced jackets applied through the continuous winding of prepreg tow which is cured after completion of the jacket, can be as effective as steel jackets for retrofits in flexural lap splice and shear applications [1]. The advantages of such a method are (i) the fiber is continuously placed in the direction where it is the most efficient, i.e. the hoop direction and, (ii) the method of application lends itself to overall efficiency and quality control at a rapid rate of completion. An example of the dimensions and reinforcement layout of a shear column test specimen are shown in Fig. 1, emphasizing the small thickness of composite needed for retrofit.

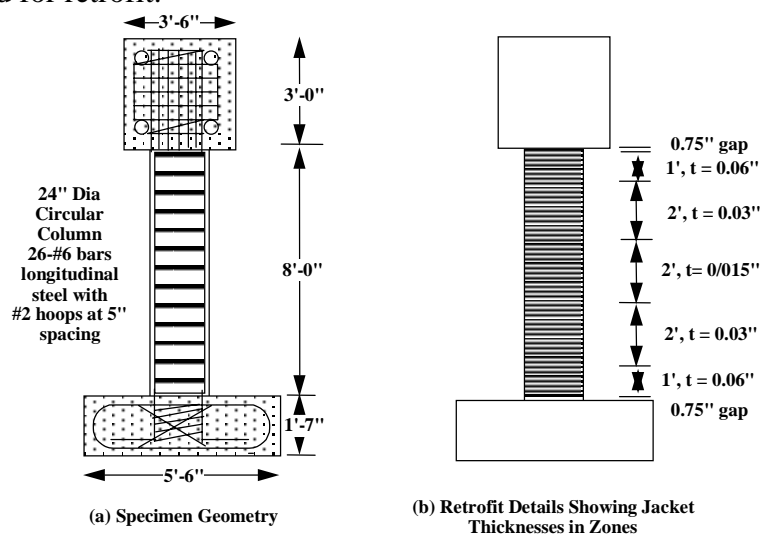


Fig 1: Example Schematic Showing Retrofit Details for a Carbon Fiber Composite Jacket for Shear Retrofit

The dimensions of zones in Fig. 1(b) depict the changes in thickness possible over five zones, thereby enabling the efficient tailoring of composite thickness related to structural demand. For the column retrofit shown schematically in Fig. 1, stable hysteresis loops were obtained on testing up to a displacement ductility level of $\mu_{\Delta} = 10.5$. Comparisons with the as-built case (without retrofit) show a clear improvement in performance. Equivalent retrofit measures with steel jackets show a slightly increased initial stiffness and load carrying capacity with increasing ductility levels due to the isotropy of the material. It should be noted that both these aspects are in fact disadvantages since they result in the transmission of higher seismic forces to adjacent structural elements. The use of composites, especially as reinforced with carbon fibers in the hoop direction (providing directed confinement) thus provides a layup that is

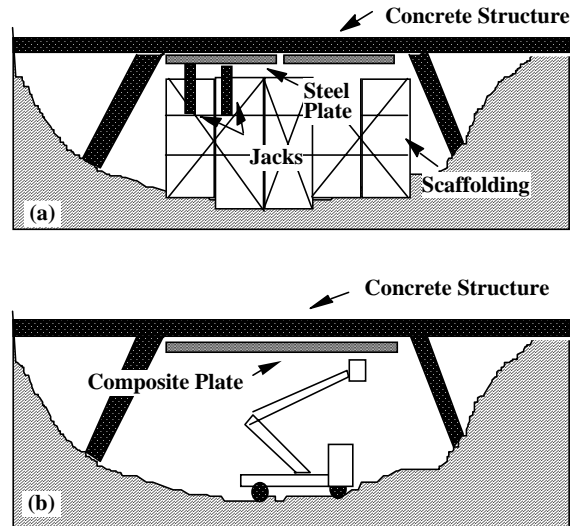


Fig. 2: Rectangular Column Retrofitted Using Carbon/Epoxy Tow Preg and Subsequently Covered With a Protective Coating

tailored for the specifics of the application, providing materials efficiencies that were not possible with conventional materials. Extensive testing has been conducted using this technology with both 40% scale and full-scale validation tests. In addition successful field demonstration applications have been conducted on the I-10 Santa Monica Viaduct in Los Angeles and a comprehensive set of design guidelines have been developed [1,2]. The application of the technique to a rectangular column is shown in Fig. 2, wherein the entire jacket was coated with a layer that served both as protection and as an aesthetic coating. The use of composites in such an application has been shown to be cost-competitive with steel retrofits while providing the potential for faster fabrication with less lane closure and

potentially far greater durability over the life-time of use. Further details related to testing and materials selection are reported in [3] and discussed briefly in a later section

External Strengthening of Decks and Girders



*Fig. 3: Schematic Comparison of Placement of External Reinforcement
(a) Steel Plates, (b) Composite Plates*

The use of techniques associated with the external attachment of composite plates to the soffit of decks and the underside of beams for purposes of strengthening and retrofit is attractive due to factors related to ease of access and decreased need for extensive changes to the existing structure. Although the bonding of steel plates has been used extensively for over two decades, this method suffers from a number of disadvantages ranging from difficulty in placement, to concerns related to overall durability. Composite plates, on the other hand, do not suffer from most of these deficiencies, due to the high stiffness- and strength-to-weight ratios, corrosion resistance and light weight (Fig. 3). Beginning with the repair of the Ibach bridge in Switzerland, a number of retrofit and strengthening projects have been completed in Europe and Japan, along with a few demonstration projects in the United States. In recent years, this method has been used for the upgrading of bridge decks to enable the use of higher load levels such as in the case of the Hiyoshigura Viaduct in Chiba, Japan where two layers of carbon fiber unidirectional fabric were bonded to the underside of a deck section in order to increase capacity from a 20 ton level to a 25 ton level [4]. The use of composites in such applications provides yet another example of how light weight tailored materials can be used effectively to enhance and increase the life of existing civil infrastructure. Details related to use and testing of such applications can be found in [5,6].

REPLACEMENT BRIDGE DECKS

It is estimated that most bridges in the US on an average last 68 years, whereas their decks last 35 years, and that “during the 1990’s, 40% of the total highway deck area in the US will become 35 years old, statistically ready for replacement” [7]. Some estimates from the mid

west and from regions where there is extensive use of road salt, put the life of a conventional bridge deck at about 10 years, thereby requiring extensive triage, or expensive replacement within a short time period. States such as Wisconsin report that with the exclusion of painting, bridge deck repair and replacement accounts for between 75 and 90% of annual maintenance costs associated with the structure. Added to the problems of deterioration are the issues related to the need for higher load ratings (HS15 to HS20, for example) and increased number of lanes to accommodate the ever increasing traffic flow on major arteries. Beyond the costs and visible consequences associated with continuous retrofit and repair of such structural components are the real consequences related to losses in productivity and overall economies related to time and resources caused by delays and detours.

Reasons such as those listed above provide significant impetus for the development of new bridge decks out of materials that are durable, light and easy to install. Besides the potentially lower overall life-cycle costs (due to decreased maintenance requirements), decks fabricated from fiber reinforced composites would be significantly lighter, thereby affecting savings in substructure costs, enabling the use of higher live load levels in the case of replacement decks, and bringing forth the potential of longer unsupported spans and enhanced seismic resistance. There has been considerable activity over the past decade in the area of composite reinforcement for concrete bridges with the reinforcement ranging from composite rebar and grids to composite cables for external and internal post-tensioning. The current application, however, emphasizes the use of fiber reinforced composites for the entire deck or as part of the actual superstructure system itself. Such a concept, in general, is not new, having been used previously in the Miyun bridge in China and the Aberfeldy Footbridge in Scotland, among others. The focus of this section will be on developments in the area of replacement bridge decks capable of being placed on pre-existing concrete and steel girders, as well as being used in new bridge systems.

The overall test program was undertaken at the University of California, San Diego (UCSD) with funding from the Federal Highway Administration (FHWA), the Advanced Research Projects Agency (ARPA), and the California Department of Transportation (Caltrans) as part of a University-Industry Consortium, and was aimed at the development of lightweight, degradation resistant fiber reinforced composite decks for primary use in replacement. The overall criteria that were used to guide the development of these decks included: (i) the development of stiffnesses through the appropriate use of face sheets and internal core configurations that would fall in the range between the uncracked and cracked stiffness of existing reinforced concrete decks, (ii) the development of equivalent energy levels at acceptable displacement levels as a means of building in a safety factor due to the elastic behavior of composite sections, and (iii) the development of processing methods that would be cost-effective and which ensured repeatability and uniformity. A building block approach was used in this program with tests being conducted at the subcomponent, component and field-size levels as depicted in Fig. 4, so as to evaluate structural response, effect of fabric architecture and the effect of different core configurations, in components subject to shear and bending as appropriate. Components were fabricated by a number of industrial partners (as listed in Fig. 4) using Wet-Layup, Pultrusion, Resin-Infusion, and processes that were combinations thereof for manufacturing. Details related to these processes can be found in [8, 9]. In order to verify repeatability and uniformity between samples, a number of components were fabricated and tested to the same specifications as well. It was generally seen that structural response and failure modes could be replicated fairly uniformly.


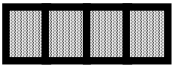






CONFIGURATION	COMPONENT SCALE			
	3' - 4'	6' - 8'	14'	15' x 7.5' Panels
 Balsa Core (Dupont)	●			
 Foam Filled Boxes (Dupont)	●		●	
 Foam Filled Truss (Dupont)	●	●	●	●
 Foam Filled Hat Sections (Dupont)			●	●
 Pultruded Profiles With Face Sheets (Lockheed-Martin)	●	●	●	
 Hybrids (Lockheed-Martin)				●
 Corrugated Core (Core-Kraft)		●		
 "Egg Crate" Core (Northrop-Grumman)			●	

Fig. 4: Matrix of Test Specimens

Fig. 5 depicts sample test results from the subcomponent level tests. Each of these used a different core configuration in order to assess the effectiveness of various strategies. The truss core configuration consisted of triangular foam cores wrapped with fabric, which were assembled within face sheets to form the structure. In order to assess the effectiveness of additional reinforcement at the nodes formed by the adjacent triangles, the second configuration used a woven fabric insert that strengthened the node area. The effect of this on the overall ductility and performance of the system is clearly apparent, as response appears to shift from linear elastic to “pseudo-ductile” with the ductility being afforded by slow matrix cracking and gradual separation between fabric layers at internal nodes and along the inclined webs (Fig. 6). The use of such mechanisms could be considered as a means for arriving at pseudo-ductile response in structures and thus enabling gradual and non-catastrophic failure of primary load-carrying elements in a safety critical application. Larger component level tests were conducted on 14 ft long beams using a test setup that consisted of two high strength concrete abutments that were set at 8 ft centers in a hydrastone bed and post-tensioned to the test floor.

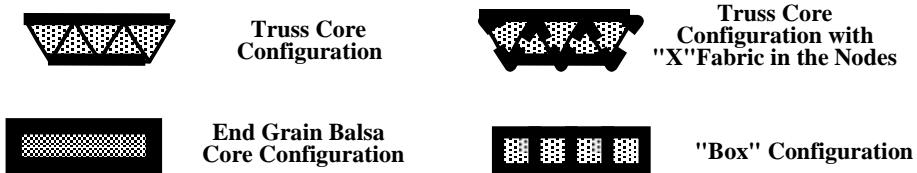
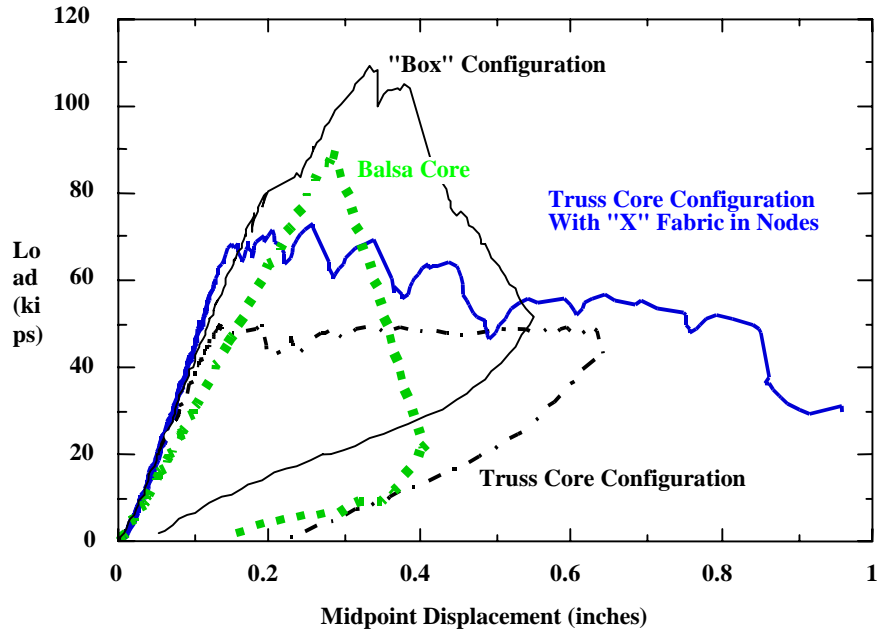


Fig. 5: : Load-displacement response of subcomponents tested in three-point bend mode

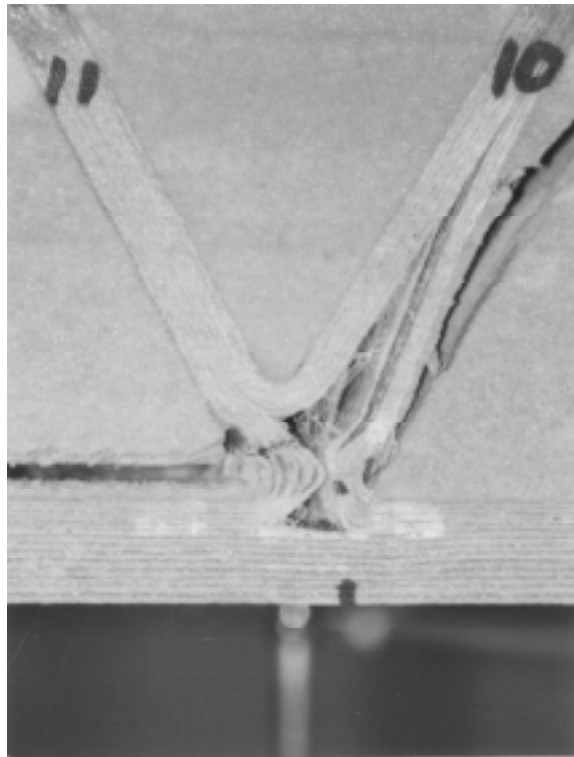


Fig. 6: Fabric Separation and Cracking at a Node

Continuity was provided on the cantilever end of the beam outside the supported span through the use of a structural steel yoke placed at the theoretical point of inflection of the adjacent span. The yoke was tied through the test floor. Each specimen was extensively strain gaged and deflection profiles were monitored using linear potentiometers. Examples of two such components are given in Figs 7 a and b.

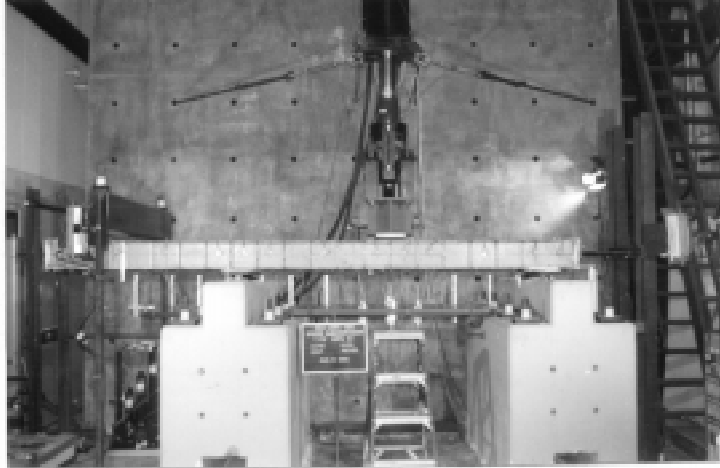


Figure 7a: "Box" Type Component Showing Support and Loading Conditions



Figure 7b: Deformation of a Trapezoidal Core Component at a Load Level of 215 kips

The fiber reinforced composite deck specimens show failure loads far in excess of that shown by the reinforced concrete specimen with initial structural stiffnesses that are comparable. The "box" configuration and the "trapezoid" configuration also show significantly enhanced energy levels as can be seen from Fig. 8. Obviously further optimization is necessary in order to achieve the appropriate performance levels at the minimum cost. Costs are directly related to the thicknesses of composite used in the skins and in the webs formed with the core configuration. A concern often voiced about the use of fiber reinforced composites for primary structure is that related to brittle behavior and catastrophic failure. In most cases, the components showed considerable load carrying capacity and continued to carry load, albeit at significantly lower levels, even after substantial cracking and fracture were seen.

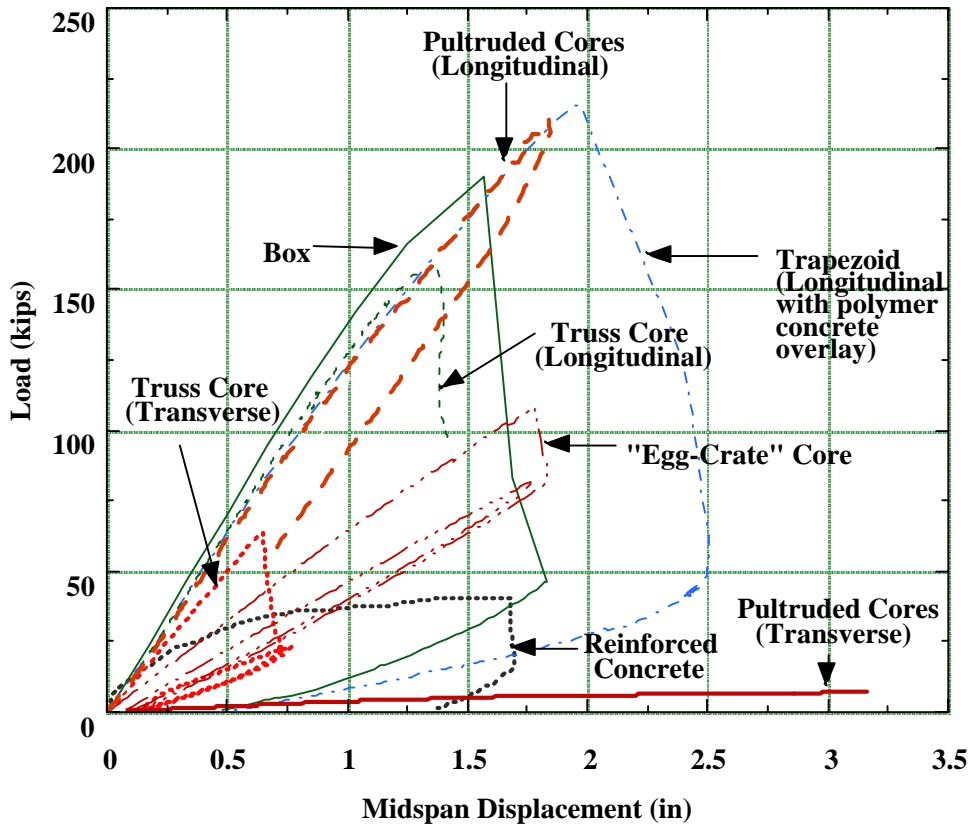


Fig. 8: Overall response of the 14 ft beam elements

— Reinforced Concrete	
— (#1) Truss Core (Resin Infused: All Glass)	62.15 kips/in
— (#2) Modified Hat Core (Wet-Layup: All Glass)	71.17 kips/in
— (#3) Modified Hat Core (Wet-Layup: Glass/Carbon Hybrid)	101.13 kips/in
— (#4) Modified Hat Core (Wet-Layup: Glass/Carbon Hybrid, Polymer Concrete Overlay)	104.78 kips/in

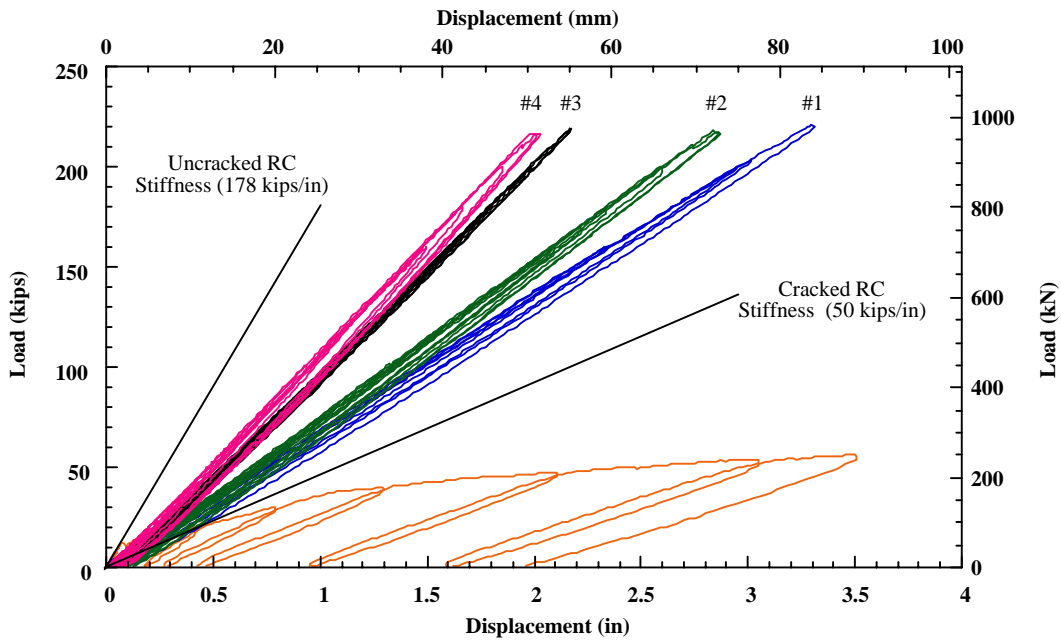


Fig. 9: Overall response of the field-scale deck panels

Further details related to strain and displacement response can be found in [10]. Field scale deck panels of size 15' x 7.5' x 9" were also tested for a limited number of concepts. These panels were fabricated in pairs, one each to be tested in the laboratory for assessment of stiffness and load-deflection response, and the other to be placed in a road test-bed for monitoring. Deck panels were fabricated following preset design criteria based on the achievement of a stiffness level between that of a cracked and uncracked concrete deck, and with the appropriate energy level to ensure safety. A panel using a glass/carbon hybrid construction was also tested, with and without a 0.75" polymer concrete overlay. All panels were approximately 8.25" thick, leaving 0.75" for the polymer concrete overlay. Panels were tested in the laboratory under simply supported end conditions with loads being introduced into the deck through two pads 6' apart and a spreader beam to approximate AASHTO HS loading conditions. Test results are shown in *Fig. 9*.

In each case, the composite decks were tested to a load of about 220 kips after which the test was terminated. It should be noted that the composite decks were 3 to 4 times lighter than the reinforced concrete deck panel which weighed about 12,500 lb., which translates into a threefold advantage, i.e. (a) lower deadweight enabling a higher live load capacity for the same supporting structure in cases of replacement decks, (b) lower dead weight enabling the use of lighter and smaller supporting- and sub-structure, in cases of new construction, and (c) lower dead weight enabling greater ease of field placement without heavy equipment.

4 deck panels (3 composite and one reinforced concrete) have been placed in a test site at UCSD in the road bed simply supported between two abutments 14 feet apart on centers traversing a hollow simulating a bridge. Deck-to-deck connections were made through the use of shear keys, backfilled with concrete. The site is on a heavily traveled road and hence affords the opportunity for field monitoring. The decks are instrumented with strain gages and linear potentiometers and response is monitored at regular intervals.



Fig. 10: Stages in the Placement of Composite Decks in a Road Test-Site

It is envisaged that monitoring will provide critical information on the actual behavior of these decks under actual traffic conditions. *Fig. 10* shows the placement of decks in the test site using fork-lifts, which emphasizes the immense advantage of lighter weight vis-à-vis field placement. This will also translate to faster completion of projects, thereby reducing time of road closures.

CONCEPTS FOR RENEWAL / NEW STRUCTURES

Although the areas of rehabilitation and retrofit offer the maximum potential for immediate application of composites in civil infrastructure, the development of new systems that combine the directionality and high performance levels of composites with the dominant characteristics of conventional materials (such as with concrete in compression) show great potential for advances in the design and construction of new civil engineering structures. One such concept is that of composite shell systems for columns, wherein prefabricated composite tubes serve the dual purposes of form-work and reinforcement, thereby replacing the reinforcing steel while enabling faster construction. In this system, the column is constructed by placing the hollow composite shell in place, and then filling it with concrete, without any steel along the height of the column. Construction details are such that it can be directly incorporated with conventional construction methods. Fig. 11 shows such a system being tested, whereas Fig. 12 depicts a section with the shell removed showing the use of ribs in the composite shell to enable continuity of deformation and stress transfer between the shell and the concrete encapsulated by the shell.

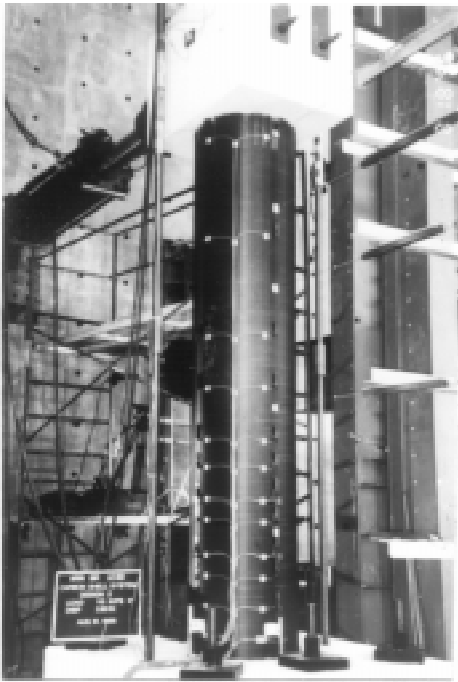


Fig. 11: Composite Shell System

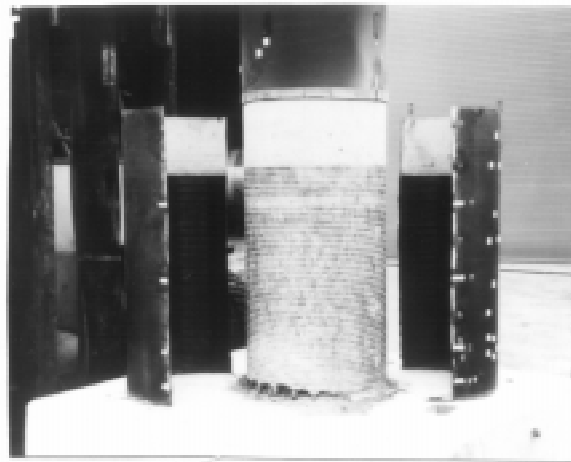


Fig. 12: Cut-Away of the Composite Shell System Showing the Shell, Ribs and Encapsulated Concrete

The composite shell system has been successfully tested using two concepts: (a) wherein starter bars from the footing extended into the column providing a conventional anchorage mechanism into the footing and/or bridge superstructure, and (b) wherein steel is completely eliminated with anchorage force mechanisms consisting of the reaction moment due to the compression force couple generated inside the footing and the frictional stresses between the composite shell and concrete [11]. The initial success of this system has led to the development of a complete bridge system, wherein the girders and columns are fabricated from composite shells [12]. An example is shown in Fig. 13a for a space truss bridge, whereas Fig. 13b depicts a concept for a dual tied arch bridge where the arches are comprised

of concrete filled carbon fiber reinforced tube segments and the tie girders are similar tubes which are post-tensioned. Cross-beams are connected to the tie girders using a Lincoln log system with joints being filled with concrete.

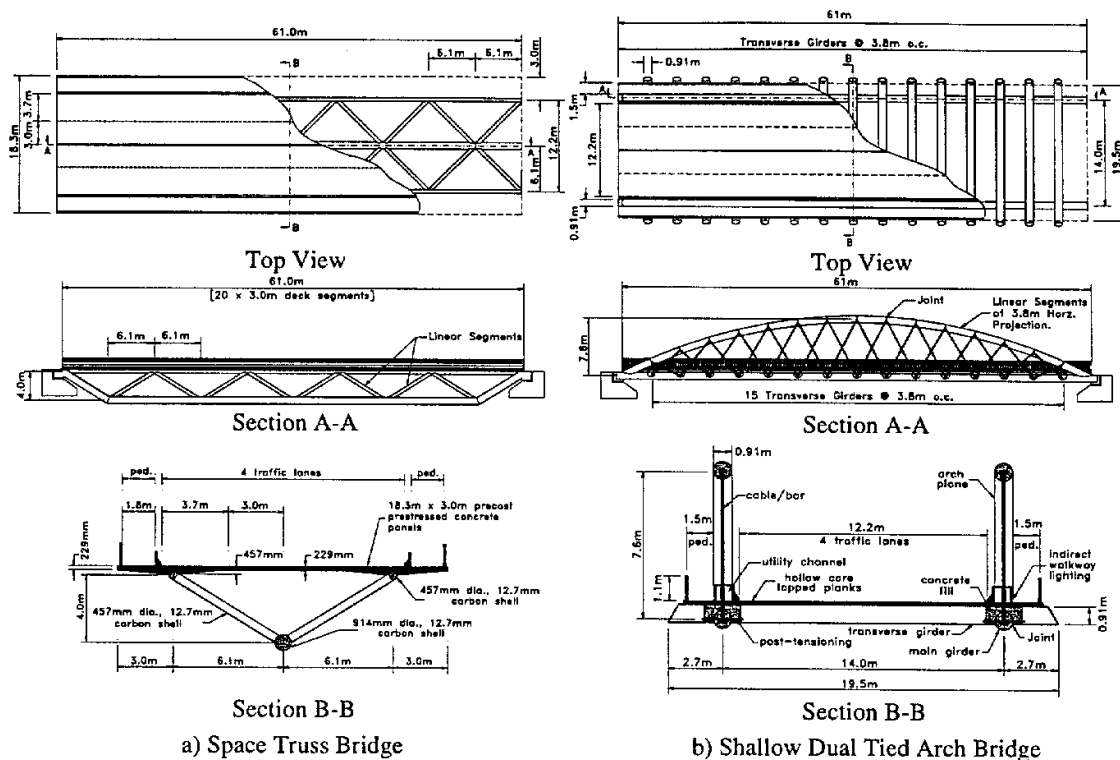


Fig. 13: Concepts for Modular Composite Shell Bridge Systems (after [12])

ISSUES RELATED TO MATERIALS AND MANUFACTURABILITY

The ultimate success of the applications described in the previous sections, as well as others being developed across the world will be dependent on the appropriate selection of materials and manufacturing methods that will enable these applications to live up to their full potential. The use of composites in civil infrastructure is different from its use in applications in the aerospace arena for a variety of reasons including (a) decreased need for very high dimensional control, (b) increased need for uniformity and standardization, even at the cost of some loss in tailorability, (c) increased need for materials that are capable of withstanding a severe environment (nature) over long periods of time with very little in-depth inspection, and a minimal amount of maintenance, and (d) increased emphasis on cost. This does not mean that civil structures will not be inspected at routine intervals, but it should be understood that the inspections will take place in the field, in conditions that may be far from ideal due to the vagaries of climate, and component position. This predicates that not all routine aerospace based NDE techniques will be viable. Also the overall safety of these structures is of paramount concern and hence materials selection and the determination of design values for characteristics of performance is very important.

The selection of a composite materials system for use in civil infrastructure needs to be predicated on the requirements of both short- and long-term performance, as well as on the

environment in which the performance is required. Although it may be tempting to choose the fiber reinforcement primarily on the basis of cost or stiffness, and the resin on the basis of cost or toughness, it is imperative that both be chosen on the basis of a number of factors including: (a) cost, (b) structural performance in terms of strength and/or stiffness, (c) damage resistance in terms of factors such as impact resistance and toughness, (d) resistance to environmental degradation and deterioration especially from aspects such as moisture, heat, freeze-thaw and alkalinity, (e) long-term performance factors such as creep and relaxation, and (f) manufacturability, including the effect of adverse field conditions on in-process defect formation. It is also important to differentiate between those applications which are stress critical, from those that are driven by the modulus of the material, and even those in which performance may be dependent, at least in part, on levels of failure strain (e.g. seismic retrofit of columns needing plastic hinge confinement).

Although some bare fibers, such as glass, may be rapidly affected by environmental factors, the degradation is significantly retarded or even nullified by the selection and application of the appropriate sizing and resin system. The engineer thus must consider the resin system not just as a medium that holds fibers together and serves as a basis for shear transfer, but also as a protective layer over the fibers themselves. Generically, a designer could consider polyesters, vinylesters and epoxies as the building block matrices for composites used for civil infrastructure applications. Of these the polyester systems are the simplest and the most economical. Orthophthalic polyesters should be avoided wherever possible since they have limited thermal stability and chemical resistance. Isopolyesters have better performance characteristics and have increased resistance to water permeation. Vinylester resins have characteristics similar to those of the Isopolyesters but often have better environmental resistance especially when used with glass fibers wherein interfacial bonding is better than with the isopolyesters. However, these resins do not bond as well to carbon fibers because of the lack of sizings that are compatible with them, resulting in decreases in shear and compressive properties. Epoxies are generically the most expensive of the three types of systems, but show the best overall performance and the least shrinkage upon cure. A number of blends are now available that combine the best characteristics of the systems and offer very good resistance to moisture penetration. The application of a gel coat or a resin-rich surface layer is also recommended for most applications using glass fibers as the reinforcing phase so as to provide a further barrier between the environment and the reinforcing fiber. Although considerable data exists for the environmental resistance of aerospace grade composites, data is not readily available for composites used in civil infrastructure. Degradation to these composites, when it occurs, usually affects strength, rather than stiffness, and hence care should be taken to apply strength reduction coefficients to designs to account for drop-offs in short-term and long-term performance levels. Table 1 gives a conservative estimate of time dependent strength reduction coefficients for E-glass, S2-glass, and carbon fiber reinforced composites.

Table 1: Strength Reduction Coefficients

Characteristic	E-Glass Composites	S2-Glass Composites	Carbon Fiber Composites
Short-Term	0.6-0.7	0.7-0.8	0.95
Long-Term	0.25-0.4	0.3-0.5	0.9

In each case, however, these should serve as guidelines only, with the actual factors being determined as far as possible taking into account the specifics of the materials systems used

and the requirements and loading regime associated with the application. Similar to the reduction factors used for short- and long-term performance on the basis of strength, factors need to be determined as related to fatigue and creep strength associated reduction. These obviously depend on the type of constituents chosen, and also on the form of the reinforcement used.

Table 2 gives an example of fatigue and creep strength reduction coefficients for E-glass reinforced composites. The table, again, serves as an example, underlying the critical need for the development of a good data base on materials to be used in civil infrastructure applications, along with the determination of appropriate materials related factors for design. Guidelines such as those given in Tables 2 and 3 should be used appropriately, keeping in mind that materials should not be blindly discarded because of the factors, since in a number of cases, the actual loading regime may not be affected significantly by the reduction coefficients (e.g. in some applications designs could call for the use of thicknesses of face sheets in order to meet stiffness or deflection critical criteria, resulting in very low stress levels even under overload conditions, which would mean that the material could still easily meet all long-term strength and creep-rupture requirements).

Table 2: Fatigue and Creep Strength Reduction Coefficients

Condition	E-glass Continuous Strand Mat in Polyester	E-glass Woven Roving in Isopolyester	Unidirectional E-glass/Epoxy
<i>Fatigue Stress Ratio</i>			
10 ³ cycles	0.5-0.65	0.3-0.45	0.4-0.6
10 ⁶ cycles	0.25-0.4	0.2-0.35	0.2-0.35
<i>Creep Rupture Stress Ratio</i>			
1000 hours	0.4-0.65	0.55-0.65	0.7-0.85

Often designs have to be developed based on limited data, or data that is deemed to be “representative” of the materials to be used. The question then arises as to what levels should be used for preliminary design allowables. Although the actual resolution of the question depends on the interplay between the manufacturing method used and degree of quality control (both of the incoming raw material stream and the finished product), reasonable values of strength allowables can be estimated through the use of one of the procedures in Table 3.

Table 3: Approximations for Strength Design Allowables

Procedure	Design Allowable
Nominal	Average - 3(Standard Deviation)
A Basis	50% of Average
B Basis	75% of Average

The selection of materials is also predicated by the specifics of the application itself. In applications where a composite is externally bonded to a concrete surface for the purposes of

strengthening, the efficiency of the measure will in large measure be dependent on the efficacy of the bond between the composite and the concrete substrate.

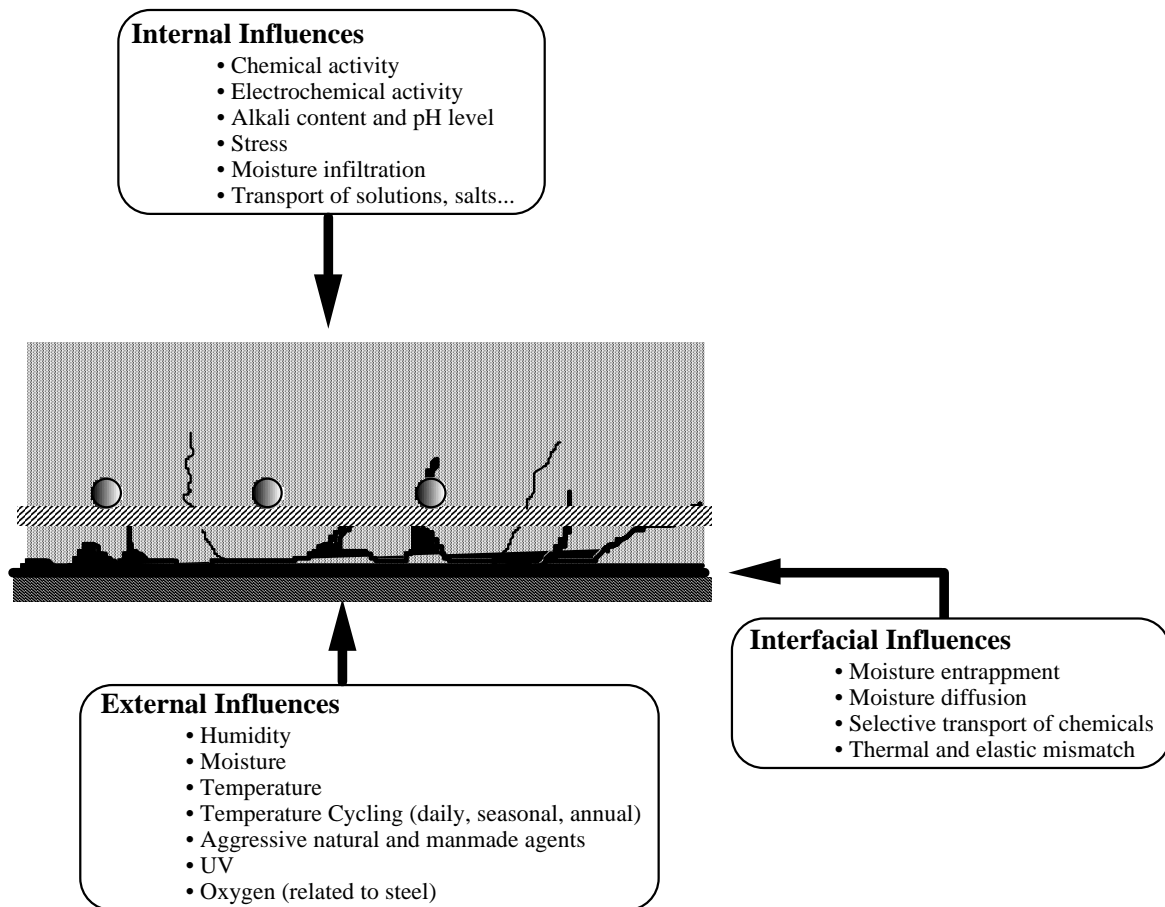


Fig. 14: Systems Level Interactions

An aspect that needs to be kept in mind during the design of such schemes is that related to the long-term environmental durability of the composite, and the durability and effectiveness of the adhesive bond between concrete and the composite. Adhesion and bond between the two are aspects that need to be looked at very closely not just because of the mechanics of rehabilitation, but also because of the influences of a variety of variables, external and internal on the response of the system (Fig. 14). It is important to remember that the strength and effectiveness of assemblies depends largely on the cohesive strength of the adhesive and the degree of adhesion between the two adherends. Of equal importance to the efficiency of the adhesive is the method of surface pretreatment of the adherends prior to the application of the adhesive. Most engineers tend to focus on the achievement of a prescribed initial bond strength but it must be noted that although important, this metric is not as important as that of bond durability as dictated by the environmental stability of the adherend-adhesive interface. This is especially true of assemblies that are subjected to the vagaries of nature, including extremes of temperatures (often within a 24 hour cycle), moisture, sustained and cyclic loading. Further details related to these aspects are reported in [6,13].

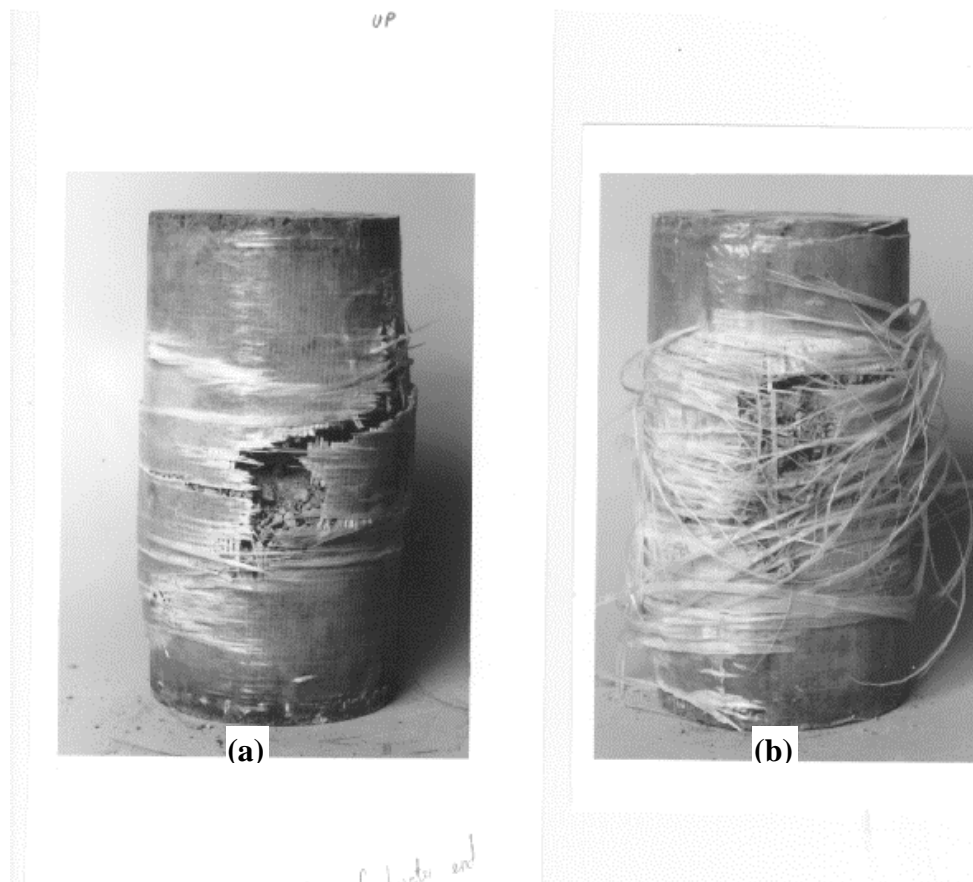


Fig. 15: Comparison of Failure Modes as a Consequence of Environmental Exposure to (a) Fresh Water Under Ambient Conditions, (b) 0° F (dry)

The use of composites in the strengthening of columns and in seismic retrofit calls for the use of reinforcement predominantly in the hoop direction. This is a fiber dominated application, with the predominant role of the composite being to enable the application of constraint to the concrete core. Although the resin then may appear to be extraneous, it serves a very useful function beyond that of a matrix in acting as a protective layer for the fibers, both from environmentally induced and accidental impact induced damage. It should however be noted that the composite, even in the undamaged state, changes response to a certain degree with the environment. A classic example is that of increase in stiffness and compression strength after exposure to 0° F (dry) temperatures due to matrix hardening. Not only can this change the response of the entire system (stiffness changes can be as high as 15-20%) but it also results in the introduction of new forms of damage and failure mechanisms. *Figs. 15a and b* show the dramatic change in failure mode of a glass epoxy wrap after short-term exposure to fresh water (at ambient temperature) and 0° F (dry) conditions. The tearing, inter-roving delamination and shredding of the hoop reinforcement in the former is traceable to the enhanced stiffness and hardening of the resin at sub-zero temperatures. Effects such as this, although not dangerous in a structural sense, do need to be taken into account during design. Effects of environmental exposure on the response of such systems are further elucidated in [14,15].

A common concern related to the use of fiber reinforced composites in civil infrastructure is the accurate determination of composite properties that can directly be used by the designer. A specific example of this is in the area of seismic retrofit where composite properties are needed for materials used in the confining jacket under loading conditions that replicate the actual situation of a confined column. Coupon level tension, flexure and shear tests which are routinely conducted to characterize composite properties do not address this important aspect. One way to determine properties which simulate those in a field wrap is to conduct a NOL ring or "burst" test, wherein a 20" diameter ring of the material in the configuration used in a jacket is placed in an apparatus and then hydraulically pressurized internally to simulate confinement and impart only circumferential stresses to the ring. An added advantage to such a test, beyond the determination of design properties, is the capability to test systems that are fabricated through the adhesive bonding of shell segments to form a jacket. Whereas tensile, or other characterization level tests would not give a true indication of structural performance, and failure mode, the NOL ring test does, even replicating failure initiation. This test can also

be used to accurately assess the effect of environmental exposure on the behavior of the retrofit system itself, including that induced by premature softening or plasticization of the adhesive, if any. It is strongly recommended that special efforts be made by the composites community to develop simple tests such as the NOL test which provide data to the civil engineering designer directly combining materials aspects with those of structural form and manufacturing.

Although the tests conducted to date on fiber reinforced composite decks have shown that they can be fabricated using a variety of processes with performance levels based on quasi-static testing that are acceptable for use in replacement strategies, a number of issues still need to be investigated before the actual implementation of such decks in the field. Some of these issues relate to response under dynamic loads, long-term durability of materials, connections between the decks and supporting girders, and connections between the decks and barriers and side rails. Due to the plethora of choices available in fiber and resin types, fabric architectures and processing methods, it is critical that specifications be developed based on performance standards, not just at the materials level, but also at the component and systems level. These standards must necessarily include recommendations on partial safety factors to accommodate variations due to differences in raw materials, quality achievable through different manufacturing processes, durability based on material choices and bridge environment, structural response and damage. It is highly probable that such deck systems will interact with pre-existing or new structural components fabricated from conventional materials and it is critical that interface issues as related to coefficients of thermal expansion, residual stresses and moduli differences are resolved without adversely affecting overall systems response. Issues such as cost-effectiveness and overall manufacturability must be addressed in the near future if such schemes are to compete with conventional strategies. It must be noted that overall cost-effectiveness is intrinsically tied to the degree of efficiency in materials conversion through the choice of a manufacturing process or processes. It is conceivable that future directions will emphasize the use of hybrid construction, encompassing not just hybrids of different reinforcing fibers, but also hybrids combining fiber reinforced composites with conventional materials such as steel and concrete. Future development in deck systems will have to consider a systems level approach based on the specifics of the application under consideration.

CONCLUSIONS

Fiber reinforced composites provide an immense palette of opportunity for the civil engineer to combine form and function in a manner not possible to date, and hence open up new vistas for the development of methods for renewal, including those involving new structural systems. Demonstrations and applications have clearly shown that these materials will be applied in future projects. However the extent of these applications will depend in large part on the resolution of outstanding critical issues that include (a) durability and fire protection, (b) reparability of composite structural elements, (c) development of validated codes, standards and guidelines of use to the civil engineering community, (d) development of cost-effective design approaches and manufacturing methods, and (e) provision of an appropriate level of quality assurance and control both during manufacturing and installation using unskilled construction labor.

Future developments in this area will probably emphasize hybrid construction wherein the most efficient aspects of composites are combined with dominant properties of conventional materials to provide the best overall structural response. It is already feasible that this technology will enable the construction of longer span bridges which meld in with the surrounding environment, providing exceptional structural response along with outstanding aesthetic features.

ACKNOWLEDGMENTS

The author gratefully acknowledges the support of the Federal Highway Administration, the Advanced Research Projects Agency, the California Department of Transportation, and the members of the ACTT/BIR Consortium.

REFERENCES

1. Seible, F., Priestly, M.J.N., Hegemier, G. and Innamorato, D., "Seismic Retrofit of RC Columns With Continuous Carbon Fiber Jackets," *ASCE Journal of Composites in Construction* (in press).
2. Seible, F., Priestly, M.J.N. and Innamorato, D., "Earthquake Retrofit of Bridge Columns With Continuous Carbon Fiber Jackets - Volume II, Design Guidelines," *Advanced Composites Technology Transfer Consortium Report No. ACTT-95/08*, UCSD, August 1995.
3. Karbhari, V.M., "On the Use of Composites for Bridge Renewal: Materials, Manufacturing and Durability," *Proceedings of the 42nd International SAMPE Symposium and Exhibition*, Anaheim, CA, May 4-8, 1997.
4. Karbhari, V.M., "Site Reports - Use of Composites in Civil Infrastructure in Japan," *WTEC/JTEC Report*, 1997.
5. McKenna, J.K. and Erki, M.A., "Strengthening of Reinforced Concrete Flexural Members Using Externally Applied Steel Plates and Fiber Composite Sheets - A Survey," *Canadian Society of Civil Engineering*, Vol. 21[1], 1994, pp. 16-24.

6. Karbhari, V.M., Engineer, M. and Eckel, D.A., II, "On the Durability of Composite Rehabilitation Schemes for Concrete: Use of a Peel Test," *Journal of Materials Science*, Vol. 32, 1997, pp. 147-156.
7. Bettigole, N.H, "Replacing Bridge Decks," *Civil Engineering*, 9, 1990, pp. 76-77.
8. Karbhari, V.M., "Fiber Reinforced Composite Decks for Infrastructure Renewal," *Proceedings of the 2nd International Conference on Advanced Composites in Bridges and Structures*, Montreal, Quebec, 1996, pp. 759-766.
9. Seible, F., Hegemier, G., Karbhari, V., Davol, A., Burgueno, R., Wernli, M. and Zhao, L., "The I-5/Gilman Advanced Composite Cable Stayed Bridge Study," *Structural Systems Research Report # SSRP 96/05*, UCSD, 1996.
10. Karbhari, V.M., Seible, F., Hegemier, G. and Zhao, L., "Fiber Reinforced Composite Decks for Infrastructure Renewal - Results and Issues," *Proceedings of the 1997 International Composites Expo*, Nashville, 1997, pp. 3C/1-3C/6.
11. Seible, F., Burgueno, R., Abdallah, M.G. and Nuismer, R., "Advanced Composite Carbon Shell Systems for Bridge Columns Under Seismic Loads," *Proceedings of the National Seismic Conference on Bridges and Highways*, San Diego, Ca, December 10-13, 1995.
12. Seible, F., Hegemier, G., Karbhari, V., Burgueno, R. and Davol, A., "The Carbon Shell System for Modular Short and Medium Span Bridges," *Proceedings of the 1997 International Composites Expo*, Nashville, 1997, pp. 3D/1-3D/6.
13. Karbhari, V.M., "Issues in Joining of Composites to Concrete - Rehabilitation and Retrofit," *Proceedings of Composites '96, Manufacturing and Tooling*, Anaheim, 1996, pp. 345-363.
14. Karbhari, V.M. and Eckel, D.A., II, "Effect of Cold Regions Climate on Composite Jacketed Concrete Columns," *ASCE Journal of Cold Regions Engineering*, Vol. 8[3], 1994, pp. 73-86.
15. Karbhari, V.M. and Eckel, D.A., II, "Effect of Environment on Axial Strengthening Capacity of Composite Jacketed Concrete Structural Elements," *Journal of Composites Technology and Research*, Vol. 17[2], 1995, pp. 99-106.

THE POTENTIAL OF KNITTED FABRICS AS A REINFORCEMENT FOR COMPOSITES

Ignaaas Verpoest, Bart Gommers, Gert Huysmans, Jan Ivens, Yiwen Luo, Surya Pandita, Dirk Philips

Department of Metallurgy and Materials Engineering,
Katholieke Universiteit Leuven, de Croylaan 2, B-3001 Leuven, Belgium

SUMMARY: Knitted fabrics have been, for a long time, considered to be useless as a reinforcement for polymer composites. This paper will show that the opposite is true: the in-plane mechanical properties are comparable with those of woven fabric composites, the out-of-plane properties (mode I fracture toughness, impact resistance) are superior. Moreover, the knitting loop structure allows for an extensional deformation of the preform; complex composite parts can hence be shaped without major difficulties in one draping operation. This paper will also highlight some novel modelling concepts, developed to predict the mechanical properties of knitted fabric composites.

KEYWORDS: textile composites, knitted fabrics, mechanical properties, modelling

INTRODUCTION

It is very surprising that it took more than 50 years before the composites community discovered the enormous variety of textile techniques. When glass fibres became commercially available in the 30's, their use as reinforcement for polymers remained basically restricted to two forms: unidirectional strands and chopped fibres.

Shortage of supplies of traditional construction materials in the aircraft industry during the second world war, incited engineers to use glass fibre composites in military aircraft. In order to optimise the mechanical properties, new fibre "architectures" like woven, braided, and even knitted fabrics were experimentally produced. The brittle nature of glass fibres required however some difficult adaptations to the existing textile machines. In the early 50's, only weaving remained as a commercially profitable textile technology for glass fibres. The advent of the even more brittle carbon fibres in the 60's would not change this picture.

During the last decade however, the composites community has rediscovered textiles. Two main reasons can be quoted for this.

First, the at that time available "preforms", namely unidirectional prepregs on one hand and chopped strand mats on the other hand, represented two extremes of in-plane mechanical properties, with nothing in between. Moreover, they both suffered from low out-of-plane properties and poor damage tolerance. It was believed that more complex fibre arrangements, as can be achieved in textiles, could help bridging the gap in the in-plane properties and improve out-of-plane properties and damage tolerance.

Second, UD-prepregs and short fibre composites also represent two extremes in production efficiency. Injection moulded short fibre thermoplastics and chopped strand mats are highly efficient techniques from a point of view of labour cost, whereas sprayed short fibre composite products require only a small capital investment. Autoclave techniques, using UD-prepreg, are on the other hand labour intensive and require high capital investments. Hence, the second driving force for the rediscovery of textiles was the pressure to reduce cost, not only of the raw materials and/or preforms, but also of the composite processing itself.

It should be emphasized that the previously drawn picture is schematic and hence might need some amendments. Indeed, woven fabrics have always been present, but were considered as a poor man's alternative for the superior UD-prepregs. Moreover, braidings continued to be used for special, mostly tubular types of applications. And finally, in the space industry, where cost was for a long time a non-issue, handicraft textile techniques (like 3D-"weaving") could be afforded. The real break-through of textile composites can be situated in the late 80's, as can be traced back in conference proceedings (ICCM, SAMPE) and journals, and in the appearance of specialised conferences (like TEXCOMP).

A multitude of textile preforms have found their way to commercial applications during the last decade [1]. New types of weaving and braiding, both two- and three-dimensionally, have been developed; stitching (or sometimes knitting) was used to combine into one package different UD-layers, and eventually to provide some through-the-thickness reinforcement. More recently, embroidery has been rediscovered, in its computer controlled form, as a highly efficient way for applying local reinforcements.

From the family of mass production textile techniques, knitting has been the last to be rediscovered by the composites community. Apart from some rare, isolated exceptions, the first scientific papers, reporting systematic studies on knitted fabric composites, appeared in the early 90's [Ref. 2-10].

The reluctance to use knitted fabrics as a reinforcement for composites was partially based on (false) intuition, partially on (true) facts.

Many composite engineers could not believe that a highly deformable and unstable fibre structure could be used as an effective reinforcement for composites. This intuitive argument was often heard when presenting initial results on knitted fabric composite properties. It overlooks however one of the basic laws in composites: as soon as the matrix is sufficiently stiff to immobilise the fibres, these fibres are fully operational as reinforcement.

A second group of arguments was based on facts. The highly curved nature of the yarns in knitted fabrics will result in mechanical properties which would never exceed those of a quasi-isotropic laminate. Moreover, looping the yarns could result in massive fibre breakage during the knitting process. As shown in Fig. 1, it was hence expected that the in-plane stiffness and strength should be situated somewhere in between those of woven and braided fabrics on one hand, and of (continuous or short fibre) random mats on the other hand.

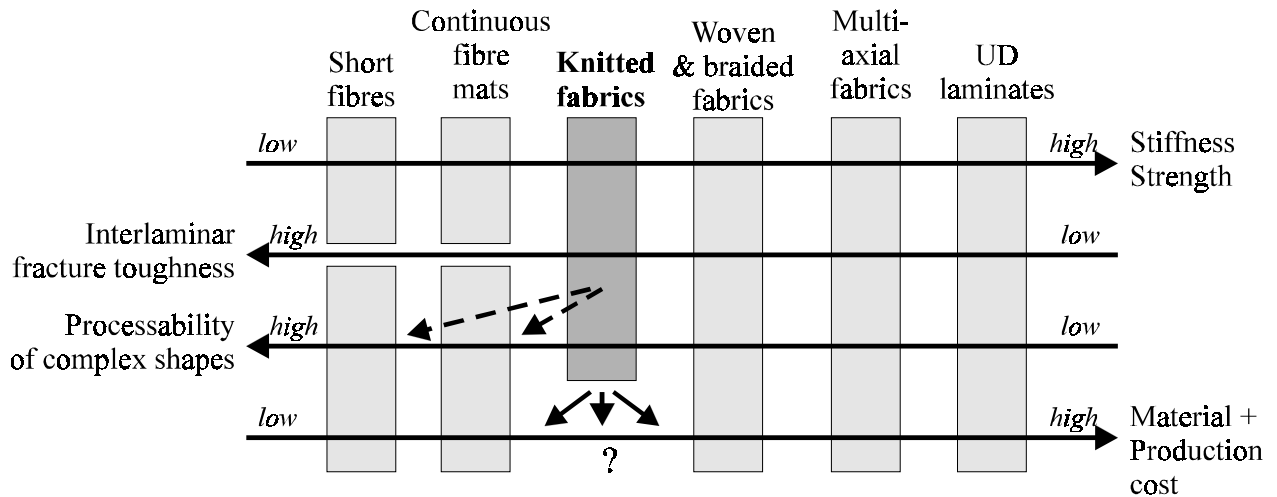


Fig. 1: Situation of knitted fabric composites in between fibre mats and woven or braided textile composites

The highly deformable nature of knits however raised the expectations that composite structures with very complex shapes could be produced in an efficient way. And finally, nobody had foreseen that knitted fabrics would possess an excellent interlaminar fracture toughness, giving hope for good damage tolerance and impact resistance. As will be shown further on, this has been achieved [5,11-15].

In the following paper, a comprehensive overview of the research on knitted fabrics, both 2D and 3D, at the Katholieke Universiteit Leuven will be presented. Where appropriate, reference will be given to results, available in the open literature, of the few other research groups active in this area.

KNITTED FABRICS

Production of Knitted Fabrics

Knitting for composite applications can be carried out on the same knitting looms on which sweaters, underwear, socks or curtains are knitted. In this way, this composite preforming technique takes advantage of the very advanced level of knitting machinery, which was optimised towards high speed production at zero defect rate.

As for clothing and house interior textiles, two different knitting techniques are used.

In the **weft knitting** technique, one single yarn is fed into the knitting machine. The yarn forms loops by the separate and consecutive movements of the needles. In this way, the knitted fabric is created row by row. The rows are usually called ‘courses’, the columns ‘wales’. The simplest weft knitting structure is the plain weft knit, shown in Fig. 2a, whereas Fig. 2b shows a more complicated weft knit, as used in our studies.

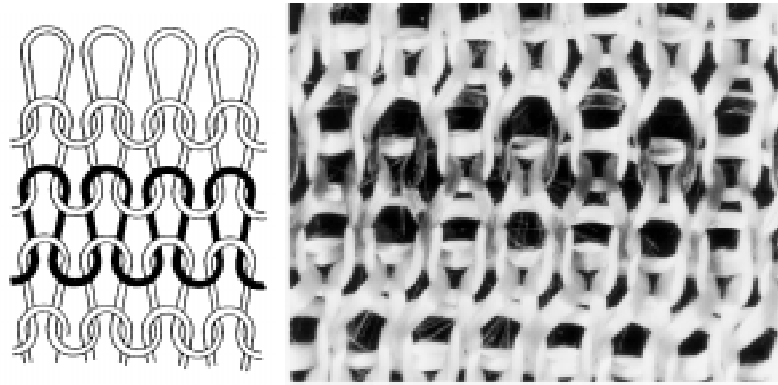


Fig. 2: Plane weft knitted fabric (a) and more complex weft knit used in this study (b)

The needle bar in the weft knitting machines can be either straight (“flat” weft knitting) or it can form a closed circle (“circular” knitting). In the former, the carrier which actuates the needles, moves back and forth, whereas in the latter it simply follows the rotational movement dictated by the circular needle bar. In mechanical knitting machines, basically each type of loop structure requires a specific machine setting; only a limited sequence of loop structures can be mechanically “programmed”, using a cam system. This lack of flexibility has been overcome in computer controlled weft knitting machines, where the needles can be actuated separately in a computer controlled way. This allows a continuous variation of loop structures in both course and wale direction, and even a variation in the external geometry of the knitted product: socks, sweaters or five-fingered gloves can in this way been knitted in one uninterrupted operation. It is evident that this potential has not yet been fully exploited in knitted preforms for composite applications.

An additional advantage of the weft knitting technique are the low set up costs, as only one yarn bobbin is needed. Furthermore, circular knitting is extremely fast because of the rotational, uninterrupted movement of the shuttle.

The **warp knitting** technique is substantially different. A large number of yarns are simultaneously fed into the machine. All the yarns make the same loops. The extent to which one yarn is connected to its neighbours is determined by the movement of a guide bar. Fig. 3a shows a 1-and-1 (tricot) knitted fabric, in which each yarn is only connected to its nearest neighbour yarn. Fig. 3b shows a more complicated structure, as used in this study.

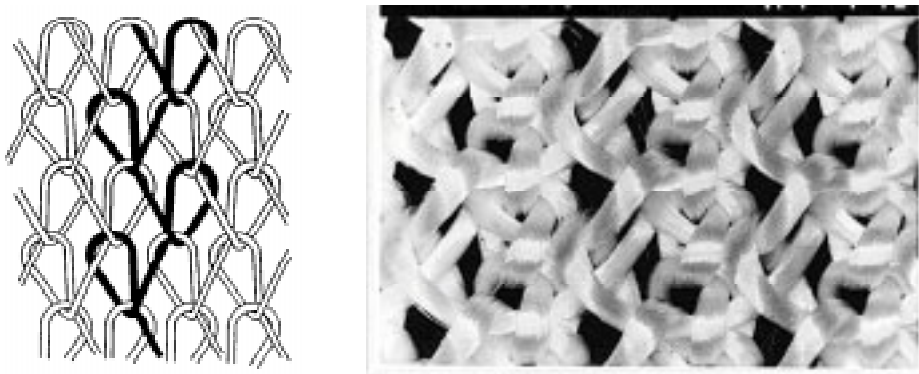


Fig. 3: (a) 1-and-1 tricot (warp) knitted fabric (b) a more complex warp knit used in this study

Already for non-composite applications (e.g. for house interior textiles) warp knitting looms with additional insertion of straight weft and/or warp yarns have been developed. It might be evident that this offers interesting perspectives for composite applications, as the curly nature of the knitted loops can be compensated by the insertion of straight yarns. Although it can be expected that the in-plane mechanical properties of the composite will improve, the price to be paid will be the loss in deformability of the preform and the loss of isotropy.

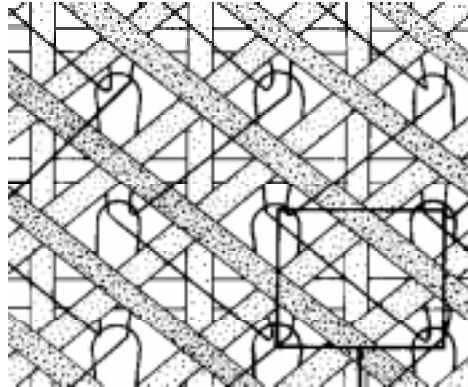


Fig. 4: Example of a weft inserted warp knit (WIWK)

From this technology, a specific type of knits for composites was developed. In the “weft-inserted-warp-knits” (WIWK), also called “non-crimp fabrics” (Fig. 4), the knitted loops (often out of a polymeric yarn) are only used to hold together the straight inserted yarns. In order to meet the specific requirements for composite applications, special looms have been developed (by a.o. Liba and Malimo). However, this type of knitting generates a kind of stack of UD-layers with different orientations, and hence should be compared with a multi-layered laminate. It will not be discussed further in this paper.

Warp knitting has the advantage over flat weft knitting that it is faster (but normally slower than circular knitting). Moreover, it offers some additional options like the use of more than one guidebar, each controlling one set of yarns, or the use of more than one needle bed. In this way “double” or multi-layered structures can be produced. - The 3D-knitted sandwich structures, discussed at the end of this paper, are a special example of this.- Finally, it has to be pointed out that “jacquard” techniques can be used like in weaving, in order to introduce a specific sequence of knitting loops, resulting in a regular pattern. It is obvious that also this potential has not yet been fully exploited for composite applications.

Although the knitting loops can be extremely complicated, they always follow a repetitive pattern (although the pattern can be distorted during consequent handling of the fabric). Hence, repetitive volume (or better: area) elements (RVE's) can be identified, identical to the unit cells in solid materials crystallography. It is interesting to observe that different knitting structures will have different degrees of symmetry, and that these symmetries can be described in a way identical to symmetries in crystals. Fig. 5 compares the symmetry elements in three knitted structures, with those in a woven fabric. Further on in this paper, it will be shown how the symmetry content of a knit will determine the elastic and strength properties of knitted fabric composites.

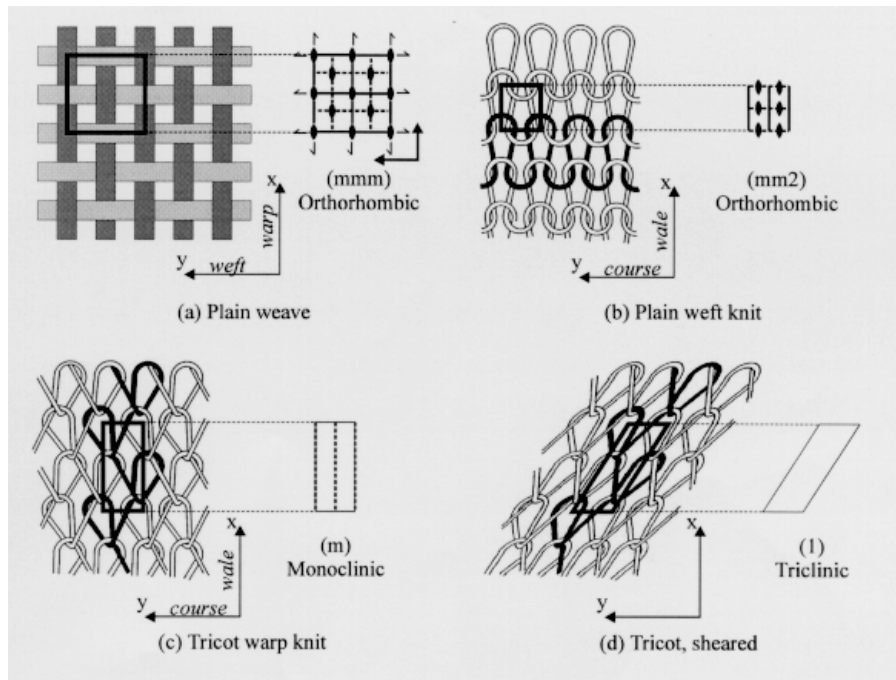


Fig. 5: Symmetry elements within knitted fabrics

Processing of Knitted Fabric Composites

Processing of composites comprises three major steps: the impregnation of the fibre bundles or preforms, the shaping or forming, and finally the consolidation (although the sequence of these steps can be altered). In this respect, knitted fabric composites are not different from all other textile based composites. Hence, only some striking differences and important advantages will be highlighted.

The **impregnation** step should be looked at differently for thermoplastic and for thermoset matrices.

Thermoplastic matrices offer the opportunity to be mixed with the reinforcing fibres *before* (using any type of combined yarns) or *during* the knitting operation (using simultaneously reinforcing and TP yarns). The big advantage of this type of pre-impregnated preform is that in principle only one additional processing step would be needed, namely simultaneous shaping and consolidation at elevated temperature of a stack of non-preconsolidated knitted fabrics. Research is ongoing to evaluate whether the resulting product quality can compete with the more conventional two-step process; for flat plates, Ramakrishnan [16] showed that acceptable mechanical properties can be achieved using such a one step process. For complex shaped composite parts, the critical point seems to be the uneven distribution of compressive stresses in a the mould, which leads to different degrees of consolidation. Replacing matched die forming by rubber stamping or diaphragm forming might offer a solution for certain composite products.

In the conventional process, different knitted layers (containing combined yarns) are preconsolidated into “organic sheets”, which are afterwards shaped into the final product geometry. Preconsolidation into organic sheets can also be realised using pure fabrics, i.e. by film stacking; this process can even be carried out continuously, using a double belt press.

The impregnation with *thermosets* is not different from that of other textile preforms. However, one major advantage has to be mentioned. The specific loop structure in knitted fabrics creates a continuous path for the liquid resin during vacuum infiltration or resin transfer moulding. As a consequence, the permeability is higher than for woven fabrics or mats (Fig. 6). In order to have a fair comparison, this permeability should be measured at equal fabric compaction load, because in reality, the knits can be compressed, either under atmospheric pressure in a semi-open mould or as a consequence of higher clamping pressures in a closed mould. This excellent permeability, under any compressive loads, has inspired the Belgian company Syncoglas to develop a unique (and patented) hybrid, sandwich type preform. In this preform, called Multimat, a central knitted layer is stitch-bonded to two outer random mats; the central knit secures the fast resin transport, whereas the random mats provide a smooth and rigid outer surface.

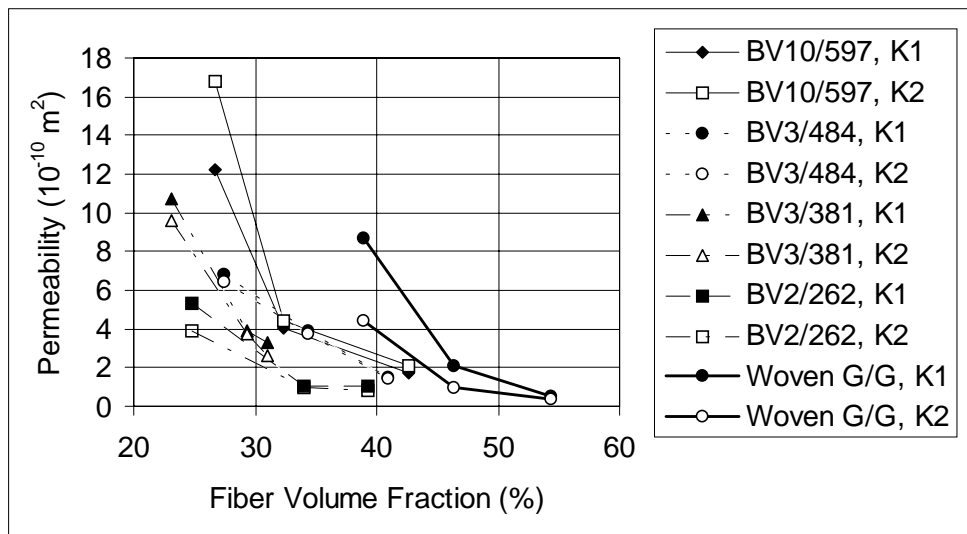


Fig. 6: Comparison of the permeability of knitted and woven fabrics

The **shaping** or **forming** step is intrinsically much easier than in any other composite processing method, because of the excellent deformability of knitted fabrics. This property is the direct consequence of the curled loop structure in knits. In fact, in each loop a certain amount of extensional deformation is built in, as the loops can be stretched. Moreover, shear deformations can be achieved by rotations at the loop intersection points. At these locations, and at high strains, additionally some yarn slippage might occur. All these deformation modes together result in an excellent drapability, which can be evaluated in different ways. Fundamental studies can be carried out on a biaxial tester, which was recently built at K.U.Leuven. (Fig. 7). Any combination of biaxial strains can be realised; the apparatus is further equipped with load cells and a centrally mounted video-microscope, so that the material resistance, and the unit cell deformation can be monitored continuously. Alternatively, deformability tests can be carried out by draping the knitted fabric over a predefined shape (a cylinder with a hemispherical top) during a diaphragm forming process. At identical processing conditions, it was shown that much more difficult shapes could be formed than with woven fabric composites, without wrinkling or tearing.

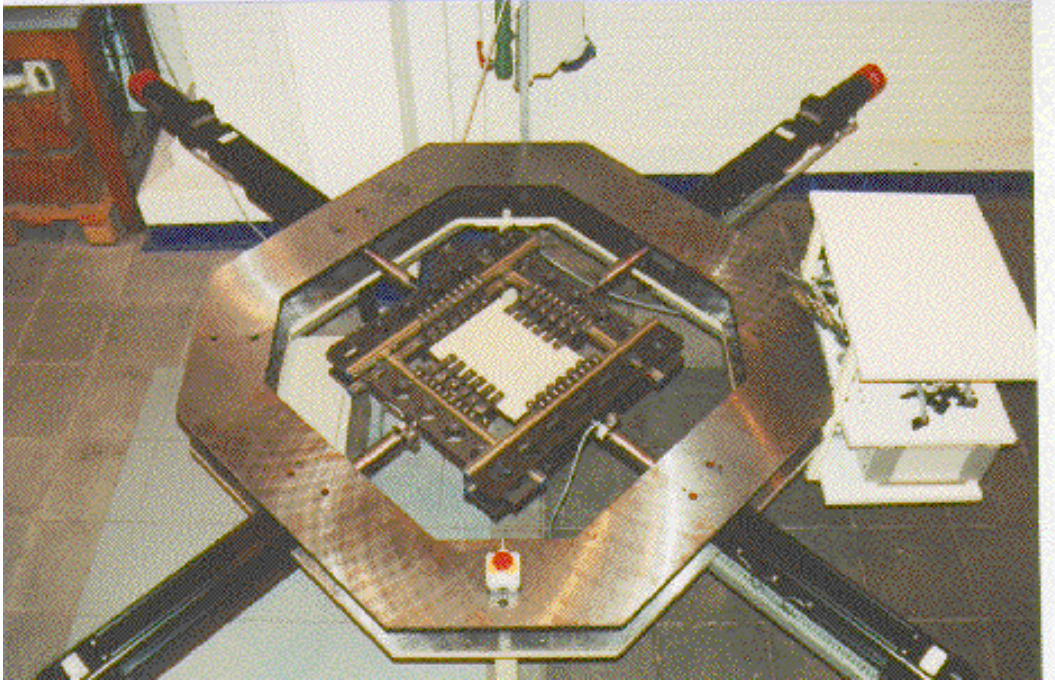


Fig. 7: Biaxial tester developed at MTM

Finally, the **consolidation phase** is in no way different from that of any other textile based composites, and does not need any further comments.

Mechanical Properties

In the following chapter, the mechanical properties of knitted fabric composites will be discussed. Emphasis will be put on weft and warp knitted glass fibre fabrics (using 68 or 136 tex yarns); - the distinction between weft and warp knits is irrelevant, because it will be shown that the anisotropy in mechanical properties are uniquely controlled by the fibre orientations, and the average properties by the fibre volume fraction and the yarn tex. Hence the way the knitting loops are produced is of secondary importance- . In order to make the comparison reliable, only one epoxy resin has been used (Hexcel F533 in film form) and all specimens have been produced in an autoclave (one hour at 125°C under a pressure of 3 bar). The fibre volume fraction was measured by the matrix burn-off method according to ASTM Standard D2584, or by a simple calculation using the areal density of the knit. The fibre volume fraction varied between 33 and 43 %, the void content between 1 and 5 %.

In-Plane Strength and Stiffness

The in-plane strength and stiffness have been measured by carrying out tensile tests in different orientations relative to the warp (or “course”) direction. Later on, a data reduction method will be presented that calculates the full in-plane compliance matrix based on only tensile test data. Besides, all the strength parameters in the quadratic Tsai-Wu failure criterion can be deduced.

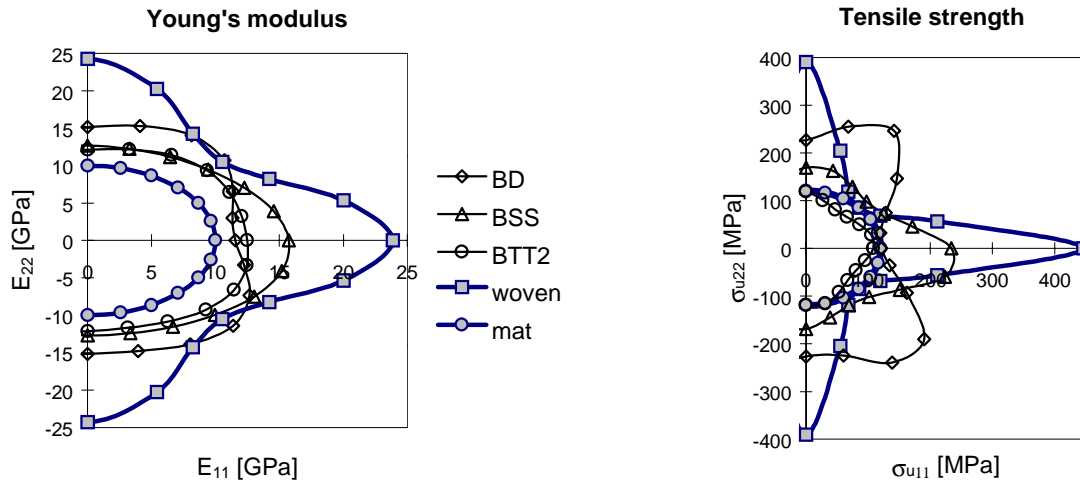


Fig. 8: Typical polar plots of the stiffness and the strength of knitted fabric composites, compared to woven fabric composites and random mat composites

First, the anisotropy is illustrated by directly representing in polar plots the Young's modulus and tensile strength of specimens, tested in different directions relative to the warp direction (Fig. 8). In contradiction to the isotropic random mats on one hand, and a typical orthogonal woven fabric (showing an outspoken weakness in the 45° direction), knitted fabrics seem to have mechanical properties which lay in between those of woven fabric and random mat composites. Moreover, knitted fabric composites can be either highly anisotropic, or almost isotropic. The latter is further outlined in Fig. 9, where the shear moduli and shear strength are represented. It is shown that, in contradiction with the highly anisotropic woven fabrics, which are very weak in warp or weft direction, knitted fabric composites are almost isotropic in shear.

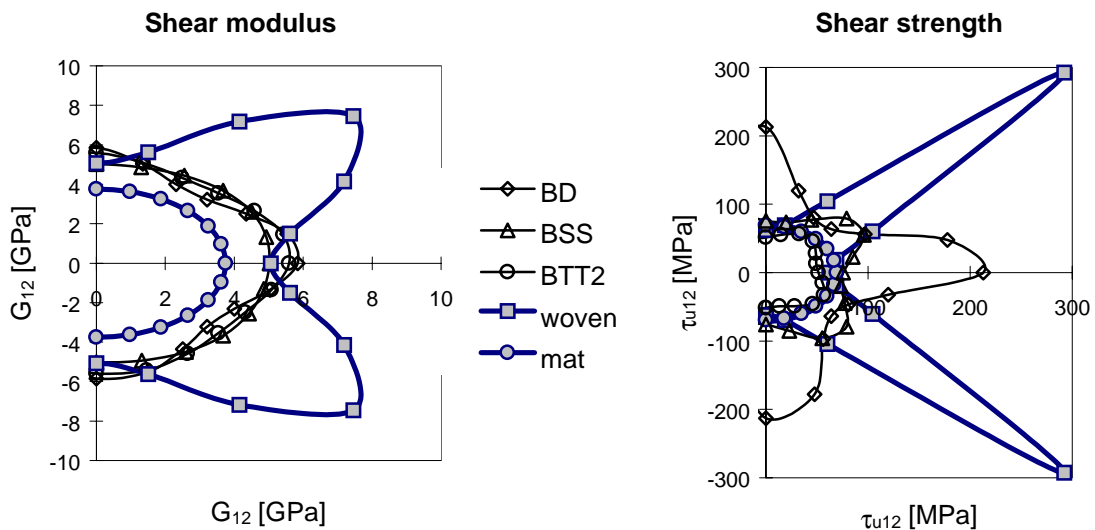


Fig. 9: Typical polar plots of the shear modulus and the shear strength of knitted fabric composites, compared to woven fabric composites and random mat composites.

The degree of anisotropy P_{an} of property P (stiffness or strength) can be represented by the following anisotropy factor:

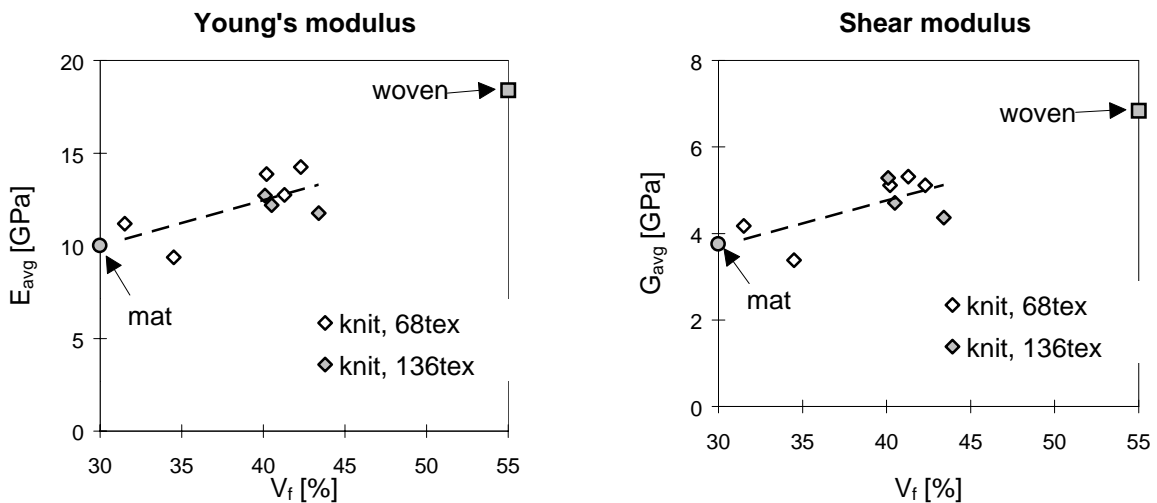
$$P_{an} = \frac{P_{max} - P_{min}}{2P_{av}} \quad (1)$$

Similarly, an average property P_{av} (stiffness or strength) can be defined as the average over all in-plane orientations. For example,

$$E_{av} = \frac{1}{S_{11,av}} \quad \text{with} \quad S_{11,av} = \frac{13}{8}(3S_{11} + 3S_{22} + 2S_{12} + S_{66}) \quad (2)$$

Similar relations can be written for the average shear modulus and for the average strength.

Recalculating the data from Fig. 8 and 9 would show that, for a similar volume fraction of 40 %, knitted fabric composites can either have a higher or lower average stiffness compared to woven fabric ; the average strength follows a similar trend. It should however be emphasized that woven fabric composites can obtain higher volume fractions at equal compaction , often leading to better average mechanical properties than knitted fabric composites produced at the same compaction load. On the other hand, random mat composites rarely exceed a volume fraction of 30%, and hence the comparison is made (in Fig. 8 and 9) with a 30% mat material. It is clear that knitted fabrics perform much better then initially anticipated. They outperform random mat composites, and they might compensate with their superior drapability the somewhat lower properties in course and wale direction in comparison to woven fabric composites in warp and weft direction. If however the overall average properties are considered, the nearly isotropic nature of most knitted fabric composites outperforms the very low bias direction properties of woven fabric composites. Whereas the degree of anisotropy is strongly dependent on the fibre orientation in the unit cell, and hence on the type of knit, the average properties do not seem to be influenced by it. This is further confirmed in Fig. 10. The average stiffness and strength values for different types of knits at different fibre volume fractions are presented. The fit is remarkable, and even woven fabrics follow the trend. This observation is interesting because knitted fabrics can now be optimised towards other properties (drapability, handleability, isotropy, damage tolerance,...) while the average stiffness and strength will remain unaffected.



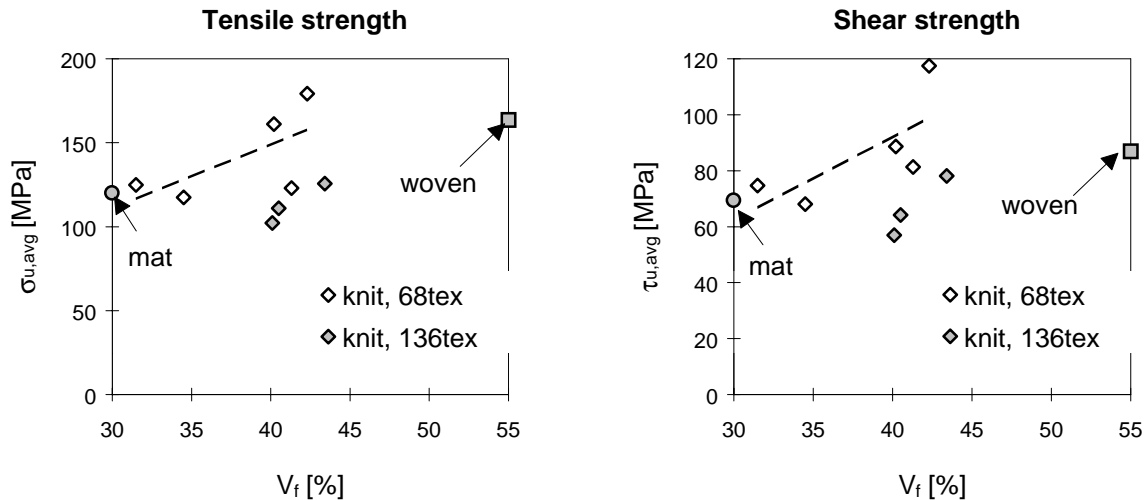


Fig. 10: Average stiffness and strength properties as a function of fibre volume fraction

Another concern might be the influence on the mechanical properties, of the deformation of the knit during the shaping and forming step of the composite processing. Preliminary results show however that, if the knitted fabric is not overstretched (leading eventually to fibre failure), the *average* mechanical properties are not basically affected; it is however unclear when the overstretching starts. The degree of anisotropy however will be affected, because the curled yarns will be gradually stretched, altering in this way the fibre orientation distribution. The ultimate anisotropy at maximum stretching will depend on the loop geometry and the biaxiality of the deformation. Studies are under way on a biaxial tester (Fig. 7) to evaluate this phenomenon.

Finally, it can be mentioned that some authors [17,18] have studied the effect of inserted straight yarns. It is obvious that in the direction parallel to these yarns both stiffness and strength will dramatically increase. The practical relevance of knitted fabrics with straight inserts is however limited to those applications where a high degree of anisotropy is requested, and where the extensional deformability in the insertion direction is not needed during the forming operation.

Fracture Toughness

When different layers of knitted fabrics are stacked and pressed, the loops of one layer will intermingle with those of the neighbouring layers. This will be more pronounced as the loop structure is more open, and as the out-of-plane orientation of the yarns is higher. An interlaminar crack will have to follow a very rough path, up and down the intermingling yarns. A straight path is impossible because massive fibre fracture would then have to occur.

As a consequence, it can be expected that the mode I interlaminar fracture toughness G_{IC} (the energy to create a unit area of crack) would be much larger than for unidirectional or woven fabric composites. Tests were carried out [19] using double cantilever beam specimens. Due to the high G_{IC} values and the rather low stiffness of the beams, compared to the conventional UD-specimens, 15 mm thick specimens had to be used. A 3 mm thick knitted fabric composite at the centre was reinforced on both sides with 6 mm thick woven glass-epoxy

laminates. Only then the crack opening displacement could be kept within reasonable limits, and bending damage in the beams could be avoided.

Fig. 11 shows that the mode I fracture toughness is about 10 times higher than for UD-specimens (using the same resin and fibre), and about five times higher than for woven fabric composites. Some other factors, like the yarn count, seem to have an influence on the achievable values. Knit BDD450, having thinner yarns, results in a higher fracture toughness. It was found that the energy absorbing crack deviation mechanism is exploited in a more effective way, because thinner yarns lead to a more tortuous crack path.

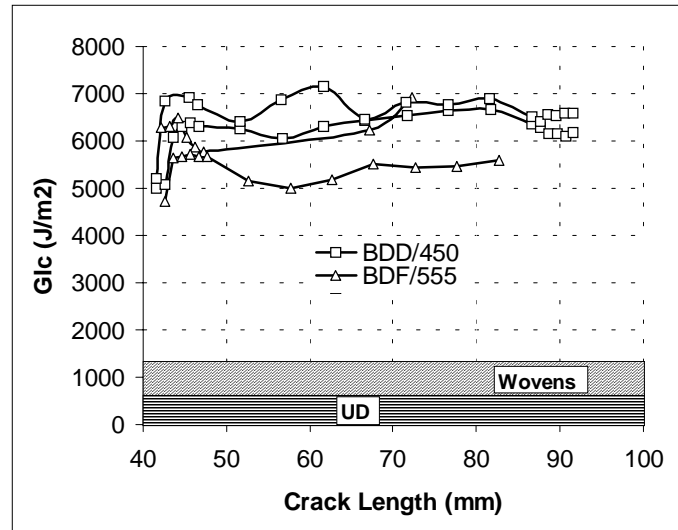


Fig. 11: Mode I fracture toughness of knitted fabric E-glass/epoxy composites BDD/450 and BDF/555 (wale direction), compared to wovens and UD's

Similar increases of mode I interlaminar fracture toughness have been found by other authors. Mayer [12] observed in a carbon fibre reinforced thermoplastic (PEEK) composites an increase by a factor 2.3 when comparing knitted with woven fabrics.

Optimisation of knitted fabrics towards maximum mode I interlaminar fracture toughness is actually being studied. Attempts to measure pure mode II values failed, because the extreme roughness of the crack surfaces would lead to interlocking and early crack arrest.

Impact and Mechanical Properties after Impact

The high interlaminar fracture toughness values of knitted fabrics suggest that the impact resistance might be excellent as well. At least when the initiation and growth of delaminations would control the impact resistance, as in UD- and woven fabric based laminates.

Impact tests have been carried out using an instrumented falling weight impact tester, applying impact energies (“incident kinetic energies”) between 1.5 and 9.2 J per mm plate thickness. Absorbed energy and maximum force were calculated from the measured loads and impactor displacements. Damage was assessed by ultrasonic C-scan and by microscopy on polished cross sections. Compression after impact tests were carried out using a Boeing-type set-up, complemented with anti-buckling guides. The same experimental procedure was applied on woven fabric composites, using the same fibres and matrix.

For the same absorbed energy, the projected damage area (measured by ultrasonic C-scan) was substantially larger in woven than in knitted fabric composites. Optical microscopy indeed showed that delaminations are absent in knitted fabric composites, and that the energy is dissipated in bending cracks at the tension side of the impact specimen. Hence, next to compression, also tensile-after-impact tests should be carried out. The normalised tensile strength of knitted fabric composites does not show a significant reduction, as shown in Fig. 12. This might indicate that most of the fibres do not break at the bending cracks, but rather bridges the cracks. During crack development, the curled fibres in the knitted fabric can slightly be stretched before they become fully loaded. The strong decrease in tensile strength of woven fabric composites is related to fibre fractures around the impacted area.

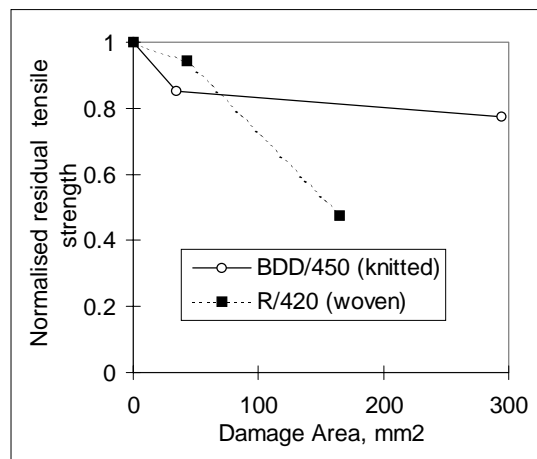


Fig. 12: Residual tensile strength of knitted and woven fabric composites as a function of damage area

As a conclusion, it can be stated that knitted fabrics are less sensitive to impact than woven fabric composites. Other authors have confirmed these findings [5,11-15].

Fatigue

The fatigue properties of composites based on UD-layers are excellent, mainly because the loads are carried by the highly fatigue resistant fibres. Cracks in off-axis plies gradually degrade the composite and initiate the final fatigue failure.

The slight out-of-plane orientations in woven fabric composites, together with the stress concentrations at the warp-weft cross-over points, reduce their fatigue properties compared to UD-based composites. As both factors are much more pronounced in knitted fabric composites, it could be expected that their fatigue resistance is lower.

Only one source has been found in the open literature [6]. Although only the fatigue properties in warp and weft direction have been compared, both for glass and carbon fibres, the knitted fabrics showed a decrease in number of cycles to failure. Also, the stiffness degradation due to damage development was more pronounced in knitted fabrics. More studies will have to be carried out to confirm these preliminary results.

Analysis and Modelling

It should be possible to explain, and even to predict, the mechanical properties of knitted fabric composites, based on the geometry of the loop structure and the fibre volume fraction, and on the properties of the composing materials.

First, an accurate and appropriate description of the loop structure, and of the yarn orientations within them, should be developed. Second, the stiffness (or compliance) matrix should be analysed, and advantage should be taken of the symmetry elements in the loop structure, because symmetry minimises the number of independent parameters. And finally, predictive models should be developed. It is beyond the scope of this paper to present in detail each of these steps. Over the past four years, researchers at K.U.Leuven have been developing a comprehensive set of solutions of the stated problems. They have been (and will be) published in the open literature, and reference will be given to them where appropriate. In the following, only the major steps in these developments will be highlighted.

Geometrical Analysis

Although for weft knitting, a machine building company has developed software to derive the loop geometry from the machine settings, it has, to our knowledge, not yet been applied to knitted fabrics for composites. If the predictions would be sufficiently accurate, this would be the most appropriate way to determine the fibre orientations in knitted fabric composites.

Up to now, experimental measurement of the yarn orientations is the only solution, but in knitted composites this is a very tedious task. One way would be to map the elliptical cross sections of fibres on a large number of parallel cuts through one unit cell. Numerous problems however arise: 3D-mapping out of a set of 2D images is cumbersome as many similar features (fibres with the same diameter and orientation) have to be followed, the mutual distance between the cuts has to be known accurately... As an alternative, the in-plane orientations are measured on the dry (non-impregnated) fabric. A major assumption has to be valid to justify this (handy) simplification, namely that the in-plane orientations will not be influenced by the consecutive composite processing steps. The out-of-plane orientations are derived from the yarn position at the maximum and minimum height; a linear interpolation in between the extremes results in the required out-of-plane orientation, after a scaling to the actual thickness of one layer of knitted fabric in the composite.

The three-dimensional orientation of a fibre fragment (in itself assumed to be cylindrical) can be described using the two spherical co-ordinate angles θ and ϕ , as defined in Fig. 13.

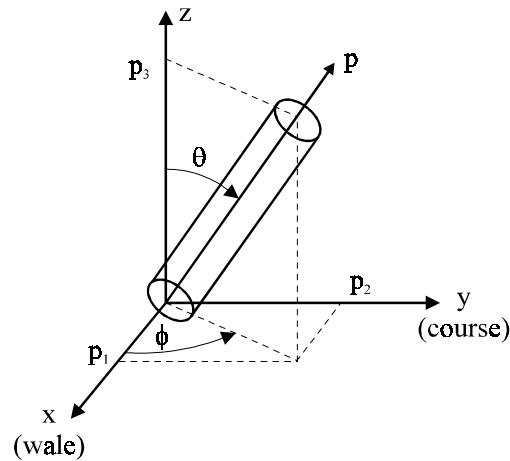


Fig. 13: Spherical co-ordinates used for the description of the yarn segment orientations

However, the out-of-plane angle varies only between $90 \pm 20^\circ$. For the calculation of certain properties in certain knitted fabric composites, this out-of-plane angle seems to be of less importance, and could hence, as a further simplification, be ignored.

By measuring the 3D co-ordinates of some 200 points along the yarns in one unit cell, the angles θ and ϕ can be calculated for individual fragments along one loop. From this, it is a small step to come up with an orientation distribution graph, as in Fig 14 (the loops have been split up in “straight” segments with an orientation difference of 15°).

Alternatively, a much smaller number of co-ordinates could be measured (about 20), and a cubic spline could be fitted through it.

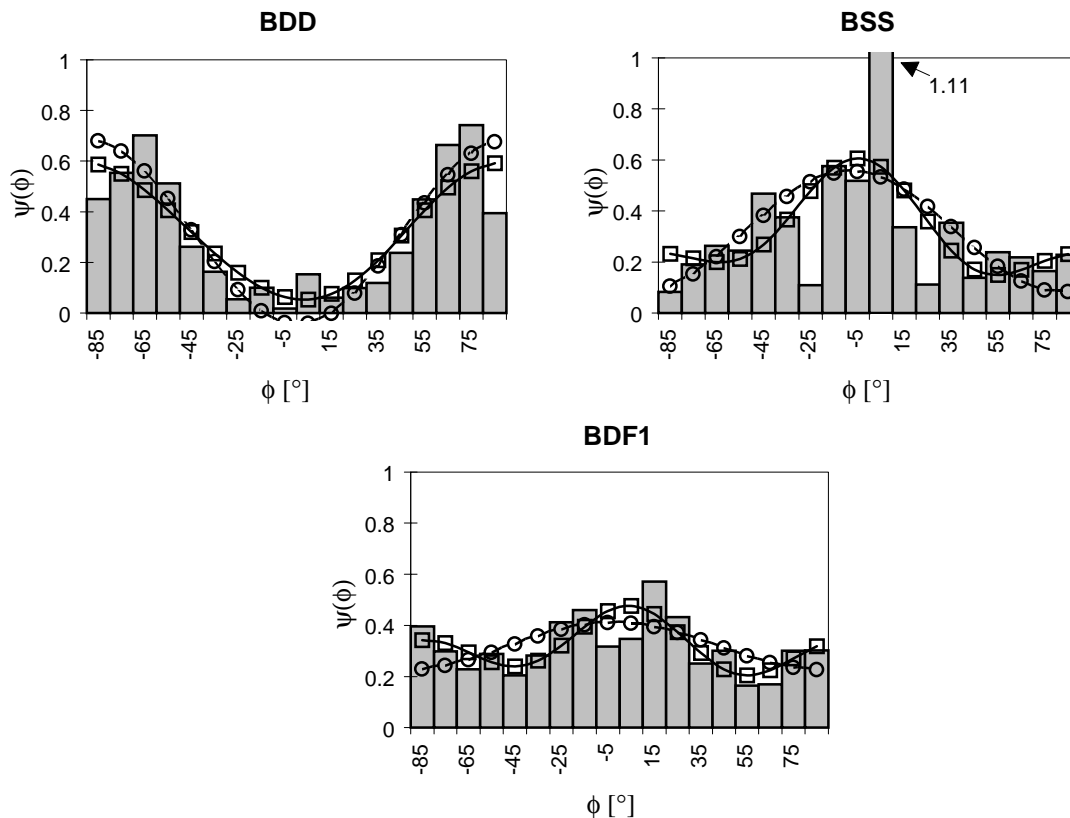


Fig. 14: In-plane orientation distributions of three types of knitted fabrics

The analysis can be rendered mathematically transparent by introducing the concept of orientation tensors [20], as they are since a long time used in short fibre composites literature. The orientation of each individual fibre fragment, defined by the angles θ and ϕ can be alternatively described by a vector \mathbf{p} , with unit components

$$\begin{aligned} p_1 &= \cos(\phi)\sin(\theta) \\ p_2 &= \sin(\phi)\sin(\theta) \\ p_3 &= \cos(\theta) \end{aligned} \quad (3)$$

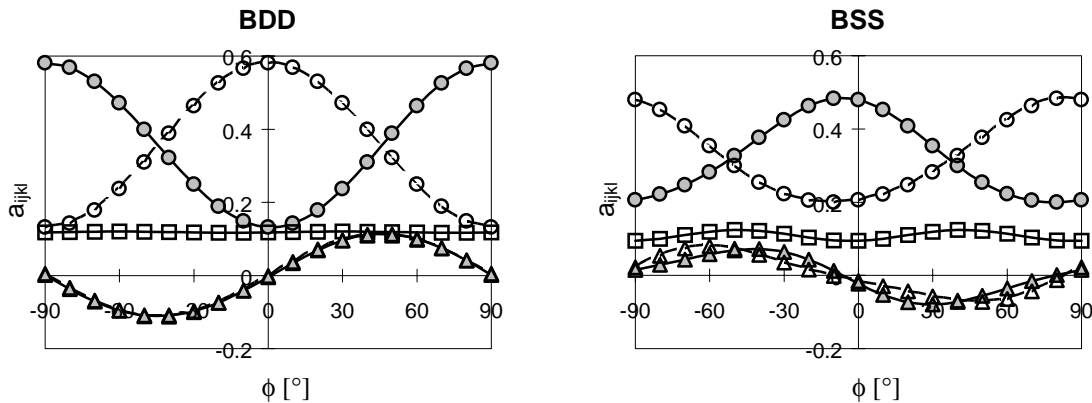
An orientation distribution function $\psi(\mathbf{p})$ can now be fitted through the experimentally measured orientation distributions, by the help of orientation tensors of the 2nd, 4th, ... nth order, defined as:

$$\begin{aligned} a_{ij} &= \oint p_i p_j \psi(\mathbf{p}) d\mathbf{p} \\ a_{ijkl} &= \oint p_i p_j p_k p_l \psi(\mathbf{p}) d\mathbf{p} \end{aligned} \quad (4)$$

It can be shown that these tensors, easily written as 3-by-3 resp. 6-by-6 matrices, are symmetric, and that they contain more zero elements for a higher symmetry order of the unit cell (for a detailed discussion, see [20]).

A complete recovery of the orientation distribution function (ODF) requires tensors with order infinity. However, it can be shown that the nth order orientation tensor contains all information from the ODF which is relevant for the orientation averaging of nth order properties. Elasticity (and strength) are 4th order properties, conductivity, thermal expansion and permeability are 2nd order. The approximation of the distribution of in-plane angles has been reconstructed using the 4th and 2nd order orientation tensors. The result is shown in Fig. 15 for 3 knits.

The orientation tensors can further be used to gain more quantitative appreciation of the symmetry in knitted fabrics. The variation with the in-plane angle ϕ of the individual in-plane components of the orientation tensor is shown in Fig. 15.



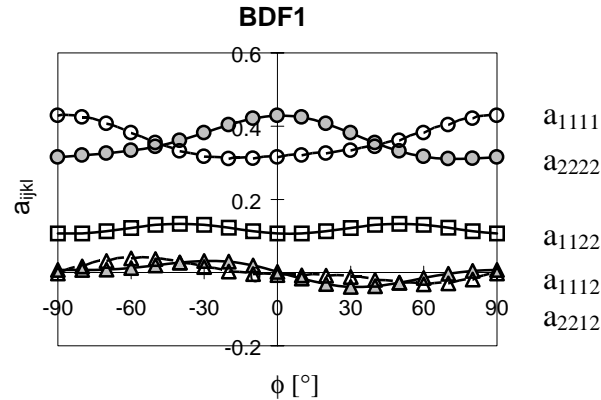


Fig. 15: Variation with in-plane angle ϕ of the components of the planar 4th order orientation tensor for different types of knitted fabric

Several minima and maxima in a_{1111} can be observed. It can be proved analytically that in monoclinic systems a_{1111} and a_{2222} must have an extremum at the same angle ϕ . In other words, at right angles to ϕ (min), a maximum must be found. Fig. 15 suggests that BDD and BSS are certainly monoclinic; in BSS, the symmetry axis is however shifted to $\phi=-4^\circ$. This “distortion” can be quantified using a_{1112} and a_{2212} (see ref. [20]).

Analysis of Elastic Constants and Strength Properties

The elastic engineering constants, Young’s moduli, shear moduli and Poisson’s ratios, can be converted into a two- or three-dimensional stiffness matrix. For unidirectional composites, which are in fact transversely isotropic, this is a well known procedure [21]. Only two tensile (0° and 90°) and one shear test are required to fully determine the in-plane stiffness matrix.

If however the degree of symmetry of the knitted fabric unit cell decreases, the question has to be answered how many tests will be required, and which are the best specimen orientations to be used. In a recent publication [22], the authors showed that four independent measurements suffice for monoclinic materials, while for triclinic materials six independent measurements are required. A data reduction method was developed, and an optimisation analysis was made in order to select a set of specimen orientations which should lead to the highest accuracy in the derived stiffness matrix. For instance for monoclinic materials, tensile tests in three directions, in which the Young’s modulus and Poisson’s ratio are determined (in case of 0° and 90° tests, leading to only 5 independent measurements) seems to be an optimum solution. It has to be emphasised that **no** shear tests are needed in order to calculate the shear related elements of the stiffness matrix. A similar procedure was suggested for triclinic materials, and for the strength parameters.

The orientation tensor approach can further be used to analyse the average stiffness (and strength) of knitted fabric composites. The average stiffness is calculated using the transformation rules for in-plane elastic constants [21], which is slightly more complicated, but also more accurate than the previous one (Eq. 2). Furthermore, it can be shown that the average value for the a_{1111} component of the orientation tensor of monoclinic materials can be calculated in a similar way. If both the average E_{11} and a_{1111} are used as normalising factors, the inverse of the experimentally measured average stiffness E_{11} is linearly related to a_{1111} (Fig. 16a).

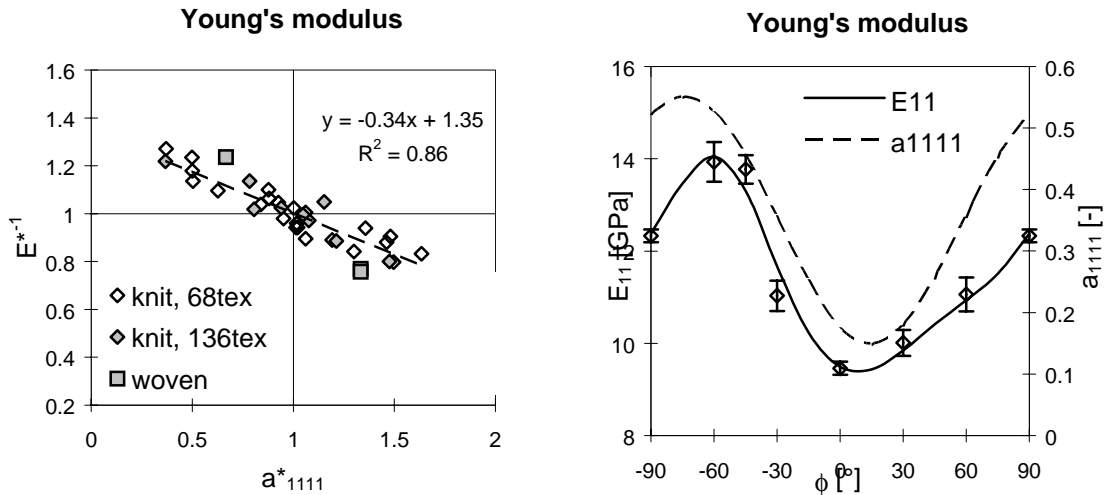


Fig. 16: Inverse normalised Young's modulus vs. normalised a_{1111} (a) and evolution of E_{11} and a_{1111} with in-plane angle ϕ (b)

For a specific knit, Fig 16b shows that indeed the Young's modulus for different test orientations follows the same trend as a_{1111} . - It has to be emphasised that E_{11} is derived from the stiffness matrix by a simple transformation of the reference co-ordinate system-. Similar results have been found for the strength parameters, and for the shear modulus.

The practical relevance of these results should not be underestimated. They indeed suggest that the ODF (measured or calculated from machine settings), together with the determination of the fibre volume fraction, should be sufficient to "predict" the Young's modulus in all the other orientations, within a certain class of knitted fabric composites (e.g. glass-epoxy). A similar procedure could be followed for the shear modulus and for the tensile strength.

Modelling of Elastic Constants and Strength Properties

Up to now, only some tools for the analysis of knitted fabric composites have been proposed, and some interesting correlations between components of the orientation tensors and the mechanical properties have been observed. These correlations however have, strictly spoken, no predictive value, as micro-mechanical models should have.

In a micromechanical model, the properties of fibre and matrix are combined with information on the fibre orientations and fibre volume fraction, in order to calculate the mechanical properties of the composite. As an intermediate step, the transversely isotropic properties of the impregnated fibre bundles are calculated first in their own co-ordinate system; then they are converted to the global co-ordinate system of the knitted fabric composite. These steps are identical for all micromechanical models (although different impregnated fibre bundle models are used). The differentiation between the models only occurs in the further modelling steps, namely where the straight impregnated yarn segments are combined with each other and with the pure matrix to form the actual textile composite.

Micromechanical models can broadly be split up in analytical and numerical models.

Analytical models, once implemented in a computer program, in general only require a short computing time compared to numerical models (like FEM-models) of textile composites. Despite their sometimes intricate mathematical formulations, analytical models provide insight in the relative importance of the different geometrical and material parameters.

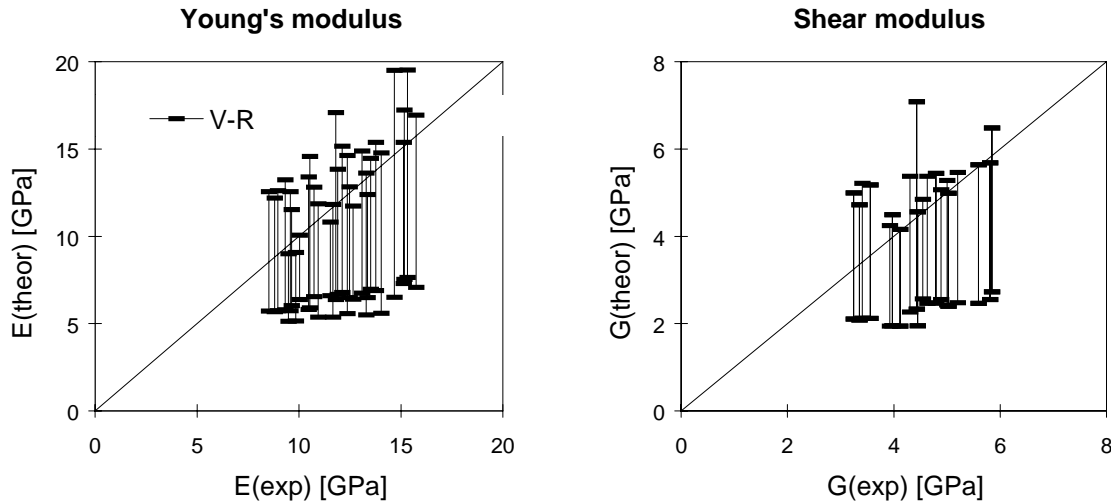


Fig. 17: Iso-stress and iso-strain predictions of the Young's modulus and the shear modulus of several types of warp knitted fabric composites

The most simple examples of analytical methods are based upon a mechanics of materials approach. The Voigt and Reuss models assume an isostrain or isostress state in the different phases of the composite, and are often used for a first approximate calculation of the elastic properties of UD-composites. For textile composites, these models lead to an over- resp. under-estimation of the elastic properties, as is shown in Fig. 17. Unfortunately, the upper and lower limits are much too far away from each other, so that an accurate estimation of the real elastic properties becomes very doubtful. - It is however interesting to remark that for the glass-fibre epoxy knitted composites studied up to now, the elastic moduli could be fairly precisely “guessed” by making a simple average between the upper and the lower limit; this might however be a pure coincidence.-

In the framework of a modelling study on woven fabric composites, Vandeurzen et. al. [23] have developed a far more sophisticated and accurate position-dependent model, using a complementary energy minimisation technique. It is actually investigated whether this model could also be applied to knitted fabric composites.

More refined analytical models, for which the Voigt-model can be treated as a special case, are based upon the so-called eigenstrain or transformation strain theory. Every yarn segment is replaced by an equivalent inclusion having the same properties as the matrix, but having a non-vanishing eigenstrain defined in such a way that both the original inhomogeneity and the inclusion have the same final stress state. The eigenstrain theory tries to correlate the local perturbation strains to a given eigenstrain distribution. Two problems are related to the use of these models to knitted fabric composites. The first one is dealing with the evaluation of the auto-correlated Eshelby tensors relating the perturbation in a given inclusion to the eigenstrain within the same inclusion. Solutions exist for ellipsoidal shaped inclusions and were originally derived by Eshelby. For curved yarn segments, complex integrations need to be carried out. To overcome this, a short fibre equivalent was introduced. In this approach, the

curved yarn segment is replaced by an ellipsoid having an aspect ratio which is a function of the local yarn curvature.

A second problem arising in the practical application concerns the evaluation of the even more complex interaction Eshelby tensors, relating the perturbation strains and the eigenstrains in different inclusions. These tensors are amongst others a function of the relative orientations and positions of the considered pair of inclusions. Therefore, several averaging schemes were developed taking into account the inter-inclusion interaction in a global sense. The Mori-Tanaka scheme has been widely used in the modelling of short fibre and particle reinforced composites, but is limited to the lower volume fraction range. In the micromechanical description of polycrystalline materials on the other hand, where the volume fraction equals unity, self-consistent averaging schemes were developed. As the yarn volume fraction in knitted fabric composites can be relatively high due to the loose packing of the fibres in the yarns, both methods were compared (Fig. 18).

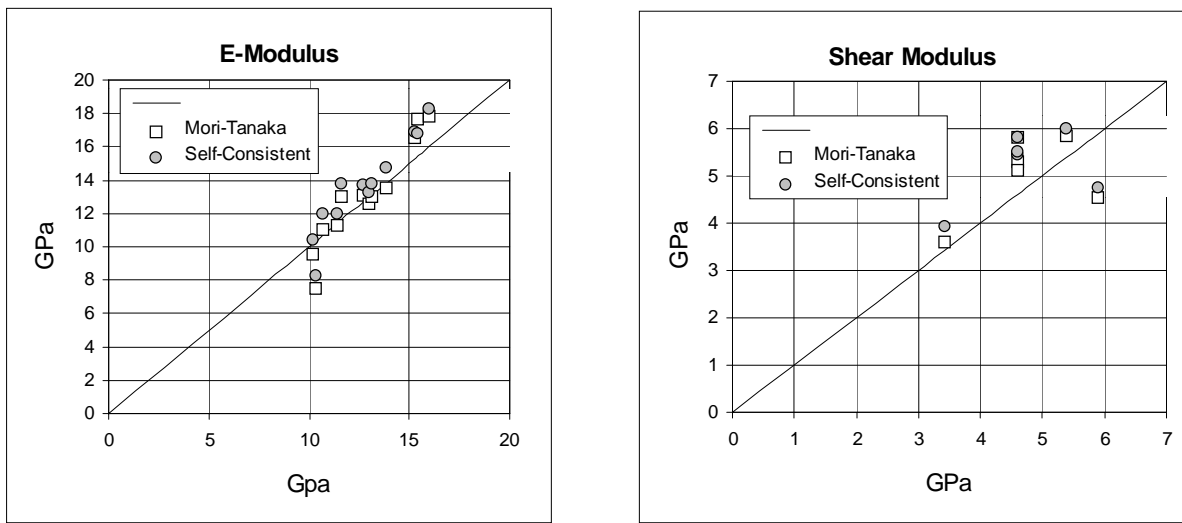


Fig. 18: Predicted E-moduli and G-moduli using the Mori-Tanaka and a Self-consistent Averaging Scheme

Although these models do not explicitly take into account the relative position of the yarn segments, the predictions are quite acceptable, as is shown in Fig. 18. Further improvements and extensions of these models are under way, and will be published soon.

Numerical models are quite cumbersome for knitted fabric composites, because of the extremely complicated loop geometries that might occur (see above 2). A fully three-dimensional modelling of a real composite (not of simple 1-and-1 structures) would quickly lead to a number of meshes and to degrees of freedom that, even with very powerful computers, are difficult to handle, if not impossible. Moreover, the mesh generation in itself is a difficult task; a mesh generating pre-processor should be in a easy-to-handle parametric format, so that variations in yarn size or cross section, fibre volume fraction, fabric deformation,... could be incorporated without having to restart the mesh generation from scratch. Only if these problems are solved, it seems worthwhile to consider FEM-modelling of knitted fabric composites.

To avoid the previously mentioned problems, the binary model, initially developed by Cox [24] for woven and braided fabric composites, was investigated. In this binary model, the composite is subdivided in one-dimensional spar elements, representing the axial properties of the impregnated yarns, and three-dimensional medium elements, responsible for the transverse and shear properties of the yarns, and for the matrix properties. This model was applied on several of our knitted fabric composites using a homogenisation scheme, in which periodic boundary conditions are applied [25]. The agreement between the binary model predictions of the elastic properties and the experimental values was quite acceptable, except for the shear modulus (Fig. 19). The major problem however is that this binary model excludes an accurate description of the local stress states, and hence cannot be used to predict strength values.

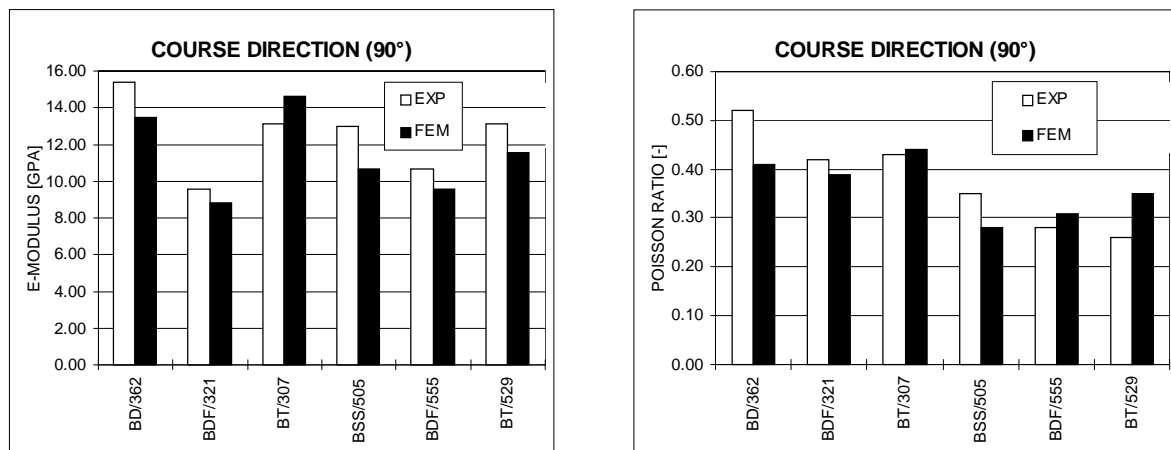


Fig. 19: Experimental Values and FEM-Predictions of E_{11} and n_{12} of 6 types of warp knitted fabric composites

3D-Knits

Over the past ten years, several new concepts for composite sandwich structures have been invented at K.U.Leuven. First, double layer woven fabrics, as used to produce velvet or carpets, have been developed to be used as preform for composite sandwich structures. Second, a similar knitted structure has been investigated. And most recently, patents have been filed for a new, continuous production concept for honeycomb cores.

Woven sandwich fabrics offer three main advantages [26]: first, skin and core can be produced in one single processing step; second, the skins are strongly bonded to the core by the pile fibres, hence preventing skin-core delamination; and third, the core can be easily filled with a foam, creating a (pile) fibre reinforced foam, so that also brittle foams (like phenolics) can be used in structural applications.

As stated earlier, woven fabrics have however one disadvantage: they only deform in shear, and hence draping over complex forms is very difficult. Extending the concept to double layer **knitted** fabrics would solve this problem. Moreover, the knitting process is much more versatile than weaving, allowing to create intricate loop structures and variable pile orientations.

The concept of 3D-knitted fabric composites will be treated in depth in another paper during this conference [27]. In the following, only some aspects will be highlighted.

3D- or double layer knits are produced on a double needle bed Raschel warp knitting loom with minimum 6 (up to 8) guide bars. The skins can be closed (like in 3D-woven fabrics), but the versatility of the knitting process allows one to create a multitude of open skin structures (Fig. 20). After impregnation and curing, a unique open skin sandwich composite can be created. Applications where a flow of liquids or gases (ventilation) is required, can be realised in this way.

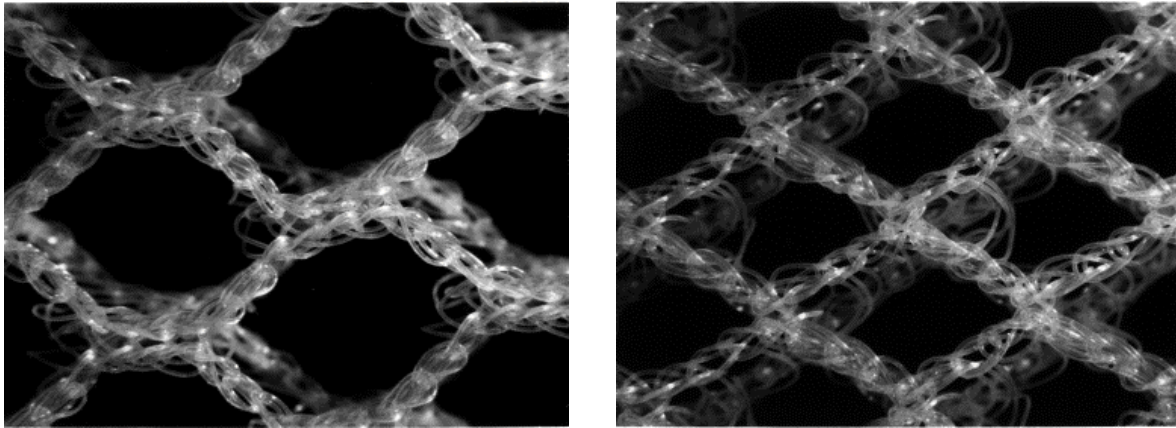


Fig. 20: Examples of hexagonal and orthorhombic cell structures

The knitting loop structure is however not so tight as the binding structure in a woven fabric. The piles are not well fixed into the skins, and the skin itself is rather unstable before impregnation. The good binding in 3D-woven fabrics makes it possible that during processing the multi-filament core yarns will stretch themselves, resulting in an open core structure. Due to the loose binding structure, self-stretching of the core is hard to realise in 3D-knitted fabrics. Thick, thermoplastic mono-filament yarns have to be added as pile yarns. If however only mono-filament yarns are used in the core, the resin will not well adhere to them, and a weak composite core is formed.

The optimum 3D-knitted fabric has now the following composition: a combination of multi-filament polymer and glass (or any other reinforcing fibre) yarns in the skins, and a combination of a mono-filament and any multi-filament yarn (polymer, glass, ...) in the core. Impregnation will then be homogeneous. The mechanical properties can be controlled by the amount of reinforcing fibres in both skin and core, by the areal density of the skins (the “openness” of the skins) and by the pile density in the core.

Each application requires an optimisation of these different parameters, which is enabled by the versatility of the knitting process. For an application where a high bending stiffness and an optimum ventilation is required, combined with a light weight, several 3D-knits were developed, impregnated and cured, and tested in bending. The results are shown in Fig. 21.

The bending stiffness can obviously be increased by adding glass fibres to the skins and by improving the impregnation homogeneity.

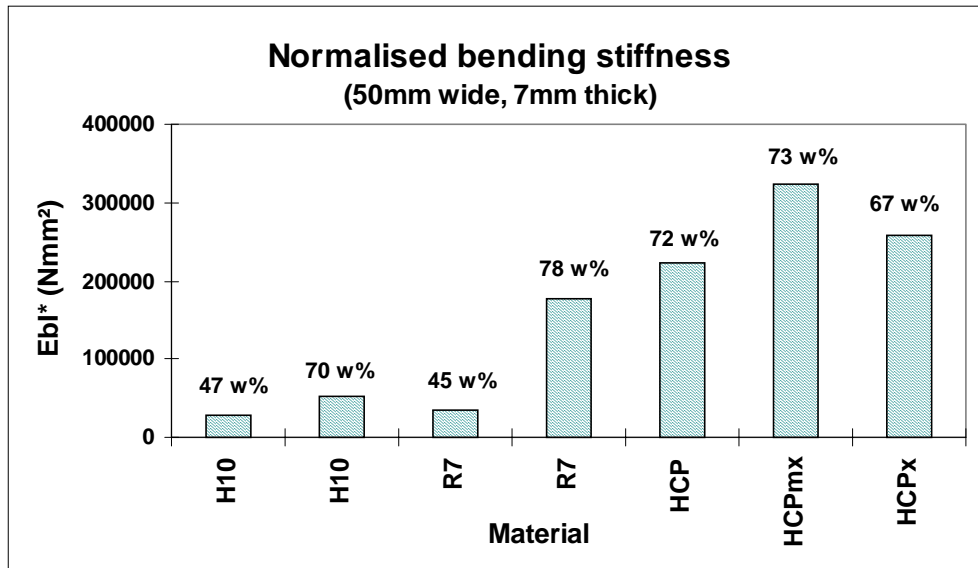


Fig. 21: Flexural stiffness of 3D knitted fabric composites; the three knits HCP contain ramie and viscose fibres (w% means: weight percentage of matrix)

A second application required a combination of good ventilation and excellent shock absorbance. The influence of the pile composition and the matrix content on the deceleration during transverse impact is shown in fig. 22. The required maximum deceleration of 150 G can be met when using at least 3 layers of 3D-knitted fabric composites.

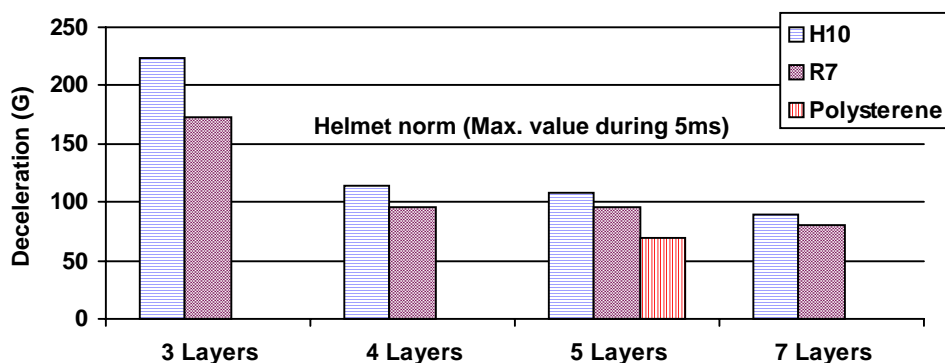


Fig. 22: Comparison between hexagonal and rhombic knitted composites and polysterene. Influence of the number of layers in the knitted composite. (Resin : 70w% Hexcel R2503)

In both aforementioned applications, the final form of the product had a complex three-dimensional shape. The high deformability of knitted fabrics allowed to realise these shapes without any problem.

CONCLUSIONS

Knitted fabrics have finally been discovered as an interesting alternative composite preform. The in-plane mechanical properties are reasonable compared to woven fabric composites, and superior to random mat composites. The out-of-plane properties (G_{Ic}) and damage tolerance are however better than most other composite preforms.

The major advantage remains the high deformability, which allows an efficient use in complex shaped composite products. A considerable decrease of processing costs can hence be envisaged. In resin transfer moulding applications, the excellent resin permeability is an additional processing advantage, allowing to impregnate large surfaces at low pressure in an acceptable time. In compression moulding applications of thermoplastic matrix composites, the extensional deformability of knitted fabrics makes the "organic sheets" behave like stampable metallic sheets.

It is however clear that the potential of knitted fabrics as preform for composites has not yet been fully exploited, and that the knitting technology is waiting for the imagination of composites engineers.

ACKNOWLEDGMENTS

The authors gratefully acknowledge the Flemish government for their support of this research in the IWT-project "Optimalisatie van breisels voor composietstructuren". This text presents research results of the Belgian programme on Interuniversity Poles of Attraction initiated by the Belgian State, Prime Minister's Office, Science Policy Programming.

REFERENCES

1. Fantino, L., Complex & architectural textile preforms AEROTIS[®] : potential applications in composite industries, Proc. SAMPE Europe, Paris 1997, pp. 185-186.
2. Rudd, C.D., Owen, M.J. and Middleton, V. Mechanical properties of weft knit glass fibre/polyester laminates. *Comp. Sci. Techn.* **39**(1990), pp. 261-277.
3. Owen, M.J., Middleton, V. and Rudd, C.D. Fibre reinforcement for high volume resin transfer moulding (RTM). *Comp. Manuf.* **1**(1990), pp.74-78.
4. Arendts, F.J. and Drechsler, K. Composites with knitted fibre reinforcement. *Proc. 3rd Int. Symp. COMP'90*, AMATEC, Greece, 1991, pp. 415-420.
5. Chou, S. and Wu, C.-J. A study of the physical properties of epoxy resin composites reinforced with knitted glass fiber fabrics. *J. Reinf. Plastics and Comp.* **11**(1992), pp. 1239-1250.
6. Chou, S., Chen, H.-C. and Lai, C.-C. The fatigue properties of weft-knit fabric reinforced epoxy resin composites. *Comp. Sci. Techn.* **45**(1992):283-291.
7. Verpoest, I. and Dendauw, J. Mechanical properties of knitted glass fibre/epoxy resin laminates. *Proc. 5th Eur. Conf. on Comp. Mat. (ECCM-5)*, Bordeaux (France), 1992, pp. 927-932.
8. Verpoest, I. and Dendauw, J. Mechanical properties of knitted glass fibre/epoxy resin laminates. *Proc. 37th Int. SAMPE Symp.*, Anaheim (USA), 1992, p.369-377.

9. Ruffieux, K., Hintermann, M., Mayer, J., Koch, B. and Wintermantel, E. Enhanced local carbon fibre knitting reinforcement of mechanically adapted bone plates. Concept of a new implant. *VTT Symposium 133: Textiles and composites '92*, Tampere (Finland), 1992, p.326-331.
10. Mayer, J., Lüscher, P. and Wintermantel, E. Knitted carbon fiber reinforced thermoplastics: structural characterization with image analysis. *VTT Symposium 133: Textiles and composites '92*, Tampere (Finland), 1992, p.315-320.
11. Mäder, E. and Bunzel, U. Influencing the properties of continuous fibre-reinforced thermoplastics by textile processing. *Proc. Techtexsil Symp.*, Frankfurt AM (Germany), 1994, paper 327.
12. Mayer, J. *Gestricke aus Kohlenstoffasern für biokompatible Verbundwerkstoffe, dargestellt an einer homoelastischen Osteosyntheseplatte*. Ph.D. thesis, ETH Zürich (Switzerland), 1994.
13. Bannister, M. and Herszberg, I. The manufacture and analysis of composite structures from knitted preforms. *Proc. 4th Int. Conf. Automated Comp.*, Nottingham (UK), 1995, p.397-404.
14. Ramakrishna, S. and Hamada, H. Impact damage resistance of knitted glass fiber fabric reinforced polypropylene composites. *Sci. Eng. Comp. Mat.* **4**(1995):61-72.
15. Leong, K.H., Falzon, P.J., Bannister, M.K and Herszberg, I. An investigation of the mechanical performance of weft knitted Milano rib glass/epoxy composites. Submitted to *Comp. Sci. Techn.*
16. Ramakrishna, S., Hamada, H., Cuong, N.K. and Maekawa, Z. Mechanical properties of knitted fabric reinforced thermoplastic composites. *Proc. 10th Int. Conf. on Comp. Mat. (ICCM-10)*, Whistler (Can.), 1995, p.IV-245-252.
17. Ramakrishna, S. and Hull, D. Tensile behaviour of knitted carbon-fibre-fabric/epoxy laminates - part I: experimental. *Comp. Sci. Techn.* **50**(1994):237-247.
18. Ramakrishna, S. and Hull, D. Tensile behaviour of knitted carbon-fibre-fabric/epoxy laminates - part II: prediction of tensile properties. *Comp. Sci. Techn.* **50**(1994):249-258.
19. Huysmans, G., Gommers, B., Verpoest, I. Mechanical properties of (2D) warp knitted fabric composites: an experimental and numerical investigation *Proc. 17th Int. SAMPE Europe Conf.*, Basel (Switzerland), 1996, pp.97-108.
20. Gommers, B., Verpoest, I., Van Houtte, P., On the use of orientation tensors in the analysis of knitted fabric reinforced composites, *Proc. Texcomp-3 Conf.*, Aachen (Germany), 1996, pp.8/1-8/18.
21. Tsai, S.W. and Hahn, H.T. *Introduction to composite materials*. Technomic Publishing co., Lancaster, 1980.

22. Gommers, B., Verpoest, I., Van Houtte, P., Determination of the mechanical properties of composite materials by tensile tests. Part I: elastic properties, Part II: strength properties, *Journal of Composite Materials*, accepted for publication (March 1997).
23. Vandeurzen, Ph., Ivens, J., Verpoest, I., Texcomp: a 3D analysis tool for 2D woven fabric composites, *SAMPE Journal*, **33**, no. 2, pp. 25-33, March-April, 1997.
24. Cox, B.N., Carter, W.C., Fleck, N.A., *Acta Met. Mater.*, **42** (1994), pp. 3463-3479.
25. G. Huysmans, B. Gommers, I. Verpoest, A Binary Finite Element Model for the Effective Stiffness Prediction of 2D Warp Knitted Fabric Composites, *Proc. 4th Int. Conf. on Def. and Fract. of Comp.*, 24-26 March 1997, Manchester, pp. 309-318.
26. A.W. Van Vuure, J. Ivens, I. Verpoest, Sandwich fabric panels, *Proc. 40th Int. SAMPE Symposium*, Anaheim, USA, May 8-11, 1995
27. Philips, D., Verpoest, I., Van Raemdonck, J., Optimising the mechanical properties of 3D-knitted sandwich structures, *to be presented at ICCM-11*.

AEROSPACE MATERIALS AND STRUCTURAL RESEARCH INTO THE NEXT MILLENNIUM

Jim C. I. Chang

*Aerospace and Materials Sciences Directorate
Air Force Office of Scientific Research
110 Duncan Avenue, Suite B115
Bolling AFB DC 20332-8050
USA*

SUMMARY: The aerospace materials and structures community has made major advances during the past fifty years. Specifically, the development of composite materials has offered design engineers the opportunities for designing high performance aerospace systems which otherwise would be impossible to attain. Today, as we approach the beginning of the next millennium, it is both academically satisfying and practically beneficial to examine where we have been and to speculate where we will be. An assessment on the state-of-the-art of the advanced composites as well as their limitations and investment strategy is presented here. All materials including, metal and polymeric, metal, and ceramic composites are discussed. The impact and challenge presented to the materials technology developers from advancement in computing and manufacturing, and from paradigm shift in structural designs philosophy such as multi-functional smart structures are also addressed. Finally, research opportunities and the next frontier of materials research are discussed.

KEYWORDS: composites, structures, solid mechanics, computer simulation materials design, smart structures, multi-functional structures, manufacturing and processing.

INTRODUCTION

The opportunity and challenge to the materials scientists in the next century are (1) to design materials for a purpose; not to design the best materials possible, and (2) to predict materials performance; not to characterize as is materials. To meet this challenge, an integrated-proactive materials research approach must be adopted. The structural material core technology (Fig. 1) concept used by the US Air Force Office of Scientific Research (AFOSR) is an excellent example of the proactive approach for materials program planning and development. The multi-disciplinary integration approach (Fig. 2) is the key for assuring the development of quality and low cost materials.

Composite materials have been used since the dawn of the civilization. Early Egyptians knew to mix straw and earth to increase toughness, and Chinese used cooked rice mixture to cement earth blocks. However, the major advancement to the understanding and utilization of composite materials has come about only within the last fifty years. For any material or material systems, the most simplified design parameters are strength and toughness. The figure-of-merit of different material systems has been discussed in Ref. 1, and they are illustrated in Figs. 3 & 4. Among all composites, polymeric composites have made the most

impact where military and civilian aircraft made of this type of composite have been built and are being flown all around the world. However, as they are being used, the knowledge based on the polymeric composites durability from usage and from environmental degradation is

found lacking. Therefore, basic research in this area is being revamped. On the other hand, because of the need of high performance air vehicles, composites having different attributes have also been extensively investigated and developed. Metal matrix composites and ceramic matrix composites are the commonly known composites where stiffness, strength and elevated temperature capability are the main development goals. Today, the material technology development process has reached a cross road where the feasibility of certain class of composites to attain the postulate performance goals must be realistically assessed. Specifically, it must be assessed against the practicality and feasibility of these materials being actually used for engineering applications. For example, can technical breakthrough realize the desire of using bulk ceramic composites for turbine engine rotating components applications? Or should other ceramic technologies, such as coatings, that offer less performance improvement but have a real possibility of success be the areas of emphasis? In the mean time, have we reached the new frontier where new advancements such as, nanotechnology and computationally materials modeling offer the scientists with the tools to “design” materials? More importantly, the materials research effort must also be compatible with the aerospace vehicle design paradigm shift. The future aerospace structures are not bonded by the conventional aerodynamically-based designed principles, i.e., tailless aircraft and smart multi-functional airframe. In this case, structural and functional composites could be one single identity, and metal and non-metal are no longer separate classes of materials but hybrid composites instead.

METAL AND METALLIC COMPOSITES

Metal is the basic material that has been used extensively for centuries. Therefore, the utilization and development of non-metal composites must be examined in light of the advancement made by the metal community. From the aerospace materials point of view, the trend toward higher temperature materials has steered the emphasis to composites. In fact, this has been precisely the trend for materials development in the last thirty years. However, the advancement made in experimental capability, processing and fundamental understanding has pushed metal into a new frontier - higher strength/stiffness and elevated temperature capability. This latest development has given the nonmetallic-composites, especially carbon-carbon and ceramic composite materials a run for its money.

For high temperature applications, metals and metal composites have definitively proven their worth beyond conventional wisdom. Fig. 5 illustrates the metal and metal composites lifecycle and investment strategy used by the AFOSR metals program. Monolithic metals, Ti, Al and Ni have reached technology maturity where only limited investment is need for specific applications. High cycle fatigue of Ti is an example. The next category, such as TiAl and NiAl, is near the tail end of basic research but substantial investment is still needed to address unique issues that prevent these materials potential being realized. Fracture toughness of intermetallics is such an example. In fact, intermetallics are strong competitors to composites for turbine fan blade applications. The majority of innovative basic research effort in metals and metal composite is in elevated temperature applications. Both Nb-Si and Mo-Si-B, have high creep resistance properties and oxidation resistance characteristics (Figs. 6 & 7), and they are true contenders to ceramic composites for high temperature applications

(Refs. 2 & 3). Fundamentally, Nb-Si is relatively stable up to 1670⁰C and is 80% lighter than Ni-superalloys. Because of these characteristics and the advancement made to date, the possibility of using these metallic systems for engine applications is much higher than that of the ceramic composites. Some other advanced metallic systems are distinguished by their unique features such as metallic glass (Ref. 4), or by their physical dimensions such as microlaminates or nanomaterials. Metallic glass (Fig. 8) is an alloy-glass systems where metal alloying and unique processing provide materials with exceptional strength and ductility. Nano-and micro-laminated materials are hybrid materials that are tailored for specific thermal or mechanical properties, and are far better than most of the single phase material or macro-multi-phases composites can ever attain (Figs. 9, 10 & 11). All these achievements are possible because advancement made in fundamental understanding and in newly developed processing techniques (Refs. 5 & 6). Nevertheless, the frontier has just been opened, new opportunity and challenge are plenty and substantive advancement in metal and metal composites is expected.

Metal Matrix Composites (MMC) have their unique characteristics that lend themselves for specific applications. These characteristics include high stiffness, low coefficient of thermal expansion and high thermal conductivity. For space structures, all these properties are desirable and essential for vibration control and for minimizing the effects from cyclic thermal environment in space. Additionally, the dimensional stability and low outgassing requirement of most space platforms makes MMC ideal materials. However, after more than three decades of research and development, the cost of making MMC and the difficulty of making quality components have prevented this materials being used extensively. At the same time, advancement of other type of materials have provided solutions to space structural applications which would otherwise depend solely on MMC.

There are still many research issues in MMC to be pursued. When answers to these issues are found, MMC may make a come back and become the materials of choice again. Issues related to quality and low cost production are the key areas that require research attention. Additionally, there are many other research issues that are applications specific. For example, the making and qualifying of MMC dimensional stability is still a challenge to space applications. Because of the high temperature infiltration and solidification processes that the matrix material experiences, substantial thermal induced residual stresses are locked in the processed composites. This process induced thermal stress is the major contributor to the MMC hysteresis loop behavior which leads to unstable structural geometry from thermal cycling during service. Innovative processing techniques to alleviate this problem, and new and rigorous thermal mechanical theory which takes care of nonlinear interaction between the thermal and mechanical stresses is needed to predict this behavior. The latter case can not bear fruit from the conventional linear thermo-elastic or thermo-plastic theory and it must start from fundamental thermodynamics.

POLYMERIC COMPOSITES

Performance, processing and manufacturing, and maintainability are the three major considerations for using any material. Because of its relative maturity, the research needs of polymeric composite are easier to define in this context. Polymeric composites become viable engineering materials following twenty years of research and development effort. As in the case of any new materials development effort, the major emphasis has been on performance. In terms of processing and manufacturing, most effort has been focused on

property improvement, and cost reduction has not been a driver. One of few processing and fabrication success stories is Resin Transfer Molding (RTM). For this reason, the usage of polymeric composites are still rather limited. Therefore, low cost processing and manufacturing requires attention.

As far as maintainability is concerned, our knowledge is very limited. Because polymeric composites have been widely used for aircraft, missile and space systems for some time, performance degradation from service environment exposure has become a major issue to the maintenance and operation of these systems. This is one of the important areas where basic research as well as engineering development effort is needed. The types of degradation we are talking about here are thermo-oxidation degradation and solvent/moisture induced degradation. In this case, the traditional approach of looking at the macroscopic scale is no longer sufficient. Specifically, thermo-oxidative degradation is a chemistry process; solvent/moisture induced degradation is a combined chemical and physical process. Therefore, in order to scientifically determine the so called "damage initiation", the physics and chemistry of the polymer molecular architecture change from processing to service must be understood. Fig. 12 illustrates one of the AFOSR polymeric composites program thrusts on polymeric composites degradation where damage initiation mechanisms are addressed in a comprehensive manner. The fundamental effects addressed include chemical structures effects and chemical degradation, network effects, mechanical stress effects, and thermoplastic processing. Each effect is a complicated one. For example, the moisture uptake depends on the time, temperature and history, and is dictated by the physical states of the polymer. One of the physical states that plays a major role to the process of degradation is porosity. There are open porosity and close porosity which dictate the probability of moisture infiltration and retention. The definition and the measurement of these types of porosity and its effects on moisture retention is at the basic research stage. Figs. 13 and 14 illustrate a technique of using positron for measuring porosity and the hole effects on controlling moisture diffusion (Ref. 7). By breaking up the porosity into static and dynamic holes, the preliminary data suggested that only the static holes control the moisture diffusion below the glass transition temperature. The stress effect on sorption is illustrated in Fig. 15. This formulation was developed by Treloar for rubber (Ref. 8), which is different from conventional polymer. However, from the fundamental chemistry point of view, this is a start.

Lastly, the issue of Non-Destructive Evaluation of polymeric composites has been addressed by engineers as measuring structural integrity or mechanical separation of materials, i.e., delamination and other damage from fabrication and usage. However, the new frontier is to be able to interrogate the chemical state of the polymer non-destructively, and to scientifically relate these measurements to the mechanical and chemically conditions of the materials. With this capability, the material engineers will be able to see and to predict actual material separation before it happens. This knowledge is important to the use of composites itself as well as to the development and usage of adhesive bonding technique which is extremely desirable but not widely used due to its low reliability.

CERAMICS AND CERAMIC COMPOSITES

Ceramic materials offer elevated temperature capability but are weak from fracture. For this reason, for more than thirty years, the ceramists have been trying to realize the high temperature capability and to improve materials toughness. Both transformation toughening and second phase reinforced ceramics have been the center of most research effort.

Unfortunately, despite substantial investment and research on different fiber reinforced ceramics, the so called “toughened ceramic composite” remains a concept. The toughness derives from the added reinforcement is no where near to be useful. Additionally, the lack of solution to alleviate oxidation problem has prevented the elevated temperature capability being realized. Investment and effort in oxidation resistance coatings for ceramic composites has been substantial but has not produced useful product. At the same time, other newly developed materials, such as strong and elevated temperature metallic systems have practically taken the steam of the ceramic composites development momentum. In fact, it is the critical time to the ceramic composite research community, and a critical self evaluation is needed in order to maintain this momentum. The reality is that without realistic probability of these materials being used in the reasonable future, and under the present fiscal environment, the resources sponsors in the government and industry can not and will not sustain the amount of investment in ceramics and ceramic composites research as they have been doing in the past twenty years. This statement does not imply that no research should be done in ceramic composites. Basic research should be focused to looking at the critical issues rather than making different kinds of composite materials. In this case, the investment will be smaller, selective and focused. For example, to use these materials for elevated temperature applications, research on ceramic composites should be focused on elevated temperature properties not on extensive analysis and testing at room temperatures. The AFOSR ceramics and ceramics composites program is a program that takes on this balanced approach.

Bulk ceramics can sustain severe compressive loads without failure. For this reason, it is ideal to use monolithic ceramics for this type of applications, such as ceramic bearings. Ceramic bearings are superior to metal bearings for their high abrasive resistance, elevated temperature capability and requiring no lubricant. Research on processing, particle size effects and failure under compression for achieving surface strengthening and toughening of bulk ceramics are all excellent issues. Fig. 16 (Ref. 9) illustrates the relationship between the particle size and the failure modes of Silicon Nitride from indentation tests. With this type of preliminary information, ceramic bearings have been fabricated and tested in the space shuttle and aircraft auxiliary power units. However, these trial runs have also revealed that the integrity of these bearings are very sensitive to contamination. Therefore, in order to use ceramic bearings, materials processing and their response to chemical/thermal/mechanical environment must be fully understood.

Other ceramics and ceramic composites applications that will result in huge cost savings are ceramic coatings - Thermal Barrier Coating (TBC) and abrasion resistance coating. TBC on engine components leads to huge saving from increased efficiency as the operating temperature is increased. Abrasion resistance coating can reduce wear loss and increase component life and operation efficiency from friction reduction. The research issues on TBC are oxidation and structural integrity of the coatings. The focus must be on the coating system which contains substrate, transition coating and the TBC itself. It is a combined chemical, thermal and mechanical issue plus materials development effort. Fig. 17 illustrates the figure-of-merit for designing a TBC for purely thermal mechanical response (Ref. 1). One should realize that the integrity of a TBC is controlled by adhesion, stress, deformation and failure modes, and these variables are nonlinearly coupled with oxidation degradation of the coating system. TBC is a hot issue in the engine community because it offers the real possibility of substantial savings for operating a engine. However, many unanswered technology questions have prevented TBC from being used to its maximum potential.

Coating for friction reduction is a different matter whereas the hardness is the figure-of-merit. In this case, diamond coating is the most desirable kind. However, basic research to date has demonstrated that ceramic coatings having near the diamond hardness could be fabricated. For example, it has been known that the theoretical hardness of CN_x (Ref. 10) could be comparable to that of the diamond. The issue is to know enough fundamentals and to process it into crystalline structures rather than in the amorphous forms which only have about one third of the hardness (around 30 GPa) as that of the diamond. A structural template approach (Fig. 18) which grows CN_x coating pseudomorphically on a template has been developed (Ref. 10). The function of the template is to provide a method to maintain minimum interfacial energy between the coating and the template materials. For CN_x coatings, TiN, ZrN and HfN are candidate template materials. With this arrangement and properly chosen controlled wavelength, typical PVD processed coating having a hardness around 60 GPa have been produced (Fig. 19).

The knowledge base on how to make toughened ceramic composites for elevated applications is much less matured. In terms of fundamental properties, two most important and also most difficult problems are oxidation and toughness. There is no good solution to prevent oxidation and no viable means to achieve toughness from second or third phase reinforcement. In terms of applications, fabricate quality components at low cost is still a long way off.

To date, the community does not have enough understanding to make a toughened ceramic composite. Therefore, it is a mistake for anyone even to try to do so. Specifically, the composite toughness is highly dependent on the as processed interface and its reaction to load transfer, and on the properties of the fibers and the matrix especially their chemical and thermal stability at elevated temperatures. However, from the engineering point of view, one can divide the research focus into near term and far term expectations. Short of a set of answers, one can still expect to develop ceramic composites for near term non-load bearing high temperature applications, such as nozzle liners, or for one time, short duration applications, such as a missile engines. For example, weaved ceramic composites having sufficient transverse strength can be used provided that the oxidation degradation is designed into the components. In this case, good oxide fibers and oxide matrix are possible candidate materials for fabrication. As far as using ceramic composites for rotating components in a jet engine, we will need better fundamental knowledge. Therefore, instead of making ceramic composites, one should attack these fundamental issues with vigor. Specifically, the best pure and high quality fibers must be developed and fabricated to alleviate oxidation problems. For long duration applications, such as jet engines, no matter what type of coating is being developed and used, cracks will develop and oxygen will get through to the fibers. In this case, none of the available oxide-fibers available fits the definition. However, some major advancements have been made in the laboratory (Ref. 11). The pure SN fibers, UG-HM, have been fabricated and tested along with standard Hi-Nicalon and Nicalon fibers for oxidation resistance and for mechanical load-carrying capability with success (Fig. 20). Let us turn our attention to the interface. To achieve the fiber debonding for toughened composites, proper chemical and mechanical characteristics must be incorporated into the interface. Specifically, one must be able to fabricate the interface that is stable chemically at elevated temperatures and will debond upon load impinging by an on-coming crack. W. P. Kriven has developed a laser deposition technique for coating the fibers to achieve this goal. Fig. 21 depicts the successful interface which is stable at a temperature up to 1450⁰C and can debond upon applied stress. (Ref. 12)

Lastly is the processing issue. The ceramics and ceramic composites processing techniques available to date can not guarantee quality and are very expensive as well. Novel methods must be developed to translate laboratory proven materials for mass production. There are a lot of on-going effort but very few lend themselves to low cost and quality processing. One method offers potential and fits under the meaning of innovation. Prof. K Sandhage and H Fraser (Ref. 11) looked at the causes of the problems associated with ceramics and ceramic composites processing - shrinkage, porosity and machining. To alleviate the shrinkage problem, they choose to add a small amount of Alkaline Earth materials, which shrink upon sintering because their oxides have smaller molar volume than the metal itself, into the ceramic precursor. In doing so, the total volume change of the mixed precursor could be close to zero. Because there is no volume change from sintering, there is no shrinkage or cracking. Additionally, the precursor is suitable to be processed the same way as those used in the powder metallurgy processing. Specifically, one can use casting or rolling processes to make the composites into final component shapes. No machining is required because this process produces no change in dimension from sintering.

SOLID MECHANICS, SMART STRUCTURES AND INTERDISCIPLINARY RESEARCH

As stated at the beginning of this paper, the challenge for materials scientists is to design a material for a purpose and to predict its behavior before this material is fabricated. For this reason, correct solid mechanics principles that connect the micro- and macro- behavior must be developed and used. Figs 22 & 23 are such examples (Ref. 13). Knowing the properties of each of the constituents of a composite, one can design composite materials and control different failure modes. However, as the materials become more complicated, the mechanics principles that have been developed and used for isotropic and homogeneous materials are no longer valid. Specifically, for any composite material, deformation and damage are nonlinearly coupled, and damage initiates only at a fraction of the ultimate load. There is no distinct “yielding” or “proportional limit” where linear deformation does not come about from material damage. For this reason, a set of new mechanics principles for composite materials must be developed to account for these behaviors. Fig. 24 depicts the processes and the needs. Good results have been generated and one of such examples is illustrated in Fig. 25 - failure criteria for various materials categories (Ref. 14).

The ultimate objective of material development is to make components and systems. The only way to achieve this goal is through close collaboration among the mechanics researchers, materials specialists and structural engineers. Only the structural engineers can define the needs. With the accurate mechanics principles, the mechanics researchers can translate these needs into material properties requirements and also use them for performance prediction. These requirements in turn become materials development goals. For this reason, the paradigm shift in structural design will have a major impact to materials research in the next century. The next generation of aerospace structures will be multi-functional i.e. designed for load-carrying, communication as well as for other smart performance such as health monitoring and self healing. These structural systems have been loosely called “smart structures” or “adaptive structures”. The relevant disciplines to achieve the “smartness” are materials, structures, aerodynamics, electronics, electromagnetic, sensors and actuators, and control. Smart structure is an integrated sensors/actuators and load-carrying system having embedded sensors and actuators that can be used for health monitoring, control feedback, communication (antenna), performance improvement and other functions. Because a smart

structure is to perform many different functions (mechanical, electrical and optical), the critical research topics are to understand and to take advantage of the interrelatedness among these disciplines. For example, one form of the smart structures is an integrated airframe and antenna system that can carry load, monitor materials integrity, communicate in the electromagnetic wave spectrum, and also must have low signature characteristics and perform well aerodynamically (good flying quality). The only means to achieve this goal is to do discipline research and carefully explore the interrelatedness issues among all these disciplines. Among the selective topics being addressed are: deformable airframe for low signature systems and tailless aircraft, distributed sensors and actuators systems, neural net coupled control, optimal energy allocation for control architectural design, MicroElectroMechanical Systems (MEMS) and host-sensor interactions. MEMS are miniature electrical, mechanical and possibly optical systems at micron-size which can be used as distributed sensors and actuators. The spin off potential of MEMS is unlimited. In addition to use them for system control purposes, they can revolutionize manufacturing, processing, robotics, space applications, etc.

A FEW WORDS ABOUT THE FUTURE

In addition to the integrated-collaborated effort, future materials research will be greatly enhanced by the new developments in instrumentation and in computing power. Today, material researchers have already demonstrated that nano-layer materials at micron level made from different materials groups, metal, polymer and ceramics, can be fabricated. The uniqueness of this development is that the traditional division lines among different materials groups have been broken for the purpose of picking the best material system to do a special job. On the computational power side, one may speculate that the future materials could be designed from atomic structures level and up. Fig. 26 illustrates a calculated electron energy density distribution of TiAl materials having different alloy composition. It is a first principle calculation (Ref. 15), but it is still far off from this technique being used to design a real material. However, the electron density distributions do provide some insight as to the relative property change from introducing different alloy into the material systems

REFERENCES

1. A. G. Evans, Implementation Challenges for High Temperature Composites, Mech-283 Harvard University Publications, 1996
2. D. M. Dimiduk, P.R. Subramanian, and M. G. Mendiratta, Acta. Metall. Sinica, 8 (1995) pp. 519-30.
3. P. R. Subramanian, M. G. Mendiratta, and D. M. Dimiduk, JOM, 48(1), (1996), pp. 33-38
4. W. L. Johnson, Current Opinion in Solid State and Materials Science, 1, 383 (1996)
5. J. J. Lewandowski, C. H. Ward, M. R. Jackson, and W. H. Hunt, Jr., eds., Layered Materials for Structural Applications, Vol. 434, Pittsburgh, PA: Materials Research Society, 1996.

6. R. G. Rowe, D. W. Skelly, M. R. Jackson, M. Larson, and D. Wachapelle, Layered Materials for Structural Applications, Vol. 434, J. J. Lewandowski, C. H. Ward, M. R. Jackson, and W. H. Hunt Jr., Eds., Pittsburgh, PA: Materials Research Society, 1996, pp. 3-13.
7. H. Hristov, B. Bolan, A. F. Yee, L. Xie, and D. Gidley, "Measurement of Hole Volume in Amorphous Polymers Using Positron Spectroscopy", *Macromolecules*, 1996, V. 29, p. 8507.
8. C. J. Wolf and H. Fu, "Stress Enhanced Transport of Toluene in Poly Aryl Ether Ether Ketone (PEEK), *J. Polym. Sci. (Phys. Ed.)* 34, 75-82 (1996).
9. S. K. Lee, S. Wuttiphan and B. R. Lawn, "Role of Microstructure in Hertzian Contact Damage in Silicon Nitride: I. Mechanical Characterization," *J. Am. Ceram. Soc.* (In press).
10. D. D. Li, M. S. Wang, Y. W. Chung, S. C. cheng, X. Chu, X. W. Lin and W. D. Sproul, "Structure & Hardness Studies of CN_x/TiN Nanocomposite Coatings." *J. of Appl. Phys. Letters*
11. M. D. Sacks, A. A. Morrone, G. W. Scheiffele, and M. Saleem, "Characterization of Polymer-Derived Silicon Carbide Fibers with Low Oxygen Content, Near-Stoichiometric Composition, and Improved Thermomechanical Stability," *Ceram. Eng. Sci. Proc.*, 16 [4] 25--35 (1995).
12. Chao M. Huang, Y. Xu, Fulin Xiong, A. Zangvil, and W. Kriven, "Layer Ablated Coatings on Ceramic Fibers for Ceramic Matrix Composites," *Materials Science & Engineering Journal*, March 1995.
13. N. Pogano, *Journal of Composites, Part B*, In press, 97
14. N. Chien, T. Honein, and G. Herrmann, "Conservation Laws for Non-Homogeneous Mindlin Plates," *Int. J. Engineering Science*, 1994.
15. Y. Song, S. P. Tang, J. H. Yu, O. N. Hryasox, A. J. Freeman, C. Woodward, and D. M. Dimiduk, *Phil. Mag. B*, 70, (r), (1994), pp. 987-1002.

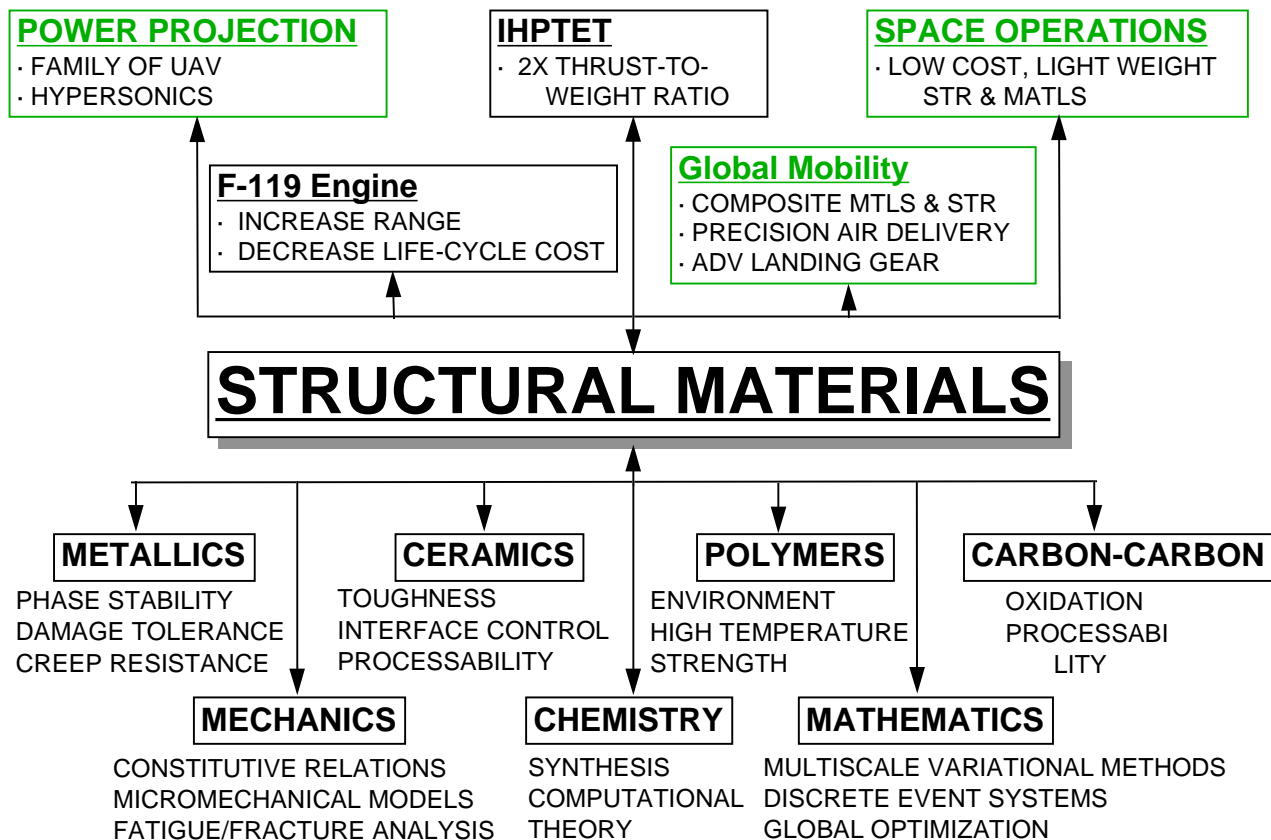


Fig. 1 AFOSR Structural Materials Core Technology

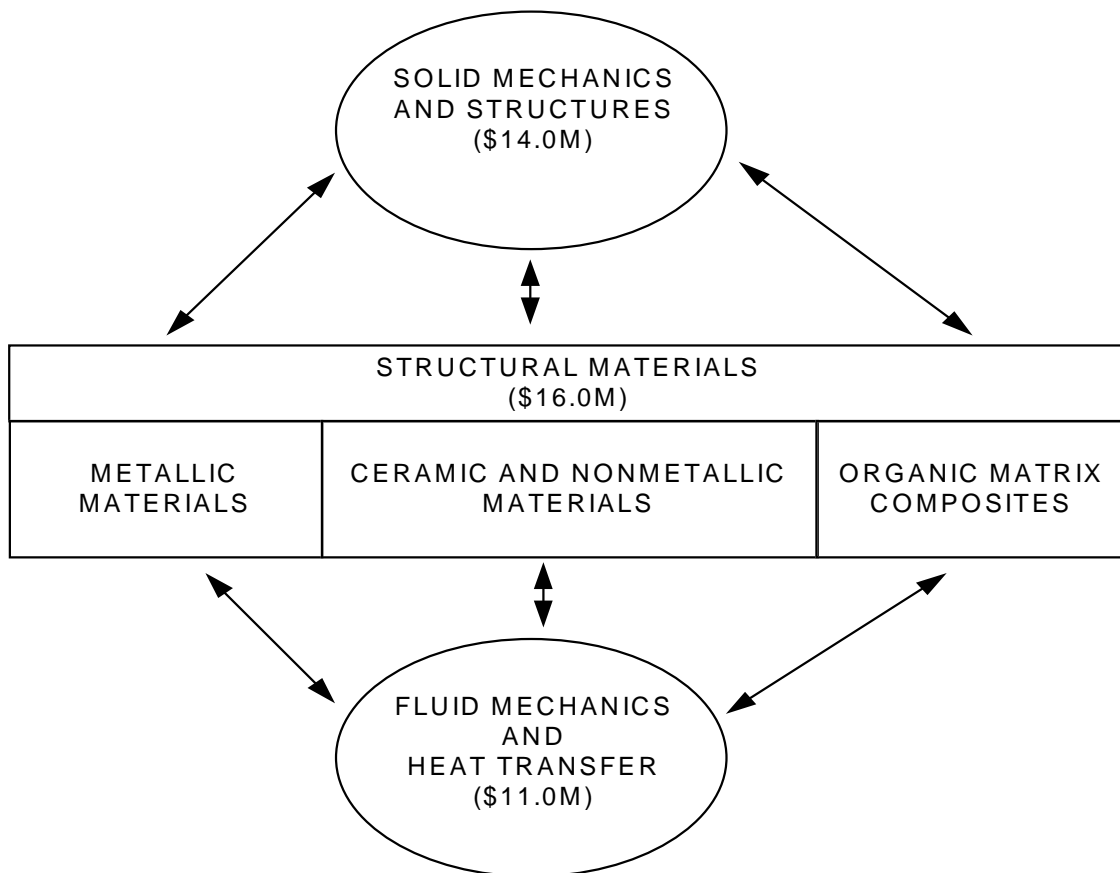


Fig. 2 Integrated-Proactive Materials Research

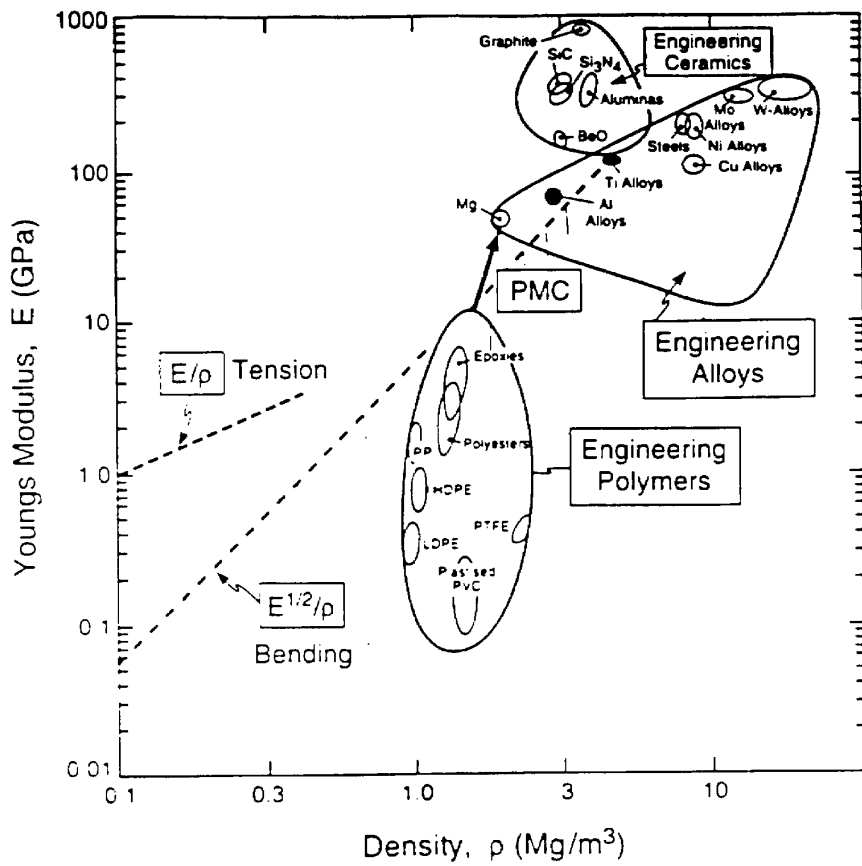


Fig. 3(a) Figure-of-Merit for Material Modulus/Density

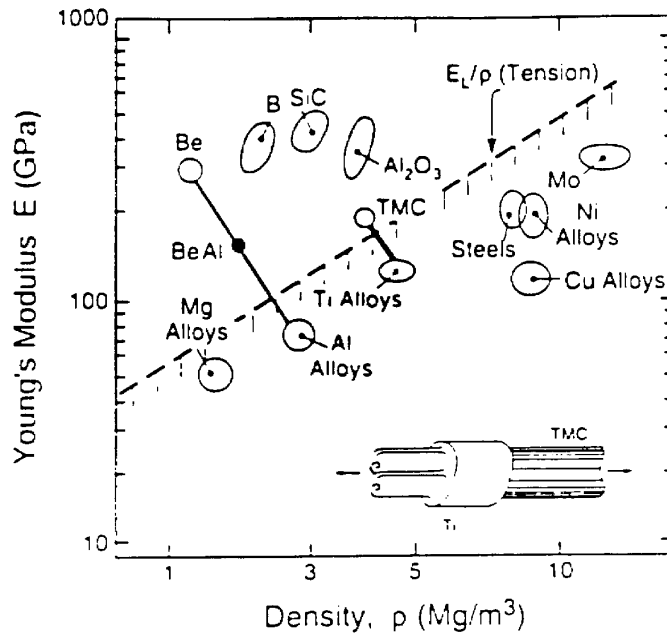


Fig. 3(b) Figure-of-Merit for Material Modulus/Density

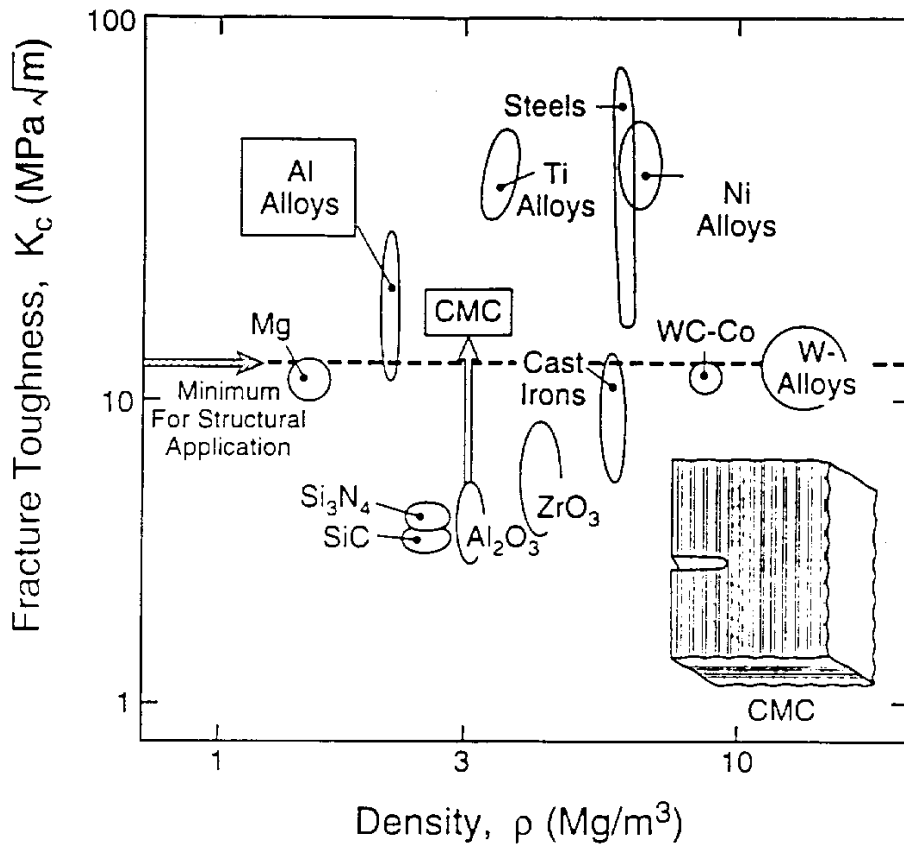


Fig. 4 Figure-of-Merit for Materials Toughness

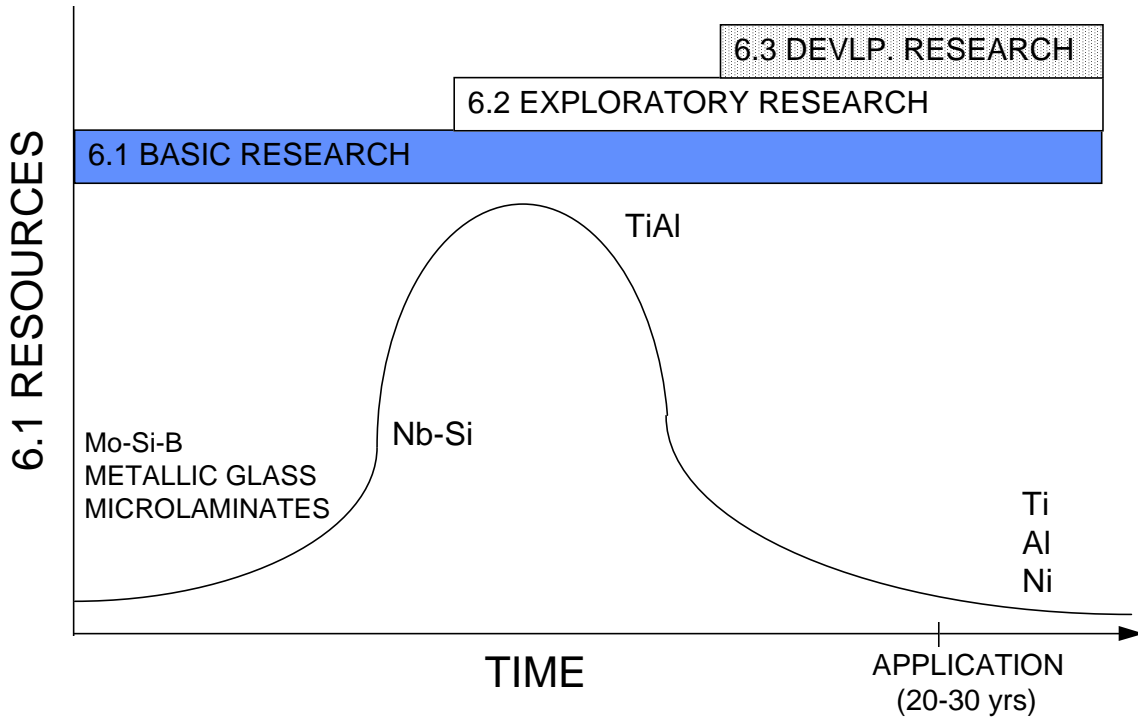


Fig. 5 AFOSR Metals/Metals Composites Research Strategy

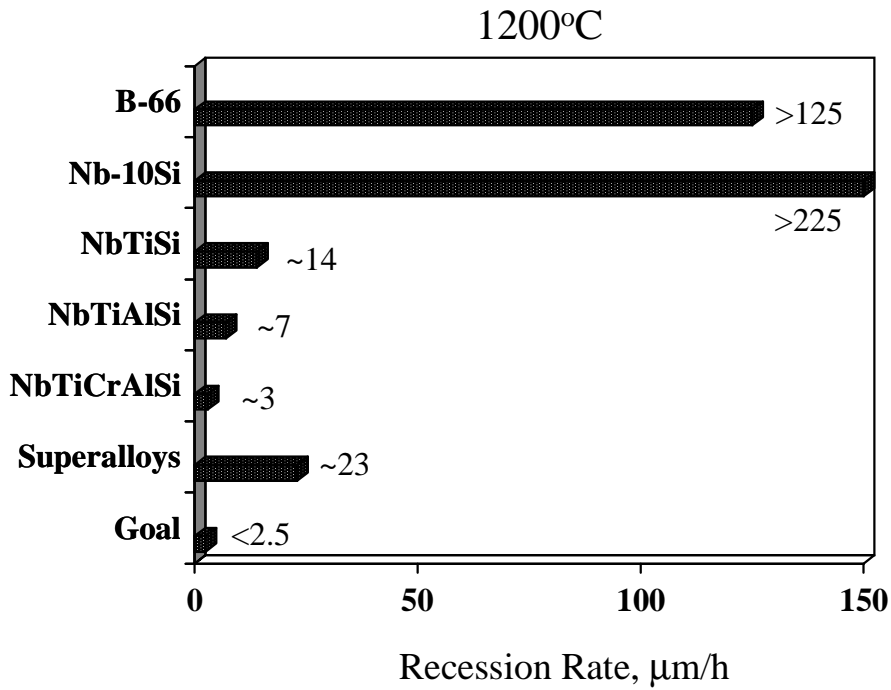


Fig. 6 Recession Rate of Various Metals/Metal Composites

- Region of relative stability to 1670°C
– Potential for use to 1300°C or higher
- Reinforcing Nb₅Si₃ very creep resistant
- Nb has low solubility for Si, but is readily alloyed with other elements
- 80% the density of Ni-superalloys

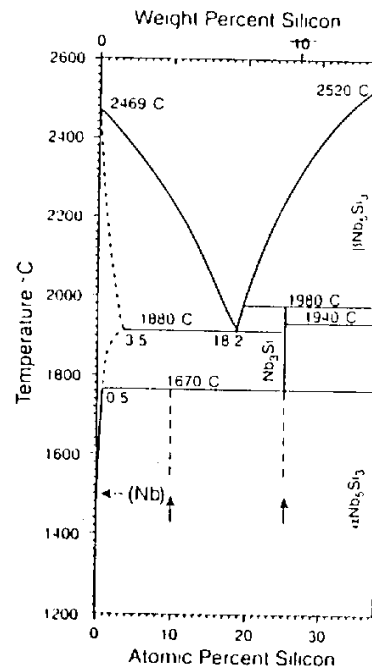


Fig. 7 Figure-of-Merit of Nb-Si

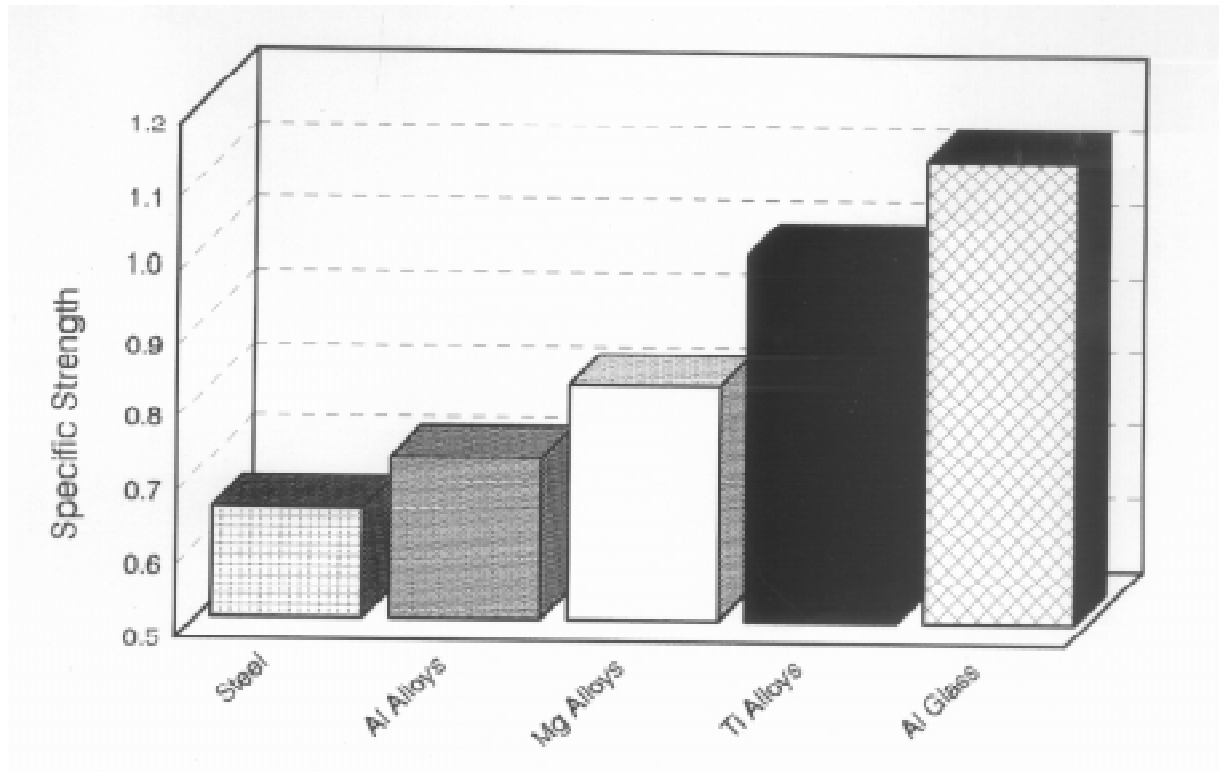


Fig. 8(a) Specific Strength of Different Metal Systems

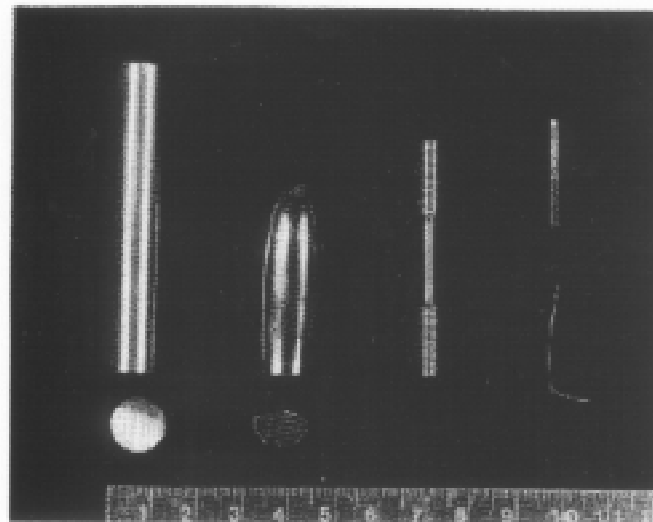


Fig. 8(b) Elongation of Metallic Glass

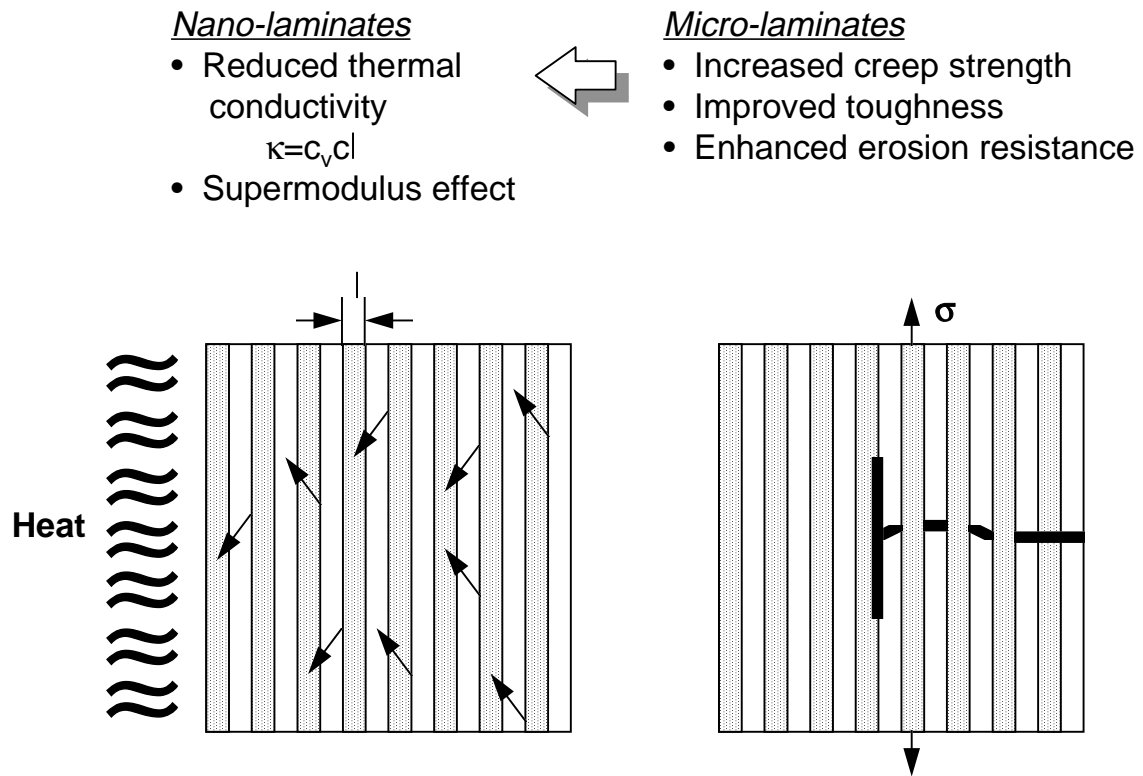


Fig. 9 Nano- and Micro-Laminates

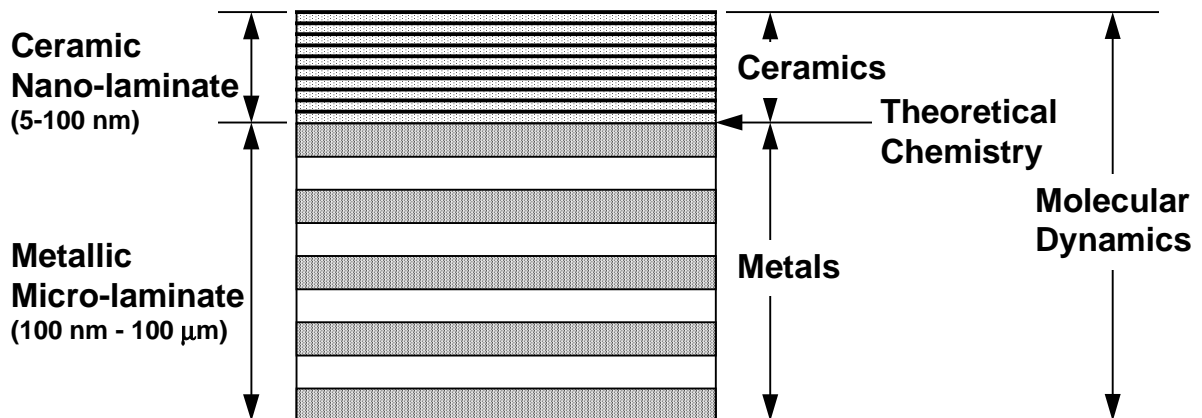


Fig. 10 Hybrid Nano- and Micro-Laminated Materials

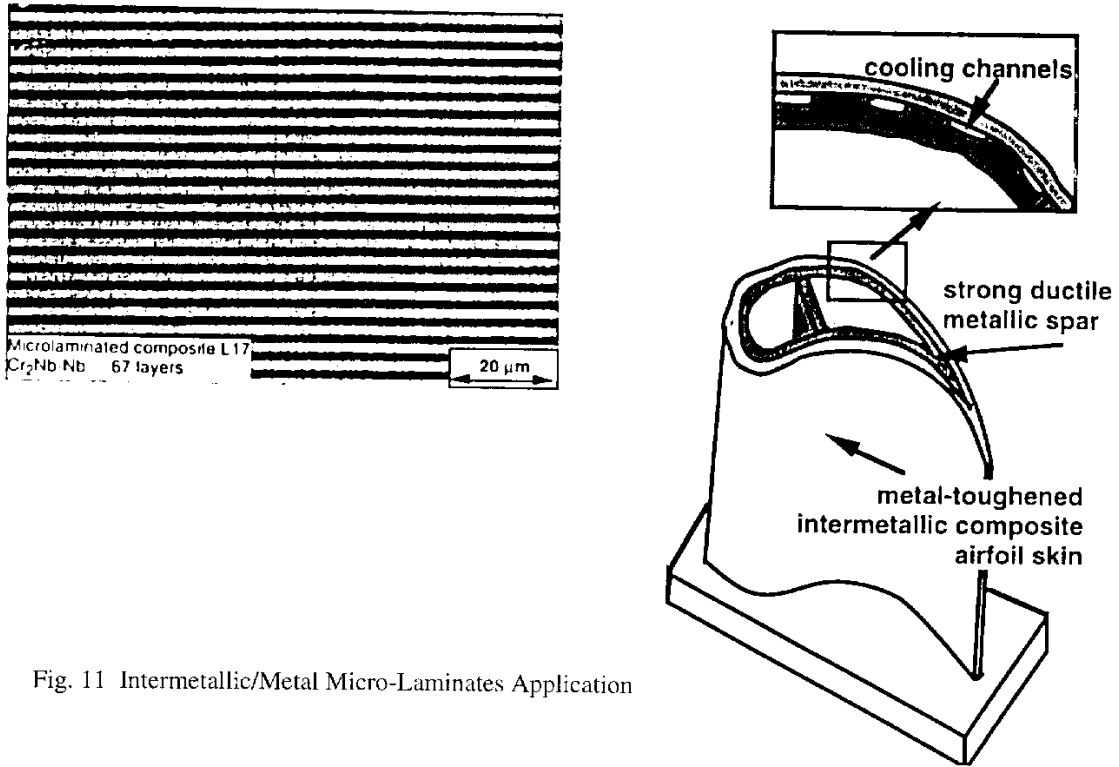


Fig. 11 Intermetallic/Metal Micro-Laminates Application

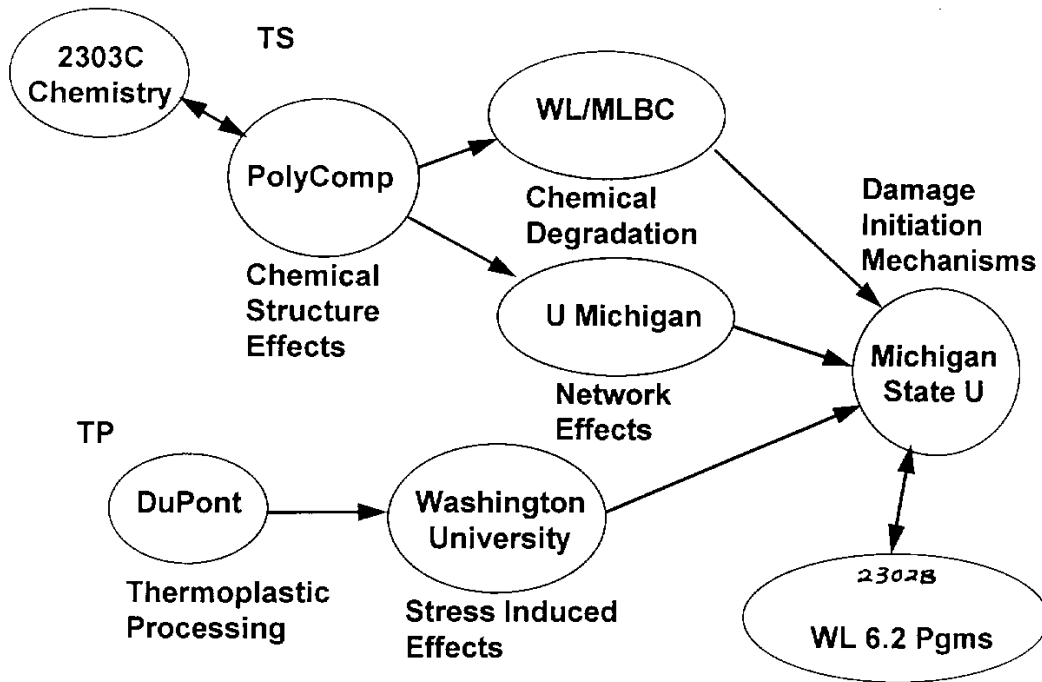


Fig. 12 AFOSR Polymeric Composite Degradation Program

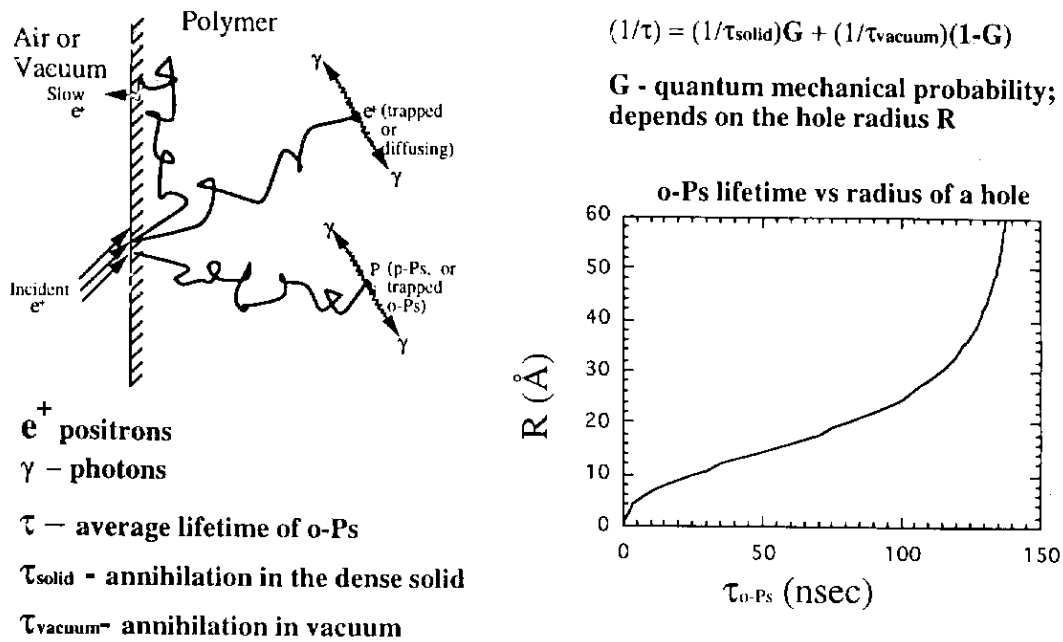
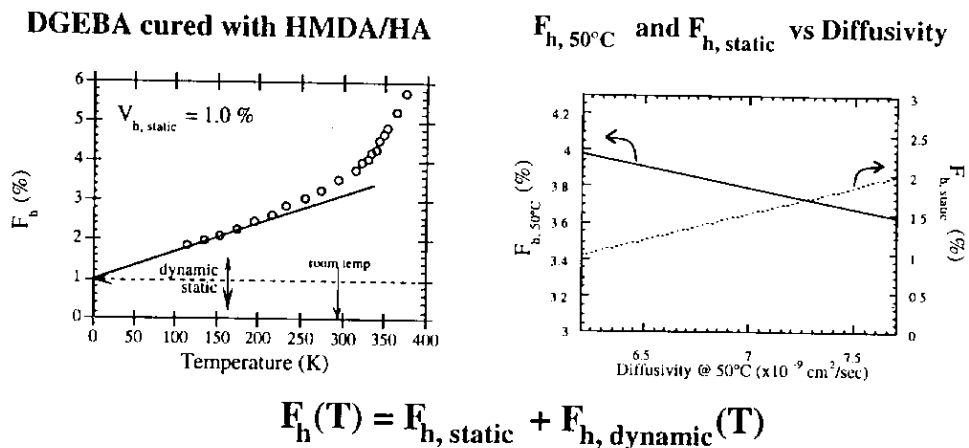


Fig. 13 Interaction of Positrons with Polymers



- Preliminary data suggest that the static holes control the moisture diffusion below T_g
- Potential life-prediction tool
 - ⇒ design cure cycles with predicted durability
 - ⇒ residual life prediction / NDE

Fig. 14 Hole Effects on Controlling Moisture Diffusion

$$t = \frac{RT}{V_1} \left[\ln(1 - v_2) + v_2 + \chi v_2^2 + \frac{\rho V_1}{M_c} v_2 \lambda^2 \right]$$

- t = tensile stress
- R = gas constant
- T = temperature
- V₁ = molar volume of penetrant
- V₂ = volume fraction polymer
- χ = Flory-Higgins interaction parameter
- ρ = density of polymer
- M_c = effective molecular weight between cross-links
- λ = extension ratio

Experimental and Calculated Toluene Volume Fraction as a Function of Stress at 22°C

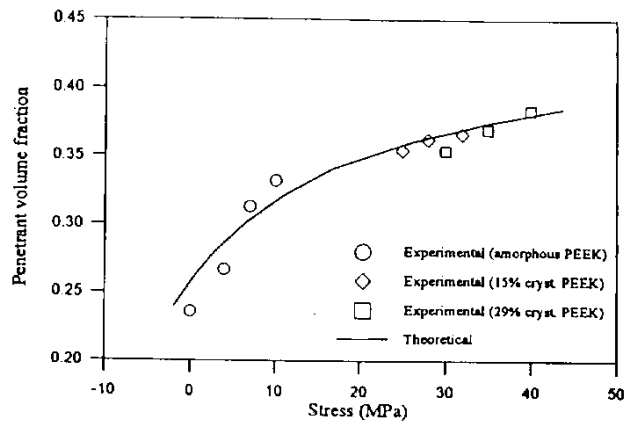
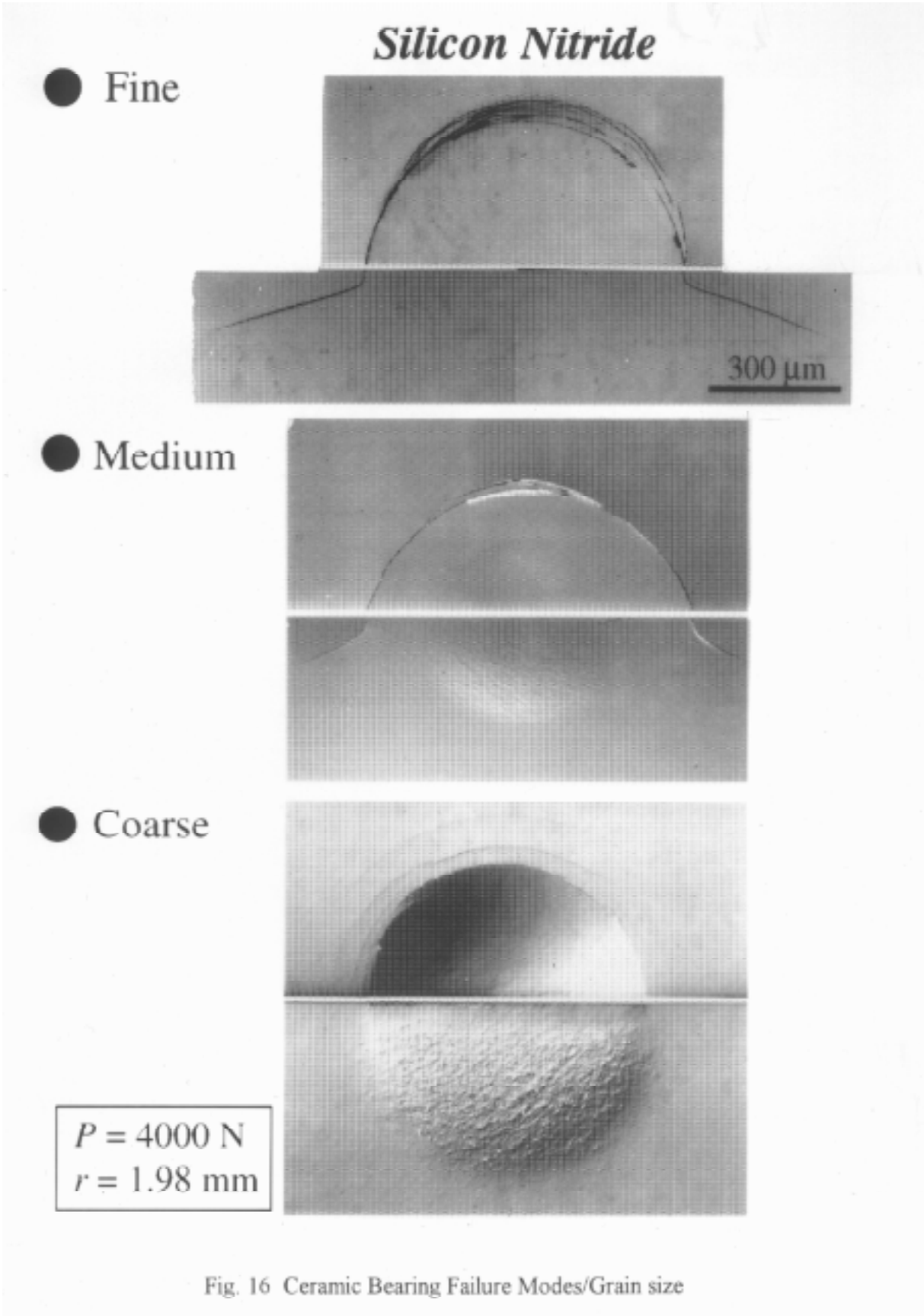


Fig. 15 Model for Sorption of Penetrant into Stressed Rubber (Treloar)



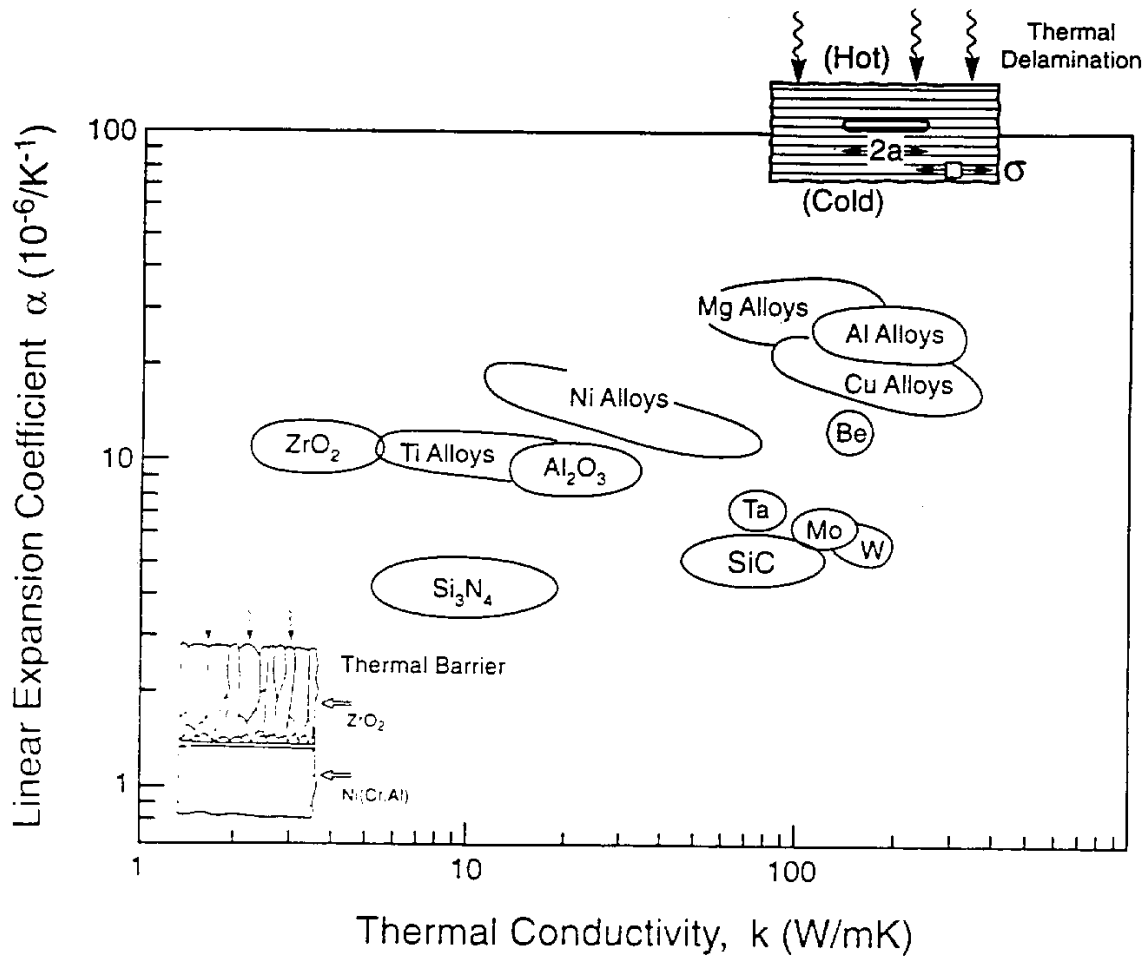
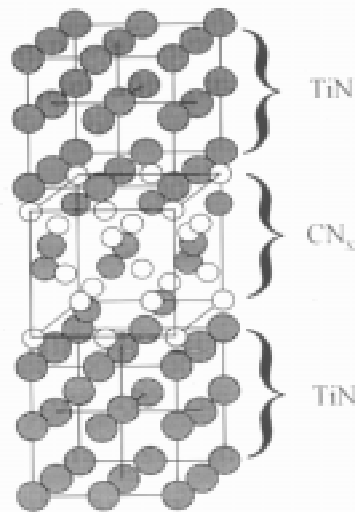


Fig. 17 Figure-of-Merit for TBC Design



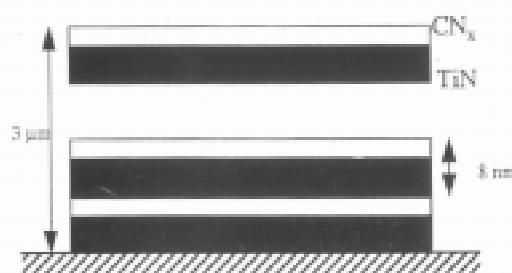
Approach - grow CN_x pseudomorphically on template

- Grown on TiN (ZrN, HfN)

- » $\beta-C_3N_4$ (0001) = 0.644 nm
- » TiN (111) x2 = 0.60 nm (-7%)
- » ZrN (111) x2 = 0.651 (1.1%)
- » HfN (111) x2 = 0.645 (0.2%)

- Interfacial energy reduction
- Surface free energy
- Phase stability induced by stress
- Strain energy

Fig. 18 Crystalline Carbon Nitride Structural Template Method



- 100% crystalline CN_x/TiN
- Hardness about 60 GPa
- CN_x structure to be determined
- Smooth top surface

- Typical PVD coating, can be scaled-up readily
- Controlled wavelength (superlattice period)

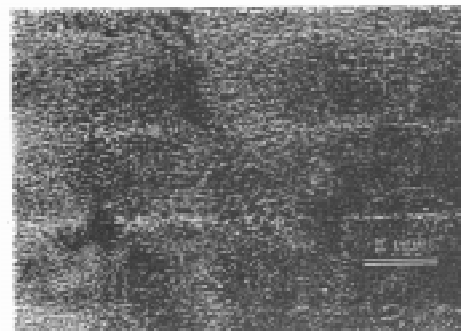


Fig. 19 Nanolayer Stabilized Crystalline Carbon Nitride

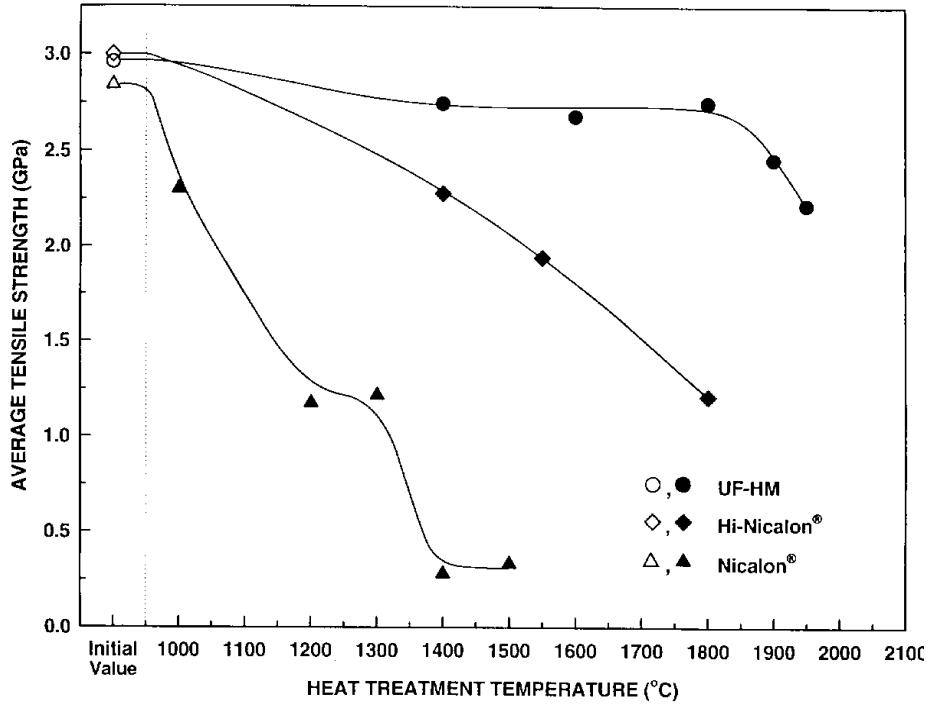


Fig. 20(a) UF-HM Fiber Performance

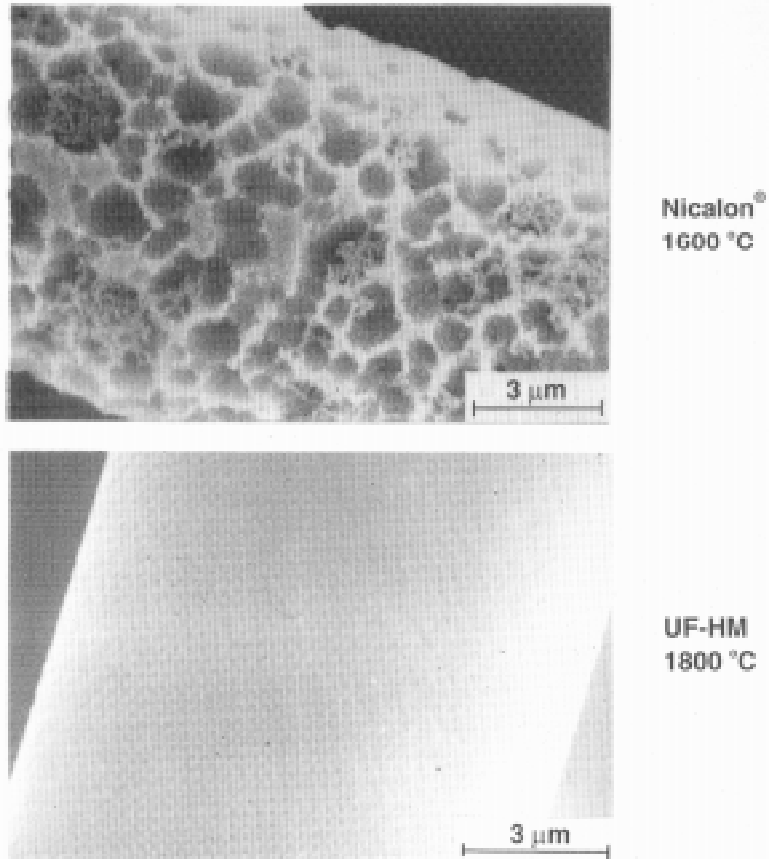
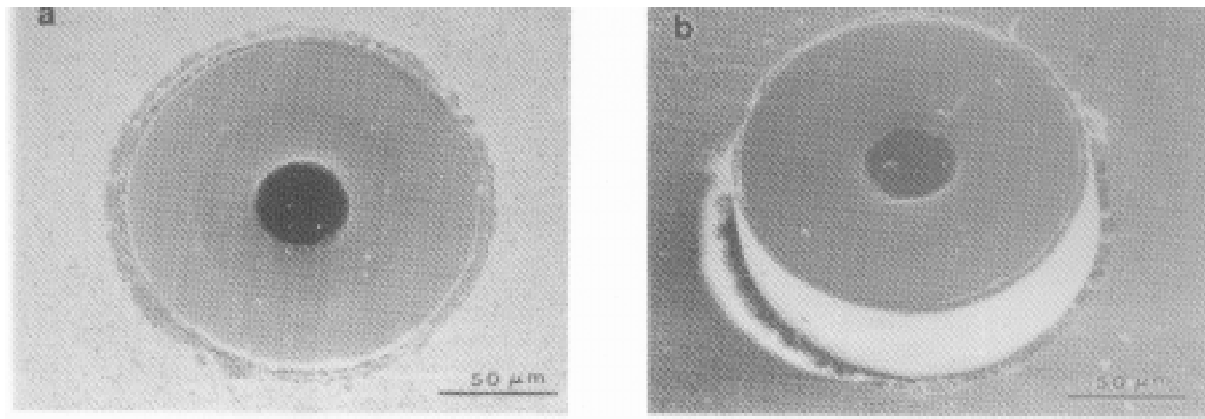


Fig. 20(b) SEM micrographs which show that Nicalon[®] fibers are extensively degraded after heat treatment at 1600°C (top), while UF-HM fibers are not degraded at all after heat treatment at 1800°C (bottom).



(a) before

and

(b) after fiber pushout tests of a SCS-0 fiber / $MgSiO_3 / ZrSiO_4$ matrix composite hipped at $1450^\circ C$ for 1 hour. The interface is weakened by the transformation and fibers can be pushout.

Fig. 21 Transformation Weakening of Interfaces

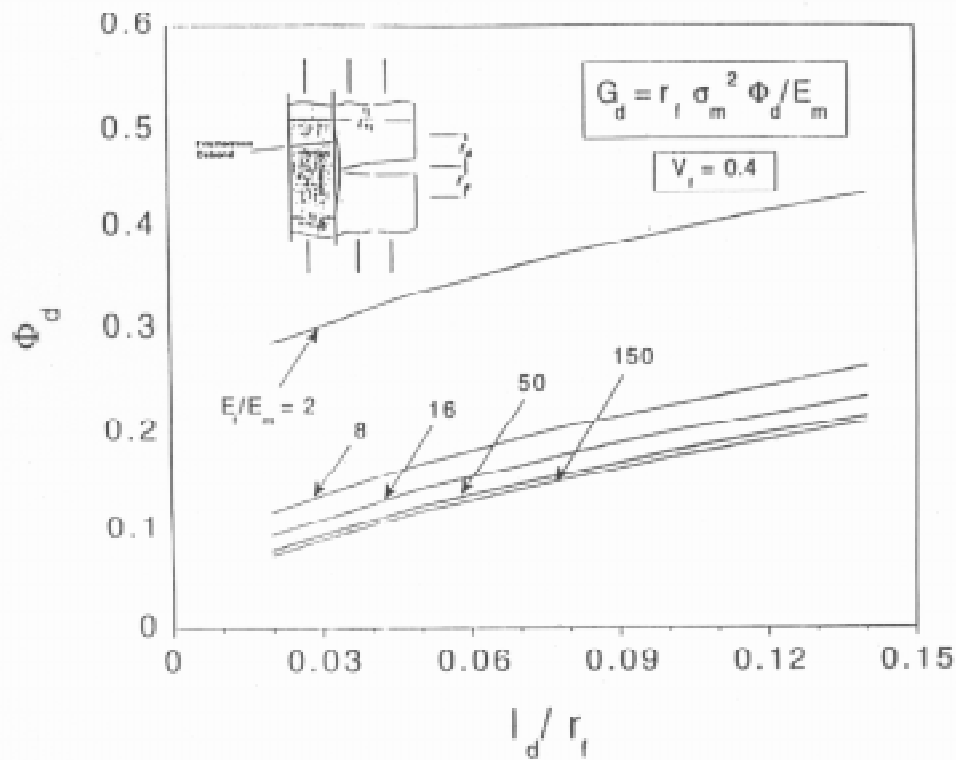
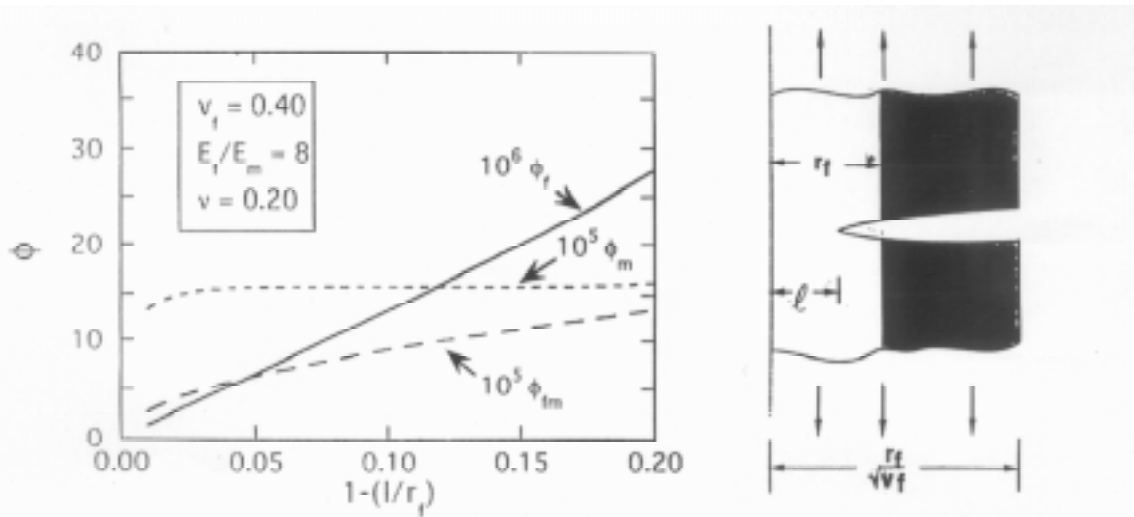


Fig. 22 Material Design Curves Debonding Mode



$$G = \frac{r_f (\phi_f \sigma_f^2 + \phi_m \sigma_f \sigma_m + \phi_m \sigma_m^2) \cdot 10^4}{\pi E_m (\ell/r_f)}$$

Fig. 23 Material Design Curves (Fiber Penetration Mode)

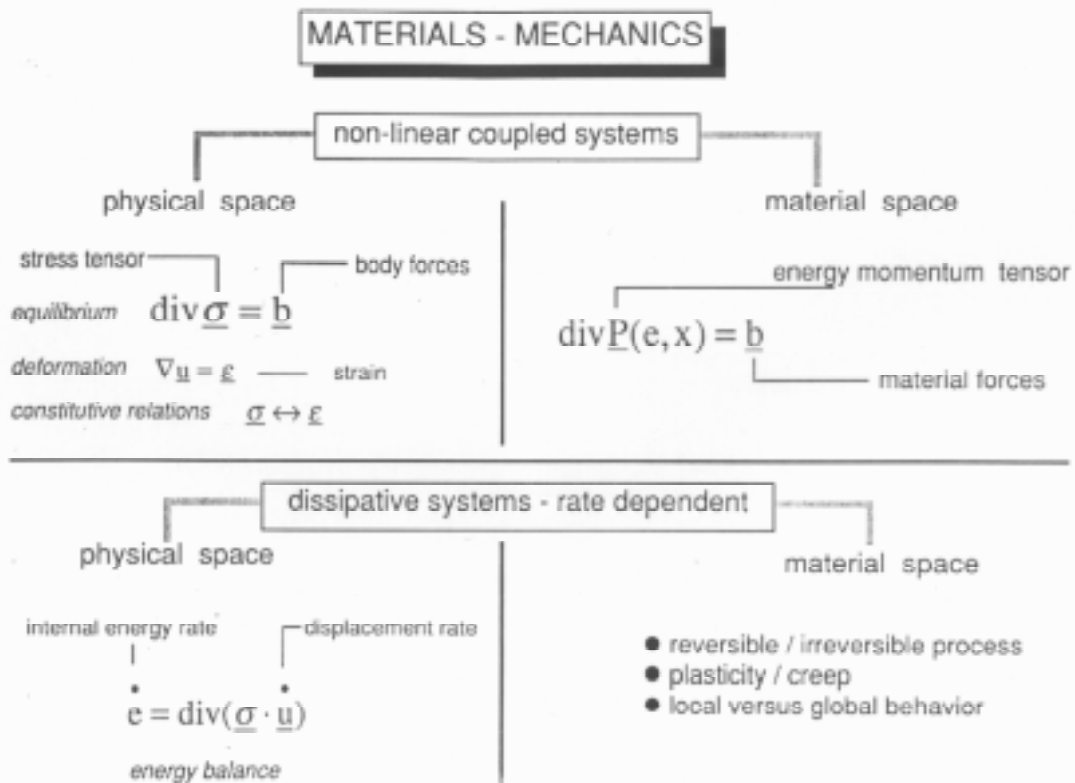


Fig. 24 Materials - Mechanics Fundamentals for Composite Materials

- Conservation Laws in Material Space - Failure Criteria

- Thermoelastic Medium

$$\int_{\partial\Omega} [u_i^k \sigma^{kj} n^j - W^e n^i + \frac{1}{2} \frac{\beta^2}{\lambda + \mu} \theta^2 n^i - \frac{\mu\beta}{\lambda + \mu} (\theta u_j^i n^j - u^i \theta_j n^j)] dl = 0 ,$$

- Viscoelastic Medium

$$\frac{D}{Dt} \left(\frac{\sigma_{ij}}{2E} \right) = \sigma_{ij} - \eta \dot{\epsilon}_{ij}$$

- Non-Homogeneous Medium

$$J_{non-h} = \int_{\Gamma} [(W n^i - t^i u_j^k) + m(W x^k n^k - t^i u_{,k}^i x^k - \alpha u^k t^k / 2)] dl = 0$$

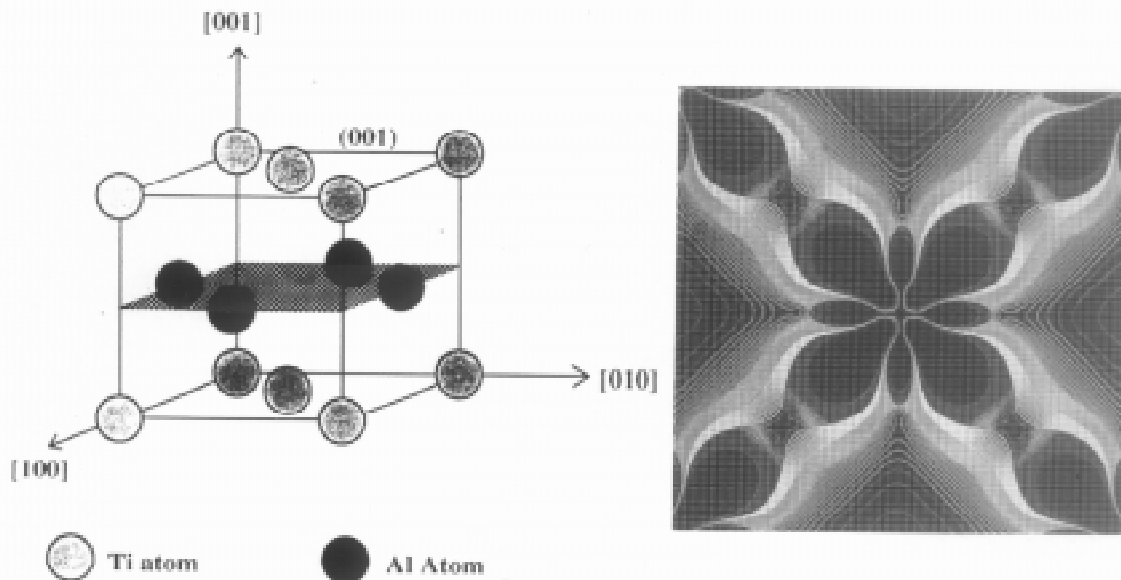
$$J_h = \int_{\Gamma} (W n^i - t^i u_j^k) dl = 0$$

$$M_h = \int_{\Gamma} (W n^k - t^i u_{,k}^i) x^k dl = 0$$

Fig. 25 Conservation Laws of Dissipative Systems

Problem:

Calculation of atomic bonding as a function of alloy composition



Approach:

Use technique based on the Fully Linearized Muffin-Tin Orbital method to calculate d-d Ti bonding in TiAl as a function of alloy content

Fig. 26 Atomic Bonding in TiAl

DELAMINATION FRACTURE IN THE PRESENCE OF THROUGH-THICKNESS REINFORCEMENT

Brian Cox¹, Roberta Massabò², Daniel Mumm³, André Turrettini⁴, and Keith Kedward⁵

¹*Rockwell Science Center, 1049 Camino Dos Rios, Thousand Oaks CA 91360, U.S.A.*

²*Department of Structural and Geotechnical Engineering, Università di Genova, Italy*

³*Division of Engineering and Applied Sciences, Harvard University, Cambridge MA 02138, U.S.A.*

⁴*McDonnell-Douglas Corporation, Long Beach, California, U.S.A.*

⁵*Department of Mechanical and Environmental Engineering, University of California, Santa Barbara, U.S.A.*

SUMMARY: Fracture concepts are discussed for delamination cracks in laminates bridged by through-thickness reinforcement. By examining limiting crack configurations, a much simplified and general depiction of the problems of suppressing crack propagation (when through-thickness reinforcement is intact) and avoiding ultimate failure (when through-thickness reinforcement has failed) can be constructed. From these concepts, the paths towards material design principles and structural reliability codes diverge. For the former, deep insight is required into the micromechanics of the through-thickness reinforcement acting as bridging ligaments, which requires detailed experiments on failure mechanisms and models of failure phenomena. For the latter, a phenomenological solution is sought, in which bridging effects are represented by a function containing the fewest possible parameters that remains consistent with micromechanical models, with the parameters to be evaluated by a few properly chosen engineering tests. The details of this divided approach will be surveyed for the particular case of mode II delamination cracks in laminates reinforced by stitching.

KEYWORDS: delamination, stitching, z-reinforcement, rods, weaving, textiles, theory, fracture, micromechanics, crack bridging.

INTRODUCTION

Through-thickness reinforcement is the most promising method of solving the endemic problem of delamination in 2D laminates used as skins or sheets. It is also attractive for avoiding the pull-off of stiffeners or other attachments when out-of-plane tensile stresses arise. Various techniques of applying through-thickness reinforcement have been developed, including stitching [1-4], the insertion of short rods (so-called “z-reinforcement”) [5-8], and interlock weaving [9]. All of these approaches work in their primary goal, but they degrade in-plane properties to some extent, because of the disruption of in-plane fibers. It is therefore important to know the expected magnitude of the effect of through-thickness reinforcement, so that overdesign and unnecessary cost are avoided and in-plane properties maintained. The requisite models will be referred to here as material design models.

Once through-thickness reinforced composites are manufactured for a given application, a second engineering problem arises – the prediction of their strength, damage tolerance

(including notch and impact sensitivity), and fatigue lifetime. Models of the performance of the through-thickness reinforcement in a structure are required, which will be referred to here as structural reliability models.

This article outlines the elements of material design and structural reliability models for stitched laminates, mainly for polymer composites but with some reference to ceramic matrix composites. The central problem is the behaviour of delamination cracks that are bridged by stitching, which shields the delamination crack tip from the applied load by imposing tractions across the crack. In plane problems, the bridging tractions, p , include mode I and mode II tractions, p_3 and p_1 , where the x_1 is the direction of crack propagation and x_3 the through-thickness direction. The bridging tractions can usually be expressed as functions of the opening and sliding crack displacements, u_3 and u_1 .[♥] Structural reliability models deal with determining the essential characteristics of $p_i(u_j)$ from calibrating experiments and the question of how the crack will propagate given $p_i(u_j)$; material design models show how $p_i(u_j)$ depends on the material and geometrical properties of the constituent materials and the mechanisms by which individual bridging stitches act.

The nature of material design and structural reliability models for through-thickness reinforcement should be as distinct as their purposes. A material design model is intended to specify the details of the optimal reinforcement. It should therefore describe the mechanisms of the bridging action of the reinforcement and the failure of the laminate in detail, relating all macroscopic phenomena via micromechanics to the material and geometrical properties of the laminate and the through-thickness reinforcement. Fiber volume fractions, fiber orientations, reinforcement architecture, fiber and matrix properties (elastic and nonlinear), microcracking, crazing, the condition of interfaces, and fiber or tow pull-out effects are all phenomena that, among others, may appear explicitly in material design models; and whose investigation by innovative experiments, often on a microscopic scale, is demanded. No detail is too fine if it can be shown to influence the bridging relation, $p_i(u_j)$. A structural reliability model, in contrast, should be as simple as possible, retaining the minimum degrees of freedom necessary to generate accurate predictions of performance in a structural application. It should be coupled to a set of engineering tests by which it is to be calibrated. The structural reliability model should unburden the structural engineer of the need to know most of the details of why the through-thickness reinforcement acts in a certain way, preserving her from error by having a form known to be correct for the prevailing mechanisms. The calibrating tests must not be microscopic, but macroscopic, usually on specimens whose geometry reflects that of the structural component.

The problem of mode II delamination cracking will be used here as the prime example. Experimental results will be quoted for one exemplary laminate consisting of a quasi-isotropic lay-up (48 plies $[45/0/-45/90]_{ns}$), with an in-plane Young's modulus, $E_1 = 44.6$ GPa, transverse shear modulus, $G_{13} = 2.6$ GPa, and in-plane Poisson's ratios $\nu_{12} = \nu_{21} = 0.3$; stitches of doubled 3650 denier S-2 glass fiber tows on a square array of side 3.2 mm; individual stitch area = 0.636 mm^2 ; total stitch area fraction $c_s = 0.062$; and laminate half-thickness $h = 3.6$ mm [10,11]. Fracture concepts for bridged delamination cracks will be surveyed, experimental observations of mechanisms described, and material design and structural reliability models introduced.

[♥] In this paper, u_1 and u_3 are defined so that the total crack sliding and opening displacements are $2u_1$ and $2u_3$.

FRACTURE CONCEPTS

In work reported in detail elsewhere, end notch flexure (ENF) tests have been performed on numerous carbon/epoxy laminates stitched with Kevlar or glass fiber tows, including the exemplary case defined in the Introduction [12]. The ENF test configuration is illustrated in Fig. 1a. The specimen has thickness $2h$ and length $2L$ and contains a delamination crack of length a along its mid-plane. In a thin, unnotched and uncracked specimen of an orthotropic, homogeneous laminate, a load per unit width, P , generates uniform shear tractions of magnitude

$$\tau_a = \frac{3P}{8h} \tag{1}$$

along the mid-plane. In analyzing the fracture mechanics of an ENF specimen, either τ_a or P can be regarded as the independent variable. In this paper, τ_a will be used and referred to as the applied shear stress and the schematic shown in Fig. 1b will be examined. The shear tractions, p_1 , represent in a continuous approximation the bridging mechanisms developed by the stitches in the bridged portion of the delamination, $a-a_0$, a_0 being the length of the unbridged portion of the crack, e.g., a notch. The behavior of the ENF specimen is obtained by superposing the solution for the problem of Fig. 1b and the solution for a specimen containing no crack or notch and subject to the external load, P [13].

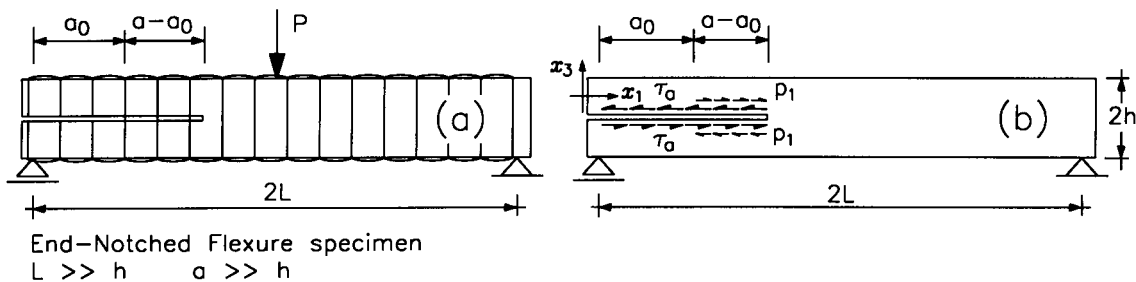


Fig. 1: The end notch flexure (ENF) test and coordinate system.

Fig. 2 shows crack opening and sliding displacements measured with great precision by stereoscopy along a typical delamination in an ENF specimen. The crack has grown from a notch and is bridged by stitches. The zone of detectable sliding displacement, which away from the notch is associated with a single interlaminar crack, extends some 20 mm from the notch. Its extremity indicates the position of the crack tip. The opening displacement is very small (effectively zero) within 2-3 mm of the mode II crack tip. Thus the tip conditions are pure mode II.[▼] The opening displacement rises to an approximately constant value in the

[▼] At a much finer scale, perhaps $\sim 1\mu\text{m}$, one might expect to find that the furthest advance of damage consists of arrays of ogive cracks, whose shapes are just such as to create pure mode I conditions at each of their crack tips when the far field stress is pure shear [14]. Such microcracks have been seen in similarly constrained layers of various brittle materials, including ceramics and epoxy resins [9]. However, the relevant scale for modeling the crack tip in Fig. 2 is $\sim 1\text{ mm}$, three orders of magnitude greater. At this scale, the stress fields must be almost entirely mode II, because the opening displacements are so much smaller than the sliding displacements.

crack wake. This is reminiscent of crack opening due to surface roughness in mixed mode fatigue crack tests in alloys. The plateau in the opening displacement corresponds there to the size of mismatched asperities. In the stitched laminates, the opening is due to the propping effect of the bridging stitches when they bend plastically within the crack. The crack of Fig. 2 remained bridged by intact stitches and propagated stably (increasing load) until it had reached the middle of the specimen. In other experiments, the stitches failed at the outset of crack propagation, which was then unstable. The nature of the fracture process depends critically on the laminate thickness, $2h$, the notch length, a_0 , and the nature of the stitching, which is embodied in the bridging law. For a mode II delamination, the bridging law is simply the dependence of shear bridging tractions, p_1 , on the sliding displacement, u_1 . For the crack of Fig. 2, p_1 may be regarded as continuous along the crack, rather than discrete, because the crack length is much greater than the stitch spacing.

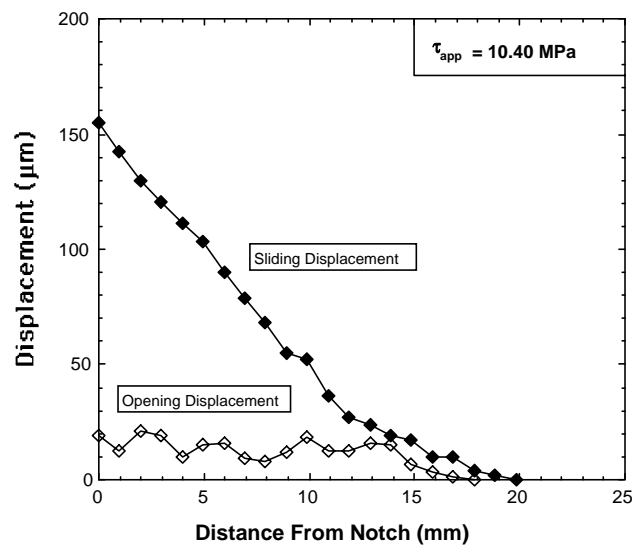


Fig. 2: Total opening and sliding displacements for a delamination crack in a carbon/epoxy laminate stitched by S-2 glass fibers (from [12]).

Two limiting crack configurations characterize the various possible fracture histories. The first is the small scale bridging limit, where Linear Elastic Fracture Mechanics prevails. The second will be referred to here as the ACK limit, in reference to the seminal work of Aveston, Cooper, and Kelly on mode I matrix cracks in fibrous composites [15]. A condition for the existence of the ACK limit is that the bridging law, $p_1(u_1)$, must be an increasing function. Experiments and models confirm that this is so.

The essential concepts introduced by the two limiting configurations can be summarized as follows (see [13] for details).

Small Scale Bridging Limit

If the bridging ligaments (stitches) fail during crack propagation, the delamination crack will eventually reach, in a sufficiently long specimen, a configuration characterized by a zone of intact stitches which is much smaller than the crack length, the notch size, and the specimen half length, L . The length of the bridging zone approaches a constant length, l_{SSB} , as the crack grows. In this limiting configuration the bridging stitches provide a constant increment, G_b , to the delamination fracture toughness of the composite, G_{II} :

$$G_{II} = G_{IIc} + G_b = G_{IIc} + 2 \int_0^{u_0} p_1(u_1) du_1 \quad (2)$$

where G_{IIc} is the delamination fracture energy of the unbridged composite and u_0 is the crack sliding displacement at which the bridging tractions vanish. The critical value, τ_{SSB} , of the applied shear stress, τ_a , in this limit follows through Griffith's energetic fracture criterion as

$$\tau_{SSB} = \frac{1}{a} \sqrt{\frac{h(G_{IIc} + G_b)}{\bar{A}}} \quad (3)$$

where a is the crack length; and \bar{A} is defined in [13] for general cases consistent with cylindrical symmetry in the ENF test and takes the value $\bar{A} = 4/E$ for the special but common case of a homogeneous, orthotropic laminate, with $E = E_1(1 - \nu_{12}\nu_{21})$. If either $p_1(0) \neq 0$ or $G_{IIc} \gg G_b$ (e.g., $G_{IIc} > 1.5 G_b$ for a linear law), then $l_{SSB} \sim (a_{IIc}h)^{1/2}$ where a_{IIc} is the mode II catastrophic length scale (a material constant):

$$a_{IIc} = \frac{4u_0}{p_0\bar{A}} \left(\sqrt{1 + \frac{G_{IIc}}{G_b}} - \sqrt{\frac{G_{IIc}}{G_b}} \right)^2 \quad (4)$$

with p_0 and u_0 the values of p_1 and u_1 at bridging ligament (stitch) failure [13]. Eq. (4) reduces for a homogeneous orthotropic laminate with vanishing G_{IIc} to

$$\lim_{G_{IIc} \rightarrow 0} a_{IIc} = \frac{u_0 E}{p_0} \quad (5a)$$

and, in the particular case of a rectilinear bridging law, the quantity $2a_{IIc}$ in this limit coincides with the mode II characteristic length

$$l_{IIch} = \frac{G_b E}{p_0^2} \quad (5b)$$

for which a well-known analogy exists in mode I [13]. When $G_{IIc} = 0$, the notch sensitivity of the laminate, i.e., its loss of strength when an unbridged notch or delamination flaw of length a_0 is present, depends on $a_0/(l_{IIch}h)^{1/2}$. When $G_{IIc} \neq 0$, notch sensitivity and other fracture characteristics depend on both $a_0/(l_{IIch}h)^{1/2}$ and the ratio G_{IIc}/G_b .

If $p_1(0) = 0$ and G_{IIc} is relatively small, a realistic case for some stitched laminates, l_{SSB} no longer is approximated by $(a_{IIc}h)^{1/2}$, but becomes very large, rising in proportion to G_b/G_{IIc} ; but l_{SSB} still scales with $h^{1/2}$.

The ACK Limit

If the bridging ligaments (stitches) do not fail and $p_1(u_1)$ is an increasing function, the delamination crack will eventually, in a big enough specimen, reach a configuration in which

the applied shear tractions are sustained in the crack wake by equal and opposing bridging tractions and the critical stress for crack propagation, τ_{cr} , approaches a constant value, τ_{ACK} , given by [13,16]

$$G_{IIc} = 2 \left[\tau_{ACK} u_{ACK} - \int_0^{u_{ACK}} p_1(u_1) du_1 \right] \quad (6a)$$

where $\tau_{ACK} = p_1(u_{ACK})$. Equation (6a) reduces for a power law $p_1 = \beta u_1^\alpha$ to

$$\tau_{ACK} = \left[G_{IIc} \beta^\alpha \frac{1+\alpha}{2\alpha} \right]^{\frac{\alpha}{1+\alpha}} \quad (6b)$$

The ACK limit is approximated when the crack has propagated beyond any notch a distance $a - a_0$ somewhat greater than a length l_{ACK} given by

$$l_{ACK} = \sqrt{a_{IIIm} h} \quad (7)$$

$$a_{IIIm} = \frac{1}{A} \left(\frac{1+\alpha}{2\alpha} G_{IIc} \right)^{\frac{1-\alpha}{1+\alpha}} \beta^{\frac{-2}{1+\alpha}} \quad (8a)$$

with the special case

$$a_{IIIm} = \frac{E}{4\beta} \quad (8b)$$

for linear bridging ($\alpha = 1$) in a homogeneous, orthotropic laminate [13]. When $a - a_0 \ll l_{ACK}$, bridging effects are weak and the crack propagates nearly as though it is unbridged, even though stitches already bridge the crack wake.

Characteristics of Fracture

Fig. 3 shows the evolution of the critical applied load for crack propagation in an ENF specimen with a notch (no stitches) of size a_0 when the bridging stitches never fail and the bridging law is linear. All curves share the asymptote $\tau_{cr} = \tau_{ACK}$. Crack propagation is unstable for small notches and stable for large notches. Defining a stable curve as one for which $\tau_{cr}(a_0) < \tau_{ACK}$, the minimum notch size for stable growth follows from Eqs. (3) and (8b) as $a_0 = (a_{IIIm} h)^{1/2}$.

Fig. 4 shows histories of the critical stress for one of notch sizes from Fig. 3 when the stitches have various finite strengths. If the stitches are strong enough (normalized strength 2.0 in the cases shown), the ACK limit is still reached without stitching failure. But for lower strengths, a period of growth without stitching failure is succeeded by stitching failure and unstable, catastrophic cracking. The specimen is rendered in two by the process. The critical stitch

strength for noncatastrophic cracking (towards the ACK limit) rises linearly with increasing notch size, a_0 , for large notches in a laminate of fixed depth, h (not as $a_0^{1/2}$, as it would in an infinite or very thick specimen). For small notches, whether cracking is noncatastrophic or catastrophic depends on the relative magnitudes of τ_{ACK} and p_0 ; or, equivalently, of the length scales a_{IIc} and a_{IIIm} [13].

The role of the length scale $(l_{IIch})^{1/2}$ in notch sensitivity is illustrated in Fig. 5, which shows how the notched ultimate strength of the laminate, τ_{ult} , depends on notch size for several bridging laws when the intrinsic delamination toughness, G_{IIc} , is zero. This will be a useful approximation in discussing the failure of stitches whenever $G_{IIc} \ll G_b$, which is probably always the case for bridged cracks in a ceramic matrix composite and will often be so in a textile polymer composite. \diamond The notch size is normalized by $(l_{IIch})^{1/2}$. When $a_0/(l_{IIch})^{1/2} > 1$, all curves converge, approaching the curve obtained for a Griffith crack in a material with toughness equal to that supplied by the bridging ligaments, G_b . Only when $a_0/(l_{IIch})^{1/2} < 1$ is there significant dispersion among the curves and even then it is modest. For vanishing notch size, the composite strength is limited by p_0 , the ligament strength. Thus $(l_{IIch})^{1/2}$ and p_0 alone are sufficient to define the ultimate notched strength to a fair approximation [13,17,18].

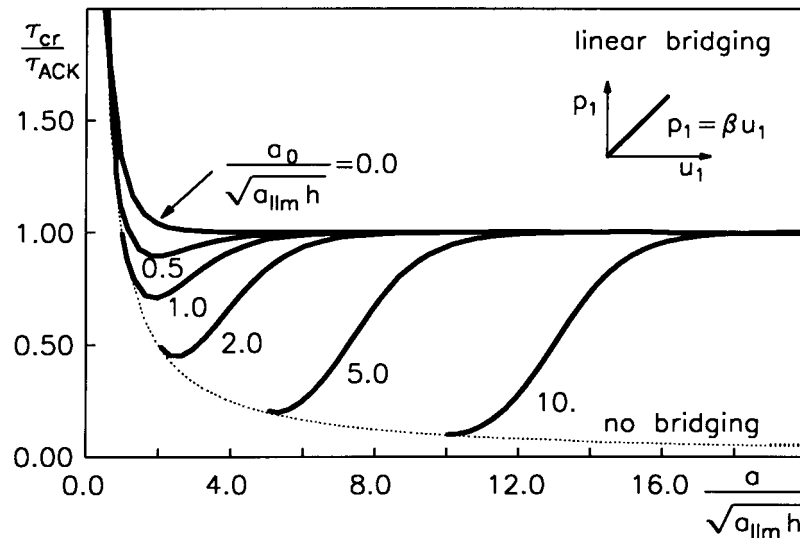


Fig. 3: Approaching the ACK limit in a mode II fracture test. The critical applied shear stress for delamination crack propagation in an ENF specimen for different notch sizes, with a linear bridging law and stitches that do not fail (from [13]).

When $G_{IIc} \neq 0$ (i.e., other than when $G_{IIc}/G_b \ll 1$, which may be the case in a composite with a tough polymer matrix), the ultimate notched strength will also depend quite strongly on G_{IIc}/G_b . It also then depends on the size of any initial bridged delamination crack (or matrix flaw). If the laminate is defect-free apart from the notch, its ultimate strength, $\tau_{ult}^{(max)}$, can be substantially higher than its ultimate strength, $\tau_{ult}^{(min)}$, in the presence of the most deleterious matrix flaw. This is illustrated for a material with a rectilinear bridging law and for a range of values of $G_b/G_{IIc} > 1$ in Fig. 6. Now the notched strength depends on p_0 , $(l_{IIch})^{1/2}$, and G_b/G_{IIc} .

\diamond Putting $G_{IIc} = 0$ is obviously not a valid step when modeling delamination crack growth, which must depend on the value of G_{IIc} , as illustrated, for example, by Eq. (6).

The concepts outlined here are of course not peculiar to mode II cracks or to delamination specimens. Similar length scales and nondimensional parameters control mode I fracture and apply to infinite specimens [18,19]. However, one important distinction of thin plates is that the lengths l_{ACK} and l_{SSB} are not material constants, as they are in infinite specimens, but material-structure parameters, involving the plate thickness, h .

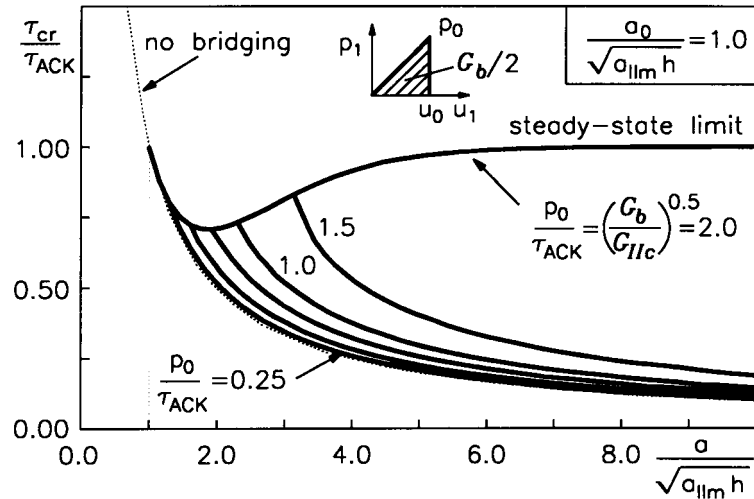


Fig. 4: Catastrophic and noncatastrophic failure. If the stitches are strong enough, the ACK limit can still be reached. Otherwise, catastrophic failure sets in after some initial extension of the bridged zone.

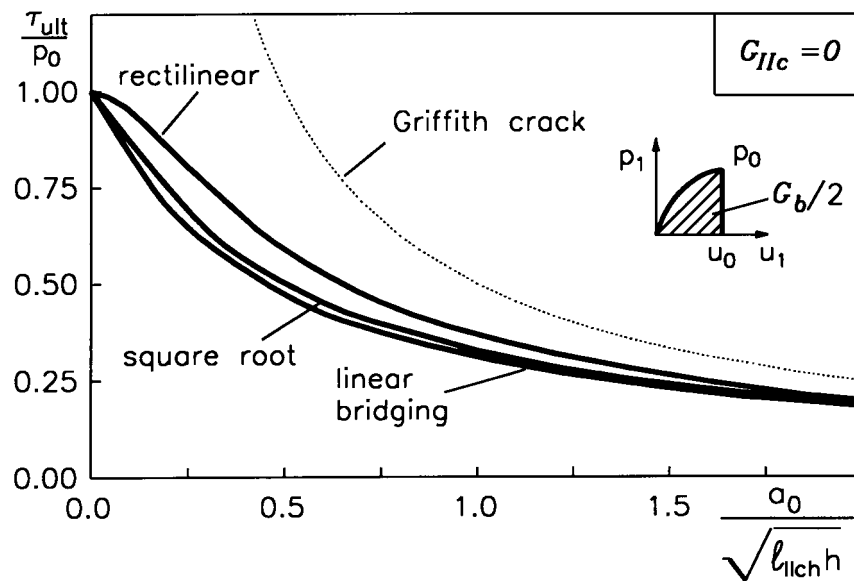


Fig. 5: The ultimate notched strength for bridging laws of various shapes in a material with no intrinsic fracture resistance (from [13]).

THE MICROMECHANICS OF MODE II BRIDGING BY STITCHES

Experiments have now revealed the mechanisms of damage that develop in a bridging stitch as the crack sliding displacement increases. Direct observations of bridging stitches in the wake of a crack were obtained by sectioning a cracked ENF specimen [20]. The specimen, a carbon/epoxy laminate with S-2 glass stitches, was first encased, loading jig and all, in a block of epoxy resin while still under load. At this point it contained a delamination crack that had grown stably approximately 20 mm from a 20 mm notch. The petrified specimen was sectioned along its length and the section gradually polished down to reveal a sequence of stitches that ranged from far ahead of the crack tip to the furthest wake near the notch.

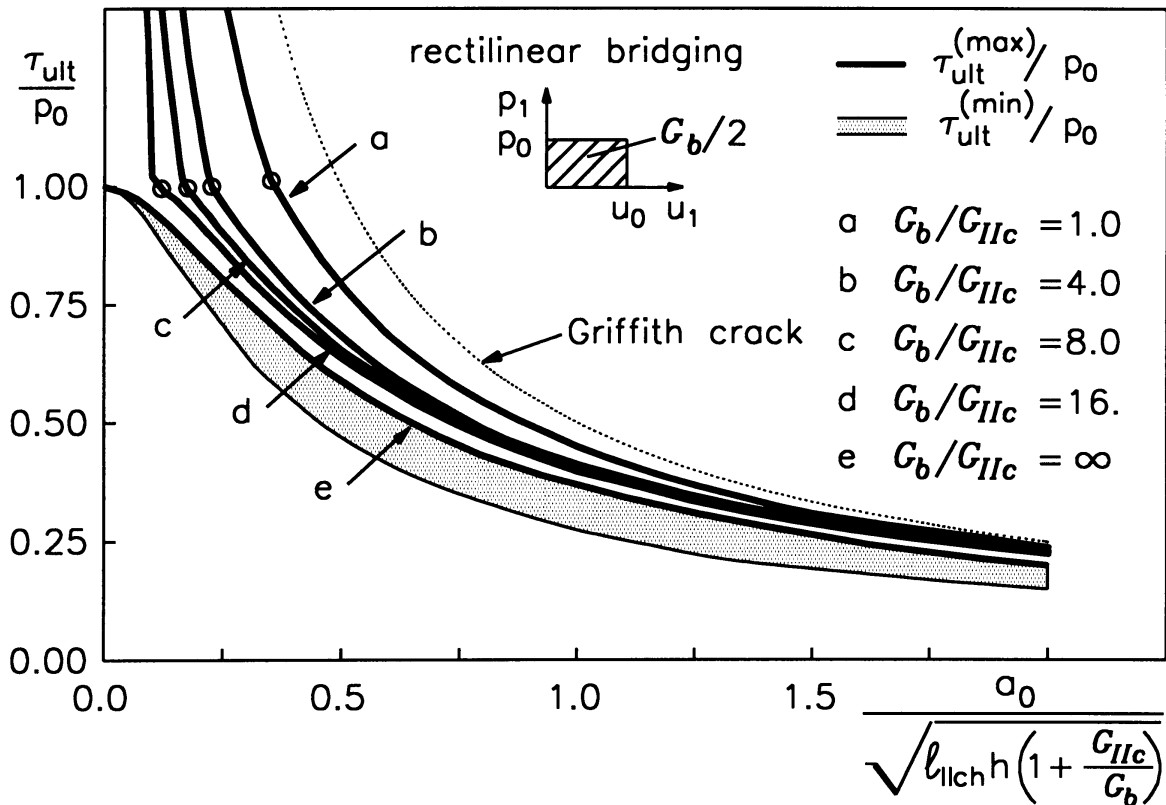


Fig. 6: Bounds for the ultimate notched strength corresponding to defect-free material and material in which a bridged delamination crack or matrix flaw already exists (from [13]). To the left of the circles on the curves for the upper bound, the ultimate strength is determined by crack initiation from the notch root; to the right by bridging stitch failure following stable propagation of a delamination crack to a finite length. The lower bound is determined by bridging stitch failure when an infinite delamination crack is presumed to exist in advance. The band shown for the lower bound covers curves for all values of G_b/G_{IIc} .

Ahead of the crack tip, the stitches were not visibly deformed or damaged. No microcracking or debonding was observed even around the last stitch in front of the crack tip. The first stitch behind the crack tip, i.e., the most recently enveloped in the crack wake, was exposed to some crack sliding displacement, but no significant opening displacement. Still no microcracking was visible around this stitch, but polarized light microscopy revealed a well demarked zone of crazing within it, extending over its whole diameter and approximately two stitch diameters away from the fracture plane on either side. Thus the stitch accommodated the crack sliding

displacement by internal plastic shear, presumed to be mediated by arrays of microcracks and crazing similar to those seen in other shear tests [9]. Stitches further back in the crack wake, where the sliding displacement was greater, had debonded from the surrounding laminate. The debond cracks involved no fiber/matrix separation, but consisted of matrix cracks that separated the stitch as a whole from the surrounding composite. They were most pronounced on the side of the stitch where local tensile stress would be expected. Around stitches subject to even greater crack sliding displacement (further back from the crack tip), significant plasticity and eventually splitting cracks and spalling were seen in the laminate.

Other observations of damage mechanisms were made during shear tests of small notched cubes cut out of a stitched laminate panel, each cube containing just one or two stitches [10]. The notch consisted of a square annular sawcut, which left a small, square island of unbroken material on the center plane of the cube. Each cube was cemented into massive, stiff grips, which were loaded in shear under displacement control. The load-displacement data from these tests should correspond directly to the bridging traction relation, $p_1(u_1)$, in the ENF specimen, with due account of volume fraction considerations. Representative results are reproduced in Fig. 7. The left ordinate is the shear stress within a stitch on the fracture plane, obtained by dividing the measured load by the cross-sectional area of the stitch (approximately 0.64 mm^2). The right ordinate is the corresponding bridging traction, p_1 , for a square array of stitches spaced 3.2 mm apart. It is obtained by dividing the measured load by the area occupied by a stitch in the array, i.e., $(3.2 \text{ mm})^2$, and does not depend on knowing the cross-sectional area of a single stitch.

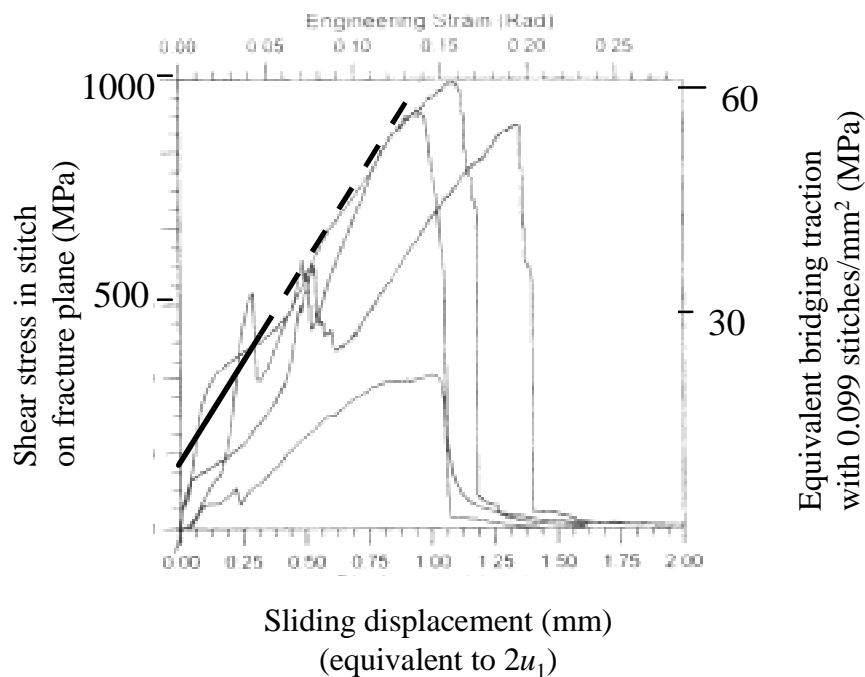


Fig. 7: Shear load/sliding displacement data from four cuboidal specimens containing just one S-2 glass fiber stitch which were tested in stiff grips. The left ordinate shows the average shear stress across the stitch on the fracture plane; the right ordinate the equivalent bridging tractions for stitches on a square array with separation 3.2 mm . The displacement is the total displacement, $2u_1$. The heavy line shows the stress expected for the traction law deduced from the sliding profile of a crack in an ENF specimen. (Figure adapted from [10].)

Three of the curves in Fig. 7 show features and stress levels that are consistent with the deformation seen around stitches in the crack wake in the sectioned ENF specimen. (In the fourth curve, for which the peak load was only one third of that recorded for the other three, the stitch was probably damaged in advance during specimen machining.) At sliding displacements less than 0.2 mm, the shear stress in the stitch at the fracture plane (left ordinate) is just a few hundred MPa. For similar polymer composite plies under pure deviatoric shear, matrix microcracking leads to large strains at stresses above approximately 75 MPa, with hardening to ~ 100 MPa as the shear strain approaches 10% [9,21]. For the stitch to support loads well above 100 MPa, it must bend near the fracture plane so that significant load is carried in tension. But the degree of bending need not be very great to achieve equivalent shear stresses on the fracture plane of ~ 200 MPa, since the stitch has such a high axial stiffness. Thus plasticity and some stitch realignment will account for the total loads found below displacements $2u_1 < 0.2$ mm. For $2u_1$ between 0.2 and 0.6 mm, the curves consistently show a sharp drop. It is unclear yet whether this corresponds to the onset of the splitting cracks in the laminate as observed in the sectioned ENF specimen or debonding of the stitch from the laminate. Sliding displacements and total load then increase fairly smoothly to ultimate failure. The peak load is approximately 20% of that implied by the manufacturer's quoted tensile strength for S-2 glass. After failure the stitch is found to have dragged through the laminate only near the fracture plane, distorting onto a roughly sinusoidal locus. But the total crack sliding displacement at peak load is much larger than could be expected if the stitch stretched only in this region. Much of the crack displacement is evidently permitted by axial sliding of the stitch: there are pronounced dimples left on the outer laminate surfaces where the stitch has been pulled down towards the fracture plane. After peak load, there is a dramatic drop in load followed by some relatively small but enduring pullout forces.

BRIDGING LAWS FROM FRACTURE TESTS

Analysis of Crack Displacement Profiles

Bridging traction laws can also be deduced from measurements of crack displacement profiles such as those in Fig. 2. In the usual solution of the bridged crack problem for a mode II delamination, the crack sliding profile, $u_1(x_1)$, is calculated given an applied load, the crack geometry, and some particular law, $p_1(u_1)$, as one step towards computing the net crack tip stress intensity factor or, equivalently, G_{II} . The necessary calculations can be performed efficiently and accurately for most laminates by plate theory [13,22]. To deduce $p_1(u_1)$ from $u_1(x_1)$, this same problem is formulated as an inverse problem [12,23].

In solving inverse problems, special measures must usually be taken to treat experimental noise, since small oscillations in the data can lead to large oscillations in the deduced function, here the bridging law. The most expeditious technique was found to be the use of restricted parametric forms for the traction law [12], which is often recommended when data contain only enough information to reveal the general shape of the function being sought and not its details. Figure 8a shows a crack sliding profile obtained by stereoscopy, with typical experimental noise, together with the profile computed once the traction law had been deduced. The traction laws deduced from linear, quadratic, and cubic trial forms are shown in Fig. 8b. Their concurrence confirms that the law is essentially linear, the variance at the highest and lowest sliding displacements being due to the data being sparse at these extremes. The offset from the origin is real: trials with a linear law passing through the origin gave

markedly inferior agreement with the data. Once the traction law is determined, the intrinsic toughness, G_{IIc} , can be deduced from the critical load measured experimentally for the particular crack length.

Analysis of Load/Deflection Data

The measured relation between the magnitude of the point load applied to the ENF specimen and the load point deflection also contains information about the bridging traction law. The load/deflection record for the specimen for which the profile data of Fig. 8 were taken (in which a stable crack grew without failure of the stitching in the crack wake) is shown in Fig. 9a. The elastic response expected of an unnotched, uncracked specimen has been subtracted out of the displacement to highlight nonlinear behaviour. Figure 9b shows a hypothetical, parametric traction law which was used to compute the load/deflection curve for the specimen and notch configuration. The traction law parameters $p_1(0)$ and β and the intrinsic toughness, G_{IIc} , were varied to optimize agreement between the data and the prediction. The data show linear elastic behaviour at low loads, up to a knee corresponding to crack initiation at a load that depends on G_{IIc} and $p_1(0)$. The slope of the subsequent data, which show the specimen response as the crack is growing, depends on $p_1(0)$ and β .

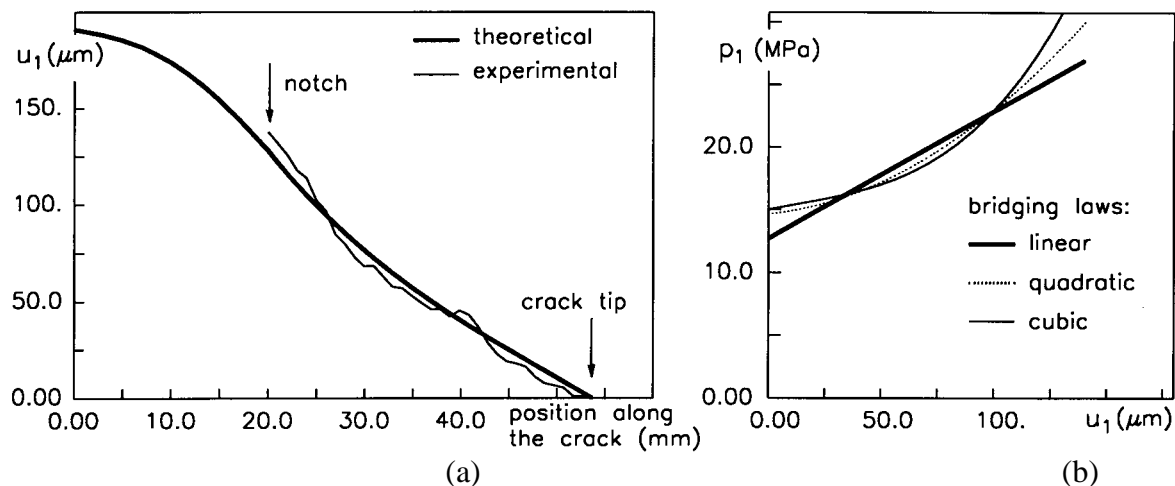


Fig. 8: Bridging laws (b) obtained by fitting crack sliding profiles (a) from an ENF test of a carbon/epoxy laminate with S-2 glass stitches. (From [12].)

The fitted parameter values for the crack of Fig. 9 are $G_{IIc} = 0.2 \pm 0.03 \text{ kJ/m}^2$; $p_1(0) = 11. \pm 0.6 \text{ MPa}$; and $\beta = 110 \pm 11 \text{ MPa/mm}$. These are in excellent agreement with the traction law deduced from crack profile data (Fig. 8b), which is an entirely independent measurement. This agreement can be illustrated by using the values of G_{IIc} , $p_1(0)$, and β deduced from the crack profiles to reproduce the load/deflection data. The result is superimposed on Fig. 9a (fine dashed curve).

The deduced traction law can be converted to the average shear stress in a stitch on the fracture plane by dividing p_1 by the stitch area fraction, c_s . The result thus obtained from the linear law of Fig. 8a with the parameters inferred from load/deflection data has been superimposed as a heavy line on Fig. 7, the data from shear tests on miniature cuboidal specimens containing just one stitch. There is some discrepancy at the lowest displacements: the shear test data go to the origin, while the deduced traction law does not. However, the interval of displacements over which this causes disagreement is exaggerated by the data of

Fig. 7, because the test jig used for the cuboidal specimens had significant compliance, which was not subtracted from the recorded displacement. The true response of the material undoubtedly rises much more steeply from the origin than the data show. The traction law deduced from either crack profiles or load/deflection data should certainly be regarded as far superior in accuracy for displacements $2u_1 < 0.2$ mm. At higher displacements, the deduced traction law (dashed extrapolation) and the shear test data are in good agreement, since the latter also show an approximately linear increase with much the same slope. Again, entirely independent measurements concur.

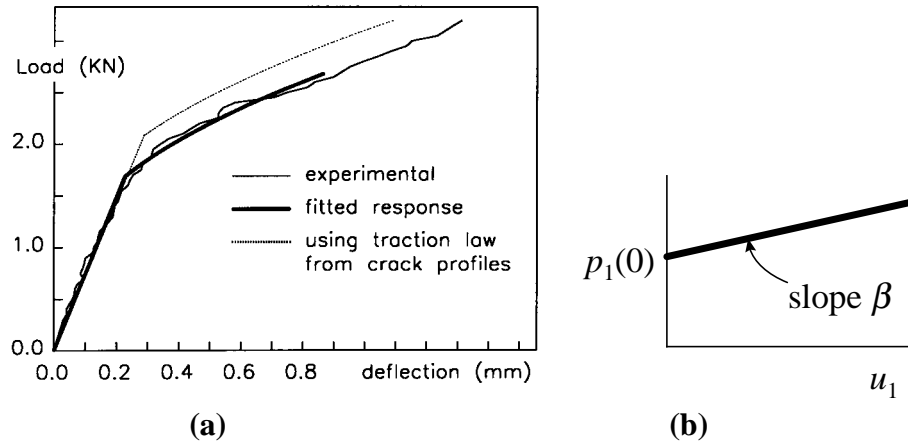


Fig. 9: (a) Load/deflection data and fitted response for a specimen containing a crack that grew stably without stitching failure. The elastic response expected of an unnotched, uncracked specimen has been subtracted from the actual load point displacement. The dotted curve in (a) is a best fit to the data obtained by varying the trial traction law shown in (b) in a crack growth simulation. The fine dashed curve shows a similar simulation using the fixed parameter values deduced from crack profile analysis. All of the curves have been terminated at a maximum crack length of 53.6 mm.

BRIDGING LAWS AND LENGTH SCALES FOR ONE STITCHED LAMINATE

From the results of the preceding section for one particular carbon/epoxy laminate stitched with S-2 glass tows, values can be assigned to the bridging parameters and length scales introduced as fundamental constants.

Characteristics of the ACK limit

The concepts introduced in the first section for the ACK limit were defined by considering bridging laws satisfying $p_1(0) = 0$, whereas in the law deduced experimentally, $p_1(0) > 0$ (Fig. 8b and 9b). However, application of the J integral and stress superposition arguments show that the basic results require only trivial modifications. For the linear law of Fig. 9b, the ACK stress becomes

$$\tau_{ACK} = p_1(0) + \sqrt{G_{IIc}\beta}. \quad (9)$$

The critical stress curve shown for zero notch size in Fig. 3 is shifted up uniformly by $p_1(0)$. Therefore, l_{ACK} , of Eqs. (7) and (8) with $\alpha = 1$ will continue to prescribe the amount of crack

growth required for τ_{cr} to approach within a given amount of τ_{ACK} . Curves for nonzero notches will begin at the same point on the dotted curve (“no bridging”), but will now rise to the new, higher asymptotic value given by Eq. (9). With these changes, the qualitative appearance of all the critical stress curves remains much the same as shown in Fig. 3. In particular, a similar role in defining notch sensitivity is played by the length scale, a_{lim} , defined by Eq. (8a). The minimum value of $a_0/(a_{lim}h)^{1/2}$ required for stable crack growth will be somewhat lower, the criterion becoming

$$(10) \quad \frac{a_0}{\sqrt{a_{lim}h}} \geq \frac{1}{1 + p_1(0)/\sqrt{G_{IIc}\beta}}.$$

From the values deduced for G_{IIc} , $p_1(0)$, and β for the exemplary glass-stitched carbon/epoxy laminate, one obtains $\tau_{ACK} = 16$ MPa and $a_{lim} = 110$ mm. Since $h = 3.6$ mm, $l_{ACK} \approx 20$ mm. Thus from Eq. (10) a notch of length $a_0 > 6$ mm is required to obtain any stable delamination crack growth in an ENF specimen of this material; and somewhat larger than this for the stable growth to be readily observed. This indeed concurs with tests executed for various notch sizes. A specimen of half length $L > 100$ -150 mm would be required to produce a crack that had approached close to the ACK limit. The analysis of crack growth in ENF tests in specimens of typical size would therefore require full solution of the bridged crack problem; no asymptotic solution would be adequate.

Characteristics of the Small Scale Bridging Limit

The traction laws of Fig. 7 contain all information required to characterize the small scale bridging limit. The total work of fracture, the area under the curves computed with the right hand ordinate, is $G_b \approx 30$ kJ/m². This is about two orders of magnitude greater than the intrinsic mode II fracture toughness of the laminate, $G_{IIc} \approx 0.2$ kJ/m². In any test in which the crack is in or near the small scale bridging limit, the influence of G_{IIc} will be virtually undetectable. While G_{IIc} was evaluated successfully by analyzing cracks approaching the ACK limit, it could not be measured by experiments on cracks propagating near the small scale bridging limit.

Again referring to the right hand ordinate of Fig. 7, one has $p_0 \approx 55$ MPa; while the critical sliding displacement $u_0 \approx 0.6$ mm. Equation (5b) then gives $l_{IIch} \approx 500$ mm. For $h = 3.6$ mm, $(l_{IIch}h)^{1/2} \approx 40$ mm. Since $G_{IIc} \ll G_b$, the quantity $(l_{IIch}h)^{1/2}$ will control the notch sensitivity of ultimate strength, much as shown by the curve for a rectilinear law in Fig. 5; and the equilibrium zone length in small scale bridging will be given to within a factor near unity by $l_{SSB} \approx (l_{IIch}h)^{1/2}$. Thus a specimen of half length L much higher than 300-400 mm would be required to achieve small scale bridging conditions. This will not be the case in specimens of common dimensions; and therefore full solution of the bridged crack problem rather than asymptotic approximations (i.e., in this regime, linear elastic fracture mechanics) is again required for fracture analysis. In particular, unless an especially long specimen is used, it will not be accurate to quote a single value for the composite fracture toughness, $G_{II} = G_{IIc} + G_b$, deduced by linear elastic fracture mechanics from a strength measurement. Unfortunately, this error has already taken up residence in the literature.

The Transition from Noncatastrophic to Catastrophic Failure

For a material in which $G_{IIc} \ll G_b$, the strength of an unnotched specimen will be approximately p_0 [13].* If $p_0 > \tau_{ACK}$, the ACK limit could then be approached, with a delamination crack fully bridged by intact stitches propagating noncatastrophically right across the specimen. However, if a large enough notch is present, the stress concentration at the notch root will cause the stitches to fail there before the applied shear stress reaches τ_{ACK} and failure will be catastrophic (i.e., the first crack will separate the specimen in two). For the material analyzed above, $\tau_{ACK}/p_0 = 16/55 = 0.3$. From Fig. 5, the transition from noncatastrophic to catastrophic failure will therefore be expected when $a_0/(l_{IIch}h)^{1/2} \approx 1.25$ or $a_0 \approx 50$ mm. Since this length is substantially greater than l_{ACK} , there are in this case smaller notch sizes for which stable noncatastrophic cracks can be expected. This is obviously so, as the results above demonstrate. However, there could be other materials in which the opposite would hold, that a notch large enough for stable delamination crack growth (i.e., $\tau_{cr}(a_0) < \tau_{ACK}$) would also be large enough for stitch failure, in which case an experimenter would search in vain for stable delamination cracks (see also Fig. 4).

The Effect of the Discreteness of Stitches

The length scales, l_{ACK} and l_{SSB} , provide a simple test of the validity of representing the effect of discrete stitches as continuous tractions: they must be much greater than the stitch spacing, d . If the stitches do not fail in the crack wake, then the bridging tractions become significant compared to the applied shear stress when the crack length, a , is somewhat greater than l_{ACK} (Fig. 3). If d is much less than l_{ACK} , then many stitches will already be involved in this stage of crack growth. For the material studied in detail above, this is the case: $d = 3.2$ mm while $l_{ACK} = 20$ mm. This also implies that stitching can have little effect in this material in suppressing the initiation of delamination cracks (i.e., the generation of cracks just a few mm long). The material relies mainly on the intrinsic delamination toughness, G_{IIc} , for resistance to crack initiation.

If the stitches do fail, then l_{SSB} is the relevant length scale. Once again, for the material taken as an example here, $d \ll l_{SSB}$ and the effects of the discreteness must be negligible. Many stitches are involved in the bridging zone and the sliding displacement experienced by the ultimate stitch must be very close to the sliding displacement calculated in the continuous traction model.

Friction on the Delamination Fracture Surfaces

Stitching does not inhibit delamination crack initiation by its action as a crack bridging entity. However, once a crack of length several mm exists, other shielding mechanisms might play an important role, especially friction arising from fracture surface roughness, and stitching has important indirect roles in determining friction. The stitching process introduces waviness in the in-plane plies, forcing the delamination fracture surface to be non-planar; and stitching restricts mode I crack opening, keeping the fracture surfaces in contact over a zone behind the crack tip that is longer than it might be in the absence of stitching. Experiments are in order to quantify these effects. Figure 2 suggests that, since the crack exhibits mode I opening at distances more than 2-3 mm from the mode II crack tip, fracture surface friction effects

* When $G_{IIc} \neq 0$, there will be in a material that behaves strictly according to the model defined in this paper, a regime of small notch sizes where stitch failure must be preceded by matrix crack initiation at a stress higher than p_0 , rising for small notches as a_0^{-1} .

operate over a zone much smaller than the bridged zone over which the stitches act. It should therefore be valid for cracks longer than a few mm to include friction effects as an enhanced value of the intrinsic fracture toughness, G_{IIc} . Further, when friction can be included in G_{IIc} and G_{IIc} is evaluated either by inverting a crack sliding displacement or by fitting load/deflection data, as reported above, the deduced value will already include the effects of friction. They are inseparable from other contributions to G_{IIc} for such measurements under these conditions.

STRUCTURAL RELIABILITY MODELS

Consider the engineering task of predicting the failure of a stitched laminate component in service. To simplify the discussion and relate it directly to the results summarized above, assume that the applied load is expected to create shear on the delamination plane and that the delamination crack is therefore a mode II crack. Of course, arbitrary applied loads might generate mixed mode conditions, but the approach to be outlined here can be generalized.

The material data from which delamination failure can be calculated are the elastic constants of the laminate, which can be regarded as known; and the intrinsic delamination fracture resistance, G_{IIc} , and the bridging traction law, $p_1(u_1)$, which must be determined. The traction law, $p_1(u_1)$, will represent the entire contribution of the stitches to delamination suppression by crack bridging. The essential step is to recognize just which characteristics of $p_1(u_1)$ need to be known and to define simple tests for their evaluation.

Noncatastrophic Cracking

Figure 3 shows that, in the absence of a notch, the ACK stress, τ_{ACK} , provides a conservative bound for the applied shear stress required for noncatastrophic delamination cracking (crack growth without accompanying stitch failure). Thus τ_{ACK} defines the proportional limit for the structure as long as delamination cracking is the first failure mechanism. (The ACK stress already serves in a similar function for engineering applications of ceramic matrix composites under aligned tensile loads, in which the first nonlinearity is the appearance of multiple mode I matrix cracks [24].) The delamination cracking stress is not reduced by the pre-existence of a delamination crack, provided it remains fully bridged by essentially undamaged stitches. For parts containing bridged delamination flaws, τ_{ACK} is a design limit.

However, if a notch exists over which the stitches have been cut – or perhaps an impact damage zone exists in which the stitches have been weakened or destroyed during the creation of a delamination crack – the stress for noncatastrophic delamination cracking, τ_{cr} , may be less than τ_{ACK} . For a bridging law like that shown in Fig. 9b, Eq. (10) specifies the critical notch size above which $\tau_{cr} < \tau_{ACK}$. Thus the controlling parameters are τ_{ACK} , $p_1(0)$, and the structure-material length scale, l_{ACK} ; or equivalently, $p_1(0)$, β , and G_{IIc} . These three degrees of freedom are all the material properties that are needed to predict the delamination performance of the part under shear loading, provided no stitches fail during the crack propagation.

To evaluate the controlling parameters and predict noncatastrophic delamination, detailed knowledge and micromechanical models of the bridging process are not required. It is enough to determine τ_{ACK} , $p_1(0)$, and l_{ACK} (or $p_1(0)$, β , and G_{IIc}) empirically. A simple and sufficient experiment would appear to be a record of load/deflection data, such as Fig. 9a.

Catastrophic Delamination

The two essential characteristics of the traction law $p_1(u_1)$ for predicting stitch failure are the peak traction, p_0 , and twice the area under $p_1(u_1)$, which is the bridging contribution to the work of fracture, G_b . Figure 5 shows that further details of the shape of $p_1(u_1)$ have negligible effect on the load at which stitches fail.

Once again, it would appear that standard ENF tests should be sufficient to evaluate these parameters. A sequence of tests with increasing notch size should replicate Figure 5; information about p_0 is contained mainly in the intercept at zero notch size and about G_b in the slope of the curve.

In laminates in which G_{IIc} is comparable to or greater than G_b , the notched strength diagram of Fig. 5 must be modified to account for the actual value of G_{IIc} [13]. But the same sequence of tests should still suffice for evaluating p_0 and G_b , which continue to be sufficient information about the bridging law for predicting catastrophic cracking..

MATERIAL DESIGN MODELS

Consider next the problem of selecting the quantity and nature of stitching tows to achieve target engineering properties in a structure, i.e., for shear loading, to achieve particular

characteristics in the traction law, $p_1(u_1)$. This is a question which demands complete modeling of the bridging process. It must be approached by considering the mechanisms of deformation of discrete stitches.

For stitches deforming in shear caused by crack sliding displacement, the mechanisms are highly nonlinear, complex, and only partially revealed by the experiments reported above (and more fully in [10] and [20]). Further experiments are needed to detail plasticity, the patterns of cracks that form around a stitch as it shears, the mechanics of stitch rupture, and the process of pullout of the stitch, which evidently begins before its rupture. With due experimental grounds, models may then be formulated to study the roles of stitching fiber properties, matrix properties, stitch size, stitch orientation, etc. Such work is in progress.

These material design models are necessarily much more complex than structural reliability models. The material and geometrical parameters that can affect $p_1(u_1)$ may be very numerous. The details must be pursued. However, it is very important to recognize that all the same details need not be carried on to the problem of formulating structural design models. As explained above, structural design models address a much more restricted question with consistently limited information about the bridging process.

ACKNOWLEDGMENTS

The authors are very grateful to Mr. Larry Dickinson for supplying stitched laminate specimens; Dr. Fred Morris for stereoscopic analysis of images; and Dr. Stefan Janssen for initiating the tests of cuboidal specimens. BNC was supported by AFOSR Contract Number F49620-94-C-0030; RM and DM by Rockwell Independent Research and Development

Funds; and AT and KW by Pratt and Whitney Aircraft under a Technology Reinvestment Project with the Advanced Research Projects Agency.

REFERENCES

1. Horton, R. E., and McCarty, J. E., "Damage Tolerance of Composites," in *Engineered Materials Handbook, Vol. 1: Composites*, ASM International, Metals Park, Ohio, 1987.
2. Smith, P. J., and Wilson, R. D., "Damage Tolerant Composite Wing Panels for Transport Aircraft," Boeing Commercial Airplane Company, NASA Contractor Report 3951, 1985.
3. Dow, M. B., and Smith, D. L., "Damage Tolerant Composite Materials Produced by Stitching Carbon Fabrics," *Int. SAMPE Technical Conf. Series* 1989, **21**, 595-605.
4. Dransfield, K., Baillie, C., and Mai, Y.-W., "Improving the Delamination Resistance of CFRP by Stitching - a Review," *Composite Science and Technology* 1994, **50**, 305-17.
5. Darbyshire, H. F., Bendix Aerospace-Electronics Company Report BDX-613-144 (1970).
6. Bradshaw, F. J., Dorey, G., and Sidey, G. R., "Impact Resistance of Carbon Fiber Reinforced Plastics," *Royal Aircraft Establishment Technical Report 72240*, Farnborough, England, 1973.
7. Krasnov, V. I., Kuznetsov, V. A., and Maksakov, A. Yu., "Automated Method of Transverse Reinforcement of Composites by Short Fibers," *Mekhanika Kompozitnykh Materialov*, **3**, 449-504, 1987.
8. Freitas, G., Fusco, T., Campbell, T., Harris, J., and Rosenberg, S., "Z-Fiber Technology and Products for Enhancing Composite Design," AGARD Conference, 1996.
9. Cox, B. N., Dadkhah, M. S., Morris, W. L., and Flintoff, J. G., "Failure Mechanisms of 3D Woven Composites in Tension, Compression, and Bending," *Acta Metall. Mater.*, 1994, **42**, 3967-84.
10. Turrettini, A., "An Investigation of the Mode I and Mode II Stitch Bridging Laws in Stitched Polymer Composites," Masters Thesis, Department of Mechanical and Environmental Engineering, University of California, Santa Barbara, 1996.
11. Dickinson, L., "Effects of Stitching Parameters on Mechanical Properties and Damage Tolerance of Stitched/RTM Composites," *Fourth NASA/DoD Conference on Advanced Composites Technology*, Salt Lake City, Utah, 1993, ed. J. G. Davis, J. E. Gardner, and M. B. Dow, NASA, 1993.
12. Massabò, R., Mumm, D. R., and Cox, B. N., "Mode II Delamination Cracks in Stitched Composites," submitted for publication.
13. Massabò, R., and Cox, B. N., "Concepts for Bridged Mode II Delamination Cracks," submitted for publication.
14. Xia, Z. C., and Hutchinson, J. G., "Mode II Fracture Toughness of a Brittle Adhesive Layer," *Int. J. Solids Structures* **31**, 1133-48 (1994).

15. Aveston, J., Cooper, G.A., and Kelly, A. (1971), Single and Multiple Fracture, in *The Properties of Fiber Composites*, Conf. Proc., National Physical Laboratory, IPC Science and Technology Press Ltd., p. 15.
16. Marshall, D.B., and Cox, B.N. (1988), "A J-Integral method for calculating steady-state matrix cracking stresses in composites," *Mechanics of Materials*, **7**, 127-133.
17. Cottrell, A.H., (1963), Mechanics of Fracture, *Tewksbury Symposium of Fracture*, University of Melbourne, Australia, 1-27.
18. Bao, G. and Suo, Z., (1992), Remarks of crack-bridging concepts, *Appl. Mech. Rev.*, **24**, 355-366.
19. Cox, B.N., and Marshall, D.B. (1994), Concepts for bridged cracks in fracture and fatigue, *Acta Metall. Mater.*, **42**(2), 341-363.
20. Mumm, D. R., unpublished work.
21. Fleck, N. A., and Jelf, P.M. (1995), Deformation and Failure of a Carbon Fibre Composite under Combined Shear and Transverse Loading, *Acta Metall. Mater.*, **43**, 3001-7.
22. Jain, L.K., Mai, Y-W. (1994), "Analysis of stitched laminated ENF specimens for interlaminar mode-II fracture toughness," *Int. Journal of Fracture* **68**(3), 219-244.
23. Cox, B. N., and Marshall, D. B., "The Determination of Crack Bridging Forces," *Int. J. Fracture* **49**, 159-176 (1991).
24. Evans, A. G., and Marshall, D. B. (1989), Mechanical Behaviour of Ceramic Matrix Composites, *Acta Met.* **37**, 2567-83 1989.

777 EMPENNAGE CERTIFICATION APPROACH

A. Fawcett¹, J. Trostle², S. Ward³

¹777 Program, Structures Engineering, Principal Engineer and DER

²777 Program, Structures Engineering, Manager

³Composite Methods and Allowables, Principal Engineer

Boeing Commercial Airplane Group, PO. Box 3707, Seattle, Washington, USA

SUMMARY: This paper presents the Boeing approach to certification of the 777 composite empennage structure. The design team used carbon-fiber-reinforced plastic (CFRP) materials for the horizontal and vertical stabilizers, the elevators, and the rudder of the new 777 twinjet. Boeing based its approach to certification on analysis supported by coupon and component test evidence in compliance with guidelines issued by the FAA and JAA. The test program validated analysis methods, material design values, and manufacturing processes. The new toughened resin material used on the 777 provides improved damage resistance over conventional thermoset materials. The 777 empennage represents a major commitment to composites in commercial aircraft service.

KEYWORDS: commercial transport aircraft, certification, structural testing, carbon-fiber reinforced plastic **Error! Bookmark not defined.**, composite structure, strength, damage tolerance, and fatigue.

INTRODUCTION

Many components on the 777 aircraft contain composite materials (figure 1). Examples include fairings, floorbeams, engine nacelles, movable and fixed wing trailing edge surfaces, gear doors, and the empennage-including the horizontal and vertical stabilizers, elevators, and rudder. Composite materials are used primarily to reduce weight and improve aircraft efficiency. For some components, composite materials are appropriate, based on other requirements such as fatigue resistance, surface complexity, corrosion resistance, or manufacturing preference.

The use of CFRP in 777 empennage structure follows developmental work and commercial service from the early 1980s. The NASA/Boeing 737 horizontal stabilizer was the first major component of composite structure certified for commercial use [1]. The company introduced five shipsets into service in 1984. The approach taken by Boeing to obtain certification and acceptance by the FAA was a key milestone in the development of composite structure for commercial aircraft applications. This certification approach complies with FAA and JAA regulations and maintains the Boeing philosophy that aircraft structure certification is shown by analysis with supporting test evidence.

Following the 737 horizontal stabilizer program, Boeing designed a composite empennage for the 7J7 airplane. Although the company did not commit this model to production, Fuji Heavy Industries (FHI) fabricated a full-scale horizontal stabiliser test article (figure 2). Japan

Aircraft Development Corporation (JADC) performed static, fatigue, and damage tolerance testing of the stabilizer test article [2].

The 7J7 empennage represented the first significant use of a toughened-resin CFRP material. The test program complied with applicable regulations and addressed items outlined in the certification agency advisory circulars for composite aircraft structures [3]. The full-scale test, along with a comprehensive ancillary test program, met all of the advisory circular recommendations. It provided full-scale validation of the design and analysis methodology, fabrication processes, and damage tolerance capability of toughened-resin materials.

Boeing has expanded the use of composite materials to other applications. The Boeing 737, 747, 757, and 767 aircraft use composite materials in wing fixed leading and trailing edge structure and control surfaces. The rudder, elevator, aileron, and spoilers on these models use CFRP sandwich construction.

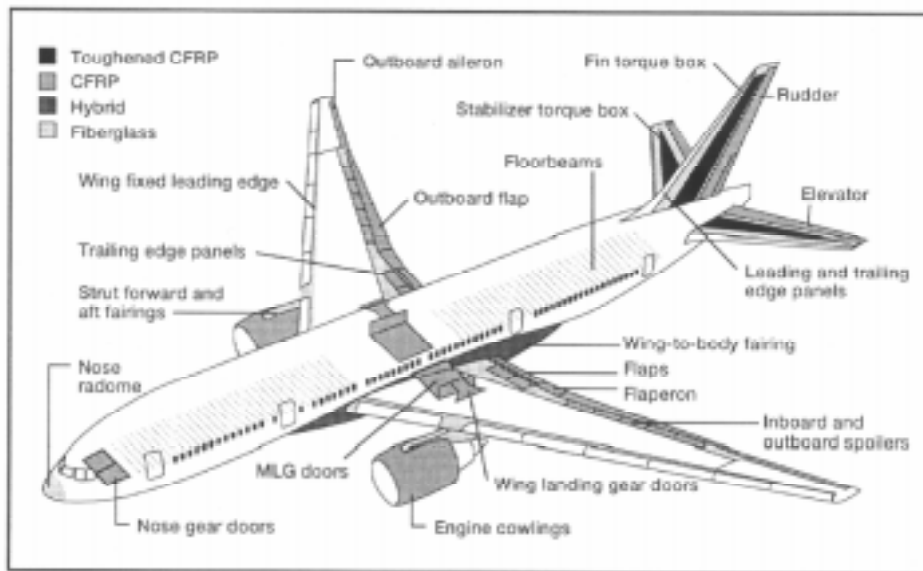


Figure 1: Composite Materials Usage on the 777

The use of composite materials on the 777 horizontal and vertical stabilizers originated as part of a company-funded program. Boeing built a prototype or preproduction composite horizontal stabiliser, based on the 767-200 planform (figure 3). Designers selected the 767-200 as a base configuration with known weight, loads, cost, and structural characteristics. The 777 preproduction horizontal stabilizer design evolved with long-term production in mind; a major objective was to validate manufacturing costs. Other objectives for the program included:

- Use composites where weight reduction can be achieved at a reasonable cost.
- Use toughened-resin materials or additional gage to increase resistance to service threats.
- Provide for a wide range of repair options, including mechanically fastened repairs.
- Provide access for maintenance, inspections, and repair.

- Design for visual in-service inspections only.
- Design to maximize automated fabrication processes.

Because of the similarity in structure, geometry, and materials, the FAA and JAA accepted the preproduction stabilizer and supporting test program as applicable experience and part of the certification basis for the 777 empennage. Full-scale testing of production aircraft structure, including the empennage components, is complete. This, together with other test data, forms the basis by which joint FAA/JAA certification has been granted. The 777-200 is in production and operating in service with the first eight customers.

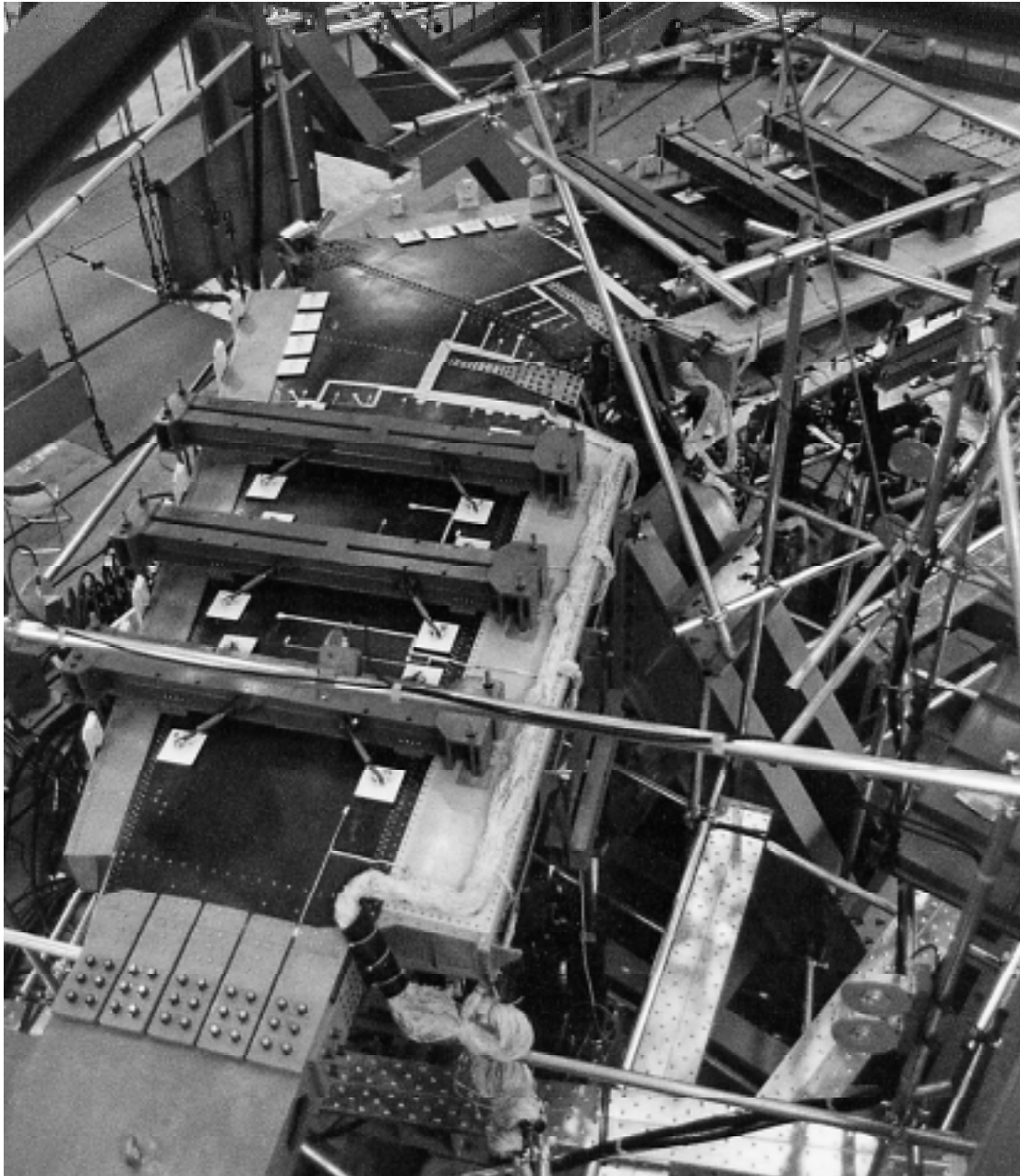


Fig. 2: 777 CFRP Horizontal Stabilizer Test Article

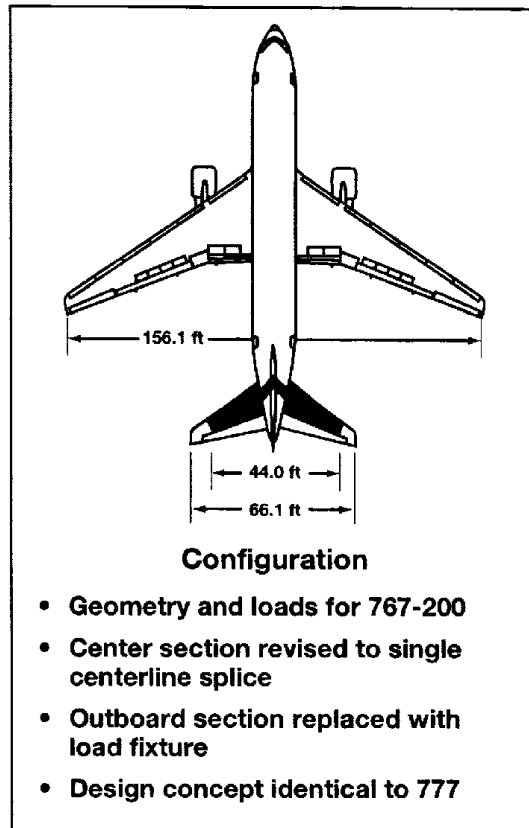


Figure 3: Configuration of the Preproduction Horizontal Stabilizer

DESCRIPTION OF STRUCTURE

The 777 empennage consists of the horizontal and vertical stabilisers, elevators, and rudder (figure 4). The design team configured each stabilizer as a two-cell box, consisting of a main structural box and an auxiliary or forward torque box, leading edges, tip, and fixed trailing edges. The main torque boxes are made from CFRP composite material: solid-laminate front and rear spars, honeycomb sandwich ribs, and integrally stiffened laminate skin panels.

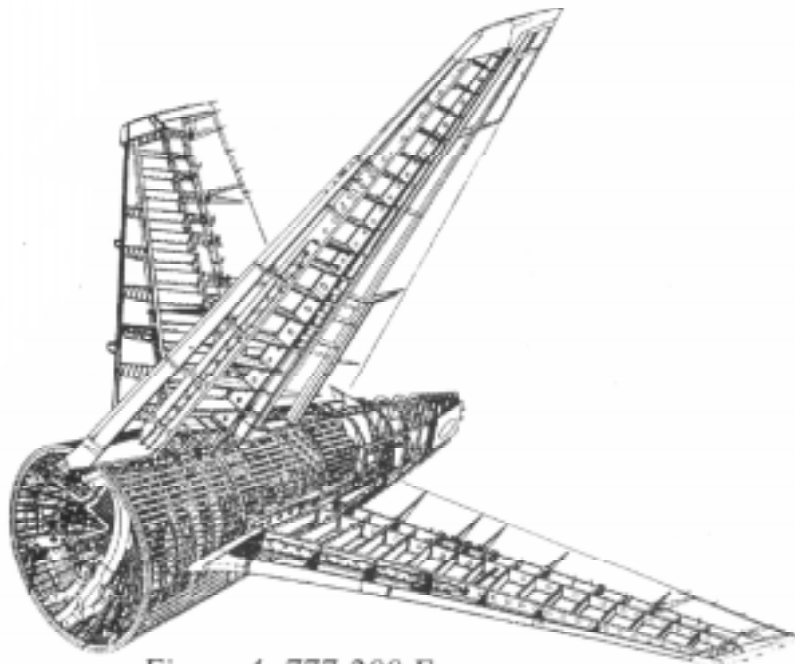
The main box panels and spars feature a toughened-matrix CFRP material from Toray. The preimpregnated fiber/resin system is T800/3900-2. It provides improved resistance to impact damage over previous brittle materials. The auxiliary torque box and fixed trailing edges are glass or glass/CFRP sandwich panels with aluminum ribs. The leading edge, tip, and auxiliary spar are aluminum construction. The Boeing Company manufactures both stabilisers at the Composite Manufacturing Center near Tacoma, Washington.

The elevator and rudder are also constructed from CFRP sandwich panels, ribs, and spars and are hinged from the stabiliser or fin fixed trailing edge. The rudder incorporates a lower tab of CFRP sandwich construction. ASTA fabricates the rudder in Australia; Hawker de Havilland fabricates the elevators. Reference 4 contains a more detailed description of the 777 empennage components.

CERTIFICATION APPROACH

This section describes the certification approach, together with the regulations and means of compliance. Topics include internal loads, environment, static strength, damage tolerance, and fatigue.

FAR Part 25 and JAR Part 25 [5, 6] define the regulatory requirements applicable to the 777 aircraft. Table I summarizes the principal requirements for structural strength, design, and construction. In addition to the regulations, the FAA and JAA have identified an acceptable means of compliance for certification of composite structure [3].



*Figure 4: 777-200 Empennage
(cover panels not shown)*

The advisory circular includes requirements in the following areas: (1) effects of environment (including design allowables and impact damage); (2) static strength (including repeated loads, test environment, process control, material variability, and impact damage); (3) fatigue and damage tolerance evaluation; and (4, other items such as flutter, flammability, lightning protection, maintenance, and repair.

The 777 empennage certification approach is primarily analytical, supported by test evidence at the coupon, element, subcomponent, and component levels and full-scale limit load test at ambient environment. The environmental effects on the composite structure are characterised at the coupon, element, and subcomponent levels and are accounted for in the structural analysis. Supporting evidence includes testing through a "building-block" approach that obtains material characterisation, allowables and analysis methods development, design concept verification, and final proof of structure (figure 5).

Experience with similar structure was important in developing the 777 certification program. The 7J7 horizontal stabilizer [2, 7] and the 777 preproduction horizontal stabilizer programs validated analytical methods, design allowab[les], and fabrication and assembly processes applied to the 777 empennage structure. Boeing has accumulated significant additional

knowledge and experience in characterising the behavior of composite aircraft structure. Boeing has augmented this experience database with the 737 composite stabilizer fleet experience and numerous other production applications in control surfaces, fixed secondary structure, fairings, and doors.

*Table 1: Regulations
Concerning Composite Structure Certification*

Topic	Reg	Subject
Material and process specifications	25.603 25.605	<ul style="list-style-type: none"> • Control of materials • Fabrication methods
Material properties	25.613 25.615 25.619	<ul style="list-style-type: none"> • Material strength properties and design values • Design properties • Special factors
Proof strength	25.305 25.307	<ul style="list-style-type: none"> • Strength and deformation • Proof of structure
Damage tolerance	25.571	<ul style="list-style-type: none"> • Fatigue evaluation • Residual strength • Discrete source damage
Other	25.581 25.609	<ul style="list-style-type: none"> • Lightning protection • Protection of structure

The FAA and JAA participated in the certification approach for the 777. They participated directly through discussion and approval of the certification plan and indirectly through Boeing designated engineering representatives (DER). FAA representatives witnessed nearly all significant subcomponent and full-scale production component tests.

Internal Loads

Load models (figure 6) based on finite element analysis (FEA) determine internal load distributions. Elevators and the rudder are part of the model and attach to the main structure with the control surface position corresponding to the load condition being analyzed. External loads representing airplane aerodynamic and inertia loads are applied as nodal loads to the entire FEA model of each respective stabiliser and control surface. The FEA model determines hygrothermal loads for superposition with mechanical loads. The horizontal stabilizer model is a stand-alone analysis; the vertical stabilizer includes the interaction effects with the fuselage as a boundary condition at the fin base, obtained from the airplane major finite element model.

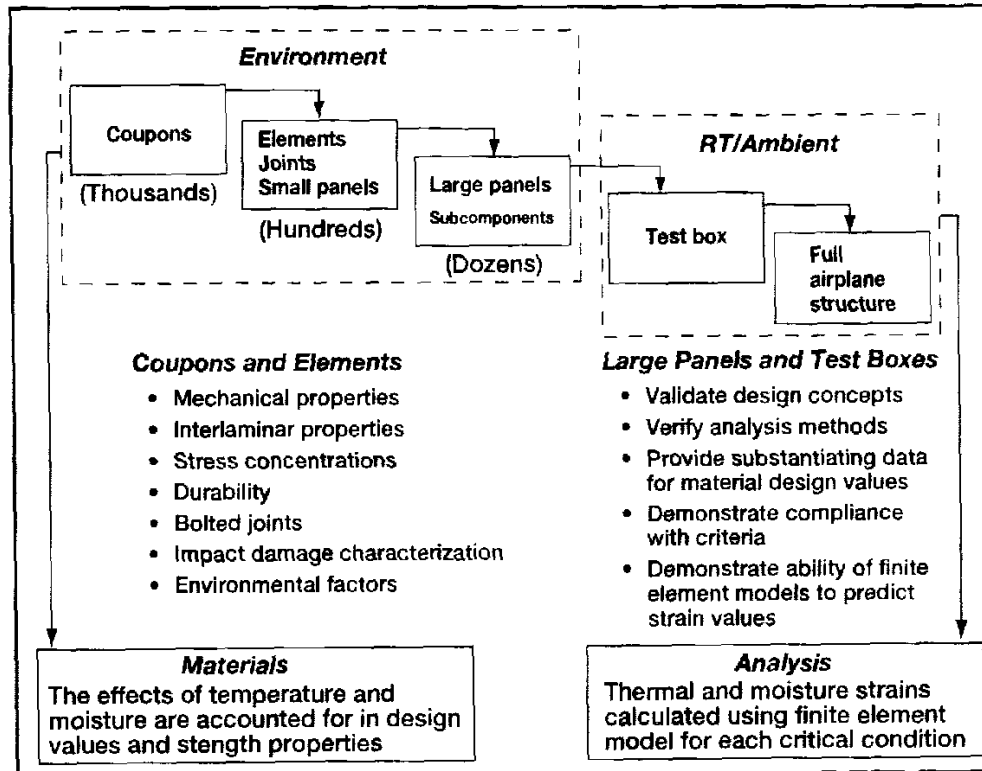


Figure 5: Building Block Approach for Design and Environmental Accountability

Design Environments

Analyses determined the most critical environment expected in airline service. In areas away from local heat sources, the thermal analysis predicts a maximum in-flight temperature of 71 CC (I 60°F) and a minimum temperature of -54°C (-65°F). Engineers studied the effect of moisture on the material systems applied in the empennage. They determined that it is highly unlikely that a moisture content of 1.1% by weight will be exceeded in service.

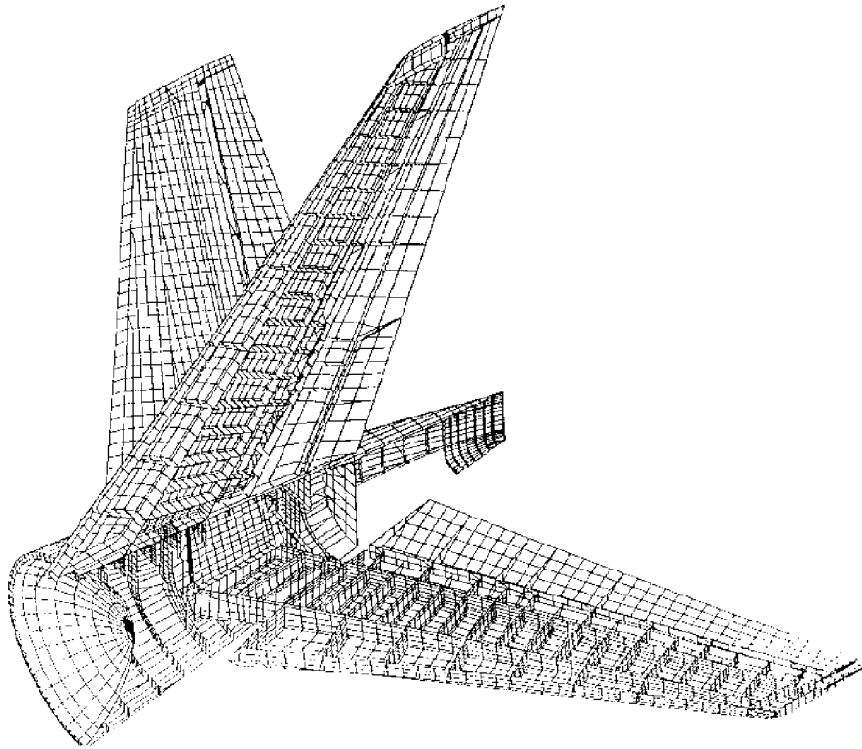


Figure 6: Finite Element Model, 777 Empennage Structure

Static Strength

The substantiation of static strength began by establishing material properties and design values utilizing coupon, element, and subcomponent data. Concurrently, engineers established methods of analysis. Stress analysis follows in which the design is analyzed using ground, flight, and inertia loads accounting for the configuration, dimensions, and properties of the structure. The analyses employ a variety of semiempirical methods, continuum mechanics, and special finite element solutions. The resulting calculated strains are compared to design values to show positive margins of safety for all critical load conditions. Strain surveys and limit load testing on the full-scale airplane confirm the accuracy of the internal loads model and analysis. Testing of elements, subcomponents, and the preproduction stabilizer provides additional evidence with ultimate load and repeated load data, including damage and environment.

A test program provided laminate-level allowable design strain values covering each failure mode and environmental condition. Corrections for material variability followed approved procedures in MIL-Handbook 17 [8]. The testing covered laminate configurations typical of the 777 empennage structure. Representative subcomponent tests accounting for the effects of environment verified detail design values.

Laminated composites are susceptible to the effects of impact damage. The 777 empennage design recognizes this by using toughened-resin CFRP materials and by limiting design strains. Subcomponent tests to establish design strains include the presence of impact damage. As a result, the composite structure design is capable of sustaining ultimate load with isolated impact damage, inflicted by any likely energy source, that cannot be detected visually. This type of damage is frequently referred to as "barely visible impact damage." Visibility studies

using a range of damages applied to several components determined the threshold of detectability.

Damage Tolerance and Fatigue

FAR and JAR 25.571 [5, 6] and the advisory circulars [3] describe two primary damage tolerance requirements: damage growth characterisation and residual strength capability. As in the case of static strength, damage tolerance certification is based on analysis supported by tests at element, subcomponent, and component levels. Considering the applied strains, Boeing selected a no-growth approach for the 777 empennage similar to that used for the 737 program [9]. This philosophy states that any damage that is visually undetectable is not critical. Structures with this type of damage must be capable of carrying ultimate load for the operational life of the airplane.

No-growth behavior was exhibited in numerous subcomponent tests and two full-scale cyclic load tests: the 7J7 horizontal stabilizer [7] and the preproduction 777 horizontal stabiliser. In each case, visible damage was inflicted on the test article that underwent spectrum type repeated loading. Nondestructive test personnel inspected damage sites for growth during the test sequence. Full-scale tests have further demonstrated the following characteristics:

- Manufacturing anomalies allowed per the process specifications will not grow for the equivalent of more than two design service lives.
- Visible damage due to foreign-object impact will not grow for the duration of two inspection intervals.
- The structure can sustain specified residual strength loads with damage that can reasonably be expected in service.
- The structure can sustain specified static loads ("continued safe flight loads") after incurring in-flight discrete-source damage.

In the case of fatigue, the 777 structure design meets or exceeds the safety and economic maintenance standards of current commercial transport aircraft. The design service life goal is the equivalent of 40,000 flights of 1.5 hours' duration, 25,000 flights of 3 hours' duration, or 10,000 flights of 9 hours' duration, whichever is critical.

Boeing based fatigue evaluation of the metal structure on established methods. Tests have characterised the fatigue behavior of the composite structure at coupon, element, and subcomponent levels, as well as in full-scale tests. The full-scale component tests have verified that deliberately inflicted damage does not grow under operating loads.

The 777 structural inspection plan will prevent catastrophic failure during the operational life of the airframe by detecting fatigue, corrosion, or accidental damage. Boeing has established an initial structural inspection and maintenance plan, based on the procedures of the Airline/Manufacturer Maintenance Planning document. This approach analyzes the airplane structure in terms of environmental and accidental damage potential with consideration for material, location, inspectability, and past service experience.

DEVELOPMENT TEST PROGRAM

The test program developed to support analysis and certification for the 777 empennage was part of an overall approach reviewed with the regulatory authorities. This section reviews tests and results, together with their place in the compliance plan: 777 preproduction stabiliser, vertical stabilizer root attachment, elements, and subcomponents.

777 Preproduction Horizontal Stabilizer Test

The 777 preproduction horizontal stabiliser test article was nearly identical to the production component. The test article was a partial span box. Designers eliminated the minimum gage outboard sections for cost considerations and replaced them with load application fixtures. The test article included typical, specification-allowed process anomalies, as well as low-velocity impact damage up to and beyond the visual threshold. Figure 7 shows the test article; figure 8 shows the test load sequence. Reference 4 contains more detailed description, including the test setup.

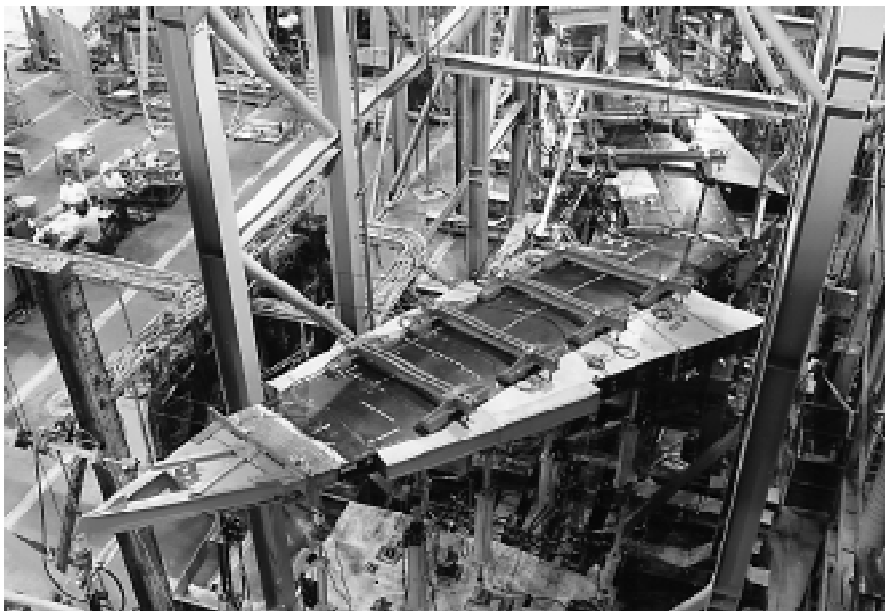


Figure 7: Preproduction Horizontal Stabilizer Test

One of the test objectives was to validate the "no-growth" design philosophy for damage [3]. To do this, impact damages were inflicted on the test box at the barely visible level. Boeing conducted fatigue testing for load cycles representative of two design service lifetimes. Periodic ultrasonic inspection revealed an absence of detrimental damage growth. This test included a 1.5S load enhancement factor to account for possible fatigue scatter associated with the flat S-N curves typical of composite materials.

Limit load strain surveys and initial ultimate load testing results demonstrated the predictive capability of the FEA internal loads model. Measured strains were at or below predicted strains. There was no indication of permanent deformation in any component.

To demonstrate residual strength capability the test box was further damaged with visible impacts. Visible damages are those that are easily detected by scheduled maintenance inspections. Fatigue testing representative of two inspection intervals again verified the

no-growth approach. Limit load testing verified that the structure was capable of carrying the required loads (FAR 25.571b) with these damages existing in the structure.

Engineers then inflicted the test box with major damage in the form of saw cuts to the front and rear spar chords and a completely severed stringer/skin segment. Testing demonstrated the capability to sustain continued safe-flight loads (FAR 25.571e). Again, ultrasonic inspection of the deliberately inflicted damages showed no detrimental growth. Residual strength testing substantiated the analytical predictions and empirical results based on subcomponent test characterisation.

Upon completion of the damage tolerance testing, mechanics repaired the cut element damages and the major through-penetration impact damages, using bolted titanium sheet metal repairs. Mechanics made the repairs using external access only, simulating in-service repair conditions. The test article demonstrated design ultimate load (DUL) capability with the repairs in place.

The test article was loaded to destruction using a symmetric down bending load case. A two-piece rupture occurred in the lower surface skin panel between ribs one and two. Final failure occurred above the required load level. Engineers predicted the skin panel failure using the analytical methods and design values derived from five stringer compression panel subcomponent tests.

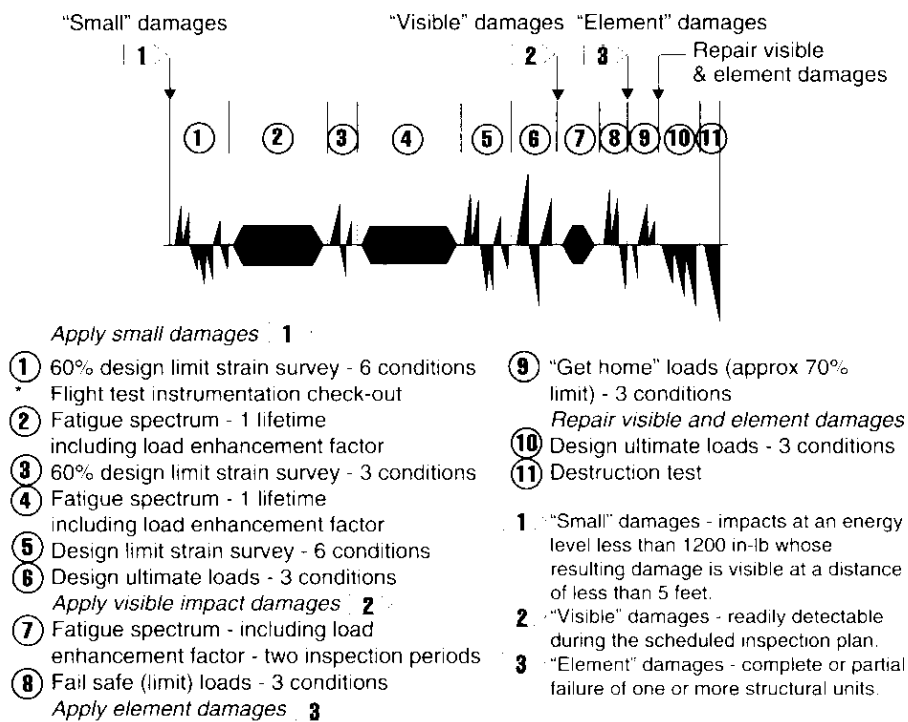


Fig. 8: Preproduction horizontal stabilizer test sequence

In summary, the preproduction stabiliser test substantiated the following findings:

- The "no-damage growth" behavior.
- The strength, durability, and damage tolerance of the 777 CFRP empennage design.

- The methods of analysis, material properties, and design values used to design and analyze a CFRP empennage.
- The capability of the ELFINI internal loads model for predicting strain distributions and deflections.
- The design and application of mechanically fastened repairs.

Vertical Stabilizer Root Attachment Test

Boeing conducted two large subcomponent tests to evaluate the primary joint of the 777 vertical stabiliser root attachment to the fuselage. The main objective of the tests was to

validate the analysis and load distribution assumptions for the joint. These tests also satisfied requests by the FAA and JAA for demonstrating ultimate load capability (FAR/JAR 25.305 and 25.307) and durability (FAR/JAR 25.571) of this CFRP/titanium joint.

The program achieved these objectives by fabricating two test articles representative of the 777-200 design, each composed of a four-bay section of CFRP skin panel and rear spar chord with two titanium root fittings (see figure 9). The first article was subjected to static testing in a series of limit and ultimate load conditions in tension and compression, culminating in a destruction test under tension loads. The final tension test loaded the article to 1.5 times DUL when the shear fasteners at the stabilizer-to-body interface failed. The skin and fittings remained intact as did the tension bolt/barrel nut connection.

The objective of the fatigue test was to find potential fatigue critical areas and investigate crack growth behavior. The second test article was tested with cyclic loads at a constant amplitude followed by a tensile residual strength test. Cracks in titanium clips and fittings developed.

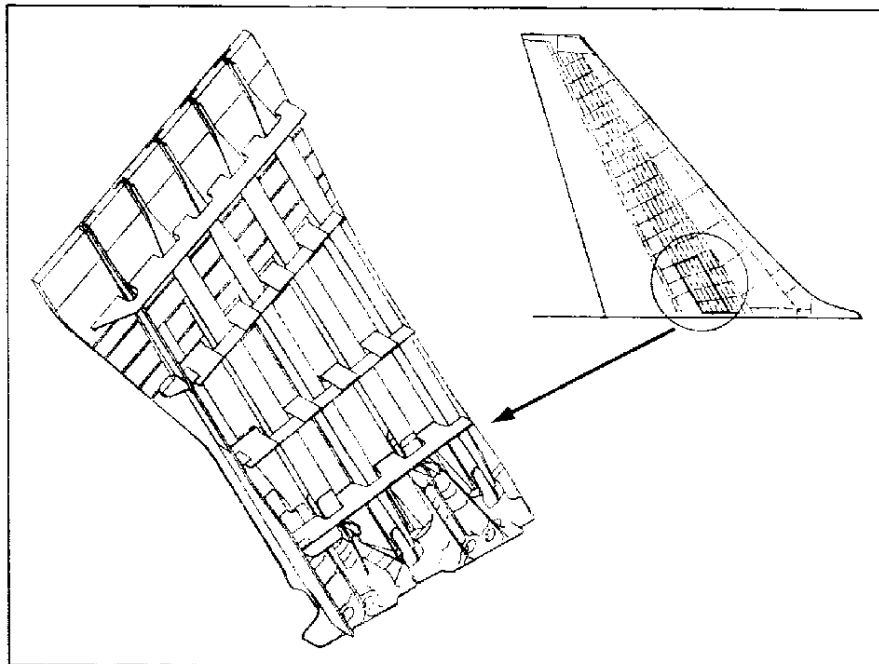


Figure 9: 777 Vertical Fin Root Joint Test Article

Post-test inspection of the cracks showed that the most detrimental crack began well after two equivalent design service lifetimes. The fatigue test was followed by residual strength tests in compression to limit load and in tension to failure. The panel failed under tension loading at approximately 1.5 times DUL, caused initially by the failure of the shear fasteners at the stabilizer-to-body interface, followed by a two-piece failure in the CFRP skin panel.

Subcomponent Tests

Subcomponent tests established point design values and validated methods of analysis for skin panel, spar, rib, trailing edge beam, and horizontal stabiliser centerline splice joint. These design values accounted for the effects of environment, the presence of barely visible impact damage, and for large damages. The Subcomponent test results comprise a significant portion of the test evidence required to validate analytical methods and demonstrate the required levels of static strength and damage tolerance for the 777 empennage.

Subcomponent test results validated the following critical design values and methods of analysis:

- Compression ultimate strength design value curve for stiffened skin panels.
- Shear-compression ultimate strength interaction curve for stiffened skin panels.
- Compression and tension damage tolerance analysis for stiffened skin panels.
- Strength of bolted and bonded repair designs for stiffened skin panels.
- Bolted joint analysis and design values for the skin panel-to-trailing edge rib joints.
- Static compression strength, tension strength, and tension fatigue performance of the horizontal stabilizer centerline splice joint.
- Analytical methods for spar strain distributions, web stability, and peak strains at cutouts.
- Analytical methods for rib shear tie and chord strength and stiffness.
- Peak strain design values for rib shear tie cutouts.

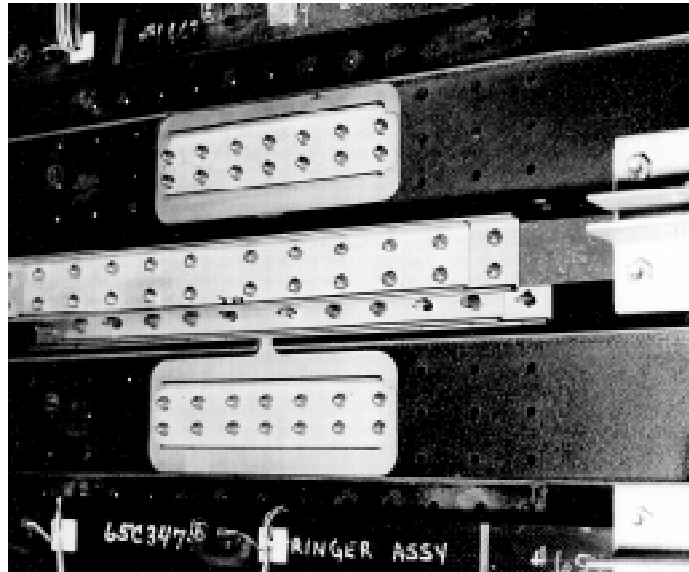


Figure 10a: Typical Bolted Repair on CFRP Skin Panel Test, Interior View

Several test types demonstrated no-growth of small damages under operational repeated loading. These tests complemented the results from the full-scale component fatigue testing and involved the following articles:

- Axially loaded flat panels.
- Shear loaded flat panels with cutouts.
- Stiffened panel with a bonded repair.
- Spar shear beams with web cutouts.
- Centerline splice joint stiffened panel.

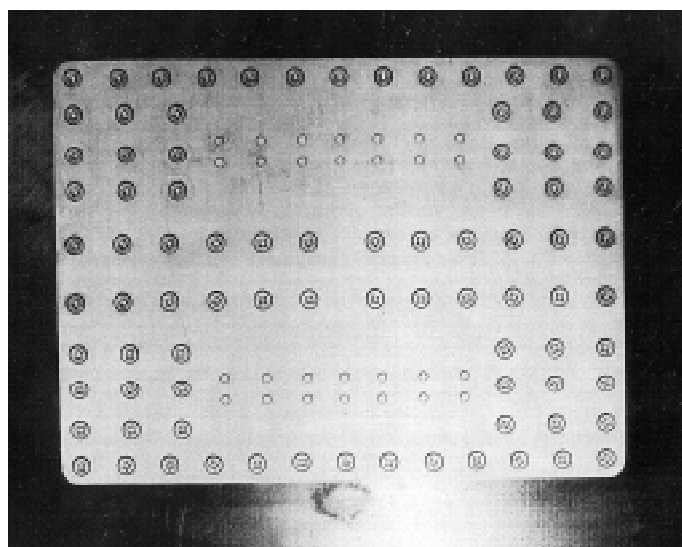


Figure 10b: Typical Bolted Repair on CFRP Skin Panel Test, Exterior View

A major focus of the empennage subcomponent test program involved the main torque box skin panels. These panels consist of an integrally stiffened solid laminate skin with I-section stringers. A series of] O five-stringer, three-rib-bay compression panels with small impact damages established the panel] design strain curve. Engineers derived the design strain values from the panel failure loads, using a modification of the classical effective width analysis technique. Tests were conducted at room temperature and hot/wet conditions and included barely visible impact damage and typical manufacturing flaws.

Tests on eight five-stringer panels validated repair concepts. Three tests contained bolted repairs using titanium doubler plates (figure 10); five tests contained bonded prepreg scarf joint repairs. All panels demonstrated ultimate load capability. Six of the panels were tested in compression; one panel of each repair type was tested in tension. Two bonded repair compression panels were tested in a hot/wet condition.

The bonded repair tension panel contained impact damages and was fatigue cycled for two lifetimes of operational loads without damage growth or disbond of the repair. Figure 11 shows a compression panel with a bonded repair under load; the moiré image clearly shows the buckle pattern of the skin panel and the location of the repair.

Tests on another 10 five-stringer compression panels and two five-stringer tension panels demonstrated capability for various large damages. Damage configurations included disbonded stringers, clearly visible impact damages, and saw cut damages to the skin and to a skin/stringer element. The first two damage types validated capability for regulatory fail-safe (FAR 25.571b) damage tolerance evaluations, while the saw cut damages validated capability for discrete source (FAR 25.571e) evaluations.

Tests on five-stringer panels loaded in combined shear and compression validated the shear-compression design envelope. Six panels with small damages were tested in a specialized test machine at several shear/compression load ratios. Engineers conducted additional stiffened panel tests to validate specific design details, including stringer runouts, the stabilizer centerline splice joint, and trailing edge rib-to-skin joints.



Figure 11:
Bonded Repair on CFRP Skin Panel Test

Subcomponent tests for the main torque box spars and ribs focused primarily on validating ultimate strength capability of these items. These tests included impact damages and environmental effects.

In summary, the subcomponent testing provided data to support the development of specific design values and to validate analytical methods. These design values and methods supported findings of compliance for FARs 25.307, 25.571, 25.603, 25.605, and 25.613. Engineers developed this supporting data using procedures that follow the guidelines in the composite structure advisory circulars [3].

Coupon and Element Tests

Boeing conducted an extensive coupon and element level test program in support of new 777 composite structure applications. These tests established material stiffness properties,

statistical allowables, and strength design values and validated analytical methods. Tests also established laminate level statistical allowables for unnotched and notched conditions, following recommended procedures [8].

Table 2: Summary of T800/3900-2 CFRP Material Coupon and Element Tests

Test Type	Number of Tests
Ply properties	235
Long-term environmental exposure	200
Laminate strength	2,334
Interlaminar strength	574
Radius details	184
Crippling	271
Stress concentrations	118
Effects of defects	494
Bolted joints	3,025
Durability	385
Bonded repair	239
Total	8,059

Testing covered laminate, joint, and structural configurations typical of the 777 empennage; temperatures from -54°C to 82°C; moisture conditioned laminates; and the effects of

manufacturing variations and anomalies allowed within the process specifications. A limited amount of impact damage testing was performed at the element level. Test article configurations ranged from simple rectangular coupons to bolted joint, angle-section, I-section, and shear panel element tests. Table 2 shows a summary of the testing.

PRODUCTION COMPONENT TESTS

The following section discusses the full-scale production component tests for the 777 horizontal and vertical stabilisers. The primary objective of this testing is limit load substantiation in compliance with FAR/JAR 25.305 and 25.307. A further objective is to verify the load distribution and analytical methodology. Previous experience from ultimate load and failure testing of the 737, 7J7, and 777 preproduction horizontal stabiliser test boxes removed the need to test the 777 production structure beyond limit load for certification

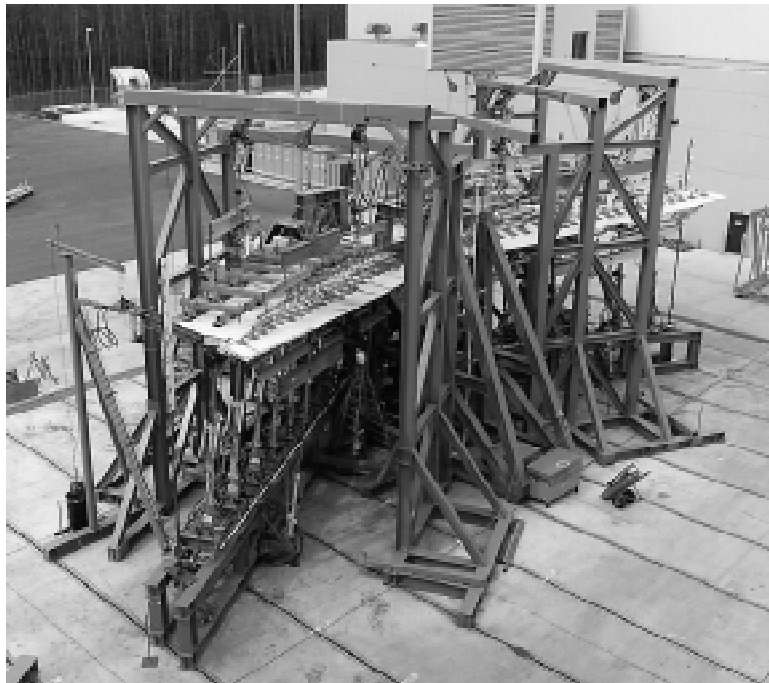


Figure 12: 777 Horizontal Stabilizer Test Setup

777 Horizontal Stabilizer Tests

Boeing tested the 777 horizontal stabiliser and elevators separately from the airplane because the attachment to the body is determinate. The test specimen was a structurally complete production article (figure 12). The test plan omitted nonstructural components and systems not essential to the structural performance or induced loading of the stabiliser.

The strakelet and tip Airings were not installed, and the elevator actuators were replaced by rigid links. The test specimen was fabricated by the same construction methods and governed by the same specification requirements as other production structure. Inspectors maintained FAA conformity on a majority of the parts during fabrication. Tests began in April 1994 and were complete in June of 1995.

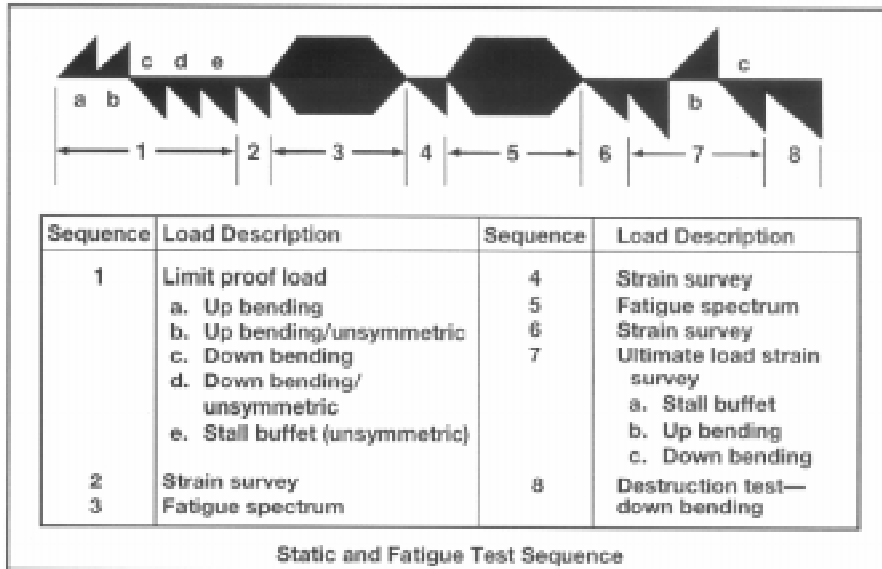


Figure 13: 777 Horizontal Stabilizer Test Sequence

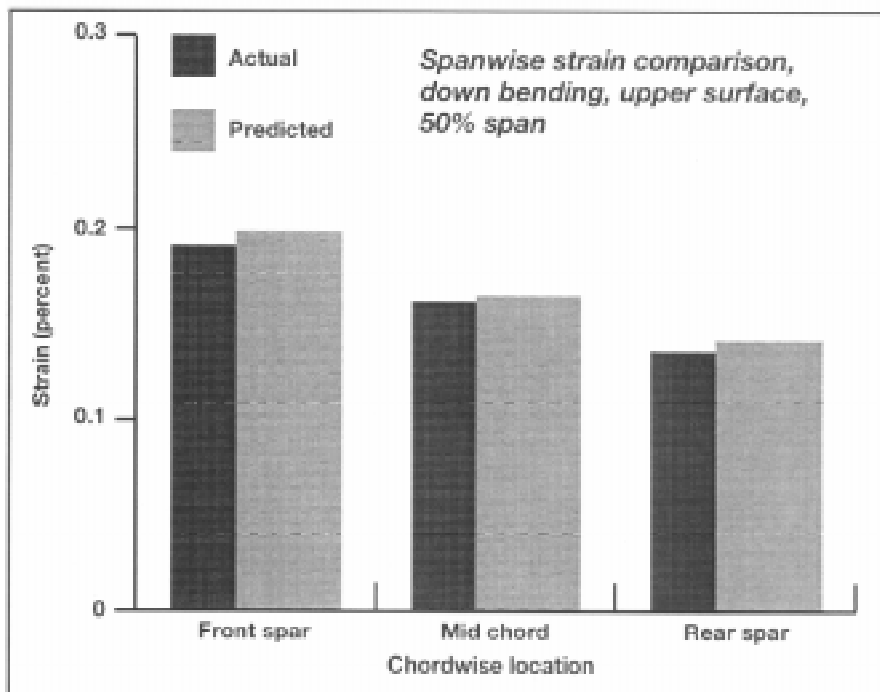


Figure 14: 777 Horizontal Stabilizer Test, Predicted Versus Actual Strains

Engineers computed test loads for each static load condition to match the required shear, moment, and torsion values. These test loads were applied to the stabiliser using hydraulic actuators connected to attachment fittings, mounted on the stabiliser structure. The stabilizer was mounted in the test fixture at the pivot and jackscrew fittings, as it would be in an airplane. The test article was instrumented with strain gages, electronic deflection indicators (EDI), and calibrated load-cells at selected locations. Instrumentation monitored structural

responses and provided data for correlation to analytical predictions during all strain surveys. Testing was conducted outdoors at ambient conditions.

The test included three critical static load conditions: up, down, and unsymmetric bending. Figure 13 depicts the loading sequence. As in the preproduction test box, limit load strain survey results demonstrated the predictive capability of the PEA model. Calculations accurately predicted measured strains (figure 14). Overall deflection along the span of the stabilizer correlated well (figure 15). There were no signs of permanent deformation.

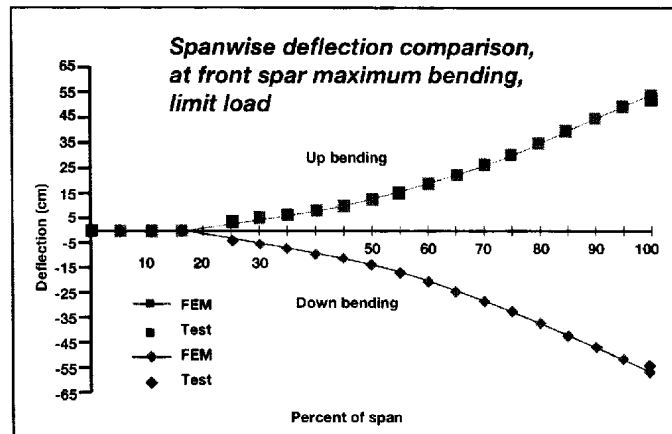


Figure 15: 777 Horizontal Stabilizer Test, Predicted Versus Actual Deflection

Additional testing that was not required for certification included fatigue, ultimate load, and destruct testing. The horizontal stabilizer was subjected to 120,000 flights of spectrum fatigue loading to satisfy the program objectives. This test verified the fatigue characteristics of the metallic portion of the stabilizer. The preproduction test box described earlier verified the composite structure.

Ultimate load and destruct testing supplemented the data that was acquired as part of the certification program. The test team ran three load cases representative of up, down, and unsymmetric bending. The critical down bending load case became the destruct run. The test box was subjected to barely visible impact damage and loaded to failure. Engineers accurately identified the failure location and predicted the failure load within 3D. Final failure occurred above the required load level.

The 777 horizontal stabilizer test program met the following goals:

- Verified compliance with FAR/JAR 25.305 and 25.307. The test article sustained limit load for critical conditions without permanent deformation.
- Verified predictive capability of analysis methods coupled with subcomponent tests. Strains and deflections closely matched the analysis.
- Verified the design service goals of the 777 horizontal stabilizer.
- Verified the absence of widespread damage due to fatigue.

777 Vertical Stabilizer Test

Boeing tested the 777 vertical stabilizer, including the rudder, as part of the airplane fullscale test (figure 16). Again, the purpose was to show limit load capability and verify the accuracy of analytically calculated strains and deflections. Tests began in June of 1994 as part of the

fullscale airplane test and were completed in April of 1995. Boeing used a second airplane with vertical stabilizer and rudder in the major fatigue test, which began in January of 1995.

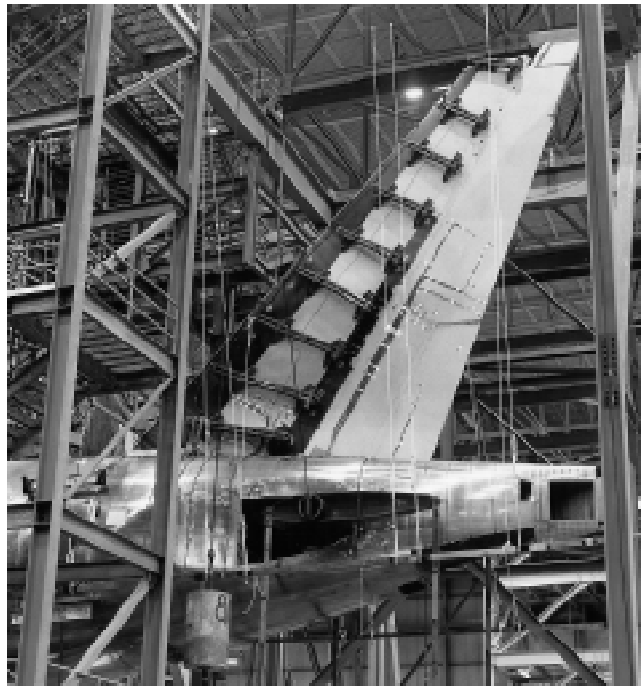


Figure 16: 777 Vertical Stabilizer Test Setup

The static test article was the second production airplane built. The aft portion of the aircraft was structurally complete except for nonstructural components and systems; the horizontal stabilizer was replaced by a load fixture attached at the pivot bulkhead and jackscrew attachment. The leading edge and tip were not installed on the vertical stabilizer, and the rudder actuators were replaced by rigid links.

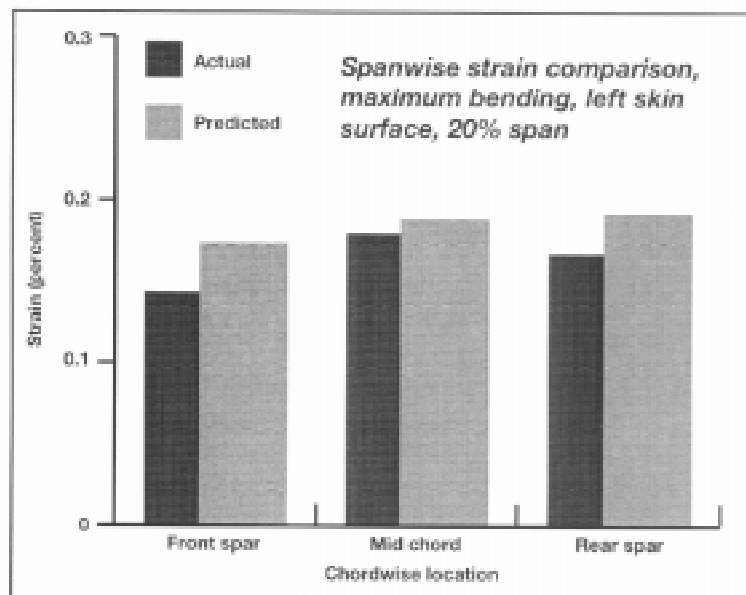


Figure 17: 777 Vertical Stabilizer Test, Predicted Versus Actual Strains

As described for the horizontal stabilizer test, engineers computed loads for critical cases, based on the external load conditions, and applied them through a series of actuators, fixtures, and pads. The test article contained a full set of instrumentation to monitor behavior and collect data for comparison with the analysis. Testing was conducted indoors at ambient conditions.

Three critical conditions tested included maximum bending (engine-out), maximum torsion (hinge moment), and maximum shear (lateral gust). Technicians applied other test conditions as part of the overall airplane test sequence, which were not critical for the vertical stabiliser. In comparison with the analysis, measured strains were accurately predicted (figure 17). Measured deflection along the span of the fin correlated well with the FEA loads model (figure 18). There were no signs of permanent deformation.

A completely separate test using another production airframe verified the fatigue behavior of the 777. This test subjected the vertical stabiliser and rudder to 120,000 flights of spectrum fatigue loading. The 777 vertical stabiliser test program exceeded the same goals as described for the horizontal stabiliser test.

CONCLUSIONS

The results of the 777 empennage certification program have provided data to show compliance with FAA and JAA regulations. The results also add to confidence in the use of composite materials in large primary structures for commercial transport aircraft. The necessary steps leading to this conclusion entail: (1) an early certification plan developed by working together with the FAA and JAA; (2) a dedicated material characterisation program:

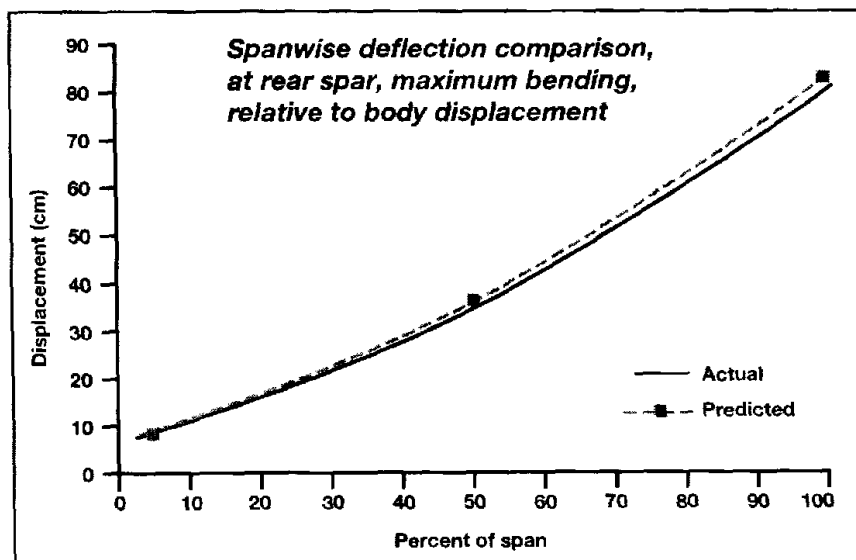


Figure 18: 777 Vertical Stabilizer Test, Predicted Versus Actual Deflection

(3) substantiation of static strength by analysis, accounting for the effects of damage and environment, and the supporting static tests; and (4) damage tolerance verification with a no-growth approach and the supporting test data. On each major item, Boeing has complied

with the guidelines established by the regulatory authorities. The resultant composite airplane components are safe and reliable.

ACKNOWLEDGMENTS

The authors gratefully acknowledge the many and diverse contributions of the 777 empennage design-build team and support staff. We also acknowledge David R. Wilson, Karl H. Schreiber, and John T. Quinlivan for their leadership in the 777 certification process. We are thankful to Stan Wood of the FAA for his oversight during the course of the program. Thanks to Peter J. Smith for his encouragement. The authors remember Ernie Dost, who always wanted to work on the 777 empennage, but instead worked to broaden our smiles and further our knowledge of impact damage resistance.

REFERENCES

1. McCarty, J. E., Johnson, R. W. and Wilson, D. R., "737 Graphite-Epoxy Horizontal Stabilizer Certification," AIAA 82-0745.
2. Takaki, J., Kimura, J., Berner, J., Hirahara, M. and Yahata, A., "CFRP Horizontal Stabilizer Developmental Test Program," presented at the Ninth International Conference for Composite Materials, Madrid, 1993.
3. FAA Advisory Circular 20-107A, *Composite Aircraft Structure*, 1984; and, companion document by the JAA, ACJ 25.603, *Composite Aircraft Structure (Acceptable Means of Compliance)*, 1986.
4. Schreiber, K. H. and Quinlivan, J. T., "The Boeing 777 Empennage," presented at the Ninth International Conference for Composite Materials, Madrid, 1993.
5. *Code of Federal Regulations, Aeronautics and Space*, Part 25, "Airworthiness Standards: Transport Category Airplanes."
6. *Joint Aviation Requirements'JAR-25*, "Large Aeroplanes."
7. Takaki, J., Kimura, J., Berner, J., Hirahara, M. and Yahata, A., "Fatigue Test for CFRP Horizontal Stabilizer," presented at the 17th International Committee on Aeronautical Fatigue, Sweden, June 1993.
8. MIL-Handbook 17, *Proceedings of Coordination Group on Allowables*.
9. Johnson, R. W., McCarty, J. E. and Wilson, D. R., "Damage Tolerance Testing for the Boeing 737 Graphite-Epoxy Horizontal Stabilizer," 5th DoD/NASA Conference on Fibrous Composites in Structure Design, NADC 81096-60, New Orleans, Jan. 1981.

LARGE COMPOSITE FAN BLADE DEVELOPMENT FOR MODERN AEROENGINES

Keith T. Kedward

*University of California at Santa Barbara
Department of Mechanical & Environmental Engineering
Santa Barbara, California 93106-5070, USA*

SUMMARY: The state of maturity of contemporary PMC's after almost 30 years of scientific and technology development has resulted in a capability that far exceeds that available in the late 1960's, and which, in 1989, prompted General Electric to engage in the notably successful development and flight certification of large PMC fan blades for their GE90 engine. In this paper an accounting of the specific enhancements in (i) constituent (fiber and matrix) property characteristics, (ii) fabrication and processing options, and (iii) design analysis methods combined with computational capabilities will be discussed. However, an equally important aspect is the variation in the design options that has resulted from evolving high by-pass ratio engine technology, which will also be addressed. The GE90 fan blade represents one of these options, being a relatively large blade designed to operate at lower tip speeds, thereby reducing the severity of the impact threat represented by the ingestion of large birds. A comparison between various modern turbofan engine fan blades and other rotor blades serves to indicate the important parameters and the difficulty of establishing a composite threshold range for rotor blades in general.

KEYWORDS: polymer matrix composite, composite fan blade, constituent properties, impact performance, textile reinforcement architectures, engine certification

INTRODUCTION

Since the ill-fated attempt by Rolls-Royce to develop large polymer matrix composite (PMC) fan blades for a large commercial turbofan engine in 1968, i.e., the RB211, this potential application had eluded the engine designer until the emergence of General Electric's GE90 engine development. But the continuing evolution in turbofan engine design has resulted in a progressive increase in by-pass ratio which has fueled a continued interest in the application of PMC's for fan blades due to the concomitant increased pay-off for high specific stiffness and strength offered by PMC's.

The state of maturity of contemporary PMC's after almost 30 years of scientific and technology development has resulted in a capability that far exceeds that available in the late 1960's, and which, in 1989, prompted General Electric to engage in the notably successful development and flight certification of large PMC fan blades for their GE90 engine. In this paper an accounting of the specific enhancements in (i) constituent (fiber and matrix) property characteristics, (ii) fabrication and processing options, and (iii) design analysis methods combined with computational capabilities will be discussed. However, an equally important aspect is the variation in the design options that has resulted from evolving high by-pass ratio engine technology, which will also be addressed. The GE90 fan blade represents one of these

options, being a relatively large blade designed to operate at lower tip speeds, thereby reducing the severity of the impact threat represented by the ingestion of large birds. A comparison between various modern modern turbofan engine fan blades is illustrated for a range of important parameters in Table 1. In addition, the vitally important factor for impact performance, the tip speed, is compared in Figure 1 for a general variety of composite rotor

Table 1. The evolving fan technology represents a major consideration - some relevant comparisons

	RB211	TRENT 800	PW4084	GE90
Blade Type	Hollow Ti	Hollow Ti	Hollow Ti	Composite
Thrust (lb.)	61k	84k	84k	84k
Fan Diameter (in.)	86	110	112	123
No. of Blades	24	26	22	22
Red Line RPM	3900	3264	3045	2386
By-Pass Ratio	4.5	6.0	7.0	8.5
Blade Chord (tip)	17.7	19.9	19.5	21.0
Blade Chord (root)	14.2	16.0	13.9	12.0
Blade Span	28.4	36.7	34.8	48.0
Aspect Ratio	2.0	2.3	2.44	2.57
Blade Weight (lb.)	19	26.4	35	36
Tip Speed (ft./s.)	1408	1430	1488	1250

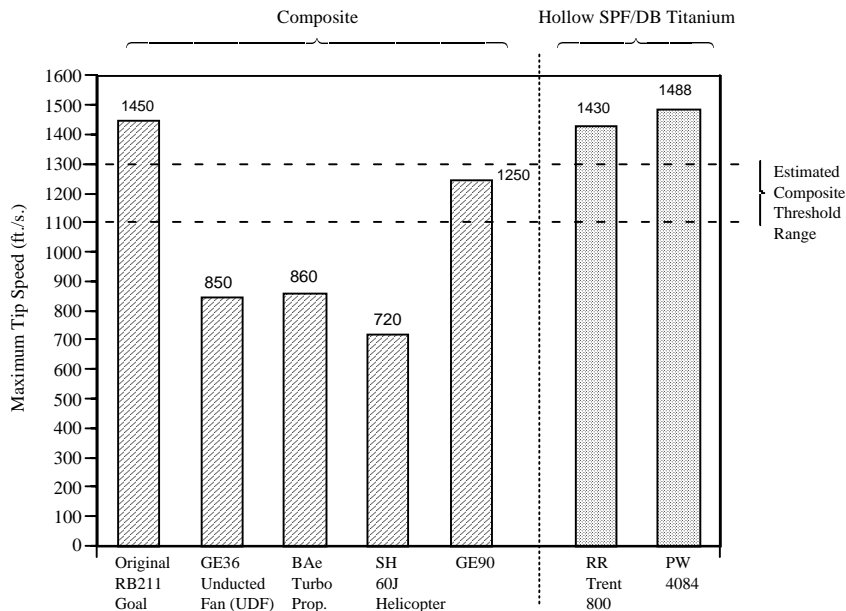


Fig. 1: A general comparison of composite vs. hollow titanium rotor blades. An estimated impact velocity threshold range for composites is also presented in this figure, although many other factors, such as aerofoil profile, angle of projectile incidence and other geometrical features will be discussed later.

The GE90 blade design, Figure 2, also serves to illustrate the critical importance of a multidisciplinary posture that enables the effective exploitation of a new technology in key hardware items for revenue generating products. The current strategies based on integrated product development teams which evidence this trend are emphasized in the discussion. Ultimately, the successful application of PMC's for large fan blades will contribute to higher aerodynamic efficiency, with lower specific fuel consumption, in concert with environmentally friendly, lower engine noise. Technology advances discussed in the paper will also focus on enhancements in analysis capabilities that facilitate high rate, large displacements and strains, together with three-dimensional (out-of-plane) modeling of severe soft body impacts inflicted during bird ingestion. Much improved simulations of both the PMC fan blade target and the soft body (bird) projectile have become feasible with the advent of supercomputing technology. This has culminated in greater insight for the engineer and subsequent improvement in composite design for higher impact resistance and reliability with less extensive, and less expensive, experimental commitments. Collectively, such capabilities will lead to a reduction in the time necessary to develop new technology-driven products.

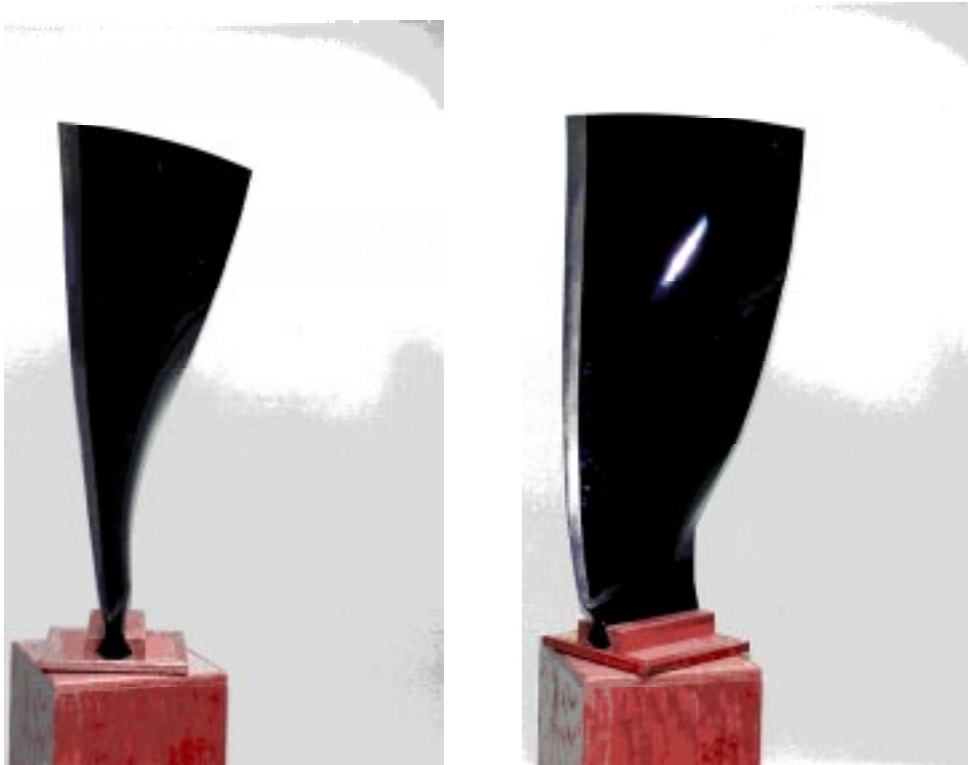


Fig. 2: The GE90 Composite Fan Blade

In the concluding section, the challenge of developing certification strategies and economics-driven issues of reparability and airline customer acceptance and confidence will be addressed.

The potential advantage of polymer matrix composites (PMC's) to the evolving development of the high by-pass ratio turbofan engine was first recognized in the late 1960's by Rolls-Royce. A major contributor to the Rolls-Royce decision of embarking on an extensive composite fan blade development program for the RB211 at that time was the emerging carbon-fiber production capability. The background of experience gained from earlier work on small glass-fiber/epoxy compressor blades provided a useful foundation and, together with the additional specific stiffness available with carbon-fiber reinforcement, also satisfied the demanding dynamic environment. Indeed, the possibility of developing a large fan blade with vibration characteristics that would eliminate the need for midspan shrouds (or "snubbers") that were necessary with similar solid titanium fan blades of that era represented a further significant incentive, i.e., these benefits translate into high aerodynamic efficiency, lower noise and improved fuel consumption.

Unfortunately, the severe bird ingestion environment presented a major obstacle and the lack of ductility and toughness characterized by the very low strain-to-failure and inferior interlaminar shear strength of early carbon fiber composites were shown to be totally inadequate. Use of metallic leading edge sheaths necessary for contributing erosion and hard body as well as ice impact resistance were subsequently shown to offer insufficient improvement in soft body impact (bird ingestion) performance.

Continuing evolution in turbofan engine design has resulted in progressive increases in by-pass ratio over a range from 3 to 9 and projections for future advanced engines indicate the possibility of significantly larger ratios. As a consequence, the potential payoff with PMC's for the resulting large fan blade application has become even more attractive, as illustrated by General Electric's excursion into PMC fan blade development for the GE90 engine, with a by-pass ratio of 8.5. Another advanced technology product, the hollow, superplastically formed and diffusion bonded (SPF/DB) titanium fan blade currently offers the only viable alternative to PMC's. Interestingly, the initial development of the hollow-titanium fan blade by Rolls-Royce, began at the same time as the original carbon fiber/PMC RB211 fan blade design was replaced by the shrouded solid titanium design. Rolls-Royce's Trent 800 engine now utilizes the proven hollow titanium version which was originally introduced over 12 years ago for the RB211-535 engine as discussed recently by Miller [1].

It will be explained more fully, later, that the fate of the original Rolls-Royce PMC fan blade for the RB211 was mainly due to its inability to satisfy the demanding bird-ingestion requirement. Further, the technological advancements in composite constituent property characteristics (fiber and matrix), fabrication options and design analysis methods, in addition to the changing requirements created by the evolution in high by-pass ratio fan technology will be described in accounting for the revitalized interest in PMC fan blades.

In general, the requirements for fiber reinforcement in a composite fan blade should comprise:

- (i) Adequate stiffness in flexure and torsion to provide resonant frequency characteristics that avoid undesirable vibration responses. It follows that flexural stiffness calls for axial (0°) fiber reinforcement preferably at aerofoil surfaces, whereas torsional stiffness similarly calls for ±45° reinforcement as close to the outer surfaces as practicable. Adequate chordwise flexural stiffness is also required for blades of low aspect ratio and this requires a reasonable percentage of transverse (90°) fiber reinforcement.

- (ii) The dominant consideration of bird (soft body) impact translates into high dynamic interlaminar shear stress in the blade root region and, probably, at the impact sites. Furthermore, for the highest level (8 lb.) bird impact interlaminar damage must be anticipated but containment of the damage by suppressing the propagation of this damage may benefit from some through-thickness fiber reinforcement. Consequently, some compromise between acceptable in-plane stiffness and strength properties and adequate interlaminar toughness would then be sought.

ENHANCEMENTS IN TECHNOLOGY

Since the early attempt at utilizing the first-generation PMC's in the form of a carbon fiber/epoxy matrix system in the late 1960's, Goatham [2, 3], Kedward [4], there have been several substantial enhancements in the properties of the fiber and matrix constituents. More reliable manufacturing technologies with a greater range of options for producing reliable products at lower cost have also matured and been applied in production. Finally, assisted by the advent of supercomputer technology a much improved range of sophisticated design analysis methods have been developed and are now on-line. In the following sections a specific explanation of the impact that these enhancements have had on the development of high performance composite fan blades is presented.

Improvements in Constituent Properties

With the early polyacrylonitrile (PAN) based fibers, the statistical variability, particularly in fiber strength properties was significant as well as the limited general quality standards available from early production processes. In the past twenty-five years both the strength and stiffness of available fibers have increased significantly. Moreover, the capability to obtain fibers with both high strength and high modulus has been developed, whereas the composites designer was previously forced to choose between one or the other. An appreciation of these enhancements in fiber properties can be gained from the historical data presented in Table 2.

Clearly, the benefits in strength, strain-to-failure and modulus of contemporary carbon and graphite fibers translate into major gains in the in-plane properties of multidirectional laminates of interest in highly efficient structurally loaded components. Similar benefits in transverse and interlaminar matrix dominated properties are realized from the gains in polymer matrix ductility, toughness and the improved understanding of the influence of the fiber-matrix interface.

Table 2. Carbon/graphite fiber property enhancements

	Manufacturer	Fiber	F_f^{tu} ksi	E_f (Msi)	$\epsilon_f^{tu}(\%)$
1967	Rolls Royce	"HYFIL"	300	30	0.94
1978	Amoco	T300	450	34	1.30
1980	Hercules	AS4	570	34	1.60
1985	Hercules	IM6	740	40	1.73
1986	Hercules	IM7	770	40	1.81
1987	Hercules	IM8	790	44	1.67

Substantial gains have evolved through the development of tougher polymer matrix systems which, in conjunction with a more extensive scientific characterization of the effect of fiber/matrix interface phenomena, has provided much needed increases in interlaminar toughness, see Table 3 and Figure 3.

Table 3. Fracture Energy of Bulk Polymer Matrix and Composite Interlaminar Cleavage

Date (Ref)	Bulk Polymer System	Matrix Fracture Energy G_{IC} (kJ/m ²)	Interlaminar (Mode 1) Fracture Energy, G_{IC} (kJ/m ²)
1974 [5]	Shell 818	0.18	0.55
1980 [6]	Hexcell 205	0.27	0.60
1980 [6]	Hexcell F-185	5.10	4.60
1986	AS4/PEEK (Thermoplastic)	*3.80	1.60
1990	IM7/8551--7 (Toughened Eposy)	*1.10	0.55

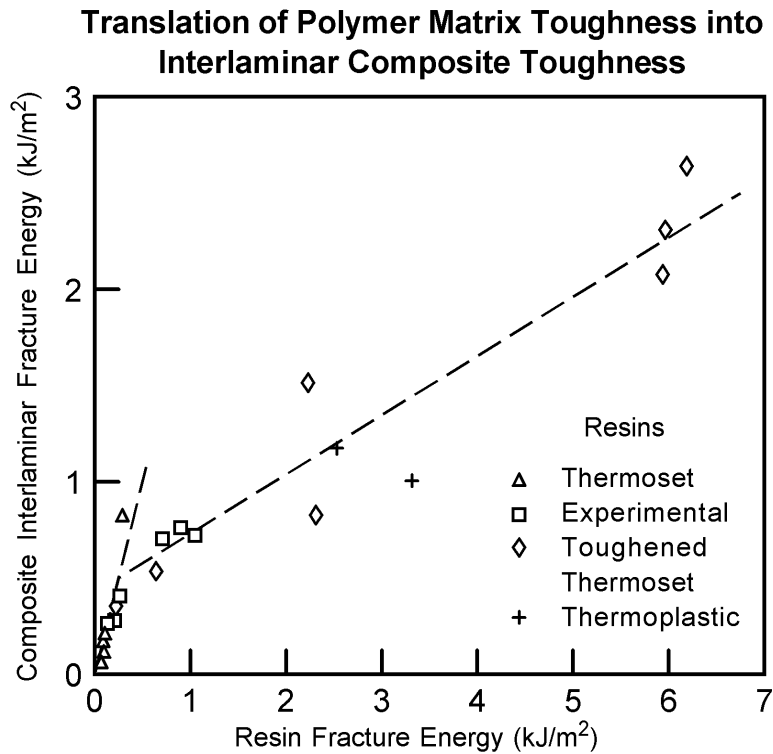


Fig. 3: Translation of Polymer Matrix Toughness into Interlaminar Composite Toughness

Much has been learned regarding the methods of toughening bulk polymer matrix materials such as the use of elastomeric particles for example. More significant is the ability to translate the enhanced toughness of the bulk polymer into improved interlaminar toughness in the composite. In first generation, relatively brittle, epoxy systems (Table 3) toughness enhancement of the matrix resulted in substantial increases in composite interlaminar (toughness particularly in Mode I (interlaminar tension)). This effectiveness is illustrated in Figure 3 for the relatively brittle epoxy matrix systems with typical values of Mode I strain energy release rates, G_{IC} , given in Table 3. It is also clear, from Table 3 and Figure 3, that the translation of bulk matrix toughness into composite interlaminar can be much less effective for the tougher polymer systems. We now appreciate that the general principle accounting for the reduced effectiveness of composite toughening is associated with the high degree of constraint imposed by the stiff reinforcing elements in PMC's with high reinforcement volume fractions.

With regard to the general subject of damage tolerance and the macroscopic structural behavior of composite structures it is also acknowledged that the proportional increase in toughness may be significantly different for Mode I (interlaminar tension) vis á vis Mode II (interlaminar shear). Typically the gains in Mode I (G_{IC}) are significantly higher than those realized for Mode II (G_{IIC}) for most candidate toughening methods. From a structural designer's viewpoint the relative importance of these factors must be interpreted from the aspect of structural configuration and loading. In the event of the high velocity impact threat the damage resistance can be strongly dependent on the Mode II toughness of the composite but this may vary for composite structural configurations subjected to hard body projectiles, e.g. ice, runway stones, etc. vs. soft body (bird ingestion) projectiles. On the other hand the damage tolerance of composite structures may be more dependent on Mode I toughness particularly for damaged structures that are loaded in compression following an impact event. For the composite fan blade application, of interest herein, the latter is probably of lesser importance than for, say, that of a composite upper wing skin for a commercial transport aircraft.

More recently the rate-dependent behavior in both Mode I and II fracture has been studied for both untoughened and toughened epoxies, see Cairns [8,9]. Although the conditions representing only low velocity impact have been addressed indications of significant rate dependence specifically for Mode II fracture properties of toughened epoxy systems are of direct interest and relevance. It is particularly noteworthy that the corresponding results pertaining to Mode I fracture are relatively insensitive to strain rate [9]. Qualitative rationalization of these observations refer to tortuosity of crack path development in the non-homogeneous toughened epoxy matrix system, local crack tip sliding deformation as well as inherent matrix toughness increases.

During the past four or five years it has been demonstrated that the interlaminar toughness of laminated composite systems can be effectively increased, at least in Mode I, by the inclusion of a small percentage of through thickness reinforcement by stitching of dry fiber preforms [10] followed by resin infiltration processing as discussed next.

Alternative Reinforcement Architectures for Toughening and Manufacturing Advantages

Recent NASA-funded research and development work at McDonnell Douglas Aerospace, Long Beach, California has demonstrated that effective toughening of laminated polymer

composites can be realized by use of a small percentage of stitched reinforcement [10]. Using the Compression-After-Impact (CAI) strength as an indicator of toughness, it was shown that only 3% of Kevlar stitch reinforcement is necessary, using the relatively brittle Hercules 3501-6 resin matrix system to attain a toughness equivalent to that of the toughened epoxy system, Hercules 8551-7. The latter is a considerably more expensive matrix material but, more significantly, the possibility of utilizing resin infiltration method such as Resin Transfer Molding (RTM) or Resin Film Infusion (RFI) methods of processing net shape structures offers potential economic advantages for manufacturing. At least for commercial transport upper wing skin and related applications this approach is most attractive and is now has serious consideration for such applications. A tolerable reduction in the critical in-plane properties must be accommodated in utilizing relatively-lightly stitched PMC systems however.

Other candidate approaches for effective interlaminar toughening are widely available through the exploitation of textile technology. One specific example is some form of "angle interlock" architecture, often defined as "2.5D fiber architecture". The need for adequate in-plane stiffness and strength properties generally precludes consideration of a full 3D-type of fiber reinforcement architecture.

As mentioned the ability of stitched fiber arrangements to suppress or contain interlaminar damage has been demonstrated, for the McDonnell Douglas transport wingskin application now under development. There is also a limited amount of data that indicates that "2.5D" or angle-interlock architectures can similarly suppress or contain damage although the impact on in-plane properties has been less well characterized as are meaningful comparisons of interlaminar tensile and shear properties of these systems.

To assess the potential of 2.5D systems, in fan blade applications a survey of the existing technology and data base should be conducted. Some relevant data is presented in Table 4, compiled from Ref. [11] but the absence of interlaminar strength properties will be noticed here.

Table 4: Data for Angle Interlock “2.5D” Reinforcement Architectures, [11]

Property	Mode	Layer-to-Layer (LTL)		Through-the Thickness (TTT)	
		Type A (4 layers) 0.22”	Type B (6 layers) 0.246”	Type A (4 layers) 0.22”	Type B (6 layers) 0.246”
E_1	Tension	12.3	11.6	11.5	10.4
Axial	Compression	12.8	11.8	12.0	10.4
Modulus (Msi)	Flexure	10.4	---	9.14	9.14
F_t , ult	Tension	142	136	122	130
Axial	Compression	97.2	101	82.7	78.3
Strength (ksi)	Flexure	150	150	155	130
E_2 Transverse (Msi) Elastic Modulus		63.5	6.13	6.16	6.64
E_3 Thru-thickness (Msi) Elastic Modulus		2.32	2.03	2.0	2.02
G_{12} In-plane shear (Msi) Modulus		0.9	0.84	0.81	0.83
ν_{12} (In-plane Poisson ratio)		0.06	0.13	0.054	0.097

In attempting to summarize the state-of-the-art on the subject as it relates to the fan blade application, the following observations are pertinent:

- (a) Typical layer thicknesses for the layer-to-layer angle interlock and through-thickness angle interlock architectures are in the range of 0.040 inch-to-0.060 inch, which is much larger than typically found in tape or fabric laminates. Hence, it may be necessary to “phase out” the interlock layers in the thinner sections of a fan blade.
- (b) It is also important to note that typical interlock systems comprise only orthogonal in-plane reinforcement (warp and fill directions) with no $\pm 45^\circ$ fibers. Incorporating in-plane angle orientations may require some development time on behalf of the preform supplier.
- (c) The effectiveness of the interlock arrangement in achieving improvements in interlaminar, tension and shear, characteristics without serious degradation in the in-plane properties demands very careful study. For example, the angle and straightness, in the thickness direction, of the warp weavers and the associated anisotropy in interlaminar property enhancement has not been adequately presented in the literature reviewed to date.
- (d) Due to the coarseness of the architecture and the related unit layer thicknesses the tendency for lower flexural stiffnesses, especially for thinner sections of the blade

should be recognized. Some of the data presented in Table 4 illustrates this tendency. Table 5 provides a concise summary of the general implications of this class of reinforcement architectures for fan blade applications in terms of some pros and cons.

Enhancements in Design Analysis Methods

With the enormous expansion of numerical methods development, such as that based on finite element technology, combined with the utilization of current supercomputing capabilities there has been phenomenal growth in our ability to conduct complex and detailed analyses. Advantages in the development and handling of databases that can effectively link the computer aided design, analysis, manufacturing and tooling functions are also derived from these developments. Numerous, special purpose software developments and design rules and systems are now available, examples such as linear and nonlinear laminated plate analysis codes and out-of-plane methodologies have emerged to support conventional laminated composite structures. More recently there is a growing capability for treating integral fiber architectures although generally a less mature design analysis at present.

However, of greater interest and relevance to PMC fan blade design are the sophisticated analysis methods now developed for soft body impact evaluation than can simulate the ingestion of large birds and predict the consequences. This particular condition has primarily been the critical design issue, and most certainly accounted for the failure of the first attempt to utilize PMC's for the Rolls-Royce RB211 engine in the late 60's and early 70's.

In attempting to account for the technology leverage existing today relative to that available in the 1968-71 era of the RB211 development, the current analysis capability represents a profound advantage for the engine designer. To put this in perspective it is appropriate to briefly review historical developments over the period from 1968 through to the present. An illustration summarizing the key developments in soft body impact analysis methods is portrayed in Figure 4. Only very crude modeling and analysis techniques for both the soft body (bird) projectile as well as the composite target (blade) were available in the late 1960's. One example of this overly simplistic idealization of the distribution, termed slice mass, of the bird onto the blade was published by Sayers [12]. Although finite element technology development, and the application thereof, was rapidly growing in the late 1960's, it was some time later (about 1975) before advanced composite anisotropic layered structures could be effectively idealized, recognizing the fact that computational capabilities permitted only relatively slow run times. The additional data input and output required for large numbers of composite layers was very cumbersome at that time.

Table 5: Some Pros and Cons Related to the Selection of Fiber Reinforcement Architecture in Fan Blade Application

	STITCHED FABRIC BASELINE	LAYER-TO-LAYER ANGLE INTERLOCK	THROUGH THICKNESS ANGLE INTERLOCK
PROS	<ul style="list-style-type: none"> • Modest dilution of in-plane properties. • Flexibility for accommodating all 0/45/90 directions. • Order of magnitude improvement in Mode I (Interlaminar Tension Strength) properties. • Amenable to selective transverse reinforcement. 	<ul style="list-style-type: none"> • Well established preform experience. • Potential enhancement of Mode II (Interlam. Shear Strength) properties. • Good prospects for automated preform development. 	<ul style="list-style-type: none"> • Well established preform experience. • Potential enhancement of Mode II (Interlam. Shear Strength) properties. • Good prospects for automated preform development. • Potentially lower cost preform rel. to layer-to-layer system.
CONS	<ul style="list-style-type: none"> • Restricted to near-normal fiber reinforcement thru thickness. • Limited enhancement of Mode II (Interlam. Shear Strength) properties. • Possibility of application to thicker sections. 	<ul style="list-style-type: none"> • Less effective reinforcement in Filler Direction (Anisotropy) • Unproven capability for accommodating ± 45 in-plane reinforcement. • Potentially higher cost preform rel to thru-thickness system. 	<ul style="list-style-type: none"> • Less effective reinforcement in filler direction (Anisotropy) • Unproven capability for accommodating ± 45 in-plane reinforcement.

By the mid 1970's the compatibility for more representative soft body simulations were beginning to emerge such as Pratt & Whitney's PW/WHAM code. In this simulation, reported and described later by Martin [13] a more accurate distribution of impact load is facilitated by a fluid finite element idealization. "Flow" of the soft body (bird) occurs at impact while the target remains solid. The postulate in such projectile models is that the material density rather than the material strength is the dominant factor and this tended to be substantiated by Barber et al [14,15,16] using metallic targets. Soft body impact was shown [15,16] to be characterized as a four-step process:

- (i) initial shock (Hugoniot pressures) caused by a sudden decrease in speed of a soft-body projectile at the initial impact (stagnation) point
- (ii) impact shock decay via relaxation waves propagating from the free surface of the projectile.
- (iii) steady-state fluid jet flow developing a stagnation pressure.
- (iv) finally flow and induced load decay.

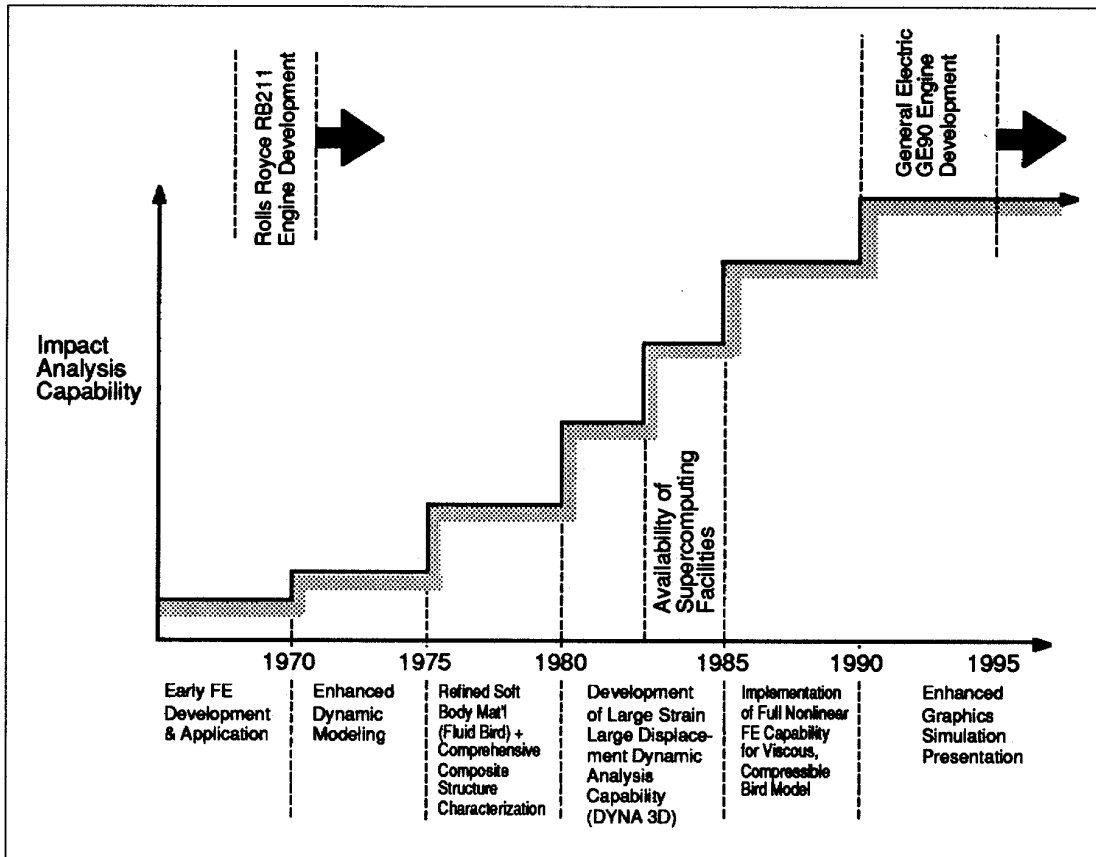


Fig. 4: Historical development of impact analysis technology

It is characteristically found that predictions based on the above approach generally concur with experimental results specifically with regard to transmitted stresses near the trailing edge several milliseconds after the initial impact. In fact damage or loss of material near the trailing edge tip is typically observed during experimental bird impact simulations and this was indeed the case in GE90 fan blade development testing. Predictions also indicated that impact induced stresses are subsequently transmitted to the root in the trailing edge area several milliseconds later; again this has been confirmed during experimental evaluations.

It was also shown that, experimentally, gelatin material was a suitable soft body substitute for bird-like projectile confirming that established and used earlier by Rolls Royce [12] and others [17,18]. Simple one-dimensional analytical predictions are also available such as that of Cassenti [19] who showed that, for perpendicular impacts the Hugoniot pressure is given by the water hammer pressure; i.e.

$$p_H = \rho_0 C_0 u_0 \tag{1}$$

where

ρ_0 is the material density at the nominal pressure

C_0 is the velocity of sound in the fluid body, for small disturbances

u_0 is the nominal initial velocity of the projectile

The stagnation pressure is given by:

$$p_s = \frac{1}{2}\rho_0 u_0^2 \quad (2)$$

By application of equations (1) and (2), a rough estimate of the pressures developed at the impact center can be obtained. The possibility that delamination damage may be created by the high, short pulse, Hugoniot pressure remains unproven with regard to its potential significance in degrading the composite target (blade) integrity.

With the advent of supercomputing capability in the mid 1980's and the development of high rate, large displacement, nonlinear flow modeling and analysis for ductile metals, represented by software developments such as DYNA 3D, growth in soft body impact analysis capability was extensive, see Niering [20]. At about the same time the capabilities for modeling geometrically complex blade targets exhibiting centrifugally load-induced nonlinear deflections and comprised of highly anisotropic, heterogeneous laminated composites had reached a relatively mature level.

Clearly, the growth in sophistication of physical simulations, and associated commercial modeling and analyses of the bird and the composite fan blade target presented a major advantage for GE's development of the GE90 blade relative to the primitive state-of-the-art existing at the time of the initial Rolls Royce RB211 fan blade development. More significantly, the designer can now conduct more meaningful evaluations of the complete containment event in developing designs for new systems to combat bird ingestion and its consequences.

INTEGRATED PRODUCT & PROCESS DEVELOPMENT PHILOSOPHY

The development of the GE90 Composite Fan Blade (Figure 2) serves as a classic example of the successful utilization of concurrent engineering approaches that embody a strong multidisciplinary posture in contemporary industry. With the adverse history of the earlier Rolls Royce experience with the RB211 engine and the negative attitudes that had "shadowed" that era of aggressive composite utilization it was a particularly formidable challenge for General Electric to commit to the GE90 fan blade development. In retrospect it is clear that GEAE had formed the vision that the increased by-pass ratio and thrust, the increased blade size and lower tip speed, see Table 1, presented a scenario that merited revisiting the application of composites. This vision is apparent from a review of the papers presented by Hauser & Elston [21] and by Elston [22] wherein credits are attributed to the excellent execution of component/product design based on the integration of material selection, manufacturing process definition and rigorous development evaluation.

Elston [22] discusses the benefits in overall engine reliability and performance and to customer (airline) acceptance derived, in addition, from the design attention to maintenance and overhaul features. Specifically the high thrust and enhanced fuel economy are introduced together with substantial reductions in noise and emissions. Numerous lessons learned from GEAE development such as the Unducted Fan (UDF) engine developed under the GE/NASA

Energy Efficient Engine program proved to be invaluable for the overall GE90 engine development.

The initiatives based on integrated product and process development (IPPD) and concurrent engineering was extended to external interactions with the airframe manufacturer, i.e. Boeing's 777 team, as well as subcontract suppliers and airline representatives.

Interestingly, Miller [1] projects the Rolls Royce philosophy advocated for the development of their advanced line of high by-pass ratio aeroengines, the RB211 and Trent families. Interdisciplinary collaboration between material scientists, design and manufacturing engineers, representative of the same concurrent engineering philosophy utilized by GEAE, was a continuing theme in the recent presentation by Miller [1]. However, Rolls Royce offers an alternative form of fan blade design, i.e. a hollow titanium construction. The engineering and manufacturing development of the wide chord hollow titanium fan blade is described by Miller [1] as, "an excellent example of simultaneous engineering-design for a controllable manufacturing process as well as for product duty". It is also noteworthy that the hollow titanium fan blade design and development began at the time that the original RB211 PMC fan blade was being abandoned to be replaced by the shrouded solid titanium design configuration, as mentioned previously.

Only time will tell which fan blade, the GE90 Composite or Rolls Royce hollow titanium, will prove to be superior over a long period of service. The comparisons illustrated on Figure 1 indicate that the latter will tolerate higher tip speeds although many other engine parameters and geometrical factors may be responsible for the operational superiority of the two competing engines. Some have expressed concern regarding the long term fatigue/durability of the hollow-titanium construction. Undoubtedly such comparisons, other than the thrust rating and specific fuel consumption (SFC), are exceedingly difficult to determine in quantitative terms.

CERTIFICATION AND MAINTENANCE ISSUES

First the general operational requirements associated with large fan blades are significantly different from those for aircraft structures for which the large proportion of data and documentaton is available [23, 24]. Moreover, these fan blade requirements also differ from those typical of other components in engine structures that are in use or under consideration regarding projected composites utilization. The differences bear close similarity with the situation for the rotorcraft industry wherein rotor blade engineering development and production receives special treatment relative to typical static, fuselage structures, fairings, etc.

As a consequence it is of no surprise that certification strategies tend to be substantially different for large fan rotor blades vis a vis other aeroengine components. Primary reasons for this situation are also associated with environmental and maintenance considerations for which extreme temperature exposure as well as low velocity damage of relatively thin gage structures represent driving concerns. For the case of large fan blades the bird ingestion criteria usually dominates the overall design approach. The range of temperature experienced by the major proportion of the fan blade configuration high bypass ratio engines does not, typically, cause major concern. This scenario results from the higher impact velocities created at take-off engine rpm in conjunction with moderate aircraft forward speeds.

A striking example of the uniqueness involved with the certification of composite fan blades was provided during the development and certification of the GE90 blade. Although the general airworthiness requirements are detailed in Section 33.77 of the Federal Aviation Regulations (FAR) Part 33 [25] it also became necessary for the Federal Aviation Administration (FAA) to develop a “Special Conditions” document [26] covering the specific design aspects of the GE90. However, as stated reference [26] does not represent a standard for general applicability to other composite fan blades. Nevertheless, future engine developers introducing composite fan blades would be advised to review [26] very thoroughly and should contemplate the possibility of a somewhat different set of special conditions. It is especially noteworthy that GEAE also faced the increased bird ingestion guidelines recently imposed by the FAA which call for a demonstrated capability for ingestion of an 8 lb. bird with a safe engine shutdown. The corresponding large bird requirement was previously 4 lb.

The economics-driven issue of maintenance also poses special challenges for composites. Current attention to related composite repair procedures have identified this subject as critical to future airline acceptance. Surveys have indicated that the cost and time of composite repair and the availability of suitable repair materials are common reasons for the concern. Again most of the surveys apply to secondary aircraft structure (airframe) repairs and therefore, with reference to composite fan blade applications, they should be taken as general operational experiences that do not usually apply directly to rotating, blade components.

Specifically for the composite fan blade scenario, results have shown that damage levels below visual detectability are unlikely to pose a threat to structural integrity. The most susceptible area experiencing moderate damage levels is usually in the vicinity of the leading edge where it has been demonstrated that the metallic leading edge guard in this area can be “dressed” in the instances to provide satisfactory structural performance as well as cosmetic appearance. Naturally, blade replacement would be necessary after incidents such as large bird ingestion.

CONCLUDING REMARKS AND FUTURE OUTLOOK

The above discussion has, hopefully, illustrated that the dramatic advances in materials performance, both fiber and matrix, together with substantial enhances in design, analysis and processing accounts for the notably successful GE90 composite fan blade. Contemporary trends in high by-pass ratio aeroengines has generally supported the introduction of composites on account of larger blade sizes and lower tip speeds. But several items of concern remain; examples being the effort required to certify large composite fan blades and the related prospect of other “special conditions” to be satisfied.

Existing capabilities for soft body impact prediction, now under consideration, should be further enhanced specifically for more rigorously characterizing the composite fan blade structure in both the aerofoil and the blade root region. Failure criteria and progressive damage models that reflect rate dependent behavior must be refined so as to provide improvements to current capabilities [27, 28] now commonly used in the available software systems such as DYNA3D and MSC/DYTRAN. These capabilities should be coordinated with carefully-instrumented experimental programs. To establish refined correlations more extensive use of of-embedded sensor technology should be utilized to effect greater insight and understanding of the characteristics of composite fan flade in operation, particularly under the critical bird ingestion loading.

There is an imminent need for more representative damage modeling and the interrelated failure criteria that are applicable to composite fan blades during the severe soft body impact condition. Better information on the strain rate effects, for which preliminary research has been reported by Cairns [8,9], could provide a useful background for conventional composites. However, the future of integral fiber architecture can only be meaningfully assessed if the analysis methods now evolving are carefully correlated with high quality experimental work.

ACKNOWLEDGEMENTS

Grateful acknowledgements are due to United Technologies, Pratt & Whitney (UT/P&W) and General Electric Aircraft Engines (GEAE). Specifically the author extends his personal thanks to *Dr. Karl M. Prewo* of United Technologies Research Center (UTRC) for several valuable discussions and for suggesting that this contribution be presented at ICCM-II and to the financial support of UTRC management during a short sabbatical as Visiting Scientist. *Dr. Tom Vasko* and several colleagues at UTRC are also acknowledged for numerous technical interactions and technical discussions during the preparation of this paper. A special thanks also to *Dr. James C. Williams* and *Douglas D. Ward* of GEAE for their kind cooperation in providing details, data and illustrations related to the GE90 composite fan blade as well as several technical discussions.

REFERENCES

1. S. Miller, "Advanced Materials Mean Advanced Engines", *Interdisciplinary Science Reviews*, Vol. 21, No. 2, 1996; Also 'The Institute of Materials, Third Finnieston Lecture', London, 5 June 1996.
2. J.I. Goatham, "Design Considerations for Large Fan Blades", SAE National Air Transportation Meeting, New York, April 21-24, 1969.
3. J.I. Goatham, "Materials Problems in the Design of Compressor Blades with Fibrous Composites", *Proc. Roy. Soc. Lond. A.* 319, pp. 45-57 (1970).
4. K.T. Kedward, "The Application of CFRP to Aero Engine Components", *Int. Conf. on Carbon Fibers, Their Composites, & Applications*, The Plastics Institute, London, 1971.
5. G.B. McKenna, J.F. Mandell, & F.J. McGarry, *Soc. Plastics Industry*, Annual Technical Conference, 1974, Section 13-C.
6. W.D. Bascom, J.L. Bitner, R.J. Moulton, & A.R. Siebert, "The Interlaminar Fracture of Organic Matrix, Woven Reinforcement Composites," *Composites Journal*, pp. 9-18, January, 1980.
7. NASA Langley Research Center, 'Tough Composite Materials: Recent Developments,' Noyes Publications, 1985.
8. D.S. Cairns, "Static and Dynamic Strain Energy Release Rates in Toughened, Thermosetting Composite Laminates," *Proc. 9th DOD/NASA/FAA Conference on Fibrous Composites in Structural Design*, November 4-7, 1991.
9. D.S. Cairns, "Static and Dynamic Mode II Strain Energy Release Rates in Toughened Thermosetting Composite Laminates," *ASTM Journal of Composites Technology & Research*, 14, 1, pp. 37-42, Spring 1992.

10. M.B. Dow & D.L. Smith, "Damage Tolerant Composite Materials Produced by Stitching Carbon Fabrics," *International SAMPE Technical Conference*, 21, pp. 595-605, 1989.
11. B.N. Cox, M.S. Dadkhah, W.L. Morris, J.G. Flintoff, "Failure Mechanisms of 3D Woven Composites in Tension, Compression, and Bending," *Acta Metall. Mater.*, Vol. 42, No. 12, pp. 3967-3984, 1994.
12. K.H. Sayers, "Design & Analysis Methods for Soft Body Impact on Laminated Composite and Metal Jet Engine Fan Blades", *Fiber Science & Technology*, 8 pp. 173-206, 1975.
13. N.F. Martin, "Nonlinear Finite-Element Analysis to Predict Fan Blade Damage Due to Soft Body Impact", *J. Propulsion*, 6, 4, August 1990.
14. J.P. Barber & J. Wilbeck, "Bird Impact Loading", Government/Industry/University Workshop on FOD of Composite Blades", NASA Langley Research Center, March 1977.
15. J.P. Barber, H.R. Taylor & J.S. Wilbeck, "Bird Impact Forces and Pressures on Rigid and Compliant Targets," Air Force Materials Lab., Wright-Patterson AFB, OH, AFML-TR-77-60, May 1977.
16. J.P. Barber, P.F. Fry, J.M. Klyce & H.R. Taylor, "Impact of Soft Bodies on Jet Engine Fan Blades," Air Force Materials Lab., Wright-Patterson AFB, OH, AFML-TR-77-29, April 1977.
17. J.S. Wilbeck, "Bird Impact Loading," *Proc. Shock and Vibration Bulletin*, Vol. 48, pp. 115-122, 1978.
18. J.S. Wilbeck, 1981, "The Development of a Substitute Bird Model," *ASME Journal of Engineering for Power*, Vol. 103, pp. 725-730, 1981.
19. B.N. Cassenti, "Hugoniot Pressure Loading in Soft Body Impacts", *AIAA Paper No. 79-0782*, 20th AIAA/ASME/ASCE/AHS Structures, Structural Dynamics & Materials Conference, April 4-6, 1977.
20. E. Niering, "Simulation of Bird Strikes on Turbine Engines", ASME, Trans., J. of Engrg. for Gas Turbines & Power, 112, October 1990.
21. A.A. Hauser & S.B. Elston, III, "Aero-Engine Reliability - A GE View", AIAA Conference, Bristol, UK, 9 October 1991.
22. S.B. Elston, III, "GE90 - The Next Era in Aircraft Engine Technology and Reliability", International Society of Flight Safety Investigation, Dallas, Texas, 2 September 1992.
23. Anon., Federal Aviation Regulations (FAR), Part 25, Airworthiness Standards: Transport Category Airplanes, Dept. of Transportation, Federal Aviation Administration, December 1978.
24. Anon., Advisory Circular 20-107, Composite Aircraft Structure, Federal Aviation Administration, July 1978.
25. Anon., Federal Aviation Regulations (FAR), Part 33, Airworthiness Standards: Aircraft Engines, Dept. of Transportation, Federal Aviation Administration, January 1994.
26. Anon., Federal Aviation Administration, 14 CFR, Part 33; Special Conditions No. SC-33-ANE-08, Special Conditions; General Electric (GE) Aircraft Engines Models, GE90-Series of Turbofan Engines, Effective Date: March 6, 1995.
27. Y. Murray & L. Schwer, "Implementation & Verification of Fiber-Composite Damage Models", DYNA3D User's Manual, Lawrence Livermore National Laboratory, Report UCID-19592, May 1989.

28. Y.D. Murray, "Fibrous Composite Laminates: An Introduction to the Theory, and Verification of the DYNA3D Implementation," APTEK Inc., San Jose, California, DNA-TR-88-191, August 1988.

CAN BRAIDED COMPOSITES BE USED FOR CRUSHING ELEMENTS IN CARS ?

Hiroyuki Hamada

*Faculty of Textile Science, Kyoto Institute of Technology
Matsugasaki, Sakyo-ku, Kyoto 606, Japan*

SUMMARY: In this paper, braided composite I-beams are considered as possible candidates for crushing elements in cars. A description is given on the braiding process and the various mechanisms which can be used to produce different types of braided preforms, including I-beams. The mechanical performance of these braided I-beams under four-point bending is presented. The I-beams are also loaded in compression to investigate their progressive crush performance. The introduction of a chamfer on one end of the beams enabled high energy absorption values to be achieved through progressive crush. Investigation into the crush zone of partially crushed I-beams was also carried out to determine the energy absorption mechanisms which exist in such structures. A database of crush performance values (specific energy absorption) of composite tubes for a range of material systems is also presented, which has the potential to be used in the design of composite beams for crush elements in cars. From the crush and bending tests, it is concluded that the use of a braided composite in a car body is highly possible. To do so, several issues need to be addressed which are identified and discussed in this paper.

KEYWORDS: energy absorption mechanism, braids, I-beam, progressive crushing, bending properties, side member, glass fibre, impact test

INTRODUCTION

Recently, the increase in vehicle numbers has led to a rise in traffic accidents compared to the development of transportation. Consequently, there is a great demand on passive vehicle safety. In experiencing large impact, a rigid passenger compartment is needed to prevent harm to the occupants, which results in an increase in the vehicle weight. However, this leads to high impact energies and decelerations in vehicle collisions which has the potential to cause irreversible brain damage to the occupants. Therefore, the structural requirements of the passenger compartment should include high strength and light weight. Application of fibre reinforced plastics (FRP) to vehicle compartments can satisfy these requirements.

In the automotive industry, FRP have been used in applications such as bumpers, side panels and bonnet components, and has also become prominent in secondary structural components. However, despite the improved performance capabilities of FRP, the inherent high-costs associated with FRP restricts their use to high-performance niche applications.

It has been reported [1-6] that FRP tubes under axial compression load display high energy absorption performance, so that it is possible to protect occupants in a front collision by arranging the composite tube in front of a vehicle body, such as behind the bumper. To initiate crushing, a chamfer trigger is incorporated on one end of the tube. Failure starts at the

chamfered end, and the crushing zone propagates down the tube without catastrophic failure. This fracture behaviour is called progressive crushing.

The crashworthy performance of materials is commonly expressed with the specific energy absorption value, E_s , which is expressed by the following equation:

$$E_s = \frac{\bar{P}}{A\rho} \quad (1)$$

where, \bar{P} , A and ρ are the mean crush load, cross-sectional area and density, respectively. A unit is expressed by kJ/kg. For example, E_s of steel tube is 30 kJ/kg, whereas E_s of a glass cloth/epoxy composite tube is 70 kJ/kg. Progressive crushing behaviour contributes to the high E_s values of FRP.

In this paper, it is discussed whether or not it is possible for braided composites to be used in a car body as crush elements. Firstly, the braiding mechanism used to produce new braided fabrics is introduced. The most important point in the mechanics of braided composites is continuity of the reinforcing fibres. Although various braided fabrics were discussed in this paper, the concept of continuity was maintained in all the braids. Also, the mass production technique, referred to as Braiding Pultrusion Processing (BPP), which is expected to lead to a wider usage of braiding, is highlighted.

Secondly, the bending properties of braided I-beams are investigated. Among various kinds of braided fabrics, an I-beam was selected for crush elements of a car. The reason for this is that in Japan, about 23% of crush accidents resulting in fatalities are attributed to side impact [7]. It is necessary to consider not only front collision but also lateral collision in the design of a vehicle. The introduction of side impact bars has the potential to prevent fatalities resulting from side impact. Side members with I-shaped cross-sections can possess high bending strength due to the large second moment of area. If braided I-beams can be produced with high bending and crush properties, they would be ideally suited as side impact members.

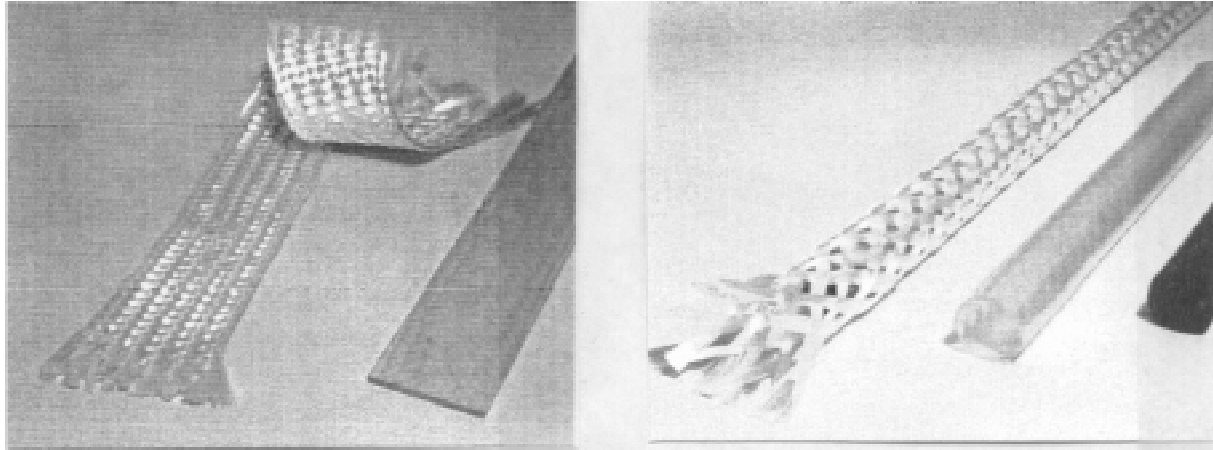
Thirdly, the progressive crush behaviour of various composite tubes are presented in detail. This includes values of E_s for many kinds of material systems. It is emphasised that precise observation of fracture aspects is important in order to clarify the crushing mechanism. Finally, the crushing performance of a braided composite I-beam is described. The braided I-beam was found to possess high crush performance with an E_s value of 70 kJ/kg. The fracture mechanism is examined through observation of the crushed I-beam cross-section. The crush behaviour of the braided I-beam was found to be similar to that of a 0/90° tube. It is concluded that the use of a braided composite in a car body is highly possible.

BRAIDED I-BEAM

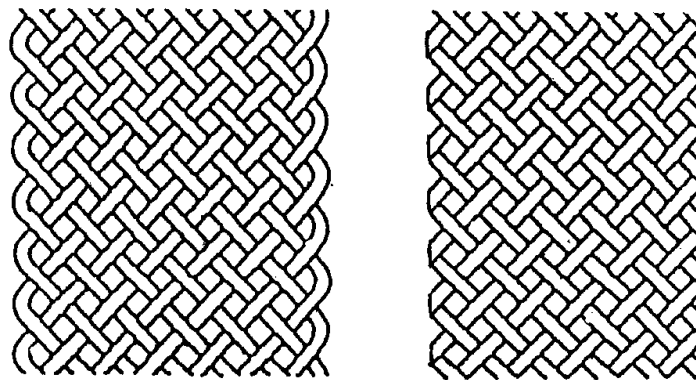
Braided Fabric

There are two kinds of basic braids; flat braid and tubular braid as shown in Fig. 1. The flat braid can be used to produce flat plates, whereas cylindrical shapes can be made from tubular braids. Fig. 2 shows schematically the fibre orientation state of the flat braid. The normal braided flat bar (see Fig. 2a) and that with the side edges cut off (see Fig. 2b) are referred to as "Non-cut" and "Cut" respectively. To compare the mechanical properties between Non-cut and Cut composites, tensile tests were carried out [8]. Tensile stress-strain curves of the composites are shown in Fig. 3. With the Non-cut specimens, the tensile stress increased linearly until it reached the maximum stress, while with the Cut specimens, the gradient of the

curve gradually decreased until the stress reached the maximum value. The maximum stress of the Non-cut specimens was much higher than that of Cut specimens. It can be said that the continuity of the fibres at the side edge strongly affects the tensile properties. Thus, in regards to continuous fibres, braided composites have superior characteristics compared to other fibre reinforced composites.



(a) (b)
 Fig. 1: Photographs of (a) flat braids and (b) tubular braids



(a) (b)
 Fig. 2: Schematic diagrams of (a) Non-cut and (b) Cut specimens

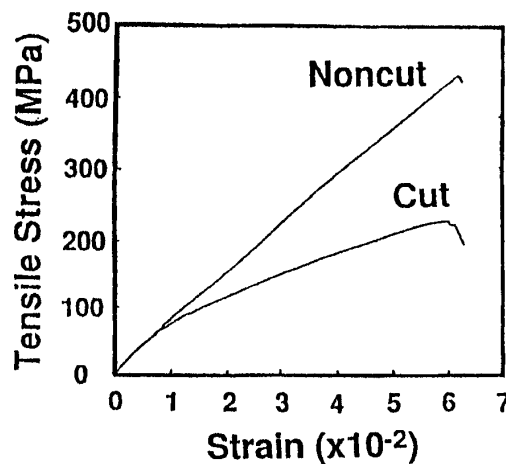


Fig. 3: Typical tensile stress-strain curves of Non-cut and Cut specimens

The importance of continuous fibres is highlighted in the mechanical joint problem. Fig. 4 shows schematically the fibre orientation around a hole. In the BH specimen, the fibre is

continuously oriented around the hole, whereas the fibres are discontinuous in the drilled hole of the MH specimen. Both specimens are used in mechanical joint test as shown in Fig. 5a. Fig. 5b indicates the load-displacement curve resulting from these joint tests. Clearly, the BH specimen has higher joint strength. Here, continuously oriented fibres are important for mechanical properties of composites, which can be easily realised by the braiding technique.

Braiding Mechanism

The conventional braiding mechanism consists of a taking up mechanism and spindle movement as shown in Fig. 6. Spindles move along the circle, which can be regarded as one-dimensional movement (1D). The formed fabric is taken up in the vertical direction, which is also regarded as one-dimensional movement (1D). Braided fabric with two-dimensional shapes such as flat and tubular braids can be fabricated with a combination of these two one-dimensional movements ($1D + 1D = 2D$).

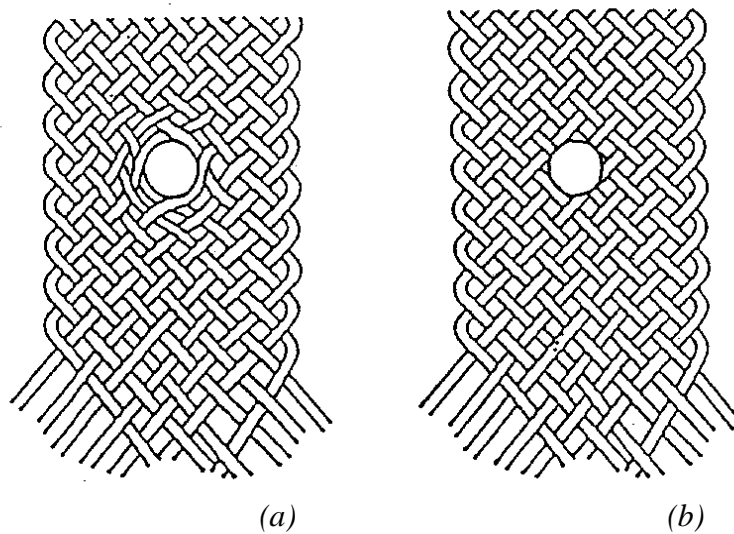


Fig. 4: Schematics of (a) braided hole (BH) and (b) machined hole (MH) specimens

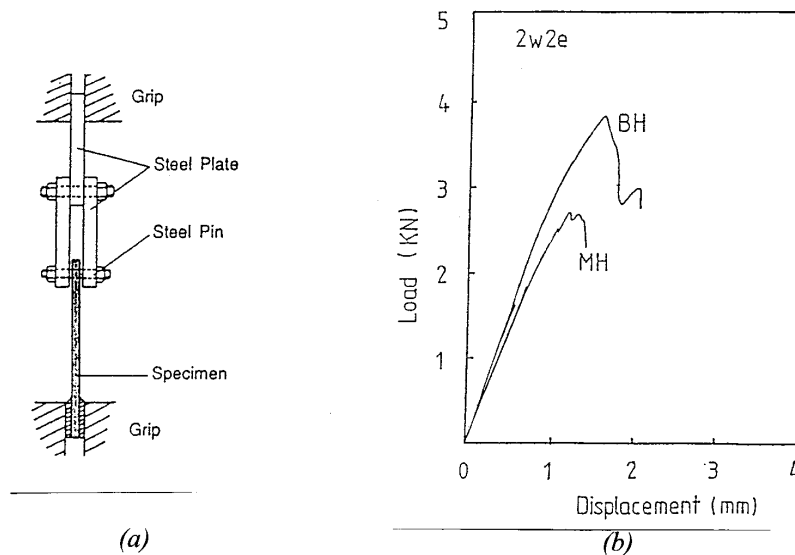


Fig. 5: Mechanical joint test: (a) Schematic of test set-up; and (b) Typical load-displacement response

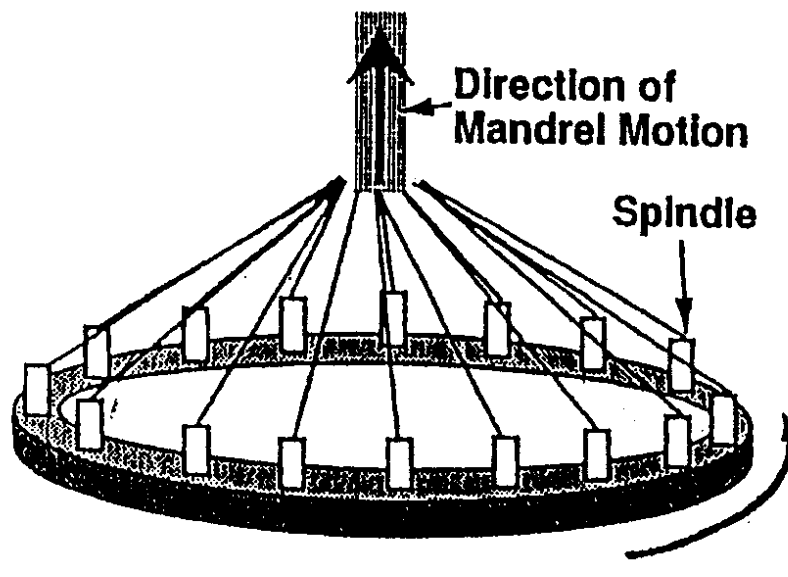


Fig. 6: The conventional braiding mechanism

Table 1: List of braiding mechanism from low to high dimension

Taking up mechanism		Spindle movement
1-DS	+	1-DS
1-DR	+	1-DS
1-DS	+	1-DM
1-DS	+	2-D
3-D	+	1-DS

In order to fabricate near-net shape fabrics, new braiding mechanisms have to be considered. The concept of two sets of movement; taking up mechanism and spindle movement are very useful for creating new mechanisms. Table 1 lists our braiding mechanisms from low dimension to high dimension. The conventional braiding mechanism is indicated by 1-DS + 1-DS in this table. S refers to one way movement in the taking up mechanism and single truck in spindle movement. According to this table, new braiding mechanisms and fabricated braids are introduced in following sections.

1-DR + 1-DS

When reverse movement is applied to the taking up mechanism, which is referred to as 1-DR, the braided fabric returns in the opposite direction as shown in Fig. 7. If this reverse movement is repeated several times at certain intervals, and also the reversible points are changed during this process, a cylindrical braided through-the-thickness fabric can be produced as shown in Fig. 8. Interlaminar delamination would be suppressed by such through-the-thickness fabric due to interlamina reinforcement [9-14].

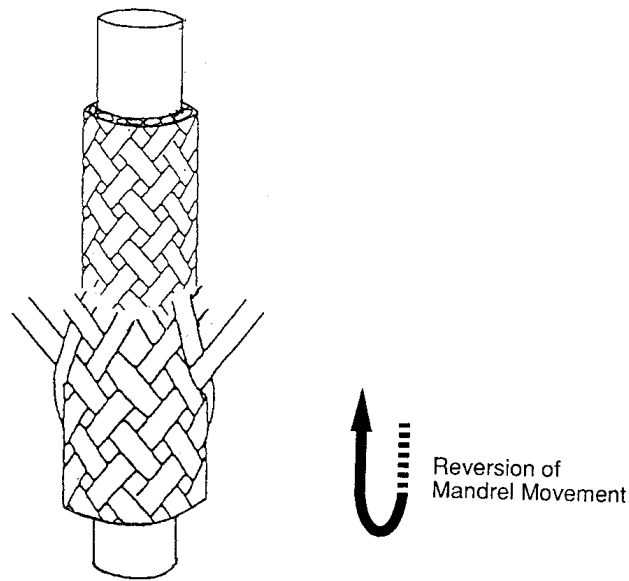


Fig. 7: The mandrel movement is reversed

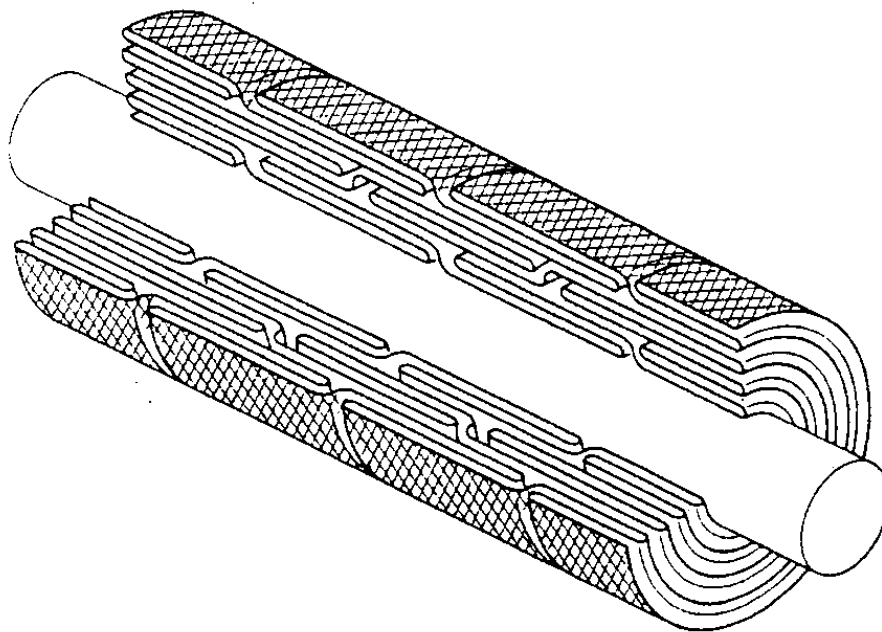


Fig. 8: Cylindrical braided fabric with through-the-thickness fabric

Static lateral compression tests are performed on new braided composite cylinders. Fig. 9 shows the relation between the lateral compressive load and displacement. The braided cylinders are also compared with conventionally laminated tubes. Specimens with only three layers were considered in this test program. As can be seen from Fig. 9, the new braided composite cylinders, referred to as multi-reciprocal tube, maintains a high load since interlamina fracture is suppressed at the reversible point where the through-the-thickness fabrics exist. Whereas a sudden load drop is observed in laminated tubes due to interlamina

fracture which is not retarded. This difference is confirmed by observation of the fractured specimens.

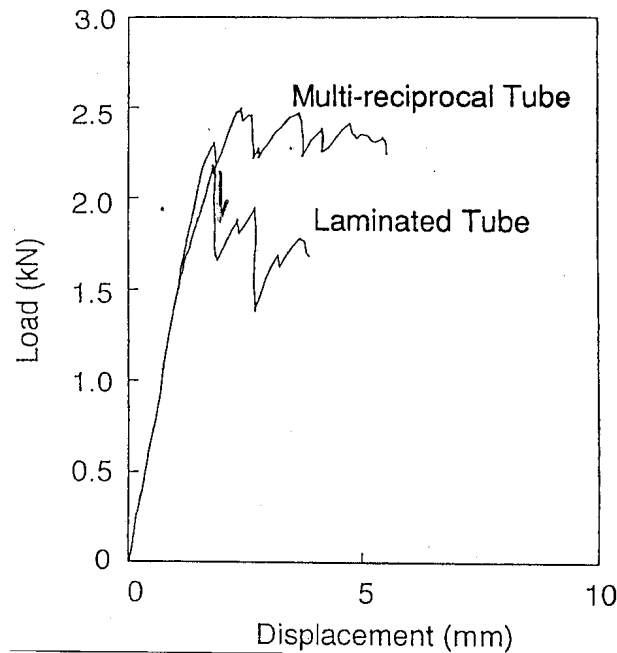


Fig. 9: Relation between lateral compression load and displacement

1-DS + 1-DM

In this process, although the taking up mechanism is still one way in one dimension, spindle movements are not single because there are several tracks. Fig. 10 shows one example of this braiding mechanism, where 3 tracks are connected at some points. The spindles can move from one track into another as shown in Fig. 10. In this case, the spindle which begins in the outer track travels into the middle track and finally the inner track. Based on this mechanism a very unique braided cylinder can be fabricated. For example, the fibre can pass from the outer layer to the middle layer, and from the middle layer to the inner layer providing interlamina reinforcement equivalent to that of the multi-reciprocal cylinder.

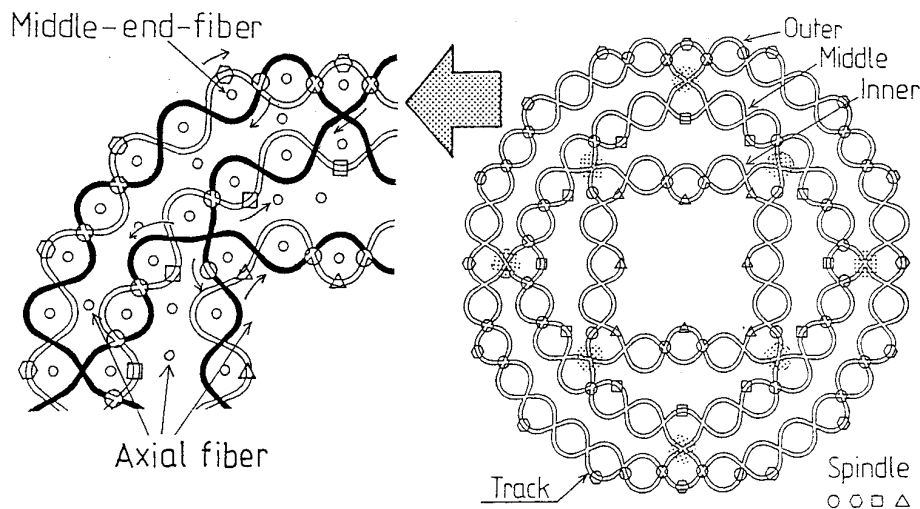


Fig. 10: Tubular braid with through-the-thickness fibres

Another example is shown in Fig. 11 and 12. A cylindrical braided fabric with core materials can be fabricated. Four core materials are inserted between inner and middle layers, and between middle and outer layers. In this braiding process, the thickness of braided fabric depends on the thickness of the inner, middle and outer layers and thickness of the core materials. A light weight and thick composite can be manufactured by adopting foam material as core material. Fig. 12 shows a cross section of the cylindrical braided composite without core material which exhibits cells which are isolated from one another. This pipe is expected to be used as multi-functional pipe which can send different fluid at once.

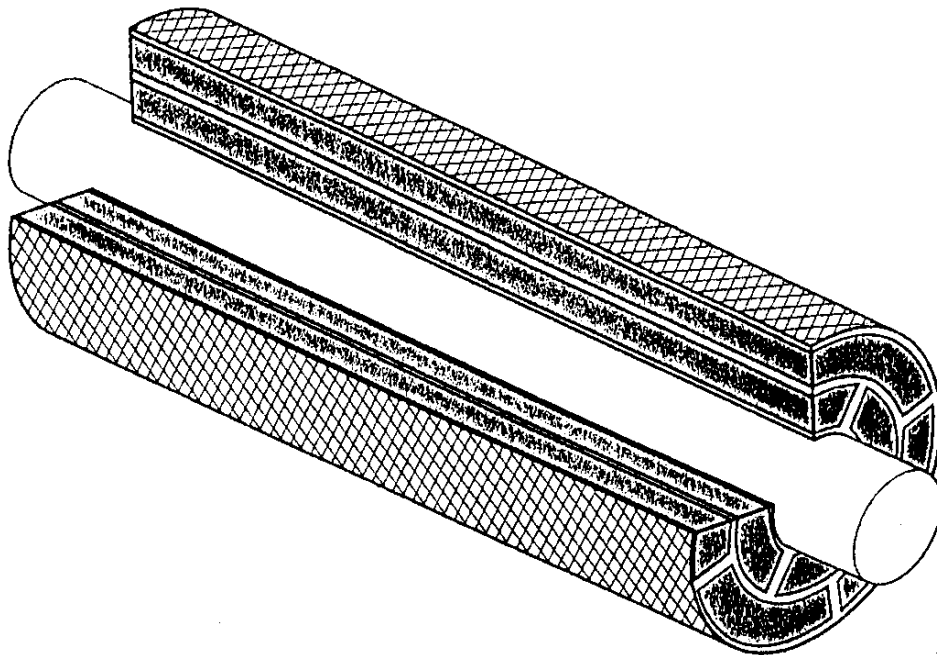


Fig. 11: Schematic of a cylindrical braided fabric with core materials

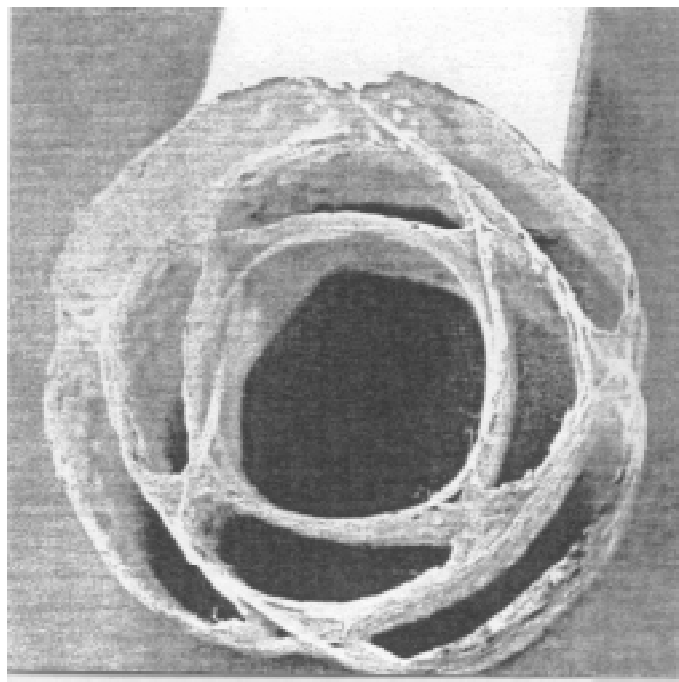


Fig. 12: Photograph of a cross-section of a cylindrical braided composite without core materials

1-DS + 2-D

This braiding mechanism is the most important in this paper, because braided I-beams can be fabricated by this process. In this process, the taking up mechanism is one dimensional and one way. The track configuration is modified two-dimensionally according to the shape of the final products as shown in Fig. 13. In this process the spindle movements become more complex than the previous braiding mechanisms. For example, inadequate initial spindle setting pattern can not fabricate braided fabrics because a collision of spindles would occur. Also, regularity of the braided fabrics is changed according to the spindle collision.

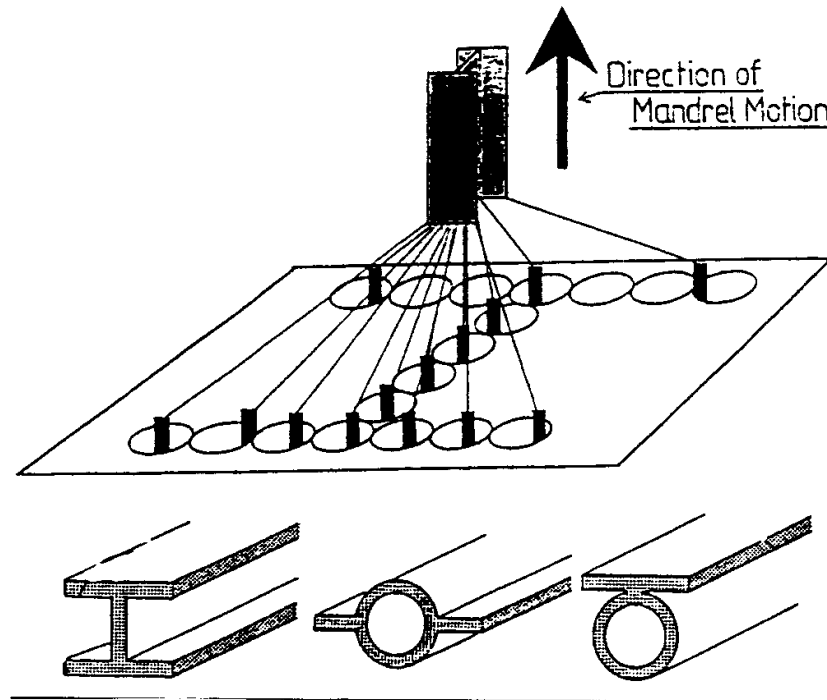


Fig. 13: Two-dimensionally modified track configuration

Computer simulation which can predict adequate initial spindle setting pattern and fibre orientation state of formed braided fabrics must be developed. Fig. 14 shows an example of results obtained from computational simulation [15]. Accordingly, complex fibre orientation state is visible. Therefore, CAE system is needed in the braiding process [16,17]. Fig. 15 shows the flow chart of the braiding CAE system (BCAE), which consists of the simulation program for the design of the braiding machine and the numerical analysis method for the design of the final component. The CAE system consists of three steps; braided fabric, braided composite and braiding machine. The track configuration of a braiding machine for integrated braids can be designed using the simulation program. The initial spindle setting patterns that could provide a braiding structure with regular weaving pattern can also be provided. Using the numerical analysis method, the mechanical properties and fracture aspects of integrated braided composites can be predicted.

Fig. 16 shows the braiding machine and track configuration used to produce the I-beam. The track configuration was obtained by BCAE. It should be emphasised that the reinforcing fibres in the braided I-beam preform are continuously oriented. In order to reinforce the I-beam longitudinally, middle-end-fibres and axial fibres can be inserted. Fig. 17 illustrates the braided fibres which are continuously oriented and surround the axial fibres. This architecture is useful in the crushing mechanism described later in the paper.

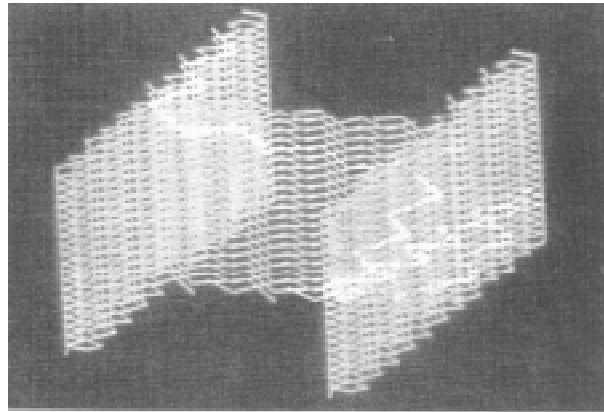


Fig. 14: A result of computational simulation

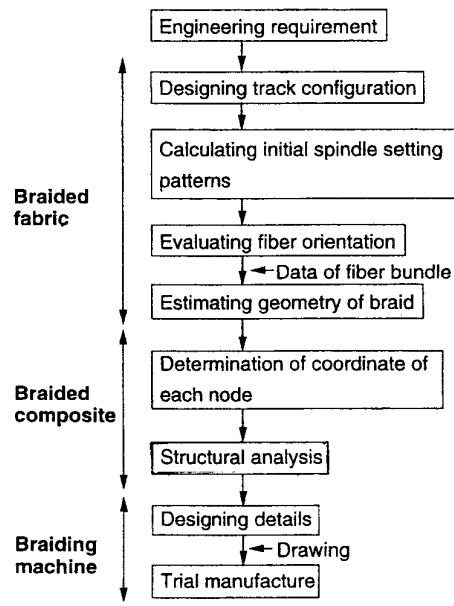


Fig. 15: The flow chart of the braiding CAE system

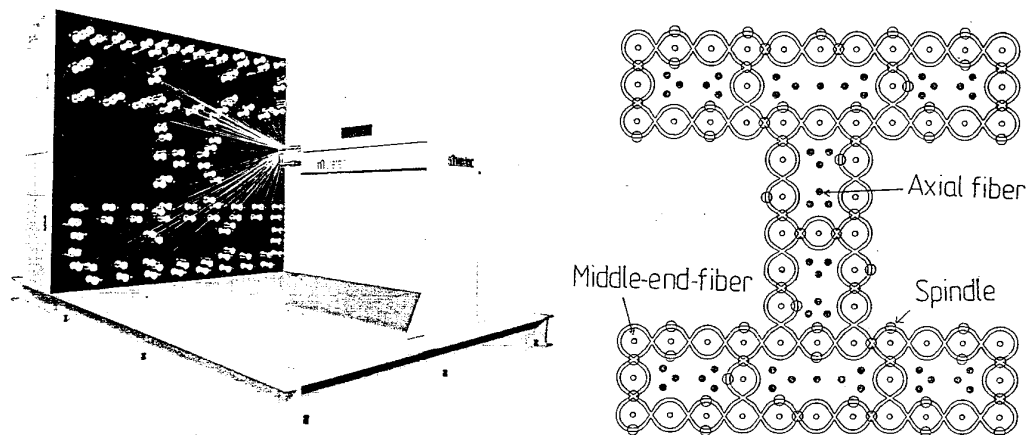


Fig. 16: Braiding machine for I-beam and subsequent track configuration

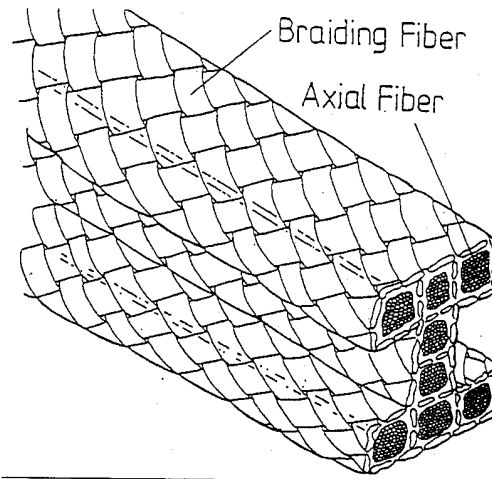


Fig. 17: Schematic of a braided I-beam with axial fibres

3-D + 1-D

This braiding mechanism is a very interesting system, where by the taking up mechanism is 3-dimensional in spite of the one dimensional spindle movement, as shown in Fig. 18. The mandrel can move up and down and also rotate in any direction. Using this braiding mechanism multi-axial pipes can be fabricated (Fig. 18). Also, reinforcing fibres are continuously oriented in these products which enables a very high joint strength to be achieved [18]. Designers do not have to pay attention to the joint strength by using this pipe. In order to make the braiding machine for these pipes, great effort was needed technically with BCAE being used to assist in machine design. Fig. 19 shows the braiding machine used to produce braids with multiple braiding axes.

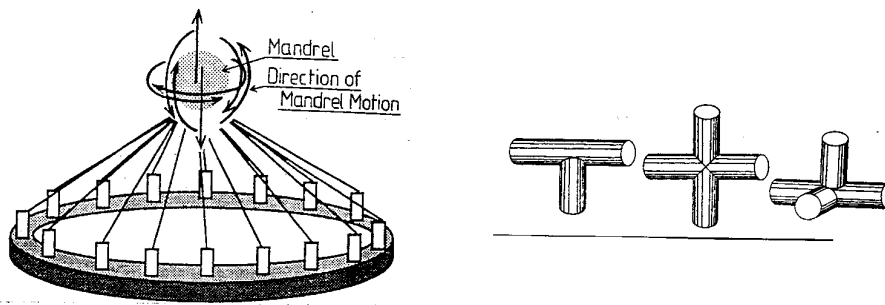


Fig. 18: Braiding mechanism for braid with multiple braiding axes

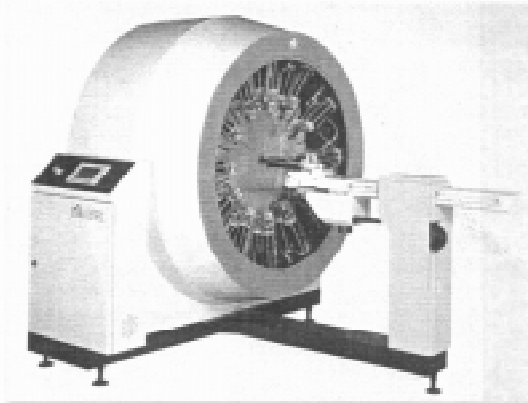


Fig. 19: Braiding machine for braid with multiple braiding axes

Braiding Pultrusion Process (BPP)

Resin impregnation for braided fabric is important mechanically and economically. Batch impregnation systems push up the cost of fabrication, so that continuous fabrication systems corresponding to mass production is needed.

Fig. 20 shows a schematic of the braiding pultrusion process [19]. Here, braided I-beams can be continuously fabricated. The impregnation device is placed between the braiding point and the braiding machine. Individual fibre strands under longitudinal tension meet the resin so that a higher degree of impregnation is achieved. Therefore at the entrance of the die, voids which may exist inside the braided fabric are squeezed out resulting in the completion of a high impregnation state. At the moment, the pultrusion conditions are as follows; pultrusion speed, pultrusion force and so on.

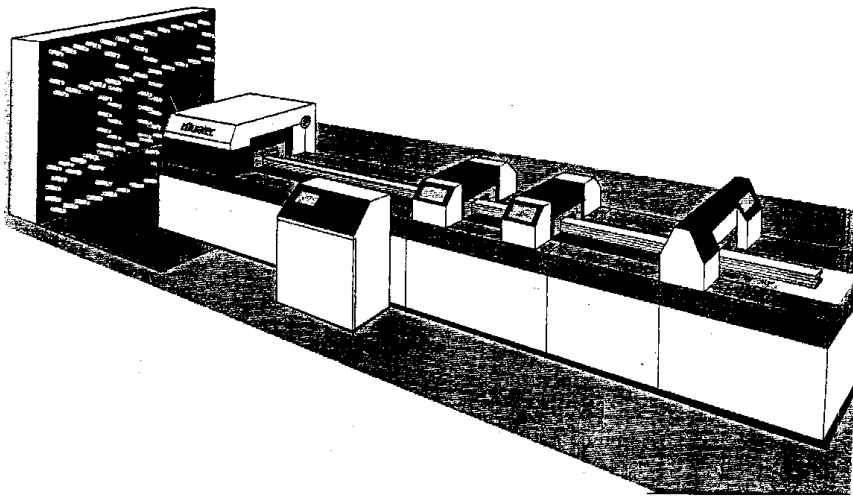


Fig. 20: Braiding pultrusion system

BENDING PROPERTIES OF BRAIDED I-BEAM

The braided fabric with I-shaped cross-section used in this paper consists of 63 glass fibre bundles (1150 tex, ER2310, Japan Electric Glass Co. Ltd.). The I-beam which consists of 100 unidirectional glass fibre bundles which were used as axial fibres in the flanges and web is referred to as G/G. While the I-beam with 76 carbon fibre bundles (800 tex, torayca, Tora Co.) used in the flanges and 24 glass fibre bundles in the web is referred to as G/CG. After impregnation with epoxy resin (EPIKOTE 828, Yuka Shell Epoxy Co. Ltd.) under vacuum, these I-beams were cured by the autoclave moulding method. The fibre volume contents were approximately 60%.

The dimensions of the bending specimen of the braided I-beam was approximately 18 mm in width and height. The thickness of both the flanges and web was 3 mm. Aluminium I-beams of the same dimensions were also prepared as a comparison. Four point bending tests with a 360 mm span and 120 mm mid span were conducted as shown in Fig. 21. Fig. 22 shows the relation between bending stress and deflection in three types of specimens. Bending properties obtained from experiment are summarised in Table 2. The bending strength of G/G and G/CG were 2.4, 2.8 times higher than that of aluminium, respectively. From these experimental results, it is understood that the braided I-beam has excellent bending properties.

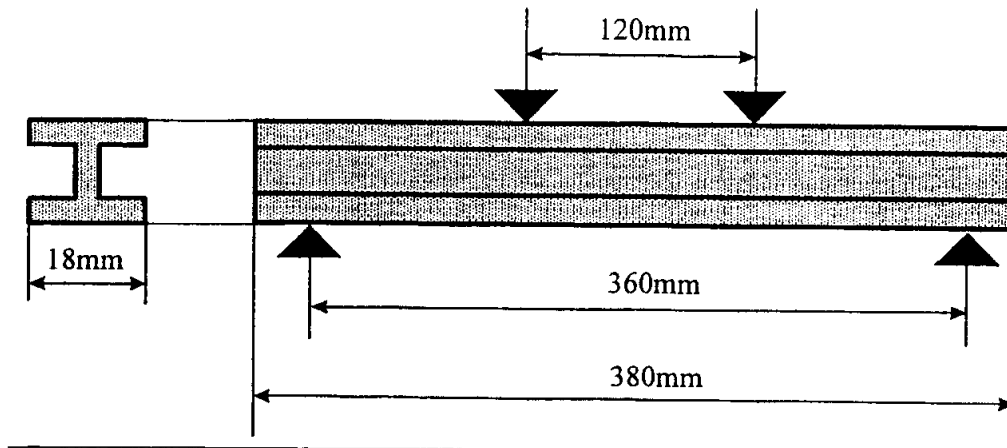


Fig. 21: Schematic of the four point bend test

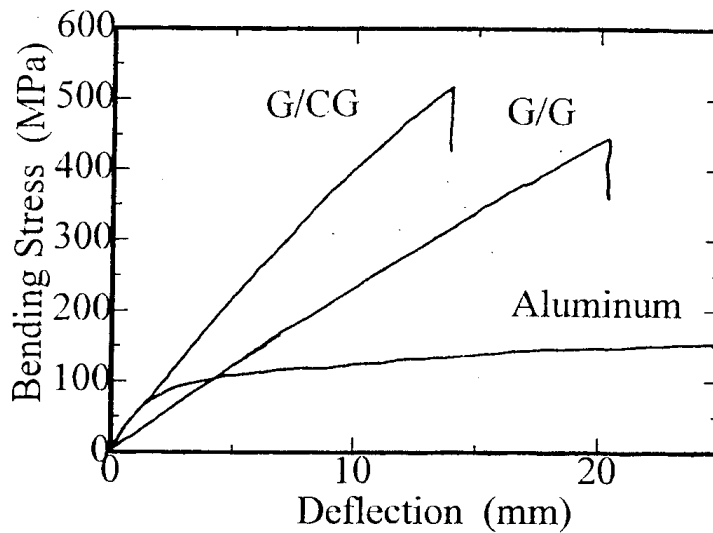


Fig. 22: Bending stress-deflection curves of three types of I-beam

Table 2: Bending modulus and strength under quasi-static condition

Specimen	Bending Modulus (GPa)	Bending Strength (MPa)
G/G	37.4	431
G/CG	73.5	520
Aluminium	71.8	183

PROGRESSIVE CRUSHING OF COMPOSITE TUBE

When an axial compressive load is applied to a composite tube, it leads to brittle fracture as shown in Fig. 23. The corresponding load-displacement curve is shown schematically in Fig. 24. On the other hand, when one end of the tube has a taper, this leads to progressive crushing because the tapered part acts as a trigger for fracture initiation. Fig. 25 shows the fracture mode and load-displacement curve of progressive crushing. The capability of energy

absorption for such a tube is very high because the enveloped area of the load-displacement curve is very large.

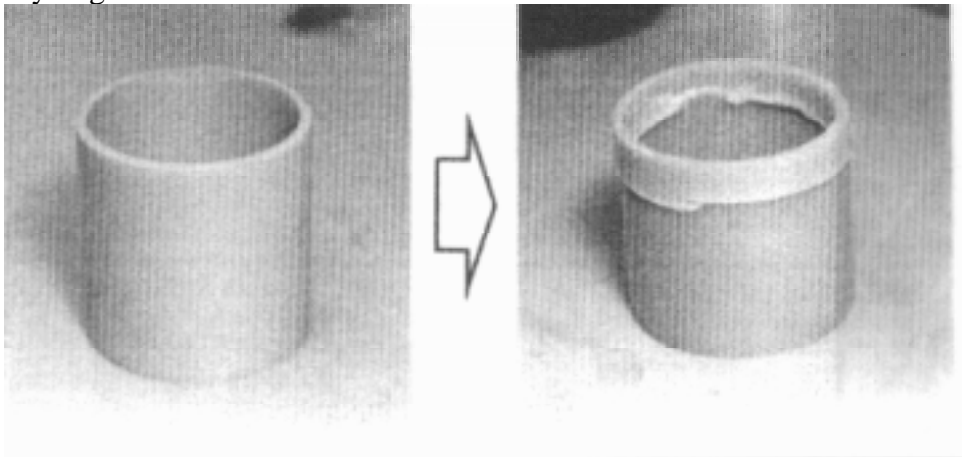


Fig. 23: Brittle fracture

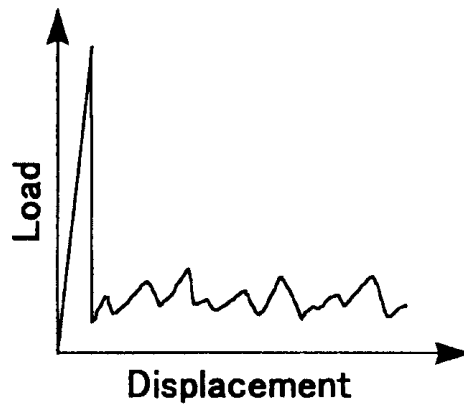


Fig. 24: Load-displacement curve of brittle fracture

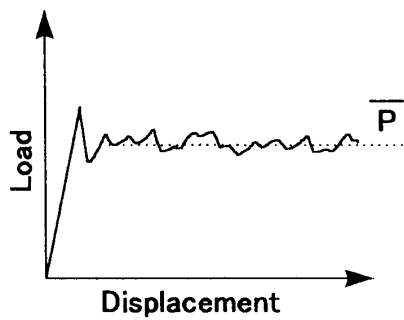
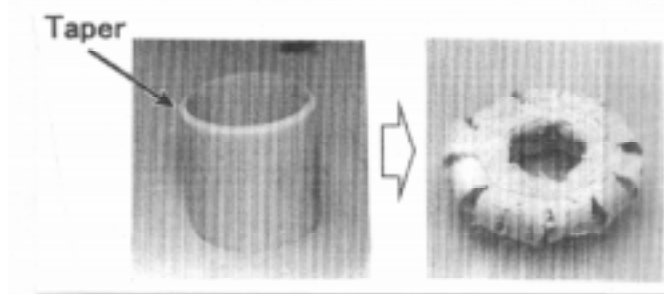


Fig. 25: Progressive crushing

Table 3 lists the specific energy absorption value (E_s) for various kinds of material systems [20-34]. E_s of carbon/PEEK exhibits the highest value and surprisingly in this data, a mean crushing load of 225 kN for a tube with an inner diameter of 50 mm and a wall thickness of 2.5 mm.

In the glass/epoxy composites, silane coupling agents are changed; one is amino silane and another is acryl silane. The former provides good adhesion but the latter does not. Fig. 26 shows the fracture aspects of crushed pipe in both material systems. The amino silane treated tube exhibits a splaying mode, whereas the acryl silane treated one shows a fragmentation mode. The properties of interface between fibre and matrix greatly affect the crushing behaviour. This result indicates the importance of interface.

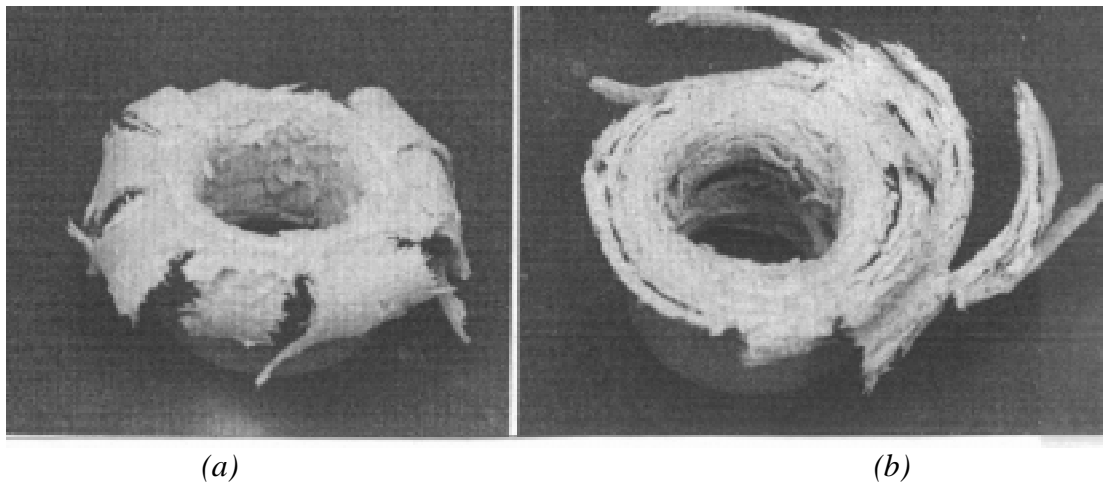


Fig. 26: Fracture aspects of glass/epoxy tubes treated with (a) amino and (b) acryl silane coupling agents

In order to understand the fracture mechanism of crushed tubes, precise observations are needed. Fig. 27 shows the polished cross section of a carbon/PEEK tube which achieved the highest specific energy absorption value. Not only are inter- and/or intra-delaminations are observed but fibre fracture into small segments can also be clearly seen.

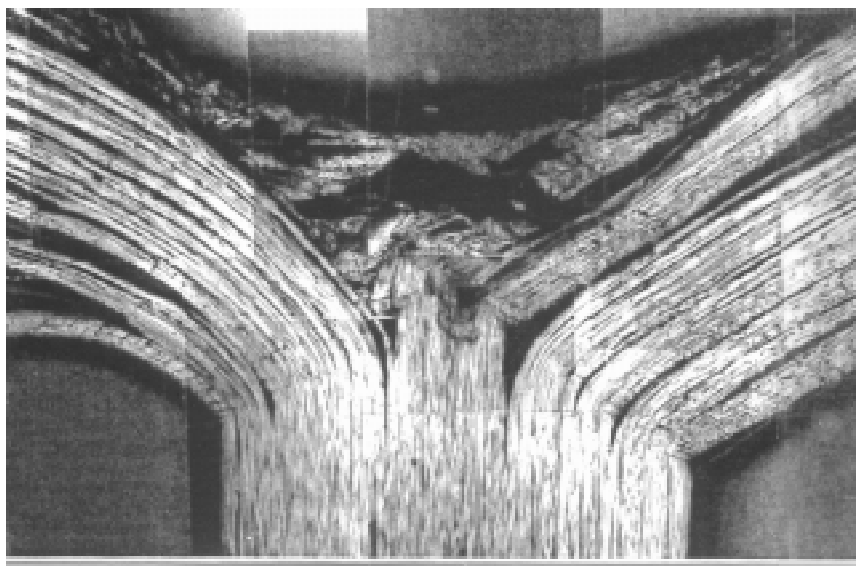


Fig. 27: Polished cross-section of carbon/PEEK

Table3-1 Energy absorption performances of metal tubes.

Material	(Quasi-static) Steel	(Impact)	(Quasi-static) Aluminum	(Impact)
Es (kJ/kg)	38.6	33.7	49.9	51.2

Table3-2 Energy absorption performances of glass cloth/epoxy tubes tested under different condition.

Test Condition	Quasi-static		Impact	
Surface Treatment	Amino	Acryl	Amino	Acryl
Es (kJ/kg)	66.6	53.0	69.5	61.4

Table3-3 Energy absorption performances of glass cloth/epoxy tubes tested at different temperatures.

Temperature (°C)	-140		-80		-40		20	
Surface Treatment	Amino	Acryl	Amino	Acryl	Amino	Acryl	Amino	Acryl
Es (kJ/kg)	104.3	90.1	96.6	68.4	79.0	57.2	66.6	53.0
Temperature (°C)	80		100		120		150	
Surface Treatment	Amino	Acryl	Amino	Acryl	Amino	Acryl	Amino	Acryl
Es (kJ/kg)	50.1	43.0	33.8	32.8	—	—	—	—

Table3-4 Energy absorption performances of glass cloth/epoxy tubes hydrothermally aged in 80°C water for different time.

Immersion Time (hrs)	0		30		100	
Surface Treatment	Amino	Acryl	Amino	Acryl	Amino	Acryl
Es (kJ/kg)	66.6	53.0	58.5	43.3	58.6	46.3
Immersion Time (hrs)	300		1000		3000	
Surface Treatment	Amino	Acryl	Amino	Acryl	Amino	Acryl
Es (kJ/kg)	51.5	32.5	48.5	30.8	44.5	29.2

Table3-5 Energy absorption performances of glass cloth/epoxy tubes exposed in weather meter for different time.

Exposure Time (hrs)	0		500		1000	
Surface Treatment	Amino	Acryl	Amino	Acryl	Amino	Acryl
Es (kJ/kg)	66.6	53.0	71.9	56.7	69.9	55.8
Exposure Time (hrs)	1500		2000			
Surface Treatment	Amino	Acryl	Amino	Acryl		
Es (kJ/kg)	71.7	56.7	73.4	55.8		

Table3-6 Effect of t/D ratio on energy absorption performances of glass cloth/epoxy tubes.

Number of Ply	2	4	6	8	16	24	32	40
t/D ratio	0.008	0.015	0.022	0.029	0.062	0.097	0.130	0.179
Es (kJ/kg)	—	—	172	172	206	207	155	141
Number of Ply	8	16	42	80				
t/D ratio	0.011	0.022	0.059	0.110				
Es (kJ/kg)	—	196	157	148				

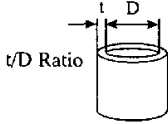


Table3-7 Effect of taper angle on energy absorption performances of glass cloth/epoxy tubes.

Taper Angle (°)	15	45	75
Es (kJ/kg)	67.9	66.0	67.1




Table3-8 Energy absorption performances of glass cloth/epoxy tubes in off-axis test.

Inclination Angle (°)	0	5	10	15	20	
Es (kJ/kg)	Quasi-static	68.8	67.2	65.3	58.1	43.1
	Impact	68.1	68.0	65.5	62.8	60.9

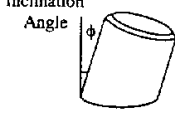


Table3-9 Energy absorption performances of glass cloth/epoxy tubes by using of the jig.

Jig	Flat Platen	For External Splaying Mode	For Internal Splaying Mode
Es (kJ/kg)			
Quasi-static	67.1	77.9	116.2
Impact	66.7	85.3	86.8




Table3-10 Energy absorption performances of glass cloth/epoxy tubes in different impact speed.

Impact Speed (km/h)	20.0	30.0	50.0
Es (kJ/kg)	68.6	71.8	69.4

Table3-11 Energy absorption performances of FW-FRP tubes with different fiber reinforcement under static condition.

Material	GF/Epoxy			CF/Epoxy			KF/Epoxy		
Fiber Orientation Angle (°)	±15	±45	±75	±15	±45	±75	±15	±45	±75
Es (kJ/kg)	39.8	25.3	40.7	70.3	22.6	53.3	25.6	33.5	41.6

Table3-12 Energy absorption performances of FW-FRP tubes with different fiber reinforcement under impact condition.

Material	GF/Epoxy			CF/Epoxy			KF/Epoxy		
Fiber Orientation Angle (°)	±15	±45	±75	±15	±45	±75	±15	±45	±75
Es (kJ/kg)	17.2	40.5	51.2	67.3	62.5	55.3	36.4	39.1	55.3

Table3-13 Energy absorption performances of CF/DF Hybrid FW tubes with different fiber architecture.

Fiber Architecture	DF100%		Interlamina CF/DF/CF		Intralamina CF/DF=1/1	Intralamina CF/DF=3/1
	±10	±30	±10	±30	±10	±10
Fiber Orientation Angle (°)	±10	±30	±10	±30	±10	±10
Es (kJ/kg)	29.0	—	67.1	31.0	48.0	76.4

cf. Dyneema is a ultra-high molecular weight Polyethylene fiber has high strength and modulus.

Table3-14 Energy absorption performances of CF/DF Hybrid Cloth tubes with different fiber architecture.

Fiber Architecture	DF100% Plain Cloth		Warp:CF, Weft:DF Plain Cloth		Warp,Weft:CF,DF Plain Cloth	
	0,90	±45	CF:0 DF:90	CF:90 DF:0	0,90	±45
Fiber Orientation Angle (°)	0,90	±45	CF:0 DF:90	CF:90 DF:0	0,90	±45
Es (kJ/kg)	32.1	—	49.5	35.5	47.3	49.0

Table3-15 Energy absorption performances of CF/PEEK tubes with different fiber orientation angle.

Fiber Orientation Angle (°)	0	±5	±10	±15	±20	±25	±30
Es (kJ/kg)	194	205	225	214	202	181	—

Table3-16 Energy absorption performances of Glass/PEEK tubes with different fiber orientation angle.

Fiber Orientation Angle (°)	0	±5	±10	±15	±20	±25	±30
Es (kJ/kg)	143	113	191	172	171	—	—

Table3-17 Effect of cooling rate on energy absorption performances of Carbon/PEEK 15° tubes.

Cooling Rate (°C/min)	Rapid Cooling -95.5	Gradual Cooling -8.2	Slow Cooling -0.7
Es (kJ/kg)	219	197	197

Table3-18 Energy absorption performances of CF/PEEK tubes under Impact condition.

Fiber Orientation Angle (°)	0	±5	±10
Es (kJ/kg)	91.2	99.3	98.0

Table3-19 Energy absorption performances of CFRTP tubes with different matrix resin.

Material (0°)	CF/PEEK	CF/PEI	CF/PI	CF/PAS
Es (kJ/kg)	225	155	131	128

According to these observations we propose an equation which describe the contribution of each fracture factors to total energy absorption value as follows:

$$U = U_{sp} + U_{lc} + U_{de} + U_{ff} + U_{fr} + U_{\sigma} + \text{others}$$

The detail of this equation is shown in Fig. 28. It is considered that the total energy absorption performance U in progressive crushing mainly consists of six energy absorption mechanisms. They are energy absorbed by the splitting of fronds, required for central crack, absorbed by delamination of fronds, required for fibre fracture, associated with frictional heating and that generated by bending deformation.

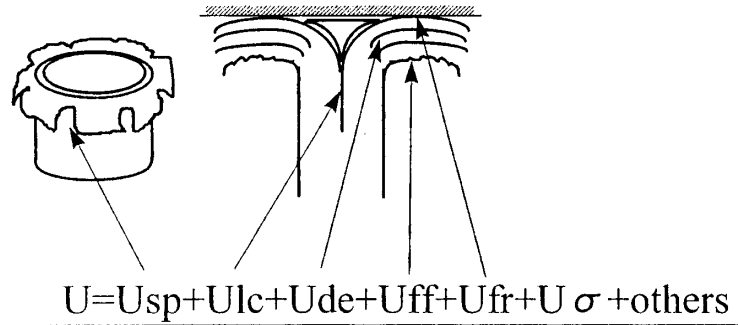


Fig. 28: Contribution of each fracture factor

It is clear that fracture aspects are very important for designing crushing elements. Therefore, a database was established for the crushing performances of composites, which can be easily used in the design of a car body. Fig. 29 shows a diagram of a system for both software and hardware. Software used in this study was for a normal database that can treat image data, because the fracture aspects should be included. The image data was input through an image scanner for published data and video signal port for a new result. In order to use large data memory an MO device was used for storing data. Main memory for using this database was only 0.6 MB.

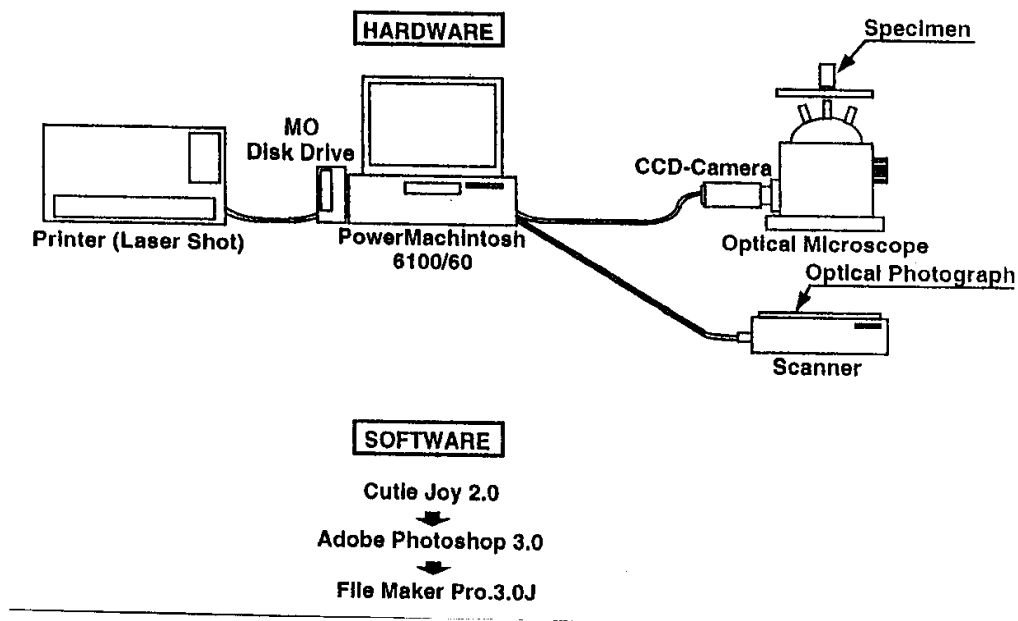


Fig. 29: Diagram of system for software and hardware

The database includes load-displacement curves, E_s values and other numerical data, out view of fractured materials, microscopic observations are included as well as material and experimental conditions.

CRUSHING BEHAVIOUR OF BRAIDED I-BEAM

Specimens and Experimental Method

Compressive tests under quasi-static and impact conditions were carried out in thickness, width and axial directions of braided I-beams (G/G type). The length of the specimens used in this study was 30 mm. To initiate progressive crushing a chamfer or notch was machined onto one end of the specimen as shown in Fig. 30. The chamfer acts as a trigger for progressive crush. The specimens compressed in the thickness direction were referred to as Type A and B. The Type B specimen had a notch machined on one end. The specimens compressed in width and axial directions respectively were referred to as Types C and D and Types E and F. Specimen Types D and F where machined with a chamfer at one end.

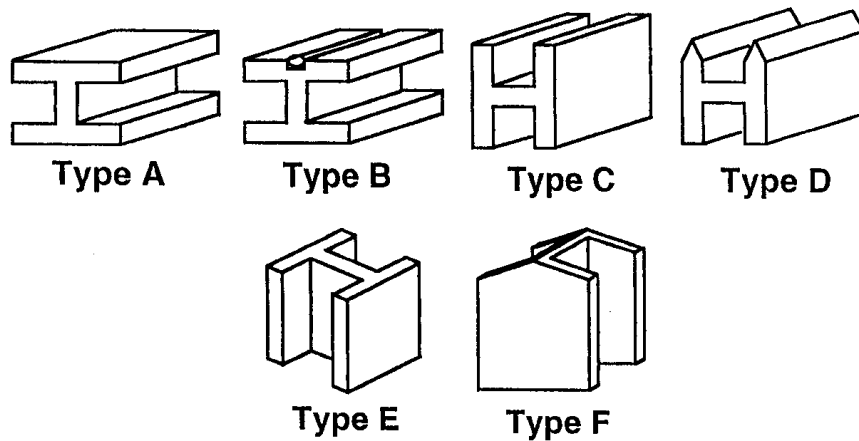


Fig. 30: Types of braided I-beams tested under compression

Quasi-static tests were performed using an Instron Universal Testing Machine (Type 4206) at a constant cross-head speed of 2 mm/min. Impact tests were performed using a drop-test facility (The Japan Automobile Research Institute). The drop plate weight of 49.0 kg was dropped from a height of 0.88 m to give an impact velocity of 15 km/h, where a stopper was set to keep a constant crushing displacement. The signals from the load cells located beneath the platform were fed to the analog-digital converter. The digitised signal was then filtered with a cut-off frequency of 1 kHz. The data representing the load-time history of the impact tests were processed to produce load-displacement curves.

The crushed specimens were cast in polyester resin to observe the crush zone morphology. The cross-sections in the web region were polished and photographed on an optical microscope.

Results

The load-displacement curves in quasi-static and impact tests are shown in Fig. 31. Types D and F specimens which had a trigger at one end displayed small load fluctuation, while Type C and E specimens which had no trigger displayed a high peak load in the early stages.

Energy absorption performances obtained from load-displacement curves are summarised in Table 4. Type F exhibited the highest E_s , about 70 kJ/kg in both quasi-static and impact tests. It was clear that braided I-beam had excellent energy absorption performances in the axial direction, similar to that found with commercial glass cloth/epoxy tubes previously studied.

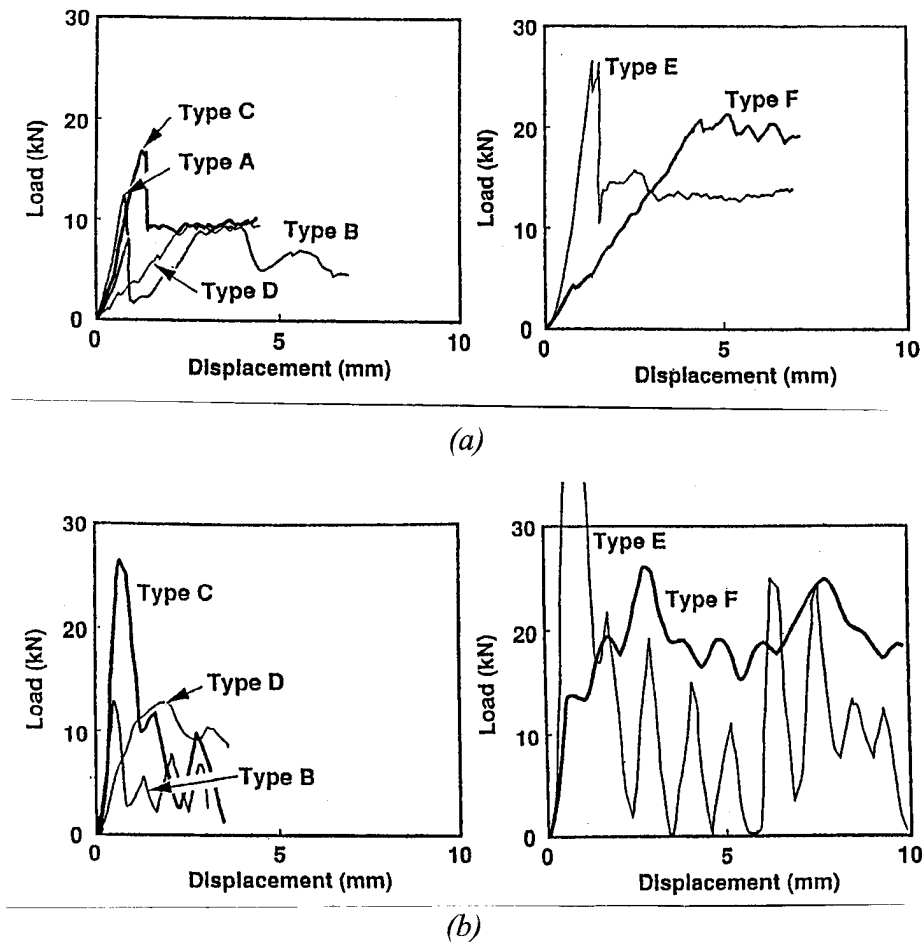
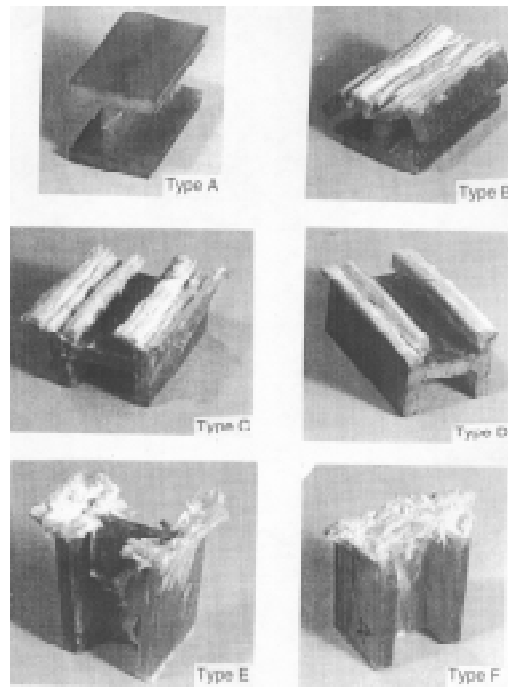


Fig. 31: Load-displacement curves of braided I-beam under (a) quasi-static and (b) impact conditions

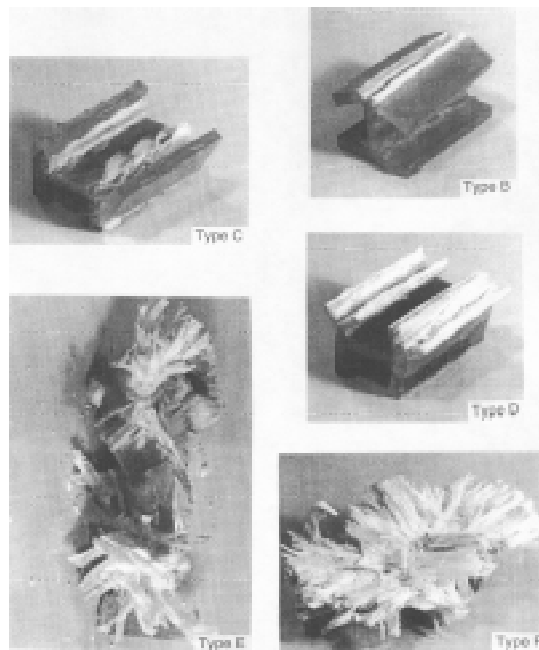
Table 4: Energy absorption performances of braided I-beams

Test Condition	Type	Mean Crush Load (kN)	Maximum Crush Load (kN)	Specific Absorption (kJ/kg)
Static	A	-	13.3	-
	B	6.3	10.0	13.7
	C	9.1	17.5	21.2
	D	9.2	10.8	21.4
	E	13.3	27.5	50.5
	F	19.0	20.9	70.0
Impact	B	5.3	13.3	11.5
	C	-	27.0	-
	D	10.5	12.9	24.5
	E	11.7	55.0	44.5
	F	19.6	26.1	74.5

Photographs of crush zones of braided I-beams after quasi-static and impact tests are shown in Fig. 32. In quasi-static tests, Types B, D and F with a trigger showed progressive crushing. Types C and E which had no trigger crushed axially from one end of the specimen, however showed a fatal crack at the web section. On the other hand, in the impact test, Types C and E crushed in a brittle manner while Types B, D, F displayed progressive crushing, same as that observed in quasi-static tests. Accordingly, for specimens with no chamfer catastrophic fractures were observed, so that the load abruptly decreased and was highly serrated. In contrast, specimens with triggers showed progressive crushing which resulted in a constant load.



(a)



(b)

Fig. 32: Photographs of crush aspects of braided I-beams under (a) quasi-static and (b) impact conditions.

Detailed photomicrographs of cross-sections cut through the crush zone parallel to the axis of the web in quasi-static tested Type F specimens are shown in Fig. 33 and their schematic diagrams are shown in Fig. 34. To clarify the crushing mechanism, the development of the crush zone in the braided I-beam was examined by observation of crush zones in four stages of partially crushed I-beams. Stage 1 represents the crush zone morphology during the increase of the load. Stage 2 corresponds to the crush zone in reaching the peak load. Stage 3 shows the crush zone at the initial stage of the stable crush load region and Stage 4 shows the crush zone during stable crushing. In Stage 1 kinking and delaminations between plies of unidirectional fibres were observed in the chamfer region. In Stage 2 the debris wedge consisting of fractured fibres and resin was seen, and a longitudinal crack had also formed beneath the debris wedge. In Stage 3 the wedge increases in size, and then in Stage 4, the central crack observed in the previous stage disappears, instead delamination at the fronds and fibre fracture are clearly observed.

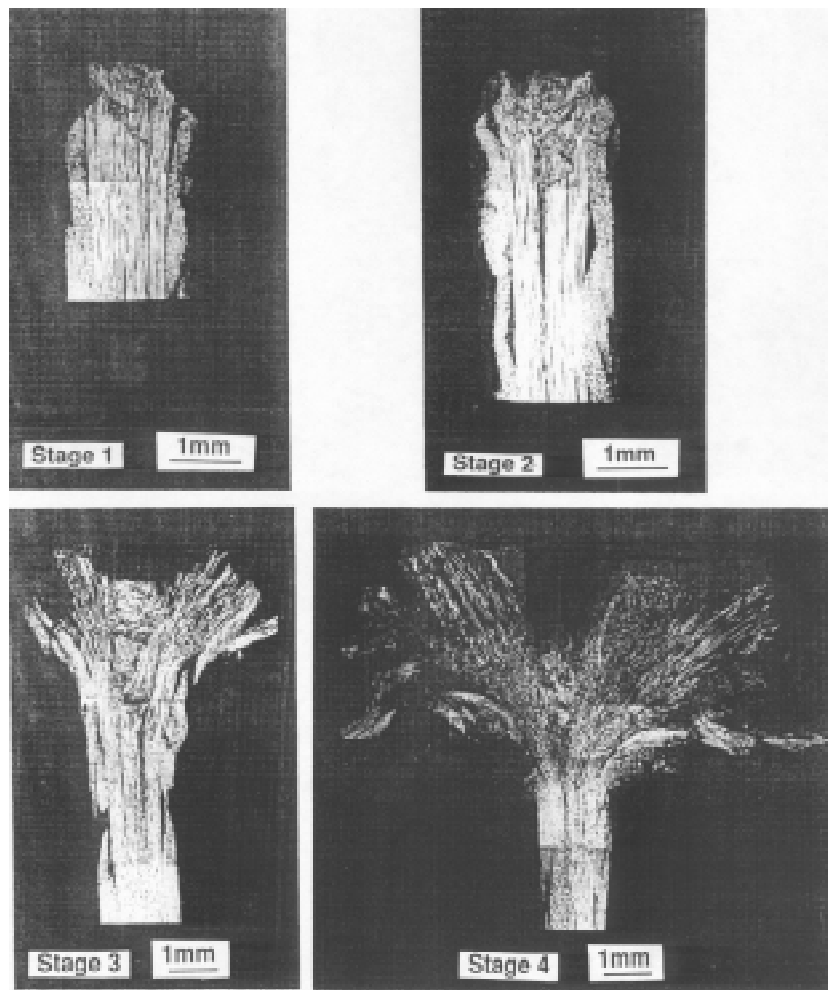


Fig. 33: Photomicrographs of web cross-sections of quasi-static tested Type F I-beams at various load stages

Discussion

For unidirectional glass fibre/epoxy composite materials, compressive strength is lower than tensile strength because of buckling and splitting in general. This is mainly due to the low fracture toughness of epoxy resin. For conditions to exhibit high crush load under axial

compression, two points are considered as follows. One is that the composites must contain many unidirectional fibres in the compressive direction. The other is that little fracture such as shear crack, splitting and so on occurred. For instance, unidirectional carbon fibre/PEEK tubes displayed the highest E_s values (200 kJ/kg) that has been recorded in the literature. This reason for this is that splitting of unidirectional carbon fibres was not seen due to high fracture toughness of PEEK resin [35].

To increase the compressive strength for glass fibre reinforced composite tubes, Hull [36] had investigated the effect of different ratios of hoop and axial fibres of composite tube on crushing performance. Several kinds of tubes fabricated from glass cloth polyester prepreg materials were prepared with different warp and weft ratios. According to his findings, the crushing performance had an optimum range between a hoop:axial ratio of 1:1 and 1:4. This is mainly due to a number of fractures occurring at the fronds such as interlaminar and fibre fracture. The hoop constraints further greatly contribute to the formation of these fractures.

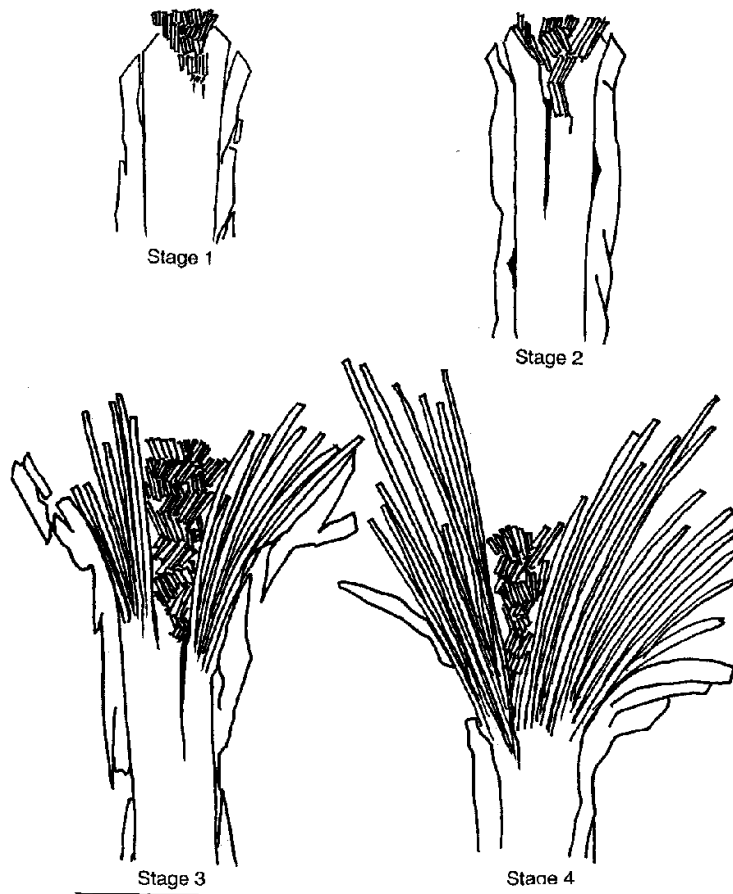


Fig. 34: Schematic of the web cross-sections of quasi-static tested Type F I-beams at various load stages

In the case of braided I-beams, the ratio of braiding fibre and axial fibre is 1 to 1.5. If the braiding fibre can be regarded as the hoop fibre, it is considered this ratio is appropriate for obtaining high stable crush load according to Hull's suggestion. The resin used in the braided I-beams have a low fracture toughness, however, still displayed high values of E_s , same as those of glass cloth/epoxy tubes. This is because the axial fibres which are placed into the braided fabric are supported by the continuous structure of the braiding fibres.

CAN BRAIDED COMPOSITES BE USED FOR CRUSHING ELEMENTS IN CARS ?

In the previous sections, details were given on two major topics; braided composites and the crushing behaviour of composites. Consequently, the braided I-beams proposed in this paper have the potential to be used as crush elements in a car body. However, there are several requirements which need to be addressed before braided I-beams can be used. Here, we would like to list these requirements and ask researchers who are interested in composite materials to address these requirements.

Integrated Composite Structure System

A braided I-beam itself possesses high bending and high crushing performance, however, a connecting method or integrated method to a car body has to be considered. A braided hole has a high mechanically fastened joint strength, as shown earlier in the paper, so it is expected that an integrated structure would also have a similar high performance.

Durability of Composite Structures

A braided I-beam may possibly be exposed to severe environments, particularly when it is designed for an outer panel of the car body. We performed some experiments for crushing behaviour of composite cylinders exposed in weather meters for long periods of time as shown in Table 3-5. The results did not show any change to the crush performance, however, environmental tests on braided I-beams has never been carried out.

Dependence of Crushing Speed

In this paper we described the results of a 15 km/h speed test. For actual usage, the dependence of crushing speed on E_s has to be measured.

Conversely, a collision or an accident at slow speed will cause a small amount of damage inside the braided I-beam. This may result in a decrease in the crushing performance for a severe accident. It is necessary to know what damage is generated in a low speed accident and preferably what damage mechanisms are introduced to estimate crushing performance of braided I-beams.

Database

The database described earlier in the paper is established for designers of car bodies to understand the crushing performance of FRP composite materials in detail. The database will be distributed in MO disk style.

However, the most important factor is that the database provides reassurance on crushing behaviour of FRP. Usually, the crushing behaviour can not be believed by the persons who have not observed actual testing. Also people misunderstand that properties of composite materials have large scatter, so that they do not believe or are not able to understand crushing.

Developing a large data base would assist in enabling everyone to understand the crushing performance. Here, four factors have been identified which need to be conquered for the actual usage of braided I-beams in car bodies. There are many other factors to be considered,

so we need to change the discussion or argument, particularly from the car industry, or undertake co-research work for appropriate usage of composite materials.

CONCLUSIONS

Braided composite I-beams were considered as possible candidates for crushing elements in cars. They were shown to possess excellent bending properties compared to conventional aluminium, important in the application of side members. The introduction of a trigger mechanism allowed composite I-beams to display excellent progressive crush characteristics, similar to those exhibited by composite tubes. Specific energy absorption values reached 70 kJ/kg for braided I-beams. The structure of the braided I-beam was found to be suitable for progressive crushing because axial fibres are tied up by braided fibre.

Therefore, it can be concluded that braided I-beams are useful for impact energy absorbers in lateral and frontal collisions. They can be introduced into the car body as side members designed to absorb both front and side impact. However, for braided I-beams to fulfil this potential, several issues need to be addressed. These include: integration of the composite structure; durability of the composite materials; dependencies on crushing speed; and the creation of a database of progressive crush characteristics.

REFERENCES

1. G. L. Farley and R. M. Jones, "Prediction of the energy-absorption capability of composite tubes", *Journal of Composite Materials*, 26-3 (1992) 388-404.
2. I. Sigalas, M. Kumosa and D. Hull. "Trigger mechanisms in energy-absorbing glass cloth/epoxy tubes", *Composites Science and Technology*, 40 (1991) 265-287.
3. H. Hamada, S. Ramakrishna and H. Satoh, "Crushing mechanism of carbon fibre/PEEK composite tubes", *Composites*, 26 (1995) 749-755.
4. H. Hamada, H. Satoh, M. Nakamura, Z. Maekawa and D. Hull, "Fabrication of carbon/PEEK composite tubes and their energy absorption performance", *Proceeding of the Ninth International Conference on Composite Materials (ICCM/9)*, Madrid, 12-16 July (1993) -197-204.
5. T. Morii, H. Hamada, N. Ikuta, M. Desaeger and I. Verpoest, "Effects of silane treatment on mechanical properties of hydrothermal aged glass fabric/epoxy laminates", *Proceedings of ICCM-10*, (1995).
6. H. Hamada and S. Ramakrishna, "Comparison of static and impact energy absorption of carbon fibre/PEEK composite tubes", *American Society for Testing and Materials*, (1996) 182-197.
7. Nikkei Mechanical, 487 (1996) 36-42 (in Japanese).

8. A. Fujita, Z. Maekawa, H. Hamada and A. Yokoyama, "Mechanical behaviour and fracture mechanism in flat braided composites. part 1: braided flat bar", *Journal of Reinforced Plastics and Composites*, 11 (1992) 600-617.
9. H. Hamada, A. Fujita, A. Nakai, A. Yokoyama and T. Uozumi, "New fabrication system for thick composites - a multi-reciprocal braiding system", *Innovative Processing and Characterization of Composite Materials ASME 95, NCA-Vol.20/AMD-Vol.211* (1995) 295-304.
10. A. Nakai and H. Hamada, "Bending properties of multi-layered braided composite tube", *Journal of Science and Engineering of Composite Materials* (in submitting).
11. A. Nakai, M. Masui and H. Hamada, "Fabrication and mechanical properties of multi-reciprocal braided composite tube", *Advanced Composites Letters*, 5 (1996) 77-79.
12. M. Masui, A. Nakai and H. Hamada, "Fabrication and mechanical properties of thick braided composite tube with through-the-thickness fibre", *Joint Canada-Japan Workshop on Composites*.
13. H. Hamada, A. Nakai, M. Masui and M. Sakaguchi, "Improvement of lateral compressive strength in braided pipe - new braided fabrication", *International Composites EXPO '97*, (1996).
14. H. Hamada, A. Nakai and M. Masui, "Mechanical properties for self-reinforced braided composite tube", *American Society for Composites 11th Technical Conference*.
15. A. Nakai, M. Masui, A. Yokoyama and H. Hamada, "Simulation for predicting dimensions of braided composite", *Journal of Textile Institute* (in submitting).
16. H. Hamada, A. Nakai, A. Fujita, Z. Maekawa, A. Yokoyama and T. Uozumi, "CAE in integrated braided composite", *Journal of Science and Engineering of Composite Materials*, 4-2 (1995) 109-120.
17. H. Hamada, A. Fujita, Z. Maekawa, A. Nakai and A. Yokoyama, "Design of braided composite tubes by numerical analysis method", *Composites for The Pressure Vessel Industry ASME 1995, PVP 302* (1995) 69-73.
18. A. Fujita, H. Hamada, Z. Maekawa, A. Nakai, A. Yokoyama, N. Ikuta and T. Uozumi, "Design and fabrication of braided preforms for 3-D composites", *Advances in Science and Technology 7, Advanced Structural Fibre Composites*, (1994) 819-826.
19. T. Uozumi, Y. Hisa, A. Fujita, H. Hamada, A. Nakai and A. Yokoyama, "Braiding pultrusion process (BPP)", *27th International SAMPE Technical Conference*, (1995) 371-379.
20. H. Hamada, J. C. Coppola and D. Hull, "Effect of surface treatment on crushing behaviour of glass cloth/epoxy composite tubes", *Composites*, 23-2 (1992) 93-99.

21. H. Satoh, H. Hirakawa, Z. Maekawa, H. Hamada, M. Nakamura and D. Hull, "Comparison of energy absorption among carbon/thermoplastic tubes", 38th International SAMPE Symposium (1993).
22. H. Hamada, H. Satoh, H. Hirakawa, Z. Maekawa and M. Nakamura, "Comparison of energy absorption among carbon/thermoplastics tubes -the highest energy absorption value ever recorded for any material-", Proceedings of JSAE Spring Convention 933 (1993) 37-40 (in Japanese).
23. H. Hamada, M. Nakamura, Z. Maekawa, T. Kashima and T. Jyono, "Energy absorption characteristics of high performance polyethylene fibre reinforced composite tubes", Proceedings of JSAE Spring Convention 933 (1993) 41-44 (in Japanese).
24. H. Hamada, M. Nakamura and Z. Maekawa, "Energy absorption characteristics of ultra-high molecular weight polyethylene fibre reinforced composites", Theses of JSAE (1994) 134-139 (in Japanese).
25. H. Hamada, S. Ramakrishna, T. Nishiwaki and Z. Maekawa, "Energy absorption characteristics of composite tubes with different cross-sectional shapes", Proceedings of 10th ASM/ESD Conference (1994) 523-534.
26. H. Hamada and S. Ramakrishna, "Scaling effects in the energy absorption of carbon-fibre/PEEK composite tubes", Composites Science and Technology, 55 (1995) 211-221.
27. H. Hamada, S. Ramakrishna, Z. Maekawa and H. Sato, "Effect of cooling rate on the energy absorption capability of carbon fibre/PEEK composite tubes", Polymer and Polymer Composites, 3-2 (1995).
28. H. Hamada, S. Ramakrishna and Z. Maekawa, "Environmental effects on the progressive crushing behaviour of glass cloth/epoxy composite tubes", Composite Interfaces, 3-1 (1995) 23-39.
29. T. Morii, H. Hamada, N. Ikuta, M. Desaegeer and I. Verpoest, "Effects of silane treatment on mechanical properties of hydrothermal aged glass fabric/epoxy laminates", Proceeding of ICCM-10 (1995).
30. H. Hamada and S. Ramakrishna, "Impact performance of glass cloth/epoxy composite tubes with different surface treatment", Composite Interface, 4 (1996) 1-10.
31. T. Nakatani, K. Kameo and H. Hamada, "Development of energy absorption parts with FRP tubes", 41st FRP CON-EX '96 Conference (1996) 157-159 (in Japanese).
32. H. Hamada and T. Nakatani, "Energy absorption capabilities of composite tubes under off-axial compressive load", 74th Symposium of JSME (1996) (in Japanese).
33. H. Hamada and T. Nakatani, "Energy absorption properties of composite beams with I-shape cross section", Proceedings of JSAE Spring Convention 965 (1996) 33-36 (in Japanese).

34. H. Hamada, S. Ramakrishna and H. Sato, "Effect of fibre orientation on the energy absorption capability of carbon fibre/PEEK composite tubes", *Journal of Composite Materials*, 30-8 (1996) 947-963.
35. H. Hamada, J. C. Coppola, D. Hull, Z. Maekawa and H. Sato, "Comparison of energy absorption of carbon/epoxy and carbon/PEEK composite tubes", *Composites*, 23-4 (1992) 245-252.
36. D. Hull, "A unified approach to progressive crushing of fibre-reinforced composite tubes", *Composites Science and Technology* 40 (1991) 377-421.

DEVELOPMENT OF A COMPOSITE FLOOR PANEL TO REPLACE PLYWOOD FLOORING IN RAIL CAR INTERIORS

H. Snaith

*Transform Composites Pty Ltd., 50 Clyde Street, Broadmeadow, NSW 2298, Australia
(Now with ADI Limited, Fitzroy Street, Carrington NSW 2294, Australia)*

SUMMARY: This paper describes the development of a lightweight composite panel which offers an alternative to conventional plywood flooring. The composite panel has the potential to substantially increase, and possibly eliminate, the re-flooring interval for rail car interiors.

The composite floor panel is economically competitive with the plywood and although the basic panel unit price is presently higher than plywood, there are potential savings in the installation, and significant savings if the through life costs are considered. Further, the long term trend in plywood price is likely to be upward as environmental considerations become more influential, (such as the restrictions placed on the import of tropical hardwood species). In contrast the composite panel price is likely to remain stable.

The panel skins and structural core are fabricated from fibre-reinforced phenolic resin. The foam fill is also phenolic. With phenolic resin used throughout the panel fire resistance is of a very high order. For floor applications the panel are made flat though curved panels for other applications are being considered. The composite panel is designed as an alternative to treated F14 stress grade structural plywood but outperforms the plywood in nearly all aspects.

The testing and evaluation of the composite floor panel are described and the various performance criteria are discussed.

KEYWORDS: phenolic panel, treated plywood, rail car floors

INTRODUCTION

Passenger rail cars in New South Wales have conventionally used treated plywood flooring. The plywood deteriorates due to the effects of water ingress and wear, and has to be replaced at regular intervals (generally between five and fifteen years depending on location within the car). The cost of rail car refurbishment involving floor replacements is high. Furthermore the availability of treated plywood of adequate quality is declining. The only Australian based manufacturer of treated plywood closed its plant in 1996. Hence an alternative flooring product is sought.

A 13mm phenolic Composite Floor Panel was developed as a direct replacement option for the 13 mm treated plywood used by the State Rail Authority of New South Wales (SRA) in its double-deck passenger rail car fleet.

The panel configuration was designed to suit this particular application but other configurations are possible.

The composite floor panels are of sandwich construction having skins of glass fibre reinforced phenolic resin, and a core consisting of glass fibre reinforced phenolic and phenolic foam. This construction provides good structural and sound attenuation properties with low panel weight and cost.

PHENOLIC COMPOSITES

Glass fibre reinforced plastics (GRP) are well established materials of construction for rail car interiors in Australia being extensively used for internal linings, luggage compartments, stairs, seating etc. These components have traditionally been manufactured from glass fibre reinforced polyester or modified acrylic resin.

The 'resol' version of phenolic resins is designed to be processed like conventional polyester resin commonly used in fibre reinforced plastics.

The advantage of phenolic resin is its outstanding heat resistance and fire performance which has been widely reported in the literature eg Gibson et al [1].

The physical and mechanical properties of the phenolic based composites, as reported by Forsdyke et al, [2] O'Brart, [3] and others, are in most cases comparable to polyester based composites with the notable exceptions of elongation, colour and surface appearance- which are generally inferior to other thermoset polymers. Phenolic composites usually require either painting or a decorative coating if good aesthetics are required for the application. Rail car flooring however is usually finished with a vinyl mat wear surface and hence an aesthetic finish is not required of the floor panel itself.

As reported by Forsdyke [4], Brown [5] and others, worldwide use of phenolic composites is growing and examples of industries using phenolic composites are the automotive, rail, aircraft, marine, offshore and building and construction. Applications in the rail industry to date include: cable supports and enclosures; live rail covers; various signal, aerial and switchgear enclosures; interior panels (with decorative coatings); luggage compartments; sleeper car partitions; diesel engine heat shields; underground station tunnel linings, and rail car flooring. Several recent developments have involved the manufacture of complete rail cars or freight wagons of composite material using filament winding, resin infusion or pultrusion. An example using pultruded carbon fibre is reported by Suzuki and Satoh [6].

SELECTION OF FLOOR PANEL CONFIGURATION

A number of panel configurations were initially considered including: steel faced plywood; aluminium faced plywood; aluminium faced pvc foam sandwich; composite faced pvc foam sandwich; aluminium or composite faced honeycomb core sandwich, 3-D distance fabric, and lastly, a sandwich construction using a moulded composite core with composite skins.

The last of these options was selected with phenolic composite chosen in preference to aluminium for both core and skins as it was considered to have better fire performance,

fatigue resistance, and potentially better corrosion resistance (reports from the rail car manufacturer indicated corrosion of aluminium in wet areas and insulation from the stainless steel structural members would be an additional requirement). The bonding of aluminium was also considered to be a major issue which could be largely avoided by using the composite option.

The plywood core options were rejected due in part to the problems experienced by the SRA and reported by the rail car manufacturer caused by water ingress (for example the stainless steel faced plywood suffered from delamination) and also due to anticipated future availability problems of good quality plywood.

The pvc foam core option was rejected on the basis of poor heat resistance and fire performance. If an aluminium faced pvc core sandwich construction were used then under fire or local overheating conditions rapid heat transmission through the aluminium to the core would lead to rapid deterioration of floor integrity.

Honeycomb core options were considered but rejected on grounds of high cost, poor availability, and on process considerations. They are however considered to have the highest ratio of stiffness-to-weight hence their widespread use in aerospace.

3-D 'distance fabrics' with phenolic matrix and foam filling appeared to offer most of the desired properties but were rejected on grounds of cost and limitations (at the time) on available dimensions and lay-up.

Attention therefore became focussed on the all composite moulded core sandwich construction as it had the most attractive combination of features from performance, cost and manufacturing considerations. The last of these, the manufacturing process, proved to be crucial.

MANUFACTURING PROCESS

With the raw material cost of the composite approaching the finished plywood panel cost, it was necessary to develop a cost effective and yet versatile, high throughput process. Existing processes that meet this description include pultrusion, the continuous laminating/sandwich panel process, and to a lesser extent, resin transfer moulding (RTM) . However none of these processes are capable of producing a hollowed cored product with the combination of section intricacy, low wall thickness, and panel width variation required for this application. A completely new process was therefore developed with the assistance of an Australian Federal Government grant.

The panel making process is sufficiently versatile to allow a wide range of lay-ups to be used for moulded corrugated core and the panel skins. Most common forms of fibre reinforcement can be used including woven and random mats, stitched, knitted and low crimp fabrics, and tissues or veils. The process allows the option of incorporating foam within the core channels. The foam filling can be complete (ie in all cavities of the corrugated core), or optionally in a portion of the core such as in alternate cavities. The incorporation of foam increases thermal insulation, acoustic attenuation, and panel compressive properties. For the floor application a phenolic foam was selected as this has good heat and fire resistance. The mechanical properties of phenolic foam are generally poor. However when incorporated into

the cavities of the corrugated core, the foam contributes to the panel compressive properties as compressive load puts the foam into partial hydrostatic compression due to its encapsulation.

The panel does not depend on the foam for its bending resistance which it derives from the corrugated composite core acting in combination with the skins.

Although one particular configuration was selected for the rail floor application, the process is sufficiently versatile to allow for many other configurations to suit other applications. A light-weight version of the panel without foam core can be used for fire resistant partitioning for example.

PANEL TESTING AND EVALUATION

Panel Load-Deflection Testing

To assess the panels suitability for the rail floor applications, a number of tests were carried out. The first set of tests included three point bending (Fig.1) to assess panel static stiffness and strength, and repeated three-point-bending (ie cyclic testing- Fig. 3)to assess retention of integrity with repeated loading. The test method was provided by the rail car manufacturer and prime contractor for refurbishment as 'Goninan Test Specification Ref. 0510E/3 parts 1 & 2'.

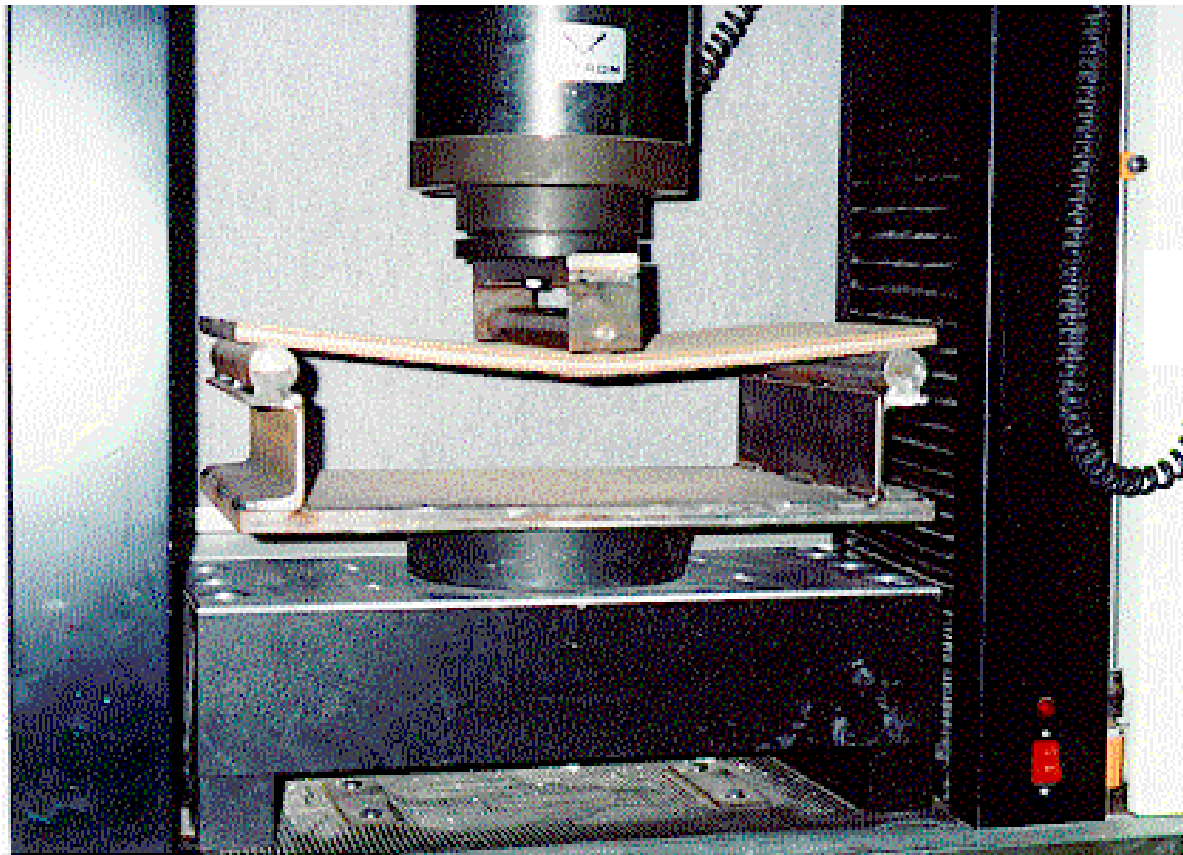


Fig. 1: Typical three-point-bend test

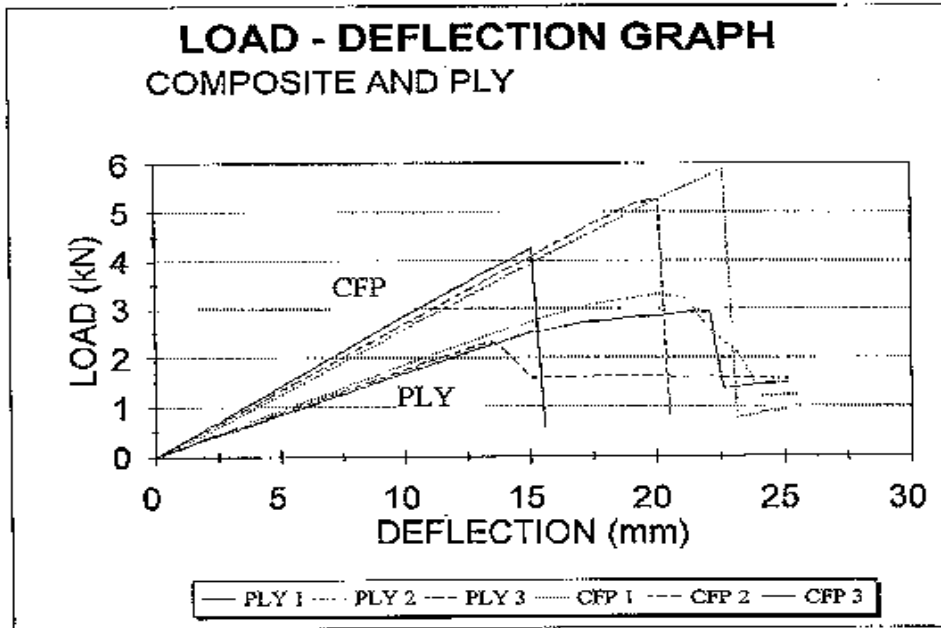


Fig. 2: Load-Deflection Curves for Composite and Plywood Panels

Typical load deflection curves for the composite and the plywood are shown in Figure 2. In all cases the composite panel has a higher load at failure than the plywood and the lowest value for the composite panel is 15% higher than the highest value for plywood. The mean value for the composite is 80% higher than the mean value for the plywood. The variation for both panels at this stage was quite high as the early panels were largely hand made. Since the testing of the early panels, the variation for the composite panel has been reduced with samples produced on the full scale pilot plant and further improvement is anticipated as refinements are made to the manufacturing process.

As well as the load to failure being higher for the composite panel than for the plywood panel, the mode of failure is considered to be safer for the composite panel. The plywood panel fails by tensile rupture of the plies starting from the underside of the panel. The residual load carrying capability is effectively zero. For the composite panel however, initial failure is by compression in the top skin with the lower skin remaining intact and capable of carrying load after initial failure. Composite panel samples will typically sustain a subsequent load of over 40% of the initial failure load, when simply supported- more with end fixity or continuity.

Panel Cyclic Load Testing

As the composite panel consists of a laminated construction it was considered necessary to subject samples to a cyclic load to assess whether or not the panel would de-laminate or deteriorate in anyway. The set-up for cyclic loading is similar to that for the static load-deflection test ie three-point-bending, but with the load applied and released in a sinusoidal fashion. The test rig is shown in Figure 3.

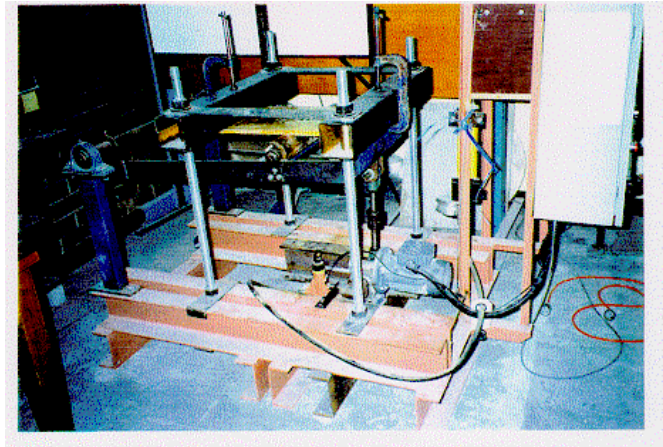


Fig. 3: Cyclic Load Test Arrangement

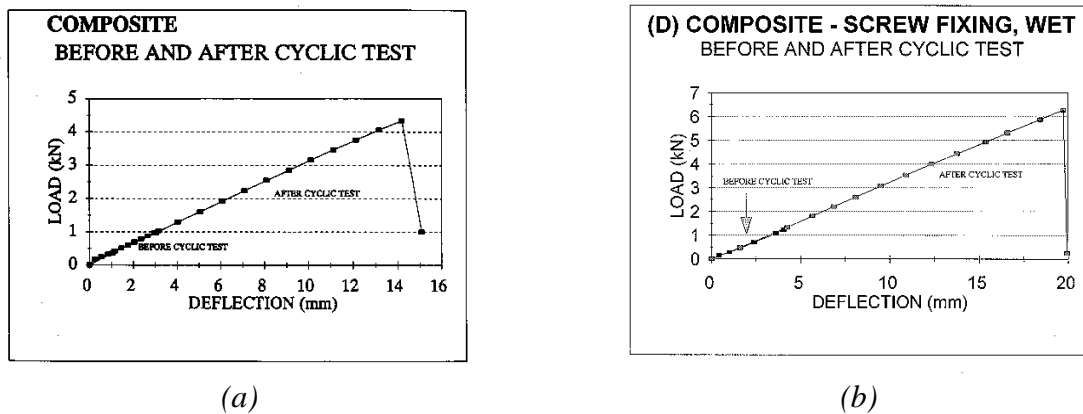


Fig. 4a: Typical results of load-deflection tests (a) after cyclic loading to 10^5 cycles with 4.5 mm central deflection (b) after cyclic loading to 10^7 cycles with 2.0 mm central deflection

The results of initial testing (ie to ‘Goninan Test Specification Ref. 0510E/3 part 2’) showed that no deterioration in panel stiffness or load carrying ability due to the cyclic loading called for in the test method was detected, despite the deflection of 4.5 mm being over twice that considered to be the maximum in service deflection ie 2 mm (Fig. 4a). It was therefore decided to test a sample for a much higher number of cycles ie 10^7 to a maximum deflection of 2mm. After this test the panel was loaded to failure and again showed no significant reduction in stiffness or load carrying ability (Fig. 4b). These results were re-assuring as it was not known at the outset of this development whether or not a laminated phenolic composite panel with corrugated core would suffer delamination between core and skins as a result of repeated flexural loading, considering that contact area between core and skin is less than 50% of the panel area.

The fatigue behaviour of uni-directional glass fibre reinforced phenolic composites is reported by Branco et al [7], including the effects of varying fibre volume fraction, fibre surface treatment and stress ratio. Their conclusions suggest that while the fatigue life of a phenolic matrix composite is less that of one based on epoxy, 10^7 load cycles can be comfortably exceeded if the normalised stress is below 20 %. The different fibre surface treatments used appear to have minor influence on the reported fatigue life.

High Heel Shoe Puncture Test

As train floors can be subjected to potentially damaging effects of high heel shoe loads, a test was undertaken using a 5mm cylindrical steel impressor (contact area 0.2 cm²) to compare the puncture resistance of the composite panel with the plywood. The set-up is shown in Figure 5.

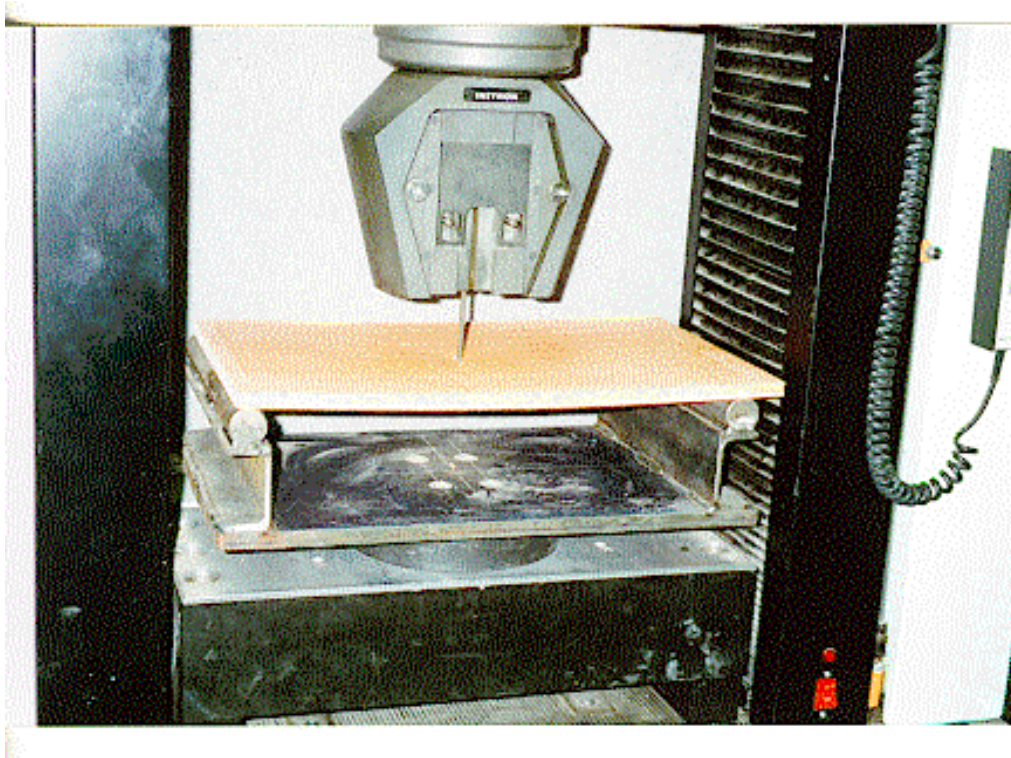


Fig 5: High Heel Puncture Test

The minimum puncture load for the composite panel was 2.31 kN (11.8 kN / cm²) which compares with a maximum value for the plywood of 1.62 kN (8.25 kN/cm²) thus representing an increase in puncture resistance of 42%. When this test was repeated placing a piece of vinyl floor covering on the panel sample, the covering became permanently marked at approximately 0.8 kN load.

Voerpost [8], considering the potential suitability of 3-D distance fabrics for rail flooring applications, reports that a typical heel loading requirement in Europe would be 150 kgf over 1 cm² (1.5 kN/cm²). This requirement is easily met by the composite floor panel, but a typical foam filled 3-D distance fabric is likely to require additional layers of reinforcement on the upper skin.

Drop Weight Impact Testing

A search for a standard impact test relevant to this type of application was unsuccessful- the ASTM method for roof panels and the drop weight 'tup' test were not considered appropriate. A simple test to assess the tolerance of the composite panel to incidental impact damage and comparing the outcome with that for plywood was devised. The test consisted of dropping a 6.7 kg steel sphere from increasing heights of 1.0 m, 1.5m and 2.0m at different locations. The arrangement is shown in Figure 6.

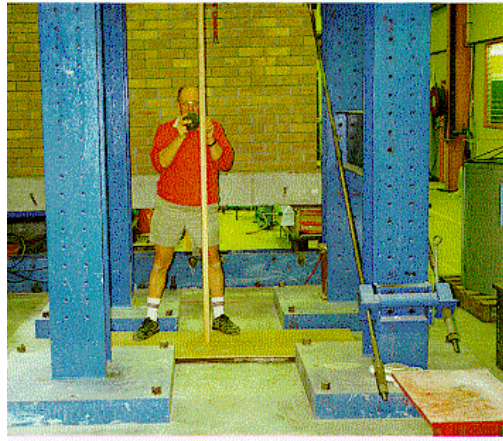


Fig. 6: Drop Weight Impact Test Arrangement

For the composite panel, no visible damage occurred in each case. For the plywood panel cracks appeared on the underside of the panel. Three-point-bend test specimens were subsequently cut from the impacted panels for residual strength testing. In this test the maximum load recorded for the plywood specimen was 1.8 kN before panel collapse compared with 5.4 kN for the composite panel which failed in compression of the upper skin (Fig. 7).

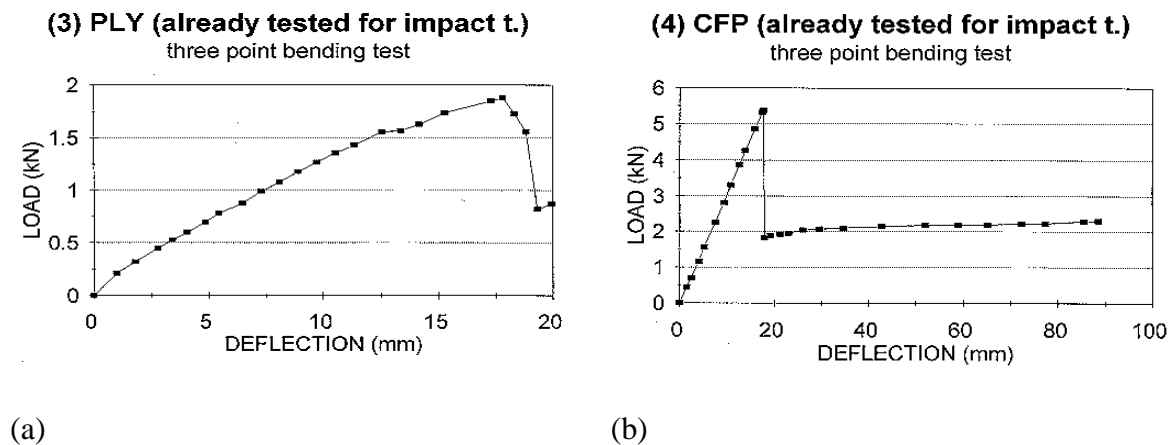


Fig. 7- Load-deflection tests after drop weight impact- (a) plywood (b) composite
Note: different axes scales

This test suggests that the damage tolerance to this type of impact of the composite panel is superior to that of the plywood which failed on the more critical (tensile) underside.

Fire Testing

Nine panel samples 600mm x 450mm were submitted to the Australian Wool Testing Authority (AWTA) for testing to Australian Standard AS 1530.3 'Simultaneous determination of ignitability, flame propagation, heat release and smoke release'. This test is a radiant panel fire test similar to other national standards such as ASTM E 162, BS 476 Pt 6 & 7, DIN 4102, NFP92-501 etc.

The result was given as indices 0,0,0,0-1 which is the best result possible for the test, thus confirming the excellent early fire resistance of glass fibre reinforced composites as reported by others.

Sound Transmission Testing

Samples of plywood (16 mm and 13 mm thickness) and composite panels (13 mm thickness), of plan area 610 mm x 610 mm were tested for sound transmission loss. Of the two composite panels tested one was 100 % foam filled while the other had no foam filling. The wideband (63- 10,000 Hz) sound transmission loss values recorded were as per Table 1.

Table 1: Wideband sound transmission loss values for ply and composite panels

16 mm Plywood	13 mm Plywood	13 mm Composite (no foam)	13 mm Composite (100 % foam)
TL = 30 dB	TL = 24 dB	TL = 23 dB	TL = 26 dB

The results indicate that the sound transmission loss for the composite panels is of the same order as for the plywood and that foam filling has the effect of increasing sound transmission loss.

Panel Installation

As main bearers in the SRA's rail cars run transversely, the composite floor panels are made in typical lengths of 5 m and with widths from 0.6 m to 1.4 m depending on location within the car. The panel edges are supported on secondary bearers which run longitudinally. Two fixing methods have been evaluated (1) self tapping screw fasteners and (2) adhesive bonding. A composite panel sample with each fixing method was subjected to the cyclic load test described above in both dry and wet conditions. No noticeable deterioration of the panel or its fixing occurred and the panels with screw fixing gave the highest residual load-to failure after cyclic loading to 10^7 cycles with 2 mm central deflection. Both fixing methods would appear to be suitable for the application. The screw fasteners used in the testing were an 'off-the-shelf' type with a shallow counter-sunk head as the skin of the composite panel is thin. Subsequently a dedicated fastener was made to specification to suit the application.

Service Trials

For trial and evaluation of the product the SRA gave permission for a double-deck car to be fitted with the composite floor panel during scheduled refurbishment. At the time of writing this car has been in service for approximately eighteen months with no problems reported after periodic inspections.

CONCLUSIONS

A plywood replacement floor panel was developed along with an novel manufacturing process for economic volume production. The replacement product was constructed of glass fibre reinforced phenolic resin and whilst of the same weight as the plywood, appears to have superior structural properties as determined by the evaluation tests described above.

Whilst the composite product is likely to be more expensive than the traditional treated plywood it replaces, it is of similar order of cost so as to minimise the impact on operating costs.

There is scope for further product development with improvements in structural properties anticipated together with the potential for reducing weight.

The product concept has potential for use in other applications. A design model is currently under development for this purpose. Material coupon test data will be incorporated in the model which is based on laminate analysis. The model will incorporate failure modes and be verified against test results on full scale panels.

ACKNOWLEDGMENTS

The author gratefully acknowledges the assistance of the following organisations during the development of composite floor panels:

City Rail, State Rail Authority of New South Wales
A Goninan & Co. Ltd., Broadmeadow NSW 2292
The University of Newcastle Research Associates (TUNRA), Callaghan NSW 2308
AusIndustry, Department of Industry, Science & Technology, Canberra ACT 2601
FORTECH, Consultants in FRP Processing, Product Development, and Marketing (UK)
Transform Composites Pty Ltd, Broadmeadow NSW 2292

REFERENCES

1. Gibson A.G., Chandler H.W., Wilcox J.A.D., Wu Y-S., and Hume J., "Fire Performance of Composite materials for Offshore Use", *Composite Materials for Offshore Use- A One Day Seminar-* Institution of Mechanical Engineers, London 17 November 1994, UK
2. Forsdyke K.L. and Hemming J.D., "Phenolic GRP and its Application in Mass Transit" *44th Annual Conference, Composite Institute, society of the Plastics Industry Inc.*, February 1989, session 3-C / , US
3. O'Brart P., "Phenolics in the Building Industry" Cray Valley Limited, *18th International Congress, British Plastics Federation* 1992 UK
4. Forsdyke K.L., "Phenolic Composites for Safety in Mass Transit Systems" *International Review Conference on Polymers in Rail Transport and Mass Transit Systems-* 19/20 November 1991 Manchester UK
5. Brown D.E., "Glass Reinforced Phenolic Mouldings in Railway Rolling Stock- A Specifiers View" GEC-Alsthom Metro-Cammell Limited, *18th International Congress, British Plastics Federation* 1992 UK
6. Suzuki Y. and Satoh., "High Speed Trains and Composite Material", *SAMPE Journal*, Vol.31 No.4, July/August 1995
7. Branco C.M., Ferreira J.M., Richardson M.O.W. and Fael P., " *Fatigue behaviour of a phenolic matrix composite*" *Int J Fatigue* 14 No. 6 (1992) pp 367-376
8. Verpoest I, Department of Metallurgy and Materials Engineering, Katholieke Universiteit Leuven (B), *One day workshop on 'Advanced 3-D Textile Sandwich Composites'*, University of New South Wales, Jan 1997 (Aus)

COMPOSITE MATERIALS AT THE CROSSROADS – TRANSITION TO AFFORDABILITY

Cecil W. Schneider

*Lockheed Martin Aeronautical Systems
86 South Cobb Drive, Marietta, Georgia 30063-0648 USA*

SUMMARY: Historical development of composite materials, trends for aerospace and non-aerospace applications, and obstacles to expanded application to aerospace products are addressed in this paper. While high performance composite materials, using carbon fiber in a polymer matrix, have matured over the past 30 years, affordable application of these materials has eluded the aerospace industry. Over the past few years, the aerospace industry and government have devoted significant resources to development of innovative manufacturing processes to reduce costs, but composite designs are still significantly more expensive than those with comparable metallic structures. This paper addresses some of the deterrents to affordable composite structures, with recommendations for future development to overcome the affordability obstacles.

KEYWORDS: design-for-manufacturing, composite manufacturing, composites affordability, composites development requirements, composite applications, trends in composites development

INTRODUCTION

Polymer matrix composites became structurally viable aerospace materials with the development of carbon fibers in the 1960s. As the technology matured in the 1970s the development focus was on performance, driven by a need to save weight on high performance fighter and V/STOL aircraft. Design and analysis methods were developed, refined and validated, providing the capability for design of large, complex aircraft structures with a high degree of confidence. During the 1980s the technology emphasis shifted from performance to cost reduction, while still maintaining high performance. The industry also began to integrate composite materials into stealth aircraft to reduce the radar signature of fighter and bomber aircraft. While usage of composite materials was still driven by the U.S. Department of Defense [DoD] vehicles, there began to be increasing applications to non-aerospace products such as high-end sporting goods.

During the past decade, there has been a dramatic shift towards affordability in aircraft application priorities, which has driven the development focus to lower cost materials and processes. The industry assessed lessons learned from development and production programs, with the result that increased emphasis must be placed on design and manufacturing integration to develop design-for-manufacturing guidelines and tools. Development activities in advanced manufacturing automation such as fiber placement and Resin Transfer Molding [RTM] are leading to significant reductions in manufacturing cost. The rapid expansion of composite material applications came to a sudden end in the early

1990's with the rapid downsizing of DoD, and subsequent termination of many government programs. These changes led to mutual recognition among users, suppliers and government that some degree of standardization of materials specification, testing, and design properties could achieve significant reductions in cost. This downturn has been reversed in the past two years as other, non-aerospace, industries have increased their applications of advanced composite materials. Because of this, future growth of the carbon fiber market will not be in military aircraft, but in commercial products with selective use of composite materials.

HISTORICAL PERSPECTIVE

The use of *composite* materials on aircraft structures is not a recent event. *Composite* aircraft structures were around even before powered flight since early gliders [Figure 1] and the Wright Flyer (which achieved the first powered flight at Kitty Hawk) were fabricated of fabric over wood, with only limited use of metal in critical areas. It was not until the thirties that aluminum took over as a primary aircraft structural material as aircraft sought ever higher speed and performance levels. The first all-aluminum aircraft was the Lockheed *Electra*, which was first delivered to airlines in 1934. Not surprisingly, those early metal applications encountered significant resistance from design and manufacturing personnel toward this 'new-fangled' aluminum material.



Fig. 1: Otto Lilienthal, 1891

While fiberglass/epoxy materials were in general use on aircraft for non-structural applications during the 1950's and 60's, there were not considered to be a structural material because of the low properties and strength-to-weight ratios. Advanced composite structures became a reality with the development of carbon fibers in the 1960's. As these materials were introduced, the development community had to overcome early problems to develop fibers, resins and prepreps that achieved strength and modulus properties that outperformed aluminum materials, while still contending with the real-world environmental and moisture concerns and issues. Just as with the introduction of aluminum materials, composite materials brought new concerns and issues to the design process as well as cultural bias about putting "burned materials on airplanes". Early concerns about the moisture intrusion [Figure 2] were resolved by development of "hot/wet" testing that accounts for the "knock-down" factors in design properties.



Fig. 2: Moisture Was An Early Concern



Fig.3: L-1011 Composite Aileron

As the technology matured in the 1970's, development activities continued to have a performance emphasis, driven by a need to save weight on high performance military fighter and V/STOL aircraft. The focus was on continued development of advanced materials to achieve higher modulus and strength to further reduce weight, with very little emphasis on affordability. Design methods were developed, refined and validated to provide capabilities for design of aircraft structures with a

high degree of confidence. However, composite materials still required a high level of development and qualification testing to get initial secondary structural applications into production. Most of the composite structures produced during this period were limited quantity runs of secondary structures to prove feasibility and obtain initial customer confidence by conducting flight evaluations. Much of these initial flight evaluation structures were fabricated under contracts from NASA [Figures 3 and 4] and the U.S. Air Force Wright Laboratories.

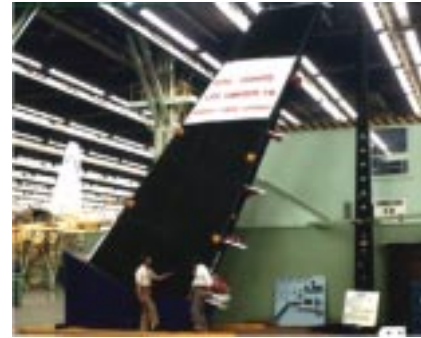


Fig. 4: L-1011 Composite Vertical Fin

During the 1980's we began to see a shift to increasing emphasis on cost reduction, while still maintaining high performance. Initial production applications of secondary structures in the early part of the decade led to application on primary structures on fighters, V/STOL and business aircraft by the end of the 1980's. Through development efforts led by NASA, advanced composite materials were transitioned to initial commercial aircraft secondary structures. However, DoD applications continued to predominate, with optimistic forecasts of usage that lead material suppliers to facilitate and develop new fiber, resin and prepreg products. The result was an expanding line of available capacity and products, but with little standardization. Manufacturing technology scale-up and automation development activities were concentrated on cost reduction. However, many of these efforts were limited in scope by focusing only on specific narrow technology areas while overlooking design or tooling aspects. The industry began to integrate composite materials into the stealth world to achieve low observable characteristics -- although most of us did not know this was occurring at the time. The majority of the structure on the B-2 Bomber [Figure 5] was fabricated from carbon/epoxy materials, coated to reduce radar signature. While production of composite materials was still driven by DoD applications, we began to see increasing application to non-aerospace products such as high-end sporting goods -- for example, golf clubs and tennis rackets.



Fig. 5: B-2 Bomber Is Mostly Composite

In the 1990's, applications have expanded into primary structures on large commercial aircraft, such as the Airbus A-320 and Boeing 777 tail structures [Figure 6]. During this decade, there has been a dramatic shift towards affordability in aircraft application priorities, which has driven the development focus toward lower cost materials and processes. The industry assessed lessons learned from development and production programs, with the result that additional development effort is required for design and manufacturing integration,

leading to design-for-manufacturing guidelines and tools. Development of advanced manufacturing automation such as fiber placement and RTM has provided fabrication processes that can significantly reduce manufacturing cost, but there is still work remaining to develop and validate optimized design methods for these processes. The proliferation of composite materials in the late 1980's came to a sudden end in the early 1990's with the rapid downsizing of DoD, and subsequent termination of many government programs. These changes led to mutual recognition among the users, suppliers and government that some degree of standardization of materials specification, testing and design properties could achieve significant reductions in cost. As the DoD usage of composite materials dramatically decreased, the supplier industry was hard hit by reductions in demand for fiber and resin.



Fig. 6: Boeing 777 Tail Structure

The Changing Environment

During the past decade, there have been dramatic changes in health and safety considerations for all materials, which has produced a much safer working environment. In the past, health and safety would be considered only after evaluating materials for performance. Today, hazardous materials are rapidly being replaced with environmentally friendly materials and processes to reduce workplace exposure. Health and safety must be evaluated prior to introduction of materials into the shops, with safe handling procedures written into the specifications prior to purchase. This has had an impact on materials development as well as applications, but the net result is a much safer working environment for employees.

Government And Industry Trends

Starting in the mid-1980's, DoD budgets began to decrease, and dramatically dropped after the collapse of the Soviet Union [Figure 7]. We have not yet seen the end of this decrease in budgets, which drastically reduced the number of airframe program new starts. The number of aerospace companies has also dramatically decreased through mergers and buyouts, and teaming on large companies has become the norm. In 1945 there were 16 major U.S. companies building military aircraft. This had reduced to 11 in 1980, 9 in 1985, 6 in 1990 and three today. With fewer aircraft programs, the demand for carbon fiber dropped, causing material suppliers to decrease their R&D investment. Today there are few new materials being developed, and most of those that are under development are focused on commercial rather than military products.

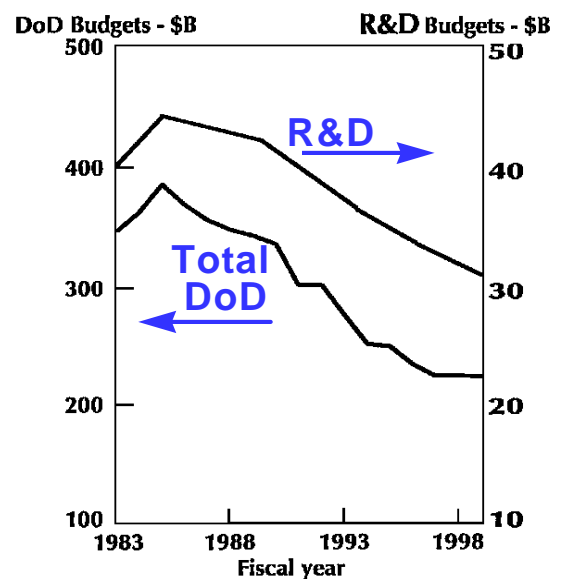


Fig. 7: DoD Budget Trends

While the decreasing DoD budgets led to consolidation changes in airframe companies, there

have been similar changes in the material supplier industry. Shipments of composite prepreg started slowing in 1989, causing ripples in an industry that had been growing at 20-25% per year. The downturn in material orders led to consolidation of the material suppliers, resulting in companies exiting the industry, bankruptcies, and buyouts. The bottom was reached in 1993, and the industry is again experiencing growth, but most of this growth is in the commercial marketplace. However, the carbon fiber suppliers are not repeating past practices of over-facilitating, which has created long lead times for carbon fiber since demand is currently exceeding capacity.

THE FUTURE PARADIGM

While the industry has been downsizing, right-sizing, consolidating and merging the U.S. government has been also been undergoing similar change. DoD initiatives are underway on conversion from government to commercial standards and specifications as well as commercial contracting practices, all of which will impact the way we procure and use materials and how we process these materials. DoD has also been evaluating the requirements for future air vehicles under their Fixed Wing Vehicle Program. The government/industry team established that affordability issues are the key design drivers, regardless of aircraft type. Requirements that drive affordability include reduced fabrication cost, reductions in development span, and reduced operational and support costs. However, requirements for reduced weight, increased fatigue life and higher structural operating temperatures are still valid design drivers that must be met with affordable designs.

F-22 Material Applications

The impact of affordability on materials decisions during the design process can be seen in the use of composite materials on the F-22 Advanced Tactical Fighter [Figure 8]. During the proposal stage on this program, the aircraft used about 40% composites to meet performance, temperature and toughness requirements. As the design progressed through successive trade studies, the amount of composite materials decreased to approximately 25% today. This reduction reflects the ever-increasing emphasis on affordability over performance – even for high performance fighter aircraft. While performance is obviously still important, the price that a program is willing to pay for this performance is lower than it was in the past.



Fig. 8: F-22 Material Applications

Design for affordability must be incorporated early in the design process to be effective. This requires better Integrated Product and Process Development [IPPD] methods and tools to permit the Integrated Product Teams [IPT] to be able to perform collaborative design and analysis among all disciplines, including manufacturing and inspection. These tools must be integrated with the business and financial systems to provide optimized design-for-manufacturing methods that integrate scheduling and cost with performance. Development of

IPPD tools is an ongoing effort at university, industry and government labs, but much more needs to be done to achieve a true virtual enterprise that is capable of supporting design at remote sites. The methods being developed must be transferred to industry development teams to fully integrate them into design tools that can be readily used by the design teams. Training of the design teams is also a critical factor that the methodology should address so that *Tutorials* are built into the software programs. The amount of time and schedule that is required to adequately train new personnel must be minimized – this should be provided via on-line training modules that are an integral part of the methods.

Design Paradigm Must Change

In addition to the development of verified collaborative IPPD tools, industry must change the approach to design for composite materials to achieve true affordability. Today, a typical airframe design is made up of lots of *bits and pieces*. The design decisions that lead us down this path are driven by many things -- a lack of knowledge on how to design for the material or process, inadequate or incomplete design tools, *tug-of-wars* and *turf-battles* between different organizations, etc.

In the example shown in Figure 9, a concept aircraft was redesigned for affordability only, resulting in a 94% reduction in parts count and a 95% reduction in fastener count. While this example is overly simplistic, it does show that affordability can be achieved by a dramatic reduction in part count and assembly operations. Development of innovative design approaches and IPPD tools that can be easily used by the entire IPT will enable design teams to achieve this parts consolidation and thereby reduce the cost of composite structures to the point that they are comparable with conventional metallic structures. Only then will we see the use of composites on aircraft structure reverse the downward trend in terms of percent use.

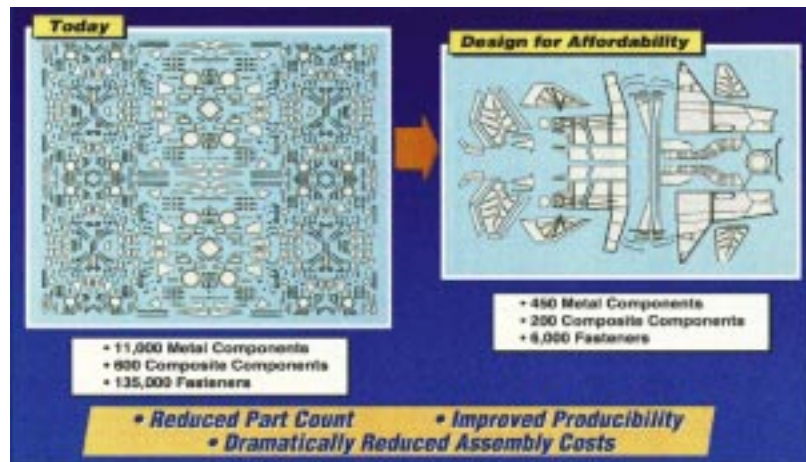


Fig: 9: Design For Affordability Involves Reduced Part Count And Assembly [1]

TECHNOLOGY NEEDS

Over the past two years, representatives of aerospace companies and Wright Laboratories reviewed past development and production programs on composite materials and structures to determine the deterrents to affordability. The primary findings of this study can be divided into design/analysis and materials/structures issues, which are itemized in the following subsections.

Design and Analysis Methods

There is a need within the industry for standardized automated design, analysis, modeling and simulation methods for composite structures that provide:

- A design database of materials properties and specifications prior to start of detail design. This will take a cooperative effort on the part of government and industry. Standardized design data and specifications are needed to provide Mil-Handbook properties (Design Allowables) on composite materials prior to initiation of the design cycle. These design properties must be based on standardized test methods so that all material properties can be compared equally.
- Standardized structural analysis methods that are available for everyone to use. With teaming the norm these days, we need easily used design and analysis methods that are available to multiple-company teams. These methods could then also be used for non-aerospace composite products.
- Design and analysis methods that include physics-based modeling and simulation techniques that cover the range from initial design to fabrication and assembly. With these tools, the design IPT can validate the design prior to release of the design drawings.
- Design-for-manufacturing tools include validated models for material processing, producibility, tool design and manufacturing planning functions. These must allow simplified custom modeling of the design in the IPT environment to provide early detail knowledge. The final output from the IPT should be a "*Build-To Package*" that includes the validated design, all Numerical Control programs, shop planning and operations instructions, inspection steps, tool designs, etc.

Some of these tools exist today, but they do not work together in an IPT environment. Many others need additional research and development and validation. The design tools need to be optimized for large unitized structures that reduce part count to eliminate or minimize tooling and assembly. Large unitized structures are an essential step to affordable composite structures, but the tools for design of such integrated structures are a long way from reality.

Composite Materials and Structures

Lower cost materials and material preforms are other key factors to achieving affordability with composite materials. The material suppliers are working toward \$5/lb carbon fibers for commercial applications -- can these low cost fibers be selectively used for aircraft applications? The aerospace industry has worked on out-of-autoclave curing resins and processes for the past twenty years, but has largely ignored these developments on production applications. Improved resins for lower temperature and pressure cure can reduce the cost of curing composite structures through simplified tooling and lower cost tooling materials. Recent developments in textile preforms also show promise of reducing cost while enhancing out-of-plane loading capabilities. Aligned discontinuous fibers have the capability to be laid out in flat patterns and subsequently post-formed into complex shapes, but development of the material with epoxy resins has stalled and needs to be resumed. Automated fiber placement has made significant progress over the past few years with the concurrent development of towpreg materials. But there is a need for epoxy or thermoplastic resins that will permit real-time cure or consolidation on-the-fly to achieve further improvements in this fabrication

process. In-situ curing resins could eliminate in-process debulk and consolidation cycles that greatly increase fabrication times for thick-section composite structures.

Closed-loop process controls are required to reduce cure cycle time and errors and improve quality of the product. Improved quality will reduce costs and eliminate rework, and provide data for resolution of problems if there anomalies in the cycle.

Innovative structural approaches are needed that will yield large unitized structures that can reduce assembly time and cost. As mentioned previously, the design and analysis methods must be capable of optimizing such designs.

While the industry has made significant progress in automation of the fabrication process, there is still a need for further improvements. Flexible automation for fabrication and assembly is required that is electronically coupled to the design data base. For each fabrication and assembly method there must be compatible process models that can be used for simulation of the entire process.

Trends In Collaboration

In the past we tended to keep everything we developed proprietary, with little sharing of data between companies. We each developed our own analysis methods, data and other tools and convinced ourselves that these provided our competitive edge. With increased teaming among the remaining aerospace companies, there are few secrets in this arena. In the past we each had adequate staff and budget to develop and maintain our methods and databases because there were always multiple production programs to support the technology base, but in today's business environment companies are investing significantly lower levels of funding in research and development, with the result that there are inadequate resources to support all of the required development activities.

We must learn to share data and information that is pre-competitive, and to maintain as proprietary only that data and information that is product related. With fewer and fewer new program starts, industry and government must learn to collaborate on the pre-competitive data and information to reduce the cost of future airframes for both DoD and commercial programs. If we can reduce the cost of airframe products, then we'll see more and more spin-off applications to commercial products.

APPLICATION TO COMMERCIAL PRODUCTS

The technology needs covered here must be addressed in a cooperative spirit between university, industry and government. If we work together to develop, validate and transition the data and methods to industrial programs then we can look forward to a future where we see dramatic increases in the application of composite materials to a wide variety of commercial products that can improve our quality of life and lower the cost of products we procure.

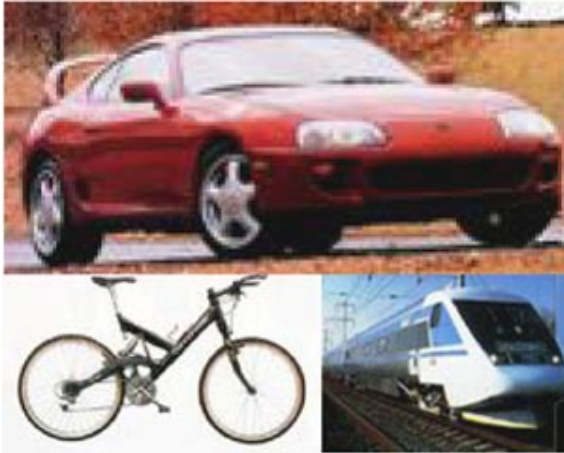


Fig. 11: Commercial Applications Are Rapidly Increasing

If we continue the ways of the past, and do not solve the affordability issues, then we can look forward to a future with diminishing use of composite materials, used only where the customer is willing to pay the premium for increased performance. We know that there are many applications where composites can be applied to increase performance, reduce weight, increase operating life, etc., if composites could be applied at equal or lower cost to other alternative materials. At least one business aircraft employed composite materials for a majority of its structure, but this

extensive use of composite materials increased the price of the aircraft sufficiently to make it unaffordable. Affordable composite designs and processes would have improved the sales potential in these cases. Applications such as bridge reinforcement for better earthquake resistance, lightweight bridges, bicycle and motorbike frames, automobile and truck frames, wind turbines, rail car frames and trucks, golf shafts, tennis rackets, etc., [Figures 10 and 11] provide us with the opportunity to apply composites to reduce weight and increase performance. If only a fraction of these opportunities are exploited, the volume of composite materials used will literally explode overnight – but not many of these opportunities can be exploited if the cost of fabricated components and parts is not decreased. It is up to us collectively to make this future one where composites are the most affordable solution to any design problem.



Fig. 10: Wind Turbines And Blades Are High Potential Application

REFERENCES

1. Westerheide, Donald, “*Design For Affordability, Manufacturing’s Influence On The Future*”, Industry Presentation at DMC95, Defense Manufacturing Conference ’95, 27-30 November 1995, Dallas, TX USA

COMPOSITE APPLICATIONS IN SPORTS EQUIPMENT: TABLE ROLLING OF COMPOSITE TUBES

Jerome S. Berg¹, John T. Kanne²

¹*Manager of West Coast Technical Service, True Temper Sports, 5421 Avenida Encinas,
Suite F & G, Carlsbad, CA 92008, USA*

²*Manager of Composite Products, True Temper Sports-Retired*

SUMMARY: Table rolling is a common and cost effective composite manufacturing process for tubular structures such as golf shafts, fishing rods, and bicycle tubes. Sheets of pre-impregnated composite material are wrapped around a mandrel which defines the inner shape of the part. A compacting tape is spirally wrapped around the uncured material to debulk the structure and to provide consolidation during the curing process. Once cured, the mandrel is extracted, the consolidation tape is removed, and the outer surface is sanded and subsequently painted. Tube rolling allows a multitude of design options by varying the material type, pattern shapes, and mandrel design. This paper presents a short summary of the table rolling process, the equipment, and potential problems and solutions common to the industry. In addition, a partial list of material, equipment, and tooling vendors associated with table rolling is included.

KEYWORDS: tube rolling, golf shafts, bike tubes, table rolling, recreation tubes, mandrel extractor

INTRODUCTION

In the field of composites fabrication, table rolling is a widely used and cost effective technique for utilizing pre-impregnated fibrous tapes which are cut into flag or pennant form for tubular structures. The individual flags become part of the total wall thickness by rolling the flags around a mandrel. The hard mandrel provides the support during cure and defines the inside dimensions of the tube.

Table rolling is utilized to fabricate a variety of products including straight tubes usually under 7.62 cm (3 inches) in diameter and up to 3.66 m (12 feet) long, and small diameter tapered tubes such as fishing rods, golf shafts, and ski poles. Flags may consist of a wide variety of fibers oriented either longitudinally (along the axis of the tube) or off set at a bias angle. In turn, tube rolling patterns are generally referred to as "longitudinal" or "bias" flags. The resin content (RC) and the fiber areal weight (FAW) of the pre-preg define the ply thickness. Since external molds are seldom used for table rolled tubes, a variety of polymer compaction tapes are used to apply an external pressure. These tapes provide the external pressure necessary to debulk and prevent flag unraveling before cure and to provide some heat driven compaction during cure.

Fibers and Resin

Carbon fiber 234 MPa (34 Msi) to 620 Mpa (90 Msi), glass “E” or “S” type, aramids polyethylene, and boron are some of the common fibers in table rolled tube manufacture.

The most common resin used to coat the fibers is the epoxy blend family, which is formulated for specific product purposes. The resin and fiber are combined and advanced slightly to a selected tac (stickiness) level. This fiber and resin combination is called “pre-preg.” Pre-preg surface tac has an important adhesive quality in table rolling which permits composite flags to adhere to one another or the mandrel without slipping during the table rolling operation.

Pre-preg is offered by specification of fiber areal weight (FAW), resin type, resin content (RC), and roll width. Fiber areal weights from 130-160 g/m² and resin contents from 30-36 percent are common in table rolling. Higher modulus fibers favor a lighter FAW to ease rolling. The epoxy in pre-preg is catalyzed, so care must be exercised in following the pre-preg vendor’s storage and handling recommendations. And because air and moisture are detrimental to the surface tac, it is important to cut and consume the flags as soon as possible after opening and unrolling the pre-preg. Dry and low tac pre-preg can influence and aggravate flag wrinkles and ply slippage, leading to voids and dimensional problems. Address tac with the pre-preg supplier to find a suitable resin formulation for the table roller’s manufacturing environment.

Design

The design of a tube rolled part depends on the fiber orientation of the plies, the type or mixture of materials, and the wall thickness. Golf shafts generally consist of $\pm 45^\circ$ layers for torsional stiffness and 0° layers for flexural stiffness. Fishing rods mainly incorporate unidirectional fiber with a fine woven glass scrim backing for hoop strength. Bicycle tubes are generally quasi-isotropic, and if the tubes are internally bonded to an aluminum lug, an inside layer of glass is utilized to inhibit galvanic corrosion. The number of layer wraps at a specific orientation is depended on the design and the ease of manufacturability. Also, it is extremely important to design the flag width to completely cover the mandrel circumference and to avoid gaps or overlays of the layers. Indexing or evening offsetting subsequent layers also helps in maintaining a uniform wall thickness and part symmetry. Occasional, however, trade-offs are sometimes accepted to simplify the manufacturing process at the sacrifice of achieving a perfectly symmetrical lay-up.

EQUIPMENT

Shear/Sheeter

Pre-preg materials are generally supplied as a roll of material. The shear or sheeter is a machine which cuts the roll to length. A number of commercially available power sheeters have hardened steel blades and include automatic feed mechanisms for the material rolls. Safety guards with interlocks are needed to prevent finger and hand injury.

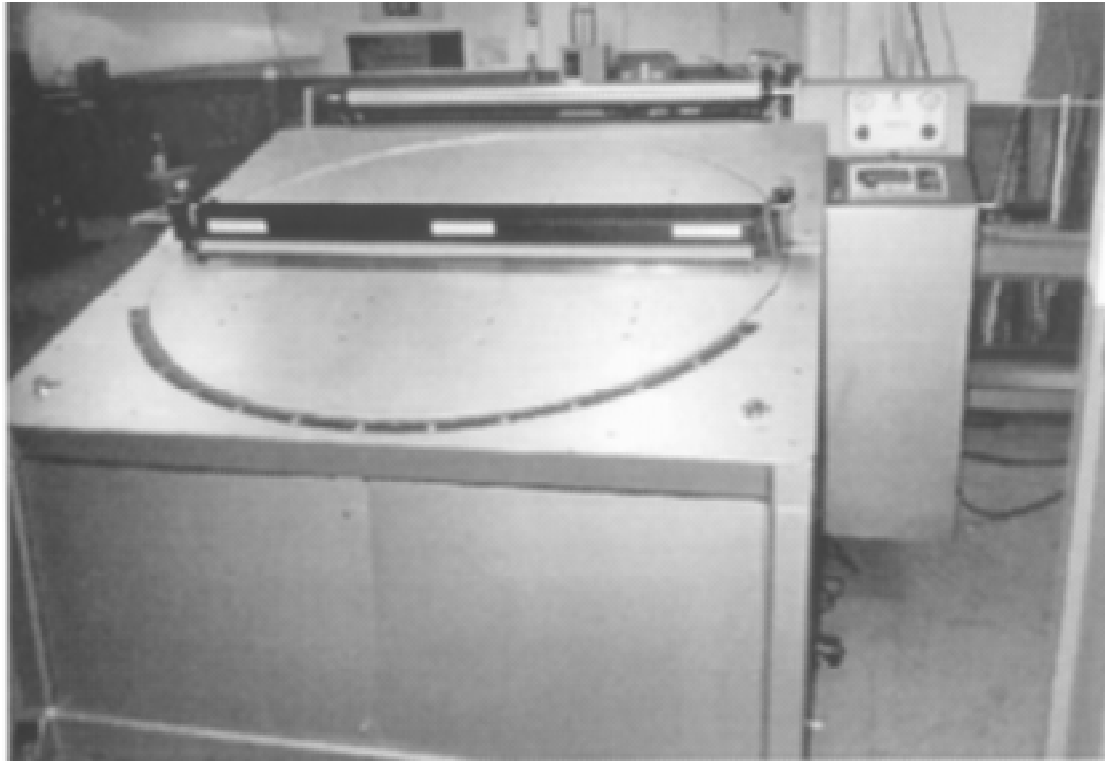


Fig. 1: Sheeter Press, Courtesy of Century Design, Inc.

Roller Press

The roller press is a machine used to press several stacked layers of pre-preg tape into individual flag or pennant patterns. The cutting tooling used in this machine is the steel rule die.

The steel rule die, the pre-preg, and an impact sheet (usually a soft plastic like polyethylene) are passed through the rotating pressure wheels of the roller press. After compaction, the impact sheet is removed to expose a stack of ready-to-assemble flags which are now nested between the blades of the die. The roller press and dies act similarly to a kitchen cookie cutter. A sharp knife and straight edge is a simple solution for prototype or small scale production flag cutting.

Rolling Table

In the 1960^s machines with a rotating and movable lower platen were specifically developed for the tubular composite industry. After activating the machine, a pivoted upper platen is lowered down upon the mandrel, and a linear motion activator in the lower platen rolls the mandrel into the pre-preg flag. These machines permit pressure ranges to be established, gaining maximum compaction and increasing the speed of rolling. The pivoted upper platen permits the combinations of parallel tube or tapered (cone-like) tube rolling. If the mandrel is parallel, then the pivot function of the upper platen will be unnecessary.

Current rolling tables include temperature controlled platens and platens with piano key-like fingers for achieving uniform pressure on tapered parts. Both flat bed and segmented bed versions are covered with canvas. This pad provides sufficient resiliency and friction to permit flags to roll without slipping, yet conform to the mandrel surfaces. A slight dusting of

talcum powder can be used to prevent pre-preg from sticking. Table rolling provides tighter and a more uniform compaction of plies than hand rolling.



Fig. 2: Roller Press, Courtesy of Century Design, Inc.

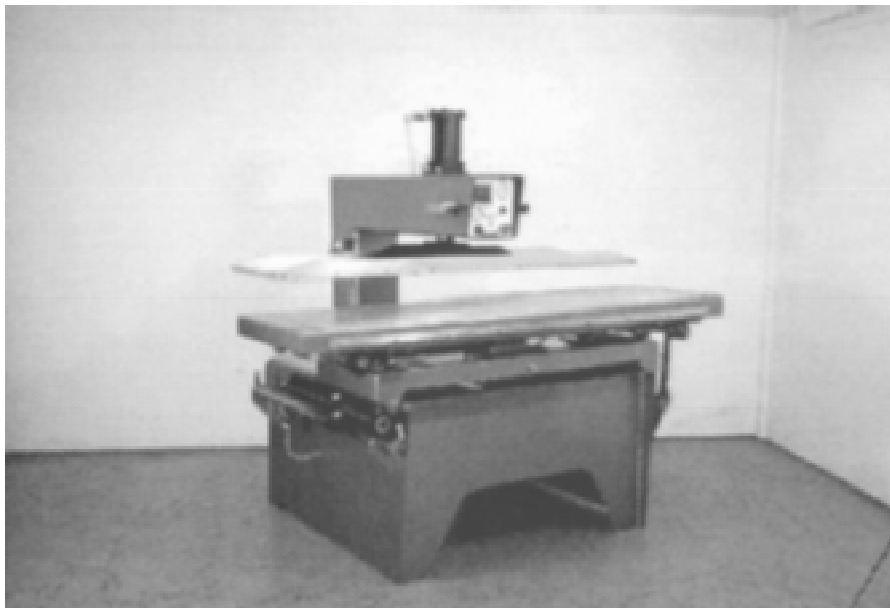


Fig. 3: Table Rolling Press, Courtesy of Century Design, Inc.

Vertical Tape Wrapper

A variety of plastic and/or cellophane tapes, 1.27 to 2.54 cm (0.5 to 1.0 inches) in width are used to compact the table rolled plies of pre-preg. Machines used to apply these tapes must permit tape tensioning to debulk the product as the tape is applied. Some applications call for multiple passes through the tape wrapper to increase the tape pressure for better compaction. As the tube diameter or the wall thickness increases, the compaction affect of the tape diminishes so additional wraps of tape are applied. Frequently, two types of tape may be used:

a release tape (polyethylene) and a secondary compaction tape (polyester or cellophane). Apply the tape as soon as possible after table rolling to prevent the flags from loosening.

Horizontal Tape Wrapper

This machine represents an alternate to the vertical tape wrapper. It is used frequently for longer, heavier parts and also for very flexible mandrels such as fishing rods. The mandrel is affixed to a chuck or mechanical coupling which rotates the parts while tape is applied. The rollers provide support for the part while motion is in place. The single or even dual tape feed spools move with the tape carriage and return to restart position.

After cure, the wrapping tapes are removed by slitting the tape longitudinally and peeling the tape away from the cured part. Wrapping tapes are then discarded.

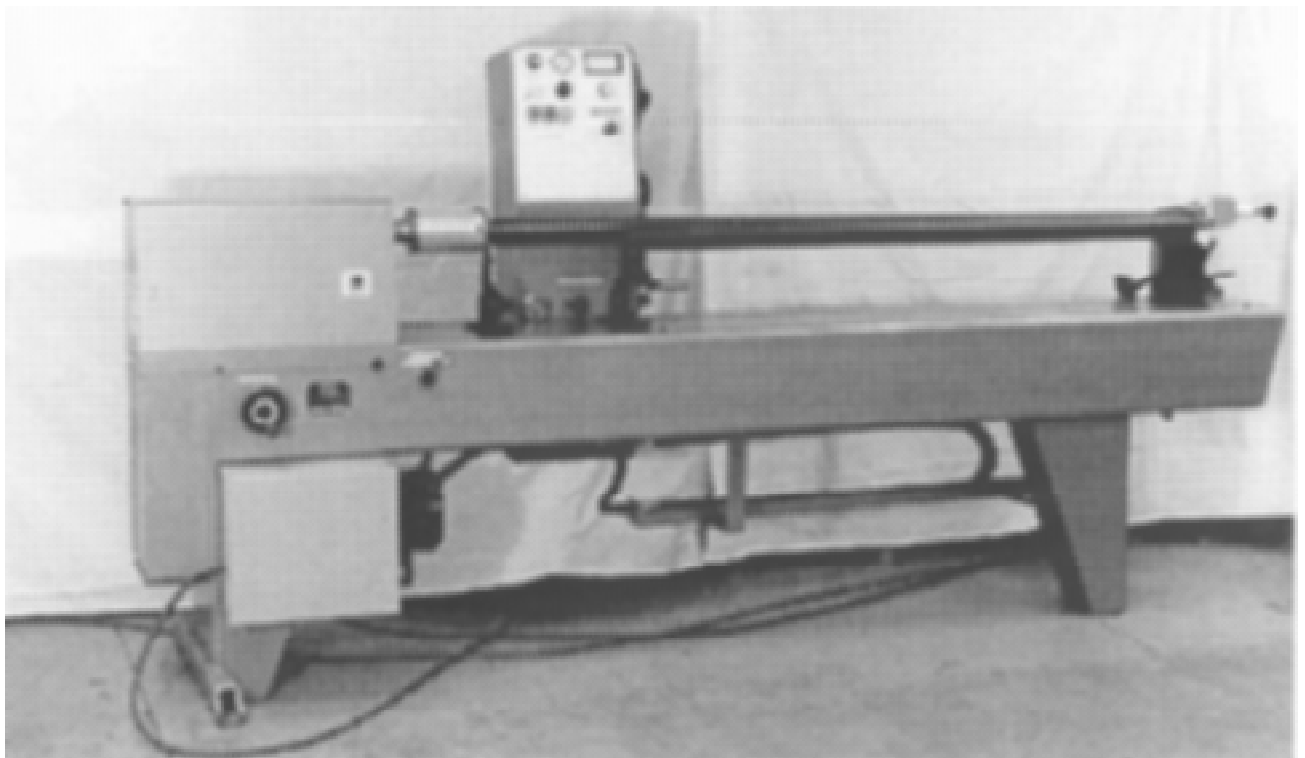


Fig. 4: Horizontal Tape Wrapper, Courtesy of Century Design, Inc.

Mandrel Extractor

Tubular parts which have been cured over a hard mandrel are all subject to mandrel removal. The mandrel extractor generally connects to a bolt on the larger shank end of the mandrel. The end of the composite tube rests against a stationary block shaped to permit passage of the mandrel but blocking the tubular part. Mandrel extractors are generally hydraulic or pneumatic. Hydraulic extractors offer a controlled extraction speed, while pneumatic extractors are faster and useful in high volume environments. Mandrel withdrawal is generally done prior to tape removal.

The type of mold release used, correct size of the stationary block, and the wall thickness of the cured part must be carefully evaluated to prevent end crushing or splitting of the tube.

Very light weight golf shafts with a wall thickness as thin as 0.5 mm (0.020 inches) are possible with the table rolling and shrink wrap process.

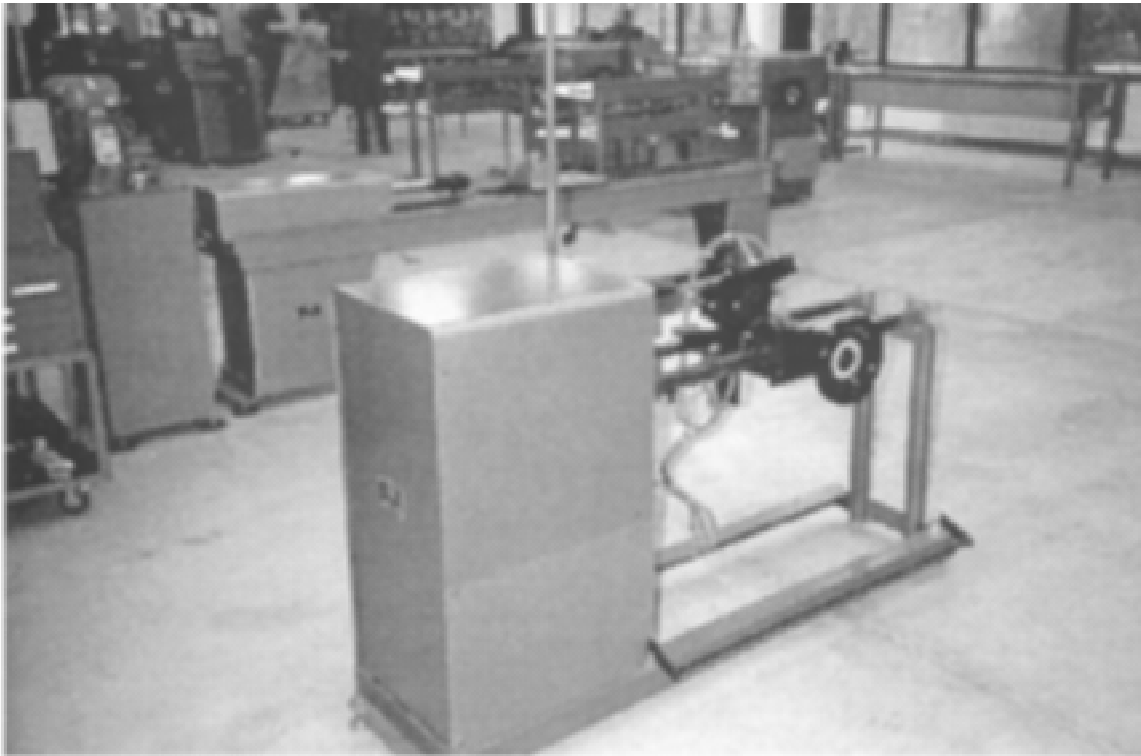


Fig. 5: Pneumatic Mandrel Extractor, Courtesy of Century Design, Inc.

Curing Ovens

Ovens used for curing the composite tubes can be either electrically or gas heated and of batch or conveyorized design. Curing temperatures ranging from 121°C to 191°C (250°F to 375°F) are most common for roll forming pre-pregs. Consult the pre-preg supplier for recommendations on appropriate cure profiles. Fine tuning of the cure profile is often needed to optimize particular roll forming operations and specific products. Ovens with thermocouples are useful in determining hot and cold spots, which may indicate oven regulation for uniform temperature control. This assures a uniform gel and uniform tape compaction within the part.

Centerless Sander or Grinder

The wrapping tapes leave a series of spiral indentations approximately 0.05 mm (0.002 inches) deep in the composite tube surface. If a smooth surface is desired for cosmetic reasons or for geometry requirements the part can be surface sanded or ground. A centerless sander basically removes a user defined controlled amount of surface material. A centerless grinder provides a more accurate finish dimension. Centerless grinders are common for the high precision required for the tip ends of golf shafts in which a tolerance of +/- 0.05 mm (+/-0.002 inches) is not uncommon. In carbon fiber golf shaft manufacture, these surface finishing techniques are also used to tailor the product stiffness by incrementally removing material along the shaft length. This changes the shaft stiffness characteristics.

TOOLING

Mandrels

The mandrels used for table rolling are usually hardened steel, sometimes aluminum or even composite. Golf and fishing rod mandrels are usually solid while larger tube mandrels are hollow. The mandrels are designed to support the pre-preg during rolling and curing and provide the inside dimensions for the part. Recalling that mandrels must be extracted in “mandrel extracting,” some negative taper is beneficial. Hard chromed and plated mandrels generally provide a longer life and easier release since scratched or dented surfaces will hamper mandrel removal.

Steel Rule Dies

These dies incorporate multiple blades embedded in a rigid backing (usually marine grade plywood) which cut the material in the roller press. The pre-preg tape (up to 20 layers) is cut between the cutting die blades and a polyethylene sheet sandwiched between the rotating press wheels. Dies with one piece blades provide the best and most continuous cuts. Dies which include weldments (as in a triangular shape flag) generally dull faster since the weldments soften the cutting edges. Ramps can be used between the cutting blades in die designs to keep the roller pressure off the blade ends. The die builder can recommend blade height and cutting edge type best suited for the task.

MATERIALS

Mold Releases

Generally, mold releases for table rolling mandrels consist of two components: A primary mold release which provides a polymer bond to the mandrel surface to prevent adhesion; and a secondary mold release which acts as a slip agent.

The secondary mold release is most beneficial in straight or slightly tapered mandrels and is reapplied between subsequent mandrel turns. A primary release can lose its effectiveness after several hundred turns and must be stripped off and recoated. A variety of quality mold releases are on the market. The fabricator should work with the release supplier to develop a coating program for the specific application. Silicone based releases should be avoided if the tube is subjected to subsequent bonding or painting.

Fibers

The pre-preg tapes can be made from longitudinal tows or woven tows of the following fibers: aramid, glass, carbon, and boron. Most material vendors have developed robust resins and standard fiber packages specifically designed for the cost conscious recreation industry. Many of the in-depth certification programs, panel testing, and other qualification programs common with the aerospace industry are not necessary.

All of these fibrous composite tapes can be cut into flags and pennants needed for the table rolling process. However, because of the brittle nature of boron pre-preg, boron is often hand cut and used generally as a longitudinal tip reinforcement in golf shafts.

TYPICAL PROBLEMS

Voids

Voids are caused by entrapped air which is not evacuated before resin gelation. The presence of voids reduces the strength bearing capabilities of the part, creates stress risers, and can contribute to surface finishing and cosmetic problems.

Voids are first minimized by working with the pre-preg supplier to assure a high quality material with uniform resin content and good “wet-out” of the fibers. Also, the material suppliers (pre-preg and wrapping tapes) must play a key role in developing a cure profile for the specific process and products.

Voids are increased by flag wrinkles which are indicative of rolling problems. The capability to perform void content checks (ASTM D3171) and photomicrographs of the laminate is extremely useful to develop and improve tube processing. Laminate photos are also very useful in operator training. Few laminates are completely void free but void contents lower than one percent are possible with the table rolling and tape wrap compaction process.

Dry and Difficult to Roll Material

Pre-preg dryness (lack of tac) can be due to low resin content, resin formulation, ambient conditions of the manufacturing environment, the age or out time of the material. Insufficient tac can cause flag movement during assembly, wrinkles, voids, and parts with a poor surface finish. Resin content and formulation can be adjusted to suit the manufacturing environment. Temperature and humidity control are very helpful in maintaining consistent material tac in the manufacturing shop. Avoid leaving cut patterns exposed since moisture in the air greatly affects the material surface tac and sometimes renders it useless. Consuming the material within two days is a good rule to follow.

Warm lay up and rolling tables can help increase material rolling ability and are generally adjusted for slight material and environmental changes. Off angle plies are difficult to roll adjacent to the mandrel and the difficulty is magnified by the higher modulus fibers. Tac tape is a narrow strip of reinforced adhesive designed to aid the adhesion of bias plies to the mandrel. Also, solvent based “tac resins” can be applied to the mandrel to ease application of the first ply. Once the first ply is tightly rolled, however, the material tac is sufficient for subsequent flags.

Part Slippage During Cure

The viscosity of the resin drops as the heat of cure begins. Occasionally, tapered mandrels and the constriction of the wrapping tape during the cure can force a part to slip down the mandrel. Golf shaft design is highly dependent on mandrel reference position for proper stiffness and geometry requirements. Slippage can first be minimized by designing a short semi-parallel section in the mandrel (as in the butt section of the golf shaft). Slippage is also reduced by overwrapping the tapes onto the mandrel at both ends to secure the part. In addition, the cure profile or the mold release can be adjusted to limit slippage.

Exposed Surface Voids

Exposed surface voids after sanding or grinding are indicative of poor rolling practices, insufficient lamination pressure, and questionable material. Exposed surface voids are sometimes referred to as “fiber pulls or picks”, which have a wood grain appearance on parts with longitudinal surface plies.

Longitudinal Ply Waviness

Tapered parts with longitudinally oriented fibers are prone to zones with a wavy or “fiber wash” appearance. The problem is amplified with multiple taper mandrels and very low viscosity pre-pregs. Cure profile modifications or alternate resins can reduce the tendency of “fiber wash”.

PARTIAL LIST OF TABLE ROLLING SUPPLIERS

Equipment

Century Design Incorporated
3635 Afton Road
San Diego, CA 92123
(619)-292-1212

Materials

Pre-preg

Newport Adhesives and Composites
1822 Reynolds Avenue
Irvine, CA 92714
(714)-253-5680
Fiberite
4300 Jackson Street
Greenville, TX 75403
(903)-457-8554

Toray
5729 Lakeview Drive, NE
Kirkland, WA 98083-2548
(206)-827-9029
Cytac Engineered Materials, Inc.
1440 North Kraemer Boulevard
Anaheim, CA 92806
(714)-666-4349

Mold Release

Frekote Products
Dexter Adhesives and Structure Division
One Dexter Drive
Seabrook, NH 03874
(603)-474-5541

Chemlease
P.O. Box 540083
Orlando, FL 32854-0083
(407)-425-2066

Wrapping Tapes

Flexicon Pacific Inc.
856 North Elm, Suite J
Orange, CA 92667
(714)-633-9820

Dunstone Company, Inc.
2104 Crown View Drive
Charlotte, NC 28227
(704)-841-1380

Tooling

Mandrels

Lynco Grinding Corporation
5950 Clara Street
Bell Gardens, CA 90201
(213)-773-2858

Steel Rule Dies

Ontario Die Company of America
2735 20th Street, Box 610397
Port Huron, MI 48061-0397
(810)-987-5060

THE NEED AND REQUIREMENTS DRIVING THE DEVELOPMENT OF POLYMER COMPOSITES FOR AUTOMOTIVE APPLICATIONS

Gilbert B. Chapman, II

*Advanced Materials Consultant, Liberty and Technical Affairs, Chrysler Corporation
30900 Stephenson Highway, Madison Heights, MI 48071, 810-583-5214*

SUMMARY: This presentation will provide an overview of the need, requirements, and constraints governing the development and application of polymer composites in automotive structures. It will discuss the efforts underway by the Automotive Composites Consortium, a joint R&D partnership among Chrysler, Ford, and General Motors, to lead the technology developments required for the cost-effective application of these new materials in mass-produced vehicles.

KEY WORDS: automotive composites, composites development requirements, automotive composites consortium, automotive polymer composites, fiberglass reinforced plastics in automotive applications

INTRODUCTION

Energy conservation, environmental protection, and the concomitant enhancement in quality of life are so important to us that much of our human endeavor is focused on these worthy, interrelated objectives. The role that materials technology plays in supporting these objectives is by no means minor, and is especially important in supporting these objectives through improvements in automotive technology. The advances in automotive products and the processes by which they are created, developed, and manufactured are dependent on prerequisite advances in materials and processes that support the automotive industry or those industries related to it. So materials technology paves the pathway for progress in automotive technology.

The need for this progress is intensifying as public awareness of our finite energy and environmental resources creates market, societal, and political pressures for safer, fuel-efficient, environmentally-friendly vehicles at the affordable costs to which we have become accustomed. The Partnership for A New Generation of Vehicles (PNGV) in the United States and other similar joint government-industry initiatives in Asia, Europe, and North America are but a few examples of efforts throughout the industrial world to develop a "Super Car".

The general requirements for this Super Car are that it must be safe, affordable, energy-efficient, environmentally-friendly, durable, and reliable with good quality and the capacity and performance to which we have become accustomed. These requirements can be reduced to two words: "Low Cost"--in the broad sense of the term. For example, a safe vehicle minimizes the cost in terms of human suffering and misery to the individual and community.

It also minimizes the losses to society, or units thereof, incurred due to inconvenience, injury, or death resulting from vehicular mishaps. An affordable vehicle provides reliable transportation at costs that are commensurate with available financial resources allowed for acquisition, operation, and maintenance. Obviously, affordability is an essential prerequisite requirement. Energy-efficiency minimizes the costs to energy resources expended for the development, manufacture, use, and disposal of the vehicle. The costs to the environment during development, manufacture, use, and disposal must also be minimized in order for the vehicle to be considered "environmentally friendly". Finally, the vehicle must provide value in terms of performance to expectations--capacity, quality, durability, and reliability must all minimize hassle, inconvenience, and the negative value concomitant with the cost of poor quality.

Hence these components of cost are but a few examples of those that all combine to comprise the total or full life-cycle cost to all of those finite resources expended to acquire, use, and dispose of the vehicle. This total cost should be counted as a "fully accounted cost" and minimized systemically by optimizing each cost component. Thus, a low-cost vehicle can enhance the quality of life by providing obvious advantages to individuals and society while maintaining good stewardship of our human, energy, and environmental resources.

Among the obvious advantages that automotive vehicles provide are a mobile society with concomitant increase in productivity, trade, and the distribution of wealth. Less obvious is the benefit brought to a society by one of the three high value-adding, wealth-creating enterprises--manufacturing. The manufacturing enterprise includes the creation, design, and development of the product and contributes significantly to the economic vitality of industrialized societies. The other two wealth-creating enterprises, mining and agriculture, also benefit by supporting the fuel needs of vehicles (petroleum "mining") and using vehicles for farm mechanization. When a society can compete in a global economy by enhancing its enterprises that create wealth and help utilize output (vehicles) from such enterprise to move goods for trade--all without the over-utilization of its natural resources--the quality of life is enhanced and long-term economic gains ensue.

Therefore, having an industry which has played such an important role in creating wealth, improving mobility, and enhancing the quality of life in industrial societies, it is very important to support this industry with technologies that will help it contribute to our drive toward better stewardship of our human, energy, and environmental resources.

Foremost among the technologies that are required to support this drive to improve automotive energy-efficiency and environmental-friendliness is materials technology. Innovative materials technology and designs will be required to meet the energy-efficiency goals of the Super Car. To meet these goals, it is estimated that a 50% reduction in the weight of both body and chassis will be required.

Several materials are current candidates that are expected to contribute to these aggressive weight reduction targets. Alloys of aluminum, magnesium, titanium, and iron high-strength steels in innovative designs, metal-matrix composites, ceramics, engineering plastics, and polymer composites are among them. Polymer composites have been among the leading candidates for years as materials for weight reduction in automotive body and chassis applications. The requirements and constraints for these composites will be outlined in this presentation. Both business and technical barriers will be addressed, along with the concomitant constraints of costs and cycle time which are so crucial to successful application

of composite materials technology in the automotive industry. These automotive requirements will be presented in the light of realistic business, engineering, and manufacturing constraints in hope that the composites R&D community will help address these needs in the context of the constraints and conditions outlined.

THE NEED FOR POLYMER COMPOSITES

As indicated earlier, polymer composites are engineering materials that hold high potential to:

- Reduce Vehicle Weight
 - Reduce Energy Consumption
 - Reduce Impact on the Environment
 - Reduce Dependence on Imported Fuel
 - Reduce Trade Deficit
- Reduce Tooling Investment Cost
 - Reduce Manufacturing Complexity
 - Reduce Break-Even Volume

The weight reduction potential is an attractive asset because of the need to improve the energy efficiency of the vehicle without sacrificing capacity or performance. The Partnership for a New General of Vehicles (PNGV) has set a mass reduction target of 50% for both body and chassis systems and an overall weight reduction of 40% in order to make its 80 mile/gallon stretch goal a realistic probability. This PNGV fuel economy goal is third among the three PNGV goals. All three PNGV goals are:

1. **Manufacturing:** Reduce manufacturing costs and product development times for all car and truck production.
2. **Near-Term Advances:** Pursue advances that increase fuel efficiency and reduce emissions of standard vehicles.
3. **Breakthrough Vehicle:** Super Car - Develop a new class of vehicles with up to 3 times the fuel efficiency of today's comparable vehicles.

The elements of goal three include:

- Triple Current Fuel Economy (80 mpg)
- Intrepid / Lumina / Taurus Size, Performance, and Cost
- Meet Current and Anticipated Safety Standards
- Improved Recyclability and Reduced Vehicle Emissions
- Concept Vehicle by 2000 and Production Prototype by 2004

This third goal is the most visible of the three PNGV goals and is often dubbed the Super Car. Other vehicle objectives include:

- 5-Passenger Capacity
- 0-60 mph in 12 Seconds
- 90 mph Top Speed
- 200 Mile Range
- Maintenance Free for 100,000 Miles
- Equivalent to Today's Full Size Cars

While progress in the development of polymer composite for automotive applications can be expected to lend support to each of these three goals as the technology evolves, it is unrealistic, however, to expect fiberglass-reinforced polymer composites alone to provide the weight reduction required to achieve the targeted fuel efficiency. Therefore, other materials and innovative designs are expected to be employed.

Among the other materials is the closely-related but more expensive cousin--carbon-fiber reinforced polymer composites. Whereas this material has high potential for reaching the weight-reduction target, it is currently priced far beyond the cost target imposed by the automotive market. Efforts are currently underway to provide carbon fiber at much less than the familiar \$12/lb. Prices at an attractive \$3 to \$5/lb. are far more economically appropriate for automotive applications.

THE ISSUE OF COST

The high-volume, mass production of low margin products is a very cost-sensitive enterprise. Capital investment manufacturing process and material costs must be optimized to maximize value to the customer. The quality and performance-to-price ratio must be maximized in order to compete in a value-sensitive and very competitive market. Therefore, material and manufacturing cost must always be kept in mind and minimized where it can be done without reducing quality and value.

The following simple calculations illustrate the small (\$3,055) margin of cost increase a value-conscious customer might be willing to pay for a "Super Car" at current fuel prices if he or she were to govern the purchase decision simply by personal economics--attributing little or no value to environmental quality.

If fuel costs for traveling 100,000 miles in a 5-passenger car at 27 miles/gallon were 3,704 gallons x \$1.23/gallon = \$4,555; and in a 5-passenger car at 82 miles/gallon were 1,220 gallons x \$1.23/gallon = \$1,500--the difference in fuel costs would be \$3,055 (plus environmental costs).

The next scenario shows a larger margin (\$8,571) available for additional vehicle cost at fuel prices of \$3.45/gallon. If fuel costs for traveling 100,000 miles in a 5-passenger car at 27 miles/gallon were 3,704 gallons x \$3.45/gallon = \$12,778; and in a 5-passenger car at 82 miles/gallon were 1,220 gallons x \$3.45/gallon = \$4,207--the difference in fuel costs would be \$8,571 (plus environmental, economic, and political costs).

The results of these simple calculations must be considered when determining the additional costs available for materials or any other technology incorporated into a Super Car in various fuel-price markets. Many customers, however, would be willing to spend more than the break-even with fuel cost in order to contribute to the societal goals of improving environmental quality. Nevertheless, cost is in most cases the bottom line.

REQUIREMENTS FOR AUTOMOTIVE COMPOSITES

The requirements and constraints imposed on automotive composites are captured by the three Rs of our industry:

- Rapid
 - High Volume Manufacturing
 - Automated

- Robust
 - Operate in a "Non-Ideal" Plant Environment
- Reasonable Cost

A "generic" list of automotive composites requirements shows:

- Low Materials Cost
- Short Cycle Time
- Robust Processing Window
- Fast, Reliable Assembly/Joining Technology
- Long Durability in Automotive Environments
- Reliable and Acceptable Crash Energy Management
- Minimal Environmental Impact
- Energy-Efficient Manufacturing
- Customer Acceptance
- High Performance-to-Weight Ratio

These requirements, although not specific, are indicative of the material requirements of the industry. There are also other needs, such as:

- Need for Low-Cost High-Modulus Fibers
- Fiber Size Developments
 - Capability for Rapid Processing (Chopping?)
 - Compatibility with low-Cost Fast-Cure Resins
- High Temperature Property Retention (>120°C)
- Long-Term Durability and Damage Tolerance
- Crash Energy Management Characteristics
- Economically Viable Recycling

In addition to the cost constraints discussed earlier, there are dominant constraints for all advanced materials. Among them are:

- Customer Acceptance (Internal Customers)
- Market Acceptance (External Customers)
- Economic Issues
- Environmental Issues (at Low and High Production Volumes)

There are also concerns that are derived from the aforementioned. These are challenges that must be overcome whenever new materials/processes/design technologies invade a long-established methodological culture.

Common Composites Concerns

- Implementation Strategies
- Design, Materials Processing, and Applications Match
- Material Supply and Processing Issues
- Development Costs and Funding
- Capital (Investment) Costs
- Manufacturing (Molding, Assembly, Coating)

- Materials Characterization and Inspection Issues
- Customer Acceptance
- Energy, Environmental, and Economic Impact

THE AUTOMOTIVE COMPOSITES CONSORTIUM

The Automotive Composites Consortium, a joint R&D partnership among Chrysler, Ford, and General Motors, was organized to lead the technology developments required for the cost-effective application of these new materials in mass-produced vehicles.

Formed in 1988, the Automotive Composites Consortium (ACC) is progressing well towards its goal of developing the technology of structural polymer composites to accelerate its application in vehicles. In cooperative programs with supplier companies and government laboratories and funding, the ACC is prototyping structural members for vehicles, demonstrating high-volume processing technology, developing design methodology for crash energy management, advancing composite joining techniques, and establishing materials test standards.

Prior to the formation of the ACC, each of the U.S. Big Three automotive companies individually conducted programs that established the performance of prototype composites in structural applications such as front rails, floor pans, side aperture panels, space frames, and crossmembers. However, manufacturing technology to produce large structural parts and vehicles which meet the high production volumes and low costs demanded by the automotive industry was not demonstrated. The ACC is striving to meet automotive productivity and cost goals using glass fiber reinforced thermoset materials made by liquid composite molding (LCM), which includes structural reaction injection molding (SRIM) and resin transfer molding (RTM).

Recently, however, the scope of the ACC has been expanded to include thermoset and thermoplastic structural composite materials manufactured by compression molding in its long-range plan and will be further broadened to include all automotive structural polymer composites, irrespective of the manner in which the composite was formed.

Supplier involvement is critical to the operation and success of the Automotive Composites Consortium. Corporations and government laboratories have participated in ACC programs through cost-sharing arrangements. These organizations share the new technology generated in the cooperative program. In addition, the ACC works with many companies and selected universities on a contractual basis and has recently become a partner with the National Institute of Standards and Technology in the Advanced Technology Program (ATP) for our Focal Project II.

Today, the ACC is an integral part of the United States Automotive Materials Partnership (USAMP), an emerging group of partnerships investigating a wide range of polymeric and metallic materials that can be used to maintain high performance levels while reducing vehicle weight. This partnership, including ACC, seeks to support the goals of the Partnership for a New Generation of Vehicles (PNGV) and the high-priority national "Super Car" initiative, which will also be briefly discussed. All of the pre-competitive R&D consortia of Chrysler, Ford, and General Motors operate under the auspices of the United States Council for Automotive Research (USCAR).

This partnership among Chrysler, Ford, and General Motors is proving to be a successful approach to developing structural polymer composites. Aggressive programs to develop and demonstrate new processing methods, design techniques for crash energy management, joining methods, and materials test standards are producing results. The ACC has successfully concluded its first Focal Project and is proceeding with its second application program, Focal Project II, to develop and demonstrate the capability to produce large LCM structures in a cost-effective, robust process.

CONCLUDING REMARKS

- Automotive Applications of Composites are Steadily Evolving
- Auto Industry Recognizes Potential for Structural Polymer Composites
- Future Growth in Automotive Composites Depends on Technological Developments and Market Demands
 - Cost Reduction
 - High-Volume Manufacturing Methods
- PNGV and Future Vehicles Offer Potential for Advanced Composite Materials

In order for the automotive industrial enterprise to continue to pursue its primary purpose, as captured by Chrysler's statement of purpose:

"To Produce Cars and Trucks that People Will Want to Buy,
Will Enjoy Driving, and Will Want to Buy Again",

while also pursuing the implementation of new technologies to meet the needs of the 21st century, we must:

- Learn About Each Other's Needs and Capabilities
- Banish "NIH"
- Promote Government Assistance on R&D to Support Strategic Industrial Initiatives

REFERENCES

1. J. E. Fillion, "Technology Developments in The Automotive Composites Consortium", proceedings of 9th Annual ASM/ESD Advanced Composites Conference & Exposition, November 1993.
2. T. J. Dearlove, E. M. Hagerman, S. N. Kakarala, D. L. Denton, D. G. Peterson, J. C. Lynn, G. T. Bretz, C. F. Johnson, D. J. Melotik, "Standardization of Test Methods for an Automotive Database", proceedings of 6th Annual ASM/ESD Advanced Composites Conference & Exposition, p. 101, October 1990.
3. Automotive Composites Consortium Materials Work Group, "Test Procedures for Automotive Structural Composite Materials", Second Edition, September 1994.
4. G. B. Chapman, II and G. M. Hagerman, "Nondestructive Inspection Technology for Quality Assurance of Automotive Composite Components", proceedings of 9th Annual ASM/ESD Advanced Composites Conference & Exposition, November 1993.

5. B. K. Larson and L. T. Drazal, "The Glass Fiber Sizing-Matrix Interphase in Polymer Matrix Composites: Resin Spreading, Fiber Wetting, and Adhesion in Liquid Composite Molding", proceedings of 9th Annual ASM/ESD Advanced Composites Conference & Exposition, November 1993.
6. G. W. Ritter, C. H. Mao, N. G. Chavka, and G. J. Cinpinski, "A Study of Cores for the Liquid Composite Molding Process", proceedings of 9th Annual ASM/ESD Advanced Composites Conference & Exposition, November 1993.
7. T. S. Ladewig and T. E. Wilson, "Cost Model Development for the Production of LCM Parts", proceedings of 9th Annual ASM/ESD Advanced Composites Conference & Exposition, November 1993.
8. C. Boggs, R. Jeryan, L. Lalik, D. Peterson, C. Venkatesan, "Design, Analysis, and Testing of an All-Composite Shock Tower", proceedings of 9th Annual ASM/ESD Advanced Composites Conference & Exposition, November 1993.
9. G. B. Chapman II, "The Automotive Composites Consortium--Partnering for Growth", to the SME/CMA Conference on Composites Manufacturing and Tooling '95, 30 January 1995, Disneyland Hotel, Anaheim, CA

APPLICATION OF ADVANCED CARBON-CARBON COMPOSITES TO A TIP TURBINE STRUCTURE OF THE ATREX ENGINE

Hiroshi Hatta¹, Yasuo Kogo¹, Muneharu Yoshizawa¹, Nobuhiro Tanatsugu¹
Hisaiichi Onabe², Masakazu Onozuka², Fumiki Tomioka²

¹ *Institute of Space and Astronautical Science, 3-1-1 Yoshinodai, Sagami-hara, Kanagawa, 229 Japan*

² *Ishikawajima Harima Heavy Industry Co., LTD, 3-5-1 Mukaidai-Cho, Tanashi-Shi, Tokyo, 188 Japan*

SUMMARY: A feasibility study was carried out to apply a carbon/carbon (C/C) composite to a turbine disk of Air-Turbo-Ram-Jet engine. The C/C composite has not been successfully applied to such a primary structure subjected to a dynamic load. The optimum design of the turbine disk made of C/C composites was explored in two kinds of structure, i.e., monolithic and joined. The monolithic structure was assumed to be composed of three-dimensionally reinforced (3D) fabrics and the joined structure divided into three components. Through the discussion, the joined structure was shown to be superior to the monolithic structure. It is due to the reason that in the joined structure the optimum arrangement of reinforcing fiber can be easily made obeying the stress distribution in the turbine disk.

KEYWORDS: carbon/carbon (C/C) composite, air-turbo-ram-jet engine, optimum design, dove tail joint

INTRODUCTION

A development study on an ATREX engine, air turbo ram jet with the expander cycle, is now under way in the Institute of Space and Astronautical Science (Japan). The ATREX engine is a combined cycle engine performing like a turbojet engine at a subsonic to Mach 2 flight and a fun-boost ramjet in the flight of Mach 2 to 6 and is planned to be applied to a propulsion system of a fly-back booster of a TSTO (Two stage to orbit) space plane. The structure of the ATREX engine under development is schematically shown in Fig.1, where main feature is that the expander cycle is adopted to improve high speed efficiency and the tip-turbine configuration is employed so as to provide compactness and light weight of the turbo machinery.

This engine is estimated to possess sufficient effective thrust up to Mach 6 at 35 km altitude. The 1/4-scale model of the ATREX engine, outer diameter of tip-turbine being about 400mm, has been fabricated using refractory metals and performance of it was tested under the sea level-static condition (Step I in Fig.1). It was reported that satisfactory performance was obtained in preliminary tests, which demonstrated that the flight speed of the Mach 6 is possibly realized [1]. Requirement for the tip-turbine structure of ATREX, shown as the shaded region in Fig.1 and in detail in Fig.2, is extremely severe due to high

temperature environment up to 1500°C and hard loading condition by centrifugal force. Because of this, conventional metallic material, such as super alloy, cannot be applied without a cooling system.

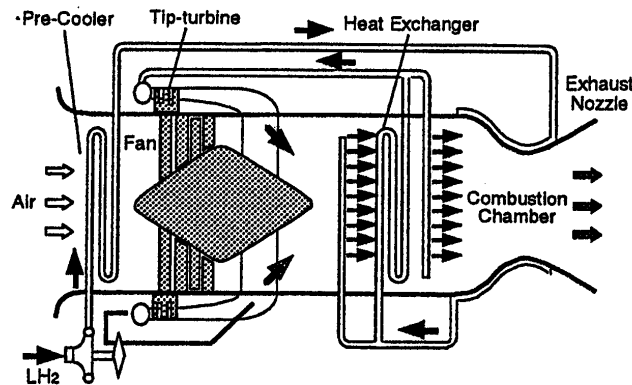


Fig.1 An explanatory diagram of the ATREX engine mechanism.

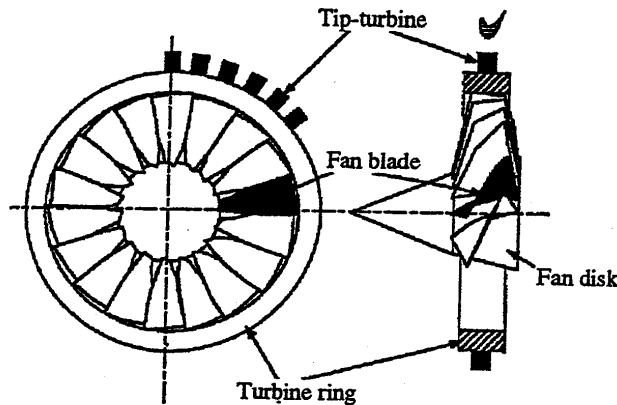


Fig.2 A schematic drawing of the turbine disk for the ATREX engine.

While the tip-turbine structure was made of heat resistant super alloy in the preliminary stage due to low temperature environment in this stage, advanced Carbon-Carbon Composite (ACC) is attempted to be employed as the material for the tip turbine structure. Since the ACCs appears to be only material that simultaneously possess low density about 1.8 g/cm³ and superior mechanical properties, high stiffness and strength, at elevated temperature more than 2000°C [2,3], utilization of the ACC is regarded as an indispensable factor to attain the flight speed of Mach 6.

Table 1 Environmental condition of the ATREX engine.

Turbine Type		Tip Turbine
Tip Speed (m/s)	Turbine	600 ~ 700
	Fan	500 ~600
Fan Inlet Diameter (mm)		300 ~ 600
Fan Inlet Air Temp. (K)		1300
Turbine Inlet H2 Temp. (K)		1800
Heat Exchanger Inlet Combustion Gas Temp. (K)		2700
Heat Exchanger Wall Temp. (K)		2000
Cycle		about 60 min. x1

As shown in Fig.2, the turbine disk has a complex shape, that consists of 2 rings, the turbine ring and the fan disk, and the fan blade connecting the 2 rings. This type of a shape is ordinary regarded as rather difficult to form by use of a continuous fiber reinforced composite material. This is due to difficulty to arrange fiber directions optimally in accordance with varying loading directions from place to place. Thus in this paper, emphasis will be placed upon how to place reinforcing fibers and how to integrate the optimally designed components into the tip turbine disk system.

STRESSES INDUCED IN TURBINE DISK

The most severe stress appeared in the turbine disk is estimated to be that due to the centrifugal force. In Fig.3 the highest stresses in the individual components, the turbine ring, the fan, and the fan disk, of the turbine disk induced by the centrifugal force are shown as a function of the rotation speed of the outer fan tip. In the calculation of Fig.3, the stress transfer between the individual elements was neglected, in other words, the stresses shown in Fig.3 is the maximum tensile stress in the each component when they rotate independently in the own place. It is obvious from this figure that the hoop stress in the turbine ring is highest and the value of the stress is about 560 MPa at 440m/s, which is the rotation speed when the flight speed is supposed to be Mach 6.

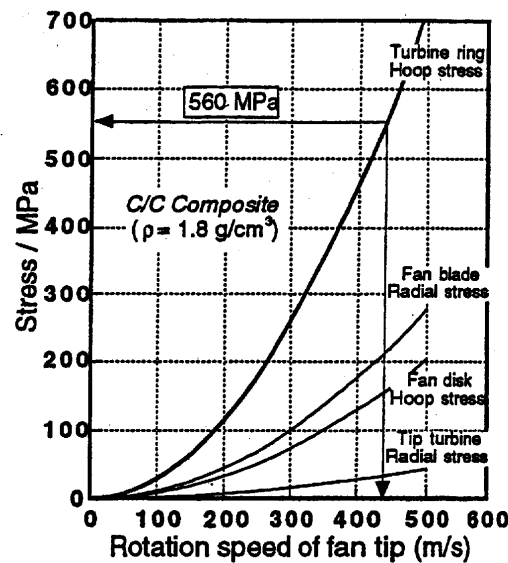


Fig.3 The maximum stress induced in each component of the turbine disk as a function of the fan tip speed.

In addition to the centrifugal force, thermal mismatch stresses should be induced due to temperature distribution of in the turbine disk. For instance in the Mach 6 flight condition, temperatures of the tip turbine, the outer tip of the fan, and the fan disk are estimated to be 1500°C, 1200°C, and 800°C, respectively. In the case of a turbine made of nickel base super alloy whose coefficient of thermal expansion, CTE, is about 8×10^{-6} , thermal mismatch displacement between the fan and the turbine ring in the radial direction yields thermal stress of about 800 MPa. On the other hand, for the case of the ACCs the CTE is extremely low ($-1 \times 10^{-6} \sim 1 \times 10^{-6} /K$), though the CTEs of laminate ACCs along the out of plane direction is

relatively high ($4 \times 10^{-6} \sim 8 \times 10^{-6} /K$). Thus the effect of thermal mismatch stress can be neglected.

PROPERTIES OF ACC

Strength and toughness of the ACCs ordinary increase with increase of temperature up to about $2500^{\circ}C$. Hence we can conservatively estimate applicability of the ACCs from the mechanical properties at the room temperature. Recently strength of a high performance ACC improved rapidly, for instance with the room temperature strength for unidirectionally reinforced one; 1400MPa and a cross ply laminate; 700 to 800 MPa [3,4]. Thus from the comparison of the predicted maximum stress of 560 MPa in Fig.3 and the above-mentioned strength of the ACCs, it can be concluded that the ACCs possesses sufficient capability to sustaine the load required for the ATREX turbine disk.

However, the ACCs have well known two kinds of drawback. First one is low strength of interlaminar. For example, interlaminar shear strength (ILSS) of a unidirectional and cross ply ACCs are 20~30 MPa and 10~20 MPa, respectively. Since complex tri-axial stresses distribution is anticipated to be induced in the turbine disk, It is concluded that three-dimensional reinforcement [5] is indispensable for the ACC application.

The other problem is low oxidation resistance of the ACC in high temperature oxidizing environment higher than $500^{\circ}C$. It is established fact that thermal barrier coating of SiC and vitreous crack shielding is effective especially against short period and low times of heat cycle oxidation in the temperature range up to $1700^{\circ}C$ [6,7]. Thus the SiC coating is assumed to be applied to the region of the fan and fun disk. For the outer side of the turbine ring and the tip turbine, the SiC coating can be omitted, because atmosphere of them is pure hydrogen, and to hydrogen, ACCs possess sufficient environmental resistance even in elevated temperature.

CONFIGURATION OF TIP TURBINE STRUCTURE

The load and shape of the turbine disk are essentially axi-symmetric. Therefore it is not difficult to estimate stress distribution roughly and locations of stress concentration in the turbine disk. High values of tensile stress are predicted in the turbine ring in circumferential direction and fans and their roots in the radial direction. To reinforce these regions and directions, two types of configurations made of the ACCs will be explored, i.e., monolithic and joined Structures.

Monolithic Structure

As for a monolithic structure, three-dimensionally woven (3D) fabrics reinforced in the directions of r, q, and z as schematically shown in Fig.6 are considered to be a most promising material as a reinforcement of the ACCs, in which z axis coincides with rotational axis. In this configuration, a thick circular disk made of the ACC may be firstly formed. Then the disk is machined into the shape of the turbine disk by cutting tools.

One of difficulties encountered in the monolithic structure is that high value of tensile stress is anticipated in the fan due to the load transfer from the expanding turbine ring by the centrifugal force. This stress appears due to variation of the centrifugal force with the radial

position, i.e., difference between large radial displacement of the turbine ring and small displacement of the fan.

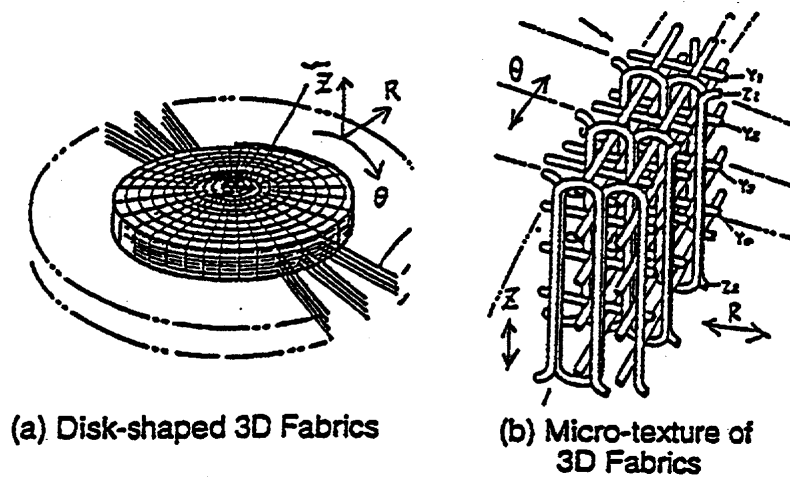


Fig.4 A3 – dimensionally reinforced fabrics for the turbine disk and its texture

It can be minimized if the radial displacement of the turbine ring can be suppressed for example by increasing Young’s modulus of the turbine ring. Figure 7 represents the effect of Young’s modulus on the tensile load of the fan blade. In the figure 1xE, 3xE, 5xE, and 10xE stand for the cases of Young’s modulus ratio of the turbine ring to the fan being 1, 3, 5 and 10, respectively. It is obvious from this figure that the fan stress drastically decreases with increase of the turbine ring modulus and, when the ratio equals to 5, the stress transfer from the turbine ring to the fan blade becomes negligible. However in the monolithic structure, volume fraction of the reinforcing fiber cannot be controlled freely so as to control the Young’s modulus.

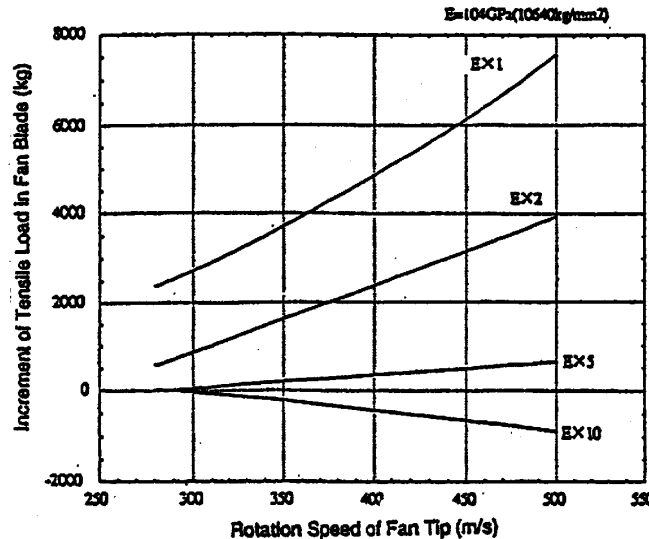


Fig.5 The effect of Young’s modulus ratio of the turbine disk on the transfer load from the turbine ring to the fan blade.

As shown in Fig.4, the maximum stress appears in the turbine ring, and this stress is tensile and in the circumferential direction. Hence, in the turbine ring heavy reinforcement must be placed in the hoop direction to sustain centrifugal force as well as to cancel load transfer from

the turbine ring to the fan. On the hand, the heaviest reinforcement in radial direction is required in the fan and nearly isotropic one in the fan disk. Thus roughly speaking, ideal reinforcing directions are hoop in the turbine ring, radial in the fan, and quasi-isotropic in the fan disk, respectively. Among them the reinforcement of the turbine ring takes priority of others as demonstrated by Fig.4.

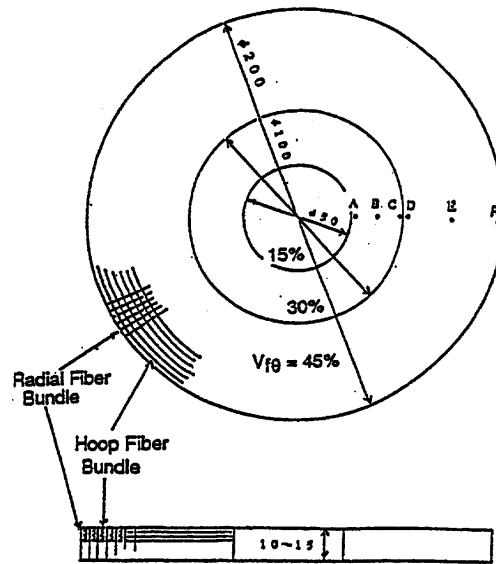


Fig.6 Volume fraction of hoop fiber in the 3-dimensionally reinforced fabric for the turbine disk.

In the meanwhile, fabrics makers say that from the view point of restriction on fabricating 3D fabrics the volume fraction of the hoop fibers in the 3D fabrics for the turbine ring is at the utmost set to 45%. With this volume fraction in turbine ring, it is not difficult to get three times difference of the fiber volume fractions between the turbine ring in the hoop direction and the fan blade in the radial direction. The ACC using the preform shown in Fig.8 has been thus fabricated, i.e. to obtain three times of the volume fraction difference, volume fraction of hoop fiber $V_{f\theta}$ is intentionally varied as shown in the figure, and machined into simplified monolithic structure model as shown in Fig.9. High speed rotation test will be carried out to ensure potential of monolithic structure.

In the monolithic structure, there is one more difficulty being necessary to be overcome. While the fan is twisted as shown in Fig.3, the radial reinforcing fiber is straight. Therefore the radial reinforcing fibers in the fan are actually cut into short fibers and radial strength in the fan must be reduced greatly. In order to get over this problem, the following two countermeasures are being explored.

To develop 3D-fabrics with the radial fiber curved along the twisted fan.

To make the fan thicker so as to maintain sufficient strength.

Joined Structure

The other configuration is a joined structure. In this configuration, the fan disk, fan blades, and turbine ring + tip turbine blades, shown in Fig.3, are first formed separately and then the fabricated each component is to be assembled into the tip turbine disk structure in the order shown in Fig.10. For this structure, strength of each components can be easily optimized in

accordance with each stress distribution, because fiber orientations and volume fractions can be easily optimized due to simplicity of component shapes.

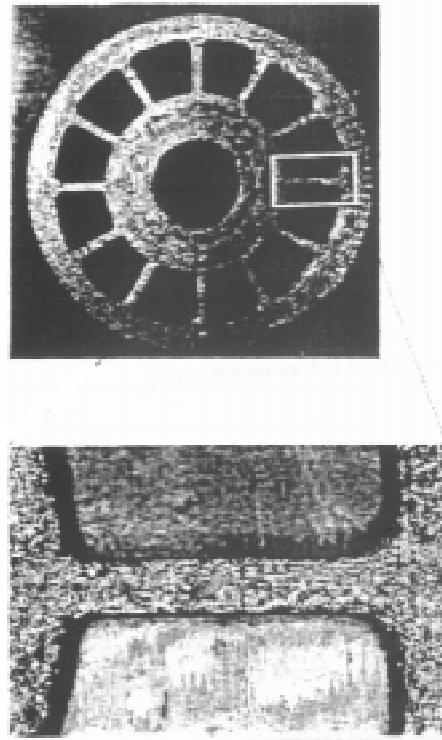


Fig.7 A simplified model for the monolithic turbine disk made of 3-dimensionally reinforced ACC.

In order to assemble the turbine disk structure efficiently, two types of joint configurations are attempted to be employed as shown in Fig.11. One of the joints is a dovetail joint between the fan blade and the fan disk, and the other is a pin joint between the fan blade and the turbine ring. Simplified component tests and analytical studies have been carried out on both type of joints.

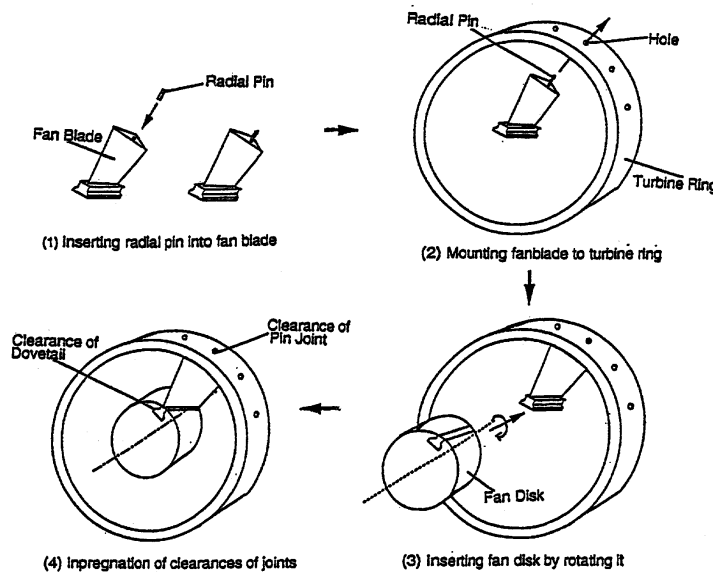


Fig.8 Assembling procedure for the joint tip turbine disk.

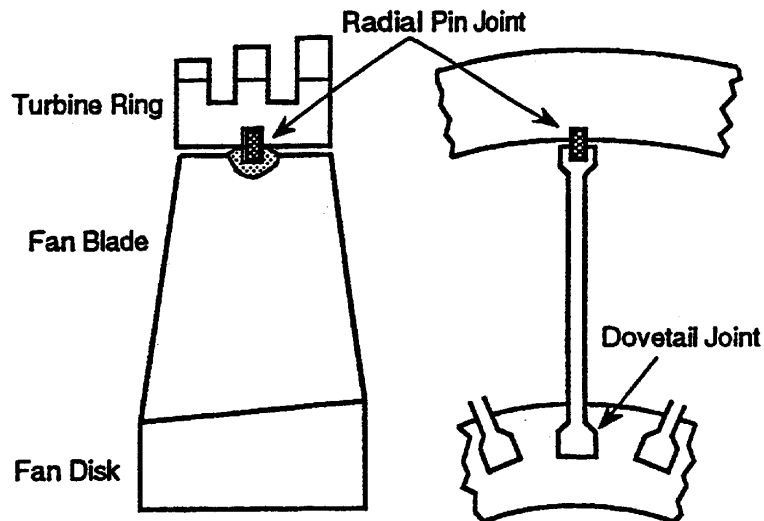


Fig.9 An schematic drawing of two types of joint adopted in the turbine disk of the joined structure

Dovetail Joints

Both of analytical and experimental studies have been carried out on simplified models of the dovetail joint to optimize the dovetail shape and reinforcing directions in ACC.

As a first step analysis, FEM study of the dovetail joint was carried out to clarify the relation between stress distribution and the shape of the joint for laminate type ACC using the two dimensional anisotropic analysis model as shown in Fig.12(a) under loading condition of 440m/s rotation. From these studies, it was shown that the ACC dovetail joint with lower shoulder angle, for example 30° , has higher load bearing capability. But as shown in Fig.12(b), which is typical results of interlaminar shear stress induced in the dovetail, maximum interlaminar shear stress is 90 MPa at the shoulder that an arrow indicate in the figure. Because it is about nine times higher than ILSS of laminate type ACC, it is concluded that laminate type ACC is not adequate for the dovetail material.

Tensile tests of a simplified dovetail joint model made of three dimensionally reinforced (3D) ACC have been carried out as a function of shoulder angle and root curvature to optimize the shape of the dovetail configuration as shown in Fig.12. Figure 13 shows preliminary results of tensile test for dovetail made of 3D ACC. As shown in the figure, maximum load is 7.2 kN. Assuming the 1/4 scale tip turbine structure model (diameter of f400 mm at fan tip), load bearing capacity in actual dovetail made of 3D ACC can be estimated as 106 kN. Considering loading conditions in actual structure of 73 kN at rotation speed of 440 m/s, experimental results suggest that 3D ACCs are possibly applicable to dovetail joints of the ATR engine, at least assuming maximum load can be applied for design. Further experimental and analytical studies are required to clarify the design limit for 3D ACCs and to optimize the shape of dovetail, because subcritical damages will be introduced during loading before final fracture.

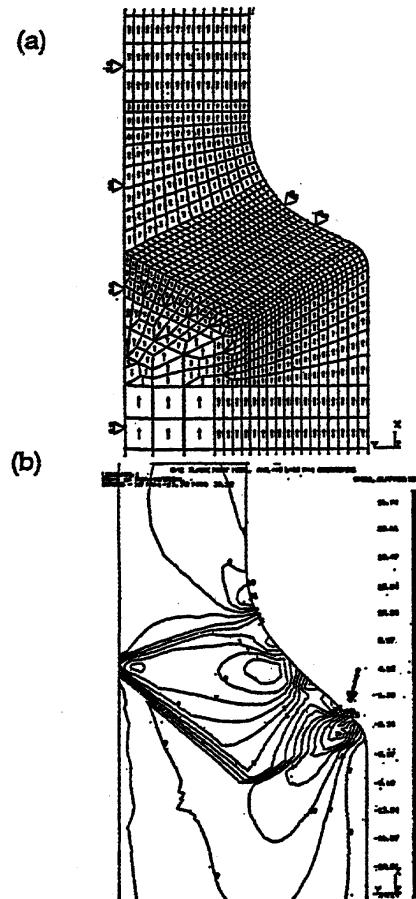


Fig.10 The FEM analysis of the dovetail joint.

(a) An analytical model,

(b) A calculation results for the interlaminar shear stress.

Pin Joints

The other is a pin joint between the fan blade and the turbine ring (Fig.11). This joint transfers the weak circumferential force but doesn't the radial force. Main problem of this joined structure is to prevent reduction of turbine ring strength. As a rule of a jet engine, holes should not be made in the turbine ring because burst rotation speeds of the turbine ring tend to be drastically lowered due to stress concentration appeared around the hole. Thus detailed study on a relaxation measure of the stress concentration around the joint holes is required to materialize this structure. Actually, the tensile test of ACC plates with a hole were carried out to rationalize the joint behavior between the fan blade and the turbine ring using specimens shown in Fig15. Typical results of tensile tests are shown in Fig.16, where stress concentrations were calculated as ratio of fracture stress averaged over minimum net section of specimen with a hole to the fracture strength of smooth specimen. For comparison, analytical results by FEM were also calculated assuming fracture will occur when the maximum strength in the specimen reaches fracture strength of smooth specimen. From these results, it was concluded that fracture stress of specimen with a hole was insensitive to stress concentration around a hole, and thus pin joint between the fan blade and the turbine ring was regarded as a quite effective structure for the case of ACCs.

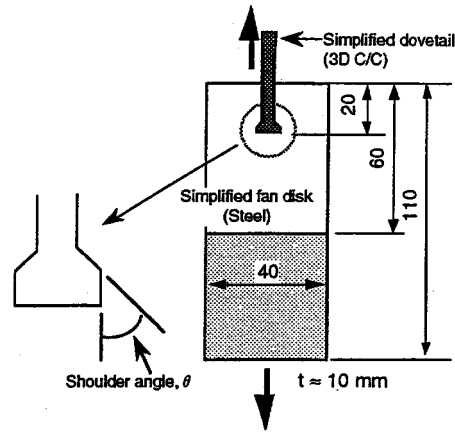


Fig.11 A test configuration for the measurement of dove tail strength

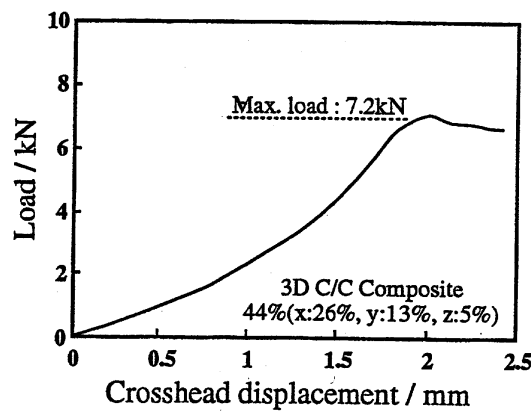


Fig.12 An Load-displacement curve of in the tensile test of the dovetail joint made of 3D ACC..

An unsettled factor peculiar to the joined structure is vibration induced by asymmetric displacement of the turbine ring during high speed rotation. The pin joints automatically tend to suppress non-axi-symmetric displacement because stiffness of the joint pin and the fan blade prevent the asymmetric displacement. However the region of rotation speed of turbine disk, where this mechanism is effective, is not clear and a simple model experiment is now in preparation.

Comparison of load bearing capability between the monolithic and joined structures leads to a tentative conclusion that the joined structure is superior to the monolithic structure, though uncertainty concerning vibration of the turbine ring is still exist..

HIGH SPEED ROTATION TEST

High speed rotation tests have been also carried out to confirm the stress distribution and the failure criteria of the tip turbine structure under rotation. Fig.17 represents schematic view of the rotation burst tester derived by an air turbine, made by Maruwa electric Co., that have the maximum rotation speed, 100000 r.p.m. In this tester, telemeters and high speed cameras are mounted to measure strain distribution and fracture initiation patterns of the rotating disk. During the rotation test, the chamber, in which the specimen is set, is evacuated by a rotary pump.

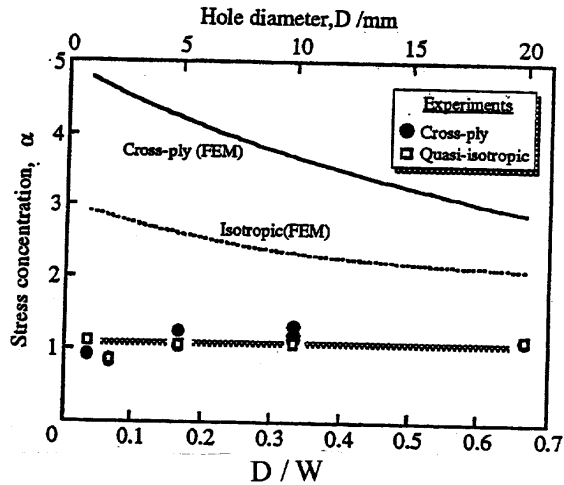


Fig.13 Stress concentration in the tensile test of the ACC specimen with a hole.

The test on a flat ACC disk with the quasi-isotropic stacking sequence of carbon fiber resulted in the peripheral velocity of the fan equal to 427 m/s at the burst point of the ACC disk. The fracture pattern of the disk specimen is shown in Fig.18. The fractured specimen was collected by thick felt sheets and rubber tire. Comparison between the results from the rotation test and that of static tensile test implied that the failure of ACC during rotation test occurred obeying the average stress condition over the radius of the disk rather than the maximum stress condition. In the next step, a high speed rotation test of simplified turbine models will be performed to explore further efficient structures.

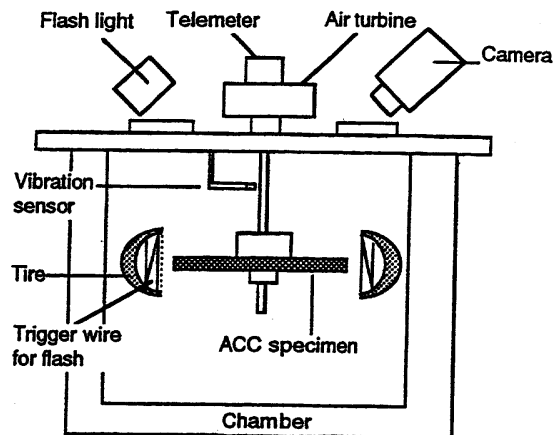


Fig.14 A schematic drawing of the spin burst tester.

FURTHER APPLICATION OF ACCS

Almost all the components of ATREX engine are to be exposed to high temperature environment as shown in Fig.19. It is obvious from this figure that the down stream region of engine becomes extremely high temperature. As shown in Fig.20 there is no other material exhibiting high strength in the temperature range higher than 1200° C. Thus to lower the weight of the whole engine system by minimizing introduction of a cooling system, utmost application of the ACCs is preferred. In our project, the next item to examine the ACC application is chosen to be the heat exchanger. Difficulties encountered in the ACC application of the heat exchanger are extremely high temperature in oxidation environment

and an extremely complex shape. By application of ACC to the turbine disk and the heat exchanger, weight reduction compared with an all-metal engine is estimated to be 35kg in the 1/4 scale model.

Table2 Stress concentration in turbine disk models.

Models	Elements	Average stress	Concentration points	Stress concentration
Monolithic structure	Ring (σ_{θ})	126 (a1)	221 (a2)	1.8 (a2/a1)
	Fan (σ_r)	74 (b1)	103 (b2)	1.4 (b2/b1)
Joined structure	Ring (σ_{θ})	323 (c1)	790 (c2)	2.4 (c2/c1)
	Fan (σ_r)	199 (d1)	312 (d2)	1.6 (d2/d1)

*1 σ_{θ} : Circumferential stress (MPa), σ_r :Radial stress (MPa)

*2 Rotating speeds: Monolithic 30,000rpm, Joined 30,600rpm

Table3 Measured strains and estimated fracture rotation speeds.

Specimens	Elements	Measured strain (5,000rpm)	Failure rotating speeds (2,000 $\mu\epsilon$)	Failure circumferential speeds
Monolithic structure	Ring (ϵ_{θ})	24.6 $\mu\epsilon$	45,083 rpm	472 m/s
	Fan (ϵ_r)	61.4 $\mu\epsilon$	28,536 rpm	298 m/s
3D-Ring	Ring (ϵ_{θ})	24.4 $\mu\epsilon$	45,267 rpm	474 m/s

*1 Measured points: center of elements

*2 Circumferential speeds : calculation based on specimen diameter ϕ 200mm

*3 ϵ_{θ} : Circumferential strain, ϵ_r : Radial strain

CONCLUSION

In order to apply ACC to the tip turbine structure, feasibility study was carried out on the two types of configurations, those were the monolithic structure and the joined structure.

Comparison of load bearing capacity by the stress analysis and component tests for both configurations, it is tentatively concluded that the joined structure is superior to the monolithic structure.

Further study is needed to optimize shape and arrangement of reinforcing fiber directions. Furthermore, vibration in the joined structure should be evaluated for materializing tip turbine structure.

REFERENCES

- N. Tanatsugu et.al.,” Development Study on ATREX Engine for Future Space Plane” , 19th ISTS, 1994-5 Yokohama, in printing.
- G. Savage, “ Carbon-Carbon Composites” , Chapmanhall, 1993.
- C. R. Thomas, “ Essentials of Carbon-Carbon Composites” , Roy. Soc. Chem., 1993.
- J. E. Sheehan, “ Carbon-Carbon Materials and Composites” , NASA Ref. Pub., Chap.8, pp.223-266, 1992.
- T. W. Chou, F. K. Ko, “ Textile Structural Composites” , Composite Material Series Vol.3, Elsevier, 1989.

DEVELOPMENT OF HIGH PERFORMANCE CARBON/CARBON BRAKE DISK FOR AN ADVANCED AIRCRAFT

Jinyong Lee, Jong-kyoo Park, Heun-seung Ha and Byung-il Yoon

4-5-3 Agency for Defense Development, P.O.Box 35-4, Yusong, Taejon 305-600, Korea

SUMMARY: This paper describes the manufacturing process and the dynamic torque test result of carbon/carbon aircraft brake disk. Through the methods of a pitch impregnation and chemical vapor infiltration using specially designed preform carbon/carbon brake disk with required properties such as friction and wear, density, thermal and mechanical properties etc. have been manufactured for the qualification test after the processes of a nondestructive test, a machining, a metal channel installation and an antioxidation treatment. All qualification tests including a dynamic torque test and a service life test were performed according to the specifications of the MIL-W-5013 and the GD16ZL001B of the Lockheed(General Dynamics) with an inertia dynamometer. From the all qualification test the brake assembly has shown superior braking performance comparing with the current qualified carbon/carbon brake disk and has passed the all requirements.

KEYWORDS: carbon/carbon brake disk, dynamic torque test, inertia dynamometer, MIL-W-5013,

INTRODUCTION

Because of their low density, excellent high temperature mechanical properties, self-lubricative and high heat absorption capability, carbon/carbon composites have been considered one of the best materials in the aircraft brake industry. Although aircraft brake is a core of the landing part, large consumed and connected directly with the safety of a pilot only several countries have succeed in developing carbon/carbon brake disk in the worldwide.

In partnership with the Daewoo Heavy Industries Ltd. We, the Agency for Defense Development have been developing carbon/carbon brake disk. In the brake disk development it is necessary to test and evaluate dynamic torque property of the brake materials using an inertia dynamometer. In accordance with the specifications of MIL-W-5013 and the GD16ZL001B of the General Dynamics (Lockheed) regarding the development of aircraft brake disk we have performed dynamic torque test consisting of 45 stops of landplane landing design gross weight, 5 stops of maximum landing design gross weight and 1 stop of maximum design gross weight(rejected take-off) for several sets of brake assembly. In addition to the test, a service life test of 500 stops under the purpose of evaluating service life and reliability of brake disk has been performed. All results from these tests have satisfied the requirements.

FABRICATION OF CARBON/CARBON BRAKE DISK

Carbon/carbon brake disks were manufactured using a typical process of liquid impregnation and carbonization. In the fabrication process PAN-based carbon fiber and coal-tar pitch were used as a reinforcement and a matrix precursor respectively. To obtain a good friction property and structural stability high modulus chopped carbon fiber after undergone heat-treated at about 2500 was used for friction surface and continuous carbon fiber fabric consisted of a center part of brake disk which plays important role in load-bearing during operation. The properties of carbon fiber and pitch used are in table 1 and 2 respectively.

Table 1: Property of carbon fiber used in the manufacturing carbon/carbon brake disk

Tensile strength (MPa)	Tensile modulus (GPa)	Elongation (%)	Density (g/cc)	Filament diameter (μm)	Specific heat (kJ/kg.K)
3,400	235	1.3	1.8	6.8	0.17

Table 2: Property of coal-tar pitch used a matrix precursor

Specific Gravity	Softening Point ($^{\circ}\text{C}$)	Carbon Yield, 1000 $^{\circ}\text{C}$ (%)	Toluene insoluble (wt%)	d002(\AA)
1.31	117	43.0	41.0	3.581

As the first step in the fabrication, green disks were manufactured using a pitch-prepreg and chopped carbon fiber with a hydraulic press and the green disk was carbonized using a furnace in a special metal container designed to suppress the green disk expanding in carbonization and then several times of impregnation and carbonization processes were performed to obtain a required density. In the middle of the densification process 2 or 3 times of a high temperature heat treatment called a graphitization were applied to facilitate a pitch impregnation and develop a matrix microstructure having a good friction property. After the liquid densification process the brake disk with a required density was suffered a chemical vapor infiltration (CVI) as a final densification. The brake disks having a enough density were evaluated by non-destructive test (NDT) an internal flaws and prepared the dynamic torque test through the processes of machining according to a drawing, metal channel installation and antioxidation coating at non-friction parts. Table 3 shows typical properties of the carbon/carbon brake disk.

DYNAMIC TORQUE TEST

Introduction

According to the specifications of the MIL-W-5013 regarding only a military aircraft development and the GD16ZL001B of General Dynamics(Lockheed), a dynamic torque test is should be performed for development of an aircraft brake with 45 stops of a landplane landing design gross weight braking, 5 stops of maximum landing gross weight braking and 1 stop of rejected take-off(RTO) similar to an aircraft maximum design gross weight. All tests

should be performed using a same brake disk assembly but RTO test can be performed using tested assembly or a new one.

Table 3: Typical properties of the carbon/carbon brake disk

Density (g/cc)	Tensile strength (MPa)	Compressive strength (MPa)	Flexural strength (MPa)	ILSS (MPa)	Thermal conductivity (W/m.K)
>1.75	80-110	110-140	100-140	10-12	25-30(∥) 80-90(⊥)

After the dynamic torque test, service life dynamic torque test which is consisted of 333 stops of landplane landing design gross weight braking and 167 stops of 74% landplane landing design gross weight braking should be performed to evaluate braking reliability and service life in accordance with the GD16ZL001B.



Figure 1: Photograph of the prototype brake assembly

Braking Performance Test

Test and Evaluation Criteria

All dynamic torque tests were performed according to the MIL-W-5013 and GD16ZL001B using a certified inertia dynamometer which can simulate kinetic energy absorbed by a brake assembly in an aircraft landing and evaluated by criteria such as a maximum braking pressure, braking stability, braking distance, tire bead and wheel temperature defined in Table 4 and Table 5 respectively. For our development program the dynamic torque tests were performed for an existing qualified disk assembly and the prototype brake disk assembly under the purpose of comparing braking performance. Figure 1 shows the prototype brake disk assembly.

Test Results

Table 6 and 7 show the dynamic torque test results for the prototype and an existing qualified carbon/carbon brake disk assembly. Considering the braking pressure needed to satisfy braking distance requirement an existing brake assembly need more braking pressure than the prototype brake assembly. It can be concluded that a prototype assembly has better braking performance than a qualified existing brake assembly in conditions of the landplane landing design gross weight braking and the maximum landing design gross weight braking. Especially in the RTO test the prototype showed superior braking performance that only as low as pressure of 1176 psi is necessary to stop an aircraft safely within a required braking distance. From the RTO result it is evaluated the prototype has more survivability in emergency landing which is being issued in a qualified current brake assembly.

Table 4: Dynamic torque test conditions

Test Conditions	A	B	C
Aircraft weight (pounds)	19,500	27,500	37,500
Braking kinetic energy (million feet pounds)	5.7	10.5	18.1
Inertia equivalent weight of dynamometer (pounds, max)	9,536	12,650	13,191
Braking velocity (knots min.)	116	137	176
Tire load (pounds)	7,380	10,147	13,811
Tire rolling radius (inches)	11.7	11.4	11.3

A : Landplane landing design gross weight braking test

B : Maximum landing gross weight braking test

C : Maximum design gross weight braking test(Rejected take-off test)

Table 5: Evaluation criteria in the dynamic torque test

Test conditions		A	B	C
Requirement				
Max. allowable braking pressure (psi)		2,300	2,300	2,300
Braking distance (feet)		2,238	3,108	5,250
Tire bead seat temperature (max. F)		400	400	410
Axle temperature (max. F)	Inboard	450	450	900
	Outboard	400	400	
Fuse plug release		No	No	After 1 min.

Table 6: Test result of 45 stops in landplane landing design gross weight

Items	Requirements	Existing brake	Results
Braking pressure (psi)	2,300 (max.)	959	506
Braking torque (in.lbs)	NA	29,494	33,286
Deceleration rate (ft/sec ²)	8.60	8.47	9.17
Braking distance (feet)	2,238	2,251	2,136
Braking temperature (°C)	NA	500-700	600-700

Table 7: Test result of 5 stops in maximum landing design gross weight

Items	Requirements	Existing brake	Results
Braking pressure (psi)	2,300 (max.)	1,486	817
Braking torque (in.lbs)	NA	34,366	41,789
Deceleration rate (ft/sec ²)	8.59	9.07	8.72
Braking distance (feet)	3,108	2,872	3,103
Braking temperature (°C)	NA	800-1200	1000-1400

From the braking torque and pressure curve, a braking performance of the prototype brake assembly showed more stable than an existing brake throughout braking. Table 8 is the result of the RTO test for the prototype brake assembly. In the test several R-type thermocouples were installed on the two stator disks in order to measure friction temperature and the temperature was monitored only up to 1700 due to thermocouples melting but the real friction temperature would be estimated as high as 2000. After the test several metal channel were melted and a fuse plug released about 100 seconds elapsed after the stopping.

Table 8: Test result of rejected take-off(RTO) test

Items	Requirements	Results
Braking pressure (psi)	2,300 (max.)	1,176
Braking torque (in.lbs)	NA	41,849
Deceleration rate (ft/sec ²)	8.40	8.74
Braking distance (feet)	5,250	5,112
Braking temperature (°C)	NA	>1700

Figure 2 shows the RTO test with a burning brake assembly.

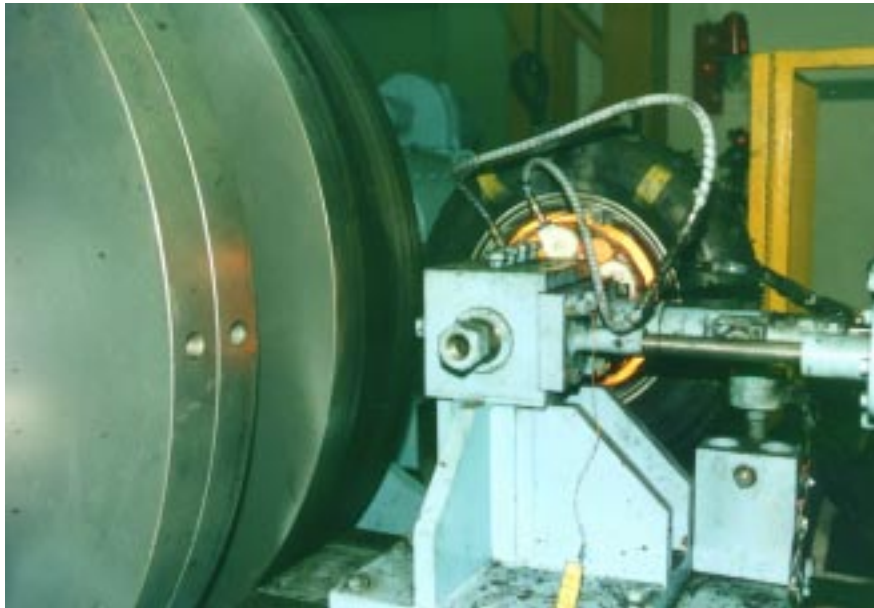


Fig. 2: Photograph showing the RTO test

RESULT OF SERVICE LIFE DYNAMIC TORQUE TEST

In accordance with the GD16ZL001B, 500 stops of service life test was performed for the prototype brake assembly. Table 9 and 10 show the service life dynamic torque test results respectively. During the service life test no brake disk failure was happened and showed superior braking performance and reliability. The service life cycle was projected more than 1000 landings.

Table 9: Test result of 333 stops of service life test in landplane landing design gross weight

Items	Requirements	Results
Braking energy (x10 ⁶ ft.lbs)	5.7	5.9
Braking pressure (psi)	2300 (max.)	542
Braking torque (in.lbs)	NA	33,432
Deceleration rate (ft/sec ²)	8.6	9.2
Braking distance (ft)	2,238	2,159
Braking temperature (°C)	NA	600-700

Table 10: Test result of 167 stop service life test in 74% landplane landing design gross weight

Items	Requirements	Result
Braking energy (x10 ⁶ ft.lbs)	4.2	4.3
Braking pressure (psi)	2300 (max.)	430
Braking torque (in.lbs)	NA	24,789
Deceleration rate (ft/sec ²)	6.4	7.0
Braking distance (ft)	2,238	2,077
Braking temperature (°C)	NA	500-600

CONCLUSIONS

In accordance with the specifications of MIL-W-5013 and GD16ZL001B dynamic torque test was performed with an inertia dynamometer for the prototype brake assembly and an existing qualified brake assembly. Comparing with an existing carbon/carbon brake disk assembly the prototype brake disk assembly showed more stable braking stability, higher braking performance due to higher friction coefficient and evaluated satisfying all the specification requirements.

500 stops of the service life test according to the GDZL001B specification was performed to evaluate a service life and braking reliability. From the test, the prototype brake assembly showed no failure and stable braking performance throughout all the test and service life was projected more than 1000 landing cycles.

REFERENCES

1. MIL-W-5013, "General Specification for Aircraft Wheel and Brake Assemblies," 1982.
2. General Dynamics Specification 16ZL001B, "Wheel and Brake Assembly : Aircraft Main Landing Gear 25.5 x 8-14 Tubeless."
3. ARP 1493, "Wheel & Brake Design and Test Requirements for Military Aircraft." 1979.
4. Park,J.K., J. Lee, Ha,H.S., and Yoon,B.I., "Analysis of Carbon/Carbon Brake Disk Protopype(1), MSDC-511-950877, ADD, 1995.
5. Park,J.K., J. Lee, Ha,H.S., and Yoon,B.I., "A Study on the Mechanical Properties of Carbon/Carbon Brake Disk, MSDC-511-970061, ADD, 1997.
6. Park,J.K., J. Lee, Ha,H.S., and Yoon,B.I., "Analysis of Carbon/Carbon Brake Disk Prototype(2), MSDC-511-970075, ADD, 1997.

THE DEVELOPMENT OF THE COMPOSITE HORIZONTAL STABILIZER FOR A FIGHTER AIRCRAFT

C. L. Ong, T. B. Hong, J. S. Chen, J. Y. Huang

*Aeronautical Reserach Laboratory/ CSIST
P. O. Box 90008-11-15, Taichung, Taiwan, R.O.C.*

SUMMARY: An advanced composite horizontal stabilizer has been developed for a newly designed fighter. The building block and concurrent engineering methodology was followed in this work. Under the constraints of stiffness, material, and maintenance, etc., the structure was optimized for weight reduction with sophisticated manufacturing methods. The assembled structure were certified by dynamic test, static test, and damage tolerance tests. The natural frequency, mode shape and damping ratio were measured during the dynamic test. In addition, the strength and stiffness of the structure were determined by the static test. The load spectrum was applied in the horizontal stabilizer fatigue test for two life times. After flush bonded boron/epoxy patching and flush bolted titanium patching repairs for the simulated damages, one more life time fatigue test was carried out. The development work has been successfully finished with unique composite corrugated understructure and certified to the military requirements. The horizontal stabilizer has been subjected to series production.

KEYWORDS: composite horizontal stabilizer, static test, dynamic test, damage tolerance, delamination, patching, inspection interval, barely visible impact damage

INTRODUCTION

To ensure that a newly developed major structure of an aircraft meets the design requirements, a series of analyses and tests ,including static strength, ground vibration, damage tolerance and flight test[1], should be performed. Laminated composites, with their high strength - to -weight ratio, offer considerable technological advances in the production of aircraft structures. In general, graphite-epoxy composites have the advantage of resistance to cracking by spectrum loading and immunity to corrosion. However, design is complex due to the nonhomogeneous nature of the material and its failure modes. For example, the delaminations in the composite skins could result in stiffness and strength loss, thereby reducing the flutter resistance and strength margin of the structures. Since that no general rules of testing for composite structures are available, sometimes individual procedures adapted to the structure has to be developed[2].

The requirements of safety, original weight, size and maintenance for large-scale composite structure is much more importance than that of small-scale composite structure. In order to develop a newly designed large-scale composite structure successfully, team-work is especially important. The development of composite horizontal stabilizer involves all kinds of specialty. Detail considerations have to be made in every steps during the designing and manufacturing process by means of concurrent engineering. In this manuscript, the

certification procedures of the assembled composite horizontal stabilizer of a fighter was discussed through the introductions of design concept, analyses and tests.

STRUCTURAL DESCRIPTION

The major structural elements of the composite horizontal stabilizer shown in Fig.1 are: 1) composite upper and lower skins, 2) composite sine wave corrugated substructure, 3) metallic leading edge and trailing edge, 4) metallic tip rib and root rib. The upper and lower composite skins were made of Fiberite T300/976 Gr/Ep prepreg. The skin were symmetric to each other and were designed as quasi-isotropic stacking sequence with 0° , 45° , 90° and -45° in about equal proportions. The zero direction of fiber was arranged along the spanwise direction. The laminate thickness varies from 16 plies near the tip of the horizontal stabilizer to 64 plies near the region of the pivot shaft. In contrast to a plane plate, the stability of the corrugated plate was influenced by many parameters including angle of corrugate, radius of corrugate, overall plate dimension and thickness of the laminate. The horizontal stabilizer is classified as a safety-of-flight structure. Skins, corrugated substructure and metallic pivot shaft are assembled with bolts and rivets.

STRUCTURAL DESIGN AND ANALYSIS

Since complex load paths are prone to fracture, especially the places with stress concentration, these regions are the candidate points for damage tolerance analysis and test. Based on the analysis results, once the thickness and percentage distribution can be obtained, the stacking sequence can be determined. The objective of the stress analysis is to provide the correct internal forces and load path for selection of impact locations. The analysis flowchart, shown in Fig.2., includes dynamic analysis, static analysis and damage tolerance analysis. In addition, an analysis had been made of the probable lightning strike zones of the fighter, guiding the design of lightning protection material. Considering that the metallic tip rib can act as a good conductor for releasing the lightning energy, no severe lightning damage will be expected on the skins.

To attain a perfect design of a composite structure, the concept of design and manufacture must be considered in all respects as shown in Fig.3. There are some special requirements to be fulfilled which made the design of the horizontal stabilizer a tough job. These requirements include weight reduction, performance promotion, cost effective, maintenance, strength, stiffness and life limit. Also, some design considerations have to be taken into account such as the source of material, configuration of the structure, operate environment, equipment capacity, schedule, budget, and quality assurance ability. The design flowchart is shown in Fig.4. Before the formal production start not only ground test but also flight test have to be implemented to certify that the design requirements were met. In the following paragraphs, only the materials and processes and the ground test which includes dynamic test, static test and damage tolerance test are introduced.

MATERIALS AND PROCESSES

The material chosen should satisfy the application requirements of sustaining temperature 115°C , hot/wet properties at 100°C and the mechanic properties loss less than 5% in the environment of salt water, hydraulic oil, fuel(JP-4) and solvent. The material was qualified

according to the physical and mechanical requirements specified in the material specification. For the sake of structure design and analysis, the design allowables was established by the material coupon tests subjected to environment, fatigue, stress concentration and damage tolerance effects for the quasi-isotropic laminates.

The process specification was developed for the fabrication of composite stabilizer. The prepreg patterns were provided by the automatic cutting machine using CATIA design data. The skins and corrugated substructure were made by the autoclave curing of vacuum bagged lay-ups using the composite tooling. In this specification, the curing cycle, process qualification tests, and the non-destructive tests were also described and implemented during the production.

TEST PROCEDURES

The full scale tests are influenced by numerous factors; for example, test procedures and boundary conditions of the test article. To get a realistic result for the structural capacity, these factors have to be clarified and defined. All the full scale test must be proceeded by tests of components to get the test parameters. The completion and review of these parameters was done by test of substructure, the bending - torsion box (B.T. box)[2], to reach the realistic test procedure to be performed in the full scale test.

The test items during the development of the composite horizontal stabilizer are shown in Fig.5. The real structural natural frequency, mode shapes and damping ratio were obtained from dynamic test. By setting the exciter at the proper locations, the response can be read out from the accelerometers. After the process of filtering, amplification and calculation of signal, the test results were then compared with the analytical results. The tested article can be suspended independently, or can be set on a fixture. Also, it can be put on the full scale airplane for testing with more real boundary simulation. The purposes of static test are : 1) verify the correctness of the analysis results, 2) to obtain the real strength of the tested structure, 3) to fulfill the requirements according to the specifications. Similar to the damage tolerance test, the strain gages should be adhered to the critical locations. The simulation of the boundary conditions is one of the key points of making a good test.

To get realistic information for the design base for the horizontal stabilizer, for instance from the damage tolerance respect, attention has to be paid to the impact test parameters on specimens or components, including impact energy, type of impactor, geometry, support conditions, material properties, specimen thickness, stacking sequence and loads. The purpose of the impact pretests is to verify the input parameters of testing the horizontal stabilizer under the realistic boundary conditions. The procedure and performance steps are as follows. First, selection of the critical areas of the horizontal stabilizer. Second, definition of test point geometry and support conditions. Third, definition of the test parameters such as impact energies and impactor size and form. Finally, damage size was measurement by A-scan as function of the impactor type and energy. The results of the impact pretests defined the reference data for the damage tolerance tests of the horizontal stabilizer. Of all the damage types which are possible during manufacture and service, delaminations, impact damage, lightning strike damage, battle damage and loose rivets were selected for damage tolerance test because of their important effects on structural capacity.

Since the artificial flaws of comparable area to impact damage produce less reduction in compressive strength[5], also considering the estimated expenditure, delaminations were simulated by serious impact damage only. There were 25 damaged-locations, including 13

barely visible impact damage (BVID), 8 visible impact damage (VID), 1 lightning strike damage, 1 battle damage and 2 loose rivets. Considering that the delamination is prone to spread under compressive loading, most of the damage (14 locations) was applied to the lower skin.

To certify the feasibility and reliability of repair technology on composite structures, two impact damaged-areas were repaired after two lifetimes of damage tolerance test. Both flush composite bonded repair and metal bolted repair were applied to the composite lower skin. Finally, on completion of four lifetimes of damage tolerance test, a static residual strength test was performed to check whether structural strength after repair implementation met the requirements. Stiffness and static strength of the composite horizontal stabilizer with and without damage were evaluated and compared.

The critical load case has to be decided together with the detailed damage locations. The load types can be expected to be the same as those for the B.T. box. The results of the impact pretest and parameters investigated by the B.T. box test defined the reference data for the damage tolerance tests of the horizontal stabilizer. According to the specifications[3,4], two design lifetimes of damage tolerance test should be performed. However, considering that the composite structure is sensitive to environmental change, which is difficult to simulate in the test laboratory for a full-scale article, the first lifetime damage tolerance test with BVID defects was carried out to assess environmental effects[2]. For the following two lifetimes of test, visible impact damage, large delaminations, lightning strike and loose rivets were applied to the horizontal stabilizer to assess the damage tolerance characteristics. Finally, one lifetime testing with magnitude of load increased to 14% was carried out to evaluate the possibilities for extending the service life of the horizontal stabilizer. Totally, the test article was subjected to four lifetimes of flight - by - flight load spectra simulating the in-service fatigue loading condition for the aircraft.

INSPECTION AND QUALITY ASSURANCE

The quality assurance people should not only execute the inspection during test, but also has to prepare for the quality assurance plan. From general inspection point of view, the inspection items involved from the beginning of material screening to the final production step, as shown in Fig.6. The major inspection work during the development of composite horizontal stabilizer is the inspection of damages during and after the damage tolerance test. During this test, strain surveys and NDI (non-destructive inspection) were carried out periodically to monitor strain distribution and to record damage growth. The exact positions to be impacted, especially at the ply termination, can be identified by measuring the thickness of the laminate with the help of portable NDI (A-scan). In addition, any existing manufacturing defects around the impact positions must be detected. Again, NDI was utilized to determine the extent of the internal damage of the structure after impact. Strain surveys and NDI inspections were taken periodically to track the strain history and damage growth.

VERIFICATION

Static strength tests of the composite horizontal stabilizer, the final and most important test item, aimed at investigating the influences of damage on structure stiffness and strength and also prove the strength of repairs. To simulate a better design limit load condition, 13 load

actuators, and the offset concept which allow the actuators to adjust their loading direction were used. For composite horizontal stabilizer without damage, the static strength attains 175% design limit load. Tensile failure modes were found at the bolted region of upper skin and pivot fitting. For the composite horizontal stabilizer with 23 damaged-areas and 2 repairs, the residual static strength attains 160% limit load, which meets the regulation , i.e. the damaged horizontal stabilizer structure must be capable of sustaining limit load without any failure or obvious partial failure. Also, two repaired regions were survived after being subjected to 160% limit load, hence structure with damage of the tested sizes and locations is repairable.

CONCLUSIONS

This paper presents the structural certification of dynamic character, static strength and damage tolerance strength in developing the composite horizontal stabilizer of a fighter. Test items include ground vibration tests, static test, and simulation of damage of composite structure by four lifetime test of flight-by-flight load spectra. Conclusions from these tests can be summarized below :

- (1) Damage to composite structure was more difficult to simulate than that of metallic structure. Very often, there are no general rules of testing for composite structures available, individual procedures adapted to the structure has to be developed.
- (2) The test results indicated that the development of the composite horizontal stabilizer is quite a success. The design is optimal and the requirements are met. The test results also provides an important reference for service maintenance.
- (3) To develop an advanced composite horizontal stabilizer, new techniques such as structural health monitoring and co-cured manufacturing could be some possible fields for researches in the future.

REFERENCES

1. Chang, Y. B., Lin, T. Y., Wang, G. R. and Chen, C. C., "Flight Load Test of the Indigenous Defensive Fighter", *J. of Aircraft*, Vol.31, No.4, 1994, pp946-952.
2. Huang, J. Y., Tsai M. Y., Chen J. S. and Ong C. L. "Damage Tolerance Certification of a Fighter Horizontal Stabilizer", *J. of Aircraft*, Vol.32, No.3, 1995, pp643-648.
3. Military Specification, Airplane Damage Tolerance Requirements, MIL-A-83444 (USAF), July, 1974.
4. Military Specification, Airplane Strength and Rigidity Ground Tests, MIL-8867B (USAF), August, 1975.

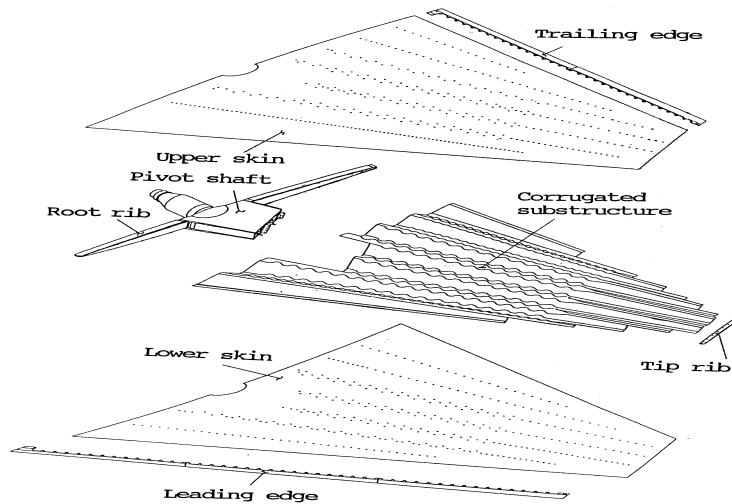


Fig.1 Composite Horizontal Stabilizer Components

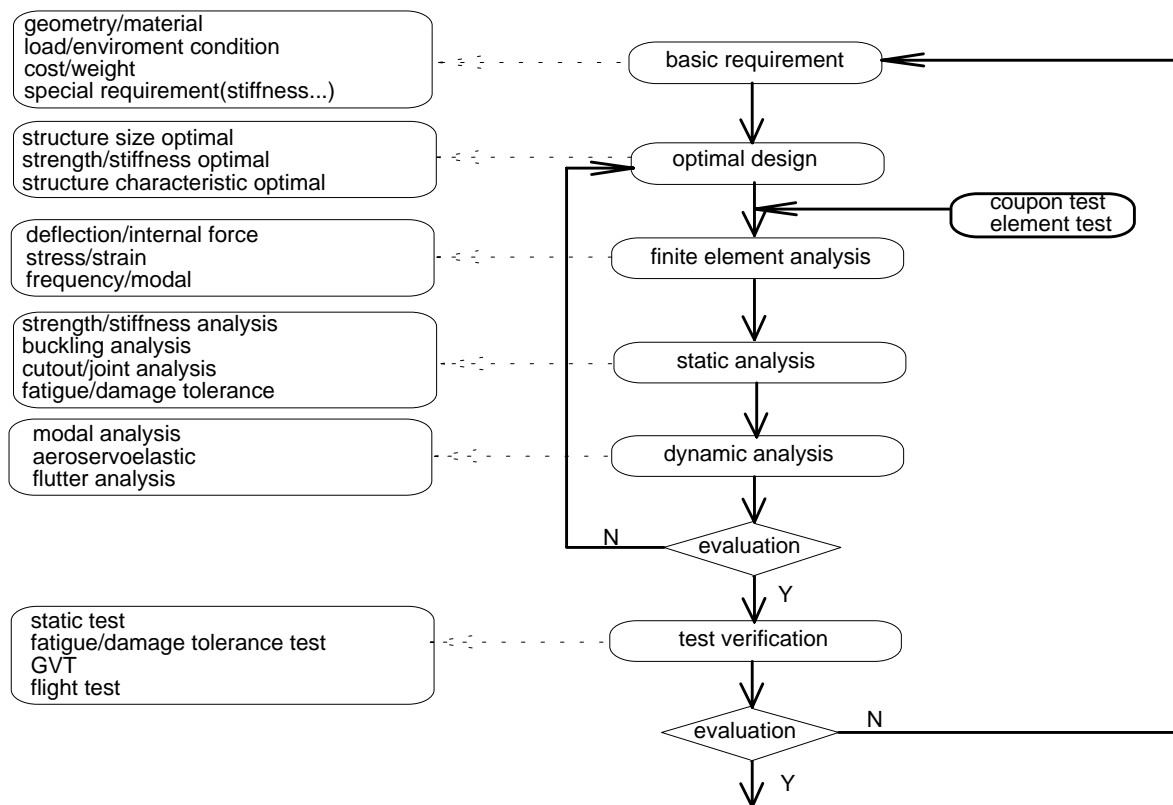


Fig.2 Structure Analysis Flowchart



Fig.3. Design requirements and Limitations of Composite structure

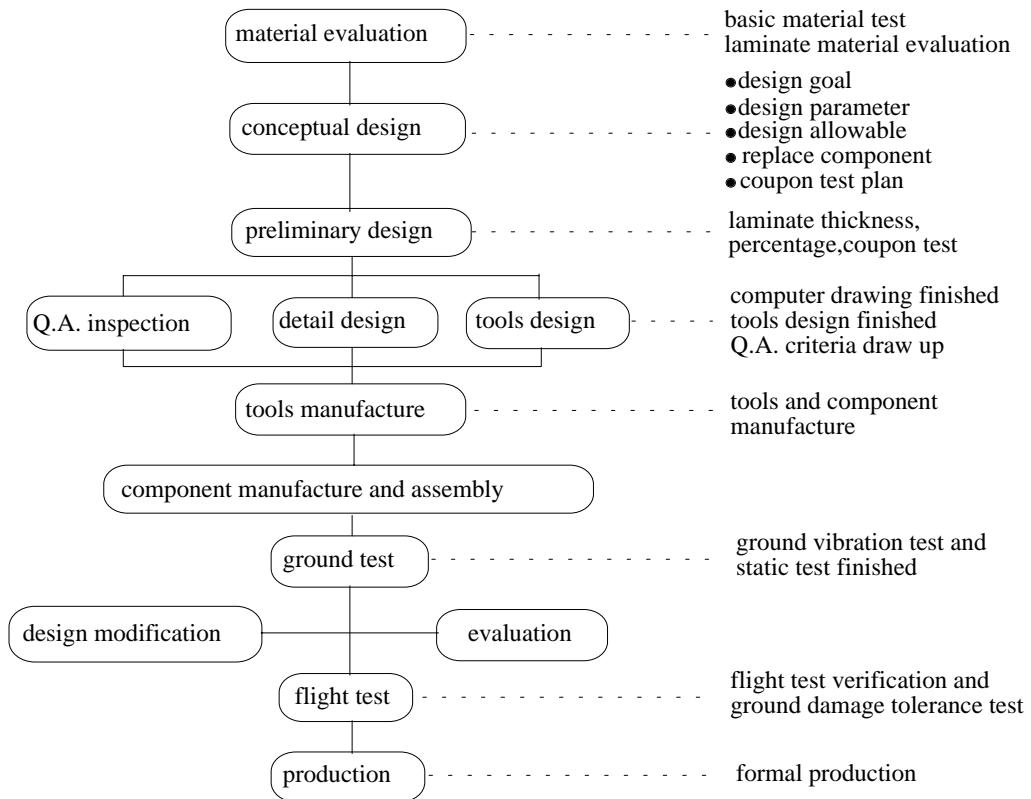


Fig.4 Composite Structure Development Flowchart

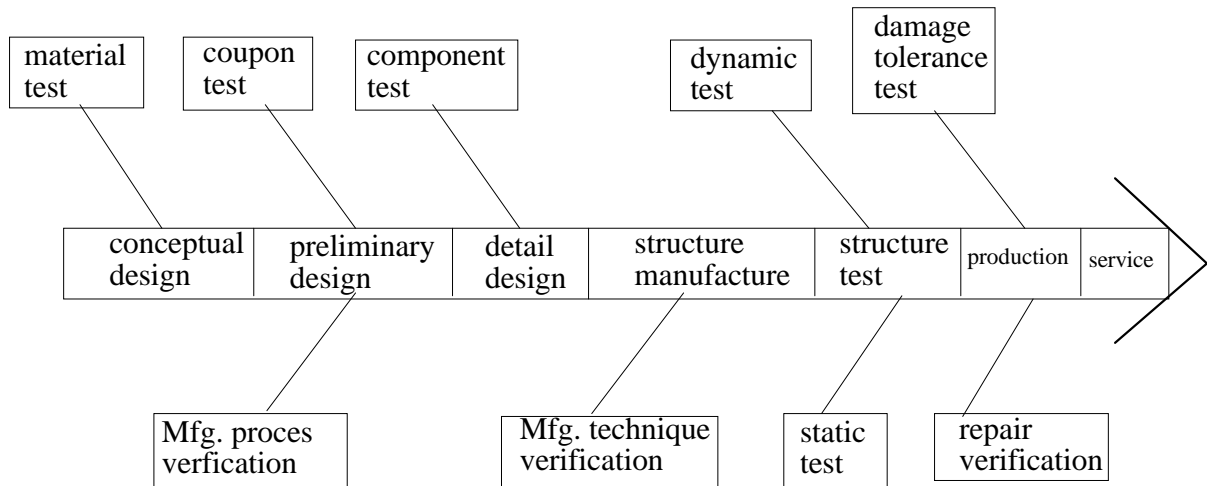


Fig.5 Test item during composite H.T. development

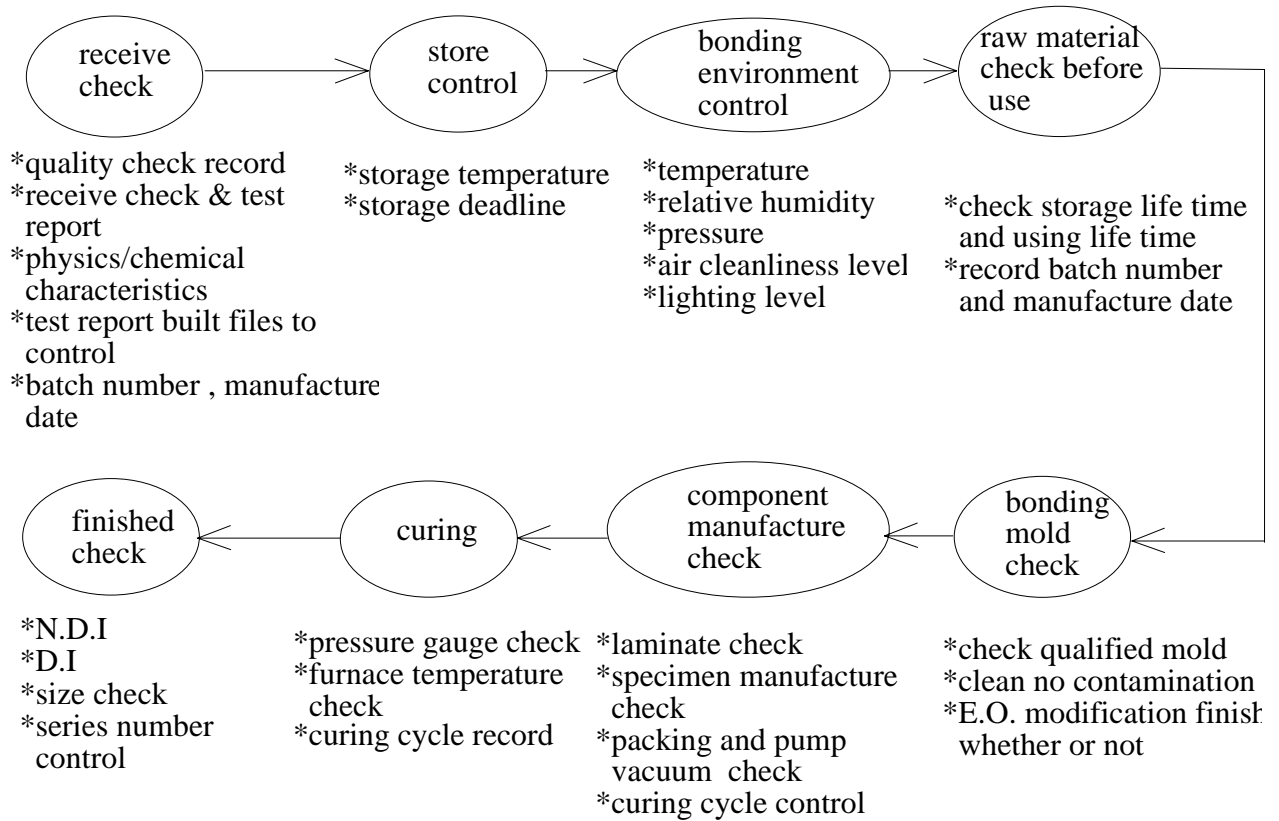


Fig.6 Quality Guarantee And Test

TOWARDS A COMPOSITE CIVIL AIRCRAFT WING

G. Clayton¹, P. Falzon², S. Georgiadis³, X.L. Liu⁴

^{1,3}*Aerospace Technologies of Australia Ltd/Cooperative Research Centre for Advanced Composite Structures Limited, 226 Lorimer Street, Fishermens Bend, Victoria 3207, Australia*

²*Cooperative research Centre for Advanced Composites, Victoria 3207, Australia*

⁴*Department of Mechanical Engineering, Monash University, Clayton, Victoria 3168, Australia*

SUMMARY: Following a visit to Germany by personnel representing the Australian Aerospace Industry in 1994 a research program was commenced mid-1995 by the Cooperative Research Centre for Advanced Composite Structures. This program undertook the investigation of cost effective design/manufacture of commercial aircraft composite wing stringers and ribs in cooperation with Daimler-Benz Aerospace Airbus (DASA) and supported by the Ministry for Education, Research and Technology, BMBF, Bonn. This paper details the research and development undertaken to progress towards cost efficient manufacturing technologies for wing stringer (T-section) production and indicates the techniques used and the outcomes derived from the early stages of the program.

KEYWORDS: wing, stringers, resin transfer moulding, tooling, test

INTRODUCTION

Conventional pre-preg stringer designs from DASA were utilised as the baseline. The overall wing tasks undertaken by the CRC-AS included design, manufacture, development, test and sub-element qualification. The program was undertaken in two phases:

Phase 1 investigated various manufacturing techniques and material types which could be used in stringer design. However, as the prime deliverables to DASA were 2 metre stringers for use on a compression test panel in a short timescale, qualified unidirectional and standard 5H satin fabrics were utilised for initial design work. These stringers represented the type 2, or intermediate stringer sections.

Resin Film Infusion and Resin Transfer Moulding techniques were evaluated for the liquid moulding.

Phase 2 covered the design and manufacture of all the outboard, or type 3, stringers for the DASA full scale wing test. This involved use of the most cost effective preform scenario, deduced from earlier studies, and the use of integrally heated RTM tooling.

The prime deliverables of the program were:-

A validated stringer design methodology compatible with the DASA wing

A validated production methodology for cost effective stringer manufacture

Manufacture of Demonstration and Full Scale Test stringers as agreed between DASA and CRC-ACS

DASA Assembly Method

The assembly method DASA proposed for the wing consists of using pre-cured stringers which are co-bonded to the prepreg wing skin during the cure of the skin itself.

This method enables simple tooling to be used for the final skin cure inclusive of stringers thus, if the stringers can be produced in a cost effective manner, assembly costs will be minimised compared to the co-curing of an integrally stiffened skin.

General Philosophy

The stringer design philosophy was heavily influenced by manufacturing technique and cost. The main structural concern was to match the strength and stiffness of the DASA prepreg stiffeners. *Figure 1* illustrates the wing FEM.

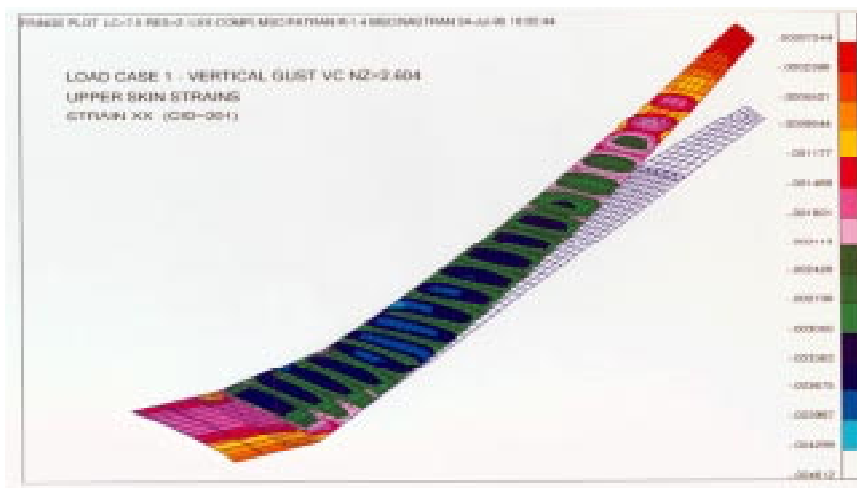


Figure 1. Wing FE Model

Coupon tests were undertaken to verify the 'lamina' strength and stiffness for use in calculations and sub-element coupons taken from the stringer to confirm structural adequacy.

A MS Excel program was developed to undertake analysis of the stringer geometric variables and this was used in conjunction with program GENLAM for generation of the requisite properties to match the DASA wing.

In addition to the technical evaluation of the stringers - compatible to the composite wing requirements - a costing exercise was undertaken. Further to material costs this evaluated various manufacturing procedures such as hand lay-up, drape forming, RTM and RFI, as appropriate to the material.

PHASE 1

Stringer Design

The deliverables to DASA for Phase 1 of the program were 3 stringers of 2 metres length for incorporation in to a large compression test panel in Germany. The stringers had to match or better the current DASA designed stringers manufactured by conventional prepreg technology.

All intermediate wing stringers (Type 2) consisted of flanges and additional core in the blade zone. Designs with no core tended to be overweight. Note also the requirement for a layer of glass fibre on the insides of the stringer for lightning strike purposes and Airtech Release Ply G on the bond surface of the flange.

Calculations were also undertaken on the stability of the blade and flange in comparison to the baseline DASA design. Damage Tolerance requirements stipulated the stringers must be capable of withstanding complete disbond from the wing between adjacent rib stations.

Properties for the stringer stiffness were obtained from lamina testing. In general stiffness properties of the fabric/RTM6 combinations compared favourably with the theoretically values given by DASA for the prepreg .

Following manufacture of the representative stringer lengths several sub-element coupons were cut from the blade and flange and tested. Prime among these tests was the compressive stringer section test where the required load at Room Temperature was specified by DASA as 295KN: see *Figure2*.

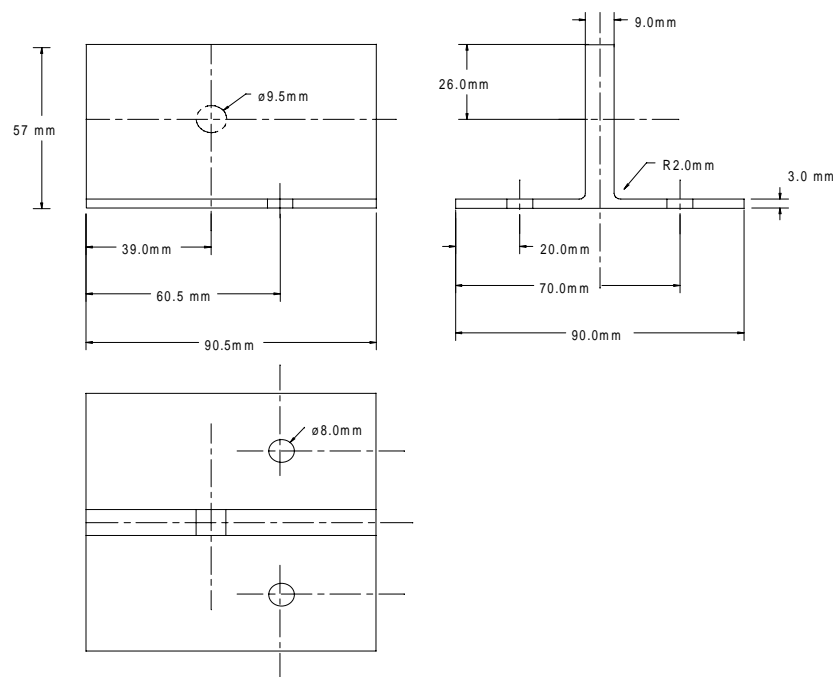


Figure 2. Compression T piece from Stringer

Stringer Manufacture

Each cure produced two stringers from an I-Beam geometry, the final stringer dimensions being obtained by trimming following cure: see *Figure 3* which shows the mandrels in the full assembly tool.



Figure 3: Mandrels in RTM tool.

The stringer manufacture can be defined as being in two stages:
Preform Manufacture
Resin Injection and Cure (RTM or RFI)

Preform Manufacture

For Phase 1 the preform was produced by drape forming the channel sections prior to assembly in the tool. The core preform was designed to fill the interstitial void during resin impregnation at a 60% fibre volume fraction. Of particular criticality are:-

- Peel Ply incorporation
- Mould preparation
- Insertion of mandrels in the tool
- Alignment of the preforms
- Incorporation of the Rohacell thermal expansion 'valves'

Resin Injection and Cure

Two methods of resin infiltration in to the preform were evaluated: Resin Film Infusion (RFI) and Resin Transfer Moulding (RTM).

RFI methods were trialed on a tool of one metre length. The RFI process produced reasonable beams but it was decided, owing to timescale restraints, to use the more familiar RTM process to produce the test panel stringers.

During the limited RFI trials undertaken during Phase 1 many lessons were learnt, in particular on the avoidance of dry spots and surface porosity, incorporation of the peel ply, the effectiveness of the end dams, cure cycle dwell times, and use of RTM6 in both the liquid and B-staged state.

Resin Transfer Moulding was the method eventually chosen to produce the stringers for Phase 1 and can be illustrated by *Figure 4*.

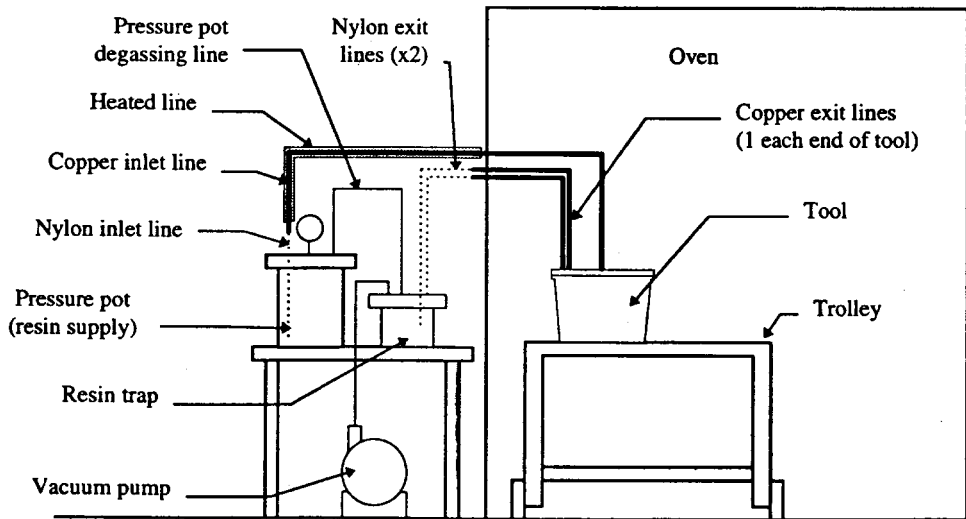


Figure 4: RTM Set Up

Stringer Machining

Two stringers were produced from each I-beam. For flange trimming a hand-held cutter was used with a steel rule guide clamped in position to locate the edge of the flange. A diamond tipped blade was then used to separate the I-beam into two stringers, this initial cut being half way up the web. Final cuts were then made for the stringer flange width using a preform mandrel and Hand Router. The web was machined to the correct height by using a milling head loaded with a small diamond tipped blade. This procedure was unwieldy and not a production friendly scenario. During Phase 2 a more automatic procedure was developed using a specifically designed machining jig on a rail system.

Quality

The compression panel stringers were delivered to DASA on schedule on July 3 1996. Dimensional control of the components was good and subsequent photomicrographs illustrated very low porosity.

Coupon Testing

Lamina tension and compression tests were devised to investigate the basic material properties for the materials used in Phase 1. Tests were undertaken in the 0°, 45° and 90° directions to evaluate the prime lamina properties. Tension tests were used to determine both the tensile and shear properties for each of the materials tested.

DASA Sub-Element Testing

It was a requirement of the project to undertake sub-element testing on components taken directly from representative manufactured stringers. The testing consisted of plain and holed compression specimens, open hole tension and bearing test coupons cut from both the stringer flange and blade.

Characteristic full stringer T-sections with holes were also tested in compression. *Figure 5* summarises typical test results.

Specimen Type	Material	Conditioning	Test Temp. °C	Ult. Failure (kN)	Ult. Stress (MPa)	Ult. Strain (µε)
T	stringer	none	RT	310.9	396	5167
A	flange	none	RT	51.9	756	9783
C - 4mm hole	flange	none	RT	60.9	516	6687
C - 6mm hole	flange	none	RT	55.8	506	6557
C - 8mm hole	flange	none	RT	54.6	496	6432
C - 6mm hole	flange	70°C/H ₂ O	70°C	42.8	393	5052
D	flange	none	RT	103.5	872	8999
D	flange	70°C/H ₂ O	70°C			
B	flange	none	RT	186.8	911.7	2096
A	web	none	RT	200.2	703	9231
C - 4mm hole	web	none	RT	225.1	492	6457
C - 8mm hole	web	none	RT	210.1	455	5967
C - 12mm hole	web	none	RT	175.9	369	4847
C - 8mm hole	web	70°C/H ₂ O	70°C	155.0	336	4420
D	web	none	RT	270.5	810	9459
D	web	70°C/H ₂ O	70°C			
B	web	none	RT	40.0	718.3	1514

Figure 5. Summary of Phase 1 results

In addition interlaminar shears, softening temperature, specific gravity and fibre content specimens were taken from the stringer flange.

Environmental conditions investigated covered conditioning to saturation in 70°C water, and MEK, fuel and Skydrol immersion.

Costing

Several companies were approached for materials suitable as preforms for both the core and the flange of the Type 2 stringer.

Shown in *Figure 6* are the basic relative cost estimates of using prepreg against an RTM solution. Costs include raw material, labour, liquid moulding or draping and curing and trimming.

PREPREG VERSUS RTM COSTS FOR TWO 6 METRE T STRINGERS

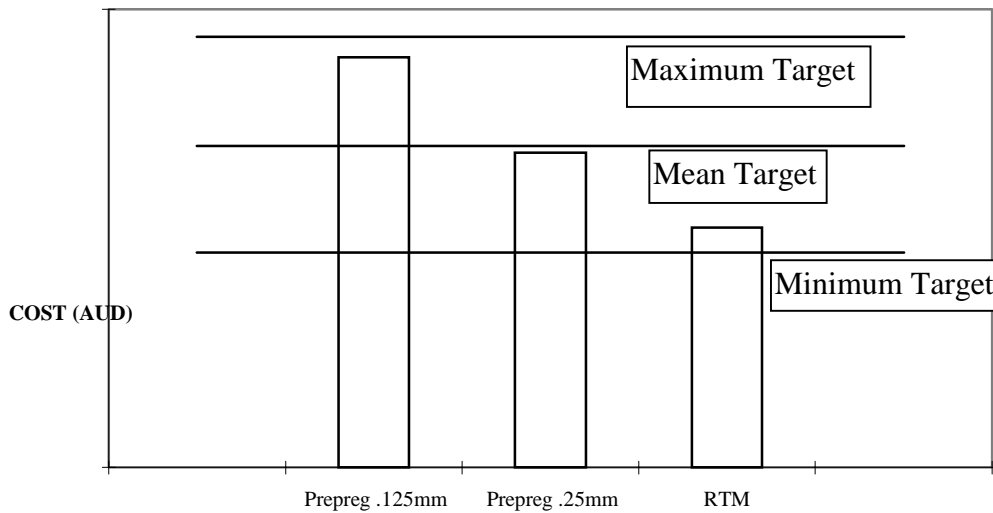


Figure 6: Comparison between pre-preg and RTM techniques

PHASE 2

Phase 2 of the research task involved finalisation of material choice based on contemporary costs for quantified volumes and production of all the outboard stringers for the DASA full scale composite wing test in Germany. The longest outboard stringer is 3.015 metres long.

Other than the design configuration of the outboard (type 3) stringers the prime thrust of Phase 2 concentrated on the design and manufacture of a 4 metre RTM integrally heated tool.

Stringer Design

The deliverables to DASA for Phase 2 of the program were 4 upper and 2 lower stringers of similar ply build-up but of different length and cross sectional dimension.

Following the material investigations undertaken in Phase 1 non-crimp materials were chosen for the stringer design. Of note is the fact that the outboard stringers (Type 3) did not have 'core material' between the flanges owing to their less demanding structural requirements, compared to the intermediate wing stringers (Type 2).

Properties of the non-crimp material were evaluated from coupon testing.

The non-crimp material was also used for an intermediate (Type 2) stringer design and effective stringer lengths produced in the Phase 1 two metre tool. DASA sub-element coupons were taken from these sections and tested for comparison to the specimens produced during Phase 1. The only structural specimen taken from the Type 3 stringers (4 metre tool) were compression T-pieces for which the target load, as specified by DASA, was 162KN.

Stringer Manufacture

As for Phase 1 the stringers were produced from I-beams, the final stringer dimensions being obtained by trimming following cure.

For Phase 2 the outboard stringer preforms were produced by a special technique developed in Phase 1.

The major difference for the Phase 2 RTM scenario was the use of an integrally heated tool. This avoided the long heat-up time associated with the oven cure used during Phase 1.

Resin Injection and Curing

The resin injection process (RTM) was similar to that used in Phase 1 and is depicted in *Figure 4*. In this case, however, an oven is not required as the tool was heated by electrical elements.

Dry thermal investigatory runs were undertaken to evaluate the integral heating scenario. Design of the heat control system, incorporating multiple local feedbacks to ensure uniform heating of the tool, was undertaken by personnel from the Mechanical Engineering Department of Monash University.

During the dry run 42 thermocouples were placed in the tool and real time temperature measurements taken for comparison to theoretical calculations.

Following satisfactory dry runs, and the ensuing calibration of the system, the internal thermocouples were removed and control of the tool undertaken by feedback from external thermocouples only.

The Heat Control Unit also incorporated automatic signals for ‘resin injection’, ‘cure complete’ and ‘ready to demold’ operations. *Figure 7* shows a typical part temperature profile during heat-up.

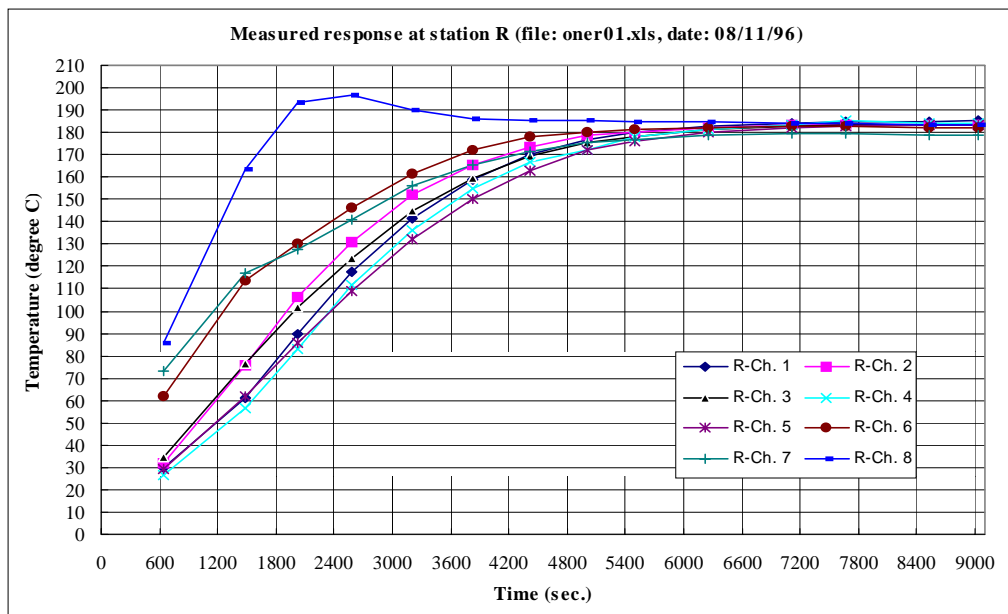


Figure 7. Typical heat up profile

Stringer Machining

As before stringers were produced by machining from the cured I-beams. A special trimming mechanism was designed and manufactured to undertake the final trimming of the stringers.

Quality

All stringers were subjected to quality assessment and controlled by a DASA configured Life Data Sheet. The Life Data Sheet included checks on the Engineering Drawing, Material Data, Fabrication, Inspection and Testing, with the appropriate signatures.

Coupon Testing

Two types of non-crimp material were used during Phase 2 and tests undertaken to evaluate basic material properties. Tests included tension and compression in the longitudinal and transverse directions, shear, and environmental aging effects on compression and shear.

DASA Sub-Element Testing

Sub-element test pieces were taken from the Type 2 stringer section and compared to the results achieved under Phase 1. This testing consisted of plain and holed compression specimens, open hole tension and bearing test coupons cut from both stringer flange and blade. A characteristic full stringer T-section with holes was also tested in compression.

A further sub-element test piece T-section with holes was taken from the Type 3 stringers produced.

Environmental conditioning investigated covered saturation in 70°C water and MEK, fuel, and Skydrol immersion.

Costing

Costing exercises during Phase 2 of the program concentrated on reducing process time with the chosen material and investigating the influence of changing from RTM6 resin to PR500.

Figure 8 illustrates costs for both the intermediary (type 2) and outer (type 3) wing stringers, at an appropriate length, using the standard and non-crimp materials. Use of the non-crimp material gave a saving of 30% over standard fabric scenarios for both the intermediate and outboard stringers. This saving was accrued in both raw material costs and reduction of assembly time.

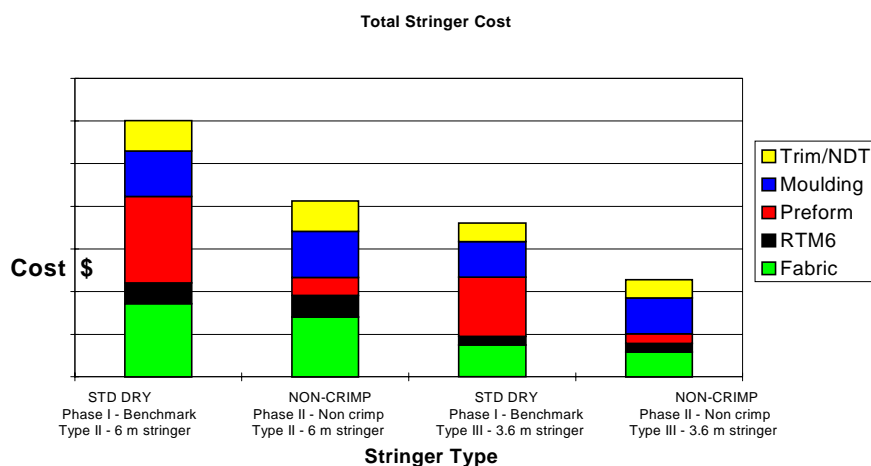


Figure 8. Cost comparisons standard v. non-crimp

The only other significant cost saving (apart from further material reductions) would be in the automation of the 'moulding operation'. If this could be purely automatic, for example, cost/metre would reduce significantly.

However, incorporation of a stringer twist requirement and thickness variation along the wing spanwise datums may introduce a significant hurdle to the use of a continuous methodology in the manufacture of pre-made stringers.

CONCLUSIONS

Phase 1 of the program culminated in the successful compression testing at DASA of a panel incorporating the stringers to the equivalent of $n=2.3$ wing loading whereupon the test was ceased. No damage of the panel was observed. Equivalent stringer panels produced in conventional prepreg failed at a lower equivalent wing loading.

Investigations during Phase 2 have revealed that the use of non-crimp preform and integral heating with RTM can significantly reduce the cost/metre of the composite stringers.

Analysis of the costing figures indicates that further automation of the preforming and resin injection methods would produce further cost savings.

Following the completion of Phase 2 the future direction of this task is likely to be on a specific aircraft design/development program.

ACKNOWLEDGMENTS

The authors gratefully acknowledge the professional and dedicated support of the CRC-AS composite wing research team without whom progress would have been impossible and the support of the Daimler-Benz Aerospace Airbus organisation, Bremen, Germany.

CONCRETE COLUMNS WRAPPED BY GLASS FIBRE COMPOSITES

Shi Zhang, Lin Ye and Yiu-Wing Mai

*Centre for Advanced Materials Technology
Department of Mechanical & Mechatronic Engineering
The University of Sydney, NSW 2006, Australia*

SUMMARY: With many structural deficiencies in bridges and off-shore structures and increasingly crumbling infrastructure elements, the needs for rehabilitation of infrastructure become critical. In this study, E-glass woven roving (WR), combined with chopped strand mat (CSM), glass fibre tape (GFT) and a vinyl-ester resin, was used to reinforce concrete columns with a wrapping procedure. The results indicate that a great reinforcing efficiency can be obtained. Finite element analysis was performed to analyse the mechanical responses of the composite wrapped concrete columns and to identify the effect of composite properties on the reinforcement efficiency.

KEYWORDS: concrete columns, wrapping technique, glass fibre composite, finite element analysis

INTRODUCTION

There is a worldwide critical need for rehabilitation of infrastructure because of aging, deterioration, misuse, lack of timely repair and maintenance, and use of improper materials and/or techniques in original construction. Especially, deterioration has been caused by a variety of factors including corrosion due to marine environments, high chloride content in the air and the use of de-icing salts. A widely used technique for concrete structures where retrofit is needed was the use of steel jackets placed around existing columns[1-2]. The use of steel encasement to provide lateral the confinement to concrete in compression has been studied extensively[3-4], which has shown to be able to significantly increase the compression load-carrying capacity and ductility of columns. However, the disadvantages of steel jacketing are corrosion and difficulties associated with the proper placement of steel jackets.

In last a few years, due to high specific strength/stiffness, design placement flexibility and resistance to corrosion, the application of polymer composites in rehabilitation of concrete structures become very attractive. Without reducing the original load-carrying capacity of the structure, the best strengthening performance can be achieved when the constituent materials and composite architecture are optimised to the specific application.

It was found that the winding of a carbon fibre/epoxy composite around square concrete columns can increase the load-carrying capacity of 8-22%, being dependent on the amount of fibres used and the treatment of the substrate[5]. The use of a novel resin infusion technique was shown to contribute to substantial improvements in composite wrap efficiency, and the use of woven glass roving as the reinforcement in the composite wraps was found to substantially increase both load-carrying capacity and deformation capability of the concrete stubs[2]. Furthermore, through the use

of glass/carbon hybrids with a epoxy resin, replication of the initial performance of concrete stubs subjected to deterioration was shown possible, with a simultaneous improvement in load-carrying capacity[6]. The effects of orientation and thickness of the composite wraps on the load-carrying efficiency and ductility of the structural concrete elements have been investigated, and it was found that the predominant use of reinforcements in the hoop direction would enable a high reinforcing efficiency[6].

The rehabilitation of deteriorated infrastructures using composites would use not only carbon fibres and epoxy resin but also glass fibres or the hybrid of carbon/glass fibres and other polymer resins such as vinyl-ester resins. Furthermore, the optimised composite architectures with a proper processing method and a compatible low cost would be an essential task of development of repairing and strengthening techniques. In this study, a E-glass/vinyl-ester resin composite jacket was introduced and effects of composite wrapping architecture were investigated.

EXPERIMENTAL PROCEDURE

Composite Architecture

The composite wrap consists of three basic architectures, shown in Figure 1, namely glass chopped strand mat (CSM), woven roving (WR), glass fibre tape (GFT). In some cases, CSM and WR are sandwiched between each other to produce better interplay adhesion of woven roving cloth layers. Meanwhile, WR is a multi-directional reinforcement with $90^{\circ}/0^{\circ}$ angle, which provides the equivalent strength in both axial and hoop directions and plays a basic reinforcing role. GFT in the hoop direction gives very good confinement and an enhanced structural integrity capacity in the hoop direction, being used as the last layers of the jacket; the tape wraps can also reduce the thickness of the composite jacket a little bit, "tightening up" the whole jacket. The tap wraps were wound using helical winding with an angle of 20° . The selection of resin curing systems is mainly concerned with the resin gel-time which is critical to the wrap processing. In general, cold setting resin systems (ambient temperature curing) should be used in this wet lay-up processing, because of the large scale and the open site condition in practical applications. Since the machine lay-up is not easy to be carried out in the wrapping process described in this study, the hand lay-up method was applied.

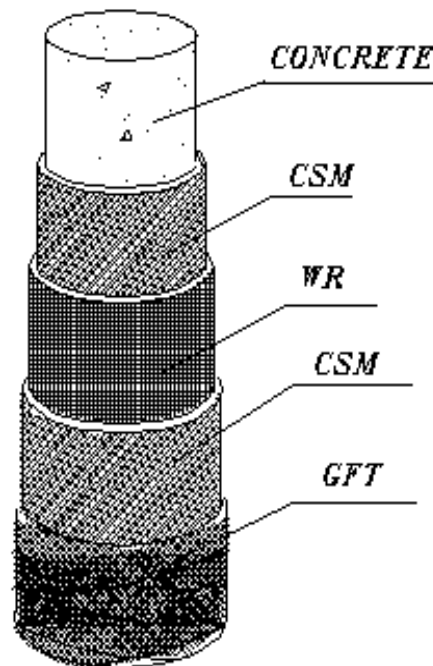


Figure 1 Concrete column wrapped by glass fibre composites

Specimens Preparation

The concrete columns were produced following the Standards Association of Australia. The columns were 300 mm high and 150 mm in the diameter using a weight mixture ratio of 1:1.4:2.3:5 (water:cement:sand:aggregate). The concrete cylinders were compacted, capped, and cured for 28 days before the tests, with an average compressive strength of 48 MPa. The surface of the concrete columns was sanded using 40# sand paper. The composite wrap types and architectures are listed in Table 1.

Table 1 Details of composite architectures used for wrapping concrete columns

Type	Details of wraps architecture
A	3 layers of WR (600 g/m ² *)
B	3 layers of WR/CSM (900 g/m ²)
C	2 layers of GFT (250 g/m ²)
D	3 layers of WR/CSM (900 g/m ²) + 2 layers of GFT

* Unit weigh of each layer

The concrete columns were wrapped using a brush and a consolidating roller. The vinyl-ester resin was mixed with 1.5% of the normal reaction MEKP catalyst at ambient temperature. Before laying the first layer, a resin coat was applied to seal micro holes on the surface of concrete columns, then each layer was wetted and rolled on to the concrete columns to ensure full consolidation. The weight ratio of glass fibre to resin for types A and type B are 1:1 and 1:1.3 respectively; 1:0.85 and 1:1.24 for types C and D respectively.

Mechanical Testing

All compression tests for the columns were conducted following the standard of AS 1012.9-1986 (Method for the Determination of the Compressive Strength of Concrete Specimens), performed on a DARTC testing machine which has a maximum axial compressive loading capacity of 2000 kN. The tests were conducted at a constant cross-head speed of 0.021 mm/s (0.05 in/min). The axial deformation data were collected using three LVDT (Liner Voltage Displacement Transducer) transducers, arranged in a circle of 120° between each other. All data of tests were continually recorded using a computer data acquisition system every 3 seconds. For each type of composite wrapped concrete columns, five specimens were tested, and the average results are presented in the following discussion.

RESULTS AND DISCUSSION

Figure 2 shows the typical global responses of the concrete columns wrapped with various composite architectures subjected to compressive loading. The results of compression tests of all the columns are summarised in Tables 2 and 3 respectively. The increase percentage was calculated as

$$\text{Efficiency \%} = \{(\text{Reinforced} - \text{Unreinforced}) / \text{Unreinforced}\} \times 100.$$

The structural stiffnesses of all columns, in terms of the initial slope of the load-deformation curve, are given in Table 4.

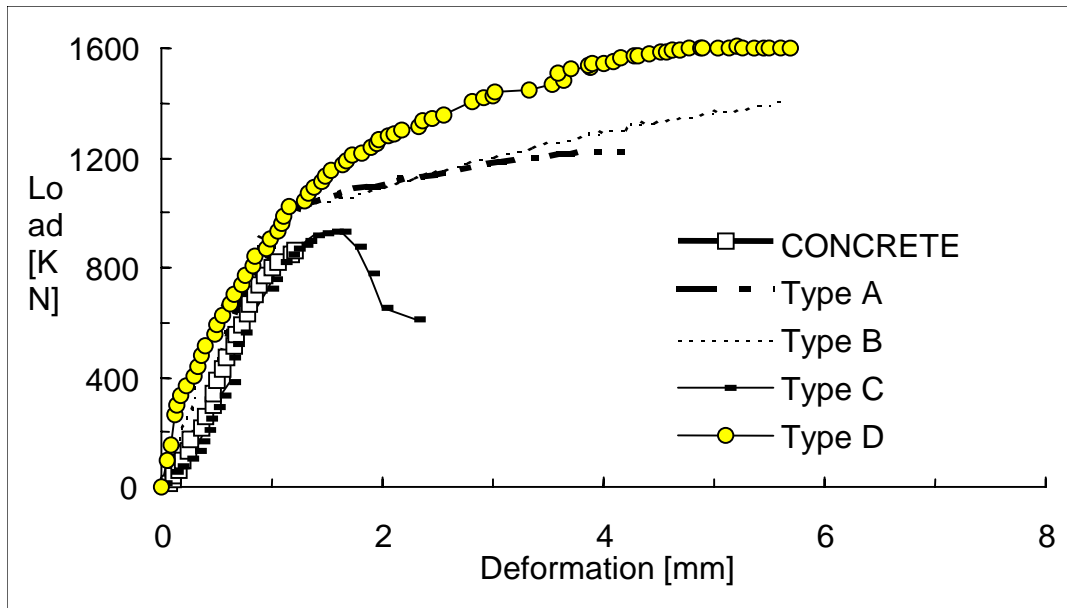


Figure 2 Typical global responses of concrete columns wrapped with various composite architectures

Table 2 Strengthening efficiency of concrete columns with different composite wraps

Type	Total Glass Content [g/m ²]	Average Load at Failure [kN]	Standard Deviation [kN]	Efficiency in Load [%]
Concrete	---	856	32	---
Type A	1800	1167	39	36
Type B	2700	1373	56	60
Type C	500	910	31	6
Type D	3200	1574	54	83

Table 3 Axial deformation of concrete columns with different composite wraps

Type	Average Deformation at Failure [mm]	Standard Deviation of Deformation [mm]	Efficiency in Deformation [%]
Concrete	1.43	0.10	---
Type A	3.77	0.58	164
Type B	5.77	0.37	303
Type C	2.52	0.17	76
Type D	6.01	0.01	320

Table 4 Structural stiffness of concrete columns with different composite wraps

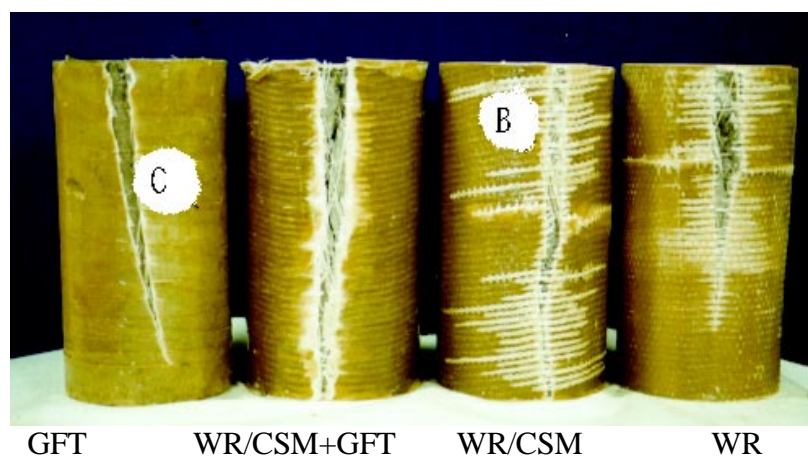
Type	E [GPa]
Concrete	12.6 ± 1.6
Type A	14.6 ± 0.9
Type B	14.2 ± 0.7
Type C	13.1 ± 0.7
Type D	15.6 ± 0.5

It was found that duplication of glass fabric layers from 2 to 4 significantly increased the load-carrying capacity, but did not change the deformation characteristics[2], shown in Table 5. However, in this study, adding chopped strand mat (300g/m²) into woven roving layers (Type B), the experimental results have shown that there are clearly increments in both load-carrying capacity and deformation capability, compared to those of Type A (Figure 1 and Table 5).

It is interesting to see that Type C wrap with only two layers of GFT provides a confinement to the concrete column and produces a significantly increase in deformation capability. However, it does not give an effectively enhancement in the load-carrying capacity, with only 6% of the increment. But when two layers of GFT wraps were applied in Type D, a clear increase in the load-carrying capacity, with 23% of the increment above Type B, is achieved (Figure 1 and Table 2).

Table 5 Comparison of reinforcing efficiency of WR and CSM/WR architectures

No	Type	Fibre content [g/m ²]	Average load at failure [kN]	Deformation at failure [mm]
1	2 layers roving cloth (800g/m ²)[2]	1600	1023.9	2.95
2	4 layers roving cloth (800g/m ²)[2]	3200	1352.3	2.93
3	3 layers of WR (600g/m ²)	1800	1167.2	3.77
4	3 layers of WR/CSM (900g/m ²)	2700	1371.3	5.77

*Figure 3 Failure appearance of concrete columns with various composite wrapping architectures*

The post failure appearance of the concrete columns wrapped with various composite architectures is shown in Figure 3. The composite jackets create a high degree of confinement to the concrete columns, meanwhile it can be seen that the failure pattern of WR on the surface of Type A composite jacket shows a brittle failure, but Type B exhibits more fibre bundle pulling failure on the surface of the WR/CSM composite jacket. However, there is not much fibre bundle pulling failure on the surface of Type D, because of the “tightening up” efficiency of the two layers of GFT as the out layers.

Since carbon and kevlar fibres are expensive, the E-glass fibre is applied in this study to match the strengthening efficiency by increasing the thickness of the composite jacket. Using the lay-up of WR/CSM, the high bonding efficiency between layers of WR can be obtained. Moreover, this type of architecture is suitable for the hand lay-up to squeeze out air bubbles. Depending on the scale of the subjects, the combined method of the machine resin wetting/hand lay-up may be applied to many cases of repair and rehabilitation of civil infrastructure using the system introduced in this study.

FINITE ELEMENT ANALYSIS

Finite Element Model (FEM)

The concrete columns in this study can be assumed to be solid cylinders wrapped with a composites shell which is perfectly bonded to the concrete[7]. Due to the axial symmetry, a two dimension model can be applied to carry out stress analysis using ABAQUS finite element package. The FEM mesh consists of 18 elements in the radial direction and 100 elements in the axial direction, shown in Figure 4. In the evaluations, the concrete and composite jacket were considered as isotropic materials, being perfect elastic-plastic and linear-elastic, respectively.

The mechanical properties of the concrete and composite (Type B) are given in Table 6. Young’s modulus and compressive strength of the concrete were determined from the compressive tests of concrete columns, and those for the composite were determined form tensile tests using coupon specimens.

Table 6 Material properties of concrete and composite

Type	Elastic Modulus [GPa]	Poisson Ratio	Compression Strength [MPa]	Tension Strength [MPa]
Concrete	12.6	0.1 [8]	48	---
Type B	14.2	0.26 [8]	---	210

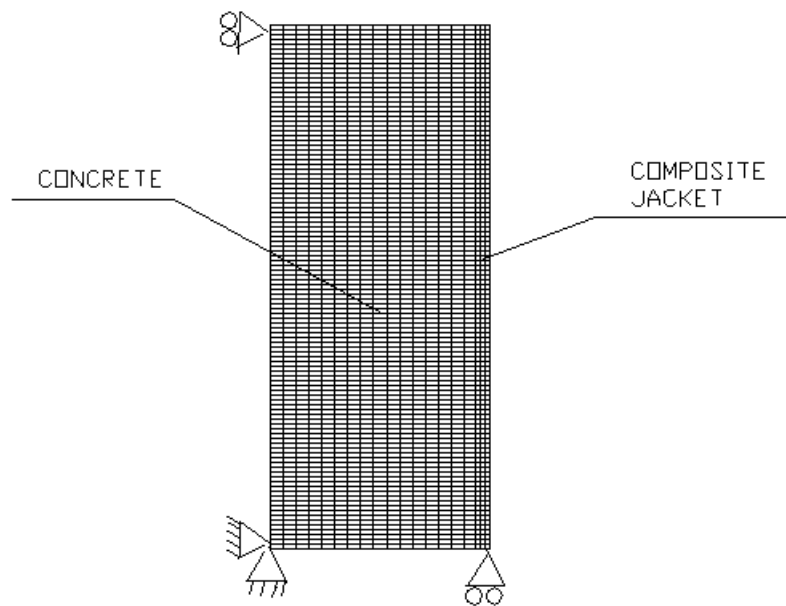


Figure 4 Mesh pattern for concrete column wrapped with composites shell

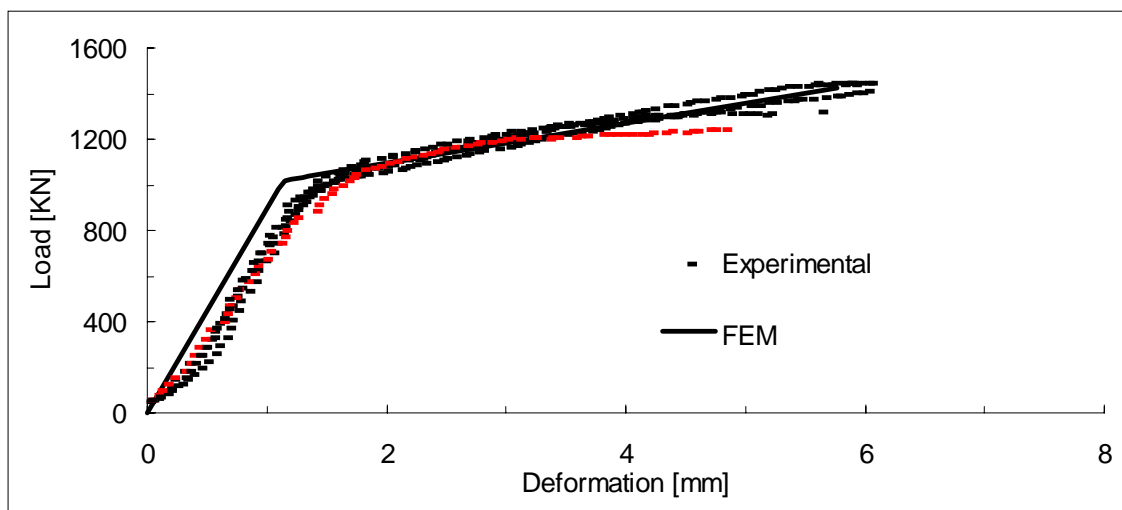


Figure 5 Comparison of FEM evaluation and experimental data for columns with Type B wraps

Load-Deformation Response

The experimental load-deformation curves (Figure 5) illustrate that the initial response is almost linear up to a yield point (kink point). The concrete began to fail beyond this point, and the curves continue almost in a linear manner with a reduced slope, with the composite wrap holding the concrete column together. Catastrophic failure occurred when the composite wrap bursted (failure point). The deformation at the failure point is a measure of the ductility of the wrapped concrete columns. The curve of FEM shows a good agreement with experimental results.

Both Young's modulus and thickness of the composite jacket can be taken as variables to identify the stiffening mechanisms of the composite jackets. Assuming the yielding strength of the concrete is 48 MPa with Young's modulus of 12.6 GPa and Poisson's ratio of 0.1, the

reinforcing efficiency of composite jackets with various composite moduli and thicknesses was evaluated for the case as follows.

- 1) the thickness of the composite jacket was assumed to be a constant ($T=3.6$ mm) and Young's modulus was enlarged from 10 GPa to 30 GPa; and
- 2) Young's modulus was assumed to be a constant ($E=15$ GPa) and the thickness was increased from 2.4 mm to 4.8 mm.

Figures 6 and 7 show effects of Young's modulus and thickness of composite jackets on the kink stress and load-deformation responses of the composite wrapped concrete columns. It can be seen that the increase of Young's modulus of the composite jackets results in increments in the kink stress, leading to higher axial stresses when the concrete fails, and significant increments in the slope of the load-deformation curve after the kink point. These results can also be achieved through the alternation of the thickness of the composite jackets.

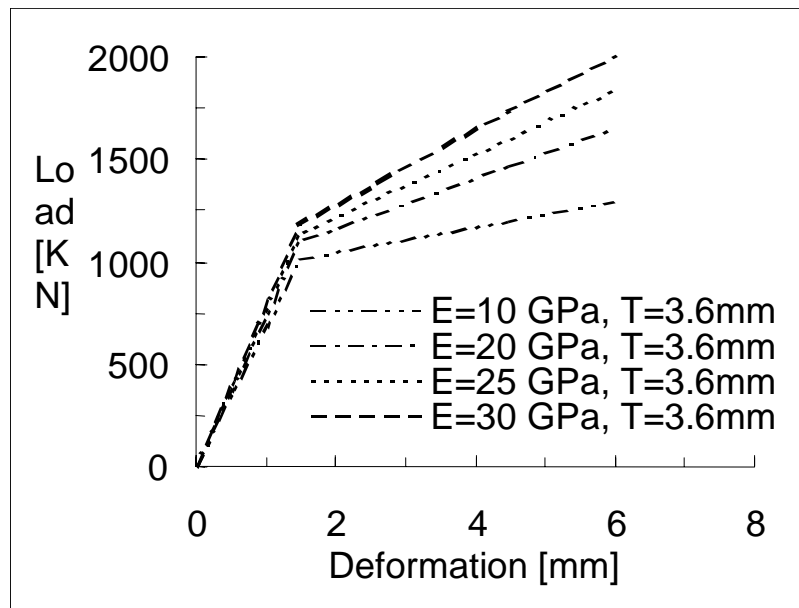


Figure 6 Effect of Young's modulus of composite jacket on kink stress

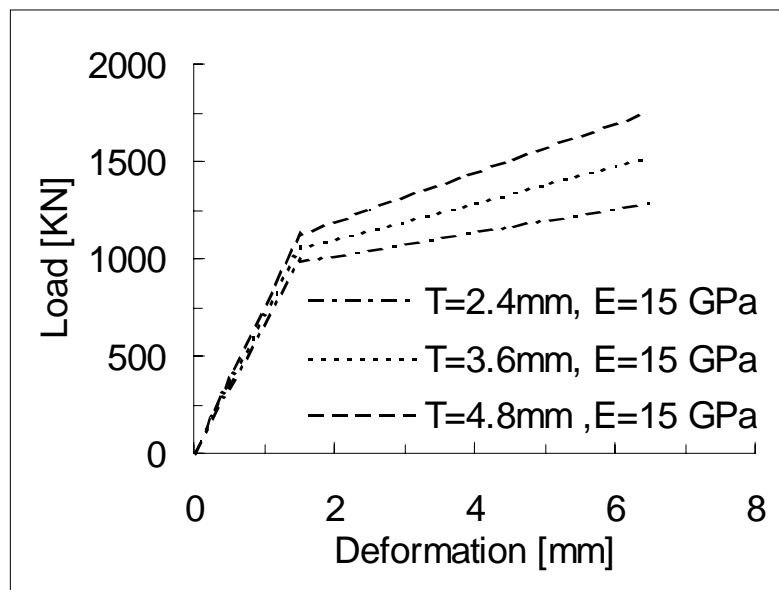


Figure 7 Effect of thickness of composite jacket on kink stress

Effect of loading condition

A finite element model was developed to examine the effect of loading conditions on the responses of the composite wrapped concrete columns. Shown in Figure 9, the curve A with the axial stress applied only to the concrete has a higher kink stress than curve B with the axial stress applied to both concrete and composite jacket. This result shows that if the top and bottom ends of the composite jacket are not subjected to the compressive load directly, the composite jacket can produce a higher strengthening efficiency to the concrete column.

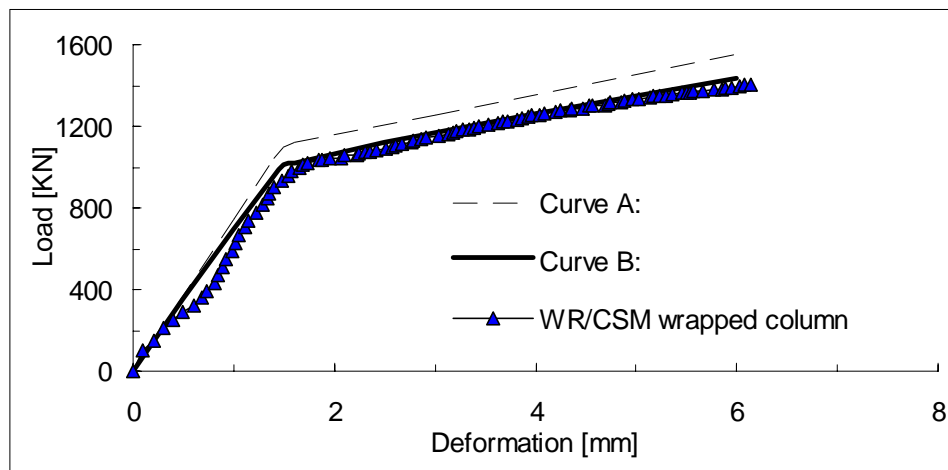


Figure 9 Effect of loading conditions on response of composite wrapped concrete column (Type B)

CONCLUSION AND DISCUSSIONS

Based on the experimental studies and the finite element analyses, the following points can be concluded:

- 1) The use of E-glass fibres and the vinyl-ester resin to reinforce concrete columns externally is effective, with a lower cost of raw materials.
- 2) The reinforcing efficiency is highly dependent on the composite architecture, with a hybrid system of roving cloth, chopped strand mat, and glass fibre tape showing highest enhancement; and
- 3) The FEM analysis can be used to tailor the design of the composite jackets.

ACKNOWLEDGEMENTS

Thanks are due to A/Professor S.G Reid for discussions on various aspects. The authors would also like to express their appreciation to the staff in the laboratory of the School of Civil Engineering at the University of Sydney for their assistance in conducting experiments. S Zhang is supported by an Australian Postgraduate Award. L.Ye wishes to thank the Australia Research Council for the support of this study.

REFERENCES

1. Japan Concrete Institute. 'Handbook for Retrofitting of Existing Reinforced Concrete Structures Gihodo-Shuuppan (In Japanese)', 1984.
2. Karbhari, V. M. 'Strengthening of Concrete Column Stubs through Resin Infused Composite Wraps', Journal of Thermoplastic Composite Materials, Vol.6, 1993, pp 93-107.
3. Furlong, R.W. 'Strength of Steel-Encased Concrete Beam Columns', ASCE Journal of Structural Engineering, Vol.93, 1967, (ST 5): pp 113-124.
4. Knowles, R. B. and Park, R. 'Strength of Concrete Filled Steel Tubular Columns,' ASCE Journal of Structural Engineering, Vol.95, 1969, (ST 12): pp2565-2587.
5. Katsumata, H., Y. Kobatake and T. Takeda 'A Study on Strengthening with Carbon Fibre for Earthquake-Resistant Capacity of Existing Reinforced Columns', Proceeding of the 9th World Conference on Earthquake Engineering, 1988, Tokyo, pp7:517-522.
6. Howie, I. 'Effect of Tow Sheet Composite Wrap Architecture on Strengthening of Concrete due to Confinement: I - Experimental Studies', Journal of Reinforced Plastics And Composites, Vol.14, 1995, pp 1008-1030.
7. Christopher, P. R. 'Analysis of a Concrete Cylinder with a Composite Hoop Wrap', 'Infrastructure: New Materials and Methods of Repair', Proceeding of the Materials Engineering Conference' Oct 1994, ASCE, Mew NY, USA. pp 192-199.
8. Timoshneko, S and Gere, J 'Mechanics of Materials', Van Nostrand Reinhold Company, 1978.

DESIGN OF COMPOSITE (FIBER REINFORCED PLASTIC) BRIDGES IN HUNGARY

László P. Kollár¹, Ákos Sapkás¹ and Adrián Horváth²

¹ *Department of Civil Engineering, Technical University of Budapest,
H-1111, Budapest, Bertalan L. u. 2., Hungary*

² *FOMTERV Rt. Consulting Bureau, H-1251, Budapest, Bem rkp. 28. Hungary*

SUMMARY: Short span (3 to 15 m) pedestrian and bicycle bridges were designed and are planned to be built in Hungary in 1998. The main driving force of the design was the cost. Glass fiber reinforced polyester was selected as the material and pultrusion as the manufacturing process. Attention was paid to the manufacturability of the elements of the bridge and their applicability in other fields. The design was governed by stiffness (displacement and vibration) and not by strength. The erection cost of the superstructure is slightly higher than that of conventional bridges, but their maintenance cost are very low.

KEYWORDS: bridge, pedestrian bridge, bicycle bridge, FRP, design

INTRODUCTION

Bridges in Hungary are usually made of conventional materials such as reinforced concrete, timber or steel. Because of the environmental effects, especially to the salting during winters, the bridges, both the old and the relatively new ones, are severely corroded. The costs of the rehabilitation of these corroded bridges are comparable to the erection costs of new ones. This is one of the main reasons why fiber reinforced plastics, due to their resistance to salt corrosion, are excellent candidates for bridge construction. Several examples of FRP bridges can be found in the literature [1-6].

SELECTION OF THE MATERIAL AND THE MANUFACTURING PROCESS

The selection of the material was based on financial considerations. Glass fiber and polyester resin were used which are significantly cheaper than graphite or epoxy. A comparison was made with conventional materials, such as timber, steel and reinforced concrete (*Fig. 1*) [7]. This comparison shows that the super-structure made of glass/polyester is slightly more expensive than the structure made of conventional materials. Pultrusion was selected, again because of financial considerations, as the manufacturing process. In the above calculation (*Fig. 1*) the price of the tooling was not included which is acceptable if big series of bridge decks are manufactured.

The use of FRP as super-structure has several advantages in addition to the corrosion resistance: because of the reduced weight the elements can be assembled without any special equipment, the abutments can be cheaper etc.

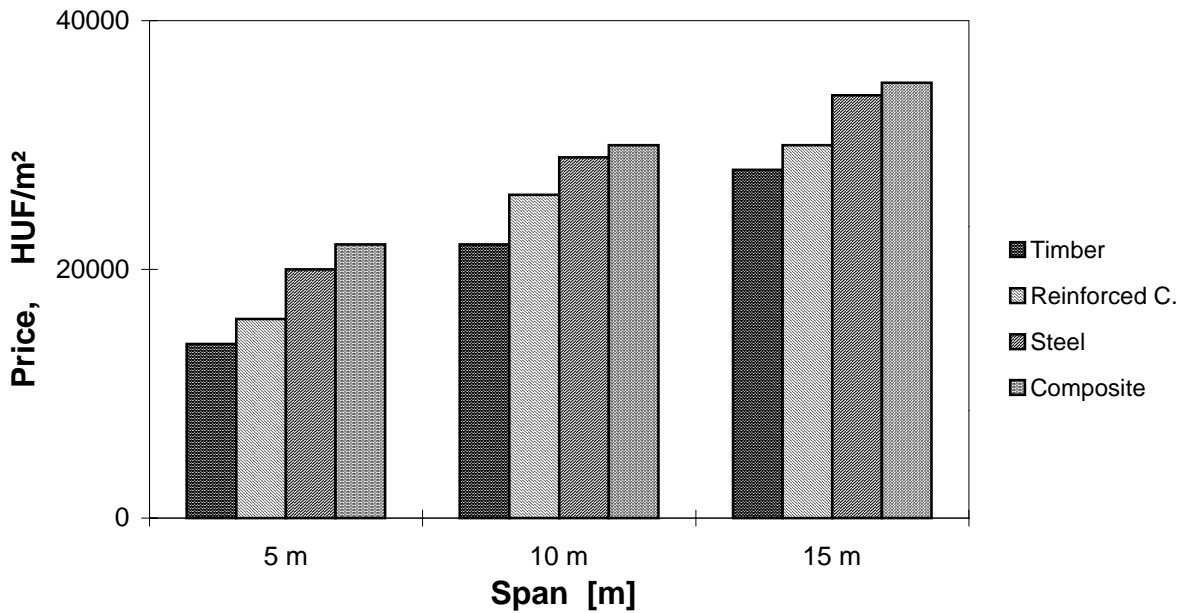


Fig.1: Price of the super-structure

DESIGN OF THE FRP BRIDGE

Two cross sections of pultruded bridge decks were considered and designed [8,9] which are shown in Fig. 2a and b. The elements can be joined together without interlocking planks (such as necessary in the ingenious bridge designed by Maunsell [1]). The closed element (Fig. 2a) behaves more effectively for concentrated loads, however its manufacturing is more complicated. The open cross-section (Fig.2b) must be strengthened by cross girders.

For short spans the beams can be used directly (Fig. 3), while for longer spans external post-tensioning were designed (Fig. 4).

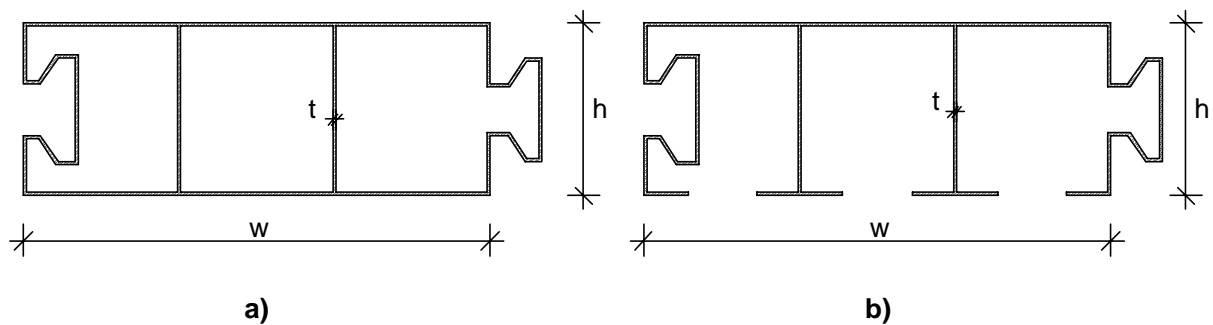


Fig. 2: Cross-section of the bridge-decks, a) closed, b) open

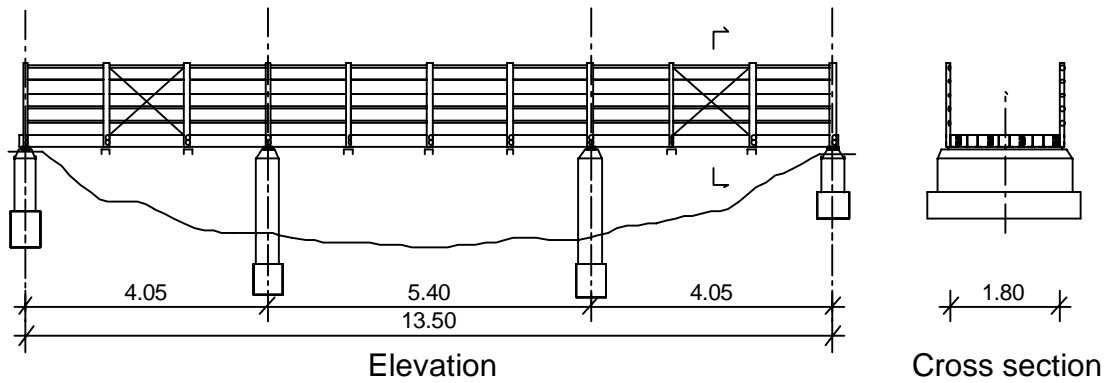


Fig. 3: Bridge deck without external post-tensioning

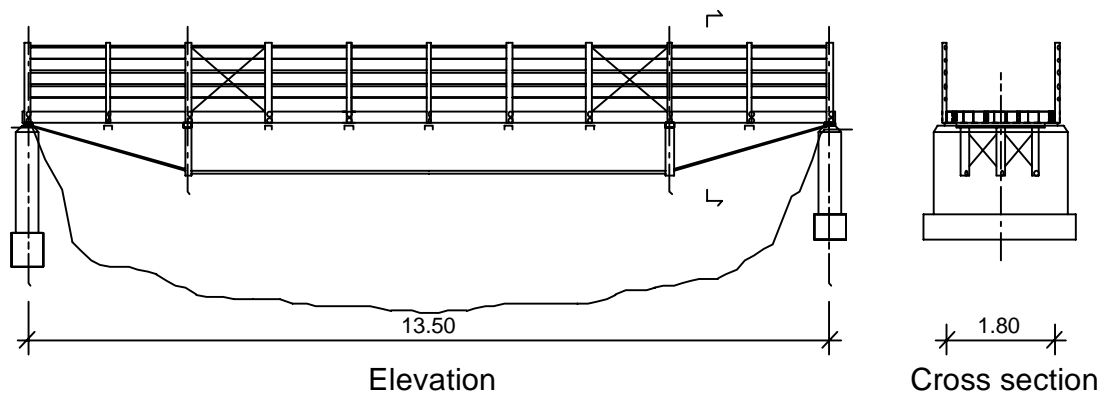


Fig. 4: Bridge deck with external post-tensioning

The pultruded elements were tested for tension and four-point bending [10], and their Young's modulus and strength were determined:

$$E=20-22 \text{ kN/mm}^2 \quad f=350-400 \text{ N/mm}^2$$

These material data and the traffic load due to the Hungarian Standard (5 kN/m² with a safety factor of 1.4) were considered.

The deflection of the middle section and the maximum stress of the bridge without external post-tensioning (*Fig. 3*) was calculated as a function of the span. The height of the cross section was $h=200$ mm, while the thickness (t) was varied between 4 and 8 mms. For simply supported bridges the results are shown in *Fig. 5*. The allowable deflection in Hungary is $L/400$, where L is the total span of the bridge. *Fig. 5* shows that this bridge can be used up to a span of 4 m. At this span the maximum stress (for the 4 mm thick section) is 24 N/mm², and hence, the safety factor of the material is ~ 15 . The required safety factor of the material is

about 3-4 [11], hence the design is governed by the deflection. The eigen frequency of the bridge is 25 Hz.

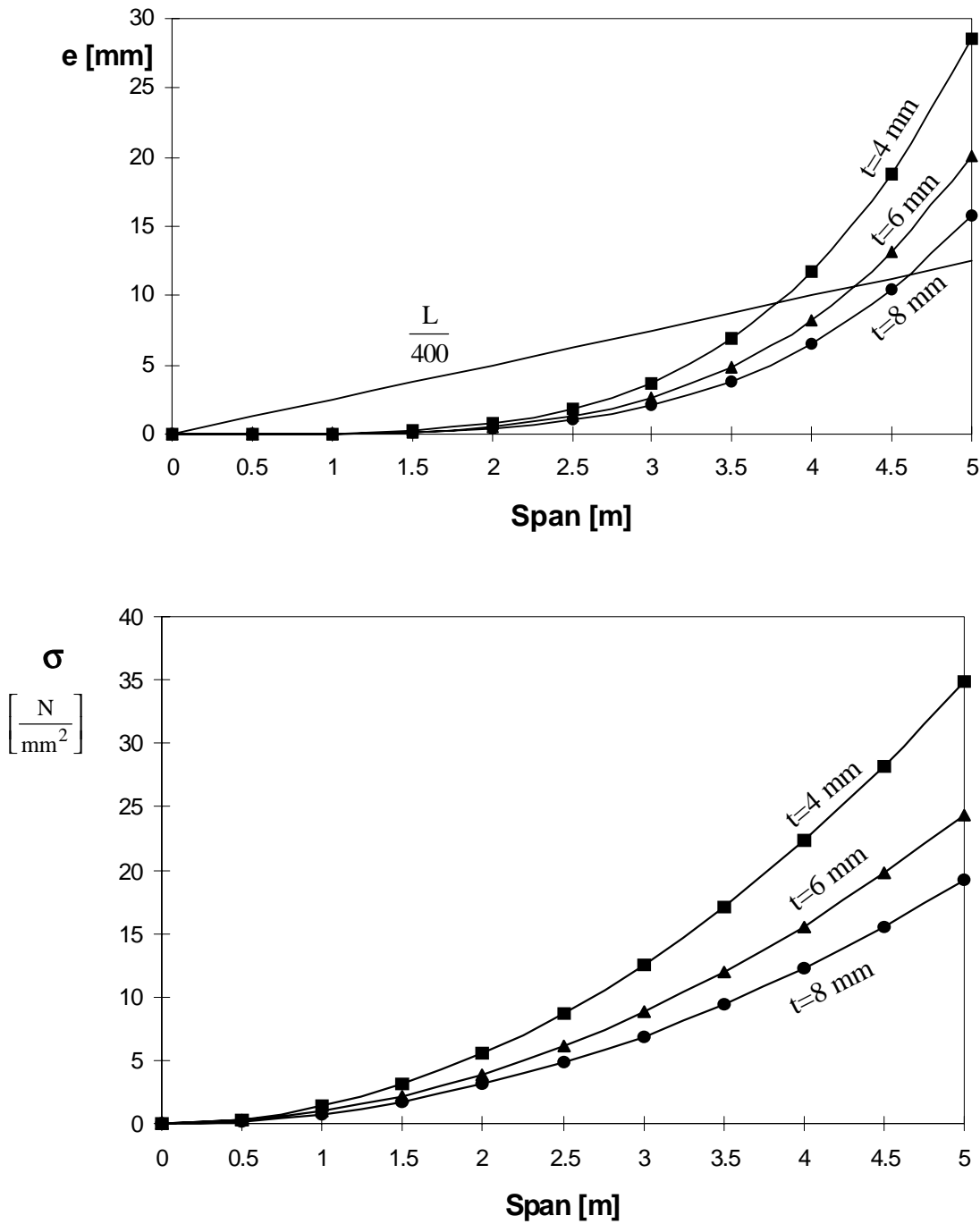


Fig. 5: Deflection and maximum stress of a simply supported bridge

If external post-tensioning is used, the bridge can be precambered by stressing the cables. The calculated deflection and the maximum stresses are shown in Fig.6. (In the calculation we assumed that the precamber of the unloaded bridge due to post-tensioning is equal to the

deflection of the bridge under the total load.) The design is governed again by deflection, the maximum span is 11 m, while the safety factor for compressive strength is again ~15.

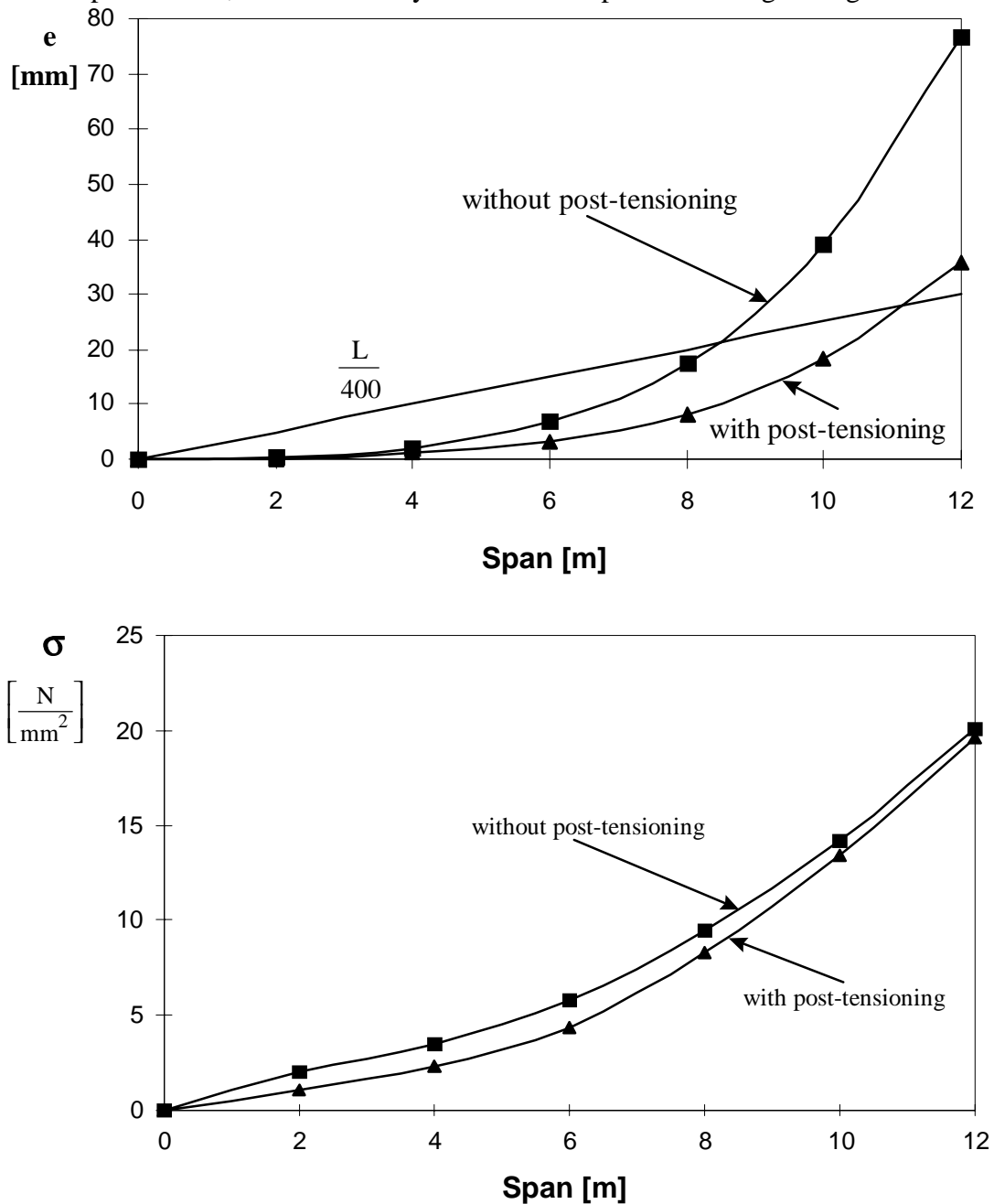


Fig. 6: Deflection and maximum stress of a bridge with and without external post-stressing

CONCLUSIONS

Preliminary design of the first Hungarian FRP pedestrian/bicycle bridge was presented. The erection cost of the super-structure is higher than that of conventional bridges. However, the maintenance cost of the composite bridge is very low. Taking the total life-time of the structure and the additional costs beyond the super-structure into account, the FRP bridges are competitive with steel or reinforced concrete bridges. The bridge deck will be manufactured

this year by the Hungarian firm NITROKÉMIA and the bridge will be built, hopefully, early next year.

ACKNOWLEDGEMENT

This project is sponsored by the OMFb fund. The writers wish to record their appreciation for this help.

REFERENCES

1. Mufti, A.A., Erki, M-A., and Jaeger, L.G. *Advanced Composite Materials with Application to Bridges*. The Canadian Society for Civil Engineering (1991)
2. Mufti, A.A., Erki, M-A., and Jaeger, L.G. *Advanced Composite Materials in Bridges and Structures in Japan*. The Canadian Society for Civil Engineering (1992)
3. Barbero, E., and GangaRao, H.V.S. "Structural Applications of Composites in Infrastructure" *SAMPE Journal*, Vol. 27, No. 6, November/December 1991, pp. 9-16
4. Erki, M.A., Yantha, P., Green, M.F., Johansen, G.E., Wilson, R., and Mauder, D. "Experimental Behavior of a Reinforced Plastic Vehicle Bridge" *50th Annual Conference, Composites Institute, The Society of the Plastic Industry Inc.*, January 30-February 1, 1995
5. Kim, D.H. *Composite Structures for Civil and Architectural Engineering* E & FN SPON, London etc. (1995)
6. Johansen, G.E., Wilson, R., Roll, F., Gaudini, P.G., Rible, S.T., Fogle, A.J., Gray, K.E., Malaki, M.R., and Choy, V.M.S. "Design and Construction of Two FRP Pedestrian Bridges in Haleakala National Park, Maui, Hawaii" *Advanced Composite Materials in Bridges and Structures 2nd International Conference* edited by M.M. El-Badry, 1996, pp.975-982
7. "Comparative Study of Pedestrian Bridges", F• MTERV Rt., 1995
8. Davalos, J.F., Salim, H.A., Qiao, P., Lopez-Anido, R., and Barbero, E.J. "Analysis and Design of Pultruded FRP Shapes under Bending" *Composites Part B: engineering*, Vol. 27B, No. 3/4, 1996, pp. 295-305
9. Khalifa, M.A., Hodhod, O.A., and Zaki, M.A. "Analysis and Design Methodology for an FRP Cable-stayed Pedestrian Bridge" *Composites Part B: engineering*, Vol. 27B, No. 1, 1996, pp. 307-317
10. Ódor, P. and Varga, L. "Report on the Mechanical Properties of the Pultruded Sections Manufactured by NITROKÉMIA", (in Hungarian) 1996
11. Structural Design of Polymer Composites, *EUROCOMP Design Code and Handbook* edited by Clarke, J.L., E & FN SPON, London etc. (1996)

GEOSYNTHETIC APPLICATIONS OF SUPER-DRAWN POLYOXYMETHYLENE FIBRES: 1. REINFORCEMENT OF ASPHALT CONCRETE

Tamikuni Komatsu¹, Hiroshi Kikuta², Yoshinobu Tuji³ and Eijiro Muramatsu³

¹*Analytical Research Center, Asahi Chemical Industry Co., Ltd.,
2-1 Samejima, Fuji, Sizuoka 416, Japan*

²*Asahi Engineering Co., Ltd., 1-8 Konan 4-Chome, Miatoku, Tokyo 108, Japan*

³*Tokyu Construction Co., Ltd., 1-15-21 Sibuya-ku, Tokyo 150, Japan*

SUMMARY: A grid was prepared from superdrawn polyoxymethylene fibers and applied to the reinforcement of asphalt concrete. The mechanical durability such as plastic flow resistance and crack resistance of the grid-reinforced asphalt concrete was assessed by the wheel tracking test. The grid-reinforced asphalt concrete showed remarkably high plastic flow resistance and crack resistance in comparison with the control without grids. The behavior of the plastic flow was explained on the basis of the general creep model and the result indicated a remarkable increase in the viscosity of the grid-reinforced asphalt concrete. The crack resistance was strongly related to the plastic flow resistance. The high durability of the grid-reinforced asphalt concrete was apparently due to the mechanical reinforcement resulting from the high rigidity of the grid layer inserted in the asphalt concrete.

KEYWORDS: polyoxymethylene fibers, geogrid, asphalt-reinforcement

INTRODUCTION

High modulus and high strength fibers such as carbon fibers, glass fibers and ultradrawn fibers are used for reinforcement of various materials. One of the applications, geosynthetics like geogrids and geotextiles that were manufactured from high performance fibers or plastics, made a technological change in the soil improvement and embankment work. In particular, using geogrids one has achieved great success in the reinforcement and stabilization of soft ground, since the invention of "Tensar", the biaxially stretched sheet developed in the mid 1970s. On the other hand, the technology of asphalt paving has supported the improvement of land traffic networks in modern societies. The asphalt pavement made from asphalt and aggregates is desired to be mechanically highly durable, but increasing heavy traffic volumes

in recent years are producing heavy damage such as wheel tracks and cracks in the pavement. Blending thermosetting resins like epoxy resin and blending elastomers like SBR with an asphalt mixture have been usually made to decrease wheel tracking. However, the conventional method is insufficient for a fundamental solution of the problems, because such modified asphalt binders only solve either of these problems and tend to be remarkably cracked by thermal shock. Recently, Aglan et al. reported that the dynamic compaction in addition to the conventional static compaction of an asphalt mixture increases both the flexural toughness and fracture resistance of the asphalt concrete.¹ This method that needs only the improved compactor instead of the conventional compactor is certainly convenient to constructors, but the improvement was several times as large as the result of the conventional compaction. Another method is an use of geosynthetics for a repair of the damaged parts: a geosynthetic is patched to a cracked part, followed by overlay with an asphalt mixture. Most of the geosynthetics used for this purpose are non-woven textiles and grids manufactured from a commodity grade of polyester yarns. Therefore, the reinforcement effect cannot be produced by this method. It is hoped that high mechanical properties of high performance fibers are effective for reinforcing the pavement, but few such applications have been reported. Recently, one of the authors developed high modulus and high strength polyoxymethylene (POM) fibers and applied the fibers to the reinforcement of rubbers and plastics.² The aim of our work is to develop the geogrids of the POM fibers. In this work, we report the durability of the grid-reinforced asphalt concrete and discuss a mechanism of the reinforcement.

EXPERIMENTAL

Preparation of Superdrawn POM Fibers and Its Grids

The superdrawn POM fibers were prepared by pressure-drawing an undrawn POM fiber at a draw ratio of 20 according to a previous method.² The diameter, Young's modulus and tensile strength along the fiber axis were 0.5 mm, 40 GPa, and 1.8 GPa, respectively. The fibers obtained were surface-activated using an activating agent comprising a mixture of resorcinol, a resorcinol-formaldehyde-latex (RFL) solution according to the continuous process described previously.² The Young's modulus and tensile strength of the activated fibers were 36 GPa and 1.5 GPa, respectively. Next the activated fibers were woven with a loom to make a grid having the 5 mm × 5 mm meshes. The grid was then coated with an emulsified asphalt, dried in air, and laminated with 15 μ m thick polyethylene film. The emulsified asphalt used was an usual tack coat used for coating of an asphalt concrete (Sin Doro Rekizai, Tack Coat PK-4) and the amount used was 300 ml per 1 m² grid. The grid thus obtained was 1.0 mm in thickness, 120 ton^f/m in Young's modulus per width and 5 ton^f/m in strength per width.

Preparation of Asphalt Concrete

A compacted asphalt mixture, so-called asphalt concrete, that was used in the following experiment was the dense-graded asphalt concrete of the surface course type 1, and this was prepared according to the asphalt pavement standard.³ The composition was 5.6% for asphalt and 94.4% for aggregates. The asphalt used was straight asphalt (Showa Shell Petroleum, STRAIGHT ASPHALT 80/100) and the aggregates used were a mixture of No.6 crushed stone (39%), No. 7 crushed stone (18%), screenings (17%), coarse sands (13%), fine sands (9%)

and limestone (4%). The asphalt and aggregates were homogeneously mixed at 160°C. The obtained hot mixture was then poured into a heated steel mold and compacted with a Marshall roller-compactor in the temperature range of 130–140°C. The molded asphalt concrete thus obtained was 300 mm^L×300 mm^W×50 mm^H. The physical properties of the asphalt concrete were confirmed to be in agreement with the standard value for the Marshall test. In the following experiment, the asphalt concrete thus prepared was used as an under block, the under part of the test sample, on which the grid is placed.

Preparation of Wheel Tracking Test Samples

The grid-reinforced asphalt concrete was prepared as follows: the under block was placed in a steel mold (300 mm^L×300 mm^W×80 mm^H), the grid was laid on the block, and the hot mix prepared in advance was then overlaid on the grid to a height of ca. 30 mm, followed by compaction at 130–140°C (grid-reinforced sample). For comparison, the control was prepared in the same way as above except that the under block was coated with the asphalt emulsion instead of laying the grid.

Preparation of Crack Resistance Test Samples

The molded asphalt concrete (300 mm^L×300 mm^W×50 mm^H) was cut into two blocks (300 mm^L×150 mm^W×50 mm^H), inserted with a cardboard between the cut planes to protect each other from adhesion, and placed in the steel mold (300 mm^L×300 mm^W×80 mm^H). The grid was laid on this under block, the hot mix prepared in advance was overlaid on the grid to a height of ca. 30 mm, and followed by compaction at 130–140°C. The reinforced asphalt concrete thus obtained was cut at a right angle to the cut planes of the under block to make three pieces of test samples (300 mm^L×80 mm^W×80 mm^H). For comparison, the control was prepared in the same way as above except that the under block was coated with the emulsified asphalt instead of laying the grid.

Measurements of Plastic Flow Resistance and Crack Resistance

The plastic flow resistance of the test sample was measured using a wheel tracking testing machine according to the asphalt pavement standard.³ A solid tire wheel was used without traveling. The experiment conditions were as follows: the sample dimension was 300 mm^L×300 mm^W×50 mm^H, the wheel load was 70 kg^f whose value is equivalent to a contact pressure of 6.4 kg/cm², the number of cycles of the wheel (or wheel revolutions) was 42 r.p.m.,

the test time was 60 min, and the atmospheric temperature was $60 \pm 1^\circ\text{C}$. A rutting depth was measured with a linear variable differential transformer and recorded to the elapsed loading times using a x-y plotter. From the deflection curve thus obtained, the ratio of deflection, RD, and the dynamic stability, DS, defined as follows, were determined:

$$DS = \frac{N(t_2 - t_1)}{d_2 - d_1}, \quad RD = \frac{d_2 - d_1}{t_2 - t_1}$$

where N is the number of cycles of the wheel; d_1 is the deflection at the elapsed loading time of t_1 ; and d_2 is the deflection at t_2 . According to the asphalt pavement standard, t_1 and t_2 were set at 45 min and 60 min, respectively. The values of d_1 at $t = 45$ min and d_2 at $t = 60$ min were expressed as d_{45} and d_{60} , respectively. Therefore, the DS and RD can be described

as follows:

$$DS = \frac{630}{d_{60} - d_{45}}, \quad RD = \frac{d_{60} - d_{45}}{15}$$

The plastic flow resistance was assessed on the basis of above DS and RD.

The crack resistance test was also carried out using the same wheel tracking test machine. A crank type solid tire wheel was used. The experimental conditions were: the sample was $300 \text{ mm}^L \times 80 \text{ mm}^W \times 80 \text{ mm}^H$; a wheel load was 100 kg^f ; the traveling distance of the wheel was $230 \pm 10 \text{ mm}$; the number of cycles of the wheel was 42 r.p.m.; the atmospheric temperature was $20 \pm 3^\circ\text{C}$. In this test, cracks were usually generated at the place close to the slit of the under block, grew to the center, and finally penetrated through the block. In order to investigate the crack-propagation process, the front face of the sample was first painted white to make cracks observable with ease, and then marked a record of time with a black pen. The crack resistance was defined as a total time until reaching to the crack-penetration.

RESULTS AND DISCUSSION

Plastic Flow Resistance

Fig. 1 shows the deflection curves of the grid-reinforced sample and the control without grids, and the results of d_{45} , d_{60} , RD and DS are listed in Table 1.

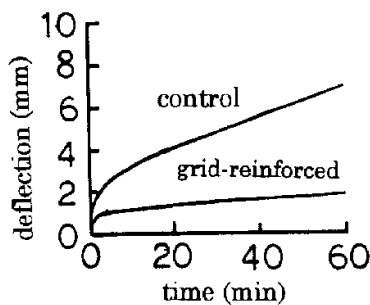


Fig. 1: The deflection curves

	grid-reinforced	control
d_{45} (mm)	1.86	5.97
d_{60} (mm)	1.95	6.97
RD (mm/min)	6.00×10^{-3}	6.67×10^{-2}
DS (pass/mm)	7000	630

The DS value of the grid-reinforced sample was over 10 times that of the control. The asphalt

concrete that is composed of asphalt as a binder and aggregates as a frame can be regarded as a kind of viscoelastic composite material. The plastic deformation behavior of the asphalt concrete at applied stress and elevated temperatures is supposed to be analogous to the creep behavior of viscoelastic materials. The rutting behavior of the asphalt concrete was then investigated on the basis of a general mechanical model that is a linear combination of a series component (the Maxwell model) and a parallel component (the Voigt mode) as shown in Fig. 2. The following general equation was used to simulate the observed rutting curves:

$$\epsilon(t) = \epsilon_1 + \epsilon_2 \{ 1 - \exp(-t/\tau) \} + \gamma t \quad (1)$$

$$\epsilon_1 = \sigma/E_s, \quad \epsilon_2 = \sigma/E_p, \quad \gamma = \sigma/\eta_s, \quad \tau = \eta_p/E_p \quad (2)$$

where $\epsilon(t)$ is the deflection at the elapsed loading time, $t(s)$; ϵ_1 is the elastic strain due to the series elastic part; ϵ_2 is the anelastic strain due to the parallel component; γ is the inelastic deflection rate due to the series viscous part; τ is the retardation time; σ is the stress; E_s and E_p are the moduli of the series and parallel components, respectively; η_s and η_p are the viscosity of the series and parallel components, respectively. The second term of the equation is dominant at the earliest regions of the deflection but is soon saturated to the value of ϵ_2 , so the deflection linearly increases with the third term after sufficiently long loading times. The sufficiently long loading time for obtaining the value of ϵ_2 and γ was set at 3600 s for convenience, that is, γ was served as RD.

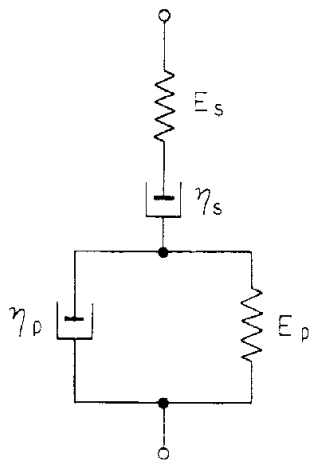


Fig. 2: Mechanical model

Table 2: Creep parameters explaining the plastic flow

	grid-reinforced	control
$\epsilon_1(\%)$	0.00	0.00
$\epsilon_2(\%)$	5.3	9.9
$\gamma(\% s^{-1})$	3.3×10^{-4}	3.7×10^{-3}
$\eta_s(\text{GPa} \cdot \text{s})$	190	17
$\tau(\text{s})$	$16.7 t^{0.50}$	$13.0 t^{0.53}$

Therefore, these parameters can be obtained in the following way: ϵ_1 is the initial deflection immediately on loading; γ is obtained as a slope of the tangent to the curve at long elapsed loading times; ϵ_2 is the subtraction of γt and ϵ_1 from the value of $\epsilon(t)$ at long elapsed

loading times; τ can be obtained from the following equation that is easily derived from the above equation.

$$\tau = -t / \ln \left\{ \left[\varepsilon_1 + \varepsilon_2 + \gamma t - \varepsilon(t) \right] / \varepsilon_2 \right\} \quad (3)$$

The relationship between τ and t was investigated, a linear line was then obtained from the plots of $\log \tau$ vs. $\log t$. The relation was therefore described by the following power function:

$$\tau = A t^n \quad (4)$$

where A is given as an intercept at $t = 1$ s of the obtained line, and n is given as a slope of the line. The results of all the parameters of the rutting behavior are summarized in Table 2. The value of ε_1 was practically zero for the reinforced sample and the control. This is because the initial strain is negligibly small because the applied load (6.4×10^{-4} GPa) is very small compared to the Young's modulus (9 GPa) of the asphalt concrete. The value of ε of the reinforced sample was about 1/2 that of the control, the value of γ of the reinforced was about 1/10 that of the control, and the value of τ of the reinforced was slightly larger than that of the control. The result means that the insertion of the grid layer into the asphalt concrete remarkably increased the viscosity of the series component.

Crack Resistance

The crack-propagation every elapsed loading time for the grid-reinforced sample and the control were investigated. In the case of the reinforced sample, the crack generation occurred at the place close to the slit of the under block, whereas in the case of the control most of cracks were generated in the inside near the surface of the sample. The cracks were generated at the place of asphalt but not in the part of aggregates. The cracks propagated along the asphalt layer around aggregates. The time until crack-generation (crack-generation time) and the total time until the fracture (crack-penetration time) of the grid-reinforced sample were eight times as long as those of the control, as is given in Table 3.

Table 3: The crack resistance

	crack-initiation time (min)	crack-penetration time (min)
grid-reinforced	375	600
grid-reinforced	413	853
control-	34	68
control-	30	93

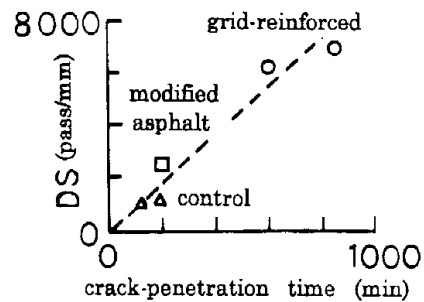


Fig. 4: Crack-penetration time vs. dynamic durability

The relationships between the vertical crack-length and the loading time were also obtained. The cracking behavior was composed of three stages, the crack-initiation stage in which

visible cracks are not observed, the crack propagation stage and the fracture stage reaching to the crack-penetration. As a result, the initiation stage showed an extrapolated linear line passing the origin and occupied 40-50% of the total time until the fracture, the crack propagation stage was linear to the time and occupied 40-50%, and the fracture stage revealed a steep upward curve and occupied 0-20%. The crack propagation stage was never shorter than the initiation stage for both the reinforced sample and the control. This means that the rate-determining stage of the fracture process is the initiation stage and the crack propagation stage and therefore suggest that the crack resistance is possibly related to steady deformation of the asphalt concrete. Fig. 4 shows a plot of crack-penetration time vs. dynamic stability. The grid-reinforced sample occupied high positions with respect to both parameters, whereas the control was near the origin. Both parameters for the reinforced asphalt concrete - appear to make a positive correlation. For comparison, the values (unpublished data) of the asphalt concrete improved by blending with polymer additives were also plotted on the same figure. The tendency for the grid-reinforced sample is not in agreement with those for the conventional asphalt concrete. This is because the reinforcing mechanisms of these samples are different with each other. The high bearing capacity of the reinforced sample is based on the mechanical reinforcement, whereas the improvement only in the plastic flow for the conventional sample is based on the hardening of asphalt by blending polymers. On the other hand, Aglan et al. presented the dynamic and static compactions to improve the crack resistance and flexural resistance, as described in the introduction. They reported that the improved properties are due to the enhanced interfacial adhesion between the binder and the aggregates that was produced by the dynamic compaction. In contrast with these methods, the improved durability by grid-reinforcing does not arise from the modification of the asphalt binder. The mechanical properties of the grid are comparable to those of a 0.1 mm thick iron plate. The insertion of the grid greatly reduced the deflection of the asphalt concrete, resulting in the high plastic flow resistance and high crack resistance of the reinforced asphalt concrete.

CONCLUSIONS

A grid was prepared from superdrawn polyoxymethylene fibers and applied to the reinforcement of asphalt concrete. The durability such as plastic flow resistance and crack resistance of the reinforced asphalt concrete was investigated using the wheel tracking test. The insertion of the grid into the asphalt mixture was very effective for increasing the durability of the asphalt concrete. The behavior of the plastic flow was analyzed using the series-parallel creep model, and the result indicated that the grid-reinforcement remarkably increases the viscosity of the series component. The crack behavior was composed of three stages and the rate-determining stage was the crack-initiation stage and crack-propagation stage. This suggests the relationship between the crack behavior and steady deformation of the asphalt concrete. Surely, the grid-reinforced asphalt concrete showed a strong relationship between the crack resistance and the dynamic stability. The high durability of the grid-reinforced asphalt concrete was apparently due to the mechanical reinforcement and this effect resulted from the high rigidity of the grid layer.

ACKNOWLEDGMENT

We wish to express our gratitude to Mr. Akira Tsutiya of Seiki Tokyu Industry Co., Ltd. for his technical advice.

REFERENCES

1. Aglan, H., Othman, A. and Figueroa, L., "*Processing Conditions-Fracture Toughness Relationships of Asphalt Concrete Mixtures*", *J. Mater. Sci.*, Vol. 29, 1994, pp 4786-4792.
2. Komatsu, T., "*Surface Modification of Superdrawn Polyoxymethylene Fibers*", *J. Mater. Sci.*, Vol. 28, 1993., pp. 3043-3047.
3. *The Asphalt Pavement Standard*, The Japan Highway Association Edition, Maruzen Ltd, Tokyo, 1996.

GRAPHITE/EPOXY COMPOSITES FOR OFFSHORE APPLICATIONS

S.T. Mear¹, H.G. Wheat¹, and H.L. Marcus²

¹*Offshore Technology Center and the Center for Materials Science and Engineering,
The University of Texas at Austin, Austin, TX 78712*

²*Institute of Materials Science, University of Connecticut, Storrs, CT 06269*

SUMMARY: The transverse fatigue crack growth rates of a graphite/epoxy composite (AS4C/E719LT) were investigated using a high pressure test system. Compact tension specimens of the as-received and conditioned composite were fatigued in ambient air, ambient seawater, 13.8 MPa (2000 psi) seawater and 27.6 MPa (4000 psi) seawater. The crack growth rates of the specimens tested in ambient and high pressure seawater were found to be approximately ten times higher than the growth rates of the specimens tested in ambient air. This was true for the as-received as well as the conditioned specimens, however, rates for the conditioned specimens were lower for all test conditions. Three possible mechanisms have been described for this change in growth rates. The first mechanism is the weakening of the fiber/matrix bond resulting in a reduced fracture toughness of the composite. Alternately, a change in the local stress field at the crack tip resulting from the presence of the incompressible seawater may be the controlling factor. A third possibility seems to result from competition between crack propagation through the matrix or along the fiber/matrix interface. If the composite is dry, as it would be in the as-received condition, both options are possible, and equally as likely, and crack propagation is accelerated in ambient or high pressure seawater. If the composite is saturated, however, the behavior is dominated by the properties of the toughened matrix, through which crack propagation becomes more difficult. These findings have ramifications for graphite/epoxy composites which would be used in offshore applications where they would be exposed to high pressure seawater.

KEYWORDS: corrosion fatigue, seawater, environmental test chamber, high hydrostatic pressure, graphite/epoxy

INTRODUCTION

The quest for oil in deep waters has resulted in a search for materials which can withstand the rigors of offshore environments. Depths approaching 3,000 meters and hydrostatic pressures of approximately 30 MPa will certainly test the materials used for deep water structures. Polymer composites are particularly attractive for deep water applications because of their light weight and high strength to weight ratios. However, many of the previous uses have focused on aerospace applications in which long term exposure to marine environments has not been a major factor.

The work of previous investigators indicates that the behavior of polymer composites exposed to high hydrostatic pressures and seawater environments is very dependent on the particular

polymer-reinforcement system as well as the reinforcement orientation, the processing and the mode of deformation. The hydrostatic pressure could act to close voids and pores and thus inhibit the uptake of saltwater [1]. In other cases, however, there may be increased moisture uptake due to high pressure [2]. The large hydrostatic pressure can suppress the longitudinal splitting of fibers or the debonding of fiber bundles and subsequent delamination [3] or close flaws and microcracks that initiate catastrophic cracking [4]. In addition, the reduced free volume of the polymer matrix brought about by the hydrostatic load may increase interlaminar strength by restricting polymer chain motion [5] or decrease transverse tensile strength and interfacial strength [6]. It has been reported that the increased matrix plasticization that results from moisture absorption degrades the mechanical performance of graphite/epoxy composites and can contribute to accelerated fatigue crack propagation [7]. The results of another study show increases of 15% in the Mode I fracture toughness and decreases of 15% in the Mode II fracture toughness at saturation for a carbon fiber composite with toughness-modified epoxy matrix [8]. The dry Mode I test specimens experienced brittle matrix failure and had good fiber/matrix adhesion, while the saturated specimens experienced ductile matrix failure and had poor fiber/matrix adhesion. The decrease in Mode II fracture toughness values was primarily due to poor fiber/matrix bonding.

Weakening of the fiber/matrix interface by moisture absorption allows increased fiber debonding and a corresponding rise in the interlaminar fracture resistance of graphite/epoxy composites [9]. Such fiber debonding causes crack bridging that reduces the stress intensity in the region of the crack tip and therefore slows crack propagation. Other studies reveal that increased matrix plasticity coupled with accelerated fiber/matrix interface degradation lowers the Mode I transverse fracture toughness of graphite/epoxy composites [10]. This behavior is attributed to the crack propagating more via the weakened interface than through the tougher matrix in wet specimens.

This paper describes an examination of a particular graphite/epoxy composite exposed to high pressure seawater environments. This composite is one which was under consideration for offshore applications. The particular concern is corrosion fatigue that could result from wave forces and hydrostatic pressures that would develop at very large depths. The following section describes the use of compact tension specimens to study the transverse fatigue crack growth in unidirectional composites subjected to axial loading and hydrostatic pressure. The main objectives were to determine the effect that pressurized seawater has on the fatigue crack growth rate in as-received and conditioned (soaked in seawater to saturation) specimens and to investigate the factors which control failure for each of the test conditions. Tests were conducted in a pressure chamber designed for studying the corrosion fatigue behavior of composite materials subjected to high hydrostatic pressure seawater. While this research is being carried out as a function of frequency, this paper will focus on the behavior at a single frequency.

EXPERIMENTAL PROCEDURES

Materials and Specimens

Compact tension (CT) specimens (25.4 mm wide) were machined from 12 ply thick panels of AS4C/E719LT graphite/epoxy unidirectional plates according to ASTM E647 [11] for metallic materials. The flat panels were fabricated using a filament winding and autoclave cure process by R-Cubed Composites from prepreg manufactured by Fiberite. The E719LT

matrix material is a thermosetting solution-based resin with two proprietary elastomer additives for increased matrix toughness.

Specimens were notched parallel to the fiber direction using a 0.51 mm wide slitting saw blade. Fig. 1 shows the geometry of the CT specimens as well as the orientation of fibers and plies relative to the machined notch. All specimens were stored in a sealed container with desiccant to prevent moisture uptake prior to testing. The elastic properties of the test materials were determined by tension and shear tests on coupon specimens and are given in Table 1 [12].

Table 1. Material properties of AS4C/E719LT.

E_1 (GPa)	E_2 (GPa)	G_{12} (GPa)	ν_{12}	V_f (%)
128.2	8.48	5.31	0.35	60

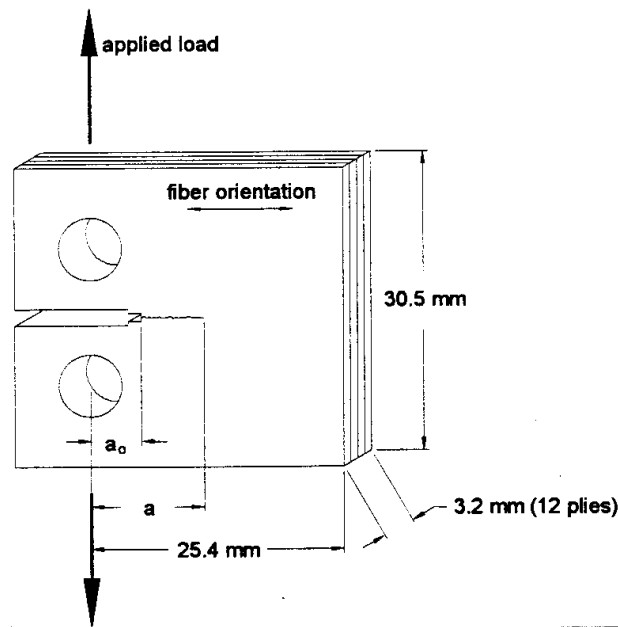


Fig. 1: Compact tension specimen geometry showing orientation of fibers and plies relative to the machined notch.

Hydrostatic Pressure Test System

The experimental test system (Fig. 2) consists of an Inconel 600 hydrostatic pressure test chamber designed by Fowkes [13] in conjunction with Autoclave Engineers. The dimensions of the test chamber accommodate a 25.4 mm wide CT specimen as well as associated grips and instrumentation. The 3.8 liter capacity chamber was also designed to maximize the environment volume to specimen area ratio and minimize the chamber surface area. The test vessel is mounted in a 100 kN MTS servohydraulic fatigue test frame, which provides control of applied loads and displacements. Data are obtained via a PC-based digital acquisition program. Pressure is monitored using an optical sensor transducer with an operating range of 0-38 MPa and an accuracy of $\pm 0.1\%$ in that range. The test system also contains a load

sensing clevis pin which was designed in conjunction with and manufactured by the StrainSert Company. This pin has the capability of accurately monitoring loads of less than 4.5 N and a maximum load capacity of 1560 N at 38 MPa. The pin has an offset load due to the hydrostatic pressure of less than 9 N at 28 MPa, minimizing errors due to pressure fluctuations resulting from ram motion or pumping of the pressurizing fluid. The remainder of the test loop consists of the system pump, fluid reservoir, fluid filter, and high pressure fittings, tubes and control valves.

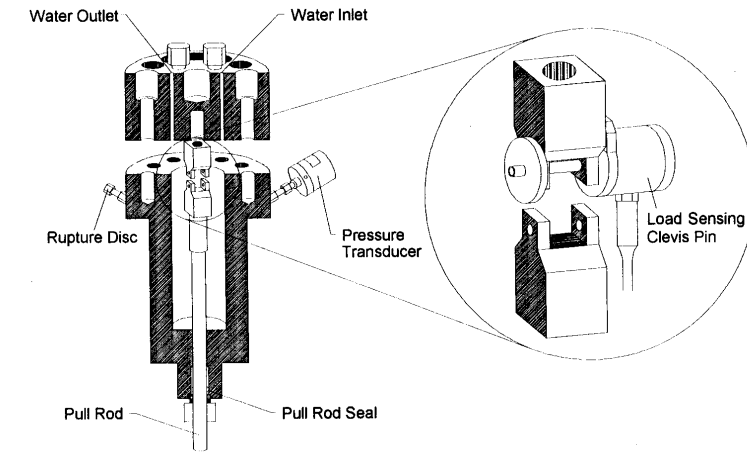


Fig. 2: Schematic of high pressure chamber and load sensing clevis pin.

Test Methods

Crack length in the enclosed chamber was monitored using the crack compliance method and the specimen compliance calibration was performed in load and displacement control. The details of the procedure have been described elsewhere [14,15]. In addition, the fracture toughness of the composite, K_{IC} , was determined from these tests according to ASTM E399 [16] for metallic materials.

Specimens were precracked in ambient air (21°C and 40-50% RH) prior to fatigue testing using the K_{max} decreasing method followed by additional precracking at the test loads. The final length of the precrack was measured under an optical microscope and was then compared with the value from the compliance calibration to ensure agreement between the actual and calculated crack lengths.

Load control tension-tension fatigue testing was performed in air, ambient seawater, 13.8 MPa (2000 psi) and 27.6 MPa (4000 psi) seawater. The mean load was 68 N with a ± 45 N cyclic load ($R=0.2$). Waveform was 2 Hz sinusoidal. The seawater solution used in all tests consisted of synthetic sea salt in distilled water. The pH and dissolved oxygen of the seawater were monitored prior to and after testing. Specimens were also weighed before and after testing to determine any possible weight gain or loss from exposure to the seawater environment. After the specimen was precracked, it was placed in the chamber, the chamber was sealed, and the seawater was allowed to circulate through the chamber for ten minutes. Next, the chamber was taken up to the test pressure and held for two minutes to allow for pressure stabilization and to check for leaks in the system.

During testing, the load and load line displacement of the specimen were monitored using a LabVIEW® based data acquisition routine. Compliance was determined by obtaining the

slope of the load-displacement curves during load-increasing cycles. The top and bottom ten percent of the data points for each curve were excluded to eliminate crack-closure and incipient plasticity effects as suggested in the *Metals Handbook* [17]. Compliance vs. number of cycles data were converted into crack length (a) vs. cycles (N) data using the compliance calibration curve. The seven-point incremental polynomial method outlined in ASTM E647 [11] was then used to generate da/dN vs. ΔK data from the a vs. N data.

After testing, specimens were removed from the system, dried, and then stored in a vacuum desiccator for subsequent failure analysis. Specimen fracture surfaces were examined using both optical and scanning electron microscopy (SEM). To prevent surface charging, specimens were coated with a 250-350 Å layer of Au-Pd prior to examination in a JEOL JSM-35C scanning electron microscope. Micrographs were made of the representative fracture surface features.

EXPERIMENTAL RESULTS

Compliance curves for the as-received and conditioned composites were plotted versus crack length. A fifth order polynomial fit [18], was used to fit the data points to the curves which were identical [14]. Fracture toughness of the AS4C/E719LT composite was determined from the load displacement curves generated during the calibration process. The average K_{IC} for the as-received composite was 3.3 MPa- \sqrt{m} .

The results of the fatigue crack growth rate tests of the as-received AS4C/E719LT are given in Fig. 3. The plots represent three tests for each condition. There was no change in the pH or dissolved oxygen content of the water during any of the seawater tests, nor was there any measurable weight gain or loss of the specimens. Crack growth rates for tests in ambient, 13.8 and 27.6 MPa (2000 and 4000 psi) seawater were almost ten times higher than those conducted in ambient air. Two mechanisms may be responsible for the increased crack growth rate in the specimens exposed to both ambient and the high pressure seawater.

The first mechanism involves a change in fiber-matrix debonding due to the presence of the seawater. The presence of the seawater may weaken the fiber/matrix bond resulting in a decrease in the composite fracture toughness. This decrease in toughness would then result in an increase in crack growth rates for specimens tested in ambient or high pressure seawater as compared to those tested in ambient air [10]. The second model involves the presence of the nearly incompressible seawater in the fatigue-induced damage zone at the fatigue crack tip. This water cannot be expelled during the relatively short down-loading time interval during the fatigue cycle. The entrapped seawater exerts pressure on the crack faces, switching a global tension/tension fatigue test into localized tension/compression cyclic stress fields in the vicinities of the cracks [19].

Both of the proposed mechanisms are rate limited by the flow of water to the crack tip either by bulk diffusion or diffusion along fiber-matrix interfaces. At crack growth rates above 2.5×10^{-3} mm/cycle, there is a possible deviation to slightly lower crack growth rates of the specimens tested in ambient seawater versus those of the specimens tested at 13.8 and 27.6 MPa (2000 and 4000 psi). This may be an indication of a slight influence of pressure on the crack growth rates at higher crack growth rates.

The results of the fatigue crack growth rates of the conditioned AS4C/E719LT are given in Fig. 4. The plots represent two tests for each condition. Again, crack growth rates for tests

conducted in ambient seawater and 27.6 MPa (4000 psi) seawater are almost 10 times higher than those conducted in ambient air. Comparison of Figures 3 and 4, however, shows that all the plots are shifted to lower rates than those for the as-received specimens in Fig. 3. This seems to support the idea that there is a competition between bulk diffusion and diffusion along fiber-matrix interfaces as well as a competition between crack propagation through the matrix and along the fiber/matrix interface. If the presence of seawater weakened the fiber-matrix bond, resulting in a decrease in composite toughness and an increase in crack growth rates, one would presume that the conditioned specimens tested in air would show higher crack growth rates than the as-received specimens tested in air. However, they did not. The rates were lower, suggesting that the saturated composite is tougher or that the saturated matrix is tougher and that crack propagation in the conditioned specimens tested in air is dominated by crack propagation through the matrix. When the conditioned specimens were tested in ambient or high pressure seawater, their rates were greater than those for the conditioned specimens tested in air because the cracks could propagate more easily through the weakened interface than the already saturated matrix.

Figures 5(a-b) and 6(a-b) show micrographs of the representative fracture surfaces for as-received and conditioned specimens, respectively. One would anticipate that the most dramatic differences would occur for the conditioned specimens tested in air and the conditioned specimens tested in seawater. However, if crack propagation in the as-received specimens takes place predominantly (but not exclusively) along the interface and if crack propagation in the conditioned specimens takes place predominantly (but not exclusively) through the matrix, then differences may be difficult to observe. Evidently this is the case. The fracture surfaces of specimens for the two cases showed no noticeable morphological differences due to either ambient or pressurized seawater. Each case showed surface features resulting from the transverse cracking, which is controlled by both fiber-matrix interface failure and matrix fracture [20]. These features include broken fibers free of matrix material, indicating a weak fiber/matrix interfacial bond, and matrix failure indicated by cleavage and river markings. Also present were manufacturing flaws such as particle inclusions and porosity.

CONCLUSIONS

The transverse fatigue crack growth rates of a graphite/epoxy composite (AS4C/E719LT) were investigated using a high pressure test system. Compact tension specimens of the as-received and conditioned composite were fatigued in ambient air, ambient seawater, 13.8 MPa (2000 psi) seawater and 27.6 MPa (4000 psi) seawater. The crack growth rates of the specimens tested in ambient and high pressure seawater were found to be approximately ten times higher than the growth rates of the specimens tested in ambient air. This was true for the as-received as well as the conditioned specimens, however, rates for the conditioned specimens were lower for all test conditions. Three possible mechanisms have been described for this change in growth rates. The first mechanism is the weakening of the fiber-matrix bond resulting in a reduced fracture toughness of the composite. Alternately, a change in the local stress field at the crack tip resulting from the presence of the incompressible seawater may be the controlling factor. A third possibility seems to be a competition between crack propagation through the matrix or along the fiber/matrix interface. If the composite is dry, as it would be in the as-received condition, both options are possible as equally as likely and crack propagation is accelerated in ambient or high pressure seawater. If the composite is saturated, however, the behavior is dominated by the properties of the toughened matrix, through which crack propagation becomes more difficult.

Post-failure optical and scanning electron microscopy did not indicate significant differences between the fracture surfaces of the specimens tested in ambient air versus those tested in ambient and high pressure seawater. This is understandable if it is assumed that crack propagation through the matrix and along the fiber/matrix interface are both possible and microscopy of selected regions of the fracture surfaces may not reveal noticeable differences. Typical fracture surface morphologies included clean broken fibers, matrix fracture, broken fibers with adhered matrix materials, and surface voids and inclusions. A more detailed statistical analysis of the fracture surfaces is needed to confirm the third possibility.

ACKNOWLEDGMENTS

This research was funded by the National Science Foundation and the Offshore Technology and Research Center. In addition, the authors express their gratitude to Harold Kleeman for his sample machining and laboratory assistance.

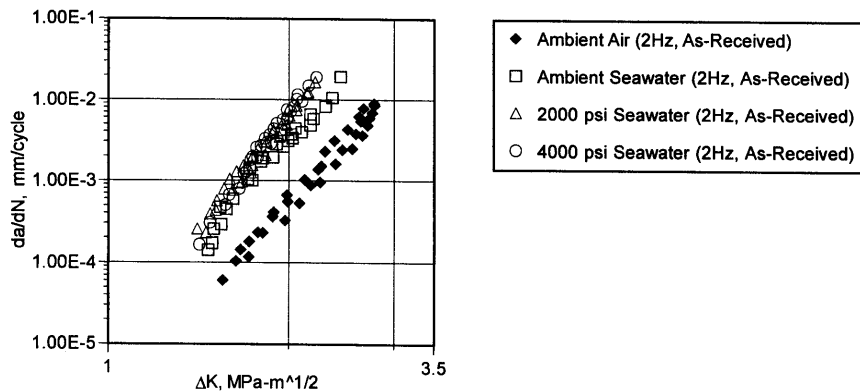


Fig. 3: Fatigue crack growth rate data for transverse cracking of as-received graphite/epoxy composites.

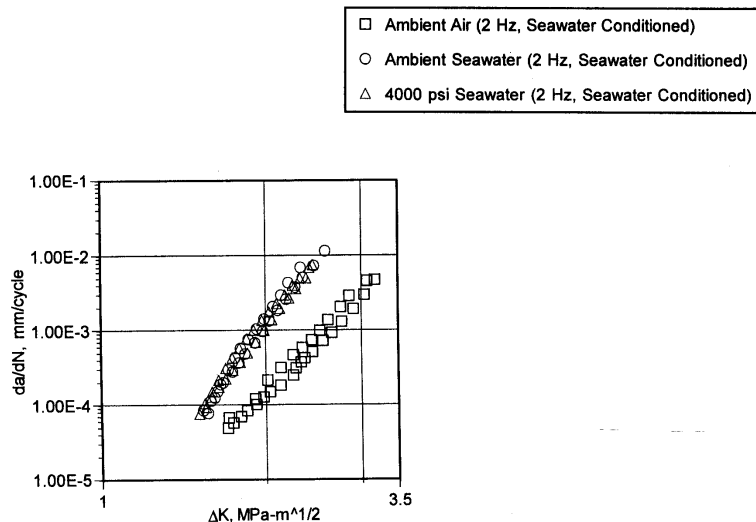
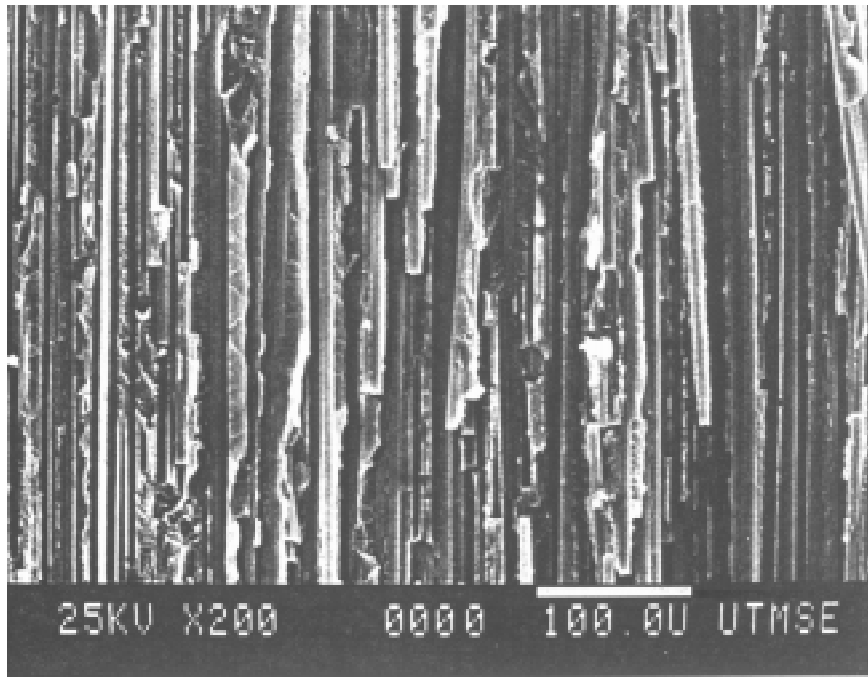
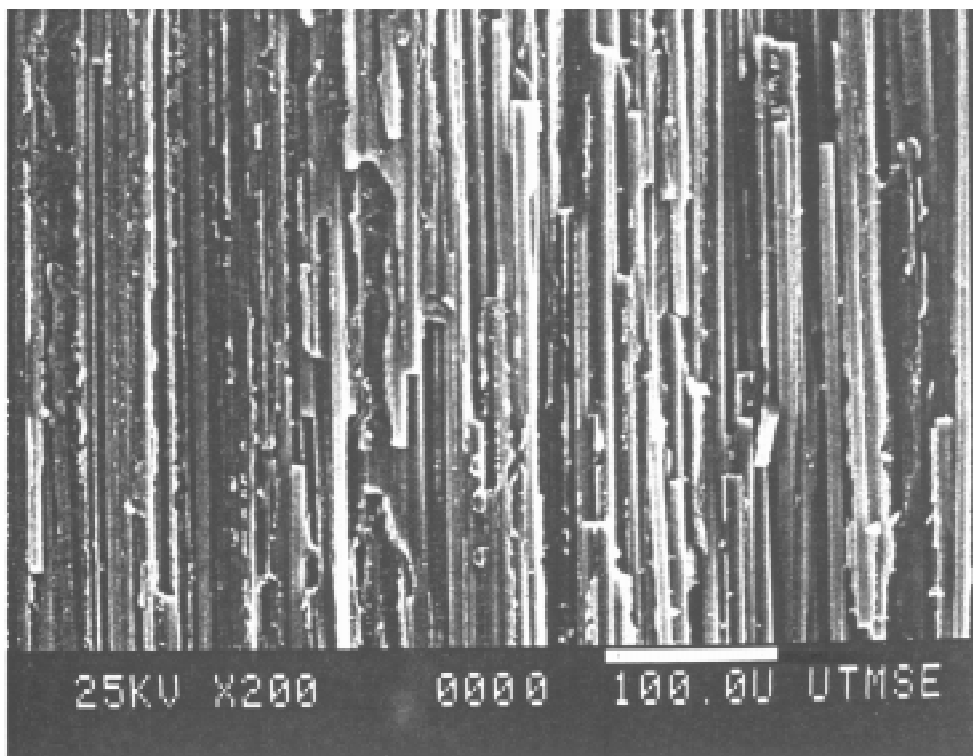


Fig. 4: Fatigue crack growth rate data for transverse cracking of conditioned graphite/epoxy composites.

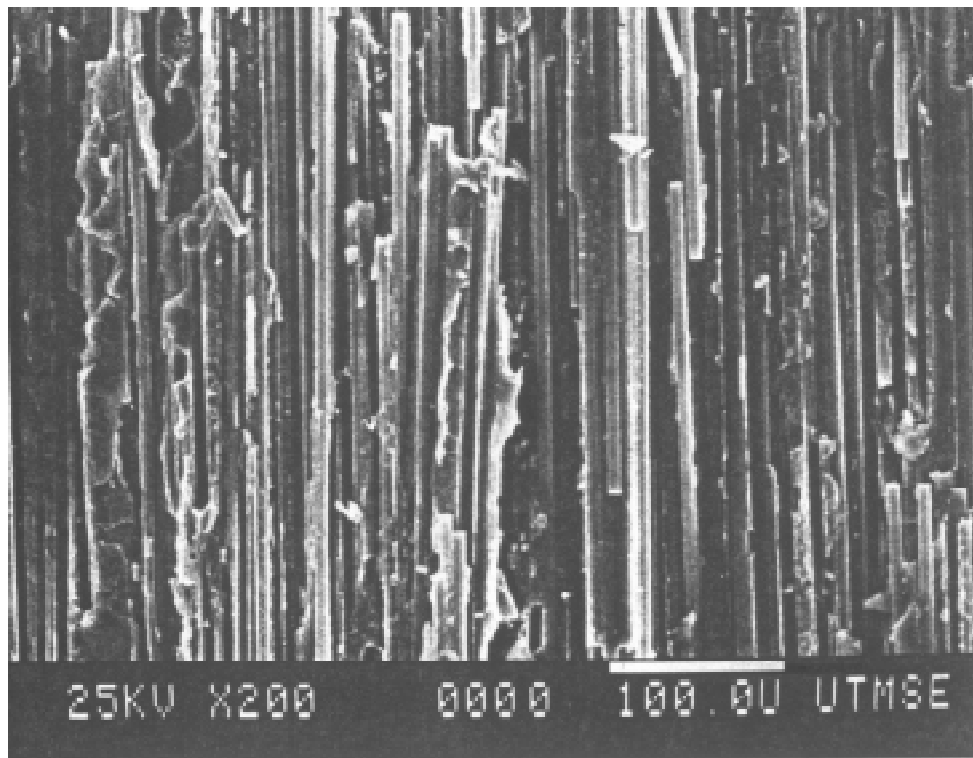


(a)

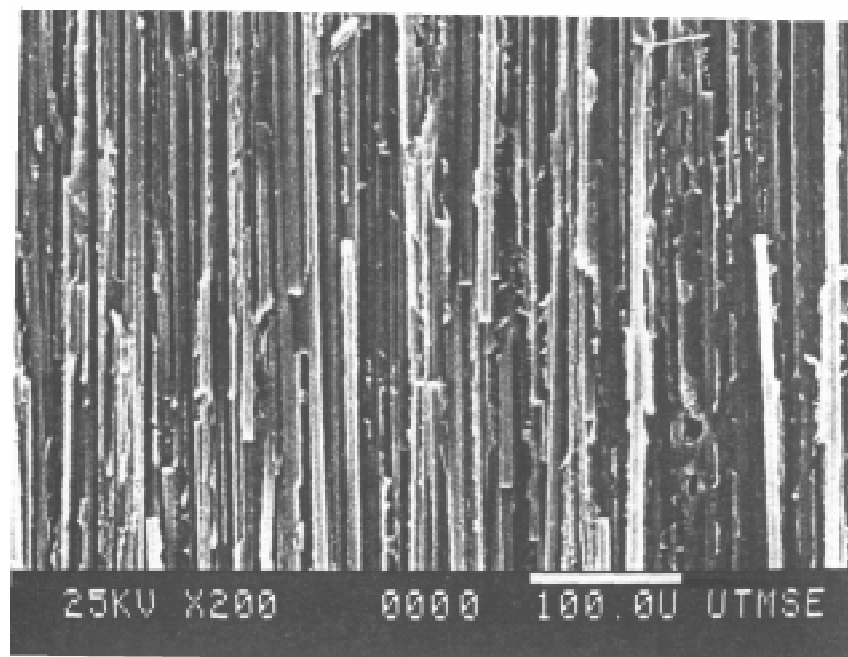


(b)

*Fig. 5: Fracture surfaces from as-received graphite/epoxy composites
a. tested in ambient air
b. tested in 4000 psi seawater*



(a)



(b)

*Fig. 6: Fracture surfaces from conditioned graphite/epoxy composites
a. tested in ambient air
b. tested in 4000 psi seawater*

REFERENCES

1. Kim, K.S., Hahn, H.T., and Williams, J.G., "Application of Composites in TLP Tethers," *Conference on Offshore Mechanics and Arctic Engineering (OMAE) Proceedings*, Vol. 3, 1988, pp. 1-7.
2. Sloan, F.E., "The Effects of Long-Term Seawater Exposure on Graphite/Epoxy Composite Materials," Dissertation, University of California, San Diego, 1991.
3. Parry, T.V., and Wronski, A.S, "The Effect of Hydrostatic Pressure on the Tensile Properties of Pultruded CFRP," *Journal of Materials Science*, Vol. 20, 1985, pp. 2141-2147.
4. Shin, E.S., and Pae, K.D, "Effects of Hydrostatic Pressure on the Torsional Shear Behavior of Graphite/Epoxy Composites," *Journal of Composite Materials*, Vol. 26, No. 4, 1992, pp. 462-485.
5. Shin, E.G., and Pae, K.D., "Effects of Hydrostatic Pressure on In-Plane Shear Properties of Graphite/Epoxy Composites," *Journal of Composite Materials*, Vol. 26, No. 6, 1992, pp. 828-868.
6. Grant, T.S. and W.L. Bradley, "An In-Situ Observation in SEM of Degradation of Graphite/Epoxy Composite Materials, *Journal of Composite Materials*, Vol 29, 1995, pp. 852-857.
7. Saunders, D.S., Clark, G., van Blaricum, T.J., and Preuss, T.E., "Graphite/Epoxy Laminate Coupon Testing Programme," *Theoretical and Applied Fracture Mechanics*; Vol. 13, 1980, pp. 105-124.
8. Jones, C.J., R.F. Dickson, et al, "The Environmental Fatigue Behavior of Reinforced Plastics," *Proc. R. Soc. Lond. A*, Vol. 396, 1984, pp. 315-338.
9. Sloan, F.E., and Seymour, R.J., "The Effect of Seawater Exposure on Mode I Interlaminar Fracture and Crack Growth in Graphite/Epoxy," *Journal of Composite Materials*; Vol. 26, 1992, No. 18, pp. 2655-2673.
10. Garg, A.C.(1986). "Intralaminar and Interlaminar Fracture in Graphite/Epoxy Laminates, *Engineering Fracture Mechanics*., Vol. 23, No. 4, 1986, pp. 719-733.
11. ASTM E647, "Standard Test Method for Measurement of Fatigue Crack Growth Rates," *Annual Book of ASTM Standards*, ASTM, Philadelphia, , 1991, pp. 1-28.
12. Schapery, R.A., Personal Communication, The University of Texas at Austin, October 24, 1994.
13. Fowkes, G.F., "An Apparatus for the Characterization of the Corrosion Fatigue Behavior of Offshore Structural Materials Under Combined Hydrostatic and Axial Loading," M.S. Thesis, The University of Texas at Austin, 1994.

14. Stolk, J.D., Mear, S.T., Wheat, H.G., and Marcus, H.L., "Corrosion Fatigue Behavior of Graphite/Epoxy Composites for Deep-Sea Structural Applications," *The Johannes Weertman Symposium*, R.J. Arsenault, et al ed., The Minerals, Metals, and Materials Society, 1996.
15. Slepetz, J.M., and Carlson, L., "Fracture of Composite Compact Tension Specimens," *Fracture Mechanics of Composites*, ASTM STP 593, American Society for Testing and Materials, 1975, pp. 143-162.
16. ASTM E399, "Standard Test Method for Plane-Strain Fracture Toughness of Metallic Materials," *Annual Book of ASTM Standards*, ASTM, Philadelphia, 1978, pp. 580-601.
17. *Metals Handbook*, "Fatigue Crack Propagation," American Society for Metals, Metals Park, Ohio, 1985, pp. 376-402.
18. Saxena, Ashok, and Hudak, S.J., Jr., "Review and Extension of Compliance Information for Common Crack Growth Specimens," *International Journal of Fracture*, Vol. 14, No. 5, 1978, pp. 453-468.
19. Kosuri, R., and Weitsman, Y., "Sorption Process and Immersed-Fatigue Response of GR/EP Composites in Sea Water," *Proceedings of the Tenth International Conference on Composite Materials, Volume VI: Microstructure, Degradation, and Design*, Anoush Poursartip and Ken Street, eds., Woodhead Publishing, 1995, pp. 177-184.
20. Garg, Amar, and Ishai, Ori, "Hygrothermal Influence on Delamination Behavior of Graphite/Epoxy Laminates," *Engineering Fracture Mechanics*, Vol. 22, No. 3, 1985, pp. 413-427.

MATERIAL AND LAMINATION DESIGN FOR DYNAMIC PERFORMANCE OF HIGH MODULUS CARBON FIBER GOLF SHAFT

Kazuro Kageyama, Isao Kimpara, Toshio Suzuki, and Isamu Ohsawa

*Department of Naval Architecture and Ocean Engineering, University of Tokyo
7-3-1 Hongo, Bunkyo-ku, Tokyo 113, Japan*

SUMMARY: High modulus carbon fibers are applied to the golf clubs. The analysis and the design of composite structures are discussed from the viewpoint of vibration control. Vibration mode, frequency and damping of high-modulus CFRP golf club are investigated experimentally and numerically. Strain energy method proposed by Gibson et al has been successfully applied to predict the structural damping. Damping factors of fibers, matrix and their interfaces are evaluated. The high modulus carbon fibers have excellent damping factors. The complicated behaviors of the structural damping has been estimated well by the proposed numerical method. Experimental visualization of the vibratory motion by using VPI technique has confirmed numerical results with very high accuracy.

KEYWORDS: vibration, CFRP, high modulus carbon fiber, golf club, damping, finite element analysis, model analysis by VPI.

INTRODUCTION

Carbon fiber has excellent potential in sport goods application because of high modulus and light weight. The higher modulus reinforcement should be applied to sport goods to achieve the better performance. Pitch-based and PAN-based high modulus carbon fibers, for example, are applied to golf shafts. When designing CFRP (carbon fiber reinforced plastic) golf shaft, not only static but dynamic performance should be taken into account. Especially, dynamic characteristics of higher order vibration modes have important effect upon feeling of impact.

Authors have applied the vibration pattern imaging (VPI) technique and finite element modeling to evaluation of vibration behaviors of composite materials/structures. The hybrid experimental/numerical approach has been successfully applied, for example, analysis of the residual strength of the impact-damaged laminates[1,2]. In the present paper, the analysis and the design of composite structures are discussed from the viewpoint of vibration control. Vibration mode, frequency and damping of high-modulus CFRP golf club are investigated experimentally and numerically.

DESCRIPTION OF CFRP GOLF CLUBS

Shafts of number 1 wood club (driver) shown in Fig. 1 are made of unidirectional CFRP. Stacking sequence of $[0_n/\pm 45_m]_T$ is applied to the laminate structures of the golf shafts as schematically shown in Fig. 2. Dimensions of CFRP shafts are shown in Fig. 3. High modulus pitch-based carbon fiber, Granox XN50 and XN80, and high modulus PAN-based carbon fiber, Toray UM46, are used as continuous reinforcement in $\pm 45^\circ$ layer, and high

strength PAN-based carbon fiber, T700, is used in 0° layer. A 130 °C cured epoxy resin is used as matrix in both ±45° and 0° layers. Material selection in CFRP golf shafts, properties of fibers and matrix are listed in Tables 1, 2 and 3, respectively. All golf shafts are prototyped and fabricated by Nippon Oil Company, Ltd.

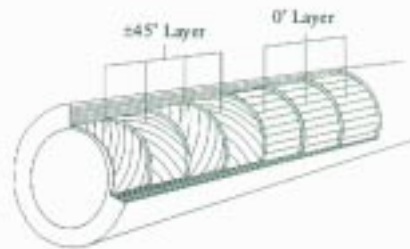


Fig. 2: Lay-up of the CFRP golf shaft



Fig. 1: CFRP golf club

Table 1: Design parameter of CFRP golf shaft

0° Layer	±45° Layer		Shaft mass g	Head mass g
	Fiber	Ply Number		
T700 4 plies	XN80	8	82.4	204.3
		9	82.0	204.5
	XN50	7	69.6	204.7
		5	60.8	202.4
	UM46	8	77.0	203.9
		6	63.8	203.6
		4	57.8	202.5

Table 2: Mechanical properties of fibers

Fiber Name	E _{Lf} GPa	E _{Tf} GPa	ρ kg/m ³
XN80	780	9	2170
XN50	490	11	2140
UM46	435	12	1820
T700	220	13	1800

Table 3: Matrix properties

Matrix	E GPa	ν	ρ kg/m ³
120°C cure Epoxy	3.5	0.3	1220

ANALYSIS AND DESIGN FLOW

Damping Factor of Composite Materials

Laminated composite structure is divided into m_1 elements. Each element is in the form of laminate consisting of m_2 plies. Total number of ply elements is $m=m_1 \times m_2$. Strain energy method proposed by Gibson et al [3, 4] is applied to every ply element, and the damping factor, η_c , of the composite structure is approximated by following form of Eqn 1.

$$\eta_c = \frac{\sum_{j=1}^m (\eta_f W_f^{(j)} + \eta_m W_m^{(j)} + \eta_i W_i^{(j)})}{\sum_{j=1}^m (W_f^{(j)} + W_m^{(j)} + W_i^{(j)})} \quad (1)$$

where $\eta_f^{(j)}$, $\eta_m^{(j)}$ and $\eta_i^{(j)}$ are damping factors of fiber, matrix and their interface, respectively, in the j -th ply element, and $W_f^{(j)}$, $W_m^{(j)}$ and $W_i^{(j)}$ are strain energy in fiber, matrix and their interface, respectively, at maximum vibratory displacement of the j -th ply element ($j = 1 \dots m$). The strain energy $W_k^{(j)}$ ($k = f, m$ and i) is given by integrating Eqn 2 over the volume $\Omega^{(j)}$ of the j -th ply element.

$$W_k^{(j)} = \frac{V_k^{(j)}}{2} \int_{\Omega^{(j)}} (\sigma_{Lk} \epsilon_{Lk} + \sigma_{Tk} \epsilon_{Tk} + \tau_{LTk} \gamma_{LTk}) d\Omega \quad (k = f, m \text{ and } i) \quad (2)$$

where $V_f^{(j)}$, $V_m^{(j)}$ and $V_i^{(j)}$ are the volume fraction of fiber, matrix and their interface, respectively, of the j -th ply element, and σ_{ijk} and ϵ_{ijk} are the stress and strain component of fiber ($k=f$), matrix ($k=m$) and their interface ($k=i$) measured in the L-T coordinates, which coincides with the orthogonal plane of material property symmetry. Volume fraction, $V_i^{(j)}$, of interface is assumed to be 0.03 in the present study.

Macro/Micro Correlation

Two-dimensional layerwise micromechanical model is applied to estimate σ_{ijk} and ϵ_{ijk} in the unidirectional fiber composite lamina. Because of continuity of stress and strain in the micromechanical model, the simple macro/micro relation is given by Eqn 3.

$$\sigma_{Tf} = \sigma_{Tm} = \sigma_{Ti} = \sigma_{Tc}, \quad \tau_{TLf} = \tau_{TLm} = \tau_{TLi} = \tau_{TLc}, \quad \epsilon_{Lf} = \epsilon_{Lm} = \epsilon_{Li} = \epsilon_{Lc} \quad (3)$$

where σ_{ijc} and ϵ_{ijc} are the macroscopic stress and strain components in the composite lamina. Stress-strain relation of fiber, matrix and their interface are given by Eqn 4.

$$\begin{Bmatrix} \epsilon_{Lk} \\ \epsilon_{Tk} \\ \gamma_{LTk} \end{Bmatrix} = \begin{bmatrix} \frac{1}{E_{Lk}} & -\frac{\nu_{LTk}}{E_{Lk}} & 0 \\ -\frac{\nu_{LTk}}{E_{Lk}} & \frac{1}{E_{Tk}} & 0 \\ 0 & 0 & \frac{1}{G_{LTk}} \end{bmatrix} \begin{Bmatrix} \sigma_{Lk} \\ \sigma_{Tk} \\ \tau_{LTk} \end{Bmatrix}, \quad k = \begin{cases} f \\ i \end{cases} \text{ or } \begin{Bmatrix} \epsilon_{Lm} \\ \epsilon_{Tm} \\ \gamma_{LTm} \end{Bmatrix} = \begin{bmatrix} \frac{1}{E_m} & -\frac{\nu_m}{E_m} & 0 \\ -\frac{\nu_m}{E_m} & \frac{1}{E_m} & 0 \\ 0 & 0 & \frac{2(1+\nu_m)}{E_m} \end{bmatrix} \begin{Bmatrix} \sigma_{Lm} \\ \sigma_{Tm} \\ \tau_{LTm} \end{Bmatrix} \quad (4)$$

where E_{ijk} are elastic moduli. Substituting Eqn 3 into Eqn 4, 9 unknown microscopic stress and strain components, σ_{Lf} , σ_{Lm} , σ_{Li} , ϵ_{Tf} , ϵ_{Tm} , ϵ_{Ti} , γ_{LTf} , γ_{LTm} and γ_{LTi} can be got. Elastic moduli of the interface layer is assumed to be average properties of fiber and matrix.

Lamina Properties

Longitudinal elastic modulus of unidirectional fiber reinforced lamina could be estimated from elastic properties of fiber, matrix and their interface by applying the rule of mixture.

$$E_{Lc} = V_f E_{Lf} + V_m E_m + V_i E_{Li} \quad (V_f + V_m + V_i = 1 \text{ and } V_i = 0.03) \quad (5)$$

Because of the difference between tensile and compressive elastic moduli of high modulus carbon fiber, the elastic modulus, E_{Lc} , under flexure load is smaller than the theoretical value estimated by Eqn. 5. In order to take the difference between theoretical and experimental elastic moduli of lamina into consideration of strain energy values, $W_k^{(j)}$, effective elastic modulus, E_{Lf}^* , of fiber, which is given by substituting the experimental lamina data, E_{Lc} , (listed in Table 4) into Eqn 5, is used in the finite element analysis.

Table 4: Lamina properties

Lamina Name	E_L GPa	E_T GPa	G_{LT} GPa	ν_{LT}	ρ kg/m ³
XN80/25P	450	6.3	5.0	0.3	1780
XN50/25P	280	7.8	4.7	0.3	1770
UM46/#118	257	7.2	4.5	0.3	1580
T700/25P	151	10.3	4.9	0.3	1580

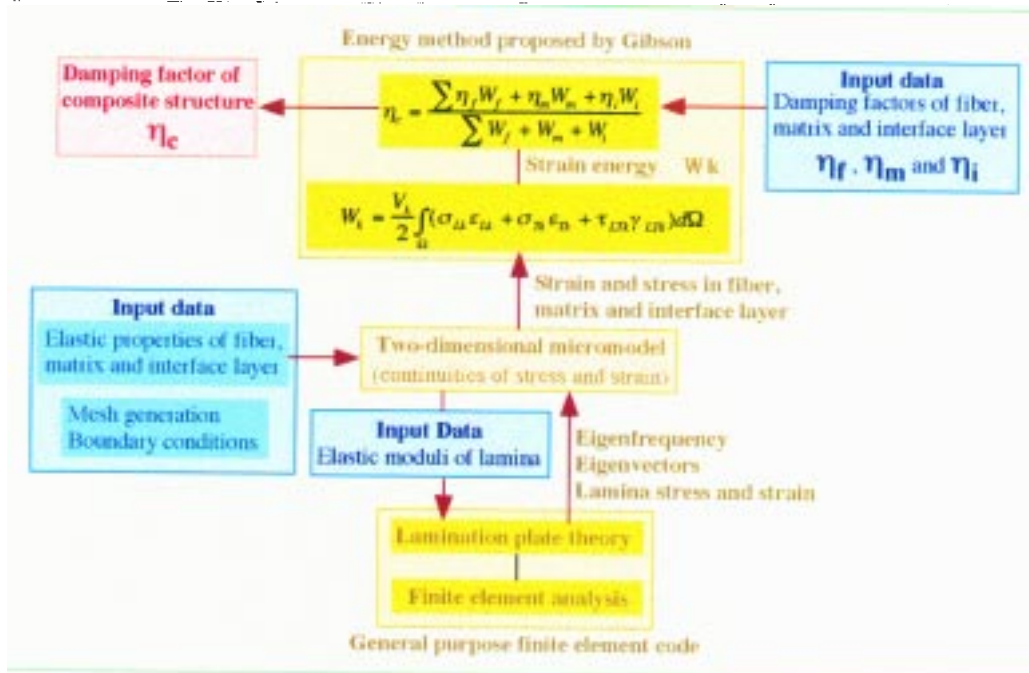


Fig. 4: Design flowchart for dynamic performance of laminated composite structures

Finite Element Model

Eight-nodes isoparametric thick shell element is used for numerical modeling of the laminated composite structure. The finite element models are solved by using general purpose finite element code, MARK K5 version, in which the stiffness characteristics of laminated element are derived from simple expansion of the theory of laminated plate. Orthotropic properties and densities of the laminae used in the present study are listed in Table 4. The stacking sequences, lamina thickness and fiber orientation are also defined in the finite element model.

Design Flowchart

A design process flowchart for vibration modes and damping of composite structures are

shown in Fig. 4. Eigenfrequency and eigenvector of displacement are calculated by applying finite element method. Stresses and strains, σ_{ijc} and ϵ_{ijc} in laminae are evaluated based on the theory of laminated plate. Stresses and strain, σ_{ijk} and ϵ_{ijk} ($k = f, m$ and i), of fiber, matrix and interface layer are approximated by applying Eqns 3 and 4. The damping factor of the composite structure are obtained by using Eqns 1 and 2.

PROCEDURES OF EXPERIMENTS

Vibration Pattern Imaging

Visualization of vibration patterns of the surfaces of composite structures are achieved by using VPI (vibration pattern imaging) technique. VPI RapidSCAN system, which are developed by Ometron Ltd., are shown in Fig. 5. It is a non-contacting measurement system that produces full field vibration images almost instantaneously with very high accuracy. The technique is based on Doppler effect of laser light emitted to and reflected from a vibrating object. Velocity distribution of the specimen surface can be obtained with the advanced laser-optic technique.

Experimental Setup

Electric shaker was mounted on the rigid foundation, and the end of the golf shaft was attached to the shaker with gripping fixture as shown in Fig. 6. An accelerometer was bonded to the gripping fixture, and the acceleration was measured at the shaking point in order to keep the amplitude of the vibration force constant. Vibration patterns of golf head were measured within the frame of scan area.



Fig. 5: VPI RapidSCAN



Fig. 6: Experimental setup

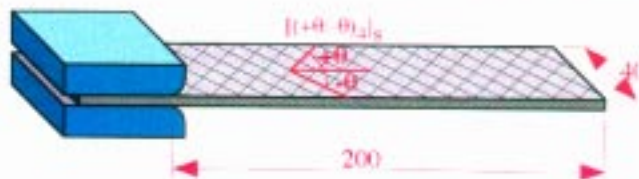


Fig. 7: $[+\theta/-\theta]_2$, angle-ply specimen

DAMPING FACTORS OF FIBER, MATRIX and INTERFACE-LAYER

Specimens and Test Method

Cantilever plates of the $[+\theta/-\theta]_{4s}$ angle-ply laminates were used to estimate the damping factor of fibers, matrix and their interfaces. Angle, θ , is chosen to be 0, 30, 45, 60 and 90 degrees. The configuration and dimension of the specimens are shown in Fig. 7. The end of the specimen was fixed to the electric shaker, and vibration load is applied under the constant amplitude condition. Vibration velocity of another end of the specimens was measured with VPI sensor. Frequency was swept near the eigenfrequency of the first bending mode. Damping factor, η_c , was defined by Eqn 6 in the present paper.

$$\eta_c = \frac{\pi(f_2 - f_1)}{f_0} \quad (6)$$

where f_0 is the eigenfrequency of the first mode, which gives the peak amplitude, A_0 , of the velocity, and f_1 and f_2 are the frequencies which give the amplitude of $A_0/\sqrt{2}$.

Results

The vibrations of the specimens are numerically analyzed as described above. The example of numerical results of strain energy, W_k ($k = f, m$ and I) of XN80 carbon fiber, matrix and interface layer is shown in Fig. 8. Similar results as Fig. 8 are obtained to all the other materials. The figure indicates that almost all strain energy is stored in fibers in the case of the $[0/0]_{4s}$ laminates. Assuming of $W_m = W_i = 0$, we estimate the damping factor, η_f , of fiber from that of the $[0/0]_{4s}$ laminates. Next, assuming of $\eta_i = (\eta_f + \eta_m)/2$, the damping factor, η_m , of matrix are estimated from that of the $[90/90]$ laminate. The estimated damping factors of fibers, matrix are listed in Table 5. Again, Damping factor of the $[+\theta/-\theta]_{4s}$ laminates are calculated. The numerical and experimental results are compared in Fig. 9. The agreement between calculation and experiment are reasonable.

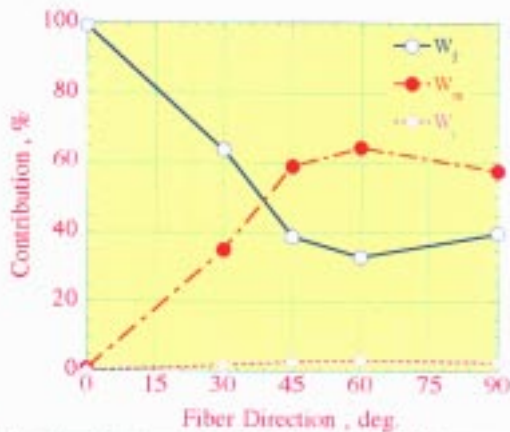


Fig. 8: Strain energy of fiber (W_f), matrix (W_m) and interface (W_i) of XN80/epoxy.

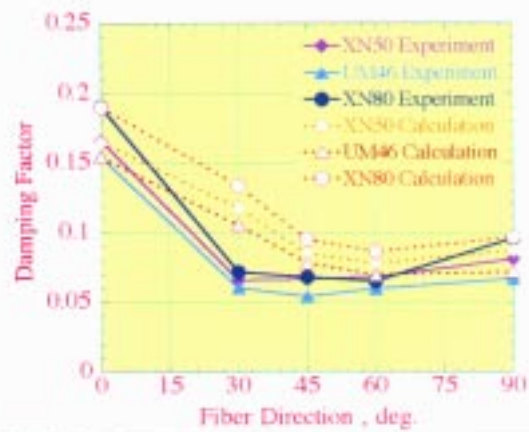


Fig. 9: Damping factor of $[+\theta/-\theta]_{4s}$ angle-ply specimen.

Table 5: Damping factor of fibers and matrix

	XN80	XN50	UM46	T700	Epoxy
Damping Factor	0.19	0.16	0.15	0.01*	0.03

* Estimated value

It should be pointed out that the high-modulus carbon fibers, XN50, XN80 and UM46, have excellent damping properties. The damping factors of the fibers are higher than epoxy resin. The properties are quite different from those of high-strength carbon fibers. Because the high-modulus carbon fibers have higher damping factor than matrix resin, the damping factor of the $[0/0]_{4s}$ laminate is higher than that of the $[+90/-90]_{4s}$ laminate as shown in Fig. 9. High-modulus CFRPs achieve excellent performance of damping at the same time.

NUMERICAL MODEL OF GOLF CLUB

Design Parameters

Design parameters in the present investigation are the fiber selection and thickness of $\pm 45^\circ$ layer as shown in Table 1. The matrix resin, the fiber and thickness of 0° layer and the other dimensions are fixed. Eigenfrequency, mode pattern and damping factor are the matters of concern in the present design. The third mode of vibration of golf club is said to have direct effect on direction-stability of ball trajectory and on the feeling of impact. We have special interest in the damping performance of the third mode vibration.

Finite Element Model

The golf shaft as shown in Figs. 1 and 2 is modeled by using thick-shell elements. The golf head is treated as an additional mass and modeled by using solid elements. The displacement of grip end of the golf shaft was fixed in order to satisfy the experimental conditions of loading.

NUMERICAL AND EXPERIMENTAL RESULTS

Eigenfrequencies of CFRP Golf Clubs

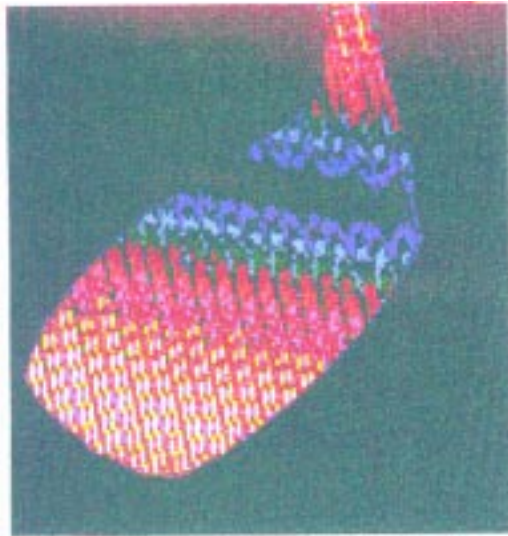
Eigenfrequencies of CFRP golf clubs that are reinforced by XN50 and UM46 fibers in $\pm 45^\circ$ layers are examined experimentally and numerically. Effects of the design parameters on the first, second and third vibration modes are listed in Table 6. With finite element analysis, the eigenfrequencies of the golf clubs can be predicted well in three vibration modes.

Table 6: Effect of the design parameters (thickness and reinforcement of $\pm 45^\circ$ layers) on the first, second and third eigenfrequencies of CFRP golf clubs.

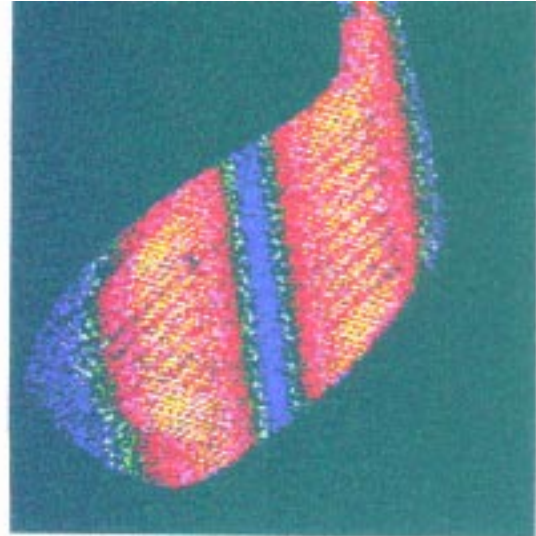
$\pm 45^\circ$ Layer		First Mode		Second Mode		Third Mode	
Fiber	Thickness	Exp.	FEA	Exp.	FEA	Exp.	FEA
XN50	0.5	3.60	3.71	43.4	43.0	56.2	60.4
	0.7	3.65	4.11	40.8	45.1	61.3	61.7
	0.9	3.66	4.12	41.0	46.2	64.8	65.5
UM46	0.5	3.63	3.71	38.0	43.1	57.5	60.4
	0.7	3.60	4.12	37.5	45.3	62.5	62.1
	0.9	3.65	4.12	40.3	46.8	64.4	65.2

Modes of Vibration

Experimental images of the second and third vibration modes of golf heads are shown in Figs. 10 (a) and (b), which are obtained by VPI technique. The finite element results are also shown in Figs. 11 (a) and (b). The location of the nodal lines of the second and third modes was indicated clearly by VPI method. Agreements between experiment and FEA are excellent.

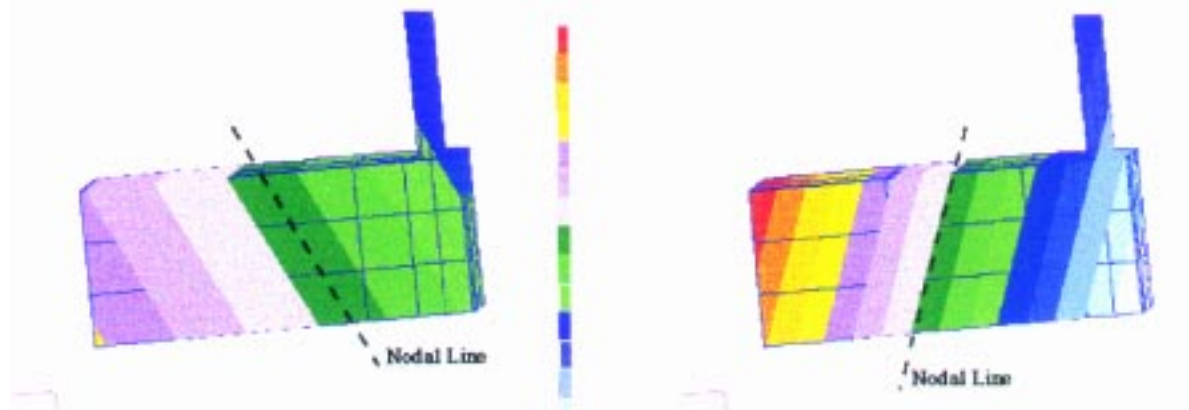


(a) The second mode (40.3 Hz)



(b) The third mode (64.4 Hz)

Fig. 10: The experimental vibration modes of golf club imaged by VPI technique



(a) The second mode (46.8 Hz)

(b) The third mode (65.2 Hz)

Fig. 11: Numerical results of vibratory displacement of the golf head.

Damping Factors

The example of fraction of strain energy obtained by finite element analysis is shown in Fig. 12. The result is in the case that the $\pm 45^\circ$ layer was reinforced by XN50 carbon fibers. The strain energy is mainly stored in the fibers and matrix of the $\pm 45^\circ$ layer. Strain energy of the interface layer is smaller than those of fibers and matrix.

In the case that the thickness of the $\pm 45^\circ$ layer is 0.5 mm, about half of the strain energy are stored in matrix of the $\pm 45^\circ$ layer, but the fraction decreases as the $\pm 45^\circ$ layer thickness increases. On the other hand, the strain energy in the fibers of the $\pm 45^\circ$ layer increases almost in proportion to the $\pm 45^\circ$ layer thickness. The tendencies appear both in the second and third modes of vibration.

In the 0° layer reinforced by T700 carbon fibers, almost all energy is stored in matrix resin. The fraction of strain energy of matrix in the 0° layer increases as the $\pm 45^\circ$ layer thickness increases in the second mode of vibration, though the fraction decreases as the $\pm 45^\circ$ layer thickness increases in the third mode of vibration. In the present analysis, the thickness of the 0° layer is kept constant.

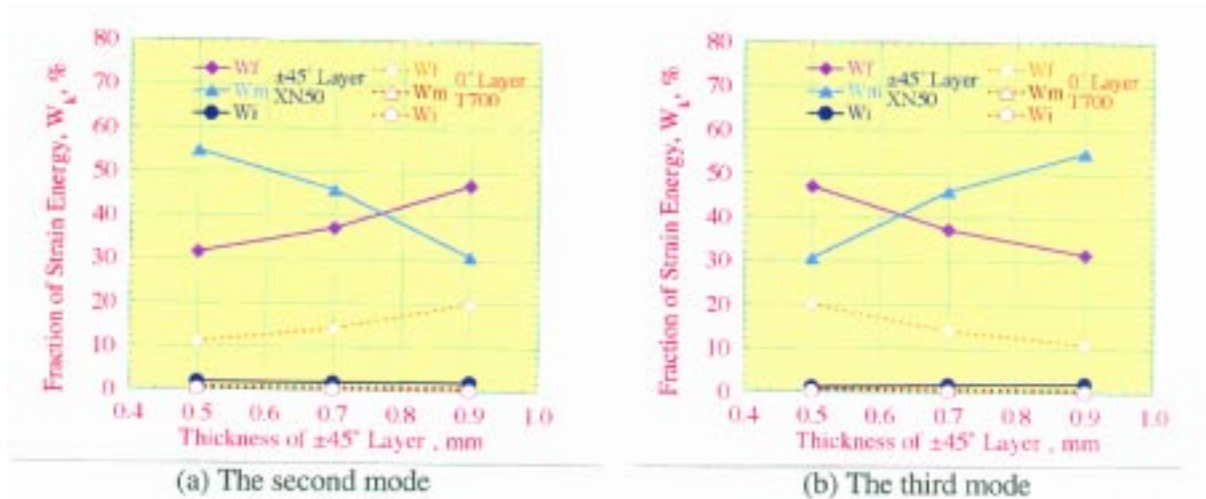


Fig. 12: Fraction of strain energy, W_k , stored in fibers (W_f), matrix (W_m) and interface (W_i) of CFRP golf club with the $\pm 45^\circ$ layer reinforced by XN50 carbon fibers.

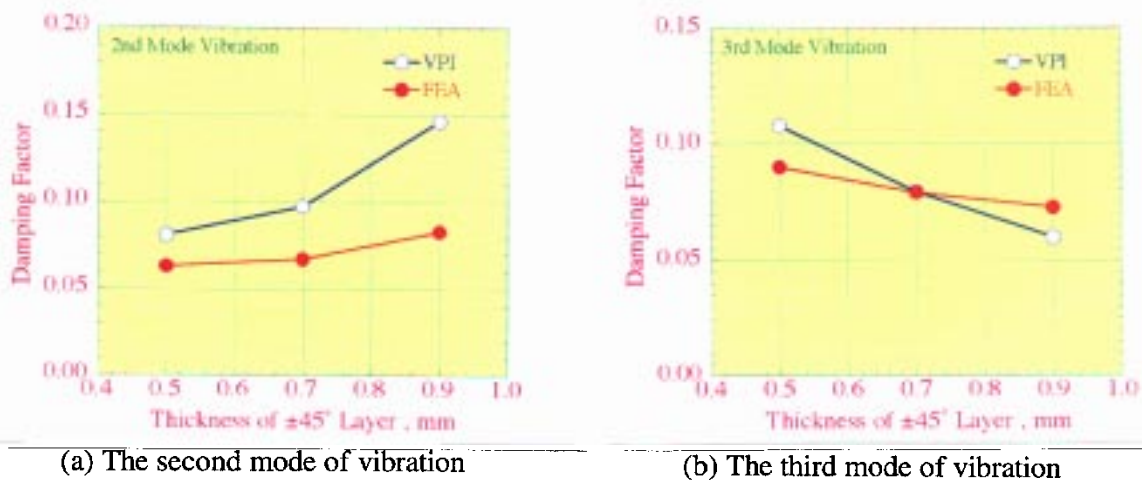


Fig. 13: Damping factors of CFRP golf club as functions of thickness of $\pm 45^\circ$ layer

Damping factors of the second and the third vibration modes are shown in Figs. 13 (a) and (b), respectively, in which the numerical results are compared with the experimental data. The damping factor of the second mode increases as the thickness of the $\pm 45^\circ$ layer increases. On the other hand, the damping factor of the third mode decreases as the $\pm 45^\circ$ layer thickness increases. The very interesting damping behavior of the CFRP golf club is predicted well by the finite element analysis proposed in the present study.

DISCUSSIONS

Longitudinal modulus, E_{Lc} , of XN80 fiber and modulus, E_m , of matrix resin are 780 GPa and 3.5 GPa, respectively, as listed in Table 4. Volume fractions, V_f , V_m , V_i , of XN80/25P are 60.8%, 36.2% and 3%, respectively. And we assumed that E_{Li} is equal to $(E_{Lf} + E_m)/2$. The modulus of the [0/0] lamina was calculated to 487 GPa by using Eqn 5. The value is about 8% higher than the experimental modulus of the lamina (E_{Lc} of 450 GPa). Equivalent elastic modulus, E_{Lr}^* , of XN80 is 720 GPa, and the value is used when applying Eqn. 4.

High-modulus carbon fibers, which are both Pitch-based and PAN-based, show the excellent damping properties. The fibers have the higher damping factors than the epoxy resin in the present paper. The behavior is quite different from that of high strength carbon fibers. Both high stiffness and high damping are achieved in the fiber direction when applying the high modulus carbon fibers to the structural members.

The deformations of the golf shaft are as follows; bending in the first vibration mode, mixed bending and twisting in the second and twisting in the third. The eigenfrequency of the first mode is independent of the thickness of the $\pm 45^\circ$ layer because the layer has small effect upon bending stiffness. Changes of eigenfrequency in the second and the third modes are small in the present design situation. The thickness of the $\pm 45^\circ$ layer has direct effect upon the damping factors. When higher damping factor of the third mode, for example, is desired, the thickness of the $\pm 45^\circ$ layer should be small. The complicated damping behaviors of the laminated composite structure can be predicted by finite element analysis when micro-mechanical effect of damping is taken into account in the structural modeling.

CONCLUSIONS

Eigenfrequencies, vibration modes and damping of the high modulus CFRP golf clubs are investigated experimentally and numerically. The strain energy method proposed by Gibson et al has been successfully applied to predict the structural damping.

Damping factors of fibers, matrix and their interfaces are evaluated. The high modulus carbon fibers, XN50, XN80 and UM46, have excellent damping factors, which are higher than that of the matrix resin, 130 °C cured epoxy. Higher eigenfrequency and higher damping are achieved when the fibers are arranged in the longitudinal direction.

Thickness of the $\pm 45^\circ$ layer, which the high modulus carbon fibers applied to, has direct effect upon the structural damping of the golf club. The complicated behaviors of the structural damping has been estimated well by the proposed numerical method.

Experimental visualization of the vibratory motion by using VPI technique has confirmed numerical results with very high accuracy.

ACKNOWLEDGEMENT

Authors express our great thank to Nippon Oil Company, Ltd. for supplying the CFRP golf clubs and the test materials which were used in the present investigation. The study is a part of the cooperative research work between Nippon Oil Company, Ltd. and us.

REFERENCES

1. Kimpara I., Kageyama K., Ohsawa I., Suzuki T. and Yamashita A., "A Proposal of Prediction Method of Compressive Residual Strength of Impact-Damaged CFRP Laminates", *Proceedings of Tenth International Conference on Composite Materials*, Whistler, Canada. August 14-18, 1995, Vol. V, pp 655-662.
2. Kimpara I., Kageyama K., Ohsawa I., Suzuki T. and Ide K., "Vibration Mode Analysis of Delaminated Composite Laminates by Means of Vibration Pattern Imaging", *Journal of the Society of Material Science Japan*, Vol. 43, No. 487, 1994, pp. 476-481 (in Japanese).
3. Hwang, S.J. and Gibson, R.F., "Micromechanical Modeling of Damping in Discontinuous Fiber Composites Using a Strain Energy / Finite Element Approach", *Journal of Engineering Materials and Technology*, Vol. 109, 1987, pp. 47-52.
4. Gibson, R.F., Hwang, S.J. and Kwak, H. "Micromechanical Modeling of Damping in Composites Including Interface Effects", *Proceedings of 36th International SAMPE Symposium*, 1991, Vol. 1, pp. 592-606.

DESIGN AND CONSTRUCTION OF A HIGH PERFORMANCE COMPOSITE CRICKET BAT

R. Brooks , S. Knowles , J.S.B. Mather

Department of Mechanical Engineering, University of Nottingham, University Park, Nottingham, NG7 2RD, UK

SUMMARY : In this paper an impact analysis and computational technique is described and applied to the design of a composite cricket bat with improved performance. The analysis combines the forced vibration during impact of a composite plate structure with Hertz contact theory to yield predictions for the peak force and coefficient of restitution during impact between a cricket ball and a composite bat. The results show that the impact characteristics and vibrational response of a composite shell structure can be tuned to give a significant improvement in hitting power and reduced impact force compared to a traditional solid wooden bat. Based on the results of the analysis, a prototype bat is designed and manufactured from Glass Mat Thermoplastic (GMT) which confirms the performance predictions.

KEYWORDS : cricket bat, composite plates, impact, mode shape function, natural frequencies, coefficient of restitution, glass mat thermoplastic, prototype bat.

INTRODUCTION

Advances in the performance of golf clubs, tennis rackets and other sports equipment in the last decade, have shown how scientific research and engineering development, particularly in the use of composite materials, can lead to significant increases in performance. Cricket, however, has seen little such development. Within a climate of dwindling supplies of willow and corresponding rises in raw material cost, the governing laws requiring a wooden blade must surely be challenged in the near future. The high impact speeds of the ball and the correspondingly high impact forces make this a very demanding application for composite materials and therefore a thorough understanding of the impact process is vital if inroads are to be made into this application area. The objectives of this paper are to show how fundamental impact theory, modified to take into account such factors as the vibrational response of a composite structure and nonlinear ball compression effects, can aid in the design of a composite cricket bat. The paper asks the question whether composite materials can offer performance improvements over a traditional wooden bat. It is also an objective to assess the manufacturing feasibility through the design and production of a prototype composite bat.

THEORY

General Analysis

The impact of a cricket ball on a cricket bat can be analysed by combining the general equation for forced vibration of a continuous uniform beam [1] with Hertz contact theory. An equation can be derived [2] which links the forcing function to the beam's vibrational response for impact at a general point $x = c$, as follows :

$$\alpha = \left[\frac{F}{K} \right]^{\frac{2}{3}} = v_o t - \frac{1}{m_2} \int_0^t dt \int_0^t F dt - \frac{1}{\rho A} \sum_{i=1}^{\infty} \frac{[X_i(c)]^2}{\omega_i \int_0^l X_i^2 dx} \int_0^t F(\bar{\tau}) \sin \omega_i (t - \bar{\tau}) d\bar{\tau} \quad (1)$$

where F = contact force k_2 = Hertz contact constant
 v_o = initial velocity m_2 = mass of ball
 ρ = beam (bat) density A = beam (bat) cross-sectional area
 x = distance along the bat
 X_i = mode shape function of the i th mode of the beam
 ω_i = undamped natural frequency of the i th mode of the beam

α is defined as the approach of the bat and ball and is given by :

$$\alpha = w_2 - w_1(c)$$

where w_2 = deflection of the ball
 $w_1(c)$ = deflection of the bat at impact point c
 $= w_{1\text{vibration}}(c) + w_{1\text{translation}}(c) + w_{1\text{rotation}}(c)$

Eqn 1, containing the forcing function on both sides, does not have an analytical solution. A numerical solution, however, may be obtained by using the small increment method, in which the contact force, F , is regarded as constant over any time increment $\Delta \tau$. The solution procedure must also take into account the nonlinear visco-elastic compression properties of the ball [3,4]. The mode shape functions, X_i , and natural frequencies, ω_i , are dependent on the beam properties and the boundary conditions as detailed in the following subsections.

Solid Bat Analysis

A solid (wooden) bat can be modelled simply as a uniform beam with a torsion spring at one end and free at the other end. The natural frequencies and mode shape functions lie between corresponding values for a simple/free beam and a clamped/free beam, depending on the stiffness of the spring [4,5]. Values of ω_i and X_i for specific beam properties and spring stiffnesses have been evaluated and used in Eqn 1 to determine how the ball and beam (bat) deflections, contact force and ball velocity vary with time.

A more accurate model for the solid bat should take into account the variable cross-section in addition to variation in material properties. Obtaining theoretical mode shape functions and natural frequencies for such a structure is difficult. To overcome this difficulty, experimental modal analysis tests for the bending modes of real bats have been used to provide the necessary data (ω_i, X_i) for incorporation into Eqn 1.

Composite Plate Analysis

For manufacturing feasibility and to reduce weight, a bat made from composite materials is likely to be a shell or plate structure. In this case the performance of the bat will depend to a large extent on the dynamic behaviour of the plate. The general theory for a uniform beam given above can also be used to model the impact of a ball on a composite plate if we assume it is supported on two sides only. In this case, the plate is modelled as a uniform beam supported at each end by torsion springs. The stiffness of these springs can be adjusted to investigate the affect of varying support conditions at the ends. ω_i and X_i for this configuration are determined in a similar way to the solid bat but in this case lie between the free/free beam and clamped/clamped beam values depending on the spring stiffness [4,5]. As before, the relevant values are substituted into Eqn 1 which can then be solved numerically for the impact variables (w_1, w_2 and F) and their time variation.

Composite Cricket Bat Analysis

To model a full composite cricket bat a combination of the methods for a solid bat and composite plate is used. The bat is assumed to be a hollow shell construction with a flat plate for the front face. Unlike the plates discussed in the previous subsection, the front face is supported along all four sides and bending modes occur in two perpendicular directions. Plate vibration theory must therefore be used. The analysis can be simplified by assuming the plate is supported on its long edges by torsion springs and at its ends on simple supports. The displacement, w_1 , of a point x, y due to a point force applied at some other point x_0, y_0 is given by [2] :

$$w_1(x,y,t) = \frac{1}{\rho h} \sum_{i=1} \sum_{k=1} \frac{H_{ik}(x,y) H_{ik}(x_0,y_0)}{\omega_{ik} \int_0^a \int_0^L H_{ik}^2 dx dy} \int_0^t F(\bar{\tau}) \sin \omega_{ik} (t - \bar{\tau}) d\bar{\tau} \quad (2)$$

H_{ik} is the mode shape function which is dependent on the plate shape and boundary conditions and readily available in the published literature [4]. h is the plate thickness. The natural frequencies of the plate, ω_{ik} , are not available in simple form for torsion spring boundary conditions, as they are for beam structures. However, it has been found that although the boundary conditions affect the peak force calculations they only have a small influence on the output speed of the ball, which is a critical performance measure. For that reason, the natural frequencies for a plate simply supported on all four boundaries have been adopted in the analysis.

The approach ($\alpha = w_2 - w_1(c)$), as before, is related to the contact force and is given by the difference between the displacement of the ball and bat. However, the displacement of the bat now has an additional term to account for the deflections of the plate as follows :

$$W_1 \langle c \rangle = W_{1plate} \langle c \rangle + W_{1beam} \langle c \rangle + W_{1translation} \langle c \rangle + W_{1rotation} \langle c \rangle$$

The bat translation and rotation are calculated from the kinematic analysis of the swing. The vibrational response of the beam (bat) is calculated as for a solid bat and the plate vibrations are calculated as described above.

EXPERIMENTAL IMPACT PERFORMANCE OF COMPOSITE PLATES

Experimental Method

To assess the relative performance of different composite materials in plate form and compare them with the performance of a solid bat, a test rig has been developed to fire a cricket ball at high speed. A compressed air gun can deliver the ball over a range of speeds up to 40 m/s. Forces of impact are measured using a force washer and ball speeds determined using an infra red sensor, both linked to a computer data acquisition system as shown in Fig. 1. Both a solid willow block and composite plates of various materials forms have been tested using the rig.

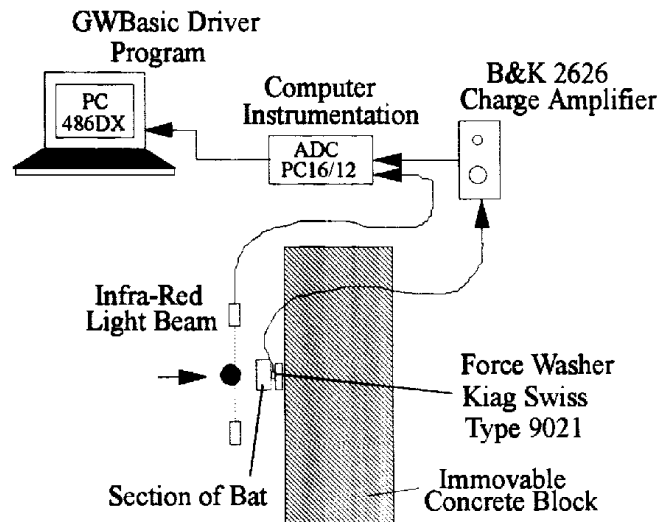


Fig. 1 Test rig for measuring ball speed and impact force during impact on either a solid willow block or composite plate

Results

Peak Force

Fig. 2 shows the variation of peak impact force (best fit lines) over a range of ball speeds (impact velocity) for the various materials tested. As expected, the impact force increases significantly with ball speed. The flexible polypropylene plate gives the lowest values whilst the stiff GRP plate gives the greatest force of all the plates. The other composite plates are intermediate between these two cases and it is clear that the small variation in thickness of the GMT plate only has a small affect on the peak force variation. In all cases the plate structures result in significantly lower peak forces compared to the willow block, 50% lower at 20 m/s, in the case of GMT, for instance. With regard to bat construction, the lower peak forces arising from a composite plate structure should also result in reduced ball damage.

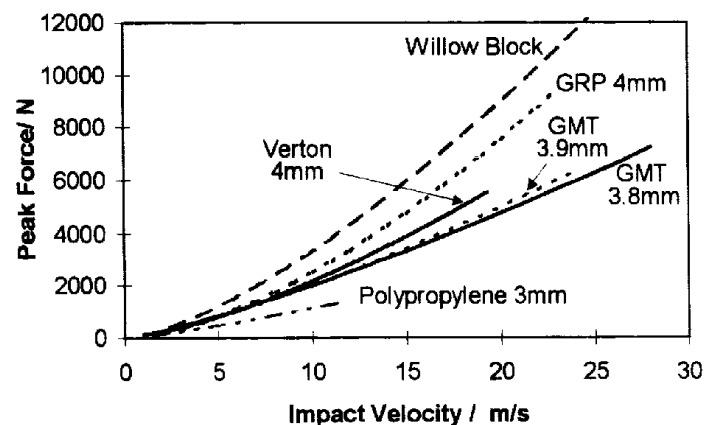


Fig. 2 Variation of peak force with impact velocity for various plates

Coefficient of Restitution

Fig. 3 shows the corresponding results for the variation of coefficient of restitution, e , (ball output speed/ball input speed). There is considerable difference between the plates tested. Results for polypropylene were only obtained for speeds up to 12 m/s, as above this speed the deflections were so great that the plate bottomed out on the steel support plate. The composite plates all give significantly higher values for e than the willow block; the 3.9 mm GMT plate, for instance, at 20 m/s, giving a value of $e = 0.75$, compared to 0.5 for the willow. It is interesting to note that the small change in GMT thickness from 3.8 to 3.9 mm thickness has a large effect on the coefficient of restitution. The higher values of e for the composite plates will clearly result in a higher output velocity of the ball and if incorporated in a bat should result in a corresponding improved performance.

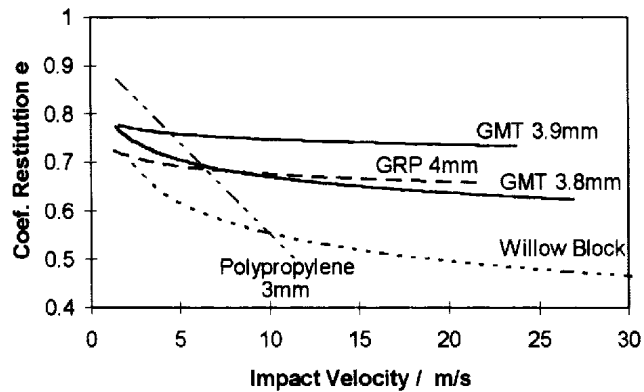


Fig. 3 Variation of coefficient of restitution with impact velocity for various plates

Damage

The plates tested above have also been assessed for damage after multiple impacts. This will be an important factor when selecting a suitable material for cricket bat construction. The results are summarised in Table 1.

Table 1 Damage in composite plates following multiple impacts

Plate Material	No. of Impacts	Speed m/s	Damage
Polypropylene (3 mm)	20	1 - 12	plastic deformation at impact & supports
GF/PAVERTON (4 mm)	1 - 20	15-30	brittle fracture - complete failure
GRP (4 mm)	20	10 - 25	matrix cracks and fibre breaks
GF/PP GMT (3.9 mm)	80	10 - 30	slight surface cracks at supports. no impact damage
GF/PP GMT (3.8 mm)	30	10 - 30	no detectable damage

The GMT plates both show good impact damage tolerance after multiple high speed impacts. One showed no sign of damage (3.8 mm) whilst the other (3.9 mm) showed only a small surface crack near the corner of a clamping block which is a region of high stress concentration. The other materials all showed poor impact performance. It should be pointed out that long term fatigue damage tolerance has not been assessed in this work.

COMPUTATIONAL RESULTS

Impact Performance of Composite Plates

Using the beam impact analysis described in the THEORY section, with twin torsion spring boundary conditions, the case of a cricket ball impacting on the 3.9 mm Glass Mat Thermoplastic (GMT) plate has been analysed. To enable comparison with experimental results in the previous section the torsion springs were set extremely stiff to represent the clamped edges in the tests. Figs. 4 and 5 show that the computational results agree very closely with both the peak force and coefficient of restitution (e) measurements over the full impact velocity range.

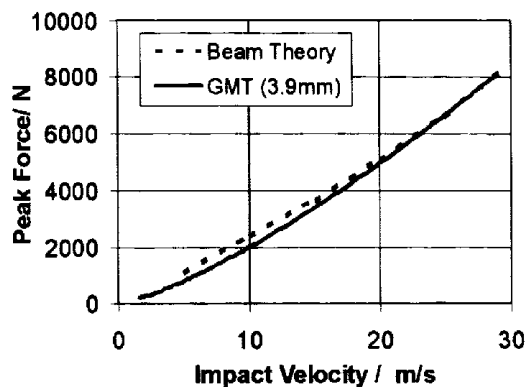


Fig. 4 Comparison of theoretical peak force with experimental values for a 3.9 mm GMT plate

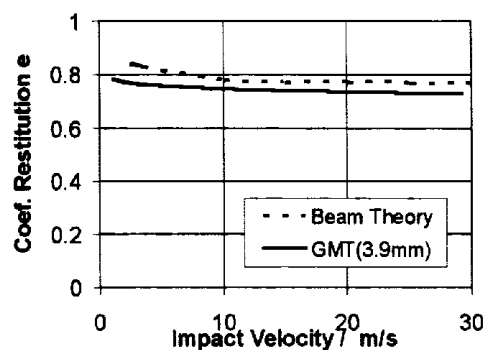


Fig. 5 Comparison of theoretical coefficient of restitution with experimental values for a 3.9 mm GMT plate

The slight overestimate of the peak force at low impact speeds is a characteristic of the nonlinear ball model used [3]. The small disagreement in coefficient of restitution is likely to be due to additional vibration modes in the plate and its fixtures. Additional results for varying spring stiffnesses show that although vibration frequencies depend on the boundary conditions, e is only marginally affected. This is an important result as it supports the use of the beam theory for accurate prediction of ball speed even if the support conditions are not well defined.

Isoharmonic Impact

During the computational analysis a particularly important observation was made. An energy analysis of the impact on a beam model for the plate shows that, as the plate mass reduces, more of the ball's energy is absorbed in vibration of the plate. Thus, as the plate becomes lighter the ball rebounds at reduced speed. In addition the contact force reduces and the duration of contact increases. However, a point can be reached where the contact time matches the time it takes for the plate to deflect and return to its original position. The energy of vibration in the plate, can then be returned to the ball giving it a high exit velocity. This matching of the plate vibrational frequency to the contact time can be termed *isoharmonic impact*. Composite plates clearly lend themselves to tuning for improved performance in this way. Furthermore, when this situation is realised, lower contact forces reduce both the losses due to the viscoelastic behaviour of the ball and damage imparted on the ball. The isoharmonic impact effect goes a long way to explaining the significant increases in coefficient of restitution (>50%) achieved with composite plates as

described in the previous experimental section. Because of its importance, patents on the principle and its application have been filed in a number of countries.

Impact Performance of a Composite Bat

The composite bat analysis (combining plate and solid bat analyses) described in the THEORY section has been used to predict the performance of a model composite bat. To facilitate direct comparison, although the model is assumed to be a shell structure, the bat was given the same mass and moment distribution properties as a solid willow bat. The front face was assumed to be made from 40%GF/PP GMT with corresponding properties. The initial ball and bat conditions were assumed to correspond to a straight drive i.e. bat linear velocity, $u_1 = 11.5$ m/s, bat rotational speed, $\Omega_1 = 18$ rad/s and ball velocity, $u_2 = 20$ m/s.

Fig. 6 shows how the output speed of the ball, following impact, varies with impact position along the blade for the model composite bat and a traditional willow bat. The two lines for the composite bat represent impact at two different positions across the width of the blade. Impact at the very edge would give results identical to the solid bat as the plate deflections are zero. It can be clearly seen that the composite bat offers a significant performance improvement. Even compared with the sweet spot for the traditional bat (in the region of 150 mm from the tip) a 50%

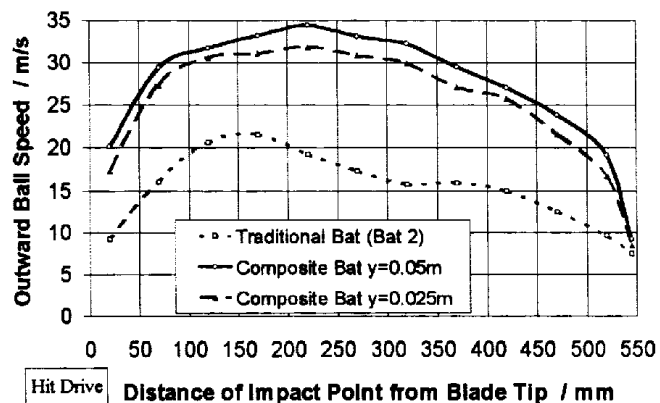


Fig. 6 Theoretical comparison of bat performance for a composite and traditional bat - straight well hit drive

improvement in hitting speed is achieved and in other regions the increase can be as large as 100%. Unlike the traditional bat, where high performance is limited to a region around the sweet spot, the composite bat shows a performance improvement over an extensive length of the blade. Fig. 6 also shows that for impact one quarter of the way across the width of the blade ($y = 0.025$ m) the performance is only marginally lower. This means that a shot hit anywhere reasonably near the centre line of the blade will rebound at a high speed due to the isoharmonic impact effect.

CONSTRUCTION AND TESTING OF A PROTOTYPE COMPOSITE BAT

Materials Selection

Both experimental and computational results have shown that the use of a composite shell structure with front face plate tailored to give isoharmonic impact should result in a bat with high performance properties. The computational design procedure, based on the theory already discussed, can be applied to the design of the front plate for a prototype bat. There are also a number of other important factors which narrow the choice of material for the complete bat :

Impact performance - The inherent brittleness of thermosetting matrices and experience from plate testing suggests a thermoplastic matrix will be the better choice for the demanding impact performance required. Specific resin choice will require data from long term impact testing.

Manufacturing - Although not the case for a prototype bat, the ultimate need will be for high volume, low cost manufacture. Again, with cycle times under one minute, thermoplastic composites offer this option. Short or long fibre injection moulded compounds have high tooling costs. Glass Mat Thermoplastics offer a possible solution with intermediate tooling costs. High performance continuous filament materials, although low in tooling costs, are only suitable for low volume manufacture and raw material costs are high. More recent commingled yarn materials offer the future potential for high performance products produced at low cost.

After consideration of the above factors it was decided to manufacture the prototype bat from 40%GF/PP GMT supplied by Symalit. There are some limitations to the surface finish of the material but in a correct design it will provide the necessary stiffness, strength and impact properties and whilst serving the initial requirements for a prototype bat will also retain the potential for high volume manufacture.

Prototype Design

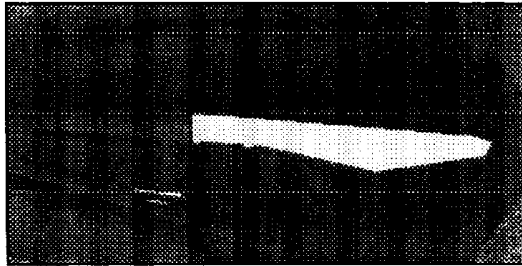


Fig. 7 Full view of prototype GMT bat

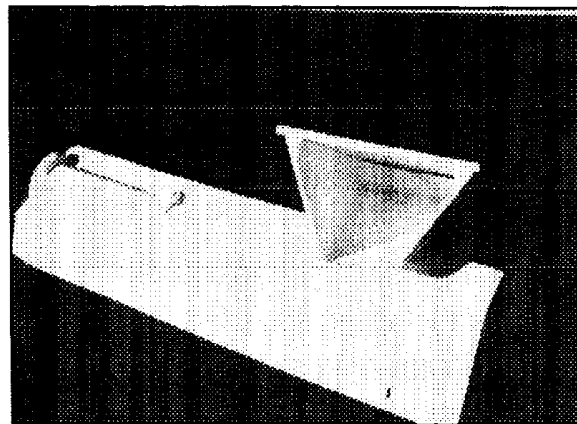


Fig. 8 Cut section of bat showing front plate and structural back. Handle insert feature can also be seen

The prototype bat, shown in Figs. 7 and 8 comprises a basic three-part structure :-

- (i) A blade back structure, compression moulded from 40% GF/PP GMT, with integral aluminium insert for the bat handle. This blade back is the main structural element to the blade and possesses sufficient depth of draw to provide both bending stiffness and strength. The design is simple with flat surfaces to reduce mould costs and allow for inclusion of internal strengthening ribs if necessary at a later stage. A low cost prototype aluminium tool has been made for producing this part.
- (ii) A flat front face plate manufactured from the same GMT as the blade back in a simple low cost picture frame compression mould. Plate thickness can be adjusted simply by changing the charge mass before moulding. The front plate is attached to the blade back by electrical resistance welding (Hot plate welding would be used in production).
- (iii) A lightweight, stiff pultruded GRP tube is fitted directly into the blade insert with an interference or adhesive connection. A stiff direct coupling reduces the energy loss in this region and allows as much strain energy as possible to go into the local plate deformation, thus utilising the isoharmonic impact effect. An outer cushioning foam fits around the handle to provide some damping from vibrations caused by impact near the blade edges.

The final prototype bat weighs about 800g, compared to 1000 - 1200g for a typical willow bat and possesses a blade flexural rigidity of 5000 Nm², equivalent to a medium weight wooden blade.

Test Results

It is difficult to perform consistent and reliable tests on a bat hitting a ball under real conditions whilst at the same time measuring parameters such as impact force and ball speeds. For that reason, the playing performance of the composite bat has firstly been assessed using experimental modal analysis coupled with the impact theory. Fig. 9 shows the computed results for the prototype GMT bat compared with a traditional bat. It can be seen that the performance of the GMT bat is significantly better than that of the traditional bat despite its lower mass and moment of inertia properties. These results agree very well

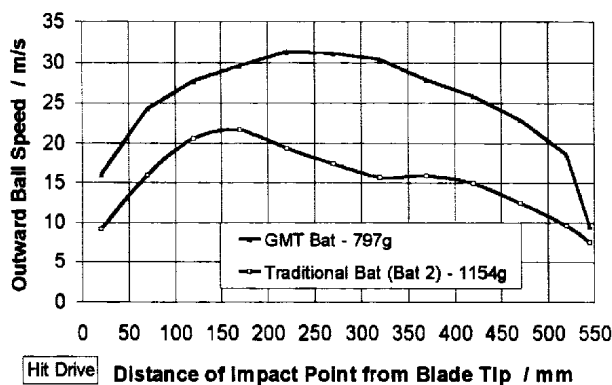


Fig. 9 Comparison of GMT prototype bat with a traditional bat, based on experimental modal analysis data.

with the results from the fully computational model (see Fig. 6) previously discussed. In addition, experimental measurements of the coefficient of restitution have been made on a second prototype GMT bat, with increased plate thickness (5 mm) and mass (1032g). For these tests the bat is clamped at the handle and a ball is dropped vertically onto the bat. Table 2 shows the results compared with a traditional bat of similar weight. The GMT bat gives consistently increased ball rebound speeds (> e), up to 90% improvement in one position. Although the clamped handle is not representative of real conditions, the results clearly confirm the existence of the isoharmonic impact effect.

Table 2 Clamped bat experimental coefficient of restitution values for a GMT prototype bat and traditional bat of similar weight.

Distance from clamp / m	Coefficient of restitution, e	
	Trad. bat (974g)	GMT bat (1032g)
0.1	0.35	0.48
0.2	0.2	0.38
0.3	0.25	0.39

CONCLUSIONS

In this paper it has been shown that a predictive model, based on beam or plate vibration analysis and Hertz contact theory, can give good predictions of the impact performance of composite plate structures and solid wooden and composite cricket bats. The theory, confirmed by experimental tests, shows that a significant improvement in ball hitting power can be achieved by a composite plate structure with a corresponding reduction in impact force and bat weight. The mechanism of impact has been termed an 'isoharmonic impact' which gives maximum performance by tuning the composite plate to the contact time during impact. It has also been shown that it is feasible to manufacture such a bat from Glass Mat Thermoplastic and that it performs in the predicted way. Future work needs to focus on the long term fatigue performance of suitable materials, high volume manufacturing methods and the thorough testing of prototype bats under real cricketing conditions. Finally, the restrictive laws of cricket in regard to bat construction need to be re-addressed if the sport is to move forward successfully into the new century.

ACKNOWLEDGEMENTS

The authors wish to acknowledge the financial support of CadCam Technology Ltd., in particular the encouragement and foresight of John Bell, and the EPSRC (UK) for the award of a CASE studentship.

REFERENCES

1. Timoshenko, S.P., *Vibration Problems in Engineering*, 2nd Edition, Von Nostrand Company Inc., 1937.
2. Goldsmith, W., *Impact, the Theory and Physical Behaviour of Colliding Solids*, Ed. Arnold Ltd, London, 1960, pp. 108-111.
3. Lieberman, B.B. and Johnson, S.H., "An analytical model for the ball-barrier impact", *Science and Golf II: Proc. of the World Scientific Congress on Golf*, E and FN Spon, London, 1994, pp 309-320.
4. Knowles, S., *Dynamic Analysis and the Use of Composite Materials in Cricket Bat Design*, PhD Thesis, University of Nottingham, 1997.
5. Gorman, D.J., *Free Vibration Analysis of Beams and Shells*, John Wiley and Sons, 1975, pp 7-16.

OPTIMIZATION OF THE CARBON-COMPOSITE WING FOR THE SKUA HIGH SPEED TARGET DRONE

D. Grygier¹, T.C. Raman²

¹*KENTRON, a Division of DENEL (PTY) LTD, P O Box 7412, Hennopsmeer 0046, Republic of South Africa*

²*ARMSCOR, Department of Aeronautics and Maritime, Aircraft Division, Private Bag X337, 0001 Pretoria, Republic of South Africa*

SUMMARY: This paper addresses the design optimization process of the all carbon-composite wing for the SKUA high speed target drone. The wing currently employs a conventional spar and rib construction, and the manufacturing process is by wet lay-up, vacuum bagging and oven cure. The design brief was to cut the manufacturing costs of the airframe and the wing by 35%, whilst at the same time reducing the mass of the drone.

Various construction techniques and manufacturing processes were investigated, and a two component integral wing structure manufactured in an autoclave was selected. The design optimization lead to a cost reduction of 40%, mainly achieved through the use of the two component structure as well as an improved manufacturing process. The integration and finishing time of the component was reduced by 60% and a mass saving of 10% was achieved. The wing was subjected to non destructive and structural testing for the qualification process.

KEYWORDS: SKUA high-speed target drone, main wing design optimization, tooling techniques, process development, structural qualification

INTRODUCTION

The SKUA High Speed Target drone (HTD) has been designed to simulate high speed attack aircraft during ground-to-air, air-to-air and ship-to-air combat exercises. Capable of flying at speeds of Mach 0.86 at 30 000 ft, the maximum instantaneous load factor is 7.5g, making this all composite airframe a highly loaded structure. The all-up weight of the drone is 680 kg, of which the airframe contributes to 180 kg.

Although the system has been in operation with the South African Airforce since 1992, to be able to compete in the international market, the design brief was to cut the manufacturing costs of the airframe by 35%, whilst at the same time reducing the mass of the drone.

For details of the HTD drone refer to Fig. 1.



Fig 1: SKUA High Speed Target Drone

DESIGN CONSIDERATIONS

The HTD wing is swept 30° at the leading edge and uses a supercritical aerofoil section with a 10% thickness to chord ratio at the root. The wing span is 3 570 mm and provision is made for mid wing and tip stores. The design specifications include the aerodynamic load caused by a 7.5g turn, a 10g launch and recovery load and a 15g landing impact load.

As the requirement for a 7.5g sustained load could not be met with the existing propulsion unit, one of the design considerations was to reduce the airframe to such size that the payload volume and the mission flight time would not be affected. The airframe was therefore reduced to 88% of full scale, and for this reason the main wing dimensions of this technology demonstrator are 88% of full scale.

WING CONCEPT DESIGN

Conventional Wing Structure

The current wing structure employs a conventional spar and rib structure bonded to the top and bottom skins. The manufacture of the spar and rib structure is a labour intensive manual operation, the skins are manufactured by a wet lay-up, vacuum bag and oven cure process. The bond lines are difficult to control and therefore the weight control on the final structure is not optimal. The wing consists of the upper and lower skins and the internal structure. [1]

Tomahawk Wing Concept

The wing for the Tomahawk cruise missile employs an internal frame structure manufactured by a hot injection moulding process. The wing top and bottom skins are made of a thermoset pre-impregnated material. The centre structure is bonded to the top and bottom wing skins and a leading edge cap ensures good bonding along the leading edge. The wing consists of only 4 parts, namely the upper and lower skin, the leading edge cap and the internal frame structure.

Integral Spar Concept

This concept makes use of an integral spar in the wing skins. The spars are moulded into the upper and the lower skins during the manufacturing process of the skins. The material lay-up for the skins and the spars are done at the same time. The wing consists of the two wings halves, which are bonded along the centre core, and a leading edge cap which assures bonding along the front split-line.

RTM Concept

The Resin Transfer Moulding (RTM) process allows the whole wing to be built in one operation. The dry skin material is put into the bottom wing mould with excess material along the leading edge. The internal webs are placed into position and thermally activated foam is used to keep it in position. The excess material is placed over the internal spars and thermal foam core, while the top half of the mould is closed and sealed. The RTM process is then activated.

CONCEPT EVALUATION AND SELECTION

The Tomahawk concept showed excellent high production volume characteristics, however, the inner spar construction carries a weight penalty, due to the relative poor mechanical properties of the short fibre injection moulded materials. As the weight constraints of the SKUA airframe are critical, to achieve the desired performance specifications, this concept was not selected.

The RTM process, has its biggest advantage in the fact that it is a one component manufacturing process ideally suited to a high production volume environment. The process was however not considered due to the time limitation on the technology program, and the associated high risks of the RTM tooling development. By process of elimination, the integral spar concept was therefor the obvious choice.

Integral Spar Concept

The integral spar concept makes use of only two spars that run along the entire length of the wing. These spars form an integral part of the wing skins, providing the wing bending and torsional stiffness. The integral spars also provide the required channels in the wing to route cables and piping. Refer to Fig. 2.

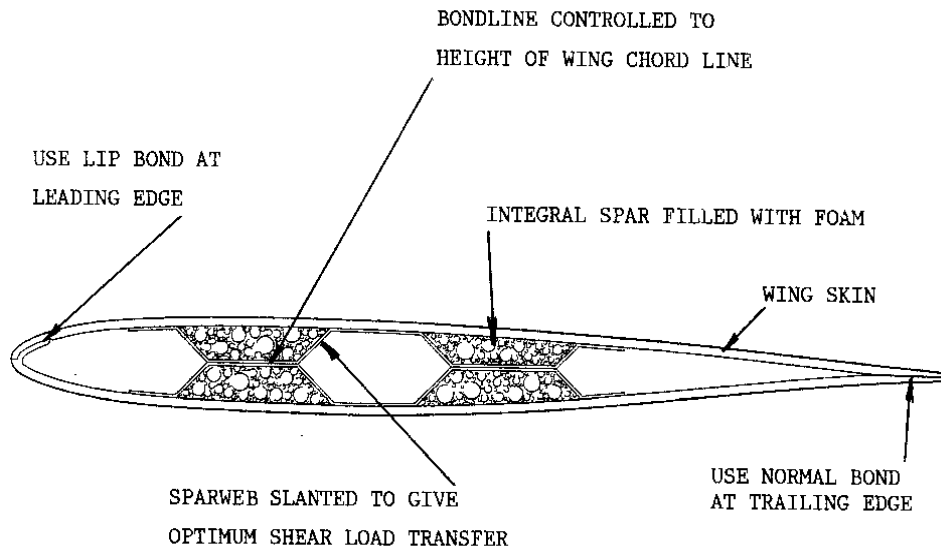


Fig 2: Integral Spar Concept

DETAIL STRUCTURAL DESIGN

Load Analysis

Based on the maximum manoeuvring capability of 7.5g, the total lift load on the main wing is 43 800 N. For the design values of the bending moments and the shear force, the wing was split into 3 sections, as illustrated in Fig. 3. An elliptical load distribution along the chord centre-line was assumed with the design values for the three sections listed in Table 1. [2]

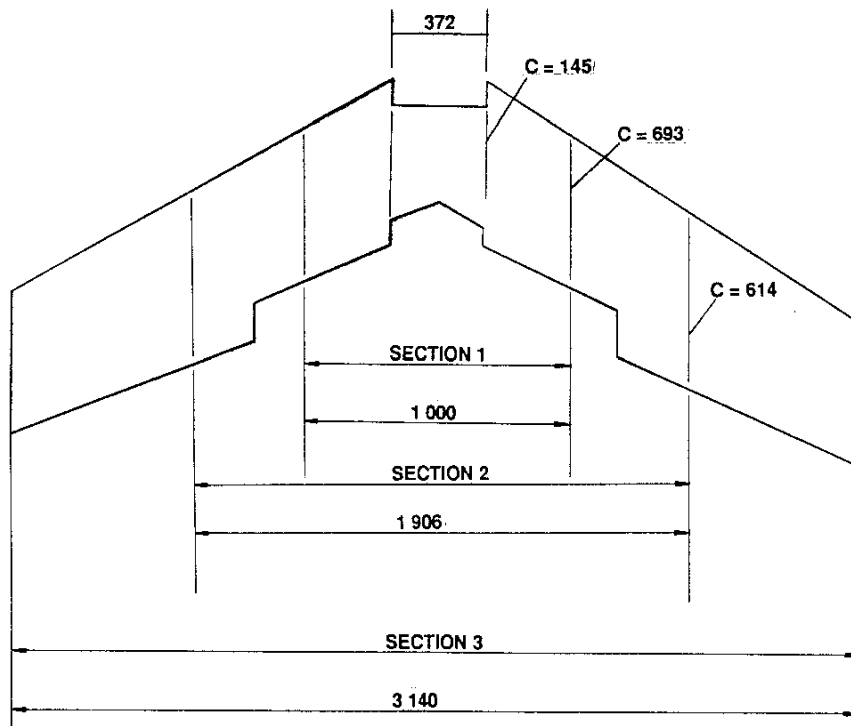


Fig 3: Wing Design and Load Analysis

Table 1: Wing Sectional Loading

SECTION	MAX SHEAR (Nm)	MAX BENDING (N)
Section 1	6 028	21 882
Section 2	4 500	12 020
Section 3	1 873	6 843

Detail Design

The conceptual design of the wing clearly highlighted the cumbersome lay-up procedures required for the integrated spar construction as presented in Fig. 2. The detail design was then adapted to an a-symmetric integral spar lay-out, whereby the spar forms part of only the lower skin. Refer to Fig. 4.

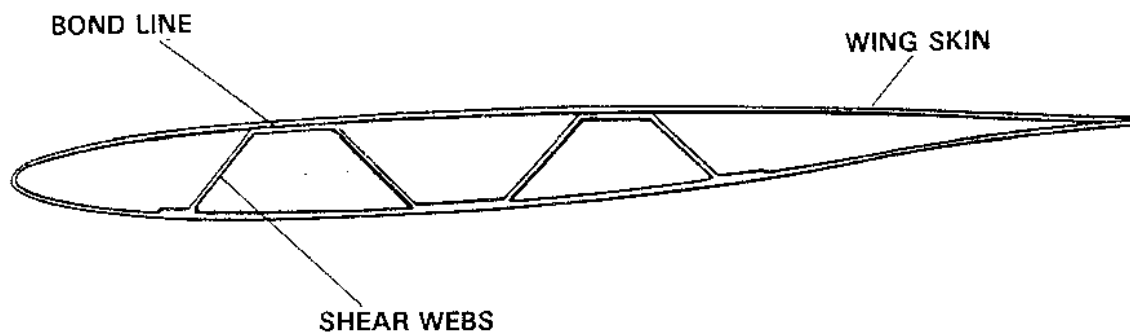


Fig 4: Optimized Integral Spar Design

The materials used in the design of the wing are listed below. The mechanical properties of these materials are not presented in this paper, as they are inherent to the products listed.

Woven Cloth:

Fibredux 920 - CX - 820 55% resin contents by weight
 T300 Carbon 2x2 twill 193 g/sqm
 Cured ply thickness 0.30 mm

Unidirectional Cloth:

Fibredux 920 - CX - TX - 133 42% resin contents by weight
 T300 Carbon 133 g/sqm
 Cured ply thickness 0.15 mm

Structural Analysis

The structural analysis was done using finite element techniques with optimization routines written for determining the optimum lamination along the wing centre-line where the

maximum shear stresses occur. The optimization process was aimed at optimizing the skin thickness and the fibre orientation in the skins. The optimization of the integral spar was driven by the manufacturing processes. The final optimization was done to ensure ease of manufacturing and minimum laminating times.

TOOLING DEVELOPMENT

Pattern

The pattern was CNC machined from a laminated block supawood. Urial or Model Lab products would have been better suited to this application due to their thermal stability for high temperature moulds. However, the supawood was selected for cost considerations. [3]

The pattern surface was prepared with a +/- 0.3 mm layer of XB5200/HY932/DY060 gelcoat, this was allowed to gel for 17 hrs at 21deg C and then coated with a 0.1 mm layer of LY5210/HY932/DY060 resin. The surface was then polished.

Moulds

The moulds were manufactured using 200 g/sqm carbon G818 in a wet lay-up process and the laminating resin was again LY5210/HY932/DY060. The mould was cured at 60° C and post-cured at 140° C. The egg-crate backing structure was then fitted to the moulds and supported by fully adjustable steel tables. The moulds were then accurately levelled with the use of a Kern ECDS theodolite system.

Tooling Jigs

The tooling required is that of the integral spar forming tool. The integral spar was machined from aluminium and bonded onto the wing skin. A carbon tool was then taken off this aluminium spar, the tool was made in the same lay-up as the wing mould. Silicon bagging was then formed to the shape of the integral spar. The integral spar tool backing is indexed with the wing mould.

MANUFACTURING PROCESS

Materials

The materials used for the skin manufacture were as specified in the detail structural analysis. To verify the tooling and the manufacturing process, and at the same time keeping the costs low, the first wing was manufactured using a thickness representative glass fibre instead of the carbon fibre. [4]

Processes

The skins were layed up according to the lay-up sequence established during the detail structural design. The spars, being part of the skin lay-up, were then formed around a silicon bladder. On completion of the skin lay-up, the tool that control the shape and height of the integral spar were fitted to the mould. The silicon bladder was then attached to the autoclave

pressure, thereby ensuring that the spar lay-up took the shape of the spar tooling. The height of the spar was directly controlled by the inner skin of the other mould. Refer to Fig. 5. The skins were then cured in the autoclave at a pressure of 7 bar and temperature of 120° C.

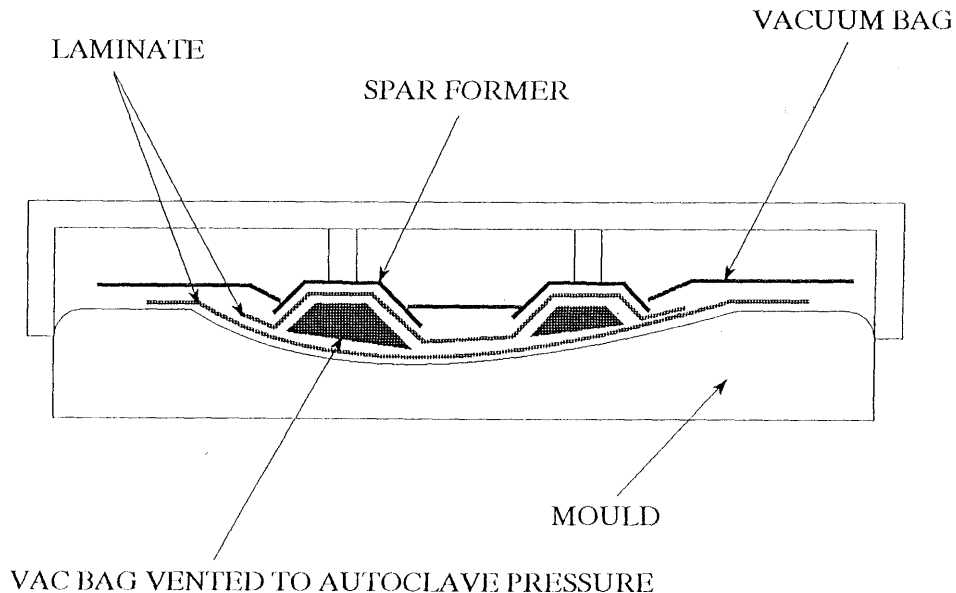


Fig 5: Integral Spar Tooling

Assembly

The two wing halves were prepared along the bonding surfaces. The tooling jigs assured the correct thickness of the bond lines along the leading and trailing edges and the centre spars. Araldite film adhesive was used along the bond lines. After bonding of the two wing halves the leading edge cap was bonded onto the wing.

TEST AND EVALUATION

Non Destructive Testing

The Non Destructive Testing (NDT) of the HTD wing was conducted with C-scan ultrasonic inspection. The original wing was used as a reference for the NDT tests, and subsequently cut open in sections, to allow for verification of the results. The C-scan ultra-sonic inspection provided good results, clearly indicating the uniform thickness of the bondlines along the full length of the integral spar/skin. No defects could be identified along the bondlines and the C-scan ultra-sonic inspection has been recommended as part of the wing qualification program. [5]

Structural Evaluation

The wing was structurally tested to 150 % design load. An elliptic load distribution was applied along the chord line by the use of a wiffle tree. Load/displacement measurements were conducted to verify the stiffness requirements.

Visual Evaluation

A wing was cut open in sections to verify the skin thicknesses and the bondlines. Good correlation was achieved between the C-scan ultra-sonic detection results and the bond lines thickness. No visible problem areas could be detected.

CONCLUSIONS

The design optimization lead to a cost reduction of 40%, this was mainly achieved through the use of the two component structure as well as an improved manufacturing process. The integration and finishing time of the component was reduced by 60%. A mass saving of 10% was achieved, and the mass variation on the production wing did not exceed 3%. Furthermore, the 2 component wing employs a minimum of bond lines, thereby reducing the use of the required NDT during the acceptance testing. The wings were subjected to structural qualification, by testing to the 150% of the 7.5g design load.

REFERENCES

1. Gouws, J.H., *Concept Design for Production Tooling on HTD Wing*, Doc No 10291-00015-715 Issue 1, Kentron, March 1995.
2. Ludick, L., *HTD 88% Wing Concept Structural Analysis Report*, Doc No 10291-00014-715 Issue A, Kentron, March 1995.

vd Merwe, H.T., *88% HTD Wing Tooling*, Doc No 10291-00017-701 Issue 1, Kentron, November 1995.
4. vd Merwe, H.T., van Wyk, J., *88% HTD Wing Manufacturing Report*, Doc No 10291-00018-701 Issue 1, Kentron, March 1996.
5. vd Merwe, H.T., van Wyk, J., *88% HTD Wing Evaluation*, Doc No 10291-00019-722 Issue 1, Kentron, March 1996.

THE HIGH-SPEED CIVIL TRANSPORT: A SUPERSONIC LEAP IN TECHNOLOGY

S. Jason Hatakeyama

*McDonnell Douglas Corporation, 2401 E. Wardlow Rd., Mailcode C071-0030,
Long Beach, California, 90807-5309, USA*

SUMMARY: Current production aerospace materials will not satisfy the requirements for a next-generation supersonic transport, currently envisioned as a Mach 2.4 cruise aircraft that carries 300 passengers over 9,260-12,000 km (5000-6500 nm) transoceanic routes. Research sponsored by the National Aeronautics and Space Administration has concluded that titanium alloys and high-temperature polymer-matrix composites are required to meet the elevated temperatures encountered on aerodynamically heated wing and fuselage surfaces during supersonic cruise. This paper presents an overview of the technology challenges facing materials developers and structural designers for the High-Speed Civil Transport (HSCT). Significant progress has been achieved in the development of lightweight, durable, damage-tolerant wing and fuselage structural concepts using advanced polymeric composites and hybrid laminate systems. Highlights of design, analysis, fabrication and test of innovative sandwich and skin-stiffened structural concepts are presented.

KEYWORDS: high-speed civil transport, HSCT, high-speed research program, HSR, SST, Concorde, sandwich, honeycomb

INTRODUCTION

For over two decades, air travelers have waited for aerospace manufacturers to launch a successor to the world's only surviving supersonic transport, the Mach 2.0 Concorde. The Anglo-French venture was hailed as a technical marvel when it entered service in 1976, but it never reached economic expectations [1]. The Russian TU-144 entered passenger service shortly after the Concorde but technical problems and two crashes led to a very brief operational career [2]. The United States' foray into the supersonic transport (SST) niche was marked with great enthusiasm during the 1960's but was eventually terminated by Congress in 1971 due to political and environmental opposition [3].

During the SST heyday, the U.S. aerospace industry also developed long-range supersonic military aircraft (B-58, XB-70, and SR-71) and high-capacity, long range subsonic airplanes (747, DC-10, and L-1011). However, the issues of airline economics, passenger safety, airframe life, airplane maintenance, airport noise, and environmental impact were significantly different for SST designs. Fortunately, Advanced Supersonic Transport research continued during the 1970's and 1980's (Fig. 1).

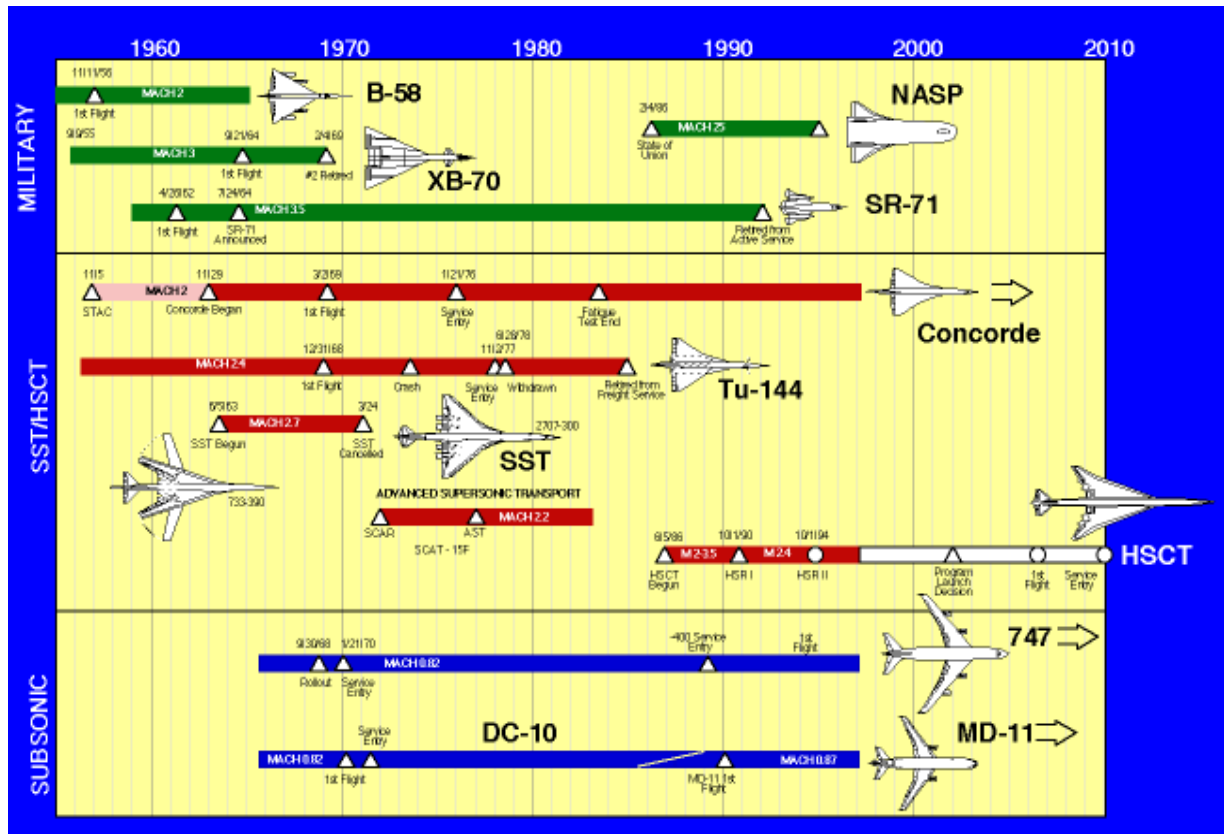


Fig. 1: Timeline of Supersonic Transport Development

Since the demise of the U. S. SST program, there has been significant technology progress that could lead to a Concorde successor that is both economically viable and environmentally acceptable. Improvements in propulsion, aerodynamics, electronic flight deck systems, and advanced materials and structures have been applied to a next-generation supersonic transport design that could see service as early as the year 2010. This High-Speed Civil Transport (HSCT) (Fig. 2) is currently under research by the United States government and industry.



Fig. 2: The proposed Mach 2.4 High-Speed Civil Transport (HSCT) will supersede the Concorde as the next-generation supersonic passenger aircraft

HIGH-SPEED CIVIL TRANSPORT DEVELOPMENT

In 1986, President Reagan announced the X-30 National Aero-Space Plane program (Fig. 3). This program was to develop two spaceplane prototypes that would demonstrate the technology required for reusable “single-stage-to-orbit,” aircraft [4]. The National Aeronautics and Space Administration, keenly aware of the benefits of hypersonic military technology applied to the development of a new commercial SST, issued contracts to Boeing and Douglas Aircraft in late 1986 to study a range of Mach numbers. Both companies selected vehicle configurations that cruised between Mach 2.0 and 2.4. These new designs became known as the HSCT.

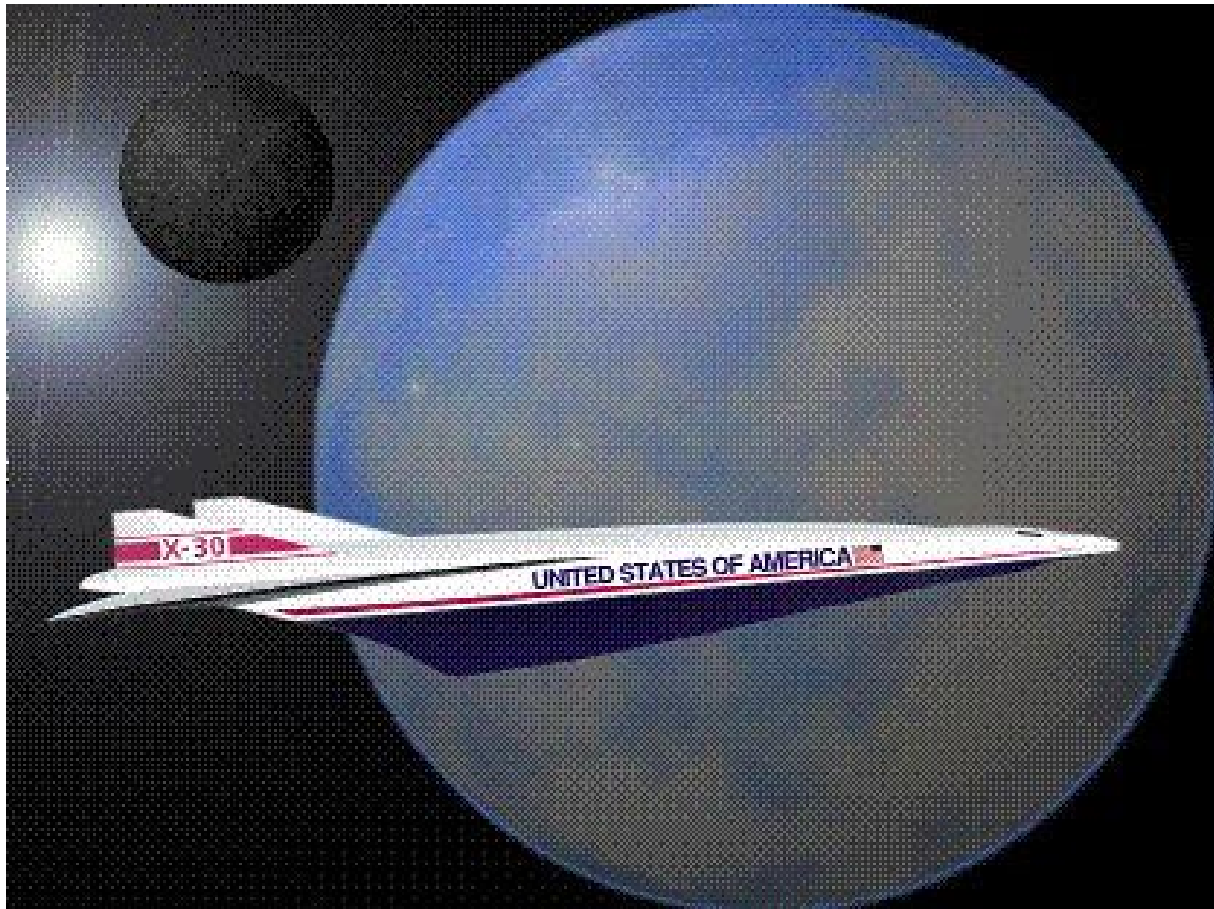


Fig. 3: X-30 National Aero-Space Plane Ushered In Renewed Aeronautics Research

World passenger traffic growth forecasts showed a considerable advantage for faster-than-sound travel between international city pairs for both passengers and the airline industry, especially for the growing Pacific Rim nations of Asia (Fig. 4). As much as 50% of the year 2015 and year 2025 total passenger markets could be suitable for a future HSCT. The success of this venture depended on an airplane that could meet the stringent airport noise restrictions along with low operating costs for the airlines and quick turnaround times at airport destinations. If an airplane could be built to fly at Mach 2.4 (2,550 kph or 1,584 mph), with a range of 9,260-12,000 km (5,000-6,500 nm), and carry 250-300 passengers, the aerospace industry would be willing to raise the multi-billion dollar investment to develop, launch, and certify the HSCT.

By 1990, NASA had formed a High-Speed Research Phase I Program (HSR I) to concentrate the efforts within the aerospace industry, government agencies, university laboratories, and material suppliers. Initially, the focus keyed in on the shortcomings of the U. S. SST, namely, ozone depletion, engine noise, and sonic boom damage.

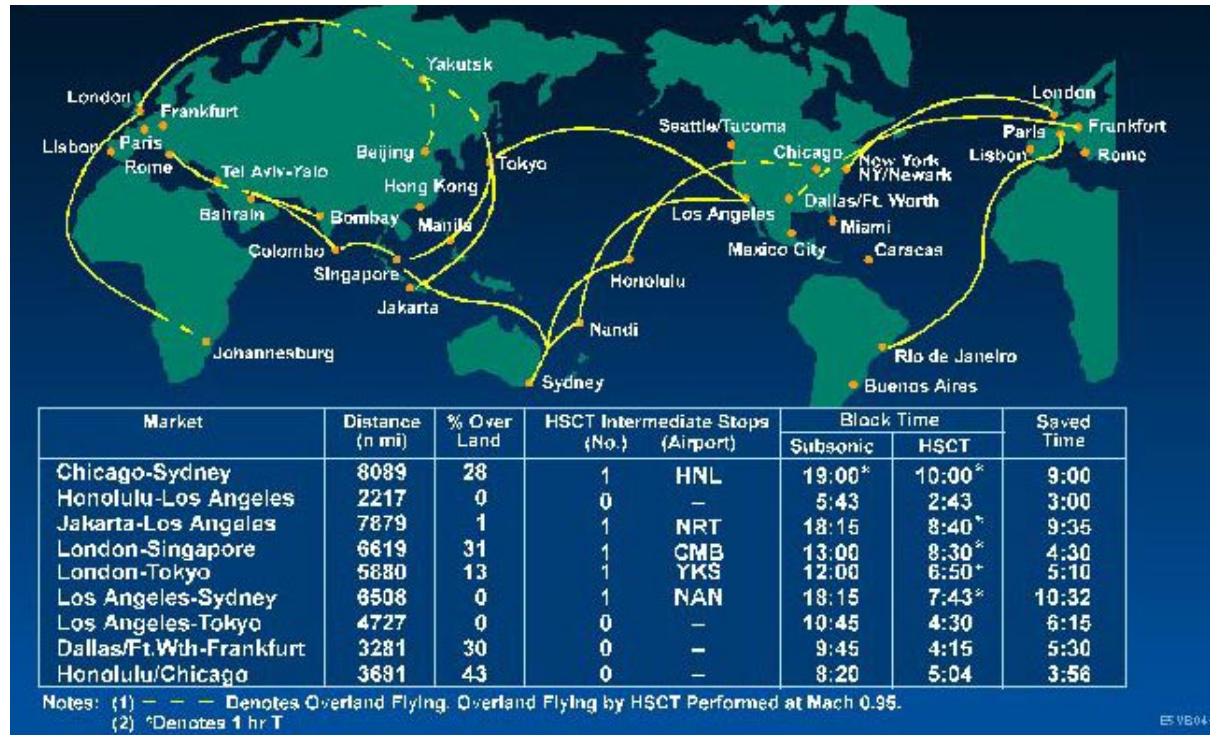


Fig. 4: HSCT Flight Time Reductions for International Routes

NASA HIGH-SPEED RESEARCH PHASE II PROGRAM

Favorable progress during Phase I of the NASA High-Speed Research Program was made in meeting the challenge of protecting the environment, thus, additional research was begun to develop the key technologies for creating a profitable airplane. These include advanced aerodynamics, efficient engines, lightweight materials and structures, and an electronic flight deck. In 1994, NASA Langley Research Center (NASA-LaRC) embarked on a US\$1.7 billion, seven-year program designated High-Speed Research Phase II (HSR II). NASA-LaRC, Boeing and McDonnell Douglas are leading the airframe technology development program, while NASA Lewis Research Center, General Electric Aircraft Engines, and Pratt & Whitney are teamed together on engine technology development. In addition, HSR II combines the talents of other aerospace manufacturers, universities, material suppliers, and small businesses throughout the country.

Early vehicle design studies conducted by Boeing and McDonnell Douglas determined tentative goals for an HSCT concept (Fig. 5): Mach 2.4 cruise speed; 300 passengers; 340,200 kg (750,000 lb.) maximum takeoff weight, and a 9,260 km (5,000 nm) range. In 1995 a common Technology Concept Aircraft baseline was agreed upon to assess the necessary technology required to launch an HSCT program. Primary emphasis was given to the

aerodynamic shaping of the wing and fuselage in order to reduce drag during supersonic cruise and to reduce noise levels during takeoff and landing.

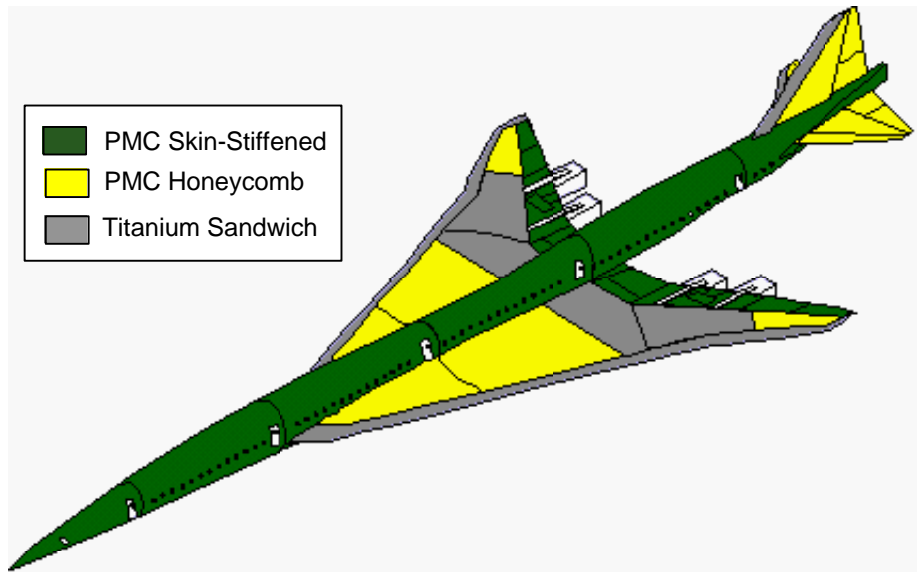


Fig. 5: HSCT Materials & Structures Selection

AIRFRAME MATERIALS & STRUCTURES TECHNOLOGY

Key to the economic success of the HSCT are lightweight materials that can withstand the elevated surface temperatures encountered at cruising speeds three times that of current subsonic jets. Moreover, these structural concepts must be durable enough to last for a lifetime of over 20,000 flights that includes 60,000 hours at cruise temperatures. The temperatures due to aerodynamic friction are in excess of that encountered by normal commercial jetliners (Fig. 6). At the nose tip, wing leading edges, and tail leading edges, the temperatures are expected to reach 177°C (350°F). This long-term thermal environment is the major driver for the airframe structure in terms of safety, weight, durability, cost, and risk.

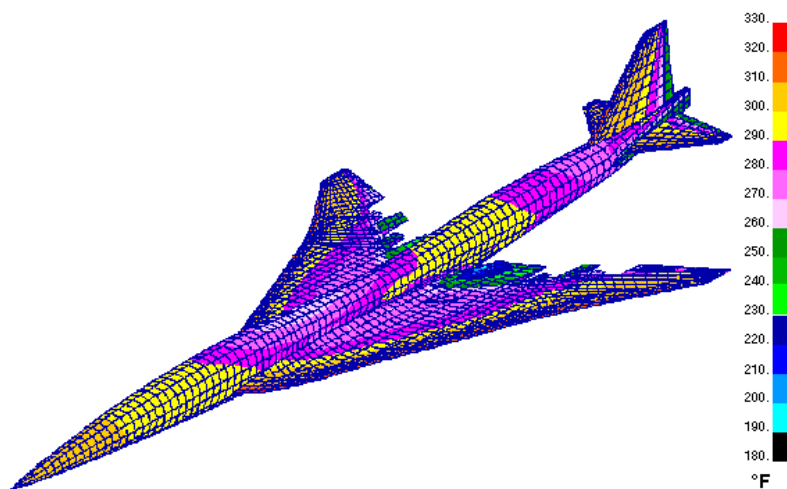


Fig. 6: Skin Temperatures During Mach 2.4 Cruise

Four major technology areas are being pursued by dedicated teams of U.S. government and industry participants. These include materials development, wing structures, fuselage structures, and airframe integration.

Materials Development

Metallic Materials

Titanium materials are being developed with 15-20 percent improvement in specific properties over conventional aerospace materials at the HSCT operating environments for up to 60,000 hours. Variations of existing titanium alloys and novel fabrication processes are under development to improve the strength, toughness, stiffness, and production cost of formed structure. The primary emphasis of the metals development is on sandwich skin panels for highly loaded wing applications (Fig. 7). Fabrication processes are being refined at McDonnell Douglas and Boeing to produce bonded titanium honeycomb and superplastically-formed, diffusion bonded titanium structure.

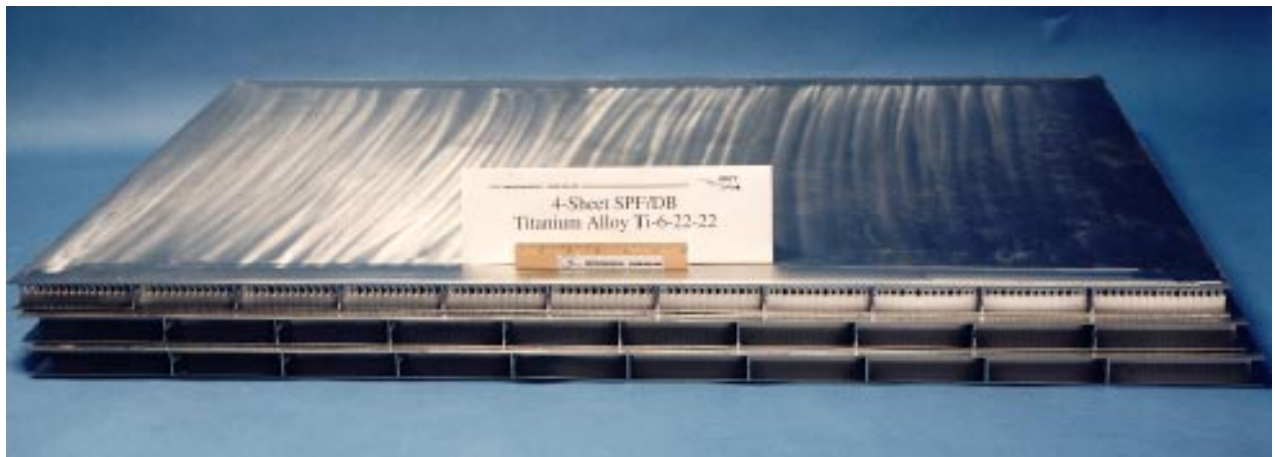


Fig. 7: Superplastically-Formed, Diffusion Bonded Titanium Sandwich Structures Use Advanced Titanium Alloys To Increase the Strength and Stiffness

Composites, Adhesives & Sealants

Long life polymer-matrix composites (PMC), adhesives, sealants, and associated material forms are also under development along with application and fabrication processes to meet the operating environment of the HSCT. Elevated temperature PMCs and structural adhesives with strength superior to existing materials are required for large acreage wing and fuselage skin panels. These bonded structures include PMC honeycomb sandwich and PMC skin-stiffened constructions (Fig. 8). Boeing, Northrop Grumman Corporation and McDonnell Douglas are producing autoclave-cured structure using polyimide resin system tape. In-situ consolidation trials are underway to produce laminates without the need for autoclave curing.

Boeing has produced a unique hybrid laminate system using interleaved titanium foil sheets between PMC plies. The titanium increases the damage tolerance of the laminate, while the PMC plies increase the fatigue life beyond the titanium failure point. Critical to the success of this laminate design is a successful surface preparation that results in a high-strength adhesive bond. Both wing and fuselage skin panels could benefit from this laminate construction.

Finally, durable high temperature fuel tank sealants are being investigated, since no sealants are currently available that can survive one airframe lifetime under HSCT thermal conditions.

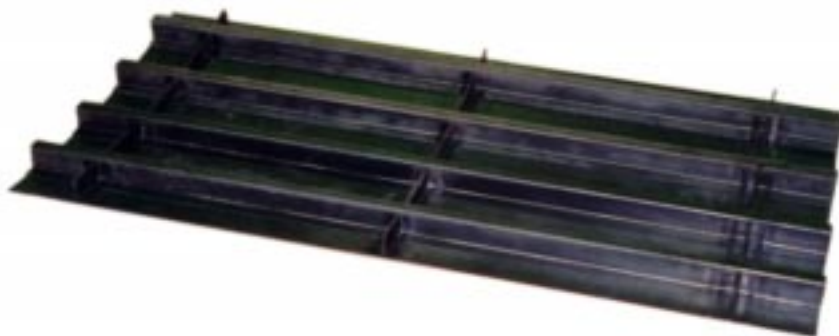


Fig. 8: Lightweight Structural Composites Will Meet HSCT Life and Temperature Requirements

Materials Durability

Critical for commercial transports, the selected materials must be able to withstand two lifetimes at temperatures much higher than those encountered during subsonic flight. A materials database will be generated that characterizes the short-term and long-term characteristics of metallic and composite materials subjected to long exposures to both elevated temperature (Fig. 9) and structural loads. PMCs are most vulnerable to long term degradation over time, and thermomechanical aging is being conducted at NASA-LaRC and California State University – Long Beach. Bolt bearing studies at Lockheed Martin Aeronautical Systems and bearing creep tests at Georgia Institute of Technology are investigating thermal effects on thick PMC laminates.

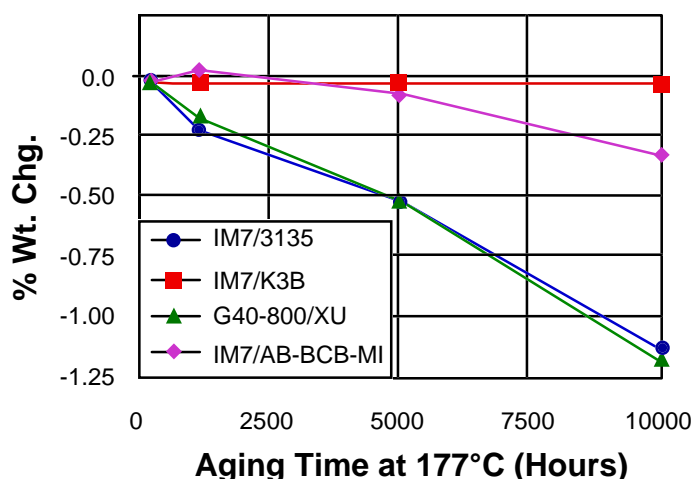


Fig. 9: Long-Term Thermomechanical Aging of HSCT Materials

Wing Structures

Metallic and composite structural concepts that meet the thermal and mechanical loads of the HSCT will be designed, fabricated, and tested. A progressive, building-block approach will be used to design and develop representative subcomponents for the main wing box, forward

strake, and outboard wing. The final validation will be led by McDonnell Douglas at the end of HSR II with a full-scale test of the HSCT main wing box (Fig. 10).

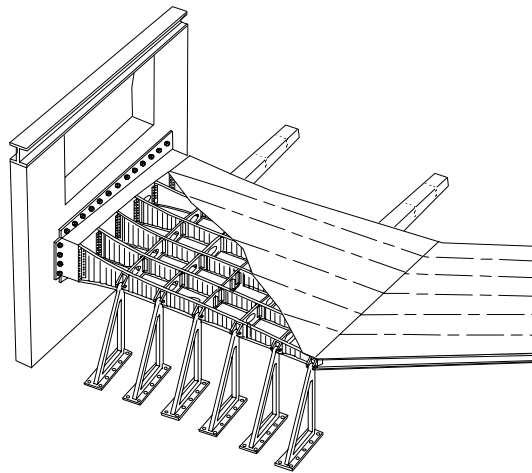


Fig. 10: Full-Scale HSCT Main Wing Box Component Test Article

Fuselage Structures

Candidate fuselage design concepts that meet the passenger safety requirements of the HSCT are also being developed. Flying at 18,300 meters (60,000 feet), catastrophic failure of an HSCT fuselage skin panel is of utmost concern. Lightweight, damage resistant structures are under development in a building-block approach for the forward, mid, and aft fuselage sections. A full-scale fuselage barrel test (Fig. 11) led by Boeing is also planned for the end of HSR II and will be tested at the NASA Langley Research Center Combined Loads Test System (COLTS) facility.

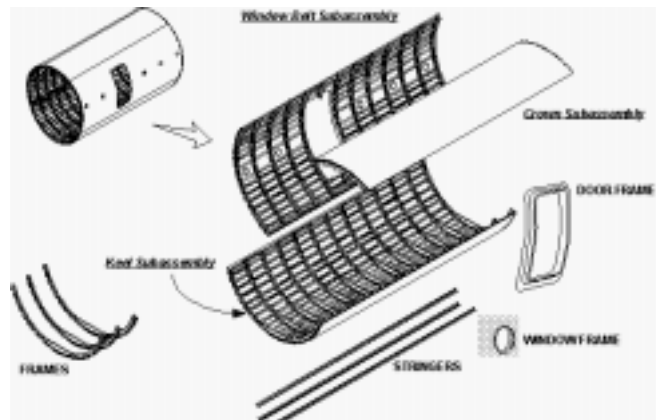


Fig. 11: Full-Scale HSCT Aft Fuselage Component Test Article Airframe Integration

Structural Dynamics

Under flight loads, the wing and fuselage experiences flutter that can affect both the HSCT performance and safety. This was one of the most challenging engineering problems associated with the original U.S. SST design. To mitigate these risks, computational methods

and wind tunnel models (Fig. 12) are being used to predict the onset of flutter and adverse aeroelastic effects without the need for additional vehicle weight.

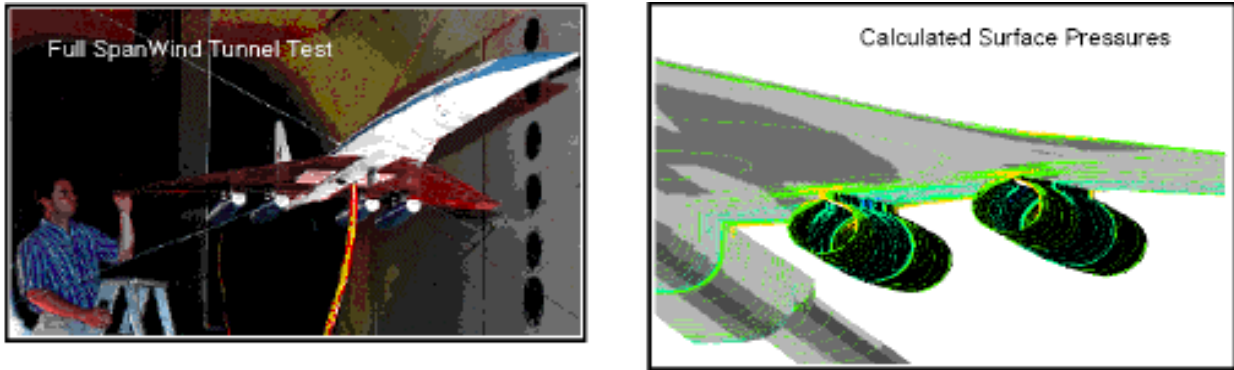


Fig. 12: HSCT Flutter Analysis Correlated to Wind Tunnel Tests

Structural Acoustics

HSCT performance and safety will be improved by eliminating sonic fatigue of structural parts due to turbulent boundary layer airflow and engine jet exhaust noise levels. Passenger comfort will be enhanced by minimizing transmission of this noise into the fuselage cabin by either active or passive suppression techniques. Using active control techniques, significant reductions in broadband noise were achieved over a large cabin volume (Fig. 13).

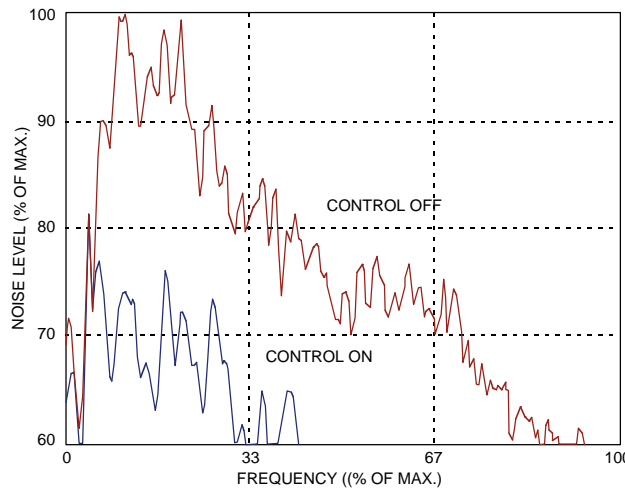


Fig. 13: Active Noise Suppression Techniques Will Minimize Cabin Noise Levels

Design/Integration Trade Studies

Airframe assessments are continually performed to reduce the overall weight of the HSCT and to integrate the various materials and structures technologies into a viable airplane design. Structural optimization uses large finite element models that represent the airframe structure to minimize the weight of each structural member.

CONCLUSION

As the United States enters the twenty-first century, the world has truly become a unified industry. International commerce and trade are now the most important factors of a balanced political and economical global culture. Although NASA is sponsoring much of the base research to develop HSCT technologies, no one company or country will be able to design and build such an airplane. Therefore, Boeing and McDonnell Douglas have joined a Supersonic Commercial Transport International Study Group to study the market needs and economics of a future HSCT. Other participants include Aerospatiale (France), Alenia (Italy), British Aerospace, Daimler Benz Aerospace (Germany), Japan Aircraft Industries, and Tupolev (Russia).

With the High-Speed Research investment by the U. S. Government through NASA aeronautics research, the American aerospace industry will be poised to help launch a fleet of HSCTs that will encourage a new future for global aviation.

ACKNOWLEDGMENTS

The author would like to thank the following individuals for providing inputs to this paper: M. Baker, M. Banuelos, M. Brunner, E. Cregger, J. Dinquel, D. Harmon, R. Hipp, W. James, M. Metwally, M. Munson, R. Ricketts, and M. Simpson.

REFERENCES

1. Owen, K., *Concorde: New Shape in the Sky*, Jane's Publishing Company Limited, 1982.
2. Moon, H., *Soviet SST: The Technopolitics of the Tupolev-144*, Crown Publishers, Inc., 1989.
3. Redding, R. and B. Yenne, *Boeing: Planemaker to the World*, Crescent Books, 1983.
4. Heppenheimer, T. A., *The National Aerospace Plane*, Pasha Publications, Inc., 1987.
5. Reithmaier, Larry, *Mach 1 and Beyond: The Illustrated Guide to High-Speed Flight*, TAB Books, 1995.

DEVELOPING OF COMPOSITE CNG PRESSURE VESSELS

B. S. Kim¹, B. H. Kim¹, J. B. Kim¹, E. J. Jun¹ and C. R. Joe²

¹ *Korea Institute of Machinery & Materials(KIMM),
66 Sangnamdong, Changwon, Kyungnam, Korea*

² *Dept. of Mechanical Design and Manufacturing, Changwon National Univ.
9 Salimdong, Changwon, Kyungnam, Korea*

SUMMARY : Development of composite CNG (compressed natural gas) pressure vessel with three-piece HDPE (High Density Polyethylene) liner and metal end nozzles was studied. The CNG environmental tests carried out for HDPE, resins and reinforcing fibers showed no significant damages. The metal end nozzle was designed to minimize the gas leak which was verified by FEM analysis. Most ideal fiber tension was obtained by experimental method and fiber volume fraction, V_f , obtained by image analyzer were 55.4% in hoop and 55.6% in helical directions, respectively. During the cure, the vessel was rotated to allow uniform resin content and when a constant internal pressure of 0.62 bar is applied, the vessels burst at 28% higher pressure and had smoother surfaces. The burst tests for under-wound and fully wounded vessel showed satisfactory results.

KEYWORDS : compressed natural gas, high density polyethylene, FEM analysis, fiber volume fraction, internal pressure

INTRODUCTION

The amount of gasoline is limited on earth and, moreover, the gasoline using vehicles pollute the air and are becoming a serious problem throughout the world. Along with solar or electric powered vehicles, the natural gas vehicles are one of the pollution-free vehicle being developed. Compressed Natural Gas pressure vessel made of Carbon/Epoxy Composite with polyethylene liner weighs about 60% less than that of Aluminum. For passenger vehicles, composite CNG pressure vessels provide much safer burst behavior as compared to that of metallic CNG. The purpose of the present study is to develop composite CNG pressure vessels for mid-size passenger vehicles. Operating and burst pressure of the vessel required are 25 and 56 bar, respectively. The liner used for CNG pressure vessels is made of HDPE and high strength carbon fibers are used for filament winding of the vessels. At each end of the vessel, the designed "Metal End Nozzle" is inserted for simpler manufacturing as well as easier injection of the natural gas.

TEST OF MATERIALS IN CNG ENVIRONMENT

In order to find out the effect of CNG environment, fibers(carbon, glass and kevlar), resins and polyethylenes have been put into a chamber with CNG environment at room temperature. The specimens were placed in a test chamber up to 1 year. To provide CNG environment, an

internal pressure of 35 bar was maintained with natural gas in the chamber. Each specimen was tensile tested before being placed into a test chamber. The specimen's tensile strength has been tested periodically during one year. Pure fibers have been tensile tested according to ASTM D3379. For all specimens, a loss of their tensile strength has been hardly observed(Fig. 1). The materials tested are vinylester (National), epoxy (Ciba-Geigy), carbon fiber (high strength, Taekwang Ind. Ltd.), fiber glass (Hankuk Fiber Glass Co.), Kevlar 49 (Dupont), HDPE1 (Honam Petroleum Ind.) and HDPE2 (SamSung Chemical Co.). All these specimens were placed in a chamber with CNG environment and tested periodically during one year.

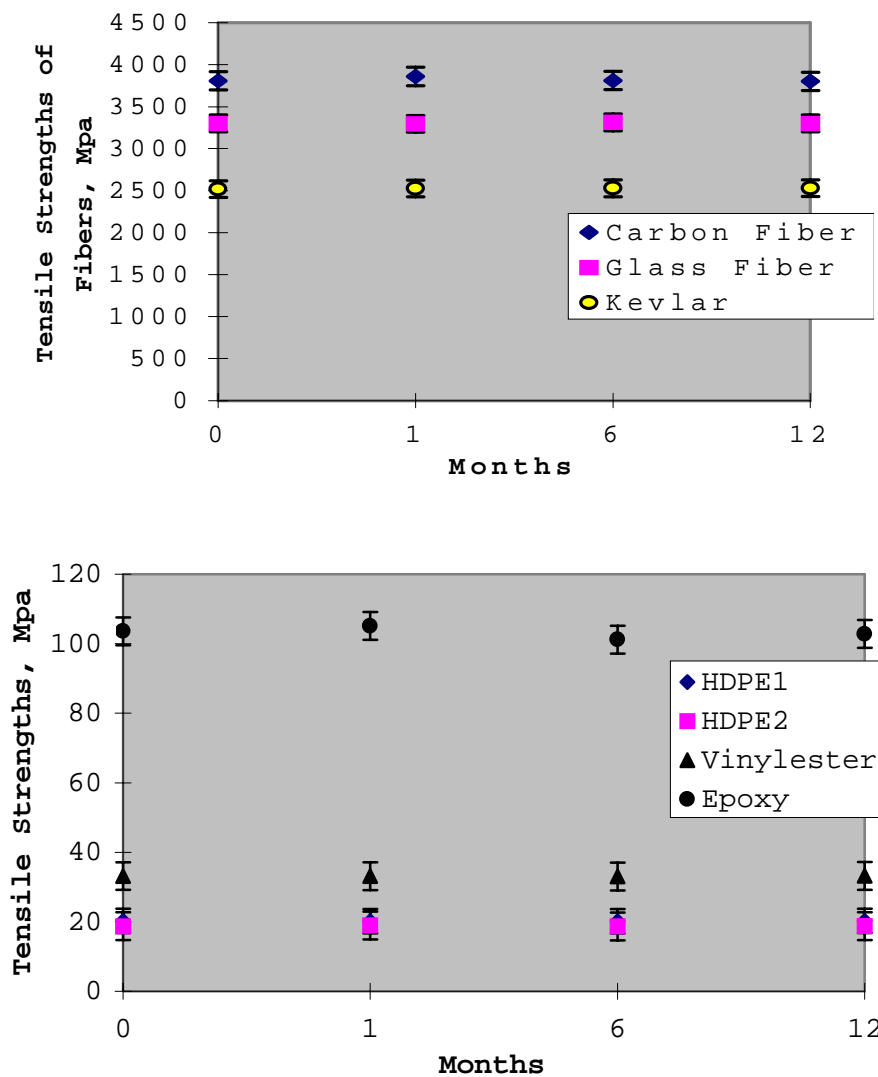


Fig. 1 : Specimens' tensile strength vs time in CNG environment (HDPE1 : Honam Petroleum Ind., HDPE2 : SamSung Chemical Co.)

DESIGN OF METAL END NOZZLE

The effective manufacturing of HDPE liner depends on the design of metal end nozzle. The design also can help to prevent gas leaks which may occur by a possible separation of metal and HDPE due to the repetitive change of internal pressure. For this reason, a metal end

nozzle has been designed and its schematic drawings are shown in Fig. 2 and 3, respectively. The thick line represents the attached area between HDPE and metal. The circled area details a notch. HDPE is filled into this notch when liner is manufactured and paste is added onto this area. When the pressure vessel is being used, internal pressure provides pressure to the paste and HDPE toward the metal which provides better sealing and seems to prevent gas leak more effectively. Moreover, in order to prevent HDPE and metal separation due to twisting of the vessel, a 3 mm x 7.5 mm x 15mm hole is carved out symmetrically at the base of the metal end nozzle(Fig. 4).

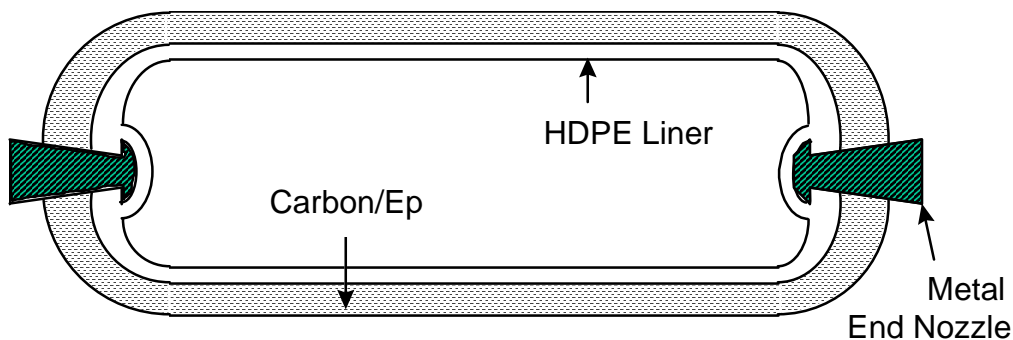


Fig. 2 : Schematic drawing of CNG vessel

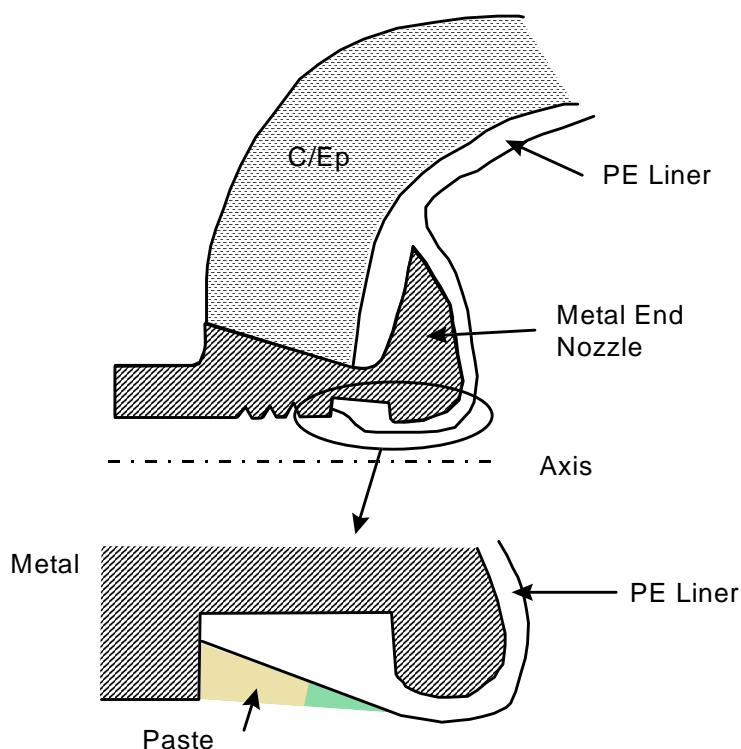


Fig. 3 : Schematic drawing of a Metal End Nozzle

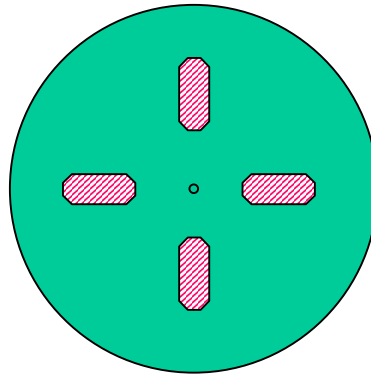


Fig. 4: Schematic drawing of symmetric holes at 3mm depths (crosshatched)

The validity of the design has been examined by NISA FEM software package. The element used for the analysis are NISA NKTP #3, axisymmetric 2D and the boundary condition was $D_{x,y,z} = 0$. Input materials properties : for metal, $E_x = 200$ Gpa, $\nu = 0.3$ and for HDPE, $E_x = 3.4$ Gpa, $\nu = 0.35$. As for load, only internal pressure of 0.62 bar was applied. One half of the nozzle shape was modeled (Fig. 5). Light colored part represent metal and dark part represent HDPE. The arrows indicate the internal pressure applied and the bunched up arrows indicate the restraints. Fig. 6 and 7 represent deformations and Von Mises stresses after the analysis.

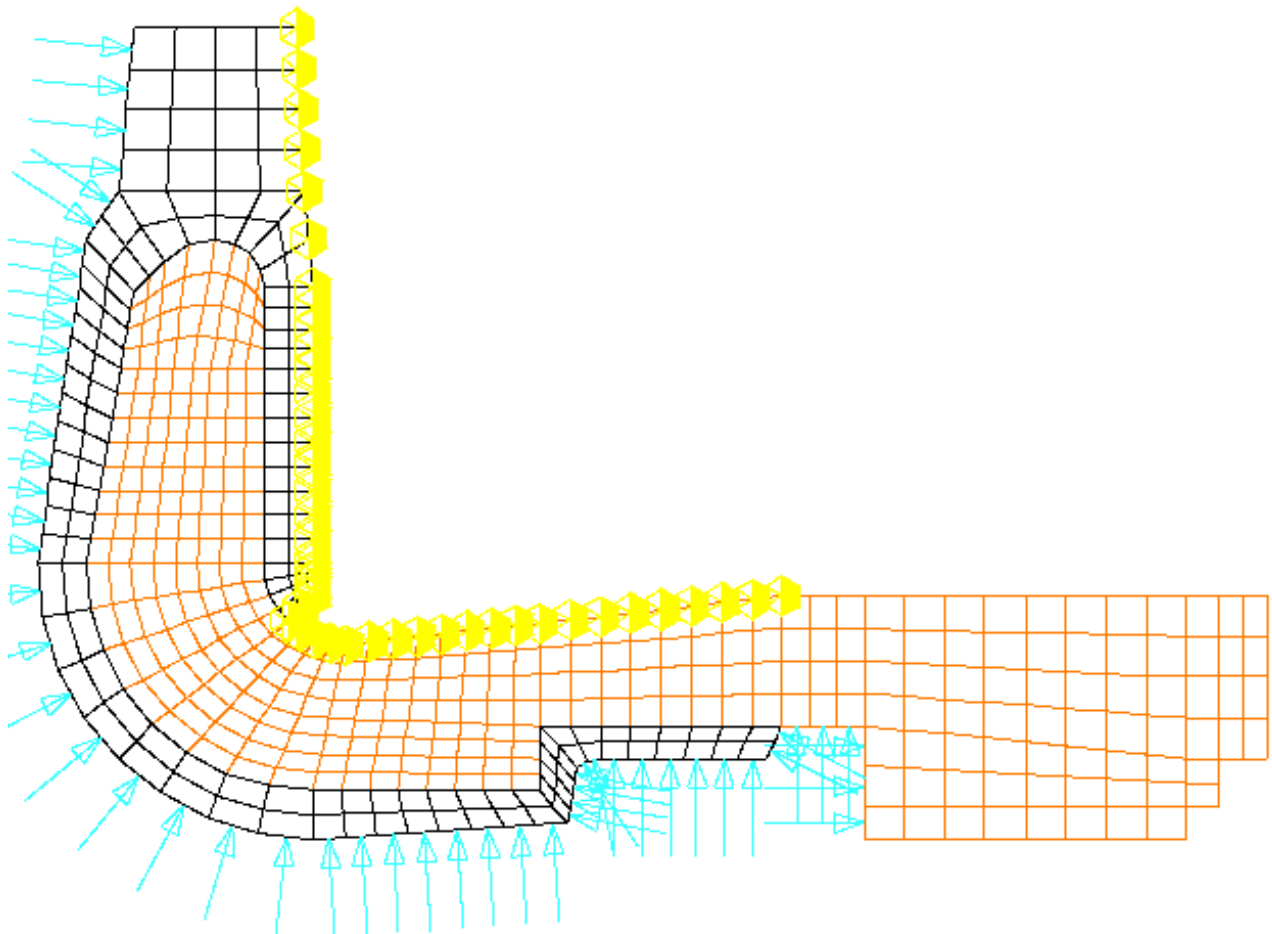


Fig. 5 : Modeling with one half of the nozzle.

The deformed shapes in Fig. 6 shows that there are no significant separation between metal and HDPE on inner part of the nozzle. Also, the maximum stress resulted in Von Mises stress analysis is only 26.36 bar in the metal which is too low to cause any significant effect considering $E_{\text{metal}} = 20,000 \text{ bar}$ and $E_{\text{HDPE}} = 340 \text{ bar}$. This result indicate that the gas leak may not occur.

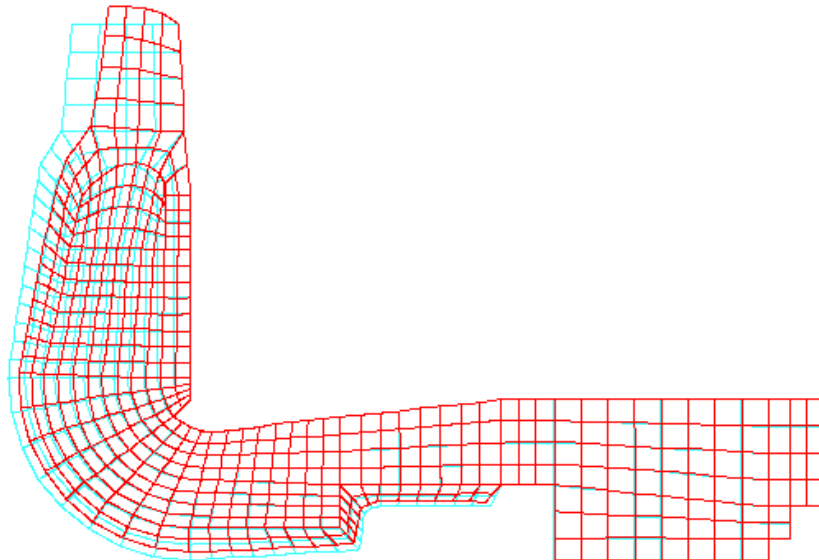


Fig. 6 : Deformations after FEM analysis

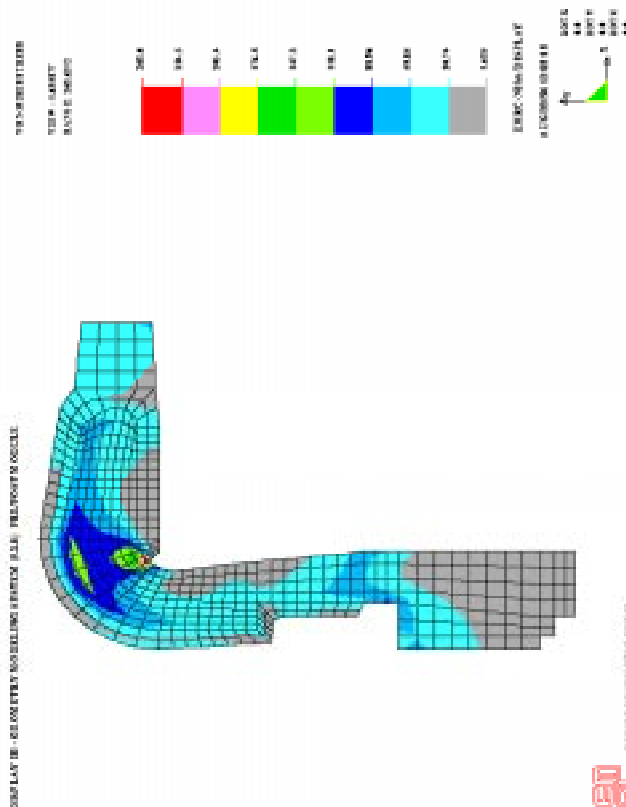


Fig. 7 : Von Mises stresses after FEM analysis

Dome area is the area that connects Metal End Nozzle and cylinder part of the vessel. Having appropriately smooth connection, the stress concentration can be avoided and easier winding can be attained. Especially, the bending moment should not exist when the internal pressure is applied such that the composite's strength in dome and cylinder part can be utilized most efficiently when in use. This dome shape can simply be achieved from the simple geometric construction around cylinder and dome area under the condition that the bending moment is zero in dome area.

Optimal V_f by Filament Winding Process

In order to achieve optimal V_f in filament winding process, the various V_f are measured by image analyzer for varying fiber tensions with various number of composite layers in hoop direction. By examining the results in Fig. 8, V_f 's were increasing with tensions higher than 1000g and decreasing with tensions lower than 750g from which the ideal tension for present filament winding machine appears to be about 800 - 850g and, with this tension, the V_f in hoop and helical directions were measured to be 55.4% and 55.6%, respectively.

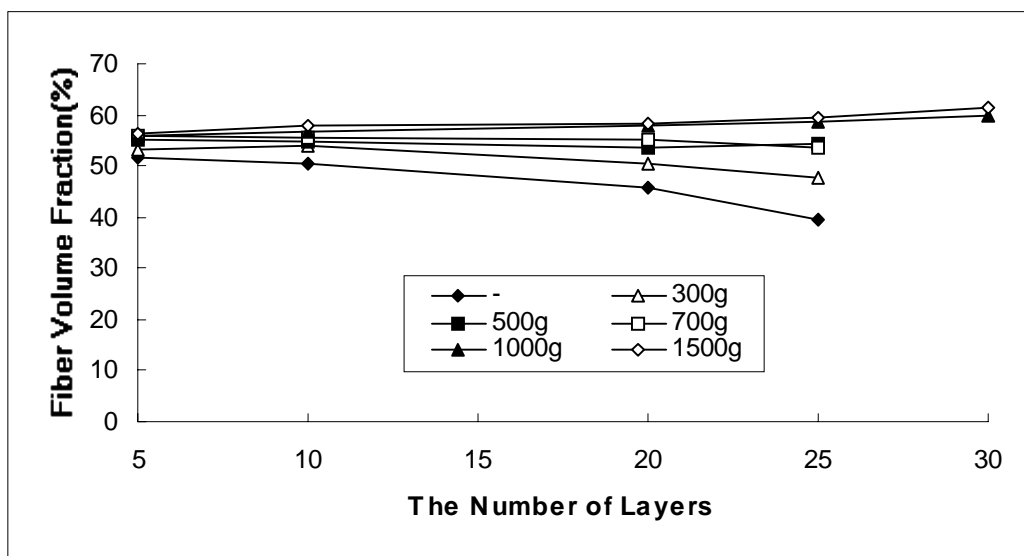


Fig. 8 : V_f vs number of layers with varying fiber tension in hoop direction

USER FRIENDLY PROGRAM

A user friendly program (KIMM - PV) has been developed to calculate most appropriate fiber directions, thickness of helical layer, thickness of hoop layer, thickness of liner, etc. This program was formulated from the laminated plate theory for cylinder and shell, respectively. The main boundary condition is the compatibility of the stresses at the boundary of cylinder and shell. This program is used to find the conditions for best structural performance for the hybrid pressure vessels. The flow chart of the program is shown in Fig. 9.

MANUFACTURING

The HDPE liner is installed in a filament winding machine. Then, the vessel is wound by use of carbon fiber strands with the specified angles and thickness. Curing is done according

to the manufacturer's recommendation. Fig. 10 represents the flow of FRP pressure vessel's manufacturing. During curing an internal pressure of 0.62 bar was applied. It prevents collapsing of HDPE during the curing process.

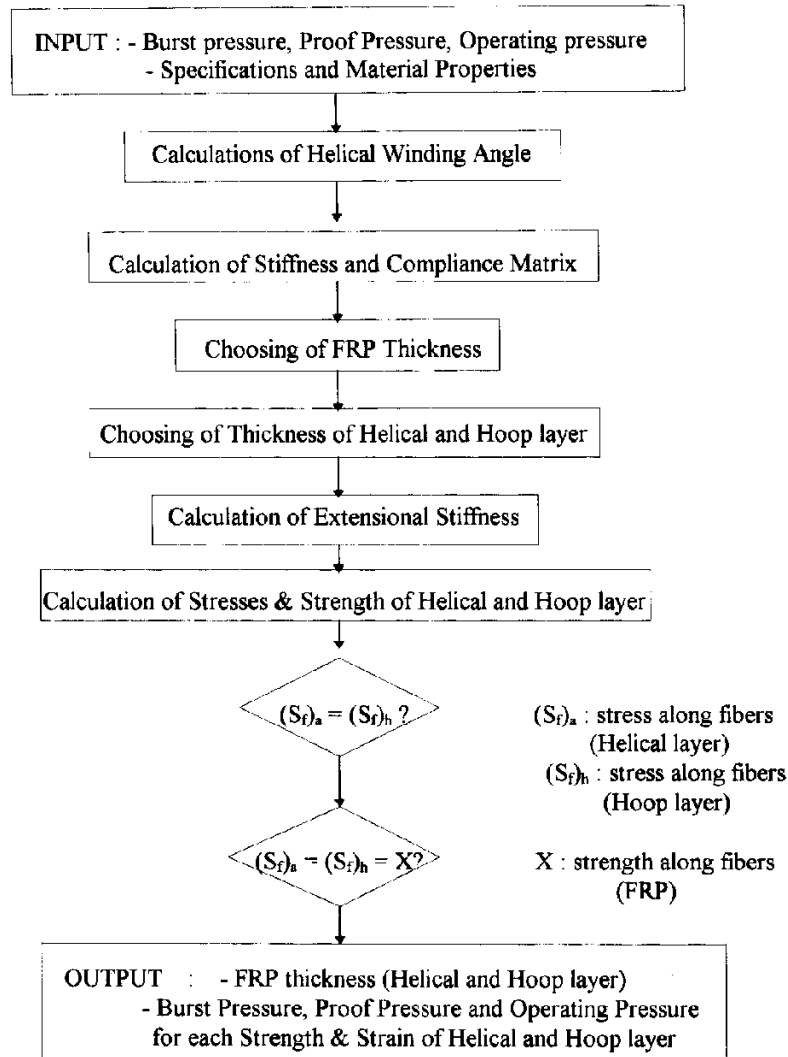


Fig. 9 : Flow chart of KIMM - PV

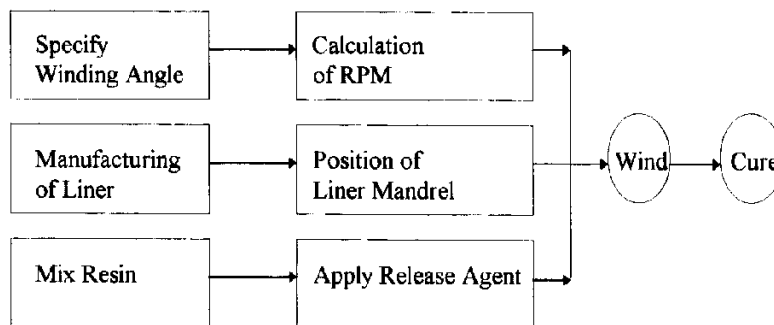


Fig. 10 : Flow of manufacturing

SPECIFICATIONS

The specifications of a CNG pressure vessel are summarized in Table 1.

Table 1. Specifications of a CNG pressure vessel

Type	F/W pressure Vessel with non-load sharing PE Liner	
Pressure	Operating Pressure	25 bar
	Proof Pressure	35 bar
	Burst Pressure	56 bar
Outer Diameter of the Liner	380 mm	
Length of the Liner	880 mm	
Weight	> 30 kg	
Internal Volume	80 liter	

BURST TEST

Specimens subjected to burst tests are summarized in Table 2 and their results are summarized in Table 3. In Table 2, K and R specimens are under-wounded compared to the ones that are to be burst at required 56 bar.

Table 2. Stacking sequences of the specimens

Specimen	Stacking Sequence	No of Layers
K 1	[15] ₂ , [90] ₂ , [15] ₂ , [90] ₃ , [15], [90] ₂ , [15] ₂ , [90] ₄	25 layers
K 2	[15], [90] ₂ , [15] ₂ , [90] ₂ , [15] ₂ , [90] ₃ , [15], [90], [15], [90] ₃	25 layers
R 1	[15], [90] ₆ , [15], [90] ₆ , [15], [90] ₆ , [15], [90] ₆ , [15], [90] ₆	40 layers
R 2	[15], [90] ₆ , [15], [90] ₆ , [15], [90] ₆ , [15], [90] ₆ , [15], [90] ₆	40 layers
S 1*	[15], [90] ₄ , [15] ₂ , [90] ₆ , [15] ₂ , [90] ₄ , [15] ₂ , [90] ₆ , [15] ₂ , [90] ₄	40 layers
S 2*	[15], [90] ₄ , [15] ₂ , [90] ₆ , [15] ₂ , [90] ₄ , [15] ₂ , [90] ₆ , [15] ₂ , [90] ₄	40 layers

Table 3. Burst test results (Internal pressure of .62 bar is applied during the cure) (1 bar = 10 Mpa)*

specimen	Burst press	[15]	[90]	Tot Wt	Fiber	Epoxy	Failure Mode
K 1	20 bar	14	11	25.4kg	7.2kg	3.4kg	Cylinder
K 2	20 bar	14	11	22.5kg	6.6kg	4.9kg	Cylinder
R 1	28 bar	10	30	27.6kg	8.6kg	6.3kg	Nozzle
R 2*	36 bar	10	30	28.5kg	8.6kg	6.7kg	Nozzle
S 1*	58 bar	16	24	29.8kg	9.5kg	7.1kg	Cylinder
S 2*	59 bar	16	24	30.1kg	9.6kg	7.3kg	Cylinder

TEST SET UP

Burst test is carried out by a safe test set up shown in the schematic drawing of Fig. 11.

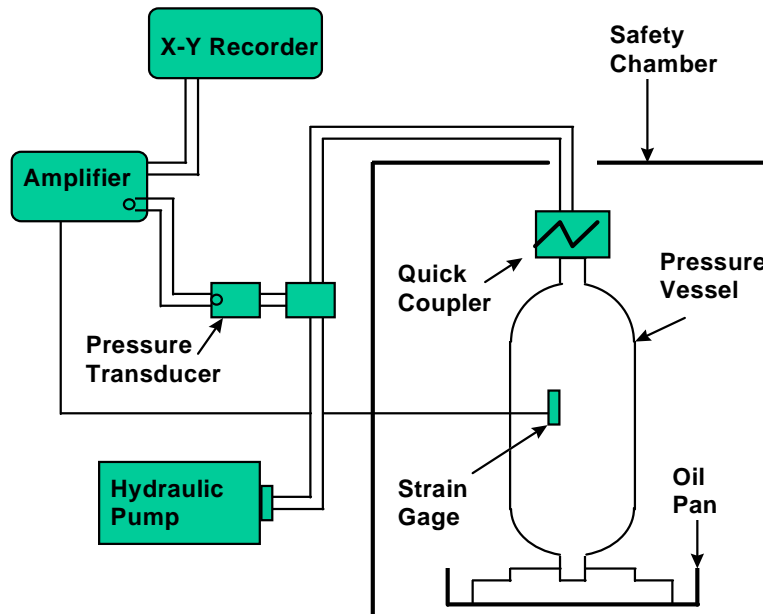


Fig. 11. Schematic drawing of safe test set up.

RESULTS

- 1) For all fibers, resins and polyethylenes tested in a chamber of CNG environment up to 1 year showed hardly any degradations.
- 2) FEM analysis showed that the metal end nozzle seems to be an appropriate design that may help prevent gas leaks.
- 3) KIMM - PV program seems to agree with burst test results.
- 4) CNG pressure vessels cured with internal pressure of 0.62 bar burst at 28% higher pressure and resulted with smoother surface.
- 5) V_f , obtained by image analyzer, were 55.4% in hoop and 55.6% in helical directions, respectively.

REFERENCES

1. E. J. Jun et al, "Development of Technology on High-precision Filament Winding Technology," KIMM Report, BSM231-1609.C, 1991. 12
2. D. V. Rosato, C. S. Grove Jr. : Filament winding, Interscience Publishers, N. Y., 1962
3. R. F. Lark, "Recent Advances in Light weight, Filament Wound Composite Pressure Vessel Technology", ASME PVP - PB - PP 17-50
4. E. J. Jun et al, Development of FRP Pressure Vessel (I, II), KIMM Report, BSN160-1244.C, 1989 - 90
5. E. J. Jun et al, Development & Application of Fiber Reinforced Plastics (FRP Pressure Vessel), BSG077-424.C, 1988
6. Lucky Polymer Technology, "Process Technology of Polyethylene", "Property & Uses of Polyethylene", Machining of Polyethylene," "Precision of Polyethylene (VLDPE)", No 11, Dec, 1989, P 10 - 43.

PWR COMPOSITE MATERIALS USE: A PARTICULAR CASE OF SAFETY-RELATED SERVICE WATER PIPES

T. Le Courtois¹ and M.-F. Pays²

¹ *Electricité de France, Engineering and Construction Division, Basic Design Department, 12-14 Avenue Dutriévoz, 69628 Villeurbanne Cedex, France.*

² *Electricité de France, Research and Development Division, Materials Research Department, Centre des Renardières, BP 1, Ecuelles, 77250 Moret sur Loing, France.*

SUMMARY: The purpose of this document is to present the broadening use of composites in French nuclear and fossil-fuel power plants. Some possible applications are presented ; the case of epoxy glass piping has been the subject of precise studies and of modeling. The general conclusions obtained are that the selected manufacturing method and materials (filament wound epoxy glass) meet the specifications of EDF. In certain areas, there is a need to go deeper into the understanding of the phenomenon, for aging particularly, because the pipeworks are expected to last the lifetime of the plant. The design rules used are convenient, but the margins need to be specified. NDT methods are available.

KEYWORDS: composite piping, power plants, selection of materials, aging, design rules, NDT, safety-related applications

INTRODUCTION

In PWR nuclear plants, steel water piping (particularly service water piping and fire pipeworks) undergo rapid corrosion. EDF has decided to install composite material piping in the latest built nuclear plant in Civaux for most of the water circuits apart from the reactor building. Some of those circuits are classified « nuclear safety », their integrity must be safeguarded. This important choice underlines the interest that EDF takes in the development of these new materials, but demands great R&D efforts (for example design studies, qualification of suppliers and quality control procedures, manufacturing and aging processes, non destructive examination either during installation or in service). These efforts ties up EDF's position with the aeronautic and aerospace industries.

Where the aeronautic and aerospace industries seek to associate functional safety and design optimization (performance/weight ratio) generally at a high price, EDF tends to seek functional safety and long term durability (40 years) at a competitive price.

Certain industries such as aeronautic, armament, and chemical take a several years lead on EDF in many fields ; alignment with them would be of great benefit for many of the research subjects mentioned above.

TECHNICAL CONSIDERATIONS FOR EDF

General Applications for EDF

Many applications are obviously possible, among which EDF gives priority to the following fields:

- piping (enlargement on Class 3 safety-related and non-classified circuits),
- structural composites (framework, roofing truss,....),
- tanks,
- fixtures and fittings within buildings (access ramps, ladders, floor grating, hand rails, guard rails like in the Petit Saut dam in Guyana);

Other applications could be considered : valves, pipe support work, raceways, cable trays, armor cladding and anti-projectile protection, fan blades for cooling towers, fuel storage pools, release flues, cable chase and ventilation shafts, tooling and equipment for live work (scaffolding, platforms,...), conductors with a composite central core, fire doors, panel boards, etc.

The materials under study are glass fiber reinforced thermoset resins (epoxy, vinyl ester and polyester). For piping applications, the filament winding technique is the most suitable. On the other hand, composite joinery (gratings, ladders, handrails, etc.) requires pultrusion techniques.

In order to develop composites for EDF's applications and to acquire the competence required to verify manufacturers' designs, R & D is necessary on three major outlines:

- knowledge of the aging process to reach a prediction of life time (resistance to hydrolysis, to creep, to acid/base/salt corrosion, to stress etc.) ;
- knowledge of the specific design rules (for multi-layer, heterogeneous, anisotropic materials) and development of the required and optimized rules and codes;
- knowledge of the different non-destructive testing methods for:
 - inspection during manufacture,
 - final inspection,
 - in service inspection.

Quality Assurance and the Materials

The nature of the materials implies the introduction of a strong quality assurance policy. The quality of supplies depends on the one of the raw materials, but above all on the manufacturing process and on the assembly of the structure on site. A procedure for the qualification of the suppliers and their operators, for the monitoring of manufacture and assembly on site, for the analysis of the feedback is necessary.

A Review of the General Use of Composite Piping

Since 1960, power stations, paper mills, chemical plants, the petrochemical industry and local councils have significantly increased their use of composite material piping throughout the world (particularly in the United States) for the following applications :

- desulfurization plants (cooling tower, piping...),
- networks for cooling water,
- networks for acids and other corrosive products,

ducts for effluent, waste water, wash water etc.,
piping for outflow, irrigation networks,
ducts for the desalination of salt water.

French Power Stations

Hydroelectric power stations do not use composite piping.

Fossil fuel power plants use this type of piping, in cooling or chlorinating circuits, in purge of wash water, and in flue gas desulfurization.

Nuclear power stations, however, are more fully equipped with composite piping (several tens of kilometers of composite piping) without any significant problem in terms of assembly or operation.

All the piping in the operating nuclear park is non-safety-related.

In the future, there will probably be a major increase in the use of composite piping, in particular within the scope of back-fitting programs for the fire-protection circuits and the safety-related service water circuits, once our selections have been justified before and approved by the French Safety Authorities.

Abroad

Hydroelectric power stations abroad do not use composite piping with the exception of the particular cases of inaccessible areas which can only be reached by helicopter and where light weight is the criterion of choice.

Fossil fuel power stations are major consumers of composite piping for the water circuits, but above all for the flue gas desulfurization system (Europe, Japan, USA). Data are available about certain American installations on the use of composite piping over a period of nearly 25 years with no apparent deterioration.

These comments are also valid for nuclear power plants. A vast inquiry, carried out at an international level (Western Europe, Japan, USA), in direct contact with the utilities, and in collaboration with the manufacturers and using data bases, reveals that the use of composite tubing in non safety-related applications is significant, but on the other hand, that in safety-related applications it is almost at zero level. Only three examples of the use of composites in safety-related piping are known to date (Belgium, USA).

The Technical Solutions

Two large families of composite structures can be used for piping:

Dual Laminate (Thermoplastic Reinforced with GRP)

This technique consists in rolling layers of resin-impregnated reinforcement (fibers or woven rovings) onto a thermoplastic liner. The liner is first heat-sealed, GRP is then built up on the outside to constitute the stress-resistant layer which bears the load.

The disadvantages in comparison to GRP (see below) are:
burdensome solution (manufacture and assembly),
limited resistance to temperature.

The advantages are:
perfect continuity of the inner-liner by heat-sealing,
excellent chemical resistance.

This latter advantage makes it a very appreciated technical solution in the chemical industry for the transfer or storage of extremely corrosive products (acid, alkali...).

GRP

In this solution, the anti-corrosion layer is a thermosetting resin lightly reinforced by a fine glass fiber fabric. The load-bearing layer, much richer in fibers, has the same chemical nature as the anti-corrosion layer. It is the best technico-economic compromise for our requirements (service water for example).

The main disadvantages of the composite material option are :

- little feedback at EDF,
- need to acquire a good knowledge of the material,
- structures sensitive to shocks,
- low level of world-wide standardization,
- few developed NDT methods.

There are however numerous advantages:

- excellent corrosion resistance (absence of significant corrosion over several decades),
- lightness,
- commercial availability in all qualities and diameters (25 mm to 9000 mm, even 11000 mm),
- minimal maintenance (no painting required),
- low pressure drop (thanks to very low roughness),
- quick and easy repair,
- very good resistance to fire (when filled with water).

For the applications in the nuclear power plants of EDF, the choice of basic material is relatively simple : GRP using a thermosetting resin. Epoxy has been chosen for the piping at CIVAUX, as it provides the best compromise between stress and chemical resistance when used for long term service water applications.

Manufacturing Method

The manufacturing methods suitable for the achievement of cylindrical sections are few:

- contact molding,
- pultrusion,
- low pressure injection,
- centrifuging,
- filament winding.

Of all these techniques, filament winding is undoubtedly the most suitable. It is possible to control the winding angle (from 0 to 90° with respect to the rotational axis).

The advantages are the following :

- fibers laid under controlled tension, in the desired direction (optimization possible),
- high fiber content,
- possibility of automation (guaranteed reproducibility).

On-site Assembly

The ways to join piping elements are butt and wrap joints, or adhesive joints (either cylindrical/conical or conical/conical), threaded sleeves, or bolted flange-to-flange connection or rotating flange (composite flange without pre-drilling).

To summarize, the safety-related composite piping at CIVAUX are made of glass fiber and epoxy resin (GRP). Straight pipes are filament wound and fittings use wound woven rovings. The adhesive joints are either cylindrical/conical or conical/conical. Joints with metal parts (pumps, valves, exchangers, etc.) use flanges.

The Economic Aspect

The decision to use piping in composite materials should be based on a full technico-economic analysis (investment, maintenance, savings in pumping energy, savings in assembly time....) of the different solutions available.

An objective comparison must therefore be made taking into account the overall costs (supply, fitting and maintenance) over the full service life of the plant. The comparison has to be made between Steel and Composite Material. The prices put forward for the design, supply, manufacture and assembly generally follow some general principles:

-for a diameter ≥ 400 mm:

The prices for GRP piping on a straight run (gallery for example) are comparable to those of coated or stainless steel. In the case of circuits including a great number of fittings or special parts (pumping station for example), the price of GRP piping is higher, due to the cost of elbows, reductions, T-joints and take-off points.

-for a diameter ≤ 250 mm:

The composite material solution is the most economical, despite the singularities (standardization of fittings in commonly available diameters).

The increased cost sometimes brought about by the use of composite materials is largely compensated by their technical advantage in terms of corrosion resistance.

THE STUDY OF SAFETY-RELATED GRP WATER PIPING

Research & Development Program

EDF has at the moment an Ongoing Research & Development Project (ORDP or PPRD in French) "Composite Materials Circuits". Priority is voluntarily given to the circuits for the nuclear power plant of CIVAUX. The efforts in terms of R & D and design studies are therefore concentrated, in the short term, on epoxy-glass piping for safety-related and non-safety-related circuits. This exercise must be a total success if a widespread development of this type of composite structure within EDF is expected in the years to come.

The objectives of the R & D program are, on the one hand, to evaluate industrial practice regarding manufacture, quality control, design rules and in-service inspection procedures and, on the other hand, to develop and validate models forecasting long term aging and mechanical behavior.

The program hinges upon the following five main axes.

1st Axis: Selection of Basic Material and Manufacturing Process,

The objective is to establish a set of guidelines to facilitate the evaluation of selection criteria for materials and existing industrial manufacturing processes.

2nd Axis: Quality Control During Manufacture,

The implementation of the quality control procedures (methods, tools, criteria) for different types of products (thin or thick structures) taking into account the basic material used (resin ductility, winding type, etc.) and the specific service conditions requires the establishment of a set of guidelines. The manufacturing defects and defects in adhesive joints have to be evaluated and the specification of the associated inspection criteria and methods to be written.

3rd Axis: Long Term Mechanical Behavior,

Through the development and validation of models of long term mechanical behavior taking into account the effects of humid environment, the long term objective is to finalize a predictive method to reach the service life of products under pressure in the presence of water.

4th Axis: Design Rules

EDF has selected standards or codes for safety-related circuits (code CASE N155-2 by ASME). They have to be evaluated, and more precisely, the margins that they allow must be clarified on the basis of the results obtained from experiments and computer modeling.

5th Axis: Non-Destructive Testing In Service.

There is a need for a set of guidelines about the methods of in-service inspection: description of the methods, implementation, performances, criteria.

Main Results

1st Axis: Selection of Basic Material and Manufacturing Process

Up to now, EDF has acquired the necessary knowledge of the industrial environment. The manufacturing processes are also well evaluated : they have been described above in accordance to the types of use they could meet. Filament winding of either roving or stripes has proven to have a better behavior than centrifugation.

A choice has been made of a set of resins that could be used in the selected possible applications in EDF power plants : the resins could be either isophthalic polyester, or vinylester, or epoxy. If the studies are restricted to a further use for water piping with safety-related applications, isophthalic polyester is not considered (it might be taken into account for joinery for example, or for non safety-related piping). A general study of the hydrolytic resistance of the macromolecular skeleton has led to a classification of the resins according to the different chemical links they bear. The links are classified in increasing order of fragility versus hydrolysis : nitrile < ester < ether.

Water uptake is a reversible phenomenon in the first place, which leads to a plastification of the macromolecular network underlined by a decrease in Young's modulus (0 to 20% for the studied resins) and of the glass transition temperature. Then, an hydrolysis occurs, and it is an irreversible phenomenon.

Epoxy resins can be synthesized with different hardeners. Epoxy-anhydride are disappointing as soon as the service temperature rises above 60°C ; for higher temperatures, EDF will prefer epoxy-amine type resins. As far as mechanics and hydrolysis are concerned, epoxy-amine and vinylester meet our requirements.

2nd Axis: Quality Control During Manufacture

The points to evaluate were the harmfulness of the manufacturing defects, the shock resistance and the non destructive control methods that could be used at this stage. Defects in straight pipes such as the core delaminations, or a delamination between the liner and the mechanical layer, an interruption in the roving, or pores in the liner don't affect the leaking pressure. A bad impregnation of the roving by the resin at least on 3 layers, is harmful for the leaking pressure. Adhesive joints present a high tolerance to adhesive defects. The following criterion have been published by the Dutch society KEMA for the harmfulness of those defects:

« The surface of the defect should be less than 25% of the total surface of the joint.

The residual length of adhesive along a generating line should be higher than 20% of the total length.

The total length of an adhesive defect leading to the inner part of the pipe should be less than 30% of the total length of the joint.

The glass transition temperature of the adhesive should be higher than the level [Optimum glass temperature of the adhesive - 30°C] ».

On the basis of those criterion, a long term program will shortly begin in order to follow the evolution versus time of instantaneously acceptable defects in adhesive joints. The bending behavior of piping is a great concern as well, for the answer to seisms. It is being studied by EDF. The MARINETECH program in Great Britain is cosponsored by EDF ; among other research themes interesting the understanding of composites, a work package deals with mechanical properties : fatigue, creep, etc. under different loading modes.

The shock resistance has been evaluated for a shock between 0 and 120 Joules. The minimum impact energy that leads to a leak has been determined for representative diameters. Until 90 Joules roughly, the leak rate stays very weak (less than 0.15 l/h for a 150 mm diameter). If plotted versus time, the leak rate of damaged pipes maintained under service pressure without end closure is annealed after a few weeks, which is favorable. This behavior had already been reported by oil producing firms, but those tests are still underway : the residual leak pressure has to be measured and the problem of testing pipes with or without end closure to be thought about.

A new non destructive method for the evaluation of the polymerization state of the resin by use of a piezoelectric implant has been designed. It is now under further study to see whether it could give an account of the aging of the structure.

3rd Axis: Long Term Mechanical Behavior

The aim, in this part of the project, was to evaluate the mechanisms and the kinetics of the damages that can occur in composite piping. A predictive model for the long term behavior and an accelerated aging method were requested. As the material is heterogeneous, and the degradation modes are complex, the adjustment of such a model is long and difficult. An additional difficulty is brought by the duration of the tests : to study the long term behavior (40 years), very long tests must be performed. Accelerated test procedures are being used to evaluate the loss of stiffness with time (for an extrapolation to 40 years). But the correlation between natural and accelerated aging is difficult and should be steadied.

The ASTM 2992 (American standard) which is called out by the Case N-155-2 code, is used to determine the long term mechanical strength of all the elements of the composite circuits in Civaux. This method has a satisfactory feedback among the oil field for example. To adjust all the parameters, a program of dismountable collars on the circuits in Civaux has been designed. It will help following the behavior of the material in service and compare the extrapolation resulting from the application of ASTM 2992 to natural aging. The results obtained and expected in those fields will be very helpful to give inputs for the model that has partially been written (for the mechanical part, not for the influence of hydrolysis for instance) and must be validated.

4th Axis: Design Rules

The critical reading of ASME's « CASE N-155-2 » code, used by EDF to design the safety-related circuits in Civaux has brought to the fore that complementary verifications are necessary to bring improvements in this design. The ruin mechanism of a composite structure depend on the type of stress and of material ; many tests have been performed at EDF on the structures used in Civaux. For the pipes and for nearly all the stresses, (pressure with end closure, pressure with end closure + bending, pressure with end closure + tension) under water pressure, a weeping is observed before the final ruin. The only exception is the test of pressure without end closure which leads directly to a wall fracture but at very high stress levels. Fittings, manufactured by stripe winding, do not weep. Their high mechanical strength leads to the fact that the weak part of the circuit around a fitting is the adhesive joint. The study of the adhesive joints proves thus to be a crucial point.

With ASTM 2992, it is possible to reach the long term mechanical strength of a pipe from weeping tests under pressure with end closure. But the circuits actually bear in service a stress with end closure and bending, so the validity of the method can be questioned. It has been proved that the short term weeping stress with end closure of a pipe is similar to this of a pipe under stress with end closure + bending.

In the calculations of the circuit's design, a flexibility factor k is introduced for the fittings ; it modelizes the flexibility of the fitting towards the straight pipe. The CASE code gives a pessimistic value for k : $k=1$, no flexibility of the fitting towards the straight pipe. An analytical formula for this coefficient has been defined and validated on the basis of tests and finite elements calculations.

5th Axis: Non-Destructive Testing In Service.

At the beginning of the R&D program, very few NDT methods (reliable, sensible and economical) for composite circuits were available. An evaluation of the 5 following techniques has been made :

IR Thermography,
differential interferometry (shearography),
ultrasonics,
acoustic emission,
X rays.

None of those techniques give all the answers. However, appropriate results have been obtained with X rays for adhesive joints bearing lack of adhesive, with ultrasonics for local controls, and with acoustic emission for the global control of pipeworks. Large scale X ray controls have been performed on joints of the Civaux power plant. These controls have put forward lacks of adhesive, sometimes of a large size. The procedures that were used for the installation (derived from the current industrial practical knowledge) have been improved and the quality of the joints is now greatly enhanced. The subsequent work (underway) is to justify the sorting criterion used, (according to the studies of the KEMA Society and together with the work by the MARINETECH Research Group) and to evaluate the harmfulness of the remaining defects.

The use of those NDT methods doesn't free from visual inspection, which is enough sensitive for most major damages (shocks for example) and gives a good general estimation of the quality of the circuits. A constant improvement of the implementation procedures would also lead to the possibility of limiting the use of expensive NDT methods through an increase in the confidence on the manufacturing and laying processes.

CONCLUSION

The installation of composite pipes in a nuclear plant in France is under way. The manufacturing methods and the products chosen are in good agreement with the specifications written by EDF. There is a need for a broadening of the knowledge about the adhesive and the fiber-matrix interface, and their behavior through aging. The leaking pressure is very tolerant to the defects in the pipes or in the joints. But the criterion followed up to now have to be validated with a higher precision. The realization of a predictive model to reach the lifetime of the materials is underway ; this action must be continued, and an accelerated aging procedure must be defined. The appropriate margin of the design rules must be reached, and specific rules for non-safety related circuits have to be proposed. Three NDT methods (acoustic emission, ultrasonics and X rays) are promising.

REFERENCES

1. Le Courtois, Thierry. 1994. "Utilisation des matériaux composites chez EDF - Cas particulier des tuyauteries - Situation en Avril 1994", Technical Note ENMEC/94.026A, Electricité De France, Villeurbanne, FRANCE.
2. Le Courtois, Thierry. 1996. « Connaissances acquises par EDF dans le domaine des tuyauteries en matériau composite. Synthèse à Février 1996, Technical Note ENMEC/96.03A, Electricité De France, Villeurbanne, FRANCE.

THERMOPLASTIC FILAMENT WINDING OF A PRESSURE VESSEL

Kurt Olofsson¹, Runar Långström¹, Tore Serrander¹ and Roland Scott²

¹ *Swedish Institute of Composites (SICOMP), Box 271, S-94126 Piteå, SWEDEN.*

² *ABB Plast, Box 273 S-94124, Piteå, SWEDEN.*

SUMMARY: This paper describes development of an all-thermoplastic pressure vessel prototype for 40 bar internal pressure, using thermoplastic filament winding. Production cost analysis indicate that a minimum prepreg winding speed of 0.4 m/s is required for efficient production. Three types of glass/PP materials have been tested as reinforcement. A conventional winding machine has been modified for thermoplastic winding. Thermal analysis indicates a maximum suitable prepreg speed of 0.4 m/s for the used heating system. Void content in manufactured hoop pipes of Plytron increased with speed and reached 1 % at 0.5 m/s supporting this speed limit. A production wet filament winding pressure vessel with thermoplastic liner has been adapted for thermoplastic winding. Mechanical analysis of the cylindrical part gave a calculated burst strength of 245 bar. Prototype vessels have been manufactured with 0.3 m/s prepreg speed using water cooled liner and stationary heating at the dome ends. Pressure testing of the prototypes gave a burst pressure of some 220 bar. A failure in the cylindrical part of the vessel was achieved indicating good dome strength. Initial degradation during the pressure test, in the form of excessive noise, occurred first at 130 bar indicating good resistance to micro cracking.

KEYWORDS : thermoplastic, filament winding, pressure vessel, glass/PP, liner.

INTRODUCTION

Much research has been performed on thermoplastic filament winding, see for instance [1]. The new class of low cost thermoplastic materials with continuous fibers that has come on the market in recent years gives potential for reduced product cost. This research is part of a four year Scandinavian research project on low cost thermoplastic composites. The intention is to develop an all-thermoplastic pressure vessel for 40 bar design pressure using glass/PP reinforcement. The studied vessel has potential for good impact, low-cycle fatigue and corrosion resistance at a reasonable cost compared to glass/epoxy reinforced vessels.

MATERIALS

Three types of glass/PP materials have been studied. Plytron is delivered as melt impregnated sheets with close to zero percent void content. It is manufactured by the Borealis company in Norway. The Plytron was cut to 5 mm width using a continuous slicing equipment. The TUT-material is a prototype material manufactured by the Tampere University of Technology (TUT) in Finland. It consist of one melt impregnated E-glass roving. Twintex is delivered in several combinations of thermoplastic matrix, fiber fraction and form manufactured by the Vetrotex company in France. It consists of co-mingled glass and thermoplastic fibers which can be woven using textile techniques since it is relatively flexible. The quality studied here consist of one 630 Tex E-glass roving with co-mingled PP fibrils. Some stiffness and strength properties for the used materials were estimated using micro mechanical formulas [2] and the

manufacturers data [3], see Table 1. Index x is fiber direction and y is transverse direction. v_f is fiber volume fraction and σ_{xB} is laminae strength in the fiber direction.

Table 1: Laminae data for glass/PP

	v_f (%)	E_x (MPa)	E_y (MPa)	G_{xy} (MPa)	ν_{xy} (-)	ν_{yx} (-)	σ_{xB} (MPa)
Plytron	35	25300	2900	1000	0.27	0.03	620
TUT	44	31500	3700	1200	0.26	0.03	600
Twintex	50	35600	4300	1400	0.26	0.03	660

EQUIPMENT

The equipment is designed for fabrication at varying fiber angles with constant prepreg speed and heating. The maximum speed for SICOMPs machine is 0.5 m/s for low angle helix layers which gives an upper limit for the possible prepreg speeds. It is a modern 4-axis winding machine with a fifth CNC-axis for control of auxiliary equipment. Compaction roller was not used for the manufacturing in this report. The heating system comprises 10 separate modules. Each module is 250 mm long, gives maximum 1000 W, uses 220 V, has ceramic lamps and allows a maximum lamp temperature of 700 °C. Each module has a temperature sensor which is used to regulate the IR-lamp temperature and hence the power output. The preheater consists of 8 modules with a total length of 2000 mm mounted on a separate chassis in the machine. An aluminium reflector is mounted under the prepreg to heat the prepreg from both sides and encapsulate it, see Fig. 1. This configuration is efficient since it combines radiation and convection heating. An isolating plate mounted under the reflector is used to protect the machine from the heat. The final heater consist of 2 modules mounted at the feed eye under the mandrel. Additional hot air heating at the dome ends was used for the pressure vessel prototypes. An equipment constraint is that fire in the prepreg is not allowed when the winding is stopped with warm preheater. The critical temperature for initiation of fire for this prepreg was tested separately in a convection oven and found to be 500 °C. It was hence decided to limit the temperature in the preheater to 450 °C to avoid this problem.

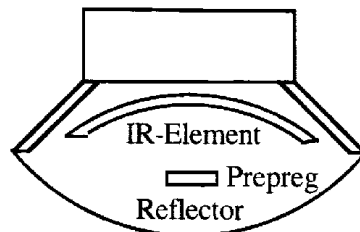


Fig. 1: Crossection of preheater

PRODUCTION COST

A typical series production line for a 3.4 l volume pressure vessel have been studied in detail to define cost sensitive process parameters, see Fig. 2. The cost model includes material (with spillage and scrap), energy, labour, administration, equipment, etc. A production line with new equipment in a medium size industry have been simulated. Two pressure vessels are simultaneously manufactured in the winding machine. The following quality control consists mainly of a test pressurisation. The cycle time is defined as the total time one vessel uses the winding machine (winding plus mounting time). The material cost for the thermoplastic liner with metal fittings is here 23 USD. The cost for Twintex and Plytron is in the range of 5-8 USD/kg. Production cost with nominal values is 70 USD with 40 USD total material cost (liner with metal fittings and prepreg) giving a material share of 57 %.

Four parameters have been varied separately:

- Prepreg speed with nominal value 0.4 m/s.
- Pressure vessel scrap with nominal value 10 %.
- Cycle time with nominal value 352 seconds.
- Prepreg cost with nominal value 7.7 USD/kg.

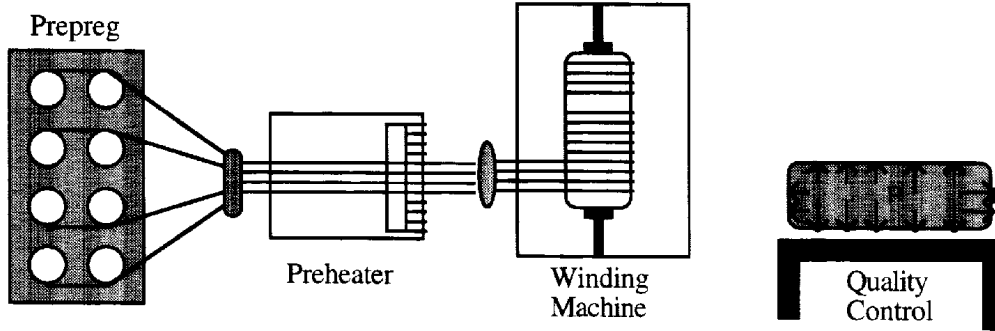


Fig. 2: Pressure vessel production

Fig. 3 shows that the cost decreases asymptotically with increased winding speed. The gain for higher speeds than 0.5 m/s is rather small. The cost is sensitive to scrapping of the pressure vessel in the quality control. A reduction of the scrap from 10 to 0 % decreases the cost with 7 USD. Presumably there exist a coupling in practice so that use of higher speeds will increase the scrap. A winding speed of 0.4 m/s was hence chosen as project goal.

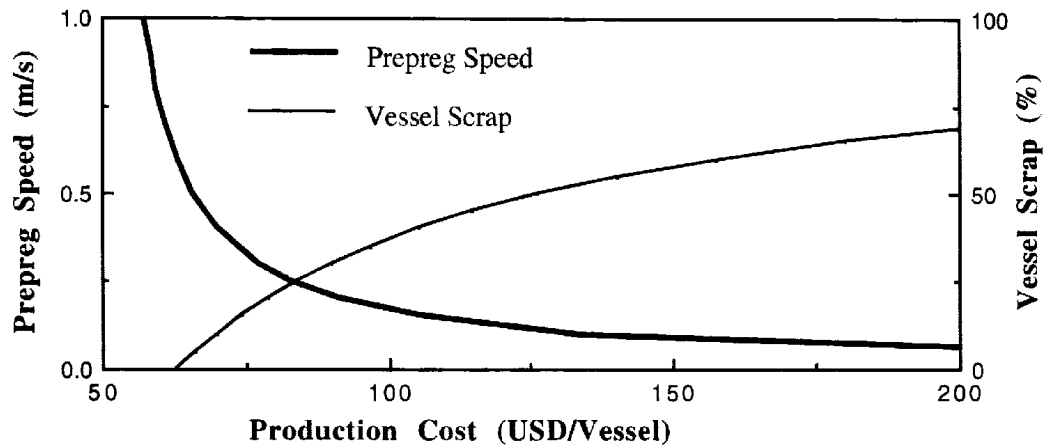


Fig. 3: Prepreg speed and vessel scrap as function of production cost

Fig. 4 shows the linear influence of total cycle time and prepreg cost. The cost is more sensitive to changes in total cycle time than changes in prepreg cost. The production cost is given by the total material cost of the vessel when the cycle time approaches zero.

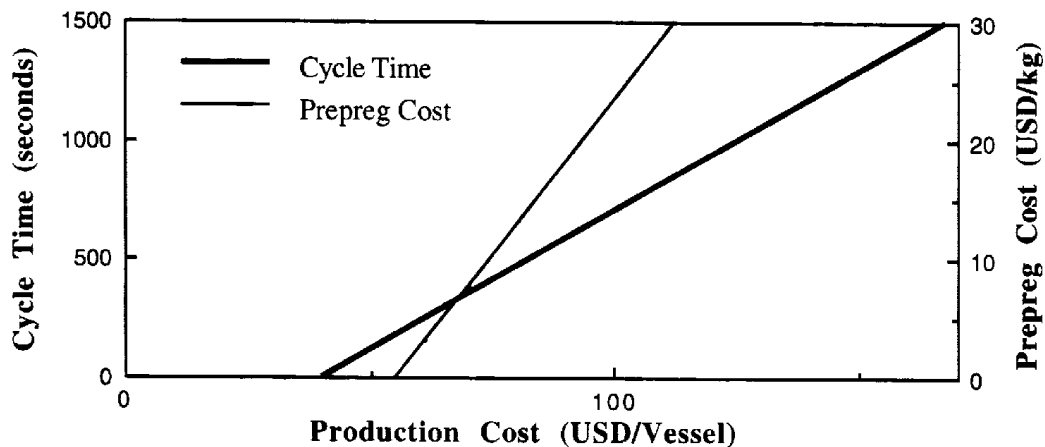


Fig. 4: Cycle time and prepreg cost as function of production cost

THERMAL ANALYSIS

Measurement

A Nickel/Aluminium thermo-couple with \varnothing 0.6 mm was connected to the upper surface of the prepreg. The prepreg was wound through the heater system, feed eye and on to the mandrel at 0.15 m/s prepreg speed. The temperature-time history was recorded.

Model

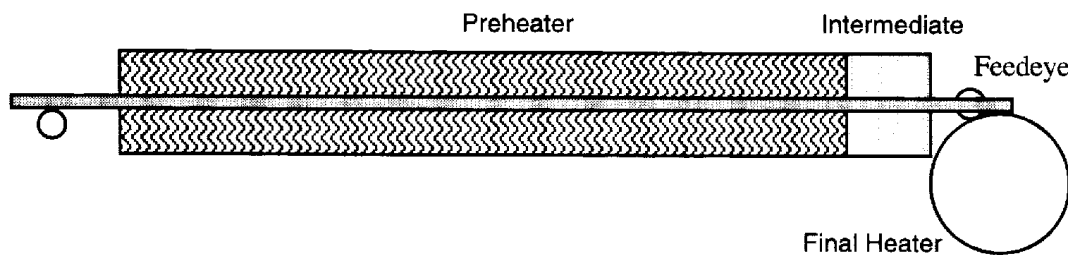


Fig. 5: Calculation model of the used heating system

The heating system model, similar to [4], is shown in Fig. 5. Intermediate is a section which can not be heated due to a geometrical constraint from the machine frame. It is simulated with the ambient temperature. The goal was to heat up the prepreg to 165-220 °C at the final heater due to a final melting temperature at 165 °C and initiation of degradation at 220 °C. One-dimensional heat analysis with a constant heat transfer coefficient was used. Even heating of the prepreg is assumed, see Fig. 6. Compensation for the thermocouple wire was included in the calculation. Material data for glass/PP with 40 volume percent glass has been used. An in-house software was used to solve the heat transfer problem. The effective heat transfer coefficient was found to be 19 W/m²°C using curve fitting on the measured temperature.

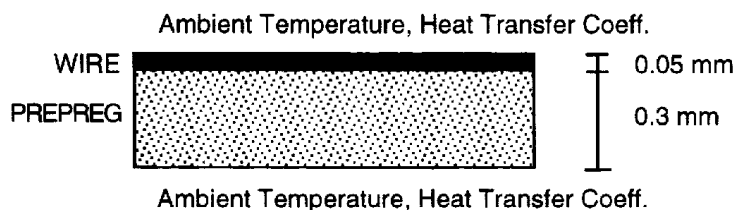


Fig. 6: Crosssection of prepreg and measuring wire with thermal boundary conditions

Calculation

Table 2: Heater process data

Heaters	0.15 m/s Prepreg Speed		0.4 m/s Prepreg Speed	
	Heater Length (mm)	Temperature (°C)	Heater Length (mm)	Temperature (°C)
Preheater	1500	380	2000	450
Intermediate	200	20	200	100
Final Heater	264	380	264	700

The heater data is in Table 2 with the results in Fig. 7. The heating system works good with a final material temperature of 170 °C. The calculation picks up the main behaviour. A cooling from ambient temperature air occurs at Intermediate. Heating occurs when the prepreg reaches the mandrel which is approximately simulated by the final heater.

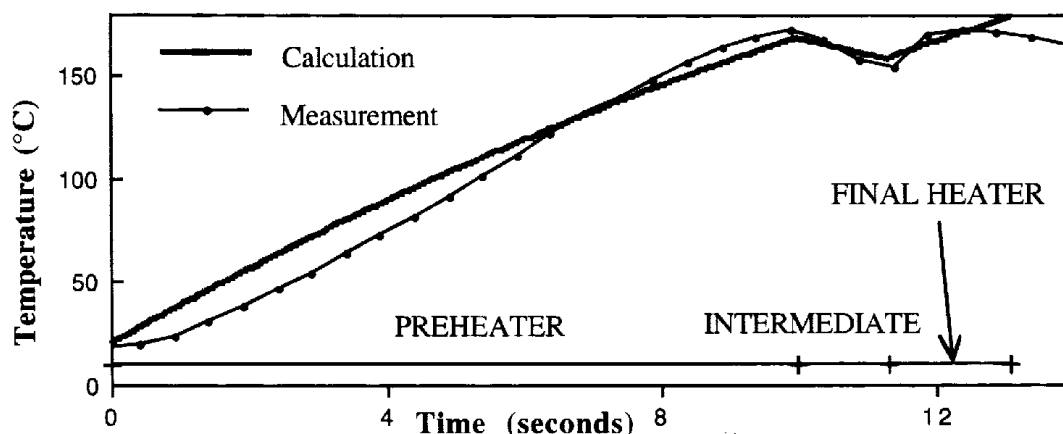


Fig. 7: Calculated and measured temperatures for 0.15 m/s prepreg speed

It was decided to increase the length of the preheater from 1500 mm to 2000 mm by adding two more heater elements. The calculation at 0.4 m/s was made with this longer preheater, see Table 2. Calculated results without thermo-couple are in Fig. 8. The heating system works good with a final material temperature of 165 °C which is the lowest acceptable value. The speed limit for the used heating system is hence concluded to be around 0.4 m/s.

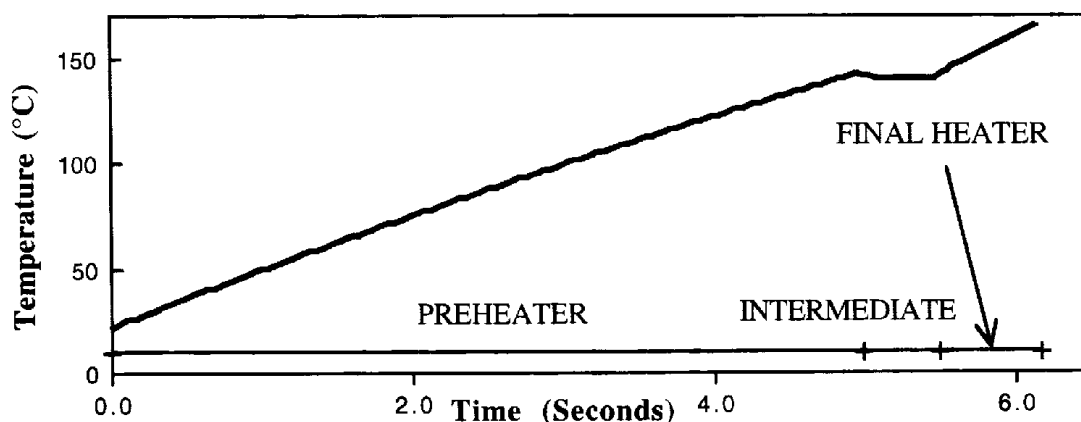


Fig. 8: Calculated temperature for 0.4 m/s prepreg speed

PIPES

Procedure

Unheated metal mandrels were used for all pipes. A thin layer of Mylar was wrapped around the mandrels before winding to give some thermal isolation from the cold metal surface. The mean fiber fraction of the pipe samples was gained from weight measurements according to ASTM D2584. Image analysis was used to measure the void content. Some initial hoop ($\pm 90^\circ$) pipes were made with the TUT-material to test the equipment and procedures. Fiber fraction, void content and local in-phase fiber buckling were studied. It was found that the achieved fiber fraction was largely unaffected by the studied process parameters. Pipes with a combination of speed, temperature and prepreg tension which indicated full melting and good compaction, showed negligible fiber buckling.

Hoop Pipes

A Plytron quality with 26 % fiber fraction by volume was used. 4 mm thick, \varnothing_i 84 mm hoop ($\pm 90^\circ$) pipes were manufactured to check the speed limit of the equipment, see pipe 1-3 in Table 3. Tension is the prepreg tension at the feed eye defined as a force, preheater and final heater is the temperature in the IR-elements, v_f is fiber volume fraction and v_v is void content. Excessive fuzz at the feedeye was generated for speeds lower than 0.2 m/s. The explanation is probably that the sliced Plytron sheet contained broken fibers. The Plytron prepreg contains zero voids as raw material. The measured void content in the thin walled pipe can hence be expected to be an indirect measure of the pipe quality since bad melting between layers will show as voids in the Image analysis. The void content increases with the winding speed and are as expected located between the Plytron bands. The results indicate that a winding speed around 0.4 m/s can be used with this heating system.

Table 3: Process data for pipes

Pipe	Angle ($^\circ$)	Prepreg Speed (m/s)	Tension (N)	Preheater ($^\circ$ C)	Final Heater ($^\circ$ C)	v_f (%)	v_v (%)	Material
1	± 90	0.2	10	420	500	28.1	0.4	Plytron
2	± 90	0.35	10	420	500	25.4	0.8	Plytron
3	± 90	0.5	10	420	500	25.8	1.0	Plytron
4	± 70	0.3	10	420	500	26.4	2.0	Plytron
5	± 30	0.35	12.5	420	500	43.2	*	TUT
6	± 15	0.35	12.5	420	500	34.0	*	TUT

*High void content.

Helix Pipes

A mandrel with dome ends was used. Plytron could not be used for low angle helix pipes due to fuzz creation at the feedeye. 2 mm thick, \varnothing_i 50 mm pipes with varying angles were manufactured to check the capacity to wind low angles, see pipe 4-6 in Table 3. The laminate quality of pipe 5 and 6 is poor due to bad consolidation in combination with crossovers in the wound band pattern. Some degradation in the material quality for low angle helix layers can however be accepted in a pressure vessel with a liner.

PRESSURE VESSEL

Mechanical Analysis Model

ABB Plast produces composite pressure vessels with thermoplastic liners. One type is a wet filament wound carbon/epoxy, 3.4 l volume, vessel with a burst pressure of more than 1000 bar. The intention with this project is to manufacture a demonstrator prototype with glass/PP reinforcement derived from this carbon/epoxy vessel. The prototype will have a much lower

burst pressure than the carbon vessel due to lower fiber fraction, weaker reinforcing fibers, lower transverse strength and thinner wall thickness. Pressure vessels are normally designed to have a similar strength of the cylindrical part and the dome. The strength in the centre of the cylindrical part is easy to calculate with laminate theory and is here used to estimate the vessel strength. The analysis indicates that transverse stresses are high so transverse micro cracking is likely to occur. The micro cracking will change the stress distribution in the vessel. This is simulated by using a low transverse modulus in the calculations (netting analysis) to predict the ultimate burst pressure for the vessel.

- Lay-up: 1.5 mm, 90 °
- 2.0 mm, ± 15 °
- 0.5 mm, 90 °
- 2 mm liner
- Outer radius of liner: 44 mm
- Calculation load: 100 bar internal pressure

Mechanical Analysis

The results are in Table 4. Index *x* is fiber direction and *y* is transverse direction. *U* denotes uncracked laminate and *C* denotes cracked laminate. The stress in the fiber direction is 245 MPa for the micro cracked laminate with the TUT material. The cylindrical part should hence burst through failure of the hoop layer at 600/245*100 = 245 bar internal pressure. The stress in the fiber direction is 251 MPa for the micro cracked laminate with the Twintex material. The cylindrical part should hence burst through failure of the hoop layer at 263 bar.

Table 4: Laminae stresses in cylindrical part

Material	± 15° Winding Angle			± 90° Winding Angle		
	σ _x (MPa)	σ _y (MPa)	τ _{xy} (MPa)	σ _x (MPa)	σ _y (MPa)	τ _{xy} (MPa)
TUT (U)	96	25	2	207	16	0
TUT (C)	112	4	3	245	2	0
Twintex (U)	95	28	3	205	17	0
Twintex (C)	113	3	3	251	2	0

Liner

The main function of the liner is to prevent leakage during operational service. The liner is 2 mm thick and made of a fatigue and temperature resistant thermoplastic material. The melting temperature is in the same range as the process window for PP. The elastic modulus at room temperature is about 100 MPa. The liner was filled completely with water before the winding started. The reason is that the water will act as a heat sink and cool the inner surface of the liner during winding. Any risk of melting the liner is hence erased. It was found that the cooled liner is sufficiently stiff to enable fast winding despite the added water weight.

Manufacturing

Prototype pressure vessels made from the TUT-material were manufactured see Table 5. Tension is the prepreg tension at the feed eye defined as a force, preheater and final heater is the temperature in the IR-elements. *v_f* is fiber volume fraction in the cylindrical part and weight is pressure vessel weight. Remark HG is two stationary heat guns placed at the dome ends. The achieved fiber volume fraction is similar to the prepregs. 5 crossover positions was used for the helix layer to improve the packing around the dome. It was difficult to obtain a good helix winding pattern around the dome for vessel 1 since the material is rapidly consolidated when it is laid down leading to thickness growth and tow gaps. This is in contrast to wet filament winding where stretching of the fibers is obtained for a full helix path. Two stationary 2000 W heat guns were hence placed at the dome ends for vessel 2 and 3 to ensure full melting at this position during the completion of the helix winding path. This process change significantly improved the fiber compaction at the dome.

Table 5: Process data for pressure vessels

Vessel	Prepreg Speed (m/s)	Tension (N)	Preheater (°C)	Final Heater (°C)	v_f (%)	Weight (kg)	Remarks
1	0.2	20	420	600	44.8	1.72	
2	0.25	20	420	500	43.8	1.72	HG
3	0.33	20	420	500	45.0	1.77	HG

Pressure Testing

The vessels were filled with water and placed in an enclosed chamber. An hydraulic equipment was used to slowly increase the pressure. Pressure versus time was recorded. The result are in Table 6. Noise pressure is the pressure when significant noise is heard indicating initiation of micro cracks. Burst pressure is the highest recorded pressure. Failure mode is either a burst dome end or a burst cylindrical part. Vessel 1 is of poor quality. Severe micro cracking of the dome ends are initiated at 20 bar. The burst pressure is only 107 bar with a failure at the dome. Micro cracks could not be observed at the cylindrical surface. Vessel 2 and 3 are much better. Noise generation is initiated at 130 bar. A burst cylindrical part is achieved for vessel 2 at 220 bar. This agrees well with the calculated value of 245 bar. Vessel 3 has a lower strength since the dome is burst. This is probably due to the use of higher winding speed during manufacturing.

Table 6: Test data for pressure vessels

Vessel	Noise Pressure (bar)	Burst Pressure (bar)	Failure Mode	Remarks
1	20, 35 +	107	Dome	No micro cracks in cylinder
2	130, 160 +	220	Cylindrical	Liner not leaking
3	130, 160 +	179	Dome	Liner leaking

CONCLUSIONS

A prototype thermoplastic pressure vessel have been developed. Winding speeds around 0.3 m/s has been used. The practical speed limit of the heating system is 0.4 m/s which is close to the machine limit for low angle winding. Prototype pressure vessels made from new qualities of the Twintex and Plytron materials will be manufactured and tested in the future.

ACKNOWLEDGMENTS

This work has been supported by the Nordic Industrial Fund (NI) and the Swedish National Board for Industrial and Technical Development (NUTEK). A special thank to Per-Morten Hansen at the Borealis company in Norway.

REFERENCES

1. Lauke B. and Friedrich K., "Evaluation of Processing Parameters of Thermoplastic Composites Fabricated by Filament Winding", *Composites Manufacturing*, Vol. 4, No. 2, 93-101 (1993).
2. Halpin J. C. and J. L. Kardos. 1976, "The Halpin-Tsai Equations: A Review," *Polymer Engineering and Science* 16(5):344-352.
3. St. John C., "Co-mingled Thermoplastic Prepregs Industrial Applications", *Proceedings of the Tenth International Conference on Composite Materials*, Whistler, Canada, August 14-18, III, 757-764 (1995).
4. Lee S. Y., Springer G. S., Arding T. and Eklund M., "Preheating Filament Wound Tows", *36th International SAMPE Symposium*, USA, April 15-18, 771-777 (1991).

INNOVATIVE APPLICATIONS WITH THERMOPLASTIC FILAMENT WINDING TECHNIQUES

R. Funck ¹, M. Neitzel ² and O. Christen ²

¹ *COMAT Ltd., Erwin-Schrödinger-Straße 58, 67663 Kaiserslautern, Germany.*

² *Institut für Verbundwerkstoffe GmbH, Erwin-Schrödinger-Straße 58,
67663 Kaiserslautern, Germany.*

SUMMARY: Filament winding is one of the most challenging technologies when axisymmetrical or even unsymmetrical composite structural shells have to be produced with continuous fibre reinforcement. This paper presents thermoplastic filament winding techniques which is an advanced method of the standard filament winding process developed for thermosets. It has the potential to overcome the drawbacks of conventional filament winding. It offers the option to achieve consolidation during the process which eliminates the need for any post consolidation processing. Studies found that thermoplastic filament winding can be more cost effective than thermoset winding.

Thermoplastic filament winding generating three dimensional shapes with continuous reinforcement following the load paths will be discussed in this paper. The feasibility of this technique is demonstrated by discussing experimental results and applications.

KEYWORDS: filament winding, thermoplastic, direct flame processing head, bicycle frame, electric motor, pressure vessel

INTRODUCTION

Thermoplastic composite materials offer a number of advantages as high fracture toughness, unlimited shelf life, recyclability, and continuous processing by avoiding the curing cycles which are characteristic for thermoset matrix composites. In addition to favourable mechanical properties thermoplastics offer a wide range of manufacturing options. Recent interest in advanced thermoplastic composites has been spurred by the promise of higher manufacturing productivity, increased quality and improved material properties.

PROCESSING HEAD

One promising thermoplastic processing method is the direct flame filament winding. Therefore a unique thermoplastic direct flame (TDF) winding head has been developed.

For direct flame processing (Figure 1) of thermoplastic matrix filament wound composites the tape supply, the tape brake and process control system are mounted on the support of the filament winding device. The TDF winding head including the heat source is installed on the

swivel axis. A mechanical brake is used to provide constant tape tension to achieve good consolidation.

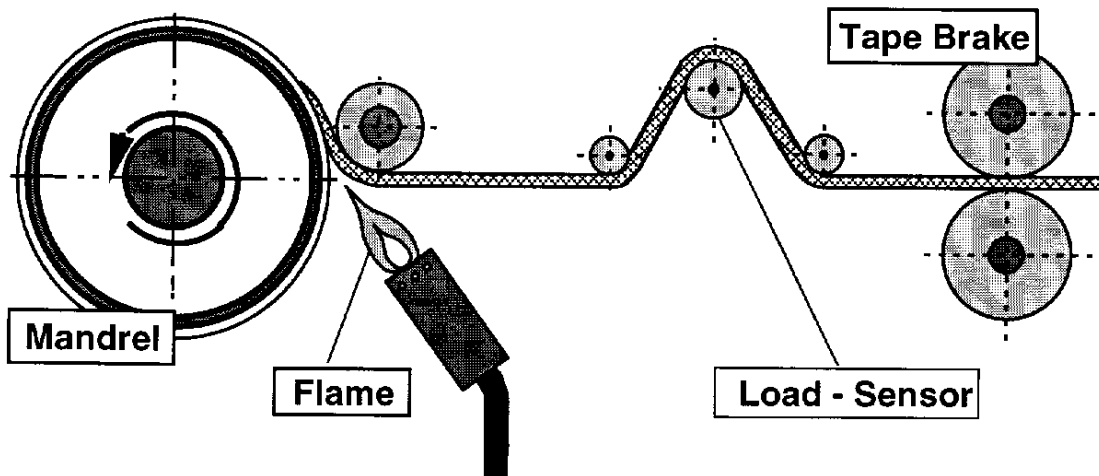


Fig. 1: Thermoplastic direct flame (TDF) processing scheme

The universal TDF winding head can easily be retrofitted to existing winding machines without any additional investment (Figure 2). The capability of the winding head has been demonstrated by manufacturing of various applications as described in this paper. Winding angles between 0° and 90° were realised. Any commercial tape material can be processed. The application of the compaction shoe is optional and depends on part geometry and winding angles.

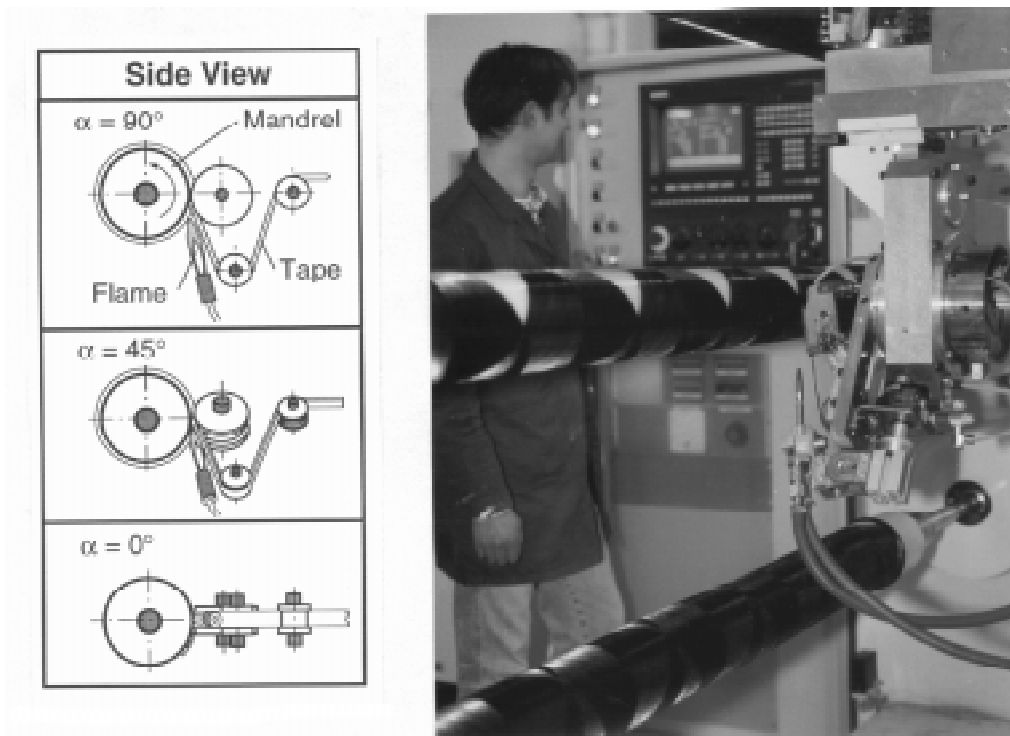


Fig. 2: TDF winding head positions

The TDF winding head incorporates a direct flame torch which gives the energy input to the tape achieving in-situ consolidation. In order to prevent matrix degradation if the winding process stops, the direct flame torch is attached to a pneumatic swivelling arm. The torch is in parking position during the process stops and turns into working position as soon as the winding process starts again.

The main objective is to generate an adequate melt zone of the thermoplastic matrix to obtain proper bonding between tape and consolidated laminate. This can be managed by focusing the flame and melting the matrix on the top surface of the laminate and the surface of the incoming prepreg tape simultaneously. The torch is directed exactly to the contact point.

BICYCLE FRAME

Composite bicycle frames for high-performance sports are predominately manufactured by filament winding or roll wrapping using thermosetting matrices. First attempts to use thermoplastic matrices speak in favour of this replacement. The main arguments for the introduction of thermoplastic composites into the road and racing bike market are: inherent vibration damping characteristics, high impact resistance, low environmental emission during processing, greater ease of recycling, possibility of thermal post-forming, absence of curing cycles and unlimited storage life of the semifinished products [1, 2].



Fig. 3: Thermoplastic filament wound bicycle frame

On the basis of manufacturing bicycle frames it is demonstrated that thermoplastic filament winding is a challenging approach for producing high-quality structural components. Finite element analysis was used to design two different bicycle frames, a conventional diamond-frame (Figure 3) and a frame with a suspending rear arm. Prototypes of both frames were manufactured using a soft flame process. Winding angles down to 17°, wall thicknesses

between 1.0 mm and 2.4 mm and speeds up to 8 m/min were realised working with a cold mandrel. In order to obtain smooth surfaces, an improved post processing technique using a compression belt was applied. Determination of the damping behaviour indicate that using thermoplastic reinforced tubes the damping properties can be improved by 8% versus thermoset tubes [3].

ELECTRIC MOTOR

The reinforcement of a 1,5 MW electric motor is manufactured using the TDF winding process (Figure 4). Such electric motors drive the German ICE trains. The electric motor incorporates 2 hoop wound rings, directly wound on the short circuit rings.

The maximum power of the electric motor was about 1 MW at 4000 revolutions per minute without the reinforcement. After increasing the number of revolutions the short circuit rings deformed unacceptable. By reinforcing the rings with carbon fiber reinforced polyetheretherketon (CF/PEEK) tape using the direct flame tape laydown the number of revolutions has been increased up to 6000 which results in 1,5 MW power. The testing of the motor in conjunction with optical microscopy indicates that high quality is achieved.

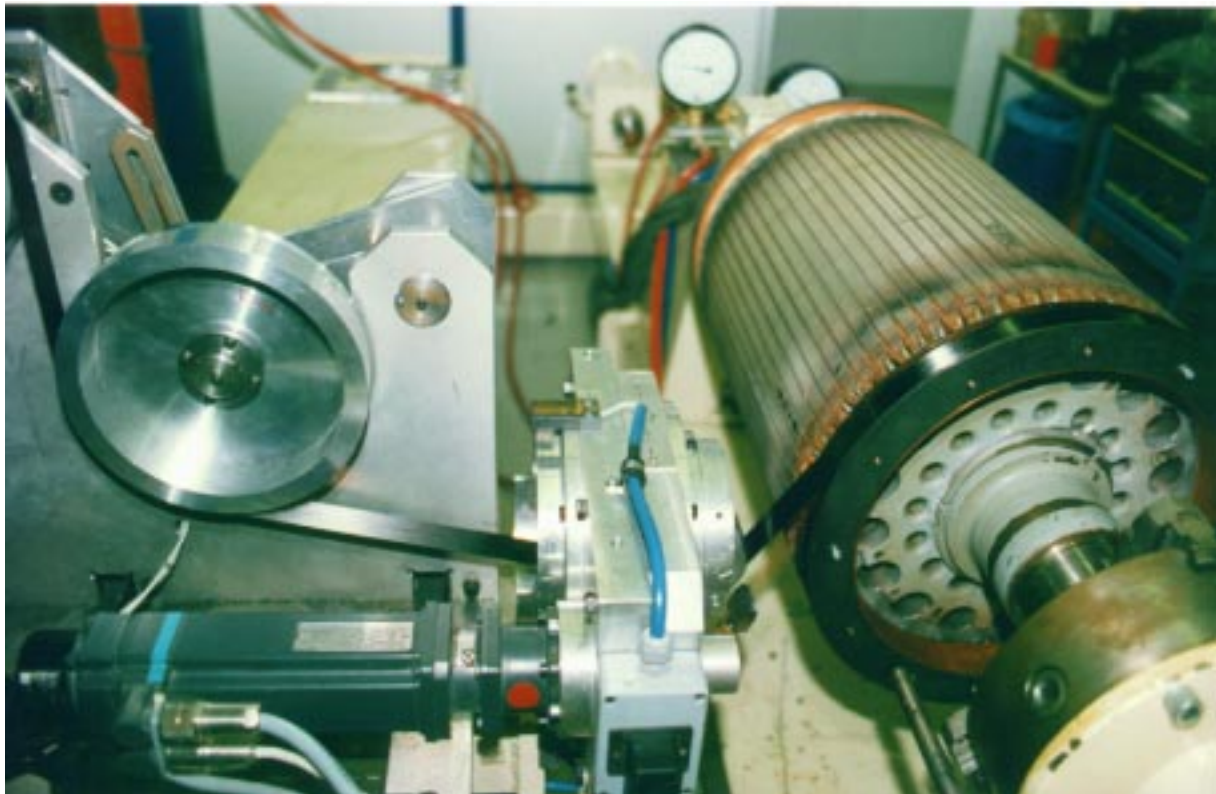


Fig. 4: Reinforcement of a electric motor

LOW PRESSURE VESSEL

Filament winding can make a significant contribution to fuel economy by reducing the dead weight of steel containers that are currently used as fuel tanks, air supply for hydraulic accumulators, operating hydraulic valves, etc.. For such applications the feasibility of using

TDF winding in conjunction with PP/GF tape (Trade name: PLYTRON® / Supplier: Borealis) was proven by fully overwrapping a blow moulded liner (Figure 5).

The structure of the reinforcing laminate of the pressure vessel was designed and programs for the computer numerical controlled winding process were developed. To demonstrate feasibility, samples of different vessel types were manufactured on a seven-axis gantry winding machine.

The vessels were hydraulically tested. The target burst pressure of 40 bar from the full composite vessel was exceeded by 22 %. The full composite vessel reduces the dead weight of a steel vessel by 55 % and enhances the safety failure mode [4].

The investigations show, that TDF winding offer new possibilities in manufacturing full composite pressure vessels.

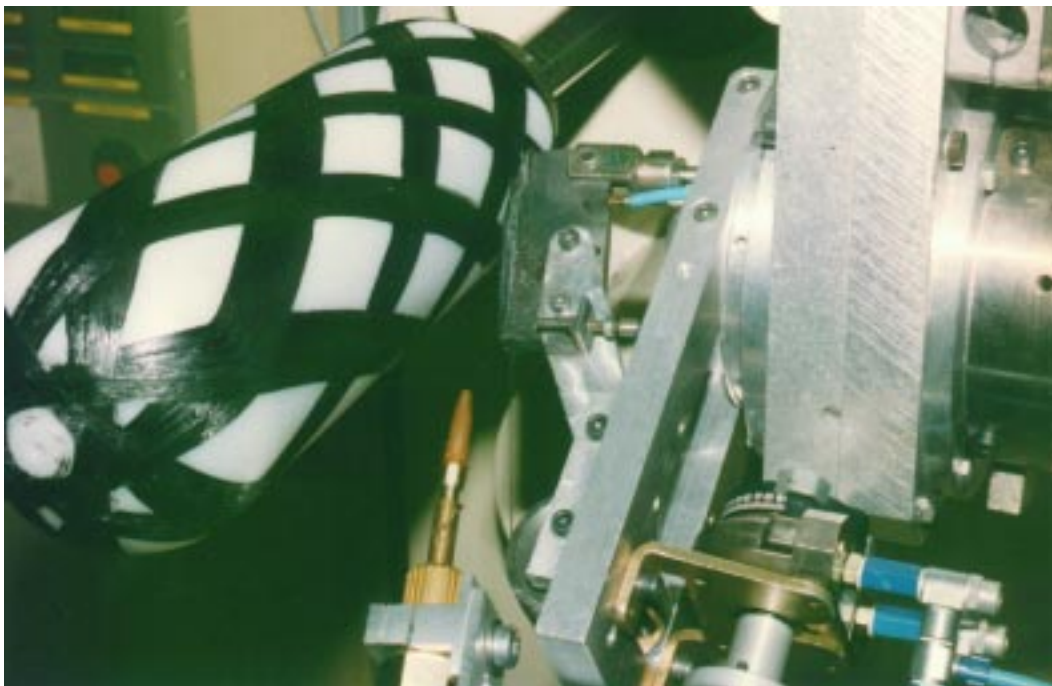


Fig. 5: Helical winding of fiber reinforced thermoplastic tape with TDF head

HIGH PRESSURE VESSEL

Thermoplastic reinforced composite pressure vessel for storage of compressed natural gas (CNG) are available on the German market. They are made of oil-quenched and tempered chromium-molybdenum powder coated steel, reinforced with an aramid fiber in the cylindrical section.

Such cylinders are used as gas storage for city buses. 7 gas cylinders (each has a volume of about 165l) are fixed on the roof of the bus (Figure 6) and operate at a pressure of 200bar which gives a operating capacity of 300 km [5]. The light weight cylinder is used in order to increase the driving behaviour of the bus without changing the bus design.

For manufacturing such light weight CNG cylinders the unique thermoplastic direct impregnation (TDI) process has been developed. The main objective of this development is to reduce the material costs by impregnating the fibers during the winding process. First experiments using the TDI process (Figure 7) show that reasonable impregnation quality can be achieved.



Fig. 6: Compressed natural gas (CNG) cylinder with hoop wound fiber reinforced thermoplastic tape

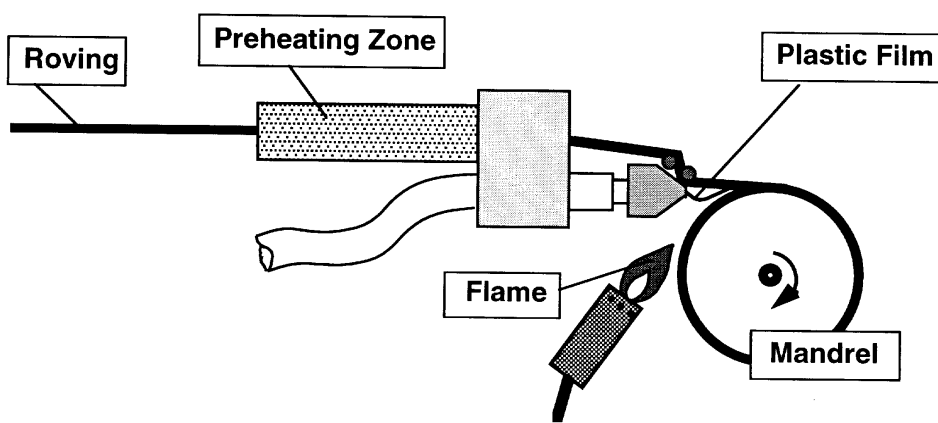


Fig. 7: Thermoplastic direct impregnation (TDI) processing scheme

CONCLUSION

This paper illustrates important methods for processing thermoplastic composite materials by filament winding. On the basis of various applications it is demonstrated that thermoplastic filament winding is a challenging approach for producing high-quality components.

A thermoplastic direct flame (TDF) winding head which can easily be retrofitted to all existing winding machines has been demonstrated.

Bicycle frames were manufactured using carbon fiber reinforced polyamide tubes with winding angles down to 17°, wall thicknesses between 1.0 mm and 2.4 mm. In order to obtain smooth surfaces, a patented post processing technique using a compression belt was applied. Electric motors were reinforced in order to increase the number of revolutions and full thermoplastic pressure vessels were manufactured by helical winding of glass fiber polypropylene tape. Also a thermoplastic direct impregnation (TDI) process has been developed in order to hoop wind light weight CNG cylinders.

All these investigations confirm, that thermoplastic winding offers new possibilities in manufacturing light weight components.

REFERENCES

1. L. Lessard, J. Nemes and P. Lizotte: Utilization of FEA in the design of composite bicycle frames. *Composites* 26 (1), (1995), p. 72-74.
2. M. Gruber: Filament Winding of Reinforced Thermoplastics. *Polymer Composites*, U.S. Department of Commerce (1990), p.121-128.
3. R. Funck, ; M. Neitzel: Challenge of Thermoplastic Composites for Bicycle Frames. *Proc. 4th Japan International SAMPE Symposium, Tokyo, September 25.-28. (1995)*, p. 1309-1314.
4. R. Funck: Entwicklung innovativer Fertigungstechniken zur Verarbeitung kontinuierlich faserverstärkter Thermoplaste im Wickelverfahren. *Fortschritt Berichte VDI* (1996), Reihe 2: Fertigungstechnik, Nr. 393
5. C. Düren, I. von Hagen, G. Junker, E. Lange, C. Rasche: Applications of Thermoplastics Reinforced with Unidirectional Fibers in the Manufacture of Composite Vessels. *The 3rd Biennial Int. Conf. & Exhibition on Natural Gas Vehicles, Conference Proceedings, Göteborg (1992)*, p. 473-500,

DEVELOPMENT OF A COMPOSITE FAIRING BAND ASSEMBLY FOR A STAINLESS STEEL SONAR DOME

Tamunoiyala S. Koko¹, Milton J. Connor² and Garry V. Corbett³

¹*Martec Limited, 1888 Brunswick Street, Suite 400, Halifax, N.S., Canada, B3J 3J8*

²*Composites Atlantic Limited, 71 Hall Street, Lunenburg, N.S., Canada, B0J 2C0*

³*DMSS 7-3-5, National Defence Headquarters, Ottawa, ON, Canada K1A 0K2*

SUMMARY: This paper describes investigations carried out to replace the stainless steel fairing band assembly components (including the fairing band, tail cap, and fasteners) for the C5 hull mounted sonar dome, with composite material. The study was motivated by the need to eliminate corrosion damage associated with the use of the stainless steel components. The investigation focused on material selection, component design, tooling and fabrication requirements for each of the components. It was shown that the fairing band assembly components could be fabricated from glass-epoxy composite materials using simple fabrication techniques such as hand layup and fasteners made of GRP material could be used to replace the non-critical stainless steel fasteners.

KEYWORDS: hull mounted sonar dome, fairing band, composite fasteners, glass reinforced plastics (GRP)

INTRODUCTION

This paper describes investigations carried out to replace the current fairing band assembly components of the C5 sonar dome with composite material. The dome has an aerofoil shape in plan and is approximately 4 m nose to tail, 1.3 m wide and 1.8 m high. Figure 1(a) shows a side view of the dome-hull interface. The dome is fastened to the flange of the dome spacer in the hull structure. The fairing band assembly is used to wrap around the dome-hull interface to provide a smooth surface, as shown in Figure 1(b), to reduce turbulence and noise. The existing fairing band assembly, comprising of the fairing band, tail cap and fasteners, is made of stainless steel material. In the presence of moisture, a cathodic corrosion mechanism is created between the stainless steel fairing band components and the mild steel dome spacer. The resulting corrosion ruins the mounting threads in the dome spacer which causes loss of the tail cap and fairing band. This requires the ship to be brought to dry dock, to perform appropriate corrective measures, thereby increasing the maintenance cost and reducing the operational readiness of the ship.

Because of their excellent corrosion resistant properties composites material are considered as suitable replacement materials for the stainless steel material to eliminate the corrosion problem. This study was undertaken to investigate the feasibility of using composite materials for the fairing band components. The investigations carried out to design and fabricate the composite fairing band, tail cap and fasteners are described in the following sections. Descriptions of the stainless steel components are first provided then, for each

component, investigations on the composite material selection, design and the tooling and fabrication requirements are provided. The challenges and lessons learned are also discussed.

DESCRIPTION OF STAINLESS STEEL COMPONENTS

Fairing Band

The fairing band is used to wrap around the sonar dome-to-hull interface, as shown in Figure 1, to provide a smooth surface in order to minimize flow disturbances. Figure 2 shows details of the fairing band. It is made of a stainless steel band which is 4.43 m long, 0.14 m wide and 0.89 mm thick. At one end of the fairing band is a latch block which fits into the front end of the dome-spacer in the hull structure. At the other end of the fairing band is a guide block which fits into the aft end of the dome spacer. The latch block and the guide block are fastened to the dome spacer by means of the fasteners designated as Types A and B. The fasteners are described below. Along the length of the band are seven space bars 19.05 mm x 9.525 mm x 73.025 mm welded to the band as shown in Figure 2. At the top and bottom of the band are 25.4 mm wide rubber gaskets for sealing the band against the hull and the dome. The stainless steel band can coil into a roll of approximately 0.914 m diameter for storage purposes.

Tail Cap

The tail cap component is a filler piece at the trailing ends of the fairing band to provide a smooth surface. Figure 3 shows the details of the tail cap component. It is made from a 200 mm x 140 mm x 0.89 mm stainless steel sheet formed to the shape of the dome at the aft end, as shown in the figure. The tail cap also consists of a stiffener and a solid bar which houses the fastener holes, and is attached to the dome spacer by means of two fasteners designated as Type C, which are described below. Strips of 25 mm wide rubber gaskets are bonded to the top and bottom surfaces of the tail cap for sealing against the dome and hull.

Fasteners

Three types of fasteners designated as Types A, B and C are used to fasten the fairing band and the tail cap components to the dome spacer in the hull structure. The dimensions and details of the fasteners are shown in Figure 4. Fastener Type A fits into the latch block at the front end of the fairing band. It is 38 mm long with 12.5 mm diameter 13 UNC screws. Fastener Type B fits into the guide block at the aft end of the fairing band. This fastener is 76.2 mm long and is fully threaded with 12.5 mm diameter 13 UNC screw threads. Finally, fastener Type C is used to fasten the tail cap sub-assembly to the ship hull. The fastener is 31.75 mm long and has 9.4 mm diameter 16 UNC screws.

COMPOSITE MATERIAL SELECTION

Fairing Band

Three composite material systems with glass, Kevlar, and high strength polyethylene (HSPE) fibers and epoxy resins were considered. These composite systems have several advantages and disadvantages for the present application. However, the material selection was based on -

cost; water absorption characteristics; ease of fabrication; and experience in marine environment. As the band is not a major structural component, it was sufficient to base the material selection on the above criteria, since other design criteria such as tensile strength, are expected to be satisfied by all three composites. In Table 1 the three composite materials are compared based on the selected criteria. Property data from Refs 1 and 2 were used for the comparison. As shown in the table, glass reinforced plastic (GRP) had several advantages over the Kevlar-epoxy and HSPE-epoxy systems. Hence, GRP was selected for this application.

Tail Cap

Because of the advantages of glass reinforced plastic (GRP) composites highlighted above GRP was also selected for the tail cap component.

Fasteners

Investigations were carried out to select suitable materials for the fasteners to be used to attach the fairing band and trailing cap to the stainless steel dome and mild steel ship hull. The main thrust was to select a material which was compatible galvanically with stainless steel, mild steel, and GRP used for the dome, hull, and fairing band/trailing cap, respectively. In order to avoid corrosion between any two components of the fairing band assembly, fasteners made of glass reinforced plastics were selected. Rather than fabricate these fasteners in-house, it was decided to purchase them from suitable suppliers, since cost was a major concern in the execution of this project. Consequently, some composite fasteners manufacturers in the United States were contacted and information on the types and capabilities of composite fasteners were obtained. The tensile and shear strengths of some glass reinforced composite fasteners from Cherry Textron [3] are compared with those of stainless steel fasteners. The shear strength of the PEEK/LQ (polyetheretherketone with long continuous quartz fiber) fastener is close to that of stainless steel, and was hence considered suitable for fastener Types A and C which are mainly loaded in shear. However, the glass reinforced fasteners could not be used for the fastener Type B because of the very large torque required to keep the fairing band flat against the dome. Hence for the Type B fastener, stainless steel with teflon coating was recommended.

DESIGN OF COMPONENTS

The approach adopted was to retain, as much as possible, the shapes and sizes of the fairing band, guide block, latch block and spacers, and replace the stainless steel material with GRP. This was necessary to reduce the amount of modifications to the ship hull-dome interface to accommodate the composite fairing band assembly. The significance of this was to keep the cost of installing the composite fairing band assembly low.

Fairing Band

Dimensions

The fairing band consists of a four-layer GRP strip 4.43 m long, 0.14 m wide. The thickness of the strip was 1.05 mm, which compares to the 0.88 mm thickness of the stainless steel band. With this thickness, the composite fairing band was flexible enough to wrap around the

gentle curve at the front end (See Figure 1) without matrix cracking. The fairing band stops short of the sharp curve at the trailing end. It is the tailing cap component which fits over this sharp curve (Figure 1). Two 25 mm wide strips of neoprene material were bonded to the top and bottom of the band on the inside face.

The guide block, latch block and spacer bars are constructed of GRP material and fabricated integrally and co-cured with the GRP fairing band to avoid secondary bond lines which would serve as areas of weakness. The dimensions and locations of the seven spacer bars are exactly the same as for the stainless steel spacer bars (Figure 2). The dimensions and shape of the composite guide block at the aft end are similar to the stainless steel block. However, a smooth transition with a 12.5 mm minimum radius is provided between the fairing band and the guide block to reduce stress concentrations.

The shape and dimensions adapted for the composite latch block required modifications to the hull dome spacer structure but eliminates the need for load bearing composite fasteners (Type A) at the front end. The modifications to the dome spacer required welding two 71 mm x 0.125 mm x 9.5 mm mild steel blocks to the web stiffeners at the front end of the dome spacer structure to provide wedges for the L-shapes GRP latch blocks. A schematic representation is shown in Figure 5. The space between the two composite latch blocks is to be filled by a 25.4 mm x 25.4 mm x 71.3 mm GRP block which is fastened to the dome spacer by a 9.5 mm diameter Type C composite fastener.

Stress Analysis

Figure 6 illustrates schematically how the tensile load is transferred from the tensioning bolts to the fairing band. During installation, the fairing band subassembly is fitted into the dome spacer by sliding the guide block between the alignment rails on the aft-end of the dome spacer. The fully threaded bolt (Fastener Type B) is backed off as much as possible to enable the front half of the fairing band to be attached to the dome spacer via the latch block. Then a torque of 40-54 Nm is applied to the fully threaded fastener to keep the fairing band tight against the dome. The torque produces a force against the dome spacer structure, which is transmitted to the fairing band via the guide block. The tensile force produced in the fairing band was estimated, using simple fastener equations [4,5], to be approximately 14.2 kN. With a safety factor of 1.5 and a 20 percent reduction of strength due to potential material degradation, the composite fairing band was found to be adequate with a large margin of safety.

Tail Cap

The trailing cap sub-assembly was fabricated as a single piece using a female mold having the shape of the trailing cap. The GRP tail cap has the same dimensions as the stainless steel cap. The main body of the tail cap consists of 4 plies of plain weave glass/epoxy prepreg. This provided a wall thickness of 1.05 mm which is close to the thickness of the stainless steel cap. The solid interior section consists of about 100 layers of plain weave GRP material.

Fasteners

Fastener Type A

The Type A fasteners fit into the latch block at the front end of the fairing band. However, with the modifications adapted for the composite latch block geometry there was no more need for the this fastener. The design required a 9.5 mm diameter GRP fastener to hold the GRP spacer block in between the two fairing band as illustrated in Figure 5. This fastener which is similar to the Type C fastener, did not carry any substantial loads and was designed only for nominal loads. Using the PEEK/LQ material and 9.5 mm diameter fasteners, the shear and tensile capacities of the bolt at installation are 25.8 kN and 13.4 kN, respectively. The fastener was treated with an adhesive thread locker to prevent it from backing off after installation.

Fastener Type B

The Type B fastener fits into the guide block at the aft end of the fairing band. This fastener was loaded mainly in tension. By the application of a torque, the fastener presses against the dome spacer structure. The axial load induced in the fastener is transferred to the fairing band via the guide block as illustrated in the free body diagram in Figure 6. The more torque applied the more the axial force and hence, the tensile force in the fairing band. The installation of the stainless steel fairing band assembly required a torque of 40-54 Nm to keep the fairing flat against the dome. A requirement for the design of the composite fairing band assembly was to provide a similar load in the fairing to ensure it stayed flat against the dome.

The torque capacity of the PEER/LQ fastener was approximately 8-10 Nm, which was significantly lower than the torque needed to induce the required tension in the fairing. In order to provide the required tension in the fairing band, stainless steel bolts with teflon coating were recommended for the Type B fasteners. The internal threads in the guide block were fabricated integrally with the fairing band by laying up the GRP on removable threaded inserts. Thus the threaded part of the teflon coated stainless steel fasteners was in contact with threaded GRP material in the guide block. Only the tip of the fastener contacted the mild steel spacer dome structure. The teflon coating on stainless steel bolt would reduce the likelihood of the generation of current between the dome spacer and the tip of the bolt, thereby reducing the possibility of corrosion damage to the fastener tip. The integrity of the threads in the GRP guide block was investigated by a simple pull-out test. Details of the experimental setup are provided in [6]. The threads sustained tensile loads greater than 34 kN without failure.

Fastener Type C

The Type C fasteners are used to fasten the tail cap sub-assembly to the ship hull. This fastener does not carry any substantial load and was hence designed for nominal loads. However, it should be noted that these fasteners screw into threaded holes in the mild steel spacer structure and have caused the most frequent corrosion damage. Hence a fastener made of composite material was essential. The PEEK/LQ fastener was used. The shear and tensile capabilities are respectively, 25 kN and 13 kN which wee adequate to hold the tail cap in place. The fastener was treated with an adhesive thread locker to prevent it from backing off after installation.

TOOLING AND FABRICATION

Fairing Band

The fairing band was fabricated from four piles of plain weave E-glass epoxy prepreg laid-up on a solid tool surface and cured with a pressure plate for even pressure distribution during cure. The flat bars, latch blocks, and guide blocks were integrally fabricated from many layers of the same material compacted and incorporated in the main lay-up. The dimensions and configurations were in accordance with the design presented above. The GRP fairing band was treated with a polyurethane coating to reduce the water absorption by the composite material. Also, a two coat antifouling agent was applied to reduce marine growth during service.

Tail Cap

The tail cap was fabricated from plain weave E-glass epoxy prepreg with the main body consisting of 4 plies, and a solid interior section consisting of a stack-up of many plies integrated with the main external plies. A female mold was used to lay up the tail cap. The two fastener holes in the tail cap were integrally fabricated using removable threaded plugs.

Fasteners

Since the fasteners were obtained from suppliers, there were no tooling or fabrication requirements for the fasteners in this study. The fastener holes in the fairing band and tail cap were integrally fabricated using removable threaded inserts as discussed in the previous two subsections.

SUMMARY

This report has provided a description of a study to replace the stainless steel fairing band assembly components (including the fairing band, tail cap, and fasteners) for the C5 hull mounted sonar dome, with composite material. The investigation focused on material selection, component design, and tooling and fabrication requirements for each of the components. Glass epoxy was selected as the replacement material to eliminate the corrosion problem associated with the use of the stainless steel components. The fairing band assembly components were fabricated from plain weave E-glass epoxy composite material using a simple fabrication technique such as hand lay up. Glass epoxy based composite fasteners were used to replace the stainless steel fasteners which sustained only nominal loads. However, it was not feasible to replace the high load-carrying stainless steel fasteners with composites fasteners because of their low torque capacities.

REFERENCES

1. Pussegoda, N., MacDonald, D., Murphy, J.G. and Malik, L., "The Effect of Environmental Exposure on the Properties of High Strength Polyethylene (HSPE) Fibre Composites," DREA CR/93/450, January 1993.
2. Niu, M.C.Y., Composite Airframe Structures, Practical Design Information and Data, ConmiLit Press Limited, Hong Kong, 1993.

3. Anon, Cherry Textron Technical Data on Advanced Composite Products, California, 1996.
4. Shigley, J.E. and Mitchell, L.D., Mechanical Engineering Design, 4th Edition, McGraw Hill Book Company, New York, 1983.
5. Langhner, V.H, and Hargan, A.D., Handbook of Fastening and Joining of Metal Parts, 1st Edition, McGraw Hill Book Company, New York, 1956.
6. Koko, T.S. and Connor, A.D., "Composite Fairing Band Assembly for the C5 Hull-Mounted Sonar Dome", Martec Report No. TR-96-23, Halifax, September 1996.

<i>Table 1: Comparison of Candidate Fairing Band Composite Materials</i>			
Property	Material System		
	GRP	Kevlar/Epoxy	HSPE/Epoxy
Water Absorption (Sea Water)(%)[1]	0.19	<1.0	0.32
Relative Cost *	1.00	4	> 4
Ease of Fabrication **	Good	Poor	Poor
Experience in Marine Environment	High	Low	Low

* Cost of fibre relative to E-glass [2], for comparison only

** Bonding between fiber and resin

<i>Table 2: Tensile & Shear Strengths of Stainless Steel & Selected Composite Fasteners [3]</i>				
Property	PEEK/L Q	Epoxy/L G	PEI/L G	Stainless Steel
Shear Strength, ksi	53	24	45	50
Tensile Strength, ksi	27	16	25	73

Notes:

PEEK/LQ = Polyetheretherketone with long (continuous) quartz fiber

Epoxy/LG = Epoxy with long (continuous) glass fiber

PEI/LG = Polyetherimide with long (discontinuous) glass fiber

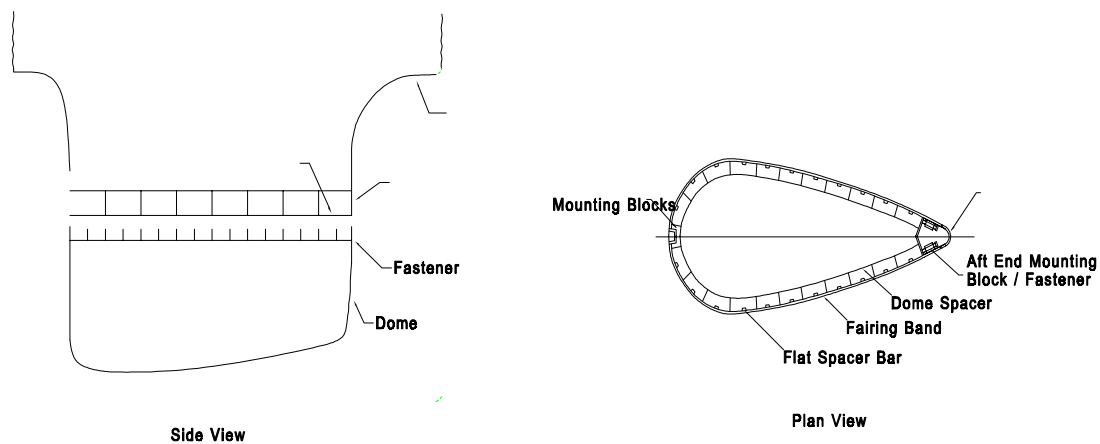


Figure 1: Dome-Hull Interface

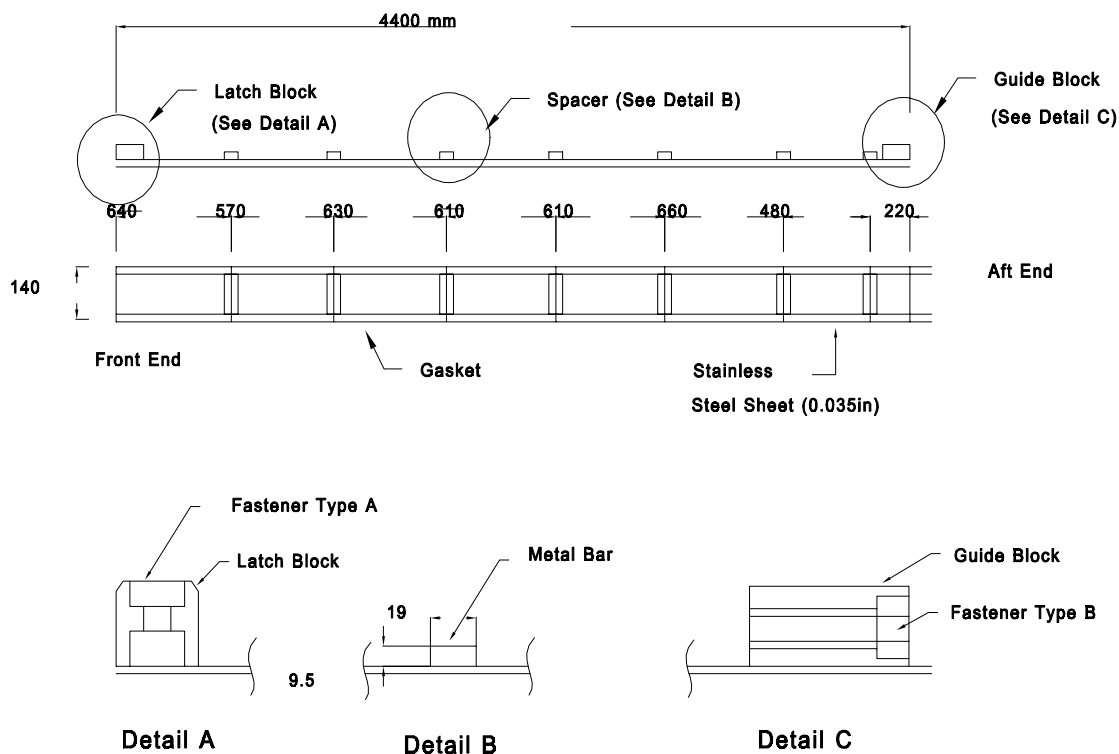


Figure 2: Details of Stainless Steel Fairing Band Assembly

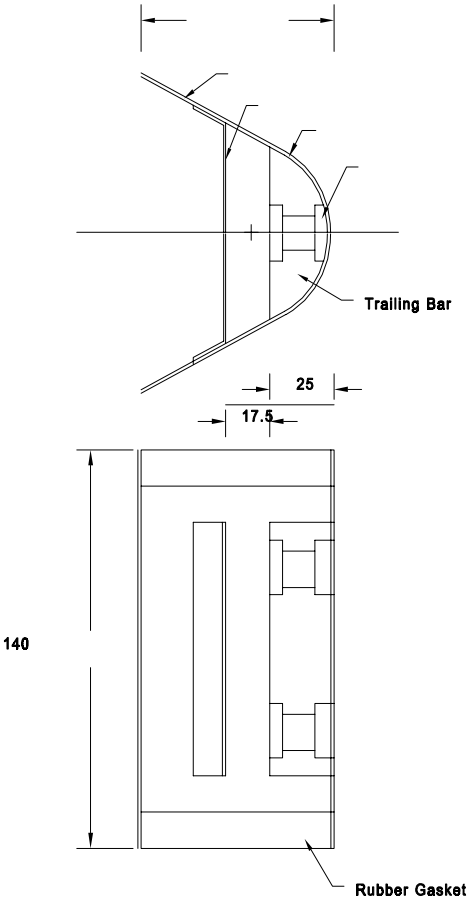


Figure 3: Stainless Steel Tail Cap

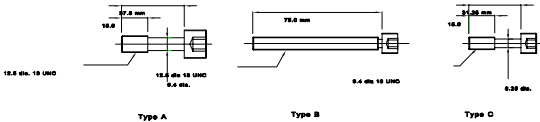


Figure 4: Stainless Steel Fasteners

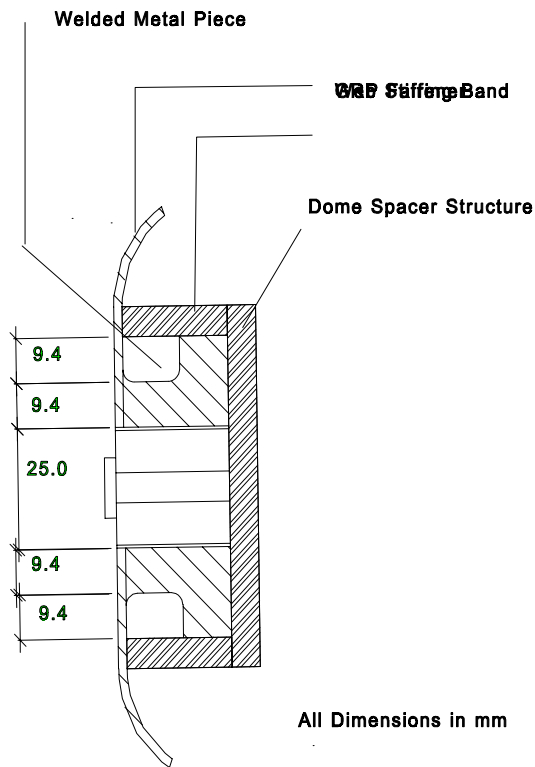


Figure 5: Modified Latch Block

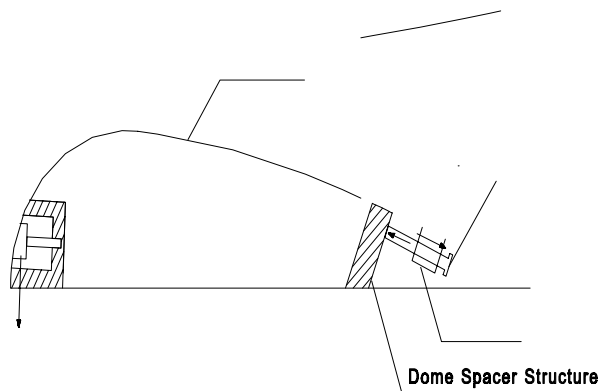


Figure 6: Load Transfer from Tensioning Bolt to Fairing Band

DESIGN OPTIMIZATION OF CENTRIFUGAL ROTOR OF COMPOSITE MATERIALS

Sung Kyu Ha¹, Jong Kweon Park², Young-Ho Kim¹ and Young-Soo Cho¹

*1Dept. of Mech. Design and Production Eng., Hanyang University
#17 Hangdang-dong, Seongdong-gu, Seoul, KOREA 133-791*

*2Machine Tool Lab., Korea Institute of Machinery and Materials
#171 Jang-dong, Yuseong-gu, Taejeon, KOREA 305-343*

SUMMARY: A procedure of stress and strength analysis has been proposed for the centrifugal rotor of composite materials of quasi-isotropic laminates. The goal in this study is to maximize the allowable rotating speed, that is, to minimize the run time with the given path length by changing the geometry and selecting the ply angles in quasi-isotropic laminate. The geometric parameters, i.e., the outer radii and the radius of tube hole are the design variables to find. Two dimensional analysis at each cross section with an elliptic tube hole subjected to internal sample pressures as well as the centrifugal body forces has been performed along the height to calculate the stress distribution with the plane stress assumption, and Tsai-Wu failure criterion is used to calculate the strength ratio. The maximum allowable rotating speed can be, then, increased by changing the radii of the outer surface along the height with the maximum strength ratio under the unit value. The optimal number of ply angles maximizing the allowable rotating speed in quasi-isotropic laminates is also found to be the half number of tube hole, and the optimal laminate rotation angle is half of $[\pi/m]$. A $\pi/3$ laminate, for instance, is stronger than a $\pi/4$ laminate for the centrifugal rotor of 6 tube hole number even though they have the same stiffness. The number of tube hole can be also optimally determined to maximize the sample volume and the allowable rotating speed as well.

KEYWORDS: centrifugal rotor, composite materials, optimum design

INTRODUCTION

The purpose of centrifuges is to separate samples containing sub-cellular and biological particles of different densities from each other by spinning the rotor containing the samples and exerting the centrifugal force on the samples in solution [1, 2]. Existing centrifuges and rotors have, however, several limitations. The majority of existing centrifuge rotors are manufactured from aluminum or titanium alloys, and their use imposes constraints in the design of the centrifuge. For instance, the lifetime of a metal rotor is limited by metal fatigue and corrosion, which restricts the number of runs at maximum speed. Additionally, enough torque must be generated to accelerate a heavy metal rotor to high speeds in reasonably short times. These factors make existing centrifuges large and heavy for the task that they perform.

The application of composite materials to centrifugation has alleviated these problems and opened up new market opportunities. Composite materials are used to reduce the weight of rotors, or to increase sample capacity and rotor efficiency, which are mostly due to their high

specific strengths and abilities of changing ply orientations. For the composite laminated rotor, the quasi-isotropic laminates are mostly used to give the structurally isotropic behavior.

In order to optimize the composite centrifuge, stresses developed in the rotor must be calculated and then reduced as much as possible by changing the geometry and selecting the proper composite materials and ply orientations. In the past, an analytic solution and finite element methods have been used to calculate the stresses of the rotor [3-5]. The general procedures of selecting the dimensions and ply orientations of a composite centrifugal rotor are, however, not presented so far.

In this study, a structural analysis of quasi-isotropic laminated composite rotor has been performed considering the geometric parameters, i.e., the number of holes, the radii of holes, the radial diameter of the rotor and the side angle of slope. All the variables are non-dimensionalized in the governing equations, boundary conditions and material constitutive equations. A strength analysis is then performed to choose the ply orientation of quasi-isotropic laminates to maximize the rotating speed.

STRESS AND STRENGTH ANALYSIS

The composite centrifugal rotor considered in this study is a fixed angle rotor with a tube angle α_0 from the axis of rotation as shown in Figure 1. The rotor can centrifuge up to $2n$ tubes located with equal spatial angles. This rotor develops centrifugal forces for the differential separation of particles. The rotor is thus subjected to both the centrifugal body forces inside the materials and the hydraulic pressures on the cavity surface due to the samples. For the design point of view, it is usually required that the rotor sustain the higher rotation speed with a larger sample volume. For that purpose, the rotor is preferably made of composite materials which have the high specific strengths. The plies are parallel to the x-y plane, and a quasi-isotropic $[\pi/m]$ laminate sequence is used with a laminate rotation angle β as shown in Figure 2. The ply angle m for the given number of tubes $2n$ has an effect on reducing the strength ratios in the materials ($m, n = 3, 4, 5, \dots$), that is, increasing the maximum allowable rotating speed ω .

STRESS ANALYSIS

The stress analysis is based on a plain stress assumption ignoring the z-directional stresses, and the stress distribution for a section parallel to the x-y plane is thus calculated. The stress distributions are thus governed by the radial and circumferential equilibrium equations which are written in cylindrical coordinates as

$$\begin{aligned} \frac{\partial \sigma_r}{\partial r} + \frac{1}{r} \frac{\partial \tau_{r\theta}}{\partial \theta} + \frac{\sigma_r - \sigma_\theta}{r} + \rho_c r \omega^2 &= 0 \\ \frac{1}{r} \frac{\partial \sigma_\theta}{\partial \theta} + \frac{\partial \tau_{r\theta}}{\partial r} + \frac{2\tau_{r\theta}}{r} &= 0 \end{aligned} \quad (1)$$

where σ_r , σ_θ and $\tau_{r\theta}$ are the radial, circumferential and shear stresses, respectively, and ρ_c denotes the density of composite materials, ω the rotational angular velocity. The length and stress are non-dimensionalized by the radius of the top plane r_0 and $\rho_c r_0^2 \omega$, respectively, and Equation (1) can be then rewritten as

$$\begin{aligned} \frac{\partial \sigma_r^*}{\partial r^*} + \frac{1}{r^*} \frac{\partial \tau_{r\theta}^*}{\partial \theta} + \frac{\sigma_r^* - \sigma_\theta^*}{r^*} + r^* &= 0 \\ \frac{1}{r^*} \frac{\partial \sigma_\theta^*}{\partial \theta} + \frac{\partial \tau_{r\theta}^*}{\partial r^*} + \frac{2\tau_{r\theta}^*}{r^*} &= 0 \end{aligned} \quad (2)$$

The superscript * thus denotes non-dimension. Since the geometry is repeatedly symmetric, only one portion is analyzed with the symmetry conditions as shown in Figure 1. The maximum radius r_{max}^* of the semi-axes of the elliptic tube hole is determined for the geometry of the given number of tube hole $2n$ and the tube angle α_o :

$$r_{max}^* = \frac{\tan \theta_n}{\tan \theta_n + \sqrt{\tan^2 \theta_n + \cos^2 \alpha_o}} \quad \text{where } \theta_n = \frac{\pi}{2n} \quad (3)$$

The distance of the tube hole center at the top plane denoted by d_o^* is dependently determined from r_{max}^* , and the distance of the tube hole center d_z^* and the surface radii r_z^* along the height z^* are expressed as a function of z^* :

$$\begin{aligned} d_o^* &= 1 - r_{max}^* \\ d_z^* &= d_o^* + z^* \tan \alpha \\ r_z^* &= 1 + z^* \tan \alpha \end{aligned} \quad (4)$$

With the notations defined as in the above, the stress boundary conditions for the portion are described as

$$\begin{aligned} \sigma_r^* = \sigma_{r\theta}^* &= 0 \quad \text{on the outer surfaces} \\ \sigma_{\xi\eta}^* &= 0, \quad \sigma_\xi^* = P^*(r^*) \quad \text{inside of the tube hole} \end{aligned} \quad (5)$$

The normal stress σ_ξ due to the pressure of the sample subjected to the centrifugal forces can be calculated using the equilibrium equation of the sample rotating with an angular velocity ω neglecting the gravitation force ;

$$P(r) = \int \rho_s r \omega^2 dr = \frac{1}{2} \rho_s \omega^2 (r^2 - r_f^2) \quad (6)$$

where ρ_s denotes the density of the sample, and r_f a pressure-free radius. The pressure is again normalized as in Equation 2 and P^* in Equation (5) is obtained ;

$$P^* = \frac{\frac{1}{2} \rho_s (r^2 - r_f^2) \omega^2}{\rho_c r_o^2 \omega^2} = \frac{1}{2} \frac{\rho_s}{\rho_c} (r^{*2} - r_f^{*2}) \quad (7)$$

For the stress-strain relationship, the equivalent isotropic material properties are used because the laminates are quasi-isotropic.

STRENGTH ANALYSIS

Solving the governing equations with the boundary conditions, the off-axis strains ε_{off} in the global x, y and z coordinates are obtained. The on-axis ply stresses σ_{on} of each ply in $[\pi/m]$ laminate are then calculated using the strain transformation matrix \mathbf{T} and the ply material properties \mathbf{Q}_{on} [6];

$$\sigma_{on} = \mathbf{Q}_{on} \varepsilon_{on} = \mathbf{Q}_{on} \mathbf{T} \varepsilon_{off} \quad (8)$$

where the transformation matrix \mathbf{T} is defined as

$$\mathbf{T} = \begin{bmatrix} \cos^2 \phi & \sin^2 \phi & \cos \phi \sin \phi \\ \sin^2 \phi & \cos^2 \phi & -\cos \phi \sin \phi \\ -2 \cos \phi \sin \phi & 2 \cos \phi \sin \phi & \cos^2 \phi - \sin^2 \phi \end{bmatrix} \quad (9)$$

In Equation (9), ϕ is a ply angle in the laminate.

The failure of the ply material can then be accessed by using a Failure Criterion; Tsai-Wu quadratic failure criterion has been used [6],

$$\sigma_{on}^T \tilde{\mathbf{F}} \sigma_{on} + \bar{\mathbf{F}} \sigma_{on} R - R^2 = 0 \quad (10)$$

Solving Equation (10) yields a strength ratio R indicating the material failure with a value greater than 1. The strength parameters $\bar{\mathbf{F}}$ and $\tilde{\mathbf{F}}$ in Equation (10) are defined in terms of the material strengths :

$$\bar{\mathbf{F}} = \begin{bmatrix} \frac{1}{X} - \frac{1}{X'} & \frac{1}{Y} - \frac{1}{Y'} & 0 \end{bmatrix} \quad (11)$$

$$\tilde{\mathbf{F}} = \begin{bmatrix} \frac{1}{XX'} & -\frac{1}{2} \sqrt{\frac{1}{XX'} \frac{1}{YY'}} & 0 \\ -\frac{1}{2} \sqrt{\frac{1}{XX'} \frac{1}{YY'}} & \frac{1}{YY'} & 0 \\ 0 & 0 & \frac{1}{S^2} \end{bmatrix} \quad (12)$$

where X and X' are the tensile and compressive strengths in the fiber direction, Y and Y' in the matrix direction, and S the shear strength.

Notice that, since the equivalent stiffness is the same for a number of angles m in a quasi-isotropic $[\pi/m]$ laminate, the off-axis strains are not changing. The distributions of the stresses and strength ratios at each ply are, however, changing with a quasi-isotropic laminate angle. The distributions of strength ratios are also dependent upon the laminate rotating angle β ; the lay-up angles of a quasi-isotropic laminate with $m=3$ and β are $[\beta, \pi/3 + \beta, 2\pi/3 + \beta]$ as shown in Figure 2. For the given geometry and loading conditions of the rotor, the optimal m and β can be thus found to minimize the maximum strength ratios in the plies.

RESULTS AND DISCUSSION

Using finite element methods, the stress analysis is performed on the composite rotor with various geometric values. Most important geometric values to design for the composite rotor are a tube hole radius r_i , radii of outer surfaces r_o and the number of tube holes n for the given radius of the top plane r_o and the fixed tube angle α_o . As shown in the analysis, all the dimensions are normalized by r_o .

The determination of radii of outer surfaces r_z^* along the height is important in reducing the stress distribution. The radii r_z^* along the height are determined to minimize the maximum stresses in each cross section with two conditions; in the first case, the radii r_z^* linearly change along the height making a constant slope angle α which is calculated as 25° , and in the second case, the radii r_z^* arbitrarily change along the height. For numerical calculation, a radius of the top plane r_o , a fixed tube angle α_o and the height are taken as 10 cm, 15° and 12.5 cm, respectively. The radius of the tube hole r_i^* is taken as 0.8 times of r_{max}^* and the number of tube hole $2n$ as 6.

The composite material used for calculation is AS4/PK and their material properties are listed in Table 1. The number of ply angle m in quasi-isotropic laminate is considered as 3 with the laminate rotation angle β zero. It is found that the maximum strength ratios always exist along the boundary. The stresses along the tube hole are thus most critical in designing the rotor. The normal stress σ_ξ^* is given by the pressure of the sample with a pressure-free radius r_f the inner point of the tube hole at the top plane and the shear stress $\sigma_{\xi\eta}^*$ is zero as in Equation (5). The specific density of the sample is considered as a constant value of 1.2. The tangential stress σ_η^* is calculated for three cases, and compared with each other. As the first case, the surface slope angle α is the same as the tube angle α_o given as 15° . For the second case, the constant slope angle α minimizing the maximum strength ratios is calculated as 25° . For the third case, the minimization of the maximum strength ratios is achieved by varying slope angle α , that is, changing the outer surface radii along the height. The stress distributions at the sections of z^* equal to 0.25, 0.75 and 1.25 for each case are shown in Figure 3. It is noticed that the variations of the stresses and the maximum values of the tangential stresses along the boundary line in the last two cases are reduced as compared to those of a case that $\alpha=\alpha_o$. The maximum allowable rotating speeds ω which are corresponding to the maximum strength ratio of unit value are, thus, increased from 31,000 rpm by 20% and 28% for the last two cases.

As a general result for the above case, or changing the ratio of the tube hole radius r_i^* with respect to the r_{max}^* , the distributions of the maximum strength ratio along the height are plotted for the above three cases as shown in Figure 4. From the contour line in Figure 4, the ratio r_i^*/r_{max}^* can be determined without any material failure for the given height z^* . Notice that the larger tube hole can exist for the given height z^* by changing the surface radii along the height as shown in Figure 4.

The maximum allowable rotating speed can be even more increased by properly choosing the number of the ply angles m in quasi-isotropic laminate and the laminate rotation angle β . In order to show the effects of m and β , the variations of maximum allowable rotating speed ω are calculated using Equation (10) and plotted by varying the angle β for four cases of m equal to 3, 4, 5, and 6 at three sections of z^* , and shown in Figure 5. The best value of m is shown as 3 which is equal to n , and the angle β is half of π/m , or 30° , except that at $z^*=1.25$

where the angle β is 6° . The maximum allowable rotating speeds ω are summarized in Table 2.

As a last example, for the constant total tube volume, the maximum rotating speed ω can be also even increased by properly choosing the number of tube hole n and are shown in Figure 6. In this example, the height z^* is taken as 1.0, the number of ply angles m equal to n , the constant angle α equal to α_o as 15° . The total tube volume V_t is normalized by r_o^3 and denoted by V_t^* . For the volume V_t^* equal to 1.2, the best number of tube hole is 3 and for V_t^* equal to 0.8, the number 6.

CONCLUSION

It is shown that the maximum allowable rotating speed of the composite rotor can be increased by changing the outer surface slope angles along the height. The maximum allowable radius of the tube hole for the given number of tube holes is also calculated by minimizing the maximum strength ratios for all the sections. The optimal number of ply angles maximizing the allowable rotating speed in quasi-isotropic laminates is found to be the half number of tube hole, and the optimal laminate rotation angle is half of $[\pi/m]$. The number of tube hole can be also optimally determined to maximize the sample volume and the allowable rotating speed as well.

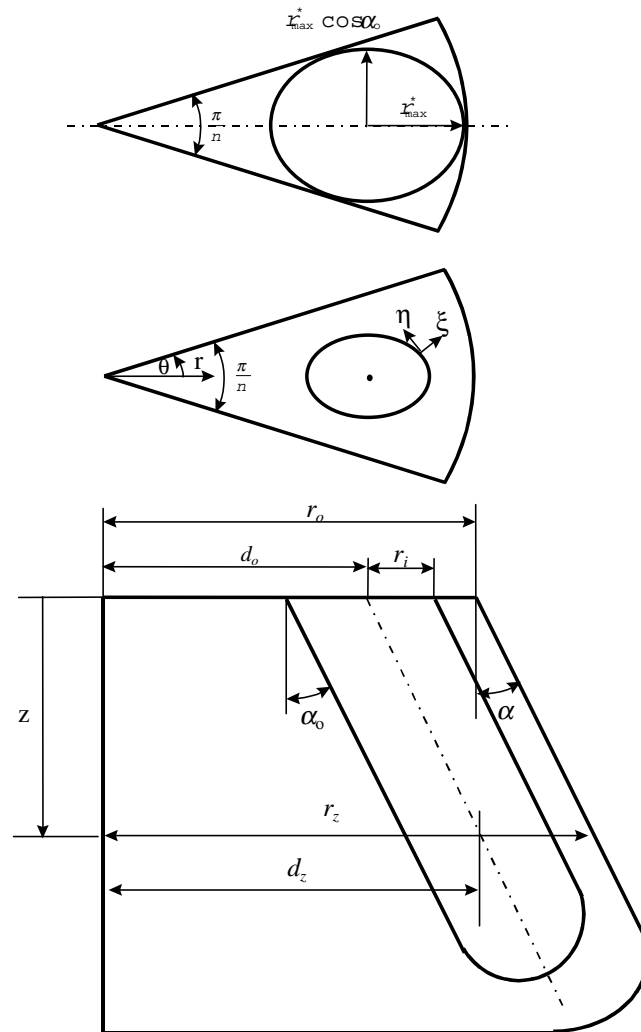


Figure 1. Geometries and coordinate systems for a fixed angle rotor with a tube angle α_o ; Determination of the maximum length of the semi-axes of the elliptic tube hole for a repeating portion of angle π/n (the top figure)

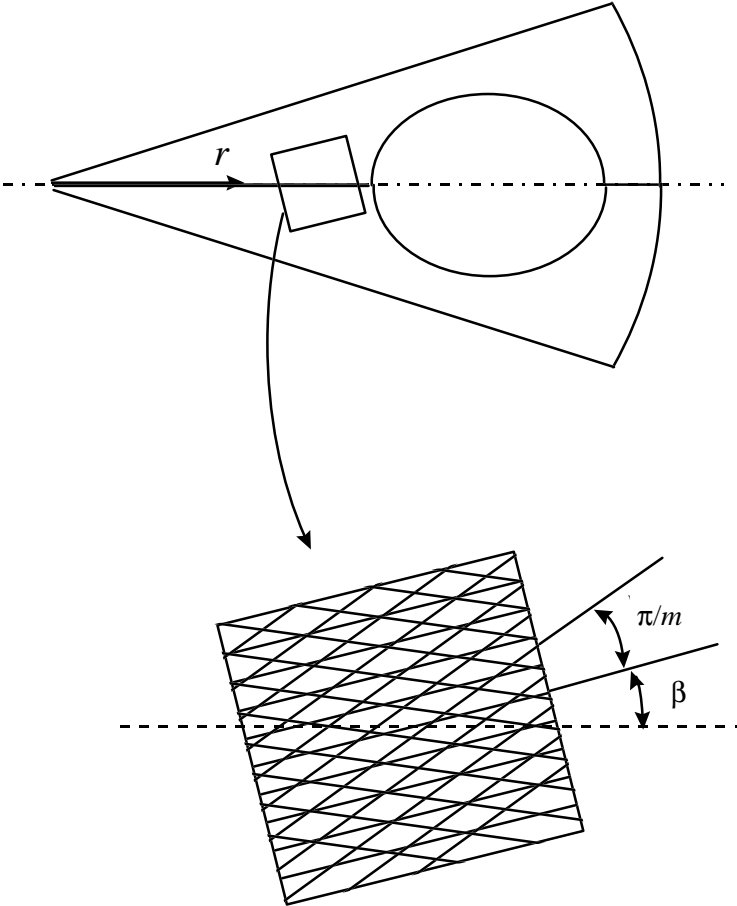


Figure 2. Geometry of layup sequence of quasi-isotropic laminate in a composite centrifugal rotor; π/m is a ply angle and β is the laminate rotation angle.

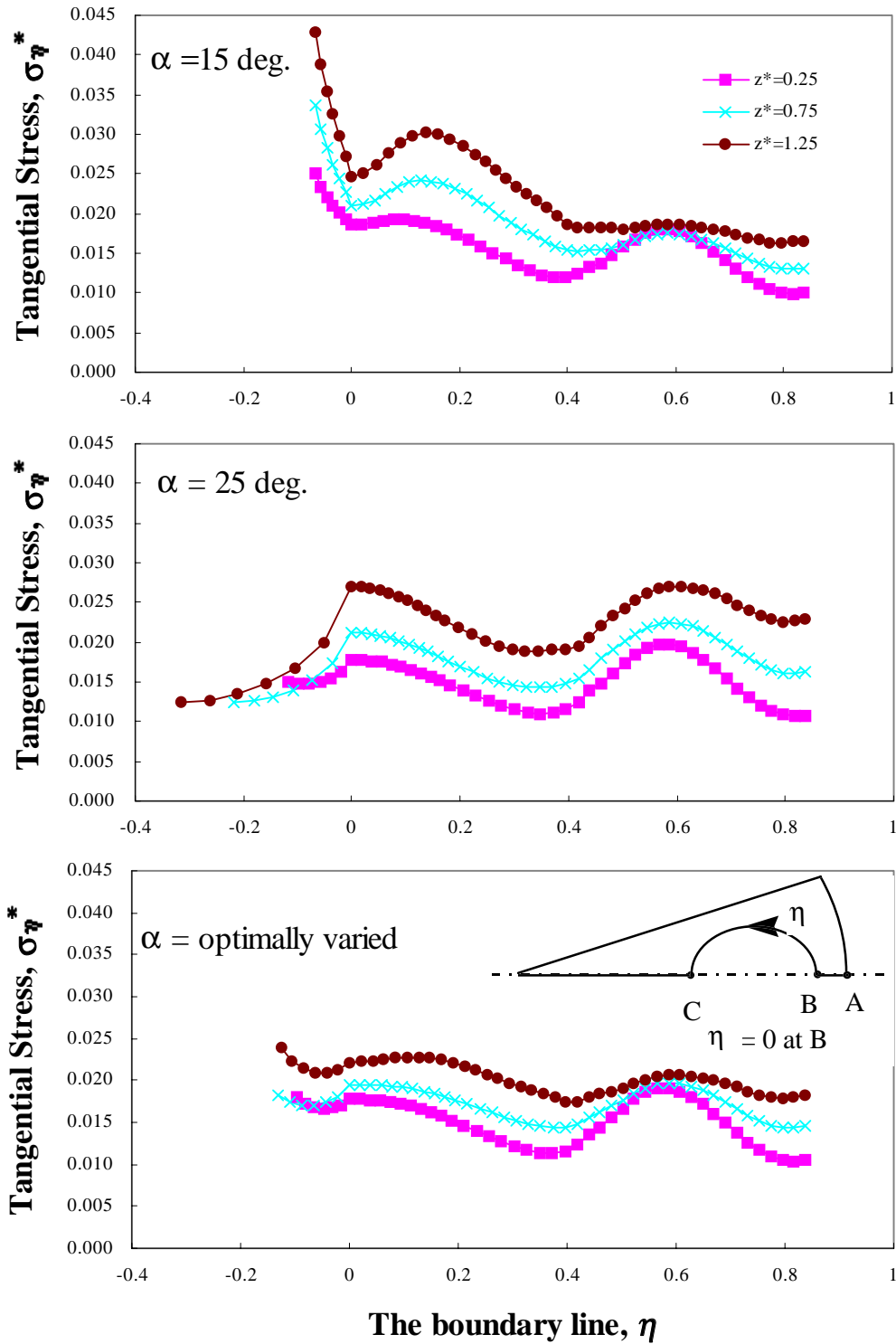


Figure 3. Distribution of tangential stresses σ_{η}^* along the boundary line η for the rotor of $r_i^* = 0.8 r_{max}^*$, $m=n=3$, $\alpha_0=15^\circ$, and $r_o=10$ cm.

Distribution of Strength Ratio, R

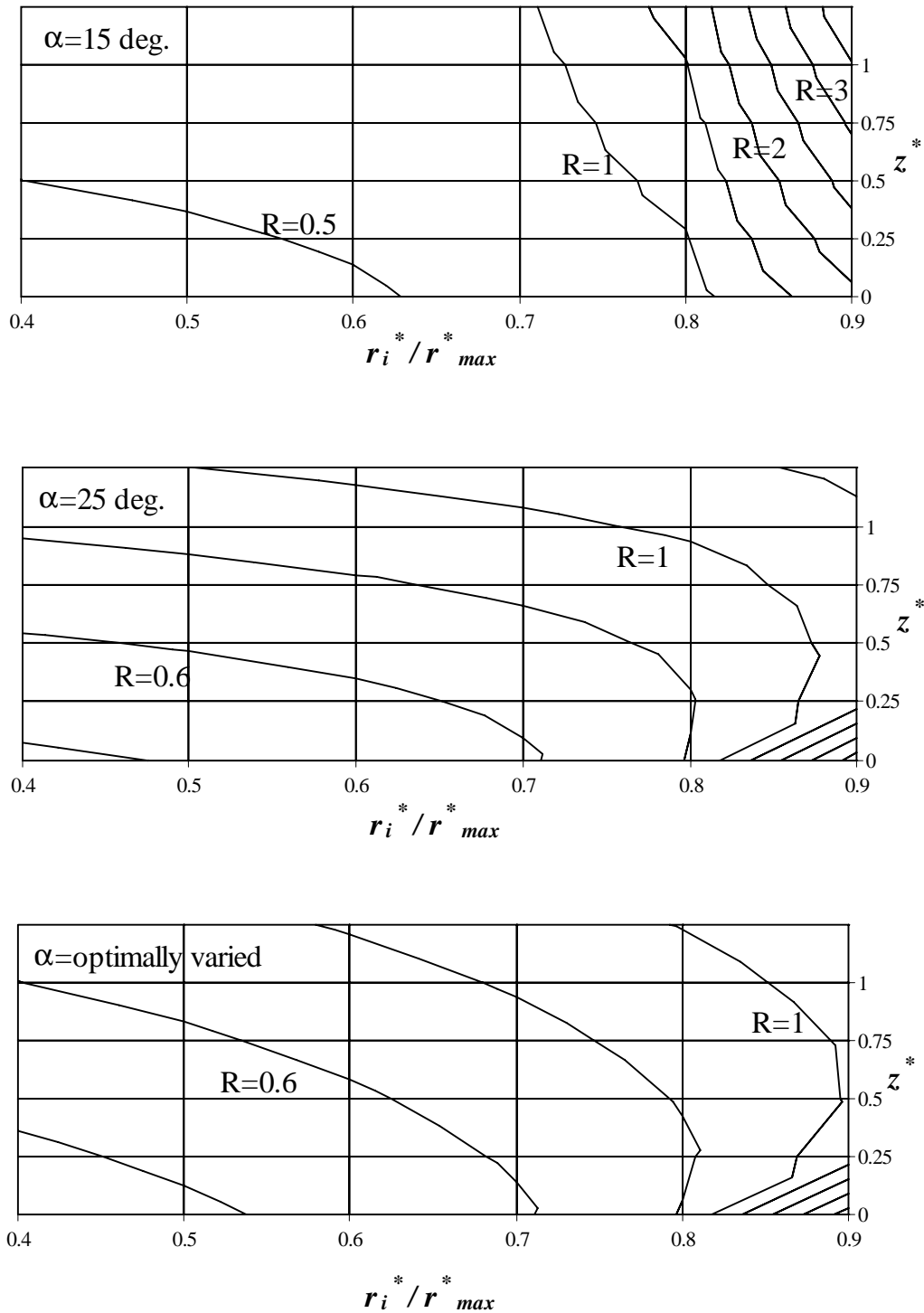


Figure 4. Distribution of maximum strength ratios R over the height and the tube hole radius r_i^* for the rotor of $m=n=3$, $\alpha_o=15^\circ$, and $r_o=10 \text{ cm}$.

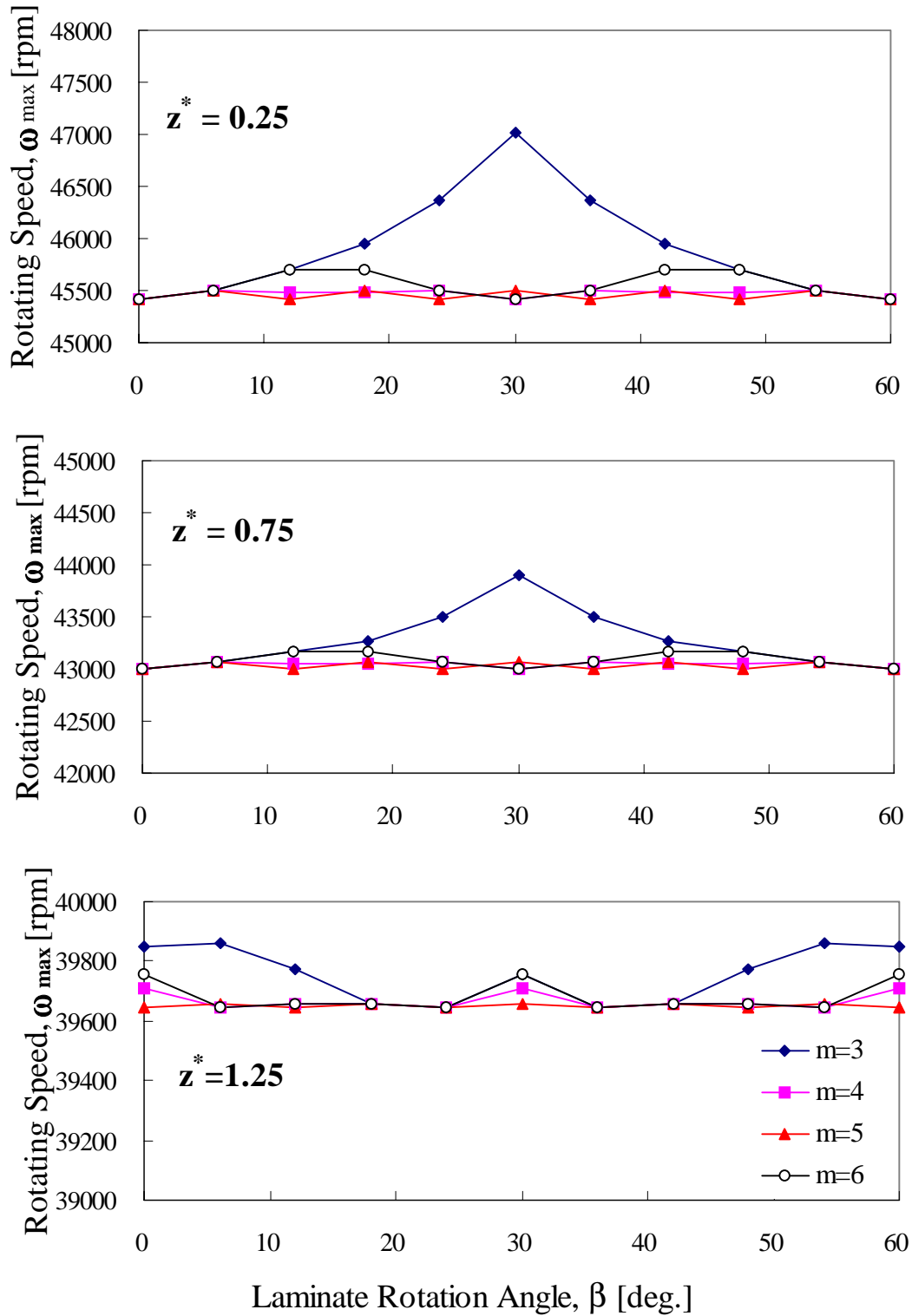


Figure 5. The maximum allowable rotating speed ω versus the laminate rotating angle β when $r_i^* = 0.8 r_{max}^*$, $n=3$, and α =optimized

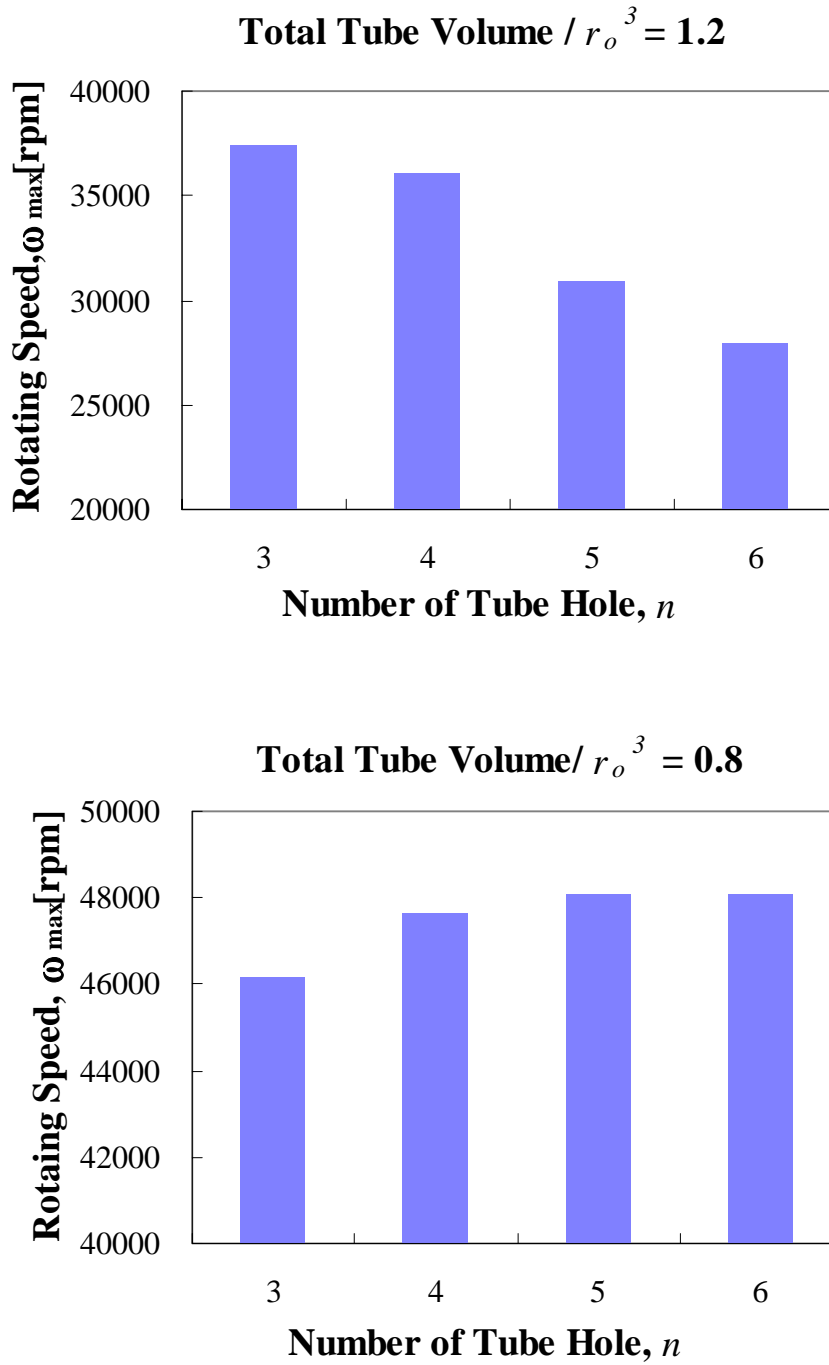


Figure 6. The maximum allowable rotating speed ω versus the number of tube hole n for the constant tube volume of 1.2 and 0.8 of the rotor of $m=n$, $\beta=0$, and $\alpha^o=\alpha=15^o$

Table 1. Material properties of centrifugal composite rotor for numerical calculation.

Material Properties (AS4/PK)	Values
Longitudinal Young's Modulus, E_x	134 GPa
Transverse Young's Modulus, E_y	8.9 GPa
Shear Modulus, E_s	5.1 GPa
Longitudinal Poisson's Ratio, ν	0.28
Longitudinal Tensile Strength, X	2130 MPa
Longitudinal Compressive Strength, X'	1100 MPa
Transverse Tensile Strength, Y	80 MPa
Transverse Compressive Strength, Y'	200 MPa
Shear Strength, S	160 MPa
Density, ρ_c	1600 Kg/m ³

Table 2. The increase of the maximum allowable rotating speed along the height z^* by varying the outer surface radii r_z^* and laminate rotation angle β ; $n=m=3$ and $\alpha=15^\circ$.

z^*	Initial ($\alpha=15^\circ, \bullet =0$)	Optimized \bullet ($\bullet =0$)	Optimized \bullet & \bullet
0	44500 rpm	44500 rpm	46900 rpm
0.25	40600 rpm	45400 rpm	47000 rpm
0.5	37600 rpm	44500 rpm	45400 rpm
0.75	35000 rpm	43000 rpm	43900 rpm
1	32900 rpm	41400 rpm	41500 rpm
1.25	31000 rpm	39800 rpm	39900 rpm

REFERENCES

1. *Ultracentrifuge Rotors*, 1995, Beckman Instruments Inc.
2. <http://www.composite.com>, 1997, Composite Rotor, Inc.
3. Kienzler, R. and Zhuping, D., 1987, "On the Distribution of Hoop Stresses around Circular Holes in Elastic Sheets", ASME J. Applied Mech., vol. 54, pp. 111-114.
4. Ku, Ta-Cheng, 1960, "Stress Concentration in a Rotating Disk With a Central Hole and Two Additional Symmetrically Located Holes", ASME, J. Applied Mech., vol. 27, pp. 359-360.
5. Timoshenko, S.P. and Goodier, J.N., 1970, *Theory of Elasticity*, McGraw-Hill, New York.
6. Tsai, Stephen W. and Hahn, H. Thomas, 1980, *Introduction to Composite Materials*, TECHNOMIC Publishing Co., Inc.

MODELLING DEFORMATION OF FILAMENT WOUND ARTERIES

Jacqueline Rebecca Postle and Ron Postle

Department of Textile Technology, University of New South Wales Sydney 2052 Australia

Summary. When artificial arteries are used in replacement surgery, it is vitally important to be able to predict the deformation of the artery under physiological conditions. The mechanical properties of the manufactured artery should ideally match the mechanical behaviour of the natural biological artery. For successful implantation, the artificial artery must support the pulsatile blood flow within certain safety limits for at least a couple of years, that is, a couple of million heart beats. In order to predict these safety measures, the deformation of the arterial prostheses must be modelled. In this paper, the strain of the artery wall under the pressure of pulsatile blood flow has been modelled in order to predict the effect on the blood flow. Also, the residue strain (or stress relaxation) due to fibre viscoelasticity is incorporated in order to predict the lifetime of artificial arteries for safe blood transport.

KEYWORDS : deformation, mechanics, fibre viscoelasticity, prostheses

Construction of Filament Wound Vascular grafts

Filament wound vascular grafts have been made from lycra in the laboratory (Hellener *et al.*, 1994). A continuous monofilament of lycra fibre was dipped in Pellathane and wound back and forth around a cylindrical mandrel. The mandrel was extracted from the lycra composite tube. These lycra fabric tubes have been shown to exhibit good biocompatibility and high porosity (Cohn *et al.*, 1992).

In terms of the tube axis coordinates, $\{x(s), y(s), z\}$, and the tangent angle $\psi(s)$ ($\psi = 0$ for all s for a straight tube), the fibre path is given by

$$\begin{pmatrix} x(s) \\ y(s) \\ z \end{pmatrix} + \begin{pmatrix} \cos \psi & -\sin \psi & 0 \\ \sin \psi & \cos \psi & 0 \\ 0 & 0 & 1 \end{pmatrix} \begin{pmatrix} 0 \\ r \cos w \\ r \cos w \end{pmatrix},$$

where r is the radius of the tube. and w is the winding angle which alternates sign as the fibre is wound back and forth along the mandrel.

Modelling deformation of Synthetic Arteries

The problem addressed in this paper is the deformation of the artery walls caused by pulsatile blood flow. Due to the viscosity of blood, the periodic pressure increase produces a gradual increase and decrease in the radial forces exerted on the artery walls. Assuming that the radial change of the deformation of the artery wall due to one pulse of the blood flow, the radius of the tube is described by

$$(1) \quad r(k) := (r_0(1 + height \exp(-(k - centre)^2/spread)),$$

where *height* is the maximum increase of the radius, *centre* is the centre of the deformation and *spread* is the length along the axis of the artery over which the radius changes due to one pulse.

Figure 1 shows a computer simulated filament-wound artery with a winding angle of 45° with a radial deformation described by Equation 1 where the input values are *height* = 0.4 and *spread* = 40. As the blood flows through the artery, the centre of the deformation would move along its axis. A computer movie has been made to simulate actual blood flow through filament-wound arteries.

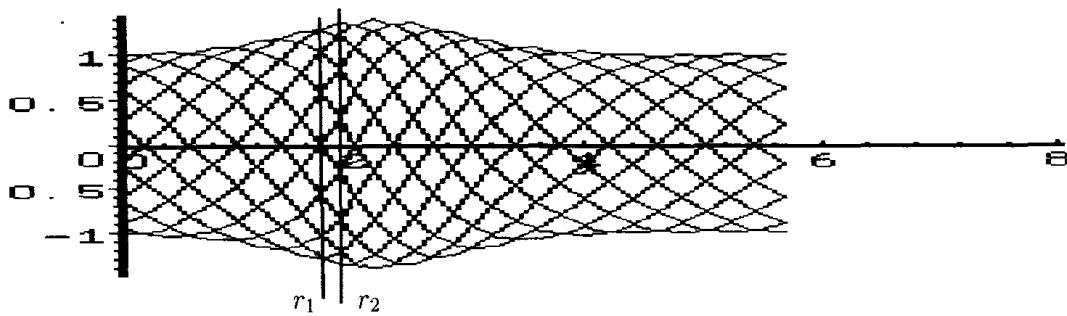


Figure 1: Filament-wound artery of winding angle 45° .

Consider a radial strip of the tube bounded by the cross-over grid points where the radius of the tube is r_1 and the adjacent grid points where the radius of the tube is r_2 . This radial strip forms a frustrum. If this frustrum is flattened out onto the plane, it would form the sector of an annulus as shown in Figure 2. The fibres lie on geodesics but are represented here as the straight zigzag lines.

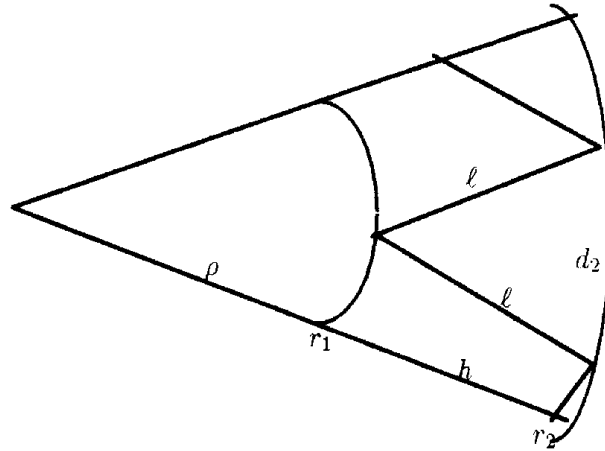


Figure 2: The frustum bounded by r_1 and r_2 of Figure 1 flattened out onto a plane forming a sector of an annulus.

Let h be the length along the artery wall of the frustum. When the frustum is flattened onto the plane, the two sides of the annulus will meet at the origin at a length of ρh from the inner radial cut r_1 . So ρ is the radius of the inner circle. If d_i is defined as the distance along the inner circle between fibre crossings, then

$$d_i = \frac{2\pi r_i}{n},$$

where n is the number of fibre paths in one direction, i.e. the number of times the fibre is wound back and forth around the mandrel. The length of fibre between crossings l is constant if the fibre is assumed to be inextensible. For extensible fibres such as lycra, the fibre length between crossings l_i will vary as the radius r_i changes.

Figure 3 shows the dimensional components of the actual artery. The difference between adjacent radii is $r_2 - r_1$, the distance between adjacent crossings along the artery wall is h and along the axis of the artery is dx . It is these variables which are needed in order to predict the final shape of the artery walls.

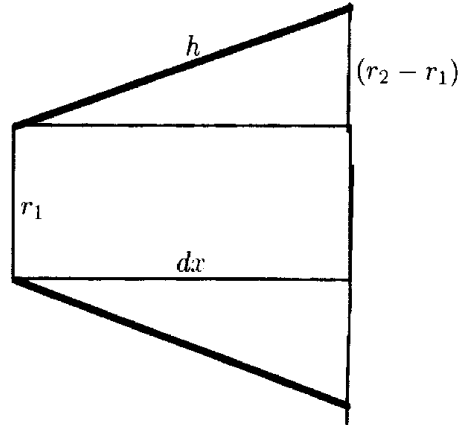


Figure 3: The dimensional components of the predicted artery.

The ratio of the adjacent radii is defined by $a = r_1/r_2$ and therefore $a\rho$ is the radius of the outer circle r_2 . Figure 4 shows the dimensions and angles associated with two portions of the fibre from the inner circle of radius r_1 to the outer circle of radius r_2 where they meet at a fibre crossing.

The fibres meet at the outer circle at angle w to the artery tube axis. The fibres are a distance d_1 apart on the inner circle and these two points are a distance ρ from the origin O of the circles along lines which are at angle θ to the tube axis. The angle between these lines to origin O and the fibre path lines of length ℓ is the angle ϕ .

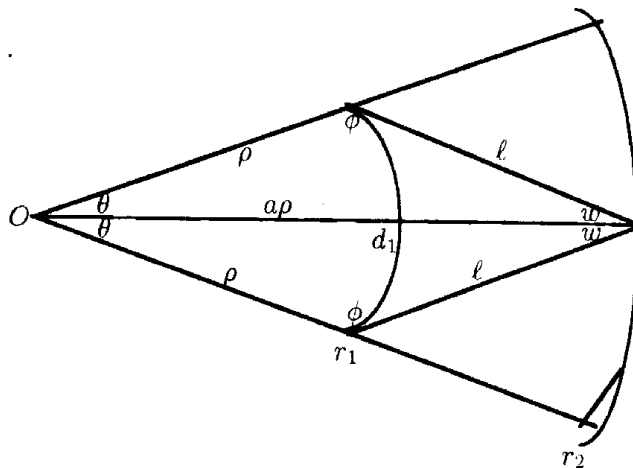


Figure 4: Two portions of the fibre of length ℓ from the inner circle of radius r_1 to the outer circle of radius r_2 where they meet at a fibre crossing.

The inner circle joined to origin O forms the sector of a circle of radius ρ and hence

$$d = 2\theta\rho$$

which can be expressed in terms of the angle at origin O as $\theta = \frac{1}{2}d/\rho$. By considering Figure 4 as two symmetrical triangles, the angles are related by

$$\phi = \pi - \theta - w.$$

Using the sine rule on these triangles for all three of the angles and the simplification $\sin \phi = \sin(\theta + w)$,

$$\frac{\sin \theta}{\ell} = \frac{\sin w}{\rho} = \frac{\sin(\theta + w)}{a\rho}.$$

Solving for the winding angle w ,

$$w = \tan^{-1}\left(\frac{\rho}{\ell} \sin \theta\right) = \tan^{-1}\left(\frac{a\rho}{\ell} \sin \theta\right) - \theta$$

and this relation was rearranged with the aid of algebraic computing to yield the analytical expression

$$(3) \quad (1 - a)\rho\ell^2 + (1 - a)a\rho^2 \sin^2\left(\frac{d}{2\rho}\right) + \ell^3 = 0.$$

From Equation (3), the radius of the inner circle ρ can be computed numerically. The radius of the outer circle is $a\rho$ and from Figure 2, the difference between the radii

$$h = (a - 1)\rho.$$

The distance along the artery axis between the adjacent grid crossings is calculated from Figure 3 by

$$dx^2 = h^2 - (r_2 - r_1)^2.$$

The Artery Compliance

The dimensional changes of a graft due to internal pressure are expressed in terms of the volumetric rigidity which is referred to as the medical compliance (Kinley and Marble, 1980). The volumetric medical compliance C_V can be resolved into the two components, C_θ the hoop compliance and C_X the axial compliance (Tu *et al.*, 1991):

$$C_V = 2\frac{\partial R}{R_0\partial P} + \frac{\partial L}{L_0\partial P} = 2C_\theta + C_X,$$

where R_0 is the radius and L_0 is the axial length of the undeformed artery. The difference in compliance between vascular grafts and host arteries reveals appropriate matching of the mechanical properties (Kidson, 1983).

The medical compliance C_V has been assumed to be equal to the hoop compliance C_θ (which is equal to the inverse of the tensile modulus of the fabric in the hoop direction) in the literature. The effect of axial deformation (i.e. change in length) is assumed negligible and thus the effect of the fabric structure is ignored.

However, the model presented in this paper is not restricted to this assumption and both the axial strain and the hoop strain is predicted according to the winding fibre structure for any winding angle. The extra prediction of axial strain of the tube is vital information for successful implantation of arterial prostheses.

Inelasticity of Arterial Prostheses

In a filament-wound or textile reinforced composite artery, a long term problem is the gradual build up of residual deformations after repeated blood pulsation cycles. The interfibre frictional moment interacts with the viscoelastic behaviour of the filaments to impose a limit on the ultimate recovery that the textile can eventually attain.

The presence of interfibre friction in a filament-wound artery can cause the build up of what may at first sight seem surprisingly large deformations in a continuing series of short blood pulsatile cycles. This problem is analogous to the build up of wrinkles in a textile fabric which is subject during wear to repeated short term deformation-recovery cycles. The level of residual deformation in a filament-wound artery is evaluated on the basis of a rheological model incorporating linear viscoelastic theory for polymeric fibres and actual measurements of frictional hysteresis during a deformation-recovery cycle.

The viscoelastic behaviour of the lycra wound fabrics were tested using an Instron extensometer by stretching the fabric in the axial direction by 10% and measuring the stress-relaxation rigidity at this constant specified strain. The stress decay constant was found to be 3.5%, i.e. the stress in the fabric was found to relax at a rate of 3.5% per decade of relaxation time.

Calculation of Viscoelastic Fabric Recovery in the Presence of Interfibre Friction

The deformation behaviour of fibres under equilibrium conditions at low strains (less than about 1%) is known to be linear viscoelastic. A rheological model of a fabric with linear viscoelastic fibres and internal frictional moment between fibres is shown in Figure 5. The interfibre frictional moment between fibres is assumed to be a constant M_0 independent of fabric strain. The linear viscoelastic fibres have a relaxation rigidity $B_0(T)$ which is equivalent to the stress relaxation as a function of relaxation time T in the absence of friction.

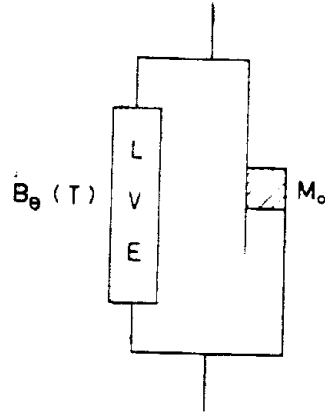


Figure 5: Fabric model for the study of repeated pulse deformation-recovery cycles. A linear viscoelastic element (LVE) characterised by a relaxation rigidity function $B_0(T)$ acts in parallel with a frictional element which gives rise to a constant opposing interfibre frictional moment M_0 .

For example, the relationship between the bending moment M of unit width of fabric and curvature K for the fabric model shown in Figure 5 is

$$M(t) = \int_0^t B(t - \tau) dK(\tau) M_0$$

where the changing sign of the curvature is always opposed by the frictional moment M_0 . We consider here a deformation-recovery sequence where at time τ , the fabric is subjected to a constant pulse deformation K_0 for a period of time t (stress relaxation) after which the fabric recovers for a short period of time under zero moment or stress, i.e. $M(t) = 0$. The linear viscoelastic element of Figure 5 recovers against the constant a frictional moment M_0 . The fabric will eventually only recover completely from deformation if the interfibre friction M_0 is zero.

In the presence of internal fabric friction M_0 following pulse deformation, the fabric would recover with time to a certain level after which fabric recovery would cease. An example is shown in Figure 6(a) for which the stress relaxation rigidity drops linearly with the logarithm of elapsed time. For an internal friction factor M_0/K_0 of four units, the fabric recovery curve after deformation for different times are shown in Figure 6(b) (Chapman, 1974).

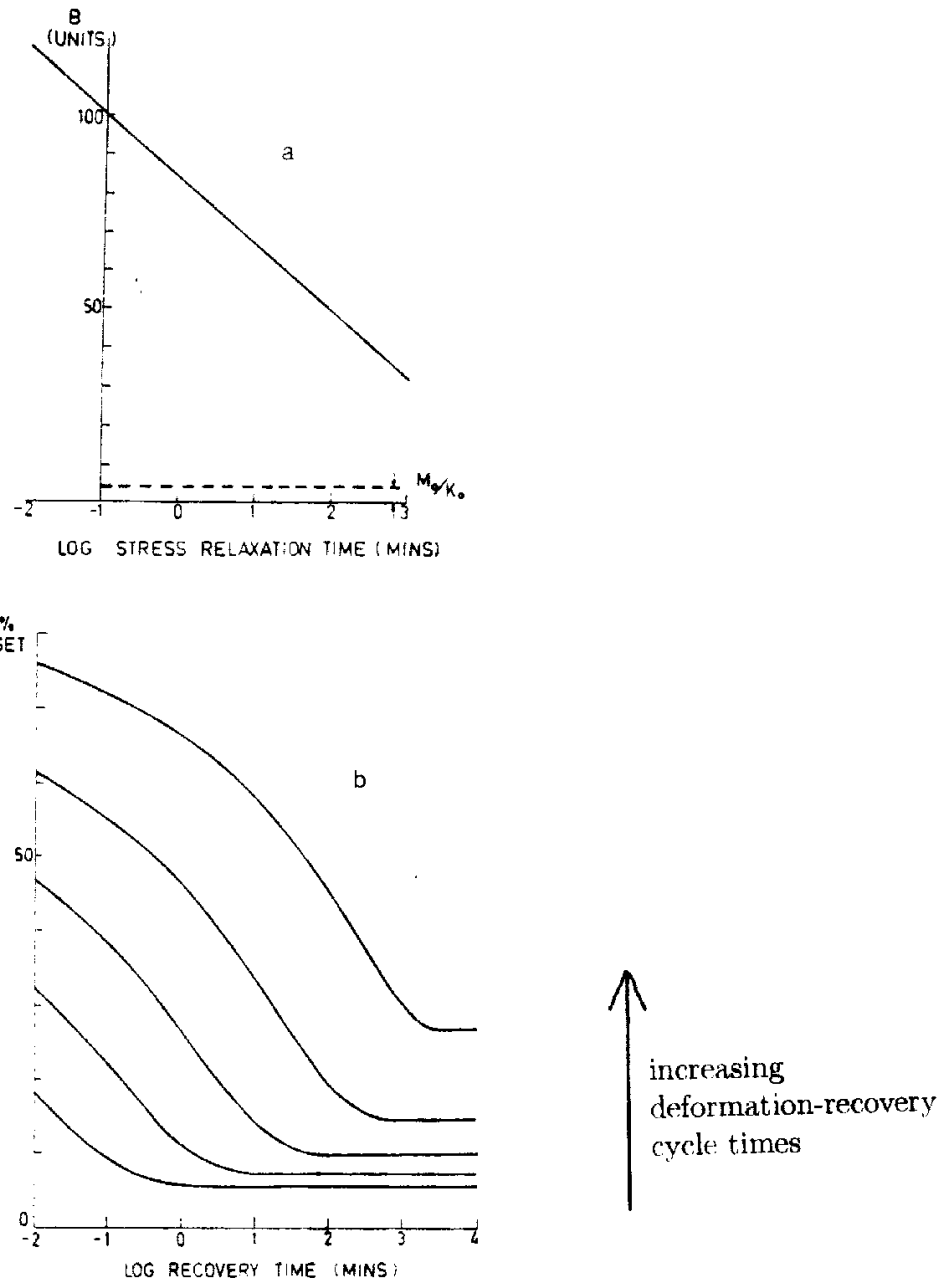


Figure 6: (a) Relaxation rigidity curve for a fabric showing the level of the frictional factor M_0/K_0 . The shape of the line is the stress relaxation per decade of relaxation time;

(b) Fabric recovery curves calculated from the data in (a), plotted in terms of % set (the residual deformation) versus the logarithm of the recovery time.

Repeated Fabric Deformation Recovery Cycles against Friction

Repeated blood pulses can be considered as mathematically equivalent to the textile problem of repeated wrinkling and recovery deformation whereby wrinkles generally develop along the same crease lines in a garment. Once the wrinkle has formed in the garment and has been allowed to recover partially, the unrecovered deformation will cause fabric wrinkling to recur preferentially along the same wrinkle line during repeated cycles (Chapman, 1975). The presence of internal fabric friction M_0 causes the build up of relatively high residual deformations in a series of short deformation-recovery cycles.

Consider the linear viscoelastic relaxation rigidity shown in Figure 7. For short times (less than t_0) the relaxation rigidity has an unrelaxed value B_0 , and at relatively long times (greater than t_2), a relaxed value B_2 . If the fabric is rapidly deformed to curvature K_0 and immediately allowed to recover, the residual curvature $K_1 = M_0/B_0$.

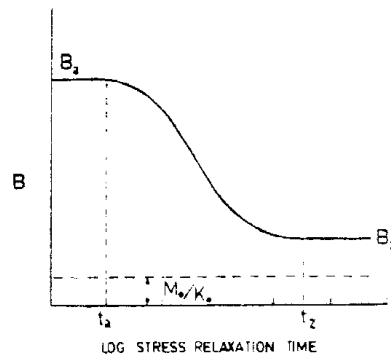


Figure 7: Idealised relation rigidity curve $B(t)$ and frictional factor M_0/K_0 used to evaluate the effect of repeated blood pulsation cycles.

The fibres are held in the deformed configuration by friction and therefore they stress-relax without further recovery until the fabric viscoelastic stress reached a value $K_1 B_2$ after time t_2 .

Following Chapman (1975), the curvature after n deformation recovery cycles is

$$K_n = \frac{M_0}{B_0} \sum_{i=1}^n (1-x)^{i-1}$$

where $x = B_2/B_0$. In the limit as $n \rightarrow \infty$,

$$\lim_{n \rightarrow \infty} K_n = \frac{M_0}{xB_0} = \frac{1}{x} K_1.$$

Since $x < 1$, a residual deformation is built up after repeated cycles which is much greater than the residual deformation after the first cycle even for blood pulsation times of approximately one second. The level of the residual deformation depends on the viscoelastic stress relaxation rate of the fabric per decade of relaxation time, the internal fabric friction factor M_0/K_0 , the exact deformation and recovery times within each pulsation cycle and the total number of pulse cycles ($n \rightarrow \infty$). Numerical calculations are performed to evaluate the residual fabric deformation for various values of these input parameters.

Conclusion

Filament wound arterial prostheses have been modelled geometrically in order to predict the deformation and recovery under physiological conditions during pulsatile blood flow. The residual deformation due to fibre viscoelastic stress relaxation in the presence of friction between fibres must be incorporated in order to predict the lifetime of artificial arteries for safe blood transport. The interfibre frictional moment in the artificial artery interacts with the viscoelastic behaviour of the filaments to impose a limit on the ultimate recovery that the textile can eventually attain after repeated cycles.

The residual deformation built up after repeated cycles is always much greater than the residual deformation after the first cycle even for normal blood pulsation times. The residual deformation can be numerically evaluated from the fibre stress relaxation rate and the interfibre friction opposing recovery within the textile artery.

Acknowledgement The author would like to thank the Hebrew University, Jerusalem for the opportunity to work in the Casali Institute of Applied Chemistry with a Golda Meir postdoctoral fellowship.

References

- Chapman, B.M. (1974). *A Model for the Crease Recovery of Fabrics*, Textile Research Journal **44**, pp. 531-538.
- Chapman, B.M. (1975), *The Importance of Interfibre Friction in Wrinkling*, Textile Research Journal **45**, pp. 825-829.
- Cohn, D., Elchai, Z., Gershon, B., Karck, M., Lazarovici, G., Sela, J., Chandra, M., Marom, G. and Uretzky, G. (1992). *Introducing a Selectively Biodegradable Filament Wound Arterial Prosthesis: A Short Term Implantation Study*, J. Biomed. Mater. Res. **26**, pp. 1185-1204.
- Hellener, G., Cohn, D. and Marom, G. (1994). *The Elastic Response of Filament Wound Arterial Prostheses Under Internal Pressure*, Biomat. **15** (14), pp. 1115-1121.
- Kinley, C.E. and Marble, A.E. (1980), *Compliance: A Continuing Problem with Vascular Grafts*, J. Cardiovasc. Surg. **21**, pp. 163-170.
- Tu, R., McIntyre, J., Hata, C., Lu, C.L., Wang, E. and Quijano, R.C. (1991), *Dynamic Internal Compliance of a Vascular Prosthesis*, Trans. Am. Soc. Intern. Organs. **37**, M470-472.

DEVELOPMENT OF A KNITTED FABRIC REINFORCED ELASTOMERIC COMPOSITE INTERVERTEBRAL DISC PROSTHESIS

S. Ramakrishna¹, S. Ramaswamy¹, S. H. Teoh² and C. T. Tan³

¹ *Centre for Biomedical Materials Applications and Technology (BIOMAT),
Department of Mechanical and Production Engineering, National University of Singapore,
10 Kent Ridge Crescent, Singapore 119260.*

² *Institute of Materials Research and Engineering (IMRE), National University of Singapore,
10 Kent Ridge Crescent, Singapore 119260.*

³ *Department of Orthopaedic Surgery, Singapore General Hospital
Outram Road, Singapore 169608*

SUMMARY: The concept of an intervertebral disc prosthesis (IVDP) has arisen from the limited success of current surgical measures to treat disc degeneration. In this study, a textile composite IVDP with a polymeric core was successfully fabricated. Issues relating to the design and process optimisation of the IVDP fabrication are discussed. In addition, the mechanical behaviour of the IVDP are compared with the mechanical behaviour of the natural intervertebral disc (IVD).

KEYWORDS: intervertebral disc prosthesis, rotational moulding, textile composites, elastomers

INTRODUCTION

In spite of their limited application thus far in the area of biomaterials, textile composites offer the potential to better match the mechanical properties of hard tissue and improve overall device performance [1]. This is due to the fact that most living tissues are three-dimensional fibrous collagen structures. In this regard, the human IVD [Fig. 1] is no exception since it comprises of fibrous composite (annular) layers that surround a gel like liquid core [2].

From a viewpoint of the mechanical requirements, an IVDP must primarily possess similar modulus and deformation properties to the natural IVD. Conventional materials cannot be exclusively considered since they cannot match the mechanical properties. For example, elastomeric polymers offer flexibility but are insufficient in modulus and tear strength. Thus, the immediate objective in this study was to apply textile composites concepts to the fabrication of an IVDP in an attempt to match the primary mechanical properties of the IVD. Two key areas are reported in this paper. These are: 1] design and process optimisation and 2] the compressive behaviour of the IVDPs.

IVDP DESIGNS

Liquid-Filled IVDP

An excised human cadaveric disc was used as the basis to fabricate open IVDP moulds. Subsequently, permanent aluminium open moulds were made [Figure 2]. Permanent aluminium closed moulds were then fabricated with a 3 mm reduction in all directions. in order to accommodate for a core polymeric region as well a composite layer to encapsulate the former.

Rotational Moulding

The natural IVD is a hollow, liquid-filled entity and to replicate this, computer controlled liquid rotational moulding (CCLRM) a method known for the making of hollow products was incorporated. CCLRM was carried out using a Kent Ridge Instruments, version RM100 workstation [Fig. 3] which also allows for environmental control of temperature and humidity [3]. The use of the computer to control bi-axial speeds allowed for greater precision in obtaining greater uniformity in thickness distribution. Optimum speed profiles for CCLRM were constructed from conducting flow visualisation studies. CCLRM requires the use of a mouldable liquid and a polyurethane elastomer (thermoset) (monothane Grade A60, Compounding Ingredients Limited (CIL), Lancashire, UK) was used because of its practicality in studying the fabrication process. The closed CCLRM of the monothane was used to make the hollow IVDP.

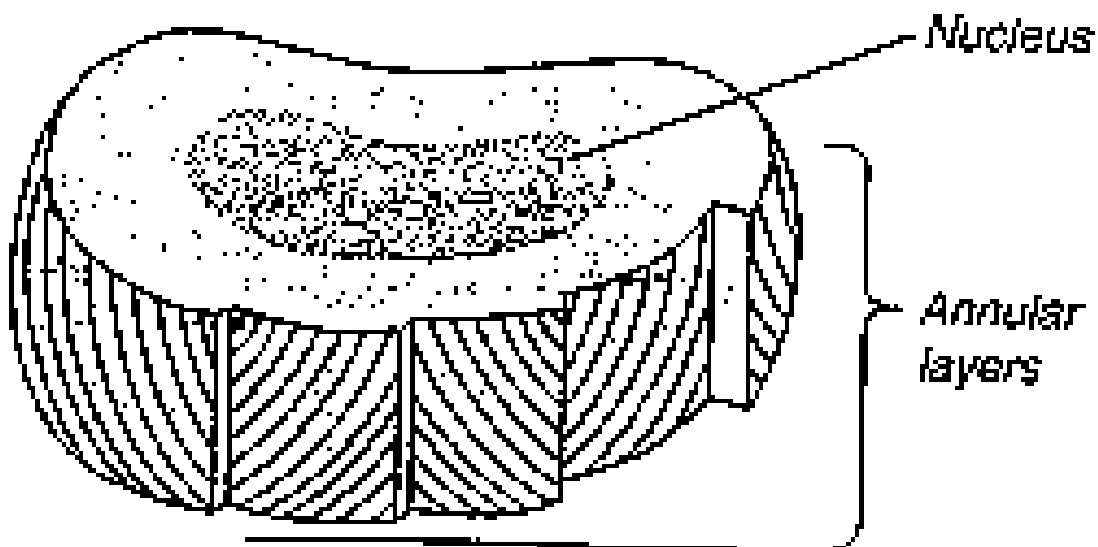


Figure 1: Intervertebral disc structure



Figure 2: Open Mould of Intervertebral Disc Prosthesis



Figure 3: Computer Controlled Liquid Rotational Moulding (CCLRM) Machine

Optimisation of Rotational Moulding

CCLRM brings with it several variables related to the mould or processing that have to be addressed in order to consistently obtain an acceptable product. Mould variables include mouldable material properties, mould quality and amount of mouldable material used. With respect to the processing variables, temperature/humidity and speeds/speed ratio have to be studied. The material to be moulded had to be liquid in nature and also have sufficient curing time to allow for adequate and complete coating of the mould interior. Monothane was found to be suited for this purpose. Furthermore, because it reached its lowest viscosity point prior to

its actual curing temperature, it went through a natural degassing stage which would prevent bubble entrapment. The permanent aluminium closed moulds allowed for a smooth and permanent surface for the moulding material to coat over. This would ensure a better moulded product. Based on a number of moulding trials, it was determined that approximately 5.4 to 6 grams of material was the ideal weight for moulding of the hollow IVDP.

It was found that monothane did not reach its minimum viscosity point when the oven temperature display indicated a temperature of 140°C (curing temperature of monothane) for approximately 15 minutes. Since this would mean that it would therefore eventually arrive at its minimum viscosity temperature when the temperature of the oven was still at 140°C, this meant that the oven temperature could be kept constant at 140°C. In order to maintain the humidity, the exhaust fan was used during the moulding cycle to maintain a dryer environmental chamber.

The speeds and speed ratios to be used for moulding is an important parameter to optimise. If the speeds were too slow, then an incomplete moulded product would result since the material would simply form a pool at the bottom of the mould surface. If the speeds were too fast, the thickness distribution of the moulded product would be very uneven and hence undesirable especially where biomaterials are concerned since this could provoke increased thrombus formation. Speed ratio is constant for a particular geometry of mould. Flow visualisation studies were conducted using an external mould with a rod attachment. Using different viscosities of a dyed and diluted fluid (Dow Corning silicone fluid 350cs, USA), the major and minor speeds were varied according to the observed thickness distribution of the liquid on the mould surface. From this, a speed ratio was determined and a speed profile was constructed as described in Fig 4.

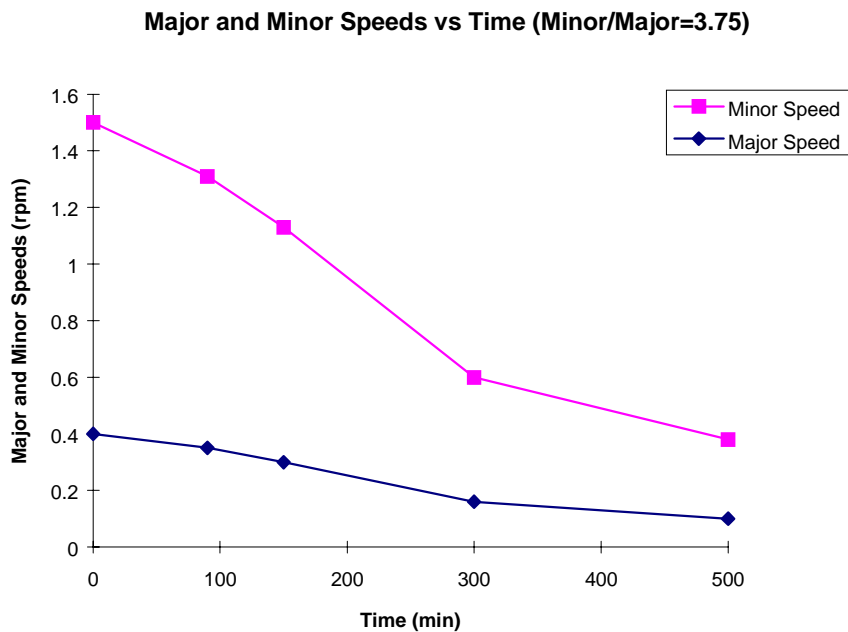


Figure 4: Speed Profile for CCLRM

Liquid-Filled Composite IVDP

Samples of liquid-filled IVDPs were inserted into a pocket that had a weft knit structure [Fig.5]. This structure was fabricated using a flat bed knitting machine and was made from aramid (Kevlar, DuPont Ltd., USA) yarns. Kevlar was chosen because of its potential use in implants [4]. The IVDP held in the knitted fabric was then dipped in monothane and was left submerged in the resin at a temperature of 120°C for two hours and then at 140°C for one hour. Subsequently, the whole set-up was placed in a larger disc cavity mould which matched the dimensions of our IVDP design requirement. The hollow composite IVDP was then injected with water.

Solid Composite IVDP

A solid IVDP was also fabricated. This was performed by complete filling of the IVDP mould cavity by liquid monothane and allowing to cure by heating for a period of 8 hours. As before, subsequent application of the composite layer was performed to encapsulate the IVDP.

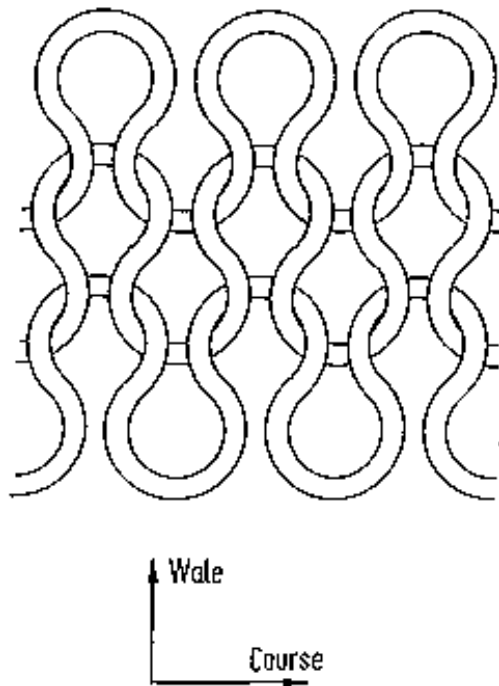


Figure 5: Weft Knitted Structure

DISCUSSION ON COMPRESSIVE BEHAVIOUR

Natural IVD

Typical stress-strain relationships for the natural IVD are depicted in Fig.6 [5]. The modulus values are seen in Table 1. An upper and lower range define the limits of a normal disc.

Beyond the upper limit, axial stiffness would be too high and below the lower limit would imply a degenerative disc. The modulus was calculated in both an initial (at less than 0.2 KN load) and final region (close to the peak modulus of the curve) (hereby called slope 1 (E_{c1}) and slope 2 (E_{c2}) respectively).

Liquid Filled IVDP

Compression testing of the three different cases of prostheses were performed. These were 1] liquid-filled IVDP, 2] liquid-filled, composite encapsulated IVDP and 3] solid, composite encapsulated IVDP. The compressive behaviour of these IVDPs can be seen in Figure 7. The curves clearly display a bi-modulus stress-strain relationship, hence the rationale for defining an initial and final region. Figure 7 has a defined strain limit of 10 % even though our IVDPs could deform in excess of 100 % when greater loads were applied. The reason for this is that in situ testing has determined surface strains on the IVD to be in the range of about 6 to 10 % for a load of 2150 N [6].

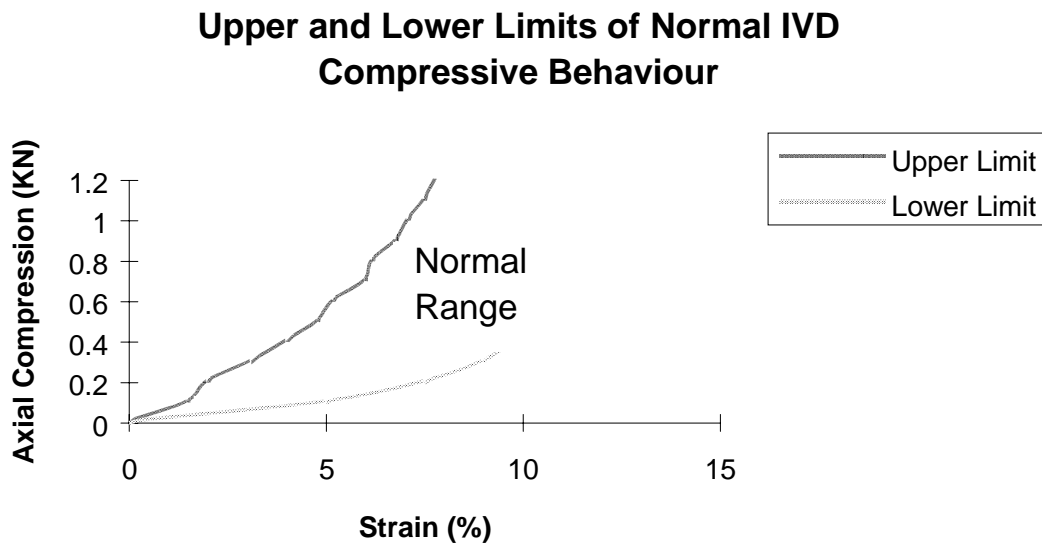


Figure 6: Upper and lower limits of a normal IVD as defined by [5]

Concentrating first on the water-filled nucleus alone, note that the steep region beyond 80% strain is not truly indicative of the sample since it was observed that leakage of the water inside occurred at roughly 10 N of load. When a large part of the water leaked out, the sample would be flattened and as a result, very little deformation could be possible at that point. Although leakage is evidence of nucleus failure, rupture, which is more catastrophic did not occur.

Although testing of the hollow, liquid-filled IVDP was not found to be optimum, it served several other purposes. Namely these were to determine a trend in the stiffness properties, to observe the compressive properties of the nucleus alone which may on its own also serve as a disc replacement and finally also to determine the benefits of a hollow, liquid-filled structure which essentially replicates the form of the IVD.

Liquid-Filled, Composite IVDP

This IVDP displayed consistent moduli values with the two slopes but were found to be lower than desired. This was perhaps due to leakage of liquid which was again observed, but was less extreme. Another related problem was that the adhesive used to seal the site of liquid injection degraded after the heating and this also caused some weakening of the matrix and resin. However, further investigation to a liquid-filled composite IVDP is necessary as the distribution of stress and the method of absorption of loads may be important in ensuring IVDP viability. This view is reinforced because fluid pressurisation is thought to be critical in equipping the means by which the IVD supports load [7].

Solid Composite IVDP

In essence, a solid IVDP without the composite layer is a representation of the compressive behaviour of the volume of monothane in use and it was thus not compared independently.

Table 1: Compressive modulus values of nucleus and IVDP at two distinct slopes

TYPE	MODULUS (KPa) (SLOPE1) [E_{c1}]	MODULUS (KPa) (SLOPE 2) [E_{c2}]
NATURAL IVD (CALCULATED FROM FIGURE 9)	$20.78 < E_{c1} < 103.90$	$74.21 < E_{c2} < 173.16$
SOLID NUCLEUS WITH COMPOSITE LAYER	17.24	40.00
WATER-FILLED NUCLEUS WITH COMPOSITE LAYER	7.41	20.98
WATER-FILLED NUCLEUS	8.36	95.62

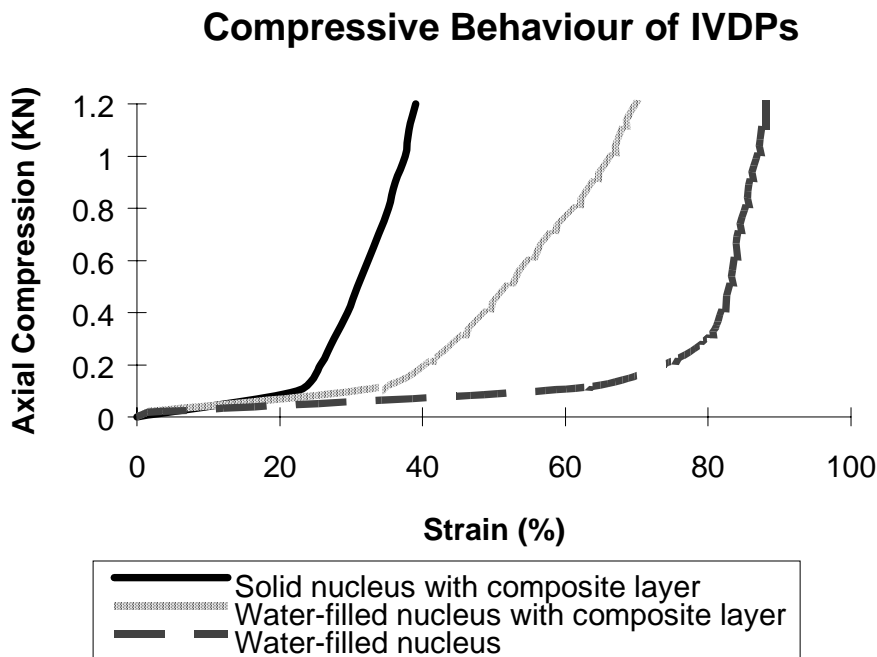


Figure 7: Compressive behaviour of IVDPs

However a solid, composite IVDP was fabricated and tested because it may sufficiently provide the required mechanical properties and as a consequence simplify the IVDP process considerably. This would enable a more consistent and desirable product.

From Figure 7, it can be seen that the solid, composite IVDP provides a compressive behaviour that limits the deformation and hence provides a higher stiffness. Secondly being solid, failure by way of leakage or adhesion loss does not occur. It was determined that the compressive modulus of a fibre reinforced solid IVDP design by [5] was 23.6 KPa in slope 1 and 86.6 KPa in slope two. A comparison between our solid IVDP and the fibre reinforced disc described in [5] describes the latter as having higher stiffness. However this is expected because the strain rates in the former are very high due to its elastomeric properties. Nevertheless, the compressive behaviour of the solid IVDP was found to be fairly adequate.

One of the difficulties in assessing optimum IVDP design is that the deformability limit of the intervertebral disc cannot be defined precisely since it is a structure which retains structural integrity from liquid movement into and out of its core. Since bone fixation effects the disc stiffness, an attempt to match excised disc mechanical properties is no longer the sole criteria, rather in addition to this, the form of the disc, i.e., fibrous nature is also equally important to the motivation for use of textile composites in the concept of an artificial disc. In this regard, a more fundamental problem is that, the importance of simulating the hollow, liquid filled form, i.e., hollow nature of the IVD, is not yet fully determined. From the viewpoint of mechanical properties and processability, it does appear however that a solid, composite IVDP is most desirable.

CONCLUSIONS

The design, optimisation and compressive behaviour our concept of the IVDP have been presented in this paper. The natural IVD was replicated successfully using weft knitted textile fabrics. The rationale for use of weft knitted fabrics is the need for elastomeric or highly compliant characteristics while improving overall stiffness. It was found that the dimensions of the IVDP (polymeric core region) were vital in order for successful encapsulation with a composite layer. For the case of a hollow IVDP, it was determined that for the sake of a uniform thickness product, speed profiles in rotational moulding are critical.

From a comparison of the compressive behaviour of the IVDPs tested, it was the solid, composite IVDP that displayed the most desired mechanical properties. This is a clear indication that while the fibrous nature of the disc allows for replication of form and properties of the natural disc, the simulation of the hollow property of the natural disc, from a mechanical point of view is not essential.

REFERENCES

1. Ramakrishna S., Ramaswamy S., Teoh S.H., Hastings G.W and Tan C.T., "Application of Textiles and Textile Composites Concepts for Biomaterials Development", *Proceedings Tex Comp 3, The Third International Symposium*, Aachen, Germany, December 9-11, 1996, Session 6: Opportunities and Applications of Composites, pp.27/1-27/27.
2. Bao Q-B., McCullen M., Higham P.A., Dumbleton J.H and Yuan H.A., "The Artificial Disc: Theory, Design and Materials", *Biomaterials*, Vol. 17, No. 12, 1996, pp. 1157-1167.
3. Teoh S.H., Sin K.K., Chan L.S., and Hang C.C., "Computer Controlled Liquid Rotational Moulding of Medical Prosthesis", *Rotation*, Vol. 3, No. 3, 1994, pp 10-16.
4. Latour Jr. R.A. and Black J., "Development of FRP structural Biomaterials: Ultimate Strength of the fiber/Matrix Interfacial Bond in In-ViVo Simulated Environments," *Journal of Biomedical Materials Research*, Vol. 26, 1992, pp. 593-606.
5. Lee C.K., Langrana N.A., Parsons J.R. and Zimmerman M.C., "Development of a Prosthetic Intervertebral Disc", *Spine* Vol. 6, No. 6 supplement, 1991, pp. S253-S260.
6. Stokes IAF. "Surface Strain on Human Intervertebral Disc", *Journal of Orthopaedic Research*, Vol. 5., 1987, pp. 348-355
7. Best B.A., Guilak F., Setton L.A., Zhu W., Saed-Nejad F., Ratcliffe A., Weidenbaum M and Mow V.C., "Compressive Mechancial Properties of the Human annulus Fibrosus and Their Relationship to Biochemical Composition", *Spine*, Vol. 19, No. 2, 1994, pp. 212-221.

LONG TERM AGING OF IMPLANTED SILICONE/SILICA COMPOSITE BREAST IMPLANTS

Clarence J. Wolf, H. J. Brandon, K. L. Jerina and V. L. Young

Materials Science and Engineering, Washington University, St. Louis, MO 63130

SUMMARY: A comprehensive study is being conducted to investigate the changes in the mechanical and chemical properties of composite (silicone/silica) breast implants as a function of implantation time. In the present study the properties of gel-filled explants with in vivo duration times ranging from 4 months to 21 years are compared to control samples. Tensile strength and elongation were measured for both explant and control shells using identical testing protocols. In addition, the tensile strength and elongation of shells which were extracted with hexane to remove non-cross linked silicones were measured. The chemical composition of the shell extracts was examined by MALDI (matrix assisted laser desorption ionization) mass spectrometry and gas chromatography/mass spectrometry (GC/MS). In addition, swelling measurements were used to determine the average molecular weight between cross-links (and/or entanglements). Low molecular weight silicones with degree of cyclization ranging from 4 to 20 were determined by GC/MS. Linear PDMS with molecular weights up to 12,000 Daltons and cyclics with degrees of cyclization up to 60 were measured by MALDI.

KEYWORDS: aging, durability, silicone elastomers, breast implants.

INTRODUCTION

The use of advanced polymeric and composite materials in biomedical applications has increased tremendously in the past few years. Of particular interest has been the use of composite materials for in vivo applications such as hip joints or artificial body parts. One particular system, silicone breast prostheses (implants), has received considerable notoriety during the past 3-4 years, primarily through the mass communication media and the judicial system. Although breast implants are not usually considered composites, the shell which contains the fluid or gel is a true composite and is composed of a cross-linked silicone rubber containing a fine particulate silica filler. The silicone/silica composite shell is used in almost all breast implants regardless of manufacturer or filling fluid. Implants have been filled with lightly cross-linked silicone gel, saline solution, and soybean oil.

In general, the shells fall into two broad classes typified by Dow Corning Silastic® I and Silastic® II. A silicone dispersion in an appropriate solvent, such as toluene or xylene, containing approximately 16% silica (SiO₂) and a small amount of cross-linking catalyst (such as chloroplatinic acid) is coated on a mandrel and thermally cross-linked after a specified thickness has been applied. The silica is added to increase the mechanical properties of the silicone elastomer. Silastic® I contains only the silicone/silica shell while Silastic® II contains an additional barrier layer of fluorosilicone or diphenylsilicone polymers or copolymers. The extra layer, usually called the "barrier coating" is added to minimize the permeation of gel fluid, typically low molecular weight silicones, through the shell.

The biomedical controversy surrounding the breast implant issue has been primarily concerned with the immunology or effect of silicone fluids on health issues. Our work is concerned with the long-term durability or aging of the silicone/silica composite shell. We have an inventory of approximately 500 explanted breast implants and 400 control implants which were manufactured at various times by different suppliers. The controls were stored in an ambient environment since their fabrication. Silastic® I implants were first used in the early 1970's while the Silastic® II's were first introduced in the early 1980's. Therefore, we have a large series of samples which were aged in vivo for time periods ranging from a few months to more than 20 years. The implants were prepared over a ten year period and as might be expected there is some variation in the exact composition and structure of an implant type even when prepared by a specific manufacturer. This report is restricted to a study of implants prepared by one manufacturer and the associated controls manufactured at approximately the same time. The data can be used to formulate general trends in material properties as a function of real time aging.

The mechanical properties and chemical composition of the silicone/silica composite shells are strongly related. Mechanical properties of specific interest are tensile strength and elongation. These properties are primarily governed by the cross-link density of the elastomer, the effect of plasticizers on the elastomer, and the nature of the silicone-silica interaction. Real-time aging is a combination of both physical and chemical aging. Physical aging includes such phenomena as plasticization while chemical aging is concerned with bond breakage or formation, i.e., cross-linking or degradation.

If the elastomer undergoes a reaction with the environment, i.e., chemical aging, a change in the cross-link density of the elastomer is to be noted. An increase in cross-link density should be accompanied by an increase in modulus and an associated embrittlement of the shell; a decrease in cross-link density suggests degradation of the elastomer and an overall loss in strength. The silica serves as bonding sites for the silicone chains and a loss in the interaction between the silicone and the silica would primarily lead to a decrease in the mechanical strength of the shell. Most of the implants contain a silicone gel with a composition similar to that of the cross-linked shell. The gel contains a large mixture of cyclic and linear silicones with a solubility parameter nearly identical to that of the elastomeric shell. Thus, the overall composition of the low molecular weight silicones, i.e., the non-cross-linked component, and their concentration sorbed by the elastomeric shell during aging is indicative of aging induced changes in the composition of either the shell or the gel which may occur during implantation.

It is particularly important to compare values obtained from a series of samples implanted for various time periods with those of samples prepared at essentially the same time, but not implanted, i.e., control samples. We used a series of mechanical testing and advanced physical chemical methods to analyze explanted samples and compare the results with a similar series of non-implanted specimens.

EXPERIMENTAL

Preparation of Samples: The elastomeric shells were wiped clean of the adhering silicone gel by gentle wiping with Kimwipes® moistened with isopropyl alcohol. Both dog-bone shaped samples (for strain/strain analysis) and rectangular pieces (approximately 3x3 cm for swelling measurements) were cut from sections of the shell and their positions were recorded. In general, five dogbone shaped samples were used for mechanical testing and three additional samples were extracted with hexane for the extraction studies.

Extraction of Shells: The samples were extracted in chromatographic grade hexane (Fisher) at 50°C for 96 hours. The samples were carefully dried to constant weight and used for subsequent analysis. The percent extractable was determined from the initial and final weights. The hexane extract was used directly for both GC/MS, and MALDI analysis.

Cross-Link Density: The cross-link density of the elastomer shells was determined by swelling measurements. After hexane extraction, which removes “all” the low molecular weight silicones, shell samples were swollen in toluene to constant weight. The samples were removed from the toluene, patted dry, and placed in a tared glass weighing jar. The cross-link density (v_c) was determined according to the Flory-Rehner theory [2] for polymer swelling:

$$v_c = \left[-\ln(1 - v_p) + v_p + \chi v_p^2 \right] \left[V \left(v_p^{1/3} - \frac{1}{2} v_p \right) \right] \quad (1)$$

where χ is the solvent interaction parameter, v_p is the volume fraction of polymer in the swollen rubber, and V is the molar volume for the swelling agent (for toluene $V = 106 \text{ cm}^3/\text{mol}$). For toluene sorption in PDMS elastomer, $\chi = 0.413 + 0.364 v_p$ [3]. The average molecular weight between cross-links (M_c) is given by the reciprocal of v_c

$$M_c = \frac{\rho}{v_c} \quad (2)$$

where ρ is the density of the polymer. The tensile modulus (Young’s) E for the membrane can also be estimated by the relation

$$E = 3RTv_c \quad (3)$$

where R is the universal gas constant the T is the temperature (K).

MALDI: Matrix assisted laser desorption ionization (MALDI) mass spectrometry is a recent development specifically designed to utilize the tremendous analytical capability of mass spectrometry for the analysis of high molecular weight compounds [4,5]. The MALDI mass spectrometer is a PerSeptive Biosystems Voyager RP with a nominal resolving power of approximately 300 and the upper mass range is approximately 50,000 Da. A few micograms of a polymer extract are placed on an inert matrix, such as 2,5 dinitrobenzoic acid, dried and ionized with a N_2 -laser (338 nm). The radiation is absorbed by the matrix and “transferred” to the polymer, with little or no fragmentation of the molecular ions.

Tensile Testing: Tensile testing was conducted on a minimum of 5 specimens cut with ASTM D412 die D half-scale. [Only 3 samples were measured for the extracted samples.] The tests were conducted to conform to ASTM D412 on an Instron 5583. The elongation data were obtained from grip extension at a cross head speed of 20 in/min.

RESULTS AND DISCUSSION

The stress/strain curves for typical Silastic® I and Silastic® II implant shells are shown in Figure 1. [The ordinate represents the engineering stress.] The curves are nearly identical for low strains but rapidly diverge for strains greater than 200%. Silastic® II exhibits the typical

stress/strain curve expected for a thin elastomer. In general, both the strain-to-failure and the stress-to-failure are considerably larger in Silastic® II controls than observed in Silastic® I controls. The toughness of Silastic® II, i.e., the area under the stress/strain, is also larger than that exhibited by Silastic® I.

The material which is extracted from the shell can result from one or more of four sources: 1) indigenous originally present in the elastomer, 2) diffuse in from the bio-environment, 3) diffuse in from the filling fluid (in this study from the silicone gel), or 4) result from the degradation of the elastomer network. Our analytical method was not designed to identify biomaterials, so case 2) is not applicable to this study. For an aging or long-term durability study, it is not important to distinguish between 1) and 3) but distinguish between indigenous and/or gel and degradation products. It is difficult to separate the compositional changes due to the variability of processing procedures used over a ten-year period (1975-1986 for Silastic® I and 1981-1992 from Silastic® II) from those changes associated with in vivo aging. However, a careful examination of a large number of specimens and controls can lead to meaningful distinction between degradation products and indigenous and/or sorbed compounds.

The strength and elongation of Silastic® I and Silastic® II implants as a function of implantation time are shown in Figures 2 and 3, respectively. Although there is considerable scatter in the data, Silastic® I shows little change in strength after 20 years in vivo, although elongation

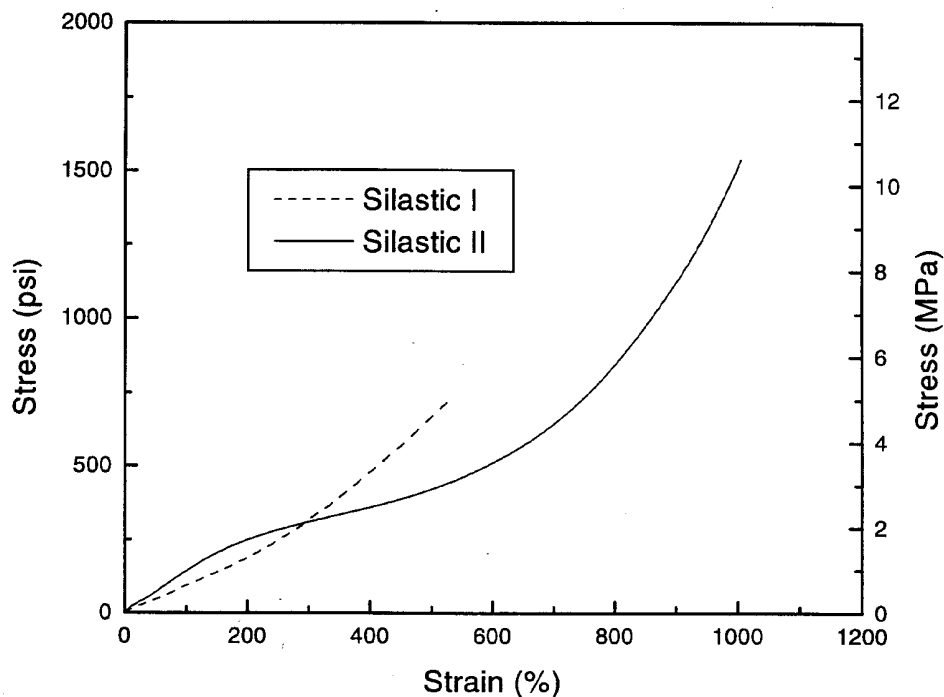


Fig. 1. Stress/strain curve for typical as-received Silastic® I and Silastic® II silicone/silica elastomeric shell.

appears to decrease on the order of 20% in the same time interval. However, Silastic® II does appear to exhibit a decrease in both strength and elongation as a function of implantation time. It is important to note that additional long-term data is needed to determine the relationship between the mechanical properties and implantation time. Do the properties decrease linearly with time, or do they reach an asymptotic value? The amount of extractables in Silastic® II shell increases with implantation time, see Figure 4. The increased

swelling of the Silastic® II samples as function of implantation time can account for a large fraction of the property decrease exhibited in Figure 3. The non-cross-linked silicone in the gel in Silastic® I shell reach an equilibrium concentration in a short time, i.e., of the order of months. Because of the barrier coating in Silastic® II, many months, or even years, are required to reach equilibrium. Therefore, the measured properties would appear to decrease even though the elastomeric network was not degraded. A comparison of the changes in mechanical properties of as-received controls and the corresponding extracted samples is given in Table 1. These values are compared to data supplied by the manufacturer on a dispersed elastomer film prepared from the same batch of material used to prepare the implant. The agreement between the values of the extracted shell and elastomeric film data is good. This data supports the hypothesis that the sorbed compounds do not degrade the elastomeric network.

MALDI provides an excellent method to analyze the molecular distribution of the extract. A typical MALDI spectrum from a Silastic® I control is shown in Figure 5. In this particular sample the amount of material extracted from the shell corresponds to 23% of its dry weight. The number average and weight average of the extract are 2618 and 4650 Da, respectively. The insert shows an expanded portion of the mass region from 1050 to 2000 Da. Two series of peaks are clearly visible, each member of the series separated by 74 mass units (corresponding to the basic siloxane unit $[\text{CH}_3)_2\text{SiO}]$. The two series are separated by 14 mass units, a methylene group. These two series correspond to linear and cyclic silicones: the structure of the linear and cyclic molecules are $\text{CH}_3[\text{Si}(\text{CH}_3)_2\text{O}]_n \text{Si}(\text{CH}_3)_3$ and $[\text{Si}(\text{CH}_3)_2\text{O}]_m$, respectively and are the characteristic materials found in the filling gel.

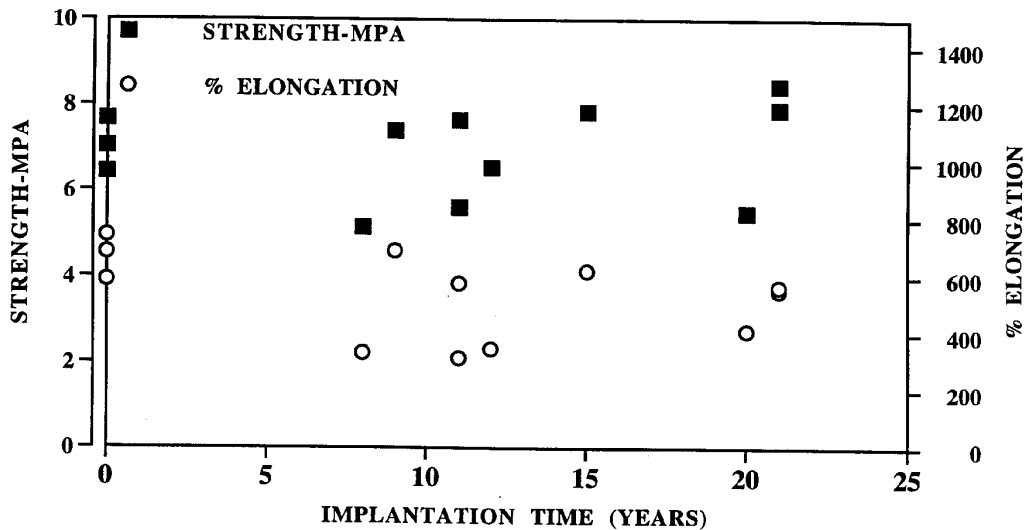


Fig. 2. Strength and elongation as a function of implantation time for Silastic® I silicone/silica shell implants.

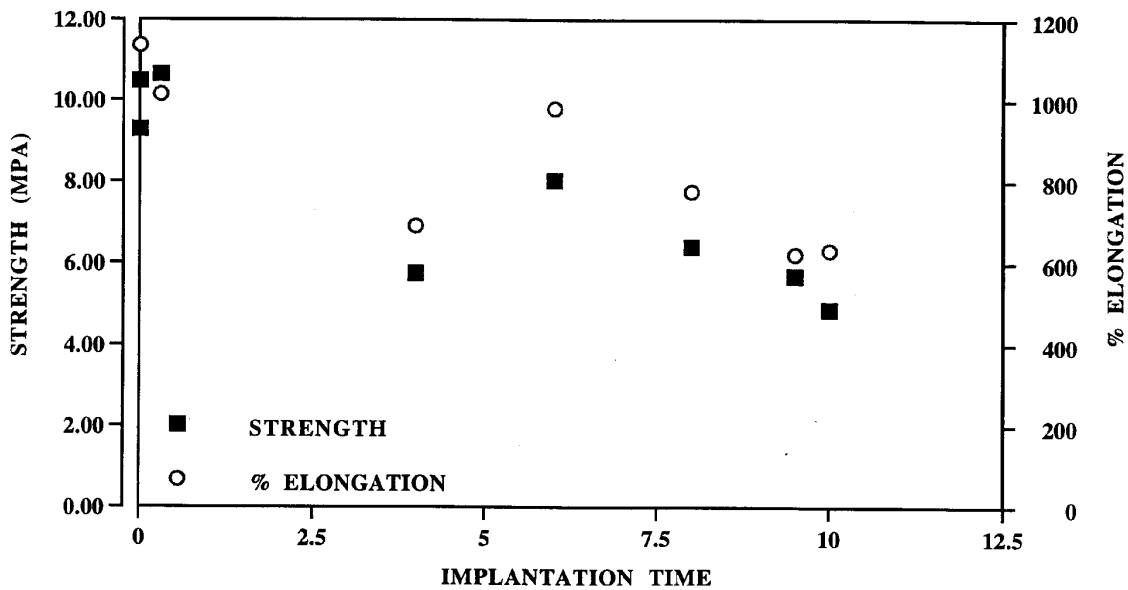


Fig. 3. Strength and elongation as a function of implantation time for Silastic® II silicone shell implants.

The number and weight average molecular weights determined by MALDI for a series of Silastic® I and Silastic® II explants as a function of implantation time are given in Figures 6 and 7, respectively. The values measured for the controls (zero implantation time) vary by 25%. The values observed in Silastic® I are, within experimental error, independent of implantation time. Although additional data is required, the preliminary studies suggest that the average molecular weight of the extract from Silastic® II increases during aging. This latter observation may result from the slow diffusion of non-crosslinked silicones from the gel into the shell.

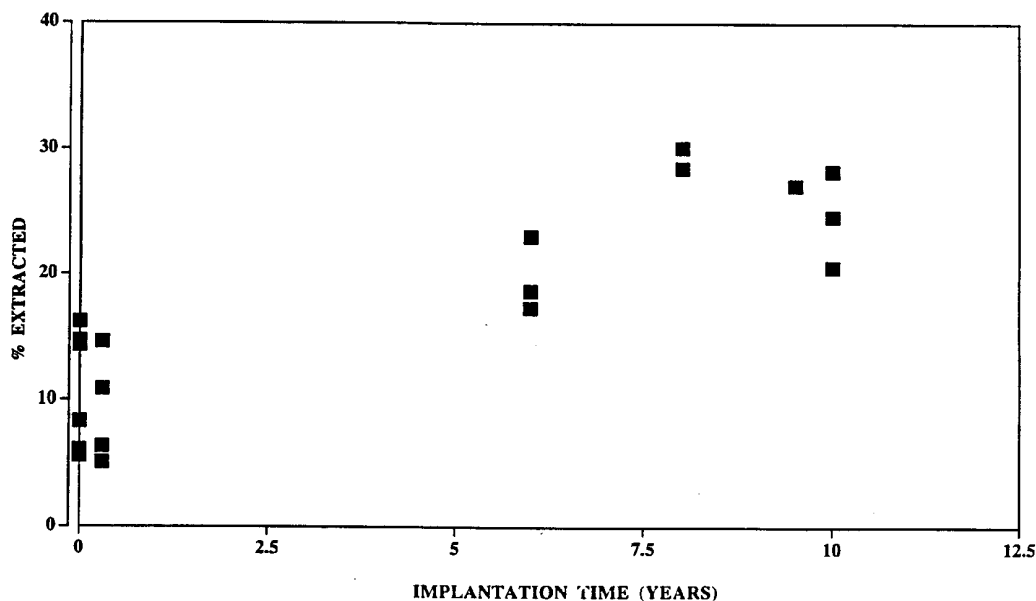


Fig. 4. Percent extractables (hexane) as a function of implantation time for Silastic® II shells.

Table 1: Comparison of Mechanical Properties of As-Received Shells, Extracted Shells, and Dispersed Elastomer Films*

	Silastic® I	Tensile Strength	
	% Extracted	MPa	% Elongation
As-Received Shell	---	5.63	397
Extracted Shell	17.0	10.86	565
Elastomer Film*	---	9.25	604
	Silastic® II		
As-Received Shell	---	10.39	921
Extracted Shell	14.7	13.83	1131
Elastomer Film*	---	12.43	1211

*Dispersed elastomeric films of the same batch prepared at the time the implants were originally manufactured.

The cross-link densities, determined from swelling measurements, as a function of implantation time for Silastic® I and Silastic® II shells are shown in Figures 8 and 9, respectively. If the elastomer embrittles, one would expect the cross-link density to increase; a decrease suggests elastomeric network degradation. The cross-link density of the Silastic® I implants is essentially independent of implantation time even after 21 years in vivo. This suggests that the silicone elastomer undergoes little or no change during implantation. The cross-link density of the Silastic® II implants may exhibit a slight increase with implantation time. However, the measured values are within the limits of the experimental error and if any change occurs, it is small. Additional work on this particular issue is needed before a definitive conclusion regarding the long-term durability of Silastic® II implants can be determined.

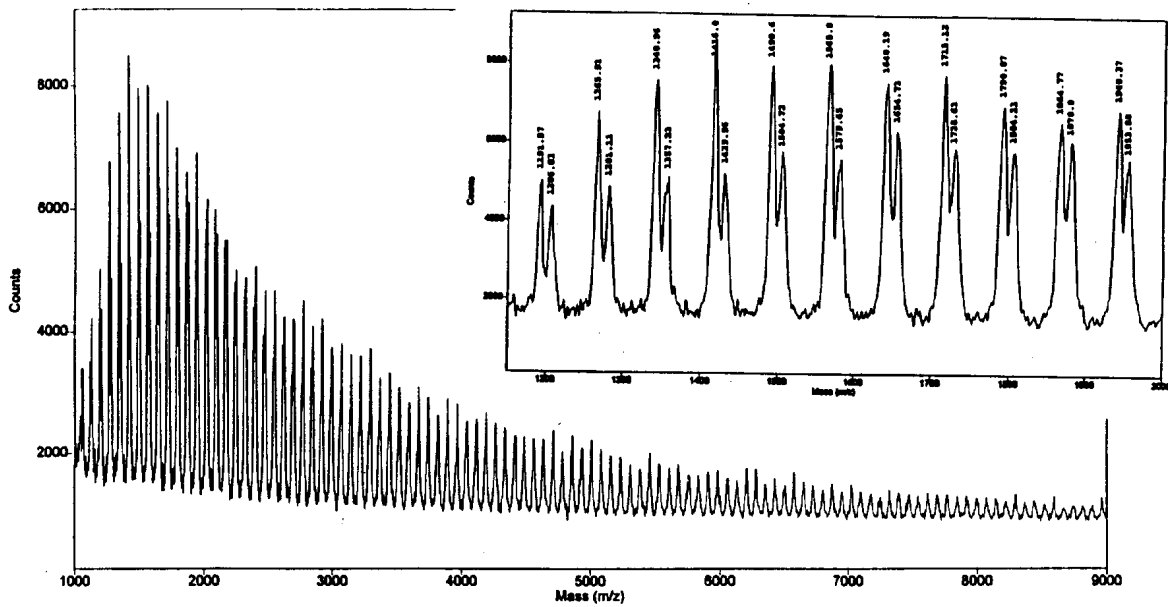


Fig. 5. MALDI Mass Spectrum from the extract of a Silastic® I silicone/silica shell. The insert shows an expanded view of the mass range from 1150 to 2000 Da.

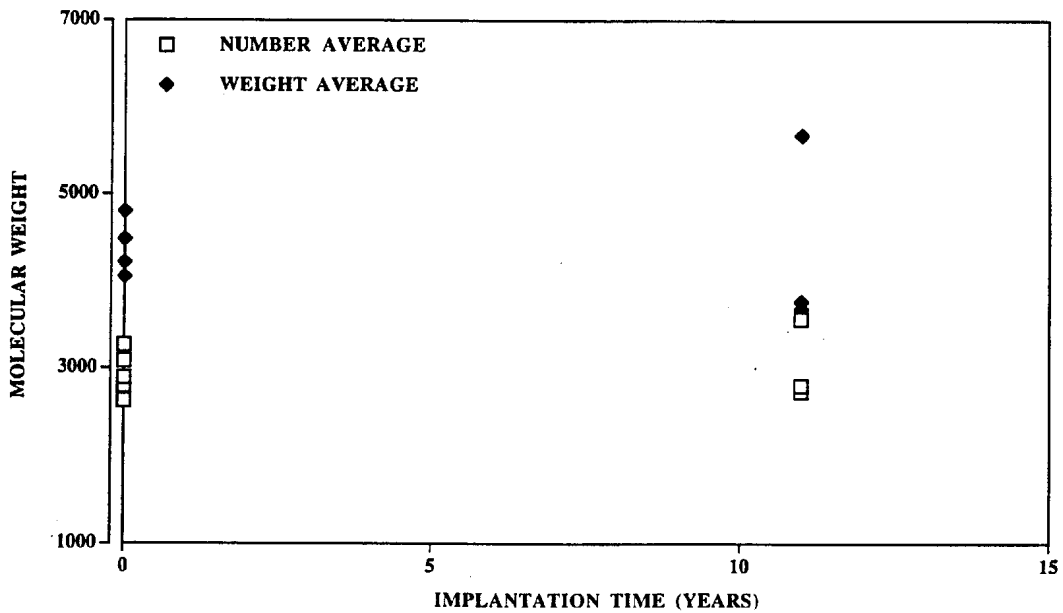


Fig. 6. Number and weight average molecular weights determined by MALDI-MS from the extract of a Silastic I shell as a function of implantation time.

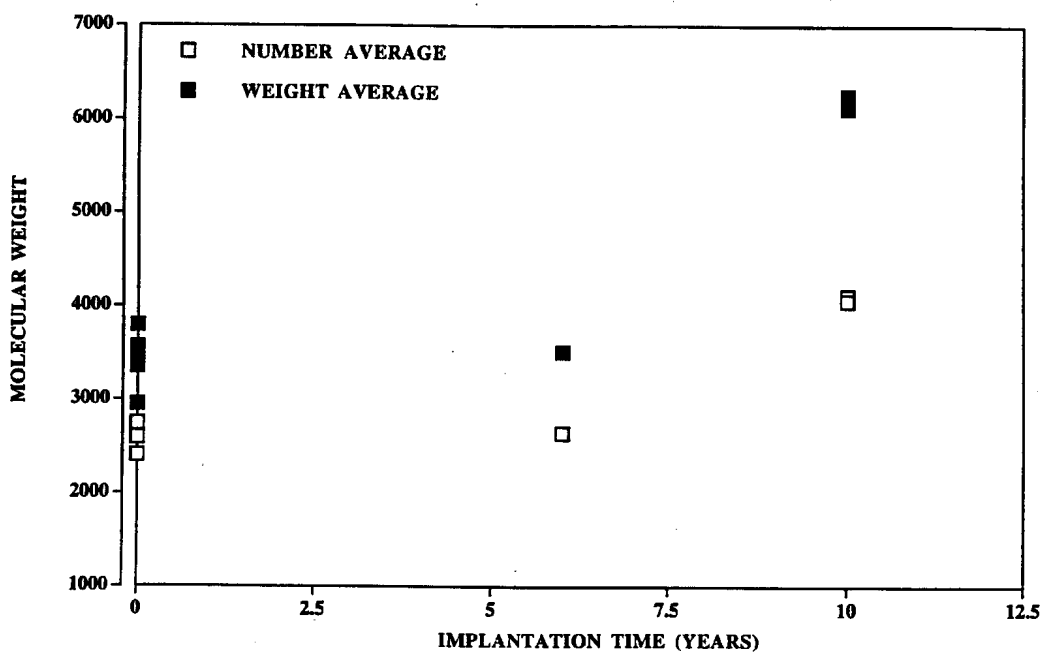


Fig. 7. Number and weight average molecular weights determined by MALDI-MS from the extract of a Silastic® II shell as a function of implantation time.

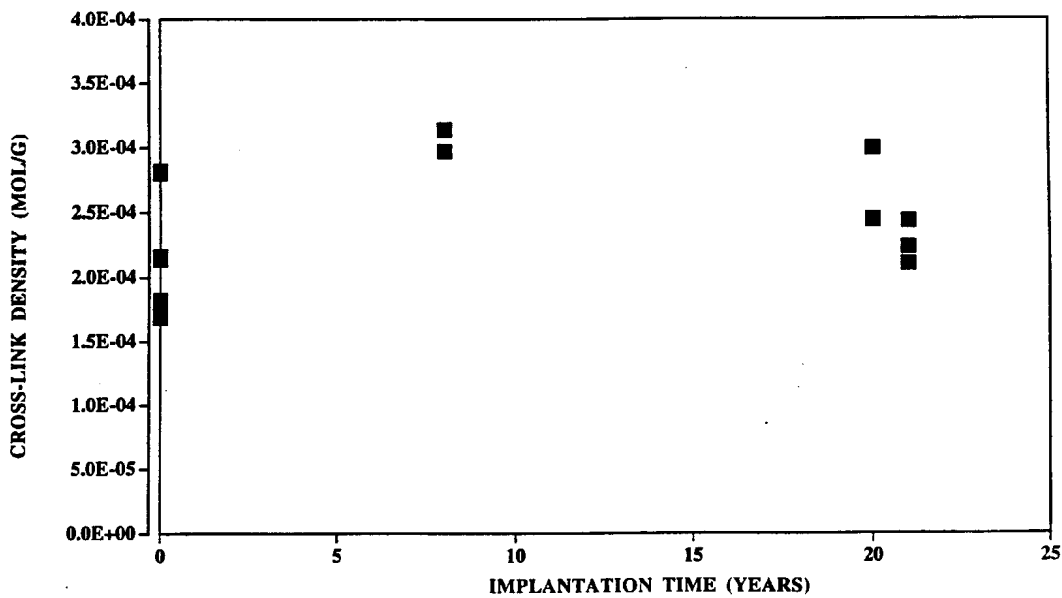


Fig. 8. Cross-link density of the silicone/silica shell as a function of implantation time for Silastic® I shells.

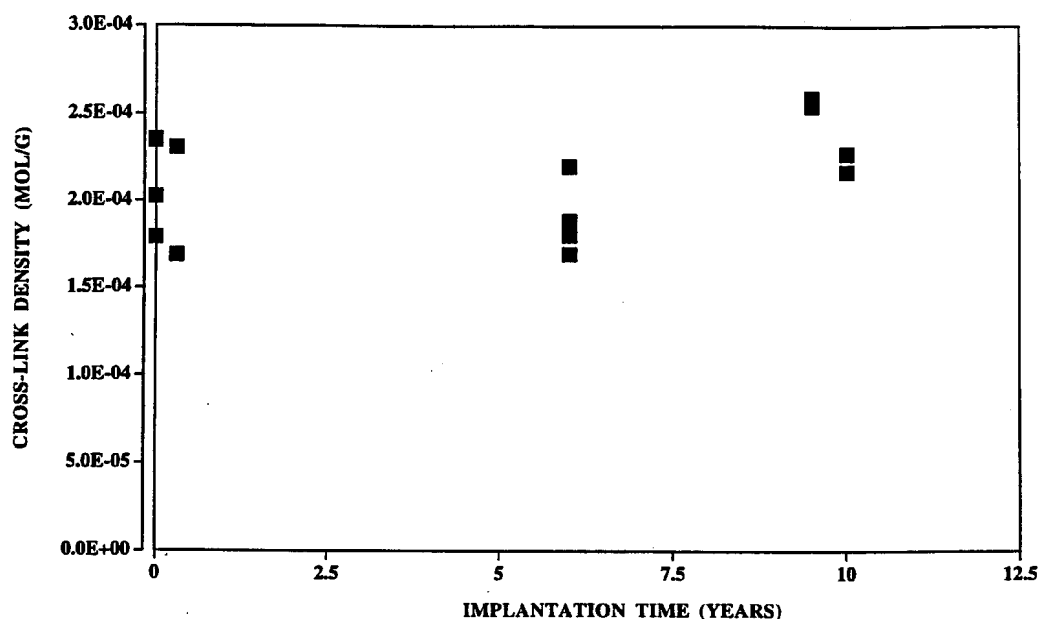


Fig. 9. Cross-link density of the silicone/silica shell as a function of implantation time for Silastic® II shells.

SUMMARY

The mechanical and chemical properties of silicone/silica explanted breast implants which have implantation times ranging from zero (controls) to 21 years were studied. Strength, elongation-to-failure, extractables, cross-link density, number and weight averaged molecular weights from extracts were determined. The Silastic® I shells, with no barrier coating, show little change in tensile strength and a slight decrease in elongation even after 21 years in vivo implantation time. Silastic® II shells, containing a barrier coating, exhibit a decrease in strength and elongation with time with a corresponding increase in silicones sorbed from the gel. The data suggest that the overall change in the silicone elastomer of Silastic® II shells is small. The integrity of the barrier coating was not examined and the influence of this coating on the long-term properties of an implant is an open question.

REFERENCES

1. Immunology of Silicones, Springer-Verlag, NY, Eds. M. Potter and N. R. Rose, (1996).
2. Floy, P. J., Rehner. Statistical mechanics of cross-linked polymer networks. II. Swelling. J. Chem. Phys. 1943; 11:521.
3. E. Favre, Eur. Polym. J., Application of Flory-Huggins Theory to Polymer-Solvents Equilibria 32 (10), 1183 (1996).
4. Hillenkamp, F., Karas, M., Beavis, R. C., Chail, B. T. Matrix-assisted laser desorption ionization mass spectrometry of biopolymers. Anal Chem. 1991; 63:1193 (A).
5. David, P. O., Kars, D. E. A facile sample preparation for the analysis of synthetic organic polymers by matrix-assisted laser desorption/ionization. Org. Mass Spectrum 1993; 28:923.
6. Wolf, C. J., Brandon, H. J., Young, V. L., Jerina, K. L., Srivastava, A. P. Chemical, physical, and mechanical analysis of explanted breast implants in Immunology of Silicones, Springer-Verlag, NY, Eds. M. Potter and N. R. Rose (1996), p. 25.

A DEVELOPMENT OF COMPOSITE ARTIFICIAL LEG SHELL USING RTM PROCESS

Moon-Kwang Um¹, Byung-Ha Kim¹, Byung Sun Kim¹ and Eui-Jin Jun²

¹ Korea Institute of Machinery and Materials, Composite Materials Laboratory
66 Sangnam-dong, Changwon, 641-010, South Korea

² Ministry of Science and Technology, Government Complex 2, Gwacheon,
427-760, South Korea

SUMMARY: Composite artificial leg shell was designed and its manufacturing process by Resin Transfer Molding (RTM) was studied. Reinforcement and resin were characterized for the optimization of the process. In order to achieve high fiber volume contents of the part, the optimal process conditions were found based on the characterization of resin viscosity. And flow analyses were performed using the model developed for irregular cross-section cylindrical shell structure. Under the selected conditions (the mold temperature and the resin feed rate), the leg shell was manufactured. The fabricated part would be tested if it satisfies required static and dynamic load conditions.

KEYWORDS: artificial leg shell, RTM process, process optimization, optimization by viscosity characterization, flow analysis.

INTRODUCTION

The resin flow plays a crucial role in the manufacturing of leg shell using resin transfer molding (RTM) process. The parameters affecting the resin flow are resin viscosity, reinforcement permeability and pressure gradient induced by the process conditions. The flow through reinforcements fabrics, therefore, can be described by the well known Darcy's law [1]

$$\bar{U}_D = -\frac{K}{\mu} \nabla P \quad (1)$$

where \bar{U}_D is the average or Darcian velocity of the resin, μ is the resin viscosity, ∇P is the pressure gradient induced in porous media and K is the permeability of reinforcements.

Permeability is only dependent on the type and the geometry of reinforcements. Widely used form for permeability is Carman-Kozeny equation [1,2]

$$K = \frac{R_f^2 (1 - v_f)^3}{4k_{ii} v_f^2} \quad (2)$$

Where R_f is radius of single fiber, v_f is fiber volume fraction and k_{ii} is Kozeny constant and it varies when the angle between resin flow direction and fiber alignments changes.

In normal RTM process, the usual fiber volume content of the part is between 10-20%. Such that the resin flow velocity is large enough to fill the mold perfectly before the gelation of resin. But if the fiber volume fraction of the part is increased, the flow resistance is increased

rapidly and the permeability is also decreased surprisingly(Fig.1). Mold filling conditions, therefore, in advanced RTM process has to be taken into account carefully. And there needs the optimization of process temperature and pressure.

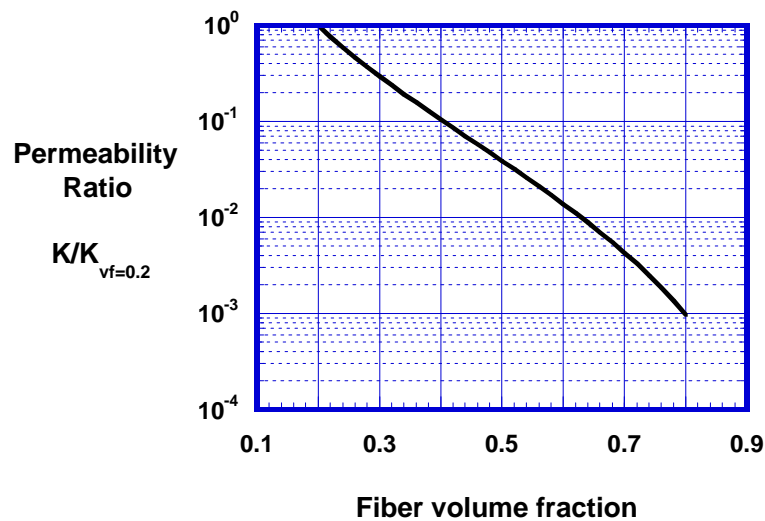


Fig.1 Permeability Ratio Based on the Permeability of $v_f=0.2$

Resin viscosity also effects largely on rein flow. Viscosity is usually a function of a temperature and an elapsed time after mixing of resin components to its gelation. If a mold is heated up, reaction of thermosetting polymer is accelerated due to the temperature effect. The optimal mold temperature should be found to maximize the resin flow.

CHARACTERIZATION OF REINFORCEMENTS

Knitted Carbon fabric(Unidirectional 6K bundle, Toray T300) is used for the reinforcements of the shell. The Pattern of the preform is given Fig.2 (here, fiber is Kevlar 49 for good observation of pattern). Cylindrical Preform is fabricated where the radius of cylinder changes. Permeability of fabrics is determined using the resin fronts measured from the experiment(Fig.3). In the experiment, constant inlet pressure is applied. Silicone oil is used . And the resin fronts as a function of time are measured. With the equation (2) and resin fronts, Permeability of preform are calculated [3,4].

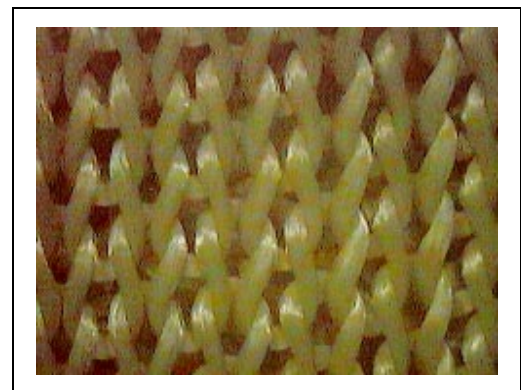


Fig.2 Pattern of the Knitted Preform used in the Process

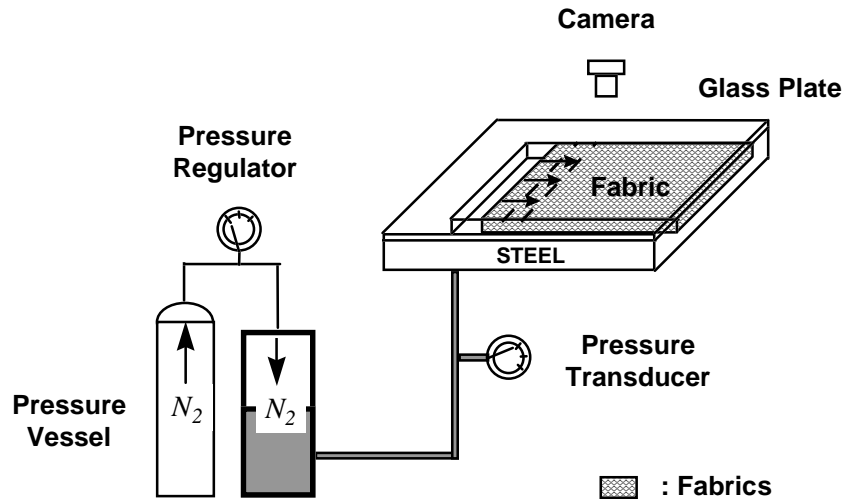


Fig.3 Experimental Setup for the Measurement of Preform Permeability

Fiber radius(R_f) is a value given by the manufacturer. Using the permeability measured in the experiments, the Kozeny constant is fitted(Fig.4). And the result is used to determine the permeability of preform when flow analysis is performed.

$$R_f = 4.0 \quad \mu\text{m} \quad (3)$$

$$k_{ii} = 0.43(4)$$

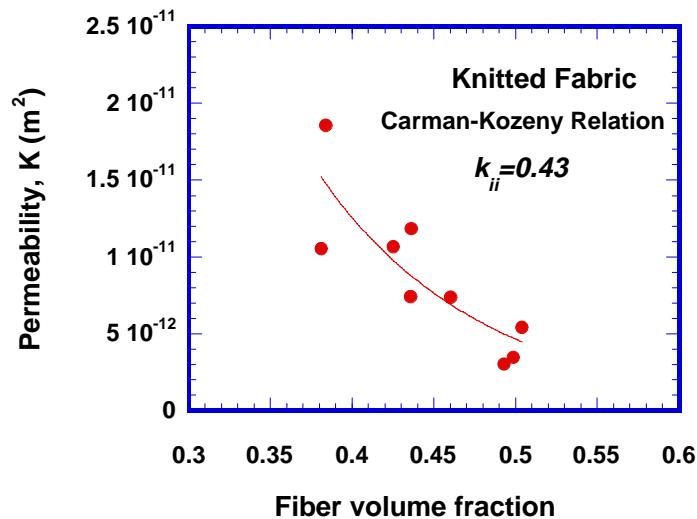


Fig.4 Experimentally Measured Permeability of the Preform

CHARACTERIZATION OF MATRIX

In RTM process for high fiber volume contents, the resin viscosity has a big effect on the mold filling time. And low viscosity CIBA-GEIGY LY564 epoxy resin is used for the matrix system and the hardener is HY2954. Recommended mixing ratio of LY564 and HY2954 by weight is 100 and 35, respectively. Resin viscosity is measured and cure of resin is analyzed.

Resin Viscosity

Viscosity(Fig.5) is measured using Brookfield cone and plate type viscometer(CAP2000). Viscosity changes as mixed resin reacts chemically with time but the change is not large in low temperature range. But total mold fill time of less than 30 minutes is preferred for the good properties of the part. Measured viscosity is used to determine optimal process.

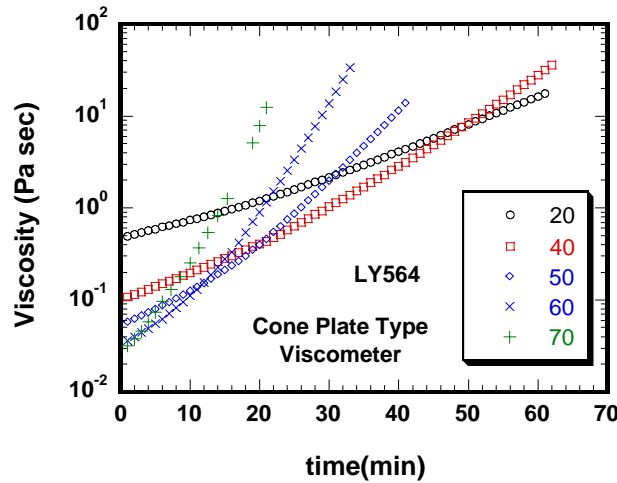


Fig.5 Measured Viscosity of Epoxy Resin(CIBA-GEIGY:LY564+HY2954)

Cure of the Resin

Cure kinetics modeling of LY564 epoxy resin can be performed by the quantification of heat released from the reaction. Released heats were measured using differential scanning calorimeter(DSC). The procedure of modeling is given in detail by reference 5. The reactive equations and the constants determined are given as follows.

$$\frac{d\alpha}{dt} = \frac{H_T}{H_U} \frac{d\beta}{dt} \quad (5)$$

where α is degree of cure, β is isothermal degree of cure, $\frac{d\alpha}{dt}$ is rate of cure, $\frac{d\beta}{dt}$ is isothermal rate of cure, H_T is isothermal heat of reaction and H_U is ultimate heat of reaction.

$$\frac{H_T}{H_U} = a + b \cdot T \quad (6)$$

$$a = -0.5984 \quad b = 4.241 \times 10^{-3} \quad (7)$$

where H_T/H_U is ratio of heat of reaction, T is absolute temperature.

$$\frac{d\beta}{dt} = (K_1 + K_2\beta^m)(1-\beta)^n \quad (8)$$

$$K_1 = A_1 \cdot \exp\left(\frac{-\Delta E_1}{RT}\right) \quad (9)$$

$$K_2 = A_2 \cdot \exp\left(\frac{-\Delta E_2}{RT}\right) \quad (10)$$

$$A_1 = -1.10 \times 10^2 \quad \Delta E_1 = -4.60 \times 10^3 \quad (11)$$

$$A_2 = 8.60 \times 10^3 \quad \Delta E_2 = -5.18 \times 10^3 \quad (12)$$

$$m = 0.25 \quad n = 1.425 \quad (13)$$

Here K_1 and K_2 are the coefficients dependent on the temperature, m and n are the constants independent on the temperature and R is the universal gas constant.

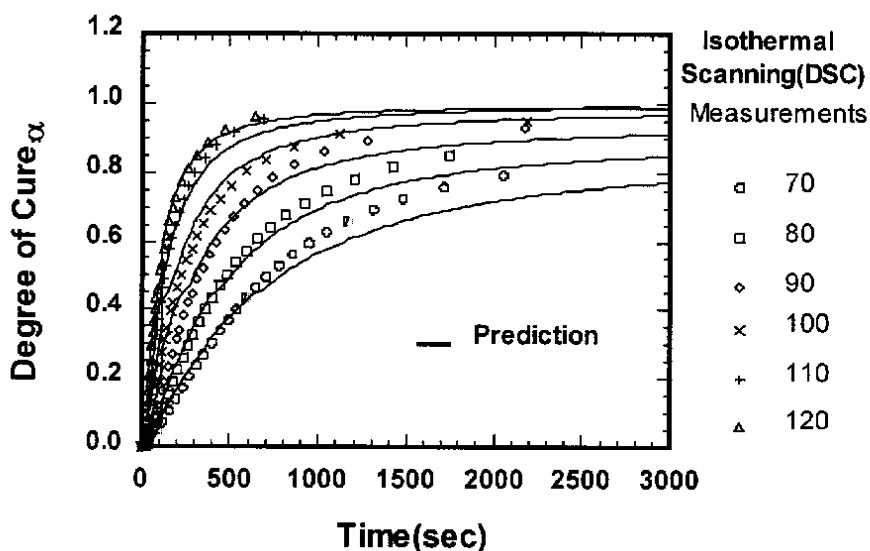


Fig.6 Comparison of Degree of Cure between measurements and predictions by the Model

To verify the model, the measured degree of cure and calculated values are compared (Fig.6). As can be seen from the comparison(Fig. 6), the measurements and the predictions show good agreements. Now if a specific cure cycle is given, the degree of cure can be calculated by integrating equation 6 with time.

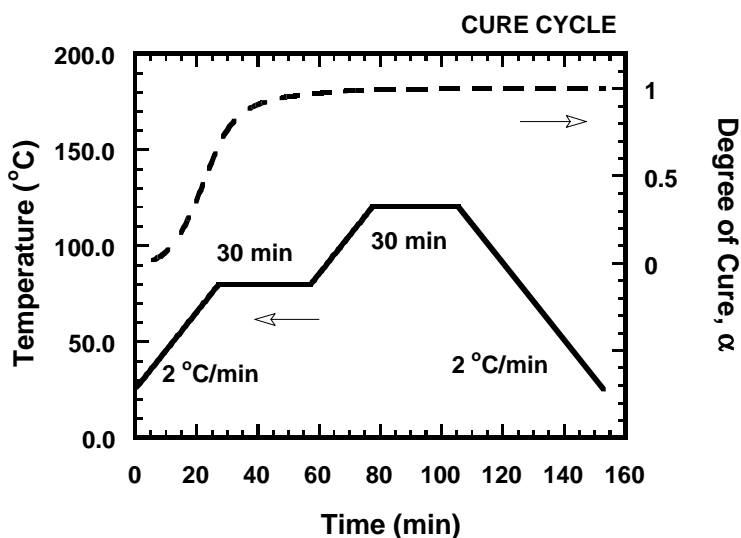


Fig.7 Cure Cycle of Epoxy Resin(CIBA-GEIGY:LY564+HY2954)

Adequate cure of the resin is needed for good mechanical property of composites parts. Two step cure is recommended by the manufacturer. Pre-cure is for low shrinkage and post-cure is for uniform cure and low internal stresses. Determined cure cycle is given in Fig.7. Here the gelation temperature is 80 and it should not be higher than absolutely necessary to maintain low shrinkage as well as low internal stresses. Second step temperature 120 is applied for post cure.

PROCESS OPTIMIZATION AND FABRICATION

A simple model to predict resin flow for any kind of irregular cross-section cylindrical shell structure is developed through the characterization of resin viscosity measured. To find optimal process conditions, parameter study was performed as a mold temperature changes. Under the determined optimal conditions, composite artificial leg shell was manufactured and processability is verified.

Optimal Process Conditions

A simple flow analysis model which can be applicable to the shape of irregular cross-section cylindrical shell structure is derived. Definitions used are given in Fig.8. $A(x)$ changes gradually. The model here is derived based on the constant flow rate.

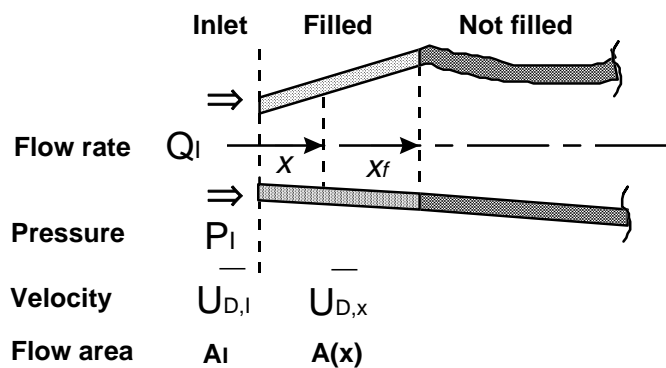


Fig.8 Calculation Domain Used for Flow Analysis

From the resin mass conservation, relation between Darcian velocity and flow area is

$$Q_I = \bar{U}_{D,I} A_I = \bar{U}_{D,x} A_x = \text{constant} \quad (14)$$

where Q_I is flow rate in inlet, $\bar{U}_{D,I}$ is Darcian velocity in inlet, A_I is flow cross-section area in inlet, $\bar{U}_{D,x}$ is Darcian velocity at specified x position, A_x is flow area at that position.

Also, from the resin mass conservation, a relation between resin front and time is

$$Q_I \cdot t_f = (1 - v_f) \int_0^{x_f} A(x) dx \quad (15)$$

where t_f is the time when the resin front reaches x_f .

Using equation 15, resin fronts as the time goes, (t_f, x_f) , can be calculated.

By integrating Darcy's law along the total flow field, inlet pressure is obtained as follows

$$\int_0^{x_f} \bar{U}_{D,x} \cdot \mu(t_x) dx = K \int_0^{P_I} dp = KP_I \quad (16)$$

The above equation is rearranged using equation 14

$$P_I = \frac{1}{K} \int_0^{x_f} \bar{U}_{D,x} \cdot \mu(t_x) dx = \frac{Q_I}{K} \int_0^{x_f} \frac{\mu(t_x)}{A(x)} dx \quad (17)$$

Optimal process condition can be obtained by minimizing inlet pressure in case of constant flow rate. In high fiber contents RTM process, to fill a mold fully high inlet pressure is necessary. And high inlet pressure can cause wrinkles of preform in early stage of filling. Gradual increase of inlet pressure, nearly the same as constant flow rate, is adequate.

As can be seen from equation 17, $\int_0^{x_f} \mu(t_x)/A(x) dx$ should be minimized to minimize inlet pressure. $A(x)$ is automatically determined if the geometry of the part is given. Therefore, minimization of $\int_0^{x_f} \mu(t_x)/A(x) dx$ is the same as minimization of $\int_0^{x_f} \mu(t_x) dx$. As $A(x)$ changes gradually, x are nearly linearly dependent on t_x . So minimization of $\int_0^{x_f} \mu(t_x) dx$ is the same as minimization of $\int_0^{t_f} \mu(t_x) dt_x$

$$\text{Minimization of Inlet Pressure} \Rightarrow \text{Minimization of } \int_0^{t_f} \mu(t_x) dt_x \quad (18)$$

Above equation means that process optimization can be easily done by the measured viscosity. The above result is more definite if the equation is derived for constant flow area.

$$P_I = \frac{Q_I}{KA_I} \int_0^{x_f} \mu(t_x) dx = \frac{Q_I^2}{\epsilon KA_I^2} \int_0^{t_f} \mu(t_x) dt_x \quad \Leftarrow \quad x = \frac{Q_I}{\epsilon A_I} \quad (19)$$

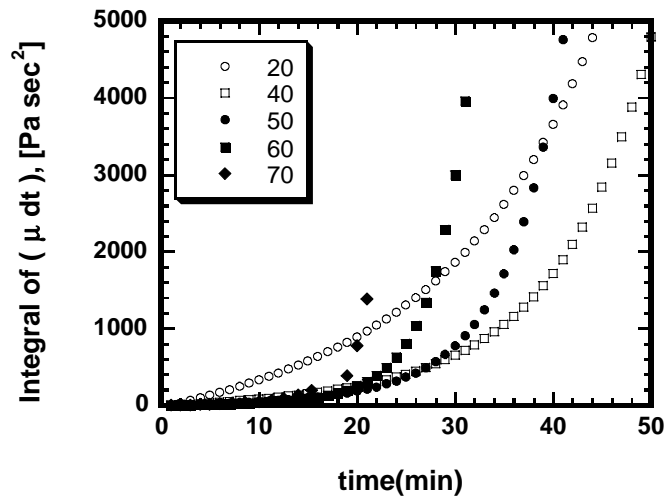


Fig. 9 Integral of Measured Viscosities with Times

The integral of $\int_0^{t_f} \mu(t_x) dt_x$ is given in Fig.9. As can be seen from the figure, there exists optimal process temperature. Ratio of Viscosity Integrations Based on the Value of Temperature 50 °C is given in Fig.10. Viscosity effect due to temperature is well shown.

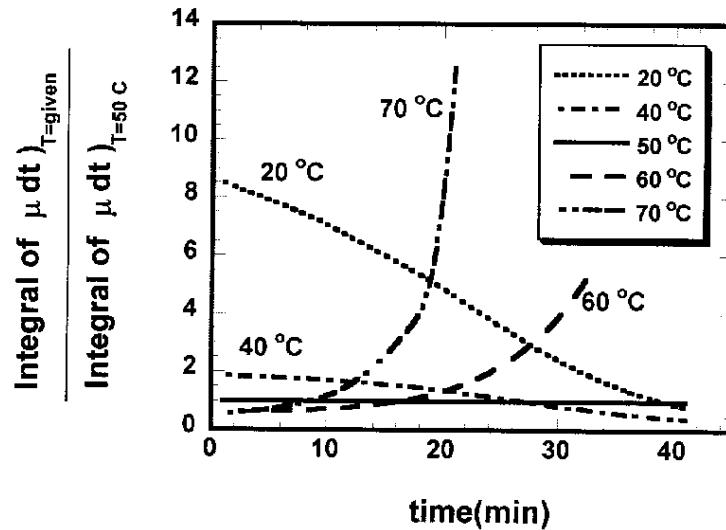


Fig.10 Ratio of Viscosity Integrations Based on the Value of Temperature 50 °C

To find adequate process conditions, parameter studies of mold filling process(Fig.11) were performed using the developed model. Fiber volume content of preform under the inner pressure and flow area of each region are

$$v_f = 0.45 \quad (20)$$

$$A(x) = 3.7699 \quad [\text{cm}^2] \quad 0 \leq x \leq 5.3, \quad \text{region I} \quad (21)$$

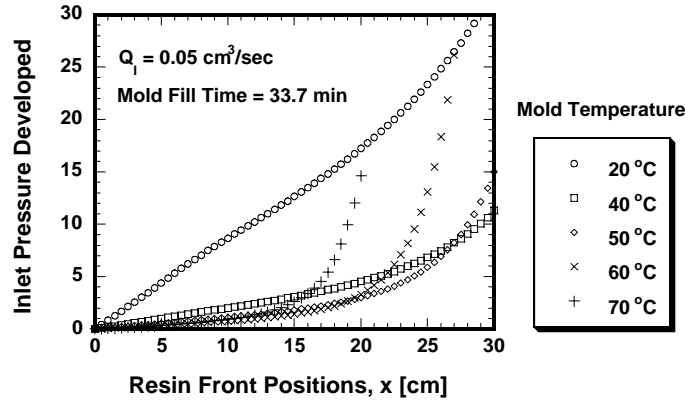
$$= 3.7699 + 0.364(x - 5.3) \quad [\text{cm}^2] \quad 5.3 \leq x \leq 10.9, \quad \text{region II} \quad (22)$$

$$= 5.8083 + 0.182(x - 10.9) \quad [\text{cm}^2] \quad 10.9 \leq x \leq 18.5, \quad \text{region III} \quad (23)$$

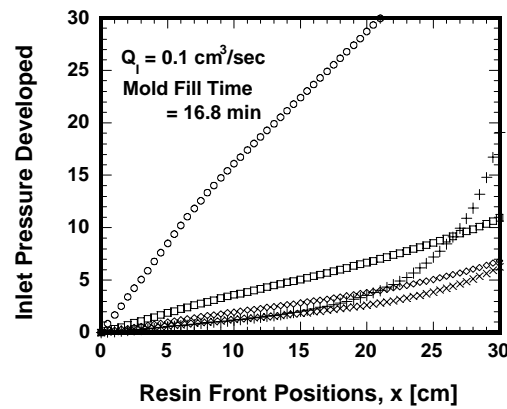
$$= 7.1915 + 0.091(x - 18.5) \quad [\text{cm}^2] \quad 18.5 \leq x \leq 26.7, \quad \text{region IV} \quad (24)$$

$$= 7.9377 - 0.6(5 - \sqrt{25 - (x - 26.7)^2}) \quad [\text{cm}^2] \quad 26.7 \leq x \leq 30.0, \quad \text{region V} \quad (25)$$

Inlet pressures are calculated as a function of temperature under the constant flow rate ($Q_I = 0.05 \text{ cm}^3/\text{sec}$, $Q_I = 0.05 \text{ cm}^3/\text{sec}$). In case of flow rate $0.05 \text{ cm}^3/\text{sec}$, mold fill time is a little longer and inlet pressure is dominated by the effect of resin cure. If the mold temperature is high enough (60, 70 °C), the resin is not filled perfectly. But if the mold temperature is low enough (20 °C), extremely high pressure is needed for perfect filling. There needs increase of flow rate.



(a) Flow Rate = 0.05 cm³/sec



Flow Rate = 0.1 cm³/sec

Fig.11 Inlet Pressure Calculated for Two Constant Flow Rate Cases

In case of flow rate 0.1 cm³/sec, adequate pressure is obtained for the mold temperature 50 ° C. Even though the mold temperature 60 ° C shows lower pressure, rapid increase of pressure is found in end region. It is due to resin cure. It is not good for optimal process because we needs time gap for oven cure, and so on. Determined optimal condition is as follows

$$Temperature_{MOLD} = 50 \quad [^{\circ}C] \quad (26)$$

Manufacturing of the Shell

For an easier application of RTM process, the shape of shell is changed a little(Fig.12). In other words, every holes and slit are filled with preform.

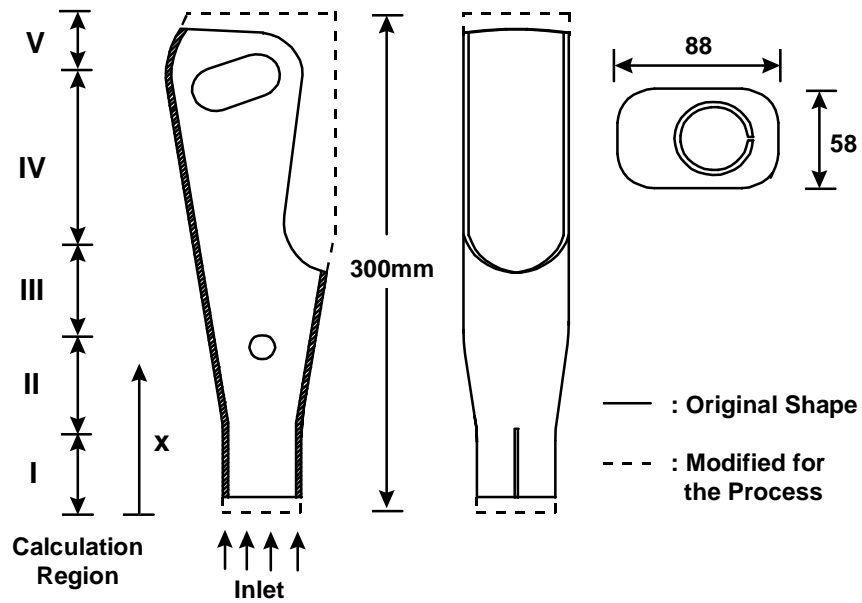


Fig.12 Shape of shell and Geometry for Flow Analysis

Mold filling process is schematically explained in Fig.13. Constant flow rate is achieved by constant movement of piston in a cylinder of resin reservoir. Piston speed is controlled by DC servo motor connected with computer. Inlet pressure is measured by pressure transducer. Polyurethane film is used inside the shell to compress the preform.

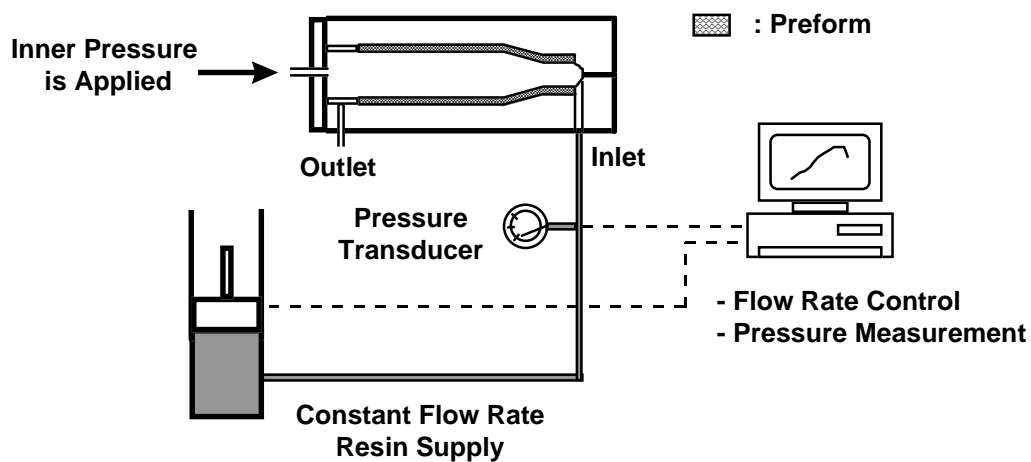


Fig.13 Schematic of Mold Filling Process

The shape of shell is supported by the pressure applied inside the shell. The pressure is supplied by nitrogen gas and it is kept on constant during the process. It is high enough compared with resin inlet pressure. After mold filling, the mold is put inside oven and the resin is cured according to the cure cycle determined(Fig.7).

$$P_{inside\ the\ shell} = 15 \quad [atm] \quad (27)$$

Steel mold is adapted to the process(Fig.14). It is composed of four pieces. Added parts for the easiness of manufacturing are cut away after the cure. And final product of the shell is given in Fig. 15.

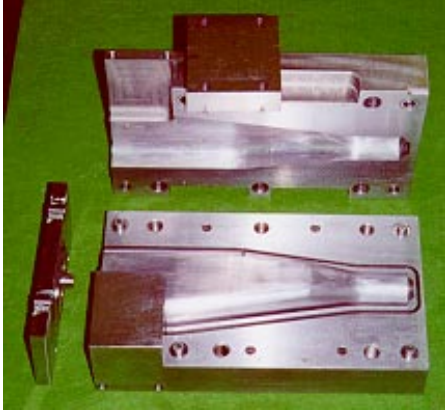


Fig.14 Picture of the Mold Used in the Process



Fig.15 Final Form of Manufactured Artificial Leg Shell

CONCLUSION

Flow analysis model based on the characterization of resin viscosity is suggested. The model can be easily applied to any kind of irregular cross-section cylindrical shell structure. To find optimal process conditions, parameter study was performed based on the model developed. Under the selected optimal conditions, composite artificial leg shell was manufactured. Now, the parts should be evaluated whether it satisfies required load conditions. And to obtain desired mechanical properties, void content of the part has to be checked.

REFERENCES

1. Kaviany, M., Principles of heat transfer in porous media, Springer-Verlag, 1991.
2. Lam, R. C. and J. L. Kardos, "The Permeability and Compressibility of Aligned and Cross-Plied Carbon Fiber Beds During Processing," Polym. Eng. Sci., 31:1064-1070, 1991.
3. Williams, J.G., C.E.M. Morris and B.C. Ennis, "Liquid Flow through Aligned Fiber Beds," Polym. Eng. Sci., 14:413-419, 1974.
4. Skartsis, L., J. L. Kardos and B. Khomami, "Resin Flow through Fiber During Composite Manufacturing Processes. Part1:Review of Newtonian Flow through Fiber Beds," Polym. Eng. Sci., 32:221-230, 1992.
5. Dusi, M.,R. et al., "Cure Kinetics and Viscosity of Fiberite 976 Resin," J. of Composite Materials, Vol.21, pp.244-261, 1987

HYDROXYAPATITE–POLYETHYLENE COMPOSITES FOR BONE SUBSTITUTION: EFFECTS OF HYDROSTATIC EXTRUSION

M. Wang¹, I. M. Ward² and W. Bonfield¹

*¹IRC in Biomedical Materials, Queen Mary and Westfield College,
University of London, London E1 4NS, U.K.*

²IRC in Polymer Science and Technology, University of Leeds, Leeds LS2 9JT, U.K.

SUMMARY: Hydroxyapatite reinforced high density polyethylene composites (HAPEX™) were hydrostatically extruded at different extrusion ratios. Their structure and mechanical properties were subsequently evaluated using various techniques. It was found that the uniform distribution of particulate hydroxyapatite in polyethylene achieved by compounding was not altered by hydrostatic extrusion. Substantial increases in the tensile properties of both filled and unfilled polyethylene were obtained in the extrusion direction. For HAPEX™ with a fixed volume fraction of hydroxyapatite, it was evident that the higher the extrusion ratio, the stronger and the stiffer the composite rod. Hydrostatically extruded HAPEX™ possesses mechanical properties that are within the bounds for human cortical bone, which indicates the potential for its load-bearing skeletal implant applications.

KEYWORDS: hydroxyapatite, polyethylene, biomaterial, hydrostatic extrusion, structure, properties

INTRODUCTION

Hydroxyapatite (HA) reinforced high density polyethylene (HDPE) composites (HAPEX™) have been developed as a bone analogue for medical applications [1]. HAPEX™ containing 40% by volume of HA possesses a stiffness approaching the lower bound of human cortical bone together with a superior fracture toughness [2]. This has led to its clinical applications such as orbital floor reconstruction [3]. The *in vivo* study showed that HAPEX™ encourages bone apposition rather than fibrous tissue encapsulation on a skeletal implant [4]. A particular advantage of HAPEX™ is that the implant can be easily shaped interoperatively for individual patients, while modification of implants made of bioactive ceramics or glasses is difficult in an operating theatre. Major progress is currently made in USA using HAPEX™ implants for otologic and maxillo-facial surgery.

For major load bearing applications, it is necessary to increase substantially the stiffness and strength of HAPEX™. Chemical coupling of HA to HDPE has resulted in improved mechanical behaviour but only limited increases in tensile properties [5]. More significant levels of improvement, however, are required.

It has long been recognised that molecular orientation in a polymer leads to a significant enhancement in the stiffness and strength along the orientation direction, as well as producing material anisotropy [6]. These effects are particularly evident with polyethylene due to its simple molecular structure [7,8]. The increase in tensile modulus has been correlated with the

average longitudinal crystal thickness in the ultra-oriented polyethylene [9]. Among several well established technologies for inducing molecular orientation in polymeric materials, hydrostatic extrusion has been used to increase substantially the tensile strength and modulus of polyethylene [8], which results in orienting the polyethylene molecules and transforming the spherulites into the fibre structure in the extruded material. It is therefore natural to investigate the possibility of hydrostatic extrusion of HAPEX™ and its effects on HAPEX™.

EXPERIMENTAL METHODS

Materials and Composite Processing

Synthetic HA (Grade P88, Plasma Biotol Ltd, UK) and an HDPE (Rigidex HM4560XP, BP Chemicals Ltd, UK) were used to produce HAPEX™ with 40% by volume of HA. Compression moulded HAPEX™ billets were manufactured via the established route [10]. Unfilled HDPE was also processed through the same procedure as a control.

The technology of hydrostatic extrusion of polyethylene (and hence HAPEX™ in the current investigation) has been described elsewhere [11]. Briefly, it involves surrounding a billet of the material with a fluid, heating up the billet to below its melting temperature and extruding the billet through a convergent die at a constant speed by pressurising the fluid. The extrusion ratio (ER) is defined as the ratio of the cross-sectional area of the billet to that of the die bore. Extrusion ratios of 5:1 and 8:1 were achieved by altering the billet and die diameters.

Methods

The hydrostatically extruded rods were cut to 50mm in length, machined into specimens to conform to ASTM E466, embedded at two ends in an epoxy resin to facilitate gripping and subjected to tensile testing on an Instron 6025 machine (Figure 1). Specimen extension was measured with an extensometer and this value was used to calculate the Young's modulus. The specimens were tested to failure and the tensile strength and fracture strain were determined.

Compression moulded materials were also tensile tested according to ISO 527, using dumbbell specimens made from square plaques. The values obtained were used as properties of HDPE and HAPEX™ at the nominal extrusion ratio of 1:1.

The distribution of HA particles in the HDPE matrix was investigated for HAPEX™ after compression moulding and hydrostatic extrusion. The polished surfaces, prepared by a standardised method [10], were lightly gold coated and examined under a JEOL 6300 scanning electron microscope (SEM). Tensile fracture surfaces of hydrostatically extruded HAPEX™ were also examined.

The molecular mass of the HDPE matrix at each processing stage was analysed by high temperature gel permeation chromatography (GPC). The measurements were made using a Waters 150CV instrument, operating at 140• C and with 1,2-dichlorobenzene as the solvent (allowance being made for the presence of filler).

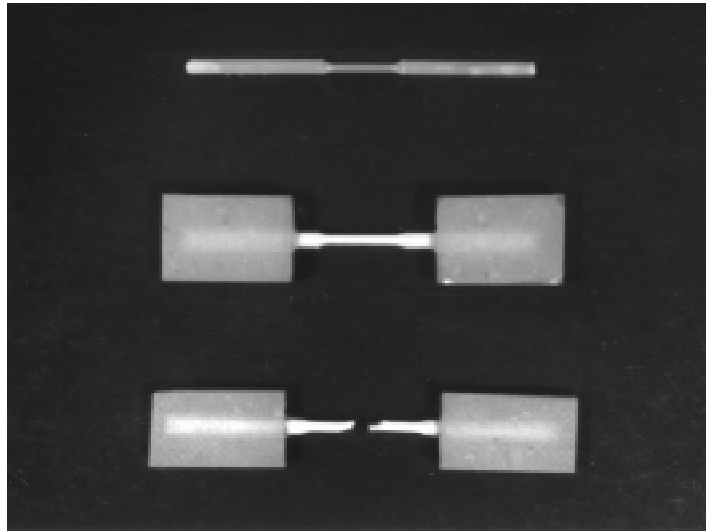


Figure 1 Hydrostatically extruded samples after machining, embedding and tensile testing

RESULTS

A homogeneous distribution of HA particles in HDPE matrix was found in both the centre and edge of hydrostatically extruded HAPEX™ rods at all extrusion ratios. Comparing the SEM micrographs taken from polished surfaces (perpendicular as well as parallel to the extrusion direction) with results obtained previously [10], it appears that hydrostatic extrusion did not alter the dispersion and distribution characteristics of HA in HAPEX™ which had been achieved by compounding using the twin screw extruder.

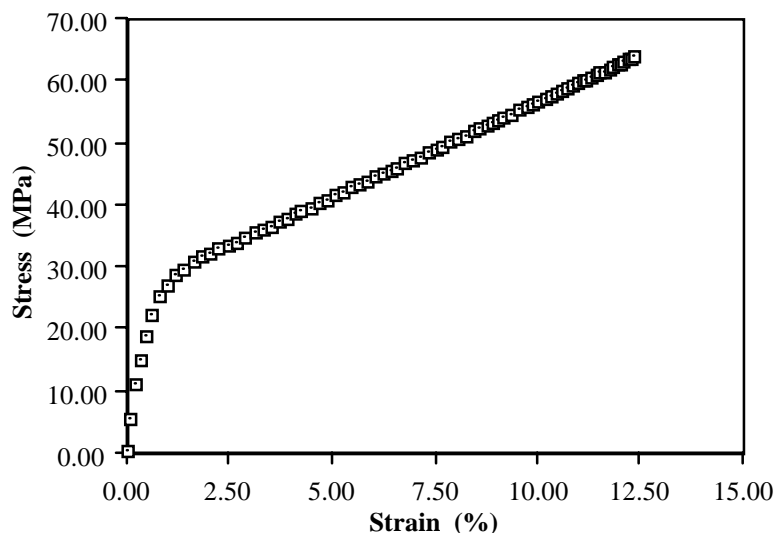


Figure 2: Tensile stress-strain curve of HAPEX™ hydrostatically extruded at the extrusion ratio of 5:1

Figure 2 shows the stress-strain curve of HAPEX™ hydrostatically extruded at ER = 5:1. HDPE and HAPEX™ samples extruded at ER = 8:1 also exhibited the same mechanical behaviour. Under an increasing tensile load, the extruded rod deformed with a gradually decreasing tangent modulus up to a certain stress level above which a near-constant tangent modulus was maintained. The rod usually fractured in this near-constant modulus region, the

fracture point depending on the volume fraction of HA and the extrusion ratio. Tensile testing results for unfilled HDPE and HAPEX™ before and after hydrostatic extrusion are listed in Table 1. Higher extrusion ratios led to higher Young's modulus and tensile strength for both HDPE and HAPEX™. The fracture strain of HAPEX™ was also substantially increased by hydrostatic extrusion, rising from 2.6% at ER = 1:1 (Sample CM40.1) to 9.4% at ER = 8:1 (Sample PC40.7). It was observed that higher modulus and strength values could be obtained from unmachined (i.e. without removal of skin of the rod) specimens than from machined (i.e. with skin being removed) specimens.

Table 1 Mechanical properties of hydrostatically extruded HDPE and HAPEX™ before and after hydrostatic extrusion

Sample Code	HA Volume (%)	Extrusion Ratio	Young's Modulus (GPa)	Tensile Strength (MPa)
CM0.1	0	1:1	0.65	17.89
PC0.100	0	5:1	2.59	61.24
PC0.24	0	8:1	4.08	158.2
CM40.1	40	1:1	4.29	20.67
PC40.1	40	5:1	5.89	64.78
PC40.7	40	8:1	9.91	91.23
PI40.2 *	40	8:1	11.4	80.84

* hydrostatically extruded sample using a billet made by injection moulding

Table 2 Weight average molecular mass of HDPE in HAPEX™ after hydrostatic extrusion

HA Volume (%)	Weight Average Molecular Mass of HDPE		
	ER = 1:1	ER = 5:1	ER = 8:1
0	271000	244000	248000
40	212000	174000	176000

* $M_w = 270000$ for as-received HDPE

The weight average molecular mass (M_w) of hydrostatically extruded HDPE and HAPEX™ is listed in Table 2. It seems that hydrostatic extrusion caused reductions in M_w . However, the extrusion ratio (5:1 or 8:1) did not appear to affect significantly the molecular mass of HDPE. (All the HDPE and HAPEX™ samples were extruded at 115°C, but with different extrusion pressures which are dependent on the extrusion ratio.)

SEM examination of fracture surfaces revealed that a core-skin structure, as shown in Figure 3a, existed in hydrostatically extruded HAPEX™. The skin may not be concentric with the centre of the rod as a varying thickness of the skin was found around the core. Figure 3b shows the skin area of the fracture surface of HAPEX™ extruded at ER = 8:1.

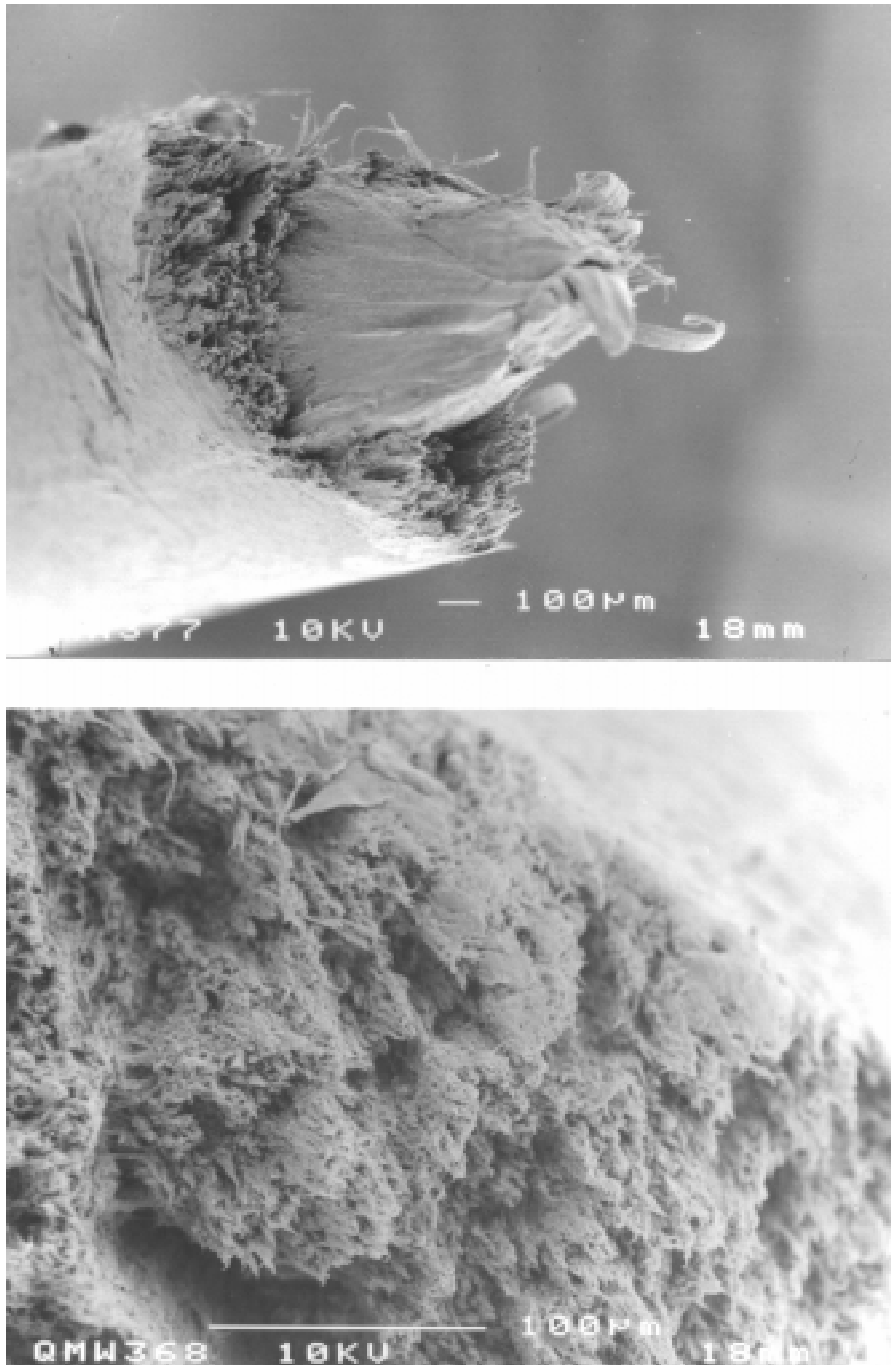


Figure 3 Tensile fracture surface of HAPEX™ hydrostatically extruded at the extrusion ratio of 8:1 , (a) a general view, (b) the skin region

DISCUSSION

Hydrostatic extrusion orients the molecular chain of polyethylene and transforms the previously folded chain morphology into one comprising extended molecular chains. Due to the high filler content (i.e. 40% by volume of HA, which is 69% by weight), HAPEX™ was hydrostatically extruded at extrusion pressures two to three times higher than for the unfilled HDPE. The extrusion temperature rather than the extrusion pressure seems to affect the

molecular weight of the HDPE matrix of HAPEX™ with a fixed HA volume fraction. It appears that hydrostatic extrusion not only improves the tensile properties of both filled and unfilled polymer in the extrusion direction but also changes their mechanical behaviour. For all the extruded rods, there are two distinctive regions as far as their tensile curves are concerned (Figure 2). Such tensile characteristics differ greatly from the behaviour of both filled and unfilled polyethylene prepared without hydrostatic extrusion. Compression moulded HDPE undergoes yielding and necking under tension, while compression moulded HAPEX™ with 40% of HA exhibits a near-linear tensile curve before fracture [10].

At the microstructural level, the investigation into the distribution of HA particles in hydrostatically extruded HAPEX™ rods has revealed the same (or at least highly similar) dispersion and distribution characteristics of hydroxyapatite in the polymer matrix as that in compression moulded samples, both exhibiting good dispersion and uniform distribution of HA particles. However, at the macrostructural level, although hydrostatic extrusion probably does not result in a core-skin structure for the unfilled polymer, it gives rise to such a structure in filled polyethylene, which has been verified by both tensile testing and SEM examination. The skin is stiffer than the core, which accounts for higher modulus values of unmachined specimen than those of machined specimen from the same sample. The thickness of the skin is probably influenced by both the ceramic particle volume fraction and the extrusion ratio.

It is evident for HDPE or HAPEX™ with a fixed HA volume fraction that the higher the extrusion ratio, the stronger and the stiffer the extruded rod (Figure 4). With an extrusion ratio of 8:1, the Young's modulus and tensile strength of HAPEX™ are 2.6 and 4.4 times higher than those of compression moulded material. An additional benefit of hydrostatic extrusion is the substantial increase in fracture strain (a measure of ductility) which is far greater than that of human cortical bone (9.4% vs 0.5-3.0%). It is also necessary to bear in mind that materials need to be processed through the compounding extruder in order to achieve larger property improvements.

Hydrostatically extruded HAPEX™ possesses mechanical properties which are within the bounds for human cortical bone. This is remarkable because the possibility of load bearing applications of HAPEX™ can now be explored. Currently, it is ideal that implants are made without removing the skin of hydrostatically extruded composites to avoid any uncertainty regarding their structure and mechanical properties. Further research in die design and optimisation of processing conditions may lead to hydrostatic extrusion of a structurally and mechanically homogeneous HAPEX™, as experience has shown that there is an optimum combination of extrusion temperature and pressure that results in the highest stiffness of polyethylene [12].

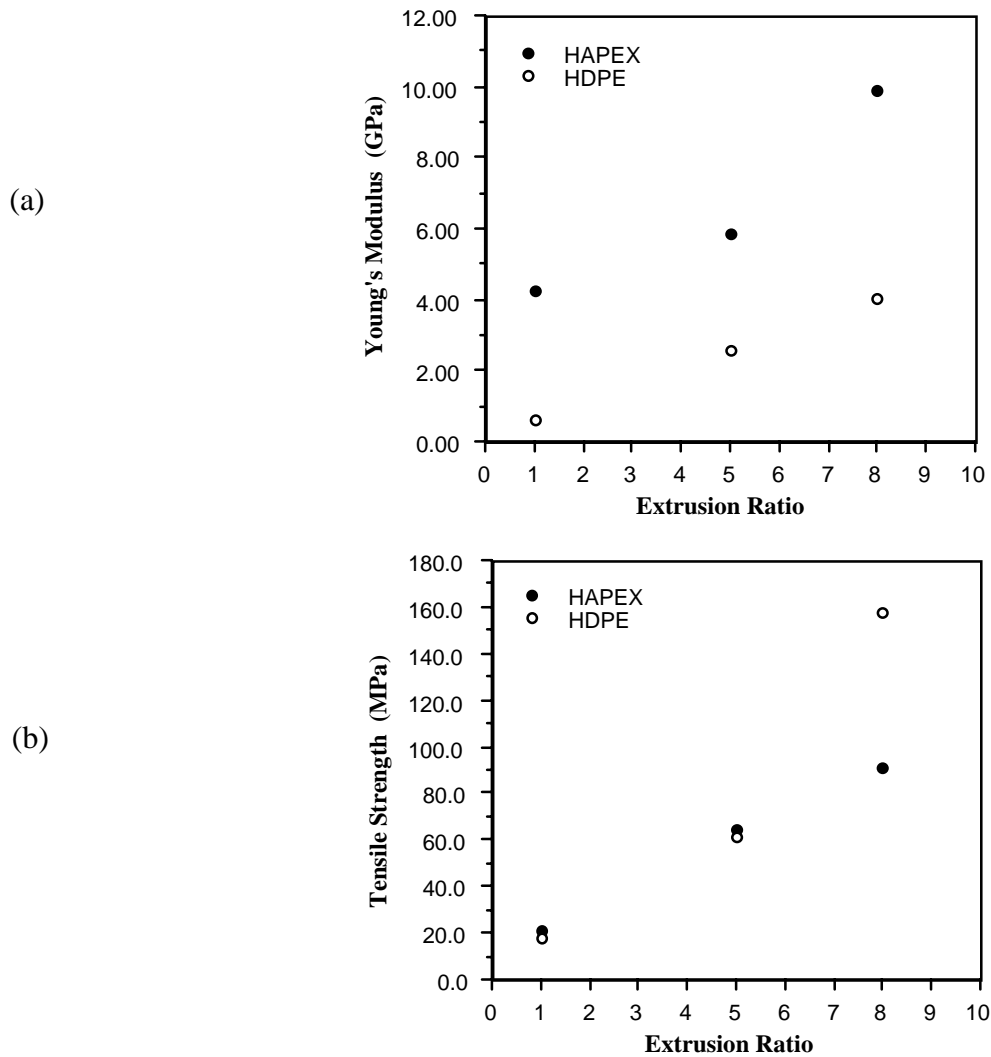


Figure 4 Effect of hydrostatic extrusion on Young's modulus and tensile strength of HDPE and HAPEXTM with 40% of HA

CONCLUSIONS

Hydroxyapatite reinforced high density polyethylene composite (HAPEXTM) containing 40% by volume of hydroxyapatite particles has been successfully hydrostatically extruded at different extrusion ratios. The resultant composite possesses mechanical properties that are within the bounds for human cortical bone together with a significantly improved ductility (and hence toughness). Therefore, HAPEXTM further processed via hydrostatic extrusion shows great promise for major load bearing skeletal implant applications.

ACKNOWLEDGEMENTS

The authors would like to thank Mr.V.Ford, Mrs.J.Huang and Dr.S.Holding (RAPRA) for their technical assistance. Dr.N.H.Ladizesky is thanked for hydrostatically extruding HDPE and HAPEXTM. Support from the UK EPSRC is gratefully acknowledged.

REFERENCES

1. Bonfield, W., Bowman, J.A. and Grynepas, M.D., "Prosthesis Comprising Composite Material", *UK Patent GB 2085461B*, 1984
2. Bonfield, W., "Composites for Bone Replacement", *Journal of Biomedical Engineering*, Vol.10, 1988, pp.522-526
3. Downs, R.N., Vardy, S., Tanner, K.E. and Bonfield, W., "Hydroxyapatite-Polyethylene Composite in Orbital Surgery", *Bioceramics*, Vol.4, 1991, pp.239-245
4. Bonfield, W. and Luklinska, Z.B., "High-Resolution Electron Microscopy of a Bone Implant Interface", *The Bone-Biomaterials Interface*, Davies, J.E., Ed., University of Toronto Press, Toronto, 1991, pp.89-93
5. Wang, M., Deb, S., Tanner, K.E. and Bonfield, W., "Hydroxyapatite-Polyethylene Composites for Bone Substitution: Effects of Silanation and Polymer Grafting", *Proceedings of the Seventh European Conference on Composite Materials*, London, U.K., 1996, Vol.2, pp.455-460
6. Frank, F.C., "The Strength and Stiffness of Polymers", *Proceedings of the Royal Society of London*, Vol.A.319, 1970, pp.127-136
7. Capaccio, G. and Ward, I.M., "Preparation of Ultra-high Modulus Linear Polyethylenes: Effect of Molecular Weight and Molecular Weight Distribution on Drawing Behaviour and Mechanical Properties", *Polymer*, Vol.15, 1974, pp.233-238
8. Gibson, A.G., Ward, I.M., Cole, B.N. and Parsons, B., "Hydrostatic Extrusion of Linear Polyethylene", *Journal of Materials Science Letters*, Vol.9, 1974, pp.1193-1196
9. Gibson, A.G., Davies, G.R. and Ward, I.M., "Dynamic Mechanical Behaviour and Longitudinal Crystal Thickness Measurements on Ultra-high Modulus Linear Polyethylene: A Quantitative Model for the Elastic Modulus", *Polymer*, Vol.19, 1978, pp.683-693
10. Wang, M., Porter, D. and Bonfield, W., "Processing, Characterisation and Evaluation of Hydroxyapatite Reinforced Polyethylene Composites", *British Ceramic Transactions*, Vol.93, 1994, pp.91-95
11. Gibson, A.G. and Ward, I.M., "Hydrostatic Extrusion of Linear Polyethylene: Effects of Molecular Weight and Product Diameter", *Journal of Polymer Science: Polymer Physics Edition*, Vol.16, 1978, pp.2015-2030
12. Hope, P.S., Gibson, A.G. and Ward, I.M., "Hydrostatic Extrusion of Linear Polyethylene: Effects of Extrusion Temperature and Polymer Grade", *Journal of Polymer Science: Polymer Physics Edition*, Vol.18, 1980, pp.1243-1256

A STUDY OF THE MECHANICAL PROPERTIES AND BIOACTIVITY OF FUNCTIONALLY GRADED TITANIUM MATRIX COMPOSITES REINFORCED WITH BIOACTIVE PARTICLES

A. E. Adoba* , H. B. McShane* , R. D. Rawlings* and I. U. Rehman*

**Dept. of Materials, Imperial College of Science, Technology & Medicine,
Prince Consort Road London SW7 2BP, United Kingdom*

**Interdisciplinary Research Centre in Biomedical Materials, Queen Mary & Westfield
College, The University of London, Mile End Road, London E1 4NS United Kingdom*

SUMMARY: A functionally graded material (FGM) has a progressively varying composition, structure and properties as a function of position within the material. Functionally graded titanium matrix composites with bioactive reinforcement have been fabricated from titanium, hydroxyapatite (HA), Bioglass® (Bg), and Apoceram (Ap) using a powder metallurgy route.

The mechanical properties of the FGMs were assessed, using three point bend tests to determine the bend strength and single edge notch bend tests to determine the fracture toughness. Microstructural studies were also undertaken of the fabricated materials and fracture surfaces. An improvement was observed in the toughness of the FGMs over the composites, with the FGMs showing a more “graceful” failure. The bioactivity of the FGMs were also assessed and the results obtained indicate the viability of these FGMs as medical implants.

KEYWORDS: functionally graded, biomaterials, biocompatibility, bioactive, titanium matrix

INTRODUCTION

Functionally graded materials (FGMs), a class of materials whose composition and microstructure vary continuously or discretely along a specific direction, are becoming more and more of a familiar concept.

FGMs are of increasing interest in advanced engines and airframes and in other applications such as armour, electric and dielectric devices and medical implants since the compositional gradient can be tailored towards specific requirements. The latter application is the one in which the work reported in this paper is aimed.

There is a fundamental requirement that an implant material and the tissues of the body coexist without either having an undesirable or inappropriate effect on the other. The phenomena related to this mutual coexistence are collectively referred to under the term of ‘biocompatibility’ defined as ‘the ability of a material to perform with an appropriate host response in a specific application’[1]. The properties required of a biomaterial are quite

complex, as the human body is known to be one of the most hostile environments within which a material can be placed.

Titanium and titanium alloys have been used increasingly in the area of bone replacement, orthopaedic surgery and dental implantation and are regarded universally as having outstanding mechanical properties, corrosion resistance and biocompatibility.

In the early 1970s it was discovered that a certain compositional range of calcium phosphate silicate based glasses did not produce a fibrous capsule when implanted in bone, but instead produced a strongly adherent bonded interface[2,3]. The term *bioactive* has subsequently been used to describe all biocompatible materials which form a bond with living tissues. Subsequently certain calcium phosphate crystalline materials e.g. hydroxyapatite and fluorapatite, and some glass-ceramics were also shown to be bioactive.

The principal limitation in the use of the glass, glass-ceramic group of bioactive materials, is that to varying extents they are weak, brittle and hard to shape, thus unsuitable for most high load bearing applications.

Bioactive glasses contain SiO_2 , Na_2O , CaO and P_2O_5 in specific proportions, namely:

- less than 60 mole % SiO_2
- high Na_2O and CaO content
- high $\text{Ca}/\text{P}_2\text{O}_5$ ratio

These features make the surface highly reactive when exposed to an aqueous medium and result in rapid formation of carbonate apatite (CA) on the surface[4]. The rate of formation of the CA layer has been shown to correlate with the bioactivity index (IB) of the material - i.e. the rate and type of bonding to tissues[5].

Bioactive ceramics, glasses and glass-ceramics have the singular advantage over other implant materials, such as titanium which is not bioactive, in that they remove the necessity for fixation and its attendant problems.

The limitations of these brittle bioactive materials were addressed by incorporating in a titanium matrix various weight percentages of bioactive reinforcement, using powder metallurgy methods[6], the aims being to obtain bioactivity from the reinforcement and superior toughness to conventional bioactive materials from the titanium matrix; with preliminary investigation of the former while the latter has been confirmed. In addition, these composite materials were studied in an attempt to first understand the mechanical behaviour of the monolithic composites, then to apply that knowledge to the study of the FGMs. Early work on titanium/hydroxyapatite FGMs was undertaken by Bishop[7]. Significantly improved mechanical properties were reported for these FGMs over the monolithic composites. Interfacial weakness between the layers however was a recurring problem. The interlayer interfacial weakness has been ameliorated in Al-SiC by providing a semi-continuous variation in composition rather than a stepwise variation by introducing a vibration stage in the pre-pressing processing [8]. The work described here builds on these earlier studies of FGMs, in particular titanium-hydroxyapatite FGMs and extends it to other bioactive reinforcement FGM systems, namely titanium - Bioglass® and titanium - Apoceram, and to the assessment of bioactivity.

The reinforcing bioactive glass-ceramic phase in the titanium matrix functionally graded composite material investigated in this paper, Apoceram, is a glass ceramic based on the

$\text{Na}_2\text{O-CaO-Al}_2\text{O}_5\text{-SiO}_2$ system with P_2O_5 used as a nucleating agent. It consists of interlocking spherulites of apatite $[\text{Ca}_5(\text{PO}_4)_3\text{OH,F}]$ and wollastonite $[\text{CaSiO}_3]$ crystal phases. The reinforcing phase of Bioglass® is also of the $\text{Na}_2\text{O-CaO-Al}_2\text{O}_5\text{-SiO}_2$ system and is a glass.

The bioactive properties of the FGMs are assessed using Fourier Transform Infrared Spectroscopy (FTIR) and Fourier Transform Raman Spectroscopy (FT Raman). The sensitivity of FT-Raman to the changes in the vibrational modes of P-O with nucleation of the CA crystallites makes it an appropriate analysis tool for the formation of the carbonate apatite (CA) layer. The C-O vibrational modes are also very intense in Raman spectra[9].

EXPERIMENTAL PROCEDURE

Material Fabrication

Titanium powder (Deeside Titanium Ltd., Active Metals Ltd.), hydroxyapatite powder (Jesse Shirley & Son Ltd.), Bioglass® (U.S. Biomaterials Corporation) and Apoceram (fabricated at Imperial College) were used to make the functionally graded composite materials. The particle size for the titanium powder was between 30 and 84 μm . The hydroxyapatite (HA) used was found to have an agglomerate particle size of between 18 and 55 μm but the individual crystal size was submicron. The Bioglass® (Bg) had a particle size range of 10 - 55 μm while the particle size for Apoceram (Ap) was below 55 μm . The different processes employed in the fabrication of the FGM systems are schematically shown in Figures 1 and 2.

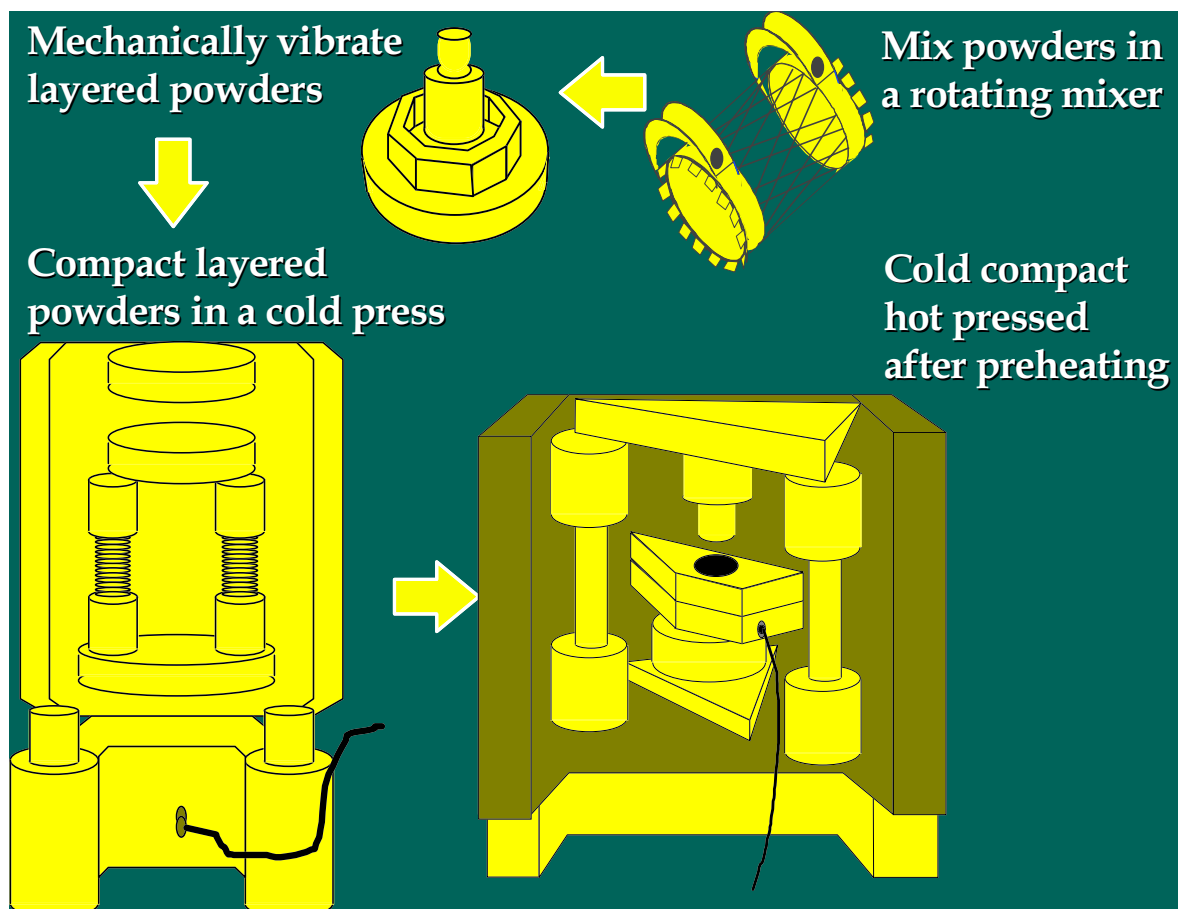


Figure 1 Fabrication using a hot pressing route

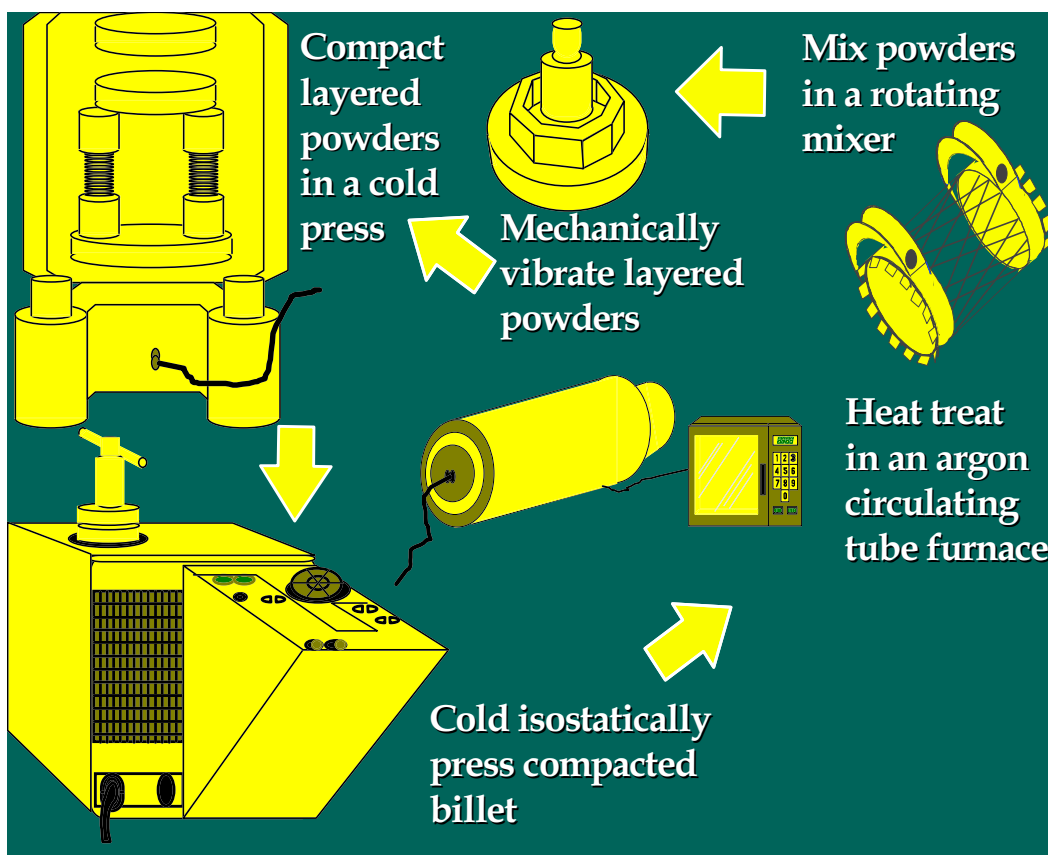


Figure 2 Fabrication using cold isostatic pressing route

Cold Compaction

The appropriate weight proportions of the titanium and bioactive reinforcement, to give 10 and 20 weight percent reinforcement, were mixed in a Turbula 3D path rotating mixer for one to one and a half hours. The powders were layered into a 60 mm steel die, pre-lubricated by zinc stearate in acetone. The die was placed in a mechanical vibrator for approximately thirty seconds, to expel air, settle the powders and make the interfaces between the layers more gradual. The powders were then compressed to produce green billets with heights between 3 and 4 cm, and approximately 70 to 80 % theoretical density.

Cold Isostatic Pressing and Heat Treatment

Selected green billets were placed in a hydraulic isostatic press and pressed for a holding time of approximately two minutes at 400 MPa. The pressed billets were heated in a controlled atmosphere furnace to 850⁰C at a rate of 150⁰C/h. The billets were cooled at the same rate to approximately 200⁰C then removed from the furnace and allowed to cool in air to room temperature.

Hot Compaction

The green billets were lubricated and then preheated in an argon circulating electric furnace to the 750⁰C for the Ti-HA FGMs and 1000⁰C for the Ti-Ap and Ti-Bg FGMs. The heated billets were transferred to a 60 mm steel die, also lubricated, in a 5 MN hydraulic press and pressed to a maximum pressure of 1.6 GPa at approximately the preheat temperature. The billets were then transferred back to the furnace and furnace cooled to room temperature

MATERIAL CHARACTERISATION

Structural Analysis

An automated diffractometer, with copper K_{α} radiation, and operating at 40kV and 40mA was used to carry out X-ray analysis on the FGM samples. Microstructural studies using ion, the titanium matrix heats up when exposed to the laser, making it difficult to analyse the surface layers.

Mechanical Tests

The flexural strength of the materials was determined using a three point bend test with specimens of nominal dimensions of 45 x 5 x 10 mm. Prior to testing, specimens were ground and polished to a 1 μm diamond finish. The fracture toughness measurements were performed according to BS 7448 : 1991 for plain strain fracture toughness testing of metallic materials. The procedure ideally should include fatigue pre-cracking from a machined notch. The brittle nature the of high reinforcement content layer made this extremely difficult, so the tests were performed without fatigue pre-cracking. It was felt that if other validity criteria were met, then the difference between fracture toughness measurements in fatigue pre-cracked samples and those that were not would be minimal. Previous work done on Tribaloys by Halstead[10] established that for fracture toughness values up to 19 $\text{MPa}\sqrt{\text{m}}$, there is very little difference between the data from samples with and without fatigue precracking.

Bioactivity Assessment

Immersion in Simulated Body Fluid

Samples of Ti-HA, Ti-Ap, Ti-bioglass® FGMs were cut to approximate dimensions of 10 x 10 mm and approximate thickness of and polished to a 1 μm finish on either side. They were then immersed in simulated body fluid (SBF) for varying periods (Table 1), at 37°C. The simulated body fluid was prepared by dissolving Ringers tablets in distilled water to the appropriate concentration, to yield the approximate ion concentration given in Table 2. When the samples were removed from the SBF, they were placed in a dessicator to dry off any excess moisture.

Table 1: Immersion Periods And Sample Compositions For Bioactivity Assessment

Sample & Composition	Immersion Period (hours)								
	1	2	6	12	18	24	48	72	120
0/10wt% HA Ti-HA FGM	✓	✓	✓	✓	✓	✓		✓	✓
0/10/20wt% HA Ti-HA FGM	—		✓	✓				✓	✓
0/10/20wt% BgTi-Bioglass® FGM	✓	✓	✓	✓	✓	✓	✓	✓	✓
0/10/20wt% ApTi-Apoceram FGM			✓	✓		✓		✓	✓
Ti-20% Bioglass	✓	✓	✓	✓	✓	✓	✓	✓	

Table 2: Ion Concentration (mM) of SBF and Human Blood Plasma[11]

Ion	Simulated Body Fluid	Blood Plasma
Na+	142.0	142.0
K+	5.0	5.0
Mg ²⁺	1.5	1.5
Ca ²⁺	2.5	2.5
Cl-	147.8	103.0
HCO ₃ ⁻	4.2	27.0
HPO ₄ ²⁻	1.0	1.0
SO ₄ ²⁻	0.5	0.5

Spectroscopic Analysis

The dried samples were analysed using Fourier Transform Infra Red Spectroscopy (FTIR) and Fourier Transform Raman Spectroscopy (FT-Raman). The FTIR was performed using a Nicolet 800 spectrometer in conjunction with a Nic-palnoe® microscope. The spectra were obtained at 4cm⁻¹ resolution averaging 256 scans. The FT Raman spectra were recorded using a Nicolet 910 spectrophotometer, equipped with an Nd:YVO₄ near-infrared laser, which eliminates the problems of sample fluorescence and photo-decomposition characteristic of conventional Raman instruments with high power lasers.

RESULTS AND DISCUSSION

Microstructure

Generally the HA containing FGMs fabricated at the lower processing temperature (750⁰C) were found to have a partially sintered Ti matrix with some porosity and unsintered agglomerate reinforcement (Figure 3). The microstructure of the Ap and Bg containing FGMs fabricated at 1000⁰C, contained less porosity in the titanium matrix (Figure 4). There was evidence of some crystallisation in the Bioglass® (confirmed in the XRD trace) and further crystallisation in the Apoceram glass-ceramic. In the Ti-HA FGM the percentage of porosity, both micro porosity and macro porosity, was higher in the reinforcement than in the titanium. Plasma spraying of metal substrates with HA has been reported as problematic because of the thermal decomposition reactions which occur at the high temperatures required[12]. It has also been reported that the decomposition of hydroxyapatite can be induced at significantly lower temperatures (850⁰C) than previously described in literature (~1300⁰C) through the presence of Ti [13]. The XRD results confirmed that the HA remained as HA, suggesting that little or no thermal decomposition of HA had taken place, despite the presence of Ti. There is also, little in the microstructural examinations to suggest the presence of reaction products with HA. It is surmised that the starting powder of titanium must have contained a thin layer of oxide which served as a passivating layer and prevented reaction between the hydroxyapatite and the titanium. The presence of titanium oxide was confirmed through secondary ion mass spectroscopy on the Ti-HA FGM. Although no quantitative analysis was available through this technique, it was concluded that the % volume content of the TiO₂ was

minimal and was not detected by XRD. There is evidence however of a reaction layer between the Ti and Apoceram (Figure 4) and Bioglass®. Theoretical thermodynamic calculations, taking into account the higher processing temperature for the Ti-Ap and Ti-Bg

FGMs suggest that reactions with the phases present in Apoceram and Bioglass® are thermodynamically more favourable and may thus account for the reaction layers observed.

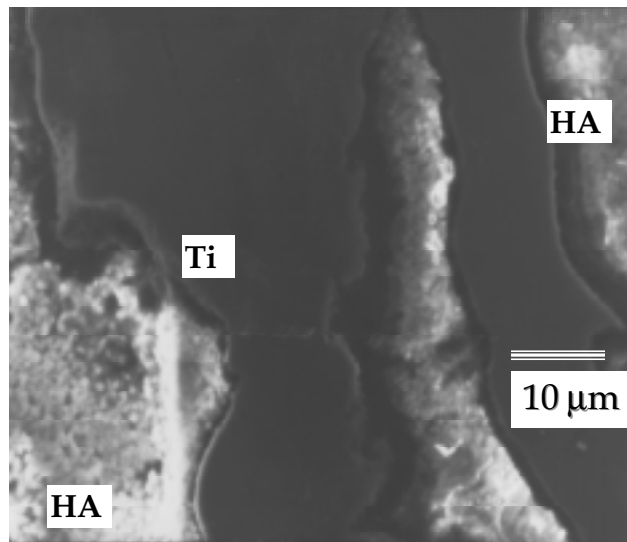


Figure 3: Secondary electron image of the 10% layer in a double layer (10/20%) titanium-hydroxyapatite FGM

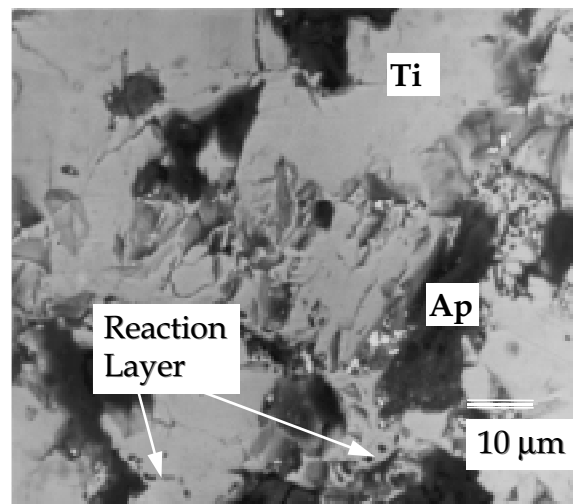


Figure 4: Back scattered electron image of the 20% layer in a triple layer (0/10/20%) titanium-apoceram FGM

Fractography

Examples of the fracture surfaces of the samples investigated indicated that the mode of micro fracture for all the composite FGMs was predominantly brittle fracture. The titanium regions

had undergone mainly cleavage fracture (Figure 5, Figure 6) although some localised ductile fracture is observed (Figure 5). Crack propagation in the composite region occurred predominantly through the reaction layer at the reinforcement/matrix interface in the Ti-Bg and Ti-Ap FGMs (Figure 6). In the Ti-HA FGM some intergranular fracture was also observed through the reinforcement. The contributory factors therefore to the improvement in fracture toughness and work of fracture (Table 3) as one moved from composite to FGM are not due to major changes in the micro fracture mechanism but are almost certainly related to crack retardation as described in the next section.

Mechanical Properties

The fracture toughness values showed a significant improvement for the FGMs over the composites and monolithic reinforcement. The FGMs demonstrated a much more graceful failure with some load carrying capacity after failure had commenced. The load-time curves presented in Figure 7 and Figure 8 are typical for both SENB fracture and three point bend tests. The graceful nature of the material failure is clearly demonstrated, leading to much greater values for the work of fracture for the FGMs. Modelling work using finite element analysis on Ti-HA FGMs [7] has shown that the high reinforcement content surface layers are under residual compressive stress.

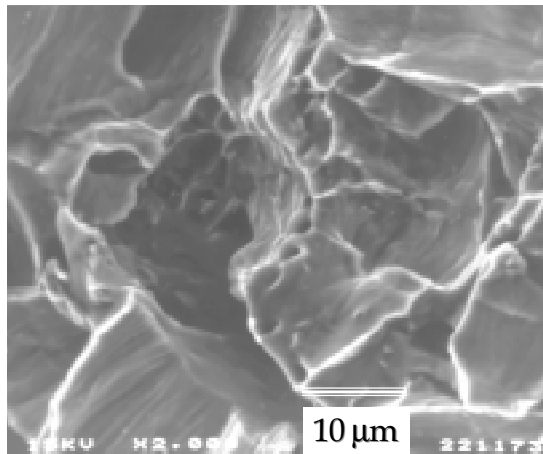


Figure 5: Secondary electron image of the fracture surface of the titanium (0%) layer in a double layer (0/10%) titanium-Bioglass® FGM

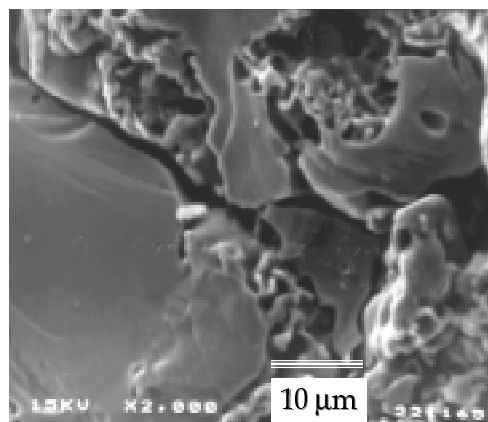


Figure 6: Secondary electron image of the fracture surface of the 10% layer in a triple layer (0/10/20%) titanium Apoceram FGM

Sample	Toughness(MPam ^{1/2})	Work of Fracture(J)
Ti-HA _{hc} FGM triple layer (10/20/30 wt% HA)	13	1.2
Ti-HA _{ip} FGM triple layer (0/10/20 wt% HA)	11	0.9
Ti-Bioglass [®] _{ip} FGM triple layer (10/20/30 wt% Bioglass [®])	12	0.1
Ti-Bioglass [®] _{hc} FGM double layer (0/10 wt% Bioglass [®])	21	3.0
Ti-Bioglass [®] _{ip} FGM double layer (0/10 wt% Bioglass [®])	11	0.1
Ti-Ap _{ip} FGM triple layer (0/10/20 wt% Ap)	9	1.3

Table 3 Mechanical Properties

This accounts for the higher K_{IC} of the FGMs compared to their conventional composites counterparts. Furthermore the interface between the layers in an FGM hindered primary crack propagation. This was particularly noticeable at the 0/10 wt% HA interface where propagation into the 0% layer usually took place after some delamination. Another feature often associated with propagation through an interface was crack branching (Figure 9) which effectively reduces K_I at the crack tip. For these reasons the FGMs have superior values for the work of fracture.

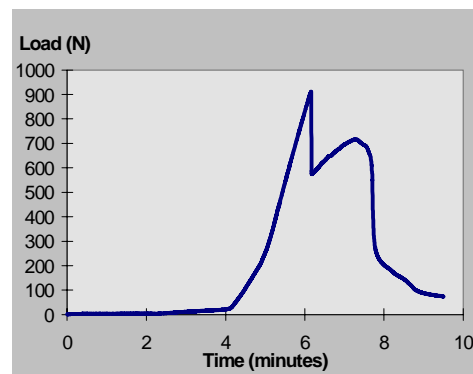


Figure 7: Load-time curve for a hot pressed Ti-HA FGM triple layer (0/10/20%) in SNEB fracture toughness testing

This accounts for the higher K_{IC} of the FGMs compared to their conventional composites counterparts. Furthermore the interface between the layers in an FGM hindered primary crack propagation. This was particularly noticeable at the 0/10 wt% HA interface where propagation into the 0% layer usually took place after some delamination. Another feature often associated with propagation through an interface was crack branching (Figure 9) which effectively reduces K_I at the crack tip. For these reasons the FGMs have superior values for the work of fracture.

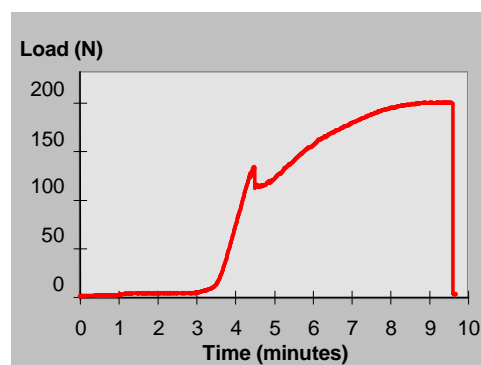


Figure 8: Load time curve for a cold isostatically pressed double layer (10/20%) Ti-Bg FGM in SNEB fracture toughness testing

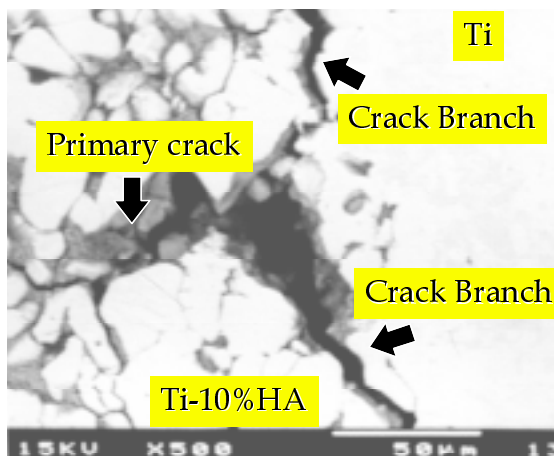


Figure 9: Back scattered electron image of the 0/10% interface in a triple layer (0/10/20%) titanium-hydroxyapatite FGM

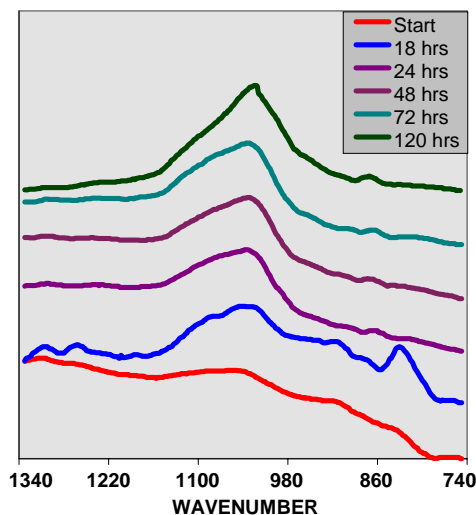


Figure 10: FTIR spectra for the 20% layer in the Titanium-Bioglass® triple layer FGM for various SBF exposure periods

Bioactivity Assessment

FTIR Analysis

The phosphate peak in the carbonate apatite layer is detected in the high reinforcement containing layer (20%Bg) and the monolithic Ti-20%Bg composite after 24 hours immersion. The peak increases with immersion time and is well defined at 120 hrs. The phosphate peak is centred at 1040cm^{-1} . A small peak, due to the C-O vibrational modes is also observed at 907cm^{-1} . The FTIR spectra for the high reinforcement containing layer in the titanium-bioglass FGM is shown in Figure 10. Figure 11 shows the FTIR spectra for the titanium-20%Bg composite. No discernible peaks of formation of carbonate apatite are observed in the spectra for the high reinforcement containing triple layer Ti-Ha and Ti-Ap FGMs prior to 72 hours exposure. After 72 hours exposure to SBF however there is an increase in the phosphate peak in the Ha containing FGM, indicating possibly, some deposition of carbonate apatite (Figure 12). The results obtained are consistent with the bioactive behaviour of Bioglass® which is known to be more bioactive than hydroxyapatite, with carbonate apatite peaks detected as

early as after 30 minutes exposure to SBF. The spectra for the 20%Ha layer in the Ti-Ha FGM is shown in Figure 12.

FT - Raman Analysis

This technique did not yield any additional information on the formation of carbonate apatite in the samples investigated. This is believed to be due to a number of reasons. One of these is that the layer is not yet crystalline and as a result does not possess a very good Raman signal.

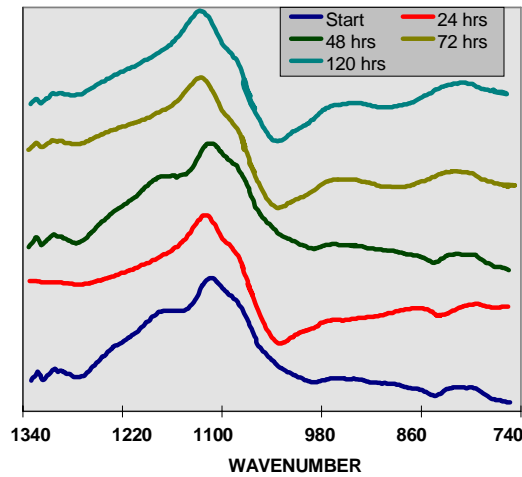


Figure 11 *FTIR spectra for the 20% layer in the Titanium-hydroxyapatite triple layer FGM for various SBF exposure periods*

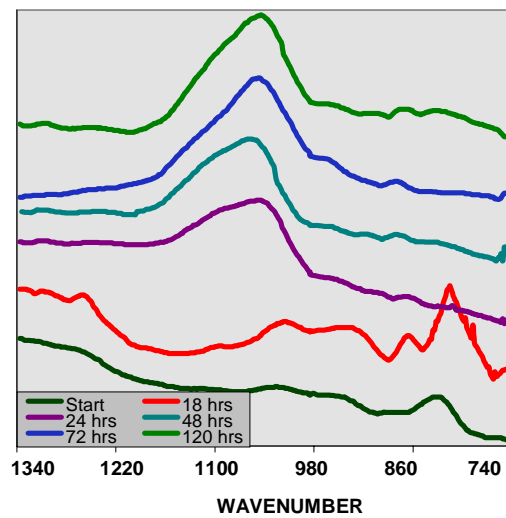


Figure 12: *FTIR spectra for the Titanium-20%Bioglass® composite for various SBF exposure periods*

In addition, the titanium matrix heats up when exposed to the laser, making it difficult to analyse the surface layers.

CONCLUSIONS

Titanium matrix composite FGMs with bioactive reinforcement were successfully produced using powder metallurgy routes, with adequate mechanical properties and “graceful” fracture behaviour. The preliminary bioactivity studies undertaken show that these functionally graded titanium matrix composites with bioactive reinforcement show promise. Further work needs to be done on assessing their performance in vivo. With optimum reinforcement compositions however, these FGM materials could herald a new and exciting future in biomedical implants.

ACKNOWLEDGEMENTS

The authors would like to gratefully acknowledge the following: Jesse Shirley and Son Ltd, US Biomaterials Corporation, The Worshipful Company of Tin Plate Workers Alias Wire Workers of London.

REFERENCES

1. Williams, D. F. “Advanced Applications for Materials Implanted Within the Human Body”, *Materials Science and Technology*, Vol. 3, October 1987, pp 797-806
2. Hench, L.L., Splinter, R.J., Greenlee, T.K., Allen, W.C., “Bonding Mechanism at the Interface of Ceramic Prosthetic Materials”, *Journal of Biomedical Materials Research*, Vol. 2, 1971, pp 117-141
3. Pitrowski, G., Hench, L.L., Allen, W.C. and Miller G.J. “Mechanical Studies of the Bone Bioglass® Interfacial Bond”, *Journal of Biomedical Materials Research*, Vol.6, 1975, pp. 47-61
4. Clark A.E., Hench L.L. and Paschall H.A. “The influence of Surface Chemistry on Implant Interface Histology ; a Theoretical Basis for Implant Materials Selection”, *Journal of Biomedical Materials Research*, Vol 10, 1976 pp. 161-174
5. Hench L.L. and LaTorre G., “The Kinetics of Bioactive Ceramics. Part IV: Effect of Glass and Solution Composition”, *Bioceramics*, Yamamuro, T., Kokubo, T and Nakamuro T., eds., V. Kyoto, Japan: Kobushi Kankokai Press, 1992, pp. 67-74
6. Adoba A. E., McShane H. B. and Rawlings R. D., “The Structure and Properties of Titanium Matrix Composites Reinforced with Bioactive Particles”, *Proceedings Seventh European Conference on Composite Materials*, London, United Kingdom, May 14-16, 1996, Vol. II, Biocomposites, pp. 461-466
7. Bishop A. M., Lin C. Y., Navaratnam M., Rawlings R. D. and McShane H. B. “A Functionally Gradient Material Produced By A Powder Metallurgical Process”, *Journal of Material Science Letters*, Vol. 12 (1993) pp. 1516-1518
8. Lin C. Y., McShane H. B. and Rawlings R. D., “The Structure And Properties Of Functionally Gradient Aluminium 2124/SiC Composites”, *Material Science and Technology*, Vol. 10, July 1994, pp. 659-664

9. Kokubo T., Kushitani H., Sakka S, Kitsugi T and Yamamuro Y, “Solutions Able to Reproduce In-Vivo Surface-Structure Changes in Bioactive Glass-Ceramic A-W³”, *Journal of Biomedical Materials Research*, Vol. 24, 1990, pp. 721-734
10. Halstead A., “Microstructure and Fracture of Two Cobalt Hardfacing Alloys”, Ph.D. Thesis, Imperial College, October 1980, p 83
11. Hench, L.L, Wilson, J. (editors), ‘An Introduction to Bioceramics’, *Advanced Series in Ceramics*, Vol 1, World Scientific, Singapore, 1993, p 332
12. Hastings G.W., Dailly D. and Morrey S., *Bioceramics*, Vol. 1, edited by Ohnishi H., Aoki H., Sawai K., Iahiyaki, Euro America (1989) pp. 353-358
13. Weng J., Liu X. and Zhang X. “Thermal Decomposition of Hydroxyapatite Structure Induced by Titanium and Its Dioxide”, *Journal of Material Science. Letters* 13 (1994), pp. 156-161

FIBRE-REINFORCED THERMOPLASTIC COMPOSITE OSTEOSYNTHESIS IMPLANTS WITH VARIABLE MECHANICAL PROPERTIES FOR BETTER TREATMENT OF BONE FRACTURES

J. Krebs¹, K. Friedrich¹, R. Heuwinkel², P. Rieger³, P. Kosack³

¹ *Institut für Verbundwerkstoffe GmbH, University of Kaiserslautern,
Erwin-Schroedinger-Str. 58, 67663 Kaiserslautern, Germany*

² *Department for Casualty Surgery, Klinikum der Universitätsstadt Kaiserslautern,
Friedrich-Engels-Str. 25, 67655 Kaiserslautern, Germany*

³ *Centre for Microelectronics, University of Kaiserslautern,
Erwin-Schroedinger-Str. 12, 67663 Kaiserslautern, Germany*

SUMMARY: A new thermoplastic composite femoral implant was designed and manufactured following the concept of semi-rigid fixation. By integrating a biodegradable polymer block into the body of the implant it was made sufficiently rigid to initially enable primary bony union but, with progressive degradation, to also enable interfragmentary movement, which promotes the proliferation of external callus and consequently a better consolidation of the fracture. In order to meet medical standards the parts of the implant were manufactured by injection moulding and near-net-shape forming. The degradation behaviour of Poly (L-lactide) was studied *in-vitro* under static and dynamic loading conditions. It was found that dynamic loading leads to mechanical degradation of the polymer long before hydrolytic degradation commences.

KEYWORDS: medical applications, osteosynthesis implants, semi-rigid fixation, resorbable polyesters, near-net-shape forming, ooly (l-lactide), CF/PEEK, biodegradation

INTRODUCTION

Historically, high performance alloys such as CoCrMo and Ti6Al4V along with ultra high molecular weight polyethylene, acrylic bone cement, and more recently, ceramics have been the materials of choice within the orthopaedic community [1]. These materials have proved their biocompatibility and mechanical properties necessary to stabilise fractured bones. With increasing understanding of the processes occurring during cortical healing of diaphyseal fractures, however, it has become obvious that both stainless steel and titanium alloy implants hold a significant drawback, that is, their comparatively high stiffness. According to recent studies, secondary bone healing, which is generally accompanied by the formation of external callus, can only take place when interfragmentary movement is enabled [2-7]. The purpose of callus, that ideally shapes around the fracture like a cuff, is to re-establish the structural integrity of the bone shortly after fracture has taken place. With progressive re-consolidation the callus cuff subsequently regresses until the bone's initial strength is fully restored. Employing metallic implants, such micro movements are strongly hampered, and therefore, in absence of external callus, union has to take place directly between the fractured bone ends. In

medical terms this curing process is described as primary or remodelling bony union. In this case, the re-consolidation process progresses extremely slow and consequently the implant cannot be removed safely for at least 18 months. Problems that may result from such a prolonged dependence are implant failure due to shortcomings in surgical technique, allergic reactions, and osteopenia. The latter encompasses all types of bone infections which mainly develop beneath very strong steel plates as a result of protection against stress which they confer. In view of these apparent drawbacks of metallic implants, advanced fibre-reinforced composites have become increasingly appealing as a new group of materials for orthopaedic bone fixation plates. Early laboratory studies on carbon fibre/polysulfone [8], carbon fibre/methylmethacrylate, carbon fibre/epoxy [9] and carbon/carbon implants in animals have demonstrated the potential advantage of composite over metallic implants. In addition, properties such as good biocompatibility, excellent fatigue properties, transparency to X-rays and, most importantly, the opportunity to individually tailor the elastic properties of the implant to that of the host bone positively add to the characteristic property profile of composite materials.

DESIGN AND CONSTRUCTION

In the frame of an ongoing project at the University of Kaiserslautern in cooperation with the Clinic of Kaiserslautern, a new osteosynthesis implant was designed made from fibre reinforced thermoplastics. Following the concept of semi-rigid fixation it was aimed to tailor the mechanical properties of the implant to the needs of the host bone. This meant, that the implant had to be sufficiently rigid in the first period after surgical fixation of the fracture in order to enable primary bony union. Then, after approximately 6 weeks, the rigidity of the implant had to subsequently decrease to allow interfragmentary movement and thus stimulate the proliferation of external callus. Prior to the design studies for such an implant with adaptable mechanical properties, a thorough literature research was conducted with the aim to select suitable materials as well as technical and geometric features. Within this survey it was found that basically only implants made from biodegradable polymers such as Poly (L-lactide) (PLLA) possess the capability to mechanically degrade by means of hydrolytic resorption. However, these materials only provide moderate mechanical properties and hence are not suitable for application in load bearing implants. Further problems still associated with biodegradable polymers are the limited processability and the virtual uncontrollable propagation of degradation which is likely to lead to an early failure of such implants. In contrast, fibre-reinforced composite implants can easily be adjusted within a wide range to the stiffness of the host bone and also provide excellent fatigue behaviour depending on the fibre/matrix system employed. For this reason, it was decided to combine the advantageous features of both by integrating a resorbable polymer block into a non-degradable fibre reinforced implant body. The limiting criterion for the selection of a suitable thermoplastic composite material was, that both fibre and matrix had to be qualified for implantation into human bodies. In view of this demand and the mechanical loading conditions that are normally imposed on such implants carbon fibre reinforced Poly (ether ether ketone) (CF/PEEK) was found to be the most appropriate choice.

Additional aspects that decisively influenced the design of the implant are briefly listed below:

- easy surgical handling,
- geometric conformity with comparable stainless steel and titanium alloy implants,

- sufficient clearance between implant and bone at the fracture for unhampered proliferation of external callus,
- geometric adaptability of the implant to the contour of the host bone,
- no exposure of fibres in the surface of the implant to prevent undesirable foreign body reactions (the reinforcements have to be fully coated by matrix material), and
- good tribological properties (wear debris can lead to inflammatory body reactions).

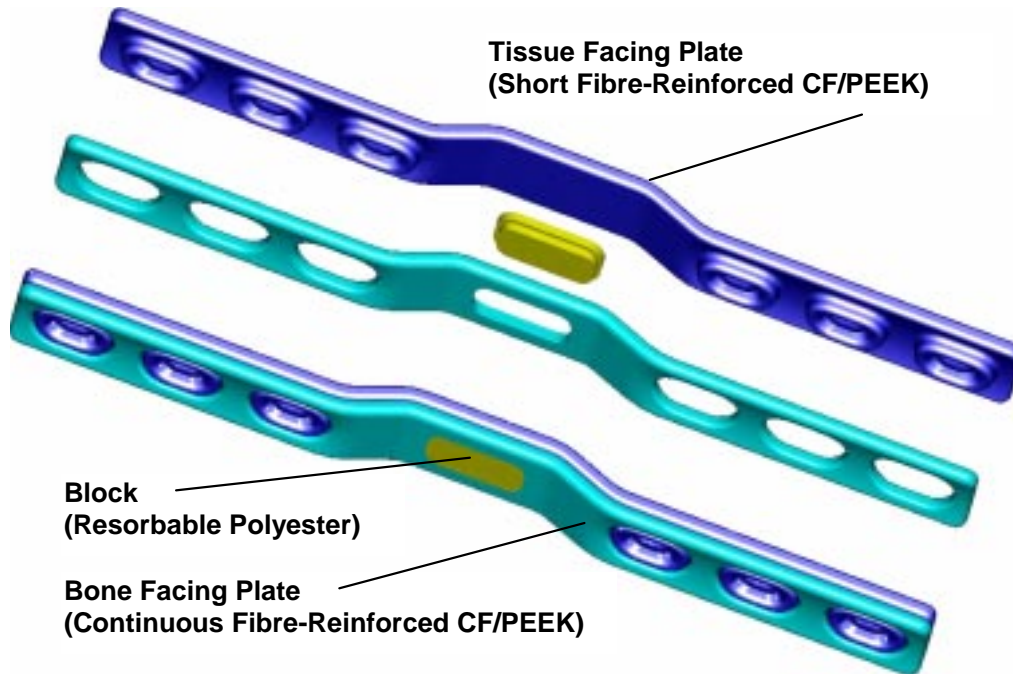


Figure 1: Isometric view of the adaptable implant

Under consideration of the demands and boundary conditions imposed on the adaptable implant from the medical, mechanical and structural point of view the following design was developed. As can be seen in Figure 1, the implant consists of three separate components; tissue facing plate, degradable block and bone facing plate. The reasons that led to this design are manifold. Preliminary experiments on injection moulding PLLA into CF/PEEK blocks with incorporated grooves showed that only poor interfacial bonding between the two polymers was achieved by virtue of the PLLA's severe shrinkage upon solidification. It was therefore decided to mount the degradable block following the principle of positive connection. This way it was also ensured that only compressive loads induced by bending moments in primary load direction can be transferred through the insert. In order to allow sufficient room for proliferation of external callus beneath the plate, a clearance of approximately 5 mm between implant and bone was allowed in the middle section. The countersunk holes were designed similar to that of titanium LC-DCP plates (Limited Contact-Dynamic Compression Plate) in order to account for dynamic compression fixation (rotation and translation of screws). The principle of limited contact was incorporated by restricting the contact area to that of the bone facing plate. This way it was also ensured that both plates can be firmly assembled.

Regarding the manufacturing of the implant, the tissue facing plate had to be made from either short or knitted fibre-reinforced PEEK due to its complex shape. Since the latter is still not commercially available short fibre-reinforced PEEK (30vol.%) was chosen for calculations and manufacture of injection moulded prototypes. The bone facing plate was made from continuous fibre-reinforced PEEK since it has to carry most of the load and the

geometry was fairly simple. The biodegradable insert was also injection moulded in order to allow for compensation of the materials processing related shrinkage through mould design.

The achievable decrease in flexural rigidity was determined by varying the dimensions of the inserted block and the tissue facing plate. The dimensions of the beams in the central section of the bone facing plate were kept constant at 2 mm for stability reasons. The maximum width of both plates was set to 17 mm which is comparable with conventional femoral implants. Dependent on the initial rigidity the maximum achievable decrease was found to be in the order of 20%. With increasing thickness of the tissue facing plate the drop in rigidity gradually declined to 13%, however, the initial rigidity then reached values in excess of 40 Nm². Naturally, such an implant would be far to rigid. According to studies by Tayton *et. al*, who implanted a series of femoral implants with different flexural rigidities into humans, values in the order of 5-10 Nm² were found to be most appropriate for good bony union and proliferation of external callus [10].

PRELIMINARY TESTS

In the preliminary testing phase mainly three different aspects were of particular interest. First, it had to be clarified if the calculated drops in flexural rigidity could be validated in an actual experiment. In addition, the degradation behaviour of the PLLA blocks had to be characterised in order to estimate the rate at which the implant's rigidity would decline.

In order to determine the rate at which the flexural rigidity of the implant decreases, four-point-bending experiments were conducted following the method of Bradley *et al*. [11]. According to his studies a femoral implant should possess an initial flexural rigidity in the order of 2Nm/° deflection. Experiments on humans showed that softer plates led to acute pain and infections in the fracture. Using simplified prototypes with manually fitted PLLA blocks, four-point-bending tests were conducted with inserted and removed degradable blocks. This way, with an initial rigidity of 2.2Nm/° deflection, a drop of 5% was measured. Naturally, for the final implant prototype this would be not satisfactory, however, it was demonstrated that even with a manually fitted block a measurable rigidity drop could be achieved.

In the next step, the degradation behaviour of the PLLA material was taken under closer investigation. Storing specimens in blood substitute solution (Ringer solution) at 37°C the Young's modulus and tensile strength were measured after predefined dwell times. It was found that after 23 weeks the modulus and tensile strength had decreased from 3.7GPa and 50MPa to 2.9GPa and 43MPa respectively. This corresponded with a drop of 20% in modulus and 14% in strength. Under dynamic loading conditions the mechanical degradation progressed at a higher rate. Exposing the PLLA specimens to cyclic tensile loads at a frequency of 15Hz, and a total of 500.000 cycles the following results were obtained. With an initial dynamic modulus of roughly 1.45GPa, which corresponded with a static modulus of 3.7GPa, increasing the maximum tensile stress resulted in higher mechanical degradation rates (Figure 2). After 500.000 cycles at 37°C in Ringer solution and a maximum tensile stress of 16MPa the specimen had lost 12.8% of its dynamic modulus. The total duration of one experiment was 18.5 hours, meaning that no appreciable hydrolytic degradation had taken place. For comparison, experiments under dry conditions and in water at ambient temperature were conducted. It was found that the elevated temperature of 37°C and the simple presence of a liquid were mainly influencing the material's mechanical degradation. Being implanted into a human however, hydrolytic degradation, which is solely dependent on the dwell time,

and mechanical degradation will act simultaneously and thus enhance the mechanical degradation rate of the PLLA. This means, that the total decrease in modulus and strength will probably well exceed that measured under load free exposure as discussed earlier. How this behaviour is then going to effect the total drop in flexural rigidity of the implant is currently under investigation.

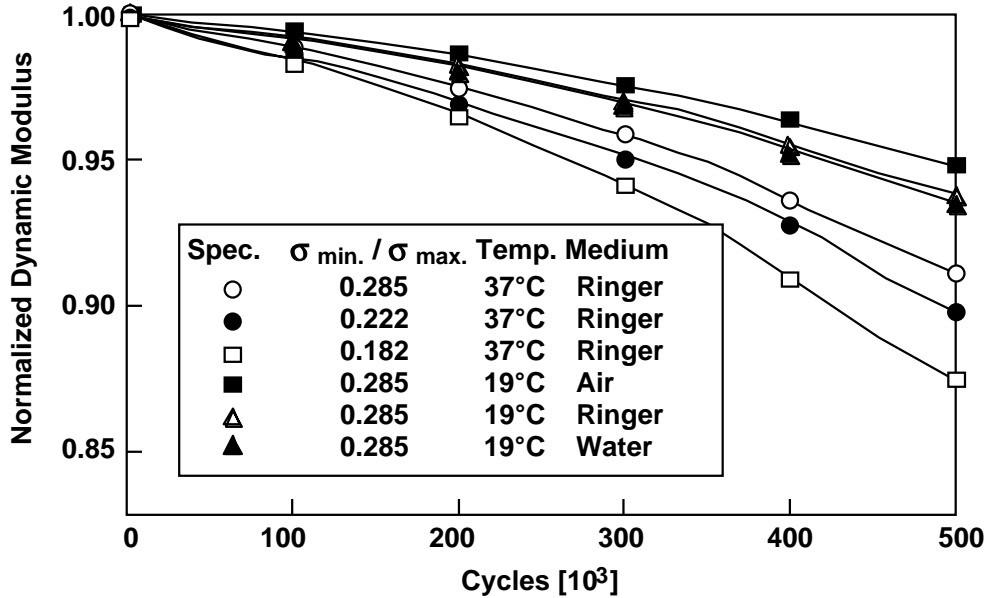


Figure 2: Normalised dynamic modulus of PLLA under cyclic loading

Another interesting effect that was observed during the dynamic testing of PLLA is its pronounced tendency to creep when exposed to Ringer solution at 37°C. Figure 3 shows the mean plastic deformation of the specimen tested under cyclic loading. It is evident that with increasing load the total deformation of the specimen also increases. However, even more significant is the fact that at ambient temperature, regardless of the surrounding medium, only marginal strain rates were measured (0.5-0.7%). This basically supports the conclusion made earlier that the temperature decisively influences the material's mechanical behaviour. Additional static tests, where a dead weight was used to apply a constant tensile stress showed similar results. Again, the specimen were put into tubs with Ringer solution at 37°C. With stresses of 3.5 and 5.5MPa mean plastic strains of 5.1 and 6.5% were measured after only 72 hours. Another 72 hours later the average strain amounted to 5.5 and 7.5%. For all specimen the transition from elastic to plastic deformation was reached after 2 hours at approximately 1.9% strain.

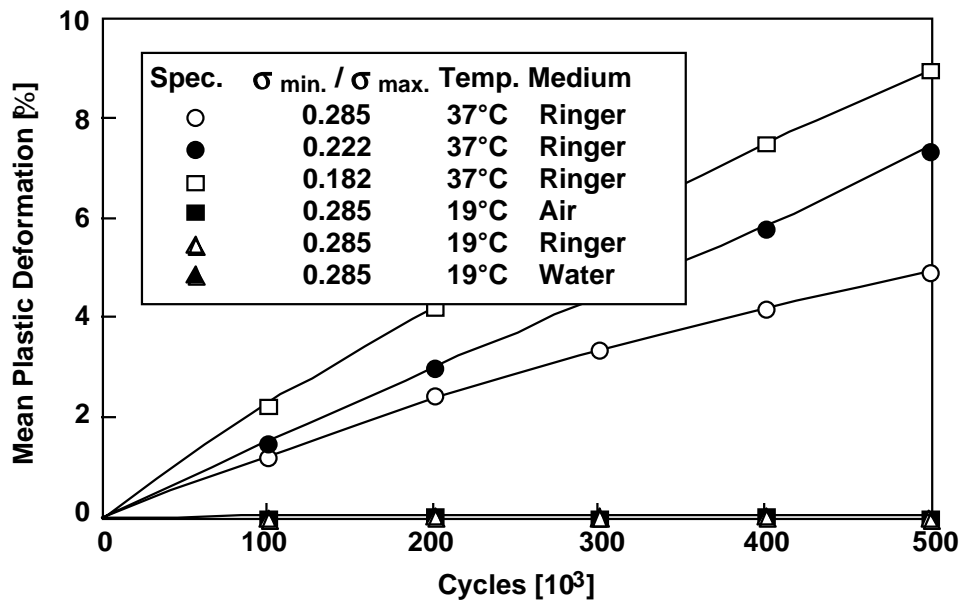


Figure 3: Mean plastic deformation of cyclic loaded PLLA specimens

Putting the results together it was concluded that the basically very brittle PLLA becomes ductile when being exposed to elevated temperatures and a liquid, in this case 37°C with water or Ringer solution. When external loads are applied mechanical degradation progresses long before hydrolytic degradation commences. However, it has to be taken into consideration that the dynamic tests had to be conducted at a frequency of 15Hz due to limitations in the testing equipment. Within the human body only frequencies of up to 5Hz do occur, meaning that the realistic situation could not be simulated. In the real situation the mechanical degradation would probably progress at a much slower rate. In order to better approximate this situation a new testing device is currently developed for dynamic four-point-bending implant prototypes with integrated PLLA blocks.

PRODUCTION OF PROTOTYPES

Prior to the production of prototypes it had to be decided on what manufacturing technique was most suited for producing the individual components of the implant. In order to satisfy the demand from the medical point of view concerning the surface finish and the coating of the reinforcements, only techniques that did not require any mechanical post-processing such as drilling or milling were taken into consideration. For the production of the continuous fibre-reinforced CF/PEEK bone facing plates, therefore, the near-net-shape technique was chosen. Figure 4 shows a photograph of the partly assembled mould. The inserts in the bottom half of the cavity, that form the countersunk holes and the gap for the biodegradable block, were removable in order to ease demoulding. For production of a part, pre-cut prepreg layers were filled into the bottom half of the mould. The assembled mould was then placed into a hot press where the material was heated to processing temperature, 420°C, at low external pressure. Once the melting temperature was reached the external pressure was increased to about 3MPa to ensure void-free consolidation.

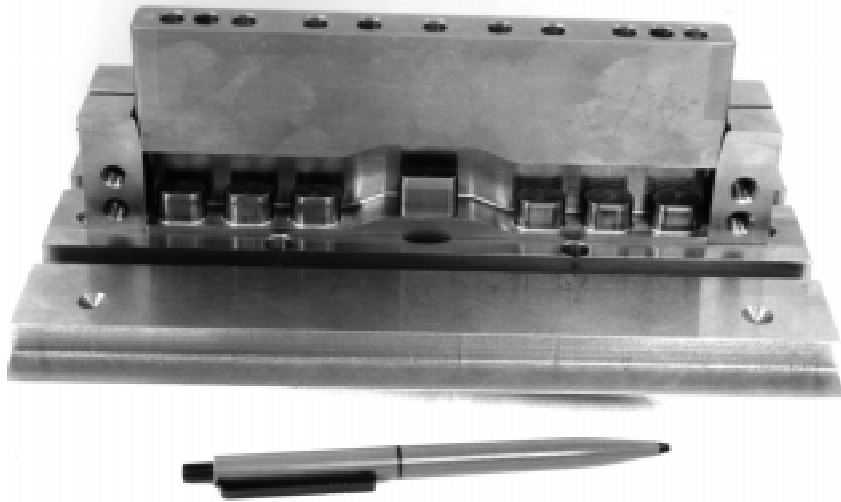


Figure 4: Photograph of near-net-shape mould for the bone facing plate of the implant

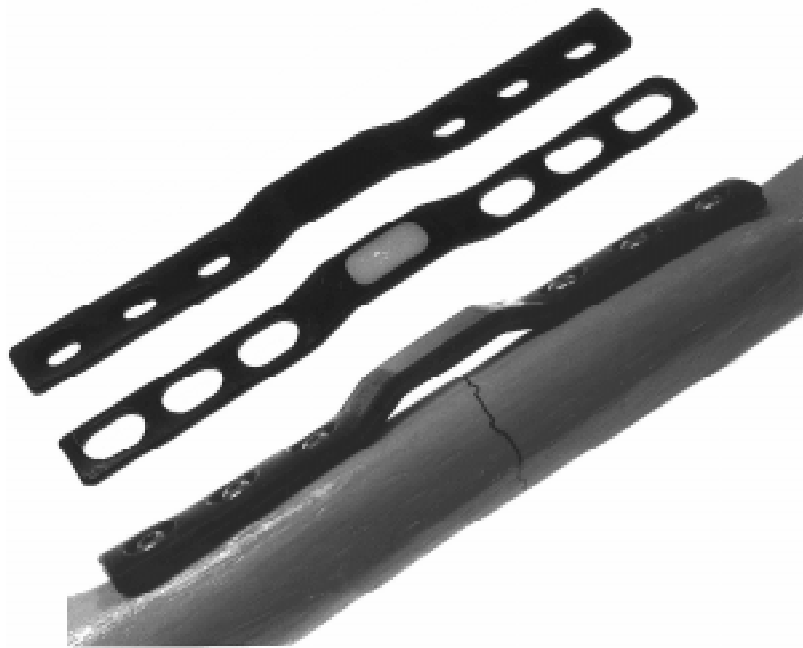


Figure 5: Photograph of implant prototype

The tissue facing plate of the implant was produced employing a similar tool to that shown in Figure 4. The degradable insert made from PLLA was injection moulded and later inserted into the bone facing plate. In order to make sure that it was tightly fitted into the gap of the bottom plate it was cooled down to -40°C prior to assembly.

RESULTS AND CONCLUSIONS

A new composite osteosynthesis implant was designed and manufactured. It consists of three individual parts, two of which are made from CF/PEEK and the third from Poly (L-lactide). The purpose of this composition was to create a property profile that subsequently allows interfragmentary movement which, according to the latest medical findings, leads to better reconsolidation of fractures bones. The main advantage of this solution in comparison with the very rigid stainless steel and titanium alloy plates is, that the implant's mechanical properties can be tailored to the patients needs. By selecting tissue and bone facing plate and the degradable block from a kit system initial and remaining stiffness of the plate can be adjusted. All components were made employing injection moulding and near-net-shape forming in order to avoid post-processing steps. This way it was ensured that the reinforcing fibres were fully coated by matrix which was required from the medical side in view of possible inflammatory reactions. Preliminary tests on simplified prototypes showed that a reduction in flexural rigidity is possible by integrating a biodegradable block into the body of the implant. According to the calculations the maximum achievable drop should be in the order of 20%. This estimation is currently validated by means of four-point-bending tests on fully detailed implant prototypes. Poly (L-lactide) was found to be rather brittle and room temperature, however, when being exposed to a liquid at 37°C its properties change drastically. Dynamic tests in Ringer solution showed that mechanical degradation occurs long before hydrolytic degradation commences. In addition it also shows a pronounced tendency to creep under those conditions. If the PLLA is best suited for reducing the implants flexural rigidity is currently under investigation.

For the final testing phase which could possibly be *in-vivo* a microelectronic testing device, which is currently designed, will be build into the body of the implant. This way, the acting bending moments, the actual temperature at the fracture site, and possible slip between implant and screws will be monitored and sent to a nearby computer via telemetry. With the data, early determination of irregularities, such as loosening of the plate or inflammatory reactions in the fracture will be enabled, allowing a more precise assessment of the actual state of bony union and restoration of mechanical and structural strength.

ACKNOWLEDGEMENTS

The authors would like to thank the „Stiftung Rheinland-Pfalz für Innovation“ for its financial support (Project No. 8036-38 62 61 61/173c) and Boehringer-Ingelheim for the free material supply. In addition, thanks are also due to M. Huisman, F. Maier, T. Pfaff, V. Kessler, H. Weber, R. Krebs, M. Barth, J. Alsfasser and A. Starck for their valuable contribution to the presented work. Professor Friedrich gratefully acknowledges the FONDS DER CHEMISCHEN INDUSTRIE; Frankfurt, for support of his personal research activities in 1997.

REFERENCES

1. Kwarteng, K.B., Stark, C., "Carbon Fibre Reinforced PEEK (APC-2/AS-4) Composites for Orthopaedic Implants", *Sampe Quarterly*, Vol. 22, No. 1, 1990, pp. 10-14.

2. Schenk, R., Müller, J., Willenberg, H., "Experimentell-histologischer Beitrag zur Entstehung und Behandlung von Pseudoarthrosen", Hefte zur Unfallheilkunde, Vol. 94, 1986, pp. 15-24.
3. Aro, H.T., Kelly, P.J., Lewallen, D.G., Chao, E.Y.S., "The Effects of Physiologic Dynamic Compression on Bone Healing under External Fixation", Clin. Orthop. Rel. Res. Vol. 256, 1990, pp. 260-273.
4. Claes, L.E., Wilke, H.-J., Augat, P., Rübenacker, S., Margevicius, K.J., "Effect of Dynamization on Gap Healing of Diaphyseal Fractures under External Fixation", Clinical Biomechanics, Vol. 10, No. 5, 1995, pp. 227-234.
5. Claes, L.E., "Knochenheilung unter dynamischer Frakturstabilisierung, *Die Plattenosteosynthese und ihre Konkurrenzverfahren*, Wolter and Zimmermann, Ed., Springer Verlag, Berlin, 1991, pp. 61-65.
6. Goodship, A.E., Kenwright, J., "The Influence of Induced Micromovement upon the Healing of Experimental Tibial Fractures", Bone and Joint Surgery (B), Vol. 67 B, 1985, pp. 650-655.
7. Wu, J.J., Shyr, H.S., Chao, E.Y.S., Kelly, P.J., "Comparison of Osteotomy Healing under External Fixation Devices with Different Stiffness Characteristics", Bone and Joint Surgery (Am), Vol. 66 A, 1984, 1248-1286
8. Hunt, M.S., "Development of Carbon Fibre/Polysulfone Orthopaedic Implants", Materials & Design, Vol. 8, No. 2, 1987, pp. 113-119.
9. Tayton, K., Jonson-Nurse, C., McKibbin, B., Bradley, J., Hastings, G., "The Use of Semi-Rigid Plastic Plates for Fixation of Human Fractures", Bone and Joint Surgery, Vol. 64-B, No. 1, 1982, pp. 105-111.
10. Tayton, K., Bradley, J., "How Stiff should Semi-Rigid Fixation of the Human Tibia be?", Bone and Joint Surgery, Vol. 65-B, No. 3, 1983, pp. 312-315.
11. Bradley, J.S., Hastings, G.W., Johnson-Nurse, C., "Carbon Fibre Epoxy as High Strength, Low Modulus Material for Internal Fixation Plates, Biomaterials, Vol. 1, 1980, pp 38-40

TAILORMADE COMPOSITE TITANIUM-BASED BIOMATERIALS

J. Breme

*Lehrstuhl für Metallische Werkstoffe,
Universität des Saarlandes D-66041 Saarbrücken Germany*

SUMMARY: Examples are given for composite tailored materials on a Ti-basis for various applications. Heart pacemaker leads with special physical properties (high capacity and conductivity) make it possible to minimize battery consumption. The improvement of the capacity was achieved by an increase of the surface by porous sintering as well as by the use of fractal coatings of highly conductive layers (TiN, TiB₂, IrO₂), for example, by PVD. In another example the realization of surface structures (porous and loops) which possess nearly isoelastic properties, as compared with the bone, is described. The new types of implants were investigated both in vitro and in vivo. The importation of bone and the new bone formation observed in animal experiments proved the accuracy of the isoelastic concept. The biological properties of Ti implants can be improved by coating with hydroxyapatite (HA) which is accomplished by the sol-gel procedure. By adapting the thermal expansion coefficient of the Ti substrate to that of HA after diffusion annealing, a maximum shear strength of the coating was achieved.

KEYWORDS: ti-composites, TiN, TiB₂, IrO₂ coatings, hydroxyapatite, sol-gel, isoelastic implants, porous sintering, surface structure

INTRODUCTION

Medical devices, implants and biomaterials must all keep in step with advances in medicine. For special applications biomaterials must often be tailor made if one single material is not able to fulfill the various requirements. Therefore composite materials must be developed if special properties are required. In most cases a surface layer which may have a biological, physical, chemical or mechanical function covers a structural material. Due to their corrosion resistance, biocompatibility and bioadhesion, titanium and its alloys are the metallic biomaterials of preference [1] for use as structural components. In the following three examples are given of composites based on Ti with special properties:

- Ti/ceramic composites with special physical properties
(heart pacemaker leads)
- Ti/porous Ti composites with special functional properties
(isoelastic implants)
- Ti/ceramic composites with special biological properties
(improved implant osseointegration)

Ti / CERAMIC COMPOSITES WITH SPECIAL PHYSICAL PROPERTIES

For artificial stimulation of the heart an electric field is required which is determined by the electrical potential and current of the pacing electrode. Inside the electrode the current is carried by electron mobility whereas outside a flux of ions is the main contributor to the current distribution. The coupling takes place at the electrode surface predominantly by the formation of an electrical double layer. The properties of the electrode tissue interface are of major importance for the pacing leads as they must serve two main functions: one is to conduct the electrical pulses from the pacemaker to the heart, and the other is to sense intracardiac signals and transmit them to the pulse generator. Pacing and sensing performance may be improved by adjusting the electrochemical and physical parameters to the interface without disturbing the biological equilibrium. For long-term stability it is essential to avoid chemical reactions which decrease irreversibly the signal amplitude and increase the threshold. The behaviour of the phase boundary can be explained by the structure of the double layer: a simplified equivalent circuit of the electrode/myocardium interface demonstrates that the potential distribution is determined by the Helmholtz capacity and the Farada impedance. If the double-layer capacity is large, the pacing losses will be low and the amplitudes of the depolarization signals will be high. This behaviour explains in general the advantage of porous over smooth electrode surfaces. The surface influence of the double-layer capacity can be described qualitatively by the relation

$$C = \varepsilon \cdot \varepsilon_0 \cdot \frac{A}{d} \quad (1)$$

where C = capacity, ε = dielectric constant of the electrolyte, ε_0 = dielectric constant of the vacuum, A = surface area and d = thickness of the layer. It is therefore clear that an increase of the surface A causes the observed favourable behaviour of porous titanium electrodes. The various surface layers (e.g. TiN) produced by PVD or CVD are able to improve the electrical conductivity of the electrode surface (Table 1). TiN is also known to have a biocompatibility similar to that of TiO₂ [2,3].

According to these considerations porous-sintered electrodes of titanium materials with conductive surface layers can have the following advantages:

- safe fixation to the myocardium due to a possible ingrowth of the tissue
- long-term stability of the electrode due to the well-known corrosion resistance and biocompatibility of titanium materials
- relatively high electrical conductivity due, for example, to a TiN surface layer
- high capacity and therefore lower losses and consequently a longer battery lifetime

For the sintering of the hemispherical shape of the electrode tip, which is shown schematically in Fig. 1, powder of cp-Ti was used. The pulverization was accomplished by HDH. Bulk material was treated with pure hydrogen under a pressure of 1.6 bar at 750 °C. Due to the pick-up of the gas the material was embrittled and could be crushed. After screening and separating a grain size fraction of 40 - 60 µm the electrodes were sintered in an argon atmosphere at 950 °C. Simultaneously with the sintering operation a contact supplying tube of commercial pure titanium was diffusion bonded to the head of the electrode tip. The temperature of 950 °C was chosen in order to guarantee sufficient bonding strength of the tube to the head and the highest possible porosity. Fig. 2 shows a cross-section of such an electrode prepared by grinding and polishing. The average porosity amounted to about 70 %, the pore size to about 50 µm.

An alternative as a conductive ceramic surface layer could be TiB_2 which, compared to TiN (Table 1) has an even lower specific electrical resistance (14.4 and 25 $\mu\Omega\text{cm}$ respectively). TiB_2 coatings on Ti electrodes can easily be produced at an increased temperature, e.g. 950°C.

Table 1: Electrical Resistance ρ ($\mu\Omega\text{cm}$)

Ti	41.8
TiO_2	10^{16}
Ir	5.3
IrO_2	49
TiB_2	14.4
TiN	25

Table 2: Heat of Formation $-\Delta H$ kJ/(mol)

TiO_2	889.41
TiN	309.15
TiB_2	319.61
IrO_2	188.39

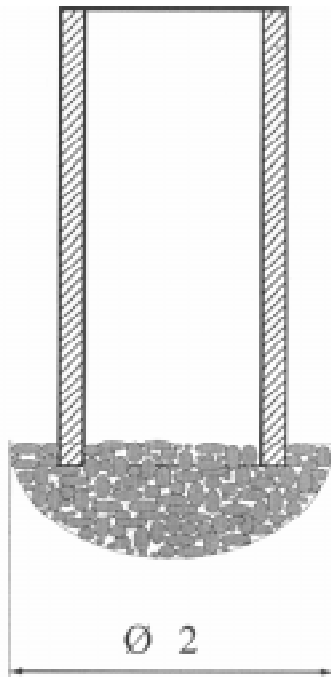


Fig. 1: Pacemaker lead (schematic)

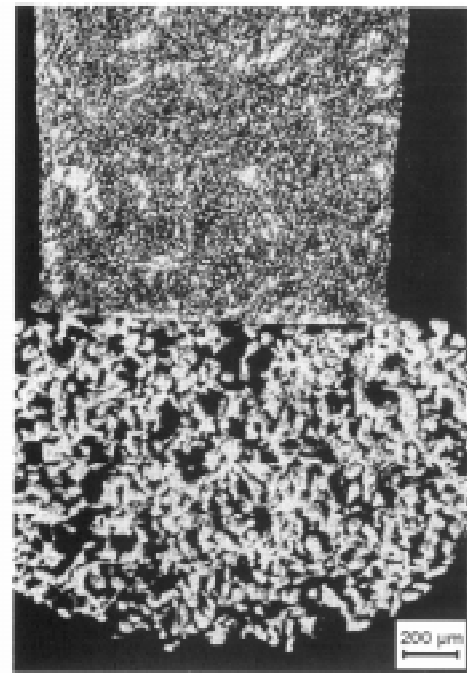


Fig. 2: Cross section of a sintered lead

For this purpose the electrodes were embedded in an oxygen-free boron powder. The sintering was performed in an argon atmosphere (1 h). The results of the impedance measurements of TiB_2 coated porous Ti electrodes are given in Fig. 3. Compared to TiN coated samples, there is no significant difference in the results. Both types of layers (TiN and TiB_2) have the crucial disadvantage of a low thermodynamic stability compared with TiO_2 (Table 2). Therefore, if anodic loading takes place, the formation of electroactive oxides, which have the disadvantage of a low electrical conductivity (Table 1), is inevitable. This problem can be overcome by the use of iridium coatings [4] which provide not only a metallic layer and an oxide layer (after anodic loading), but also high conductivity and improved impedance (Fig. 3). The Ir layers can be produced by different methods such as PVD and CVD. for the latter

process metalorganic precursors such as iridium tri-acetylacetonate ($\text{CH}_3\text{COCHCOCH}_3$)₃Ir can also be used [5].

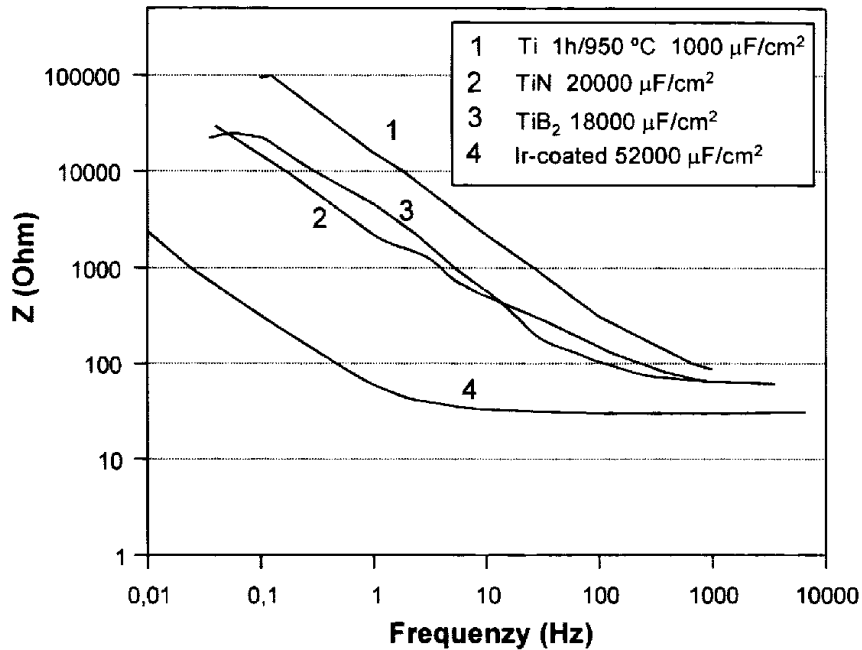


Fig. 3: Impedance measurement of pacemaker leads with different coatings

Ti / POROUS Ti COMPOSITES WITH SPECIAL FUNCTIONAL PROPERTIES

The surface structure of an implant has a significant influence on its anchorage and on the adhesion strength to the tissue. Since this strength is defined as the ratio of the loading force to the area on which the force is exerted, the load under service conditions can be greater the larger the area is. From this simple consideration it is clear that a smooth implant surface with a small contact area to the tissue will show a lower adhesion strength than a structured surface. This behaviour was demonstrated by implanting to the legs of rabbits flattened cylinders made of titanium alloys and of varying surface roughness. After an exposure time of 84 and 168 days respectively, the tensile strength was measured in tear-off tests. A measurable adhesion strength to the bone was present only when a certain degree of surface roughness ($>22 \mu\text{m}$) existed. With increasing roughness the tensile strength was enhanced [6].

From the point of view of applied mechanics, the ingrowth of the bone into surface cavities has a favourable influence. The shear stress, which is generated by the functional loading of the implant at the interface implant/bone, is decreased because, similar to the thread of a screw, the load at this interface causes, in addition to the normal stress perpendicular to the inclined area, only a small shear stress effective in the inclined area.

Besides the favourable influence on the implant anchorage, there is further important advantage in the use of surface structuring. The ingrown bone, which will be subjected to strain by compression or by tension, produces calcium, resulting in the stimulation of new

bone formation. It is clear that the appearance of this phenomenon will be enhanced in proportion to the improvement of the load transfer. From the mechanical point of view, the load transfer will improve as the stiffness of the implant decreases in the area of the ingrown bone. The stiffness S can be described by the product of the moment of inertia and Young's modulus E :

$$S = E \cdot I \quad (2)$$

Since the moment of inertia is given in most cases by the geometry of the "landscape", the Young's modulus value of the material must be lowered in order to decrease the stiffness of the implant in the direction of the bone. Because of the value of Young's modulus for Ti and its alloys, which amounts to only about 50 % of that of the CoCr alloys and of stainless steel, it is possible to produce with titanium a stiffness in the porous surface layer with a lower porosity than with the other materials. The reduction of implant stiffness and of Young's modulus by means of porous sintering results in a change in the remaining mechanical properties, especially in a decrease in the strength properties.

Since, under service conditions, dental implants are subjected to relatively low loads, the isoelastic concept is easily realized with this type of implant. A titanium alloy, Ti30Ta, has been developed which can be directly diffusion welded with alumina. Due to a high portion of the β phase this alloy has a decreased Young's modulus ($E = 80\,000$ Mpa) as compared to cp-titanium. In the martensitic structure, which can be produced by annealing in the β phase field at $900\text{ }^\circ\text{C}$ and by subsequent water quenching, Young's modulus amounts to only about $60\,000$ MPa and is already very similar to that of the cortical bone ($10 - 20\,000$ MPa). In order to achieve an isoelastic behaviour to the bone a further decrease in Young's modulus has been obtained by porous sintering (Table 3, [7]). A powder was produced from Ti30Ta by means of

Table 3: Influence of microstructure and porosity on the mechanical properties of Ti30Ta

	Porosity (%)	Compression Yield Strength (Mpa)	Youngs' Modulus (%)
cp-Ti		250-300	105000
Ti30Ta ($\alpha+\beta$)		610	81220
Ti30Ta (martensitic)		598	63680
Ti30Ta ($\alpha+\beta$)	12.3	520	59430
Ti30Ta (martensitic)	12.3	515	50120
Ti30Ta ($\alpha+\beta$)	30.4	203	25530
Ti30Ta (martensitic)	30.4	189	23630

the HDH procedure (hydrogenization-dehydrogenization). The irregularly shaped powder can easily be pressurized to produce a green body for sintering in a vacuum or in a high vacuum. By varying the sintering parameters (pressure, temperature, time, powder grain size) porous samples with different mechanical parameters were produced. Young's modulus and the yield strength were measured with strain gauges. Young's modulus and the yield strength depend on the porosity of the sintered samples (Fig. 4). The yield strength decreases with increasing porosity. At a porosity of 30 % the yield strength amounts to 190 MPa, a value which is sufficient for application as a dental implant, because, considering that even in the case of the maximum measured biting force of 800 N, [8], the compression stress is not greater than 50 MPa. Samples and implants with a porous surface layer can be produced with a specific porosity whereby the strength properties can be optimized by the sintering parameters. In addition to the porosity itself, the pore size also plays an important role. It must be sufficiently

large (approx. 50 - 100 μm) to allow the ingrowth of the bone [9]. Besides the porous sintered implants, another type of implant with a special surface structure decreasing the implant stiffness and imitating the natural anchorage of teeth has been developed. A spiral of cp-

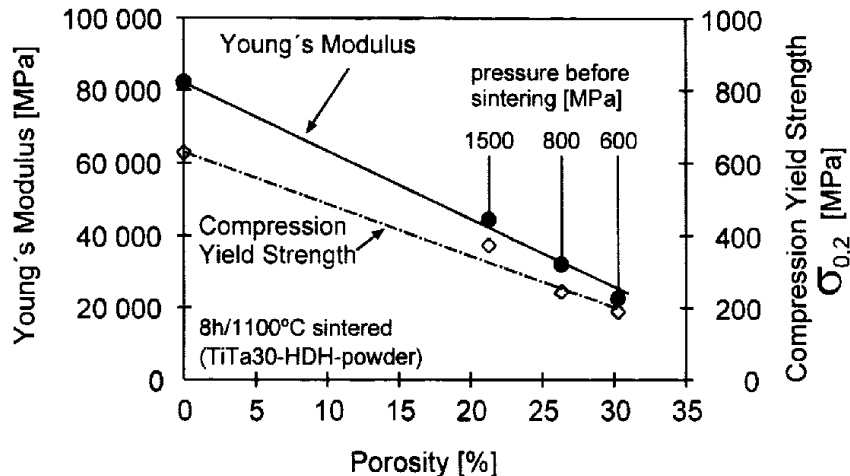


Fig. 4: Influence of porosity on the mechanical properties of Ti30Ta

titanium wire was diffusion welded (24 h at 1100 °C) on a core consisting of the alloy Ti30Ta. The ingrowth of the bone into the produced loops imitates the natural suspension by transmitting a damping capacity to the implant similar to the Sharpey fibres of the tooth. The functionality of both implant types was determined in vitro as well as in vivo. For the in vitro experiments an artificial jaw was constructed from a plastic material with the same elastic properties and geometry as a human jaw with the inner part ($E = 3000 \text{ MPa}$) corresponding to the spongy bone and the outer part (12000 MPa) corresponding to the cortical bone. The implants were inserted in the model. The model and the implants were loaded in a testing apparatus in which the strain, and therefore the stresses, of both were measured by means of strain gauges. In order to achieve a clear result concerning the influence of the stiffness of the implant, a systematic change in Young's modulus was studied by a comparison of implants consisting of various materials (alumina, steel, cp-titanium and the isoelastic implants). The measurement of the in vitro functionality of implants embedded in an artificial jaw showed that the implant with the loops on the surface have an elasticity very similar to that of the bone (Fig. 5). For the functional loading during the in vivo tests in adult fox hounds a special design was necessary. The surface layers of the implants for the animal experiments had a porosity of 20 %, a pore size of 103 μm , a Young's modulus value of 45 000 MPa and a yield strength of 340 MPa. The layers were produced from Ti30Ta powder with a grain size of 200 - 315 μm by sintering at 1100 °C for 24 h in an argon atmosphere. The implants were inserted into the lower jaws of the dogs. After a healing period of three months the implants were provided with a dental prosthesis. After functional loading for a period of six months the implants underwent histological investigation which was preceded by the preparation of microsections according to the method proposed by Donath. In all implants a good interlocking of the bone and a close bone contact to the implant surface were observed. Implants with a porous surface layer showed bone ingrowth into the open porosity. Especially in the case of the implants with surface loops an ingrowth of bone was observed.

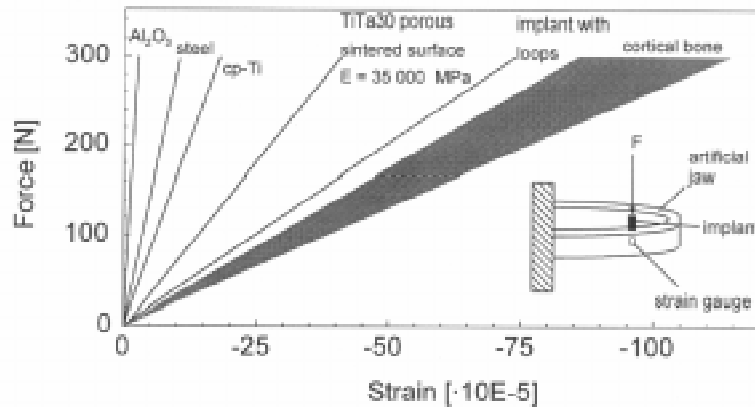


Fig. 5: In vitro investigation of dental implants with different stiffness

Ti / CERAMIC COMPOSITES WITH SPECIAL BIOLOGICAL PROPERTIES

Implants consisting of titanium materials possess an adhesion with a high shear strength to the bone. This adhesion has a mainly mechanical character because the bone grows in close contact with the implant and penetrates cavities and grooves on the implant surface due to the inert behaviour of the titanium materials caused by the constant presence of an oxide layer which has an isolating effect due to its high dielectric constant ($\epsilon = 78$) corresponding to that of water. Because of this fact and in order to provide a high shear strength between the bone and the implant during the healing period, any perceptible relative implant/bone motion must be avoided. Therefore, during this period, which takes about 100 days, implants such as hip prostheses should be loaded only to a slight degree.

By the use of hydroxyapatite (HA) with its osteoconductive properties, the healing period can be decreased to about 20 days and the bone is able to bridge the gap to the implant by the formation of a chemical bonding to the HA. Since hydroxyapatite has inadequate mechanical properties, it is only of advantage if it is used as a coating for a composite material based on a metallic material, i.e. a titanium alloy. Because of this fact the problem of the implant anchorage is shifted to the metal/ceramic interface. Nevertheless, a dense HA layer with a high adhesion strength to the metallic substrate is required. The adhesion strength can be achieved only by a chemical bonding, i.e. by diffusion annealing. The difficulty of the production of a dense HA coating on titanium arises from the thermal expansion coefficient α of Ti which amounts to only 60 % of that of HA, producing according to equation (3) high residual stresses:

$$\sigma_{R5} = \bar{E}(\alpha_M - \alpha_C)\Delta T \quad (3)$$

\bar{E} = Young's modulus of the interlayer metal/ceramic

$\alpha_{M,C}$ = thermal expansion coefficient of the metal and the ceramic respectively

ΔT = temperature difference annealing temperature/RT

Therefore, in order to overcome this problem causing a predamaging of the ceramic after diffusion bonding, it was intended to develop a corrosion resistant biocompatible titanium

alloy with adequate mechanical properties (similar to those of standard alloys) and a thermal expansion coefficient adapted to that of HA. However, in accordance with theoretical considerations, the HA coating layer should be as thin as possible because in the case of implants like hip prostheses, which are loaded by bending, the maximum bending strength (tension) is found on the lateral side in the surface fibre which consists of the HA ceramic. Because of this fact, especially thick HA layers risk being damaged.

Since, on the one hand, manganese, as compared to titanium, has an extremely high thermal expansion coefficient ($\alpha = 22 \cdot 10^{-6} \text{ K}^{-1}$ and $\alpha = 8.4 \cdot 10^{-6} \text{ K}^{-1}$ respectively between 20 and 100 °C) and, on the other hand, it is, like Fe, an important trace element in the human organism, it has been chosen as an alloying element in order to adapt the expansion coefficient of Ti to that of HA.

Fig. 6 gives the results of the measurement of the thermal expansion coefficient of the various alloys compared with the coefficients of cp-Ti and HA. With increasing Mn content the misfit between Ti and HA is reduced. For a content of 6 % Mn the difference between the metallic alloys and the ceramic is less than 20 %.

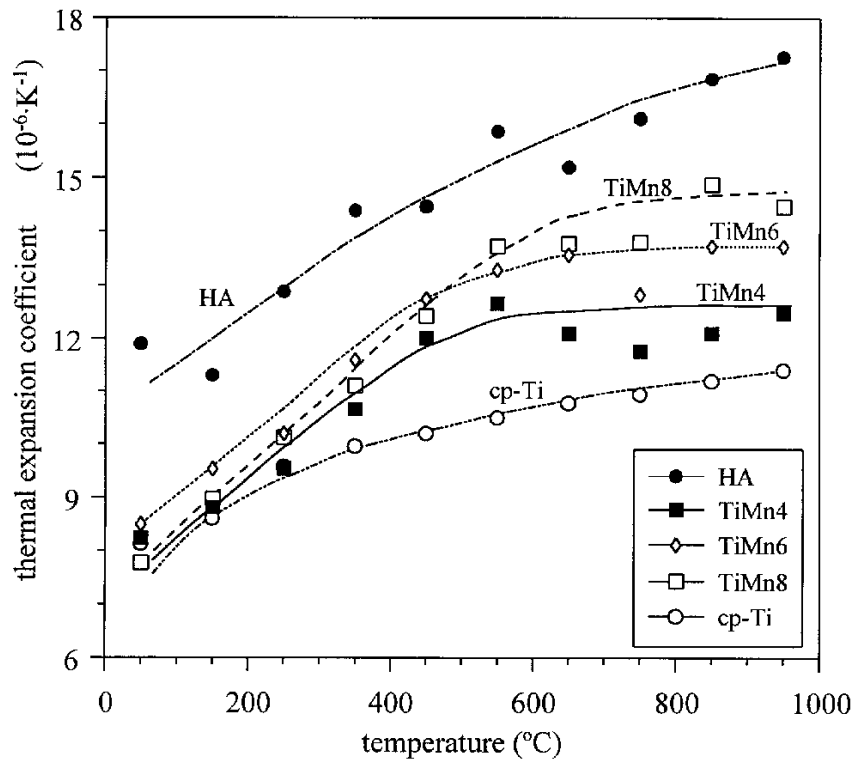


Fig. 6: Expansion coefficient of TiMn alloys

Chosen as a coating method was the sol-gel procedure shown schematically in Fig. 11. The starting materials were a solution of CaO and an organic compound triethylphosphate $\text{PO}(\text{OC}_2\text{H}_5)_3$ and trimethylphosphate $\text{PO}(\text{OCH}_3)_3$ respectively. The samples were dip coated with a mixture of the starting materials. The dip coating was followed by drying for 1 h at 130 °C, leading to the production of a gel. Finally, by annealing at 600 - 800 °C (5 - 15 min) the coating was developed. With both methods cylindrical samples of Ti8Mn were coated in order

that traction adhesive strength tests could be performed. The resulting HA coatings were characterized by x-ray studies.

The HA produced at 600 °C was seen to be more amorphous than the material produced at 800 °C.

The investigation of the traction adhesive strength of the layers produced at 600 and 800 °C respectively shows that no real value could be determined because the rupture always occurred in the glue. Since the tensile strength of the applied glue was indicated and also measured to be about 70 N/mm², the value of the adhesion strength of HA applied by the sol-gel process to the Ti8Mn alloy must be even higher than 70 N/mm².

A further advantage of the sol-gel method is the possibility of changing the Ca:P ratio within close limits. The interaction of HA with differing Ca contents and with cells was studied in proliferation tests. After a γ sterilization of Ti samples coated with different Ca:P ratios, L132 cells were cultured on the surface of these samples. After an exposure time of 72 hours the survival rate of the cells was determined by counting and then comparing the result with a standard sample of plastic. The percentage of proliferation was calculated as the ratio to the number of initially cultured cells. Fig. 7 shows the proliferation on the different coatings. There is no significant difference between the crystalline and amorphous coatings. Nevertheless, a certain content of tricalcium phosphate seems to stimulate the proliferation of the cells.

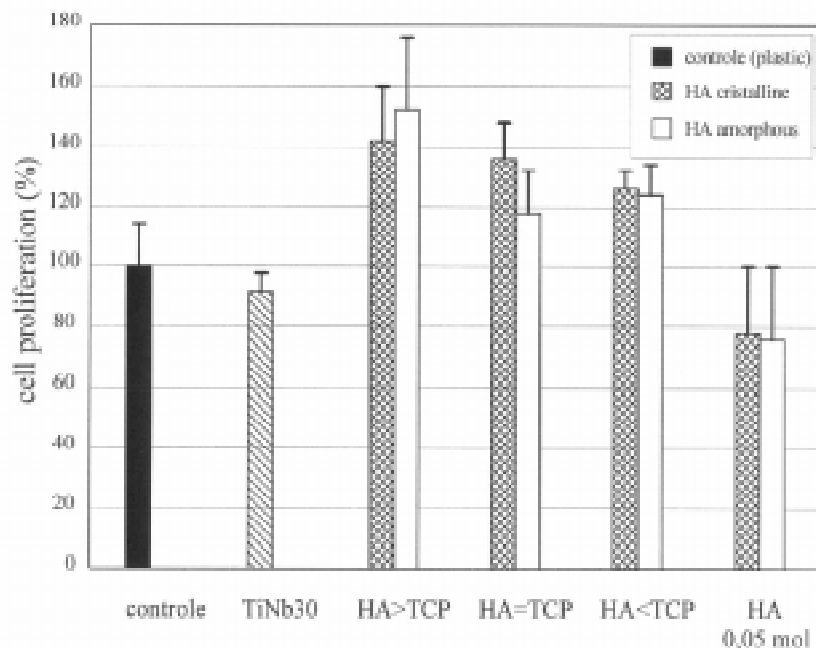


Fig. 7: Cell proliferation on HA coatings with different Ca:P ratios

CONCLUSION

By an optimization of the process parameters composite biomaterials on a Ti-basis with improved physical, functional and biological properties can be tailor-made. The physical properties can be improved with IrO₂ coatings (pacemaker leads), the functional properties (dental implants) with special surface structures and the biological properties with HA coatings (endosseous implants).

ACKNOWLEDGMENTS

The support of the Bundesministerium für Bildung, Wissenschaft, Forschung und Technologie and of the Deutsche Forschungsgemeinschaft is gratefully acknowledged.

REFERENCES

1. Breme, J. "Titanium and titanium alloys, the metallic biomaterials of preference", Plenary Lecture, Sixth World Conference on Titanium, Cannes, 1988, *Mém. Etudes Scientifiques, Revue de la Métallurgie*, 86, 1989, pp. 625-638.
2. Schaldach, M., Hubmann, M., Hardt, M., Weikl, R. and Weikl, A., "Titannitrid-Herzschrittmacher-Elektroden", *Biomed. Techn.*, 34, 1989, pp. 185-190.
3. Schaldach, M. and Bolz, A., "Longterm Stability of TiN", *Proceedings Conference Bioceramics and the Human Body (IRTEC-CNR)*, Faenza, 1991, pp. 82-88.
4. Riedmüller, J., Rzany, A., Fröhlich, R., Bolz, A. and Schaldach, M., "Langzeitstabilität bei elektrischer Belastung von galvanisch abgeschiedenem Iridiumoxid", *Biomedizinische Technik*, 40, 1995, pp. 37-39.
5. Gelfond, N.V., Igumenov, I.K., Boronin, A.I., Bukhtiyarov, V.I. Smirnov, M.Yu, Prosvirin, I.P. and Kwon, R.I., "An XPS study of the composition of iridium films obtained by Mo CVD", *Surface Sciences*, 275, 1992, pp. 323-331.
6. Schmitz, H.J., Gross, U. Kinne, R., Fuhrmann, G. and Strunz, V., "Der Einfluß unterschiedlicher Oberflächenstrukturierung alloplastischer Implantate auf das histologische Zugfestigkeitsverhalten des Interface", 8. *Sitzung des DVM-Arbeitskrieses Implantate*, DVM, Ed., Berlin, 1988, pp. 163-172.
7. Breme, J., Biehl, V., Schulte, W., d'Hoedt, B. and Donath, K., "Development and functionality of isoelastic dental implants of titanium alloys", *Biomaterials*, 14, 1993, pp. 887-178.
8. Schwickerath, H., "Kaukraft-Kaudruck-Belastbarkeit", *Dtsch. Zahnärztl. Z.*, 31, 1976, pp. 870-873.
9. Hulbert, S.F., Young, F.A., Matthews, R.S., Klawitter, J.J., Talbot, C.D. and Stelling, F.H., "Potential of ceramic materials as permanently implantable skeletal prosthesis", *J. Biomed. Mat. Res.*, 4, 1970, p. 433-439.

C-130 COMPOSITE FLAP DESIGN DEVELOPMENT AND CERTIFICATION

Doug McPherson¹, Scott Reeve², Dewey Meadows², Arun Sibal²

¹*Hawker de Havilland Ltd. 361 Milperra Road, Bankstown NSW 2200.*

²*Lockheed Martin Aeronautical Systems, 86 S. Cobb Dr. Marietta, Georgia 30063 USA.*

SUMMARY: The C-130 Composite Flap Programme resulted from the need for redesign of the existing metal flaps which suffer throughout their life from severe acoustic fatigue cracking. The total development programme up to delivery of the first flight set, including static and acoustic fatigue testing, was completed within 12 months. To achieve this ambitious schedule it was necessary to integrate design, manufacturing and certification into a united team with comprehensive understanding of the materials and technologies to be utilised. The C-130J Composite Flap is testimony to this harmonious blend which is so essential to the successful integration of composite material into a production environment.

KEYWORDS: C130 flap, design, development, certification, analysis, manufacturing, testing, integrated product team

INTRODUCTION

The reasons for new C-130J composite flaps can be attributed to associated maintenance problems on older C-130 in-service aircraft. All Hercules aircraft prior to the C-130J model were equipped with centre and outer wing flaps made of aluminium construction with classic rib and thin sheet skins. There has been a large number of reported flap skin cracks from operators over a long period of time. C-130E and C-130H maintenance records showed a high incidence of cracking in flaps and the USAF considered these to be a major maintenance burden on C-130 aircraft. Most of the flap cracks are a result of sonic fatigue in an adverse acoustic environment due to engine propeller wash and exhaust. Corrosion was a lesser contributor, but was also a consideration.

Several new designs were studied as an alternative to the existing aluminium configuration flaps. Different skin gages and materials such as ARALL skins were considered. Carbon fibre/resin composite was selected to be the best and most optimum flap design for the operating conditions.

DESIGN REQUIREMENTS AND SPECIFICATIONS

Most composite marketing is focused on the potential weight savings that can be obtained from extolling the virtues of orthotropic material, however this benefit is usually gained at the expense of manufacturing simplicity. The C-130 composite flaps were not designed for weight efficiency, the composite flap being similar in weight to its metal predecessor. The principal design parameter was durability. The flap had to withstand a very harsh acoustic

environment and the fatigue behaviour of the composite material proved far superior to the aluminium alloy material when used in the conventional skin, spar and rib configuration. In fact, the structural configuration is nothing new and falls into the much maligned description of first generation composite design known as 'black aluminium'. (Refer Fig.1).

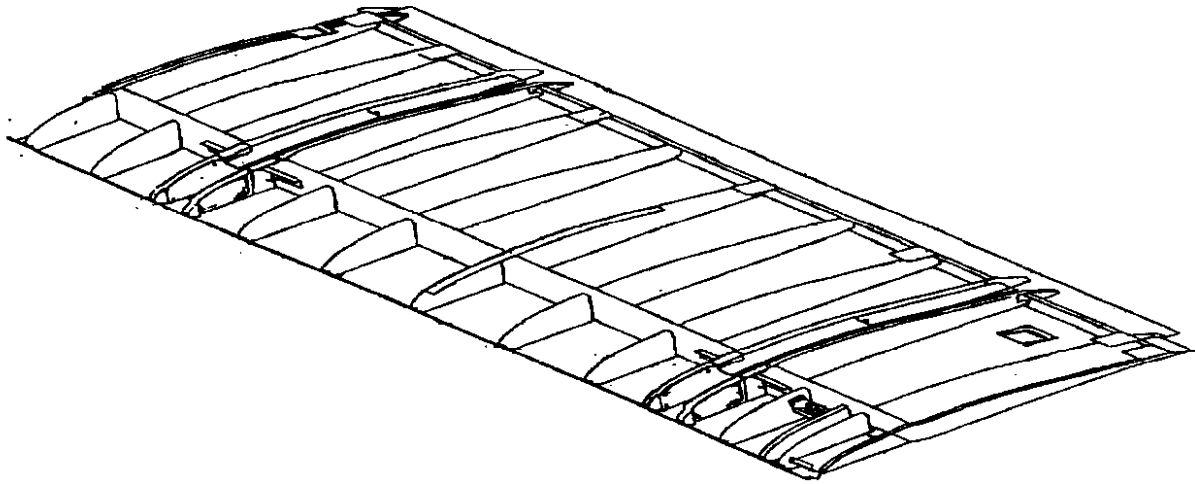


Fig. 1: Structural Arrangement - Centre Wing Flap

The re-design required that the flap basic loft contour be retained and the flaps interface with aircraft structure remain the same. The new composite flaps must be structurally and functionally interchangeable with existing metal flaps.

Hawker de Havilland (HdH) was awarded responsibility for the design and build of centre and outer wing flaps using reinforced thermoset resin materials. The separate components were to be mechanically fastened together with titanium, monel and stainless steel fasteners. The flaps must conform to the requirements of Lockheed Martin Aeronautical Systems (LMAS) specifications and standards as well as Federal Aviation Authority (FAA) regulations.

LMAS was responsible for supplying HdH with flap loft contours in CATIA models and all pertinent specifications and standards.

DESIGN BUILD TEAM

The challenge confronting HdH and LMAS was to design and manufacture a set of production flaps for the C-130J within a 12 month time frame of awarding the contract. In order to achieve such a demanding task there had to be full focus on a successful design and build implementation more commonly known these days as Integrated Product Teams (IPT). The seeds for the success of this team were sown by previous programmes at HdH and LMAS. The lessons learnt by HdH on the MD Explorer, Boeing 777 and Boeing 737 IPT, with regard to designer, builder and customer relationships were invaluable to the programme.

Having established a successful tender to win the contract, the goal HdH set itself was to resist the temptation to change the design during the preliminary design phase. HdH despatched 4 designers, 2 manufacturing engineers, 1 analyst/test engineer and 1 acoustic analyst to work on location at LMAS over a 7 week period of concept design. The heavy

emphasis on manufacturing engineering highlighted the focus on a balanced design/build integration. As well as the 'on site' team, the project organisation set up at HdH Bankstown clearly showed the priority and authority that needed to be vested in the project. The acoustic analysis was provided by Vipac Engineers and Scientists Ltd under contract from HdH. The design was consolidated on electronic media using CATIA and NASTRAN and strict discipline applied to ensure the accuracy of the model was at all times preserved. The nickel plated layup mandrels for the skins commenced manufacture during the concept phase with CATIA information sent directly to Express Plastics (UK) for N.C. profiling of the masters. A successful Preliminary Design Review (PDR) allowed the electronic 'model' to be frozen and commencement of Detail Design Phase at HdH.

The Detail Design Phase produced drawings concurrently with the tools. These two operations have traditionally been sequential and the need to parallel the activities required complete trust and close liaison between designer and manufacturer. Also paramount in the success of this phase was the co-location of a LMAS team at HdH. LMAS were the applicant for submission of the design to the certifying authority and therefore worked in unison with HdH to ensure the product met all its specification requirements. The flap design and structural analysis were approved by the LMAS engineering onsite team, including all drawings and reports. Without the onsite team the design, build and delivery of the flaps could not have been accomplished in time for C-130J flight test. The team effort worked extremely well between the two firms and established a healthy on-going relationship which was helpful through the flap installation and flight test programme. This phase was concluded with a successful Critical Design Review (CDR).

With all the tools designed and manufactured and all the drawings released the effort now converted to manufacturing. The design engineers transitioned into development engineers enabling fast resolution of problems and quick response for drawing change.

FAA CERTIFICATION PLAN

As part of the overall C-130J type certification to the FAA regulations, the composite centre and outer wing flaps needed to comply to FAR 25 and advisory circular AC 20-107A. The certification plan for the flaps consisted of:

- Material Qualification Testing
- Submittal of all material and process specifications used in design and manufacture
- Submittal of all engineering drawings
- Submittal of structural analysis
- Structural Qualification Testing

A comprehensive set of design verification tests were conducted on coupons and elements to evaluate specific design details. These tests provided valuable information as part of the design effort. The tests were not part of the formal certification plan since the Structural Qualification tests included all structural features and the effects of critical design conditions. The design verification test results were made available for FAA review.

As certification applicant, LMAS coordinated the certification plans with the local FAA office. Material specifications, process specifications, and engineering drawings were submitted to FAA Designated Engineering Representatives (DER) at LMAS. The structural

analysis was submitted to the DER for recommendation and forwarding to the FAA. Fabrication of material test panels and structural test components at HdH were witnessed by Civil Aviation Safety Authority (CASA) representatives acting under the bilateral FAA/CASA agreement. The Structural Qualification Tests were witnessed by FAA DER's.

COMPOSITE MATERIAL SELECTION, QUALIFICATION AND ALLOWABLES

The selection of materials was an important parameter in keeping manufacturing costs to an acceptable level. Poor choices in this area of design have been the downfall of many promising composite projects in the past.

To meet schedule and cost objectives, the composite material for the C-130 flaps had to meet the following criteria:

- Existing data base and allowables
- Production experience
- FAA approved specifications
- Lower cost relative to newer materials.

LMAS had proposed Hercules AS4-3501-6 carbon/epoxy, however HdH was predominantly using Hexcel's T650/F584 carbon/epoxy materials for MD Explorer and other programmes and proposed using the same material for C-130 Flaps with some cost savings over the use of AS4-3501-6 material. Based on a review of the available T650/F584 data and cost savings, LMAS accepted the use of this material for C-130 Flaps.

For ease of material handleability and fabrication, prepreg plain weave fabric was selected as the material of choice. The qualified material is a solution coated fabric which has excellent drape characteristics.

To allow the use of T650/F584 material on the C-130 Flaps, LMAS developed two new material specifications for tape and fabric materials. These specifications defined all the laminae and laminate material qualification requirements and were approved by the FAA.

All the material qualification work was performed by Hexcel. Hexcel had previously qualified T650/F584 tape and fabric materials for 82°C (180°F) applications to McDonnell Douglas Helicopter Company (MDHC) specifications. This data was FAA approved. Hexcel used this available data and generated additional required data to complete all the data required for LMAS specifications for 104°C (220°F) applications.

All the test panels and test specimens used for generating new data were conformed by FAA-DER who also participated as witness to the qualification testing.

The qualification data was used to adjust the material specification requirements and the design allowables, and then the data and specifications were submitted to the FAA for final approval.

COST EFFECTIVE DESIGN

The HdH proposal based its selection of design concept on its prior experience of the MD Explorer helicopter project. The need was to keep construction simple, there was insufficient development time to steer away from a very conservative approach. To this extent the design

excluded carbon/epoxy tape, honeycomb, film adhesives and secondary bonding. Low cost fasteners were selected that were not necessarily industry standard for this type of construction.

Standardisation of parts and fasteners received heavy focus in the design. Ribs, clips and angles are common wherever possible to minimise different tools. The constant thickness skins and substructure reduced tool complexity and simplified ply layup.

The layup of the material is quasi-isotropic to increase the bi-directional bearing properties and replicate stiffness characteristics of the existing metal flap. Ply drop offs are non existent except where required by material roll width constraints.

Copper foil prepreg was added to the outside surface of the flaps to allow dissipation of lightning strike.

ANALYSIS

Based on the preliminary allowables, the initial analysis of internal loads in critical areas was performed by hand (again due to time constraints) prior to PDR. In parallel, a coarse Finite Element Model (FEM) was developed to assess overall stiffness in bending and torsion and to confirm the internal load distribution. These two activities (hand analysis and coarse FEM) gave a reasonable assurance concerning the structural soundness of the proposed design in a matter of weeks, well before PDR. Factors like thermal expansion of the wing and the forced bending of the flap due to wing deflection were also accounted for at this early stage.

One of the most important components of the analytical side of the project was the use of a fine mesh FEM to determine internal loads and margins of safety. By the time the model was developed, more detailed information concerning wing deflection and the compliance of flap attachment points were available. This information was then included into the model, which was run for all critical load cases. It was noted early in the programme that the amount of information provided by the FEM would not be processed before the scheduled certification activities. For that reason, instead of generating the internal load data, the model was set to provide direct output in terms of safety margins, based on ply by ply analysis performed by NASTRAN. The subsequent practical task was enormously simplified, with a single glance of the strain contour display sufficient to identify hot areas and levels of strain. This automated process provided data output to include directly into the stress reports, without the need to generate safety margins by hand.

Due to the utilisation of blind fasteners (NAS 1919) it was prudent to check the issue of tension loads generated in the fasteners. For this reason, all the parts of the flap were modelled as separate entities and subsequently “sewn” together using Multi-Point Constraint (MPC) elements. This, in turn, enabled direct assessments of tension load in each fastener and the fastener load distribution along the rivetted joint. Consequently, the proper sizing of fastener diameter and pitch in critical areas was determined based on reliable data. The tape with the model data and results was then included in the stress reports.

MANUFACTURING

Extensive producibility and developmental trials were conducted during the pre-manufacturing phase and information constantly fed back into the design.

Minimisation of total parts count was a prime focus of the programme. Innovative production and assembly techniques as well as strict process control are features of the C130 Flap manufacture.

All major tools and assembly jigs were verified and qualified using computer aided theodolite instrumentation which referenced numerical information to the engineering master model data.

TESTING, CERTIFICATION AND FAA INVOLVEMENT

The test programme consisted of three phases:

- Material Qualification Testing (discussed earlier)
- Design Verification Testing
- Structural Qualification Testing.

The Design Verification Tests consisted of elements and coupons to evaluate specific design details. These tests were not part of the formal certification effort. The tests included:

- High cycle fatigue of laminates to evaluate material behaviour in a sonic environment.
- High cycle fatigue of skin/substructure joints.
- Skin panel buckling.
- Skin panel shear strength.
- Skin panel strength with impact damage.
- Skin panel strength after repair.
- Carriage to flap joint.
- Interlaminar tension of substructure angles.
- Fastener pull through.
- Fastener lap shear joint strength.
- Sonic fatigue of flap sections.

Some testing also included elevated temperature and wet environments to simulate the critical design conditions.

The Structural Qualification Tests were conducted on articles representing full scale centre and outer wing flaps. All the structural and loading requirements for the flaps were included in these tests. All full scale static tests were conducted by Aeronautical and Maritime Research Laboratory (AMRL). FAA DER's were involved in the witness of all tests. The tests were:

- Static test of the centre flap.
- Static test of spar and rib components.
- Static test of the outer flap.
- Lightning strike of flap skin.
- Flight testing.

The centre flap static test was conducted under the critical design environment of elevated temperature, wet conditions. Temperature was 93°C (200°F) and the relative humidity was 85%. The flap included Barely Visible Impact Damage (BVID) in the skins at critical

locations. Separately, full scale spar and rib components were tested under the same conditions of elevated temperature, wet environment with impact damage. Results of the test demonstrated that the flap could withstand 225% design limit load without failure.

The outer flap static test was conducted at room temperature, ambient conditions with impact damage. The environmentally compensated test load was applied to account for material strength degradation at environment.

In general, the tests confirmed some important conclusions obtained in the process of FEM analysis. The tension loads in fasteners generated by buckling skin were within safe limits and therefore the use of blind fasteners was justified and overall the correlation between the test and analytical data was excellent.

CONTINUOUS IMPROVEMENT

In the never ending quest to drive manufacturing costs downwards without compromise to the quality of the product, the following technical innovations are planned for future evaluation:

- Hot Drape Diaphragm Forming (Ribs and Spar).
- Resin Transfer Molding (Ribs)
- Composite Pultrusion (Spars)
- Robot drilling and fastener installation. (Assy).

CONCLUSION

By utilising an Integrated Product Team approach and adopting a schedule which required severe overlapping of traditionally sequential activities HdH and LMAS have achieved technical and commercial success in the design, manufacture and certification of the C-130 composite flaps.

The design criteria for the flaps focused on a robust, cost efficient structure using composite material. This paper confirms that composite structure designed for durability may well have a future market with as much potential as composite structure designed for weight efficiency.

CERTIFICATION OF STRUCTURAL COMPOSITE COMPONENTS USED ON THE MD900 HELICOPTER

Stuart E. Dutton¹, R. A. (Dick) Lofland²

¹*Cooperative Research Centre for Advanced Composite Structures Ltd
361 Milperra Road, Bankstown, NSW, Australia, 2200*

²*McDonnell Douglas Helicopter Systems, 5000 E. McDowell Rd, Mesa AZ 85215-9797*

SUMMARY: This paper will discuss the application of structural composites used on the McDonnell Douglas (MD900) Explorer Helicopter. It will concentrate on Hawker deHavilland's part in the selection, qualification, and certification of composites materials used on the helicopter. It will also discuss the design and manufacturing concepts and some of the manufacturing processes used to achieve the light weight and high performance characteristics of this machine.

KEYWORDS: FAA certification, material selection and qualification, composite structural testing, and composite manufacturing.

INTRODUCTION

The MD900 Explorer helicopter is the first new versatile rotorcraft of the 21st century. The eight place, twin-engine MD Explorer is the safest, quietest helicopter in its class. The helicopter features the composite NOTAR (No Tail Rotor) anti-torque system, bearingless all-composite rotor system, and many applications of composites in the fuselage.

HDH INVOLVEMENT IN THE MD EXPLORER

Hawker deHavilland Ltd. (HDH) began its involvement with McDonnell Douglas Helicopter System (MDHS) in the McDonnell Douglas (MD) Explorer program in 1988 when it became the first of several off-shore US companies to participate in the collaboration.

Originally, the brief was to design and manufacture the fuselage, tailboom and empennage structures. However, later the effort was scaled down slightly and MDHS retook responsibility for the boom and tail.

A very challenging target for vehicle empty weight was issued and it was apparent from the outset that novel structures would be required to meet these performance goals.

The cooperative arrangement was that MDHS would, as applicant for Certification, retain design responsibility but that HDH would carry out the detail design to MDHS approved procedures. External loading was included in the detail design specification provided by MDHS.

In order to minimize certification and maintenance costs, it was agreed that a common system of materials would be used. This was particularly significant with respect to the composites selected. A common set of (composite) materials meant that testing could be shared and data pooled between the two companies.

FUSELAGE STRUCTURE

The MD Explorer fuselage shown in Figure 1 is a hybrid with carbon fiber epoxy composite selected for the external body shells and some internal structure such as floors, keels and fuel cell support structure. Aluminum alloy is used for the supporting framework of the shell and also on the transmission deck. These choices were made for the following reasons:

- The external shape was highly curved.
- The internal structure had many interfaces with systems under the design control of MDHS which were expected to be subjected to a high rate of change through the design process.
- The deck temperatures were too high for the composite material systems that were under consideration.
- Issues of survivability in the event of a crash landing dictated a metal frame to support the machinery above the cabin area.

The consequence of the first was that components, particularly in the cockpit area, were of extremely complex shape and presented design and manufacturing challenges. The door pillar for instance is a hollow section created by bonding two Z section moldings together with adhesive in a secondary operation. The final assembly has a developed length of around 8.2 feet or 2.5 meters and has severe twists and bends along its length. The mating halves need to match closely if the bonding is to be successful. This has presented significant challenges in the tool design and manufacture.

Secondary bonding is used in the construction of all the cockpit details and in some of the remaining shell structure. Early production models had tub shell assemblies that involved a secondary bonding operation for the longerons and a tertiary bonding operation for installation of the fuel cell support ribs. Later versions dropped the latter processes in favor of mechanical fasteners (blind rivets) which are also used to attach the composite shell to the aluminum substructure.

The composite structure was of both stiffened (solid) laminate and honeycomb cored design. Much of the stiffened laminate was designed in the highly post-buckled range with buckling ratios up to seven in some locations.

ROTOR SYSTEM

The rotor composite components shown in Figure 2 consist of five main rotor blades which utilize S-2 Glass/Epoxy, E-Glass/Epoxy, Nomex Honeycomb Core, Titanium and Nickel (abrasion strips) and Stainless Steel (bushings). The blades are manufactured in components using filament winding and hand lay-up, they are inspected and then co-bonded. The root end bushings are then secondarily bonded and then machined. The abrasion strips and trim tabs are then secondarily bonded.

The five flexbeams are manufactured using S-2 Glass/Epoxy, E-Glass/Epoxy and Stainless Steel Bushings. The processes are filament winding and hand lay-up. They are then assembled in a closed mold and co-cured. After trim and inspection some secondary bonding takes place.

The five pitchcases are made from IM-7 Carbon/Epoxy, 8 Harness Broadgoods/Epoxy and Titanium and Stainless Steel. The parts are manufactured on a split mandrel using filament winding and hand lay-up. They are then placed in a closed mold internally pressurized and autoclave cured.

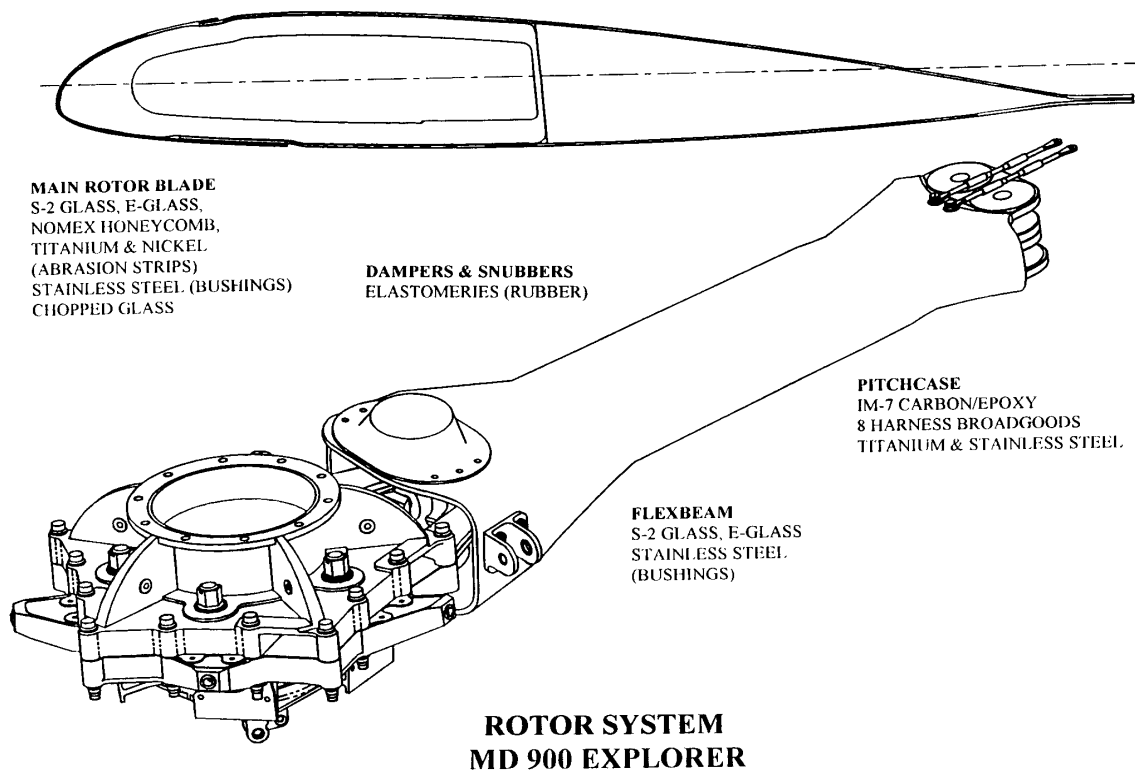
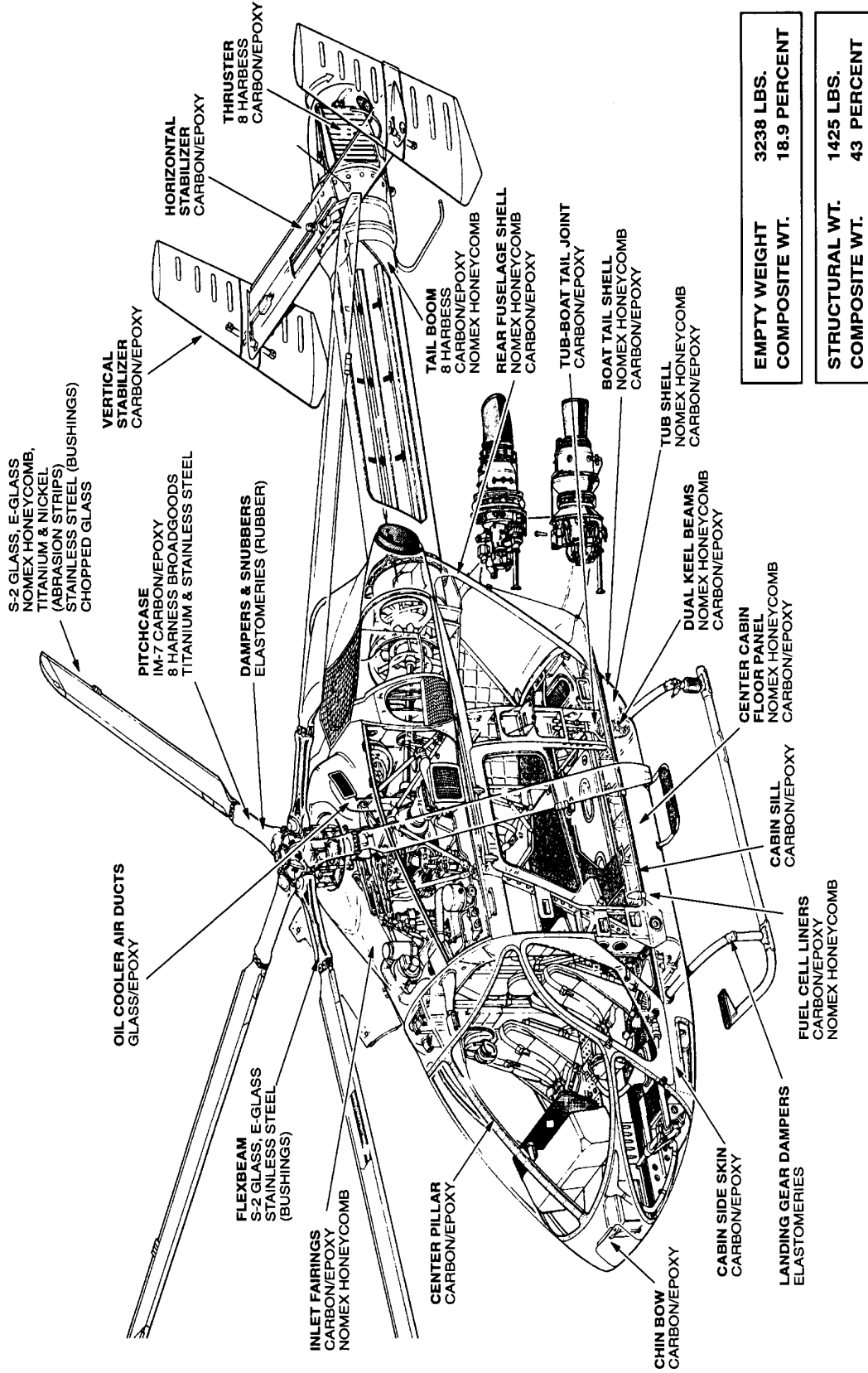


Figure 2

MD 900 EXPLORER



EMPTY WEIGHT	3238 LBS.
COMPOSITE WT.	18.9 PERCENT
STRUCTURAL WT.	1425 LBS.
COMPOSITE WT.	43 PERCENT

Figure 1

CERTIFICATION APPROACH

The certification basis was FAR 27 with AC20-107 (A) providing guidance in particular for the certification of the composite materials.

While composite rotor blades are quite common, the MD 900 is the first US certified helicopter to extensively employ composite materials in primary airframe structure. Specification documents for these new materials, and the processes for their fabrication were issued by MDHS after development with the HDH team.

The certification of materials, and components followed the now established “Building Block” approach, i.e. Materials and Process Qualification (coupon testing), Designallowables (coupon testing), Verification of Allowables (details testing), Sub-component and Full Scale Testing.

The design was certified by analysis and verified by test. This relies on using analyses to establish the critical loading cases and minimum margins of safety and by performing tests to establish (a) the accuracy of loading (Flight Testing) and (b) the adequacy of structural modeling and conformation of the failure modes (Structural Testing). An additional complexity that arises in the testing of hybrid structures at the full scale level occurs due to the fact that the reduction in composite materials performance under hot-wet environmental conditions is normally compensated for by enhancing (increasing) the test loads to be applied at room temperature. This has the affect of overloading the metal structure.

COMPOSITE MATERIAL - SELECTION AND TESTING

As mentioned, the cost of qualifying multiple materials on new aerospace projects is prohibitive and the approach on the Explorer was to choose a single resin system to be used in conjunction with several reinforcing materials from a single supplier. The resin selected was Hexcel's F584 epoxy resin available as a prepreg with T650 3k plain weave carbon and carbon tape, Kevlar 149, and 108, 120 and 181 style glass fiber.

The choice was based on cost and impact resistance (although damage tolerance rather than resistance turned out to be the key design parameter). While F584 is not strictly a toughened material, it does behave in a relatively non-brittle manner and gave significantly better impact resistance than the first generation materials in use at HDH on other programs at the time. A fully toughened system then being used on the Beechcraft Starship was considered but rejected due to its high cost.

Initially 250 °F oven curing systems were considered. However, the lower glass transition temperatures and consequently lower hot-wet properties together with the need to secondarily bond - also at 250°F - mitigated against their selection.

Also in its favor the F584 material has good tack and flow properties that help in processing. An additional factor in the selection was that the material was being considered by McDonnell Douglas Long Beach for the MD12 and subsequently qualified for the MD11. Significant cooperation was provided by Hexcel to the extent of their assisting with the provision of materials and manufacture of test coupons as well as technical support.

The specification written required that the material achieve defined mechanical properties at room temperature, cold-dry and hot-wet conditions. This was somewhat unusual in 1989 but is standard practice today. To qualify the specification, three batches of material were used to manufacture coupons (at MDHS, Hexcel and HDH). Tests were designed to sufficiently characterize the material such that should an alternative be introduced during production, then only these tests would require repeating rather than all the subsequent coupon and component testing. Material Qualification tests were performed on laminate specimens, the former to fix the elastic constants and the latter to provide initial failure strains. This testing gave early warning that the compression after impact property would be the minimum design value.

Design allowables testing was subsequently carried out also by both companies. MDHS carried out coupon testing using the angle minus loaded ply (AML) approach while HDH tested design specific laminates. Table 1 shows the total amount of coupon testing conducted for both material qualification and design allowables. Much of the HDH testing was concerned with the effect of manufacturing flaws in the laminates. This was necessary in order to validate the Non-Destructive Inspection (NDI) acceptance criteria. The flaws were simulated with teflon inserts placed in the laminate during fabrication. Discs of various diameters representing flaws both above and below the threshold of detectability were located in the critical test section of each coupon.

Location	Material	Test Type	Number of Specimens
MDHS	Carbon/Epoxy	Qualification Static	666
	Aramid/Epoxy	Qualification Static	222
	Repair Resin	Qualification Static	251
	Syntactic Foam	Qualification Static	21
	Adhesive Creep	Qualification Static	54
	Carbon/Epoxy	Allowables Static & Fatigue	1170
	Carbon/Epoxy	Qualification Static	612
HDH	Aramid/Epoxy	Qualification Static	195
	Carbon/Epoxy	Allowables Static & Fatigue	719
	Film Adhesive	Allowables Static	95
	Paste Adhesive	Allowables Static	96
	Fasteners	Allowables Static	22
		TOTAL	4123

Table 1 Composite Coupon Tests

The conclusions from the design allowables testing were as follows: From the static tests on the solid laminates at HDH the central hole specimens were more critical than either the central or the edge-flawed specimens at Room Temperature Dry (RTD) conditions. However, the open edge flaws were more critical after exposure to elevated temperature and moisture.

The knockdown factor for the central hole stress raiser was around 40% and 50% while the knockdown factor for environmental soaking was between 25% and 50%. The testing showed that the worst case B Base design value was greater than the initial design value chosen from the results of the laminate tests under the Material Qualification Program. When compared with the (AML) data generated at MDHS for open hole specimens the HDH point

design laminate had higher average and B Base reduced values. From the cyclic fatigue tests at HDH: At Room Temperature / Ambient (RTA) (ambient temperature and humidity), the endurance limit of the (flawed) specimens was greater than 60% of the ultimate failure load (which in turn was greater than the design value strain, see above). At elevated temperature Hot Temperature Wet (HTW) the endurance limit was more than 30% greater than the design limit strain. All cycle testing was carried out with a load range $R=0.5$.

From the testing on sandwich panels, it was shown that static failure strains were again higher than the design values and the fatigue is not a design consideration for this construction. Similarly comforting results were obtained from the testing of joints in which the composite elements consistently outperformed the metallic elements. In support of the Design Allowables testing described above, a number of detail design elements were tested in order to confirm that design values from coupon testing could be applied to component details. This included compression testing of stiffener sections, impact testing of sandwiched and stiffened panels, shear and compression testing on stiffened panels in damaged state and after repair, and fastener tests in composite laminates. The last mentioned was performed in answer to questions raised on the use of locked spindle blind fasteners in composite material. The small head and tail profiles were thought likely to pull through under loading. However, this was not found by the testing.

Since carbon is only a moderate conductor of electricity there is a need to provide shielding against both lightning strike and radio magnetic interference to on-board avionics equipment. This was affected by an expanded aluminum mesh co-cured over the outer carbon fiber ply of the tub and aft fuselage sections. The same protection system was employed at MDHS for the main rotor blades, pitchcase, tailboom and empennage assemblies. Testing was conducted at Lightning Technologies Inc. in the USA on panels fabricated by HDH. The results showed that lightning damage was less catastrophic to the (protected) composite surface than to similar gage aluminum alloy sheet.

The majority of the full scale testing was carried out at MDHS. HDH carried out a number of static and fatigue tests on representative sections and joints within the fuselage and also on the cabin floor. Three full scale fuselages were delivered to MDHS for structural testing two for static tests (pre-production and production versions) and one for fatigue. In addition a number of roof structures were provided; four of these were fatigue tested while one was used for static testing.

CONCLUSIONS

The test program was highly successful and validated a conservative but still light weight design. Only two small beef-up modifications to HDH delivered components were shown necessary by the static testing, only one of these to a composite part. No premature failures have been reported from the fatigue testing.

REFERENCES

1. Christ, Richard A., "Certification Testing of a Hybrid Helicopter Airframe", presented at the American Helicopter Society 52nd Annual Forum, Washington, D.C. June 4-6, 1996.
2. FAA Advisory Circular AC 20-107A, "Composite Aircraft Structure", dated April 25, 1984.

3. Federal Aviation Regulation Part 27, “Airworthiness Standards: Normal Category Rotorcraft, Change 21”, effective April 5, 1995.

TECH TRANSFER MECHANISMS FOR COMPOSITE MANUFACTURING FROM UNIVERSITIES TO INDUSTRY - A SURVEY OF SUCCESSFUL MODELS

Michael J. Martin

Virginia Tech Intellectual Properties, Inc., 1900 Kraft Dr., Blacksburg, VA 24060

SUMMARY: There has been a significant investment in Universities for research into advanced materials synthesis, design and processing. What has been lacking has been an efficient system to commercialize the results of this research funding. Technology transfer is more than licensing or turning over information, especially for composites. This paper will present successful case histories.

Technology development and transfer, as it is more broadly practiced, is a process.... a process of establishing relationships along the development cycle. In order to consider the adoption of technology development process as an operating strategy for technology transfer, any organization - university, business - requires: an ability to characterize the development cycle and define its role in a success; a team based management style based on trust; and an ability to integrate the "voice of the customer" in setting operating priorities.

KEYWORDS: technology transfer, knowledge-based economy, research organizations

UNIVERSITY - INDUSTRY TECHNOLOGY TRANSFER PROCESS

Product Development Cycle

A successful product development process is characterized by an understanding of the research and development process; and a reorganization to meet the needs of an information based economy.

Commercialization pathways for basic research in the United States vary in their design and in their success. The majority of \$250 billion spent on research and development, some estimate 85-90% of the R&D budget, is applied to solving problems with existing products [1]. Most of the estimated 10-15 % left for basic discovery research is spent at Universities and US Federal Labs. The Industrial share of basic research is less than 20 % of the Federal budget. This varies by technology - from 20% for biotechnology to 10% for composites.

The investment from the Federal Government has resulted in the creation of the largest research engine in the world. However, in the last decade it became evident that the US lacked a transmission for this engine - an innovation transmission. The US lacked an efficient mechanism to transfer the basic research results from the university and federal labs. One study found that companies in Japan and the United States are roughly equally fast to market with internally generated ideas, but Japanese companies are almost twice as fast to market with externally generated ideas--U.S. companies much slower [2].

Eventhough the US had the competitive advantage of the enormous basic research capacity, basic discoveries are a long way from commercialization. The risk capital required for commercialization is 10 to 100 times that required for the basic concept development. In a study for a Consumer Products Company by Battelle, they found that it took \$5.7 million to recover the cost of developing the wining idea plus another \$9.3 million for culling out losing ideas along the way [3].

It takes 7 to 10 years for the innovation process to translate a basic research discovery into a set of commercial products that then create sales and profits. Every organization in the technology transfer process should understand how research projects are initiated, continued, killed, or commercialized. Most U.S. companies organize the commercial development process either as:

- the "build a better mousetrap" approach - which assumes the customer will buy the improved mousetrap if it is priced right, even if there is no need; or the "flash of genius"; or
- "another Xerox" approach - which assumes a unique individual will discover a solution that overwhelms or creates a market, ignoring the cost of supporting the genius until a discovery is generated [4].

Projects are demanded by the marketing organization and handed to the customer with little or no involvement. Research agenda are reactive to production problems or competition.

Most university research agendas are set by individual faculty who investigate problems either based on curiosity or potential for peer recognition. The federal laboratories have their research agenda defined by the strategic defense of the nation, potential for peer recognition, or by legislative edict.

Figure 1 characterizes the traditional commercialization process as a "funnel". New concepts are generated by basic research centers; transferred to the applied development centers using publications; where, possibly, investment is made to generate prototypes and consequently products. The "funnel" becomes narrower closer to the market place, as concepts are filtered out according to various sets of criteria - mostly financial [5].

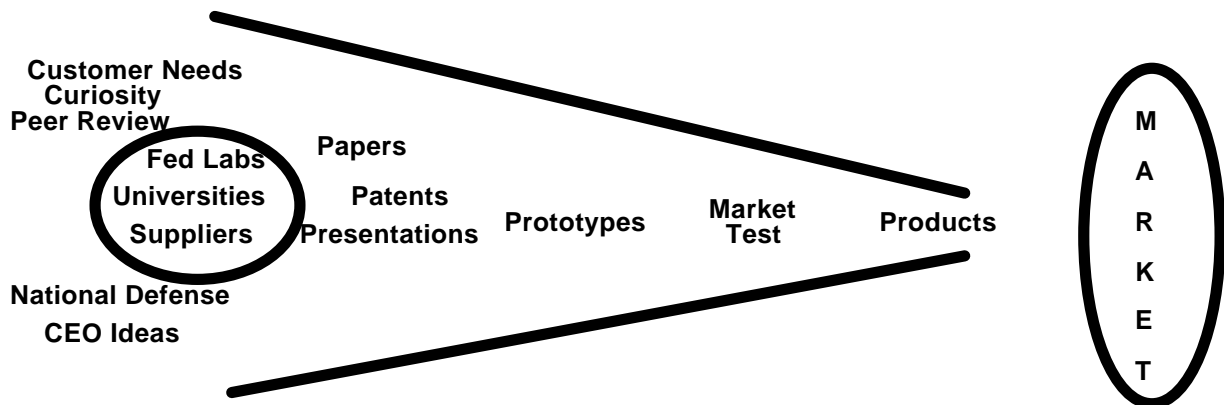


Figure 1. Development Cycle

The other factor mentioned for the relative lack of success in the innovation is the inability of traditional organizations to modify themselves for the new "knowledge based" economy, applying old hierarchical structures used in commodity based economies. There are two

distinct types of "industry" - commodity-based and information /knowledge based. Manufacturing is now uncoupled from labor and non renewable resources. From 1973 to 1985 manufacturing increased 40% in production, and did so with five million fewer people. It is forecasted that by the year 2010, only 10% of the labor force will be involved in manufacturing, which is a potential loss of six million jobs. Manufacturers are substituting knowledge and capital for labor.

In some industries, the largest contributor to cost now is overhead. The engineering or knowledge content of products is uncoupling manufacturing from scarce resources. Today 50 pounds of fiber optics carry more information than one ton of copper wire, and require one tenth of the energy to produce. Semiconductor chips only require 12% labor, but 70% knowledge; and in pharmaceutical, there is only 15% labor, and 50% knowledge content [6].

In traditional organizations, the market or customers do not have much input on the research agenda or the criteria used to screen projects as they move through the "funnel". Most developmental dollars are spent at the end of a project - right before commercialization or after the first order, the best chance to correct earlier "misunderstandings" - not at the beginning where it would have the most value. It is difficult to justify expenditures of today's cash on tomorrow's market promises and a preliminary understanding of the technical barriers, the scientist and the business manager need to develop a market-driven screening method. Preferably one that combines qualitative measurements of the potential technical and commercial difficulties; with the forecasted quantitative costs of development and the return on that investment.

The "New" Knowledge-Based Development Organizations

A number of organizations, both businesses and universities, are now in a period of transition where they are attempting to learn how to implement a market driven research agenda even at the basic discovery level and then to expedite the knowledge transfer process to become "fast to market". The first step for any organization to seek the "voice of the customer" is to realize that that the basic processes of businesses have changed. Now it is mass customization, knowledge based products, activity based costing, and the virtual corporation. The "new" organization needs to define who the "customers" are and what are their expectations. Finally, these "new" organizations determine if the existing organizational structure needs to be thrown out, modified, or optimized.

Most existing development organizations are organized around a hierarchical structure that started thousands of years ago in the Chinese Empire and, was improved by the Romans. In those days, information transition was measured in months, and could be easily compartmentalized. Hierarchy established power by controlling access [7]. Now, with local area networks, electronic mail, computer data bases, and CNN, every employee has as much information as the CEO. "Global" organizations utilize their ability to move information across national boundaries, and then modify it locally to implement a regional development strategy. The role/paradigm of management has changed from information channlers and samplers of work to facilitators - leaders that define the vision and then get out of the way.

The competitive battles looming ahead will be based upon speed - "fast to market" - and expanding the corporate imagination - developing new markets that do not exist today. "Fast to market" companies are aware of the latest technologies. They willing to risk development capital based on preliminary justification developed in a team environment [8]. "Fast to

market" organizations expand the "funnel" - expand the corporate imagination - with a "window" on technology. A "window" on technology should be able to scan the basic scientific work at University Laboratories to screen technology opportunities at the concept or proof of concept stage. These organizations ask of the results of basic research are: *derivative* - problem solving for existing products or processes; or, *platform* - involve significant product/process changes but not with new technologies; or *breakthrough* - establishment of new core products or processes often defining new markets by their creation. "Fast to market" organizations are new but have demonstrated real value. AT&T reduced the design cycle for its 4200 cordless phone from two years to one year. They achieved: lower costs, higher quality, and one additional year of sales income [9].

“New” University Organizations

Universities are reorganizing their Technology Transfer/Commercialization functions to recognize the value of industrial collaboration and their role in the national economic development policy. More than 100 U.S. Universities have started financing new companies to commercialize faculty discoveries and to promote regional economic development. In 1985, MIT began to target small growth business for licensing of University technology. Now over 60% of their license agreements are with small companies, and eight percent are with new companies created around the technology. Patent applications have doubled because of these efforts, and it has had a profound effect on the state economy. The Bank of Boston has estimated that 636 business started by MIT Alumni and faculty have generated more than 300,000 jobs in the state of Massachusetts and at least \$10 billion in annual income [10].

The United States university intellectual property market, as reported by the Association of University Technology Managers, increased to \$422 million in FY 1994, an 11% increase over FY 1993. This is double what was received in FY 1991. The number of licenses increased to 2,484 in FY 1994, a 63% increase in activity since FY 1991. Universities are becoming more aggressive in their marketing efforts. They are hiring more personnel -- the number of advertised positions for tech transfer associates has increased 50% in the last two years. Universities are actively seeking industrial partners.

Industry is also actively seeking university technology. However, each participant in the market must deal with the reality of different cultures but similar pressures: changing funding, aging demographics, hierarchy moving to team based organizations, and global competitors. Universities and industry do view the world differently. Each has a different reward system; set research priorities according to different criteria; and even have a different measure of time as shown in the following matrix.

	University View	Industry View
Rewards	Grad. Students, Facilities, Salary, Peer Recognition	Profit, Bonuses, Standard of Living
Research Priorities	Peers, Curiosity	Market, Executives
Values	Freedom, Collaboration, Openness	Independence, Competition, Risk Reduction
Time	Semesters, Ph.D. Cycle	Weeks, Annual

The barriers to collaboration or licensing from a university that companies mention most often are:

- Lack of understanding by the faculty of the value of protecting technology.
- Most faculty know-how is difficult to access. Written records can be faulty or missing.
- Technology is overvalued by faculty, especially for early stage discoveries.
- University administration focused on the deal, not the relationship.

Lack of a realistic appraisal of time, facilities, and capital required for commercialization.

The cooperation that other global competitors enjoyed with their governments and universities prompted the establishment of a number of opportunities for partnership at the basic and applied research level. Significant government actions include:

- National Cooperative Research and Development Act of 1984, allows firms to jointly fund and/or conduct "pre-competitive" research. For example, the Automotive Composite Consortium (ACC) was formed by Chrysler, Ford, and General Motors to develop large structural polymer composite parts at high production rates.
- Federal Centers of Excellence, now NSF and Department of Defense research center funding requires technology transfer, especially small businesses. Two examples are the S/I/U/CRC Low Cost, High Speed Composite Processing Center at Michigan State University and the NSF Science and Technology Center on High Performance Polymeric Adhesives and Composites at Virginia Tech.

COMPOSITES DEVELOPMENT ORGANIZATIONS

Commercial Composite Development

The materials industry development structure, which is the basis of the composites industry, has some characteristics which are a combination of history and the capital requirement for production. When new materials are synthesized either at a University research center or in a corporate lab, they must be mixed with additives to make them useful for the targeted applications. The composites industry is structured into:

1. Basic Materials Suppliers - Large Chemical companies that synthesize and or polymerize materials; for the
2. Compounders or Formulators - Combination of small and large companies that blend materials to meet specific market needs; from the
3. End users - Combination of small and large companies that design, fabricate and or add value to manufactured parts with advanced materials.

A number of composites end users are entering into new collaborations because the traditional approaches have not generated the necessary goals of low cost parts with high structural performance. Composites have always been attractive to the aerospace industry because of their weight to performance ratio to metals. The US government and the commercial aircraft industry have invested significant moneys to realize these properties but growth has been limited because of cost. Some aerospace company have invested in alternative organizations to combine their knowledge of high performance with Automotive knowledge of low cost commercial manufacturing techniques. As an example, Northrop Grumman acquired Ticom,

a directed preform and custom molding automotive RTM parts manufacturer, and became a prime contractor for the Advance Technology Transit Bus Project. Both have provided new technology for the core businesses to utilize at a lower costs and in less time to transfer the knowledge as depicted in figure 2 [11]

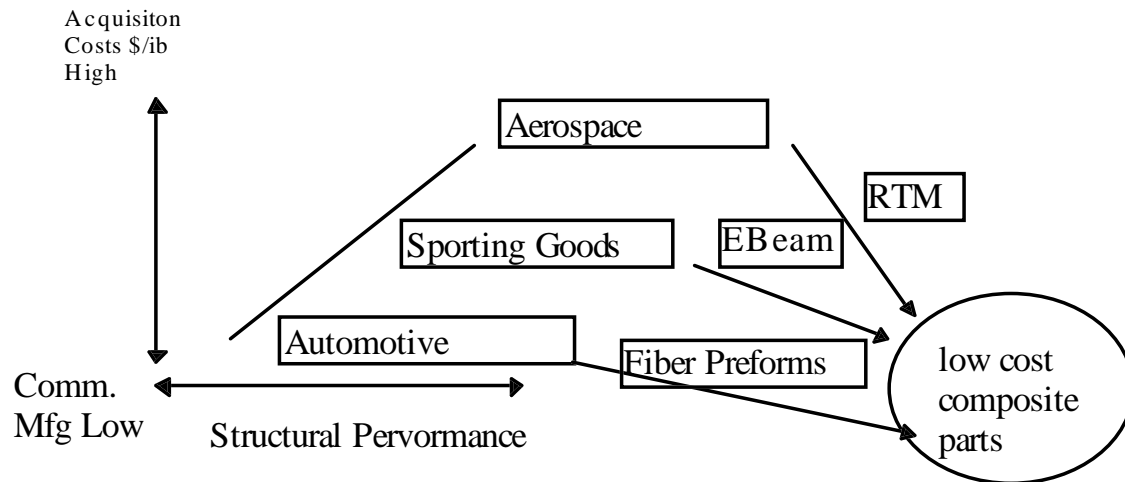


Fig 2. Goal of Composites Research Programs

University Composites Development

Industry involvement in Composites research at Universities occurs in three levels: 1) - industry affiliate; 2) - Industrial/Government Consortium; and 3) - Industry Advisory Board at a Engineering Research Center or Science and Technology Center. Typically in an industrial affiliate program, a firm joins for a set fee and then is granted a variety of rights, ranging from: newsletters, to regular research review meetings, to access to professors for consulting and students for hiring; to review of research proposals; to advising on research agenda, to intellectual property. MIT has approximately 11 industrial affiliates programs with 1 in the materials area. Eight companies are in the Materials Affiliates program and they review research proposals. Stanford has 34 industrial programs with one in the materials area. 15 companies are in the materials industrial affiliation and they attend one annual two meeting.

NSF currently supports 18 Engineering Research Centers, 52 Industry University Cooperative Research Centers, and 10 recently developed State Industry University Cooperative Research Centers. The idea was to increase the level of cooperation between industry and the university by leveraging State and Federal money with industry and with that commitment gain direct involvement.

An example of University/Industry interaction is the work of Dr. Ken Reifsnider - Alexander Giacco Professor of Engineering Science and Mechanics; Director, Center for Composite Materials and Structures; and Director, Virginia Commonwealth Center for Material Systems. Dr. Reifsnider is originator of the MRLife performance simulation code for the prediction of remaining strength and life. That code has been used by many major industries to estimate the durability and damage tolerance of composite materials and structures, especially under complex loading and environmental conditions such as high temperature service in aggressive

environments. The code is being integrated into the design codes of industries, including Babcock and Wilcox, General Electric, United Technologies, and others.

This work has also resulted in the spin off of Durability, Inc. This small business, located in the Corporate Research Park at Virginia Tech, provides material characterization, design, and analysis of composite material systems. Corporations can choose where it is most efficient to conduct life cycle research for composites. Either on the university campus as part of the MRLife consortium or off campus in a small business. The university and the Commonwealth of Virginia win in either instance. If the company elects to fund the work on campus then additional basic research is conducted and the education of graduate students is funded who can become future employees. If the work is funded at Durability, the class room of Dr. Reifsnider is enriched with real world experience, plus employment opportunities are created for graduates of Virginia Tech.

Virginia Tech Intellectual Properties, Inc. - "New" Development Organization for Composites

Traditional technology transfer is based on the belief that a University exists only to educate students; obtain research grants; and to publish papers. Therefore, patents are a hindrance and research funding by industry is a defacto conflict of interest. Traditional technology transfer consists of:

- Faculty develop areas of expertise based on obtaining federal funds in a competitive proposal process where the research agenda is established in a review by their peers.
- Commercial interests will read peer reviewed articles and identify the "best" science to fund to continue development, as long as it does not become too applied, and will then pay the University a license to practice the patents.
- Administration will periodically publish a list of patents or technologies under development, and commercial interests will contact them to negotiate a license

Virginia Tech Intellectual Properties, Inc. (VTIP) was formed in 1985 to identify, legally protect, and market intellectual properties resulting from research at Virginia Tech which have the potential of becoming commercially attractive technology. VTIP was also charged with being financially self-sufficient after sharing royalties with the inventors according to the University's Intellectual Property Policy. After a decade of success, VTIP is growing and changing to ensure further successes, adopting a more proactive effort to generate opportunities for license negotiations and income. VTIP brings some unique competitive advantages to this market.

1. *Equity in Lieu of License Fee and/or Patent Expense.* All start-ups have one thing in common. They don't have enough cash. VTIP has directly taken equity in lieu of license fees and/or patent expenses in three firms and indirectly in three more firms. One has gone public and another is on track with a second round of financing.
2. *Incubation of For-profit Subsidiary.* VTLS was a for profit subsidiary of VTIP that to commercialized a software technology. VTIP brought access to the technology and provided a financial umbrella. The inventor brought an existing customer base and a will to win. The exit scenario was a management buyout with an IRR of 25% to VTIP.
3. *Investment in Seed Venture Capital.* The probability of institutional investment is inversely proportional to the distance that the fund managing partner must travel. VTIP

along with the Virginia Tech Foundation, has invested in Zero Stage, Triad/University Partners, InterSouth, and SpaceVest. These investments in seed venture capital provide excellent opportunities for Virginia Tech start-ups to present their business plans.

4. *Investment in "Bridge Funding"*. VTIP, along with Johns Hopkins and some private investors, funded Triad which invests in early stage technologies. Technologies that have significant potential but are too early stage to attract commercial interest. An example is the work of Dr. Judy Riffle and Dr. Jack Lesko - "Thermoplastic Sizing for Carbon Fiber Composites". Dr. Riffle and Dr. Lesko have developed various sizings for carbon fiber reinforced composites with vinyl ester matrices. These composites offer cost advantages relative to epoxy matrices as well as better environmental stability. But in which part of the materials developmental chain should it be licensed in order to attract the risk capital for development - the fiber company, or the resin company, or the compounder, or the parts fabricator. Triad provided the risk capital to further development. Now patents are being prosecuted and licensees are being sought.

RECOMMENDATIONS

Additional development capacity for the university can be gained through strategic alliances, partnerships, joint ventures and consortiums with other research centers. Once the mission of the various research partners is defined, then the appropriate technology development organization can be implemented to achieve its unique growth plan. The strategic direction will define the effective research mix for the resources available and will determine the need for leverage for partnerships. It will also be the first screen for new ideas. Technology Development and Transfer is not a threat to intellectual freedom; but a catalyst for a university to recognize its total contribution to the creation of wealth in a state economy. Faculty would increase their choices for implementation of their discoveries and would identify new colleges that had not been available to them. New technology transfer mechanisms from the largest research engine in the world provide significant opportunities for U.S. businesses to "leap frog" their global competitors.

REFERENCES

1. Merrified, D., *Creative Destruction in the New Millennium*, Pridco Management Corp., October, 1996.
2. Mansfield, B., *Industrial Innovation in Japan and the United States*, "Science 30 Sept. 1989, pp. 1769-1774.
3. Razgaltis, R., *Commercialization of Early Stage Technologies: Case Histories and Lessons Learned*", Presentation to Association of University Technology Managers, February 15, 1993
4. Bacon, F., Butler, T., *Planned Innovation*, University of Michigan, 1981.
5. Clark, K., "Product Development in the World Auto Industry", University of Michigan International Automation Industry Conference, 1989.

6. Drucker, R. F., "The Changed World Economy", Foreign Affairs, Vol. 64, No. 4, 1986, pp. 768-792.
7. Peters, T., "The Destruction of Hierarchy", Industry Week, August 15, 1988, pg. 33-35
8. Hamel, G., Prahalad, C., "Corporate Imagination and New Competitive Space", Harvard Business Review, 1991.
9. Dumaine, B. "How Managers Can Succeed through Speed", Fortune, February 14, 1989.
10. Gupta, U., "Turning University Research into a Profitable Business", Wall Street Journal, June 12, 1990.
11. "Northrop Grumman Perspective: Nontraditional Applications of Aerospace Technologies", Society of Manufacturing Engineers, January 30, 1995.

DAMAGE TOLERANCE OF COMPOSITE AIRCRAFT STRUCTURES: ANALYSIS AND CERTIFICATION

Peter Shyprykevich

FAA William J. Hughes Technical Center Atlantic City Int'l. Airport, NJ 08405, USA

SUMMARY: The capability of current analytical methods based on stress and/or fracture mechanics principles, is reviewed with the objective of establishing whether the technology is sufficiently mature to be able to satisfy damage tolerance requirements of composite aircraft structure by analysis with some testing. In other words is it possible to establish initial delamination requirements in critical areas of the structure and then by analysis show that the structure is fail-safe - analogous to the assumed initial crack size in metals. Examples of usage of analytical methods in the design process are identified. Perceived barriers to the widespread use of these analysis methods in design and certification are also discussed. These include computational complexity, lack of standards for determination of material fracture properties, large amount of testing to obtain needed material constants and properties, and lack of independent verification test data.

KEYWORDS: damage tolerance, delamination initiation, impact damage modeling, crack tip element, fracture mechanics material properties, delamination buckling

INTRODUCTION

Damage tolerance of civil aircraft composite parts is addressed by requiring ultimate load strength capability in the presence of barely visible damage (BVID), limit load capability with visible damage, and a specified load below limit load with discrete source damage (DSD). This is illustrated in Fig. 1 by a plot of the required residual strength capability versus damage size. Three distinct damage zones are shown, each defined by specific regulation: Federal Aviation Regulation (FAR) 25.305 for ultimate load in the presence of BVID, FAR 25.571(b) for allowable damage limit, and FAR 25.571(e) for DSD. The two larger damages must be repaired and the structure restored to ultimate load capability at the next scheduled maintenance activity or in the case of DSD at the next airport stop. The admissible damage sizes that set ultimate, limit, and ferry flight loads are tied to damage detectability, see Fig 1. Thus the structure must be capable of sustaining ultimate load with undetectable damage, limit load with detectable damage, and ferry flight load with immediately obvious damage (to the pilot). The damage size at limit load is set at the boundary between detectable and readily detectable damage size, with the expectation that the aircraft will not be flying understrength for a long period of time.

The certification requirements outlined above are usually complied with by test. Elements, components, or full-scale structure containing damage induced by impact or Teflon inserts are tested to demonstrate ultimate or limit load capability for static and after fatigue loading. Usually no analysis is performed to show that the residual strength is adequate and that the

damage or delamination will not grow in service. As new analytical methods of strength and life predictions of damaged composite structure are being developed there is a need to integrate this technology into the certification process. Likewise, the developing American Society for Testing and Materials (ASTM) methods for characterization of fracture properties being established concurrently must be integrated with analysis and certification requirements.

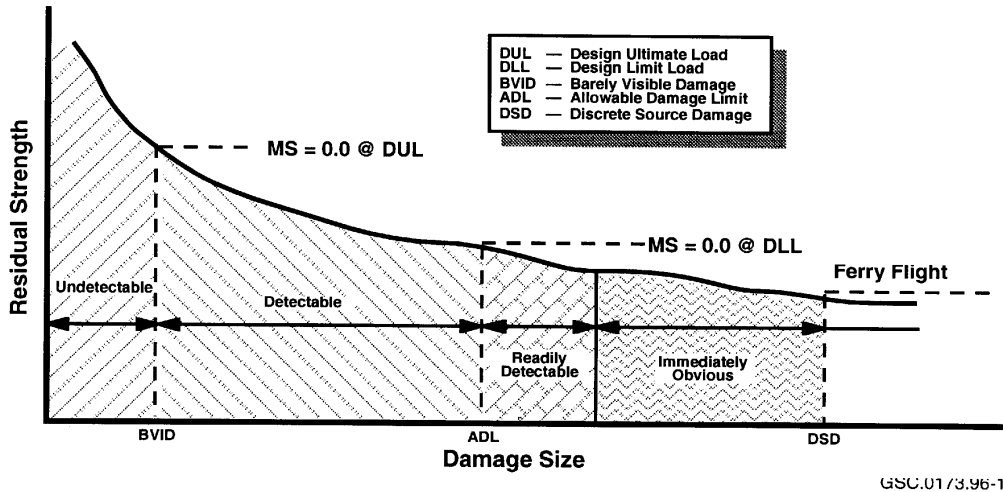


Fig. 1: Allowable damage sizes

In this paper, the capability of current analytical methods, some developed under Federal Aviation Administration (FAA) sponsorship, and the test methods for material property determination are reviewed with the objective of establishing whether the technology is sufficiently mature to be able to satisfy damage tolerance requirements by analysis with some testing. In other words is it possible to establish initial delamination requirements in critical areas of of the structure and then by analysis show that the structure is fail safe - analogous to the assumed initial crack size in metals. Examples of usage of analytical methods in the actual design or repair process are also identified.

ANALYTICAL MODELING

For the analytical methods to have wide application they must be capable of computing stresses, strains, and strain-energy-release rates for a variety of problems common in composite airframe construction. Figure 2 identifies some locations where delaminations can be deleterious to structural integrity. These are either locations where high interlaminar stresses exist and delaminations can form (free edges, bonded joints, ply drop-offs, curved parts) or in the case of compression or shear loading pre-existing delaminations have a propensity to grow. In addition to modeling delaminations at diverse locations, the analysis should be capable of treating impact damage.

Detailed Finite Element Analysis (FEA) is capable of obtaining solutions to the problems posed in Fig. 2, but, because of many locations to be analyzed this quickly becomes impractical. FEA, however, is a useful tool to treat specialized problems and is used extensively as a check solution. To reduce the analysis complexity other methods have been developed to solve some of the cases shown in Fig. 2. These methods are based on (1) stress

analysis where computed stresses are compared to interlaminar material strengths, (2) stress analysis with empirical reduction of properties in the damage area, (3) sublaminates delamination buckling followed by fracture mechanics considerations, and (4) rigorous fracture mechanics with fracture mode decomposition.

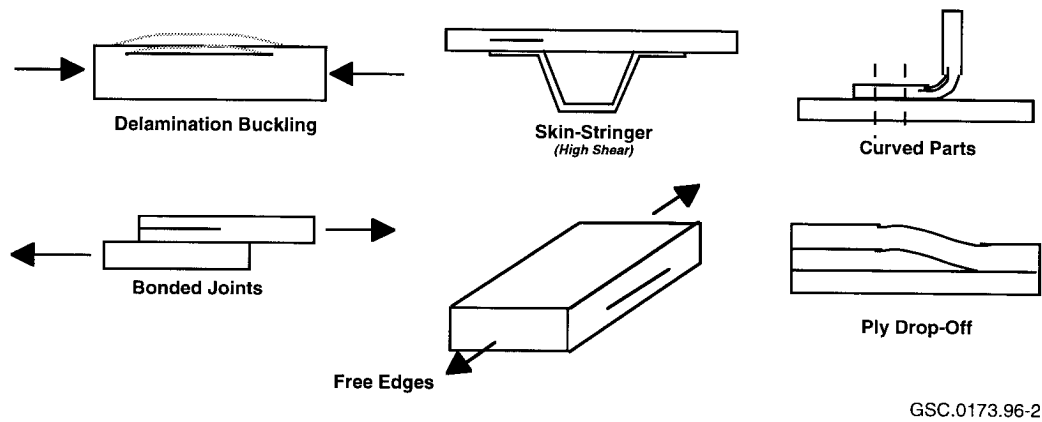


Fig. 2: Critical locations of delaminations

Although stress analyses by themselves are not capable to model structural details containing a delamination, they are useful in locating high interlaminar stress areas before proceeding to a fracture mechanics analysis. Thus the availability of specialized program that can provide a quick assessment where the critical delaminations should be considered for a damage tolerance analysis is almost a pre-requisite. This will reduce the number of critical locations to manageable numbers. In Ref. 1, the following interlaminar or out-of-plane problems are addressed: (1) induced stresses in laminate corner radii, (2) induced stresses due to ply drop-off, (3) induced stresses due to panel buckling, (4) direct stresses due to fuel pressure loads, and (5) induced stresses due to stiffener runouts. The last problem was also addressed in [2]. In [1], an analysis method has been developed for each problem above together with companion software, and as these methods have been developed under FAA and U.S. Navy sponsorship they are available to the industry, at least in the United States. Free edge problem, see Fig. 2, is not addressed in [1], but there are many solutions available in the literature, [3] and [4] being representative.

Analytical prediction of the residual strength of a composite structure damaged by impact can be separated into two types of analysis. The first type should have the ability to characterize damage knowing impact parameters such as velocity, mass, shape of impactor, and the stiffness properties of the structure in question including support conditions. The second type of analysis would use the damage information from the first analysis to compute residual strength or damage growth. As at this time there is no widely accepted method to characterize damage analytically, the recourse has been to use stiffness reduction techniques to model the damage with the amount of reduction based on correlation with test data. In one such semi-empirical model [5], the degree of stiffness reduction is assumed to depend on the impact energy and the material system. The parameters considered are laminate lay-up, laminate thickness, material toughness, support conditions, and impactor size and geometry. Although this model is available to the industry there is a general lack of acceptance primarily due to the large amount of test data required to establish empirical constants. For example, description of the impact parameter requires five constants.

Solutions to the delamination buckling problem illustrated in Fig. 2 were developed in [6,7] under FAA and Navy sponsorship. Both are closed form solutions based on energy methods

but use different functions to model the displacement of the buckled portion of the laminate. Both solutions assume the unbuckled region does not displace and hence the formulation breaks down for thin laminates or for midplane delaminations. The solution first determines the buckling load for the thinner sublaminates and then proceeds to grow the delamination according to whether the critical total strain energy release rate has been exceeded. Failure is defined as initiation of delamination growth. The problem that is solved is an embedded elliptical delamination shown in Fig. 3. The permissible loading in [6] is axial load and bending moment in one direction, see Fig. 3. Reference 7 admits bi-axial loads, but no moments. Reference 6 also allows variable boundary conditions for the local buckle ranging from fully fixed to simple supports which is controlled in the computer program by a fixity factor coefficient, γ , ranging from 0 to 1. This factor can be used as a correlation factor between analysis and test. Figure 4 shows a comparison of test data and analysis results using [6] for a compression loaded 24 ply specimen with three different delamination configurations. Specimen DSC2 had a 50.8 mm (2 in.) diameter delamination embedded four plies deep from one surface; specimen DSM1 had an additional identical delamination embedded four plies deep from the opposite surface; specimen DSM2 was identical to DSM1 with a third 50.8 mm (2 in.) diameter delamination embedded at the specimen midplane. In the analysis the near surface delamination controls the failure and hence the prediction is the same for all three specimen types. The prediction is within 3% for DSC2 and DSM1 specimens as compared to test data using $\gamma = 0.33$. For specimen DSM2 better correlation was obtained by increasing the fixity coefficient to $\gamma = 0.7$ (closer to simple supports) to more realistically reflect the degraded stiffness of the inner portion of the laminate.

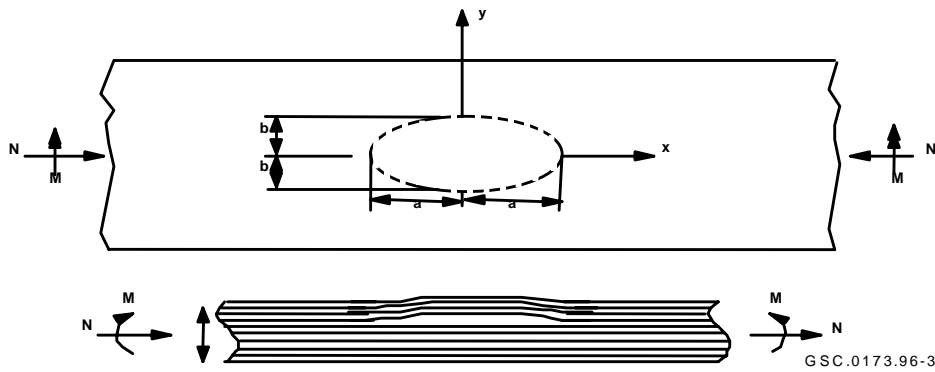


Fig. 3: Laminate with an elliptical delamination

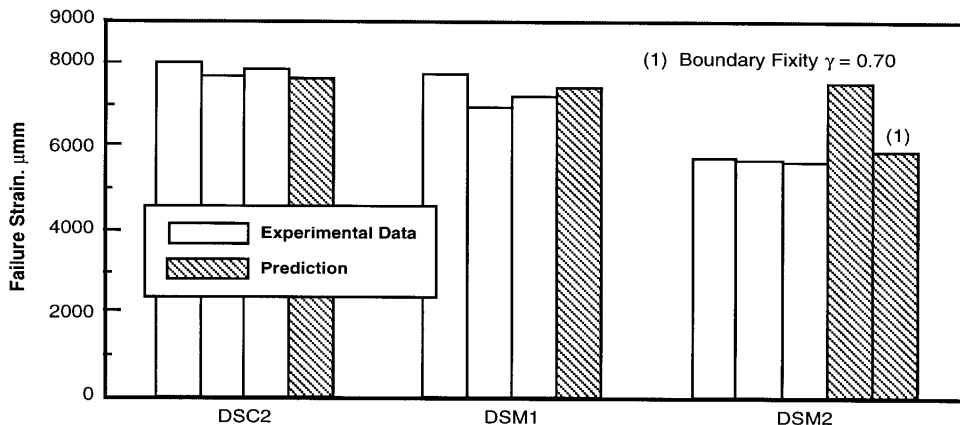


Fig. 4: Comparison of observed and predicted failure strain of a 24-ply laminate with multiple delaminations

Reference 7 also employs an empirical factor, a knockdown of the buckled sublaminates' bending stiffness [D] matrix, β , which is being used to expand the delamination buckling program to model impact damage. This adjustment is guided by the observation that after an impact event many delaminations exist across the thickness. By interrogating every interface of the laminate, selecting the most critical one, and selecting β , a prediction of compression strength after an impact can be made by the software of [7]. Figures 5 and 6 from [7] show the degree of correlation for brittle and toughened resin materials that can be obtained. The predictions, made with $\beta = 0.5$, are good, particularly for the stiffer laminate. It should be noted that these predictions were made for fairly thick laminates; for thinner laminates this method may be unconservative. It should be noted that thinner laminates may have penetration damage with attendant fiber breakage as a result of impact damage and hence the assumption that delaminations control residual strength may not be applicable. The use of the delamination buckling formulation to model impact damage may be the only practical application of this formulation as a single delamination in a laminate, unless it is large, is not critical in compression loaded structure when compared to strength reductions due to notches.

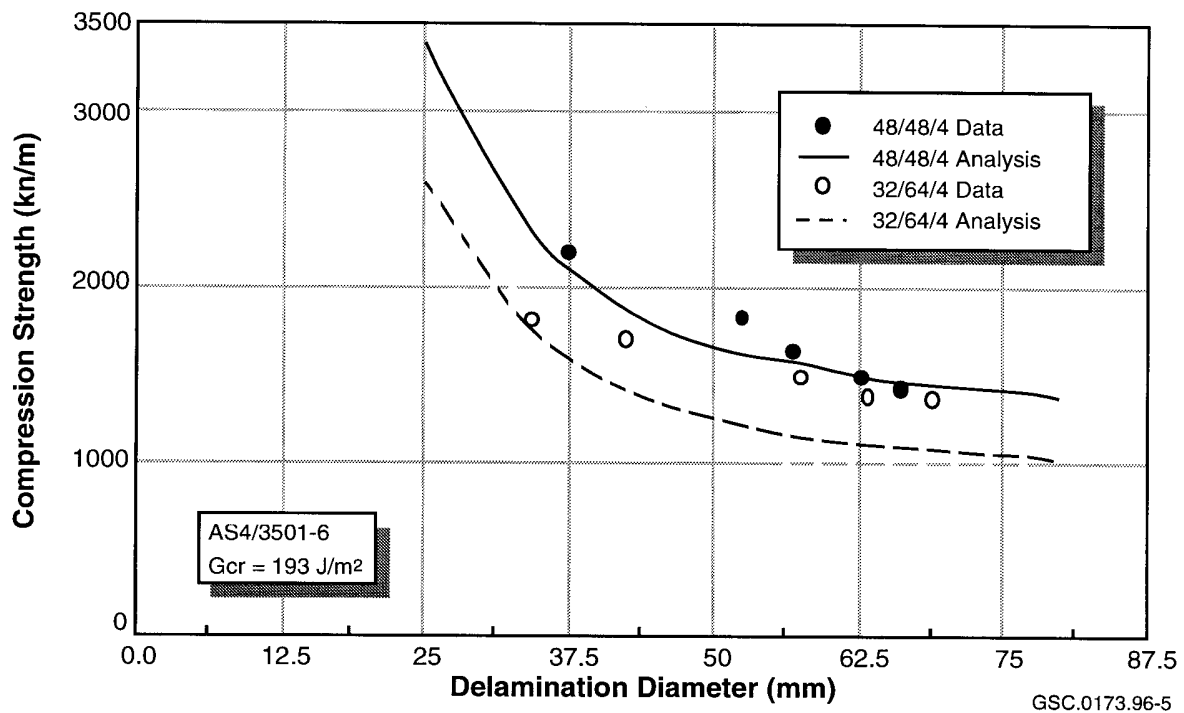


Fig. 5: Compression strength of impacted Gr/Ep laminates

The analytical delamination buckling methods developed in [6,7] were extended to a laminate with a central fastener. For this case the delamination is constrained in the center but grows outwards as a ring. These analytical models are useful for determining residual strength of laminates damaged as a result of improper assembly. An engineering methodology that can address the delamination growth problem for all the delamination locations shown in Fig. 2 is being developed by Davidson under partial FAA funding. This prediction methodology [8] uses a crack tip element (CTE) analysis based on classical plate theory [9]. The CTE provides a closed form expressions for mode mix and energy release rate (ERR) in terms of force and moment resultants in the vicinity of delamination tip which are usually available from FEA of the structural component. As this procedure is computationally efficient it can be used at a large number of interfaces where

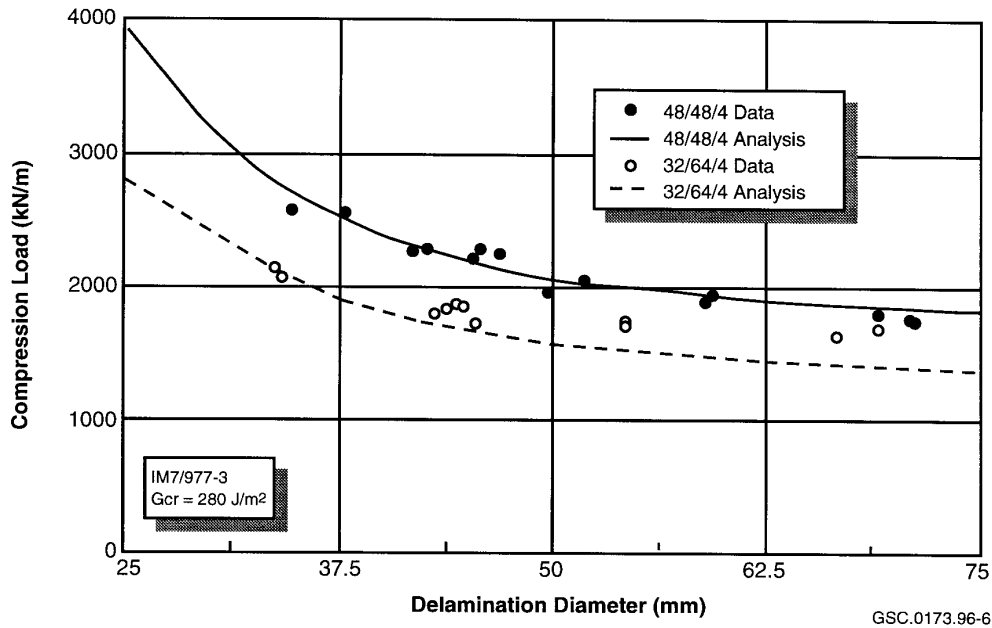


Fig. 6: Compression strength of toughened impacted Gr/Ep laminates

delamination growth is likely. Once ERR is calculated it is compared to material toughness at the appropriate mode mix ratio to determine delamination growth initiation. The material toughness in terms of ratios of G_I and G_{II} is determined experimentally using tests described in the next section. In addition, the CTE approach allows non-classical definitions of the individual ERR components. This is useful for many laminated composites when the classical linear elastic fracture mechanics (LEFM) are inapplicable. For those cases where the near-tip damage zone is small and the classical definitions of ERR apply, solutions by the CTE approach have been compared to FEA showing excellent correlation and computing efficiency [8,9]. For non-classical LEFM, a series of experiments are required to predict delamination growth. One set, to determine the “appropriate definition” of the ERR components and mode ratio and the second set to determine the toughness vs. mode mix relation for the material of interest. These experiments are described in the next section.

DETERMINATION OF CRITICAL STRAIN ENERGY RELEASE RATES

The success of fracture mechanics analysis to predict delamination initiation and growth strongly depends on having reliable test methods to determine critical strain energy release rates. These are needed for all three fracture modes and their interactions. ASTM has been standardizing these test methods, but the progress has been very slow. For mode I there is a published standard (D5228-94) for static determination of G_{Ic} using a double cantilever beam (DCB) test, but it is unavailable under fatigue loading. For other fracture modes, including mixed modes, status of ASTM standards is at varying stages of completion. Work to date has shown that for mode II, G_{IIc} as determined by end notch flexure (ENF) test is characterized by large scatter (20%). At this time it is not clear whether it is an indication of the scatter in this material property or a consequence of the test method.

Standard tests determine G_c 's by growth of delaminations in symmetrical specimens between plies in the same direction, usually 0 plies. One such plot obtained from [8] is shown in Fig. 7. The symbols show the mean of the data (a minimum of 5 test points) while the bars show

the variability by ending the bars at ± 1 normal standard deviations. The data was generated using DCB, ENF, Mixed-Mode Bending (MMB) and Single Leg Bending (SLB) specimens [8]. Mode decomposition for mixed-mode tests were by FEA for SLB, and by closed form approach for MMB [10], and also by CTE and Williams' [11] method for all tests. For these symmetric specimens containing midplane delaminations the same values of mode mix (G_{II}/G) were obtained by all of the different mode decomposition techniques resulting in consistent G_c 's. That is for a symmetric laminate with a midplane delamination any reasonable definition of mode mix will collapse to the singular field based result.

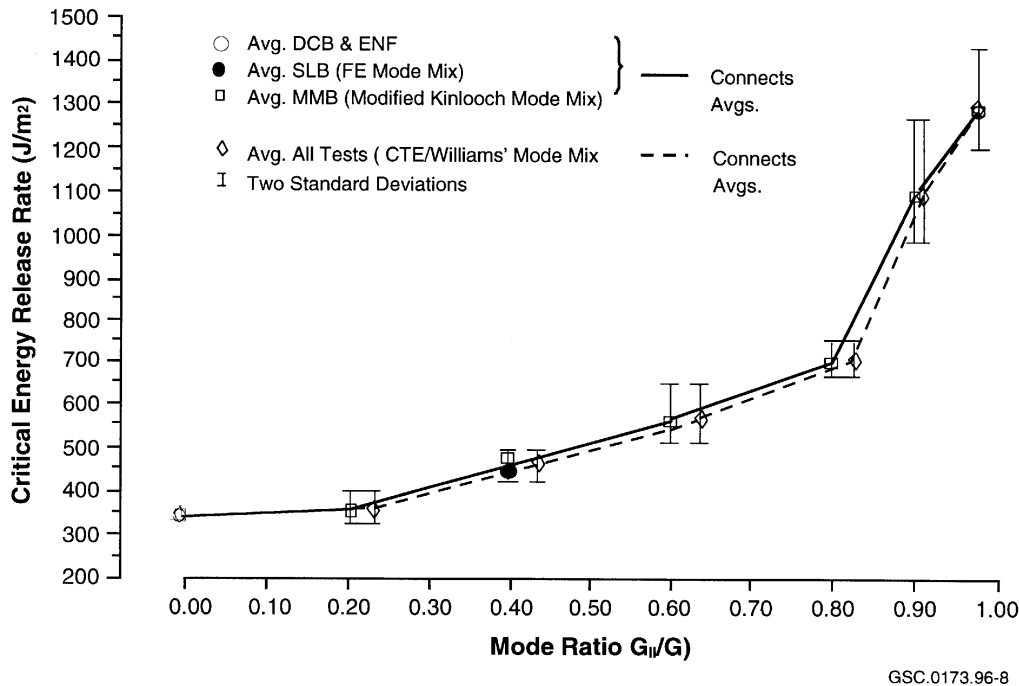


Fig. 7: G_c vs G_{II}/G for Gr/Ep midplane delaminations

Unfortunately, in realistic aircraft structures critical areas for growth may be between dissimilar orientation plies and at unsymmetrical locations. In these instances, the prediction of mode mix using the classical approach may be significantly in error, either due to large near-tip damage zones or bridging. Davidson [8] has been investigating what value of G_c should be used in these cases. Figure 8 shows a plot of data obtained from [8] in which G_c is plotted versus mode ratio for specimens with unsymmetrically placed delaminations. The location of the delamination is shown as a slash in the legend. For example, 25/5 indicates that the starter delamination was placed 25 plies deep in a 30 ply laminate. If LEFM methods are used to reduce the data, represented in Fig. 8 by upright triangles and squares, poor correlation is obtained when compared to symmetrical specimen data of Fig. 7 and reproduced in Fig. 8 as the solid and dashed lines connecting means. One would expect G_c to be a material property independent of location in a unidirectional laminate. In order to obtain better correlation, the mix mode coefficient, Ω , from the CTE, was used as a fitting parameter instead of the singular field based Ω , available as a function of thickness in [9]. This resulted in inverted triangle data points in Fig. 8, see [8] for definition of Ω . Three points to be made here are: (1) that symmetrical ASTM specimens were not sufficient to determine critical G_c at G_{II}/G ratios greater than 0.5 for this particular material, (2) additional tests to the symmetrical ASTM specimens are needed to assess if the classical definitions of ERR and mode mix solutions are valid, and (3) CTE analysis can provide a framework, until the time when the interlaminar physical behavior is understood, to make empirical adjustments to reflect reality

of delamination locations and/or to account for large damage zones. Although the CTE method has been shown to work well for unidirectional laminates its application to general lay-ups and interfaces has yet to be demonstrated. This work is presently in progress.

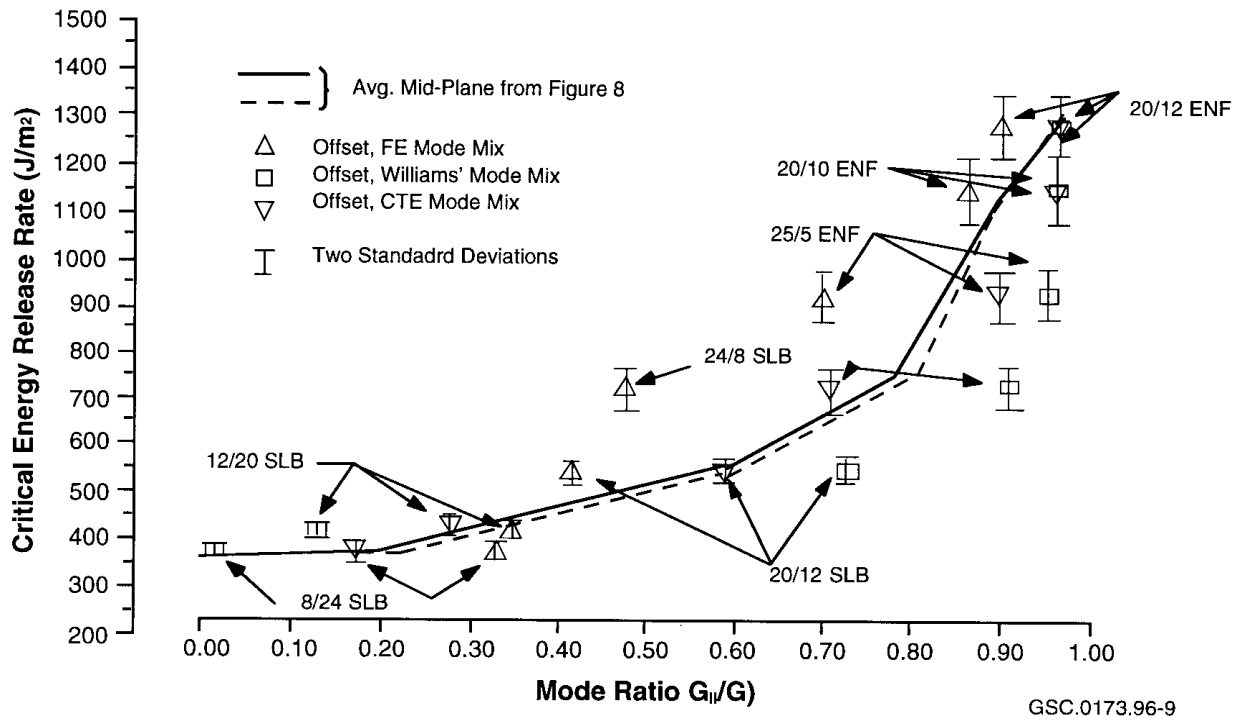


Fig. 8: G_c vs G_{II}/G_I for Gr/Ep midplane and offset delaminations

ANALYTICAL METHODS USAGE

There are very few examples of analytical methods usage in the industry. At this time these methods have not found their way into the mainstream of the design or certification. The methodology has been used to predict or understand element or component test results, primarily disbond failure of the skin/stringer interface. The analyses of [12,13,14] used FEA models to compute strain-energy release rates to determine delamination growth for these disbond problems.

One example where fracture mechanics approach was used was the evaluation of military aircraft control surface components that were damaged during manufacture. The results of the analysis provided the means of deciding whether the discrepant part could meet the durability requirements or should be repaired. The structure that was analyzed consisted of a Syncore sandwich where one side of the facesheet plies was inadvertently severed during the Syncore trimming operation. The resulting sandwich, idealized in Fig. 9, created a situation where under load the initial slit would progress by means of matrix cracks until it reached a stiff layer at which point a delamination would initiate. The question of durability then became a question whether these delaminations grow to a size that can be found by normal ultrasonic inspection. As ultrasonic inspection over the life of these parts was not planned, the analysis assumed an inspection threshold size as the in-situ delamination and a no-growth criterion was postulated under a simulated two lifetimes spectrum fatigue or that G_{th} would not be exceeded.

Because of the relatively complex construction and hybrid materials in the sandwich panels (Fig. 9), standard fracture mechanics tests such as DCB were not used to determine G_{th} but rather were back-calculated from test specimens that were more representative of the actual panel construction. This meant that the tests contained mixtures of modes I,II and III crack-opening displacements.

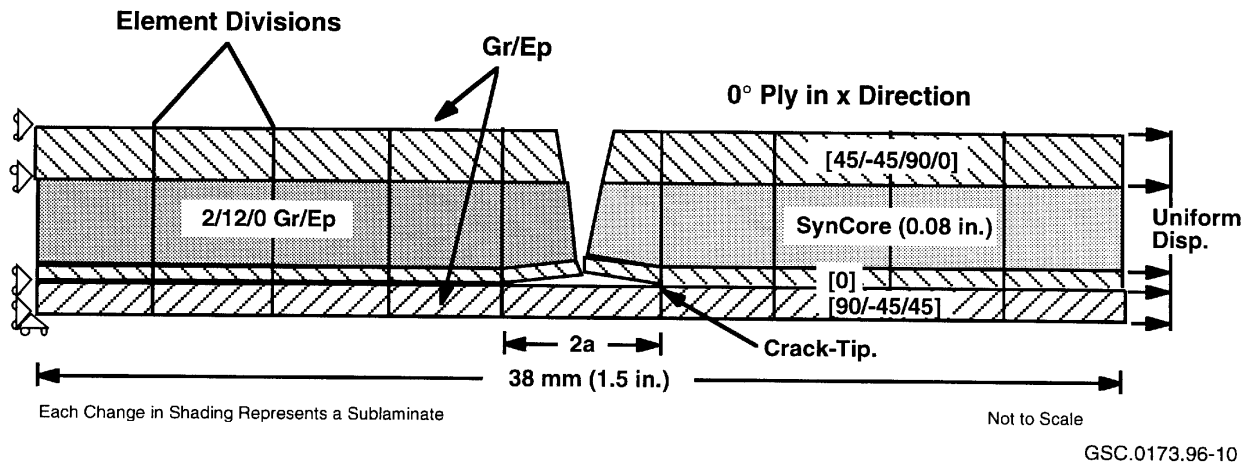


Fig. 9: Idealization of axial specimen used for strain-energy-release-rate analysis

The strain-energy-release-rate calculations were made for data reduction of test specimens, as shown in Fig. 9 for tensile loading (These were also done for compression and shear.), and actual component panels using [15]. Reference 15 treats the composite structure as an assemblage of sublaminates. Each sublaminate is treated as a higher-order plate, with shear flexibility and through the thickness stretching. When the plates are stacked the interlaminar stresses at the interfaces can be accurately evaluated. The resulting equations are solved exactly in closed form. Plates can be connected end-to-end so that complex cross-sections can be represented. However, the cross-section must be constant. A stiffness-derivative method was used to determine the total G . Alternatively, virtual crack closure method [16] was used to find the total G and its mode components. The calculated G 's for the panels were compared to the test G_{th} 's to determine margins of safety.

CONCLUDING REMARKS

Analytical methods to predict damage initiation and growth have been reviewed as to their readiness to be useful in the certification process. The review has ascertained that there are available methods that can obviate the computational complexity of FEA and can replace or at least reduce testing, particularly at the element and subcomponent level. All the methods reviewed require fine tuning for specific applications using built-in correlation factors. These factors have to be obtained by test, similarly to what is done in the analysis of notched laminates. This is not a criticism, as one would not expect a purely analytical method to be able to model such complex problems. However, because of the experience required to apply these semi-empirical methods, they are usually non-transferable between companies. This leads to the main barrier why these methods have not seen widespread use and that is a lack of independent verification test data.

Determination of material G. at various mode mixes requires further research as to their applicability to a general problem. Recourse can be taken by testing coupons simulating the actual situations instead of using ASTM, or other widely used, tests on unidirectional specimens, as was illustrated by the industry usage example.

ACKNOWLEDGMENTS

The author is grateful for the help and advice he received in writing this paper from Dr. Barry D. Davidson at Syracuse University and Dr. Han-Pin Kan from Northrop Grumman.

REFERENCES

1. Paul, Philip, C., et al., "Out-of-Plane Analysis for Composite Structures," Vol. I and II, DOT/FAA/CT-91/22-I,II, September 1994.
2. Shah, C.H., Kan, H.P., and Mahler, M., "Certification Methodology for Stiffener Terminations," DOT/FAA/AR-95/10, April 1996.
3. Flanagan, G.V., "An Efficient Stress Function Approximation for the Free-Edge Stresses in Laminates," *Int. J. of Solids and Structures*, Vol.31, No.7, 1994.
4. Kim, T. and Atluri, S.N., "Analysis of Edge Stresses in Composite Laminates under Combined Thermo-Mechanical Loading, Using a Complementary Energy Approach," *Computational Mechanics*, Vol.16, No.2, May 1995.
5. Horton, R. E., et al., "Damage Tolerance of Composites," Vol. I,II,III, AFWAL-TR-87-3030, July 1988.
6. Kan, H.P., "Delamination Methodology for Composite Structures," DOT/FAA/CT-93/64, February 1994.
7. Wanthal, S.P., et al., "Delamination Methodology for Composite Structures," Vol. I and II, DOT/FAA/CT-94/55-I,II, August 1994
8. Davidson, B. D., "An Engineering Methodology for Delamination Growth Assessment," 11th DOD/NASA/FAA Conference on Fibrous Composites in Structural Design, Fort Worth, TX, August 1996.
9. Davidson, B.D., Hu, H. and Schapery, R.A., "An Analytical Crack Tip Element for Layered Elastic Structures," *Journal of Applied Mechanics*, Vol. 62, 1995.
10. Bhashyam, S. and Davidson, B. D., "An evaluation of Data Reduction Methods for the Mixed-Mode Bending Test," Proceedings of the 37th AIAA/ASME/ACSE/AHS/ASC Structures, Structural Dynamics and Materials Conference, Part 2, Salt Lake City, Utah, April 1996, (to appear in AIAA Journal).
11. Williams, J.G., "On the Calculation of Energy Release Rates for Cracked Laminates," *International Journal of Fracture*, Vol. 36, 1988.
12. Minguet, P.J. and O'Brien, T.K., "Analysis of Composite Skin/Stringer Bond Failure Using a Strain Energy Release Rate Approach," Proceedings of ICCM-10, Whistler, B.C. Canada, August 1995.
13. Martin, R.H., "Local Fracture Mechanics Analysis of Stringer Pull-off and Delamination in a Post-Buckled Compression Panel," Proceedings of ICCM-10, Whistler, B.C. Canada, August 1995.
14. Li, J., O'Brien, T.K., and Rousseau, C. Q., "Test and Analysis of Composite Hat Stringer Pull-off Test Specimen." Proceedings of the American Helicopter Society Forum-52, Washington, D.C., June 4-6, 1996. (also available as NASA TM 110263, June 1996)

15. Flanagan, G.V., "A General Sublaminar Analysis Method for Determining Strain Energy Release Rates in Composites," Proceedings of the 35th AIAA/ASME/ACSE/AHS/ASC Structures, Structural Dynamics, and Materials Conference, Hilton Head, NC, April 1994.
16. Rybicki, E.F. and Kanninen, M.F., "A Finite Element Calculation of Stress Intensity Factors by a Modified Crack Closure Integral," *Engineering Fracture Mechanics*, Vol.9, 1997.

OVERVIEW OF COMPOSITE PROJECTS AT THE FAA AIRWORTHINESS ASSURANCE VALIDATION CENTER

William W. Shurtleff¹, Dennis P. Roach¹, Michael T. Valley¹

¹ Sandia National Laboratories, Box 5800, Albuquerque, NM, 87185-0615, USA

SUMMARY: The Airworthiness Assurance NDI Validation Center (AANC) was established by the Federal Aviation Administration (FAA) William J. Hughes Technical Center at Sandia National Laboratories in 1991 to support nondestructive inspection (NDI) technology development and assessment. The evaluations are done using a variety of characterized test specimens and test beds including entire transport and commuter aircraft. Although the initial work at the Center concentrated on metallic structure, the FAA has more recently expanded the AANC's charter to include projects directed at composite repair and inspection. The three projects briefly described in this paper are: 1) the validation and technology transfer of a thermographic technique for composite inspection, 2) the development of generic composite laminate and honeycomb calibration reference standards, and 3) the certification of the use of a boron epoxy doubler on a Lockheed L-1011.

KEYWORDS: NDI, validation, reference standards, boron-epoxy doublers, thermography

INTRODUCTION

The AANC was established by the Federal Aviation Administration FAA at Sandia National Laboratories to support nondestructive inspection (NDI) technology development and assessment. The major objective of the Center is to provide the developers, users, and regulators of aircraft needing NDI, maintenance, and repair information with comprehensive, independent, and quantitative evaluations of new and enhanced inspection, maintenance, and repair techniques.

The roles of the Validation Center are:

- To provide test specimens and procedures and do realistic assessments (technical and economic) of aircraft inspection, maintenance, and repair techniques,
- To provide quantitative reliability data on the field application of inspection and repair technologies,
- To serve as a catalyst for new technique development with subsequent technology transfer to industry.

Some examples of successful projects include: 1) The validation and transfer of a safer and more economical inspection technique for the Douglas DC-9 Tee Cap to industry use, 2) The development of an inspection technique for the Piper PA25 wing spar that became the basis for an airworthiness directive, 3) The development of an inspection procedure for United

States Coast Guard HU25 window posts to look for cracks and the subsequent baselining of over 30 USCG aircraft.

Although the initial work at the Center concentrated on metallic structure, the FAA has more recently expanded the AANC's charter to include projects directed at composite repair and inspection. The rest of this paper discusses three of these projects.

INSPECTION VALIDATION USING COMPOSITES

The expanded use of composite structures and the development of new composite repair techniques on United States Air Force (USAF) aircraft has created the need for improved portable, quantitative NDI methods and systems. Recent advancements in thermal imaging technologies could provide new inspection capabilities that can be used by field-level NDI personnel to reliably inspect aircraft composite structures and repairs. Under the sponsorship of the Warner Robins Air Logistics Center, Robins, Georgia, the AANC recently started a project to provide the USAF with a field-level thermal imaging NDI capability for inspection of bonded composite structures and repairs on USAF aircraft. This project targets two applications on Air Force aircraft: 1) bonded composite doublers on the C-141 wing plank, and 2) composite honeycomb structure on the F-15 rudder. The composite honeycomb structure is boron epoxy skin to aluminum honeycomb.

PROJECT OVERVIEW

This project will produce new composite inspection capabilities ready for use on operational USAF aircraft. The work is divided into five phases:

Phase I - System Evaluation

Produce a list of candidate thermography systems for formal testing and evaluation,

Phase II - Structured Validation Experiments

Evaluate USAF selected thermography systems in a series of statistically valid, structured experiments to determine which system best meets the USAF inspection requirements,

Phase III - Calibration Standards

Develop and deliver composite calibration standards and manufacturing procedures for the standards,

Phase IV - Field Evaluation

Support field level evaluation of the USAF selected thermography system, and

Phase V – Documentation

Provide the final NDI procedures manual, calibration standards with manufacturing procedures, expanded training syllabus (including a practical hands-on section), and prototype commercial thermography inspection system.

PROJECT STATUS

Candidate thermography systems have been selected for formal testing and evaluation. The experiment design and protocols are complete, the test specimens and calibration standards have been manufactured, and the data acquisition and grading methods have been developed. The structured experiments are underway and will continue throughout the summer of 1997. The on-aircraft field evaluations will be conducted during the first quarter of 1998, with the program completion scheduled for the third quarter of 1998.

The experiments primarily emphasize the detection and quantification of disbonds (e.g., honeycomb core to composite skin disbonds, structural element skin to repair disbonds), interlayer delaminations, and fluid ingress. The manufactured test specimens simulate an F-15 rudder, a C-141 weep hole reinforcement, and a composite repair on a C-141 fuselage. Although this project focuses on specific F-15 and C-141 inspection applications, it is expected that the implemented technology will be transferable to numerous USAF composite inspection requirements.

COMPOSITE INSPECTION REFERENCE STANDARDS

After developing a Composite Inspection Handbook, the Commercial Aircraft Composite Repair Committee (CACRC) Inspection Task Group identified a need for a set of "generic" composite reference standards for use by operators in setting up their inspection equipment. The reference standards would include typical composite flaw scenarios - delaminations, disbonds, and inclusions/porosity - and incorporate structural configurations of Boeing, Douglas, Airbus, and Fokker aircraft. The AANC's participation in this effort was solicited by CACRC personnel because it was felt that the AANC could develop and evaluate the standards in an independent manner and the results reflect the inspection needs of all aircraft designs.

PROJECT OVERVIEW

The purpose of this project is to develop a set of composite calibration standards (laminate and honeycomb) to be used in NDT equipment calibration for accomplishment of damage assessment and post-repair inspection of all commercial aircraft composites. The project includes a number of steps: 1) review composite structure designs of each Original Equipment Manufacturer (OEM) and discuss unique reference standard needs with them, 2) develop processes for producing the various engineered flaws in the specimens, 3) apply NDI techniques to the resultant test specimens and assess their applications and limitations, and 4) produce new or enhance existing composite NDI procedures through the use of the reference standards and possible application of improved NDI equipment. The project tasks described below address both solid laminate and honeycomb composite reference standards. The solid laminates and composite honeycomb are both carbon graphite and fiberglass materials. The composite is Nomex skin bonded to fiberglass honeycomb.

Solid Laminate Composite Reference Standards

Task Definition - Conduct a series of tests on existing OEM laminate composite standards in order to assess the variations in ultrasonic inspection results. Compare the NDI results

(material properties) from different laminates which have been manufactured in accordance with Douglas, Boeing, and Airbus specifications. The NDI issues include signal attenuation and velocity through the laminate.

Test Plan - Use 5 MHz and 10 MHz broad band transducers and perform inspections in a UT immersion tank in order to eliminate the coupling variable. This will allow comparison of the material properties of the different laminates. The test results will be used to establish a single, existing reference standard (or new one with a generic material) and to determine a series of correction/conversion factors to accommodate inspections on other materials.

Deliverables - 1) a series of NDI output curves such as signal attenuation vs. laminate thickness, laminate material, and inspection frequency, and 2) recommendations for a single laminate composite standard and a table of conversion factors to accommodate composite laminate inspections on all transport aircraft (i.e., other materials).

Honeycomb Sandwich Composite Reference Standards

Task Definition - Apply multiple conventional NDI techniques to a series of composite honeycomb reference standards which have been constructed with different fabrication options and flaw scenarios. Items to be varied include core thickness, core weight, skin material, cell size, skin thickness, and core material. Develop processes to reliably produce specimens with engineered flaws. Identify the important variables which should be included in composite honeycomb reference standards. Produce a design plan which describes how the variables should be combined and a fabrication plan to reliably produce consistent standards. Assess the effects of each variable on NDI in order to provide justification for minimizing the number of calibration standards.

Test Plan - Apply multiple NDI techniques to the suite of test specimens. Experiments will be performed using: 1) thru-transmission ultrasonics, 2) tap test, 3) Staveley Bondmaster (pitch-catch, swept, and MIA), 4) Zetec Sondicators. The application of these NDI techniques will be carried out using a method to control the probe pressure.

Deliverables - 1) series of flawed composite honeycomb specimens which isolate individual composite fabrication variables, 2) a lab report describing the effect of each variable on different inspection techniques and procedures, and 3) a corresponding series of recommendations for a set of void detection (disbond/delamination) standards.

PROJECT STATUS

The AANC has completed the design, fabrication, and evaluation of a trial honeycomb test specimen for the project. Figure 1 shows the specimen which was fabricated in the Northwest Airlines composite shop. The specimen contains the following features:

- numerous duplicate flaws were implanted get some statistics on how well each approach works
- the laminate was individually cured
- the laminate was joined to the honeycomb using a secondary bond
- disbonds were generated by machining recesses in the honeycomb material; this produced air gaps between the honeycomb and the composite laminate

- delaminations were generated using the four methods shown in Figure 1: 1) teflon inserts, 2) "pillow" inserts, 3) teflon pull tabs, and 4) stainless steel pull tabs.
- the pillow inserts consisted of 3 layers of 1 mil thick paper enclosed by 2.5 mil, high temperature Kapton tape; the paper stack interrupts an NDT signal and simulates an air gap between adjacent plies
- the stainless steel pull tabs were treated with a chemical release agent to prevent any connection to the adhesive.

The trial test specimen from Fig. 1 was evaluated using four different nondestructive inspection techniques. The results below are very preliminary and a more comprehensive assessment will be performed on the full set of test specimens.

Thru-Transmission Ultrasonics (TTU) - Figure 2 shows a C-scan obtained using through-transmission ultrasonics. All of the flaws are visible although the 0.5" wide pull tabs are less obvious than the 0.5" diameter delamination inserts. This technique rates all flaw production methods as equally effective.

Bondtester (resonance mode) - The Staveley Sonic Bondmaster (165 KHz and 330 KHz probes) was able to detect all of the delamination flaws. Large signal deviations, which exceeded preset alarm levels, were obtained from both the 1" and 0.5" delaminations. The disbands could not be detected.

Bondtester (MIA mode) - The Staveley Sonic Bondmaster (range of 2.5 to 12 KHz) produced unsatisfactory results in MIA mode. With the gain set to its maximum of 49.5 dB and an equipment-picked frequency of 5.9 KHz, it was possible to get small signal deviations over the flaws. The pull tab and insert delaminations produced signal movements of 3 divisions while the disbands produced 1.5 divisions of signal movement (8 divisions is preferred to make a call). These results are considered inconclusive and further work is needed to determine the applicability of MIA to composite honeycomb inspections.

X-ray - The insert delaminations were visible in X-rays, however, the smaller, 0.5" diameter delaminations were quite difficult to see. Slight shadowing could be discerned in the area of the pull tabs but this would only be detected if one knew where to look. The disbands did not appear on the X-ray images.

Based on the results of the NDI experiments, a final test specimen configuration was designed and approved by the CACRC. The suite of test specimens, which isolate critical design and flaw variables, are currently being fabricated.

APPLICATION OF BORON-EPOXY DOUBLERS TO COMMERCIAL AIRCRAFT

The AANC is conducting a technology evaluation project on Boron-Epoxy doublers with Delta Air Lines, Lockheed Martin, Textron, and the FAA. The project focuses on applying a bonded, composite doubler in place of a riveted, metallic doubler. By focusing on a specific commercial aircraft application - reinforcement of the L-1011 door frame - and encompassing all "cradle-to-grave" tasks such as design, analysis, installation, and inspection, this program is designed to objectively assess the capabilities of composite doublers. The final phase of this project includes the installation of a composite doubler on an L-1011 in Delta's fleet.

This will represent the first (non-decal) bonded composite doubler on a U.S. commercial aircraft.

Repairs and reinforcing doublers using bonded composites have numerous advantages over mechanically fastened repairs. Adhesive bonding eliminates stress concentrations caused by additional fastener holes. Composites are readily formed into complex shapes permitting the repair of irregular components. Also, composite doublers can be tailored to meet specific anisotropy needs thus eliminating the undesirable stiffening of a structure in directions other than those required. Other advantages include corrosion resistance, a high strength-to-weight ratio, and potential time savings in installation.

PROJECT OVERVIEW

To demonstrate the capabilities of composite doubler reinforcement technology in an area of known fatigue cracking, this project included the following technical activities: 1) structural design of the doubler, 2) development of doubler installation procedures, 3) structural evaluation of the design, 4) inspection procedures, and 5) laboratory and flight tests of a composite doubler installed on an operating aircraft. The general issues addressed were:

Doubler design - strength, durability and reliability issues, flaw containment, optimum adhesive properties, and critical patch parameters.

Doubler installation - surface preparation, tooling, heat sinks, effect of underlying rivets, difficulties of field installation field work.

NDI techniques used to qualify and accept an initial installation and to perform periodic inspections. The NDI equipment will be required to inspect for flaws at three different structural levels: 1) in the parent material (crack or corrosion growth), 2) in the adhesive bond (debonds), and 3) in the composite doubler (delaminations).

The overall distribution of tasks among the team participants is listed below. These tasks, along with the flow of activities are summarized in Figure 3.

Composite Patch Design and Analysis (Lockheed)

Installation Process and Material Properties (Textron and Lockheed)

Structural Verification Testing, NDI Development, and Overall Project Management (Sandia Labs AANC)

Composite Doubler Installations, Aircraft Testing, and Process Specifications (Delta Airlines)

Oversight and Certification (FAA Aircraft Certification Office)

PROJECT RESULTS

References [1-8] provide detailed results from the tasks described above. The data stemming from this study serves as a comprehensive evaluation of bonded composite doublers for general use. The associated documentation package, which is resident at the FAA Aircraft Certification Office, provides guidance regarding the design, analysis, installation, damage tolerance, and nondestructive inspection of these doublers. Figure 4 illustrates the damage tolerance capabilities of bonded composite doublers. An AANC test series demonstrated that even in the presence of extensive damage in the original structure (cracks, material loss) and in spite of non-optimum installations (adhesive disbonds), the composite doubler allowed the

structure to survive more than 144,000 cycles of fatigue loading. Installation flaws in the composite laminate did not propagate over 216,000 fatigue cycles. Furthermore, the added impediments of impact - severe enough to deform the parent aluminum skin - and hot-wet exposure did not effect the doubler's performance [3, 5, 6, 8].

Multiple NDI techniques were assessed to inspect the doubler installation for disbonds and delaminations [1, 2, 7]. The optimum method to achieve both field deployment and ease of signal interpretation involves the use of Pulse-Echo C-Scan ultrasonics. Extensive testing has shown that the two-dimensional, color coded images produced by manual and automated scanners are able to reliably detect disbond and delamination flaws on the order of 0.50" in diameter. Time savings, human factors issues, and repeatability are some of the main advantages associated with C-Scan ultrasonics. Figure 5 shows a bonded doubler test article and the C-Scan image which was produced using the pulse-echo method and a scanning device. The AANC NDI study also showed that crack detection in the parent, aluminum material can be accomplished using conventional X-ray techniques. X-ray inspections are as effective as before the doubler was installed. The Boron-Epoxy material does not impede the X-ray inspections. Power and exposure times can be adjusted to accommodate the presence of the doubler and achieve the required film density and resolution.

SUMMARY

Although there are three separate projects described here, it should be noted that all benefit from the techniques and results of the others. For example, the test and calibration specimens for the USAF will be produced using the same techniques as the specimens for the composite reference specimens although some of the materials may be different. And the inspection techniques such as resonant bond test and ultrasonic thru-transmission developed for the boron epoxy doubler inspection will be used with the composite references.

The unique charter of the AANC allows the results from these and other experiments to be easily used by the community at large. Although the thermographic validation experiment and the boron epoxy doubler on the L-1011 are aimed at specific inspections, the results can be used as a basis for more widespread applications. Further the composite reference standards are designed to be widely applicable.

ACKNOWLEDGEMENTS

This work was sponsored by the Federal Aviation Administration Hughes Technical Center under Sandia National Laboratories contract number DTFA-03-95-X-90002 and the United States Air Force under FD20609695068. Sandia is supported by the United States Department of Energy under Contract DE-AC04-AL85000.

REFERENCES

1. Roach, D., Moore, D., and Walkington, P., "Nondestructive Inspection of Bonded Composite Doublers for Aircraft", Proceedings of SPIE Conference on Nondestructive Evaluation of Aging Aircraft, December 1996.

2. Roach, D., Walkington, P., "Validation of Nondestructive Inspection Techniques for Bonded Composite Doublers in Commercial Aircraft Applications", FAA Report SNL96ER007 and inspection procedure AANC-PEUT-Comp-5521/4-004 under Atlanta Aircraft Certification Office Project SP1798AT-Q, December 1996.
3. Roach, D., Graf, D., "Damage Tolerance Assessment of Bonded Composite Doublers for Commercial Aircraft Applications", FAA Report SNL96ER0189 under Atlanta Aircraft Certification Office Project SP1798AT-Q, November 1996.
4. Roach, D., Graf, D., "Structural and NDI Validation Tests for L-1011 Composite Doubler Design: Benchmark Testing to Support Lockheed Analysis", FAA Report LG95ER0157 under Atlanta Aircraft Certification Office Project SP1798AT-Q, November 1996.
5. Roach, D., Carter, A., and Marshall, J., "Introduction of Bonded Composite Doublers to Commercial Aircraft", Proceedings of the 11th American Society for Composites Technical Conference, October 1996.
6. Roach, D., "Validation of Bonded Composite Doubler Technology Through Application Oriented Structural Testing", Proceedings of 11th DoD/NASA/FAA Conference on Fibrous Composites in Structural Design, August 1996.
7. Moore, D., Roach, D., Swanson, M., Walkington, P., "Nondestructive Inspection of Adhesive Bonds in Composite and Metallic Materials", Materials and Process Challenges: Aging Systems, Affordability, Alternate Applications, SAMPE Publication Vo. 41, ISBN 0-938994-74-3, 1996.
8. Roach, D.P., "Performance Analysis of Bonded Composite Doublers on Aircraft Structures", Proceedings of Int. Conf. on Composite Materials, August 1995.

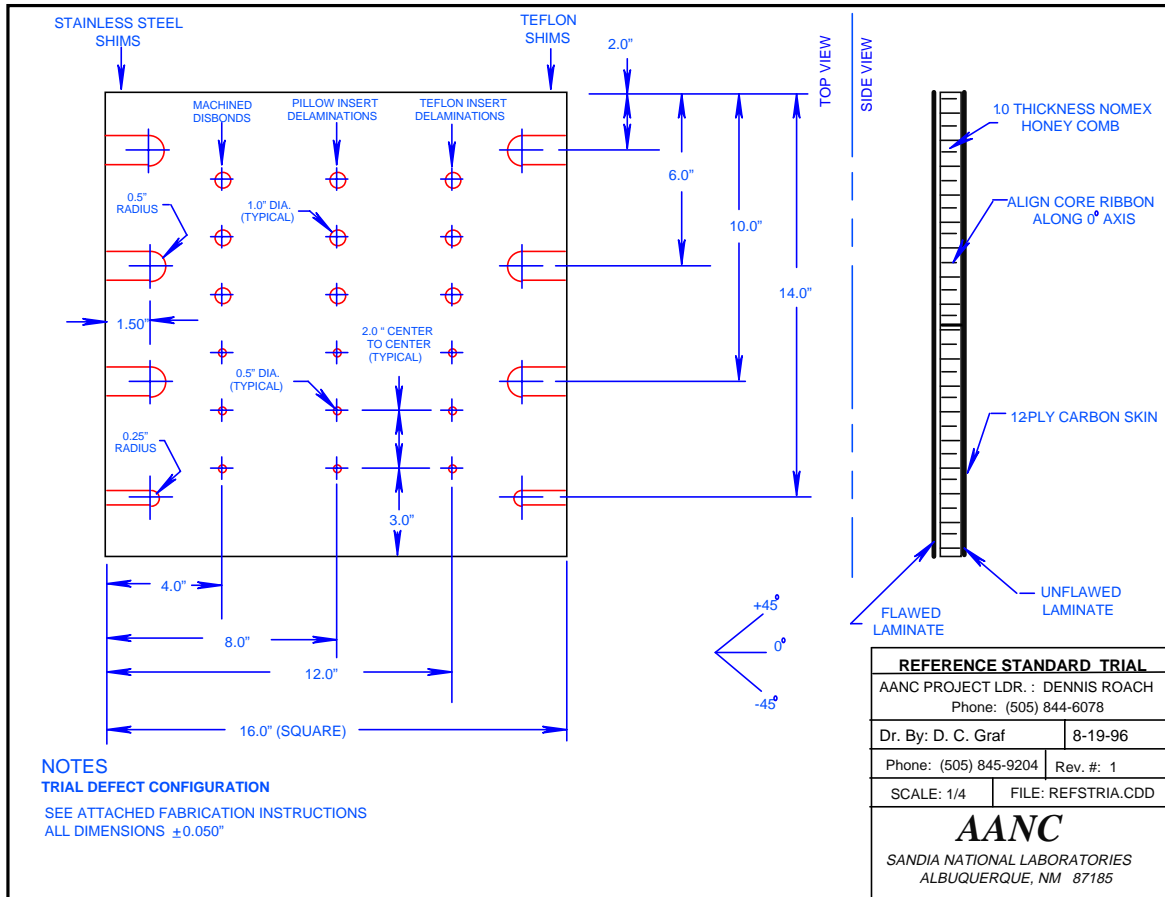


Figure 1: Trial Composite Reference Standard Specimen

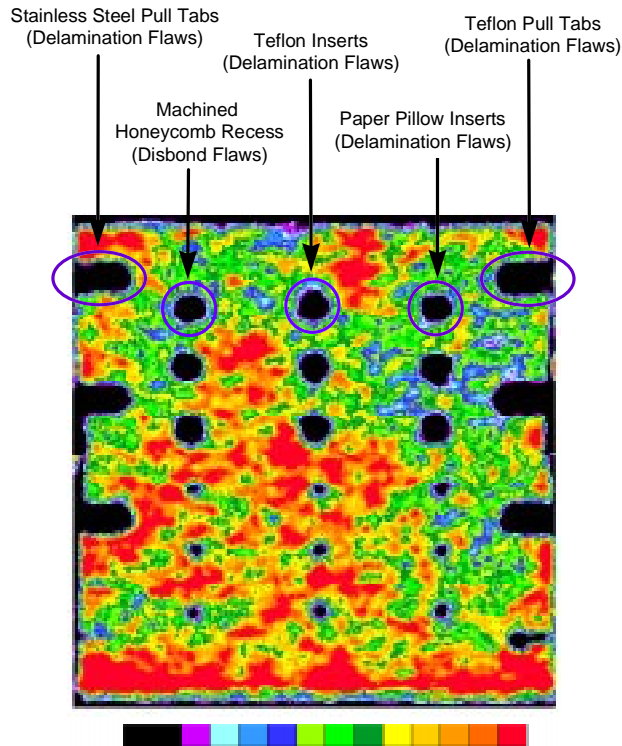


Figure 2: Through Transmission Ultrasonic C-Scan of Composite Reference Standard Trial Specimen

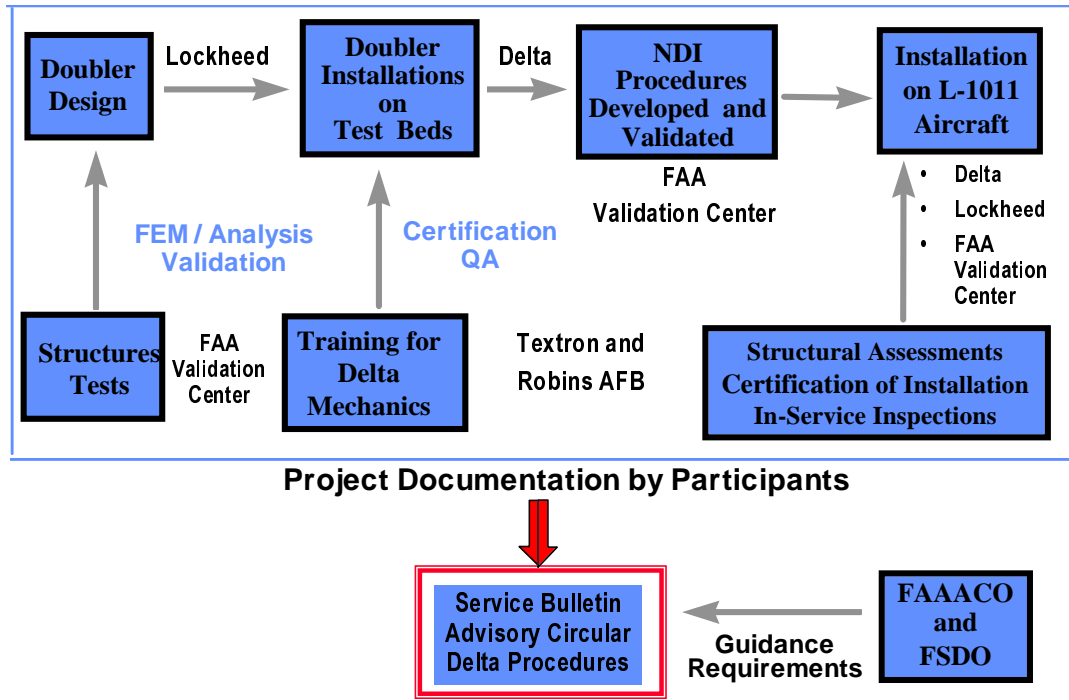


Figure 3: Roles and Responsibilities of Participants in the Bonded Composite Doubler Validation Project

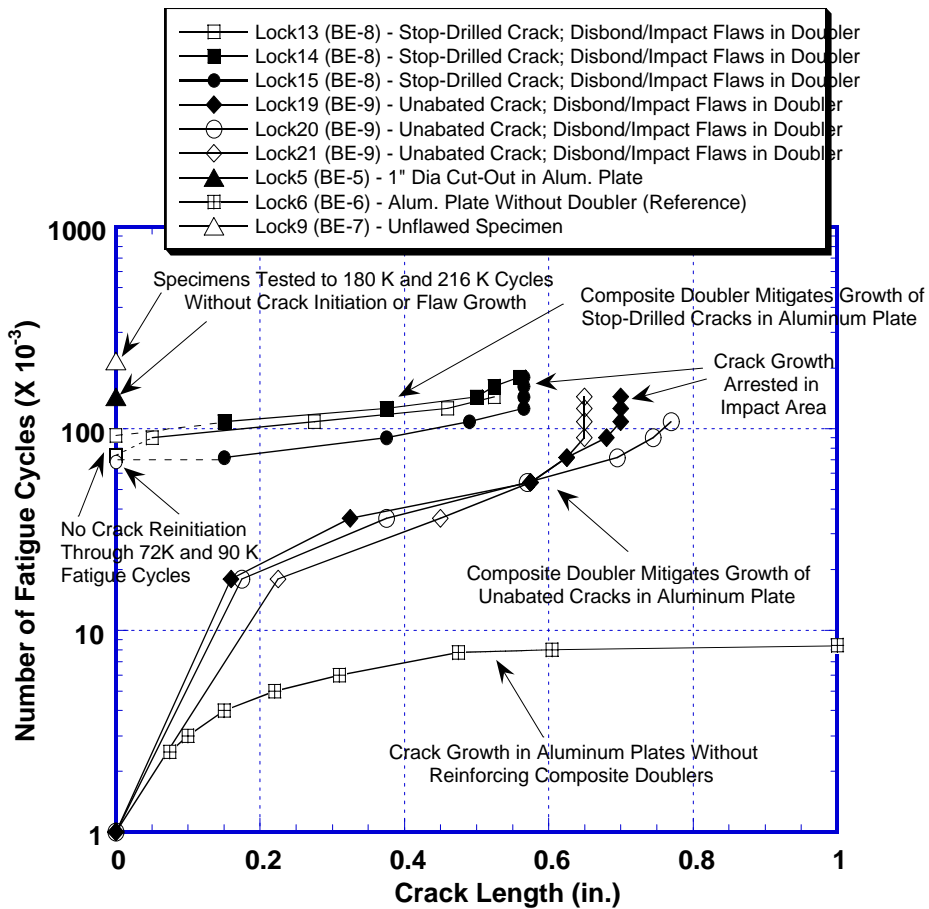


Figure 4: Fatigue Crack Growth in 2024-T3 Plates With and Without Reinforcing Composite Doublers

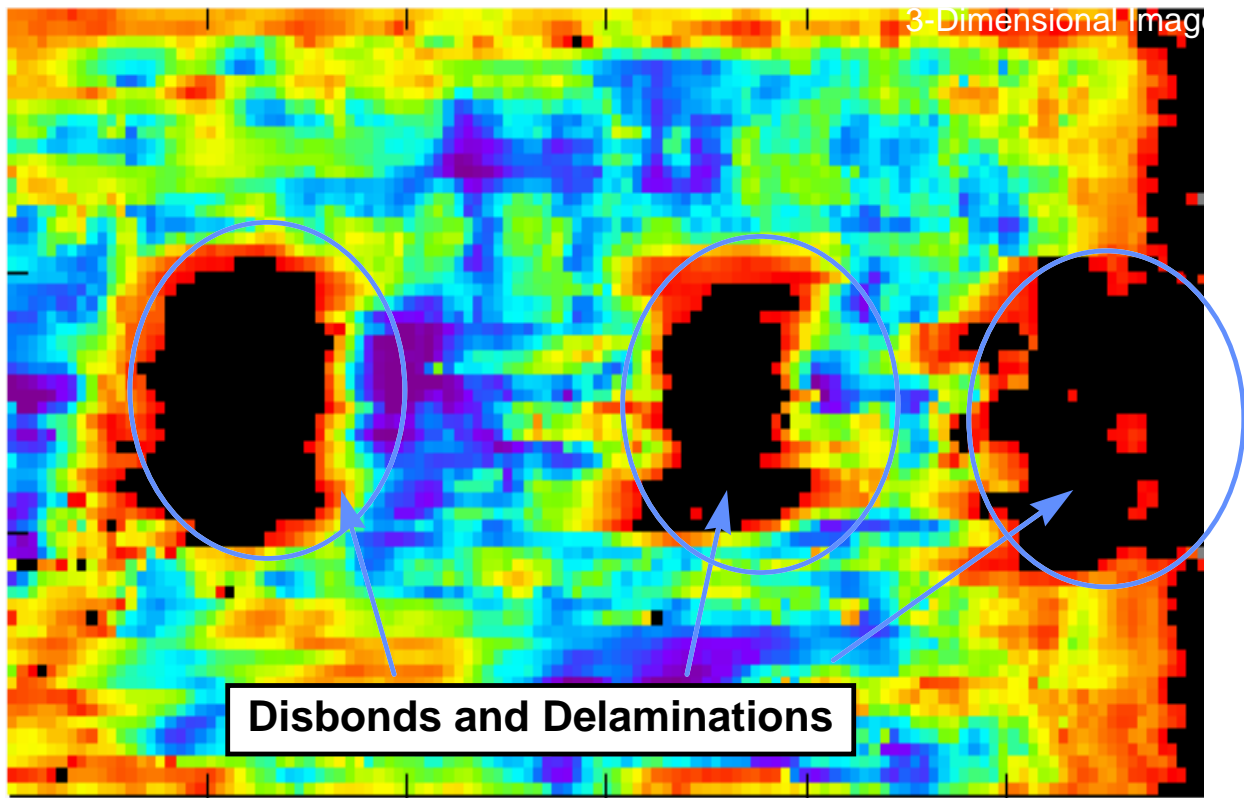
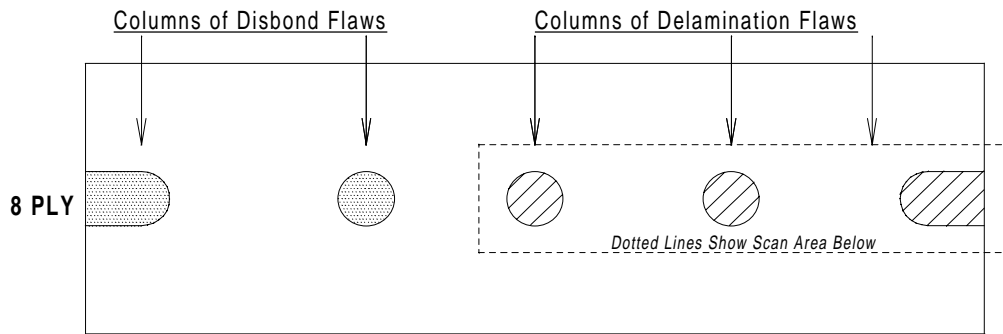


Figure 5: Pulse-Echo Ultrasonic C-Scan of Engineered Delamination Flaws in Bonded Composite Doubler Test Article

DEVELOPMENT OF A COMPOSITE AXLE HOUSING: A CASE STUDY IN MULTIDISCIPLINARY TECHNOLOGY TRANSFER MECHANISMS

A. MacDonald¹, W.M. Banks² and A. Desport³

¹ *Albion Automotive, 1187 South Street, Scotstoun, Glasgow, UK, G14 0TD*

² *Dept of Mechanical Eng, University of Strathclyde, James Weir Bldg, Glasgow*

³ *Centre for Advanced Structural Materials, University of Strathclyde, Glasgow*

SUMMARY: This paper outlines a Teaching Company Scheme (TCS) project between Albion Automotive Driveline Division and the University of Strathclyde. The TCS acts as a technology transfer mechanism between universities and industry. The aim of the project is to produce an automotive structural component through the innovative use of fibre reinforced plastics (FRP). This project plays an important part in the company drive towards technological innovation. The attractiveness of composite materials to the automotive industry has been the opportunity for parts consolidation, weight savings and increased freedom of design. In meeting the project aim the requirements for the development of medium to high volume automotive composite componentry are met by the use of an integrated design and manufacturing methodology. This is coupled with an appreciation of the financial and marketing aspects required for the development of the components involved. The use of such an integrated and concurrent approach to the development and manufacture of an FRP component is an illustration of technology transfer in product design.

KEYWORDS: technology transfer mechanism, fibre reinforced plastics, feasibility study automotive structural components, integrated design and manufacturing methodology

INTRODUCTION

The transfer of technology provided by the TCS project is the introduction of an innovative design procedure encompassing several factors. These factors include the methodology of product, design, manufacture, marketing and financing. In the automotive industry which is generally concerned with mass production of components, the opportunity has arisen for the manufacture of components from composite materials. Such components are car body parts, springs and drive-shafts for commercial and other vehicles. There are new composite materials being developed which are giving potential for cost savings. New production procedures are making mass production more viable. The TCS is designed to provide companies with expertise to solve a problem that would otherwise lie dormant. The solution provided aims to be of strategic importance to the future development of the company. The university provides supervision and background expertise and makes this available to the Teaching Company Associate.

THE TCS SCHEME

The Centre for Advanced Structural Materials is a multidisciplinary unit within the University of Strathclyde, at the forefront of delivering innovative research and technology transfer solutions. The Centre is especially recognised for its work with Small to Medium Sized Enterprises (SMEs) which have been identified as crucial for the long term economic growth of the UK. One particularly successful technology transfer mechanism which the Centre employs is a UK government funding initiative called the Teaching Company Scheme (TCS).

The TCS is a collaborative programme where experts from higher education establishments participate in projects which are demonstrated to be central to specific industrial companies' plans for strategic development. The project work is carried out in the companies by young graduates known as Teaching Company Associates (TCAs) under the joint supervision of academic and industrial staff. The companies involved benefit from the research deliverables, the technology transfer process and by the training of a young graduate who not only develops technical skills but is also trained in the wider commercial implications of the research and development process. The academic institutions benefit from industrially significant case study material and develop their research capabilities in an innovative field of technology. The TCS is a vehicle for stimulating, developing and implementing innovative ideas.

ALBION AUTO INDUSTRIES

Albion Automotive as it is known today is an independent company formed on 26 November 1993 in a management buy out when the company DAF went into receivership. However it has been in existence since 1899 when the company was formed under the original name of Albion Motor Car Co Ltd in Glasgow. The company originally produced complete commercial vehicles in the form of light vans and also cars. In 1912 it took the decision to concentrate on the manufacture and development of commercial vehicles. Albion Automotive presently concentrates its business on the following areas of commercial vehicle manufacture; axle design and production, chassis component design and manufacture and crankshaft manufacture. The current product range caters for vans up to four tonnes and light/medium 4 x 2 and 4 x 4 wheel drive commercial and military trucks [1].

DESIGN METHODOLOGY USED FOR TCS PROJECT

The designer faces a different challenge when considering working with composites especially when the proposed component is to replace something which has been designed and constructed with traditional materials in mind (such as metals). Basically there are a whole set of new design considerations to be taken into account. The manufacturing process associated with it has also to be considered in detail as there may not be an existing process suitable. The creative element of product design in FRP materials covering shape, geometry, colour and surface texture is but one issue; the underlying emphasis being the technical aspects of the choice of materials, their properties, failure criteria, fabrication and processing methods.

There has to be an optimum integration of the above factors. Traditional materials (such as metals) have many design codes and material properties' data that allow for the accurate prediction of component performance. The costs of traditional materials are generally low

and therefore there may not be such a pressing need for optimisation. Perhaps the most important factor of all is that they are isotropic and essentially homogeneous.

From the first there has to be an understanding of the technical aspects of a new material. Such factors as reduced weight, freedom from corrosion, easier mouldability and fabrication need to be considered. This enables the technical benefits and drawbacks of the implementation of the new material to be thoroughly understood [2]. As soon as an assessment of the potential technical and performance benefits has been gained, it is then necessary to commence an assessment of the financial implications. This can be achieved by constructing a list of potential income and savings benefits against potential costs. The design methodology used in the project is based on the design methodology developed by Smith [3]. The component specification is based on one of Albion Automotive's current product range. However in the interests of aiming to avoid merely reproducing a copy of an existing part, the only restrictions placed upon the design of the component are at the interfaces between connected componentry in the design envelope.

Albion currently employ the use of advanced computer aided design (CAD) combined with finite element analysis (FEA) techniques in the design of their products. It is the concurrent development of a suitable manufacturing process and product design which is new to the company. Previously the company's policy has been to buy in rough castings of their products which are then machined to customers design specifications. The TCS project aims to deliver an appropriate design together with the manufacturing process to the company for the FRP component. This will enable the company to produce the product entirely in house which will alleviate the company's dependency on rough component suppliers. These have been competitors of Albion in the past and therefore the transfer of manufacturing technology in parallel with component design is seen as an important aspect of the project. The manufacturing method under consideration is the Resin Transfer Moulding (RTM) process.

DESIGN IMPLICATIONS FOR ALBION AUTO INDUSTRIES

Feasibility Study of the Rear Axle Casing

The component chosen for development at the start of the project was a rear axle casing (see fig.1). A feasibility study on the axle component was carried out. This was in order to assess the viability of the component's development in FRP where the financial and technical benefits were evaluated. The initial specification was based on the rear axle casing which Albion produce for the LDV 200 series van. The loads exerted upon the rear axle casing were determined in order to initialise suitable material selection.

The axle casing would have to be moulded in halves to allow the component to be manufactured by a satisfactory moulding process. The spindle ends would have to remain fabricated from metal due to customer / supplier demands for product compatibility. Attachments for suspension and brakes would have to remain metallic to avoid the potential redevelopment of the brakes / suspension. This problem could be addressed by incorporating metal inserts into the mould. However this would inevitably increase manufacturing costs with the incorporation of extensive adhesive bonding technology and additional forging / casting of metal inserts.

The rear axle casing would need to incorporate a driving gear system and metal spindle ends for stub axle attachment. The spring seats/suspension brackets were to be flexible in the design approach. It was thought that some form of cooling device would be necessary in the design to dissipate the heat generated by the driving head. The composite axle casing was to be based on the current old design incorporating a banjo casing as illustrated below in Fig 1.

The current rear axle casing alone for which a composite alternative is being considered is approximately 13 % of the entire rear axle assembly. There would be a potential 40 % approximate weight saving in the casing, by producing the casing only, from FRP instead of traditional steel. The benefit of the overall reduction in the axle mass is small when the complete axle assembly is considered. There are many design restrictions due to the driveline components; driving head and halfshafts, and the spindle ends. The geometry would have to remain similar to that of the current casing with the additional problem of heat dissipation from the driving head.

Another of the main design problems was the stiffness of the axle casing arm where the springseat and damper brackets would be mounted for the attachment of suspension components. It is envisaged that an uneconomical amount of FRP would be required to match the stiffness of the current steel casings. The flexural rigidity of the FRP would provide problems due to the containment of the drive axle within the axle arm. The drive axle is rigidly attached to the wheel and the driving head. The loading on the axle arm is a resultant of the horizontal and lateral forces exerted upon the wheel combined with the mass load of the vehicle. An FRP axle arm would be subjected to undesirable bending moment loadings. The driving gear is mounted inside the casing and has to be isolated from movement in order to maintain the spline alignment in the gears. Any displacement in the axle arm would result in detrimental damage to the driving components. However in the long term, if the manufacturing strategy of Albion Automotive is to develop a complete in-house manufacturing facility for solid rear axle casings then FRP materials are a solution. This is due to the greater cost and facility requirements that a steel forging plant would have in comparison to that required for a high volume, low pressure and low tooling costs, composite component manufacturing plant.

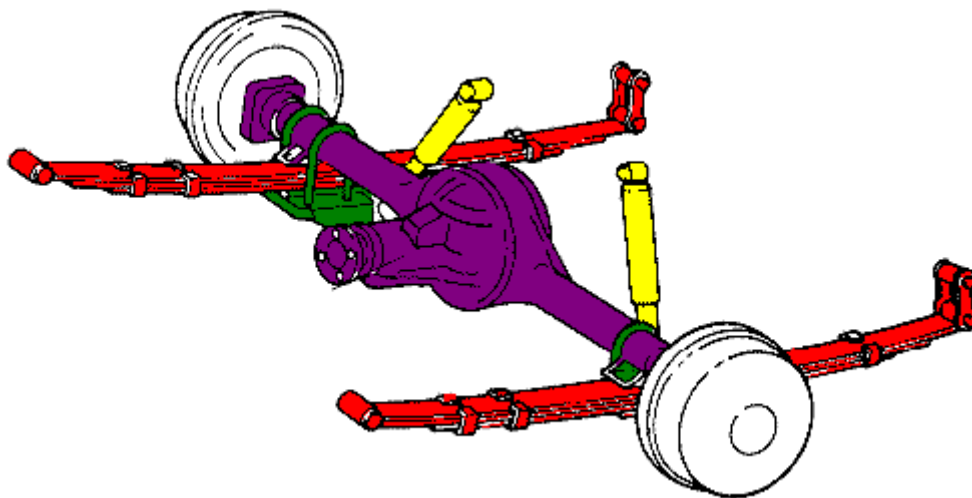


Fig 1 : A typical rear axle

Thus after a detailed examination of the rear axle casing it was concluded from the study that the existing design gave little opportunity for the application of composites. This is due to the manufacturing difficulties and design restrictions that the casing faces. These collectively go against the philosophy of composite component engineering, principally in the areas of parts consolidation and the non suitability of merely replacing a metal component with a composite one of similar design. This can be viewed in the potential costs for the casing halves and machining / design costs for the metal. The design issues concerning the metal inserts and the requirement for additional adhesive bonding technology will still be addressed and should be valuable to future product development.

An Independent Suspension System

Since the increase in production costs when compared to the steel axle currently manufactured are not justified by the technical benefits offered by a composite rear axle casing an independent suspension system was considered. The development of an FRP independent suspension system will provide the technological understanding and the basis upon which a composite rear axle casing could become a realistic proposal.

The development of an independent suspension system would also allow a better understanding of the requirements for an in-house production facility. Many of the problems facing the production of a solid rear casing do not exist in the design of an independent suspension system. At the same time it would provide adequate challenges in the development of the necessary adhesive bonding technology, FEA requirements and manufacturing process technology. Also there is the potential for incorporating the suspension as an integral part of the suspension arms through the realisation of the potential of composite material's physical properties.

The design of the components would be aimed at parts consolidation in the suspension geometry and a two piece driving head housing. The concept of an independent rear suspension is in line with the current automotive industry trend of research and development into vehicle suspension systems.

The problem of rigidity facing the solid rear axle casing is solved if the requirement for a rigid case is removed by the use of independent suspension. The strength/flexural modulus of the FRP could become an advantage in the design of the structural elements. One of the biggest problems facing the design of an independent suspension system are the packaging problem in terms of stress bearing areas in relation to the suspension volume. In the earlier designs incorporating five links the upper links intruded into the baggage compartments. However with the use of the half shaft as one of the upper links this problem has been solved by allowing the reduction in the size of the suspension arms. Part of the design specification of the project will be to investigate the parts consolidation potential offered by designing with FRPs.

The most efficient route for designing an independent suspension system is to have an axle module manufactured so as to be adaptable to a wide variety of chassis designs and applications. To date designers have tended to think of independent suspension vehicles rather than independent suspension modules for use on such vehicles. If designed and manufactured on a modular basis for application in a variety of vehicles this would be a logical approach and one that Albion currently use in the design of their current axle range. Live axle suspension systems are close to their optimum in regard to ultimate development.

Independent suspensions for heavy vehicles provides a whole range of possibilities³. This could be in the use of active suspension systems that could be controlled to suit the terrain or vehicle.

The FRP properties will be utilised to produce components that will be mechanically superior in terms of performance and cost effectiveness to current independent suspension system design using traditional materials. There will be less tooling requirements and less material requirements than those of the currently proposed FRP rigid axle casing. The requirement for reinforcement fibres around driving head casing will be less than that of the suspension linkage due to the reduction of structural forces seen by the driving head casing. Through the use of an appropriate resin system, the thermal conductivity and distortion problems of the application of composites in such an environment will be successfully tackled. Such a resin system is the DSM Daron hybrid resin system. The DSM hybrid resins allow for short processing times without the compromise on structural properties such as heat distortion, stiffness and strength.

Manufacturing Considerations

The advent of new RTM process changes have seen RTM move from a commercial, low performance process, to one that can be utilised for the fabrication of primary structural composite parts [4]. Therefore it is seen as a viable manufacturing process for consideration in this project. The RTM moulding process is very dependent on the properties of the polymers, fillers, reinforcements, moulds, and mechanical equipment. These are the key areas that the project is addressing concurrently with the component design. RTM composites can meet or surpass the properties exhibited by other fabrication methods, including autoclaved prepreg parts. Labour and part variability can be reduced while productivity can be increased. RTM provides the advantages of lower volatile organic compound (VOC) emissions with a closed mould process in terms of product uniformity (glass loading, thickness and physical properties) combined with relatively low investment costs.

These factors are all important to the success of implementing an FRP component manufacturing facility in the company. This is due to RTM being a low pressure process unlike many traditional composite manufacturing cold mould processes (sheet moulding compounds (SMCs) and reaction moulding compound (RIM). The compression moulding and injection moulding processes are well established but have considerable processing costs in terms of tooling and energy / high pressure requirements. The processes of RTM and reinforced reaction injection moulding (RRIM) in comparison offer the same capabilities but with much reduced plant costs. RTM is considered to offer the greatest potential for low volume production of complex components. RRIM is being considered also.

The design of the suspension componentry aims to allow the manufacturing process to involve heated flat sheets of FRP stamped into a three dimensional preform shell and subsequently installed over a moulded foam core. After the addition of some small, high performance attachment point preforms at certain high stress areas, the assembled preform is transferred to a heated steel tool for resin injection.

MARKET ANALYSIS

As equally important to the development of the design and manufacturing for the component are the market and financial considerations of using an FRP material in a market dominated by traditional materials and manufacturing methods. The consideration of these aspects on a concurrent basis with design and manufacture are not necessarily new to the company. However the project provides a forum for the successful combination of all of these aspects.

In the truck industry today, there is, and has been in the past, a limited application of composites and plastic materials. This can be partly explained by the overall truck industry's lack of acceptance of new material technology in structural applications. There has been widespread use of composites and plastic materials in tertiary applications in the cabs of trucks, especially of FRP. There are many components used in structural applications on trucks that have only been modified slightly in design over a period of decades in order to meet perhaps a heavier application. In cars Ford [5], Mercedes [6] and Rover [7] are examples of automotive manufacturers who have applied FRPs to structural applications in development work. The market acceptance of new components, conceptually different from the current products, is a big concern. This needs to be developed in order to estimate the sales-volume, selling-price/sales-revenue for an expected time period which would involve producing a business plan. Albion Automotive through the development of these new products hopes to enter new markets with possibly new product ranges.

Financial Implications

The use of composites is on an exponential increase with their application being applied across a wide field of technology. Fibre-reinforced composites, play an essential role in the aerospace industry where their properties have earned huge savings by reducing mass and providing the possibility for better aerodynamics, leading to huge fuel savings (one of the biggest costs in the industry). From the very early days of considering whether to use a new material or not, it is necessary to consider the financial aspects. Usually, there has to be an understanding first of the technical aspects of a new material. However, as soon as an assessment of the potential technical and performance benefits has been gained, it is then necessary to commence an assessment of the financial implications of the use of such a new material.

Commonly it is found that the initial use of the new material appears to increase the cost of production rather than decrease it. A new material may be in small-scale production compared with bulk production for previously-used materials and consequently costs much more per unit weight or volume. There is a requirement for the forward projections of output quantities and raw material volume-needs, in order to see how the price of the incoming raw material would fall with increased production. Also, a re-assessment of the design of the proposed new product is necessary to determine the benefits of the new material. These can be used to further reduce the number of components in the product giving parts consolidation leading to more efficient manufacturing procedures. From this procedure, other design benefits which can further give an overall reduction in production costs may arise.

The costs of new skills needed to carry through the R & D exercise and later manufacturing implementation needs to be taken into account early. This will include the increased cost of recruiting and training new skills in the areas of research work, design work and engineering

work. The later stages may involve the need for recruitment and training of manufacturing staff with better qualifications.

Tooling costs would be substantial area of concern when a new material/product is to be implemented. Composites can provide a reduction in tooling costs. For example, if RRIM materials are used instead of straight thermoplastic materials it is possible to not only reduce the cost of a moulding machine from potentially several hundred thousand pounds to several tens of thousands of pounds but the tooling costs drop from an average of many tens of thousands of pounds to merely some thousands of pounds [8].

At the initial stages in the product evaluation a market research assessment is necessary to determine the potential for the product. This will assess the customers' understanding of the product which the company is trying to sell them. The customer may have had no previous dealings with composite components and therefore be unaware of its potential when compared to traditional materials such as steel and aluminium.

The on-going costs which a manufacturer will have to consider include the increased cost of the up-keep of the new skills in research, design, engineering etc., which have been recruited. The comparison in the form of a cost benefit analysis will consider the new plant requirements, installation and maintenance. This would initially identify whether the new plant would be more profitable than the old plant (this would not be strictly applicable if the new plant was for the manufacture of a new product and was not for replacing existing machinery). The material costs are probably one of the initial hurdles to overcome in that composites are generally more expensive than the traditional metals but as production volumes increase this will decrease. The cost of new test procedures and test facilities must be taken into account. Often there is a higher cost initially with new materials than with the older materials since frequency of testing is usually higher in the early years. If the new material has been chosen wisely this cost usually declines to less than previous costs when adequate experience has been gained. From the above considerations the immediate and recurring costs can be estimated and combined to give an overall estimate of the costs of replacing the existing material/component with the composite material/component.

CONCLUSIONS

The TCS project outlined is providing Albion Automotive with an excellent opportunity to become an industry leader in the development of FRP automotive structural components. The research and development stages integrate material suppliers, educational establishments and the customers. A high profile approach backed with sound marketing can help the company create and sell such a product. The customers will have to be made aware of the benefits of such a product with any uncertainties in its ability to withstand the working conditions. A single marketing strategy is not suitable for application to the marketing of a new component manufactured from composites due to the current lack of market presence of composite components in the truck industry especially in the primary structural side of the market. Composites require an integrated design approach. Drucker [9] indicated that there are two distinct types of manufacturing industry: material based and information/knowledge based. This highlights that today the major driving force in the world economy is not the availability of materials but the availability of technology based innovation.

In the manufacture of composites components it is possible to target niche markets with economical short production runs. This is due to the design flexibility offered by composites which is necessary for the “fast to market” requirements of a flexible multi-vehicle chassis component manufacturer. The economic advantages are the reduction in costs associated with machining hours, assembly time, automated processes and lower cost modular tooling that could be adapted to suit a range of components.

In the company’s future strategic development involving FRP materials the TCS project between Albion Automotive and the University of Strathclyde is an excellent example of the two way transfer of technology from the university to industry. The adoption of a fresh approach to the design of existing components for application in composite materials using suitable composite design guidelines will ensure the success of the project for all parties involved. The project illustrates a successful product development process designed to give the desired performance for the optimum use of material with the manufacturing process concurrently developed alongside.

REFERENCES

Historical information taken from Albion Automotive marketing literature.

1. Day, G.S *Strategic Market Planning: The Pursuit of Competitive Advantage*, St Paul, M.N: West Publishing Co,1992.
2. Smith, G *Design Methodology for Application of Engineering plastic in Structural Components*. University of Warwick. Internal publication.
3. Fowler. G, Phifer. S, Annual Conference, Composites Institute, The Society of the Plastics Industry, Inc. February 7-9, 1994.
4. Beardmore,P., *Composite Structures for Automobiles*, Composite Structures, Elsevier Applied Science Publishers LTD, 1986.
5. Kuch, I, Daimler-Benz AG, Basic and Product Research , *Development of FRP Rear Axle Components*, Materials and Processing- Move into the 90`s.1989.
6. Smith, G.F., Pinfold, M., Walker, M., Elmendorp, De Groot, H.R. *Design and Fabrication of a Composite Subframe*, University of Warwick. Internal publication.
7. Reasbeck, P, OBE. *The Financial Aspects of Using New Materials*, Paper No.5 of PROMAT Profit Through Materials Technology, published by the National Engineering Laboratory. 1987.
8. Martin, M.J., *Understanding Composite costs: Comparison of Five Fabrication Techniques*, 46th Annual Conference, Composites Institute, The Society of the Plastics Industry, Inc. February 18-21, 1991.

A SYSTEM FOR THE DESIGN AND AUTOMATED LAY-UP FOR THE MANUFACTURE OF COMPOSITE COMPONENTS

Rodney Peck¹, Israel Herszberg¹, Sabu John²

¹ *Royal Melbourne Institute of Technology, Department of Aerospace Engineering, The Sir Lawrence Wackett Centre for Aerospace Design Technology, GPO Box 2476V, Melbourne, Victoria, 3001, Australia*

² *Department of Manufacturing Systems Engineering, Royal Melbourne Institute of Technology, Bundoora East Campus, Bundoora, Melbourne, Victoria, 3083, Australia*

SUMMARY : This paper describes the development of a low cost system for the automated manufacture of composite laminates made from prepreg and dry fabric. Tackling the task of laying up composites via robotic means requires more than just mechanical ingenuity. A systems approach needs to be employed which focuses on the area adding most to a parts quality namely the design engineer. Development of the overall systems architecture has evolved by having the design engineer as the focal point. The result of this is that, not only the software and systems, but also the hardware is developed about this focus point. Automation used for the layup process enables the plies to be layed and consolidated according to the requirements of the design engineer. Information generated during the engineering draping analysis is used to control the automation. An important feature of the automated process is the relatively simple low-cost hardware used to achieve the required draping and consolidation of the plies. The system is designed for cost effective manufacturing by minimising human intervention during manufacture and the maximum exploitation of a unified computer database.

KEYWORDS: Automated Layup, Robotics, CAD/CAM/CAPPS, design for manufacture (DFM)

INTRODUCTION

Several attempts have been made to automate the layup process with varying success. In all, the result has been to provide a means for mechanically laying up the material, with little regard for the upstream processes, such as design and analysis. There has been very little synthesis between CAD/CAM and CAPPS in developing automated layup systems [2-5] although Jarvis et al [1] have made some significant inroads into synthesising the tasks. Because of the highly directional nature of fibrous composites, the misalignment of fibres whilst draping the material can produce parts with properties much different to those used by the engineer during analysis. This means that the design/analysis of the composites must be an integral part of any automated layup system for it to be used successfully in industry. Identifying that the engineer provides a pivotal role in determining a parts quality, means that the human must be considered at all stages of development from system design right through to the design of the automation.

SYSTEM PHILOSOPHY

Having the human as the focus means that the less tangible aspects of human performance need to be considered when developing the hardware for the system. These include ensuring the system provides an environment in which the design engineer is encouraged and supported in attempting to provide optimally designed parts. Such a system needs to allow the parameters used in defining the layup in the design stage to be used during manufacture so as to ensure the parts made are representative of the parts designed and analysed.

Defining the layup for a composite requires the path used to lay the ply to be fully defined. The reason being that the in plane shearing of the fabric that occurs whilst rolling out a layup path is what determines the final orientations of the fibres. Invariably the path is not considered during the design stage and hence during the layup there exists little control over replicating the orientations used in design whilst laying up. Having the path defined as part of the design allows the layup to be performed so as to replicate the path chosen. The end result is control of the fibre orientations at the design stage. Existing projects focus not on the engineer, but more on the mechanical means for holding and manipulating the fabric. As a result, the orientations for the fibres need to be assessed while performing the layup, wasting time and money, and resulting in a system unable to respond quickly to the demands of the market - thus detracting from the quality of the part.

The automation used had to reflect the demands of the system objectives, this resulted in the need to predict, upfront, the constraints imposed upon the fabric from the handling device. This could have been done using the most common handling technique of using multiple grippers and analysing their effects on constraining the ply deformation during layup. A system by Buckingham et al [2] used a similar system in which the fabric deformation was used to control the position of the ply grippers during layup. The system however, imposed a restriction on the design engineer in that the use of many grippers results in a modified draping path in order to avoid collisions between the draping robot and the grippers holding the ply. In addition the extra automation required to hold more complex plies results in increasing complexity and expense.

The system decided upon looked at clearing the entire ply area of obstructions to enable a draping path to be specified by the design-engineer, and then followed uninterrupted by the automation during layup. In addition, the system had to obviate the need to reconfigure for different shaped parts, allowing the creativity of the engineer to be exploited as optimal solutions to the part layup were investigated.

The structure of the system aims to provide a means for producing identical parts from the one set of process plans. In this way the part produced can be used as direct feedback for the engineer on its performance.

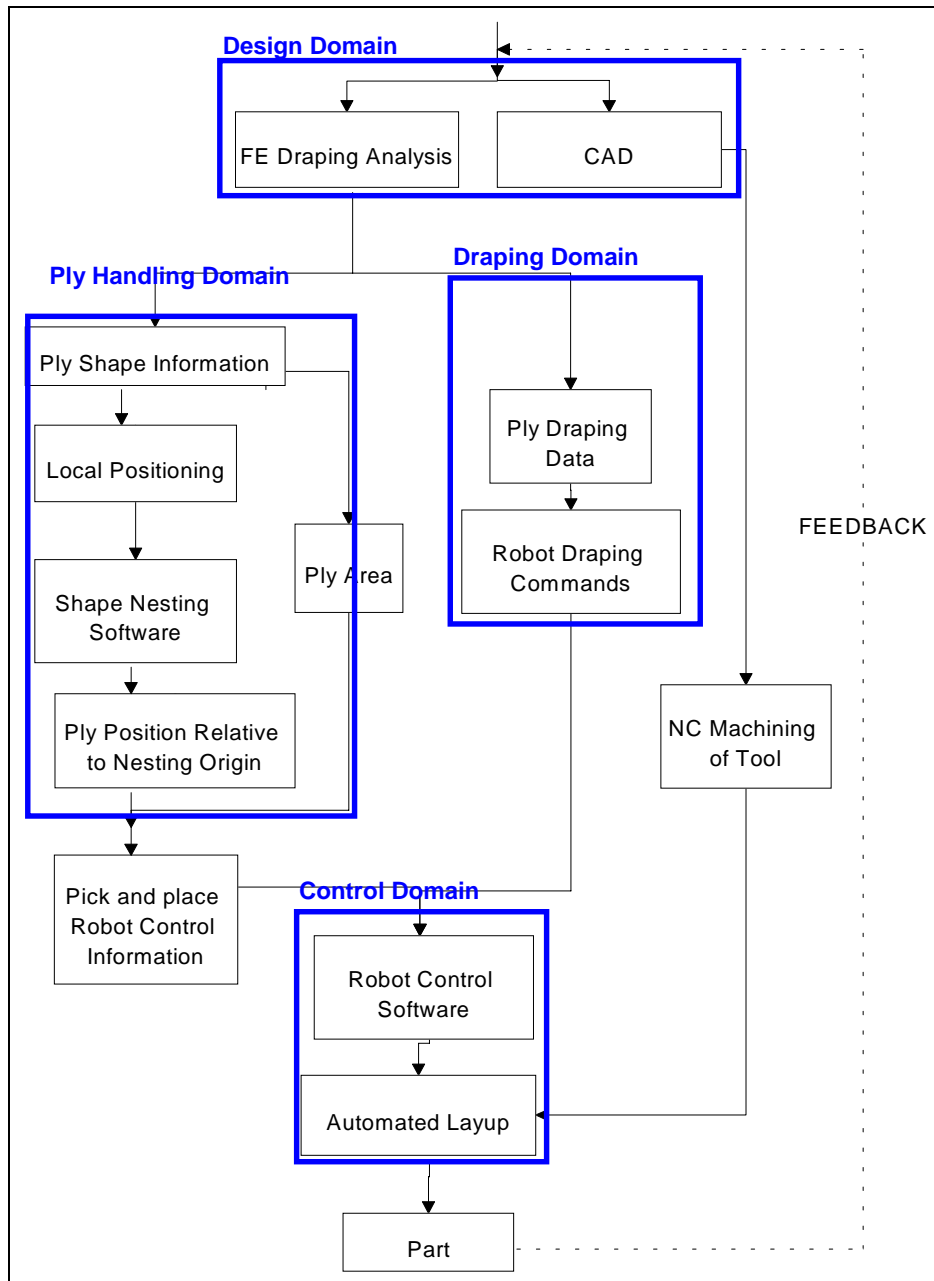


Figure 12: System Structure

COLLISION AVOIDANCE

Collision avoidance was a key issue in developing a system that focussed on the engineers decisions. If each ply needed to undergo a collision analysis to prevent the handling and draping robots from hitting one another, the draping path from design to final product is altered and the information flow becomes cluttered. This leads to reduced speeds at which the products can reach their market. Additionally, the specific design information defining the composite would be lost. The loss of information arises as robot programmers define the path needed to drape the ply to avoid collisions, hence, effectively designing the products properties by altering the fibre directions. Robot programming necessarily contains some form of manual interaction, in most cases a large portion. Again, this would reduce the ease and speed at which a product could be transformed from design to finished part.

Of the automated layup systems published, very few tackle 3D broadgoods layup, as such flat box style end effectors have sufficed for handling, avoiding the need for complex robotic manipulation. Buckingham et al [2], and Ruth et al [4], both developed systems that layed up onto 3D surfaces. Buckingham laying up onto complex curved surfaces and Ruth only onto developable singly curved surfaces. Both provide solutions for laying up using automation, however, neither provide a simple method for handling varying shaped ply without the loss of draping information. As such, they do not provide a method for effectively laying up in an environment that encourages quick time to market.

The crucial issue was to ensure the final layup was as defined by the engineer. Achieving this requires careful design of the automation and in particular, the overall system.

END EFFECTORS

Several robotic handling devices to date have been tested, none producing satisfactory results. This is due to the restrictions placed on the automation in trying to create the desired working environment. The handling devices tested have all been of a flat pad variety, as this satisfies the criteria for uninterrupted draping of the picked up ply, and also allows any shaped ply to be held. Restricting the shapes the engineers can use, restricts the creativity used during design and was considered inappropriate. Past work by Jarvis[1] and Kolluru[6] successfully used flat boxes for picking up the material. The major difference with these two projects and this one, is the objective in this project to lay up onto complex curved surfaces. For this, the pad needed to be very flexible.

The initial trials produced a suction pad that could hold and release the material without difficulty, performing the same basic tasks that both Jarvis and Kolluru's performed. Problems were encountered, however, when selectively picking of the ply from within its nested position. To overcome these, tests were performed to determine the height at which the suction could be applied and still lift the ply. 4 mm was found to be a rough practical limit. Any ply within the 4 mm distance could be picked up, while the ply at 5 mm distance did not have the pressure differential created across it to be lifted by the suction pad. To selectively pick the ply, the pad needed to be pressed down at one point on the ply causing the ply to be sucked onto the pad. The pad and ply were then raised approximately 5 mm off the table. At this time the suction throughout the rest of the pad was activated which resulted in the parts of the ply nearest the attachment point to be sucked up onto the pad, until the entire ply was sucked up onto the pad. This method was fraught with problems, in hindsight, being a little ambitious. The pad required far too much power to apply the necessary suction, mainly due to the pressure gains along long lengths of small diameter tubing. And, due to the large air flow rate needed, the tubing supplying the suction across the pad was large and resulted in a stiff pad, unable to follow complex curved surfaces. However, for the manipulation of plies without the need to selectively pick them from a nested position, as in Kolluru's case, this end effector pad works well. For the problem at hand, however, it was not sufficient.

Work is continuing on developing an end effector suitable for the specified work environment.

CELL AUTOMATION

The automation cell used to trial the system philosophy consisted of two robots, one materials handler and the other for draping. A Mitsubishi Movemaster was used for performing the

simple pick and place movements; and a Yamaha MXY for draping. An additional degree of freedom in the vertical plane was attached to the Yamaha, allowing X, Y, Z and horizontal rotational positioning. In addition to this the rotational degree of freedom of the Yamaha was supplemented with an end effector able to rotate in the vertical plane. This was used for orientating the end effector so that it was normal to the tool surface. The resulting configuration allowed for positioning of the end effector normal to the surface anywhere over the three dimensional contoured tool. Although the setup provided many limitations (one of the major ones being that three separate controllers were being used to control the positioning) its purpose was to set a base structure for a manufacturing cell capable of working with the system philosophy.

The Movemaster was used to hold a frame with the pad attached. Using only one robot for robot handling limited the size of the ply to test pieces of around 250 mm square. The Yamaha had an airline attached, capable of applying 20 N of force onto the ply, a force found by [1] and individual tests, to be representative of light manual rolling. Using air pressure to generate the force meant that larger forces were possible for those regions that were difficult to lay (ie. required more shearing force to fit the contour). Positioning of the Yamaha was controlled from data extracted from the computer draping model.

The basic procedure involved sending the pick and place robot the coordinates (extracted from a shape nesting file) for picking up the ply. The ply was picked up and moved to the correct position in the tool, at which point the draping robot forces the ply down using pressurised air. The path traversed by the robot is defined by the design engineer in the computer draping model. This path, along with the tool surface geometry, define the resulting fibre orientations and ply shape.

When finished the proposed operations are for the draping robot to move away, clearing the area, and the pick and place robot to return for the next ply. The afore mentioned problems with the end effector for handling the ply has prevented a full run of the system to be performed to date.

SOFTWARE

The software is used to provide a means for effortlessly convert the computer model of the part into process plans for laying up. It does this by searching the computer model for the data needed to develop the process plan. The process plan for controlling the automation is automatically generated for each of the plies in the model. Once generated, the process plan can be executed at the computer terminal. To use the software, an interface is used, Figure 2, in which the user simply chooses the computer model file, and the file containing the nested ply data. Next the button labelled '1- Run Analysis' is pressed to analysis the data and generate the process plans. This step generates:

- the information for scanning the flat ply
- coordinate data to control the draping robot over the contoured surface (Figure 3)
- coordinate data for controlling the robot to locate and place the ply
- data for operating the high pressure air lines during layup
- the entire process plan for laying up the part (a program created by combining the results from 1-4)

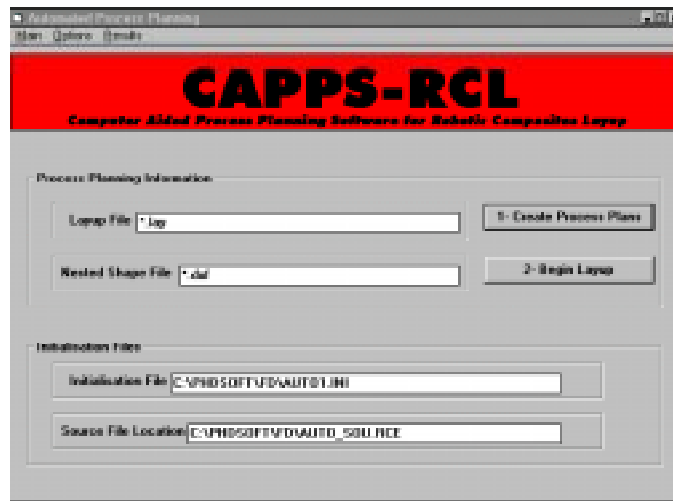


Figure 13: Software Interface

Following the generation of the plans the user will then be able to press the button ‘2- Begin Layup’ and activate the automation to begin the layup.

In the test case, no automated cutter was available so positioning of cut plies has been done by hand to represent the location of a nested ply cut using an automated cutter. A file containing the relative positions of the automation is created by the user when the automation is first set up. The positioning of plies was achieved using a common axis system throughout the entire computer design process, and referencing this in the beginning to the cutting table origin. The software uses this common axis system to generate the final process plan.

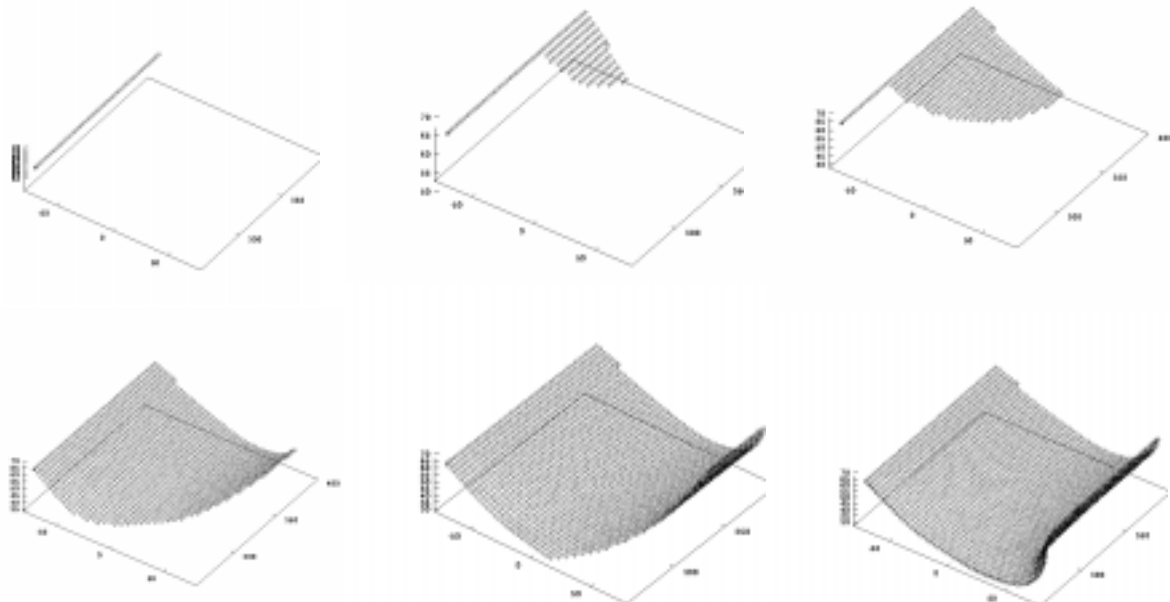


Figure 14: Computer generated draping sequence

CONCLUSIONS

A system philosophy has been created with the objective of improving the quality of laminated composites in regards to the demands of today's global work environment. In doing this the focus has been on developing a system able to provide the design engineers with the means for realising their designs during manufacture. The software has been developed that simplifies the process such that the engineer remains the focus, and although the hardware to compliment the system has been tested as a trial manufacturing cell with mixed success, the basic principles for a workable system have been tested.

REFERENCES

- [1] S. D. H. Jarvis, Wilcox, K., Chen X.Q., McCarthy R., Sarhadi M., "Design of a Handling Device for Composite Ply Lay-up Automation," *IEEE*, 1991.
- [2] R. O. Buckingham and G. C. Newell, "Automating the Manufacture of Composite Broadgoods," *Composites Part A*, vol. 27A, pp. 191-200, 1996.
- [3] G. C. Newell, R. O. Buckingham, and K. Khodabundehloo, "The Automated Manufacture of Prepreg Broadgoods Components - a Review of the Literature," *Composites Part A*, vol. 27A, pp. 211-217, 1996.
- [4] D. E. Ruth and P. Mulgaonkar, "Robotic Lay-up of Prepreg Composite Plies," presented at IEEE International Conference on Robotics and Automation, 1990.
- [5] R. B. Hans-Joachim Becker, "Industrial Multi-arm Handling System for Automated Manufacture of Composite Broadgoods," *17th June 1992 IEEE Colloquium Multi-arm Robotics*, 1992.
- [6] R. Kolluru, K. P. Valavanis, A. Steward, and M. Sonnier, "A Flat-Surface Robotic Gripper for Handling Limp Material," *IEEE Robotics and Automation Magazine*, 1995.

MODELING OF LAMINATED COMPOSITE STRUCTURES FOR COMPUTER AIDED DESIGN AND MANUFACTURING SYSTEMS

Takeshi Takatoya¹, Isao Kimpara² and Kazuro Kageyama²

*¹Airframe Division, National Aerospace Laboratory,
7-44-1 Jindaiji Higashimachi, Chofu-shi, Tokyo 182, Japan*

*²Division of Engineering, The University of Tokyo,
7-3-1 Hongo, Bunkyo-ku, Tokyo 113, Japan*

SUMMARY: The present paper aims at developing computer aided design and manufacturing systems for laminated composite structures, in order to achieve light-weight structures. As laminated panels were made by layup process step by step, laminated composite structures are handled not only as materials, which modeling is used in general purpose systems, but also as stratum structures. Then a new model of laminated composite structures is proposed in the present paper, which modeling is based on object oriented inheritance concept. According to the new modeling, some prototypes of CAD/CAE/CAM systems are developed and demonstrated. It shows that the developed systems are effective in designing lamination, analyzing laminated panels with finite element analysis and assisting of manufacturing tool mold.

KEYWORDS: modeling, CAD/CAE/CAM, object-oriented language, shell structure, light-weight structure, design methodology, layerwise analysis, tool mold manufacturing

INTRODUCTION

Advanced Composite Materials (ACM), such as Carbon Fiber Reinforced Plastics (CFRP), have recently been applied to shell structures which are required stiffness and strength for out-plane pressure and light-weight. For example, shell structures are America's cup challenging yachts, wing panels of small aircraft and so on. ACM have a big potential for archiving a light-weight structure, however, material design, structural design and fabrication technology should nearly be entangled in achieving a significant weight saving.

In design process of composite structures, material design, structure design and manufacturing process design are closely related with each other. Then, many design simulations are involved, such as selections and combinations of constituent materials, determinations of fiber orientation angles, determinations of laminate stacking sequences, choices of failure criteria, determinations of cutting and layup plans and so on [1].

It should be efficient to apply computer systems in the design process, however, the conventional CAD/CAE systems are not suited for the design of composite structures in the point of design flexibility. Because they have been developed mainly for isotropic materials, anisotropic laminated materials have been put in an additional position [2]. For this reason,

the present paper insists that computer aided design and manufacturing systems for composite structures have need to be developed.

MODELING OF LAMINATED COMPOSITE STRUCTURES

In order to develop computer aided design and manufacturing systems for laminated composite structures, a new model of laminated composite materials is required. The conventional modeling which are applied in conventional CAD/CAE systems, take laminated materials as only material data for each finite element. This modeling involves two problems. One is that lamination would be dependent on finite elements as shown in Figure 1. The other is that stacking sequences would be converted to different materials. This cause many materials in the structures.

As laminated materials were made by layup process step by step and laminated materials were put together to structures, laminated composite structures should be handled not only as materials but also as stratum structures. In the present paper, laminated composite structures consist of five stratum, that is, fiber and matrix as base materials, lamina, ply, laminated structure, main structure as shown in Figure 2. Lamina is composed of fiber and matrix, which means that lamina has thickness, strength and modulus as single-ply plate. Ply means that lamina is defined on tool mold with some area and fiber direction. Laminated structure consists of plies with stacking sequence. After laminated structures are treated as stratum structures in the computer systems, a designer can easily make models of laminated structures according to the images.

CONCEPTS AND CONSTRUCTIONS OF DEVELOPING A SYSTEM

It is one of purposes in the present paper, that computer systems are developed by using of the new model. Figure 3 shows a flowchart of laminate design and process design. The computer aided design and manufacturing systems should have three characteristic points, as follows: laminate definition easily and high response to design change, layerwise structural analysis and evaluation easily and making tool mold accurately.

LAMINATE DEFINITION AND DESIGN CHANGE

A mold is necessary for curing laminate plates. It is considered two ways in the coordinates with which laminate plates are defined. One is global coordinates, the other is surface oriented coordinates which are origin on the mold. A designer define a laminate concerned with direction of fiber as surface oriented coordinates and laminated area as global coordinates. As coordinates are converted each other in the systems as shown in Figure 4, a ply is defined easily with some area and fiber direction.

It is important to change design easily in the point of design spiral. The adaptation of the new model made it possible to response easily to design change in the developed systems. The indispensable data should be used properly in design, analysis and manufacturing with the use of scope controls.

In the present paper, the developed systems were suggested to be programmed by object-oriented language C++ [3]. It is possible that laminate stratum structures are defined accurately by classes and class inheritances in object-oriented languages, and it is easy to change laminate design by replacement of classes.

LAYERWISE STRUCTURAL ANALYSIS AND EVALUATION

After definition of laminates, it is efficient to analyze structures by means of finite element methods. Since finite element meshes belong to the laminated structure model, design change requires regeneration of meshes. In the view point of design spiral, it is desirable to generate finite element meshes automatically.

In the present paper, automatic mesh generation was achieved by means of mapping functions. The fundamental is square orthogonal base was mapping to quadrangle field on the surface. And a finite element is formulated as a thick shell element, in which special attention is paid to anisotropic principal axes, which are one of the most important characteristic of composite materials [4].

In a laminate, as the properties of layers are very different each other, then it is necessary to analyze layerwisely. And it is also required to display and evaluate stresses about each layer. That is to say, a layerwise postprocessor system is required. It is made possible to display same layer extend over different stack sequences, in spite of discrepancy in layer numbers, in the developed systems.

ASSISTING OF MAKING TOOL MOLD

In general, large scale composite structures are made by using of male mold or female mold. Female mold method is the method which is available to get accurate surfaces of product. However it costs very high. If smooth male mold was used, outer surface becomes uneven, then product need to be puttied to smooth surface. It is required to make products with smooth surfaces by using of male mold.

In the developed systems, stacking sequences and layup areas are defined on mold surfaces. Then it is easy to generate surfaces which are offset from smooth outer surfaces with thickness of laminates. Figure 5 shows a schematic of relations between mold surfaces and lamination. It is available that an uneven male mold is made by using of numerical controlled cutting machine with the generated surface data. After lamination of every plies on the uneven mold, it hopes that product has smooth surfaces.

EXAMPLE OF DEVELOPED SYSTEMS

The result of a hull of IOR cruiser under uniform pressure was introduced and discussed for example of the developed systems.

Figure 6 shows a schematic of IOR cruiser which is made by using of another surface CAD system [5]. Figure 7 shows a output of the developed systems, when IGES data was read in the systems. The laminate was defined uniformly [0/45/-45]_s in the developed systems. A keel line was fixed as boundary condition and uniform outer pressure was loaded. After finite elements were generated and calculation, the results of longitudinal stress distributions in the 45deg. layer are shown in Figure 8.

As the calculated stress is exceeded allowance, lamination has to be changed as shown in Figure 9. The finite element meshes were changed as shown in Figure 10. Figure 11 shows distributions of longitudinal stress of each plies in the developed systems, which means that it

is possible to display same layer extend over different stack sequences, in spite of discrepancy in layer numbers.

After lamination design finished, offset surfaces are generated in the systems. Figure 12 shows a schematic view of offset surfaces on the local coordinates which are projected to hull surfaces.

CONCLUSIONS

The new modeling of laminated composite structures is proposed, which is based on the concept that laminated composite structure consists of five stratum: fiber and matrix, lamina, ply, laminated structure, main structure. According to the new modeling, some prototypes of CAD/CAE/CAM systems was developed by means of object oriented language. the systems has been demonstrated. It has been shown that these systems are effective in the point of designing, analyzing and manufacturing of laminated composite structures.

REFERENCES

1. Miki, M., and Sugiyama, Y., "Expert Systems for Composite Design with Object-Oriented Language", Proc. Japan-U.S. CCM-V,1990
2. Bernardon, E., Lee, T. and Luby, S.C., "Composite Fabric Design Tool", Proc. 38th Int. SAMPE symposium, 1993, pp. 2077-2082
3. Kimpara, I., Kageyama, K. and Takatoya, T., "Development of Computer Aided Design Systems for Advanced Composite Marine Structures", Proc. Japan-U.S. CCM-VII, 1995, pp.709-716
4. Takatoya, T., Kimpara, I. and Kageyama, K., "Development of Computer Aided Design and Manufacturing System for Advanced Composite Marine Structures(3rd Report: Application of Finite Element Analysis for Anisotropic Laminated Materials)", J. S. Naval Arch. of Japan, Vol.178, 1995,pp.593-599 (In Japanese)
5. MacSurf Pro v5.3, Decision Japan Corp., 1995

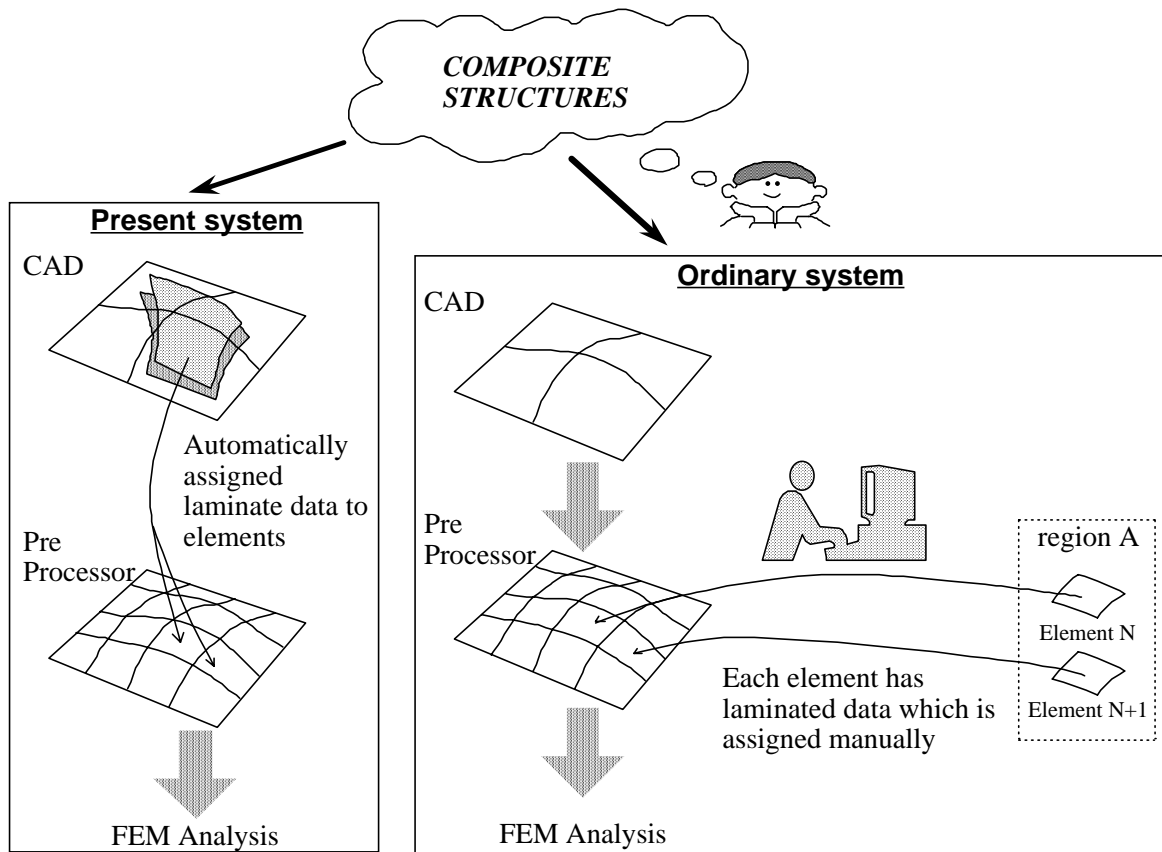


Fig. 1: Relations between lamination and finite element in the ordinary system

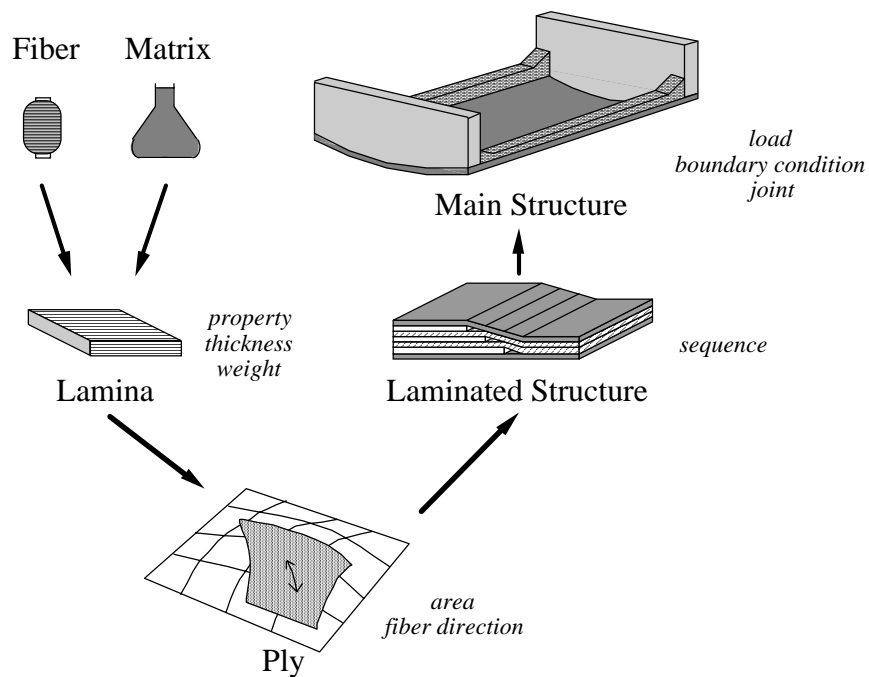


Fig. 2: Stratum of laminated composite structures

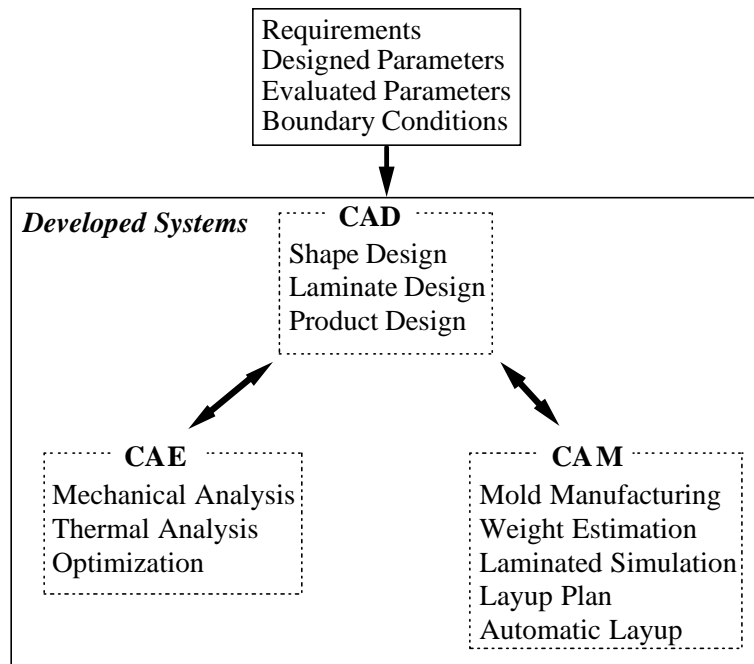


Fig. 3: Flowchart of laminate design and process design for composite structures

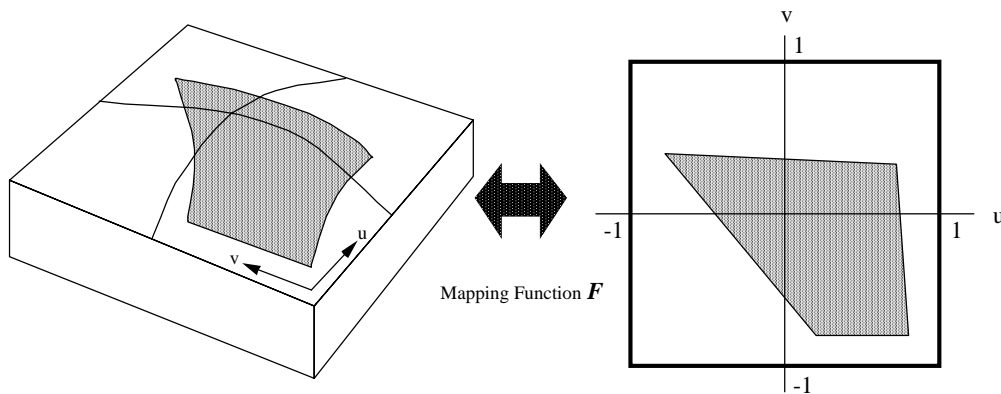


Fig. 4: Relations between local coordinate and global coordinate

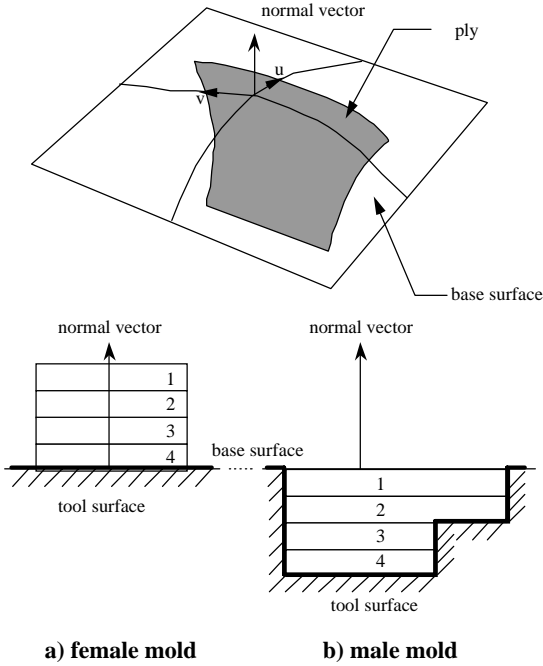


Fig. 5: Relations of laminates and base surface on male and female mold

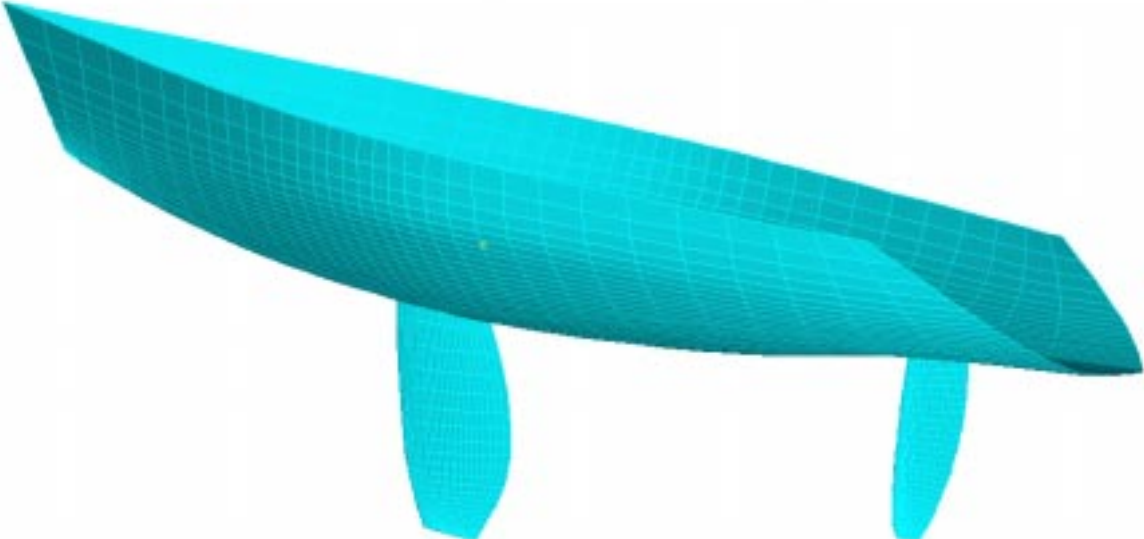


Fig. 6: Schematic of IOR cruiser

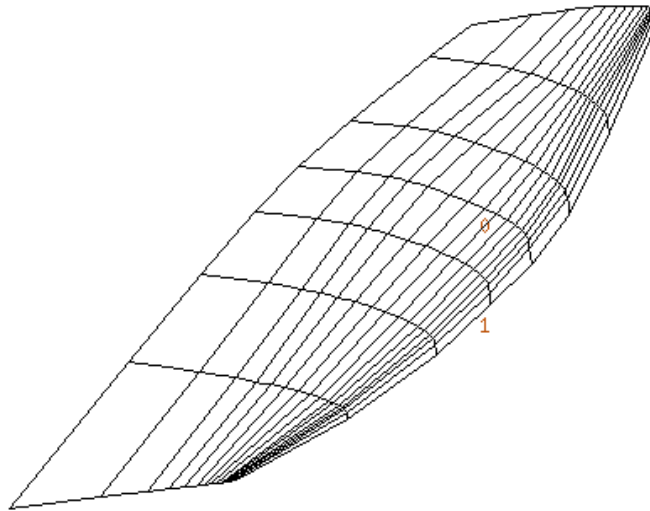


Fig. 7: Output of graphical user interface when IGES data was read in

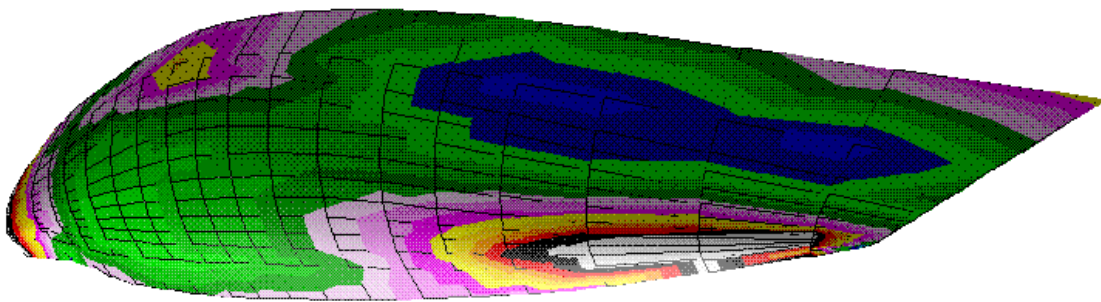


Fig. 8: Distributions of longitudinal stress of IOR hull under pressure

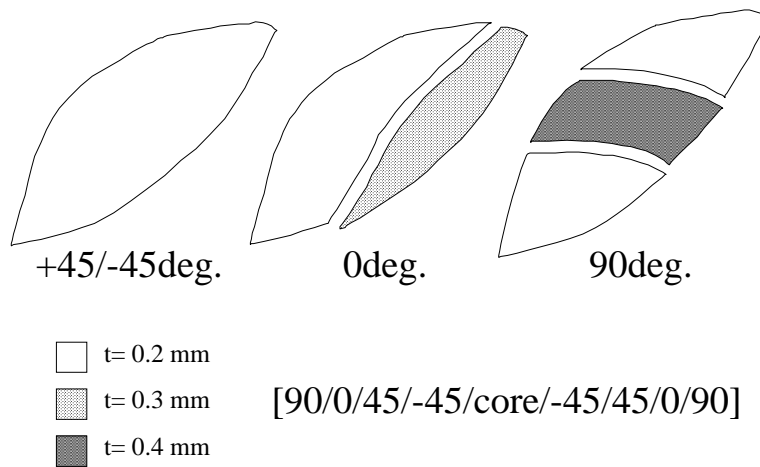


Fig. 9: Schematic of lamination plan

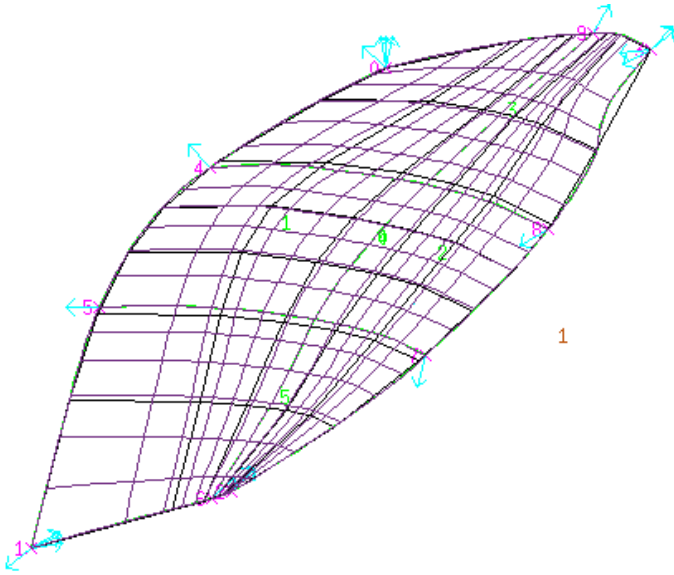


Fig. 10: Finite element meshes after changing lamination

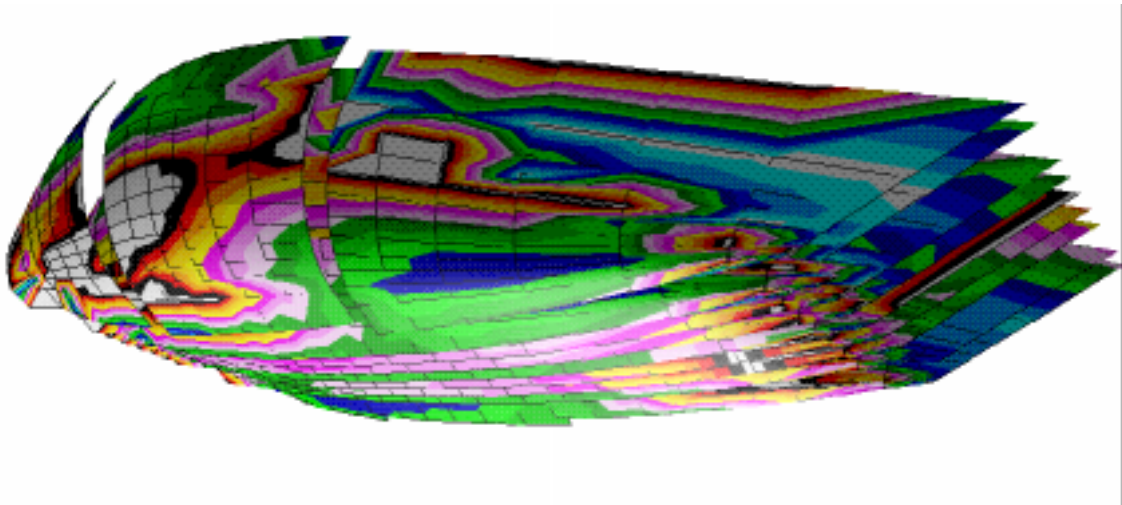


Fig. 11: Distributions of longitudinal stress in every layer after changing lamination

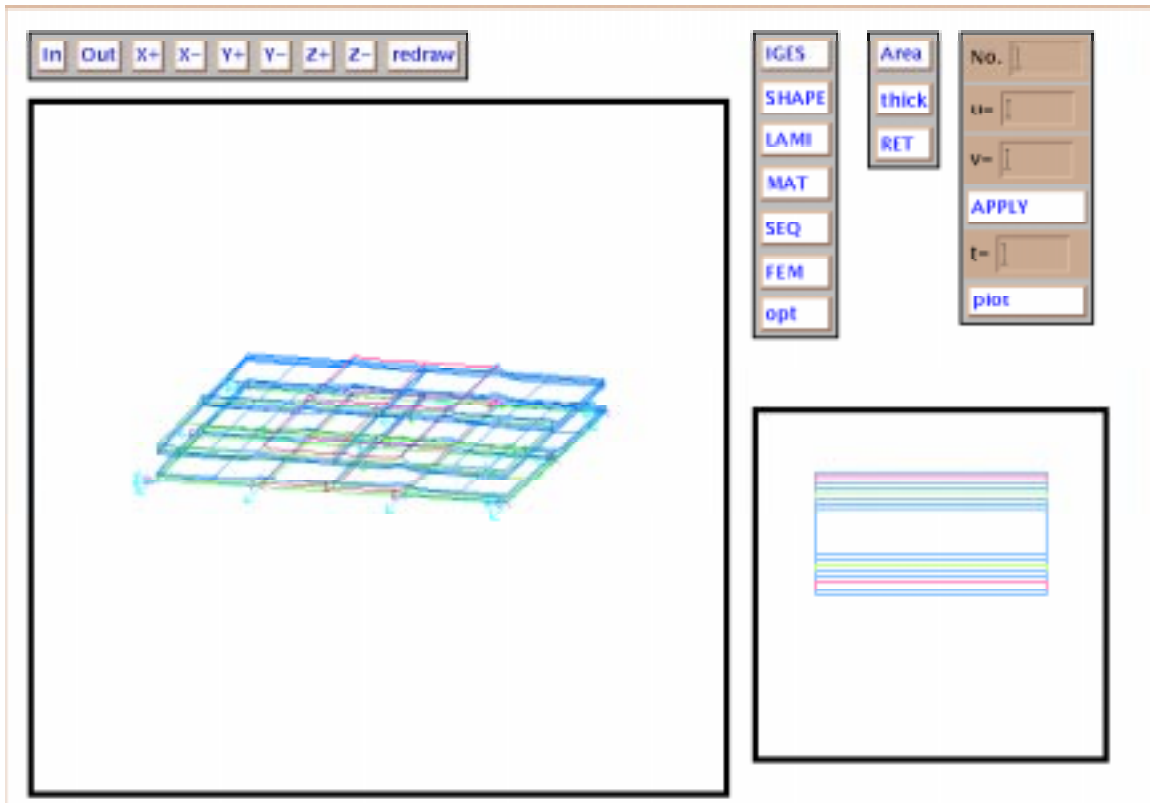


Fig. 12: Schematic of male mold surface in local coordinate

THE DESIGN AND APPLICATION OF TAILORED FIBRE PLACEMENT

P.J. Crothers¹, K. Drechsler², D. Feltin³, I. Herszberg¹, M. Bannister⁴.

¹*Sir Lawrence Wackett Centre for Aerospace Design Technology, Royal Melbourne Institute of Technology, P.O. Box 2476V, Melbourne, Victoria, 3001, Australia.*

²*Daimler Benz AG, Research and Technology, P.O.Box 80 04 65, 81663 Munich, Germany.*

³*Institute for Polymer Research, Dresden, Hohe Straße 6, D-01069 Dresden, Germany.*

⁴*Cooperative Research Centre for Advanced Composite Structures (CRC-ACS) Ltd, 506 Lorimer Street, Fishermens Bend, Victoria, 3207, Australia.*

SUMMARY: Tailored Fibre Placement (TFP) is a highly automated fibre preforming process based on embroidery technology. Its main advantage, compared to other textile technologies, is the ability to arrange the reinforcing fibres in any direction in the plane (0° - 360°) in curvilinear format. This paper reports on the design methodologies which promise the best exploitation of the TFP technology. Several of these methodologies were tested in their abilities to relieve a stress concentration in a notched composite. The design and manufacture of the components is described, with the testing setups used and results of testing also being presented. TFP was shown to offer distinct advantages in areas of stress concentrations.

KEYWORDS: tailored fibre placement, composite design methodologies, notched composites.

INTRODUCTION

The anisotropic properties of fibre reinforced composites are not being fully exploited. Maximum mechanical properties, like strength and stiffness, only exist along the fibre direction. If this direction differs from that of the applied stress, the effective properties are reduced. Flexible production equipment designed or adapted to take advantage of fibre-composite anisotropic properties can improve quality and strength-to-weight characteristics, and reduce costs.

Tailored Fibre Placement (TFP) is an invention of the Institute of Polymer Research Dresden (IPF-Dresden). The process, based on the well-known embroidery technology, is highly automated. The main advantage of TFP, compared to other textile technologies, is the ability to arrange the reinforcing fibres in any direction in the plane (0° - 360°) in curvilinear format. The fibre layup of the embroidery machine is numerically controlled, ensuring high accuracy, and the machine controlling program is generated by computer-aided design. The process is described in detail in a separate paper [1].

In combination with innovative design and production techniques, TFP shows excellent potential for the creation of a great variety of textile preforms fibres aligned in the stress field and in the third direction. Well established automated design and production technologies ensures short times from design initiation to preform production and makes TFP an exceptional fast prototyping technique.

This paper reports on the design methodologies which promise the best exploitation of the TFP technology. Several of these methodologies were tested in their abilities to relieve a stress concentration in a notched composite. The manufacturing of the components, the testing setups used, and testing results are also presented.

DESIGN METHODOLOGIES

Composite materials are unique because they allow the engineer to design the material to meet the specific application. Unlike isotropic, homogeneous materials, the directional dependence of strength and stiffness of these materials can be tailored to match the loading environments of the structural elements. Fibre reinforced composite materials are particularly versatile in this regard. The individual layers, indeed, the individual fibres, can be orientated to align their principal material directions with the principal load directions.

Recently, computer-aided or -created design techniques have been under investigation. The coupling of Finite Element Modelling/Analysis (FEM/FEA) with increasingly powerful computing power has allowed researchers to produce optimised structural designs using the algorithm of their choice.

Curvilinear Fibre Placement Design Philosophies

Traditionally, the tailoring of fibre reinforced composite structures has been done by varying the orientation of straight-fibre prepregs or the total thickness of the laminate. Recent developments in manufacturing techniques, such as fibre and tow placement technologies, make it possible to fabricate composite structures with fibre orientations that vary from one location to another. For flat panels, varying the orientation of the fibres along the plate axes results in a curved fibre format.

Mattheck [2] introduced a method known as Computer Aided Internal Optimisation (CAIO). The CAIO method calculates the principal stress trajectories along which the shear stresses are zero. Orientating the fibres along these trajectories, one obtains a pattern in which there are no shear stresses between the fibres. After several iterations when the fibre adjustment required becomes negligible, the procedure is finished and the final fibre pattern has been produced.

Hyer *et al.* [3,4] developed a similar methodology, using finite element models of panels with curvilinear fibre format to improve strength and buckling performance. This philosophy modelled an increase in tensile failure load of up to 89% when compared to a baseline quasi-isotropic laminate. However, buckling loads were adversely effected, rendering up to a 15% decrease compared to the baseline. A buckling optimised design increased the modelled buckling load by up to 197% but was impractical for manufacture due to discontinuity in fibre directions. A compromise design yielded 30% improvement in buckling load and a 35% improvement in tension load. This result shows that both multiple load cases such as buckling and tensile properties can be improved using the curvilinear fibre concept.

Cooper [5] adapted energy methods for isotropic structures to establish optimal conditions for 'trajectorial reinforcement'. He found that the fibre orientation for maximum or minimum stiffness or strength was dependent on the elastic constants and the ratio of the principal stresses. Cooper concluded that "trajectorial reinforcement is inherently highly efficient, and more so than conventional reinforcement methods, when applied to structures or structural or mechanical parts in which the principal trajectories are distinctly non-linear." This statement points distinctly toward the complex states of stress found in the area of a stress

concentration. Therefore, what Cooper refers to as ‘trajectorial reinforcement’ is most advantageous in complex states of stress such as stress concentrations. He found that trajectorial fibre reinforcement yields an estimated 47% reduction in the stress concentration factor for a notched composite plate.

Kelly [6] reported on a procedure to map load paths. He defines a load path as the trajectory taken by a unit of applied load through a structure from the point of application to the points where they are reacted. It was noted that the equations proposed by Kelly state that there is a substantial shear stress between the fibres. This implies that the resin of the fibre composite must carry a shear load. The shear load could perhaps provide the critical loading in the lamina.

An example of the different paths mapped by the load path and principle stress algorithms is given in Fig. 1.

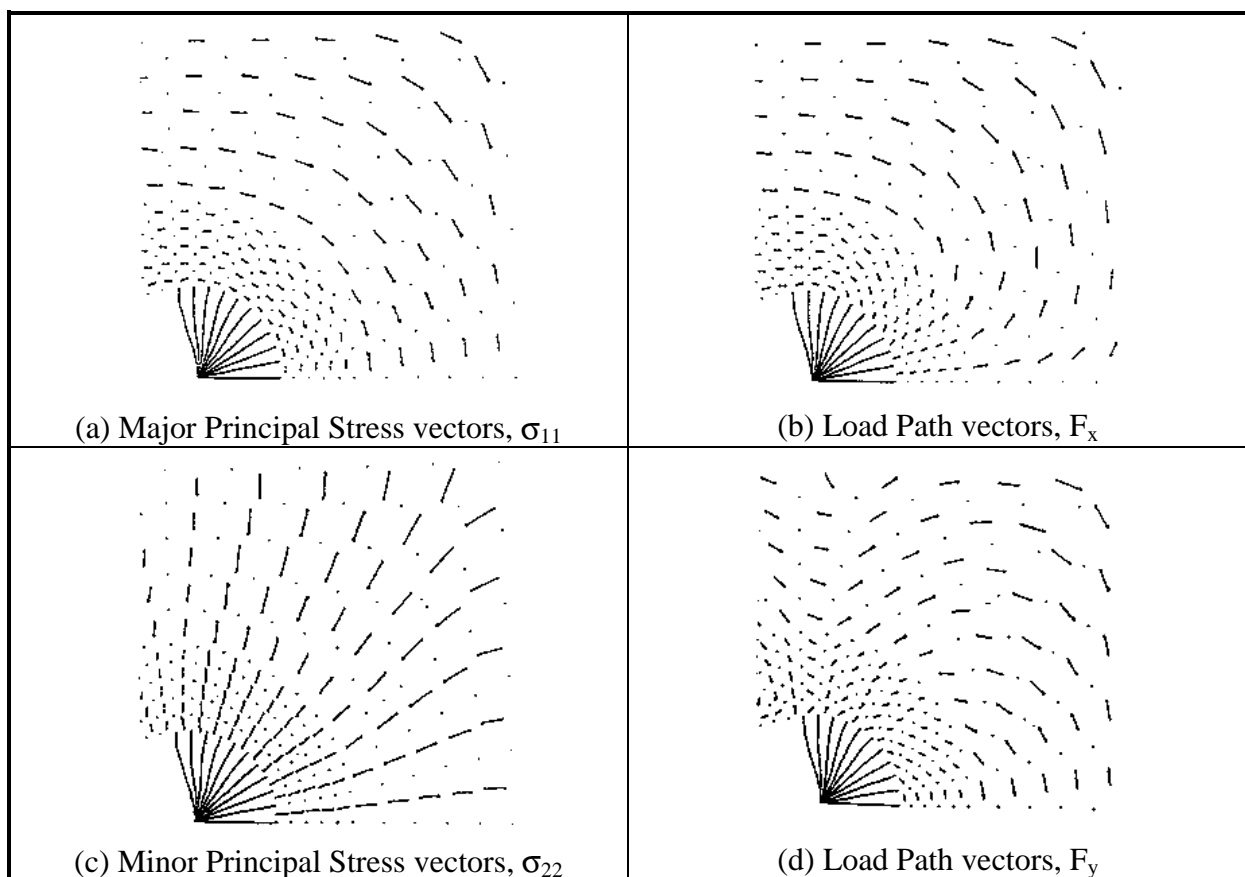


Fig. 1: Principal stress and load path vectors near a loaded hole [6].

Sensitivity studies offer perhaps the most flexible method of fibre placement design. Designing in this way will ensure that the part is optimised in the form desired and critical failure criteria are met. For example, the advantages of the CAIO algorithm seem to be limited to load cases which impart a tensile loading on the reinforcement fibres. If you were to use the CAIO for a load case which is critical in buckling, the fibre design yielded would not give the optimum buckling strength, as is demonstrated by the studies of Hyer *et al.* [3,4].

Several restrictions must be placed on a design algorithm for a true optimum design to be yielded. Manufacturing restrictions must also be considered.

EXPERIMENTAL DETAILS

Test Component Selection

The application chosen to test the fibre placement design methodologies was a notched plate creating local stress concentrations. Due to the low productivity of the TFP process in producing a fabric surface when compared to weaving, it was concluded that TFP should be used to provide local reinforcement to a base material. A quasi-isotropic Multi-axial Warp Knitted (MWK) fabric, representing a typical structure, was chosen as the base material. It was delivered as a four layer fabric $[0^\circ/45^\circ/90^\circ/-45^\circ]$ of 1 mm thickness and an areal weight of 1000 g/m^2 . Both the TFP and MWK were glass fibre due to its common usage in industry and its lower cost when compared to carbon fibre. RTM6 resin was chosen due to its well defined properties, and its common usage in industry. Fig. 2 shows the test component specifications.

The tension plate was designed for open-hole tension. The bearing plate was designed for a bolt loaded in double-shear. The dimensions of the bearing plate were chosen such that edge distance to bolt diameter ratio (e/D) = 4 and the part width to bolt diameter ratio (W/D) = 4.

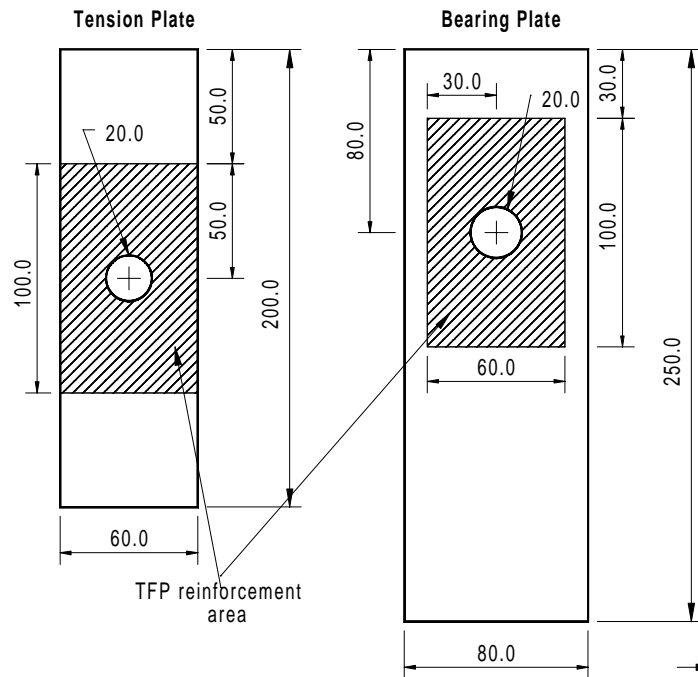


Fig. 2: Test component specifications.

TFP Design

The design for the local reinforcement of the notched plate was completed using the CAIO program of Ref. 2 and the Load Path algorithm of Ref. 6. Fig. 1 shows the calculated directional vectors for each algorithm and Fig. 3 shows the resultant fibre patterns for each load case. These patterns were compared to a pattern used in Ref. 7 which showed dramatic improvements over optimised, straight-fibre layups. This pattern will be referred to as “Star”.

TEST PROCEDURES

A bolt of 20mm diameter was used for load introduction in the case of bearing. Lateral constraints in the form of washers (ϕ 45mm) were used on the bolt to reinforce against loading in the third direction. It was endeavoured to create a 2-dimensional loading case as was modelled in the FEM calculations. Both the open-hole tension and bearing components were loaded at rate of 5mm/min.

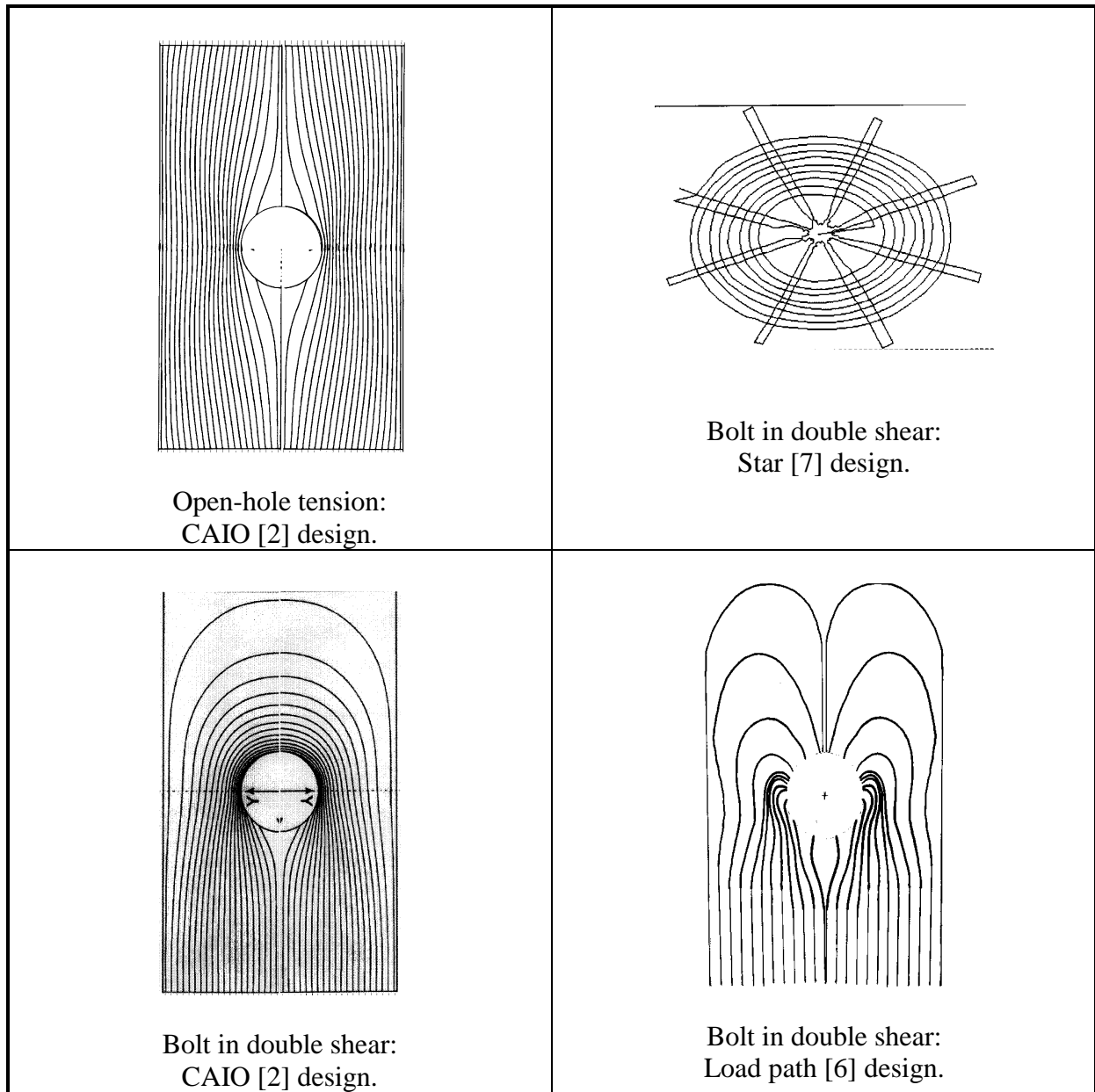


Fig. 3: Resultant fibre patterns for TFP reinforcement of test components.

Test Component Manufacture

In addition to the testing of different TFP design algorithms, several different methods of manufacture were investigated. The basic methods of component infiltration were wet Resin

Film Infusion (RFI) and Vacuum Bag Resin Infusion (VBRI). The three different manufacturing cases used were:

- (1) TFP directly on the MWK base material (being preformed as halves) before VBRI infiltration. Bond halves together. *To be used only for the tension plate,
- (2) MWK base material infiltrated using RFI. TFP preforms produced on thin, non-structural base material and infiltrated using VBRI. Bond TFP on MWK, and
- (3) TFP preforms produced on thin, non-structural base material and hand stitched on MWK base material before RFI infiltration.

For manufacturing case (3), several layup variations were trialed for the bearing plate. Fig. 4 shows the formats used. Table 1 shows the designations used. In the bulging sections, it was necessary to accommodate the locally varying cross section of the TFP reinforcement. Pressure was applied across the full surface by the use of silicon rubber sheet on both sides externally supported by solid metal caul plates. In the flat cases only the metal caul plates were used.

Six test pieces of each designation (Table 1) were manufactured and tested. The fibre volume fractions of the MWK base material was very consistent ($V_f \approx 50 \pm 2\%$). However, these fractions varied in the areas of TFP, depending on the manufacturing format (up to 60-65%).

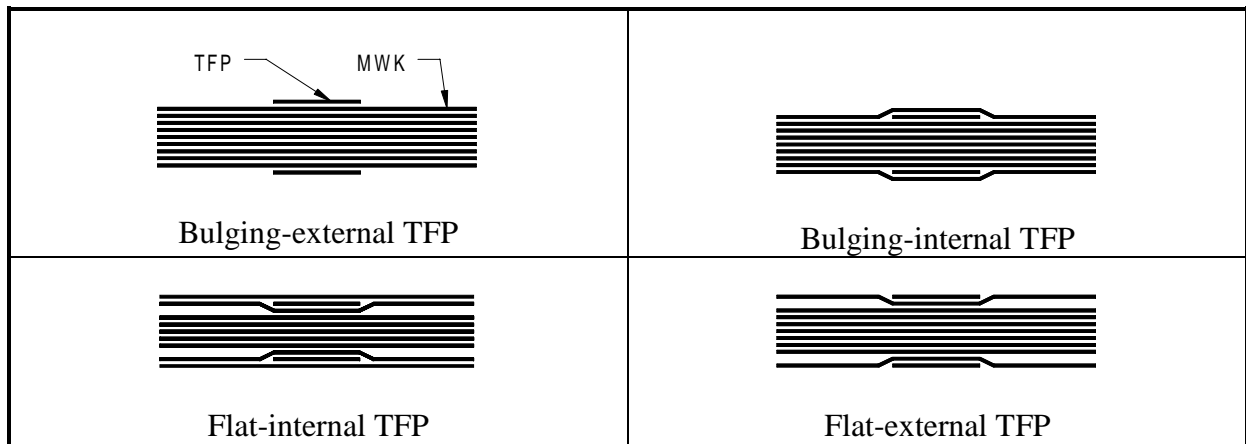


Fig. 4: Layup variations for the bearing plate in manufacturing case (3).

Table 1: Component designation format.

Tension Plate	Bearing Plate
A: No hole.	A: No reinforcement.
B: No reinforcement.	B1: CAIO design, manufacturing case (2).
C1: CAIO design, manufacturing case (1).	B2: CAIO, (3), flat-external.
C2: CAIO design, (2).	B3: CAIO, (3), bulging-internal.
C3: CAIO design, (3), bulging-external.	B4: CAIO, (3), flat-internal.
	B5: CAIO, (3), bulging-external.
	C1: Star, (2).
	C2: Star, (3), bulging-external.
	D1: Load path, (2).
	D2: Load path, (3), bulging-external.

RESULTS & DISCUSSION

Tension Plate with Open Hole

Fig. 5 shows the results of open hole testing. The test components with TFP all exhibited similar failure patterns. Initial failure was due to tension failure of the TFP reinforcement at the net section. Due to the diminished strength of the TFP reinforcement, the failure then emulated the modes observed for MWK basic material without reinforcement, i.e., shear failure initiated at the hole edge. The failure of the TFP reinforcement in tension is ideal. The CAIO design philosophy places the fibres in pure tension or compression to gain its ultimate strengths. This failure mode shows that the reinforcement fibre is used to its full potential.

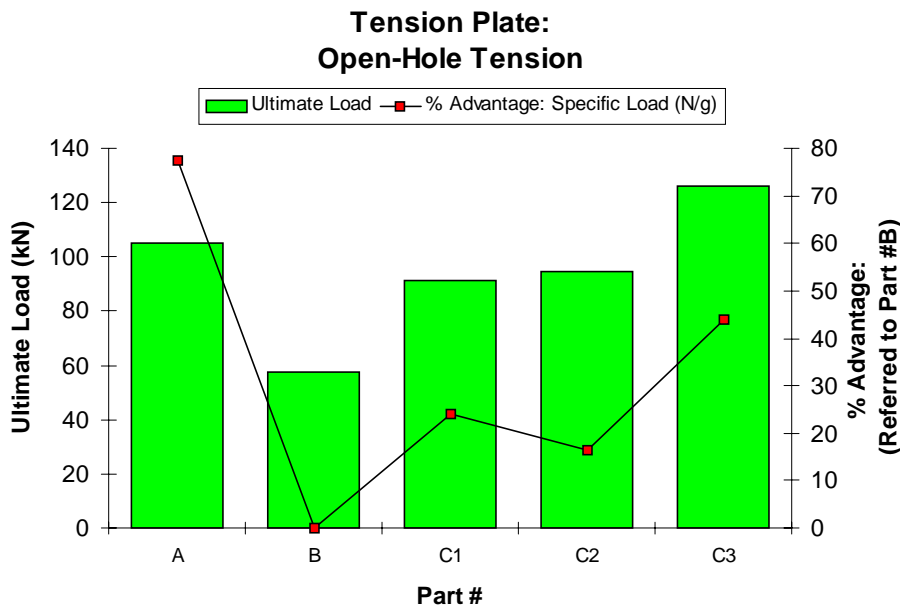


Fig. 5: Results of testing of open-hole tension testing.

Interlaminar stress transfer between the reinforcement and basic material was most efficient in manufacturing case (1) and (3) where the composite was moulded as one piece allowing fibre nesting between the TFP and MWK reinforcement fibres. However, direct TFP on the MWK basic material, in case (1), caused damage to the basic material, due to average stitching densities of up to 30 stitches/cm², and reduced the failure loads of the test piece in tension. In manufacturing case (2), the adhesive layer reduces the efficiency of stress transfer between the TFP and MWK and also adds significant weight to the test piece. Manufacturing case (3) provided the stress transfer efficiency of case (1) without stitching damage. For these reasons, manufacturing case (3) provided the best specific load characteristics.

It should be noted that the addition of just two layers of CAIO designed TFP reinforcement was capable of more than doubling the maximum load of the test component. In addition, the surface area of the TFP reinforcement was not optimised, only the fibre structure, so that the ideal weight savings were not realised. Hence, the realised 45% improvement in specific strength can be enhanced dramatically.

Bearing Plate with Bolt in Double-Shear

Bearing failure was the only mode of failure observed in all component testing. Fig. 6 shows the typical loading behaviour of bearing plates with and without TFP reinforcement. The unreinforced part (A-3) is subject to catastrophic failure at a stroke of ~1.75mm. In contrast,

catastrophic failure for TFP-reinforced components was generally between 4-7mm. The addition of TFP reinforcement does not increase the bearing stiffness of the component. Also, minor failure or a losses of bearing stiffness can be seen at approximately the same stroke as failure of the unreinforced component. However, the component is still able to support an increasing load at a slightly lower stiffness. The TFP supports the bearing area after initial failure by transferring the critical loads to other less stressed areas of the component. In the Fig. 6, the ultimate load of the TFP reinforced component has been doubled and the stroke to failure is over three times that of the unreinforced component.

The segmented failure behaviour of a TFP reinforced component could be quite valuable in service. Damage to the component could be detected at loads well below ultimate allowing repairs or replacement.

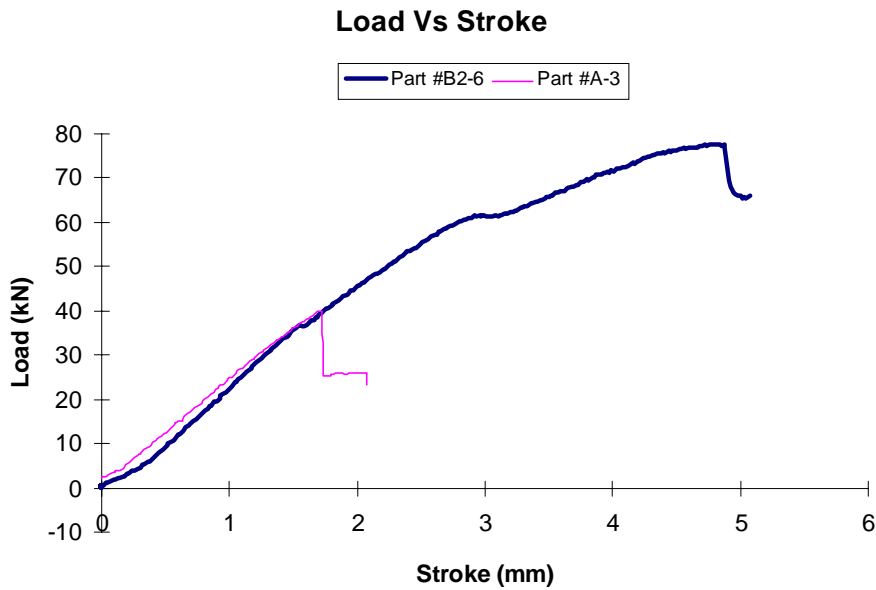


Fig. 6: Loading behaviour of bearing plates.

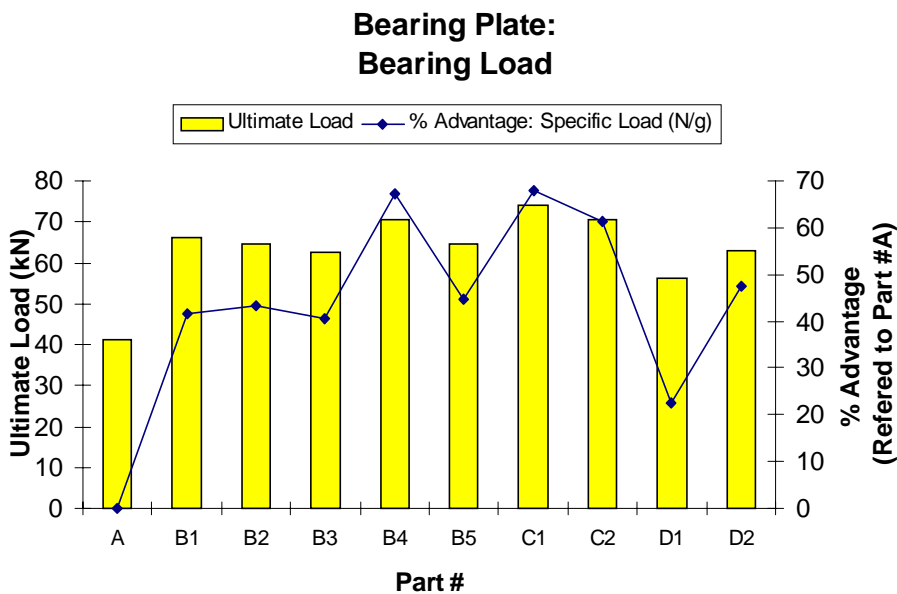


Fig. 7: Results of bearing testing with reference to bearing load.

In all cases, the addition of TFP increased the ultimate and specific loads yielded (Fig. 7). When compared to the unreinforced components, the percentage increase in specific load gained was between 23-68%. The greatest increases in specific load were shown by the Star design and the B4 variation of the CAIO design. The Star design has the advantage of being able to place the greatest mass of reinforcement in the critical bearing area and thus yielding higher loads without a significant increase in component weight. The B4 variation of CAIO also has the advantage of placing a higher fibre volume ($V_f \approx 65$) in the critical bearing area of the part. This is due to the increased compaction to give the component a flat surface. The use of the TFP reinforcement internally (B4) serves to limit interlaminar stresses and delamination of the TFP from the base material and thus gains a higher load than for the external TFP variation (B2). However, from the ultimate and specific loads alone the efficiency of the fibre patterns is still unclear.

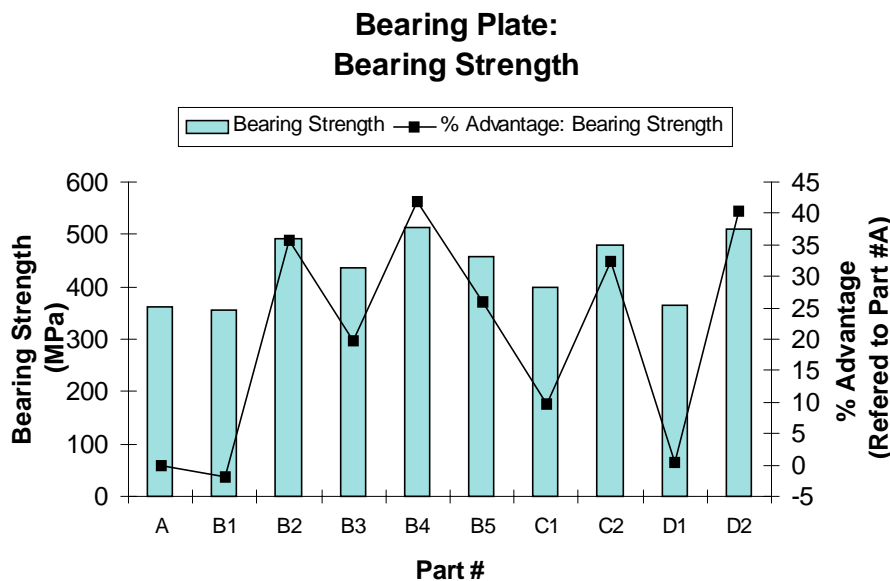


Fig. 8: Results of bearing testing with reference to bearing strength.

The bearing strengths of Fig. 8 show the efficiencies of the various component formats. The bonding of TFP reinforcement (components B1, C1, & D1) is the least efficient conversion of fibre properties. The layer of adhesive adds thickness to the part without a proportional increase in bearing resistance. The highest increase in bearing strength in this case being only 10%. In one-piece moulding, the greater efficiency of the flat variations of CAIO (B2 & B4) when compared to the bulged variations (B3 & B5) is due to the compaction of the same mass of fibre reinforcement into a smaller thickness. This gives a higher fibre volume fraction in the critical bearing area which decreases in the areas of lower stress away from the hole. In the flat variations, internal TFP (B4) shows greater efficiency due to its greater resistance of interlaminar shear and delamination. In the bulged variations, external TFP (B5) shows better bearing characteristics due to the base material remaining uncrimped and thus exhibiting its full strength.

The most efficient fibre patterns for bearing applications are shown in the comparison of the bulging-external TFP configurations (B5, C2, & D2). The most efficient pattern is given by the Load Path design methodology (D2). This is surprising because this pattern has the least amount of fibre in the critical bearing area. However, the design places fibres in opposition to the load input and thus allows direct compression of the reinforcement fibres. In contrast, the

CAIO design places fibres perpendicular to the incoming load, reducing their effectiveness to an inverse of their longitudinal properties. The Star design has a combination of both but lacks the ability to transfer the load away from the hole as efficiently as the Load Path design.

CONCLUSIONS

A study has been undertaken to investigate the application of Tailored Fibre Placement (TFP) to reinforce a notched, fibre reinforced composite component. Several different design and manufacturing variations have been tested in open-hole tension and bearing loading using a bolt in double-shear. Several trends of behaviour of the TFP reinforcement were established:

- a 45% increase in load can be yielded when using TFP reinforcement for open-hole tension,
- up to a 67% increase in specific bearing load can be yielded when using TFP reinforcement,
- p to a 45% increase in bearing strength can be yielded when using TFP reinforcement.

TFP supports the bearing area after initial failure by transferring the critical loads to other less stressed areas of the component. In all cases, the ultimate load of the TFP reinforced component has been doubled and the stroke to failure is over three times that of the unreinforced component.

The Load Path methodology yields the most efficient design for bearing because it provides fibres in direct opposition to the load and a path to transfer the load away from the critical area.

The TFP is used most effectively when it is used in a flat-internal configuration giving higher volume fractions in the areas of higher stress. This configuration gives a higher fibre volume fraction in the critical bearing area and also greater resistance of interlaminar shear and delamination.

Using TFP in a notched composite shows distinct advantages in both loading behaviour and ultimate loads reached. Combined with the appropriate design and manufacturing methodologies, its applications to areas of stress concentration, higher strength, and/or higher stiffness shows tremendous potential.

ACKNOWLEDGEMENTS

Mr Crothers would like to thank the Cooperative Research Centre for Advanced Composite Structures (CRC-ACS), Daimler Benz AG, and the Institute for Polymer Research-Dresden (IPF-Dresden) for their support during all stages of the research presented.

REFERENCES

1. Feltin, D., Gliesche, K. (1997) "Preforms for Composite Parts Made by Tailored Fibre Placement." To be presented at ICCM-11.
2. Mattheck, C. (1994) "Design in Nature." *Interdisciplinary Science Reviews*, Vol. 19, No. 4. The Institute of Materials. pp. 298-314.
3. Hyer, M.W., Charette, R.F. (1991) "Use of Curvilinear Fibre Format in Composite Structure Design." *AIAA Journal*, Vol. 29, No. 6. pp. 1011-1015.

4. Hyer, M.W., Lee, H.H. (1991) "The Use of Curvilinear Fibre Format to Improve the Buckling Resistance of Composite Plates with Central Circular Holes." *Composite Structures*, Vol. 18. pp. 239-261.
5. Cooper, A.A.G. (1972) *Trajectorial Fibre Reinforcement of Composite Structures*. Ph.D. Thesis. Sever Institute of Washington University, St Louis, Missouri.
6. Kelly, D.W. (1996) "Load Path Calculations and Applications Using Finite Element Analysis." *First Australasian Congress on Applied Mechanics*. Feb. 21-23. pp. 625-630.
7. Mueller, J. (1975) *Spannungsverteilung an gelochten ueber einen Bolzen belasteten Staeben aus kohlenstoff-faserverstaerktem Kunststoffe*. Ph.D Thesis, Zuerich.

APPLICATION OF EVOLUTIONARY ALGORITHMS TO BUCKLING DESIGN OF FRP LAMINATED CYLINDRICAL SHELLS

Yoshio Aoki¹ and O-II Byon (Goichi Ben)²

¹ *Department of Precision Machinery Engineering, College of Science & Technology,
Nihon University, 7-24-1, Narashino-dai, Funabashi, Chiba, 274, Japan*

² *Department of Mechanical Engineering, College of Industrial Technology, Nihon
University, 1-2-1, Izumi-cho, Narashino, Chiba, 275, Japan*

SUMMARY: The objective of this study is the optimum buckling design of a filamentary laminated circular cylindrical shell subjected to axial compression and/or external pressure using evolutionary algorithms. The shell is composed of FRP orthotropic laminates whose principal axes coincides with the shell axes. In order to maximize the buckling load of simply supported FRP laminated cylindrical shells, the optimization of stacking sequence is studied by use of evolutionary algorithms. After various genetic parameters including the population size, the probability of mutation and the probability of crossover are tuned by the trial calculations, the evolutionary algorithms which are the combination of the global search by a genetic algorithm with local search algorithm is proposed.

KEYWORDS: stacking sequences, genetic algorithm, FRP, optimization, buckling, cylindrical shell, numerical analysis, evolutionary algorithms, orthotropic laminates

INTRODUCTION

In recent years, a FRP laminated cylindrical shell have been widely used in space vehicles and pressure vessels due mainly to their potential for creating significant weight savings relative to metals. It is necessary to give full consideration to the buckling strength for the various kinds of loading such as axial compression, shear, bending and external pressure. Although, a buckling analysis of the FRP laminated cylindrical shell was carried out by many researchers, the design of an optimum satcking sequences that maximizes a buckling load calculated was a few. Hirano[1] investigated the buckling problem of six-ply, axially-compressed cylindrical shell. Starting from different initial points, his optimization procedure converged at different local maximum, and showed the multi-maximum characteristics of the objective function. Nshanian and Pappas[2] also used a nonlinear programming to determine the optimum design of laminated cylindrical shell having symmetric laminates about the mid-surface. Onoda[3] proved that the buckling load of laminated cylindrical shell was uniquely determined by 12 lamination parameters for any given material characteristics of the layer. Sun[4] developed a two-step optimization procedure combined Powell's method with a random search.

The efficiency of this procedure demonstrates for four-ply laminated cylindrical shells of various length-to-radius ratios involving three typical material systems. In the case of the nonlinear programming, it is pointed out that the optimum solution changes from the difference of the initial values. And, it is important that an optimization algorithm is able to search a global optimum solution. The genetic algorithm (GA) is recently applied to the

various optimization of composite structures [5]-[7] and is widely noticed as a new key to solution of optimizations problem.

The objective of this study is the optimum buckling design of a filamentary laminated circular cylindrical shell subjected to axial compression and/or external pressure using evolutionary algorithms. The shell is composed of FRP orthotropic laminates whose principal axes coincides with the shell axes. In order to maximize the buckling load of simply supported FRP laminated cylindrical shells, the optimization of stacking sequence is studied by use of evolutionary algorithms. After various genetic parameters including the population size, the probability of mutation and the probability of crossover are tuned by the trial calculations, the evolutionary algorithms which mean the combination of global search by a genetic algorithm with local search algorithm is proposed. In addition, EA is also applied to the multi-objective optimization that searches the maximum buckling load of FRP laminated cylindrical shell under axial compression and external pressure.

BASIC EQUATION

Let the mid-surface of the circular cylindrical shell be the reference surface, and the origin of the coordinates be located at one end of the cylindrical shell, as shown in Fig.1. The coordinates x , y and z are the axial, circumferential, and normal directions, respectively. The cylindrical shell has length L , radius R , and thickness t . Under the assumption that i th ply contains the same number of fibers in the $+\theta_i$ and $-\theta_i$ directions and they uniformly distribute through the thickness, the coupling stiffness coefficients of A_{16} , A_{26} , B_{16} , B_{26} and D_{26} in the laminates vanish. Using the linear strain displacement relations and the classical laminate constitutive relations, the shell buckling equations can be derived as follows.[8]

$$\begin{aligned}
 & A_{11}u_{,xx} + A_{12}(v_{,xy} + \frac{w_{,x}}{R}) - B_{11}w_{,xxx} - B_{12}w_{,xyy} + A_{66}v_{,xy} + A_{66}u_{,yy} - 2B_{66}w_{,xyy} = 0 \\
 & A_{66}v_{,xx} + A_{66}u_{,xy} - 2B_{66}w_{,xxy} + A_{12}u_{,xy} + A_{22}v_{,yy} + A_{22}\frac{w_{,y}}{R} - B_{12}w_{,xxy} - B_{22}w_{,yyy} = 0 \\
 & B_{11}u_{,xxx} - B_{12}v_{,xxy} + 2B_{12}\frac{w_{,xx}}{R} - D_{11}w_{,xxxx} - 2D_{12}w_{,xxyy} + 2B_{66}v_{,xxy} - A_{12}\frac{u_{,x}}{R} + 2B_{66}u_{,xyy} \\
 & - 4D_{66}w_{,xxyy} + B_{12}u_{,xyy} + B_{22}v_{,yyy} + 2B_{22}\frac{w_{,yy}}{R} - A_{22}(\frac{v_{,y}}{R} + \frac{w}{R^2}) - D_{22}w_{,yyyy} + N_x w_{,xx} + N_y w_{,yy} = 0
 \end{aligned} \tag{1}$$

where u , v , w are displacements in the x , y and z directions, respectively. N_x , N_y are stress resultants (positive in the case of compression); A_{11} , B_{11} , D_{11}and D_{66} are components of the stiffness matrices[9] and subscript with comma indicates partial differentiation. The solutions to Eq.(1) are assumed to be

$$\begin{aligned}
 u &= u_{mn} \cos(\bar{m}x) \cos(\bar{n}y) \\
 v &= v_{mn} \sin(\bar{m}x) \sin(\bar{n}y) \\
 w &= w_{mn} \sin(\bar{m}x) \cos(\bar{n}y)
 \end{aligned} \tag{2}$$

where $\bar{m} = m\pi/L$, $\bar{n} = n/R$; m is the number of half-waves in the x -direction, n is the number of waves in the y -direction. These displacement functions satisfy the S-2 simply-supported

boundary conditions (that is : $w=0, M_x=0, N_x=0, v=0$). Substituting Eqn(3) into Eqn(1), the buckling loads N_x and N_y of the FRP laminated cylindrical shell under axial compression and the external pressure can be derived as a solution of an eigen value problem

$$N_x = \frac{(T_{11}T_{22} - T_{12}^2)T_{33} + 2T_{12}T_{13}T_{23} - T_{13}^2T_{22} - T_{23}^2T_{11}}{m^2(T_{12}^2 - T_{11}T_{22})} \quad (3)$$

$$N_r = \frac{(T_{11}T_{22} - T_{12}^2)T_{33} + 2T_{12}T_{13}T_{23} - T_{13}^2T_{22} - T_{23}^2T_{11}}{n^2(T_{12}^2 - T_{11}T_{22})}$$

where

$$T_{11} = -(A_{11}\bar{m}^2 + A_{66}\bar{n}^2)$$

$$T_{22} = -(A_{66}\bar{m}^2 + A_{22}\bar{n}^2)$$

$$T_{12} = (A_{12} + A_{66})\bar{m}\bar{n}$$

$$T_{13} = \frac{A_{12}}{R}\bar{m} + B_{11}\bar{m}^3 + (B_{12} + 2B_{66})\bar{m}\bar{n}^2$$

$$T_{23} = -\frac{A_{22}}{R}\bar{n} - B_{22}\bar{n}^3 - (B_{12} + 2B_{66})\bar{m}^2\bar{n}$$

$$T_{33} = -\left\{ \frac{2B_{12}}{R}\bar{m}^2 + \frac{2B_{22}}{R}\bar{n}^2 + \frac{A_{22}}{R^2} + D_{11}\bar{m}^4 + 2(D_{12} + 2D_{66})\bar{m}^2\bar{n}^2 + D_{22}\bar{n}^4 \right\}$$

In the present work, the objective function may be derived as

$$f_{axial} = \text{maximize} \{ \text{minimize} [N_x(\theta_1, \theta_2, \dots, \theta_N, m, n)] \} \quad (5)$$

$$f_{external} = \text{maximize} \{ \text{minimize} [N_r(\theta_1, \theta_2, \dots, \theta_N, m, n)] \} \quad (6)$$

with the restrictions: $m > 1, n > 0, 0 < \theta_i < 90$ ($i=1, 2, \dots, N$). That is, m and n should be selected to minimize the buckling loads θ_i is furthermore decided to obtained the maximum value of the buckling loads N_x and N_r .

OPTIMIZATION PROCEDURE

Evolutionary algorithm (EA) is a calculation model or algorithm imitate a process of group heredity/evolution of a creature. EA includes Genetic algorithm, Evolution Strategies and Evolutionary Programming etc. EA has four different points compared with other optimization method[10]

EA starts to searches from multi-points in a popuration, not a single point.

EA uses a fitness function, not derivatives or other auxiliary knowledge.

EA uses probabilistic transition rules, not deterministic rules.

Various individuals are appeared in the process of the crossover and mutation, then an individual having high fitness value is retained by the selection.

Design variables in this problem are considered to the ply angle and the stacking sequence of laminated cylindrical shell. It is difficult to control and manufacture a fiber orientation precisely within 3 degree in the production of FRP cylindrical shell. From this point, fiber orientation angle of each lamina θ_i converts the binary number which increase one binary every 3 or 6 degree. The example of six-ply laminates as follows.

$$[0^\circ/60^\circ/30^\circ/48^\circ/78^\circ/90^\circ] \Rightarrow [0000|1010|0101|1000|1101|1111]$$

Next, the solution space for this optimization problem be characteristic of

It is difficult to find a global optimal value since there are many local optimum values and their differences are small.

The number of lamina increase with increasing the local optimum value.

Accordingly, the suitable methods for crossover, selection and the fitness function are determined from following reasons.

Selection ; The high fitness individuals are retained to the next generation by a selection and a roulette selection, rank selection, tournament selection and elitist sampling were proposed[11]. In this problem, the elitist sampling that always retains the best individual in the population is adopted.

Crossover ; It is exchange the section of the individual for that of another individual by a crossover and one-point crossover, multiple-point crossover and uniform crossover were proposed[12]. The central one-point crossover is adopted in this problem because it does not break a schema.

Fitness function ; The fitness function is used the difference of the buckling load and their minimum value in a population. But, since the average fitness of population goes up with the difference of fitness becomes very small, the scaled fitness function (scaling to second power or third power) is of much practical use is adopted as follows.

$$\begin{aligned} F_{\text{axial}} &= (N_x - N_{x_min})^3 \\ F_{\text{external}} &= (N_r - N_{r_min})^2 \end{aligned} \tag{7}$$

Next, various genetic parameters including the population size, the probability of crossover and the probability of mutation are tuned by the trial calculations. If the appropriate value of these parameters was not selected, the local optimum values are easy to be calculated. Thereupon, an appropriate value of the genetic parameter is tuned by using the following expressions are the capability of the optimal value search[13].

$$\text{Online performance} \quad P_{\text{on}}(T) = \frac{1}{T} \sum_{i=1}^T f_E(i) \tag{8}$$

$$\text{Offline performance} \quad P_{\text{off}}(T) = \frac{1}{T} \sum_{i=1}^T f_E^*(i) \tag{9}$$

Where T is the number of evaluation, $f_E(i)$ is the value of the objective function obtained at ith iteration and $f_E^*(i)$ is their maximum value until ith iteration.

Population size ; The effect of the population size was evaluated in the range from 10 to 150 individuals. The on-line and off-line performances are excellent at 100 individuals within the range of the probability of crossover 0.1~0.9 and the probability of mutation 0.01~0.05.

Probability of crossover ; Crossover preventes the convergence to a local optimum value. The crossover probability is evaluated within the range of 0.1~0.9. In the case of high

crossover probability for small population size(10~40) and comparatively low crossover probability for middle population size (50 or more), the on-line/off line performance is good. The crossover probability of 0.4 is regarded as an appropriate value in condition of population size of 100 individuals within the range of the mutation probability 0.01~0.05.

Probability of Mutation ; The mutation reverses the code number at an arbitrary bit of the design variable θ_i and there is possibility of find a local optimum values when the mutation probability is increased to the same as a random search (5% or more). Because the finest performance was obtained with the mutation probability 2-3% in the case of population size of 100 individuals, crossover probability 0.4~0.7, this value is regarded as an appropriate value.

From the results mentioned above, the population size of 100 individuals, the probability of crossover 0.6 and the probability of mutation 0.02 are adopted in the numerical examples of optimum stacking sequences search problems.

Figure 2 shows the change of the average fitness(the mean value of F) and the maximum fitness until 1000 generations in the case of under axial compressions. After, the average and maximum fitnesses increase until early dozens of generation, the average fitness repeats up and down due to the crossover. The maximum fitness increases rapidly as the generations by using the elitist sampling and then becomes constant at about 350 generations. Although it is seems that optimum value search is finished at this generation, the variance of the fitness of each individuals is still large (see Fig.3(b)). Therefore, the evolutionary algorithms which means the global search by the genetic algorithm and then the local search is proposed as follows:

Global search by the genetic algorithm(Exploration)

If the maximum fitness does not changed within 500th of generation continuously and the fitness over 10~20% of the population is lower than the average fitness before 500th of generations, it is decided that the global search finished. It has in remembrance all individual information of this generation and then the local search is started.

After crossover is suspended, the local search is started under the condition of the mutation probability is 5~4.5%. When the ratio of the difference between the maximum and average fitness at nth generation to the difference of both at the start of local search become to 50%, the mutation probability is changed to 4%. The mutation probability is reduced until 1% whenever this ratio reduces to 10%.

If the fitness of the individuals over 90% of population satisfies the condition of $F > F_{\max} - (F_{\max} - F_{\min})/10$, the calculation is finished.

The change of the fitnesses using by EA is shown in figure 4. The local search is started at 860th of generations because of the maximum fitness does not change after 360th of generations. The average and maximum fitness increase again, then the most of fitness are nearly equivalent to the maximum fitness is shown in Fig.3(c).

From the mentioned above, the evolutionary algorithms is used for the optimum stacking sequences search problem of FRP laminated cylindrical shells.

NUMERICAL RESULTS AND DISCUSSIONS

FRP Laminated Cylindrical Shells Under Axial Compression

In order to show the validity of the present method, the results of the optimum stacking sequences of the simply supported Boron/Epoxy 6-ply laminated and Graphite/Epoxy 4-ply laminated cylindrical shell are compared with the results by nonlinear programming[2] and [5] in Table 1 and Table 2, respectively. Material properties of the Boron/Epoxy composites are the following values, $E_L=207\text{GPa}$, $E_T=20.7\text{GPa}$, $G_{LT}=6.89\text{GPa}$ and $\nu_{LT}=0.3$. The length L , radius R and thickness t of cylindrical shell are 0.3m , 0.1m and $1.524 \times 10^{-3}\text{m}$. Material properties and dimensions of Graphite/Epoxy composites are $E_L=146\text{GPa}$, $E_T=10.8\text{GPa}$, $G_{LT}=5.78\text{GPa}$, $\nu_{LT}=0.29$, $L=0.1436\text{m}$, $R=0.0825\text{m}$ and $t=5 \times 10^{-4}\text{m}$. In Table 1, nine kinds of optimum and near optimum stacking sequences and the buckling stresses are shown in the order of decreasing the buckling stress. As being pointed out by Onoda[3], our method gives many kinds of stacking sequences having almost the same buckling stress under the axial compression. Also, the numerical results of optimum stacking sequences and buckling stress are almost agreement with three kind of results in Ref.[2](# mark). The buckling stress of the six-ply optimum Boron/Epoxy shell is slightly higher than the value of four-ply shell and it is not shown in Table 1.

FRP Laminated Cylindrical Shells Under External Pressure

Table 3 and 4 show the optimum stacking sequences and buckling load of Graphite/Epoxy six-ply and four-ply laminated cylindrical shells under external pressure, respectively. In these table, all of the buckling mode are (1,7) mode and the similar optimum stacking sequences each other are obtained. It seems that the change of middle layers of laminates are not affect so much on the buckling load. A frequency of appearance in the Table 3 and 4 means the percentage of the obtained number of stacking sequences to the total number of the optimum popuratioin also shown. If the frequency of appearance is over one percent, that stacking sequence appears one time without fail in the calculation. In these tables, the numerical results of Graphite/Epoxy laminated cylindrical shell under external pressure are compared with the results by the two-step approach combined Powell's method with a random search(@ mark) and they nearly agree with each other. Then, both algorithms can be used as the method of optimal design for practical purposes. However, the evolutionary algorithms seem to less possibility of reaching the local optimum values than the nonlinear programming or the two-step approach. Furthermore, this approach has a clear advantage of computational resources over conventional nonlinear programming or the two-step approach.

Application of Multi-Objective Optimization

The evolutionary algorithm is applied to the optimum stacking sequence and the buckling stress under both loading of axial compression and external pressure. It does not consider the interaction of the axial compression load and the external pressure in this problem. The optimum solutions are obtained by utilizing the fitness function F_{multi} , that is, the magnitude of the position vector with respect to the maximum buckling load [$f_{\text{axial_max}}$ and $f_{\text{external_max}}$] as follows.

$$F_{\text{multi}} = \sqrt{\left(\frac{f_{\text{axial}}}{f_{\text{axial_max}}}\right)^2 + \left(\frac{f_{\text{external}}}{f_{\text{external_max}}}\right)^2} \quad (10)$$

And the evolutionary algorithms added in the following procedure to the global search by GA is developed.

- 1) 50 individuals are selected by using Eq.(10) in the population.
- 2) 20~30 elite individuals which mean the individuals have high fitness are selected by each objective function are selected in the above 50 individuals and they are left to the next generation. The other individuals which are left to next generation decides by only the crossover and the mutation.
- 3) They are evaluated by only Eq.(10) in the local search.

Fig.5 shows the example of the multi-objective optimization process by EA. The initial individuals are dispersed widely in the solution plane in Fig. 5(a). After the fitness does not increase by the gloval search at 400 generations, their dispersion becomes small although each individuals are gathered to pareto plane[Fig.5(b)]. The dispersion of all individuals becomes the line in the pareto plane at 1000th generetions by the local search proress[Fig.5(c)] and validity to use the fitness finction of Eq.(10) is confirmed.

Table 5 shows the optimum stacking sequences of CF/PEEK six-ply laminated cylindrical shell under both loading of axial compression and external pressure. The material properties of CF/PEEK are $E_L=134\text{GPa}$, $E_T=12.9\text{GPa}$, $G_{LT}=6.75\text{GPa}$ and $\nu_{LT}=0.298$ and the dimensions of the cylindrical shell are $L=0.3\text{m}$, $R=0.1\text{m}$ and $t=0.001\text{m}$. In Table 5, $N_x/N_{x_{\max}}$ and $N_r/N_{r_{\max}}$ are the ratio of the buckling both loading to each buckling load under pure axial compression [$N_{x_{\max}}$] and pure external pressure[$N_{r_{\max}}$], respectively. The optimum stacking sequences of CF/PEEK laminated cylindrical shell obtained by EA have many similar ones under the external pressure. It seems that the change of the fiber orientation angle of the outside layers(θ_1 , θ_2 , θ_5 and θ_6) gives effects influence largely to both of buckling load. The result of the optimum stresses under both loading are about 85% of the each maximum buckling load under single loading and the pareto optimality is satisfied. Accordingly, it consider that EA is one of useful search method for the multiobjective optimization problem.

CONCLUSION

Evolutionary algorithms (EA) is applied to the optimization of the stacking sequence in order to maximize the buckling load of FRP laminated cylindrical shell. When EA is used in the optimization pobleem, an optimum value of various parameters of EA and the reduction of the calculation time is also considered. In adition, EA is also applied to the multiobjective optimization, that is, to obtain the maximum buckling load of FRP laminated cylindrical shell under both loading of axial compression and external pressure. The following conclusions are obtained.

- 1) The numerical results of FRP laminated cylindrical shell under axial compression or external pressure obtained by the evolutionary algorithms nearly agree with the results of conventional nonlinear programming and the two-step approach.
- 2) The evolutionary algorithms seem to be less possibility of reaching the local optimum value than the nonlinear programming or the two-step approach. Furthermore, this approach has a clear advantage of computational resources over the conventional nonlinear programming or the two-step approach.

- 3) EA is also applied to the multiobjective optimization of CF/PEEK six-ply laminated cylindrical shell under both loading of axial compression and external pressure. The result of the optimum stacking sequence is $[\pm 90/\pm 24/\pm 54/\pm 54/\pm 30/\pm 90]$ laminates and the pareto optimality is satisfied. It seems that EA is one of useful search method for the multiobjective optimization problem.

REFERENCES

1. Y.Hirano, Journal of the japan society for aeronautical and space sciences, Vol.32, No.360, 1984, pp46-51
2. Y.S.Nshanian and M.Papas, AIAA Journal, Vol.21, No.3, 1983, pp430-437
3. J.Onoda, AIAA Journal , Vol.23, No.7, 1985, pp1093-1098
4. G.Sun, Composite Science and Technology, Vol.36, 1989, pp243-253
5. R.L.Riche et al , AIAA Journal , Vol.31 , No.5, 1993, pp951-956
6. Fukunaga and Sekine, Journal of the japan society for aeronautical and space sciences, Vol.42, No.485, 1994, pp371-380
7. Todoroki, Watanabe and Kobayashi, Transaction of the Japan society of mechanical engineering, Vol.60-A, No.573, 1994, pp146-151
8. J.Tasi, AIAA Journal, Vol.4 , No.6, 1966, pp1058-1062
8. Composite Material Handbook, Nikkan Kogyo Shinbun Co., 1989 chapter 1.,
9. D.B.Fogel, An Introduction to Simulated Evolutionary Optimization, IEEE Trans. On Neural Networks, Vol.5, 1994, pp.3-14
10. S.Iba, Basis of the Genetic algorithms, Ohm Co., 1994, pp93-103
11. D.E.Goldberg, Genetic Algorithms in Search Optimization & Machine Learning , Addison-Wesley Pub. Co., 1989
12. J.J.Grefenstette, Optimization of Control Parameters for Genetic Algorithms, IEEE Trans. On Systems, Man, and Cybernetics, Vol.SMC-16, No.1, 1986

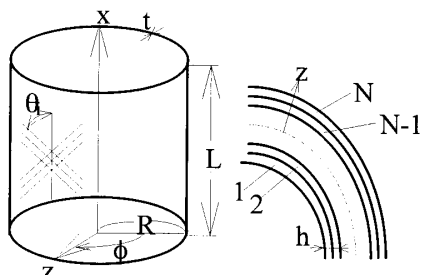


Fig.1 FRP laminated cylindrical shell

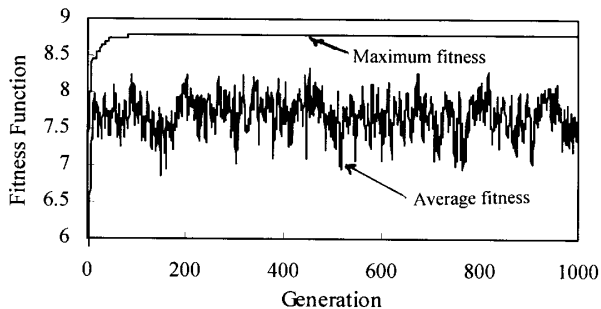


Fig.2 Change of the fitness with the generation(only GA)

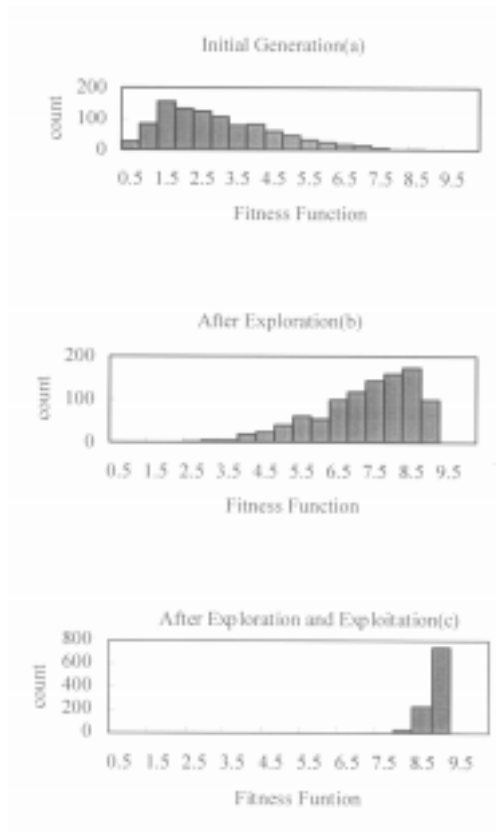


Fig.3 Variance histogram of individuals in the population

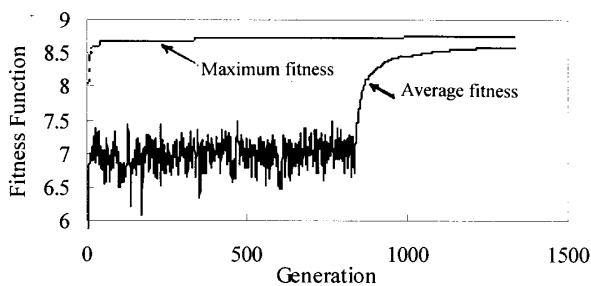


Fig.4 Change of the fitness with the generation(EA)

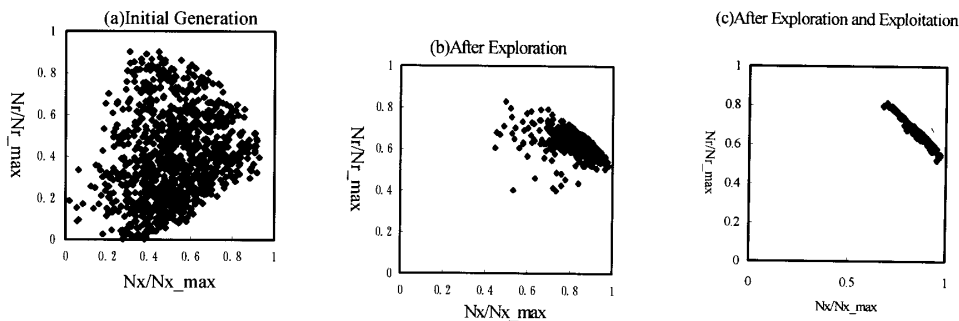


Fig.5 Change of individual distribution for multi-objective optimization

Table 1 Optimum configurations for Boron/Epoxy six-ply laminated cylindrical shell under axial compression

Optimum stacking sequences	(N _x /t) [MPa]	Buckling Type
[±30/±84/±60/±6/±48/±54]	755.7	asymmetry
[±66/±18/±30/±78/±60/±30]	755.6	asymmetry
[±24/±72/±60/±12/±30/±60]	755.6	symmetry
#[±28/±65/±86/±5/±27/±63]	754.9	
[±24/±84/±42/±42/±6/±66]	755.4	asymmetry
[±66/±6/±48/±48/±84/±24]	755.4	asymmetry
[±36/±84/±0/±60/±42/±48]	755.4	asymmetry
[±54/±6/±90/±30/±48/±42]	755.4	asymmetry
#[±50/±9/±87/±7/±54/±40]	750.5	
[±36/±90/±0/±54/±48/±42]	755.2	asymmetry
[±54/±0/±90/±36/±42/±48]	755.2	asymmetry
#[±55/±2/±82/±45/±35/±48]	756.7	

Table 2 Optimum configurations for Graphite/Epoxy four-ply laminated cylindrical shell under axial compression

Optimum stacking sequences	N _x [KN/m]	Buckling mode (m,n)
[±30 / ±84 / 0 / ±60]	101.3	(1,6)
#[±32 / ±84 / 0 / ±53]	104.1	
[±60 / ±6 / ±90 / ±30]	101.3	(13,3)
#[±59 / 0 / ±90 / ±28]	101.7	
[±30 / ±84 / ±3 / ±63]	101.2	(1,6)
[±30 / ±84 / ±0 / ±57]	101.1	(13,0)
#[±33 / ±85 / 0 / ±53]	104.1	
[±30 / ±87 / ±3 / ±57]	101.1	(3,10)
#[±33 / ±89 / ±3 / ±53]	104.1	
[±30 / ±87 / ±6 / ±57]	101.1	(3,10)

Table 3 Optimum configurations for Graphite/Epoxy six-ply laminated cylindrical shell under external pressure

Optimum stacking sequences	N _r [KPa]	Frequency of appearance(%)
[±90 / ±78 / ±12 / ±18 / ±54 / ±90]	147.2	30.8
@[±90 / ±79 / ±14 / ±16 / ±54 / ±90]	147.3	
[±90 / ±78 / ±6 / ±18 / ±54 / ±90]	147.2	6.5
@[±90 / ±76 / ±5 / ±19 / ±55 / ±90]	147.3	
[±90 / ±78 / ±0 / ±18 / ±54 / ±90]	147.2	0.1
[±90 / ±78 / ±12 / ±12 / ±54 / ±90]	147.2	1.2
@[±90 / ±77 / ±14 / ±13 / ±55 / ±90]	147.3	
[±90 / ±78 / ±18 / ±12 / ±54 / ±90]	147.1	0.8
[±90 / ±78 / ±18 / ±6 / ±54 / ±90]	147.1	2.5
[±90 / ±78 / ±0 / ±24 / ±54 / ±90]	147.0	5

Table 4 Optimum configurations for Graphite/Epoxy four-ply laminated cylindrical shell under external pressure

Optimum stacking sequences	N _r [KN/m]	Frequency of appearance(%)
[±90 / ±12 / ±27 / ±90]	12.13	28.2
@[±90 / ±13 / ±27 / ±90]	12.13	
[±90 / ±15 / ±24 / ±90]	12.13	1.2
[±90 / ±9 / ±30 / ±90]	12.13	14.9
[±90 / ±18 / ±21 / ±90]	12.12	10.3
[±90 / ±6 / ±33 / ±90]	12.12	1.7

Table 5 Optimum configurations for CF/PEEK six-ply laminated cylindrical shell under axial compression and external pressure

Optimum stacking sequences	N _x /N _{x,crk} (%)	N _r /N _{r,crk} (%)	Frequency of appearance (%)
[±90/±24/±54/±54/±30/±90]	0.83	0.85	3.2
[±90/±24/±54/±54/±30/±84]	0.84	0.85	0.1
[±90/±24/±60/±48/±30/±90]	0.83	0.86	1.4
[±90/±24/±60/±42/±36/±90]	0.82	0.86	2.3
[±90/±24/±54/±48/±30/±90]	0.83	0.85	0.2
[±90/±24/±60/±48/±30/±90]	0.83	0.85	0.3
[±90/±24/±54/±54/±24/±90]	0.84	0.85	0.1
[±90/±24/±48/±60/±30/±90]	0.84	0.85	0.3
[±84/±24/±60/±54/±30/±90]	0.84	0.84	0.4
[±90/±24/±60/±42/±36/±84]	0.82	0.86	0.1

MATERIALS AND PROCESS SELECTION FOR COST-PERFORMANCE EFFECTIVE LAMINATES

Michael G Bader

*Department of Materials Science & Engineering
University of Surrey, Guildford, Surrey GU2 5XH, UK*

SUMMARY: Composite materials offer the designer a very wide range of choice of reinforcing fibre, reinforcement format, matrix and manufacturing route. A successful design must meet the technical specification and production requirements at an acceptable cost. The production rate, total production run and availability of processing facilities will further influence both choice of materials and manufacturing route. A methodology is proposed for cost and performance prediction so that the alternatives may be evaluated on the basis of an objective assessment of cost and performance. The concept of a cost-performance index is introduced. This requires that a value be established for critical parameters of performance, e.g. stiffness and mass. This is illustrated with reference to a simple notional component.

KEYWORDS: cost, mechanical performance, continuous fibre laminates.

INTRODUCTION

Composite materials must compete with traditional materials and with each other in the engineering market place. The generally perceived advantages of composites lie in their greater structural efficiency, their ability to be tailored for specific applications, their possibilities for parts consolidation and a number of secondary advantages such as reduced corrosion. These advantages must be offset against the generally higher costs of the raw materials and the need to use unfamiliar manufacturing processes. In order to be able to compare the relative performance and economic aspects of different materials choices for a given application it is necessary that both performance and cost must be effectively analysed and predicted. It is also desirable that an equivalence between performance and cost should be established. It must be possible to answer the question: What is the value of an increase in performance? If we confine ourselves to a consideration of structural efficiency. Performance might be defined in terms of the mass of a component or structure to meet a given service loading scenario. We may then establish a monetary value for mass saving expressed in terms of \$/kg. This may then be used as a yardstick for comparison of alternative materials and manufacturing choices.

Structural Efficiency

This may be measured simply in terms of the mass of the part or structure which just meets the requirements of the mechanical specification. The critical performance parameter may be stiffness, or some aspect of strength, e.g. tension, compression, shear, creep, fatigue or

fracture toughness. In general all of these parameters may be assigned a numerical value. Furthermore the well developed methodologies of micro-mechanics, laminate plate analysis and finite element modelling techniques enable a good estimate of performance to be attained if the key elements of the constitution and structure of the composite are known. These are generally the properties of the fibre and those of the matrix, the fibre fraction, V_f , and the overall reinforcement architecture. In the present work flexural stiffness is used to illustrate typical aspects of performance.

Estimating Cost

This is rather more difficult and inexact due to the complexity of the problem and the lack of accurate data. Every effort has been made to obtain meaningful data but it is accepted that the values used may not all be realistic. Never-the-less they serve to illustrate the principles necessary to make objective cost-performance comparisons. The key aspects of the cost analysis are:

- Raw materials
- Conversion
- Tooling
- Labour
- Plant
- Consumables
- Materials utilisation

Raw materials: This is the cost of the basic fibre and resin in the case of conventional fibre reinforced polymer composites. Fibre costs vary quite considerably from the order of \$1/kg for the most basic forms of E-glass to in excess of \$1000/kg for the more exotic boron and SiC mono-filaments. Resin costs are less variable but there are still significant differences between a commodity resin such as an unsaturated polyester or polypropylene at a few \$/kg and the high temperature thermosets, such as polyimide or thermoplastics such as poly-ether-ether-ketone (PEEK) which may cost more than \$50/kg.

Conversion includes processes like weaving, braiding and pre-pregging in which the reinforcement is converted from the basic continuous roving, which is the usual format for primary supply, into a sheet, web or bulk format, possibly incorporating the resin, which is a more suitable feedstock for certain downstream processing operations. The cost of the conversion process may be offset by a more convenient and cheaper overall process. In some processes, such as filament winding or pultrusion, the fibre roving may be converted into the final product in a single processing operation. Such processes have the advantage of using the raw materials in their most basic, and least costly format. In other cases the fibre may be woven into a cloth, then impregnated with resin, cut into shapes and then laminated onto a tool. The cost of the intermediate conversion and handling operations may be substantial but the overall process may still be viable due to better performance or greater productivity.

Tooling costs may also be significant. A critical consideration is the required rate of production and the total number of parts to be manufactured. Simple disposable tooling may be used for "one off" applications, especially for very large mouldings. The whole cost of the tool then contributes to the cost of each part. More durable, but still cheap, tools may allow the manufacture of up to 100 parts from a single tool set. This allows the mould cost to be amortised over the greater number of parts. Very complex metal tools used with the more

highly automated processes, such as injection moulding, may be good for the production of tens of thousands of parts at very high rates. In general processes using simple tooling tend to be slow and labour intensive whilst the reverse is true for the highly automated processes. Another aspect of the choice of tooling and process is that achievable levels of performance may be a function of the process. Hand laid laminates using uniaxial prepreg may be the most structurally efficient and are also more flexible in that the lay-up, and hence structural performance, may be easily modified. In contrast, a reinforced thermoplastic injection moulding compound has very limited fibre content and there is much less control of the overall fibre orientation. Thus, performance and cost are lower but productivity is much higher. In the examples considered below the actual tooling costs are generally quite a small proportion of the final cost of the part, but labour costs can be a major factor.

Another important contribution to cost is the capital cost of the required plant and its operating costs. This is probably the most difficult aspect on which to obtain meaningful data. It is easy to establish that an autoclave, say, may cost several million dollars to purchase and commission. However, the way in which this capital expenditure is allocated to the cost of the parts subsequently manufactured is shrouded in uncertainty due to varying accountancy practices and local taxation laws. The principle used in the present work is to assume a plant life of 10 years and that it is operated continuously for the manufacture of parts similar to the standard moulding discussed.

The remaining factors are consumables and materials utilisation. In some processes, particularly autoclave moulding of prepreg, quite large amounts of relatively expensive consumables are used. These include bleeder and breather materials and bagging film. They can seldom be used more than once and therefore contribute directly to the cost of the product. Materials utilisation, often termed the “fly to buy ratio” in the aerospace industry, is simply the fraction of the bought-in materials which finishes up in the product. Again for prepreg there is considerable wastage so that the utilisation factor may be as low as 0.5. For a fibre reinforced thermoplastic injection moulding, where sprue and scrap may often be directly recycled, the value approaches 1.0.

ANALYSIS METHODOLOGY

The basis of the present analysis is to use a simple generic component for comparison of mechanical performance when using different materials and cost using different materials and manufacturing routes. The component is a 1 m² stiffened panel with a gentle single curvature. It is supported across the two curved edges and uniformly loaded in bending. This shape is typical of composite components used in many different applications: e.g. A hood for a car, a fuselage panel on an aircraft, part of the hull for a yacht or a storage tank for containing liquid or particulate materials. The performance requirements and economic constraints would, however, be very different for these applications and would lead to different choices of composite system and manufacturing process.

This component lends itself to manufacture by a wide variety of processes ranging from autoclave consolidation of prepreg, through resin film infusion [RFI] and resin transfer moulding [RTM] variants, to injection moulding from a moulding compound. The range of processes and materials considered together with the identification codes used are set out in Table 1. The laminates are based on E-glass, a typical high-strength carbon [HC] and an

intermediate-modulus carbon fibre [IM]. All laminates are in a quasi-isotropic configuration. For each material and process combination the panel thickness and stiffener dimensions

Table 1: Materials and processes considered

LAMINAT E CODE	FIBRE	FORMAT	PROCESS	V_f	IN-PLANE STIFFNESS E_1 [GPa]
GF-RM-IM	E-glass	BMC	Injection mould	0.25	6.5
GF-RM-CM	E-glass	SMC	Press mould	0.30	7.5
GF-RM-RT	E-glass	Random mat	RTM	0.30	9.9
GF-WR-RT	E-glass	Woven cloth		0.45	14.9
HC-WR-RT	HS carbon	Woven cloth		0.45	37.1
GF-NC-RT	E-glass	Non-crimp fabric	RTM	0.50	18.3
HC-NC-RT	HS carbon				45.6
GF-NC-PM	E-glass	Non-crimp fabric	RFI	0.55	19.8
HC-NC-PM	HS carbon		Press mould		49.5
IM-NC-PM	IM carbon		61.2		
GF-NC-AC	E-glass	Non-crimp fabric	RFI	0.55	19.8
HC-NC-AC	HS carbon		Autoclave		49.5
IM-NC-AC	IM carbon		61.2		
GF-PP-AC	E-glass	UD Prepreg	Autoclave	0.60	22.0
AR-PP-AC	Aramid				30.0
HC-PP-AC	HS carbon				55.0
IM-PP-AC	IM carbon				68.0

have been adjusted so that all panels have similar initial flexural stiffness in bending. The mass of each variant is then estimated and is used as the basis for assessing structural efficiency. The cost of materials and manufacture has also been estimated. This, of course, would vary according to the scale of production. The basis used here is to set the annual productivity on the number of components which could be produced from a single set of tools in a factory working a single shift system for 250 days/year. The only variation is for the two most automated processes considered, the press-moulded sheet moulding compound [SMC] and the injection-moulded bulk moulding compound [BMC] which are notionally operated on a 3-shift, 24 hours/day basis also for 250 days/year. Inevitably the materials purchase costs and the estimates of process costs must be approximate, but they are based on previous work [1-6], actual quotations and the best available information obtainable from toolmakers and suppliers. It should be mentioned that many commercial organisations are reluctant to release any detailed cost data.

RESULTS

The basic results are summarised in Table 2. This shows the thickness and mass of the different options and the cost, with a breakdown showing contributions of materials, tooling, plant amortisation and operation and labour as percentages of the total.

Table 2: Performance and cost analysis

CODE	THICK-NESS [mm]	MASS [kg]	PARTS p.a.	UNIT COST [\$]	COST BREAKDOWN [%]			
					Matls	Tooling	Plant	Labour
GF-RM-IM	5.50	11.07	45x10 ³	128	90	1	3	6
GF-RM-CM	5.00	10.36	12x10 ³	182	79	2	2	17
GF-RM-RT	4.25	8.66		459	13	15	4	68
GF-WR-RT	2.85	7.32	750	581	22	12	3	63
HC-WR-RT	1.68	2.92		723	39	9	3	49
GF-NC-RT	2.70	6.46	750	602	24	12	3	61
HC-NC-RT	1.45	2.55		683	37	10	3	50
GF-NC-PM	2.70	6.30		782	30	8	4	58
HC-NC-PM	1.35	2.40	500	823	37	6	5	52
IM-NC-PM	1.10	1.93		1162	56	4	3	37
GF-NC-AC	2.70	6.30		2161	11	6	36	47
HC-NC-AC	1.35	2.40	250	2321	18	6	34	42
IM-NC-AC	1.10	1.93		2712	30	5	29	36
GF-PP-AC	2.48	5.87		2582	19	5	31	45
AR-PP-AC	1.75	3.04	250	2823	27	4	28	41
HC-PP-AC	1.25	2.19		2391	15	6	33	46
IM-PP-AC	1.00	1.76		2583	22	5	31	42

It will be observed that there is almost an order of magnitude difference between the masses of the most and least structurally efficient system, whilst the costs range over three orders. The processes using autoclave consolidation are the most costly. There is no economic gain from using cheaper fibres for the prepreg-autoclave variant. This is because the laminates need a greater number of plies with consequent additional labour cost.

COST-PERFORMANCE INDEX

In order to facilitate an objective evaluation of the relative performance and cost, a *cost-performance index*, I_{pc} , is proposed. This requires that a value, v_p , be set for mass reduction. Values for v_p ranging from 1 to 10000 \$ per kg of mass saved have been used. The lower figure might be appropriate for automotive and general engineering and the higher values for spacecraft. The index is defined by:

$$I_{PC} = \frac{c_o + (m_o - m_i)v_p - c_i}{c_o} \quad (1)$$

where m_o and c_o are the mass and cost of a reference system, usually the cheapest of those being considered, and m_i and c_i the mass and cost of the system to be compared. The index will be zero for the reference system, a positive value of the index indicates a cost-performance advantage and a negative index a disadvantage. The quantity $(m_o - m_i)v_p$ is simply the added value due to mass saving. In the example the comparison has been made on the basis of stiffness and mass but any other performance criterion could be substituted for

stiffness. The results of this computation are given in Table 3 and illustrated graphically in Figs. 1-5 each for a different assumed value of ν_p .

Table 3: Cost-performance index

SYSTEM	COST-PERFORMANCE INDEX - I_{PC}				
	For indicated values of ν_p				
	1 \$/kg	10 \$/kg	100 \$/kg	1000 \$/kg	10000 \$/kg
GF-RM-IM	0	0	0	0	0
GF-RM-CM	-0.42	-0.37	0.13	5.13	55
GF-RM-RT	-2.57	-2.40	-0.70	16.24	186
GF-WR-RT	-3.51	-3.25	-0.61	25.76	289
HC-WR-RT	-4.58	-4.01	1.72	59.02	632
GF-NC-RT	-3.67	-3.34	-0.10	32.31	356
HC-NC-RT	-4.27	-3.67	2.32	62.23	661
GF-NC-PM	-5.07	-4.74	-1.38	32.16	368
HC-NC-PM	-5.36	-4.75	1.34	62.30	672
IM-NC-PM	-8.01	-7.36	-0.94	63.33	706
GF-NC-AC	-15.85	-15.51	-12.16	21.38	357
HC-NC-AC	-17.07	-16.46	-10.36	50.60	660
IM-NC-AC	-20.12	-19.47	-13.05	51.22	694
GF-PP-AC	-19.13	-18.77	-15.11	21.45	387
AR-PP-AC	-20.99	-20.43	-14.78	41.68	606
HC-PP-AC	-17.61	-16.99	-10.74	51.70	676
IM-PP-AC	-19.11	-18.45	-11.91	53.55	708

It will be noted in Table 3 that the index for the reference system is always zero. The value of the index for the comparison systems is dependent on the value chosen for ν_p and tends to be greater when a high value has been chosen. The best system is that with the highest positive index, the appropriate boxes are highlighted in Table 3. Thus for ν_p of 1 and 10 \$/kg the reference system, the injection moulded BMC is the most cost-performance effective. At 100 \$/kg the non-crimp high-strength carbon fabric processed by RTM is best, at 1000 \$/kg the RFI press-moulded IM carbon non-crimp fabric is favoured, whilst only at 10000 \$/kg does the most structurally efficient IM carbon prepreg become the system of choice, with the press-moulded RFI variant in close second place. This analysis has emphasised the economic disadvantages of autoclave based processing and the advantages of RTM and RFI in combination with non-crimp fabrics which offer the possibility of relatively high structural efficiency. It also shows that the choice of carbon in preference to E-glass may often be justified on cost-performance grounds. In real design situations the comparison will normally be over a much narrower range than that illustrated and more realistic materials and processing costs should be available. The methodology described should provide a useful tool at the preliminary stages of design.

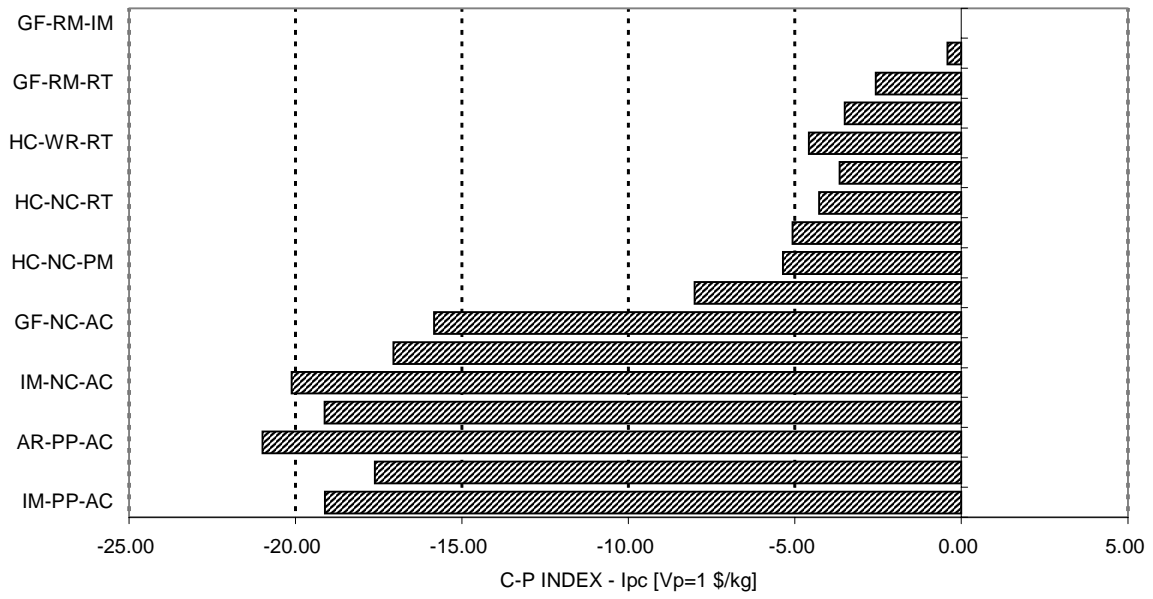


Fig.:1 Cost-performance index for $v_p=1$ \$/kg

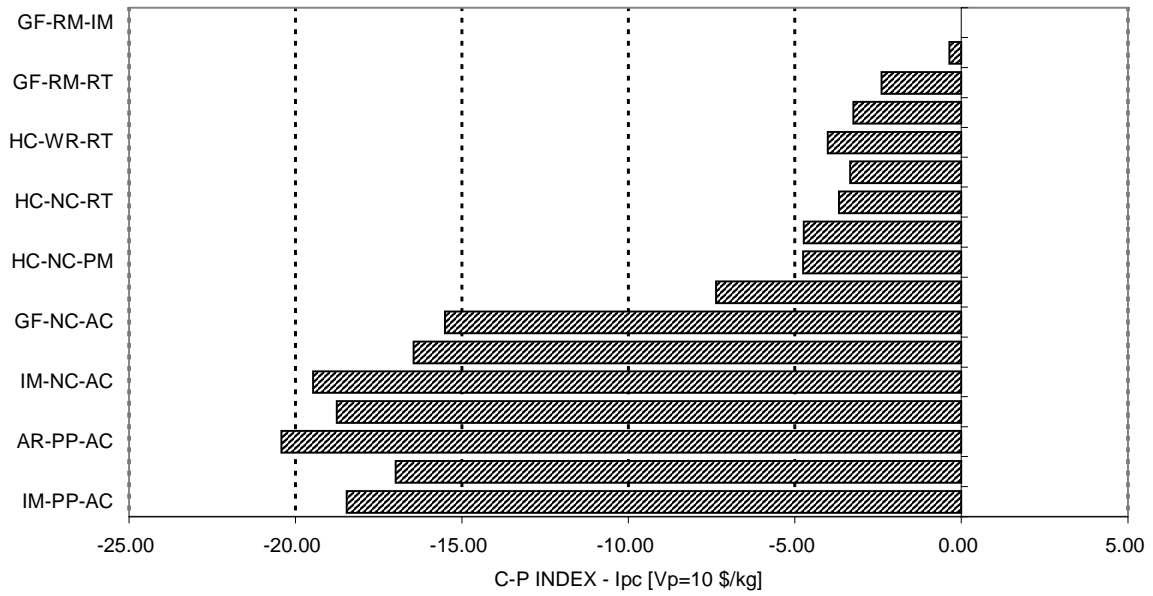


Fig. 2: Cost-performance index for $v_p=10$ \$/kg

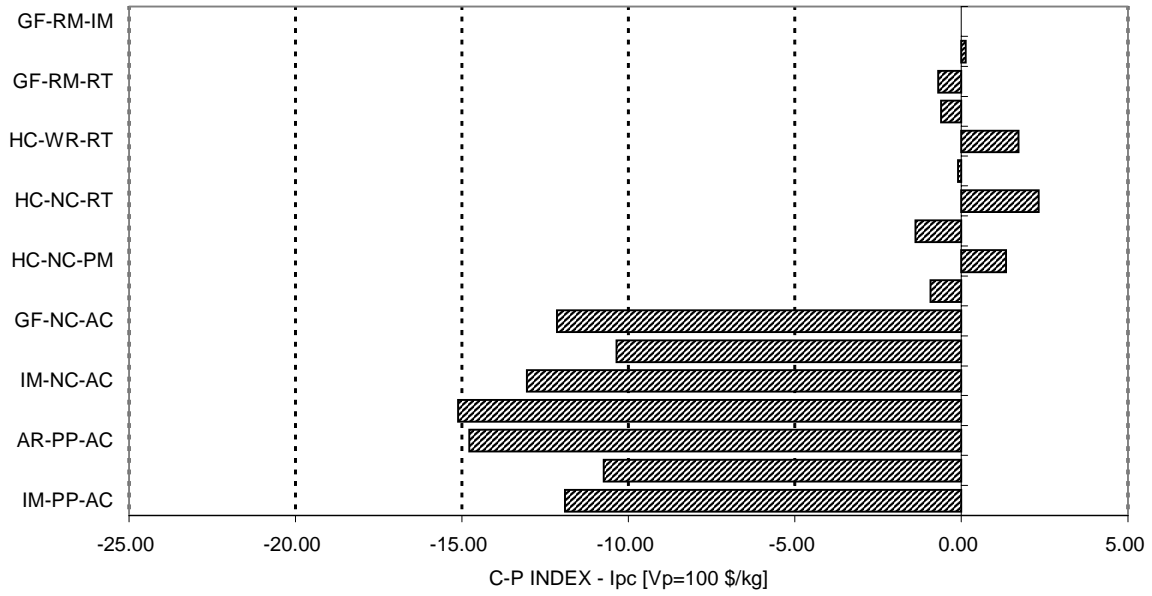


Fig. 3: Cost-performance index for $v_p=100$ \$/kg

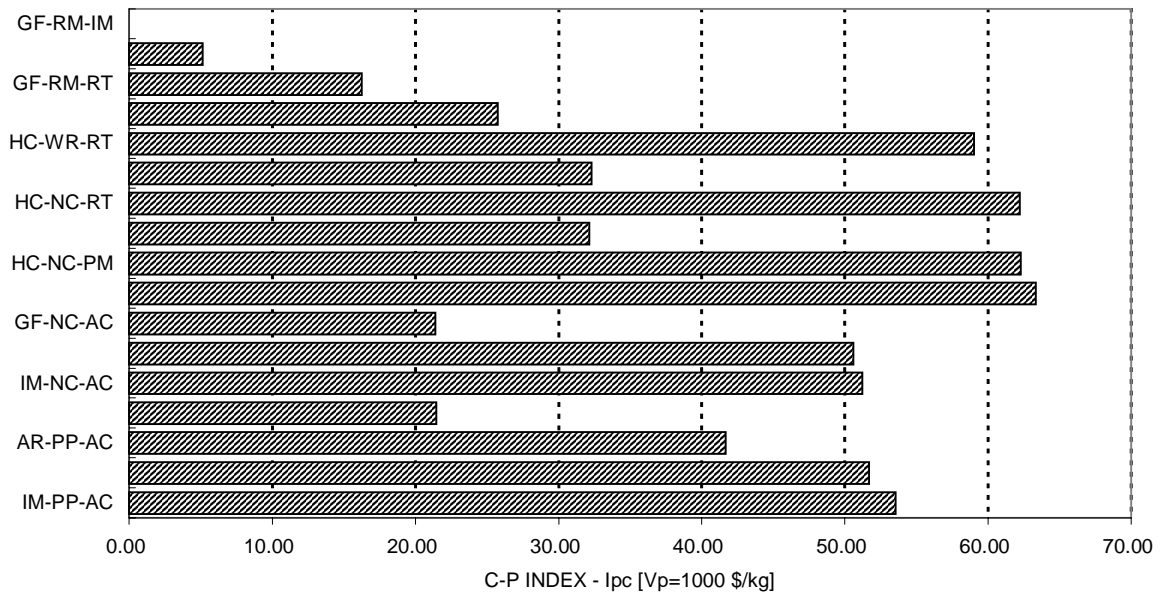


Fig. 4: Cost-performance index for $v_p=1000$ \$/kg

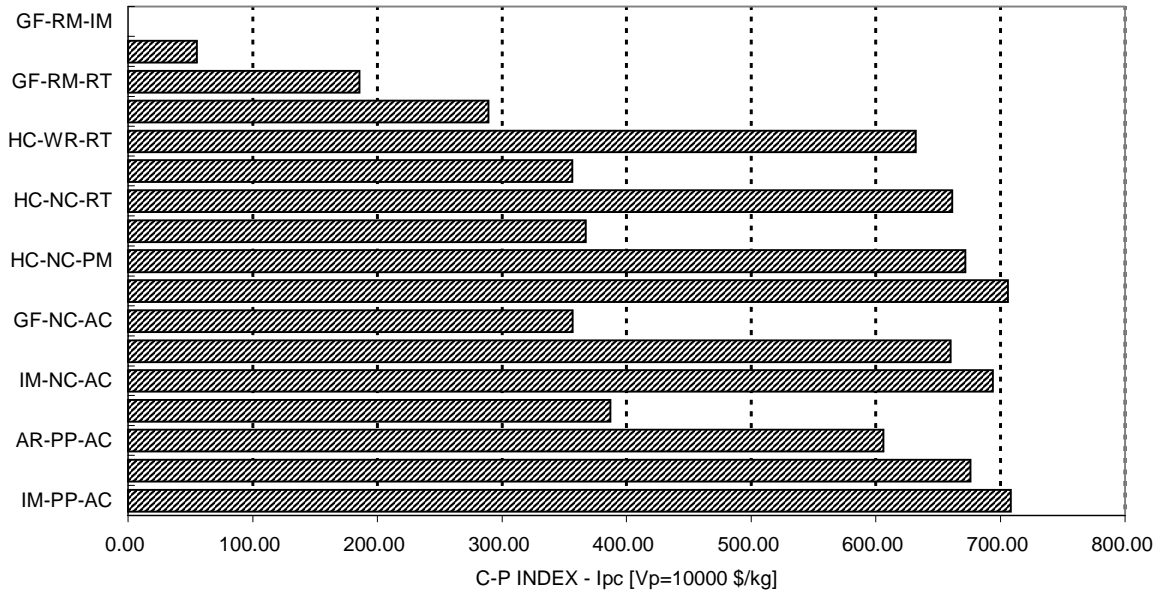


Fig. 5: Cost-performance index for $v_p=10000$ \$/kg

REFERENCES

1. Foley M & Bernardon E., Thermoplastic composite manufacturing cost analysis for the design of cost effective automated systems. SAMPE J. 26, 4, 67-74 (1990)
2. Gutowski T, Henderson R & Shipp C., Manufacturing costs for advanced composites aerospace parts. SAMPE J., 27, 3, 37-43, (1991)
3. Gutowski T, Hoult D, Dillon G, Neoh E-T, Muter S, Kim E & Tso M., Development of a theoretical cost model for advanced composite fabrication. Composites Manufacturing, 5, 231-239, (1994)
4. Silverman E M & Forbes W C., Cost analysis of thermoplastic composite processing methods for spacecraft structures. SAMPE J.,26,6,9-15,(1990)
5. Wang E & Gutowski T., Cost comparison between thermoplastic and thermoset composites. SAMPE J.,26, 6, 19-26, (1990)
6. Bader M G, Designing composite laminates for cost-performance effectiveness. Proc. 25th Japanese FRP Conference, March 18-19, (1996), Doshisha University, Kyoto, Japan. Pp I - VI.

A COMPUTER SYSTEM FOR LIFECYCLE COST ESTIMATION AND MANUFACTURABILITY ASSESSMENT OF COMPOSITES

Mengchen Li, Elizabeth Kendall, Jayanthi Kumar

*Computer Systems Engineering, Royal Melbourne Institute of Technology
City campus GPO Box 2476v, Melbourne VIC 3001, Australia*

*This work is funded by the Cooperative Research Centre for Aerospace Structures,
506 Lorimer St. Fishermens Bend, VIC 3207 Australia*

SUMMARY: The aim of this paper is to describe a computer based system that i) determines how a composite component should be manufactured, ii) measures the complexities of the part (based on a model verified at MIT [2,8,10]), and then iii) estimates the cost of manufacturing the component. The computer system architecture centers on cost, process, and manufacturability knowledge stored in a database that is accumulated, stored and then retrieved for future usage. This paper will describe the overall design of the computer system using object oriented analysis and design (OOA&D). The paper will show how to represent manufacturing knowledge in a computer based system, and also demonstrate how to store and retrieve a suggested processing tree for a given component, key aspects of the database design. Recent developments in object oriented technology, patterns and patterns language[3] will also be discussed in this paper.

KEYWORDS: cost estimation, manufacturing, object-oriented database management system

INTRODUCTION

Lifecycle costs and manufacturability are today the key aspects of large composite components. Much of the high cost associated with composites results when the specifications for the product do not correspond with the capabilities of the manufacturing processes. Therefore, in the composites industry, there is a need to develop the ability to evaluate new concepts and designs on the basis of their manufacturability along with their structural integrity and other measures of performance. There is also a need to integrate the preliminary structural design with the proposed manufacturing approach to minimise the cost and duration of development.

The aim of our project is to develop a computer based system to i) determine how a composite component should be manufactured, ii) measure the complexities of the part (based on a model verified at MIT[2,8,10]) and iii) estimate the cost of manufacturing the component. The system will also be used to evaluate alternative designs for a component so that the most effective design, in terms of manufacturability and lifecycle costs, could be utilised.

This paper will describe the overall design of the computer system using object oriented analysis and design(OOA&D). "Object-oriented" means that software is organised as a collection of discrete objects that incorporate both data structure and behaviour [6]. Both the Rumbaugh [6] and the Booch methodologies [5](software engineering techniques) will be applied in this paper. An object oriented database system (OODBMS) is used to store and retrieve objects, even very complex objects such as those found in composite manufacturing

(for example, an aircraft undercarriage door and its associated manufacturing procedures and resources). Patterns and patterns languages [3] will also be discussed in this paper as expert, masterful, software designs for real, difficult problems in computer representation. Patterns are the key to an approach to the challenges in representation that are inherent to the problem of lifecycle cost estimation and manufacturability assessment.

METHODOLOGY

Object Oriented Database Management Systems (OODBMS)

An OODBMS is a system that can store, retrieve, and manipulate objects that directly model or reflect physical objects in the real world. OODBMS keep the object [4] data, but also store behaviour, and relationships between objects. For certain kinds of applications, for example manufacturing, this is a significant advantage over relational databases. Real objects, for example machines, have behaviour. Objects are also related to each other through inheritance (specialisation), association, and aggregation (containment) relationships. An OODBMS has the ability to maintain all this information in an integrated fashion.

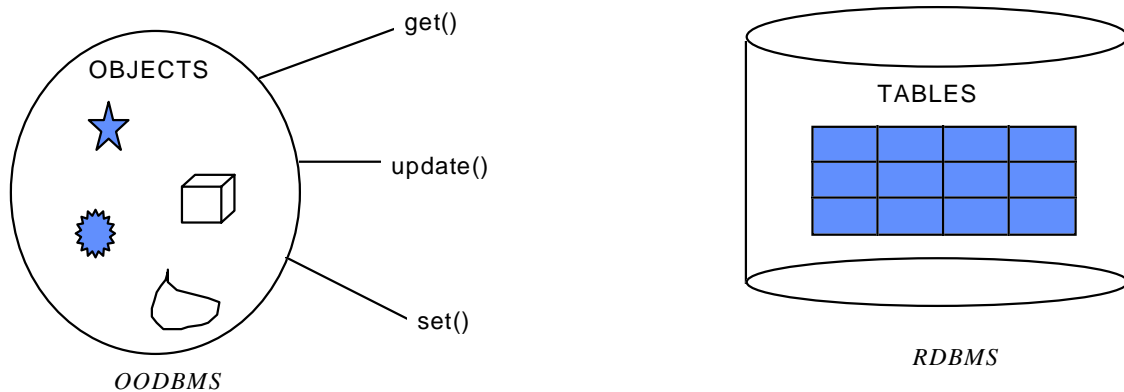


Figure 1. The Difference between Object Oriented and Relational Databases

An OODBMS is event-driven compared with a RDBMS (Relational DBMS) which is value-driven. The difference is shown in Figure 1. All the operations can be stored with the objects, eg. set and update operations; this models what happens in the real world. Users and software engineers do not need to specify such operations outside the OODBMS. An RDBMS is different because only the data(table) are stored; users have to figure out the relationships or the path to the behaviour. This makes the computer representations very complicated, and some representations may be impossible.

An OODBMS has both the benefits of a conventional database, like persistence, concurrency, change management, recovery and security, and the advantages of object-oriented technology, such as encapsulation, inheritance, polymorphism, reusability, etc.

Patterns and Pattern Languages

The computer system described in this paper addresses a complicated area of manufacturing. For this application, computer representation is important because we need to represent

complex relationships between objects, such as different resources and different manufacturing processes. Patterns in software engineering describe tested software engineering solutions to particular problems.

A pattern language defines a collection of patterns and the rules to combine them. Pattern languages describe software frameworks or families of related systems. Patterns and pattern languages are ways to describe good designs. In this project, patterns have been used to address particularly challenging areas with reusable, portable, and extensible object oriented software.

Notation

The notation we use here is the OMT (Object Modeling Technique, developed by Rumbaugh[6]) notation.(Figure 2).

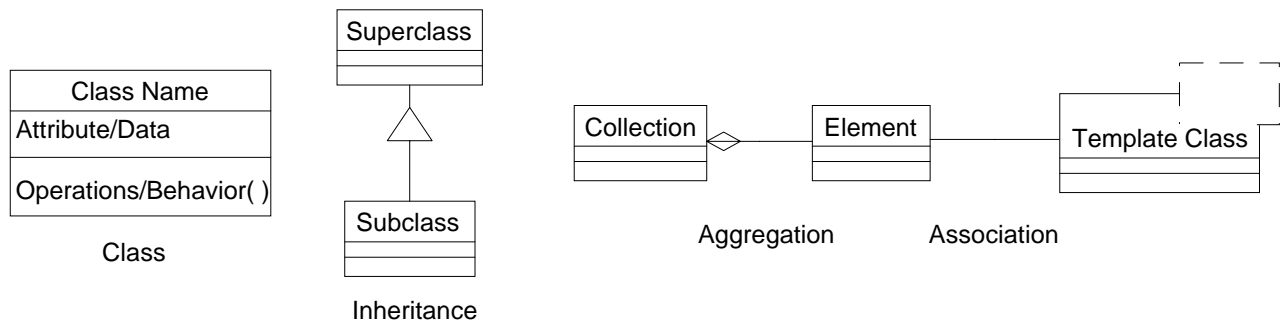


Figure 2. Object Notation

System Overview

The system is depicted in Figure 3, in a use case representation. A use case diagram indicates use cases (ways the system can be used), actors (users in certain roles), and relationships between use cases and actors. The main subsystems are the following:

- CAD System(MicroStation™)
- Patran™ P3 Laminate Modeller
- Complexity Analysis
- Manufacturing Plan Generation
- Manufacturing Cost Estimation
- Database (ObjectStore®)

There are three levels to the computer system from the architectural point of view. The first level is the Manufacturing Cost Estimation, which calculates the cost. The cost is related to the processing tree which is also associated with the component complexity. Different process fabrications yield different costs and use different complexities, this is the second level: Complexity Analysis and Manufacturing Plan Generation. In a composite component, we not only have the geometric information, which includes dimensions and tolerances, but also the laminate complexities. The sources of all this information are the CAD System and the Laminate Modeller, which is the third level of this system. MicroStation™ 95 is chosen as the CAD System. The Patran™ P3 Laminate Modeller uses IGES files from the CAD system for

modeling. All these three levels make up the system. This paper concentrates on the first and second levels (described in the following sections), while Kumar’s paper[7] describes level 3 in detail.

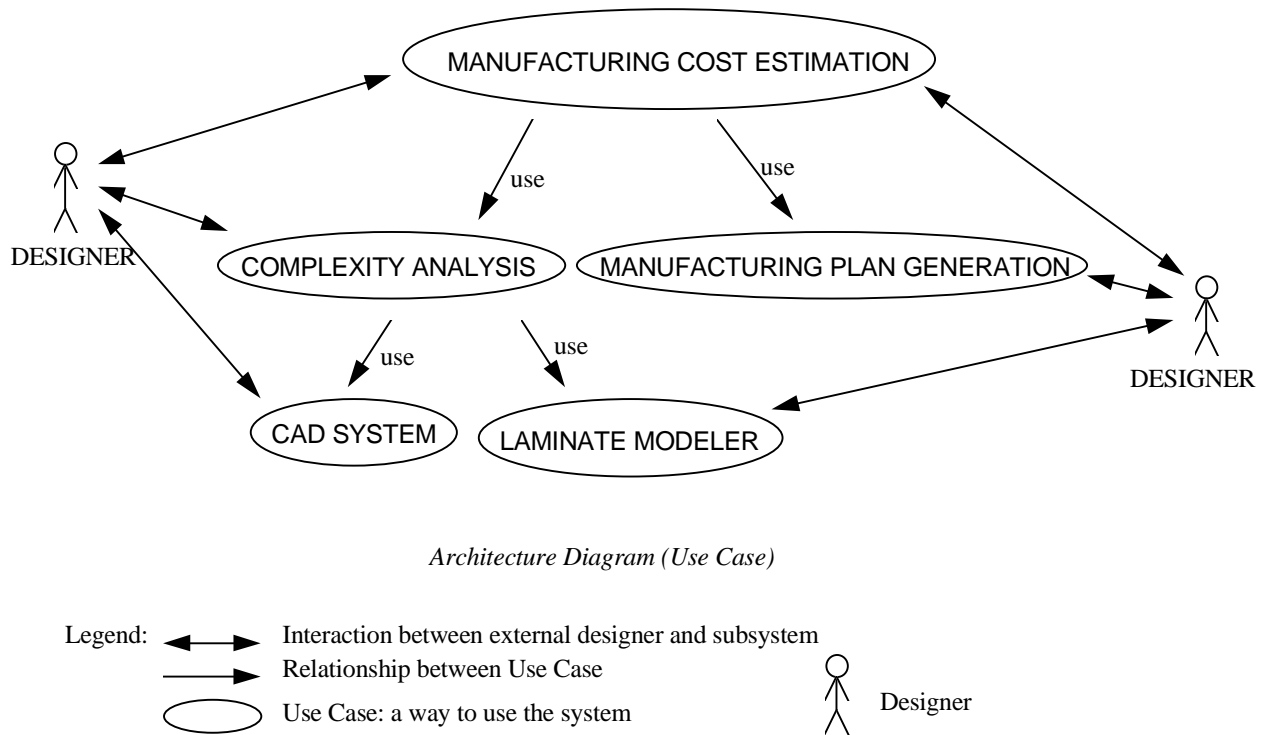


Figure 3. Use Case Representation of the Computer System

MANUFACTURING PLAN GENERATION

Manufacturing Process Representation

A manufacturing plan is made up of processes, and every process has its own resources. Equipment is a kind of resource, so are labor, tool, composite tool, and even a compound resource (a set of multiple resources that are always used together). The Composite pattern [3] is applied to represent all these resources. The Composite pattern “composes objects into tree structures to represent part-whole hierarchies. It also lets clients treat individual objects and compositions of objects uniformly.”[3]. The key to this pattern is an abstract class[4] *Resource* (Figure 4, using the notation provided in Figure 2) that represents both primitives, such as *Equipment*, *Labor*, *Non_Composite_Tool*, and *Compound Resource*. A *Compound Resource* is not only the aggregation of *Resource*, it is inherited from or specialises *Resource* as well. That means a compound resource is a resource. By using this pattern, users can group the resources to form a compound resource, which in turn can be grouped to form still more complex resource recursively. (The Composite pattern is used in other aspects of the computer system, for example compound components.)

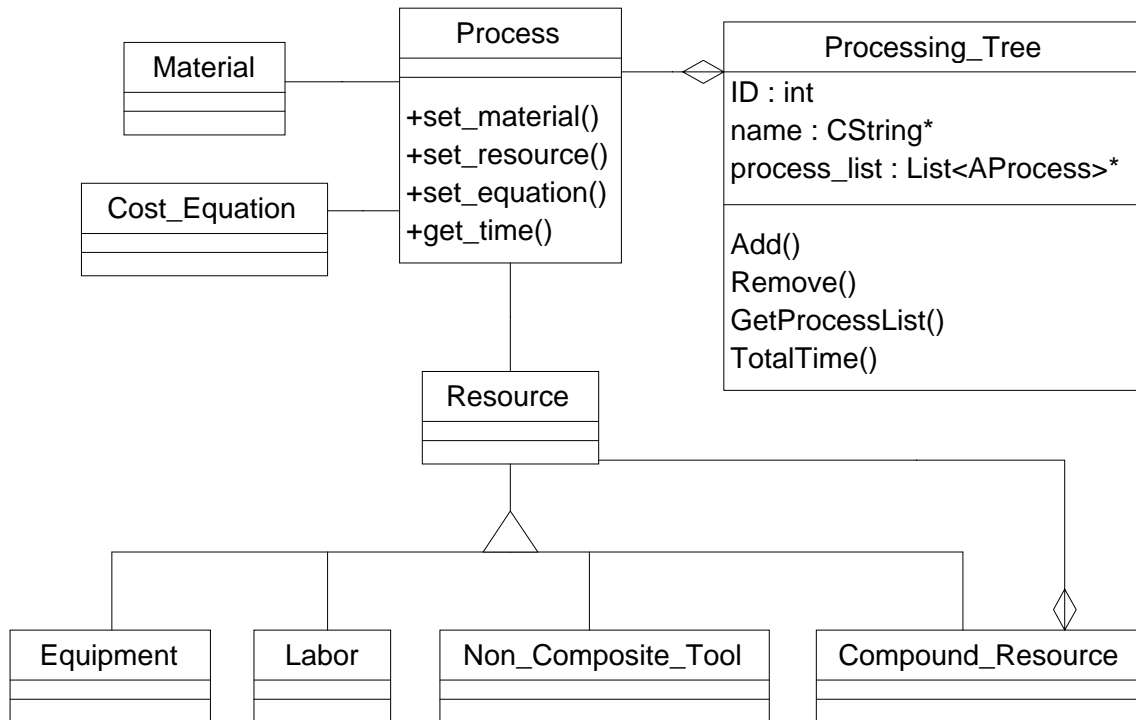


Figure 4. The Manufacturing Process Representation

Process has *Resource*, *Material*, process name, ID and strategy to calculate the time spent on this process as shown in Figure 4. The *Process* class uses *Cost_Equation* class as the strategy to calculate the cost (Fig 4). There are six equations according to the MIT model [2]. All the equations are inherited[4] from the *Cost_Equation* class. This makes all these equations have the same interface, and makes our system more flexible as any new ways to calculate cost can be easily added. This design uses the Strategy pattern [3].

Processing Tree Representation

The processing tree representation is also shown in Figure 4. A *Processing Tree* is an aggregation of *Process*. It has *name*, *ID* and a *process list* (or, more accurately a graph) which holds all the processes. *Processing Tree* has behaviours. For example, *Add()* provides a way to add a new process to the processing tree for a component, *Remove()* can be used to delete a process from an exist processing plan, *GetProcessList()* iterates over the processing tree, and *TotalTime()* supplies the method to calculate the total manufacturing time of the component. The database stores the processing trees for the various components which can be retrieved later on to generate a processing plan for a new or similar part. The pseudo code for entering, retrieving and generating a processing tree for a component can be shown below:

1. `open_database();`
2. `query_and_select_process_from_database();`
3. `process=pick_up_process(ID);`
4. `processing_tree=add_process_to_processing_tree(process);`
5. `add_processing_tree_to_container();`
6. `close_database();`

First, open the database (1), then query and select the process for a new component (2), then go to the database to pick up the process by ID number or any of its properties (3), after that, add all the necessary processes in the processing tree (4), store this processing tree in a container of the database (5), and finally save into the database by closing the database (6). Because tooling for a composite or laminate component is almost as complicated as the component itself, we mention it here explicitly. Basically there are two kinds of tooling. One is non composite (metal), and we regard this as a resource. The other is composite tool, and we think of this as another composite component that must be manufactured.

COMPLEXITY ANALYSIS AND COST ESTIMATION

Manufacturing Cost Estimation

The aim of this project is to estimate the cost of manufacturing the component. For each of the manufacturing steps, the cost considerations are materials; resources, which include the cost of equipment, labor, tool, and floor space; labor time, which is related to extensible parameters or measurements of the component; and complexities of the process that are significant cost drivers. A cost model for composite manufacturing should incorporate measures that a designer can easily obtain.

The *Material* class is for materials, see Figure 4, with cost or price as an attribute. Once geometric and complexity measurements have been made and stored in the database, we can call the operation in the material class to calculate the cost.

CAD Translation and Complexity Measurements

The CAD system used for the analysis is MicroStation™ 95, chosen for its ease of use. The design models can easily be exported from and imported to any other CAD systems by the use of the standard Initial Graphics Exchange Specification (IGES). MicroStation™ provides access to the extensible parameters or measurements, such as dimensions, surface area, volume, etc. These parameters are then written into the database [7].

The most important geometric complexity is the curvature angle of the part. This is determined using the Patran™ Laminate Modeller. The Laminate Modeller generates files that give the weft and warp coordinates of the fibres. The curvature bend angle can be numerically calculated from the knowledge of warp and weft fibres. The fibre orientation and ply count can also be read from the files that are generated in the Patran™ Laminate Modeller. Laminate complexities can be calculated with knowledge of extensible parameters, fibre orientation angle, and ply count. All of this geometric and laminate complexity information can then be stored in the database, and be queried when calculating the cost or time of a process for a component.

Another complexity of the part is determined by the sum of the dimensions required to describe the part and the tolerances on those dimensions. We consider these dimensions and tolerances as another complexity metric. This simpler approach could be used for fairly rapid comparison of alternative designs.

PROCESSING COST

In terms of processing cost, we take equipment, labour, tools and compound resource into account, with labor and processing cost dependent on the estimated time to process a given part. The time required to complete a processing step is related to the extensible parameters and complexities of the part. Extensible parameters are length, surface area, weight, volume, etc., and various manufacturing processes scale with certain extensible parameters. For instance, the time for hand layup is proportional to the surface area of the part. If the part has a complex shape, the linear or simple measurement is not sufficient, and MIT's approach [8] determines the amount of information required to represent a complex shape. Complexity can then be measured by an information metric [8].

There are six cost equations (two examples are provided in equations 1 and 2 in Figure 5) which take all these into consideration. The equation class is shown in Figure 4, and *Process* object uses *CostEquation* when calculating the processing time.

$$\text{Minutes} = \left[\left(\frac{\text{Setup}}{\text{Run}} \right) + \left(\frac{\text{Delay}}{\text{Operation}} \right) \left(\frac{\text{Operations}}{\text{Run}} \right) \right] \frac{(\text{Parts/Shipset})}{(\text{Parts/Lot})(\text{Lots/Run})} \quad (1)$$

$$\text{Minutes} = \left[\left(\frac{\text{Setup}}{\text{Run}} \right) + \left\{ \left(\frac{\text{Delay}}{\text{Operation}} \right) + \sqrt{\left(\frac{V_1}{v_{o1}} \right)^2 + \frac{2t_1 V_1}{v_{o1}}} \right\} \left(\frac{\text{Operations}}{\text{Run}} \right) \right] \frac{(\text{Parts/Shipset})}{(\text{Lots/Run})(\text{Parts/Lot})} \quad (2)$$

Figure 5. Two Sample Cost Equations

Learning Curve Effects

Learning curves must be taken into account. They are expressible by the number of parts made when the time per part levels off and stops decreasing significantly. This effect is for a new part, a new process, or a new labourer. Learning curve can also impact material scrap rates. We consider these learning curves as additional database objects.

CASE STUDY

We are investigating an airplane undercarriage door design as a case study for the computer based cost estimation system. This undercarriage door is a redesign, and the investigation involves comparing the new design to the original one. Our objective is to estimate the cost for the two new different designs, comparing them both to the old design.

The new cocured stiffened design involves the following processing steps:

- Layup the exterior skin over the main tool
- Put honeycomb with template
- Layup the ribs and spars
- Layup the interior skin
- Cure the whole part

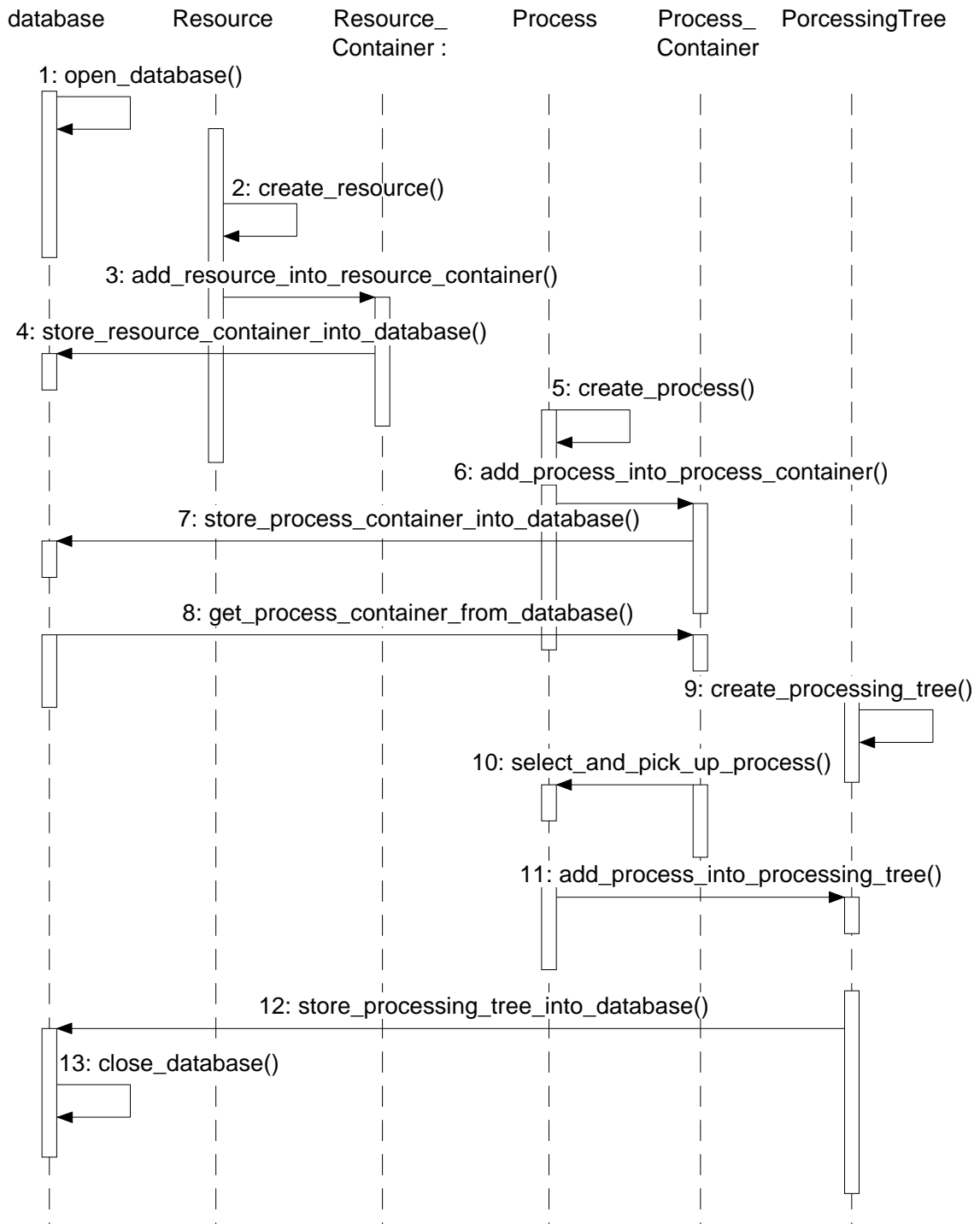


Figure 6. Sample massaging for Undercarriage Door Cost Estimation

The event trace of a scenario (Figure 6) describes how the system would be used for this case study. The text on the top of each vertical line is the class[4] name, which can be found from Figure 4, a horizontal arrow line indicates a message or behaviour between two objects, and a little rectangular box on a vertical line stands for an operation of the class that would be carried out in response to the message.

First of all, we instantiate and store the resources which are used to manufacture the component. We open the database (message 1), and instantiate or create all the instances that

are not already in the database, such as equipment (Gerber Cut and Core Cover), and labourers (Manager and Inspector), from resource class *Resource* (message 2). Then, we put all these resources in *Resource_Container* (message 3), which is a container of the database. All these resource objects are stored in the database by message 4.

Second, we install any needed processes into the database, making objects of class *Process* (message 5), such as “layup manual prepreg fabric”, “cure autoclave”, “position manual mylar template”. With resources, only processes that are not already present in the database must be instantiated, and the parameters are initialised when the processes are created. Then all these processes are placed in the *Process_Container* of the database (message 6). Finally we store all the process information into the database, this is message 7. Similar operations are carried out for the *Material* class, setting cost parameters to take material cost into account.

Third, we generate the processing plan for this component (These steps would be required whenever a new processing tree is under consideration and must therefore be added to the database). We get the *Process_Container* from the database (message 8), and next instantiate the class *ProcessingTree* to hold the processing plan for our undercarriage door (message 9). Then we can select and pick up all the processes we need for the component from the *Process_Container* (message 10). At this stage, we should take the complexity information into account, querying and therefore obtaining this information from the database for the appropriate process (detailed in [7]). After that, we add the processes to the *ProcessingTree* object (message 11), then we install this processing tree for the undercarriage door (message 12) and close the database (message 13).

If all the processing information was already stored in the ObjectStore[®] database, we could estimate the cost of manufacturing the component merely by querying and picking up the processing tree from the database. Then, the cost estimation would be accomplished by the processing tree calling its *TotalTime()* operation, which in turn calls the *get_time()* operation of each process.

CONCLUSION

The MIT model for cost estimation [2] has been the basis for this computer based system. The comparison with Australian data has been reported, but additional comparisons are ongoing. While the cost estimation is done automatically, the manufacturing process plan generation is done manually. This means we need to query the process database manually, under the direction of a manufacturing expert, in order to generate the manufacturing plan. Semi-automatic plan generation is our next step. It will allow for some steps in the processing tree to be copied or repeated for a new component that is similar to an existing one. More automated processing tree generation may be possible by “intelligent” retrieval and extension according to the part’s complexity and specification.

Through the case study, we have been applying object oriented technology to aerospace composite manufacturability successfully. The benefits of this approach, as compared to a relational database, are extensibility and reusability. These issues will become important as new components, new processes, and additional lifecycle costs are considered. And, an object oriented approach is necessary for addressing manufacturability.

ACKNOWLEDGMENTS

The authors wish to thank CRC-AS's research engineers Jaya Motipalli, Chris Granatir, and Daniel Bitton, and Boeing chief estimator Trevor Warren Smith for their invaluable contributions to this project. We also would like to thank the Aerospace Engineering Department, RMIT.

REFERENCES

1. Bindu R. Rao. *Object-Oriented Databases Technology, Applications, and Products*. McGraw-Hill. 1994
2. Ein Teck Neoh. Adaptive Framework for Estimating Fabrication Time. *MIT Thesis*. 1995
3. Erich Gamma, Richard Helm, Ralph Johnson, John Vlissides. *Design Patterns Elements of Reusable Object-Oriented Software*. Addison Wesley. 1995
4. Giri Krishnan, Elizabeth. A. Kendall, "Object Oriented DataBases and Techniques Applied to Composites", ICCM-11, Australia, 1997
5. Grady Booch. *Object Oriented Design with Applications*. The Benjamin/Cummings Publishing Company, Inc. 1991
6. James Rumbaugh, Michael Blaha, William Premerlani, Frederick Eddy and William Lorensen. *Object-oriented Modeling and Design*. Prentice Hall International Editions. 1991
7. Jayanthi Kumar, Liz Kendall. *Cost Estimates of Composite Aerospace Structures Based on Complexity*. ICCM-11 conference, Australia. 1997
8. Mawuli Tse. Design Cost Model for Advanced Composite Structures. *MIT Thesis*. 1992.
9. Object Design, Inc. *OBJECTSTORE[®] C++ API User Guide Release 4.0.1*.
10. Stuart Muter. Cost Comparisons of Alternate Designs: An Information Based Model. *MIT Thesis*. 1993.

COST ESTIMATES OF COMPOSITE AEROSPACE STRUCTURES BASED ON COMPLEXITY

Jayanthi Kumar, Elizabeth Kendall, Amit Satyawadi, Chand Kumar Malu

*Computer Systems Engineering, Royal Melbourne Institute of Technology,
PO Box 2476V Melbourne, Victoria 3001 Australia*

*This project is funded by the Cooperative Research Centre - Aerospace Structures
506 Lorimer Street, Fishermens Bend, Victoria 3207 Australia*

SUMMARY : The focus of this paper is a computer based system for measuring the complexity of a composite part, based on information theory, according to a model from MIT. Metrics such as geometric complexities and laminate complexities are considered, and these will be read from files of the Patran™ Laminate Modeler. Other metrics known as extensible parameters will be read from the files generated by CAD (Computer Aided Design). All these metrics are calculated and stored in an OODBMS (Object Oriented Database). These complexity metrics will then be retrieved and incorporated into the MIT cost model to predict the cost to manufacture a particular composite component. With this system, cost predictions will be readily available during the preliminary design phase.

KEYWORDS: computer aided design and manufacture, cost estimation, design

INTRODUCTION

Advanced composites have had considerable impact on the aircraft industry due to their low weight and high strength, as well as the flexibility they offer in designing parts with specific structural properties. However, this has been hampered by their high material and fabrication costs. Studies indicate that a large percentage of the final cost is determined in the design phase, and a major cost driver in composite manufacturing is the complexity of the part.

The aim of this project is to develop a computer based system for measuring the complexity of a part, based on information theory, according to a model from MIT[1]. The MIT complexity model has been manually verified. (Further verification is still under investigation.) The computer based model will reproduce the manually generated results that have been obtained to date. The inputs to the system are CAD (Computer Aided Design) data of the component from Microstation™ [17] and from the Patran™ Laminate Modeler [18].

Extensible parameters such as volume, surface area, perimeter, and dimensions, etc. of the design will be obtained from the CAD system. These parameters are used in first order (zero complexity) cost calculations. Geometric complexities of composite parts, like stretch and shrink flange angles, and laminate complexities, such as ply counts, drop off plies, and ply orientations are being determined from the Patran Laminate Modeler.

This paper will describe how the extensible parameters are calculated and retrieved from the CAD System. It also explains how the curvature of the complex surface and the laminate complexities are determined from the Patran Laminate Modeler. The complexity of a part increases manufacturing time beyond the first order or zero complexity prediction. Ply drop-offs and multiple ply orientations require more cutting and more pieces per unit volume. Complex curvature parts are more difficult to manufacture as they imply a change in manufacturing procedures, especially more manual effort.

All these complexity metrics will be calculated and stored in an OODBMS(object oriented database). The complexity metrics are then retrieved and incorporated into the MIT cost model to predict, during preliminary design, the cost to manufacture a particular composite component. Details of the approach are provided in this paper.

BACKGROUND

M.I.T Model

It was shown that complex parts require more fabrication time than simpler parts[3]. The MIT Cost Model [2] incorporate complexity factors, and demonstrates that each complexity factor is unique and is either empirically or intuitively derived and is usually a process specific multivariable parameter. Muter[1] proposed an approach to define part complexity based on the idea that the information required to make a part is embodied in the detail part drawings, and, further, that complexity is completely determined by information content. An information theory approach is therefore taken to quantify the complexity associated with each nonredundant dimension on a part drawing. The information content of a part is then the sum of the individual dimension information terms, given by Eqn 1.

$$I = \sum_{i=1}^N \log_2 \left(\frac{\text{dimension}}{\text{tolerance}} \right) \quad (1)$$

Cost estimates produced using this equation were found to exhibit a similar degree of accuracy when compared to estimates performed by an experienced estimator [1].

It was shown[2] that measurements of complexity for composites were simplified by the fact that the constitution of the material, in terms of fiber volume fractions and fiber arrangements, was predetermined by the designer. Tse[2] developed a model for estimating manufacturing time which predicts recurring labor for a range of advanced composite material manufacturing processes for aircraft fuselage stiffeners. The model used an information metric for shape complexity. Tse chose the fibers to be the information carriers and identified three kinds of fiber information: bending, torsion and alignment or positioning.

Information Content of Composite Fibers

Fig. 1 shows the discrete model of an individual fiber. The model is based upon the use of a linear detector to measure discrete angle changes. The model assumes an equiprobable angular range of θ , and a minimum linear detection distance of δ . The minimum angular unit is denoted by ζ . The information content of one discrete fiber bend based on Eqn 1 is given by Eqn 2

$$I = \log_2 \left(\frac{\theta_{\max}}{\zeta} \right) \quad (2)$$

The total information content for a single curve of a fiber of radius ρ , of length S , which consists of N independent bends is given by Eqn 3

$$I = N \log_2 \left(\frac{\theta_{\max}}{\sqrt{\frac{\delta}{2\rho}}} \right) = \theta \sqrt{\frac{2\rho}{\delta}} \log_2 \left(\frac{\theta_{\max}}{\sqrt{\frac{\delta}{2\rho}}} \right) \quad (3)$$

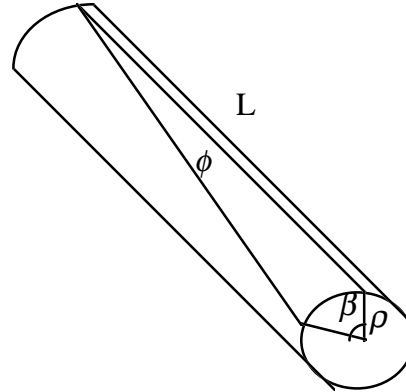
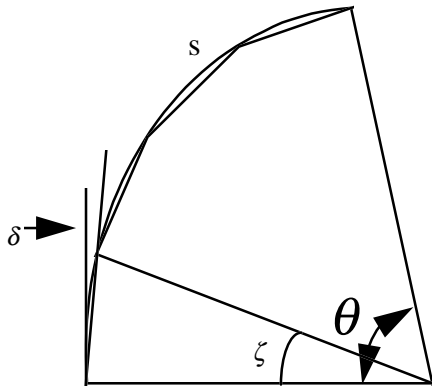


Fig. 1: Discretization of a single curve in a fiber [2].

Fig. 2: Torsion in a single fiber [2]

Hence the information stored in curved fiber is linearly proportional to the enclosed angle θ . Further, the information, I , of the part is simply the sum of the information for all the fibers in the part.

Torsion Information

Torsion information is a measure of the amount of twist introduced in a fiber during forming.

Torsion information of Fig. 2 is given in Eqn 4.

$$\tau(s) = k(s) \tan(\alpha)$$

$$\phi = \tau L$$

$$I_{torsion} = \frac{\phi}{\zeta} \log_2 \left(\frac{\zeta}{\phi_{\max}} \right) \quad (4)$$

The angle of attack α relates the radius of torsional curvature to the bending curvature of the line, $k(s)$. ϕ is the angle of twist and L is the length. Though torsional information was found to be quantifiable, its effect on labor time appeared to be small. That is, parts with different amounts of calculated torsional information did not display an appreciable difference in labor forming time.

Positioning Information

Positioning information represents the probability of placing adjoining fibers in certain positions relative to each other. Positioning information is at a minimum when identical elements are butted against each other. Positioning information identifies the complexity in aligned fiber parts with no fiber bending. The part shown in Fig. 3 (a) has been defined to have no positioning information. The part in Fig. 3 (b) will have information based on the relative rotation of the fibers at the corner.

It has been shown[4] the complexity that arises in the lay-up of composite laminates is associated with the location and placement of successive plies on top of one another. In the ply configuration of a particular part, the lay-up of plies can be considered as a stack on N

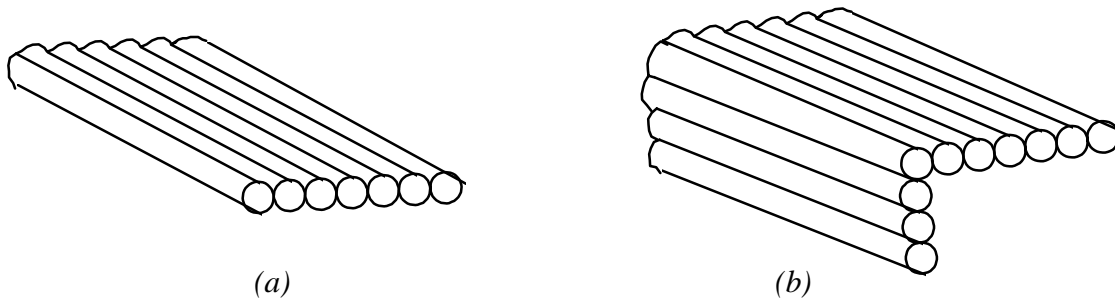


Fig. 3: (a) Ply arrangement without measurable information content. (b) Ply arrangement having positioning information but no bending information [2]



Fig. 4: Various ply stack-ups [4]

elements, where each element is a ply. As shown in Fig. 4(a), if all N elements are identical, only one configuration is possible. In order to quantify this type of complexity, from an information theory approach, the probability of this configuration is 1. If there are m different ply sizes or shapes the number of possible configuration also changes. Fig. 4(b) shows two different configurations for the same N and m. The information content of a ply stack-up is given in Eqn 5 as

$$p = \frac{1}{m^N}$$

$$I = \log_2 \left(\frac{1}{p} \right) = \log_2 (m^N) = N \log_2 m \quad (5)$$

m types of plies are abstracted as ply drop-offs plus one from a design. Eqn 5 can be rewritten as:

$$I = (\# \text{ of plies}) \times \log(\# \text{ of ply dropoffs} + 1) \quad (6)$$

Summary of Labor Time

The first order model or zero complexity model for labor time is characterised by a time constant, τ and a final velocity, v_o [2]. The first order model is based on the idea that labourers can attain a final velocity for any task, and that their time to complete is a function of this velocity and an extensible parameter of the component to be built. The process task time for a large distance x , is given by the simple Eqn 7 [2]. The time constant, τ , is given by Eqn 8 [2].

$$T = \tau + \frac{X}{v_o} \quad (7)$$

$$\tau = \tau_o (1 + bI) \quad (8)$$

The constants τ_o and b are determined by the process. I is the scaling parameter that represents the complexity of the part. Tse[2] reported that for the manual hand lay-up process the time constant equation is given by Eqn 9

$$\tau = \tau_o (1 + b_m I_m + b_f I_f) \quad (9)$$

Where the subscript m refers to male type bends and the subscript f refers to female type bends. For additive processes such as tape lay-up, the time taken for n strips of width w and length x_i , for a ply, is given in terms of area A ,

$$T = \sum t = \sum_1^n \left(\tau + \frac{x_i}{v_o} \right) = n\tau + \frac{1}{v_o} \sum_1^n (x_i) = n\tau + \frac{A}{v_o w} \quad (10)$$

For N plies of thickness h , the time to make a part is given in terms of part volume V ,

$$T = \sum_1^N \sum_1^n t = nN\tau + \frac{V}{v_o wh} \quad (11)$$

The Eqn 11 is further reduced to a time-weight relation by introducing material density, as shown in Eqn 12,

$$T = nN\tau + \frac{W}{v_o wh\rho} \quad (12)$$

The Eqns 10, 11 and 12 form the basis of the MIT cost estimation model, first presented by Tse[2]. Depending on the nature of a particular part or process, any of these equations can be applied.

METHODOLOGY COMPUTER MODEL

A cost model for composite manufacture should incorporate measures of complexity that a designer can easily abstract from a design with readily available design tools. The computer system under development for the CRC -AS in Australia aims to accomplish this. The computer model is based on object oriented techniques. Each component and its

measurements (extensible parameters and complexities) are considered as objects. The advantages of this concept is that it provides extensibility in terms of components, measurements and processes in the model [12][15].

CAD SYSTEM

The CAD system used for the analysis is Microstation™ 95, which was chosen for its ease of use. The design models can easily be exported and imported to or from any other CAD system by the standard Initial Graphics Exchange Specification(IGES) format. Microstation features extensive measuring capabilities for extensible parameters through a macro library called Microstation Basic. This provides access to the memory block of Microstation, where the measurements such as dimensions, surface area, volume, etc are stored. These parameters are then written into a database. Microstation also provides the designer with an easy to use graphical user interface to facilitate user inputs for a component's name or measurements.

The designer has to select the appropriate component from the CAD design model and this in turn invokes Microstation to take measurements. These measurements are then written into a text file for export to the database by invoking a macro written in Microstation Basic.

Patran™ Laminate Modeler

Patran is an open, integrated CAE (Computer Aided Engineering) software system which enable a common model for analysis. It shortens the design process by eliminating the need for engineers to recreate design geometry for analysis. The Patran Laminate Modeler is a Patran module for aiding the design, analysis, and manufacture of laminated composite structures. The user can simulate the application of layers of reinforcing materials to selected areas of a surface to ensure that a design is realisable. Layers are then used to build up the composite construction in a manner that reflects the manufacture of the structure. Finite element properties and laminate materials are automatically generated so that accurate models of the structure can be evaluated rapidly. By enabling the concept of concurrent engineering, the Laminate Modeler facilitates the design of structures which take full advantage of these materials in the aerospace, automotive, marine, and other markets. It also defines fiber orientations.

Theory

The curvature of the fiber on the part surface is represented by in plane and out of plane curvature [3]. Normal or out of plane curvature is the type of curvature required to make singly curved parts (simple bends). Inplane curvature, or geodesic curvature, represents double or compound curvature parts. Hence over a section of constant curvature, the enclosed angle θ is

$$\theta^2 = \theta_n^2 + \theta_g^2 \quad (13)$$

where θ_n is the enclosed angle, for the out-of -plane bending of a fiber, and θ_g is the in-plane enclosed angle. For parts with different degrees of curvature, the in-plane enclosed angle is given by[3]

$$\bar{\theta}_g = \frac{1}{A} \sum \theta_{gi} \Delta A_i \quad (14)$$

A is the total area of the part, θ_{gi} is the enclosed angle for a given fiber or a region, and ΔA_i is the corresponding area for that fiber or that region. On a fiber by fiber basis, the equation is given as

$$\bar{\theta}_g = \frac{1}{A} \sum_{i=1}^{N_f} \theta_{gi} s_i \Delta s_n \quad (15)$$

s_i is the length of the fiber and Δs_n is the width of the fiber unit. N_f is the number of fibers. The enclosed angle θ_n (out-of-plane bend angle) for any arbitrary fiber orientation is given [2] in Eqn 16. Ψ is the fiber orientation angle, α is the angle between the two planes or surfaces.

$$\theta_n = \pi - 2 \cos^{-1} \left[\sin \psi \cos \left(\frac{\alpha}{2} \right) \right] \quad (16)$$

Out-of-plane and in-plane shear slip required to deform an initially flat laminate into their respective enclosed angles is illustrated in Fig. 5. It was shown by Tam and Gutowski in [11], the shear slip for the appropriate plane is defined as

$$\Gamma = \frac{\delta}{H} \quad (17)$$

Hence from [11]

$$\theta = \Gamma \quad (18)$$

Incremental shear from a fiber mapping is defined as

$$d\Gamma_{12} = \frac{ds_1 - ds_0}{du} \quad (19)$$

ds_0 and ds_1 are incremental lengths along two adjacent fibers, and du is the inter-fiber spacing as shown in Fig. 6. It was shown that the in-plane shear deformation is related to the geodesic curvature of a fiber as

$$\Gamma_{12} = \int_0^L k_s(s) ds \quad (20)$$

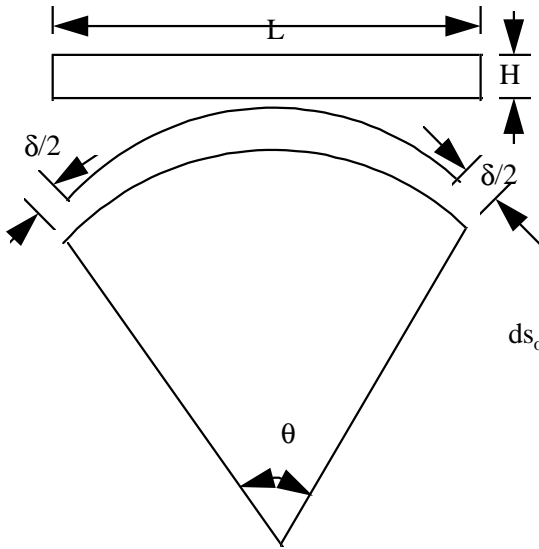


Fig. 5: Shear slip required to deform a flat laminate in the appropriate plane [11].

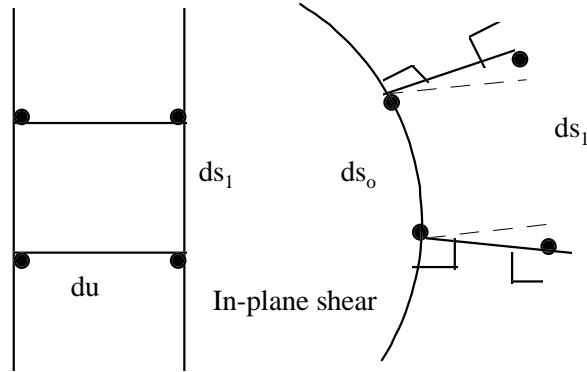


Fig. 6: In-plane local incremental shear [11].

By using Eqns 13, 16, 19 and 20, the enclosed angle is calculated numerically.

Ply drop-offs for different ply orientations are calculated using the equations derived by Neoh E.T [3]. These use the extensible parameters that are being calculated and stored in a text file by Microstation. The fiber orientation and ply count are read from the files that are generated in the Patran Laminate Modeler.

Summary of the Method

The CAD data of the component in standard IGES file format will be input into Patran™. The advantages of using the Patran Laminate Modeler is that it generates files that have information about the lay-up details such as fiber orientation, warp and weft fibers, ply count and the fiber thickness. Though the file in the Laminate Modeler does not give the fiber enclosed angle (as shown in Fig. 1) directly, it can be numerically calculated with the knowledge of the warp and weft fiber co-ordinates.

The surface to be laid with composite material is first meshed using finite elements. Using the laminate modeler tool, lay-up is carried out. The designer needs to input the composite material, the warp and weft angle if scissor draping is selected and also the thickness of a single ply. The laminate material and its properties are defined using the standard Patran methods of material definition. Once the reference direction is specified for the fiber placement, the ply lay-up will be done and the files containing information about the fibers will be exported. During the analysis, it is possible to visually observe the amount of strain on the surface of the part. This is indicated by different colours, with each specific colour representing the percentage of the maximum strain. This indicates the difficulty of lay-up and also it gives the pattern of the lay-up fabric.

DATABASE

After evaluation, ply drop off and fiber angle is written into a text file. This text file is then used to export this data to an ObjectStore [16] database that has the cost calculating equations [12].

ObjectStore is a comprehensive object oriented database management system (OODBMS). It is based on the storage of entities as objects. The advantages of using this kind of database are the following [12][15]: a) Since the entities are stored as objects, different kind of entities can be stored in the database, and the objects can be interrelated in ways that go beyond the relational model. b) It provides extensibility in terms of the number and kind of objects. This means that any number of measurements and components can be stored in the database. c) This system uses the powerful features of object oriented analysis, design and implementation such as polymorphism, delegation, containment, inheritance, etc. With an object oriented approach, the data and behavior are fully integrated. This results in a superior representation than one that could be done with a relational approach, especially for manufacturing applications.

The problem has been analysed using object oriented methodology[13][14]. OMT(Object Modeling Technique, developed by Raumbaugh[13]) notations shown in Fig. 7 is used in building the object model shown in Fig. 8.

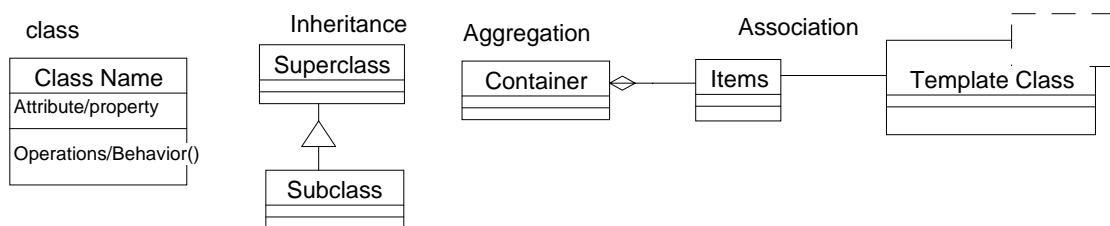


Fig. 7: Basic notation used in Object Model.

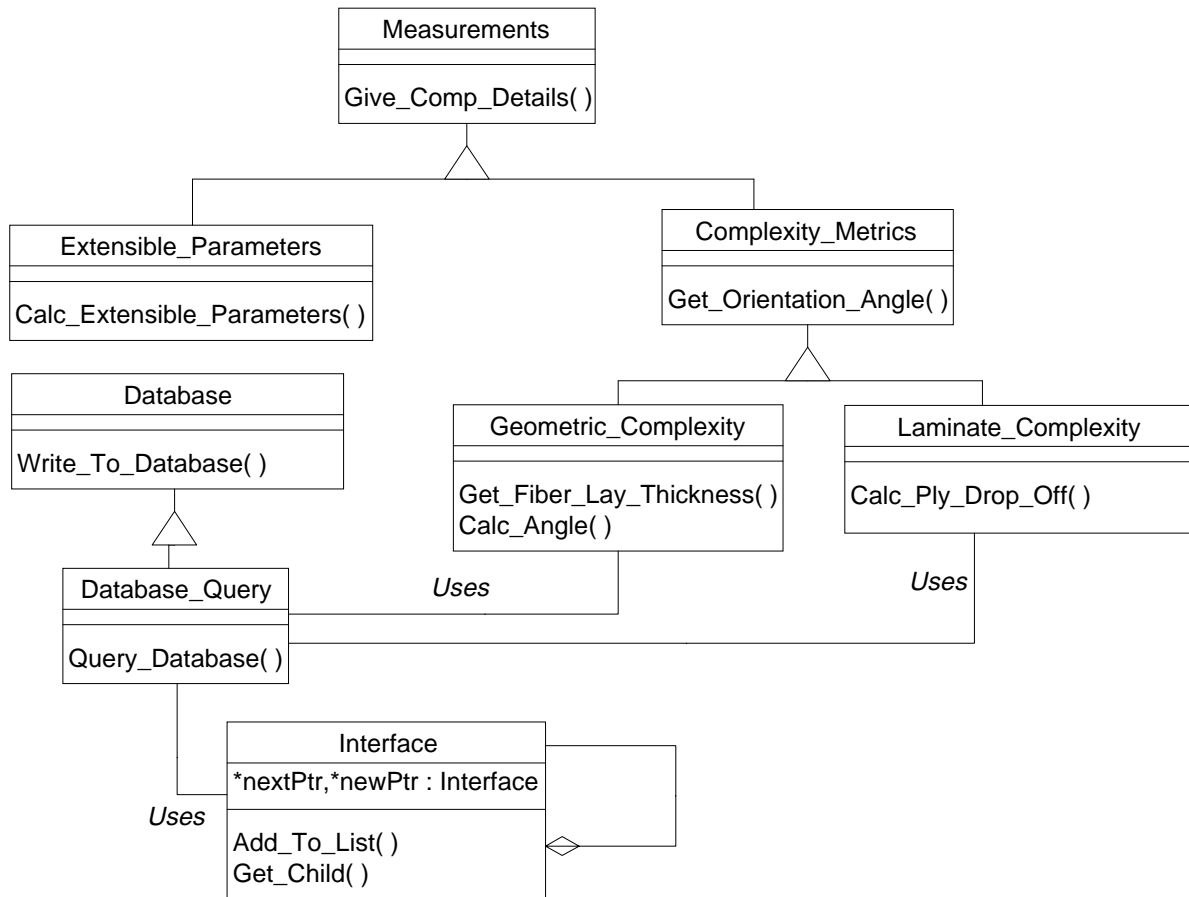


Fig. 8: The Object Oriented Model of the Complexity Metrics

The Object model shown in Fig. 8 describes an Object Oriented Interface between a CAD system and an OODBMS. There are eight classes in this model. The class Measurements is a superclass for Extensible_Parameters and Complexity_Metrics. It has commonality in terms of attributes and behaviour for the two sub-classes. The class Extensible_Parameter (inherited from Measurements) specialises its behaviour to take the Extensible Parameters from the CAD system (like length, area, volume, etc).

The class Complexity_Metrics (inherited from Measurements) specialises its behaviour to take Complexity Metrics from the Laminate Modeler. It has two subclasses Geometric_Complexity and Laminate_Complexity. Each of them specialises in the type of complexities (geometric or laminate). However each of these classes use the extensible parameters stored in the database to calculate complexities (uses Database).

The class Database is a superclass for Database_Query describing the interface for the database operations (like opening a database, writing data to a database and closing the database). The subclass Database_Query (inherits from Database) describes the interface for the querying operations to be performed by the user in the event of changing of any data in the database. The class Interface describes the interface for transferring the data from the CAD system and Laminate Modeler. It essentially describes a link list that is later stored in the database (uses Database).

CONCLUSIONS AND FUTURE WORK

The system developed will automatically generate complexity metrics like extensible parameters, curvature angle, and laminate complexities. These complexity metrics are stored in an OODBMS and then will be retrieved and input into the cost equations[12]. These equations give fabrication time, which takes care of geometric complexities and laminate complexities of the part. Knowing the fabrication time, actual cost of the component can be determined at the design stage.

Most of the computer based system has been designed and implemented, although full integration to the Patran Laminate Modeler has not yet been completed. The cost predictions have been verified in the USA, and some verification has been carried out in Australia. However, additional work with CRC industrial partners is being done currently. Case studies, including an aircraft carriage door, are under investigation.

ACKNOWLEDGMENTS

We would like to acknowledge the useful discussions we had with research engineers Jaya Motipalli, Chris Granatir, and Daniel Bitton, of the CRC-AS on the manufacture of composite parts. Also we would like to thank the Aerospace Engineering Department, RMIT.

REFERENCES

1. Mutter S, "Cost Comparisons of Alternate Designs", Masters Thesis, Department of Mechanical Engineering, MIT(Massachusetts Institute of Technology), 1993.
2. Tse M., "Design Cost Model for Advanced Composites Structures", Masters Thesis, Department of Mechanical Engineering and Technology and Policy Program, MIT, 1992.
3. Neoh E.T, "Adaptive Framework for Estimating Fabrication Time", Phd Thesis, Department of Mechanical Engineering, MIT, 1995.
4. Kim C.E, "Composites Cost Modeling: Complexity", Masters Thesis, Department of Mechanical Engineering and Technology and Policy Program, MIT, 1993.
5. Gutowski T, Hoult D, Dillon G, Muter S, Kim E, Tse M, E-T Neoh, "Development of a Theoretical Cost Model for Advanced Composite Fabrication", Composites Manufacturing, 1994.
6. Gutowski T. G, E-T Neoh and Dillon G, "Design Scaling Laws for Advanced Composites Fabrication Cost", Advanced Composites Technology Conference, 1994.
7. Cutkosky M. R and Tanenbaum J.M, " A Methodology and Computational Framework for Concurrent Product and Process Design", Mechanism and Machine Theory, 1989.

8. Foley M and Bernardon E, "Computer-Based Manufacturing Cost Analysis for the Fabrication of Thermoplastic Composite Structures", conference on Composites in Manufacturing, 1990.
9. Gonzalez-Zugasti J, "Computer Modelling of Advanced Composites Forming" Masters Thesis, Department of Mechanical Engineering, MIT, 1991.
10. Tam A.S, "A Deformation Model for the Forming of Aligned Fiber Composites" Phd Thesis, MIT, 1990.
11. Tam, and Gutowski T.G, "The Kinematics for forming ideal Aligned Fiber Composites, Composites Manufacturing, Vol. 1, No. 4, 1990.
12. Li M, Kendall E.A, Kumar J, "A Computer System for Lifecycle Cost Estimation and Manufacturability Assessment of Composites" , ICCM-11, Australia, 1997.(to be presented)
13. Raumbaugh J, Blaha M, Premerlani W, Eddy F and Lorensen W, "Object-Oriented Modeling and Design". Prentice Hall International Editions. 1991.
14. Booch G, "Object Oriented Design with Applications", The Benjamin/Cummings Publishing Company, Inc. 1991, California.
15. Krishnan G, Kendall E.A, "Object Oriented DataBases and Techniques Applied to Composites", ICCM-11, Australia, 1997.(to be presented)
16. Object Design, Inc. OBJECTSTORE[®] C++ API User Guide Release 4.0.1., May 1996, Burlington, MA.
17. Microstation[®] 95, Academic Suite[™] , © 1995 Bentley Systems, Inc.
18. MSC/Patran Version 5.0.
19. IGES Version 5.0

METHODOLOGY FOR DESIGNING COMPOSITE LAMINATE BOX BEAMS

Aaron S. Blicblau¹ and David Wallace²

¹*School of Mechanical and Manufacturing Engineering, Swinburne University of Technology
P.O.Box 218 Hawthorn Victoria, 3122 Australia*

²*Sutton Tools Pty. Ltd., 378 Settlement Road, Thomastown, Victoria 3074 Australia*

SUMMARY: This work describes the theoretical basis and design implementations for the prediction of the mechanical behaviour of fibre reinforced plastic box beams under various bending conditions. A computer assisted design package, called 'Buckle' has been developed as an aid for the design of these box beams. The design of the box beams is simplified with an inter-active approach to specifying constituent materials, overall geometric dimensions and loading situations. By incorporating an iterative approach, a comparison of materials and geometric structure leads to an appropriate selection and specification of fibre reinforced plastic beam performance requirements. The program implements a procedure for the prediction of the deflection and failure stresses in a box beam for a particular application. It enables the optimisation of fibre reinforcement orientation to minimise excessive deflections; determine buckling, and provides a comparison with similar behaviour of traditional structural materials

KEYWORDS: box-beam, bending, stiffness, deflection, computer-aided design

INTRODUCTION

Increasing use of fibre reinforced plastic (FRP) composites in structural applications is being made as manufacturing techniques, materials and improved analysis techniques are developed[1,2,3]. One reason that FRP composites are increasingly being used in engineering applications is their low specific mass compared to traditional construction materials such as steel and concrete. The low elastic modulus of FRP means that in structural applications it is best used where the shape of the member provides optimal stiffness[1,2,4]. For rectangular hollow box beams this is one of the most efficient forms of utilising FRP in terms of both stiffness and mass. These applications include stiffeners in the bodies of transport vehicles, interiors of boats and aircraft, ladders and office partition supports in buildings[5]. There is the potential to extend the use of FRP box beams further to include structural applications where the loads applied are higher and larger cross sections must be used. When using large beams, with thin walls, the chance of buckling occurring before the beam fails in shearing is high[6].

To achieve the appropriate combination of properties including lightness, resistance to deflection and buckling, the use of different laminate thicknesses or reinforcement orientation for different parts of the beam seems appropriate. In this work the authors developed a microcomputer based model for the design and analysis of laminated FRP box beams under

transverse loading conditions. A schematic diagram of the box beam configuration is shown in Fig.1 which also indicates the direction of applied loads and specific corner geometries. The computer design model enables the user to specify the composite material, or individual constituents, the arrangement of the plies and laminates, the angles of fibre reinforcement in the laminates and so optimise the geometry and material properties of the box beam. The results of the analysis provide appropriate guideline for beam strength, buckling resistance and weight for a given application. The program provides a comparison with steel, aluminium and timber beams of the same external dimensions. The model further enables prediction of the buckling and ultimate failure stresses in the beam to determine the suitability of that beam for a given application.

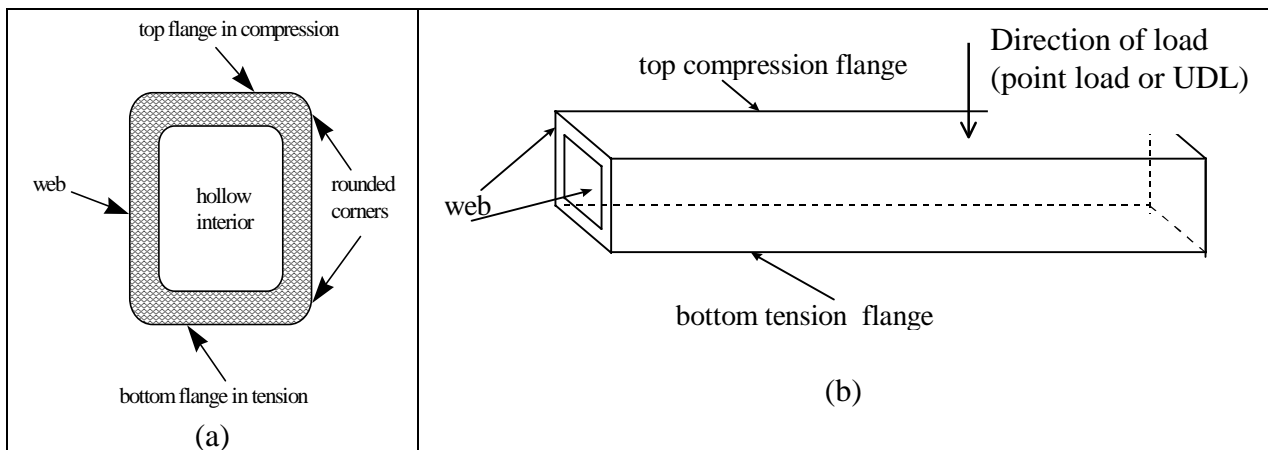


Fig. 1. Schematic diagram of the (a) cross-section of a rectangular hollow beam - enlarged view and (b) overall depiction of the beam, indicating general load direction either as one or more point loads, or a uniformly distributed load(UDL).

STRUCTURAL APPLICATIONS

Traditionally, the major areas of use of fibre reinforced plastic composites in structural engineering have involved utilising the material in the form of laminated sheets. Most applications use the composite material either as a skin or as a roofing material which is stressed in tension or formed to support its own mass[1,2]. The use of FRP sections such as beams to support transverse loads much greater than the beam mass is less common. Investigations into efficient beam design has mostly been carried out for other structural materials. This is not surprising given the relatively recent emergence of sophisticated FRP composite materials[3,4].

In the civil engineering sector composite materials including concrete have been widely used for some time. Concrete is used primarily as a composite in its own right and as a macro-composite with the addition of steel reinforcement. Much work has been done in research, development and testing to optimise reinforced concrete beam sections for strength and weight[9,10,11]. This work has led to the widespread use of box beams of varying cross sections which are designed specifically against shear and buckling failure[11]. While the investigations into the use reinforced concrete box beams clearly show the advantages of optimising the cross section of a beam for strength, the methods used for the calculation of beam parameters are largely not applicable to other materials. Although design algorithms

used for reinforced concrete box beam design deal with transverse buckling conditions they tend to be highly specific in nature. Due to the high specific gravity of concrete combined with its negligible tensile strength, steel reinforcement is used in a different manner to that of the fibres in a FRP material. Steel is used primarily either to prestress the concrete or act as an externally supportive structural member.

Investigations into the design of FRP box beams determined the way in which fibre orientation in the flanges of a box beam reacted in its resistance to buckling[2]. This involved the fabrication of box beams each with differing laminate structures in the web, compression and tension flanges. The values of Poisson's ratio, longitudinal and transverse elastic moduli was experimentally evaluated from samples taken from the beams. The overall wall thicknesses were then measured and values for the second moment of for each beam were calculated. These beams were constructed with diaphragms included at regular intervals to avoid premature localised buckling at the point of loading. Theoretical critical buckling stress values for the top flange (compression), bottom (tension) and sides (web) of the beam were calculated using elastic stability theory and classical bending theory[6]. The beams were then tested for the mid span deflection under a load of 1.0 kN. All of the beams failed by buckling of the compression flange.

From the data obtained it was concluded that while the use of longitudinal reinforcement in the compression flange gave the lowest deflection, bidirectional reinforcement increased the resistance to buckling at the expense of ultimate longitudinal strength. It was found that the experimentally obtained results with one exception were within plus or minus 15% of the theoretical predictions. This showed that the behaviour of a laminated FRP box beam could be reasonably well predicted using elastic stability and classical bending theory as applied to experimentally established laminate properties.

An analysis of the optimum fibre reinforcement orientations in laminated plates for resistance to compression and shear buckling was carried out to study specifically the behaviour of symmetric laminates used in long simply supported plates[12]. Using the assumption that the stiffness of the plate was entirely due to the fibres, elastic theory was applied to determine the buckling characteristics of the plate - where theoretical optimum fibre orientation for compression buckling resistance was found to be with fibre alignment at $\pm 45^\circ$ to the longitudinal plate axis, though this arrangement gave a theoretical laminate compressive strength of zero. The optimum fibre orientation for resistance to shear buckling was found to be with $\pm 60^\circ$ fibre orientation, which this did not give maximum shear strength. This research showed that the theoretical optimum fibre orientations must be considered in conjunction with the strength characteristics of the laminate.

Investigations to describe the buckling behaviour of a reinforced plastic box section under axial loading were undertaken[13,14] with varying results. These approaches involved finding buckling coefficients which could be used to modify elasticity equations commonly used for the prediction of buckling behaviour of plates[6]. The equations obtained were then applied to predict the buckling characteristics of a unidirectional fibre reinforced plastic box section. No conclusion was drawn by the authors regarding the accuracy of this approach when extended to the box section, nor was there any experimental validation of the calculated results. These investigation were inconclusive regarding the application of equations modified by coefficients to the buckling of the box section.

Moreover, the buckling analysis of FRP box beams was often tedious and required many iterations for optimisation. To facilitate this analysis, a number of microcomputer programs are available which can be used for the analysis of the composite box beams under various loading conditions. These included programs which combine micro mechanical theory, classical laminate plate theory and a finite element analysis of the structure to generate solutions[15]. There remains the need for care when designing large section thin walled beams using these programs.

BASIS FOR THE CURRENT ANALYTICAL DESIGN PROCEDURE

The analytical design procedure adopted for this work on the mechanical performance of laminated FRP box beams is divided into two main areas. The first deals with the characteristics of the FRP material used for the beam construction whilst the second deals with classical bending and elastic stability theory to determine the buckling, bending and stresses of the loaded beam[6,8].

Characteristics of the FRP Material

Consider a FRP laminate as a structure composed of thin sub layers(lamina). The layers may have differing alignments of fibre reinforcement. The material properties of the FRP composite laminate properties may be established using a number of approaches; those utilised in this work are the well established micromechanical theories for strength and stiffness [1,2,3], i.e. elastic modulus, shear modulus specific gravity and Poisson's ratio. Whereas a macromechanical approach was employed to analyse the stress and strain relationships within a lamina. Plate laminate theory was utilised to calculate the laminate properties[7]. The strength of the laminate was determined using a quadratic failure criteria to establish upper and lower bounds[16,17].

Bending and Elastic Stability

Classical bending theory was used to determine beam deflection under a given load,. This is based on the longitudinal modulus of the material and the second moment of inertia of the beam cross section[6,8]. Calculation of the maximum compressive and tensile stresses and maximum bending moment in the box beam were carried out also using these classical bending equations. For a laminated FRP box beam having the flanges and webs made from different laminates, there is no common longitudinal modulus throughout the beam. To simulate an isotropic material the longitudinal elastic modulus of the compression flange is taken as a baseline. The mid equivalent or transformed thicknesses as function of the transformed moduli for the webs and tension flange were determined. These transformed thicknesses are used to calculate the second moment of area of the beam using the parallel axis theorem. Using the transformed thicknesses, the effective areas of the web and flanges can be calculated. In addition the deflection caused by the selfweight of the beam is considered as a uniformly distributed load. The mass of the composite beam is determined by applying the rule of mixtures to the specific gravities of the fibre and matrix constituents and multiplying the composite specific density by the beam volume.

IMPLEMENTATION OF THE DESIGN

A computer program called "BUCKLE" was developed to predict the performance of laminated FRP box beams under transverse loading conditions. It provides information and guidelines about the viability of beams regarding resistance to buckling and failure due to exceedence of ultimate strength. Other outputs include the deflection of the beam compared with steel, aluminium and timber beams having the same external dimensions, and the performance of the steel, aluminium and timber beams with regard to buckling and ultimate strength. Shown in Fig. 2 is a flow chart of the major steps required in the design analysis. BUCKLE has been designed with an open program structure to allow the user to experiment by allowing the designer to quickly change parameters and observe the effects on beam performance.

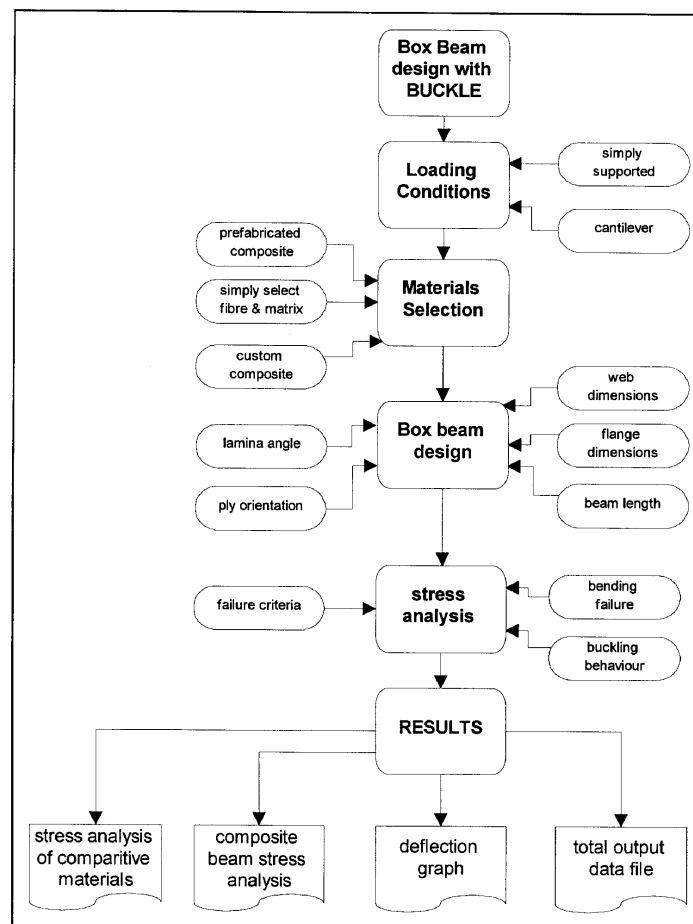


Fig 2. Flow chart describing the design procedure

It is important to recognise that the designation of the tension and compression flanges depends on the loading condition applied to the beam. In this design procedure, simply supported and cantilever beams have the top flange as the compression flange while for cantilever beams the compression flange is the lower flange (as shown in Fig.1). A corner radius has been included in the program input parameters, as industry practice in making these beams is to employ a corner, radius to minimise stress concentration.

To enable the analysis of beams under a variety of situations, the program allows for five distinct loading conditions to be selected. These include, a simply supported beam with any of a point load, two point load or a uniformly distributed load (UDL), or a cantilever beam with any of point load or UDL. For each loading condition a schematic diagram is presented on the computer video screen so that a reference is available to ensure correct entry of data. Fig. 3 shows a sample screen of the format for the required data involved in the analysis together with a diagram of a cantilever beam with a uniformly distributed load. Any of the data may be amended, and further analyses carried out to determine new performance characteristics.

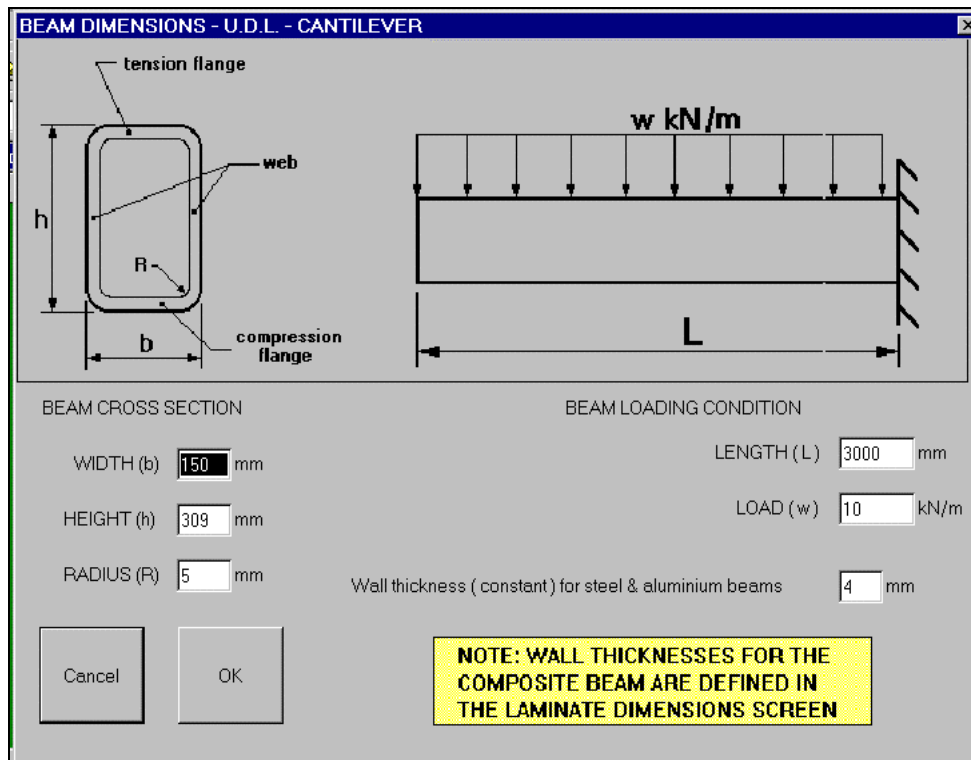


Fig. 3 A sample screen for the input of various beam configuration data and loading requirements.

RESULTS OF THE DESIGN PROCEDURE

Sample Analysis

A sample representative analysis of a composite beam was undertaken. The material selected was an E-glass epoxy such that the self-weight of the beam was 23.9 kg. The lamina was four plies thick with five repeats to give a total of 20 plies. The output data file combines the output data with the beam dimensions, laminate configuration, loading condition and material used. Included are the maximum deflections of the beams and the calculated critical and predicted stresses induced by the applied load.

Stresses in Composite Beam

The maximum strength of the composite beam is displayed according to the first or last ply failure modes[7]. These modes represent the failure stresses of the weakest ply and the

ultimate stress to failure of the laminate (ie the last ply in the laminate to fail) respectively. This data allows the designer to compare lower and upper bounds of the failure stresses in the laminates the stresses. Concomitantly, beam failure stresses are determined if failure is due to any of the buckling modes, or exceedence of the chosen strength criteria. For similar box beam steel and aluminium beams the stresses in the web and flanges together with the buckling stress is determined. A sample output of the stresses for the various beam materials is shown in Fig.4. For the timber beams (which are solid) only the maximum failure stress is determined.

LOADING CONDITION		
CANTILEVER BEAM - UNIFORMLY DISTRIBUTED LOAD	LOAD =	10 kN / m
STEEL BEAM - STRESS CONDITION		
	web shear stress	stress in flanges tensile & compressive
ALLOWABLE STRESS (BUCKLING)	252.9 MPa	1064.7 MPa
MAXIMUM STRENGTH	400 MPa	MPa
STRESS DUE TO LOADING	18.4 MPa	155 MPa
ALUMINIUM BEAM - STRESS CONDITION		
	web shear stress	stress in flanges tensile & compressive
ALLOWABLE STRESS (BUCKLING)	126 MPa	566.7 MPa
MAXIMUM STRENGTH	MPa	MPa
STRESS DUE TO LOADING	18.3 MPa	152.3 MPa
TIMBER BEAM - STRESS CONDITION		
	shear	tensile
MAXIMUM STRENGTH	MPa	MPa
STRESS DUE TO LOADING	19.6 MPa	1 MPa

Fig.4. Sample screen of comparative behaviour of beam materials.

Thus, the design analysis enables a comparison of failure behaviour to be made for the different materials at given loading conditions. Optimisation of the composite structure can be made by specification of varied materials and box beam dimensions.

Comparative Buckling Behaviour

For the present sample cantilever beam analysis, the critical buckling stress of the web is found to be 102 MPa and for the compression flange, 112 MPa. The web shear strength was 72 MPa and the compression flange strength 609 MPa. The web reinforcement was then set to $\pm 45^\circ$ with the flange reinforcement unchanged. The critical buckling stress of the web was shown to be reduced to 65 MPa while the beam deflected further than for the previous case. The web reinforcement was then set to $\pm 60^\circ$ and the compression flange reinforcement to $\pm 45^\circ$ which gave the highest values for the critical buckling stresses in both cases. The deflection of the beam under its own mass however was doubled from the previous case. The web shear strength remained constant but the strength of the compression flange was found to be less than one third of that for uniaxial reinforcement. Previous work has shown that the optimum fibre orientations for resistance to buckling was found in the compression flange to be $\pm 45^\circ$ and that for resistance to shear buckling in the web $\pm 60^\circ$, this gave the optimum

orientation for resistance to buckling. However, that these orientations did not provide for the maximum strength[2,12,13].

Comparative Deflection Behaviour

The deflection of a cantilever beam (as a rectangular hollow composite box structure) with a uniformly distributed load on the top surface, is compared with the deflection of similar beams of steel, aluminium and timber members with the same outside dimensions and interior geometries. A graph of the deflection of the composite beam versus distance along the beam is presented along with the deflections of the steel, aluminium and timber beams (Fig. 5). The deflections of the beams under their own mass may be obtained by setting the applied load to zero.

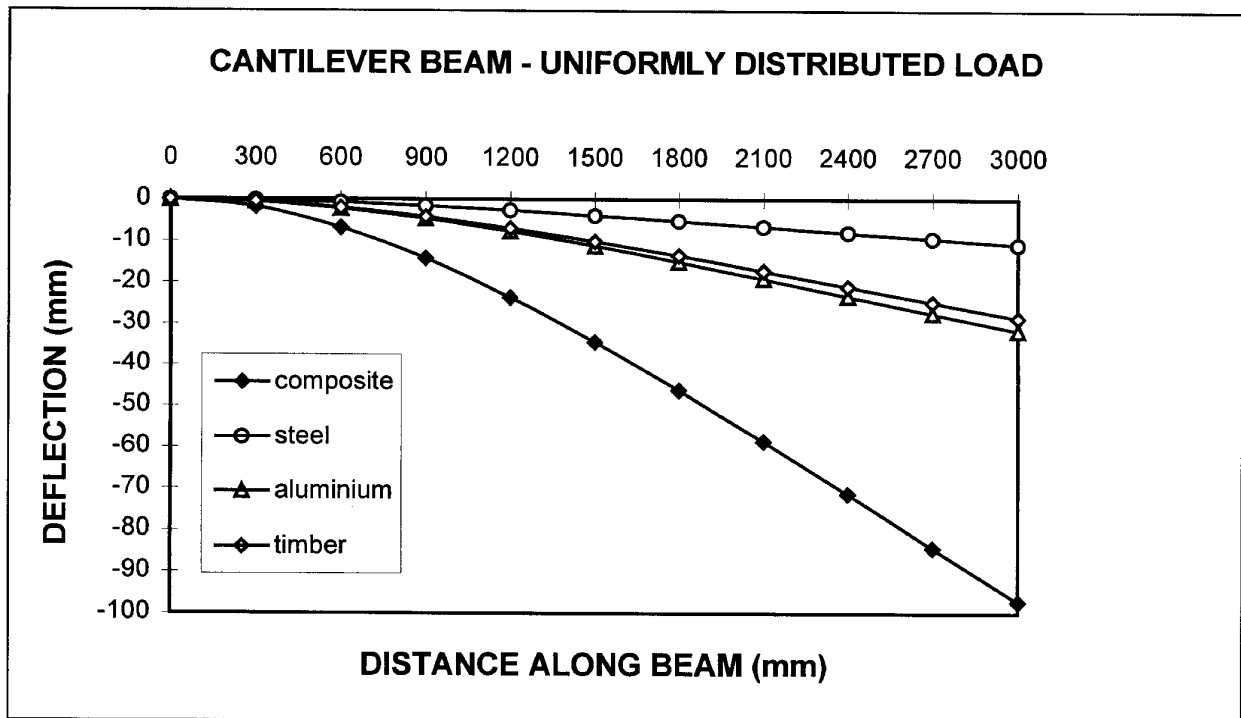


Fig. 5. Example of the comparative deflection of the different beams.

The results of the design iterative procedure indicate that the composite beam has an allowable deflection before failure of approximately ten times that of steel, and about six to seven times that of aluminium and timber. This design process is seen as a useful tool for the initial process in selecting appropriate beams, materials and geometries for specific loading conditions. Similar iterations may be carried out for other geometries, material combinations and loadings. Further design procedures for other loading conditions (point load and UDL on both a cantilever beam and a simply supported beam) indicated the benefits of using composite materials for the box-beams.

CONCLUDING COMMENTS

The investigations undertaken in this work led to the development of the BUCKLE program as an aid for the design of laminated FRP box beams. The computations of this program are based on well established bodies of theory which have in other applications been found to give good agreement with experimental results. Predicted results generated by the program should be used with caution. It is expected that further work in this field will be undertaken to determine the validity of the program output.

REFERENCES

1. Herakovich, C.T and Tarnopol'ski, Y.M., *Handbook- of Composites, volume 2, Structures and Design*, North-Holland, Amsterdam,1989.
2. Holmes, M. and Just, D.J., *GRP in Structural Engineering*, App. Sc. Pub. London, 1983.
3. Mallick, P.K., *Fibre-Reinforced Composites, Materials, Manufacturing and Design*, Marcel Dekker, Inc., New York, 2nd Ed. 1993.
4. Benjamin, B.S., *Structural Design with Plastics*, Van Nostrand, New York, 2nd Ed., 1982.
5. Schwartz, M.M., *Composite Materials Handbook*, McGraw-Hill, New York,1984.
6. Timoshenko, S.P. and Gere, J.M., *Theory of Elastic Stability*, , McGraw-Hill, New York, 2nd Ed., 1961.
7. Tsai, S.W., *Composites Design*, Think Composites, Dayton, 4th Ed., 1985.
8. Roylance, D., *Mechanics of Materials*, J.Wiley and Sons, New York, 1996.
9. Abeles, P.W., *Prestressed Concrete Designer,-Handbook*, Viewpoint Publications, Stough, 3rd Ed., 1992.
10. Neville, A.M., *Properties of Concrete*, , Pitman, London, 3rd ed., 1991.
11. Bradford M.A. and Wong,T.C., "Local Buckling of Composite Box Girders under Negative Bending", *UNICIV Report No. R-292*, Univ. of NSW, Kensington, Oct. 1991.
12. Rothwell, A, "Optimum Fibre Orientation in Plastics and Polymers", *Fibre Science and Technology*, Vol. 2, No.3, 1969, p111.
13. Banks, W.M., and Rhodes, J., "The Buckling Behaviour of Reinforced Plastic Box Sections", *The Reinforced Plastics Congress '80*, Brighton, Nov. 1980.
14. Heitzer, J. and Feuch, M., "Buckling and Postbuckling of Thin Elliptical and Anisotropic Plates, *Computers and Structures*, Vol.48, No.6, 1993, p17.
15. Think Composites, A Division of ILT Corporation, Dayton, Ohio.
16. Sih, G.C., *Failure Mechanics of Composites*, North-Holland, Amsterdam, 1985.
17. Tsai, S.W. and Wu, E.M., "A general theory of strength for anisotropic materials", *J. Composite Materials*, Vol.5, 1962, p58.

SANDWICH PLATES WITH "FULLY POTTED" INSERTS: A HIGH-ORDER APPROACH FOR ANALYSIS AND DESIGN

Ole Thybo Thomsen

*Institute of Mechanical Engineering,
Aalborg University, Pontoppidanstråde 101, DK-9220 Aalborg East, Denmark*

SUMMARY: A high-order sandwich plate theory, which includes the transverse flexibility of the core, is introduced. The theory includes separate descriptions of the face sheets and the core material, and general specification of loading and boundary conditions. The theory has been adapted especially for the analysis of sandwich plates with hard points in the form of inserts, and special attention is focused on the problem of sandwich plates with inserts of the "fully potted" type. The governing equations are formulated as a set of coupled first order differential equations, which are solved numerically using the "multi segment method of integration". Analysis results obtained for sandwich plates with "fully potted" inserts subjected to axisymmetric and non-axisymmetric loading conditions are presented. The paper is concluded with a discussion of design aspects.

KEYWORDS: sandwich plates, load introduction, fully potted inserts, transverse core flexibility, high-order theory

INTRODUCTION

Advanced structural sandwich elements are used extensively for lightweight structures for spacecraft, aircraft and other applications. The introduction of loads into such elements is often accomplished using inserts, which can be of the "through-the-thickness", "fully potted" or "partially potted" type, see Fig. 1. The "ideal" load transfer mechanism is disturbed significantly in the regions close to the inserts, where the face sheets will tend to bend locally rather than about the middle surface of the sandwich panel. Such local bending phenomena cause severe local stress concentrations that might lead to premature failure. Local bending effects cannot be accounted for using the classical "antiplane" sandwich plate theories summarised in Plantema [1], Allen [2] and Zenkert [3], as these theories do not include the transverse flexibility of the core material.

The importance of including the transverse core flexibility in the study of local bending phenomena has been pointed out in several investigations. Among others, Thomsen [4], and Thomsen et al. [5, 6] adopted a two-parameter elastic foundation approach for the analysis of point loading effects and face sheet thickness change effects in sandwich panels.

Frostig et al. [7], Frostig and Baruch [8], Frostig [9, 10] and Frostig and Shenhar [11] took a different approach by the development of a high-order sandwich beam theory, which includes the transverse flexibility of the core. The high-order sandwich beam theory inherently

incorporate both global and localised bending effects, and the basic assumptions as well as the quality of the predictions of the theory was verified experimentally by Thomsen and Frostig [12] through photoelastic measurements.

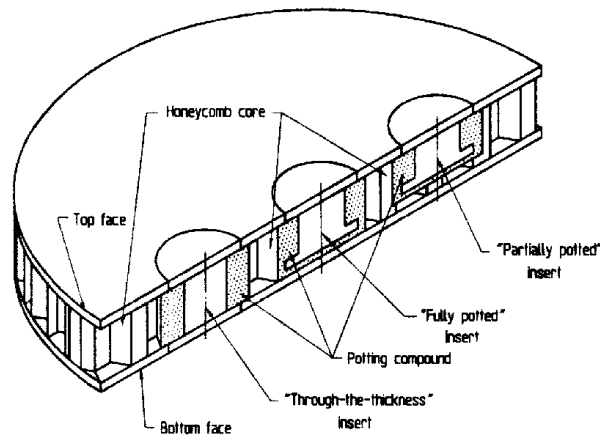


Fig. 1: Potted insert types typically used for structural sandwich panels.

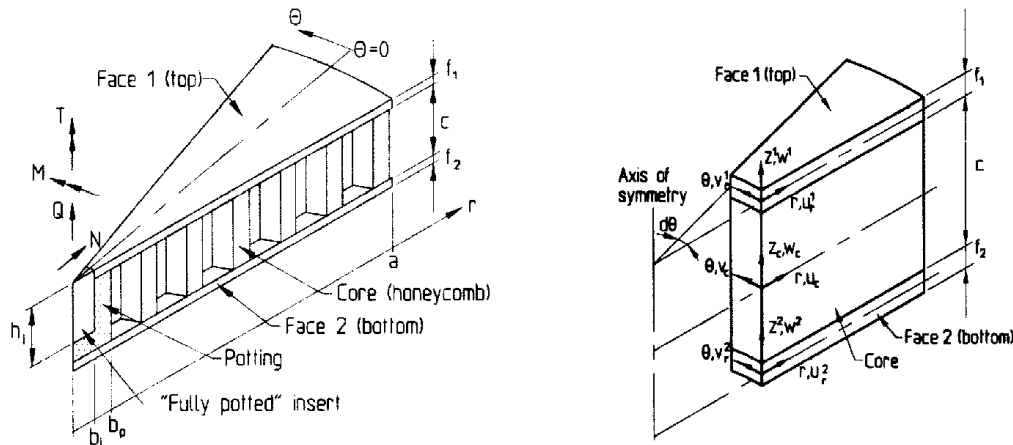


Fig. 2: Cut-out of sandwich plate with “fully potted” insert subjected to general loading conditions. Geometrical definition of sandwich plate element.

The present paper addresses the problem of analysis of sandwich plates with inserts of the “fully potted” type, which together with inserts of the “through-the-thickness” type are used extensively for practical sandwich structures. The problem is formulated by adapting and extending the principles behind the high-order theory developed for sandwich beams [7-11] to circular sandwich plates. Previously sandwich plates with “through-the-thickness” inserts were analysed using the same principles by Thomsen [13] and Thomsen and Rits [14].

MATHEMATICAL FORMULATION

It is assumed that interaction between adjacent inserts, as well as interaction between inserts and the plate boundaries or other local disturbance sources, can be ignored. Fig. 2 defines the constituent parts, the geometry and the possible external load cases.

As suggested in refs. [7-11] and [13-14], the core material is described as a transversely isotropic solid where only the “through-the-thickness” stiffness is accounted for. Setting up

the core equilibrium conditions, and using the kinematic and constitutive relations for the core, yields a set of equations describing the core stress and displacement fields in terms of the transverse core coordinate z_c (see Fig. 2):

$$\begin{aligned}
 \tau_{rz}(r, \theta, z_c) &= \tau_{rz}(r, \theta) \\
 \tau_{\theta z}(r, \theta, z_c) &= \tau_{\theta z}(r, \theta) \\
 \sigma_c(r, \theta, z_c) &= \frac{E_c}{c} \{w^1 - w^2\} - \left\{ \tau_{rz,r} + \frac{1}{r} \tau_{rz} + \frac{1}{r} \tau_{\theta z,\theta} \right\} z_c \\
 w_c(r, \theta, z_c) &= w^1 + \frac{\{w^1 - w^2\}}{c} \left\{ z_c - \frac{c}{2} \right\} - \frac{1}{2E_c} \left\{ \tau_{rz,r} + \frac{1}{r} \tau_{rz} + \frac{1}{r} \tau_{\theta z,\theta} \right\} \left\{ z_c^2 - \frac{c^2}{4} \right\} \\
 u_c(r, \theta, z_c) &= u_{0r}^1 - \frac{\beta_r^1}{2} \left\{ f_1 - \frac{z_c^2}{c} - z_c + \frac{3c}{4} \right\} - \frac{\beta_r^2}{2} \left\{ \frac{z_c^2}{c} - z_c + \frac{c}{4} \right\} + \frac{\tau_{rz}}{G_c} \left\{ z_c - \frac{c}{2} \right\} \\
 &\quad + \frac{1}{2E_c} \left\{ \tau_{rz,rr} + \frac{1}{r} \tau_{rz,r} - \frac{1}{r^2} \tau_{rz} + \frac{1}{r} \tau_{\theta z,\theta r} - \frac{1}{r^2} \tau_{\theta z,\theta} \right\} \left\{ \frac{z_c^3}{c} - \frac{c^2 z_c}{4} + \frac{c^3}{12} \right\} \\
 v_c(r, \theta, z_c) &= u_{0\theta}^1 - \frac{\beta_\theta^1}{2} \left\{ f_1 - \frac{z_c^2}{c} - z_c + \frac{3c}{4} \right\} - \frac{\beta_\theta^2}{2} \left\{ \frac{z_c^2}{c} - z_c + \frac{c}{4} \right\} + \frac{\tau_{\theta z}}{G_c} \left\{ z_c - \frac{c}{2} \right\} \\
 &\quad + \frac{1}{r2E_c} \left\{ \tau_{rz,r\theta} + \frac{1}{r} \tau_{rz,\theta} - \frac{1}{r} \tau_{\theta z,\theta\theta} \right\} \left\{ \frac{z_c^3}{c} - \frac{c^2 z_c}{4} + \frac{c^3}{12} \right\}
 \end{aligned} \tag{1}$$

In Eqns 1 E_c , G_c are the core elastic constants, σ_c is the core transverse normal stress, τ_{rz} , $\tau_{\theta z}$ are the core shear stresses, u_c , v_c , w_c are the core displacement components, and u_{0i}^1 , u_{0i}^2 , w^i ($i=1,2$) are the displacement components of the top and bottom faces, see Fig. 2. From Eqns 1 it is seen that τ_c and τ_θ are constant, that σ_c varies linearly, that w_c varies quadratically, and that u_c and v_c varies cubically over the core thickness. The core is coupled with the face sheets by requiring continuity of the displacements and stresses across the core/face interfaces.

The modelling of the face sheets are achieved using a Mindlin-Reissner type of plate theory formulation, which allows inclusion of out-of-plane shearing effects. The face sheets are treated as homogeneous, isotropic and linear elastic. This is a simplifying assumption as FRP face sheets are used in many applications. The approximation is reasonable, however, as strongly orthotropic face-laminates are hardly ever used around inserts. Instead, following the design principles adopted for riveted and bolted joints in composite structures, local reinforcements in the form of angle plies are added around inserts such that the resulting laminates appear as quasi isotropic.

Formulating the equilibrium, kinematic and constitutive equations for the top and bottom face sheets, and combining those with the "core equations", Eqns 1, and the continuity requirements, yields the governing set of partial differential equations. The order of the governing equations is 24, and consequently they can be reduced to 24 first order partial differential equations. If the 24 unknowns, henceforth called the fundamental variables, are those quantities that appear in the natural boundary conditions at an edge $r=\text{constant}$, then the boundary value problem can be stated completely in terms of these variables. The fundamental variables are:

$$\begin{aligned}
 \{y(r, \theta)\} &= \{u_{0r}^1, u_{0\theta}^1, w^1, \beta_r^1, \beta_\theta^1, N_r^1, N_{r\theta}^1, M_r^1, M_{r\theta}^1, Q_r^1, \tau_{rz}, q_r, \tau_{\theta z}, q_\theta, \\
 &\quad u_{0r}^2, u_{0\theta}^2, w^2, \beta_r^2, \beta_\theta^2, N_r^2, N_{r\theta}^2, M_r^2, M_{r\theta}^2, Q_r^2\}
 \end{aligned} \tag{2}$$

where $\beta_r^i, \beta_\theta^i$ are face rotations, N_r^i, N_θ^i are in-plane face stress resultants, M_r^i, M_θ^i are face moment resultants, and Q_r^i are face transverse shear stress resultants ($i=1,2$). In Eqn 2 two new “core variables” q_r, q_θ have been introduced

$$q_r(r, \theta) = \tau_{r,r}, \quad q_\theta(r, \theta) = \tau_{r,\theta,r} \quad (3)$$

The governing equations can be reduced to the form

$$\{y(r, \theta)\}_{,r} = \Psi(r, \theta, \{y\}, \{y\}_{,\theta}, \{y\}_{,\theta\theta}, \dots) \quad (4)$$

where Ψ denotes 24 linear functions in $\{y(r, \theta)\}$ and its derivatives with respect to θ . The dependency of θ is eliminated by Fourier series expansion of the fundamental variables thus reducing the problem to 24 first order ordinary differential equations. The resulting set of field equations can be written in the form (n =number of “harmonics” in Fourier series):

$$\begin{aligned} \text{symmetric about } \theta = 0: \quad & \{y_n(r)\}_{,r} = [A_n(r)]\{y_n(r)\} + \{B_n(r)\}, \quad n = 0 \rightarrow \infty \\ \text{skew - symmetric about } \theta = 0: \quad & \{\tilde{y}_n(r)\}_{,r} = [\tilde{A}_n(r)]\{\tilde{y}_n(r)\} + \{\tilde{B}_n(r)\}, \quad n = 0 \rightarrow \infty \end{aligned} \quad (5)$$

where $\{y_n(r)\}, \{\tilde{y}_n(r)\}$ are 24×1 matrices of r -dependent coefficient functions of the Fourier-series expanded fundamental variables; $[A_n(r)], [\tilde{A}_n(r)]$ are 24×24 coefficient matrices; and $\{B_n(r)\}, \{\tilde{B}_n(r)\}$ are 24×1 matrices of non-homogeneous load terms.

STATEMENT OF BOUNDARY CONDITIONS

The insert is modelled as a thick top face plate, even though it is recognised, that this is rather inaccurate. However, the insert will appear as a rigid body compared with the core and the thin face sheets, and the results obtained for the insert itself are therefore of no interest.

The system equations contain elements of the type r^{-1}, r^{-2} and r^{-3} . Thus, the system equations show singular behaviour for $r \rightarrow 0$. In order to avoid this the problem is rephrased slightly, now assuming that the plate centre defined by a small radius $r=b_0$ (“inner rim”) is removed. If b_0 is sufficiently small, this hardly influences the solution away from the plate centre.

The order of the system equations is 24, thus implying that 12 boundary conditions needs to be specified at $r=b_0, r=b_i$ and $r=a$. The actual statement of the boundary conditions varies slightly from load case to load case, but are derived from the following assumptions:

$r=b_0$: Bottom face (face 2): Free edge conditions are imposed.

 Potting (core) material: Free edge conditions are imposed.

 Top face (face 1): The external loading is applied to the insert as surface loading distributed over the top surface of the insert.

$r=b_i$: “Continuity” of fundamental variables, except for u_{0r}^1 and τ_{rz} , which changes discontinuously.

$r=a$: Simple support conditions are assumed for the face sheets and the core.

The boundary conditions at $r=b_0, r=b_i$ and $r=a$ are stated by specifying linear combinations of the fundamental variables. The resulting boundary value problem is solved numerically using the “multisegment method of integration”, see [13] and Thomsen [15] for details.

EXAMPLES

Definition of geometry, material properties and loading conditions

To illustrate the mechanical behaviour of sandwich plates with “fully potted” inserts, two examples are presented. The first example deals with the out-of-plane load case, and the second deals with the bending moment load case, see Fig. 2. Both examples are based on a symmetric insert/sandwich plate system defined by the following geometrical and material characteristics (properties are typical for spacecraft applications):

Geometry: $h_i=9.0$ mm, $b_o=0.1$ mm (“inner rim”), $b_i=7.0$ mm, $b_p=10.0$ mm, $a=60.0$ mm, $c=20.0$ mm, $f_1=f_2=0.2$ mm.

Face 1: Aluminium face-plates; $E_f=71.5$ GPa; $\nu_f=0.3$.

Face 2: As face 1 (symmetric sandwich panel), i.e., $E_2=E_f$, $\nu_2=\nu_f$.

Insert: Same material properties as the face-plates (i.e. aluminium).

Potting: Bulk epoxy polymer, $E_p=2.5$ GPa, $G_p=0.93$ GPa.

Honeycomb: HEXCEL Al-honeycomb 3/16”-5056-0.0007”, $E_h=310$ MPa, $G_h \approx (G_L + G_W)/2 = 138$ MPa.

The external loads specified for the two examples are:

Q load case: $Q=-1$ kN (compressive loading). *M* load case: $M=1$ kNmm.

Example 1: Out-of-plane loading *Q* (axisymmetric)

The load $Q=-1.0$ kN (compressive loading) is applied as a transverse normal load distributed uniformly over the top surface of the insert.

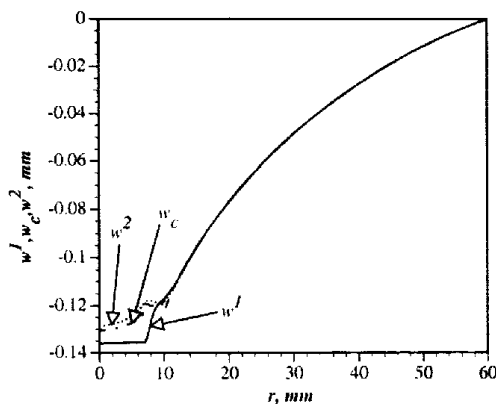


Fig. 3: w^1 (top face), w^2 (bottom face), w_c (core midsurface). $Q=-1.0$ kN.

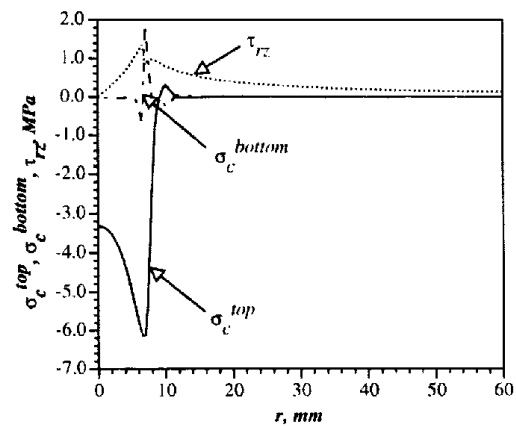


Fig. 4: τ_{rz} , σ_c^{top} , σ_c^{bottom} . $Q=-1.0$ kN.

Fig. 3 shows the out-of-plane deflections of the face sheets (w^1 , w^2), and the core midsurface ($w_c(z_c=0)$). It is observed that w^1 , w^2 and w_c are nearly identical for $r > b_p = 10$ mm, while this is not the case for $r < b_p$. It is further seen that the insert (i.e., the top face for $r \leq b_i$) deflects as a rigid body. For $r < r_p$, the deflections of the potting material (w_c) and the bottom face-plate (w^2) differs significantly from w^1 (insert/face-plate 1), which is due to the indentation of the insert into the potting. It is further seen that the relative difference between w^1 and w_c is larger

than the relative difference between w_c and w^2 . This implies that the change of thickness of the potting is not “homogeneous”.

Fig. 4 shows the radial distribution of stresses in the potting and honeycomb materials. The values of σ_c are given at the interface between face 1 and the potting/honeycomb (σ_c^{top}), and at the interface between face 2 and the potting/ honeycomb (σ_c^{bottom}). It is observed that the most severe stresses are located in the potting compound ($r < b_p = 10$ mm). As expected, σ_c^{top} is predominantly compressive underneath the insert, and is displaying a non-uniform radial distribution. σ_c^{bottom} is compressive and of very small magnitude except very close to $r = b_i$ where a tensile peak is encountered. It is further observed that τ_{rz} raises from zero at the plate centre to a peak value at $r = b_i$. After the peak τ_{rz} decreases with increasing r -values*.

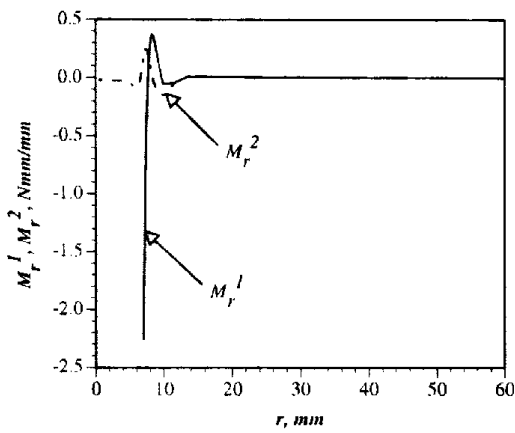


Fig. 5: M_r^1, M_r^2 . $Q = -1.0$ kN.

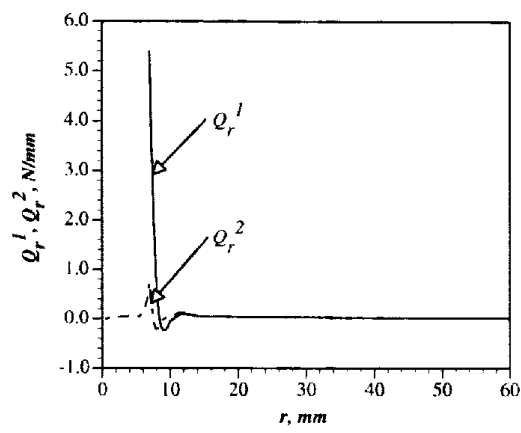


Fig. 6: Q_r^1, Q_r^2 . $Q = -1.0$ kN.

Fig. 5 shows the radial distribution of the bending moment resultants M_r^1, M_r^2 . It is seen that significant bending moment concentrations are present in face 1 close to the insert/sandwich plate intersection at $r = b_i = 7$ mm. Face 2 is only transferring small bending moments.

Fig. 6 shows the radial distribution of the transverse shear stress resultants Q_r^1, Q_r^2 . It is observed that only face 1 is subjected to significant shear loading and that a steep decay of Q_r^1 is seen with increasing r -values. This shows that the core takes over the “shear-transfer role” as r is increased. Thus, for $r > r_p$ the mechanical response of the sandwich plate is identical with the predictions of classical sandwich plate theories (e.g., refs. [1-3]).

* A special feature of the τ_{rz} distribution is, that a discontinuous “jump” is seen to occur exactly at $r = b_i$. This discontinuous jump is a consequence of the “continuity” conditions imposed at $r = b_i$, which requires continuity of the transverse shear stress resultants across $r = b_i$, i.e.

$$(Q_r^1)^- + (c + f_1 - h_i)(\tau_{rz})^- + (Q_r^2)^- = (Q_r^1)^+ + c(\tau_{rz})^+ + (Q_r^2)^+ \Rightarrow$$

$$(\tau_{rz})^- = \frac{c}{(c + f_1 - h_i)}(\tau_{rz})^+ \text{ as } (Q_r^1)^- = (Q_r^1)^+ \text{ and } (Q_r^2)^- = (Q_r^2)^+.$$

Superscript “-” means approaching $r = b_i$ from the left, and superscript “+” means approaching $r = b_i$ from the right.

Example 2: Bending moment loading M (non-axisymmetric)

The case of sandwich plates with “fully potted” inserts subjected to bending moment loading M is highly realistic, even though it is generally recommended to avoid this kind of loading through proper design. It is, however, not possible to eliminate this type of loading completely. In the present case, M has been applied to the insert as a radially uniform surface load that varies as $\cos(\theta)$ in the circumferential direction*.

Fig. 7 shows the out-of-plane displacements w^1 , w^2 and $w_c(\text{midsurface})=w_c(z_c=0)$ along $\theta=0$ (these functions vary as $\cos(\theta)$). Considering the displacements of the top face sheet it is noticed that the “insert” itself (i.e. $r \leq b_i$) primarily rotates as a “rigid” body. For $r > b_i = 7$ mm the top face deflects as a deformable body, and significant curvature change is experienced next to the potting/honeycomb intersection at $r = b_p = 10$ mm. Considering the deflectional response of the core midsurface $w_c(z_c=0)$, the overall pattern is very similar to that of the top face. Pertaining to the deflectional behaviour of the bottom face, it is very similar to that of the core midsurface $w_c(z_c=0)$.

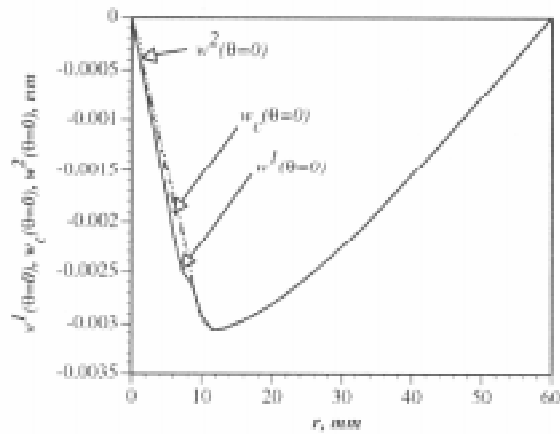


Fig. 7: $w^1(\theta=0)$, $w^2(\theta=0)$, $w_c(z_c=0)$, $\theta=0$.
 $M=1$ kNm.

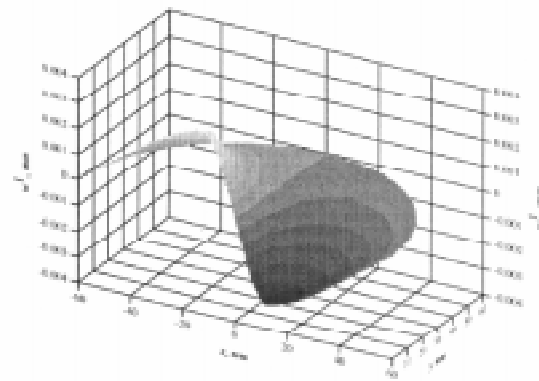


Fig. 8: Deformed top face. The “x”-axis is coincident with $\theta=0$.

To provide a better impression of the deflectional response of the considered insert/sandwich plate system Fig. 8 shows a surface plot of face 1 (top face) in its deformed state. The deformed configuration is symmetric about $\theta=0$, and only one half of the deformed top face is shown. The central part of the deformed top face sheet, extending from $(x,y)=(0,0)$ to $r=(x^2+y^2)^{1/2}=7$ mm in all directions, corresponds to the central insert, which rotates as a rigid body.

Fig. 9 shows the distribution of stresses in the potting and honeycomb materials. Four stress components are shown: σ_c^{top} , σ_c^{bottom} , τ_{rz} , which are given along $\theta=0$ (they vary as $\cos(\theta)$), and $\tau_{\theta z}$, which is given along $\theta=\pi/2$ (varies as $\sin(\theta)$). The stress distribution in the core is very complex, and it is seen to be dominated by severe transverse normal stresses along the top and bottom surfaces of the potting compound.

* The external bending moment load case can be considered as “symmetric” about $\theta=0$ (see Fig. 2), and it is only necessary to use “first-order harmonics” (e.g. $n=1$) in the Fourier-series expansion of the fundamental variables $\{y\}$. Thus, variables which are “symmetric” about $\theta=0$ varies with θ as $\cos(\theta)$, and variables which are “skew-symmetric” about $\theta=0$ varies with θ as $\sin(\theta)$. When variables are displayed in the forthcoming, it will be specified explicitly if they are given for $\theta=0$ or $\theta=\pi/2$.

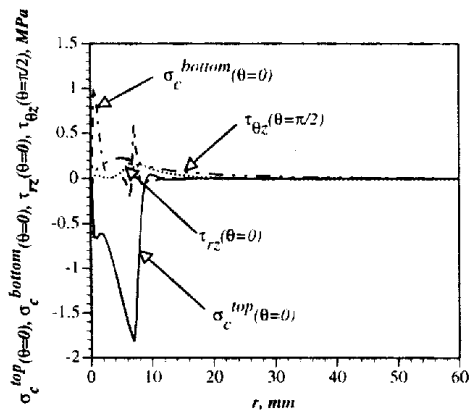


Fig. 9: $\sigma_c^{top}(\theta=0)$, $\sigma_c^{bottom}(\theta=0)$, $\tau_{r2}(\theta=0)$, $\tau_{\theta z}(\theta=\pi/2)$. $M=1$ kNmm.

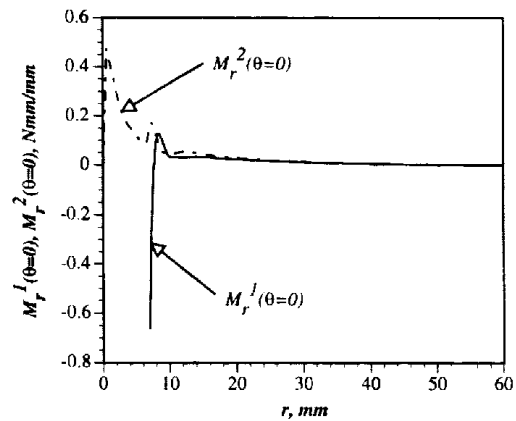


Fig. 10: $M_r^1(\theta=0)$, $M_r^2(\theta=0)$.
 $M=1$ kNmm.

Fig. 10 shows the distribution of radial bending moment resultants M_r^1 , M_r^2 along $\theta=0$ (i.e., M_r^1 , M_r^2 varies as $\cos(\theta)$), and it is observed, that the bending moment resultants are only present underneath (bottom face) or very close to the “fully potted” insert[†]. The peak value of M_r^1 (in top face plate exclusive insert), which is negative, is seen to be located at the interface between the insert and the face at $r=b_i=7$ mm. With respect to the bottom face it is seen that M_r^2 is very similar to M_r^1 for $r>b_p=10$ mm. For $r<b_p$, however, M_r^2 attains positive values, which increase towards the plate centre.

DESIGN CONSIDERATIONS

It has been demonstrated that severe stress concentrations are induced in sandwich plates with “fully potted” fully inserts, and initiation and progressive development of failure may occur at several locations. Based on practical experience, ESA Insert Design Handbook [16], combined with analysis results, it is possible to specify a number of distinct failure modes and their likely locations. Thus, “bearing” or “buckling” (wrinkling or dimpling) failure might occur in the top face sheet. However, structural failure usually occurs due to core failure, and the most likely failure modes are honeycomb shear and micro buckling which occur simultaneously (or at least are impossible to separate) [16]. Potting interface failures are observed occasionally, but can usually be avoided through proper pretreatment of the insert surfaces. Interface failure between face sheets and honeycomb are hardly ever seen, and can be avoided completely by adopting proper manufacturing procedures.

Based on the results presented, as well as results presented in refs. [13-16], a number of guidelines for design of plates with “fully potted” inserts have been specified:

1. If possible, the radial extension of the potting should at least be $0.5b_i^{\ddagger}$. This will ensure maximum relief of the face sheet bending stresses, while, at the same time, the full stress transfer capability of the potting compound is utilised.

[†] The calculated bending resultants in the insert itself are not displayed, as modelling of the insert using plate theory (as is being done) does not provide a good description of the insert.

[‡] It should be noted, that b_p is a quantity usually determined by the manufacturing process rather than a parameter, which can be specified freely by the designer. Thus, b_p-b_i is usually smaller than the recommended optimum value.

2. If possible, the ratio of the potting stiffness to the honeycomb stiffness, E_p/E_h , should be chosen to $E_p/E_h \approx 3-4$. This will ensure a good compromise between the peak stress level in the top face and in the potting and honeycomb materials.
3. It is generally recommended to avoid external bending moment loading (M load case). This can be achieved by load application through groups of "fully potted" inserts loaded in the out-of-plane direction (Q load case).
4. If severe external loads are to be introduced, a strong advise is given to use "through-the-thickness" inserts instead of "fully potted" inserts.
5. The capability of top face to resist the peak bending and shear stresses adjacent to the insert can be improved considerably by reinforcing the top face in the zones where inserts are mounted. Such reinforcements can be made by adding extra plies (UD or multi directional prepregs) to the upper surface of the to face sheet.

CONCLUDING REMARKS

A high-order sandwich plate theory, developed in refs. [13, 14] for the analysis of sandwich plates with "through-the-thickness" inserts, has been adapted for the study of sandwich plates with "fully potted" inserts. It has been demonstrated that the mechanical response encountered in sandwich plates with "fully potted" inserts is very complex, and generally exhibits more complicated features than is the case for sandwich plates with "through-the-thickness" inserts. The reason for this is the inherently asymmetric load introduction in sandwich plates with "fully potted" inserts, which prevents "proper collaboration" between the faces of the sandwich plates.

The developed procedures for analysis and design of sandwich plates with "through-the-thickness" inserts will be implemented in the composites analysis and design software package ESAComp[®] [17], which is being developed for the European Space Agency.

REFERENCES

1. Plantema, F. J., *Sandwich Construction*, John Wiley & Sons, New York, 1966.
2. Allen, H. G., *Analysis and Design of Structural Sandwich Panels*, Pergamon Press, Oxford, 1969.
3. Zenkert, D., *An Introduction to Sandwich Construction*, Chameleon Press Ltd., London, 1995.
4. O. T. Thomsen, "Theoretical and Experimental Investigation of Local Bending Effects in Sandwich Plates", *Composite Structures*, Vol. 30, 1995, pp. 85-101.
5. O. T. Thomsen, W. Rits, D. C. G. Eaton and S. Brown, "Ply Drop-Off Effects in CFRP/Honeycomb Sandwich Panels - Theory", *Composites Science & Technology*, Vol. 56, 1996, pp. 407-422.
6. O. T. Thomsen, W. Rits, D. C. G. Eaton, O. Dupont and P. Queekers, "Ply Drop-Off Effects in CFRP/Honeycomb Sandwich Panels - Experimental Results", *Composites Science & Technology*, Vol. 56, 1996, pp 425-427.

7. Frostig, Y., Baruch, M., Vilnai, O., Sheinman, I. "High-Order Theory for Sandwich-Beam Bending with Transversely Flexible Core", *Journal of ASCE, EM Division*, Vol. 118, No. 5, May 1992, pp. 1026-1043.
8. Frostig, Y., Baruch, M., "High-Order Buckling Analysis of Sandwich Beams with Transversely Flexible Core", *Journal of ASCE, EM Division*, Vol. 119, No. 3, March 1993, pp. 476-495.
9. Frostig, Y., "On Stress Concentration in the Bending of Sandwich Beams with Transversely Flexible Core", *Composite Structures*, 24, 1993, pp. 161-169.
10. Frostig, Y. "High-Order Behaviour of Sandwich Beams with Flexible Core and Transverse Diaphragms", *Journal of ASCE, EM Division*, Vol. 119, No. 5, May 1993, pp. 955-972.
11. Frostig, Y. and Shenhar, Y. "High-Order Bending of Sandwich Beams with a Transversely Flexible Core and Unsymmetrical Laminated Composite Skins", *Composites Engineering*, Vol. 5, pp. 405-414, 1995.
12. Thomsen, O. T. and Frostig, Y., "Localized Bending Effects in Sandwich Beams: Photoelastic Investigation versus High-Order Sandwich Theory Results", submitted.
13. Thomsen, O. T., "Analysis of Sandwich Plates with Through-the-Thickness Inserts Using a Higher-Order Sandwich Plate Theory", ESA/ESTEC Report EWP-1807, 1994.
14. Thomsen, O. T. and Rits, W., "Analysis and Design of Sandwich Plates with Inserts: A Higher-Order Sandwich Plate Theory Approach", submitted.
15. Thomsen, O. T., "Analysis of Sandwich Plates with Fully Potted Inserts Using a Higher-Order Sandwich Plate Theory", ESA/ESTEC Report EWP-1827, 1995.
16. *Insert Design Handbook*, European Space Agency, PSS-03-1202, Issue 1, 1987.
17. Saarela, O., Palanterä, M., Häberle, J. and Klein, M., "ESACOMP: a Powerful Tool for the Analysis and Design of Composite Materials", Proc. of "Int. Symp. on Advanced Materials for Lightweight Structures", ESA-WPP-070, ESTEC, Noordwijk, The Netherlands, 1994, pp. 161-169.

THERMOELASTIC AND 3D FAILURE ANALYSES OF CARBON-CARBON COMPOSITE BRAKE DISKS

Chun-Gon Kim¹, Jung-Seok Kim¹, Jae-Seok Yu¹, Chang-Sun Hong¹, Byung-Il Yoon²

¹*Department of Aerospace Engineering, Korea Advanced Institute of Science and Technology
Taejon 305-701, Korea*

²*Agency for Defense Development, Taejon 300-600, Korea*

SUMMARY: For the proper design of a carbon-carbon brake disk system, the transient thermoelastic and 3D failure analyses were done using finite element methods. The angular velocity history of the rotor disk was obtained by energy balance method and compared with experimental results. In this study, the 7-disk brake system was studied and tested. In the transient thermoelastic analysis, it was assumed that there is no energy dissipation such as wear. The results of transient thermoelastic analysis such as pressure, friction force and temperature were imposed to the 3D failure analysis for the most severe operating conditions. Then, 3D failure analysis was performed using cyclic symmetry condition. The results of thermoelastic analysis were compared with those of dynamometer test especially for the angular velocity history. The history of angular velocity shows good agreement between the numerical and the experimental results. For the considered brake system, the maximum pressure and the temperature occur at the first friction surface. The disk used in the 3D finite element analysis is the first rotor disk with the first and second friction surfaces. From 3D failure analysis, Tsai-Wu failure index was surveyed for the model. The analyses showed good agreement with the test result and possibly can be used for the slot design of carbon-carbon brake disks.

KEYWORDS: carbon-carbon, brake disk, thermoelastic analysis, 3D failure analysis

INTRODUCTION

In aircraft brake systems, kinetic energy is transformed to heat energy. Aircraft brake systems are usually composed of multiple disks, in which the wheel-driven rotors are sandwiched between stators held stationary by brake structure. Braking action is achieved by pressing the disks using hydraulic pressure, and heat is generated on the contact surfaces of disks. Therefore, materials of brake disks should possess high thermal conductivity and high specific strength at high temperatures. Unlike metals and ceramics, carbon-carbon composites retain their strength at very high temperatures. High thermal conductivity and low thermal expansion give carbon-carbon materials an excellent resistance to thermal shock. Also, the use of carbon-carbon composite brake disks offered 60% weight saving compared with steel[1]. The analyses of temperatures and stresses in the friction disks were performed for steel multi-disk systems[2, 3].

In this study, the transient thermoelastic analysis for carbon-carbon composites was performed and the angular velocity was calculated by energy balance method. In the transient

thermoelastic analysis, it was assumed that there is no energy dissipation such as wear. Then, 3D failure analysis using cyclic symmetry condition was performed.

GOVERNING EQUATION

An implicit transient heat equation is [4, 5]

$$\begin{aligned} & ([C_T] + \beta \Delta t [K_H]) \{T\}_{t+\Delta t} \\ & = ([C_T] - (1 - \beta) \Delta t [K_H]) \{T\}_t + \Delta t \{ (1 - \beta) \{R\}_t + \beta \{R\}_{t+\Delta t} \} \end{aligned} \quad (1)$$

The elastic equation is [4, 5]

$$[K] \{U\} = \{F_f\} + \{F_m\} + \{F_T\} \quad (2)$$

ENERGY BALANCE METHOD

The angular velocity of the rotor disk is a function of the kinetic energy of the aircraft. Therefore, the angular velocity of the rotor disk can be calculated from reduction of kinetic energy by heat generation. The heat generation during Δt is

$$\Delta t \{ (1 - \beta) \{R\}_t + \beta \{R\}_{t+\Delta t} \} \quad (3)$$

TRANSIENT THERMOELASTIC ANALYSIS

This problem is a special case of the contact problem because it is non-isothermal and contact points appear simultaneously on many surfaces. In contact problem, the actual contact area is unknown in advance, therefore, iteration technique is needed. In each friction surfaces, a pair of contacted nodes are defined. One of the nodes is designated as the master node and the other as the slave node. The continuity of axial displacements at this interface is required for the each pair of contact nodes, however, discontinuity of the radial displacements can take place due to the slip.

By the continuity condition of the temperature field, nodal temperatures on the friction surfaces have the following constraint condition.

$$T_{at M} = T_{at S} \quad \text{when } P > 0 \quad (4)$$

By the relation $q^* = \mu Pr \omega$, heat is generated on the contact nodes of the friction surfaces.

$$\begin{aligned} q^* &= \mu Pr \omega \quad \text{when } P > 0 \\ q^* &= 0 \quad \text{otherwise} \end{aligned} \quad (5)$$

Fig. 1 shows the finite element model with elastic boundary conditions.

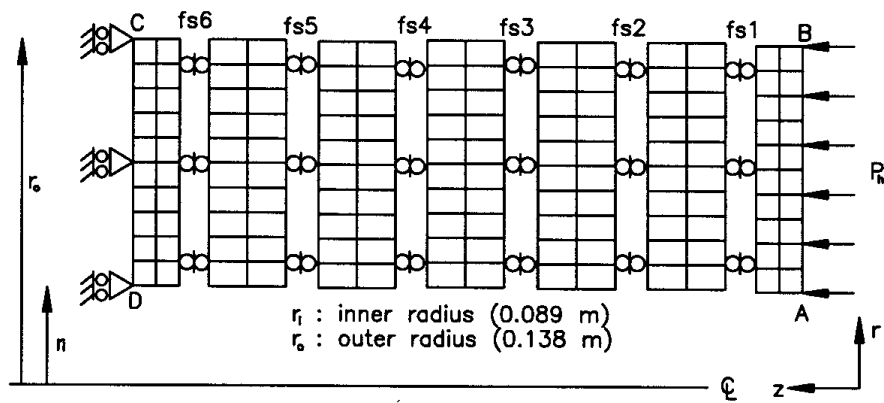


Fig. 1: Axisymmetric finite element model for elastic analysis.

The A-B surface along the radius of the right-end disk at $z=0.0$ [m] is pressed by the hydraulic pressure P_h and called the pressure plate. The C-D surface along the radius of the left-end disk at $z=0.03488$ [m] is fixed and called the end plate. In the present model, there are a pressure plate, an end plate, three rotors and two stators. The thicknesses of the pressure plate and the end plate are 0.01016 [m] and 0.00972[m], respectively. And, the thickness of the rest disk is 0.015 [m]. The inner radius r_i and the outer radius r_o of the disks are 0.089[m] and 0.138[m], respectively. Axisymmetric 8 nodes isoparametric elements were used in the finite element analysis of the brake disk. There are 20 elements and 85 nodes per disk. The model contains 7 disks and the whole system has 140 elements and 595 nodes. Fig. 2 shows the finite element model with heat boundary conditions.

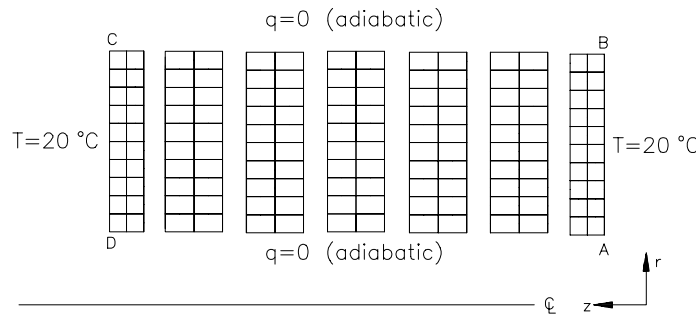


Fig. 2: Axisymmetric finite element model for heat analysis.

The heat boundary conditions are as follow; the adiabatic condition is applied to the two surfaces, the B-C and A-D surfaces bounded by the outer radius r_o and the inner radius r_i and the temperature on the A-B and C-D surfaces has prescribed temperature boundary condition, $T=20$ °C by the assumption of the cooling state like air-blowing. Fig. 3 shows history of hydraulic pressure. The hydraulic pressure in experiment varied to keep the torque of brake disk constant. In this study, the history of hydraulic pressure was approximated from the results of dynamometer test. The implicit transient time step $\Delta t = 0.01$ second was used in the calculations. The initial kinetic energy and the initial angular velocity of the brake system were 7752kJ and 209rad/sec.

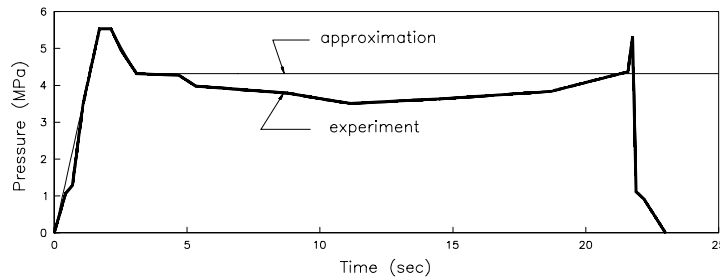


Fig. 3: History of hydraulic pressure.

Table 1 shows the material properties of carbon-carbon composites for the axisymmetric transient thermoelastic analysis.

Table 1: Material Properties of Carbon-Carbon Composites For the Transient Thermoelastic Analysis.

Properties	Symbol	value
Elastic modulus in r	E_r	^a 59 GPa
Elastic modulus in z	E_z	^a 3.46 GPa
Shear modulus in r-z	G_{rz}	1.38 GPa
Poisson's ratio	$\nu_{r\theta}$	0.3
Poisson's ratio	ν_{rz}	0.2
Thermal expansion coeff. in r	α_r	0.31×10^{-6} 1/K
Thermal expansion coeff. in z	α_z	0.29×10^{-6} 1/K
Thermal conductivity in r	k_r	50 W/(m K)
Thermal conductivity in z	k_z	10 W/(m K)
Density	ρ	^a 1.72×10^3 Kg/m ³
Specific heat	c	1.42×10^3 J/(Kg K)
Friction coefficient	$\mu_{t=0}$	^a 0.33

^a: material properties measured from material testing.

RESULTS OF TRANSIENT THERMOELASTIC ANALYSIS

Fig. 4 shows the measured and calculated histories of angular velocity. From Fig. 4, the braking time measured from the dynamometer test was 23 seconds and the one obtained from the analysis was 20 seconds. Therefore, the history of angular velocity shows good agreement between the numerical and experimental results and the angular velocity decreased linearly to keep a constant deceleration. Fig. 5 shows the calculated history of kinetic energy, From the Fig. 5 the kinetic energy decreased exponentially. Fig. 6 shows the calculated history of maximum pressure at first rotor disk. The maximum value is 0.93MPa and occurs at $t = 8$ seconds. After $t = 8$, the maximum pressure decreased almost linearly up to braking time.

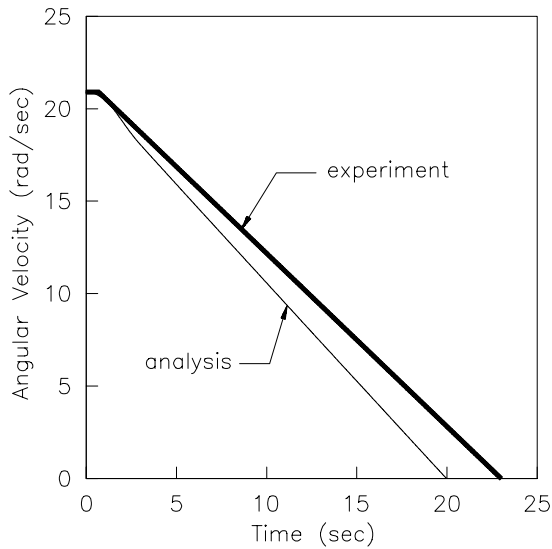


Fig. 4: History of angular velocity.

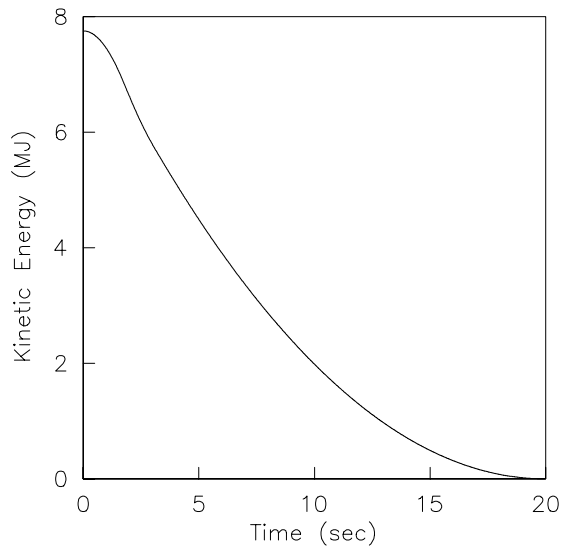


Fig. 5: History of kinetic energy.

Fig. 7 shows the history of maximum temperature at first rotor disk. The maximum value is 1330°C and occur at $t = 9$ seconds. After $t = 9$, the maximum temperature also decreased up to braking time.

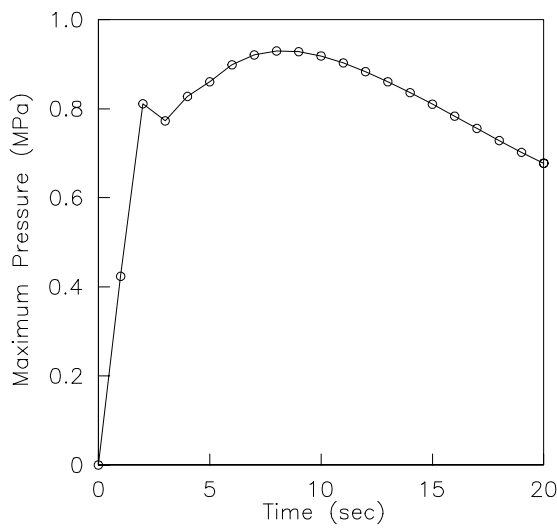


Fig. 6: History of maximum pressure.

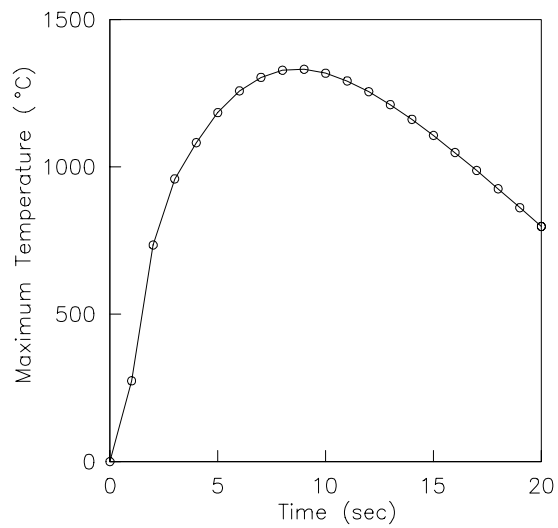


Fig. 7: History of maximum temperature.

3D FAILURE ANALYSIS

The first rotor disk of the 7-disk brake system was observed to be in most severe operating condition, so the first rotor disk with the first and the second friction surfaces was selected for 3D failure analysis. The results imported to 3D analysis are pressure, friction force and temperature. In the present 3D analysis, the modeling of full disk is impossible, because it requires huge computer memory and computing time. However, the rotor has five slots equally spaced along the outer circumference, so the rotor disk is cyclically symmetric with respect to Z axis in terms of geometry and loading. Therefore, for the efficiency of computation, the one fifth of full disk is modeled using cyclic symmetry condition. Fig. 8

shows the cyclic symmetry model of brake system used in this study and displacement boundary condition.

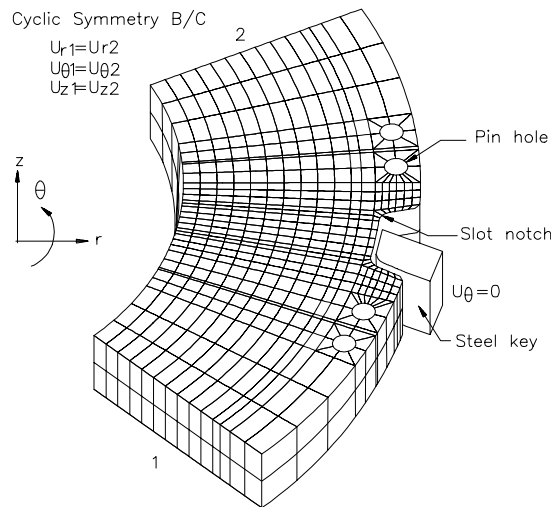


Fig.8: Finite element model and boundary condition of 3D failure analysis.

The 3D failure analysis was performed using commercial package, NISA-II. The 3D model has 944 elements and 5745 nodes. The cyclic symmetry condition means that the displacement of face 1 is the same as the displacement of face 2 as Eqn 6

$$\begin{aligned} U_{r1} &= U_{r2} \\ U_{\theta1} &= U_{\theta2} \\ U_{z1} &= U_{z2} \end{aligned} \quad (6)$$

This condition was imposed by the multi-point constraints (MPC) in NISA-II. The rotors of brake disk have five key slots. The steel keys connected to the wheel of aircraft are inserted to the key slots. When the braking action is started, the forces generated at the key slots by the keys are equivalent to the friction force. At that time, the displacement of θ -direction at the slots is constrained by the key. Therefore, the boundary condition at key slot is imposed such as Fig. 8. The failure criterion used in 3D failure analysis is Tsai-Wu failure criterion. The Tsai-Wu failure criterion is

$$\begin{aligned} f(\sigma_k) &= F_i \sigma_i + F_{ij} \sigma_{ij} = 1 \\ i, j, k &= 1, 2, \dots, 6 \end{aligned} \quad (7)$$

RESULTS OF 3D FAILURE ANALYSIS

The 3D failure analysis was performed for the most severe operating condition. The maximum pressure distribution of the brake system occurred at 8 seconds after the application of the hydraulic pressure. Therefore, at that time, the 3D failure analysis was performed. Table 2 shows the material properties of carbon-carbon composite used in the 3D analysis. Some properties were measured by the material tests for this study.

Table 2: 3D Material Properties of Carbon-Carbon Composites.

Properties	Symbol	value
Elastic modulus in r, θ	E_r, E_θ	^a 59 GPa
Elastic modulus in z	E_z	^a 3.46 GPa
Shear modulus in $r-\theta$	$G_{r\theta}$	2.41 GPa
Shear modulus in $r-z$	G_{rz}	1.38 GPa
Shear modulus in $\theta-z$	$G_{\theta z}$	1.38 GPa
Poisson's ratio	$\nu_{r\theta}$	0.3
Poisson's ratio	$\nu_{rz}, \nu_{\theta z}$	0.2
Thermal expansion coeff. in r, θ	α_r, α_θ	0.31×10^{-6} 1/K
Thermal expansion coeff. in z	α_z	0.29×10^{-6} 1/K
Tensile strength in r, θ -dirn.		^a 103 MPa
Compressive strength in r, θ -dirn.		^a 90.1 MPa
Tensile strength in z -dirn.		^a 3.01 MPa
Compressive strength in z -dirn.		^a 118 MPa
Shear strength in $r-\theta$ plane		34 MPa
Shear strength in $r-z$ plane		^a 5.71 MPa
Shear strength in $\theta-z$ plane		^a 5.71 MPa

^a: material properties measured from material testing.

Fig. 9 shows the Tsai-Wu failure index contour of brake disk. From Fig. 9, maximum failure index was 0.59 and occurred at the slot notch. In this failure analysis, stress concentration around the pin holes was not severe.

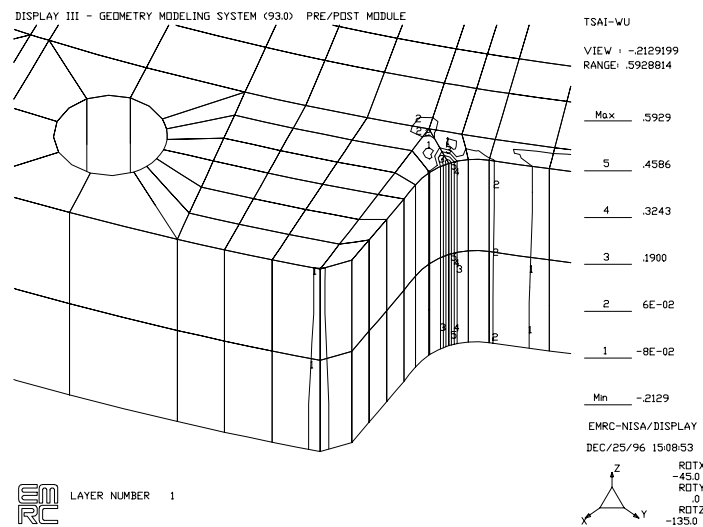


Fig. 9: Tsai-Wu failure index contour of the carbon-carbon brake disk at slot.

CONCLUSIONS

For carbon-carbon composite brake disk system having 7 disks, the transient thermoelastic and 3D failure analyses were performed. The transient thermoelastic behaviors of composite brake disk based on the experimental dynamometer test conditions were investigated and the angular velocity history was calculated by energy balance method. The hydraulic pressure was approximated from the results of dynamometer test. The history of angular velocity showed good agreement between the numerical and experimental results and decreased linearly. The histories of maximum pressure and the maximum temperature increased until $t=8$ and $t=9$ seconds, respectively and then decreased up to the braking time for the first rotor that is the most severely loaded one. In the 3D failure analysis, the results of transient thermoelastic analysis such as pressure, friction force and temperature were imported to the 3D analysis. The 3D failure analysis was performed at the time of maximum pressure and for the first rotor disk. The maximum failure index occurred at the slot notch and stress concentration around the pin holes was not severe.

REFERENCES

1. Kennedy, F.E. and Ling, F.F.," A Thermal, Thermoelastic and Wear Simulation of A High-Energy Sliding Contact Problem," *J. Lubr. Technol.*, Vol. 97, 1974, pp. 497.
2. Zagrodzki, P.," Numerical Analysis of Temperature Fields and Thermal Stresses in The Friction Discs of A Multidisc Wet Clutch," *Wear*, Vol.101, 1985, pp. 255-271.
3. Zagrodzki, P.," Analysis of Thermomechanical Phenomena in Multidisc Clutches and Brakes," *Wear*, Vol.140, 1990, pp. 291-308.
4. Sonn, H.W., Kim, C. G., Hong, C. S., and Yoon, B. I., "Transient Thermoelastic Analysis of Composite Brake Disks," *J. of Reinforced Plastics and Composites*, Vol. 14, Dec., 1995, pp. 1337-1361.
5. Sonn, H.W., Kim, C. G., Hong, C. S., and Yoon, B. I., "Axisymmetric Analysis of Transient Thermoelastic Behaviors in Composite Brake Disks," *J. of Thermophysics and Heat Transfer*, Vol. 10, No. 1, 1996, pp. 67-75.
6. EMRC NISA-II, *User's Manual*, 1992.

HIGH PERFORMANCE COMPOSITE STRUCTURES FOR HIGH PRECISION PARTICLE DETECTORS

Claude Hauviller

PPE Division, CERN, 1211 GENEVA 23 - Switzerland

SUMMARY: After some background on High Energy Physics (HEP) and the future accelerator and its detectors, tracking detector principles are shortly described. Sources of errors which impinge the resolution of these so-called trackers are then analysed. It is shown that to achieve a measurement accuracy at the level of few microns over a huge detection volume of many cubic meters, it is of a prime importance that the support structures are as light as possible while providing a very high stability.

Optimisation leads to the choice of high performance composite structures. But an hostile environment leads to major concerns on the micron level stability of these structures: ionising radiations, temperature gradients, humidity transients, vibrations,... together with inherent mechanical behaviour: internal stresses, creep...

This general presentation will be enlighten with specific examples of composite structures for high precision particle detectors.

KEYWORDS: high energy particle physics, precision detector, lightweight structures, high performance composites, mechanical stability, environmental degradation

HIGH ENERGY PHYSICS AND ACCELERATORS

To satisfy the constant quest of the physics community to look deeper into matter, more powerful accelerators are always requested.

Now, with the LEP machine, the latest and largest of CERN's accelerators with a collision energy in the range of 200 GeV, we can probe the structure of matter down to the level of 10^{-18} meter. But new fundamental questions arose: yet undetected particle families leading to a better understanding of the dark matter in the Universe, why W and Z particles have such a high mass whereas a photon is massless,... and many ideas and scenarios for a better understanding of our so complex world. To get answers or at least clues, we need to achieve one order of magnitude in resolution down to 10^{-19} meter and that implies collision energies in the TeV range at the constituents level.

The LHC (Large Hadron Collider) is designed for that purpose [1]. This 27 km long proton-proton collider of 14 TeV centre-of-mass energy will recreate the conditions prevailing in the Universe just 10^{-12} second after the "Big Bang" when the temperature was 10^{16} degrees. But a high luminosity is also required to benefit from this increase of energy. The 10^{34} cm⁻²s⁻¹ design luminosity of LHC leads to events generated by the collisions with a huge number of particles to be analysed in some nanoseconds and an unusual high radiation level.

To analyse in fine details such complex interactions, detectors will have millions of measuring channels which should give accurate information on the mass, the charge, the momentum and the trajectory of each of the generated particles.

DETECTORS

A typical detector for LHC, shown in figure 1, will be installed around one of the interaction points. It has an overall cylindrical shape with both diameter and length up to 20 meters. The particle beams go through the detector along its axis and collide at the centre. Weighing up to 15,000 tons, a detector consists basically of three sub-systems embedded one inside the other like Russian dolls: an inner detector or tracker, the calorimeters and completely enclosing the others the muon system. In addition, a magnetic field deflecting particles to measure charge and momentum, is generated by one (or more) powerful electro-magnet.

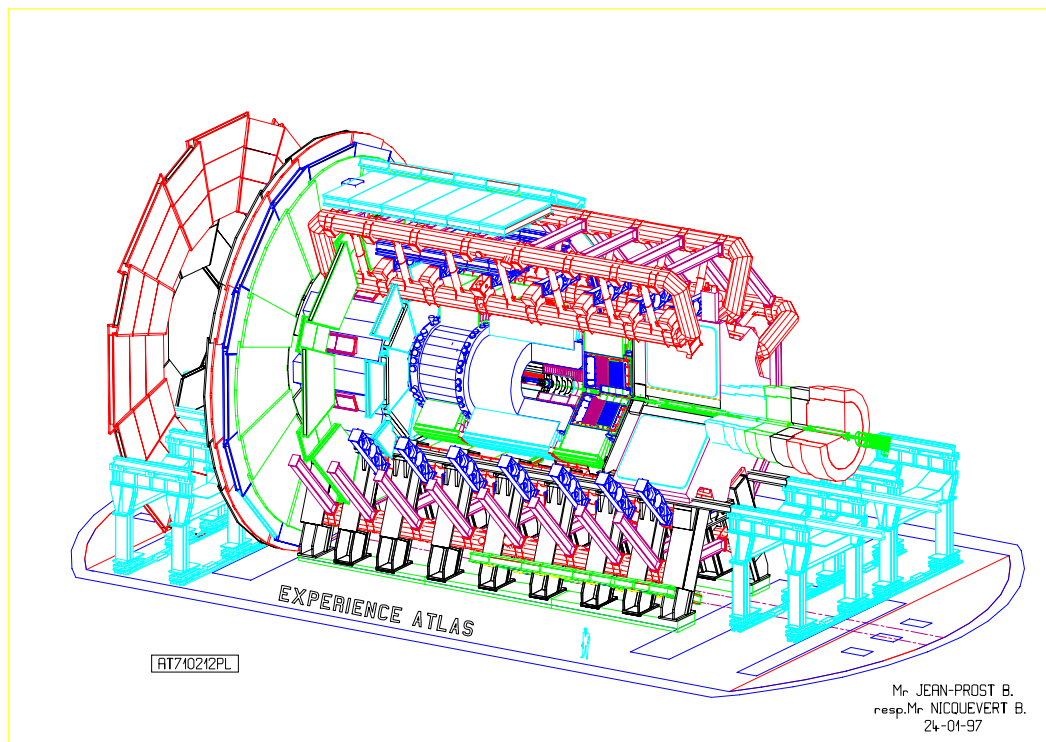


Fig1.: LHC detector (scale is given by a person in front)

HIGH PRECISION DETECTORS: TRACKERS

General

If the precision is a major concern for all the elements of the detector, the more stringent specifications are found in the innermost part, the tracker.

A tracker, located in the immediate vicinity of the interaction point, is like any other detector a system which could be divided into a series of sub-systems : the detecting elements (the heart of the detector), the support structure, the electronics and data acquisition and the services: active gases, cooling (liquid and gas), power, alignment and survey.

Detecting Elements

As most of all the present detectors, the measuring techniques of the tracking detectors are based on the ionization and excitation phenomena produced by charged particles in gases and solids. The most common and oldest ones, the Wire Chambers measure the ionization produced by a charged particle in a gas; generated electrons produce a signal on precisely positioned wires. The accuracy currently achieved is only in the order of 100 microns. Moreover, the too high density of tracks at LHC leads to spatial separation difficulties and the rather slow time for signal development of about 100 ns, is incompatible with the LHC repetivity rate of 25 ns (time between two subsequent particle bunches collisions).

Momentum measurements and particle identification require now a precision in the reconstruction of the particle trajectories in some cases better than the ten microns level. The more precise devices are the silicon or gallium arsenide or diamond strip detecting elements. The first ones are the most common ones. They are made of high resistivity doped silicon wafers, 300 microns thick. The two other types are based on the same principle with a different substrate, with the advantage of a better radiation resistance.

Narrow strips are ion implanted with a pitch of usually 50 microns. The signal is measured at the strip end in less than 20 ns and the measurement precision is around 10 microns and even could go down to 3 microns with the most sophisticated electronics devices. It is even possible to measure two co-ordinates with a double-sided detector or with an other type of device, the pixel detector where the electrodes are in the form of pads.

In the detectors presently taking data, this strip technology is only applied in rather small volumes, some decimetre cube.

Other types of detecting elements are used when the required accuracy is only around 50 microns: the Microstrip Gas Chambers (MSGC), the Straw tubes and the Scintillating fibres.

The Support Structure

Except very seldom cases, the detecting strips/wires are laid either parallel or perpendicular to the particle beams axis to simplify (or even permit) the tracks reconstruction. Therefore, the support structures have quite simple overall shape : planar or cylindrical. They are manufactured from shells, plates and cross-braced lattices. But, as it will be shown later, space and mass constraints complicate drastically the design.

DETECTOR RESOLUTION

If it has been possible to work at a resolution better than 10 microns in small detecting volumes, now the aim for the near future is to achieve almost the same precision inside huge volumes of tens of cubic meters. This step in the technology is obviously a major challenge.

To fully use the very high intrinsic resolution of the detecting elements, it is of the utmost importance not to spoil it in the fully assembled detector. Main sources of errors on the measurement of a particle trajectory are mainly due to the intrinsic resolution of the detecting element and the performance of its electronics, the multiple scattering created by all the materials of the detector and the mechanical positioning and stability in the 3-dimensional space. The total error is the r. m. s. of these errors.

Multiple Scattering

Electrically charged particles suffer multiple scattering caused by electromagnetic interactions with electrons and nuclei when traversing a medium. Loss of energy is small but large scattering angles are major sources of errors in the momentum definition.

The r. m. s. scattering angle θ_p is given by

$$\theta_p = \frac{0.014}{\beta p} \sqrt{\frac{L}{X_0}} \quad (1)$$

where

$\beta = v/c$

p in GeV/c

L length of material traversed by the particle

X_0 radiation length is a physical property of the material

Its approximate value, expressed in meters, is

$$X_0 = 7.16 \frac{A}{\rho Z(Z+1) \ln(287/\sqrt{Z})} \quad (2)$$

where

ρ is the density

A is the atomic mass

Z is the atomic number

In first approximation, X_0 is roughly inversely proportional to ρZ .

Positioning Stability

The mechanical design of the support structures is based on deflection and, usually, not on stress. Many sources of vibrations (inherent to the earth itself or to the infrastructure : pumps, motors, ventilation,...) exist in an experimental hall and will undoubtedly generate displacements in the microns range. Therefore, it is necessary to maximise the rigidity which could be expressed in general terms as the product of the Young's modulus (E) (the material should behave in its elastic range) by a length (L). Taking into account the necessary minimisation of the multiple scattering, the previous product can be written as $E X_0$, an expression depending only upon the material. As a consequence, this product $E X_0$ can be used as figure of merit for all the structural materials of the detectors and both the Young's

modulus and the radiation length should be as high as possible. Figure 2 shows a comparison of some of the best representatives of material families available on the market (unidirectional properties).

All these materials are also known for their high specific stiffness (E/ρ) and it is therefore obvious that the selection criterion $E X_0$ will lead to a choice very similar to the one for aeronautics and space [2],[3].

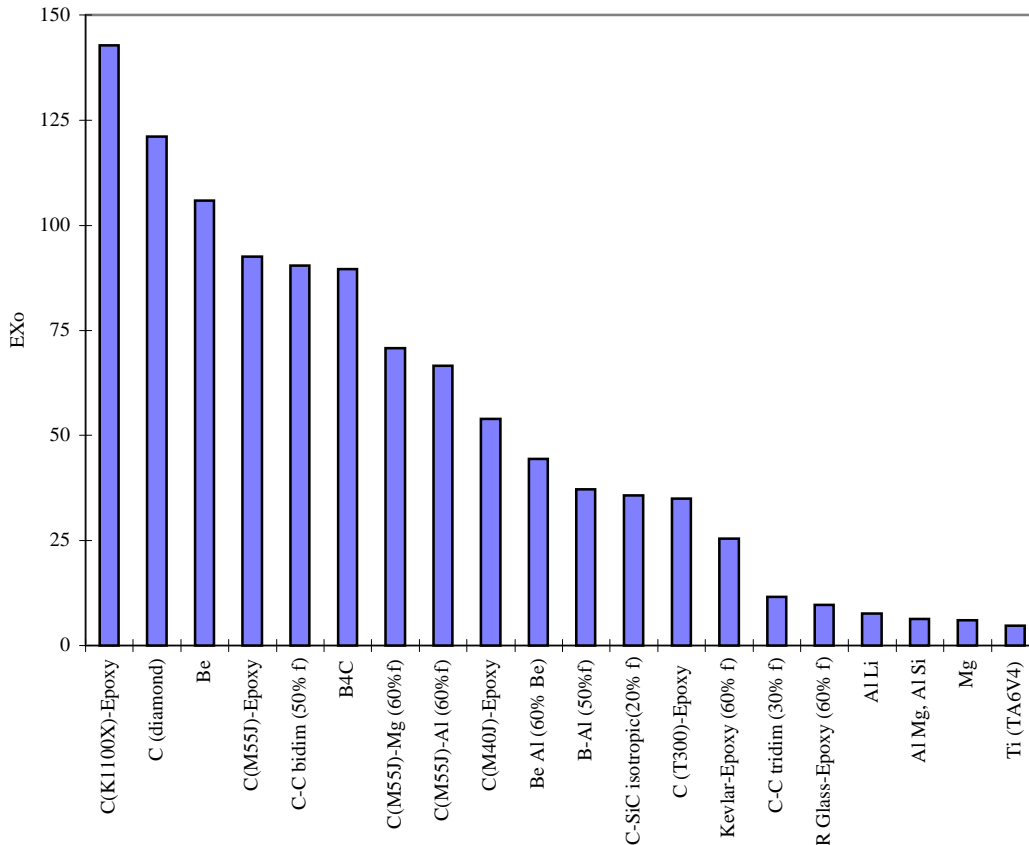


Fig. 2: Figures of merit for structural materials for trackers.

LIFE CYCLE OF A TRACKER

Operational Life

Design and construction of the present detectors will extend over more than ten years. The detectors will be assembled and fully tested in temperature and humidity controlled clean rooms. But the environmental conditions during the transport to and installation inside the underground hall will be more or less the atmospheric conditions.

The detectors are designed for ten years of operation in the radiative environment of the LHC. Each year of operation will be basically split into two equal periods: the data-taking period and the maintenance period. The tracker should stay very precise during the data-taking period, at least between two tricky on-line calibrations. During the maintenance period, the irradiation is stopped but temperature and humidity excursions may be large.

Environmental Conditions

A stiff structure will not necessary be stable, especially if the environmental conditions are too harsh. One should take into account the radiation, the temperature, the humidity and the vibrations . Table 1 summarises these parameters.

The very high luminosity of the LHC generated by a high radiative environment inside the detectors is largely above the radiation level in the present accelerators. The expected fluences inside the tracker volume are, for an integrated luminosity of 10^{42}cm^{-2} (ten years of LHC running at nominal conditions), for the charged particles, $\phi = 1.3 \cdot 10^{17}/r^2 \text{ cm}^{-2}$, where r is the distance from the particle beam axis in centimetres and for the neutrons, $\phi = 3 \cdot 10^{13} \text{ cm}^{-2}$, constant inside the tracker volume.

The resulting integrated dose goes therefore up to the Megagray range.

Dynamic measurements on present detectors have shown movements in the range of some microns. These movements have two origins [4]: the ground motion (seismic) in the low frequency range (below 1Hz), the man-made vibrations/noise created by ventilation, fluids in tubes, pumps (in particular cryogenics),...

Table 1: Typical environmental conditions (detecting element dependant)

	Data-Taking	Assembly/Maintenance
Radiation	Yearly integrated dose up to 100 KGray	None
Temperature	Nominal temperature between -15 °C and 30 °C Stability +/- 1 °C Local hot spots (electronics)	Nominal temperature between 5 °C and 25 °C
Humidity	Dry gas : N2, CO2 Some % relative humidity	Atmospheric, between 20% and 80% relative humidity
Vibrations	Ground (seismic) motion Man-made noise	Ditto

MATERIALS SELECTION

Optimal Material

In résumé, an optimal structural material for a tracker should fulfil the following criteria:
 light (high X_0),
 stiff (high E),
 radiation resistant (radiation index > 6),
 insensitive to temperature variations (low CTE),
 insensitive to humidity variations (low CME and moisture absorption),
 stable with time.

It is not very surprising to find that no material can fulfil all these requirements selection. A relative priority should be set between the different criteria. But this material choice should also be directed largely by other major factors:

the way to tackle the safety problems,
the availability of the material in rather small quantities,
the technological limitations,
and last but not least of the final cost of the manufactured parts.

Selection

The first two criteria (X_0 and E) are used as bases for the choice. Figure 2 shows that some metals, metal based composites and ceramics stand very high in the comparison, but they are hampered by serious drawbacks, mainly technological limitations and cost.

Manufacturing large structures in beryllium has been demonstrated in the space program. But it is not only costly, safety hazards are not negligible. Moreover, the technology to connect elements is difficult, leading to too bulky elements, even if welding is now becoming possible.

All these arguments are also true for beryllium - aluminium alloys. The only parts which have been manufactured yet with the others competitors (diamond, carbon-carbon, boron-carbide, metal matrix composites, silicon-carbide) are too small to be considered in the short term despite a good resistance to radiation and a relative insensitivity to humidity.

Carbon Fibre Reinforced Plastics

The material chosen is therefore the Carbon Fibre Reinforced Plastics (CFRP) family with high and ultra-high modulus fibres. The detailed choice of the components of the material for each structure depends upon its specifications. Pan fibres are the classical ones but pitch fibres are preferred when compressive stresses are small and when high thermal conductivity is a must to avoid local hot spots.

Environmental conditions specified earlier may create serious difficulties which are examined thereafter.

The plastics should be high performance plastics in order to resist radiation. An extensive source of information prepared at CERN like [5] are used as guidelines. It has been found that, for most of the plastics, one finds a correlation between the curing temperature and the radiation resistance. The two selected families of resins in terms of radiation and also in terms of manufacturing possibilities are the epoxies and the cyanate-esters.

In terms of behaviour versus temperature, CFRP is very good. The thermal properties are well known; it is possible to use lay-ups giving an almost zero coefficient of thermal expansion (CTE) and the transients in time are very short.

But in terms of the behaviour versus humidity, one finds major drawbacks: all the resins absorb humidity (up to 6% for epoxies) and the transients are in the range of months, which could lead to a large shortening of the data-taking period due to the instability of the structures. Limited work has been done in this field, but one can see in figure 3 that humidity

transients may lead to large strain variations: it takes more than two months to start to stabilise for a 0.5mm thick sample after a jump in relative humidity of only 20% [6].

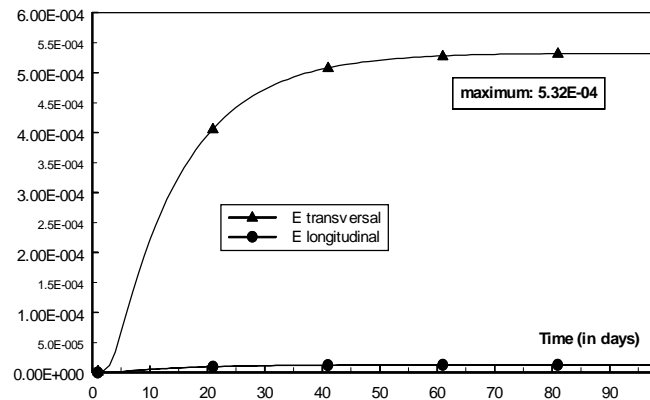


Fig.3: Hygroscopic strains (*Hercules 3501-5/T300 uniaxial composite*)

Above that, one should also take into account the macroscopic phenomena changing materials properties with time: creep occurs even at a low load level, internal stresses built-in during the manufacturing process relax more or less quickly (one should note that a lower curing temperature will limit the level of the internal stresses, but this requirement will be in conflict with a higher curing temperature for a better radiation resistance), micro-cracks propagate slowly, and the coupling effects of radiation is basically unknown.

Moreover, in the case of materials in contact with the highly pure detecting gas of a detector, resins with low outgassing should be chosen in order to avoid any pollution.

EXAMPLES OF COMPOSITE STRUCTURES FOR TRACKERS

If High Modulus Carbon Fibre Reinforced Plastics has been chosen as base material for the high precision detectors of the future, one sees that a large series of phenomena are not really entirely understood. The present design is based on the present knowledge, but specific development are going on to try to understand better how the specific environment will worsen the performances of the detectors and to try to avoid bad surprises. A large series of diverse composites structures are under design and prototyping with a construction to be completed by the end of the century. Two examples are presented below.

The ATLAS TRT Barrel Structure

This full CFRP structure (Figure 4) holds precisely positioned axial detecting elements assembled in a cylindrical overall shape (2 m in diameter, 1.6 m in length). The end faces are cross braced structures designed to minimise the material quantity and to give as much space as possible to the data acquisition equipment and the services. The two end faces are connected together by two thin cylinders. The only support points are two rails.

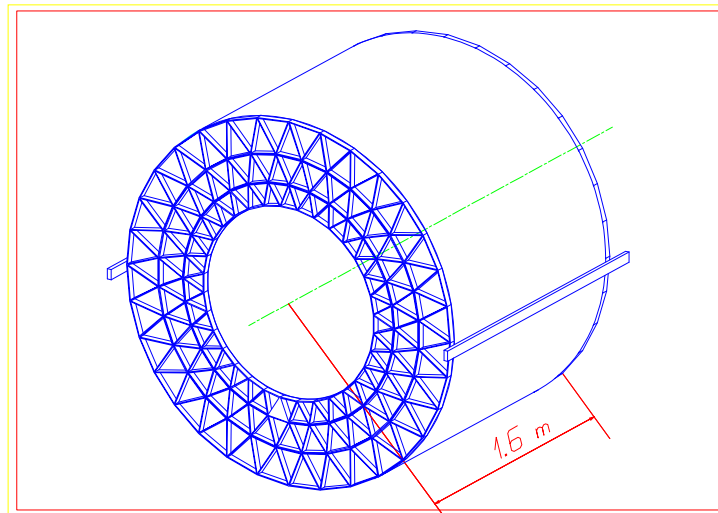


Fig.4: The ATLAS TRT barrel structure

If the trusses (5x20mm) are made of uniaxial fibres, major difficulties lay in the treatment of the connections: how to transfer the forces without increasing the dimensions of the nodes. First prototypes made by simply gluing the trusses together show unexpectedly large deflections, very different from the ones obtained by FEM analysis. More complex solutions like continuous winding could be an alternate, but costly solution.

The CMS MSGC Barrel Structure

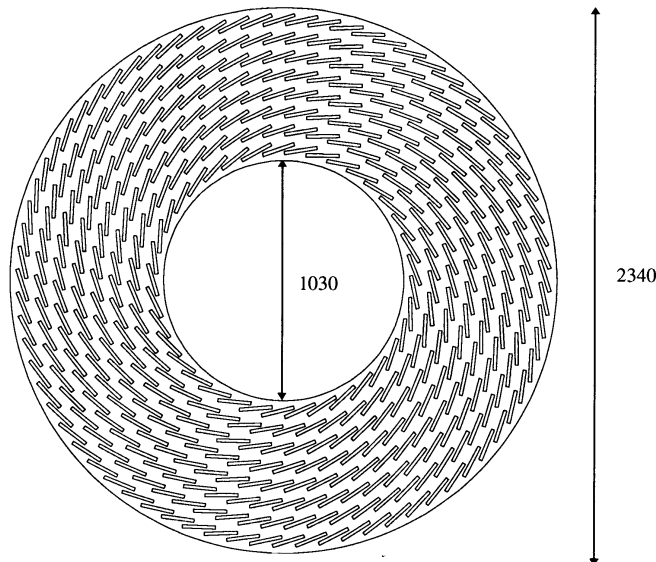


Fig. 5: A CMS MSGC barrel end-plate

This large structure is also cylindrical, but with larger dimensions: 2350 mm in diameter and 2300 mm in length. The two carbon-fibre end-plates (figure 5) support rigid composites slabs

housing the detecting elements and their services. The slots supporting the slabs should be precisely machined in a sandwich plate. The end-plates are connected together by two cylinders and two extra thinner plates reinforce the structure and minimise the sag of the slabs.

CONCLUSION

A tracker is an assembly of a series of sub-systems and its performances will be dependant of the worse of these sub-systems. The detecting elements have an outstanding behaviour and the support structures should behave accordingly. An approach of cost-effective design has led to high performance dimensionally stable structures for space applications manufactured in Carbon Fibre Reinforced Plastics. Even if the operational life, in particular the environmental conditions, of the future HEP trackers will be different, the principles and methods developed for space are applicable to the manufacturing of these structures. CFRP is presently the only technologically sound material for these applications but major concerns still exist, in the lack of knowledge of its behaviour versus parameters like humidity and moreover about possible coupling between environmental parameters leading to unexpected properties degradation. In these conditions, it is a major challenge to build reliable structures at the uppermost limit of the technology.

Finally, the HEP community has definitively one common interest with the Space community, the High Performance Composites Structures and in the near future the loop will be closed when sophisticated particle trackers will be sent into space to study matter far from all the perturbations of our Earth [7].

REFERENCES

1. LHC, the Large Hadron Collider Accelerator Project, *CERN/AC/93-03*, November 1993, see also <http://www.cern.ch/>
2. Nicquevert, B. and Hauviller, C., Eds., International Workshop on Advanced Materials for High Precision Detectors, *CERN 94-07*, September 1994.
3. International Workshop on Advanced Materials for Lightweight Structures '94, 22-25 March, 1994, ESA-ESTEC, Noordwijk, The Netherlands
4. Juravlev, V.M., et al., Seismic Vibration Studies for Future Linear Colliders, Fourth European Particle Accelerator Conference (EPAC 94) London, UK, June 1994.
5. Schönbacher, H. and Tavlet, M., Compilation of radiation test data, *CERN 89-12*, Geneva, 1989.
6. Kanoute, P., et al., Diffuse and hygroelastic behavior of reinforced composites materials, European Conference on Surfaces and Interfaces in Polymers and Composites, Lausanne, Switzerland, June 1997
7. Battiston, R., Astro-Particle Physics with Alpha Magnetic Spectrometer (AMS), Workshop on Frontier Objects in Astrophysics and Particle Physics, Vulcano, Italy, May 1996

TRANSVERSE SHEAR EFFECTS IN DISCRETE OPTIMIZATION OF LAMINATED PLATES UNDER BUCKLING AND FPF CONSTRAINTS

A. Muc and P. Saj

*Institute of Mechanics & Machine Design,
Cracow University of Technology ul. Warszawska 24, 31-155 Kraków, Poland*

SUMMARY: The aim of the paper is to discuss the optimal design of laminated biaxially compressed plates. The design goal is to maximize buckling load subjected to lamina failure and bimodal constraints. The analysis is conducted for two plate theories, ie. the Love-Kirchhoff and the first-order transverse shear deformation theories to illustrate the influence of transverse shear effects on optimal loads and composite topologies. The laminate is assumed to be symmetric, balanced and made of 0_2° , $\pm 45^{\circ}$, 90_2° plies. Genetic algorithms are employed in the analysis. A particular attention is focused on the choice of the appropriate variants of genetic algorithms - the effects of the selection and mutations are demonstrated. A lot of numerical examples illustrate the discussed problems.

KEYWORDS: plates, buckling, optimization, transverse shear effects, first-ply-failure, genetic algorithms

INTRODUCTION

Laminated composite materials are more and more applied in fields where one-component materials cannot satisfy the requirements any longer. On account of their special physical, chemical and mechanical properties composites are not only employed in the aircraft and spacecraft industries but also in several fields of technology. However, in order to meet the steadily increasing requirements made on the specifications for machinery and plants and to use the specific (anisotropic) properties of composites, the individual components must be designed in an "optimal" way.

In particular, the optimal design of laminated composite plates has been a subject of research for many years. Designs have been studied with respect to layer thickness and ply angles orientations for plate structures subjected to various constraints (buckling, FPF etc.), boundary and loading conditions. A thorough review of various approaches and results in this area is given by Adali [1].

Due to variety of used assumptions and simplifications the optimal design of laminated thinwalled composite structures may be established and classified in the following way:

- structural modeling taking especially into account 2D approximations of 3D structures

- numerical modeling of structures
- optimization algorithm

It should be pointed out that the majority of optimization problems for rectangular plates has been solved with the use of the classical Love-Kirchhoff hypothesis - see Ref. 1. On the other hand now it is obvious that for laminated composites the use of the L-K theory is strongly limited even for thinwalled structures - see eg. Noor, Burton [2]. Therefore, different modeling of structures used in the formulation of optimization problems may lead to discrepancies in optimal configurations and failure loads - the examples have been discussed and demonstrated in Ref.3.

In the present paper we intend to look deeper insight the above problems and the results are related closely with results obtained in Refs [3,4,5]. In details, the present paper intends to provide a contribution to the analysis of the following problems:

- the influence of the applied plate theories on optimal configurations of laminated plates subjected to buckling and FPF constraints
- the choice of appropriate variants of genetic algorithms to the discussed optimization problems.

In the present paper we shall not dwell on the detailed description of genetic algorithms since more information can be found eg. in Refs [6,7,8].

FORMULATION OF THE PROBLEM

Let us consider the simply supported plate loaded in x and y directions by λN_x and λN_y , respectively, with λ being an amplitude parameter. Its longitudinal and lateral dimensions are a and b, respectively. The total thickness of the plate is equal to t. The plate is constructed of an arbitrary number N of orthotropic layers of thickness t/N. The laminate is assumed to be symmetric, balanced and made of $0_2^{\circ}, 90_2^{\circ}, \pm 45^{\circ}$ plies, each of thickness 2t/N. As the result only N/4 ply orientations are required to describe the laminate configuration. An analysis based on the linear, first-order-transverse-shear deformation plate theory (FSDT) can be used to determine buckling loads (see Muc[3]). The buckling load parameter λ for the half wave numbers (m,n in the x and y directions, respectively) is given by:

$$\lambda_b = \frac{m^2 \pi^2}{N_x (1 + K \beta_m^2)} \left[\frac{T_{33} + \zeta (1 + \beta_m^2) T_{44}}{1 + \zeta T_{55} + \zeta^2 T_{44}} \right] \quad (1)$$

where

$$\begin{aligned} T_{33} &= D_{11} + 2(D_{12} + 2D_{66})\beta_m^2 + D_{22}\beta_m^4 \\ T_{44} &= \frac{12}{t^3} [D_{11}D_{22} - D_{12}^2 - 2D_{12}D_{66} + D_{66}(D_{11} + D_{22}\beta_m^4)] \\ T_{55} &= \frac{12}{t^3} [D_{11} + D_{66} + \beta_m^2(D_{22} + D_{66})] \end{aligned} \quad (2)$$

Here: $K = N_y/N_x$, $\beta_m = an/(bm)$ and $\zeta = m^2 t^2 \pi^2 / 12 a^2 k_{13}^2 G_{13}$.

For the classical Love-Kirchhoff plate theory the similar relations can be easily obtained from Eqn 1 inserting $\zeta = 0$, i.e. $t/a=0$ or $G_{13} \rightarrow \infty$.

In the absence of the applied shear loads, the laminate strains ϵ_x , ϵ_y can be calculated in the global coordinate system from (geometrically linear theory):

$$\epsilon_x = \lambda_s N_x \frac{A_{22} - K A_{12}}{A_{11} A_{22} - A_{12}^2}, \quad \epsilon_y = \lambda_s N_x \frac{K A_{11} - A_{12}}{A_{11} A_{22} - A_{12}^2} \quad (3)$$

Using the classical transformation rules the strains for the k-th ply in the local coordinate system can be calculated:

$$\epsilon_{11}^{(k)} = \epsilon_x \cos^2 \theta_k + \epsilon_y \sin^2 \theta_k, \quad \epsilon_{22}^{(k)} = \epsilon_x \sin^2 \theta_k + \epsilon_y \cos^2 \theta_k, \quad \epsilon_{12}^{(k)} = (\epsilon_y - \epsilon_x) \sin(2\theta_k) \quad (4)$$

where θ_k denotes fibre orientation of the k-th ply and in the present discrete optimization problem belongs to the set: $[0_2^{\circ}, 90_2^{\circ}, \pm 45^{\circ}]$. Comparing each of the above strains with the ultimate ones or using the relations (4) in the arbitrary quadratic strain or strength FPF criterion (eg. the Tsai-Wu criterion), finally, one can find (with the use of Eqns 3) the value of the λ_s parameter corresponding to FPF load for the analysed plate.

As it is well known the buckling analysis is always associated with searching for a such wavenumber that corresponds to a minimal buckling load. However, in optimization problems of laminates subjected to buckling constraints one can encounter a variety of solutions where optimal angle orientations (or thicknesses of each individual plies) are not connected with one wavenumber m or n. Figure 1 is an example where an optimal stacking sequence cannot be reached for a given wavenumber in buckling either for 0° or for 90° fibre orientations. The optimum exists as the buckling parameter λ_b is identical for m and m+1, i.e.:

$$\lambda_b(m, n) = \lambda_b(m + 1, n) \quad (5)$$

The above condition is called as **bimodal** solution. For continuous ply orientations the relation (5) can be satisfied exactly and one can find even analytical solutions - Muc [5].

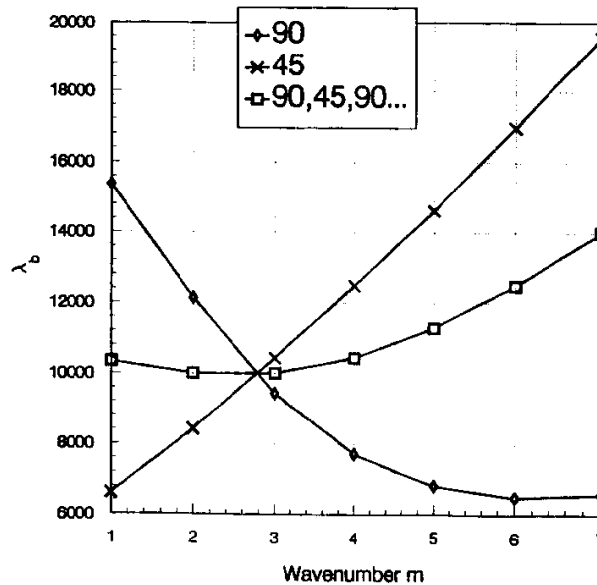


Fig. 1: Bimodal solutions in discrete optimization.

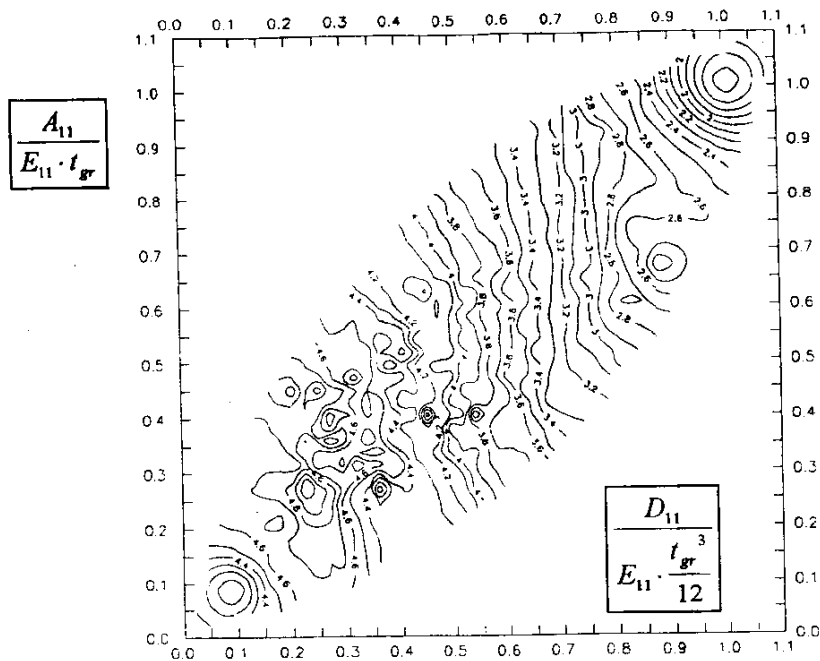


Fig. 2: Contour plots of buckling loads - FSDT.

For discrete optimization variables usually Eqn 5 is satisfied in an approximate manner only. However, as it may be observed in Ref.5 the bimodal condition has a great influence both on the optimal buckling loads as well as optimal laminate topologies and cannot be neglected in the optimization analysis.

Having all basic relations one can formulate now the optimization problem:

Find

$$\text{Max}_{S_i} \text{ Min}_{m,n} \lambda_b(S_i; m, n) \quad (6)$$

subjected to the inequality constraint:

$$\lambda_b(S_i; m, n) \leq \lambda_s(S_i; m, n) \quad (7)$$

and the equality constraint in the form given by Eqn 4. λ_s is the FPF load parameter computed with the use of Eqns 3,4 and an appropriate FPF criterion, whereas S_i constitutes a set of $3^{N/4}$ locations of plies oriented at 0° or 90° or $\pm 45^\circ$ in the laminate.

To simplify the optimization problem formulation the problem (5-7) has been replaced by the equivalent in the following form:

Find

$$\text{Max}_{S_i} \text{ Min}_{m,n} \lambda_b^m - r_s(\lambda_b^m - \lambda_s^m)^2 - r_{bim}(\lambda_b^m - \lambda_b^{m+1})^2 \quad (8)$$

The positive variables r_s and r_{bim} control the magnitudes of the penalty terms in the above objective function.

APPLICATION OF GENETIC ALGORITHMS

The existence of multiple relative or local optima is a characteristic feature of composite 2D structures, independently on the type of design variables used in the analysis, i.e. continuous, discrete or integer - see Fig.2. Let us notice that the contour plot shown in Fig.2

fills only a part of the space $A_{11} - D_{11}$ since fibres can be oriented at 0° , $\pm 45^\circ$ and 90° . Therefore, the problem of the relative optima cannot be unique to linear programming methods. The solution of the problem by the latter methods is usually liable to depend on the initial design from which the design procedure is started. This difficulty can be alleviated by repeating the computations from different starting points and comparing the solutions until reasonable confidence is built up that the global optimum has been achieved. In the area of the optimization of 2D thinwalled structures two approaches are introduced: 1) two-level multi-start optimization algorithms and 2) genetic (probabilistic) algorithms.

Two-level optimization algorithms are particularly directed to the analysis of continuous design variables, such as fibre orientations θ_k and layer thicknesses. At the first phase of the optimization, the layer thicknesses are kept constant and the conditional global optimal orientations are determined to maximize failure loads using multi-start optimization method. At the second level the optimal layer orientations are kept unaltered and the conditional global optimal thicknesses are designed including also multi-start optimization methods.

The obvious advantage of genetic techniques over the previously discussed algorithms is based on probabilistic search method linking both multi-start optimization algorithms, the possibility of the effective optimization analysis for disjoint or nonconvex design spaces and the existence of zero-one integer variables simplifying the computer coding. Mathematical programming methods will find the optimum in convex problems where there exists a single global optimum.

There are essentially three basic components necessary for the successful implementation of a genetic algorithm. At the outset, there must be a code or scheme that allows for a bit string representation of possible solutions to the problem. It is assumed that the fibres oriented at 0° are represented as 1, at $\pm 45^\circ$ as - 2, and at 90° as - 3. Next, a suitable objective function must be devised, for instance in the form given by Eqn 1. The final component is the development of transformations functions, with the use of random variable generators, that mimic the biological evolution process, i.e. recombination and mutation. The above three factors may be easily adopted to the optimal design strategy for 2D thinwalled composite structures.

However, it should be emphasized that the correctness of the genetic search as well as the total number of iterations depend on various factors, such as: 1) the number of multiple relative and local optima, 2) the length of the bit string (equal to $N/4$) - for discrete optimization problems the better results can be obtained as N increases, 3) the initial population size, 4) the probability and number of crossover, 5) the probability of mutation, 6) the selection rule in the recombination process. There is not known in advance how for a particular optimization problem the optimal values of the above factors can be selected or prescribed.

Due to the lack of space we present herein some numerical results only but in our opinion they demonstrate some general trends occurring in optimization of 2D laminated composite structures. In general, the numerical experiments have been designed to study how genetic information is carried by populations. Two aspects have been analysed in details, i.e. the influence of the selection and mutation operations on the genetic search optimization process and optimization results.

The selection is based on the best choice of individuals (according the assumed criterion) in an old population that can be a future parent and create a new population. Referring to Fig.2 the selection is equivalent to the choice of the subspace in the $A_{11} - D_{11}$ space

such that it contains the global optimum.

Four selection methods have been proposed and tested herein:

1. The classical roulette random operation.
2. For the old population the average fitness value (\bar{f}) is determined and then the individuals having the fitness values greater than eg. $0.5\bar{f}$ are selected to the new population. The rest of the new population is randomly generated among the individuals having $f \geq \bar{f}$.
3. The selection rule is the same as in the procedure 2 but each of the worst individuals ($f \leq \bar{f}$) is replaced by the best individual in the old population.
4. In the old population the worst individuals are mutated in order to obtain the better genetic material.

Variations of the average fitness values with the selection methods are shown in Fig.3. As it may be seen the selection methods 3 and 4 are the best. Let us resemble that they represent the search procedure where in the old population the best individuals only can offer their genetic material for new generations. It is worth noting that similar results have been obtained for different numerical examples studied herein.

As the next example let us consider the influence of the mutation probability on the average of the fitness value - Fig.4. Mutation is a stochastic parameter that protects from a complete loss of genetic material by changing at random a bit in a string. Then, as it is decided whether or not the mutation can be applied to a string, a second random number decides which bit can be mutated. The numerical experiments plotted in Fig.4 prove evidently that mutation has a negligible effect on the results obtained for laminated composites since the effectiveness of genetic algorithms increases as the mutation probability decreases. The identical results have been obtained also by Haftka et al. [7].

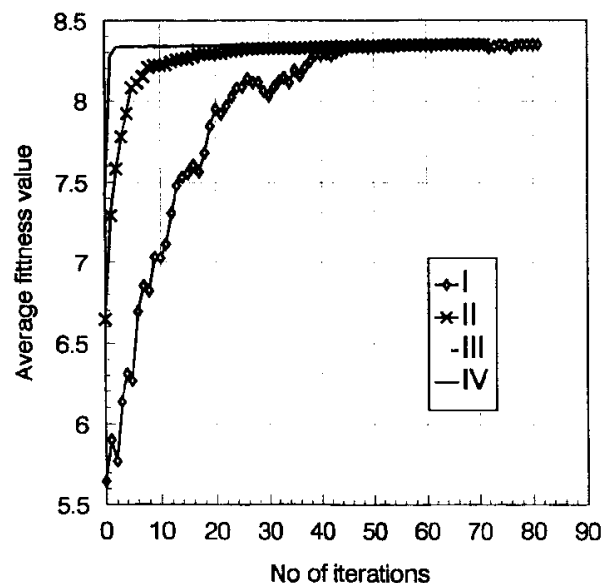


Fig. 3: The influence of selection methods.

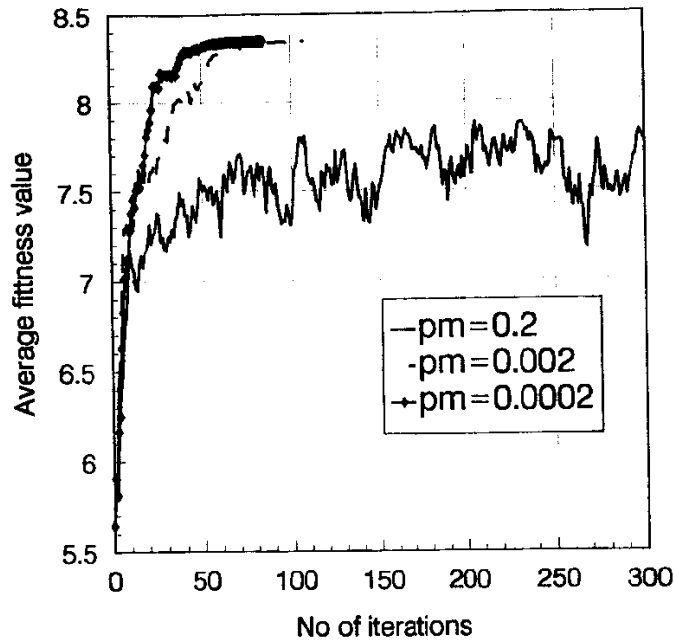


Fig. 4: Effects of mutation probability.

It is obvious that a good selection method may accelerate significantly an optimal search. In our opinion, for laminated composites there is only few representative parameters that decide what configuration is optimal or not and they are connected directly with the form of an objective function. For instance, for compressed composite plates in Ref.[5] it has been proved that angle-ply orientations are optimal as ply orientations are continuous variables. In that case just angle-ply orientations play a role of the representative parameter, ie. they select and cut off a set of allowable solutions. As it may be seen in Figs 3,4 the choice of the best individuals in populations always give convergent solutions since they possess the representative genetic material for the optimal search. Therefore, the search for the best selection method is necessary and it should be supported by theoretical considerations of a particular optimization problem because as numerical results demonstrate in fact genetic algorithms are not completely a random process.

NUMERICAL RESULTS

In 2D approach for laminated composite thinwalled structures transverse shear effects should be taken into considerations as values of: the geometrical (thickness) ratio (eg. t/a) are high, and Kirchhoff's transverse shear moduli G_{13} , G_{23} are low. To analyse the influence of those both opposite ratios we propose to introduce the parameter ζ - Eqn 2. Figure 5 is a plot of optimal buckling loads versus ζ . It exhibits that with the increase of the ζ parameter optimal buckling loads decrease rapidly and it is associated with the variations of the optimal strings. Such a behaviour is independent on the value of the K parameter describing uniaxial ($K=0$) or biaxial ($K>0$) compression. Using such plots it is possible to establish easily the region where the classical Love-Kirchhoff hypothesis may be used or not in computations of both buckling loads as well as in the evaluation of optimal string. Let us note also that comparing the results plotted in Figs 2 and 5 one may observe simply that any change of optimal strings may result in the rapid change

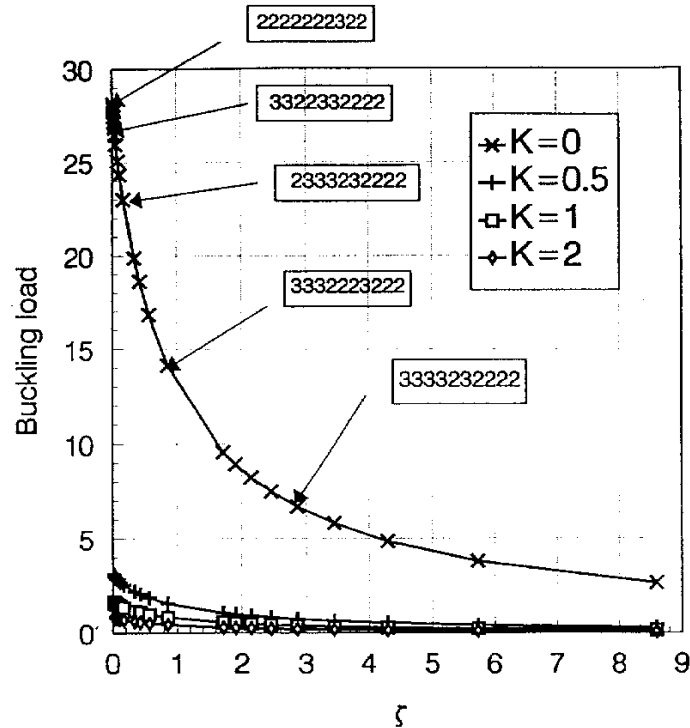


Fig. 5: Variations of buckling loads with the ζ parameter ($b/a=0.25$).

(decrease) of optimal buckling loads.

The similar to the above set of comparative results obtained for L-K and FSDT plate theories is presented also in Table 1.

Table 1: Optimal loads and strings ($K=0.5, b/a=0.25, t/b=0.048, N=48$ plies).

Failure	Mode	Load		Optimal string	
		L-K	FSDT	L-K	FSDT
Buckling	Unimodal	9999.37(3)	9603.86(3)	333322323232	233222332223
	Bimodal	9999.15(2)	9603.34(2)	332322332223	222232233322
Buckling+FPF ϵ_{max}	Unimodal	9998.2(3)	9603.86(2)	222222323223	233222332223
	Bimodal	9994.84(2)	9603.86(3)	22322233232	233222332223
Buckling+FPF Tsai-Wu	Unimodal	9310.01	9310.01	111212222233	111212222233
	Bimodal	9310.01	9310.01	111212222233	111212222233

Although for FSDT optimal buckling loads do not change drastically comparing with the optimal designs for L-KT, however even few percents may play an important role taking into account the total weight saving factor of the whole structure. It should be pointed out that both for L-KT and FSDT the optimal configurations cannot be derived analytically.

Table 1 shows also the differences in failure pressures and optimal strings for buckling and buckling with FPF constraints. As it may be seen the use of FPF criterion may decrease failure loads comparing with the pure buckling analysis only and change completely the optimal string. Although for ϵ_{max} criterion the discrepancies are negligible they may become drastic as we use more accurate quadratic Tsai-Wu relations. Of course, there is no difference in FPF loads and optimal strings between L-K and FSDT since for plates membrane and bending states are uncoupled, and FPF loads are determined with the use

of the membrane relations - Eqns 3,4. It should be emphasized that FPF is a dominating failure mode as the t/a thickness ratio becomes higher.

The pairs of rows in Table 1 demonstrate also the numerical results as the equality bimodal condition (5) has been taken into considerations or not. Of course, in the unimodal approach it is possible to obtain almost the same results, however, in that case it is necessary to analyse the whole spectrum of the wavenumbers m, n , in order to satisfy correctly the objective function in the form given by Eqn 6. To demonstrate that in fact buckling loads should satisfy the bimodal condition (5) let us analyse the results presented in Table 2. It gives the comparison of buckling loads for two neighbourhood wavenumbers using the objective function in the form (8). For the optimal strings buckling loads are almost identical so that the effectiveness of genetic algorithm in the proposed formulations is very good. In fact for the classical L-K theory the presented in Table 1 results are also with the very good agreement with those obtained by Haftka et al [7].

The results presented herein were obtained for a graphite/epoxy plate having the following material properties:

$$\begin{aligned} E_1 &= 127.59GPa, E_2 = 13.03GPa, G_{12} = 6.41GPa, G_{13} = G_{23} = 0.5G_{12}, \\ \nu_{12} &= 0.3, \epsilon_1^{max} = 0.008, \epsilon_2^{max} = 0.029, \epsilon_{12}^{max} = 0.015. \end{aligned} \quad (9)$$

It is worth to mention also that both material assumptions and the assumed form of fibre orientations eliminate automatically the term Q_{45} in the stiffness matrix so that enables us to decouple sine and cosine terms in buckling analysis.

Table 2: Bimodal solutions.

Failure	Load		Optimal string	
	L-K	FSDT	L-K	FSDT
Buckling	9999.15(2)	9603.34(2)	332322332223	222232233322
Buckling	9999.95(3)	9604.46(2)	332322332223	222232233322
Buckling + FPF (ϵ_{max})	9994.84(2)	9605.31(2)	223222233232	233222332223
Buckling + FPF (ϵ_{max})	100051.82(3)	9603.86(3)	223222233232	233222332223

CONCLUDING REMARKS

The optimal design of laminated composite plates is presented. The design goal is to maximize buckling load of the plate. The constraints are imposed on: lamina failure and bimodal solutions. Genetic algorithm is presented and applied to the optimal design. The objective function is formulated for two particular plate theories, i.e. the first-order transverse shear deformation theory and the classical Love-Kirchhoff theory using geometrically linear approach. The examples are solved to demonstrate the importance of the selection procedures in genetic algorithms and to highlight the significance of transverse shear effects in optimization problems.

The choice of the selection method seems to be one of the most important factor in genetic optimization procedures. It is shown that the selection procedures may significantly reduce the total number of iterations required in the optimal search. In our opinion the search for the best (effective) selection procedures is necessary. However, now not only

numerical implementation of different variants of genetic algorithms is required but also a deeper, theoretical explanation of the assumed choice.

The present study shows the effectiveness of genetic methods for optimal design of plates using both the first-order shear deformation theory and the classical Love-Kirchhoff theory. It is worth to emphasize that for laminated thinwalled structures the resulting optimal laminate topologies and failure loads are very sensitive to the applied type of 2D plate approximations. The proposed parameter ζ may be used as the representative measure of transverse shear effects. It has been proved that the use of classical shell theories may lead to completely wrong results both in the estimation of buckling loads and in the determination of optimal laminate configurations (strings) for orthotropic materials. For more accurate description of the optimization problems under buckling and FPF constraints it is necessary to apply more refined shell theories based on the local (laminatewise) rather 3D models as eg. delamination problems will be taken into account.

A variety of numerical results may be treated as a guideline in the evaluation of optimal topologies for laminated composite plates.

Numerical results demonstrate evidently that the fulfillment of the bimodal condition may be conducted in two equivalent ways: imposing directly the bimodal constraint on the objective functional (using the penalty method) or to search for the minimal optimal load over the prescribed spectrum of wavenumbers in buckling.

As it is shown various first-ply-failure criteria may be analysed in the similar manner. However, each of them may result in various optimal topologies and even in the change of the dominant failure mode, ie. buckling or FPF.

ACKNOWLEDGEMENTS

The support from the KBN grant PB-232/T07/95/08 is gratefully acknowledged.

REFERENCES

1. S. Adali, *Buckling and postbuckling of composite plates* (eds G.J.Turvey, I. H. Marshall), Chapman and Hall 1995, pp.329-366.
2. A.K. Noor, W.S. Burton, *Appl. Mech. Rev.*, **42**,1989,pp.1-13.
3. A. Muc, in *Proc. WCSMO-1* (eds N.Olchhof, G.I.N.Rozvany), Pergamon 1995, pp.275-281.
4. A. Muc, in *Proc. ICCE/3* (edt D.Hui),1996,pp.924-5.
5. A. Muc, *Composite Structures*,**9**,1988,pp.161-72.
6. R.T. Haftka, Z. Gurdal, *Elements of Structural Optimization*, Kluwer Academic Publishers 1993.
7. R.T. Haftka, R. Le Richie, in *AIAA J*, **31**, 1993, pp.951-6.
8. R.T. Haftka, J.L. Walsh , *AIAA J*, **30**, 1992, pp.814-19.

THERMOELASTIC ANALYSIS OF FOAM-CORED SANDWICH CONSTRUCTION TEE-JOINTS

J. M. Dulieu-Smith¹, P. J. C. L. Read² and R. A. Shenoi²

¹ *Department of Mechanical Engineering, University of Liverpool,
Brownlow Street, Liverpool, L69 3GH, U.K.*

² *Department of Ship Science, University of Southampton,
Highfield, Southampton, SO17 1BJ, U.K.*

SUMMARY: The nature of load transfer through the thickness of a foam-cored sandwich construction tee-joint is analysed using the thermoelastic technique. A method for thermoelastic calibration of the quasi-isotropic foam-cored material is described. The thermoelastic results are compared to those obtained from a finite element model of the tee-joint; the differences in the results are discussed in detail.

KEYWORDS: thermoelastic stress analysis, SPATE, foam-cored sandwich structures, tee-joints, finite element analysis

INTRODUCTION

The thermoelastic stress analysis technique is a now well established experimental method and has been used in a wide range of engineering applications. The technique is based on the measurement of the small temperature change induced in a material subjected to elastic cyclic stresses. In a linear elastic, isotropic, homogeneous material the temperature change is directly proportional to the sum of the principal stresses in the material [1]. The small temperature change is measured by the use of highly sensitive infra-red detectors.

The current industry standard equipment for thermoelastic stress analysis is the SPATE (Stress Pattern Analysis by Thermal Emissions) system [2]. The equipment incorporates a single cell cadmium-mercury-telluride infra-red detector. The detector unit houses two mirror drive systems which allow the detector to operate in a point-to-point scanning mode over a predefined area of a test specimen or component. Over a period of around 1 hour a full-field representation of the stresses is developed on a computer monitor. The test specimen requires only minimal surface preparation, in that a thin coating of matt black paint is applied to the surface which provides a constant emissivity and as a bonus enhances the thermoelastic response of the material.

The design and analysis of composite tee-joints is currently an area of major importance and is of particular relevance in the ship building industry. The thrust of the work has concentrated on single skin constructions [3], the interest being in the failure mode of the joint and the load transfer mechanism from the joint web to the flange. Detailed static and fatigue loading test programmes have been carried out (e.g. [4,5]). These provided the magnitude and position of the failure in joint; the data obtained from the work has been used as a basis for characterising the structures. Recently [6] a thermoelastic analysis of a single-skin tee-joint has demonstrated the potential of the technique for evaluating such structures. The work focused on the load transfer from the web to flange through the thickness of the material. The SPATE results provided

detailed full-field stress information and highlighted variations in the tee-joint structure caused by the manufacturing process.

The present paper deals with the analysis of foam-cored sandwich construction tee-joints. Thermoelastic stress analysis is particularly attractive in the analysis of foam-cored structures as the technique is non-contact and requires no supplementary attachments, such as a strain gauge, which could locally reinforce the material. SPATE scans are taken from the end of a tee-joint, subjected to combined bending and tension loading, so that the through-thickness stresses can be analysed. The results of the thermoelastic analysis are calibrated so that they can be compared with data derived from a finite element analysis of such structures. The potential of the technique in the analysis of foam-cored structures is clearly demonstrated.

TEE-JOINT CONSTRUCTION

A diagram of the tee-joint used in the thermoelastic work is shown in Fig. 1. The joint is 100 mm in width and consists of a 100 mm thick flange and a 50 mm thick web. The flange and web are 800 mm and 280 mm respectively in length. Different foam materials are used for the flange and the web; Divinycell H130 for the flange and Divinycell H80 for the web. Both the flange and the web are bounded by a 6 mm thick 1200 gm^{-2} quadriaxial (i.e. $0, 90^\circ, \pm 45^\circ$) woven roving E-glass/epoxy skin. The flange and the web are joined directly using an epoxy adhesive. A 7 mm fillet is formed at the junction of the flange and the web using colloidal silica filled epoxy. A 6 mm thick boundary angle skin consisting of 900 gm^{-2} glass/epoxy $\pm 45^\circ$ woven rovings is bonded around the fillet. A summary of the relevant material properties of the tee-joint constituents is provided in Table 1 [7].

Table 1: Properties of the tee-joint constituents

Constituent	Tensile Modulus (MPa)	Compressive Modulus (MPa)	Shear Modulus (MPa)	Compressive Strength (MPa)	Tensile Strength (MPa)
Web Core	80	85	31	1.2	2.2
Flange Core	140	175	52	2.5	4.2
Laminate	17000	-	5000	240	360
Fillet Resin	3300	-	3500	-	85

THERMOELASTIC THEORY

For a linear elastic, isotropic, homogeneous material it is readily shown [1] that the small temperature change, ΔT , induced in a material under elastic cyclic loading conditions is related to the stresses in the material as follows:

$$\Delta T = K T (s_1 + s_2) \quad (1)$$

where K is the thermoelastic constant (i.e. $\alpha/\rho C$, where α is the coefficient of linear thermal expansion, ρ is the density and C is the specific heat of the material), T is the absolute

temperature of the material and $(\sigma_1 + \sigma_2)$ are the changes in the principal stresses. When an infra-red detector is used the output from the detector, i.e. the thermoelastic signal, S , is related to the stresses by the following:

$$s_1 + s_2 = AS \quad (2)$$

where A is a calibration constant that is a combination of K , the detector properties and the surface emissivity of the material. In equation (2) $(\sigma_1 + \sigma_2)$ are the principal stress changes on the surface of a material or test specimen. The assumption is made that the temperature change occurs adiabatically. This is ensured by cyclically loading the specimen at such a rate that no conduction can take place. Equations (1) and (2) imply that the mean stress in the specimen is of no consequence so that the temperature change is only dependent on the range of the stress. It has been shown [8] that the mean stress is important if the elastic constants of the are highly temperature dependent. For most materials, at room temperature, the temperature dependence of Young's modulus and Poisson's ratio is small and these have a negligible effect on the thermoelastic signal.

For orthotropic materials equation (2) must be modified to incorporate the different coefficients of expansion of the material [6] i.e.

$$s_p + \alpha s_t = A'S \quad (3)$$

where α is the ratio α_t/α_p , A' is a further calibration constant and the subscripts p and t denote values in the principal material directions.

In the case of the single-skin tee-joints the orthotropic boundary angle material has been analysed [6] and equation (3) must be used. Methods for determining the calibration constant A' and α are described in detail in ref. [6]. In the design of foam-cored sandwich structures it is expected that only a shear load will be carried by the core. However, initial static tests on the tee-joint [7] have shown that for certain loading cases the joints fail in compression. This is seen as an important consideration as the compressive strength of the foam is around 50% of that tensile strength (see Table 1). Therefore any significant compressive stresses developed in the core could result in early fatigue failure of the joint. Shear stresses are detected as zero stress by the SPATE system because of the nature of equation (2). Any deviations from the shear loading design condition will therefore appear prominently in the SPATE data from the foam core. In this paper only the foam core is dealt with (a full analysis of the tee-joint will be presented elsewhere); as the material is quasi-isotropic equation (2) is used as the basis for the thermoelastic work described in the following sections.

Thermoelastic Calibration Of Foam-Core Material

It is possible to derive A (see equation (2)) using material property values from the literature and the characteristics of the detector. This approach produces unreliable results mainly due to variations in the material. An experimental approach is far more reliable and also takes account of any variations in paint emissivity and detector output. A description and a critical appraisal of thermoelastic calibration techniques is given in ref. [9]. A possible approach would be to bond strain gauges to the foam material and measure the strain at that point and compare this to the thermoelastic signal. However this is impractical as the gauges will cause local reinforcement. A better approach is to devise a means of direct calibration (i.e. where the material is loaded in

such a way that the stress distribution is known). To facilitate this a block of material, 180 mm in length and of 26.5 mm x 11.5 mm cross section was machined from the flange and a block 130 mm in length and 28 x 11.5 mm cross section was machined from the web of a tee-joint. (As the flange and web incorporate different foams, a separate calibration constant is required for both.) The most straightforward means of direct calibration is to load the material in tension. In this case there is only one principal stress in the specimen (i.e. the applied stress, σ_{app}) which can be calculated by simply dividing the applied load, P, by the cross sectional area of the specimen. This value can be substituted into equation (1) so that the calibration constant, A, can be determined from the thermoelastic signal from the specimen i.e.

$$A = \frac{S_{app}}{S} \quad (4)$$

A diagram of the flange test specimen and the loading jig used in the calibration studies is shown in Fig. 2. As the foam is very weak, 1 mm thick aluminium alloy stiffeners were bonded to each end of the specimens. The load is transferred from the end grips to the foam test specimen via the two pins. These were used to ensure an even loading across the specimen and to reduce any stress concentration effects. (The web calibration specimen was identical except the length between the pins was 116 mm instead of 168 mm.) Anti-bending shackles were attached to each end of the specimens prior to the assembly being mounted in an Instron 8501 servo-hydraulic test machine. Because of the flexible nature of the specimens the load control mode of the test machine could not be used. It was therefore necessary to apply a constant longitudinal strain to the specimens of ranges 2.38×10^{-3} for the flange and 3.44×10^{-3} for the web. These were multiplied by the tensile modulus values given in Table 1 to give stress ranges of 0.45 MPa for the flange material and 0.28 MPa for the web material. Throughout the tests the straining frequency was maintained at 8 Hz.

The foam test specimens were coated with 2 passes of R.S. matt black paint before conducting the thermoelastic work. The SPATE detector was set at a working distance of 600 mm giving a scanning spot size of 0.8 mm. (This is larger than the deflection range of the specimens which was 0.4 mm and therefore negates the requirement for any motion compensation.) The average thermoelastic signal recorded for the specimens was 633 U (Uncalibrated signal unit) for the flange material and 958 U for the web material. During both tests the variations in the signal were large giving standard deviations of around $\pm 15\%$. There is a high level of "noise" in the data which can be attributed to the cellular nature of the material. Substituting the σ_{app} values and the signal values into equation (4) provides A values of 7.07×10^{-4} MPa U⁻¹ for the flange material and 2.89×10^{-4} MPa U⁻¹ for the web material. Using the detector properties and material property values from the literature A was derived as 6.12×10^{-4} MPa U⁻¹ and 3.77×10^{-4} MPa U⁻¹ the flange and web respectively. This shows a very encouraging agreement considering the variability in the material and the other error sources [9] associated with calculating A in this manner.

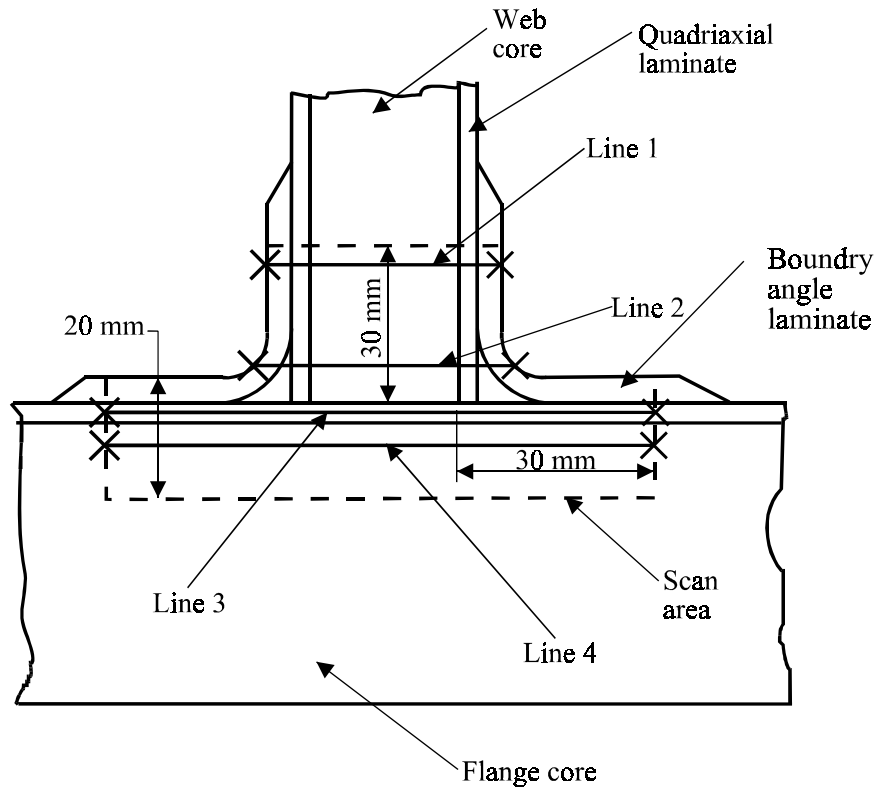


Fig. 1 Tee-joint configuration and dimensions of SPATE scan area

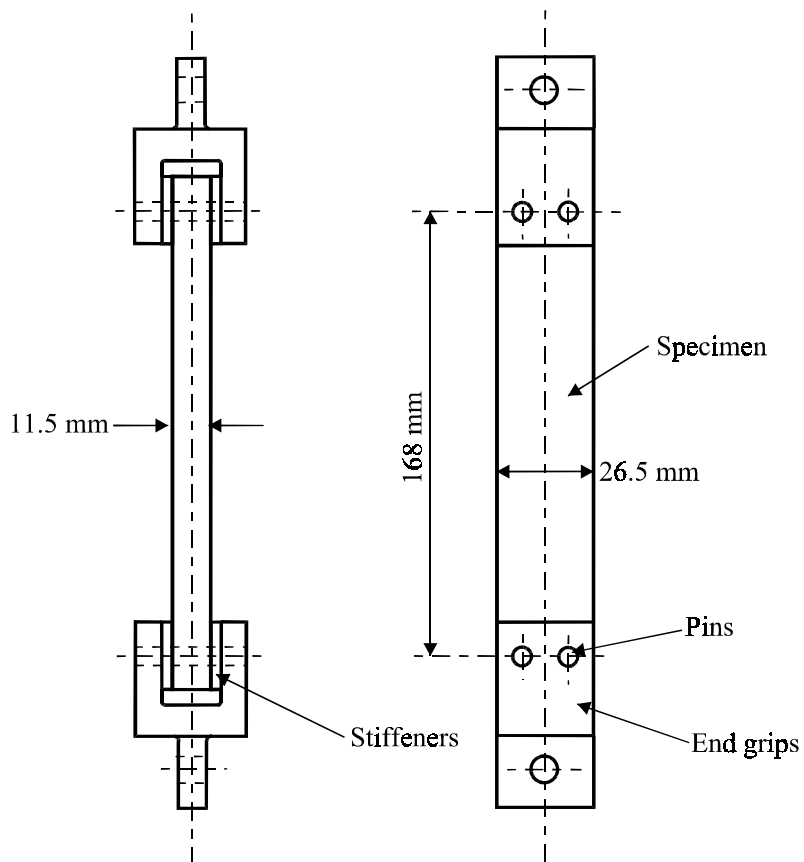


Fig. 2 Flange material calibration specimen and loading jig

Thermoelastic Analysis Of Tee-Joint

Consideration of the in-service loads experienced by the tee-joints suggested that combined bending and tension loading would most adequately model the in-service conditions. To this end a test set-up was configured in a specially designed test-rig known as FORTReSS [10] which is located at the University of Southampton. A steel beam was fixed at an angle of 45° in the FORTReSS structure. The flanges of the tee-joint were clamped symmetrically about the centre of the joint; the spacing of the clamps being 240 mm centre to centre. A hydraulic ram was positioned horizontally on the FORTReSS structure and connected to the upper end of the web. This configuration produces a combination of tensile and bending loading, i.e. a 45° pull-off load. The tee-joint was subjected to a load cycle of 0.7 ± 0.405 kN at a frequency of 8 Hz and coated with 2 passes of R.S. matt black paint prior to testing. The SPATE detector was set at a working distance of 350 mm which gave a scanning spot size of 0.6 mm. SPATE area scans were taken from both sides of the specimen, the dimensions of the scan area are shown in Fig. 1; the scans took approximately 2.5 hours to complete.

Four line plots were taken through both sets of data. The approximate positions of these are indicated in Fig. 1. Two plots (lines 1 and 2) were taken across the web; one away from the fillet the other through the root of the fillet radius. One plot (line 3) was taken along the skin on the flange. Another plot (line 4) was taken along the flange core material. Lines 1 and 2 were calibrated using the A value of 2.89×10^{-4} MPa U^{-1} and line 4 was calibrated using the A value of 7.07×10^{-4} MPa U^{-1} . The line plots from both the front and the back of the tee-joint specimen are shown in Figs. 3 and 4 respectively. (The a, b and d figures show calibrated data. The c figures are uncalibrated data for the skin material and are shown for completeness.) Fig. 3a, b and Fig. 4a, b are plots from the flange and in all cases $\sigma_1 + \sigma_2$ never exceeds 0.2 MPa; the departures at the edges are readings from the skin. This indicates, as predicted, that virtually all of the load is carried in shear. The plots through the flange skin (Figs. 3c and 4c) show positive and negative peaks at the junction with the web. The two spikes in Fig. 3c are accounted for by voids in the material at the fillet. Most interesting are the plots along the flange core shown in Figs. 3d and 4d. Here much larger stresses of the order of 0.5 MPa in compression and 1 MPa in tension are developed in positions in line with the junction of the flange and the web (i.e. 20 mm and 80 mm into the plot respectively). The plots cross zero at around 50 mm close to the centre of the joint.

Finite Element Analysis Of Tee-Joint

The finite element analysis (FEA) package used in the current work was ANSYS 5.1. The tee-joint was modelled as a two dimensional slice in plane strain with non-linear geometric properties (i.e. large deflection analysis). The element type used throughout the model was Plane82; a 2-D solid element with orthotropic material properties capability. The model was constructed of one element through the thickness of the web and flange skins, one element through the thickness of the web core and four elements through the flange core. The boundary angles consisted of one element per overlaminated layer producing four elements through the thickness at the root of the joint radius. The model was restrained to represent the clamping arrangement used during experimentation and a force vector was applied near to the top of the web to simulate the 45° pull-off. The material properties used for the foam-core and the laminated skin are given in Table 1.

To produce comparable data to that of the SPATE scan line plots shown in Figs. 3 and 4, stress results of the FEA were extracted along two lines cut through the model at the same positions as SPATE lines 2 and 4 (see Fig. 1 for line positions). Principal stress values σ_1 and σ_2 were

calculated along each line from the nodal results and then added together to produce the data required. Fig. 5 shows the FEA results for the sum of the principal stresses along lines 2 and 4. Fig. 5a shows that the stress sum through the entire core is zero indicating that the load is carried in shear. Fig. 5b shows a negative peak of -0.29 MPa 30 mm into the plot and a positive peak of 0.38 MPa 80 mm into the plot. The plot crosses zero at around 50 mm close to at the centre of the tee-joint.

DISCUSSION

The SPATE plots through the web core shown in Figs. 3a, b and 4a, b show that $(\sigma_1 + \sigma_2)$ is close to zero confirming the shear carrying capability of the core and that only a small amount of bending is being carried by the core. The signal from the skin shown in Figs. 3a, b and 4a, b is high, especially in the side of the joint loaded in tension, indicating, as expected, that the skin is carrying the bending stresses. However, it should be noted that in all the SPATE line plots only the core has been calibrated and that the values shown for the skins can only be seen as a qualitative indication of the stress levels in the skin. (A further more detailed analysis of the joint is planned which will cover both the skin and the core.) Figs. 3d and 4d show that in the flange core there are significant bending stresses and these should be taken into account in any failure analysis of the entire joint. The maximum value shown in compression is around 1 MPa which is 40% of the failure load of the material and may have detrimental effects on the fatigue life of such joints. A further factor is that the load range used in the SPATE tests of 0.81 kN is low; it is expected that the joints will experience higher in-service loads which in the case of the flange core could initiate damage.

A quantitative comparison of the SPATE data from the front and rear sides of the joint shows that there is some difference in the plots, most noticeably in the line 4 (Figs. 3d and 4d). This could be attributed to some out-of-plane loading and slight alignment errors in the SPATE equipment. A more likely cause relates to the variations in the core material and other defects occurring in the manufacturing process. Fig. 3c shows a plot along the skin material and through the fillets. At the fillets (30 mm and 85 mm) there are large spikes in the data. These were caused by the absence of filler material between the boundary angle and the skin. The voids could prevent adequate load transfer into the boundary angle and result in the flange core carrying more of the load and would account for the higher stress values in Fig.4a. Further confirmation of this is the virtually identical plots obtained from both the front and back of the web which would not be affected by the voids.

There is a very good qualitative agreement between the FEA results and the SPATE data. Only the data from the core can be quantitatively compared as the FEA from the skins is just $\sigma_1 + \sigma_2$ and the SPATE data is proportional to $\sigma_p + \alpha\sigma_t$ (see equation 3). The FEA shows that in the web core there is virtually no bending. However, the SPATE data (lines 1 and 2) show that there is a slight bending load carried by the core. Comparing the data for line 4 shows a difference between the FEA and SPATE results. The FEA gives values of around 60% less than those from the SPATE. Apart from the manufacturing defects which are not modelled by FEA other factors may be contributing to this difference. Firstly, the applied load range of 1.4 kN is very low and within the noise limits of FORTReSS. This means that the actual applied load may be in error of the order of 10% to 15% and would result in differences between the experimental and predicted results. Furthermore, initial load-deflection tests [10] have shown that the FEA model under-predicts deflections (i.e. that the joints are more flexible) resulting in smaller stress values. This needs to be confirmed and further work is underway to calibrate the causes of the difference. The important feature however is that the trends predicted by the FEA are very similar to the SPATE results.

CLOSURE

The work described in the present paper to the authors' knowledge is the first thermoelastic work on foam-cored sandwich structures. The results are very encouraging and provide a full field representation of the stresses, which highlights any manufacturing defects. The work has clearly demonstrated the potential of thermoelastic analysis in the experimental evaluation of such structures. Of particular importance is the fact that the flange core material is experiencing significant bending stresses which could result in premature failure. Further work is underway to model the full range of behaviour under a variety of loading and bending conditions.

REFERENCES

1. Stanley, P. and Chan, W.K., "Quantitative stress analysis by means of the thermoelastic effects", *J. Strain Analysis*, Vol.20, 1985, pp 129-137.
2. Harwood, N. and Cummings, W.M. (eds.), *Thermoelastic Stress Analysis*, IOP Publishing Ltd., Bristol, 1991.
3. Sheno, R.A. and Hawkins, G.L., "Influence of material and geometry considerations in the behaviour of bonded tee connections in FRP ships", *Composites*, Vol. 23 1992, pp 335-345.
4. Dodkins, A.R., Sheno, R.A. and Hawkins, G.L., "Design of joints and attachments in FRP ships' structures", *Marine Structures*, Vol. 7, 1994, pp 365-398.
5. Sheno, R.A., Read, P.J.C.L. and Hawkins, G.L., "Fatigue failure mechanisms in fibre reinforced plastic laminated tee-joints", *Int. J. of Fatigue*, Vol. 17 1995, pp 415-426.
6. Dulieu-Smith, J.M., Sheno, R.A., Read, P.J.C.L., Quinn, S. and Moy, S.S.J. "Thermoelastic stress analysis of a GRP tee-joint", *J. App. Composite Matls.*, in press.
7. Hicks, I.A., Read, P.J.C.L. and Sheno, R.A., "Tensile, compressive and flexural characteristics of tee-joints in foams-cored sandwich structures", *Proc. of 3rd Int. Conf.on of Sandwich Construction, Southampton*, 1995, pp 579-590.
8. Wong, A.K., Jones, R. and Sparrow, J.G., "Thermoelastic constant or thermoelastic parameter?", *J. Phys. Chem. Solids*, Vol. 43, 1987, pp 749-753.
9. Dulieu-Smith, J.M., "Alternative calibration techniques for quantitative thermoelastic stress analysis", *Strain*, Vol. 31 1995, pp 9-16.
10. Sheno, R.A., Read, P.J.C.L., Walters, C.L. and Thelu, S.C.M., "The development of a flexible multiple-configuration structural test facility", *Int. J. of Fatigue*, Vol. 15, 1993, pp 317-323.

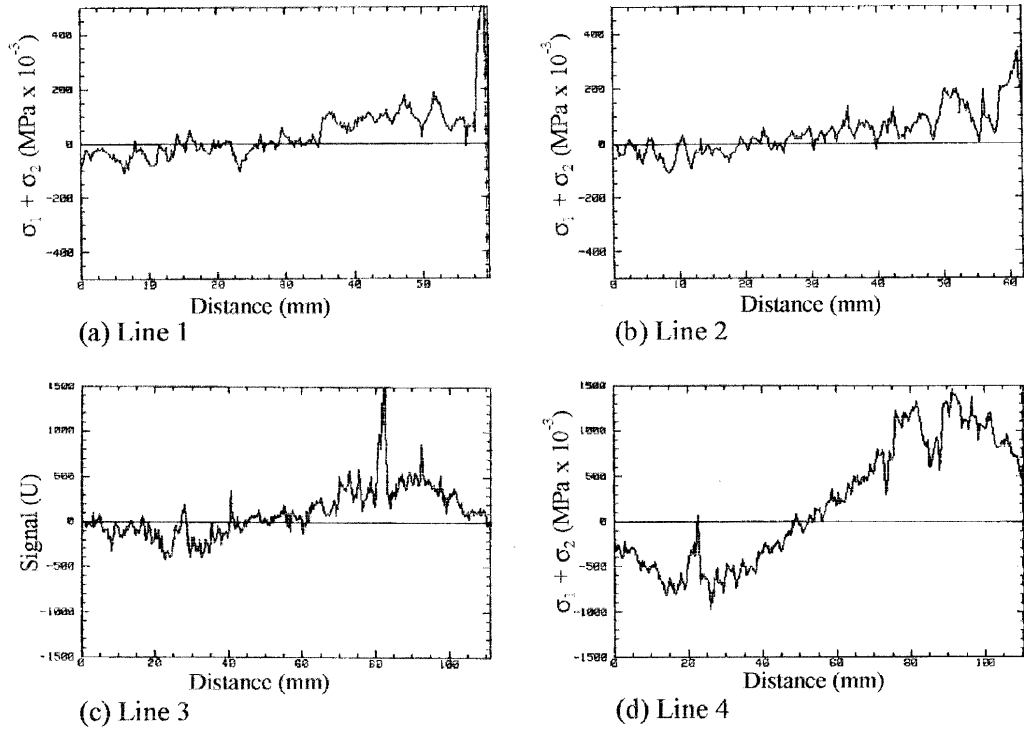


Fig. 3 Line scans on front side of tee-joint

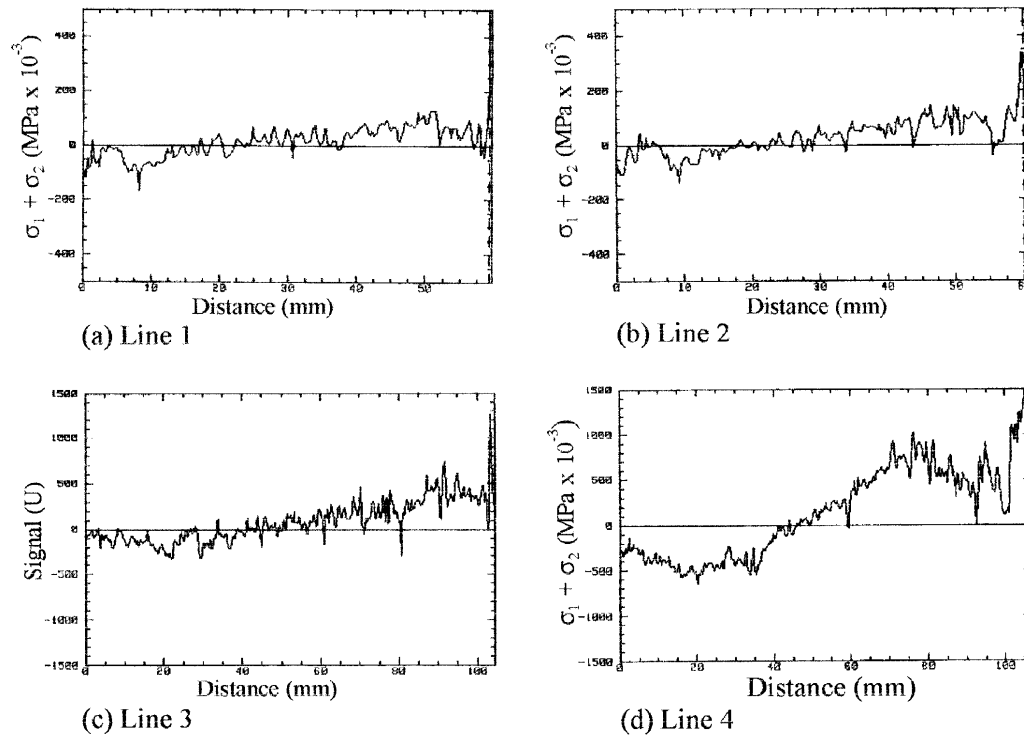
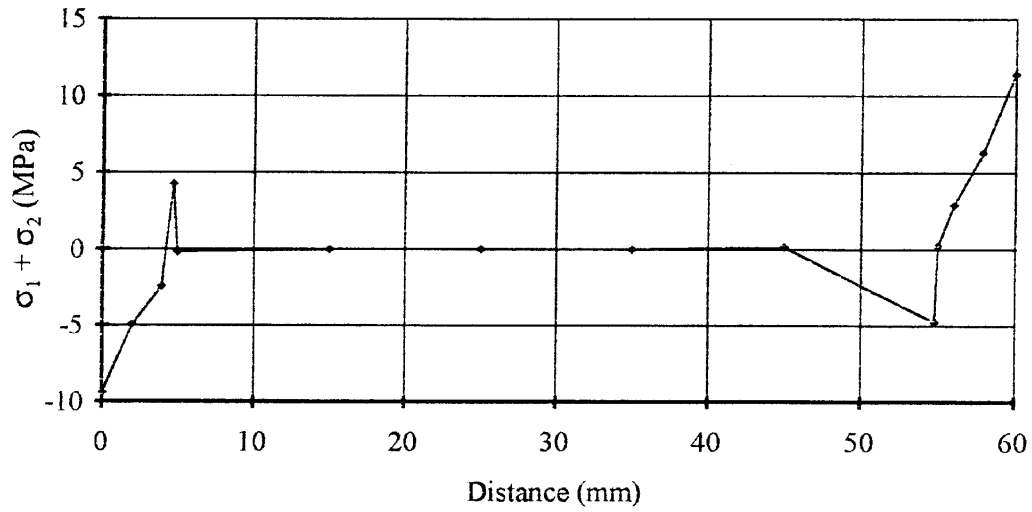
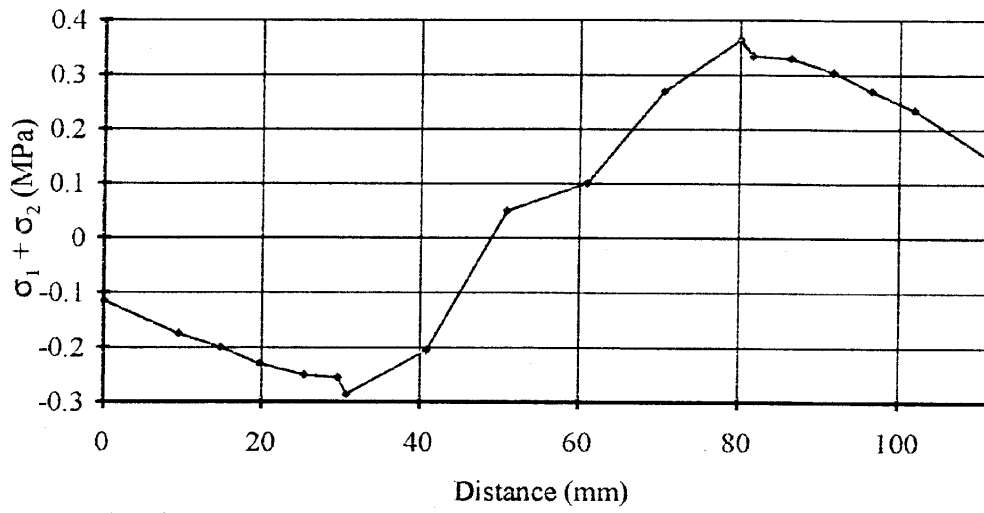


Fig. 4 Line scans on rear side of tee-joint



(a) Line 2



(b) Line 4

Fig. 5 Line plots derived from FEA results

STRESS ANALYSIS OF UPRIGHT COMPOSITE FLANGES

James M Whitney

*Department of Civil & Environmental Engineering and Engineering Mechanics,
University of Dayton, 300 College Park, Dayton, Ohio, 45469-0243, USA*

SUMMARY: A stress analysis, with emphasis on interlaminar stresses, is performed in conjunction with the curved section of an upright composite flange. The analysis is based on a higher order shell theory which utilizes shear deformation and transverse (through-the-thickness) normal strain. Closed form solutions are obtained for specially orthotropic laminates. Interlaminar stresses are determined by integrating the equilibrium equations of classical theory of elasticity in conjunction with inplane stresses obtained from the higher order shell theory. Because of the relatively large radius-to-thickness ratio of many in service flanges, it is necessary to investigate the validity of the higher order shell theory by comparing numerical results with exact solutions from classical theory of elasticity. Comparison between the two theories for both inplane stresses and interlaminar stresses shows excellent agreement. Thus, the higher order shell theory provides an excellent tool for performing stress analysis of upright flanges.

KEYWORDS: composite flanges, interlaminar stresses, ply stresses, theory of elasticity, laminated shell theory

INTRODUCTION

Numerous composite components utilize upright bolted flanges for attachment. The weight and strength of the flange attachment is critical to the success of the composite application. Much of the current state-of-the-art in the design of composite material upright bolted flanges is based on thick, tapered geometry. This design causes difficulty in manufacturing which often leads to voids in the curved area of the flange. Such voids promote delamination at a relatively low load. Thus, designs are sought which lead to thin flanges of constant thickness. In general, flatwise tension failures in the curved region is the predominate failure mode encountered in composite flanges. In order to execute a more efficient design it is necessary to develop a fundamental understanding of the stresses developed in the curved region of the flange. Special emphasis must obviously be placed on interlaminar stresses.

The work by Adsit and Goulding [1] is typical of current stress analysis modeling in conjunction with upright flanges. Their analysis consisted of two steps. In the first step the flange is modeled using effective orthotropic properties in conjunction with the NASTRAN finite element code. Bending moments from the finite element analysis are used in conjunction with an isotropic curved beam model to calculate the tangential stresses and radial stresses. In addition to not considering orthotropic properties, such an approach does not recognize the discontinuity in elastic stiffnesses which exist from ply-to-ply. Such discontinuities can have a significant effect on interlaminar stresses.

Lekhnitskii [2] obtained an exact elasticity solution for homogeneous, orthotropic curved beams

with end loadings of the same form as utilized in upright flanges. Using a stress function in conjunction with force and moment boundary conditions, the solution for homogeneous beams does not require obtaining displacements associated with the state-of-stress in the flange. Martin [3] applied Lekhnitskii's solution to the analysis of data obtained in conjunction with interlaminar tensile failure of unidirectional curved beams. The closed form elasticity solution was supplemented by a finite element analysis. This work was later extended to laminated curved beams by Martin and Jackson [4]. However, the laminate closed form elasticity solution is based on an analysis presented by Ko and Jackson [5] in which the displacements are incorrectly presented. For laminated systems the displacements must be obtained in order to enforce displacement continuity between plies.

In the present paper a higher order shell theory which includes transverse shear deformation and linear transverse normal strain is utilized to obtain the stresses in the curved region of an upright flange. Because engineering applications of upright flanges often involve thick sections, i.e. small radius-to-thickness ratios, it is necessary to compare shell theory results with solutions obtained from classical theory of elasticity. The laminated curved beam elasticity solution is obtained by using a stress function at the ply level in conjunction with plane stress assumptions in the same manner as Ko and Jackson [5]. Corrected displacement functions are presented. Continuity of displacement and interlaminar stresses are obtained at all ply interfaces.

DESCRIPTION OF ANALYTICAL MODEL

A segmented free-body diagram of a typical upright flange with constant cross-section is shown in Fig. 1. Forces and moments applied to the curved section are illustrated. The analytical model for the curved section is shown in Fig. 2. Although only half of the semi-circle is applicable to the flange, it is convenient in the analysis to use the entire region $0 \leq \theta \leq \pi$.

SHELL THEORY ANALYSIS

The laminated shell analysis is based on a higher order shell theory which includes transverse (through-the-thickness) shear deformation and linear transverse normal strain, i.e. the theory is based on the following displacement field [6, 7]:

$$u(\theta) = u^0(\theta) + z\psi_x(\theta), \quad v(\theta) = v^0(\theta) + z\psi_\theta(\theta), \quad w(\theta) = w^0(\theta) + z\psi_z(\theta) + \frac{z^2}{2} \phi(\theta) \quad (1)$$

where u , v , and w denote displacements in the axial, tangential, and transverse directions (see Fig. 2), respectively. It should be noted that the shell theory uses a z coordinate in place of the r coordinate of classical theory of elasticity. In particular, for the shell theory

$$z = r - R \quad (2)$$

where R is the radius of the midplane of the laminated composite. Denoting partial differentiation by a comma, interlaminar stresses can be determined in this model by integrating the equilibrium equations from classical theory of elasticity with the result

$$\begin{aligned} \tau_{\theta z} &= -\frac{1}{R(1+z/R)^2} \int_{-h/2}^z (1+z/R)\sigma_{\theta,\theta} dz + \frac{(1-h/2R)^2}{(1+z/R)^2} \tau_{\theta z}(-h/2) \\ \sigma_z &= -\frac{1}{R(1+z/R)} \int_{-h/2}^z (\sigma_\theta - \tau_{\theta z,\theta}) dz + (1-h/2R)\sigma_z(-h/2) \end{aligned} \quad (3)$$

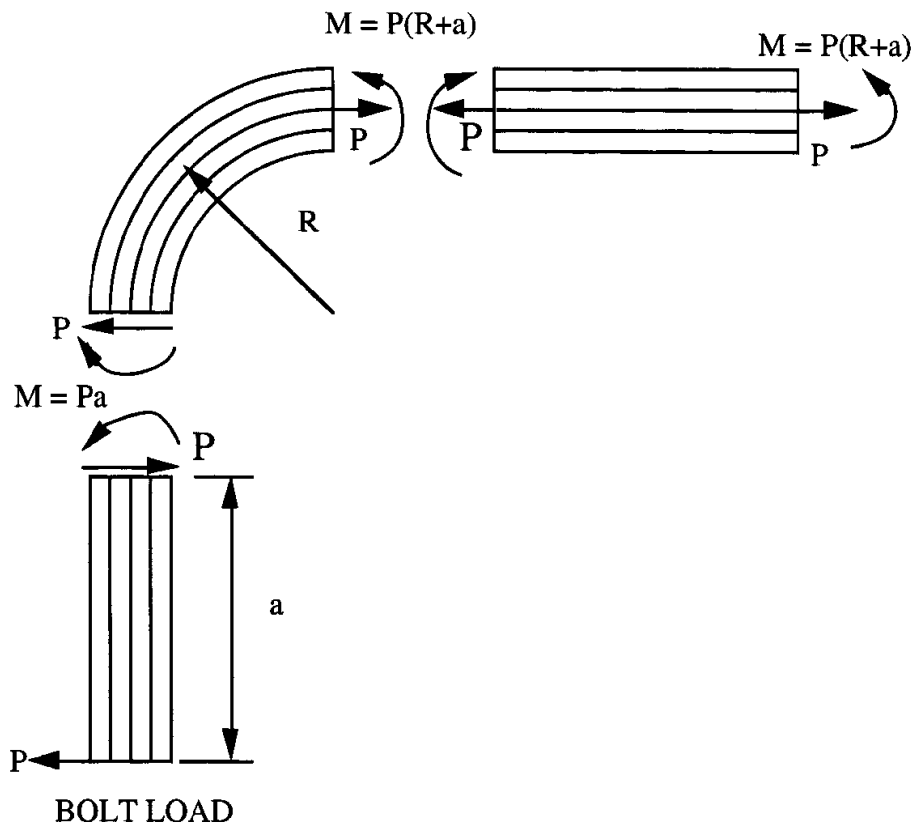


Fig. 1: Schematic of flange showing isolation of curved section

The shell theory is written in terms of the following force and moment resultants:

$$\begin{aligned}
 (N_x, N_z, N_{x\theta}, Q_x) &= \int_{-h/2}^{h/2} (\sigma_x, \sigma_z, \tau_{x\theta}, \tau_{xz})(1 + z/R) dz \\
 (N_\theta, N_{\theta x}, Q_\theta) &= \int_{-h/2}^{h/2} (\sigma_\theta, \tau_{\theta x}, \tau_{\theta z}) dz \\
 (M_x, M_z, M_{x\theta}, R_x) &= \int_{-h/2}^{h/2} (\sigma_x, \sigma_z, \tau_{x\theta}, \tau_{xz})(1 + z/R) z dz \\
 (M_\theta, M_{\theta x}, R_\theta) &= \int_{-h/2}^{h/2} (\sigma_\theta, \tau_{\theta x}, \tau_{\theta z}) z dz
 \end{aligned} \tag{4}$$

In addition, the theory includes higher order moments defined as follows

$$S_x = \frac{1}{2} \int_{-h/2}^{h/2} \tau_{xz}(1 + z/R) z^2 dz, \quad (P_\theta, S_\theta) = \frac{1}{2} \int_{-h/2}^{h/2} (\sigma_\theta, \tau_{\theta z}) z^2 dz \tag{5}$$

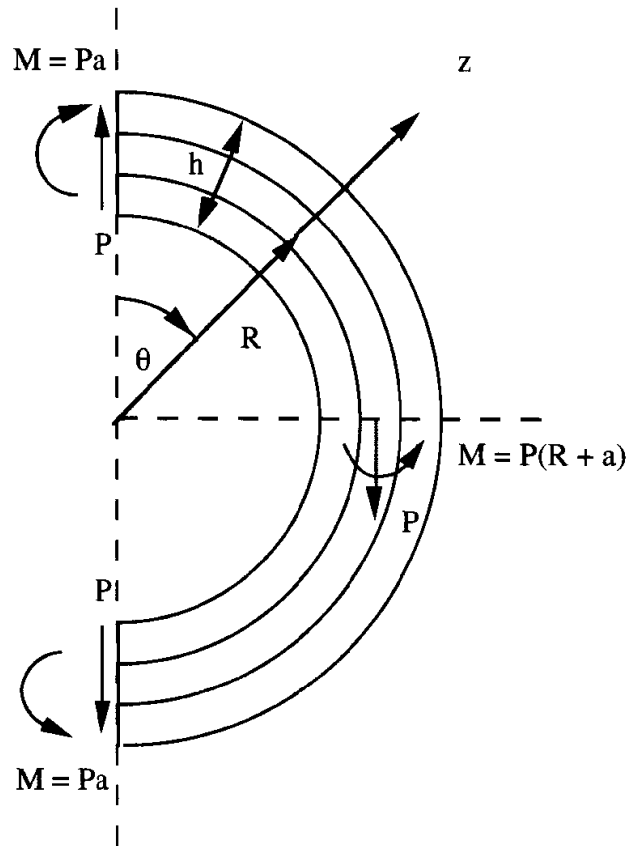


Fig. 2: Analytical model of curved section

Constitutive relations are obtained between the force and moment resultants and displacements through elastic stiffnesses in the form

$$(A_{ij}, B_{ij}, D_{ij}, F_{ij}, H_{ij}) = \int_{-h/2}^{h/2} C_{ij}(1, z, z^2, z^3, z^4) dz \quad (6)$$

where C_{ij} denote elastic compliances. Detailed constitutive relations are too lengthy to be presented here, but can be found in Ref. [6].

Equilibrium in terms of force and moment resultants are given by the relations

$$N_{\theta,\theta} + Q_\theta = 0, \quad Q_{\theta,\theta} - N_\theta = 0, \quad \frac{M_{\theta,\theta}}{R} - Q_\theta = 0 \quad (7)$$

$$\frac{R_{\theta,\theta}}{R} - \frac{M_\theta}{R} - N_z = 0, \quad \frac{S_{\theta,\theta}}{R} - \frac{P_\theta}{R} - M_z = 0$$

These relationships reflect the fact that all forces and moments are independent of the x coordinate (i.e. θ dependence only)

.For the shear loading, we assume

$$Q_\theta = -P \cos \theta, N_\theta = P \sin \theta, M_\theta = -PR \sin \theta \quad (8)$$

These forces and moment satisfy the first three equilibrium relations in eqs. (7), and the fourth relationship becomes

$$\frac{R_{\theta,\theta}}{R} - N_z = P \sin \theta \quad (9)$$

Combining the constitutive relations with eqs. (8) and (9) and the fifth relationship in eq. (7) leads to five differential equations in the displacement variables. A solution for the displacements is assumed to be of the form

$$\begin{aligned} u^0 = 0, v^0 = A \cos \theta - C\theta \sin \theta, w^0 = C(\sin \theta + \theta \cos \theta) \\ \psi_x = 0, \psi_\theta = B, \psi_z = D, \phi = E \end{aligned} \quad (10)$$

where A, B, ..., E are undetermined coefficients. Substituting eqs. (8) into the equilibrium equations leads to five algebraic equations in the five unknown coefficients.

For the pure moment loading we assume

$$M_\theta = -Pa \quad (11)$$

The displacements are assumed to be of the form

$$u^0 = \psi_x = 0, \psi_\theta = \frac{v^0}{R} = A\theta, w^0 = B, \psi_z = C, \phi = D \quad (12)$$

where as previously A, B, C, and D are undetermined coefficients. The form of the assumed displacements leads to vanishing of the transverse shear stress, i.e.

$$Q_\theta = R_\theta = S_\theta = 0 \quad (13)$$

Taking eqs. (11) and (13) into account, the equilibrium equations reduce to

$$N_\theta = 0, N_z = -P \frac{a}{R}, \frac{P_\theta}{R} - M_z = 0 \quad (14)$$

Combining eqs (12) with the constitutive relations and substituting the results into the equilibrium relations, eqs. (11) and (14), leads to four algebraic equations in the unknown coefficients A, B, C, and D. A total solution for the shell problem is obtained by combining solutions for the shear loading and the pure moment loading. The hoop stress for the kth layer can be determined from the ply constitutive relation

$$\sigma_\theta^{(k)} = C_{22}^{(k)} \epsilon_\theta + C_{23}^{(k)} \epsilon_z \quad (15)$$

where ϵ_θ and ϵ_z can be expressed in terms of the displacements, eqs. (1). The interlaminar shear stress is determined by integrating the equilibrium equation as given in eqs. (3). The interlaminar normal stress is obtained by integrating the second of the expressions in eqs. (3). It should be noted that the ply constitutive relations in conjunction with the strain-displacement relations determined from the assumed displacement field, rather than the relationship obtained

by integrating the first of eqs. (3) is utilized in conjunction with $\tau_{\theta z}$ in this calculation, i.e.

$$\tau_{\theta z}^{(k)} = G_{\theta z}^{(k)} \gamma_{\theta z} \quad (16)$$

where the interlaminar shear strain is a function of the displacements in eqs. (1) and $G_{\theta z}^{(k)}$ is the interlaminar shear modulus of the k th ply. Because the strain is continuous through-the-thickness and the shear modulus varies from ply-to-ply, eq. (16) produces a discontinuous shear stress at ply interfaces. The integration process in eq. (3), however, assures continuity of the interlaminar normal stress, σ_z , at ply interfaces.

ELASTICITY SOLUTION

A theory of elasticity solution can be obtained for the case of either plane stress or plane strain in conjunction with a laminated plate of constant curvature subjected to the loading illustrated in Fig. 2. However, the layers must be orthotropic with respect to the curved plate coordinate system. For a homogeneous curved plate a stress function solution in polar coordinates is obtained [2] such that

$$\sigma_r = \frac{1}{r} \Phi_{,r} + \frac{1}{r^2} \Phi_{,\theta\theta}, \quad \sigma_\theta = -\Phi_{,rr}, \quad \tau_{r\theta} = -\left(\frac{\Phi}{r}\right)_{,r\theta} \quad (17)$$

where the a comma denotes partial differentiation and Φ is the stress function. The plane stress compatibility equation for orthotropic materials is of the form [2]

$$\begin{aligned} S_{22} \Phi_{,rrrr} + \frac{2S_{22}}{r} \Phi_{,rrr} - \frac{S_{11}}{r^2} \Phi_{,rr} + \frac{S_{11}}{r^3} \Phi_{,r} + \frac{(S_{66} - 2S_{12})}{r^2} (\Phi_{,rr\theta\theta} - \frac{\Phi_{,r\theta\theta}}{r}) \\ + [2(S_{11} - S_{12}) + S_{66}] \frac{\Phi_{,\theta\theta}}{r^4} + \frac{S_{11}}{r^4} \Phi_{,\theta\theta\theta\theta} = 0 \end{aligned} \quad (18)$$

where S_{ij} are orthotropic compliances relative to the r - θ coordinates. A similar type equation is applicable for plane strain.

For the loading shown in Fig. 2, two solutions are superposed. The first solution involves the shear load, P and is of the form [5]

$$\begin{aligned} \sigma_r &= \left(\frac{A}{r} + \beta B r^{\beta-1} - \beta D r^{-(\beta+1)}\right) \sin \theta \\ \sigma_\theta &= \left[\frac{A}{r} + \beta(1+\beta) B r^{\beta-1} - \beta(1-\beta) D r^{-(\beta+1)}\right] \sin \theta \\ \tau_{r\theta} &= -\left(\frac{A}{r} + \beta B r^{\beta-1} - \beta D r^{-(\beta+1)}\right) \cos \theta \end{aligned} \quad (19)$$

where

$$\beta = \sqrt{\frac{(S_{11} + S_{22} + S_{66} - 2S_{12})}{S_{22}}}$$

Equation (19) is applicable to both orthotropic and isotropic materials.

For the case of the applied moment, $M = -Pa$, the stresses are of the form [3]

$$\begin{aligned}\sigma_r &= 2A + (1 + K)Br^{(K-1)} + (1 - K)Cr^{-(K+1)} \\ \sigma_\theta &= 2A + K(1 + K)Br^{(K-1)} + K(1 - K)Cr^{-(K+1)}, \quad \tau_{r\theta} = 0\end{aligned}\tag{20}$$

where

$$K = \sqrt{\frac{S_{11}}{S_{22}}}$$

For the case where $S_{22} = S_{11}$, the solution takes the form

$$\sigma_r = 2A + \frac{B}{r^2} + (1 + 2 \ln r)C, \quad \sigma_\theta = 2A - \frac{B}{r^2} + (3 + 2 \ln r)C, \quad \tau_{r\theta} = 0\tag{21}$$

For homogeneous materials displacements are not required, as the boundary conditions are in terms of stresses. In particular, for the shear load σ_r and $\tau_{r\theta}$ must vanish at the inner and outer boundaries, while at $\theta = 0$

$$\int_{r_1}^{r_2} \tau_{r\theta} dr = -P\tag{22}$$

where r_1 and r_2 denote the radius of curvature of the inner and outer boundaries, respectively. For the moment loading σ_r and $\tau_{r\theta}$ must also vanish at r_1 and r_2 . In addition,

$$\int_{r_1}^{r_2} (r - r_0) \sigma_\theta(r) dr = -Pa\tag{23}$$

where r_0 denotes the location of the neutral axis for this pure bending case. We note that for pure bending

$$\int_{r_1}^{r_2} \sigma_\theta(r) dr = 0\tag{24}$$

Thus, the pure moment condition reduces to

$$\int_{r_1}^{r_2} \sigma_\theta(r) r dr = -Pa\tag{25}$$

In the case of laminated curved plates the displacements are required in order to satisfy continuity conditions between adjacent plies. For shear loading, the displacements are of the form

$$\begin{aligned}u_r &= [(k_1 + k_2 \ln r)A + k_3 Br^\beta + k_4 Cr^{-\beta} + D] \sin \theta + k_1 A \theta \cos \theta \\ u_\theta &= [(k_5 + k_2 \ln r)A + k_6 Br^\beta + k_7 Cr^{-\beta} + D] \cos \theta - k_1 A \theta \sin \theta\end{aligned}\tag{26}$$

where u_r and u_θ are radial and tangential displacements, respectively, k_i are functions of elastic properties, and A, B, and C are undetermined constants. It should be noted that the displacements presented in Ref. [5] are incorrect. In particular, the terms $k_1(\sin \theta + \theta \cos \theta)$ and $-k_1 \sin \theta$ were omitted from u_r and u_θ , respectively. For the moment loading, the displacements are of the form

$$u_r = 2k_8 A - k_9 2B + (2k_8 \ln r - k_9)Cr, \quad u_\theta = 4k_{10}Cr\theta\tag{27}$$

where k_i are again functions of material properties and A, B, and C are undetermined constants.

For laminates continuity of σ_r , $\tau_{r\theta}$, u_r , and u_θ must be obtained at all interface boundaries. In this case the stress and displacements equations are written for each individual ply. Boundary conditions along with ply continuity conditions are sufficient to obtain all of the undetermined coefficients. Details of the solution for a laminate are not presented here. It should be noted, however, that the r dependence for both σ_r and $\tau_{r\theta}$ are identical in the shear force problem. Thus, it is only necessary to enforce ply continuity and vanishing of the top and bottom tractions in conjunction with one of these two stress components. For the pure bending moment case, vanishing of $\tau_{r\theta}$ reduces the number of conditions needed to be enforced.

NUMERICAL RESULTS

In order to compare the elasticity analysis and the shell theory, stress distributions are obtained in conjunction with a $[0^\circ/90^\circ]_S$ laminate with the following ply properties

$$\frac{E_L}{E_T} = 14, \quad \frac{G_{LT}}{E_T} = .533, \quad \nu_{LT} = 0.3, \quad \nu_{T3} = 0.5 \quad (28)$$

where E_L and E_T denote moduli parallel and transverse to the fiber direction, respectively, and G_{LT} denotes the shear modulus relative to the fiber direction. The Poisson's ratios ν_{LT} is determined by measuring the transverse strain while uniaxial tension is being applied parallel to the fibers. In a similar manner ν_{T3} is determined by measuring through-the-thickness strain while applying uniaxial tension transverse to the fibers. The properties in eq. (28) are typical of contemporary graphite/epoxy unidirectional composites. It should be noted that this material is assumed to be transversely isotropic, i.e. the transverse shear modulus (relative to the T-3 plane) is determined from the relationship

$$G_{T3} = \frac{E_T}{2(1 + \nu_{T3})} \quad (29)$$

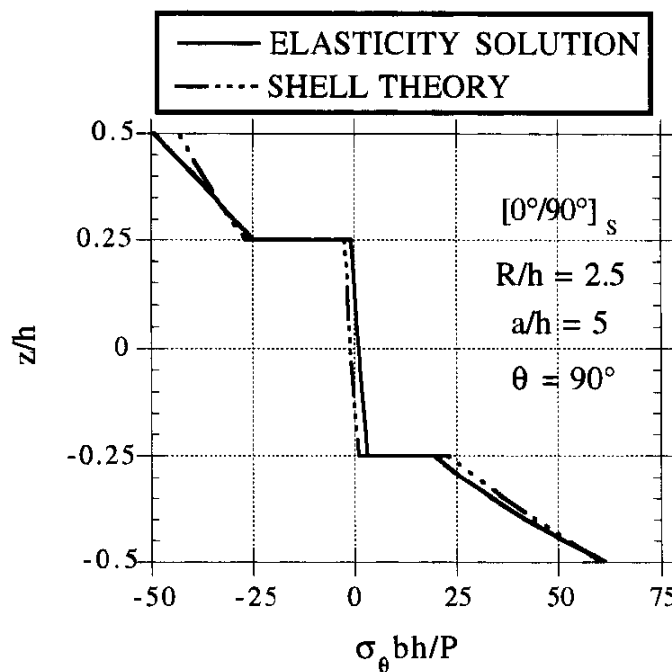


Fig.3: Through-the-thickness distribution of hoop stress

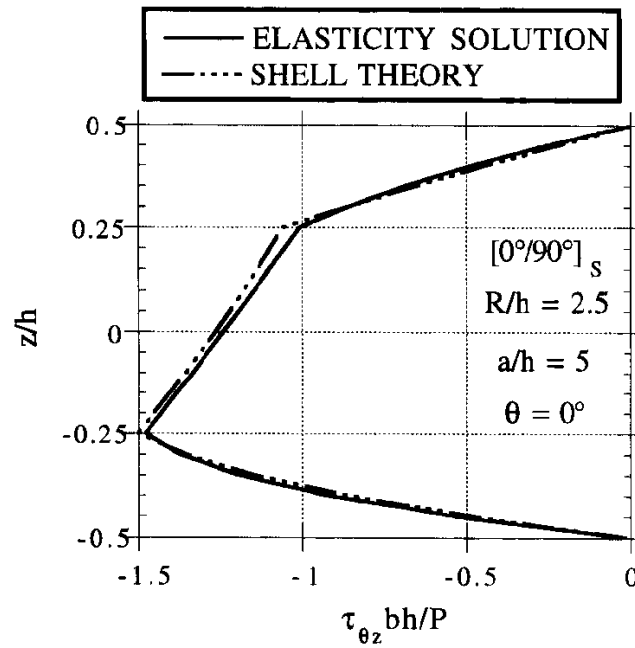


Fig. 4: Through-the-thickness distribution of interlaminar shear stress

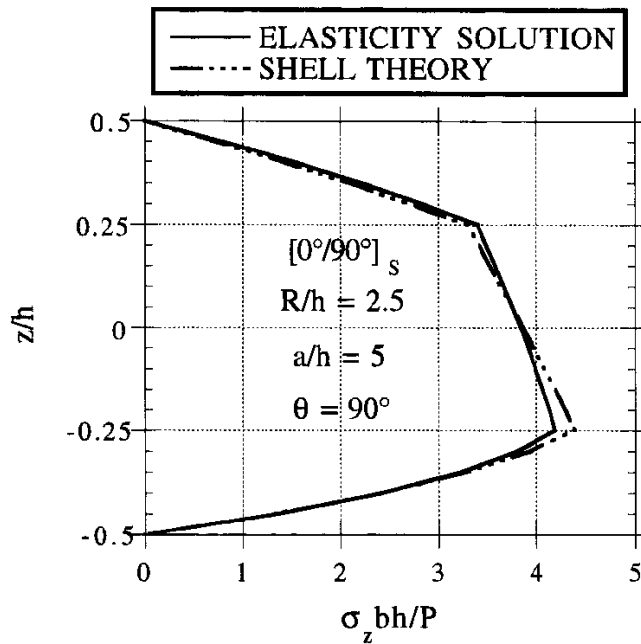


Fig. 5: Through-the-thickness distribution of interlaminar normal stress

Numerical results are shown in Figs. 3-5. The R/h and a/h ratios shown here are typical of current flanges being produced for engine applications. All stresses are normalized by the average shear stress applied at the boundary. Plate width is denoted by b .

The hoop stress distribution through-the-thickness is shown in Fig. 3 at $\theta = 90^\circ$, which is the location where this stress component is maximum. We note that good agreement is obtained between the shell theory and classical theory of elasticity even though a low ratio of R/h is being utilized.

Through-the-thickness distributions of the interlaminar stresses are shown in Figs. 4 and 5, at the location of maximum stress, where excellent agreement is obtained between the shell theory and classical theory of elasticity. It is also important to note that the transverse normal stress is tension across the entire laminate thickness. In addition the magnitude of the maximum interlaminar normal stress is very large, making this laminate configuration very vulnerable to delamination.

CONCLUSIONS

Excellent agreement is obtained between the higher order laminated shell theory and the closed form elasticity solutions as shown in Figs. 3-5. Such agreement for low values of radius-to-thickness ratios indicates that the shell theory is a very valuable tool in performing stress analysis in conjunction with the curved section of upright flanges. In addition, the large magnitude of the interlaminar stresses indicates the potential for flange delamination.

ACKNOWLEDGMENT

The author wishes to acknowledge the Ohio Aerospace Institute, Cleveland, Ohio for supporting this project under a core research grant.

REFERENCES

1. Adsit, N. R. and Goulding, J. R. "A New Design for Composite Flanges", *Proceedings of the 20th International SAMPE Technical Conference*, SAMPE, Covina, CA, 1988, pp. 289-301.
2. S. G. Lekhnitskii, *Anisotropic Plates*, Translated from the Second Russian Edition by S. W. Tsai and T. Cheron, Gordon and Breach, New York, 1968, pp. 95-101.
3. Martin, R. H., "Delamination Failure in Unidirectional Curved Composite Laminate," *Composite Materials: Testing and Design Tenth Volume, ASTM STP 1120*, Grimes, G. C., Ed., American Society for Testing and Materials, Philadelphia, 1992, pp. 365-383.
4. Martin, R. H., and Jackson, W. C., "Damage Prediction in Cross-Plied Curved Composite Laminates," *Composite Materials: Fatigue and Fracture, Fourth Volume, ASTM STP 1156*, Stinchcomb, W. W., and Ashbaugh, N. E., Eds., American Society for Testing and Materials, Philadelphia, 1993, pp. 105-126.
5. Ko, W. L., and Jackson, R. H., "Multilayer Theory for Delamination Analysis of a Composite Curved Bar Subjected to End Moments", *Composite Structures 5*, Marshall, I. H., Ed., Elsevier Applied Sciences, London, pp. 173-198.
6. Whitney, J. M. and Sun, C. T. "A Refined Theory for Laminated Anisotropic, Cylindrical Shells", *Journal of Applied Mechanics*, Vol. 41, No. 2, June 1974, pp. 471-476.
7. Sun, C. T., and Whitney, J. M., "Axisymmetric Vibrations of Laminated Composite Cylindrical Shells", *Journal of the Acoustical Society of America*, Vol. 56, No. 6, June 1974, pp. 1238-1246.

STUDY OF THE SPRING-IN PHENOMENON

Lalit K. Jain¹, Brian G. Lutton², Yiu-Wing Mai³ and Rowan Paton⁴

¹ Cooperative Research Centre for Advanced Composite Structures (CRC-ACS) Ltd.,
361 Milperra Road, Bankstown, New South Wales, 2200, Australia.

² Hawker De Havilland, 361 Milperra Road, Bankstown, New South Wales, 2200, Australia.

³ Centre for Advanced Materials Technology, Department of Mechanical and Mechatronic
Engineering, University of Sydney, Sydney, New South Wales, 2006, Australia.

⁴ Cooperative Research Center for Advanced Composite Structures (CRC-ACS) Ltd.,
506 Lorimer Street, Fishermens Bend, Victoria, 3207, Australia.

SUMMARY: Residual stresses always build up during the manufacture of composite components. In the case of channel or angle components, these stresses lead to a reduction in the enclosed angle. This phenomenon of the reduction in the enclosed angle is referred to as spring-in. To study this behaviour, sample composite angle components were fabricated from pre-preg tape and fabric, as well as from dry carbon fabric and resin using resin transfer moulding (RTM) technique. The effects of various factors such as ply stacking sequence, part thickness, tool angle, tool radius and tool material were investigated. In addition, comparison with the theoretical model developed by Jain and Mai [1] is provided and a good agreement is found.

KEYWORDS: residual stresses, spring-in, composite laminates, angle components, pre-preg material, resin transfer moulding, manufacturing

INTRODUCTION

Residual stresses are the internal stresses that develop during composite part processing. These stresses build up due to the shrinkage of the polymeric matrix around the reinforcement. The two main components that contribute to these stresses are: (1) the volumetric shrinkage of the resin during curing and (2) the mismatch in the coefficients of thermal expansion of the matrix and the reinforcement.

The most common residual stress effect observed in manufacturing composites is deformation of angled and curved parts after cure. In the case of isotropic materials, the configuration of a curved section is preserved and the contraction upon cooling is uniform. The change in shape of composite components upon cooling is therefore attributed to the anisotropic nature of the composites. For the case of a composite component the out-of-plane contraction is always larger than the in-plane contraction. This results in the two curved sides to approach each other and hence leads to a reduction in the enclosed angle. This change in the enclosed angle is referred to as spring-in [2-5]. This phenomenon mainly occurs because of the difference between the in-plane and out-of-plane strains in the plies due to the change in temperature and moisture content and resin shrinkage. Figure 1(a) shows the typical angle section. Figures 1(b) and 1(c) show change in volume in an isotropic material and residual stress induced distortion (in addition to the volume change) in an anisotropic material, respectively; the parameters ϵ_r and ϵ_θ are strains in the radial and tangential directions, and Φ_1 and Φ_2 are the enclosed angles.

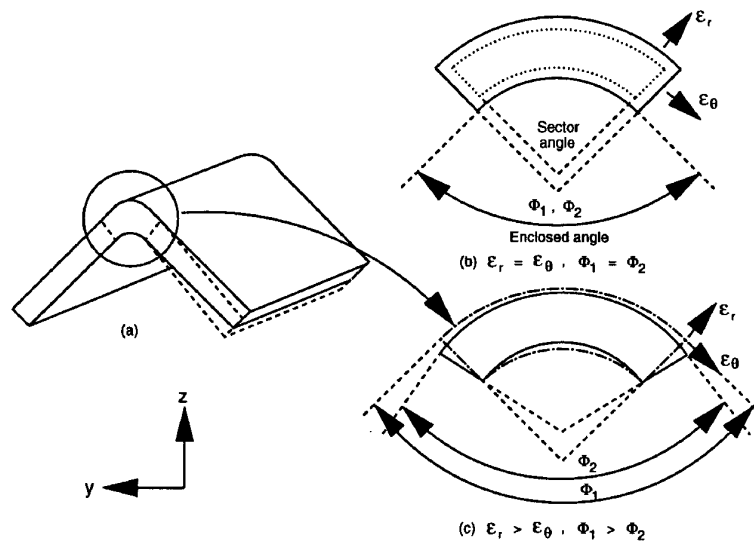


Fig. 1: (a) Typical angle section (b) Change in the volume of a cylindrical segment of isotropic material. (c) Change in the shape of a cylindrical segment of anisotropic material.

Spring-in causes considerable difficulty and expense for composite manufacturers. Currently, tool angles are modified to compensate for part spring-in. The amount of modification is based on either “rules-of-thumb” from past experience or on trial-and-error. For angular parts, the compensation is normally between 1 and 2.5⁰. The most common problem found with using a standard factor is that the spring-in may vary with lay-up, material, cure temperature, etc. Therefore, what worked once does not necessarily work next time. In such instances, retooling may be required until an acceptable part is manufactured. If spring-in from residual stresses could consistently and easily be predicted, tooling could then be compensated for specific part characteristics without having to make a series of test specimens.

Therefore, the purpose of this paper was to validate the spring-in model developed by Jain and Mai [1] by fabricating some sample angle components. This spring-in model would enable the tool designer to predict the spring-in for a given part and thus assist with the tool design.

SPRING-IN MODEL

The model developed by Jain and Mai [1] analyses the cylindrical or the curved part of the component. The model includes the effect of resin shrinkage and also takes into account various factors that can affect the degree of spring-in such as tool radius, ply stacking sequence, part thickness, symmetric/non-symmetric lay-up, curing temperature, thermal expansion coefficients of the fibre and the matrix, enclosed angle and volume fraction.

The degree of spring-in and the residual stresses can be determined by solving the following constitutive equations [1]:

$$\begin{Bmatrix} N_x \\ N_y \\ N_{yx} \\ M_x \\ M_y \\ M_{yx} \\ M_{xy} \end{Bmatrix} = \begin{bmatrix} \\ \\ \\ K \\ \\ \\ \end{bmatrix} \begin{Bmatrix} \varepsilon_x^0 \\ \varepsilon_y^0 \\ \omega_1 \\ \omega_2 \\ \kappa_x \\ \kappa_y \\ \tau_2 \end{Bmatrix} - \begin{Bmatrix} N_x^T + N_x^c \\ N_y^T + N_y^c \\ N_{yx}^T + N_{yx}^c \\ M_x^T + M_x^c \\ M_y^T + M_y^c \\ M_{yx}^T + M_{yx}^c \\ M_{xy}^T + M_{xy}^c \end{Bmatrix} + \begin{Bmatrix} \frac{T_{120}}{R} \\ \frac{1}{R} \left(T_{220} - \frac{T_{221}}{R} + \frac{T_{222}}{R^2} - \frac{T_{223}}{R^3} \right) \\ \frac{1}{R} \left(T_{260} - \frac{T_{261}}{R} + \frac{T_{262}}{R^2} - \frac{T_{263}}{R^3} \right) \\ \frac{T_{121}}{R} \\ \frac{1}{R} \left(T_{221} - \frac{T_{222}}{R} + \frac{T_{223}}{R^2} - \frac{T_{224}}{R^3} \right) \\ \frac{1}{R} \left(T_{261} - \frac{T_{262}}{R} + \frac{T_{263}}{R^2} - \frac{T_{264}}{R^3} \right) \\ \frac{T_{261}}{R} \end{Bmatrix} \quad (1)$$

where R is the mid-plane radius of the curved section, N_x , N_y , M_x , M_y , etc. are the force and moment resultants defined as:

$$[N_x, M_x] = \int_{-h/2}^{h/2} \sigma_x \left(1 + \frac{z}{R} \right) [1, z] dz, \quad [N_y, M_y] = \int_{-h/2}^{h/2} \sigma_y [1, z] dz, \quad (2a)$$

$$[N_{xy}, M_{xy}] = \int_{-h/2}^{h/2} \sigma_{xy} \left(1 + \frac{z}{R} \right) [1, z] dz, \\
 [N_{yx}, M_{yx}] = \int_{-h/2}^{h/2} \sigma_{yx} [1, z] dz, \quad (2b)$$

and

$$T_{ijm} = \int_{-h/2}^{h/2} \bar{Q}_{ij} f(z) z^m dz. \quad (3)$$

The z coordinate is measured in the through-thickness direction with origin in the mid-plane and h is the total thickness of the laminate. The parameters N_x^T , N_x^c , M_x^T , M_x^c , etc. are the force and moment resultants from thermal and resin shrinkage strains. \bar{Q}_{ij} are the reduced material stiffnesses in the global coordinate system and $f(z)$ is the through-thickness expansion or the thickening term with contributions from thermal expansion, in-plane residual stresses and shrinkage strains. The K matrix may be regarded as the stiffness matrix. The various terms of the K matrix are given in Ref. [1]. σ_{ij} are the stress components and ε_x^0 , ε_y^0 , ω_1 and ω_2 relate to the mid-plane strains and κ_x , κ_y , τ_1 and τ_2 relate to the curvatures. The other details of the model and the assumptions involved may be found in Ref. [1].

With the use of appropriate boundary conditions and constraints, equation (1) has to be solved iteratively for mid-plane strains and curvatures since the thickening term $f(z)$ cannot be

determined unless the strains components are known. Once all the strain components are known, the degree of spring-in, $\Delta\Phi$, is simply given by

$$\Delta\Phi = \kappa_y R(180^\circ - \Phi) \quad (4)$$

where Φ is the enclosed angle.

EXPERIMENTAL INVESTIGATION

The test specimens were manufactured from unidirectional pre-preg tape and from dry fabric and resin transfer moulding (RTM) technology. The results for carbon/epoxy plain-weave pre-preg fabric were taken directly from an earlier spring-in study conducted by Lutton [6].

Fabrication of Pre-preg Samples Using Unidirectional Tape

These samples were fabricated from Fiberite T300/934 carbon/epoxy pre-preg tape and were cured at 177 °C. Both the male and the female components of the RTM tool (discussed in detail later) were used to produce these components. This allowed us to examine the effect of type of tooling on the spring-in. The following lay-ups were considered for this study: [0/0]_s, [30/-30]_s, [45/-45]_s, [60/-60]_s, [90/90]_s, [90/0/90/0]_s, and [0/90/0/90]_s. The first five lay-ups allowed us to study the effect of the orientation angle of the angle ply laminates. The last two allowed us to examine the effect of the lay-up sequence. In addition, three different tool radii were considered for the female tooling, 4, 7, and 8 mm, and two different radii for the male tooling, 3 and 6 mm. This allowed us to examine the effect of tool radius on the spring-in.

The nominal thickness of each ply was approx. 0.2 mm. The fibre volume fraction was approximately 65 percent and typical properties of a unidirectional laminate as estimated from micromechanics relations are given in Table 1. In predicting the cure shrinkage strains, the linear resin shrinkage during cure was assumed to be 1.5 percent. The parameters E, G and ν represent the Young's modulus, the shear modulus and the Poisson's ratio. The parameters α and ϵ_c represent the coefficient of thermal expansion and the cure shrinkage strain.

Table 1: Material properties of Fiberite T300/934 carbon/epoxy unidirectional laminate.

E_{11} (GPa)	E_{22} (GPa)	E_{33} (GPa)	G_{12} (GPa)	ν_{12}	ν_{13}	ν_{23}
150.76	7.93	7.93	3.7	0.2525	0.2525	0.30

α_1 ($10^{-6}/^\circ\text{C}$)	α_2 ($10^{-6}/^\circ\text{C}$)	α_3 ($10^{-6}/^\circ\text{C}$)	ϵ_c^1	ϵ_c^2	ϵ_c^3
-0.8×10^{-6}	27.62×10^{-6}	27.62×10^{-6}	-0.125×10^{-3}	-0.7×10^{-2}	-0.7×10^{-2}

Fabrication of Pre-preg Samples Using Plain-Weave Fabric

These samples were fabricated from the Hexcel W3L282-42"-F584 material. The nominal resin content in the pre-preg was 40 ± 3 percent by weight, the fibre areal weight (density) was 193 ± 8 g/m² and the standard cured ply thickness was 0.19 mm. To study the effect of tooling material, three different tooling materials, namely, aluminium, steel and carbon/epoxy

composite, were used. In addition, to analyse the effect of the tool angle, four tool angles were taken into consideration: 45° , 70° , 90° and 135° . All the tools were male tools with a constant tool radius of 2 mm. The effect of laminate thickness was studied by increasing the number of plies. The lay-ups consisted of 4, 6 and 10 plies with the orientations: $[0/0]_s$, $[45/45]_s$, $[0/45]_s$, $[0/0/0]_s$, $[45/45/45]_s$, $[0/45/0]_s$, $[0/0/0/0/0]_s$, $[45/45/45/45/45]_s$, and $[0/45/0/45/0]_s$.

These samples were also cured at 177°C . The material properties for a fabric laminate (with 0° lay-up) as estimated from micromechanics relations are given in Table 2. Again, the resin shrinkage was estimated to be 1.5 percent.

Table 2: Material properties of plain-weave carbon/epoxy 0° laminate.

E_{11} (GPa)	E_{22} (GPa)	E_{33} (GPa)	G_{12} (GPa)	ν_{12}	ν_{13}	ν_{23}
80.05	80.05	8.68	4.0	0.0275	0.2525	0.2525

α_1 ($^{\circ}\text{C}$)	α_2 ($^{\circ}\text{C}$)	α_3 ($^{\circ}\text{C}$)	ϵ_c^1	ϵ_c^2	ϵ_c^3
1.73×10^{-6}	1.73×10^{-6}	44.42×10^{-6}	-0.6×10^{-3}	-0.6×10^{-3}	-0.9×10^{-2}

Fabrication of RTM Samples

These samples were fabricated from Ciba Geigy “uniweave” Injectex (GU230-E01) fabric and RTM6 resin using resin transfer moulding (RTM) technology. The uniweave fabric has 90 % 3K carbon tows in the warp direction and 10 % 1K carbon tows in the weft direction.

Steel was chosen to construct the RTM tool because of its relatively smaller coefficient of expansion. This would minimise the effect of the tool material on the spring-in angle. The tool used had two parts which are best described as male and female “V - Blocks” with a 90° enclosed angle (see Figure 2). The male part had a machined recess for an “O” ring seal and a machined, two-stepped rebate to accommodate the preform; one step was 1 mm deep and the other was 2 mm deep. The tool radii machined into the apex were 3 mm and 6 mm in the case of 1 mm rebate and 6 mm in the case of 2 mm rebate in the male part. Accordingly, the tool radii for the female part were 4 mm, 7 mm and 8 mm. Thus the components produced were 1 mm (with internal radii 3 mm and 6 mm) and 2 mm (with internal radius 6 mm) thick. Also, the male part had three resin outlets common to each of the three preform at the apex of the “V”. The female part had two off peripheral inlets.



(a) (b)
Fig. 2: RTM tool in (a) unassembled form and (b) assembled form.

The lay-ups considered for each RTM run were as follows: (1) [0/0]_s, [0/0]_s, [0/0]_{2s}, (2) [30/-30]_s, [30/-30]_s, [30/30/-30/-30]_s, (3) [45/-45]_s, [45/-45]_s, [45/45/-45/-45]_s, (4) [60/-60]_s, [60/-60]_s, [60/60/-60/-60]_s, and (5) [90/90]_s, [90/90]_s, [90/90/90/90]_s. The first two lay-ups for each run were identical with inner radii of 3 mm and 6 mm, respectively, and 1 mm thickness. The third lay-up had an inner radius of 6 mm and was 2 mm thick. The lay-ups considered allowed us to study the effect of the radius, thickness and the orientation angle of the angle ply laminates.

From the thickness of the laminate, the areal density of the “uniweave” Injectex (220 g/m²), and the density of T300 carbon fibres (1.75 g/m²), the volume fraction of the lay-ups was determined to be 50.3%. The resin cure shrinkage was estimated to be 1.5 percent. The laminate properties, determined from micromechanics relations, are given in Table 3.

Table 3: Material properties of “Unidirectional” carbon/epoxy RTM laminate.

E₁₁ (GPa)	E₂₂ (GPa)	E₃₃ (GPa)	G₁₂ (GPa)	v₁₂	v₁₃	v₂₃
106.3	16.67	5.44	2.43	0.09	0.275	0.275
α₁ (°C)	α₂ (°C)	α₃ (°C)	ε_c¹	ε_c²	ε_c³	
0.145×10 ⁻⁶	13.0×10 ⁻⁶	53.25×10 ⁻⁶	-0.32×10 ⁻³	-0.32×10 ⁻²	-0.12×10 ⁻¹	

RESULTS AND DISCUSSION

The cure temperature for the pre-preg samples was 177 °C (350 °F) and for the RTM samples was 160 °C. The ambient temperature was assumed to be 21 °C.

Figure 3 shows the model predictions as a function of radius/thickness (R/h) ratio for all three composite materials considered in this study. It can clearly be seen that for (R/h) ratio greater than 1, the degree of spring-in remains constant and does not depend on the radius of curvature or the thickness of the laminate. For the lay-ups considered in this study, the R/h ratio was greater than 1. Therefore, while calculating theoretical spring-in values, only one R value was considered. It should also be noted here that although the cure temperature for RTM laminates was lower than that for the pre-preg laminates, higher spring-in angles are predicted by theory for the RTM laminates because of higher coefficient of expansion and resin shrinkage in the through-thickness direction.

Table 4 summarises the results for the Fiberite T300/934 unidirectional tape material. The parameter R_t in this table is the tool radius and R_i is the internal radius. It can be seen from this table that there is considerable scatter in the spring-in data. The spring-in data given for each lay-up is an average of three values, measured from a single specimen at three different places. The difference between the results from male and female tooling can be attributed to the matrix bridging observed in the components produced from female tooling. The matrix bridging could be defined as the accumulation of excess resin due to resin flow during curing at the corner of the component on the surface away from the tool. No matrix bridging was observed in components produced using male tooling. In the case of female tooling, both matrix bridging and a resin rich layer (on the tool side) were more pronounced for smaller tool radius (i.e. the 4 mm tool radius). For this reason, very large spring-in angles were observed for [45/-45]_s and [60/-60]_s lay-ups from female tooling for 4 mm tool radius. Also,

the amount of matrix bridging was not consistent in different specimens produced from the same tooling. In the case of thicker laminates, no noticeable matrix bridging was observed in components produced from female tooling and therefore similar spring-in results were obtained in components manufactured on both male and female tooling. However, in general, there was a lot more scatter in the data from female tooling for different tool radii.

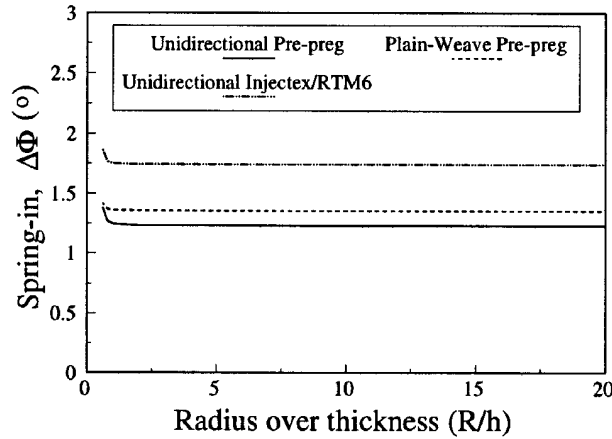


Fig. 3: Effect of (R/h) ratio on the spring-in of a cross ply [90/0/90/0]_s laminate.

Figure 4 shows the comparison between theoretical predictions and experimental data for components produced using male tooling. The agreement between the two is not so good. This could have resulted from the difficulty in measuring the spring-in angles with good accuracy because the specimens were very thin and could deform quite easily while measuring the angles. However, for thicker laminates (8 ply lay-ups) shown in Table 4, the agreement between experimental data and predictions is excellent in the case of male tooling and is within experimental error in the case of female tooling. This verifies the validity of the spring-in model. It should also be noted here that the results for both [90/0/90/0]_s and [0/90/0/90]_s lay-ups are quite similar (for male tooling) and independent of the tool radii and thus indicate that for symmetric lay-ups, the effect of the lay-up sequence on the degree of spring-in is insignificant.

Table 4: Experimental and Theoretical Results for Unidirectional Pre-preg Material.

Lay-up	Male Tool		Female Tool			Theory R _i = 3 mm
	R _t = 3 mm	R _t = 6 mm	R _t = 4 mm	R _t = 7 mm	R _t = 8 mm	
[0/0] _s	0.2	0.75	0.57	0.68	0.73	0.0
[30/-30] _s	0.21	0.19	0.91	-0.24	-0.49	0.45
[45/-45] _s	0.88	0.70	2.94	0.96	1.38	1.11
[60/-60] _s	1.02	1.20	3.36	0.95	0.78	1.28
[90/-90] _s	1.15	1.24	1.29	0.40	0.42	1.023
[90/0/90/0] _s	1.23	1.26	1.05	1.0	1.02	1.233
[0/90/0/90] _s	1.20	1.28	1.37	1.25	1.40	1.233

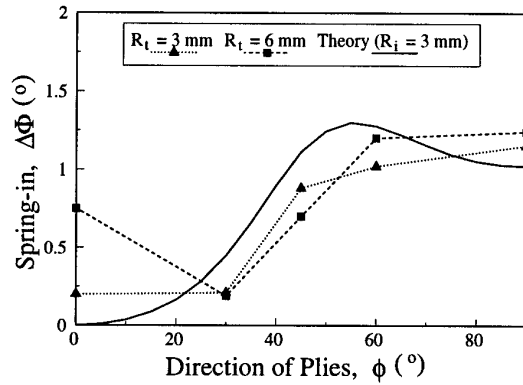


Fig. 4: Effect of the orientation angle of an angle ply $[\phi/-\phi]_s$ laminate on the spring-in in the case of unidirectional pre-preg material.

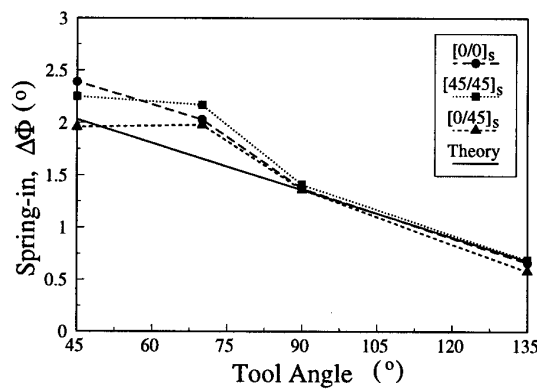


Fig. 5: Magnitude of spring-in observed for the four ply lay-ups cured on aluminium tooling.

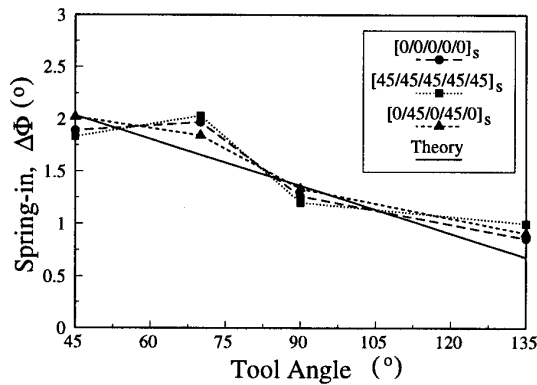


Fig. 6: Magnitude of spring-in observed for the ten ply lay-ups cured on aluminium tooling.

For the plain-weave fabric material, only male tools with tool radius of 2 mm were used to fabricate the samples. Figures 5-6 illustrate the magnitude of spring-in observed for the 4 and 10 ply aluminium tooled lay-ups. It can clearly be seen that ply orientation angles do not have any significant effect on the degree of spring-in. The theoretical predictions are also shown in these figures and a good agreement with experimental data (except for a tool angle of 70°) can be observed. It can also be seen that, in general, spring-in decreases with an increase in the tool angle. Figure 7 shows that an increase in thickness by increasing the number of plies does

not have any significant effect on the degree of spring-in. This is consistent with the theoretical predictions. The results for lay-ups cured on steel and composite tools were similar to those for lay-ups cured on aluminium tool and are therefore not shown in graphical form. Since the model predicts that for fabric laminates the spring-in angles do not depend on the thickness of the laminate or on the ply orientation angles, to provide comparison between tool materials, an average spring-in values for each tool angle was determined. Figure 8 shows the comparison between theoretical predictions and average spring-in angles for components cured on different tool materials. It can be seen from this figure that tool material has negligible effect on the spring-in angles. This validates the assumption made in our theoretical analysis that spring-in does not depend on the tool material.

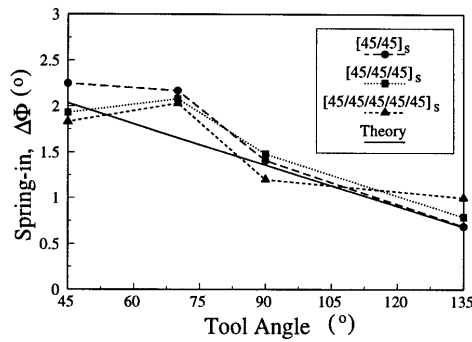


Fig. 7: Spring-in observed for the 45° orientated ply lay-ups cured on aluminium tooling.

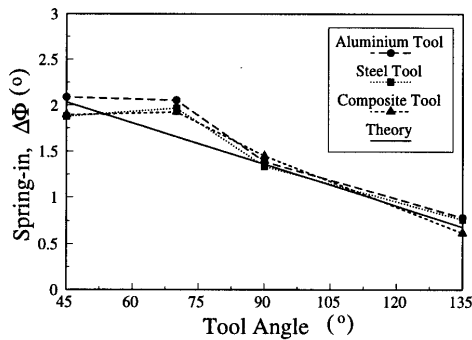


Fig. 8: Comparison between average spring-in angles and theoretical predictions.

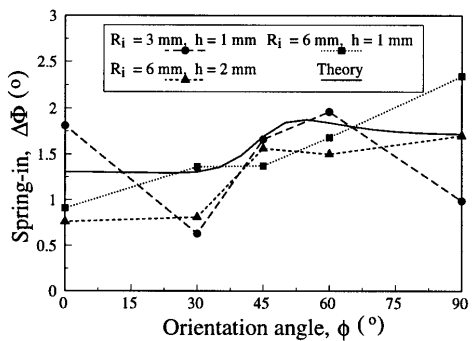


Fig. 9: Magnitude of spring-in observed in RTM samples for different internal radii and laminate thicknesses for angle ply $[\phi/-\phi]_s$ laminates.

The spring-in results for the RTM samples along with the theoretical results are shown in Figure 9. The predictions are found to lie between the experimental results. The RTM tool

was designed to reveal information on the effect of tool radius and the thickness of the laminate on the magnitude of spring-in. However, from the experimental data it is not possible to identify any trends in the spring-in angles as a function of the internal radius (R_i) or the thickness of the component. Since theoretical predictions are independent of the internal radius and the thickness of the laminate, a comparison between average spring-in angles and theoretical predictions is shown in Figure 10 and a good agreement is found.

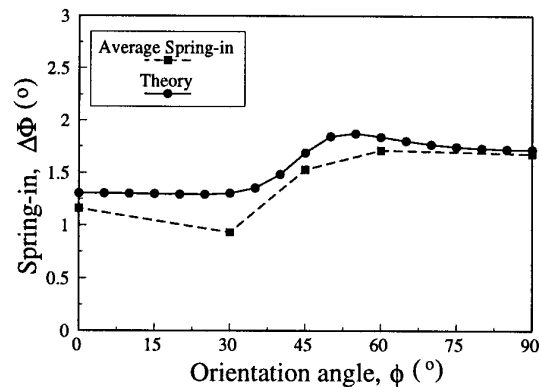


Fig. 10: Comparison between theoretical predictions and average spring-in angles for the RTM samples.

CONCLUSIONS

In this study, spring-in model developed by Jain and Mai has been evaluated. Reasonable agreement is found between experimental results and theoretical predictions. Therefore, the spring-in model developed could be used to assist tool designers with the tool design. For radius-to-thickness (R/h) ratios greater than one, spring-in is found to be independent of the radius or the thickness of the laminate. In addition, it is found that the magnitude of spring-in does not depend on the lay-up sequence (for symmetric lay-ups) or the tool material, and that the spring-in angle decreases with an increase in the tool angle. In the case of fabric laminates, the orientation of the plies does not affect the degree of spring-in.

REFERENCES

1. Jain L.K. and Mai Y.-W., "Stresses and Deformations Induced During Manufacturing. Part I: Analysis of Composite Cylinders and Shells," To appear in the *Journal of Composite Materials*, Vol. 31, No. 3, 1997.
2. Zahlan, N. and O'Neill, J.M., "Design and Fabrication of Composite Components; the Spring Forward Phenomenon," *Composites*, Vol. 20, pp. 77-81, 1989.
3. O'Neill, J.M., Rogers, T.G., and Spencer, A.J.M., "Thermally Induced Distortions in the Moulding of Laminated Channel Sections," *Mathematical Engineering in Industry*, Vol. 2, pp. 65-72, 1988.
4. Kollár, L.P., "Approximate Analysis of the Temperature Induced Stresses and Deformations of Composite Shells," *Journal of Composite Materials*, Vol. 28, pp. 392-414, 1994.
5. Nelson, R.H., "Prediction of Dimensional Changes in Composite Laminates During Cure," *Proceedings of 34th International SAMPE Symposium*, pp. 2397-2410, 1989.

6. Lutton, B.G., Analysis of Flange Springback in Carbon/Epoxy Composite Angled Parts, B.E. Thesis, University of Technology, Sydney, Australia, 1991.

Table 5: Experimental and Theoretical Results for Plain-Weave Fabric Pre-preg Material.

Lay-up	Aluminium Tool				Steel Tool				Composite Tool				Theory ($R_i = 2 \text{ mm}$)			
	45°	70°	90°	135°	45°	70°	90°	135°	45°	70°	90°	135°	45°	70°	90°	135°
[0/0] _s	2.39 ⁰	2.03 ⁰	1.37 ⁰	0.66 ⁰	2.02 ⁰	1.90 ⁰	1.27 ⁰	0.61 ⁰	2.25 ⁰	2.12 ⁰	1.63 ⁰	0.67 ⁰	2.03 ⁰	1.66 ⁰	1.36 ⁰	0.68 ⁰
[45/45] _s	2.25 ⁰	2.17 ⁰	1.41 ⁰	0.69 ⁰	1.98 ⁰	2.02 ⁰	1.30 ⁰	0.45 ⁰	1.80 ⁰	2.03 ⁰	1.50 ⁰	0.62 ⁰	2.03 ⁰	1.66 ⁰	1.36 ⁰	0.68 ⁰
[0/45] _s	1.96 ⁰	1.98 ⁰	1.36 ⁰	0.58 ⁰	1.97 ⁰	1.87 ⁰	1.23 ⁰	0.58 ⁰	2.0 ⁰	1.9 ⁰	1.6 ⁰	0.7 ⁰	2.03 ⁰	1.66 ⁰	1.36 ⁰	0.68 ⁰
[0/0/0] _s	2.0 ⁰	2.34 ⁰	1.74 ⁰	0.95 ⁰	2.24 ⁰	2.36 ⁰	1.50 ⁰	1.05 ⁰	1.98 ⁰	2.02 ⁰	1.53 ⁰	0.53 ⁰	2.03 ⁰	1.66 ⁰	1.36 ⁰	0.68 ⁰
[45/45/45] _s	1.93 ⁰	2.08 ⁰	1.48 ⁰	0.79 ⁰	1.79 ⁰	2.15 ⁰	1.64 ⁰	0.85 ⁰	1.97 ⁰	1.85 ⁰	1.37 ⁰	0.53 ⁰	2.03 ⁰	1.66 ⁰	1.36 ⁰	0.68 ⁰
[0/45/0] _s	2.52 ⁰	2.05 ⁰	1.32 ⁰	0.60 ⁰	1.93 ⁰	1.94 ⁰	1.43 ⁰	0.68 ⁰	2.05 ⁰	1.97 ⁰	1.44 ⁰	0.63 ⁰	2.03 ⁰	1.66 ⁰	1.36 ⁰	0.68 ⁰
[0/0/0/0/0] _s	1.89 ⁰	1.97 ⁰	1.26 ⁰	0.86 ⁰	1.85 ⁰	1.77 ⁰	1.18 ⁰	0.84 ⁰	1.85 ⁰	2.02 ⁰	1.50 ⁰	0.55 ⁰	2.03 ⁰	1.66 ⁰	1.36 ⁰	0.68 ⁰
[45/45/45/45/45] _s	1.83 ⁰	2.03 ⁰	1.20 ⁰	1.00 ⁰	1.82 ⁰	1.80 ⁰	1.41 ⁰	1.03 ⁰	1.59 ⁰	1.57 ⁰	1.28 ⁰	0.63 ⁰	2.03 ⁰	1.66 ⁰	1.36 ⁰	0.68 ⁰
[0/45/0/45/0] _s	2.02 ⁰	1.84 ⁰	1.33 ⁰	0.91 ⁰	1.35 ⁰	1.90 ⁰	1.07 ⁰	0.77 ⁰	1.57 ⁰	1.87 ⁰	1.18 ⁰	0.70 ⁰	2.03 ⁰	1.66 ⁰	1.36 ⁰	0.68 ⁰
Average	2.09 ⁰	2.05 ⁰	1.39 ⁰	0.78 ⁰	1.88 ⁰	1.97 ⁰	1.34 ⁰	0.76 ⁰	1.89 ⁰	1.93 ⁰	1.45 ⁰	0.62 ⁰	2.03 ⁰	1.66 ⁰	1.36 ⁰	0.68 ⁰

Table 6: Experimental and Theoretical Results for RTM Samples.

Lay-up	R_i (mm)	RTM Tool (Exptl.)	Theory
[0/0] _s	3.0	1.81 ⁰	1.30 ⁰
[0/0] _s	6.0	0.91 ⁰	1.30 ⁰
[0/0/0/0] _s	6.0	0.76 ⁰	1.30 ⁰
[30/-30] _s	3.0	0.63 ⁰	1.30 ⁰
[30/-30] _s	6.0	1.36 ⁰	1.30 ⁰
[30/30/-30/-30] _s	6.0	0.81 ⁰	1.30 ⁰
[45/-45] _s	3.0	1.66 ⁰	1.69 ⁰
[45/-45] _s	6.0	1.37 ⁰	1.69 ⁰
[45/45/-45/-45] _s	6.0	1.56 ⁰	1.69 ⁰
[60/-60] _s	3.0	1.96 ⁰	1.84 ⁰
[60/-60] _s	6.0	1.68 ⁰	1.84 ⁰
[60/60/-60/-60] _s	6.0	1.50 ⁰	1.84 ⁰
[90/90] _s	3.0	0.99 ⁰	1.72 ⁰
[90/90] _s	6.0	2.34 ⁰	1.72 ⁰
[90/90/90/90] _s	6.0	1.70 ⁰	1.72 ⁰

FINITE DIFFERENCE METHOD FOR THE ANALYSIS OF FILAMENT WOUND COMPOSITE SHELLS

E.V. Morozov¹ & E.G. Evseev²

¹ *Department of Mechanical Engineering, University of Natal, Durban 4041, South Africa*

² *Department of Mechanics and Optimisation of Processes and Structures, State University of Technology, 27 Petrovka Street, 103767 Moscow, Russia*

SUMMARY: The present paper deals with the application of finite difference method to the analysis of thin-walled composite structures. The mechanical models and numerical techniques are developed for laminated composite structures reinforced by various elements and layers. The numerical solutions of the static problems of thermoelasticity are discussed for composite filament wound orthotropic shells of revolution.

All of the methods are based on the applied theory of thin-walled composite structures which allows for transverse interlaminar shear strains. The equations of the shell theory of this type were derived on the basis of three-dimensional theory of elasticity (see: Vasiliev [1], Vorobey, Morozov, and Tatarnikov [2]).

KEYWORDS: filament wound composite shells, finite difference method, thermoelasticity, transverse shear strain

INTRODUCTION

Composite materials and structures can be designed to meet the special set of requirements. The composite thin-walled structures operating under conditions of both the high-temperature heating and mechanical loading are used for some aerospace applications. Carbon-carbon composites are most appropriate materials in this case. In the present paper the filament wound composite shells of revolution are considered. They consist of the number of elementary unidirectionally reinforced helical layers with different angles of orientation. The main parameters describing a particular laminated composite structure are the mechanical and physical properties of unidirectional elementary layer, fibre orientation, thickness distribution, stacking sequences, and the number of layers. For the structures considered the elementary layer consists of two plies symmetrically oriented at angles of $\pm \phi$. In order to take into account all of the main features of the material, structure and operational conditions the appropriate mechanical models and mathematical approaches should be developed. In this paper the variant of refined applied theory of thermoelastic composite shells is used as the basis for modelling procedure and analysis of stress-strain state. The mechanical properties of composite elementary layers were obtained experimentally as a result of special mechanical tests. The finite difference method of approximation has been used in order to calculate the displacements of the shell, stress and strain distributions for elementary layers of composite material. Cubic spline interpolation has been used to define the data for numerical analysis during the computational process.

THEORY OF THIN-WALLED COMPOSITE STRUCTURES

Composite shells of revolution with the symmetrical structure of reinforcement are considered. The shell is produced by filament winding with the angles of fibre orientation $\pm \phi(y)$ to the meridian line of the initial surface of the shell (see Fig.1). The type of fibres and matrix is the same for the whole shell. It gives the opportunity to use simplified constitutive equations relating force and moment resultants to the strain components of the initial (middle) surface. The reinforced layer is referred to a co-ordinate system coincided with the layer's symmetry axes (1,2,3). Axes 1 is directed along the fibre orientation, axes 2 defines the transversal direction, and axes 3 is orthogonal to the plane (1,2).

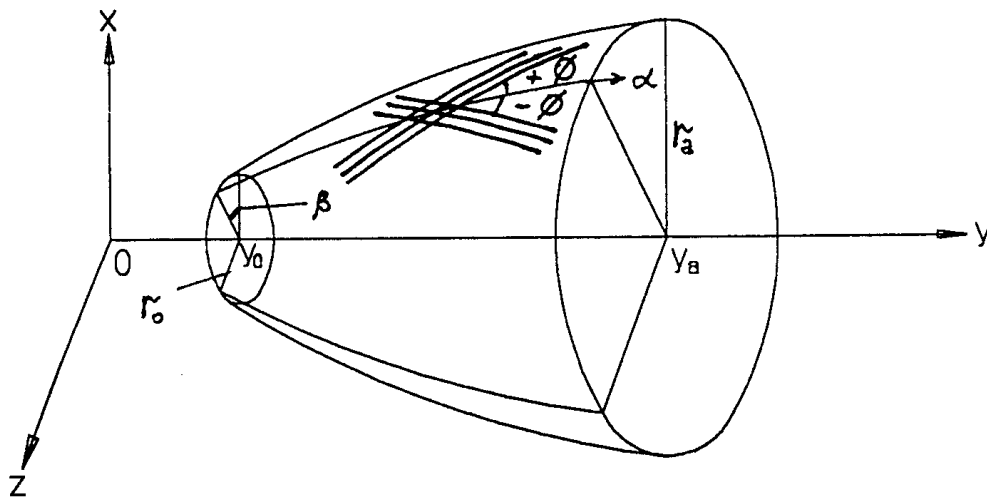


Figure 1. Filament wound shell of revolution

The shell is referred to a cylindrical coordinate system as presented in Fig.1. The coordinates α, β are the curvilinear surface coordinates coinciding with the principal directions (longitudinal and circumferential respectively) of the middle surface of the shell.

The equilibrium equations are presented as follows:

$$\frac{d(rN_\alpha)}{dy} - \bar{r}N_\beta - \frac{rr''}{1+(r')^2} Q_\alpha = 0, \quad \frac{d(rM_\alpha)}{dy} - r'M_\beta - r[1+(r')^2]^{1/2} Q_\alpha = 0, \tag{1}$$

$$\frac{d(rQ_\alpha)}{dy} + \frac{rr''}{1+(r')^2} N_\alpha - N_\beta + r[1+(r')^2]^{1/2} p(y) = 0,$$

where $N_\alpha, N_\beta, Q_\alpha, M_\alpha, M_\beta$ are the stress resultants; the y-axis is the axis of the shell ; $r(y)$ is the radius of cross-section; $r' = dr/dy$. The strain-displacement relationships can be written as

$$\begin{aligned}\varepsilon_\alpha &= u'[1+(r')^2]^{-1/2} - r''w[1+(r')^2]^{-3/2}, & \varepsilon_\beta &= (r'u+w)[1+(r')^2]^{-1/2} / r, \\ \kappa_\alpha &= \theta'_\alpha[1+(r')^2]^{-1/2}, & \kappa_\beta &= r'\theta_\alpha[1+(r')^2]^{-1/2} / r, \\ \varphi_\alpha &= \theta_\alpha + w'[1+(r')^2]^{-1/2} + r''u[1+(r')^2]^{-3/2},\end{aligned}\quad (2)$$

where u is the displacement of the initial surface along the axis α , w is the displacement orthogonal to the plane which is tangent to the initial surface of the shell, θ_α is the angle of rotation of the element which is orthogonal to the tangent plane; $\varepsilon_\alpha, \varepsilon_\beta, \kappa_\alpha, \kappa_\beta$ are the strain components, ψ_α is the transverse shear strain. In the case considered in this paper constitutive equations of thermoelasticity are given in the form

$$N_\alpha = C_{11}\varepsilon_\alpha + C_{12}\varepsilon_\beta - T_\alpha^{(0)}, \quad N_\beta = C_{12}\varepsilon_\alpha + C_{22}\varepsilon_\beta - T_\beta^{(0)}, \quad (3)$$

$$M_\alpha = D_{11}\kappa_\alpha + D_{12}\kappa_\beta - T_\alpha^{(1)}, \quad M_\beta = D_{21}\kappa_\alpha + D_{22}\kappa_\beta - T_\beta^{(1)}, \quad Q_\alpha = C_{55}\psi_\alpha,$$

where

$$C_{mn} = h\bar{B}_{mn}, \quad D_{mn} = h^3\bar{B}_{mn} / 12 \quad (m, n = 1, 2); \quad C_{55} = hG_{\alpha\gamma}; \quad T_{\alpha,\beta}^{(k)} = \int_{-h/2}^{h/2} \bar{B}_{mi} t^k d\gamma; \quad k = 0, 1;$$

In these formulas \bar{B}_{mn} , \bar{B}_{mi} , are the stiffness and the thermal coefficients of the layer reinforced under the angle ϕ (these coefficients can be calculated for given material structure using the known equations of mechanics of composite materials [1], [2]); C_{55} - is the coefficient of transversal shear stiffness and $G_{\alpha\gamma}$ is the transversal shear modulus. The modulus $G_{\alpha\gamma}$ can be presented in terms of the shear moduli G_{13}, G_{23} of the unidirectionally reinforced material. These moduli should be determined experimentally or calculated using the micro-mechanical models of composites.

The equations (1)-(3) can be rearranged to the following system

$$\begin{aligned}\frac{d(\bar{r}Q_\alpha)}{d\bar{y}} + \frac{\bar{r}''\bar{r}}{a^2} N_\alpha + r_0\bar{r}p_0\bar{p}(\bar{y})a - \frac{C_{12}}{r_0a} (u' - \frac{w\bar{r}''}{a^2}) - \frac{C_{22}u\bar{r}'}{r_0\bar{r}a} - \frac{C_{22}w}{r_0\bar{r}a} + T_\beta^{(0)} &= 0, \\ \frac{d(\bar{r}M_\alpha)}{d\bar{y}} - \frac{D_{12}\bar{r}'}{ar_0} \theta'_\alpha - \frac{D_{22}(\bar{r}')^2}{ar_0\bar{r}} \theta'_\alpha + r_0\bar{r}aQ_\alpha + T_\beta^{(1)}\bar{r}' &= 0, \\ \frac{d\theta_\alpha}{d\bar{y}} + \frac{D_{12}\bar{r}'}{D_{11}\bar{r}} \theta_\alpha - \frac{r_0a}{D_{11}} (M_\alpha + T_\alpha^{(1)}) &= 0, \quad \frac{dw}{d\bar{y}} + r_0a\theta_\alpha - \frac{\bar{r}''}{a^2} u - \frac{r_0a}{C_{55}} Q_\alpha &= 0,\end{aligned}\quad (4)$$

$$\frac{du}{d\bar{y}} + \frac{C_{12}\bar{r}'}{C_{11}} u + \left(\frac{C_{12}}{C_{11}\bar{r}} - \frac{\bar{r}''}{a^2} \right) w - \frac{r_0a}{C_{11}} (N_\alpha + T_\alpha^{(0)}) = 0,$$

$$N_\alpha - \bar{r}'Q_\alpha = p_0r_0 \frac{a}{\bar{r}'} \int_{\bar{y}_a}^{\bar{y}} \bar{p}(\bar{y})\bar{r}'\bar{r}d\bar{y}$$

where $\bar{y} = y / r_0$; $\bar{r} = r / r_0$; $\bar{p} = p / p_0$; $a^2 = 1 + (\bar{r}')^2$; r_0 , p_0 , are the specified parameters of the shell and load respectively. The equations were accomplished by the following boundary conditions:

$$u = 0; w = 0; \theta_\alpha = 0 \text{ for } y = y_0; \quad N_\alpha = 0; Q_\alpha = 0; M_\alpha = 0 \text{ for } y = y_\alpha. \quad (5)$$

If we have solution of the system (4) the strain components of the initial surface of the shell can be calculated using equations (2). After that we can calculate the strains e_α , e_β for any point of the wall of the structure by the following way

$$e_\alpha = \varepsilon_\alpha + \gamma \kappa_\alpha, \quad e_\beta = \varepsilon_\beta + \gamma \kappa_\beta.$$

The strain components for elementary unidirectional layer can be calculated as follows

$$\begin{aligned} \varepsilon_1 &= e_\alpha \cos^2 \phi + e_\beta \sin^2 \phi, & \varepsilon_2 &= e_\alpha \sin^2 \phi + e_\beta \cos^2 \phi, \\ \varepsilon_{12} &= (e_\beta - e_\alpha) \sin 2\phi \end{aligned} \quad (6)$$

Normal stress σ_1 acting along the fibres, normal stress σ_2 acting in the direction orthogonal to fibre orientation, and shear stress τ_{12} can be calculated for each elementary layer and cross-section of the shell using the following equations

$$\begin{aligned} \sigma_1 &= \bar{E}_1 (\varepsilon_1 + \mu_{12} \varepsilon_2) - \bar{E}_1 t (\alpha_1 + \mu_{12} \alpha_2), \quad \sigma_2 = \bar{E}_2 (\varepsilon_2 + \mu_{21} \varepsilon_1) - \bar{E}_2 t (\alpha_2 + \mu_{21} \alpha_1), \\ \tau_{12} &= G_{12} \varepsilon_{12} \end{aligned} \quad (7)$$

where $\bar{E}_{1,2} = \bar{E}_{1,2} / (1 - \mu_{12} \mu_{21})$, $\bar{E}_{1,2}$ - are the longitudinal and transverse Young's moduli of unidirectionally reinforced material respectively, G_{12} - is the shear modulus, t - change of temperature at the given point of the wall, α_1, α_2 - are the coefficients of thermal expansion along the fibres and in the orthogonal direction respectively, and μ_{12}, μ_{21} are the Poisson's ratios. The stresses acting in the wall of the shell can be calculated in terms of the stress resultants from the following equations [2]

$$\begin{aligned} \sigma_\alpha &= N_\alpha / h + 12 M_\alpha \gamma / h^3, & \sigma_\beta &= N_\beta / h + 12 M_\beta \gamma / h^3, \\ \tau_{\alpha\beta} &= N_{\alpha\beta} / h + 12 M_{\alpha\beta} \gamma / h^3, & \tau_{\alpha\gamma} &= (1.5 / h - 6\gamma^2 / h^3) Q_\alpha \end{aligned} \quad (8)$$

where $\tau_{\alpha\gamma}$ - is the transversal shear stress.

The approach presented above has been used for the analysis of stress-strain state of carbon-carbon composite shells of revolution operating in the conditions of high-temperature heating jointly with the different types of mechanical loading.

NUMERICAL METHODS

The finite difference method has been used in order to obtain numerical solution of the problem determined by equations (4) and boundary conditions (5). The system (4) was approximated by the first order finite differences. Cubic spline interpolation was implemented to represent the geometry and shape of the shell $\bar{r}(\bar{y})$, thickness of the wall $h(\bar{y})$, internal pressure distribution $\bar{p}(\bar{y})$ and the pattern of filament winding $\phi(\bar{y})$ in the following general form

$$S(\bar{y}) = \sum_{p=0}^3 Q_{pq} (\bar{y} - y_q)^p; \quad \bar{y}_{q-1} \leq \bar{y} \leq \bar{y}_q$$

where $\bar{y} = y / r_0$, $\bar{p} = p / p_0$; r_0 is the radius of the initial cross-section of the shell (see Fig.1), and p_0 is the value of the pressure for the same cross-section. Dispelling method has been used in order to determine the coefficients of cubic spline Q_{pq} . As the result we obtain the system of linear algebraic equations. The system contains $6(n+1)$ variables, namely $u_i, w_i, \theta_{\alpha i}, N_{\alpha i}, Q_{\alpha i}, M_{\alpha i}$ for the $(n+1)$ points and consists of $5n$ equations written for the $n+1$ points on the basis of the first five equations from the system (4). The sixth equation of the system (4) which has been integrated in explicit form gives another $n+1$ algebraic equations and five equations have been obtained from the boundary conditions (5) as follows:

$$u_1 = 0, w_1 = 0, \theta_{\alpha 1} = 0 \text{ for the point 1,}$$

$$\text{and } Q_{\alpha_{n+1}} = 0, M_{\alpha_{n+1}} = 0 \text{ for the point number } n+1.$$

Resulting system of linear algebraic equations has the band type matrix and solution of this system gives the values of basic unknown functions $u(\bar{y}), w(\bar{y}), \theta_{\alpha}(\bar{y}), N_{\alpha}(\bar{y}), Q_{\alpha}(\bar{y}), M_{\alpha}(\bar{y})$ for $n+1$ points of the analysis (radial cross-sections of the shell). Corresponding stresses and strains are calculated according to equations (6) - (7).

NUMERICAL RESULTS

Analysis of the cylindrical composite shell loaded by uniformly distributed internal pressure has been used in order to verify computer algorithm and optimise parameters of finite difference grid. Results of calculations were compared with the analytical solution. As an example of application of the method suggested a numerical analysis for filament wound carbon- carbon composite shell of revolution has been produced. Mechanical characteristics of the unidirectional carbon-carbon composite were determined experimentally: $E_1 = 157.4$ GPa, $E_2 = 19.2$ GPa, $G_{12} = 9.0$ GPa, $\mu_{21} = 0.3$.

For unidirectionally reinforced material $G_{12} = G_{13}$. In order to calculate transversal shear modulus $G_{\alpha\gamma}$ we need to know modulus G_{13} . It could be shown that for unidirectional composite the following equation is appropriate [3]

$$G_{23} = G_m \frac{\kappa_m + \xi + \eta \frac{G_m}{G_f}}{\eta \kappa_m + (1 + \xi \kappa_m) \frac{G_m}{G_f}}$$

In this equation G_f, G_m are the shear moduli of fibres and matrix respectively; ξ and $\eta = 1 - \xi$ are the volume contents of the fibres and matrix ; $\kappa_m = 3 - 4\mu_m$, where μ_m is the Poisson' ratio for matrix material. Using the experimental values for E_1 and E_2 we can find the values E_m and ξ for specified material. For carbon-carbon material considered in this paper $G_{23} = 9349$ MPa (Young's modulus for fibres was assumed to be equal to 250 GPa). The geometry of the shell and pressure distribution are shown in Figure 2.

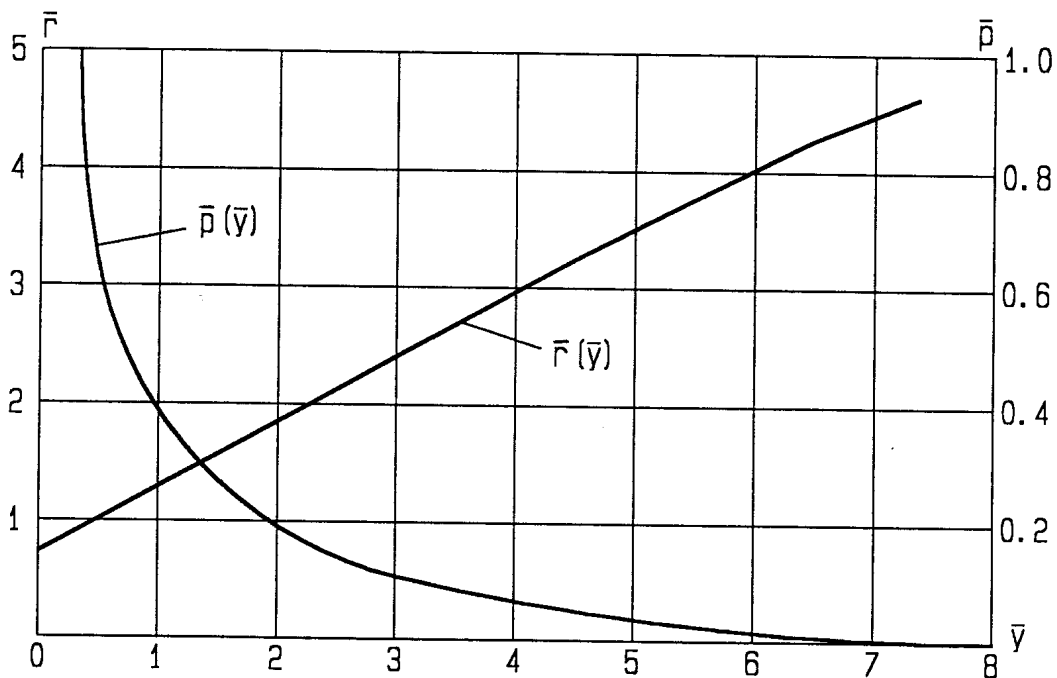


Fig.2: Geometry of the shell and load distribution ($\bar{r} = r / r_0$)

Filament winding pattern function and thickness distribution are presented in Fig. 3. Some results of numerical solution are presented in Fig.4 and Fig.5. In Fig.4 normal displacement distribution $\bar{w}(\bar{y})$ of the shell is shown. Distribution of the stresses acting in the elementary layers of material are given in Fig.5. The main feature of carbon-carbon material produced by filament winding is the very low tensile transverse strength (for material discussed this mechanical characteristic is equal to 6.6 MPa). According to this the distribution of the transverse stresses over the structure is of significant interest. The results of calculation of transverse stresses σ_2 and shear stresses τ_{12} are presented in Fig.5 for both external and internal surfaces of the shell . As shown in Fig.5 the level of values of tensile transversal stresses is quite high and practically determines the strength of the shell for given load.

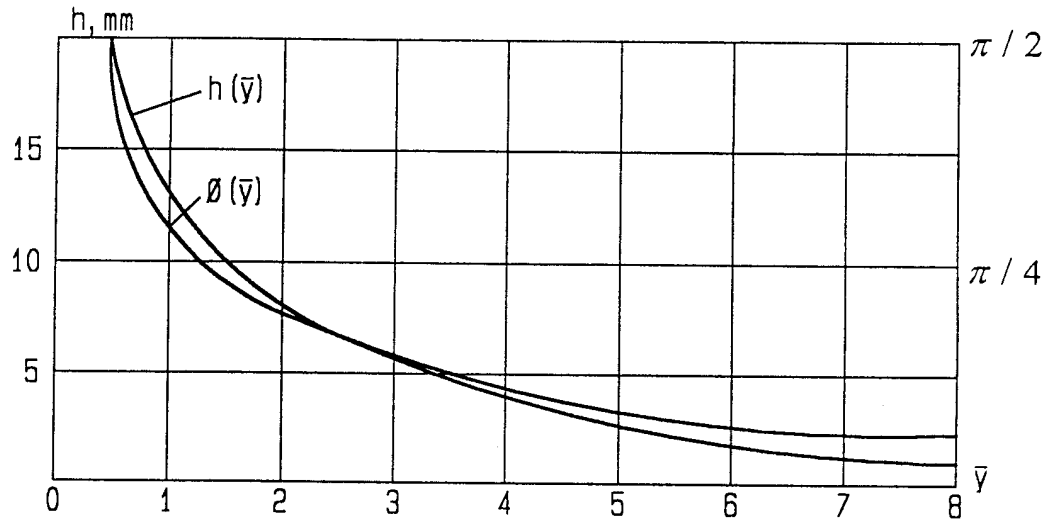


Fig.3 Filament winding pattern and thickness distribution

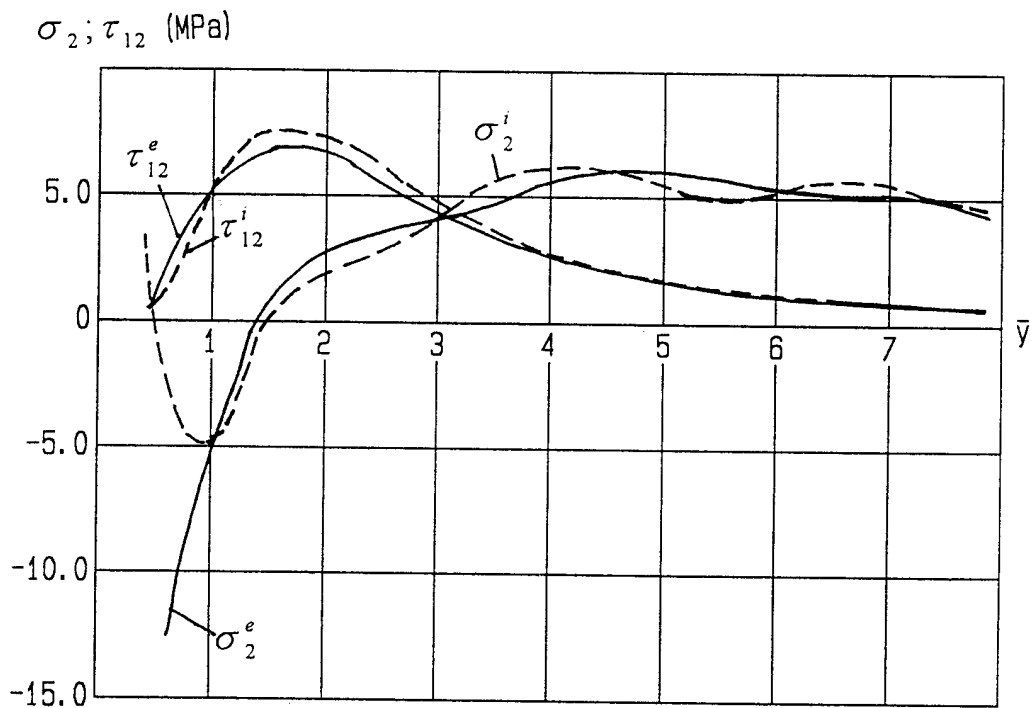


Fig.4 Distribution of the stresses in the elementary layer: $\sigma_2^i, \tau_{12}^i, \sigma_2^e, \tau_{12}^e$ - are the transverse and shear stresses for the internal (i) and external (e) surface of the shell.

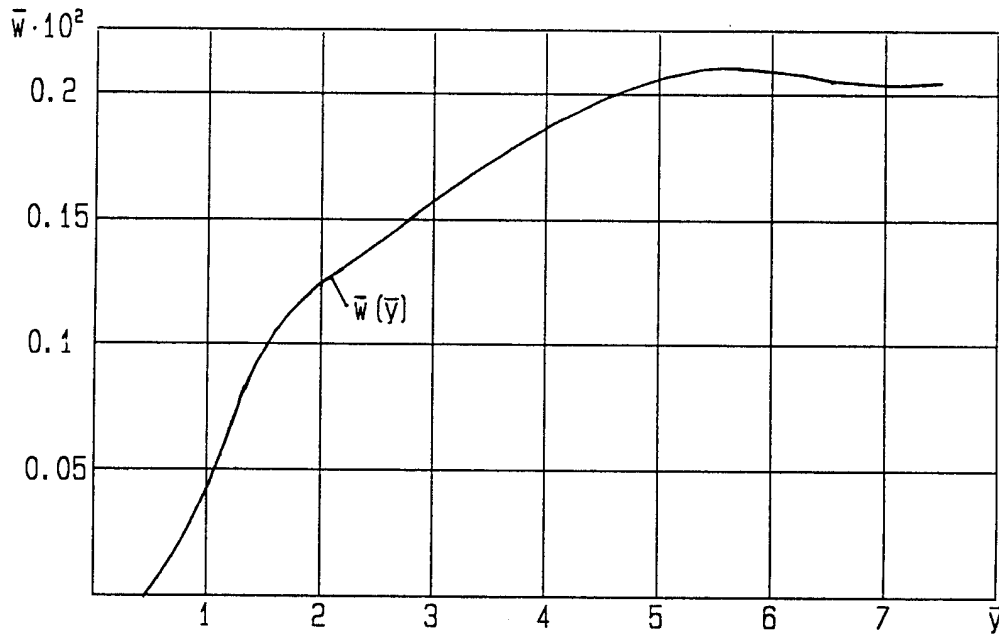


Fig.5 Normal displacements of the shell

CONCLUSIONS

The method presented in the paper gives the possibility to produce stress-strain state analysis of thermoloaded composite shells of revolution. Numerical technique and algorithm implemented were verified and tested using the exact analytical solution obtained for the cylindrical shell. This solution has been used in order to optimise the parameters of finite difference discretization as well. Numerical analysis of carbon-carbon composite shell of revolution has been produced and the displacements, stresses, and strains were calculated. The numerical results obtained allow to estimate strength and stiffness of the shell. Such an assessment of the failure could be produced on the level of elementary reinforcing composite layer. All the necessary information for it could be obtained as the result of computational process. The method presented in the paper could be implemented as a part of optimisation procedure as well. In this case it can be used as a method of direct analysis of mechanical response of composite structure to be optimised.

REFERENCES

1. Vasiliev, V.V., Mechanics of Composite Structures, Taylor & Francis, 1993.
2. Vorobey, V.V., Morozov, E.V. and Tatarnikov, O.V., Analysis of Thermoloaded Composite Structures, Mashinostroenie, Moscow, 1992.
3. Vanin, G.A., Micromechanics of Composite Materials, Naukova Dumka, Kiev, 1985.

DESIGN AND BEHAVIOR OF A GRADIENT CFRP BEAM

Patrick Kim¹ and Toshio Tanimoto²

¹*School of Engineering and*

²*Department of Materials Science and Ceramic Technology, Shonan Institute of Technology,
1-1-25 Tsujido Nishikaigan, 251 Fujisawa, Kanagawa, Japan*

SUMMARY: This work examines the advantages that can be gained for laminated flexural composite beams by spatially varying the fiber volume fraction. Design equations are given for a gradient beam whose depth varies while keeping the total fiber content constant. Beam shapes are calculated for a constant surface stress, to reduce the likelihood of failure at the beam root. These solutions are compared to uniform fiber content, all-CFRP beams with the same bending stiffness but with a constant cross-section or a constant surface stress, tapered profile. The gradient beams gave a similar or higher failure load and a lower mass for a given stiffness. The higher resin content also gave an improved vibration damping of the beam. The gradient design leads to a more effective material use. It can be applied to lightweight, dynamically loaded structures such as leaf springs.

KEYWORDS: material gradient, layered beam, cantilever, interlayer, damping, leaf spring, structural optimization

INTRODUCTION

Gradients in composition and properties are a means to improve the performance of structural components. While one may want to apply a material with a desired property or functionality locally while making the rest of the structure of different materials, the interface between dissimilar material leads to processing stresses and stress concentrations during loading. A gradient in properties helps to reduce these stresses and thus to improve the performance of material or part. On a broader level, parts may be designed with material gradients in order to control the overall distribution of stresses. Functionally gradient materials (FGMs) are thus a means to optimize the use of materials and increase reliability.

Current FGM research is focused in particular on metal and ceramic matrix composites [1]. However, polymer composites and related materials with a gradient in properties have been the subject of very few studies to this date [2, 3]. A major practical difficulty is to produce the desired compositional and microstructural gradient [2]. The aim of the present work is to investigate the design and behavior of gradient CFRP cantilever beam with a gradient in effective fiber volume fraction along its length (Fig. 1). Unlike all-composite beams with a uniform fiber content and a tapered profile, this solution avoids the problem of stress concentrations and delamination-related failures common with laminate designs using ply drops [4]. The design objective is a constant stress at the beam surface, in order to improve the strength or reduce the mass of the beam for a given stiffness, and thus improve the effectiveness of material use.

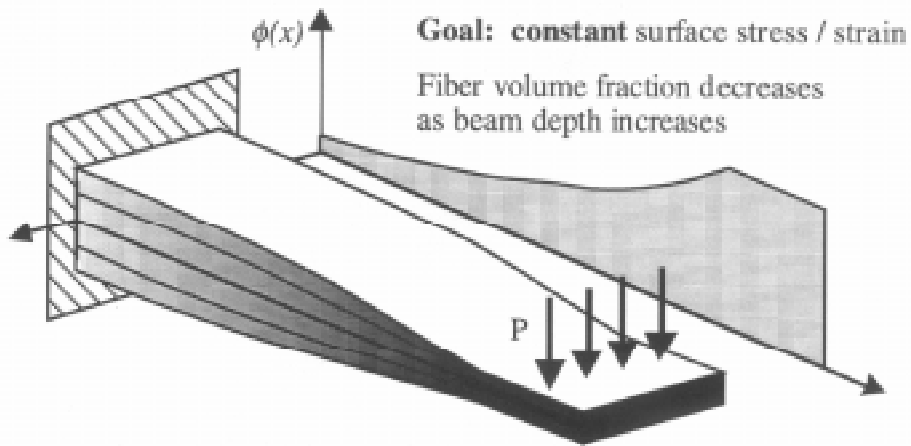


Fig. 1: Schematic representation of a CFRP cantilever beam with a gradient in fiber content.

BEAM DESIGN

The beam under study is shown in Figure 2. It is shown as a cantilever, but could also represent half of a simply supported 3-point bending beam. The beam is taken as a unidirectional composite with a fiber orientation corresponding to the beam's longitudinal axis. The total fiber content is constant over the entire length of the beam, while the effective fiber volume fraction changes with the depth of the beam. The beam, of total length L , has a tip length a of constant thickness y_0 and fiber volume fraction, ϕ_0 . For $x \leq a$, the cross section is constant, and a force P applied to the beam tip leads to linearly increasing surface strains. In the rest of the beam, the depth $y(x)$ increases gradually while the fiber volume fraction $\phi(x)$ decreases. The fiber volume fraction is given by:

$$\phi(x) = A_f / y(x)b(x) \tag{1}$$

where $b(x)$ is the beam's width and the total fiber area A_f is constant along the beam's length.

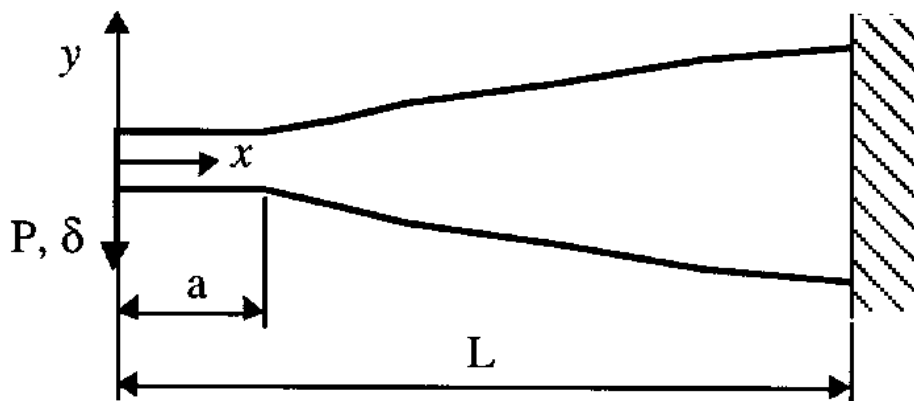


Fig. 2: Definition of the geometry of the cantilever beam

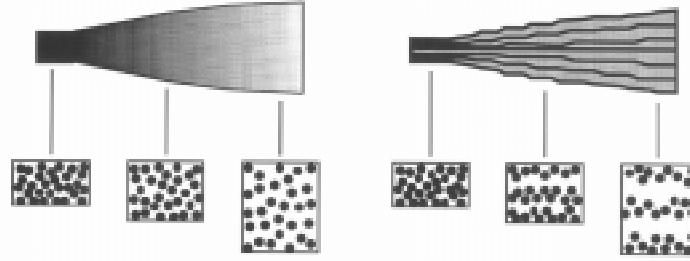


Fig. 3: Ideal (left) and layered (right) gradient beam cross sections. Fibers are represented by black dots.

Two cases are considered: an ideal gradient composite beam in which the fibers are distributed evenly within a cross-section across the beam's thickness at any point along its length, and a laminated beam, in which resin layers are introduced between composite layers (Fig. 3).

In the case of an ideal gradient beam with fibers distributed uniformly in a cross-section, the composite's longitudinal modulus is:

$$E(x) = (\phi(x)R + (1 - \phi(x)))E_m \quad (2)$$

where $R = E_f/E_m$ is the ratio of fiber to matrix modulus. The bending stiffness of any section along the length of a beam of constant width is:

$$(EI)_{eq}(x) = \frac{E_m y^2(x)}{12} (A_f(R-1) + y(x)b) \quad (3)$$

The surface stress for $x \geq a$ is given by equilibrium:

$$\sigma_{surf}(x) = \frac{My(x)}{2I(x)} = \frac{6Px}{y^2(x)} = const. \quad (4)$$

The beam profile for a criterion of constant surface stress σ^* at the beam's surface is thus:

$$y = \sqrt{6Sx} \quad \text{where } S = P/\sigma^* \quad (5)$$

For $x \geq a$, the surface strain is:

$$\epsilon_{surf}(x) = \frac{My(x)}{2(EI)_{eq}(x)} = \frac{6Px}{(A_f(R-1) + y(x)b)E_m y(x)} = const. \quad (6)$$

Setting this strain constant, ϵ^* , for $x \geq a$, gives a quadratic equation that can be solved for y :

$$y = \frac{1}{2} \left(-B + \sqrt{B^2 - 4C} \right) \quad (7)$$

where $B = (R-1)\phi_o y_o$ and $C = -6Tx/E_m$, $T = \frac{P}{\epsilon^*} = \frac{2E_o I_o}{ay_o} = \frac{E_o y_o^2}{6a}$ (8)

where E_o and I_o are the modulus and moment of inertia of the composite beam for $x \leq a$. The deflection of the beam is calculated by the method of complementary virtual work:

$$\delta = \int_0^L \frac{M(x)}{(EI)_{eq}(x)} M_v(x) dx$$
 (9)

Giving the compliance:

$$\frac{\delta}{P} = \int_0^a \frac{12x^2}{(B+y_o)y_o^2 E_m} dx + \int_a^L \frac{12x^2}{(B+y)y^2 E_m} dx = \frac{a^3}{3E_o I_o} + \int_a^L \frac{12x^2}{(B+y)y^2 E_m} dx$$
 (10)

or, simplifying,
$$\frac{\delta}{P} = \frac{2a^2}{3Ty_o} + \int_a^L \frac{4x}{T(\sqrt{B+24Tx/E_m} - B)} dx$$
 (11)

The deformation due to shear is negligible for long beams as examined here. For continuity, the surface stress or strain for $x \geq a$ is set equal to the stress or strain at $x=a$,

$$\sigma^* = \frac{P a y_o}{I_o} \text{ OR } \epsilon^* = \frac{P a y_o}{2E_o I_o}$$
 (12)

From Eqn (5) for constant stress or (7) and (8) for constant strain, and Eqn (11), the thickness y_o and the profile $y(x)$ of the tapered part of the beam can be calculated iteratively for a beam tip of given length a , modulus E_o , fiber volume fraction ϕ_o , and a desired compliance. The profiles of beams with a constant section tip $a=0.2L$ are given for different ratios $R = E_f/E_m$ in Fig. 4. The lowest curve gives the profile of a homogenous beam with constant surface stress. The upper curve, for $E_f/E_m = 500$ is practically the limiting profile for very high fiber-to-matrix moduli ratios. Increasing the ratio to 10000 would change the calculated maximum thickness by less than one percent.

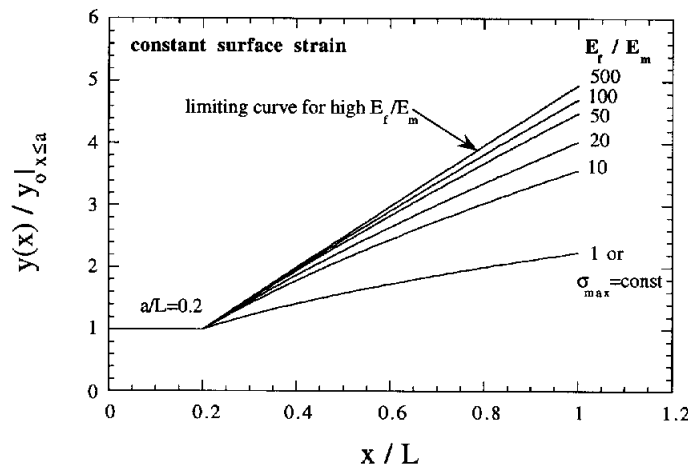


Fig. 4: Beam profiles for constant surface stress or strain. The ratio of fiber to matrix modulus is indicated on the graph.

In the second case, the gradient beam is analyzed by simple beam theory for layered beams. The beam's length is divided into segments of constant sectional properties:

$$(EI)_{eq}^j = \sum_i E_i b \left[(t_i^j)^3 / 12 + t_i^j (\bar{y}_i^j)^2 \right] \quad (13)$$

where t_i^j is thickness and \bar{y}_i^j the distance from the beam's neutral plane of layer i in segment j . For given layer properties, the thickness of the layers in each segment are calculated iteratively to obtain a constant surface stress along the beam's length and a desired flexural compliance, calculated by Eqn (11).

EXPERIMENTAL

The cantilever beams tested in the present study were made of a unidirectional pitch-based CFRP prepreg (Nippon Steel Corporation, Japan), and an epoxy adhesive film (Toho Cytec, Japan). The processed CFRP prepreg had a thickness of about 0.18 ± 0.02 mm, a longitudinal modulus of 200 GPa, and a relative density of 1.64. Its strength, measured from bending tests, was 965 MPa. The epoxy film contained an approximately 10% volume fraction of woven glass fiber carrier fabric. Its average thickness was 0.075 mm, with an in-plane modulus of 8 GPa and a relative density of 1.35.

Various beam geometries, described in Table 1 and Fig. 5, were investigated. The effective fiber volume fraction in a cross-section was varied along the beam's length by inserting the adhesive film between the prepregs. The adhesive film layers were evenly distributed between the prepreg plies through the thickness of the beam. Short beam samples of constant thickness, with one layer of epoxy film at their midplane were tested in three-point bending with a span to depth ratio of 10 to determine the strength of the bond between the prepregs and adhesive film. As none of the samples failed in the adhesive or the interface, the bond was considered to be strong enough not to form a detrimentally weak plane. Finally, samples with varying thicknesses, and in particular samples designed for constant surface stress or strain, were tested and compared to the values for constant cross-section, all-CFRP beams.

Table 1: Sample description

Sample ID	Description
C	Only CFRP
I	Constant thickness CFRP, 0.075mm interlayer at mid-plane
G2	Layered beam, reduced surface stress
G3	Layered beam, constant surface stress (& strain)

The composite was laid up by hand in 125mm x 250mm plates with the fiber direction along the long axis of the plate. It was then cured in an autoclave at 140°C and 5 bar for 60min, with a heating rate of 2°C/min and slow cooling. As the plates were cured on a flat plate half-tool, they had one flat and one convex face. The cured plates were cut into 15mm wide beams with the fibers parallel to the long axis of the beam. Half beams were used for the cantilever tests, with a clamping length of 15mm, while three-point bending tests were conducted on the whole beam. The final fiber distribution through the thickness of the beams was determined from optical micrographs of the polished beam edges. The measured values were then used to back-calculate the processed beam's stiffness and stresses using the multilayered beam model.

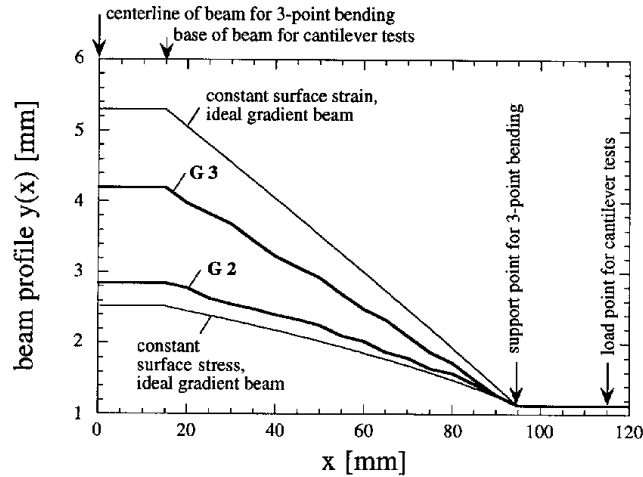


Fig. 5: Profile of multilayered gradient beams G2 and G3. The profiles of ideal gradient beams for constant surface stress or strain are also shown.

The gradient beams were tested statically as a cantilever and in three-point bending. The bending stiffness, the load at first damage, the maximum load, and the residual bearing capacity after failure were obtained from quasistatic tests on an Instron load frame, at a tip deflection rate of 2mm/min. The quasistatic test were run with the flat face on the compression, as well as on the tension side of the beam. The load-deflection curve was recorded for all tests, and the strain was measured at five points on the G3 gradient beam using strain gauges.

RESULTS AND DISCUSSION

Table 2: Cantilever test results for the G2 and G3 beams, L=100mm. Calculated values, in parentheses, are given for constant cross section and constant surface stress all-CFRP beams having the same stiffnesses as the gradient beams.

Beam ID	Thickness [mm]	Mass M [g]	P / δ [N/mm]	(P/δ)/M [N/mm/g]	P _{max} [N]
G2	2.85 / 1.13 *	4.12	5.24 (5.38)	1.27	56 (99)
Const section	(1.91)	(4.70)	5.24	(1.11)	(88)
Const surf. stress	(2.37 / 1.06) *	(4.06)	5.24	(1.29)	(68)
G3	4.20 / 1.13 *	4.78	10.1 (9.09)	2.11	91 (149)
Const section	(2.38)	(5.85)	10.1	(1.73)	(137)
Const surf. stress	(2.95 / 1.32) *	(5.06)	10.1	(2.00)	(105)

*Max / min thickness

The bending stiffness and maximum load capacity of the gradient beams loaded as cantilevers with a length of 100mm are reported in Table 2. They are compared to the calculated values for all-CFRP beams with the same bending stiffness but a uniform fiber content and of constant cross-section or designed for a constant surface stress. The bending stiffness of the beams is also given normalized by the mass of the beams. The expected maximum load was calculated based on the measured bending strength of the CFRP (965MPa) and the maximum stress at the beam's surface. Both gradient beams have the lowest or close to the lowest mass, and the highest strength per unit mass for a given stiffness. For a stiffness-based design, they thus represent a more weight-effective solution, and further use less carbon fiber

reinforcement fiber. The constant-section beam, although it has a slightly higher expected strength than the all-CFRP beam with a constant surface stress, has a significantly higher mass.

The results of the instrumented cantilever test for beam G3, with five strain gauges on both the compression and tension sides of the beam, are given in Fig. 6. The graph shows the calculated and measured axial stress as a function of position along the surface of beam. As the surface layer consisted of CFRP throughout, this also corresponds to the strain distribution. The measured stresses correspond adequately to the calculated values. Also shown is the linear stress distribution expected for a constant section beam with the same bending stiffness. The maximum stress in the latter is slightly higher than for the gradient beam, and the strength, assuming tensile failure of the surface CFRP layer, is thus correspondingly lower (Table 2).

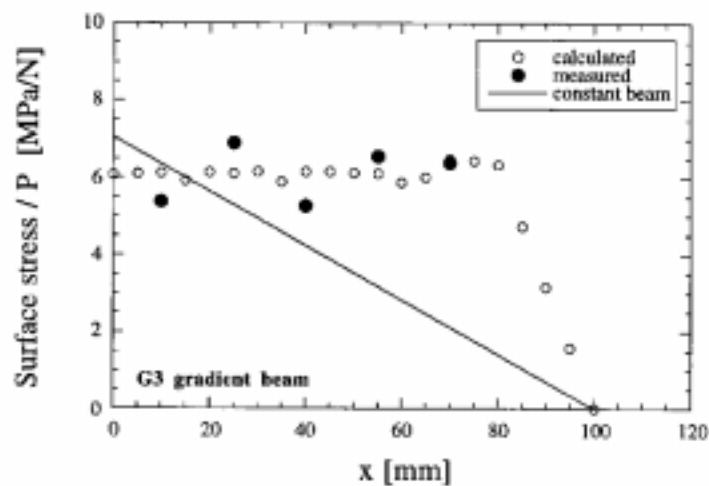


Fig. 6: Strain as a function of position at the surface of gradient beam G3.

Table 3: Three-point bending test results, $L=190\text{mm}$. Calculated values, in parentheses, are given for constant section and constant surface stress all-CFRP beams with the same stiffness.

Beam ID	Thickness [mm]	Mass M [g]	P / δ [N/mm]	$(P / \delta) / M$ [N/mm/g]	P_{\max} [N]
G2	2.85/1.13 *	9.02	15.15 (15.63)	1.68	160 (214)
Const section	(2.05)	(9.58)	15.15	(1.58)	(213)
G3	4.20/1.13 *	11.16	28.57 (30.30)	2.56	235 (334)
Const section	(2.54)	(11.86)	28.57	(2.41)	(328)

*Max / min thickness

The bending stiffness and maximum load capacity of the gradient beams loaded in three-point bending with a span of 190mm are reported in Table 3. They are compared to the calculated values for beams of same stiffness but with a constant fiber content and cross-section. In this test configuration, the gradient beams did not have the constant section tip like the cantilever. As the design for constant surface stress holds only for a given tip length a , the G3 beam does not have a constant surface stress for this test geometry. However, in this case as well, the gradient beams have a lower mass and equivalent predicted strength for a given beam stiffness.

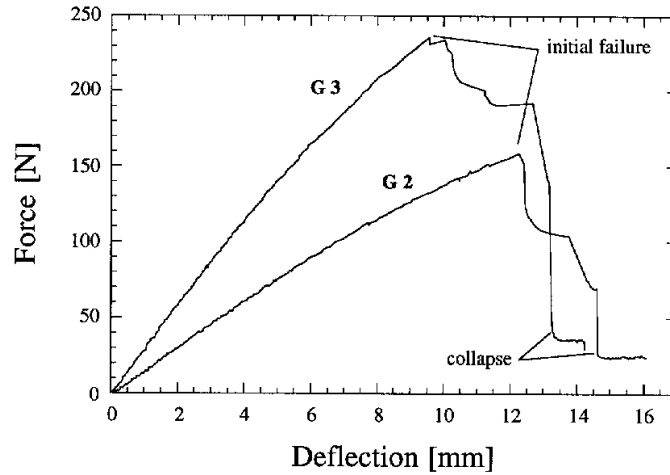


Fig. 7: Force-deflection curves for gradient beam samples G2 and G3 under 3-point bending, span=190mm.

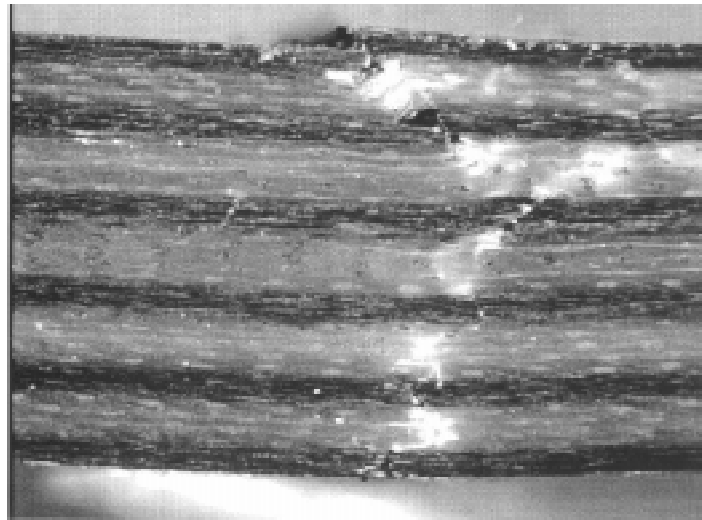


Fig. 8: Fracture through the thickness of gradient beam G3, three-point bending test. The load application point is slightly left of the failed area. The dark layers are the CFRP lamina, the light ones are the adhesive film.

Constant-section CFRP beams, tested in three-point bending at various spans ranging from 16mm to 100mm, all collapsed suddenly as a result of tensile failure of the CFRP at mid-span. The gradient beams, on the other hand, had a more gradual failure (Fig. 7). For beam G2, a more or less simultaneous damage of the resin layers and tensile failure of the CFRP were observed, although the former very likely preceded the latter. On the other hand, the first evidence of damage was clearly observed in the resin layers in beam G3. This damage developed in steps through successive layers (Fig. 8), starting with the topmost, compressively stressed layer. This was followed, after extensive damage leading to a reduction of the bending stiffness, to a tensile failure of the CFRP and final collapse of the beam. As the damage leading to failure started in the resin layers, the gradient beams did not reach the maximum expected load calculated on the assumption of a tensile failure of the CFRP. The ductility of the gradient beams was calculated as the area under the load-deflection curve from the initial failure to collapse divided by the area before failure, and is

expressed in percent in Table 4. It is highest for the G3 beam, which has the highest resin content in the highly stressed zones close to the surface of the beam.

Table 4: Post-failure behavior, three-point bending test results, $L=190\text{mm}$. Calculated values are given for a constant cross section all-CFRP beams having the same stiffnesses as the gradient beams.

Beam ID	P_{\max} [N]	Residual load [N]	Res. load [% P_{\max}]	Ductility [%]
G2	160	103	64%	20
Const section	(213)	--		< 10
G3	235	193	82%	58
Const section	(328)	--		< 10

Introducing layers of epoxy increased the damping of the beams, even for the constant thickness, all-CFRP beam with a single 0.075mm layer at the midplane. This results from the higher damping of the epoxy film compared to the CFRP. The first mode loss coefficient of the gradient beams, which contained a much larger proportion of epoxy interlayers, was five to six times higher than that of the all-CFRP beams. This agrees with previous findings [5, 6] that improved damping is obtained through the use of low-stiffness interlayers in CFRP.

Table 5: Vibration frequencies and damping of gradient and constant cross section all-CFRP cantilevers, $L=100\text{mm}$. Calculated values in parentheses are obtained by Raleigh's method.

Beam ID	1st mode freqs [Hz]	1st mode loss factor[%]
C	196 (230)	0.18
I	176 (216)	0.20
G2	338 (466)	1.13
Const section	(341)	--
G3	499 (646)	0.90
Const section	(425)	--

Overall, the static and dynamic performance of CFRP beams is improved by the use of a material gradient. By adapting the stiffness of the beam to the load by increasing the content of lower density and lower cost resin, a beam of a desired stiffness is made lighter and with an equivalent strength using a smaller amount of composite prepreg. Furthermore, as the material distribution in the beam is changed gradually, there are no deleterious stress concentrations that could lead to failures related to delaminations, as is the case with ply drops in all-composite beams. The next step is to improve the performance of the beams investigated here by achieving a true material gradient without property jump at the CFRP/resin layer interface.

CONCLUSIONS

The design and behavior of gradient CFRP flexural beams have been investigated. The design equations are presented for an ideal gradient beam, with a uniform fiber distribution in cross-sections along the length, and for a layered beam. The latter is a practical approximation to a true gradient beam, and was produced and tested in this work. This type of beam has demonstrated good performance in terms of low mass and equivalent strength for a given bending stiffness. The gradient beam designed for constant surface stress weighed less than all-composite beams with the same stiffness and had the highest bending stiffness and strength per unit of mass of all beams examined. It failed in a more ductile manner than

the constant-section CFRP beams, and had an improved vibration damping. The behavior of the gradient beams is predicted accurately by the multilayered beam model.

REFERENCES

1. Markworth, A.J., Ramesh, K.S., Parks, W.P., Modelling studies applied to functionally graded materials, *Journal of Materials Science*, Vol. 30, 1995, pp. 2183-2193.
2. Choe, C.R., Park, M., Functionally gradient type of polymer composites, *Proc. of the 5th Symp. of Interfacial Materials Science (SIMS-V)*, Fukuoka, Japan, 1996, pp. 262-265.
3. Amada, S., Munekata, T., Nagase, Y., Ichikawa, Y., Kirigai, A., and Zhifei, Y., The mechanical structures of bamboos in viewpoint of functionally gradient and composite materials, *Journal of Composite Materials*, Vol. 30, 1996, pp. 800-819.
4. Botting, A.D., Vizzini, A.J., Lee, S.W., Effect of ply-drop configuration on delamination strength of tapered composite structures, *AIAA Journal*, Vol. 34, pp. 1650-1656, 1996.
5. Fujimoto, J., Tamura, T., Kimpara, I., Tanimoto, T., Damping properties under flexural vibration for CFRP/damping material laminates, *Journal of the Japan Society for Composite Materials*, Vol. 20, pp. 144-153, 1994.
6. Liao, F.-S., Su, A.-C., Hsu, T.-C., Vibration damping of interleaved carbon fiber-epoxy composite beams, *Journal of Composite Materials*, Vol. 28, pp. 1840-54, 1994.

DESIGN OF IMPACT DAMAGE TOLERANT COMPOSITE LAMINATES

Chen Puhui¹, Liu Junshi¹, Shen Zhen¹, Yang Xu²

¹ Aircraft Strength Research Institute, P. O. Box 86, Xian, Shaanxi 710065, P. R. China

² Aircraft Design Institute, P. O. Box 725, Shenyang, Liaoning 110035, P. R. China

SUMMARY: In this paper, the effect of laminate stacking sequence on compression strength after impact of a T300/5405(BMI) composite were studied. Failure stresses and strains as a function of stacking sequence are governed by three parameters defined by effective elastic moduli. The optimisation of these three parameters is very useful to damage tolerant composite laminate design. Moreover, a high in-plane shear modulus skin concept is proposed. It is more reasonable than the so-called low stiffness skin concept for damage tolerant composite stiffened panel design. The $\pm 45^\circ$ kevlar and glass fibre plies coated on carbon fibre reinforced laminates can offer superior impact resistance and raise compression strength after impact.

KEYWORDS: impact damage, impact resistance, compression strength after impact, in-plane stress concentration, in-plane shear modulus, impact damage tolerance design

INTRODUCTION

Composite materials subjected to impact may suffer a significant loss in compression strength. Impact damage arises on composite aircraft structures due to dropped loads and runway debris etc. In order to overcome impact threat and to provide composite aircraft structural integrity, the impact damage tolerance aspect must be introduced into the initial sizing criteria during structural layout, i.e. the method to determine required thickness and lay-ups [1]. At present, only the limited amount of work has concentrated on effect of laminate stacking sequence on impact resistance and, especially compression strength after impact (CAI).

In this paper, a systematic study was conducted on above mentioned issues for a carbon fibre/BMI composite.

EXPERIMENTAL

Material

A carbon fibre/BMI T300/5405 composite was used in this study. Laminates of 4 different number of plies (15-, 35-, 37-, and 53-ply), 31 different lay-ups of 0° -, $\pm 45^\circ$ -, 90° -plies were tested and evaluated, including fifteen 15-ply, fifteen 35-ply, two 37-ply and one 53-ply laminates denoted by [x% 0° : y% $\pm 45^\circ$: z% 90°]. Among these, two 37-ply laminates are

identical to a 35-ply laminate with a lay-up of [30:60:10] coated respectively with $\pm 45^\circ$ kevlar fibre plies and glass fibre plies.

Impact Tests

Specimens were impacted by a free-falling steel impactor with a hemispherical end of 1-inch-diameter. The specimens of 15-, 35- and 53-ply were impacted with energy of 14J, 47J and 93J. Since two 37-ply laminates have different thickness, their values of impact energy were respectively 58.6J and 56.1J which were calculated from energy per unit thickness of the 35-ply laminate. During impact, the specimens were clamped between two steel plates with a central rectangular opening whose centre was aligned with those of the specimens and the impactor. The impactor was captured after impact to prevent secondary strikes. After impact the specimens were inspected by a penetrant enhanced X-radiography. Dent depths were measured with a micrometer.

Compression Tests

Compression test fixture includes upper and lower load introduction devices and anti-buckling guides. The load introduction devices are similar to those of NASA RP 1142. Two stiffened thin steel plates with a central opening of 60 mm diameter were designed to prevent global buckling of the specimens. They are very effective for compression tests of thinner specimens. In order to reduce the friction between the anti-buckling plates and the specimens, their contact surfaces were separated with Teflon.

RESULTS AND ANALYSIS

Compressive Failure Stresses and Strains after Impact

Laminates with Constant Percentages of $\pm 45^\circ$ -Plies

Figure 1 displays trends of failure stresses and strains as a function of 0° -ply share for impacted 15- and 35-ply laminates. The failure stress increases with the increase of the percentage of 0° -plies. The failure strain in figures 1(a) and 1(c) initially decreases and then increases, i.e. exhibits concave curves. While the failure strain in figures 1(b) and 1(d) monotonically decreases as the percentage of 0° -plies increases. The two concave curves are due to high failure strains of the two laminates corresponding to the last points in figures 1(a) and 1(c). Measured data shows these two laminates have much smaller dent depths than others, indicating a very small number of fibre breakages in them. The high strains may be caused by very small dent depths of the two laminates. If damage sizes of these two laminates were identical to those of other laminates in figure 1, a drop in failure strain would be expected to be significant, yielding monotonically decreasing trends. This will be further discussed later.

Laminates with Constant Percentages of 0° -Plies

Figure 2 displays trends of failure stresses and strains as a function of $\pm 45^\circ$ -ply share for impacted 15- and 35-ply laminates. Both failure stress and strain increase as the percentage of $\pm 45^\circ$ -plies increases.

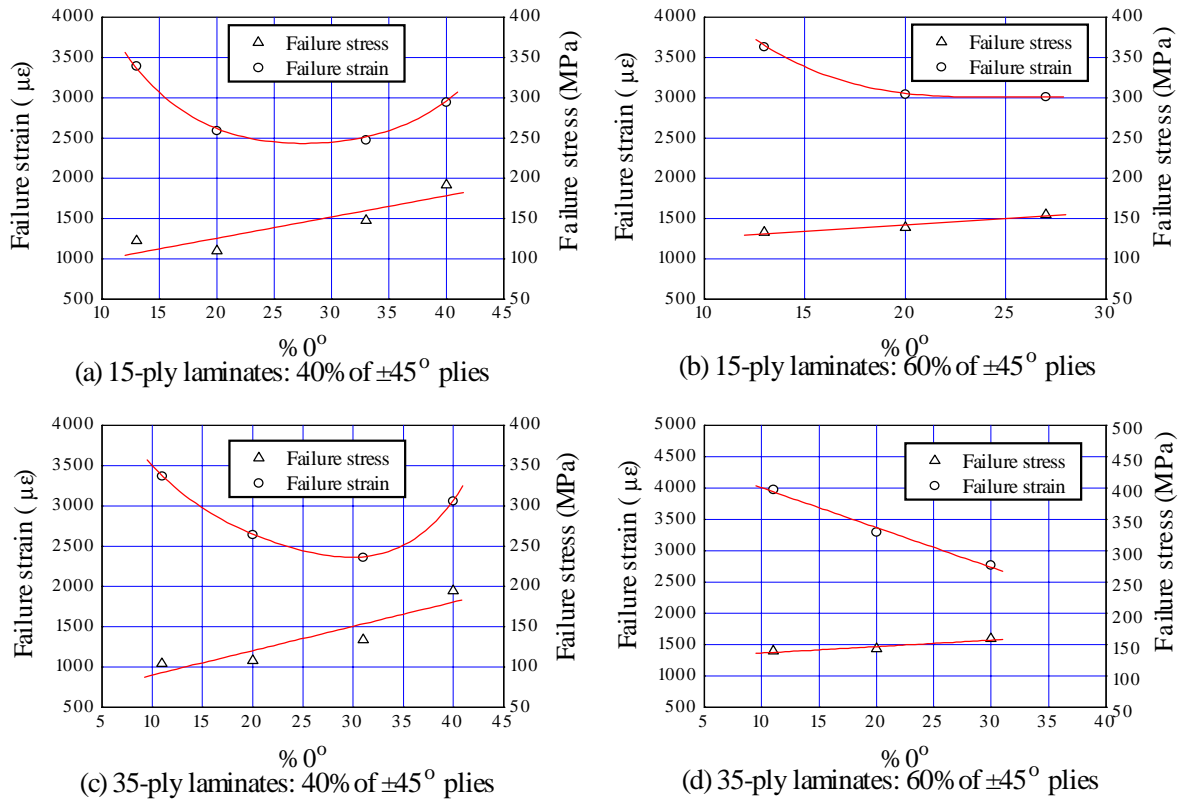


Fig. 1 Failure stress and strain vs % 0° of laminates with constant % $\pm 45^\circ$

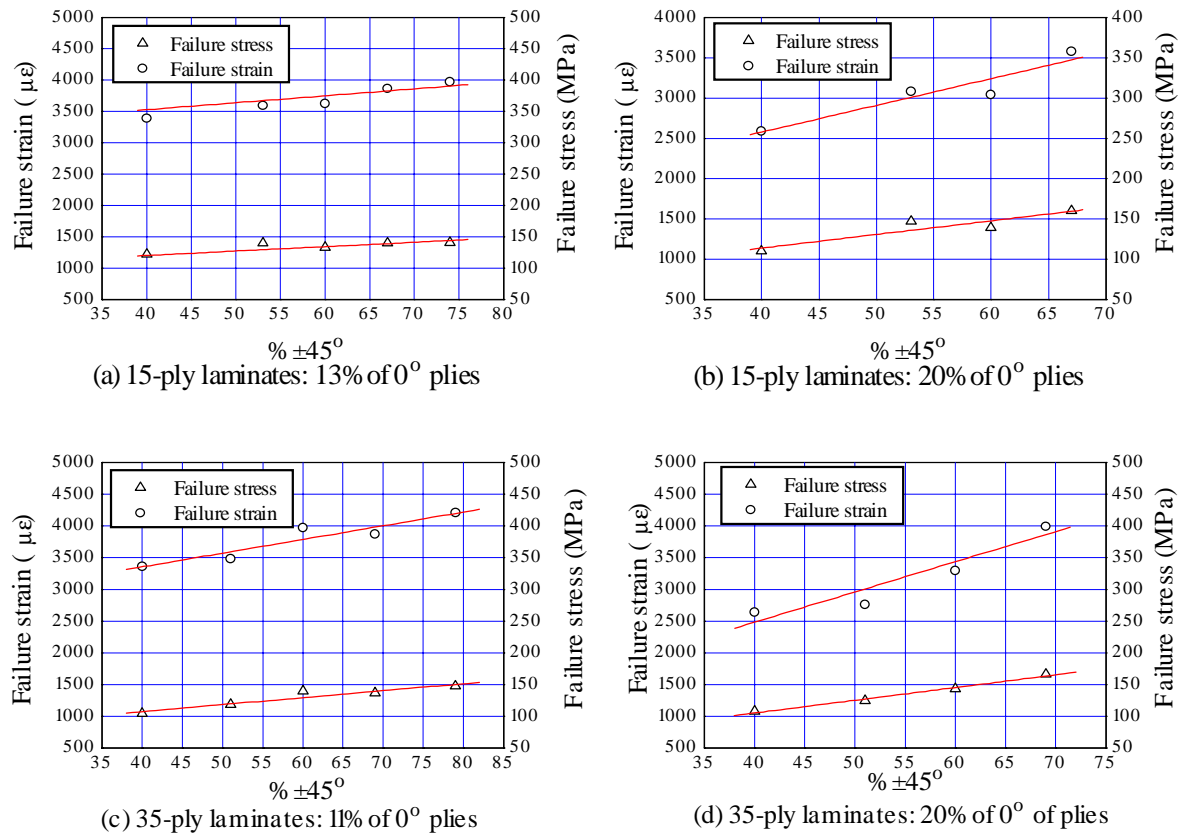


Fig. 2 Failure stress and strain vs % $\pm 45^\circ$ of laminates with constant % 0°

Laminates with Constant Percentages of 90° Plies

Figure 3 shows trends of failure stress and strain as a function of ±45° -ply share for impacted 15- and 35-ply laminates. As the percentage of ±45° -plies increases, the failure stress increases while the failure strain decreases.

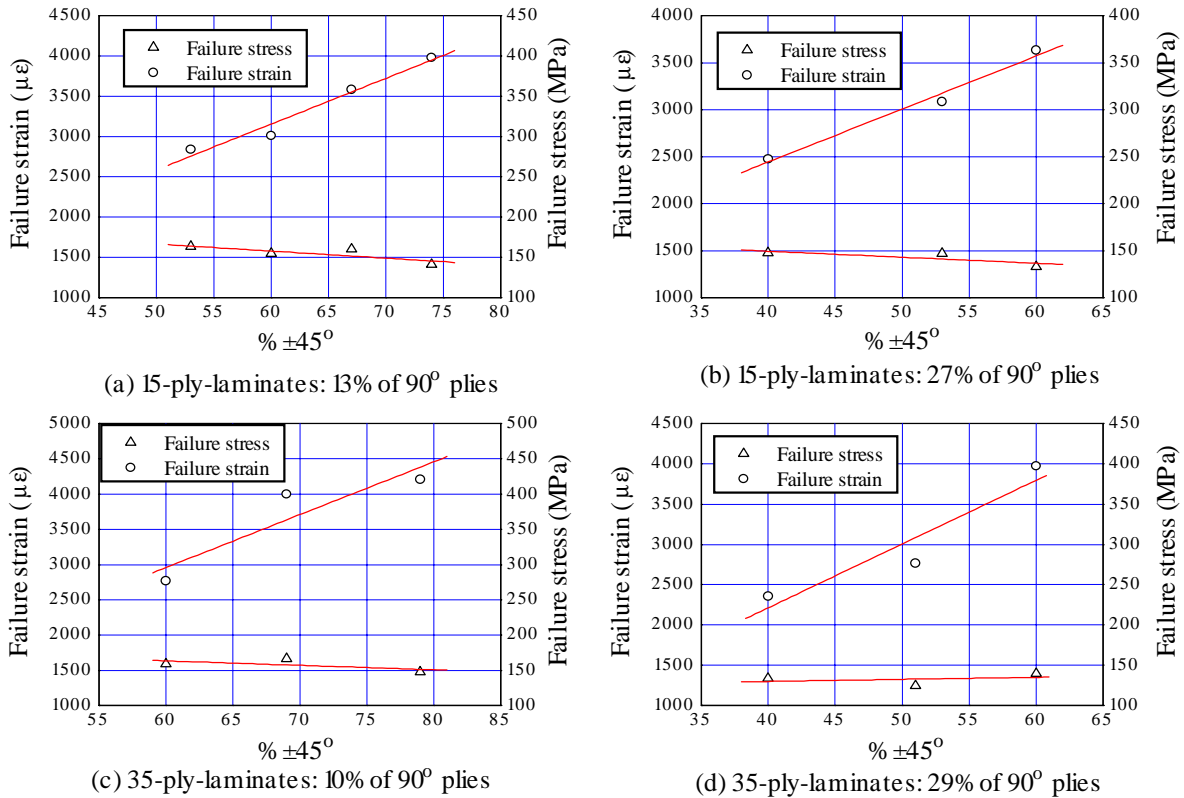


Fig. 3 Failure stress and strain vs %± 45° of laminates with constant % 90°

Governing Factors of Compression Strength after Impact

Stress Concentrations Due to Impact Damage

The failure strength of a damaged laminate strongly depends on damage induced stress concentrations. As well known, the stress concentration due to holes in orthotropic materials depends on their elastic constants. For example, a central hole in a infinite width orthotropic laminate generates a stress concentration [2] of

$$K_t = 1 + \sqrt{2 \left(\sqrt{\frac{E_y}{E_x} - \nu_{yx}} + \frac{E_y}{2G_{xy}} \right)}$$

where E_y , E_x , G_{xy} and ν_{yx} are the effective laminate normal moduli, shear modulus and Poisson's ratio, respectively, and the respective y and x are parallel and transverse to the loading direction.

In-plane and out-of-plane stresses redistribute around impact damage due to changes in local stiffness which may occur due to fibre failure and/or sublaminar instability. It is believed that the stress concentration is a key factor affecting compression strength after impact of a laminate [3].

The stress concentration type which is dominant for impacted laminate failure must be identified. It can be done with an understanding of compression failure modes of impacted laminates, i.e. separating the critical growth modes from those that occur as a consequence of laminate failure [4]. Extensive experimental work on damage response and growth modes during compression tests of impacted laminates indicated that, both brittle and tough materials exhibit delamination growth at time very close to the final failure. In other words, the delamination growth and the final failure are nearly simultaneous. Moreover, observations show that the delamination growth only occurs near the non-impacted surface of a laminate. The delamination growth near the impacted surface of the laminate is a consequence of the final failure. It seems to be that the delamination growth near the non-impacted surface has no ability to cause the final failure of the laminate. Experimental observations show that the final failure is dominated by local post-buckling of all sublaminae as a whole. This kind of post-buckling effectively reduces local stiffness, which increases the in-plane stress concentration. As the in-plane stress concentration is increased to a critical value, it leads to the failure of the laminate. In addition, post-failure patterns of impacted laminates show a typical shear-crippling failure mode except two buckled surface sublaminae. This further verifies the governing role of the in-plane stress concentration in compression failure of impacted laminates.

The serious fibre failure can largely change the local stiffness and causes a significant increase of the in-plane stress concentration. Consequently the compression strength after impact is largely reduced by the serious fibre failure. Evidently, the major cause of the concave curves in figures 1(a) and 1(c) are the very low extent of fibre failure in the two laminates corresponding to the last points in figures 1(a) and 1(c). The impact induced fibre failure has a large effect on the compression strength after impact.

Characterisation of Compressive Failure Stresses and Strains after Impact

As is the case for holes, one can link compression strength after impact with the in-plane stress concentration or elastic modulus. It may be an effective way to get a deep insight into the influence of lay-ups on compression strength after impact. Insight gained from the stress concentration formula of holes leads to an attempt of correlating three parameters

$$\alpha_1 = \sqrt{\frac{E_y}{E_x} - \nu_{yx}} + \frac{E_y}{2G_{xy}}$$

$$\alpha_2 = \frac{E_y}{E_x}$$

$$\alpha_3 = G_{xy}$$

with compression stresses and strains after impact.

Figure 4 shows the failure strain versus the parameter α_1 for all the 15- and 35-ply laminates respectively. It is seen that the failure strain increases as α_1 decreases. But the failure stress is not uniformly consistent with α_1 . It strongly depends on the parameter α_2 . The higher the modulus of elasticity in the loading direction compared to that transverse to it, the higher is the failure stress, as shown in figure 5. But the failure strain can not be characterised by α_2 .

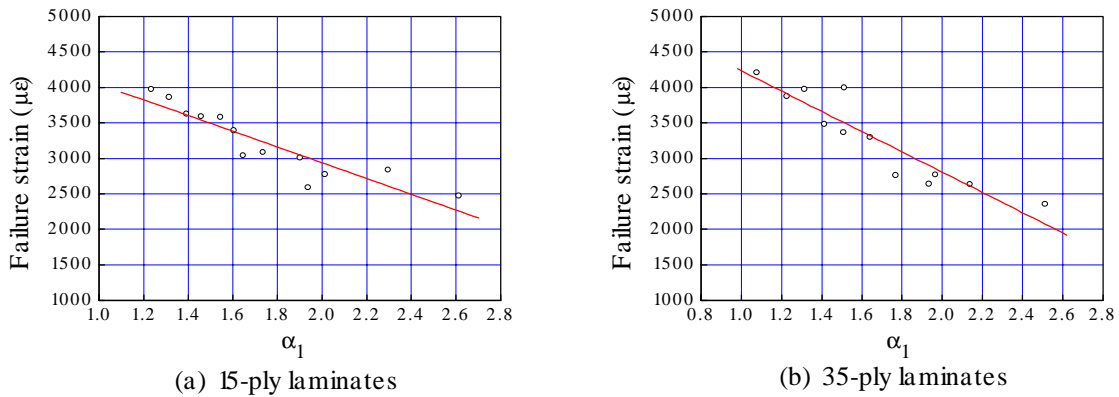


Fig. 4 Failure strain vs parameter α_1

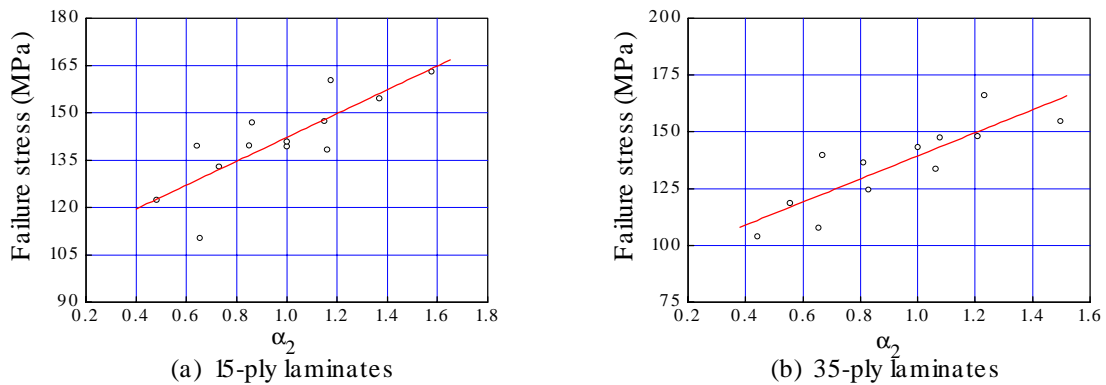


Fig. 5 Failure stress vs parameter α_2

As was indicated above, in the case of constant percentages of 90° - or 0° -plies, the failure strain increases with the increase of $\pm 45^\circ$ -ply share. By linking the failure strain with the stiffness in the loading direction, it is found that, in the case of constant percentage of 90° -plies, the failure strain increases with the decrease of the stiffness in the loading direction. This forms a base of the so-called ‘low stiffness skin’ concept for design of impact damage tolerant composite stiffened panels. In the case of constant percentage of 0° -plies, however, the stiffness in the loading direction is nearly unchangeable. In this case, one can not correlates the failure strain with stiffness in the loading direction. But in both cases, it is found that the failure strain increases with the increase of in-plane shear modulus, G_{xy} . Figure 6 is the trends of failure strain versus in-plane shear modulus, G_{xy} .

In the case of constant percentages of $\pm 45^\circ$ -plies, as the percentage of 0° -plies increases, the in-plane shear modulus is unchangeable while the stiffness in the loading direction increases. Therefore, the failure strain decreases with the increase of the stiffness in the loading direction.

Design of Impact Damage Tolerant Composite Laminates

The 'low stiffness skin' or 'soft skin' concept has been successfully used in design of the damage tolerant composite panels. This design incorporates a low stiffness skin with a predominance of $\pm 45^\circ$ -plies and a low percentage of 0° -plies. The low stiffness skin is damage tolerant to high strains. The primary axial load-carrying reinforcement, that is, 0° fibres, is concentrated at the stiffeners.

Based on the above discussion of the governing factors of compression strength after impact, a 'high in-plane shear modulus skin' concept is proposed. The new concept is more reasonable than the old one because a laminate with a higher in-plane shear modulus has higher ability to redistribute load from damaged to undamaged areas than a laminate with a lower shear modulus. $\pm 45^\circ$ -ply share is a key factor in design of impact damage tolerant stiffened panels of aircraft. Generally, a damage tolerant to high strain laminate can be achieved by increasing $\pm 45^\circ$ -ply share. But the laminate with a predominance of $\pm 45^\circ$ -plies and a low percentage of 0° -plies is damage tolerant to high strains but not to high stresses.

It should be emphasised that this approach is much less attractive for a skin which is a axial load-carrying element. For example, it is effective for a thick wing, but it is much less attractive for a thin wing, where it is more efficient to keep primary load-carrying material near the outer surface for great effectiveness in bending. Therefore, it is more attractive and desirable to design a laminate which is damage tolerant not only to high strains but also to high stresses. It can be done by choosing stacking sequences with low α_1 , high α_2 and high G_{xy} . Of course, there exists a match of these three parameters. For instance, among the laminates of this study, stacking sequences of [20:67:13] of 15-ply and [20:69:10] of 35-ply laminates satisfy the above requirement of low α_1 , high α_2 and high G_{xy} and are comparably damage tolerant to both high strains and stresses.

It should be noted that, in selection of the damage tolerant laminates, the requirement of low impact resistance should be considered. A combination of the low impact resistance and the above design method will leads to an excellent impact damage tolerant laminate design.

Impact Resistance and Compression Strength after Impact of Laminates Coated with $\pm 45^\circ$ Kevlar or Glass Fibre Plies

Two 37-ply laminates (denoted by L_k and L_g) are identical to the 35-ply laminate with a lay-up of [30:60:10] (denoted by L) coated respectively with $\pm 45^\circ$ kevlar fibre plies and glass fibre plies. Since these three laminates have different thickness, an identical impact energy per unit thickness was used, as mentioned above.

The $\pm 45^\circ$ kevlar and glass fibre plies coated on carbon fibre reinforced laminates greatly decrease impact induced fibre breakages and cause very small dents, as shown in figure 7. Therefore, the $\pm 45^\circ$ kevlar and glass fibre plies effectively improve the impact resistance of carbon fibre reinforced composites.

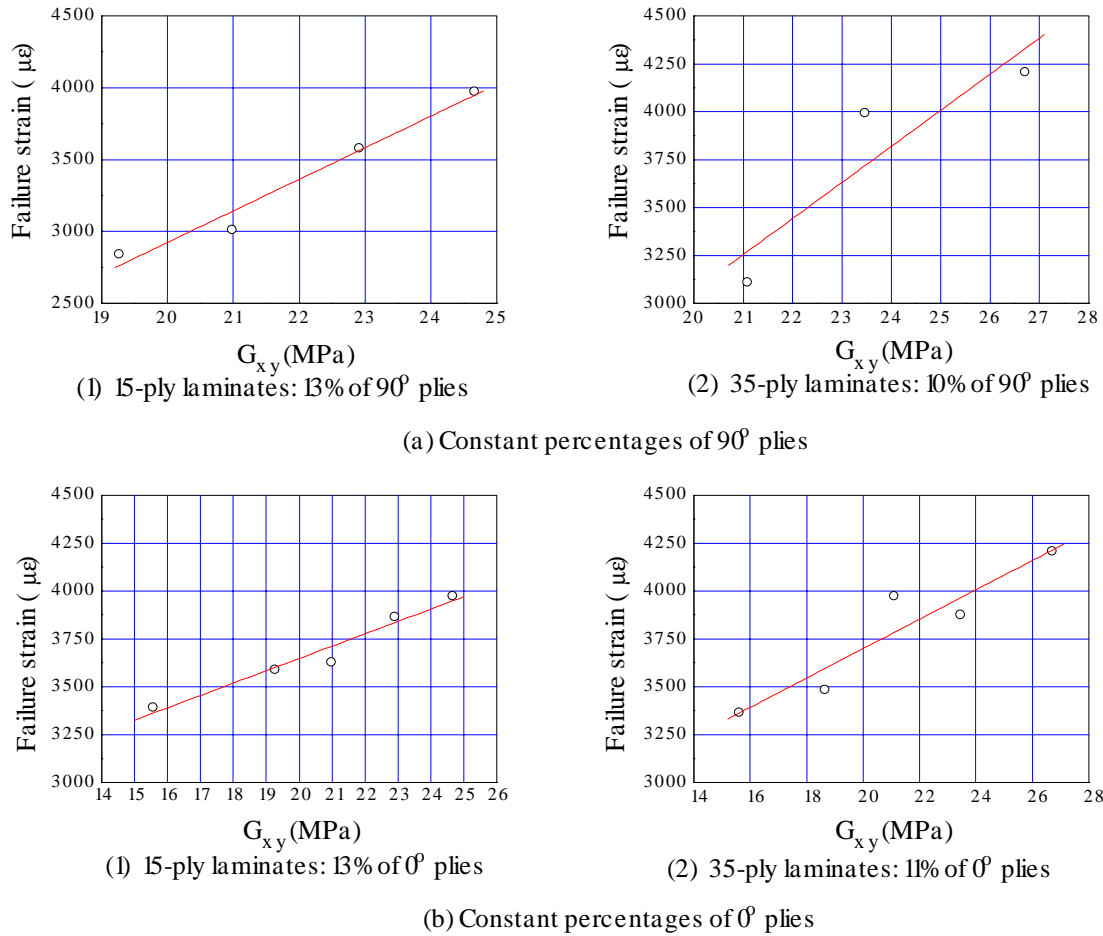


Fig. 6 Failure strain vs in-plane shear modulus G_{xy}

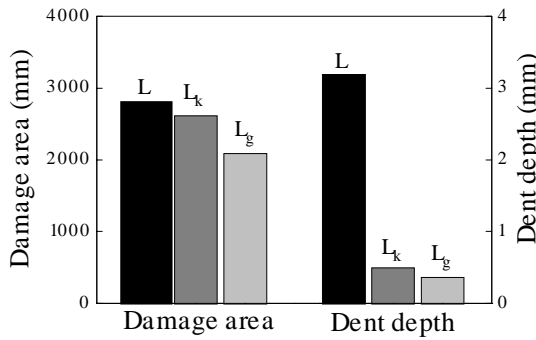


Fig. 7 Sizes of impact damage

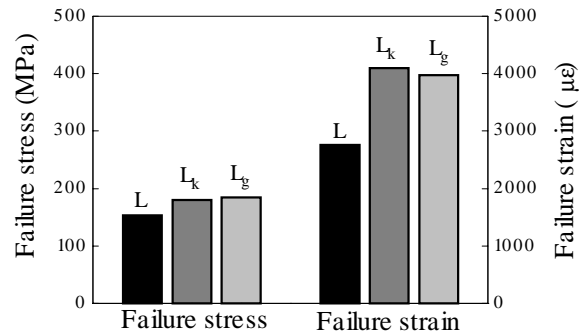


Fig. 8 Compression strength after impact

Due to very small dent depths of the two 37-ply laminates, they show much higher post-impact strengths than the 35-ply laminate, as show in figure 8. Since the test data shows no significant differences in damage areas, the high increase of the strength is obviously caused by the low extent of the fibre breakage. Because the fibre breakage can largely reduce the local stiffness and enhance the in-plane stress concentration, it strongly affects compression strength after impact.

Damage areas are commonly used to characterise impact damage while dent depths are hardly considered. Without analysis to link the dent depth with the impact damage, compression strength as a function of damage area may be misleading in some cases. The impact damage must be characterised by both damage area and dent depth.

CONCLUDING REMARKS

The most important conclusion drawn from the study is that the failure stress and strain after impact are strongly affected by the in-plane stress concentration and their trends as a function of lay-ups are governed by three parameters defined by effective elastic moduli. The optimisation of these three parameters is very useful to damage tolerant composite laminate design. A high in-plane shear modulus skin concept is proposed. It is more reasonable than the so-called low stiffness skin concept for damage tolerant composite stiffened panel design. The $\pm 45^\circ$ kevlar and glass fibre plies effectively improve the impact resistance of carbon fibre reinforced composites.

REFERENCES

1. J. Bauer, G. Günther and R. Neumeier, "Allowable compression strength for CFRP-components of fighter aircraft determined by CAI-test", AGARD Meeting, November 1992
2. Seng C. Tan, *Stress Concentrations in Laminated Composites*, Technomic Publishing Company, Inc., Lancaster, U. S. A.
3. I. Kröber, "Effect of impacts on CFRP Structures, Results of a Comprehensive Test Program for Practical Use", AGARD Meeting, November 1992
4. Larry B. Ilcewicz, Ernest F. Dost and Randy L. Coggeshall, "A model for compression after impact strength evaluation", *Proc. of 21st int.. SAMPE Tech. Conf.*, September 25-28, 1989

EFFECTS OF STACKING SEQUENCES ON THE HYDROELASTIC BEHAVIOR OF COMPOSITE PROPELLER BLADES

H. J. Lin¹ and J. J. Lin²

*Dept. of Naval Architecture and Ocean Engineering, National Taiwan University,
73, Chou-Shan Road, Taipei, Taiwan, R.O.C.*

SUMMARY: A finite element method coupled with analysis of a non-cavitating lifting surface was used to assess the performance of a composite marine propeller, including thrust, torque, efficiency coefficients and deflections. An MAU 3-60 propeller was analyzed with different stacking sequence of T300/1076E. The hydroelastic behavior of the propeller with balanced and unbalanced stacking sequences were investigated and discussed. Stacking sequences effects have been shown to influence the performance of composite propeller in region of low advanced coefficient, J.

INTRODUCTION

Hydrodynamic aspects of the design of a marine propeller attract attention for the purposes of predicting the deflection and strength of the propeller blade and increasing its efficiency. A procedure to calculate the blade strength must involve numerical methods because of the nonlinear phenomenon of the blade deflection and its loading. A geometrically non-linear calculation is needed to calculate the quasistatic deflection of the blade that results from the centrifugal force and the distribution of pressure in the fluid.

The first approach to solve the strength problem of the blade was proposed by Taylor[1], who considered a propeller blade to be a cantilever rigidly attached to a boss. The stresses were calculated with elementary beam theory using cylindrical blade sections having a straight face and a curved back. The cantilever beam theory yields reasonable estimates of stresses at certain selected points of relatively straight and narrow blades. Modified forms of this theory are proposed for a wide propeller blade, but limited knowledge of the structural response of the blade is available. The approach of shell theory was first proposed by Cohen[2], who considered a propeller blade to be a helicoid shell of variable thickness and infinite width. This approach was limited when applied to a blade of the finite width. Conolly[3] developed a thin-shell approach in parallel with an experimental program. This approach was demonstrated to be successful for a wide blade, but symmetrical forms and the assumption that the normal deflection of a section was invariant limited the application of the method. Moreover theories of shell type that incorporate broad assumption are involved for routine design work.

The reason to choose of the finite element method is its lack of any additional assumption about the behavior of the displacements. Genalis[4] used a triangular plane element and Atkinson[5] used a parabolic and curved element of a thick shell model to analyze the mathematically defined propeller. These results are compared with calculated and

experimental results presents by Conolly. The conclusion is that a thick-shell model is satisfactory to calculate the response of propeller blade. Ma[6] applied the isoparametric solid element model to analyze a highly skewed propeller the computed results are compared with measured deflections and stresses under a steady pressure . Sontvedt[7] applied a triangular thin-shell element to analyze moderately screwed and highly screwed propeller under hydrodynamic loading of frozen type . The calculated results of stresses and deflection are compared with experiments. Atkinson and Golver[8] applied a curved superparametric thick-shell element model to analyze three types of propellers. The surface loading was calculated according to a steady lifting surface analysis developed by Szantyr[9]. In this process, the surface pressure is first obtained on assuming that the structure is rigid and the resulting surface pressure is imposed on the structure to calculate the structural response. An iterative procedure is applied to calculate a new geometry of blade and to modify the surface loading. The process is repeated until a new stable condition is achieved. Thus this approach is applied in an uncoupled manner.

The developed procedure of the coupled fluid-structure analysis[10] was used in the evaluation of effects of stacking sequences on hydroelastic behavior of composite propeller blades. The geometrical non-linear finite element procedure for structural analysis and non-cavitating lifting surface theory for fluid analysis were considered. The Newton-Raphson procedure was used in the equation solver.

FLUID-STRUCTURE INTERACTION

The finite element equation for a geometrically non-linear three-dimensional degenerate shell element is written as

$$([K_o] + [K_L] + [K_G] - [K_R])\{u\} = \{F_{ext}\} + \{F_I\} + \{F_R\} = [K_T]\{u\} \quad (1)$$

in which $[K_o]$, $[K_L]$, $[K_G]$ and $[K_R]$ are the linear stiffness, initial displacement, geometric and rotational matrix, $\{u\}$ is the nodal displacement, $\{F_{ext}\}$ are the external forces excluding fluid forces $\{F_I\}$, $\{F_R\}$ are the centrifugal load.

The steady and noncavitating lifting surface analysis procedure used in the present work is that of Kerwin and Lee[11]. The strengths of the sources representing the blade thickness are pre-determined by a stripwise application of thin-wing theory at each radius, leaving only the vortex strengths to be determined. The horseshoe vortex strengths, Γ , on each blade can be expressed in terms of those on the key blade.

$$\sum_{j=1}^{(N \times M)} A_{ij} \Gamma_j = G(u) \Gamma_i = -\vec{n}_i \cdot (\vec{V}_\infty + \vec{V}_\Omega + \vec{V}_q^{source})_i = rhs(u) \quad i = 1, 2, \dots, N \times M \quad (2)$$

The forces of the fluid acting on the blades are expressed as:

$$F_I = \int_A N_s^T n N dA \cdot \{\Delta P\} = [B]\{\Gamma^{vortex}\} + \{C\} \quad (3)$$

In which, $[B]$ is the coupled matrix of interaction between fluid and structure, $[C]$ is the matrix determined from the distribution of the blade thickness of the blade that can be neglected if the thickness effects of the blades is ignored.

The finite-element equations (1) and (3) coupled with equation (2) is expressed as

$$\begin{bmatrix} K_T(u) & -B(u) \\ 0 & G(u) \end{bmatrix} \begin{Bmatrix} u \\ \Gamma \end{Bmatrix} = \begin{Bmatrix} F_R(u) + F_{ext} + C \\ rhs(u) \end{Bmatrix} \quad (4)$$

The Newton-Raphson method was used to solve these equations. Three convergence criteria was adopted in structural, the displacement, external forces and external work, and two in fluid, wake velocities just behind the trailing edge and the strength of the singularity, for every iteration.

NUMERICAL RESULTS AND DISCUSSION

An MAU 3-60 propeller was analyzed. The MAU 3-60 propeller has three blades as shown in Fig. 1. Its expansion ratio is 0.6, diameter D is 150 cm. Table 1 shows geometrical data of the MAU 3-60 propeller. The generation line of propeller blade is taken as the reference of fiber direction θ of composites. The fiber from root to the leading edge is positive. Two stacking sequences $[0/90/\theta_2]_s$ and $[0/90/-\theta_2]_s$ were considered. The number of layer was account for from middle surface to upper and lower surface of propeller blades. Thus different location has different number of layers.

Table 1: The geometric characteristics of MAU3-60 propeller

r /R	C/D	P/D	Skew	Rake/D	t /D	f /D
0.2	0.174	1.455	0.000	0.0	0.0434	0.0430
0.25	0.202	1.444	2.328	0.0	0.0396	0.0395
0.3	0.229	1.433	4.655	0.0	0.0358	0.0370
0.4	0.275	1.412	9.633	0.0	0.0294	0.0344
0.5	0.312	1.361	13.948	0.0	0.0240	0.0305
0.6	0.337	1.285	18.378	0.0	0.0191	0.0247
0.7	0.347	1.200	22.747	0.0	0.0146	0.0199
0.8	0.334	1.112	27.145	0.0	0.0105	0.0161
0.9	0.280	1.027	31.575	0.0	0.0067	0.0134
0.95	0.210	0.985	33.788	0.0	0.0048	0.0140
1.0	0.000	0.942	36.000	0.0	0.0029	-

Number of blades, 3; expended area ratio, 0.6; design advanced coefficient, 0.5.

The number of structural mesh is 12×12 and of the fluid mesh is 8×8 for every blade. The results appear in Fig 2 ~ 5, for thrust coefficient K_T , pitch ratio P/D and camber distribution C . General agreement between the present approach and PSF2 (Propeller Steady Flow) [11] analysis in the region of high advanced coefficient J ($J=V_a/nD$, V_a : advance velocity of ship, n : rotation speed of propeller), leads to the conclusion that the present nonlinear approach is satisfactory for calculating the response of a propeller blade. The stacking sequence effects on thrust are shown in Fig. 2. The thrust of composite propeller with stacking sequence of $[0/90/-\theta_2]_s$ are very close to the results of PSF2, in which a rigid structure is considered. Due to the stacking sequence effects, the thrust of composite propeller with $[0/90/\theta_2]_s$ are larger than those with $[0/90/-\theta_2]_s$ in region of low advanced coefficient. The larger of the angle θ , the higher the thrust increases. Fig. 3 and 4 show the variation of pitch ratio in different locations and different advanced coefficients. The pitch variation increases of blades with $[0/90/-\theta_2]_s$ and decreases with $[0/90/\theta_2]_s$. The higher of the pitch is, the larger the thrust. Therefore the phenomena of variation of pitch may use to describe the variation of thrust of composite blade with different stacking sequences. The camber of the blade dose not vary much in the blade, its maximal variation occurs near the tip of the blade. Hydroelastic effects have been shown to influence the performance of composite propeller and can improve the numerical results.

CONCLUSIONS

A geometrical non-linear finite element method coupled with analysis of a non-cavitating lifting surface was used to assess the performance of a composite marine propeller blades. The hydroelastic behavior of the propeller with unbalanced stacking sequences of $[0/90/\theta_2]_s$ and $[0/90/-\theta_2]_s$ were investigated and discussed. Stacking sequences effects have been shown to influence the thrust, pitch ratio and camber of composite propeller blades, especially, in region of low advanced coefficient.

ACKNOWLEDGMENTS

This work was supported by the National Science Council of the Republic of China, under the Grant No. NSC 85-2611-E-002-027.

REFERENCES

1. Taylor, D.W., "The Speed and Power of Ships", Inc., Washington, 1933.
2. Cohen, J.W., "On Stress Calculations in Helicoidal Shells and Propeller Blades", NRC report 215.
3. Conolly, J.E., "Strength of Propeller", RINA, Vol.103, 1974, pp.139-204.
4. Genalis, P., "Elastic Strength of Propellers - An Analysis by Matrix Methods", Ph.D.Thesis, University of Michigan, USA, 1970.
5. Atkinson, P., "On the Choice of Method for the Calculation of Stress in Marine Propeller", RINA, Vol.110, 1968, pp.447-463 ()
6. Ma, H., "Stresses in Marine Propellers", Journal of Ship Research, Vol.18, 1974, pp.252-264.
7. Sontvedt, T., "Propeller Blade Stresses, Application of Finite Element Methods", Computers and Structures, Vol.4, 1974, pp.193-204.
8. Atkinson, P. and Glover, E.J., "Propeller hydroelastic effects", SNAME on the propeller's '88 Symposium No.21, 1988.

9. Szantyr, J.A., "A New Method for the Analysis of Propeller Cavitation and Hull Surface Pressures", Trans. RINA, Vol.127, 1985, pp.153-167.
10. Lin, H.J. and Lin, J.J., "Nonlinear Hydroelastic Behavior of Propellers Using a Finite Element Method and Lifting Surface Theory", Journal of Marine Science and Technology, Vol.1, No.2, 1996, pp.114-124.
11. Kerwin, J.E. and Lee, C.S., "Prediction of Steady and Unsteady Marine Propeller Performance by Numerical Lifting-Surface Theory", SNAME, Vol.86, 1978, pp.218-253.

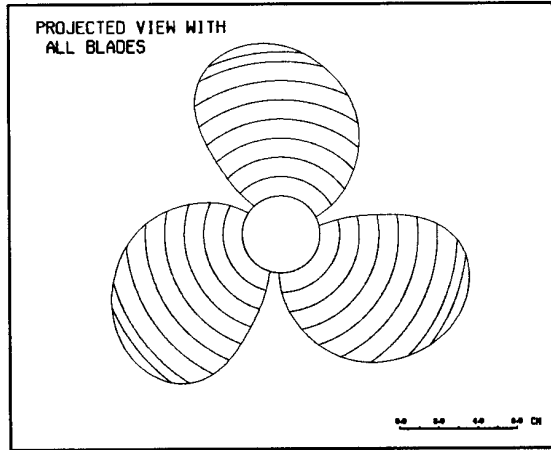


Figure 1: The projected view of MAU3-60 propeller

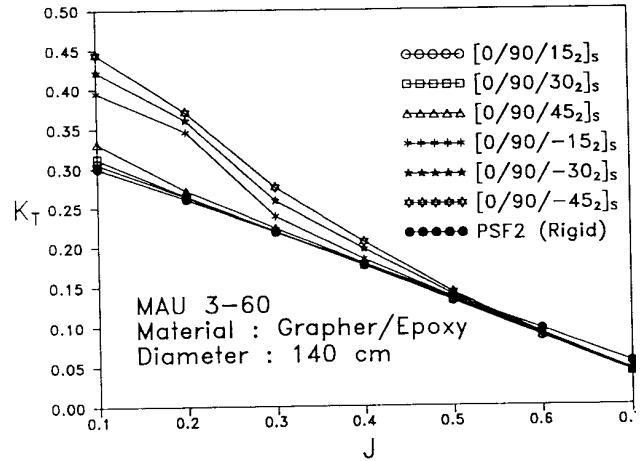


Figure 2: The thrust coefficient characteristics of the MAU3-60 propeller

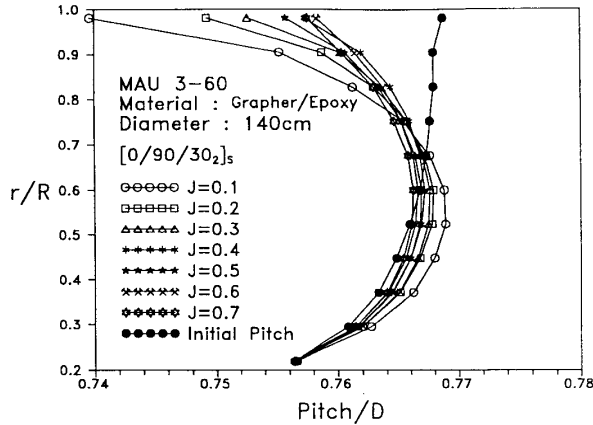


Figure 3: Pitch variation of blade with $[0/90/30_2]_s$

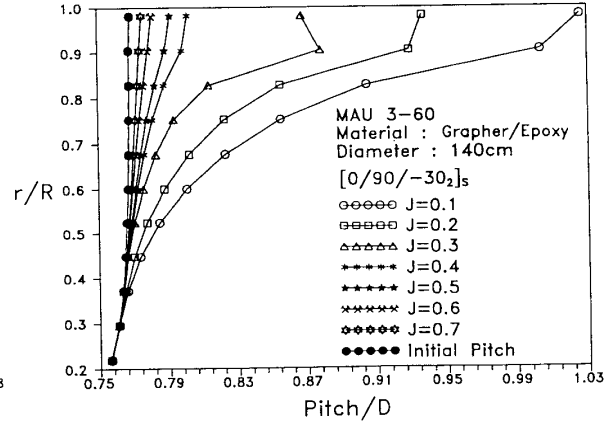


Figure 4: Pitch variation of blade with $[0/90/-30_2]_s$

PLYDROPS FOR TAPERED DESIGN OPTIMIZATION OF COMPOSITE PLATES

Phillippe M. Manne* and Stephen W. Tsai

*Department of Aeronautics & Astronautics,
Stanford University, Stanford, California 94305-4035, U.S.A.
manne@structure.stanford.edu - stsai@leland.stanford.edu*

SUMMARY: Design optimization of composite plates implies weight minimization. Maintaining concurrently easy manufacturability usually is conflicting. Plydrops are thus proposed to help design and fabricate simple low weight tapered plates. Sublaminates, made of multiple plies at various orientations, combining one or more materials, are repeated or dropped in different zones of the structure, yielding the plydrops taper while ensuring physical continuity of the fibers in all composite layers. The orientation and thickness of each ply group in this reference sublaminate as well as its number of repetitions in the zones across the structure are optimized. Plydrops appear very well suited for handling multi-purpose optimization; their influence on the toughness of laminates and on the pattern of the layups is also investigated.

KEYWORDS: plydrop, taper, sublaminate, optimization, manufacturability, strength, stiffness.

KEYWORDS: plydrop, taper, sublaminate, optimization, manufacturability, strength stiffness

Introduction

The weight of a composite structure is minimized by optimizing its layup and by tapering its thickness. Complex rules of design, often made without a rational basis, are frequently used and require intensive labor for manufacturing, the cost of which may outweigh the benefits of lightness. The number of ply angle and stacking sequence combinations limits the usefulness of unconstrained computer codes. Their output, if not very complicated and hence expensive to build, can simply not be manufacturable at all. It is quite common to end up with scores of oddly shaped and overlapping layers, resulting into fiber discontinuities and ply mismatches (Figure 1).

On the other hand, in current industrial practice, engineers tend to restrict their space of design variables so drastically that, although guaranteeing manufacturability, their product misses most of the advantages of composite materials, since approaching a not as light quasi-isotropic design.

To address these deficiencies and lower costs, a new approach is envisioned: low weight and easy manufacturing requirements must be combined. Adequately using plydrops can achieve this double objective. One has then to determine where and how many plies must be dropped or added as well as optimize their orientations. The total number of

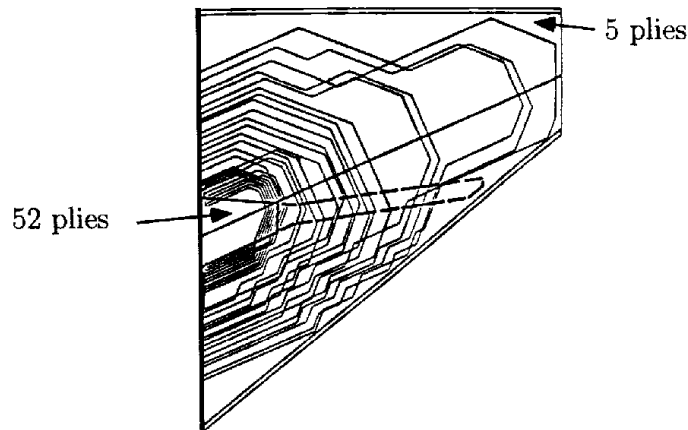


Figure 1: General Dynamics F-16 A/B. Plydrops in the horizontal stabilizer.

such plies provides then the taper, zone by zone. Simplifying even further, groups of plies are dropped simultaneously and along straight lines. Finally, using the same fibers in the same relative proportions and orientations everywhere solves many manufacturing problems.

Comprehensive details and extensions of the present article can be found in Manne & Tsai [1-3].

2 Manufacturing cost factors

The main cost factors [4] of a composite part are the cost of material, correlated with the weight of the part, and the cost of manufacturing, often quite significant and correlated with the complexity of the layout. The main manufacturing related items are :

- Templates. A conform copy of each layer is kept for shape inventory.
- Eyebrows. The complement of each template is used as positioning device. Laser positioning is however taking over nowadays.
- Tooling and cutting. More sophisticated tools are needed for curved edges.
- Debulking and bagging. A vacuum is applied after every few layers are laid up, for compaction. Overlapping and small cutouts tend to increase the quantity of voids.
- Mismatches. Positioning errors induce mismatches, wrinkles, gaps.
- Scrap. Sophisticated shapes incur lots of residue waste.
- Labor. Because of all these complications, most composite parts are still laid up by hand, which is very time consuming and expensive.
- Storage. Cumbersome inventories of plies, templates must be preserved at all times.

Cost factors are thus reduced by simplifying the final design, such as squaring plies down to four-sided quadrilaterals and limiting their quantity to avoid tiny components.

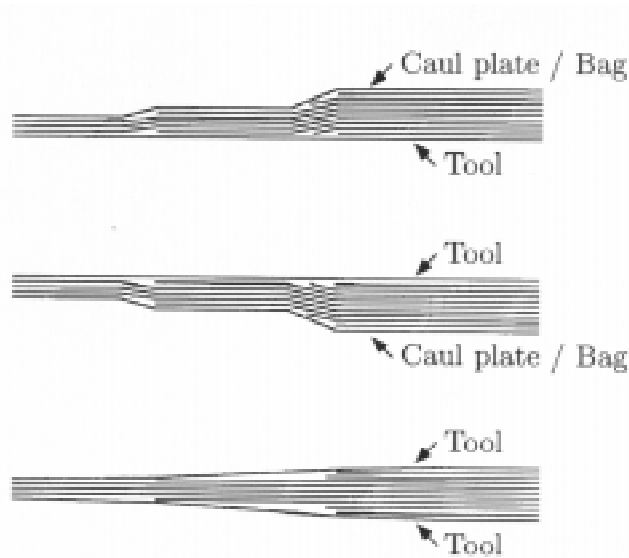


Figure 2: Examples of external plydrops (top, middle) and internal plydrops (bottom).

3 Plydrops

3.1 Tapered structures

Except in pressure vessels, thickness tapering is desirable since stresses tend to vary significantly within a structure. Tapering saves indeed weight by removing unnecessary material in low stress areas [5]; it also helps conforming to geometric shape requirements, such as those dictated by aerodynamics.

Tapering of metal structures is essentially done by removing material whereas tapering of composite structures is done by selectively building up material. Indeed, the external layer is first laid out on a mandrel or a mold, yielding a smooth surface. The remaining plies are laid up suitably, producing the desired thickness taper. Starting and stopping a ply is referred to as a *plydrop*. Several dropping schemes (Figure 2) [6] are possible: external (upper-side or lower-side) and internal (symmetric or unsymmetric).

A plydrop may consist in dropping a single ply or a group of plies, the latter being pursued here. In particular, a sublaminates is defined as a reference group of plies, to be either added or dropped as a whole.

3.2 Sublaminates

The laminate on the left in Figure 3 is made of nine plies of individual thickness h_0 , at three different orientations and sequenced as $[(\theta_1)_2/(\theta_2)_4/(\theta_3)_3]$. According to laminated plate theory [7], its mechanical behavior remains unchanged if identical adjacent plies are merged together, as in the laminate on the right in Figure 3 where the sequence is $[\theta_1/\theta_2/\theta_3]$ and the corresponding ply thicknesses are $2h_0$, $4h_0$, and $3h_0$. These consolidated plies are referred to as *superplies*. It follows from laminated plate theory that potentially critical stresses and strains are always extreme on the outer surfaces of the superplies, never at their internal ply interfaces. So, in the present case, only four interfaces must be

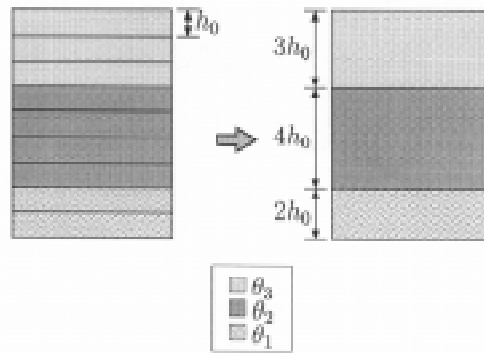


Figure 3: Sublaminate : stack of plies or superplies (group of identical individual plies).

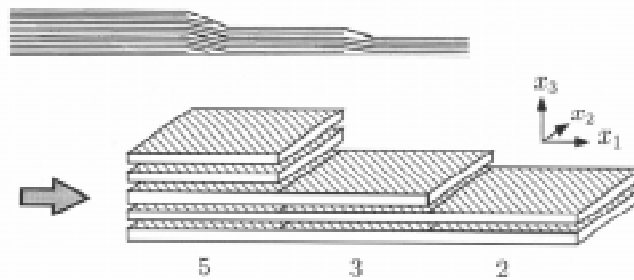


Figure 4: Plydrops by addition/subtraction of sublaminate. True aspect and corresponding F.E.M. model with 5,3,2 repeated sublaminate.

checked for failure instead of ten.

A reference stack of superplies is called a *sublaminate*. The sublaminate shown in Figure 3 is made of nine plies or three superplies. Finally, a sublaminate repeated a given number of times, forms a laminate.

3.3 Sublaminate plydrops

3.3.1 Description

The parts shown in Figures 1 and 2 feature general plydrops. No special repetitive pattern is involved: plies are dropped individually and anywhere in the structure.

Instead, we propose to repeat or drop entire sublaminate at once. In Figure 4, our sublaminate is repeated five times on the left, three times in the middle section and only twice on the right. In other words, the laminate successively drops from five to three to two sublaminate.

Besides, the structure is divided into a regular grid of design zones (Figure 5). Each zone is modeled as a four-sided quadrilateral, excluding automatically small cutouts and

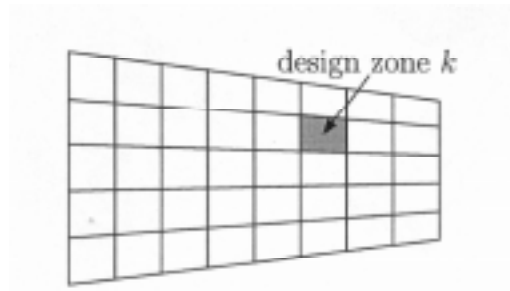


Figure 5: Division of a plate into a grid of design zones.

weird shapes. Cutting costs are thus again reduced, positioning of the layers becomes a less awkward task and fewer debulks are probably needed.

In conclusion, anywhere in the structure, the stacking sequence of the laminate is

$$\left(\left[(\theta_1)_{n_1}, \dots, (\theta_m)_{n_m} \right]_{r_k} \right)_s \quad (1)$$

where r_k stands for the *repetition factor* of the sublaminates in design zone k .

The staircase model (Figure 4, bottom) is an idealized Finite Elements model of the real smoothly staggered plydrops (Figure 4, top).

3.3.2 Features

Designing tapered structures by dropping sublaminates is fostered by the combined benefits of tapered structures and sublaminates repetitions. The main advantages of ply-drop tapering are lower weight, shape conformity, and a smooth surface contour by laying out the external ply on the mandrel or mold and building up layers inwards.

The design enhancements proper to repeated sublaminates are:

- Existence of a unique reference sublaminates throughout the structure, requiring much fewer design variables in the optimization process.
- Absence of fiber discontinuities within a layer: neither layup mismatches nor weakening internal butt-joints.
- Repetition homogenizes the global laminate properties by alternating ply sequences: lower interlaminar stresses increase toughness and hence delay delamination.
- Easier manufacturing process and lower production costs.

3.3.3 Secondary issues

A detailed design involving plydrops raises some secondary issues, which are irrelevant to the conclusions of a preliminary design process, limited to first ply failure [2, 8–11]:

- Stress concentrations at drop-off line. Beneficial influence of plydrop staggering. Local effects of the drop-off scheme (Figure 2): inside, outside, combined or middle drops.
- Drop-off steepness rate: how many plies can be dropped at once.

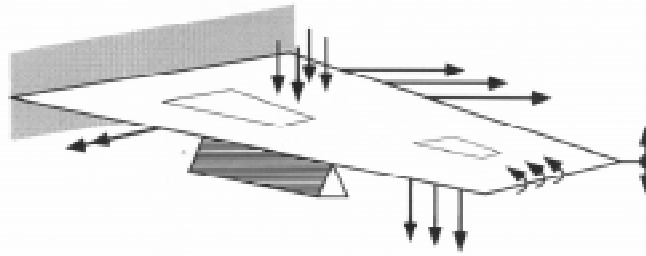


Figure 6: Problem geometry. Quadrilateral plate subjected to multiple loadsets and boundary conditions.

- Drop-off spacing rate: how close neighboring plydrops can be.
- Potential development of delamination or hinge effects leading to premature buckling at drop-off lines.
- Behavior of resin pockets developing in the plydrop fillets.

4 Design optimization

SUNSPOT [1-3, 11] was conceived as an advanced preliminary design tool for plane composite structures. Beams and quadrilateral plates (Figure 6), with optional cutouts, subjected to multiple complex loadsets and any boundary conditions, are optimized by using plydrops.

The optimization objective [2, 11] is minimum weight and is subject to one or more constraint classes, some of which are optional:

- Strength [Compulsory]. The optimized structure may nowhere fail in strength. Tsai-Wu's first ply failure [7] constitutes the limit, calculated with the quartic failure criterion which enables direct scaling of the thickness of the laminate [1].
- Stiffness [Optional]. Four maximum displacement values may be prescribed: the displacement components u_0 , v_0 , w_0 , and d_0 , the displacement modulus, defined as $d_0 = \sqrt{u_0^2 + v_0^2 + w_0^2}$. If more than one such constraint is specified, the worst case rules (active constraint), fulfilling automatically the other ones [1, 2].
- Manufacturing complexity [Optional]. Manufacturing complexity is evaluated by a manufacturing complexity index [1] which adds a penalty to the optimization objective function.

Usage of plydrops in conjunction with reference sublaminates for the layup of the structure, strongly reduces the number of design variables. They are [2, 11]:

- Angle (θ_i). The m ply orientation angles of the reference sublaminate.
- Number of plies (n_i). The number of plies at the corresponding angles, in the sublaminate layup.

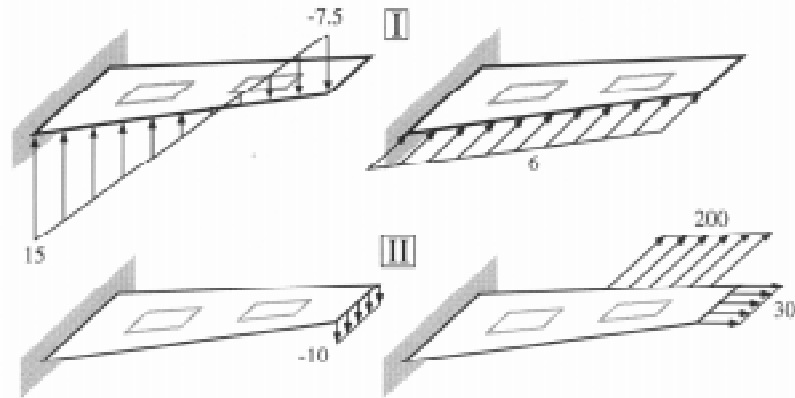


Figure 7: Trapezoidal cantilever plate with two openings. Two loadcases (#1 on top — #2 on bottom). Linear load intensities given in kN/m.

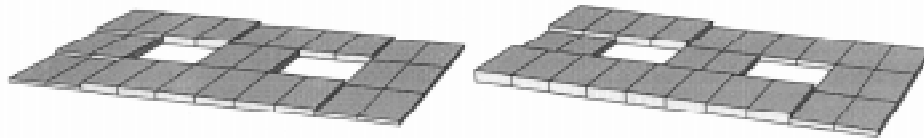


Figure 8: Cantilever plate made of AS/H3501. Plydrops results for strength (left) and combined strength/stiffness (right) by *SUNSPOT*.

- Repetition number (r_k). The number of times the sublaminates is repeated in design zone k (Figure 5). The stack of r_k sublaminates is then mirrored symmetrically (s in Eq. 2), yielding the layup in zone k as

$$\left(\left[(\theta_1)_{n_1}, \dots, (\theta_i)_{n_i}, \dots, (\theta_m)_{n_m} \right]_{r_k} \right)_s \quad (2)$$

5 Example

A 3 meter long cantilever plate with two equally spaced openings is optimized with plydrops for two sets of criteria. It is subject to two distinct loadcases (Figure 7). The following and other more complex cases are elaborated in [2, 3, 11].

5.1 Strength optimization

The base sublaminates of the optimum plydrops design is $[5_9/40_2/-51_3/3_9]$ for graphite-epoxy AS/H3501. It is repeated between one and three times, symmetrically (Figure 8, left). The optimum uniform thickness design is 16% heavier than the plydrops one. The best quasi-isotropic design is 110% heavier.

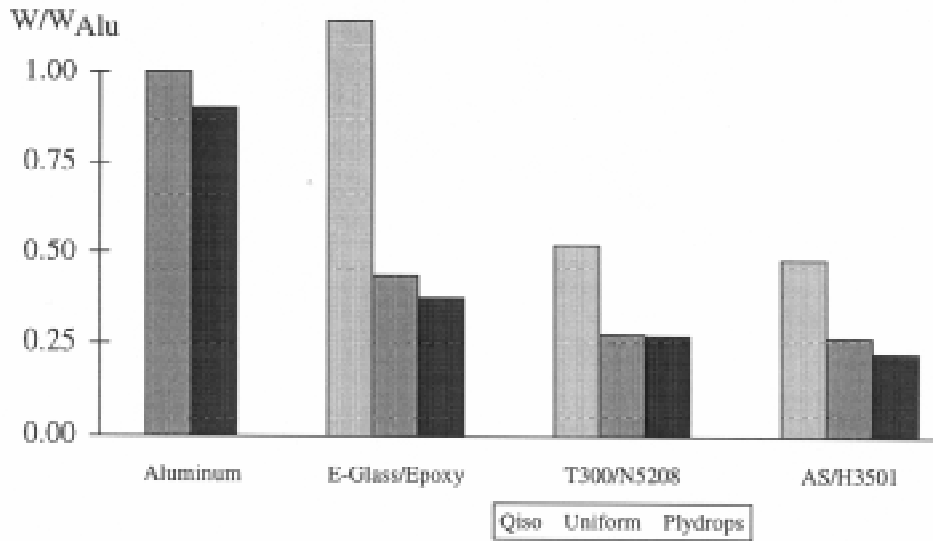


Figure 9: Cantilever plate made of Aluminum, E-Glass/Epoxy, T300/N5208, AS/H3501. Comparison of strength optimized weights: quasi-isotropic, uniform thickness, and plydrops designs. Reference: uniform thickness aluminum design.

5.2 Combined strength and stiffness optimization

Combined strength and stiffness optimization ensures a structure that neither fails nor defects like a “spaghetti”. Our strength optimized AS/H3501 plate deflects by 4.68 m. Bounding the maximum deflection to 0.50 m, the new plydrops optimum uses a slightly different sublaminates and a new layout (Figure 8, right), while increasing weight by only 125%.

6 Conclusions — Sublaminates plydrops

Adding and dropping entire sublaminates has many advantages but also side-effects.

6.1 Advantages

Sublaminates plydrops enjoy many qualities:

- Their usage as global entities ensures fiber continuity in all layers. There are no internal butt-joints. It is either the same fiber throughout or it is being dropped.
- Repetition of the same reference sublaminates everywhere strongly reduces the number of optimization variables and, hence, the computation time.
- Repeating a sublaminates, made of different plies, prevents or at least discourages the apparition of thick stacks of identical plies. They are better spread out, thus increasing structural toughness and reducing the risk of delamination. However, such homogenization limits strength efficiency of the individual plies inside the complete laminate in bending problems.

- Used as standard building blocks, sublaminates offer simpler shapes, straight cuts, less scrap residue and easier manufacturing possibilities.
- Automatic generation of local reinforcements in the structure (Figure 8).

6.2 Disadvantages

The defaults of sublaminates have to do with their repetition and own thickness.

- When strength efficiency is crucial, the most efficient plies try to be stacked in large numbers on the periphery. However, repeating the reference sublaminate spreads them out across the thickness and caps their efficiency. The common result is minimal repetition, once or twice, of quite thick sublaminates, as expected. Most practical design problems have multiple loads and rarely deal with extreme stress variations.
- Steep tapering, when required, may be inhibited. Other plydrop patterns, such as individual ply drop-offs, may be better suited. In such case, the basic principles of the present design methodology are still applicable. As mentioned beforehand, the multi-ply sublaminate plydrops are a modeling of smoothly staggered individual plydrops (Figure 4).
- When designing larger structures, dividing them up into multiple design areas is recommendable: a same sublaminate may be reasonably efficient across a large area but may be not all over. The current approach of layup uniformity would then be applied to each design area.

6.3 Toughness constraints

Laminate toughness is often upheld by repeating sublaminates but not systematically. Enforcing laminate toughness essentially constrains the stacking of its plies: only a handful of plies of same orientation may be stacked together. By doing so, freedom of optimization is hindered, weight increases as a result and the underlying homogenization lowers the strength efficiency of the constitutive plies. The final layup will lean more towards quasi-isotropy, missing the benefits of anisotropy!

Acknowledgments

I would like to thank Professor Stephen W. Tsai, my PhD adviser, for his support and guidance, for generously sharing his experience and suggestions. I am very grateful to Professor László Kollár, of the Technical University of Budapest, for his insightful discussions regarding this research.

This research was supported by the National Science Foundation, the Fulbright Foundation, Kenetech Windpower, the National Renewable Energy Laboratory, and the Industrial Technology Research Institute of Taiwan.

Bibliography

- [1] P. M. Manne and S. W. Tsai, "Design Optimization of Composite Plates. Part I — Design Criteria for Strength, Stiffness, and Manufacturing Complexity of Composite Laminates," *Journal of Composite Materials*. Submitted for publication.
- [2] P. M. Manne and S. W. Tsai, "Design Optimization of Composite Plates. Part II — Structural Optimization by Plydrop Tapering," *Journal of Composite Materials*. Submitted for publication.
- [3] P. M. Manne and S. W. Tsai, "Practical Considerations on the Design of Composite Structures," *Journal of Mechanics of Composite Materials and Structures*. Submitted for publication.
- [4] S. Metschan, D. Graesser, G. Mabson, M. Proctor, D. Tervo, and L. Ilcewicz, "Manufacturing Data for Costade Analysis of Composite Fuselage Panels," in *Boeing's Advanced Technology Composite Aircraft Structures Program Presentations*, 5th Advanced Composite Technology Conference, August 1994.
- [5] A. Miravete, "Optimization of Symmetrically Laminated Composites Rectangular Plates," in *Proceedings of ICCM 7*, vol. 3, (New York, NY), pp. 289–294, International Academic Publishers / Pergamon Press, 1989.
- [6] M. Niu, *Composite Airframe Structures*. Hong Kong: Conmilit Press Ltd., 1992.
- [7] S. W. Tsai, *Theory of Composites Design*. Dayton, OH: Think Composites, 1992.
- [8] A. Botting, A. Vizzini, and S. Lee, "The Effect of Plydrop Configuration on the Delamination Strength of Tapered Composite Structures," in *Conference Proceedings*, vol. 1 (Structures I), pp. 40–47, 33rd AIAA/ASME/ASCE/AHS/ASC Structures, Structural Dynamics and Materials Conference, April 1992.
- [9] W. Cui, M. Wisnom, and M. Jones, "Effect of Step Spacing on Delamination of Tapered Laminates," *Composites Science & Technology*, vol. 52, no. 1, pp. 39–46, 1994.
- [10] J. Curry, E. Johnson, and J. Starnes, "Effects of Dropped Plies on the Strength of Graphite-Epoxy Laminates," *AIAA Journal*, vol. 30, no. 2, pp. 449–456, 1992.
- [11] P. M. Manne, *Design Optimization of Composite Plates*. PhD thesis, Department of Aeronautics & Astronautics, Stanford University, Stanford, CA, May 1996.

STEALTH AIRFRAME DESIGN METHODOLOGY FOR HIGH ALTITUDE REAL-TIME RECONNAISSANCE DRONES

D. Grygier

*KENTRON, Division of DENEL (Pty) Ltd
P O Box 7412, Hennopsmeer, 0046, Republic of South Africa*

SUMMARY: This paper presents the design philosophy behind the development of a Stealth Unmanned Air Vehicle (UAV) for real-time reconnaissance applications. The aspects of the threat analysis, the mission analysis and the Radar Cross Section (RCS) requirement definition leading to the design concept of the airframe, are introduced. The Electro Magnetic (EM) design requirements for low radar signature are derived and brought into context with the development of the composite airframe.

The stealth design methodology of the radar absorbing composite structure is illustrated on the inward slanted dorsal fin of the specific UAV. The paper addresses the use of analytical modelling techniques for low RCS geometric shaping and presents a detailed design of the fin employing the electro-magnetically tuned composite materials. The special tooling and manufacturing processes of the stealthy fin are discussed. The work is concluded with a summary of the results of the electro-magnetic tests, the environmental tests and the structural qualification of the dorsal fin hardware.

KEYWORDS: stealth airframe design methodology, radar absorbing composite structures, radar cross section reduction, dorsal fin design and development

INTRODUCTION

Designing a composite airframe structure is as technically challenging as it is complex by nature. However, by taking this composite structure, and introducing the requirements for a low radar cross section signature airframe, a new dimension of complexity is added in terms of the design, materials, manufacturing and processing techniques.

The airframe geometry, its structure and the internal layout, is dictated by the system requirement specifications. For an airframe with a low radar cross section signature, these are not only defined through the design guidelines for aerodynamic, structural and material inputs, but also by the requirement for a specific electro-magnetic performance.

The materials required for the airframe structure, conventionally defined to perform to certain mechanical characteristics, now need to be defined by their electro-magnetic performance, ie the properties of permeability and the transmissivity. A whole new design methodology needs to be established which takes into consideration the aspects of geometric shaping, structural optimization and the application of electro-magnetically tuned composite materials.

The inward slanted dorsal fin of the Flowchart 2 Stealth technology demonstrator, an Unmanned Air Vehicle (UAV) for use as a high altitude real-time reconnaissance drone, is used in this case study to demonstrate the various aspects of low observability design. Refer to Fig.1.

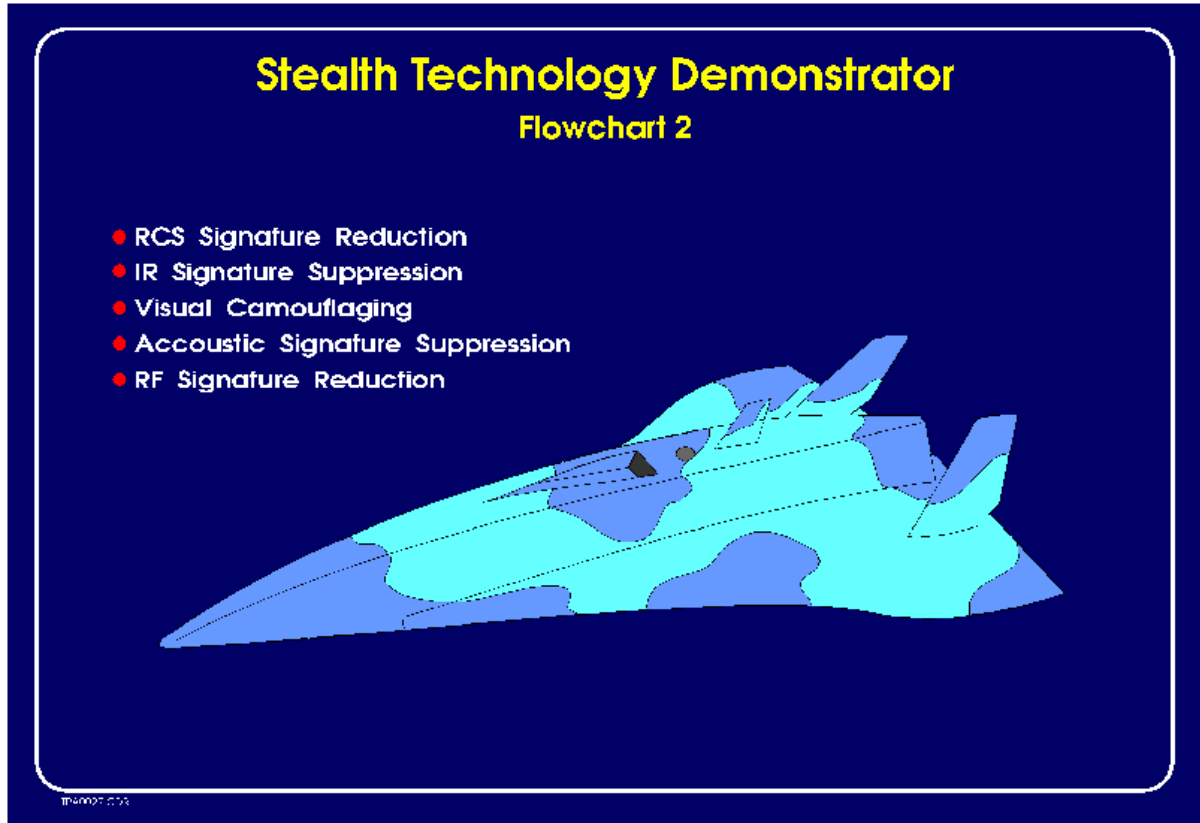


Fig 1: Flowchart 2 Stealth Technology Demonstrator

STEALTH REQUIREMENT ANALYSIS

A brief introduction into the field of stealth technology is presented, to illustrate how the design of an airframe is driven by the system requirement for low observability. The chronological steps involved in the stealth requirement analysis [1] are discussed below. Refer to Fig. 2.

Threat Analysis

In the threat analysis the target scenario that is to be encountered, is established. This entails the identification of the different threat radars and air defence systems, such as Surface to Air Missile systems (SAM's) and Anti Aircraft (AA) gun systems, which are employed at the target area. The different threats are then characterized and prioritized in terms of their potential influence on the mission effectiveness.

Mission Analysis

In the mission analysis the primary mission is specified and the type of system required to conduct this mission is selected. The system requirement specifications define the type of airframe and provide inputs to the airframe performance. The mission profile is then defined to ensure maximum mission effectiveness.

Radar Cross Section Requirement Definition

The RCS requirement definition establishes the maximum allowable RCS for the airframe, to ensure that the primary mission is conducted successfully with a high degree of survivability. From the threat scenario and the planned mission profile, the radar illumination angles during the mission are calculated. The type of electro-magnetic scattering mechanisms and the expected radar return, ie the RCS of the airframe, are analysed with the use of analytical methods. The data is then used to define the basic geometric shape of the airframe. [2]

Survivability Study

The survivability study forms part of the strategic analysis. Analytical modelling techniques are employed to determine the threat performances, such as radar detection ranges, kinematic ranges, system accuracies, flight profiles and time over target, etc. Based on this the probability of detection [3] and ultimately the survivability and mission effectiveness of the airframe is established.

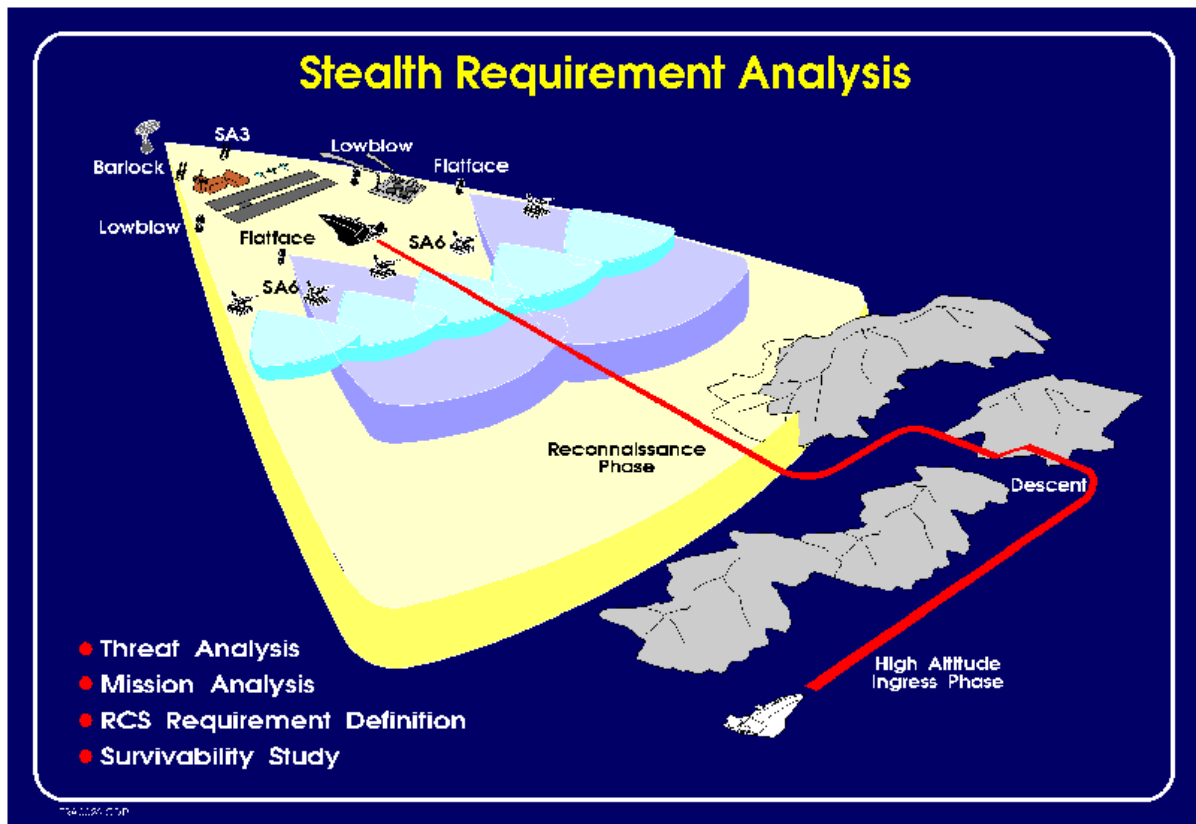


Fig 2: Stealth Requirement Analysis

AIRFRAME DESIGN

The system requirement specifications for the Flowchart 2 high altitude real-time reconnaissance drone are presented. The design methodology for low RCS signature is then illustrated in a case study on the UAV's inward slanted dorsal fin.

System Requirement Specifications

The system requirement specification for the UAV dictate high subsonic speeds at an altitude of 40 000 ft during its ingress and egress phase. It descends to the reconnaissance level while maintaining the high subsonic speed throughout the reconnaissance phase. The airframe is designed to a sustained load factor of +5g and -3g with a maximum instantaneous load factor of +8g. The UAV falls in the 1 000 kg class and with an unspecified payload capability it has an approximate flight time of 60 minutes.

The airframe is ground launched with the use of two discardable solid rocket boosters, accelerating the airframe at 10g during the launch phase. Recovery is induced through the use of a drag and a main parachute. Inflatable landing bags are used to absorb the landing loads, which are limited to 15g. Emphasis is placed on the requirement for an all composite airframe structure, which is easily containerized in standard ISO containers to ensure ease of transportability and rapid deployment.

From the stealth requirement analysis the main threat radars in this potential threat scenario have been identified as mono-static radar systems, operating in the C- and X-band. With the primary mission being reconnaissance, a high - low - high flight profile is required. For this flight profile, the biggest threat of detection occurs when the UAV is in its final sector of the ingress phase. Under this condition the airframe is primarily subjected to radar illumination angles in the forward sector defined by -5° to $+15^{\circ}$ in elevation and $\pm 35^{\circ}$ in azimuth.

To ensure a probability of detection of less than 90% during the final ingress phase, the RCS requirement definition implies that the maximum RCS of the airframe must not exceed -10 dBsm (fictitious value) in the direction of the threat radars transmitter/receiver. Although the design is optimized for mono-static radar systems, the maximum RCS from any aspect angle should not exceed -12 dBsm (fictitious value). This system requirement is applicable for the full frequency range in the C and X band, for both planar and circular polarized radar systems.

Detail Design: Case Study Dorsal Fin

The system requirement specifications dictate a range of design constraints on the dorsal fin. [4] These are summarized:

- i) aerodynamic design, defined by factors such as the aircraft flight envelope, manoeuvrability, drag, aerodynamic efficiency, etc.
- ii) structural design, defined by the aerodynamic and inertia loads, and the combination of aerodynamic and structural interaction, the aero-elastic behaviour.
- iii) electro-magnetic design, defined by the requirements for low observability through geometric shaping and the application of electro-magnetically tuned composite materials.

- iv) materials, the composite materials have to provide certain mechanical properties to ensure structural integrity, as well as electro-magnetic properties to ensure the low RCS signature.

To achieve the system requirement specifications and satisfy the aerodynamic, structural, electro-magnetic design constraints, an iterative approach had to be taken to derive at the optimal fin structure.

Aerodynamic

A 65A008 NACA profile was selected for the dorsal fin to ensure optimal aerodynamic efficiency during high altitude high subsonic flight conditions. The leading edge was swept back through 25° and the trailing edge through 15° . The root chord was 400 mm and the fin 600 mm long. The fin loading was based on FAR 26, whereby the worst case aerodynamic load condition occurred at $Cl = 0.6$ (a side slip angle of 15° at VA), where VA was 300 knots. The resulting design load at these conditions was 2 000 N.

Structural

The structural design of the fin was based on ultimate load at 150% and yield at 120% of the design load of 2 000 N. In the load analysis an elliptical load distribution along the centre chord was used. A preliminary structural design was conducted to establish the skin construction and fibre lay-up. The basic dimensions of the 20% and 60% spars were established and the concept for the finbox at the fin/wing intersection was defined. Maximum fin deflection and flutter was investigated.

Electro-magnetic

At the C- and X-band frequencies the electro-magnetic wavelengths are far shorter than the length of the airframe, implying that the design is driven by high frequency scattering mechanisms. For this high frequency scattering mechanism, the effects of detail geometric shaping and the use of electro-magnetic material parameters become critical. (For resonant and/or Rayleigh type scattering regimes, this would be less applicable). [5]

A software code, based on Physical Optics (PO), was developed to establish the backscattered field for a conductive constant chord reference fin. The code was then hybridized with the Geometrical Theory of Diffraction (GTD) code, to enable further evaluation of the fields of diffraction. The analytical model was subsequently upgraded to include the effects of the different electro-magnetically tuned composite material parameters. From this analytical model the main contributors to the RCS and their relative contributions were established.

The model was then upgraded to enable the RCS prediction of the fin within the surroundings of the fuselage and the main wing. Given the system/fin boundary conditions, the electro-magnetic scattering mechanisms could be established. The highest contribution to the RCS was due to a combination of reflection and diffraction along the fin leading and trailing edge, with surface wave energy propagating along the skin surface. The interference reflection between the fin and the fuselage formed a large contribution to the RCS of the airframe.

The plan shape of the fin was subsequently optimized. The sweepback angle of the fin leading edge was increased, the fin tip was smoothed and a radius along the root of the fin base was added. To reduce the high reflection/diffraction off the fin leading edge, a low impedance RAM was selected in this area. To reduce the surface wave energy along the skins, and due to a limitation in skin thicknesses, a high impedance RAM was employed along the skins. The material construction was that of an outer dielectric skin (Epoxy/glass fibre), a Nomex RAM core and an inner dielectric skin (Epoxy/glass fibre). The skin thicknesses had to be impedance matched and it was critical to the optimal performance of the RAM that the dielectric skins did not vary in thickness.

To prevent direct illumination of the inner mechanics of the fin, ie the main spars, the electrical connections, the control rods, etc, this area was covered with a conductive inner skin. This inner skin formed part of the wing torsion box, whereby the skin was made of Epoxy/carbon fibre to the correct fibre lay up, satisfying the bending and torsional stiffness requirements. The shape of this inner skin was critical to achieve a low RCS, and had to be optimized for minimal radar return for the main threat illumination angles. For details of the design concept of the dorsal fin cross section, refer to Fig. 3.

The carbon spars were bonded to the inner conductive skin and continued into the fin root box, to transfer the fin loads to the airframe bulkheads. Details such as control panels and the control surface interface increase the complexity of the stealthy fin design considerably. The discussion of these aspects have not been included in this paper.

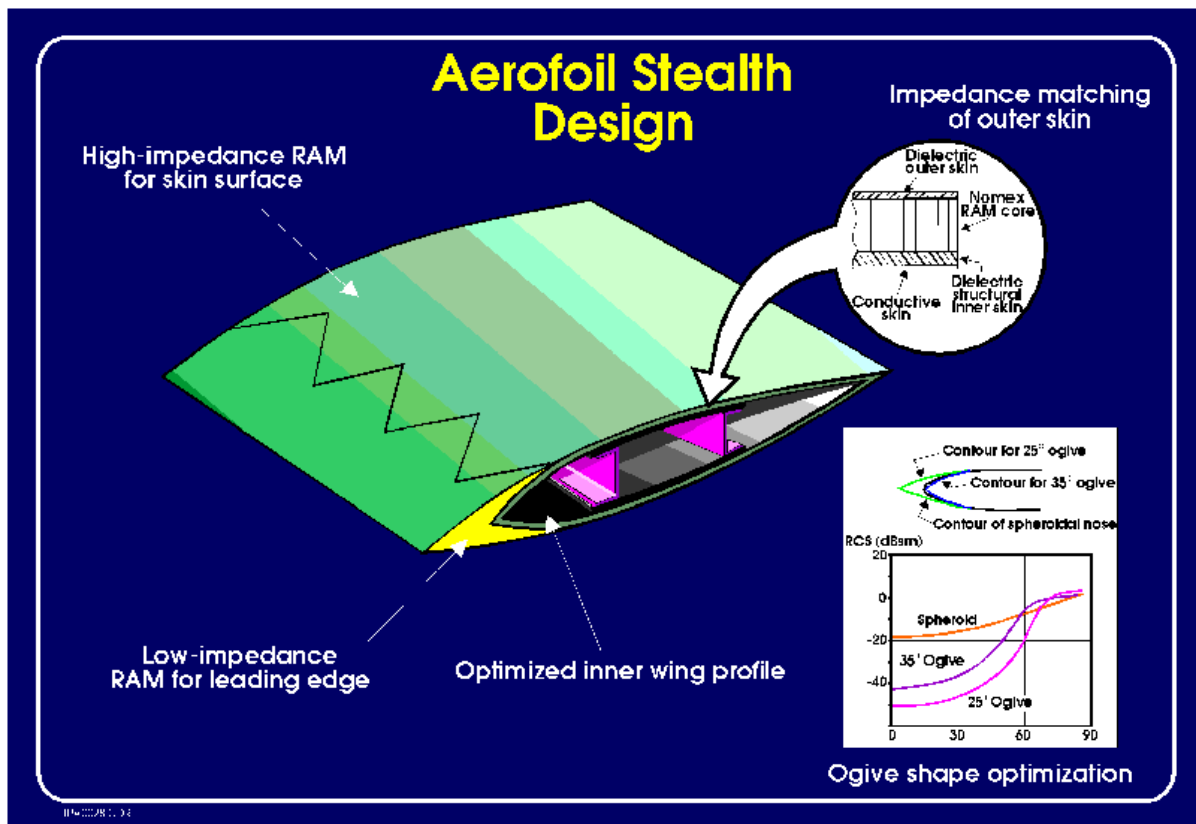


Fig 3: Dorsal Fin Stealth Design

MANUFACTURE AND PROCESSING

The additional tooling and the complexity in the manufacturing processes for the construction of the stealthy fin, is discussed. The problems associated with the different RAM, the storage, handling and the environmental threats etc, are briefly mentioned.

Tooling

The basic tooling for the fin resembled that of conventional composite material tooling. The fin pattern was CNC machined from a type 65 aluminium block. A carbon composite mould, cured at a temperature of 60° C, was taken off the aluminium pattern and postcured at 120° C. The mould was subsequently stiffened with a carbon backing structure. Additional aluminium tooling had to be machined for the forming of a silicon insert which was required for shaping the inner conductive leading edge skin. Tooling was also required for the manufacture and positioning of the main spars.

Manufacture

The complexity in the manufacture of the fin was brought about by the fact that the different layers of composite materials, ie, the outer dielectric skin, the RAM core and the inner dielectric skin, were not allowed to vary in thickness by more than 5% over the total surface area. To maintain the transmissivity of these dielectric materials, the fibre matrix ratio's were not allowed to vary by more than 5%, as this again was critical to the optimal impedance matching of the RAM structure.

The leading edge RAM was CNC machined and bonded into position. The Nomex RAM was pre-cut and formed part of the skin lay-up procedure. Extreme care had to be taken during the integration of the RAM, that no air was allowed to be trapped in the construction and no resin was allowed to migrate towards the RAM core. This had to be achieved while at the same time maintaining good bonding between the surfaces to ensure the required structural integrity.

Material Handling

The environmental and health hazards associated with some of the RAM formed a major problem. Special storage facilities were required, whereby protection against contamination of the raw materials was ensured. The facilities had to ensure good environmental control, as some of the materials only had a limited shelf life. The high toxicity and the combustibility of some materials, made it paramount to ensure strict safety regulations. Special handling methods needed to be implemented, and the personnel had to wear protective clothing due to the health hazards associated with some of the RAM.

TEST RESULTS

The dorsal fin was subjected to extensive environmental, static and dynamic structural tests and electro-magnetic performance measurements. The electro-magnetic evaluation of the radar absorbing materials in the free space measurement facility, for the qualification of the materials, is not discussed in this paper. [6] & [7]

Structural Testing

The structural tests were conducted in the Structural Research and Test Laboratory at Kentron. The tests were grouped into static and dynamic load cases. In the static load case, the fin was initially subjected to yield loading at 120% of the design load, and subsequently to ultimate loading at 150% of the design load. In the dynamic load case, the fin was subjected to twice the fatigue life cycle spectrum of the airframe. [8]

The full set of structural tests were repeated after completion of the environmental tests, to establish whether the environmental testing had any negative effects on the structural integrity of the fin. [9]

Environmental Testing

The environmental tests were conducted to establish the effects of the different environmental conditions on the structural integrity and the electro-magnetic performance of the RAM. These tests included Ultra Violet (UV) tests, fungal growth, humidity and temperature cycling. Furthermore the structure was subjected to aircraft fuels, low viscosity lubricating oils and cleaning agents for extended periods of time. [9]

Electro-magnetic Testing

The electro-magnetic tests were conducted in a radar test facility representing far field conditions, to establish the design efficiency in terms of the RCS signature. One fin, coated with a conductive outer skin, was tested to establish a baseline and to determine the geometric constraints. The tests were then repeated with the stealthy fin, which incorporated the different radar absorbing materials. [8]

The electro-magnetic tests for the stealthy fin were repeated after the fin was subjected to the environmental tests, to establish whether the electro-magnetic testing had any deteriorating effects on the electro-magnetic performance of the fin. [9]

CONCLUSION

To optimize the design of low observable composite aircraft structures, the system requirements for aerodynamic design, structural design and electro-magnetic design have to be optimally harmonized. Furthermore, from a materials aspect, the use of advanced composite materials, in combination with electro-magnetically tuned materials, require the development of completely new design, manufacturing and processing techniques.

A design methodology was established for the design of stealthy composite material airframe structures. This was illustrated by a case study on the inward slanted dorsal fin of the Flowchart 2 high speed reconnaissance drone. It was successfully demonstrated that the RCS requirement specifications were achieved and that the associated technologies are well established. For the UAV and associated airframe components, such as engine intakes, wings, canards, etc, the above design methodology can now be applied.

REFERENCES

1. Grygier, D., *Flowchart 2 - Airframe Stealth Requirement Specification*, Kentron Doc No 10204-00021-701, Issue 1, 1992.
2. Ruck, G.T., Barrick, D.E., Krichbaum, C.K., *Radar Cross Section Handbook*, Plenum Press, 1970.
3. DiFranco, J.V., *Radar Detection*, 1993.
4. Pieterse, B., *Flowchart 2 - Low RCS Vertical Tailfin Design and Development*, Kentron Doc No 95-10204-02 Issue 1, 1995.
5. Skolnik, M.I., *Radar Handbook*, Mc Graw-Hill Inc, 1970.
6. Pieterse, B., *Flowchart 2 - Environmental Testing of RAM*, Kentron Doc No 10204-00037-701 Issue 1, 1992.
7. Dr Odendaal, *Flowchart 2 - Measured Data For RAM Characterization*, Kentron Doc No VLG 95/027, Issue 1, 1995.
8. Dr Odendaal, Vledder,WD., *Flowchart 2 - Electro-magnetic and Structural Evaluation of the Vertical Fin*, Kentron Doc No 10204-00058-701, Issue 1, 1995.
9. Grygier, D., Dr Odendaal, Vledder,WD., *Flowchart 2 - Electro-magnetic and Structural Evaluation of the Vertical Fin*, Kentron Doc No 10204-00058-701, Issue 2, 1995.

STRUCTURAL ANALYSIS OF CORD-REINFORCED RUBBER COMPOSITES

Ramana M. Pidaparti

*Department of Mechanical Engineering, Purdue University at Indianapolis (IUPUI)
723 W. Michigan Street, Indianapolis, IN 46202, U.S.A.*

SUMMARY: The mechanical behavior of cord-reinforced rubber composite structure under tension, bending and torsion was investigated using a three-dimensional (3D) beam finite element method. The extension-twisting coupling due to the twisted nature of the cords as well as the coupled extension, bending, and twisting deformations characteristic cord-rubber composite structures were included in the finite element model. The accuracy of the present approach is demonstrated by comparing the results of coupled stiffness obtained from the finite element analysis to the available experimental data in the literature. The effect of cord orientation on the relative deformation/stiffness under tension, bending and torsion is presented to illustrate the effects of coupled behavior of cord-reinforced rubber composite structures.

KEYWORDS: finite element model, belt structure, stiffness couplings, twisted cord, rubber, structural analysis and design

INTRODUCTION

Cord-reinforced rubber composite structures with $\pm\alpha$ cord orientations find applications in automotive and aerospace engineering industries. The mechanical behavior of cord-reinforced rubber composite materials is generally complex due to the nonlinear geometric and material properties, and exhibit coupled axial-bending-twisting behavior under different loading conditions. The complexity of cord construction (as the cord itself is not a single filament but many filaments twisted together) results in the cords exhibiting coupled extension-twisting coupling behavior. It is important to include the coupled axial-bending-twisting behavior for the realistic analysis of cord-rubber composite structures and also to develop analysis techniques to design durable cord-reinforced rubber composite structures.

Several authors analytically investigated the response of cord-rubber composite laminates subjected to different loading conditions [1-8]. An exact expression for torsional stiffness of a single cord-rubber ply was developed by Bert and Chang [1] using St. Venant torsion theory. Akasaka et al. [2,3] studied the coupled extensional-torsional and bending-shear deformations of cord-rubber structures subjected to extension and bending. The torsional behavior of cord-rubber belt structures was studied by Akasaka et al. [4] including the interply shear deformation and torsional-extensional deformations. Robbins and Clark [5] presented an engineering analysis of bending stiffness of cord-rubber laminates based on laminate theory. They did not consider the interlaminar shear or coupled bending shear deformations. Bert [6] presented a theoretical treatment to predict the out-of-plane bending stiffness of a laminated composite plate under cylindrical bending based on classical lamination theory. Shield and

Costello [7] studied the extension-twisting coupling behavior of single-ply and two-ply cord-rubber composites using an energy approach based on the Ritz method.

It was experimentally shown by Turner and Ford [9] that significant interply shear strains exist when a two-ply composite structure is subjected to simple tension. These interply shear strains are believed to be mainly responsible for fatigue induced delamination in cord-rubber composite structures. Finite element analysis of cord-rubber composites was studied by many investigators [10-17]. Ford, Patel and Turner [10] have applied the axisymmetric finite element method to Turner and Ford's model of cord-rubber composites. Hsieh [11] and Cembrola and Dudek [12] presented finite element models for studying the behavior of cord-rubber laminates. De Eskinazi et al. [13] compared the results of interply shear strains from 2D and 3D finite element analysis and showed that the results were significantly different when 3D analysis was used. Pidaparti and Kakarla [14] presented a three-dimensional finite element model to study the non-linear extensional behavior of two-ply cord-rubber composite laminates. Later, they extended their study to analyze the three-dimensional torsional behavior of cord-rubber laminates [15]. The results indicated that coupled bending-shear and twisting shear deformations are important for a realistic analysis of the behavior of two-ply cord-rubber composite structures. Recently, bending analysis of two-ply cord-rubber composites and twisted cords was studied by Pidaparti using a hierarchical finite element approach [16].

In this study, a belt structure made from a cord-reinforced rubber composite and subjected to tension, bending and torsion was investigated using a recently developed three-dimensional beam finite element [16]. The extension-twisting coupling due to the twisted nature of the cords as well as the coupled extension, bending, and twisting deformations of cord-rubber composites was included in the finite element model. The accuracy of the present approach is demonstrated by comparing the results of coupled stiffness obtained from the finite element analysis to the available experimental data in the literature. The effect of cord orientation on the relative deformation/stiffness under tension, bending and torsion are presented to illustrate the effects of coupled behavior of cord-rubber composite structures. The three-dimensional finite element model presented would help in better understanding the mechanical behavior of cord-rubber composite structures under combined loading conditions.

FINITE ELEMENT ANALYSIS

Figure 1 shows the finite element modeling of a two-ply cord-rubber composite structure. The finite element model treats a two-ply composite composed of three layers through the thickness: two cord-rubber layers and a rubber layer as shown in Figure 1.

A recently developed finite element model [16] was used in this study. The present finite element model consists of a beam element and a warping element. The beam element is a three-node isoparametric finite element whereas the warping element is an eight node isoparametric element. The cross-section of the laminate consisting of cord-rubber and rubber layers was modeled using 8-node isoparametric finite elements (see Fig. 1). The finite element has beam nodes and warping nodes. Each beam node has three translational degrees of freedom and three rotational degrees of freedom (dof), respectively. Each warping node has a single dof in the beam direction but is normal to the deformed cross-section. The finite element model takes into account stiffness couplings due to axial, bending, twisting and warping deformations. The details of this beam/warping element can be found in Refs. [16,

17]. The present 3D beam element is computationally inexpensive as compared to the 3D solid finite element model.

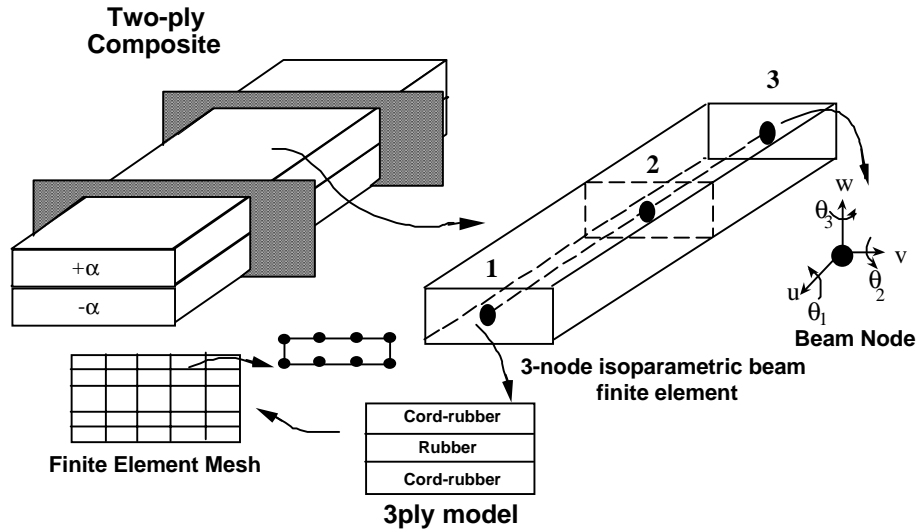


Fig. 1. Finite element modeling of two-ply cord-rubber composite structure

The stress-strain relationships for the rubber and cord-rubber materials are assumed to be linear isotropic and linear orthotropic, respectively. The rubber elasticity is defined in terms of Young's modulus (E_m) and Poisson's ratio (ν_m). It is important to consider the extension-twisting coupling behavior of twisted cords in the material model for a realistic analysis of cord-rubber composite structures. Shield and Costello [7] developed a material model for a unidirectional lamina of cord-rubber composite by assuming it to be monocyclic and taking into account the twisted nature of the cords. Their material model was derived from an energy approach and the Shield-Costello equations for a unidirectional cord-rubber composite are given by:

$$E_1 = E_m + c_1 E_c v_c \left[1 - \frac{6c_2 c_3 v_c (1 + \nu_m)}{c_1 (\bar{A} \bar{h}^2 \bar{E} + 6c_4 v_c (1 + \nu_m))} \right] \quad (1)$$

$$E_2 = \frac{4E_m [c_1 E_c v_c + E_m] + \frac{24(1 + \nu_m) v_c E_c}{\bar{A} \bar{h}^2} (c_4 E_m + C E_c v_c)}{[4E_m + 4(1 - \nu_m^2) v_c c_1 E_c] + \frac{24(1 + \nu_m) v_c}{\bar{A} \bar{h}^2 \bar{E}} (c_4 E_m + C E_c v_c (1 - \nu_m^2))} \quad (2)$$

$$\begin{aligned} G_{12} &= G_m (1 - v_c) \\ \nu_{12} &= \nu_m \end{aligned} \quad (3)$$

where ν_m is the Poisson's ratio of rubber material, $\bar{A} = A_c / R^2$, $\bar{h} = h / R$, $\bar{E} = E_m / E_c$, A_c is the area of the cord, h is the thickness of cord-rubber ply, R is the outer radius of the cord and v_c is the cord volume fraction. The cord properties are described by Young's modulus of cord (E_c) and Poisson's ratio (ν_c). The constants c_1 , c_2 , c_3 , c_4 and $c = c_1 c_4 - c_2 c_3$ are used to describe the extension-twisting coupling and are determined analytically by Shield and Costello [7]. These constants depend on the helix angle of the cord and the ratio of inner wire

diameter to outer wire diameter. Recently, Shield and Costello applied this material model to study the mechanical behavior of single ply and two-ply cord rubber composite plates [7] and obtained good results. The above material model is included in the present finite element model.

Cord-rubber composites have different properties in tension and compression. In this study it is assumed that the properties in tension and compression are the same for all the cord-rubber elements. However, for a more realistic prediction, this bimodular properties [18] should be included in the present model. Linear static analysis is carried out to estimate the stiffness and relative deformations for a two-ply cord-reinforced rubber composite belt structure.

RESULTS AND DISCUSSION

A cord-rubber composite belt structure having $\pm\alpha$ cord orientation and subjected to tension, bending and torsion is considered. The geometry of the belt structure is 250 mm long, 63 mm wide and 3.7 mm thick as shown in Figure 2. The cord-rubber layers have a thickness of 1.45 mm and the rubber layer has a thickness of 0.8 mm. Since most composite belt structures have cord orientations of 10° to 40° to achieve best performance, these orientations were considered for finite element analysis.

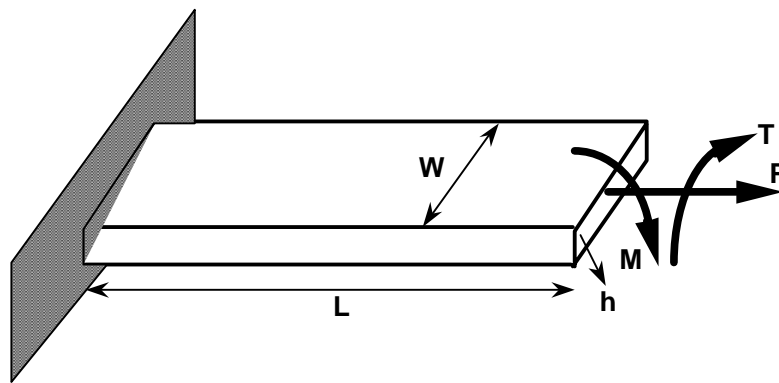


Fig. 2. Geometry, loading and dimensions for a two-ply cord-rubber composite belt structure

The following material properties were used for the finite element analysis and were obtained from Refs. 4 and 5.

Rubber Properties:

$$E_m = 18.4 \text{ Mpa and } \nu_m = 0.5.$$

Steel cord geometric and material properties:

$$E_c = 184.0 \text{ GPa and } \nu_c = 0.3.$$

$$\text{Number of yarns} = 5, d = 0.25 \text{ mm}, d^* = 0.213 \text{ mm}, \text{ and } R_j = 0.088 \text{ mm}.$$

$$t_{piyarn} = 5, t_{picord} = 3, \text{ helix angle} = 81.4^\circ, \text{ and } \nu_c = 0.2976.$$

The constants for twisted cords $c_1=0.967$, $c_2=0.0828$, $c_3=0.187$ and $c_4=0.0723$ were taken from Ref. [7].

After conducting a convergence study, the two-ply steel cord-rubber belt structure was modeled using four beam elements (along the length) and twenty 8-noded elements over the cross-section. Coupled strain ratio which is defined as the coupled torsional-extensional deformation and torsional-bending deformation, generally present in angle-ply composites, was calculated from the finite element analysis. In order to validate the present finite element model the results obtained were compared to the experimental data for torsional loading and four-point bending for different cord orientations.

Figure 3 shows the variation of axial and torsional stiffness with cord orientation. It can be seen that the axial stiffness decreases as the cord-orientation is increased, whereas, the torsional stiffness increases as the cord-orientation is increased. The torsional stiffness is almost 3.8 times higher than the corresponding axial stiffness for a 20 degree cord orientation. However, this increase in torsional stiffness as compared to the axial stiffness increases when the cord orientation is increased. The bending stiffness variation with cord orientation is shown in Fig. 4. The bending stiffness decreases upto a cord-orientation of 15 degrees, increases up to a cord-orientation of 25 degrees and changes after that. It can be seen from Figs. 3 and 4 that tire belt stiffness is strongly dependent on the cord-orientation.

The coupled axial-twist deformation variation with cord-orientation is shown in Fig. 5 for both axial tension and torsional loading. It can be seen that the coupled deformation is higher for axial tension as compared to the torsional load. The coupled axial-twist deformation under axial load is almost 5 times higher than the corresponding coupled axial-twist deformation under torsional load for a 20 degree cord orientation. However, this increase in coupled axial-twist deformation under axial load as compared to the torsional load increases when the cord orientation is increased. The results presented in Fig. 5 illustrates the coupling effects under different loading conditions. Therefore, it is important to capture these coupled deformations for a realistic analysis of cord-rubber composite structures.

The results of coupled deformations and stiffnesses obtained from the present finite element analysis were compared to the experimental data for validation. Figure 6 shows the comparison of coupled torsional-extension deformations for different cord orientations under torsional loading. It can be seen that the present finite element results are in reasonably good agreement with the experimental data [4]. The results of bending stiffness for cord orientations of 15 to 30 degrees under four-point bending for the two-ply cord-rubber composite structure are compared to the results obtained from the present finite element analysis [16] in Fig. 7. It can be seen that a good agreement is found between the present finite element results and the experimental data [5]. The bending stiffness decreases as the cord orientation is increased. Good agreement of the above results validates the utility of the present finite element model for the analysis of cord rubber composites subjected to different loading conditions.

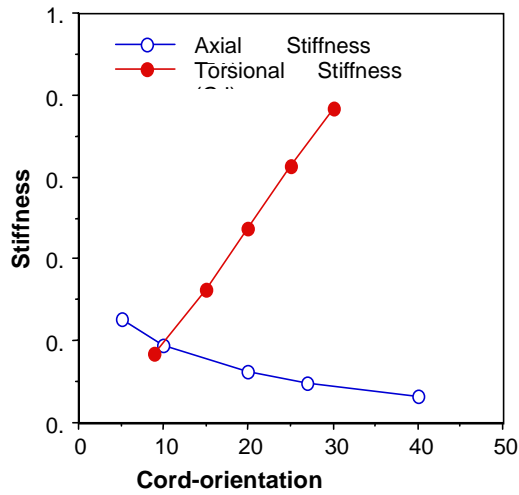


Fig. 3: Axial and torsional stiffness variation with cord-orientation

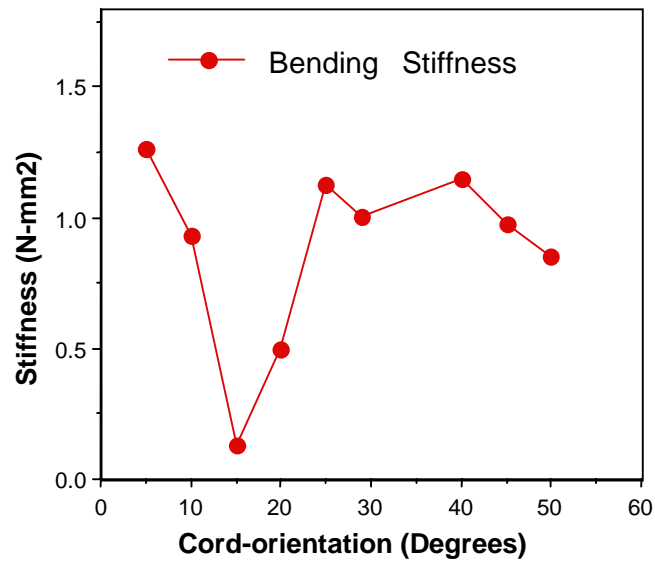


Fig. 4: Bending stiffness variation with cord-orientation

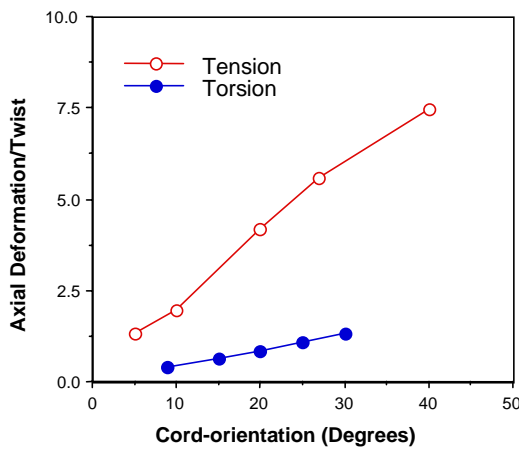


Fig. 5: Ratio of axial deformation to the twist variation with cord-orientation under tension and torsion.

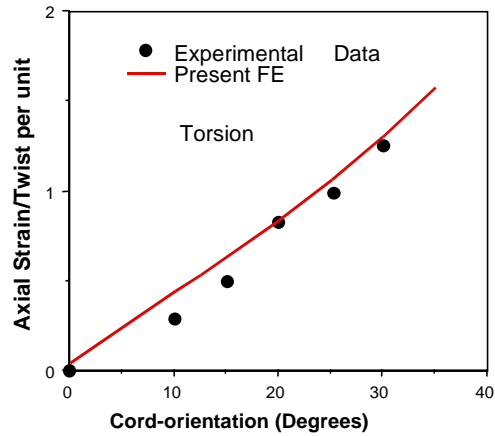


Fig. 6: Comparison of coupled torsional-extensional strain for different cord orientations under torsion.

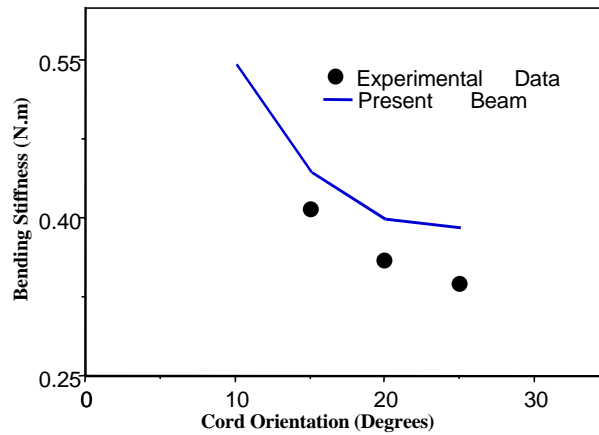


Fig. 7: Comparison of bending stiffness variation with cord orientation for a two-ply steel reinforced rubber structure.

CONCLUSIONS

The structural response of a cord-rubber composite belt structure subjected to axial tension, bending and torsional loading was investigated using three-dimensional beam finite element analysis. The present 3D beam element takes into account the coupled extension, bending, and twisting deformations as well as the twisted nature of the cords. The accuracy of the present model is demonstrated by comparing the results for torsional and bending loadings to the existing experimental data. The results presented indicate that cord orientation has a strong effect on coupled strain ratios. The results presented indicate the usefulness and applicability of the present finite element model to analyze cord-rubber composite structures under complex loading conditions.

ACKNOWLEDGMENTS

Support for this work was provided by the U.S. National Science Foundation under the grant MSS-9109683.

REFERENCES

1. Bert, C.W. and Chang, S., "Analysis of Twisting Stiffness for a Multifiber Composite Layer", *Journal of Applied Mechanics*, Vol. 17, No. 9, 1974, pp. 658-662.
 2. Akasaka, T., Hirano, M. and Motomura, K., "In-plane Bending Rigidity of Biasply Laminated Composite Strip", *Journal of Composite Materials and Structures*, Vol. 3, 1974, pp 12-16.
 3. Akasaka, T., Kabe, K. and Sako, K., " Bending Stiffness of a Tire-belt Structure with Steel Cords ", *Composites Science and Technology*, Vol. 24, 1985, pp 215-230.
 4. Akasaka, T., Katoh, M. and Makinouchi, H., "Torsional Stiffness of a Steel-Cord Reinforced Belt Structure ", *Tire Science and Technology*, Vol. 17, 1989, pp 274-290.
 5. Robbins, D.H., and Clark, S.K., "Bending Characteristics of Textile-cord Reinforced Rubber, " *ASME*, 64-WA/RP-7, 1964, pp. 1-12.
 6. Bert, C.W., "Simplified Prediction of Ply Steer in Radial Tires, " *Journal of Tire Science and Technology*, Vol. 8, 1980, pp. 3-9.
 7. Shield, S.K. and Costello, G.A., " The Effect of Wire Rope Mechanics on the Mechanical Response of Cord Composite Laminates: An Energy Approach ", *ASME, Journal of Applied Mechanics*, Vol .61, No. 1, 1994, pp 9-15.
 8. Patel, H.P., Turner, J.L. and Walter, J. D., "Radial Tire Cord-Rubber Composites, " *Rubber Chemistry and Technology*, Vol. 49, 1976, pp 1095-1110.
 9. Turner, J.L. and Ford, J.L., "Interply Behavior Exhibited in Complimentary Composite Laminates", *Rubber Chemistry and Technology*, Vol. 55, 1982, pp 1079-1094.
 10. Ford, J.L., Patel, H.P. and Turner, J.L., "Interlaminar Shear Effects in Cord-Rubber Composites, " *Composites Science and Technology*, Vol. 17, 1982, pp 255-271.
 11. Hsieh, K.T., "Modeling of Cord-reinforced Rubber Laminates," Ph.D. thesis, University of Texas at Austin, Austin, Texas, 1985.
 12. Cembrola, R.J. and Dudek, T.J. "Cord/rubber Material Properties," *Rubber Chemistry and Technology*, Vol. 58, No. 4, 1985, pp 830-856.
 13. De Eskinazi, J., Ishihara, K., Volk, H. and Warholic, T.C., "Towards Predicting Relative Belt Edge Endurance with the Finite Element Method", *Journal of Tire Science and Technology*, Vol. 18, No. 4, 1990, pp 216-235.
 14. Pidaparti, R.M.V. and Kakarla, V.P., "Three-dimensional Stress Analysis of Two-ply Cord-rubber Composite Laminates," *Journal of Composite Structures*, Vol. 28, 1994, pp 433-440.
 15. Pidaparti, R.M.V. and Kakarla, V.P., "Torsional Stress Analysis of Cord-rubber Composite Laminates," *Mechanics of Composite Materials and Structures*, Vol. 2, 1995, pp 93-109.
 16. Pidaparti, R.M.V., "Hierarchical Bending Analysis of Cord-Rubber Composites," *AIAA Journal* , Vol. 33, No. 12, 1995, pp 2359-2363.
 17. Pidaparti, R.M.V., "Stiffness Characteristics of Twisted Cords for Cord-rubber Composites," *Journal of Composite Structures*, Vol. 24, 1993, pp 291-298.
- Bert, C.W., " Model for Fibrous Composites with Different Properties in Tension and Compression", *ASME, Journal of Engineering Materials & Technology*, Vol. 99, 1977, pp 344-349.

DESIGN OF A ROLL-CONTROL SUSPENSION LINK USING COMPOSITE MATERIAL

Xiao-jing Gong ¹, Donald Hearn ¹, Shahram Aivazzadeh ¹,
Georges Verchery ¹, Frédéric Moll ²

¹ *Institut Supérieure de l'Automobile et des Transports (ISAT) - Université de Bourgogne
49, Rue Mademoiselle, Bourgeois, B.P. 31 58027, Nevers Cedex, France*

² *GEC/Alstom, Rue Baptiste-Marcet, B.P. 42 - 71202 - Le Creusot Cedix, France*

SUMMARY: The aim of this study was to reduce the weight of the current all-steel forged suspension link fitted on French Railways TGV (High Speed Train) bogies by incorporating composite materials. Weight saving of the order of 30% was specified.

A previous analysis of the part function and its working environment had been performed in order to decide whether a partial or a total substitution of composites for steel was appropriate.

The first part of the study assessed engineering feasibility by a global approach to materials systems and selection. The result showed that the most cost-effective and technologically viable solution was to retain the existing forged steel rod-ends and replace the shank by a bonded composite material tube.

Prototypes consisting of steel-on-steel, glass/epoxy on steel and carbon/epoxy on steel combinations were made and tested. The steel on steel specimen was used as a benchmark for the others. Results on glass/epoxy tubes showed good correlation during static testing. However, their relatively low resistance to cyclic loads led to the replacement of the glass/epoxy material by carbon/epoxy tubes.

A total of three carbon/epoxy on steel suspension links were used in the test programme. The 30% weight saving was confirmed. These specimens met the design requirements and performed well when compared to the theoretically predicted values both in static and fatigue testing modes. It is intended to put two prototypes into service on a bogie.

KEYWORDS: application of composite materials, testing, static and fatigue behaviour

INTRODUCTION

This study was commissioned by the ACR works of GEC-Alstom with the aim of using composite materials technology to make weight savings in certain applications. The part chosen for the study was a suspension link forming part of the anti-roll system of a high speed train (TGV) bogie. Being a feasibility study only the mechanical behaviour aspects were to be examined; no account was taken of the long-term effects on composite material performance.

Expected weight saving was set at least at 30%. There are four links per bogie of average weight 10kg which in fact represents a relatively insignificant gain however it was felt that a successful link design could be fitted to a bogie without any safety implications.

The study was broadly divided into four main sections covering the following topics:

- a) Analysis of the existing suspension link and its working environment. Exploration of various ways of introducing composite materials into the construction.
- b) Finite element analysis to optimize the choice of composite materials and bond-line geometry.
- c) Fabrication of full size test samples and validation through mechanical testing.
- d) Optimization of the chosen solution to meet the specified requirement.

After the completion of the test programme three composite suspension links were manufactured in conformity with the specification, two of which were fitted to a bogie for testing under real conditions.

FUNCTIONALITY OF THE EXISTING LINK

The current part is made from a forging of AF42 steel (yield stress 42 MPa) and weighs 10 kg. It is fitted to the bogie and the anti-roll bar through silentbloc bushings pressed into the end eyes and held by circlips. Service loads are tension and compression only, static rating being ± 50 kN and the dynamic rating ± 30 kN in fatigue. Life expectancy is 30 years although the actual number of cycles this represents is difficult to verify. Simple dimensional analysis showed that in the shank the safety factor is 6 in monotonic loading and 3 in fatigue which obviously represents considerable overdesign.

The first part of the study was a research exercise on a solution that would possibly give the most weight saving. A link made up of light alloy end fittings incorporated into a filament-wound composite structure has been studied. The reduction in weight was estimated to be about 6 kg which is appreciable. However the approach was not justified from time scale and cost considerations as well as the potential development difficulties.

A second and more pragmatic approach was being simultaneously conducted which consisted of replacing the central solid steel part of the suspension link by a light-weight composite tube as showed in Figure 1.

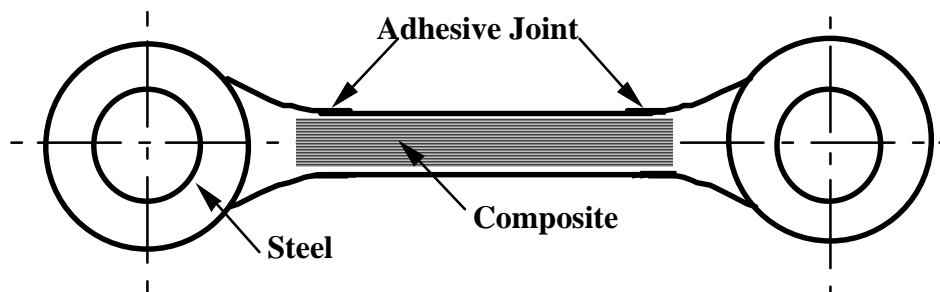


Figure 1 Suspension link with shank made from UD composite tube

As the service loads in this section are limited to tension and compression only since the bushings remove any applied moment at the ends, then a tube made from unidirectional composite material was thought to be a good choice.

It was intended that assembly between the composite material and the steel end-fittings should be by adhesive bonding. Initial estimations showed that the 30% weight-saving was theoretically possible, thus meeting the specification, provided the tube was of maximum length compatible with a sound adhesive bond.

Literature shows [1] that composite materials fatigue behaviour is generally good so it was felt the performance of the new link would depend largely on the efficiency of the adhesive bond.

DESIGN OF THE BONDED JOINT

In view of the importance of a correctly designed bond [2-6] the dimensioning of the end fittings was performed using finite element analysis. The calculations were done using ACCORD-2D which is a two dimensional elastic model. To ensure a favourable stress distribution it was decided to vary bond line thickness and to allow for geometry changes at the highly stressed end of the joint.

Basic materials properties used in the calculation are presented in Table 1.

Table 1. Basic materials properties used in the finite element calculation

Material	Young's modulus E (GPa)	Poisson's ratio •
Steel	210.0	0.30
Epoxy resin for the bond	1.4	0.33
unidirectional glass-epoxy tube	40.0	0.35

The results of the calculations enabled the joint configuration to be defined as showed in Figure 2. Bondline thickness was fixed at a nominal 0.4 mm.

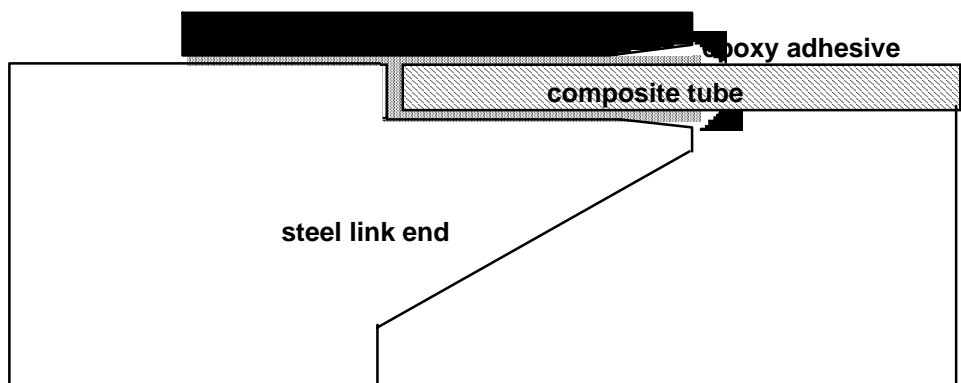


Figure 2. Bond geometry defined by finite element calculation

By assuming that the failure criterion should be maximum shear stress in the bond and applying it to the numerical data it is possible to predict overall joint performance. Taking the shear elastic limit of the epoxy adhesive; $\tau(\text{yield}) = 20 \text{ MPa}$; $\tau(\text{failure}) = 37 \text{ MPa}$, which give a notion of the safety factors. However this is not the case in fatigue; a reasonable assumption is that the fatigue strength is limited to between 10 and 20% of the static strength.

In the event that bond strength should need to be optimized after initial testing, then this could be done by increasing bonding contact area or by the choice of a more rigid composite material such as unidirectional carbon/epoxy.

TEST SAMPLE PREPARATION

Materials and Joint Dimensions Configuration

Each sample consisted of a composite tube middle section and two steel end-fittings to enable the adaptation to the test machine to be made either by pinning or by bolting. The fittings were machined from XC 48 steel which has very similar characteristics to the original forged suspension link. Bonding was carried out at 120°C.

The finite element analysis had showed that the composite tube should be of a material having an elastic modulus at least as high as unidirectional glass/epoxy ($V_f=60\%$). At the time of making the samples no unidirectional glass/epoxy composite tube in the required dimensions was available, hence the initial samples were made using tubing reinforced by glass woven roving having a warp/weft ratio of 60/40. Materials properties of the samples are presented in Table 2.

Table 2. Materials properties of the test samples

Material	E(GPa)	ν	τ -yield(MPa)	τ -failure(MPa)
Steel XC 48	210.0	0.33	400	700
Epoxy PERMABOND ESP 110	1.4	0.33	20	37
			X ⁺ (MPa)	X ⁻ (MPa)
Woven glass/epoxy tube (warp)	30.0	0.35	690	375
UD carbon/epoxy tube	230.0	0.35	3530	

The first samples were made to the dimensions given by the numerical calculation and the joint length was set at 30 mm (Fig. 2). In the first static tests premature cracking at the joint free edge was observed and the design load was not attained. This was thought to be due to the nature of the glass fibre composite used so it was decided to increase the bond length to 38 mm. This allowed the design load to be attained so all subsequent samples had the same joint length.

In order to attain the fatigue load, one test sample was made with steel XC 48 tubes and three made with unidirectional carbon/epoxy composite tubes.

Bonding and joint preparation

All bonded surfaces were prepared using 200 then 400 grade emery paper to produce a smooth mat surface. Degreasing was done by trichlorethylene dip and warm air drying.

The thickness of the internal diameter bond layer at 0.4 mm was maintained by a machined recess in the tube fitting onto a shoulder on the end piece. The outside diameter bond thickness was obtained by using four slips of thin rubber to centre the two half shells. The

slips did not run the full joint length to avoid creating any stress concentration and no significant loss of bond area was incurred by this technique.

Bonding time was a full two hours at 120°C followed by oven cooling.

TESTING

As this was a feasibility study and the main area of interest was in the performance of the bonded joint, no particular precaution was taken to monitor the behaviour of the composite tube. Apart from some static testing to provide reference values all the testing was in the dynamic mode.

The fatigue tests were carried out at the ACR plant by GEC-Alsthom on a Schenck 160 kN dynamic testing system.

Static loading

As the study progressed it was found necessary to make different types of specimen in order to reach the specified performance. However all specimens were geometrically identical and thus underwent the same testing schedule.

Static testing in tension and compression was done using loading speeds of 80 or 160 N/s. All the static test results obtained on various samples are presented in Table 3.

As a general rule local cracking of the samples in tension was seen at the free stressed end of the bond well in advance of any non-linear behaviour on the load/elongation curve. By increasing the bond length from 30 mm to 38 mm the initiation of the local cracking occurred at a much higher load level which lead to corresponding increases in joint yield and breaking strengths. Under compression loading, any global non-linear behaviour occurring was observed before the failure of the composite tube. One of the samples (N.5) was tested in compression up to 100 kN and then in tension to the failure; no significant effect of compression on tensile strength was observed.

Table 3. The static test results obtained on the samples with glass/epoxy composite tube

L1=50 mm, L2=30 mm, P(kN)					
N0	Load	P-crack	P-yield	P-break	Failure mode
1	tension	58	75	139	bond
2	tension	55	98	140	bond
3	tension	50	102	132	bond
4	compression			156	composite tube
5	compression then tension	50	86	137	bond joint
Tension: Pc=53±5 kN, Py=90±6 kN, Pb=137±3 kN.					
Compression: Pf=156 kN					
L1=50 mm, L2=38 mm, P (kN)					
6	tension	66	92	152	bond
7	tension	85	100	140	bond
8	tension	65	90	144	bond
9	compression			120	composite tube
Tension: Pc=72±13 kN, Py=94±6 kN, Pb=145±7 kN.					
Compression: Pf=120 kN					

One of the samples with carbon fibre tube was tested in tension only. Crack initiation at the free stressed edge was around 110 kN after which the load/elongation curve behaved non-linearly. This value is some 50% higher than previous values obtained with glass fibre

samples and confirms the well-known fact that sound bonds are made between members of similar stiffnesses. The breaking load of this sample was 158 kN.

Tensile failure occurs in the bond length while compression failure occurs in the composite tube. Examination of a failed bond shows fragments of composite tube adhering to the steel substrate and traces of epoxy resin on the tube indicating that the failure line oscillated between both substrates. This evidence confirms the choice of adhesive and the assembly technology.

Overall static behaviour was good and the results were well with the specification.

Fatigue testing

Fatigue testing was carried out under severe conditions going from 30 kN in tension to 30 kN in compression following a sinusoidal variation. Throughout the test sample stiffness was measured as a function of the number of cycles. The signal was processed by a personal computer set-up.

Fatigue life of glass/epoxy samples

For glass/epoxy samples, the test programme was started by fatiguing directly two specimens to failure with no prior mechanical loading being imposed. As is showed in Table 4 the fatigue life was fairly low and the usual cracking at the free stressed end of the joint was observed. As a result it was decided to pre-load the sample to 70 kN before starting the fatigue cycling. This load value represents the onset of local cracking. As can be seen in Table 4 this treatment seems beneficial although more testing would be necessary to confirm the trend.

Table 4. The fatigue test results obtained on the samples with glass/epoxy composite tube

NO.	Loading (f=12Hz)	Fatigue life (number of cycles)	failure mode
1	fatigue ± 30 kN	$209 \cdot 10^3$	bond joint
2	fatigue ± 30 kN	$232 \cdot 10^3$	bond joint
3	static tension 70kN fatigue ± 30 kN	$506 \cdot 10^3$	bond joint

A number of conclusions were drawn from these preliminary tests which lead to some modification in the programme.

- The results showed that fatigue life was well below that expected.
- Pre-stressing might be a useful means of increasing fatigue life.
- Bonds fail showing adhesive-cohesive behaviour.
- Sample stiffness remained fairly constant until the few minutes preceding bond failure.
- Concomitant with bond failure the local temperature in the bond zone increased by about 10°C.
- The stress concentration at the free joint end seems responsible for the low fatigue life.

Fatigue life of steel sample

This sample was prepared using a tube and end fittings made from the same steel in order to investigate the role of part stiffness on bond fatigue strength. Apart from the material used the sample was identical to its composite counterparts.

The fatigue testing was begun with no prior static loading of the part. Test conditions were ± 30 kN at 5 Hz.

The now classic local cracking was observed at about $400 \cdot 10^3$ cycles with no apparent change in overall stiffness. With still no evolution in stiffness the frequency was increased to 12 Hz from $1.3 \cdot 10^6$ cycles onwards. The test was stopped at $6 \cdot 10^6$ cycles with no apparent change in overall stiffness.

This one-off test was seen to indicate that a high modulus composite solution would be viable.

Fatigue life of carbon/epoxy sample

In the same way as the steel sample a unidirectional carbon/epoxy part (their characteristics are presented in Table 2) was prepared using exactly the same bonding configuration. The test results obtained are presented in Table 5. The loading spectrum is somewhat varied as rapid confirmation of the usefulness of the solution was required. As the test continued without apparent loss of sample stiffness the frequency was progressively increased to gain time. Probably the load conditions of ± 30 kN were too low but it was felt inappropriate to modify the specification at this stage.

During the test crack initiation occurred at about $300 \cdot 10^3$ cycles, slightly lower than the steel version. An attempt to measure the extent of crack propagation was made using infra-red thermography. The test frequency was deliberately increased in order to initiate local heating that could be detected. In spite of an increase to 20 Hz during about $60 \cdot 10^3$ cycles nothing was found. Any temperature increase was uniform and corresponded with an increase in the hydraulic actuator temperature. It was concluded that any crack propagation must be slight and have no significant effect on fatigue life in this case. Thereafter the load was increased until bond failure at $11.1 \cdot 10^6$ cycles.

Table 5. Fatigue test results obtained on the samples with carbon/epoxy composite tubes

Frequency	Load	Cycles	Observations
5 Hz	± 30 kN	$296 \cdot 10^3$	local cracking at the free joint end crack propagation detection using infra-red thermography
20 Hz	± 30 kN	$357 \cdot 10^3$	
10 Hz	± 30 kN	$450 \cdot 10^3$	failure in bond
20 Hz	± 30 kN	$1.5 \cdot 10^6$	
20 Hz	± 40 kN	$10.0 \cdot 10^6$	
20 Hz	± 50 kN	$10.5 \cdot 10^6$	
20 Hz	± 60 kN	$11.0 \cdot 10^6$	
20 Hz	± 60 kN	$11.1 \cdot 10^6$	

Based on this performance it was decided to proceed with the fabrication of three prototype suspension links, two of which were to be fitted to commercially operated trains for field trials.

CONCLUSIONS

This study has showed the feasibility of making steel to composites bonds that can have significant mechanical strength and fatigue life.

The best compromise was found to be a unidirectional carbon/epoxy tube due to its high modulus.

Inspite of high performance some local cracking at the free stressed end of an adhesive bond is inevitable though not necessarily important.

The combination of carbon/epoxy and steel enabled a weight saving of 30% to be made as required by the specification.

REFERENCES

1. Carlson R.L. and Kardomateas "An introduction to fatigue in metals and composites", Published by Chapman & Hall, 1996.
2. Kinloch A.J. "Adhesion and Adhesives", Published by Chapman & Hall, 1987.
3. Adams R.D. "Structural Adhesive Joints in Engineering", Elsevier Applied Science Publishers Ltd, 1984.
4. Apalak M.K. and Davies R. " Analysis and design of adhesively bonded corner joints: fillet effect", Int. J. Adhesion and Adhesives, Vol. 14 Number 3, 1994.
5. Wassell G.C., Clarc J.D., Crompton J.S. and Dickson R.F. "Fatigue within adhesive bonds", Int. J. Adhesion and Adhesives, Vol. 11 No. 2 April 1991.
6. Dennis J. Damico, Thomas L. Wilkinson, Jr., and Sandra L. F. Niks, "Composites Bonding", ASTM STP 1227, Eds. American Society for Testing and Materials, Philadelphia, 1994.

SIMULATION OF THERMO-MECHANICAL BEHAVIOR DURING QUENCHING PROCESS OF METAL MATRIX COMPOSITES

Dong-Ying Ju

*Department of Mechanical Engineering, Saitama Institute of Technology,
Fusaiji 1690, Okabe Saitama 369-02, Japan*

SUMMARY: In this paper, a numerical model is presented which aims to simulate the occurrence and evolution of residual stresses during quenching process of metal matrix composites. Because the residual stresses on the interface are related to void formation, growth and coalescence, it is important to consider the variation of temperature, phase transformation and stress fields in a quenching process. Here, a set of coupled equations of the heat conduction, stress/strain and phase transformation of materials is given in the framework of metallo-thermo-mechanical theory. A method of numerical calculation by the finite element method considered the coupling of the thermo-mechanical behavior incorporating the variation of temperature, phase transformation and elastic-plastic deformation. As an example, simulation of a quenching process associated with a metal matrix composites of Ti-Fe matrix reinforced unidirectionally by SiC-ZrO₂ fiber is engaged in this study. In results of this simulation, the micro-structure behavior and residual stress on the interface of the fiber-matrix is evaluated, and the effect of fiber size is also discussed.

KEYWORDS: metallo-thermo-mechanical theory, interface behavior, metal matrix composites, quenching process, inelastic constitutive equation, jump conditions, finite element analysis

INTRODUCTION

In the heat treatment process of metallic material, such as quenching and tempering, complicated coupling effect of material behavior is sometimes important to be taken into account in the computer simulation. Metallo-thermo-mechanical theory[1-4] and some numerical method[5-7] capable to describing such interaction among phase transformation, effect of coupling between temperature, micro structure change due to phase transformation had been developed by many researchers based on continuum thermodynamics.

Recently, the development of some metal matrix composites depends strongly on controlling the physical and chemical properties at the fiber-matrix interface which are utilized by quenching process. However, because the residual stresses on the interface are related to void formation, growth and coalescence[8], it is important to consider the variation of temperature, phase transformation and stress fields in the quenching process. Here, in order to forecast thermo-mechanical behavior, three basic problems have to be considered. The first one is that phase transformation is strongly nonlinear with respect to time and location and it affects the mechanical behavior on the interface of the matrix composites. The second is the effect of size rate between the fiber and matrix composites; and the third is the jump of about

temperature, stress/strain fields on the interface due to variation of material properties in the fiber and matrix composites. For solving these problems, here, a set of coupled equations of heat conduction, stress/strain and phase transformation of materials is given in the framework of metallo-thermo-mechanical theory. A numerical model is presented which aims to simulate the occurrence and the evolution of residual stresses during the quenching process of metal matrix composites. The method of numerical calculation by the finite element method is considered for coupling the thermo-mechanical behavior incorporating the variation of temperature, phase transformation and stress/strain fields. In the calculation for stresses, an elastic-plastic and creep constitutive model is employed. As an example of calculation, simulation of a quenching process associated with a Ti-Fe alloy reinforced unidirectionally by SiC-ZrO₂ fiber is engaged in this research. In results of this simulation, thermo-mechanical behavior and the residual stresses of the composites is evaluated, and some effect due to fiber-matrix size are also presented.

GOVERNING EQUATIONS

The detail of introducing the governing equations in the framework of thermodynamics capable of describing the governing equations for temperature and stress/strain fields incorporating metallic structures are already reported elsewhere[5]. Here, the fundamental equations are summarized in the following:

Mixture rule

When a material point undergoing a heat treatment process is assumed to be composed of multi-phase structure, an assumption is made that a material parameters χ is described by the mixture law[9]

$$\chi = \sum_{I=1}^N \chi_I \xi_I; \quad \text{and} \quad \sum_{I=1}^N \xi_I = 1, \quad (1)$$

where ξ_I denote the volume fraction for the I-th phase.

Heat Conduction Equations

The local energy balance or the first law of thermodynamics is usually given in terms of the internal energy $e = g + T \eta + (\sigma_{ij} \epsilon_{ij}) / \rho$, as

$$\rho \dot{e} = \sigma_{ij} \dot{\epsilon}_{ij} - \frac{\partial h_i}{\partial x_i}, \quad (2)$$

with stress power $\sigma_{ij} \dot{\epsilon}_{ij}$. Here, ρ and h_i are the density and heat flux, respectively. η is the entropy of the thermodynamic state. Introducing the expressions for specific heat $c = T(\partial \eta / \partial T)$, Equation (2) is reduced to a heat conduction equation

$$\rho c \dot{T} - \frac{\partial}{\partial x_i} (k \frac{\partial T}{\partial x_i}) - \sigma_{ij} \dot{\epsilon}^p_{ij} + \sum \rho_I l_I \dot{\xi}_I = 0, \quad (3)$$

where k and l_I denote the coefficient of heat conduction and the latent heat produced by the progressive I-th constituent.

The boundary conditions of heat transfer on the inner surface is assumed to be

$$-k \frac{\partial T}{\partial x_i} n_i = h(T - T_w), \quad (4)$$

where h and T_w are the heat transfer coefficient and the temperature of coolant on heat transfer boundary with unit normal n_i , respectively.

Constitutive Equation

Total strain rate $\dot{\varepsilon}_{ij}$ is assumed to be divided into elastic, plastic, thermal strain rates and those by structural dilatation due to phase transformation and creep such that

$$\dot{\varepsilon}_{ij} = \dot{\varepsilon}_{ij}^e + \dot{\varepsilon}_{ij}^p + \dot{\varepsilon}_{ij}^T + \dot{\varepsilon}_{ij}^m + \dot{\varepsilon}_{ij}^c . \quad (5)$$

Here, elastic and thermal strains are normally expressed as

$$\varepsilon_{ij}^e = \frac{1+\nu}{E} \sigma_{ij} - \frac{\nu}{E} \sigma_{kk} \delta_{ij} , \quad (6)$$

and

$$\varepsilon_{ij}^T = \alpha(T - T_0) \delta_{ij} , \quad (7)$$

with Young's modulus E , Poisson's ratio ν and thermal expansion coefficient α , respectively. Here, T_0 is the initial temperature of material.

Strain rates due to structural dilatation and transformation plasticity depending on the I -th constituent read

$$\varepsilon_{ij}^m = \sum_{I=1}^N \beta_I \xi_I \delta_{ij} , \quad (8)$$

where β stands for the dilatation due to structural change.

The plastic strain rate is reduced to the form when employing temperature dependent materials parameters

$$\dot{\varepsilon}_{ij}^p = \lambda \frac{\partial F}{\partial \sigma_{ij}} = \hat{G} \left(\frac{\partial F}{\partial \sigma_{kl}} \dot{\sigma}_{kl} + \frac{\partial F}{\partial T} \dot{T} + \sum_{I=1}^N \frac{\partial F}{\partial \xi_I} \dot{\xi}_I \right) \frac{\partial F}{\partial \sigma_{ij}} , \quad (9)$$

with a temperature dependent yield function

$$F = F(\sigma_{ij}, \varepsilon^p, \kappa, T, \xi_I) , \quad (10)$$

with hardening parameter κ , where

$$\frac{1}{\hat{G}} = - \left(\frac{\partial F}{\partial \varepsilon_{mn}^p} + \frac{\partial F}{\partial \kappa} \sigma_{mn} \right) \frac{\partial F}{\partial \sigma_{mn}} , \quad (11)$$

The creep strain rate is assumed to follow a simple Norton creep law as

$$\dot{\varepsilon}_{ij}^c = \frac{3}{2} A_c^{1/m} \bar{\sigma}^{(n-m)/m} \bar{\varepsilon}^{c(m-1)/m} s_{ij} . \quad (12)$$

Here, s_{ij} , $\bar{\sigma}$ and $\bar{\varepsilon}$ are deviatoric stress, equivalent stress and equivalent strain, respectively. Either isotropic or kinetic hardening type of yield function F is available to be used in the paper. Symbol A_c , n and m are material parameters based on Norton creep law. Either isotropic or kinetic hardening type of yield function F is available to be used in this paper.

Kinetics of Quenching Process

In the case of quenching, two kinds of phase transformation are anticipated: One is governed by the diffusionless or martensite mechanism. From thermodynamic consideration, the formula for this type of reaction from austenite is assumed to be governed by the modified Magee's rule[10] as

$$\xi_M = 1 - \exp[\phi(T - T_M) - \varphi(\sigma_{ij})] , \quad (13)$$

with

$$\varphi(\sigma_{ij}) = A_1 \sigma_m + A_2 J_2^{1/2} , \quad (14)$$

where T_M is the martensite-start temperature under vanishing stress. The parameters A_1 and A_2 can be identified if we have the data of the martensitic transformation depending on the applied stress.

The other type of phase transformation is controlled by diffusion mechanism, and the volume fraction of developing phase such as pearlite may be expressed by modifying the Johnson-Mehl relation[11] as

$$\xi_p = 1 - \exp(-V_e) \quad , \quad (15)$$

where V_e is defined by

$$V_e = \int_0^t \bar{f}(T, \sigma_{ij})(t - \tau)^3 d\tau \quad . \quad (16)$$

Here, we separate the function $\bar{f}(T, \sigma_{ij})$ into two independent function of temperature and stress as

$$\bar{f}(T, \sigma_{ij}) = f_1(T) f_2(\sigma_{ij}) \quad . \quad (17)$$

Since the time-temperature-transformation *TTT* diagram under the applied mean stress σ_m in logarithmic scale deviates from the one without stress which is represented by the function $f(T)$, the kinetic equation of diffusion type is often applied to the variations of pearlite or ferrite structure in quenching processes. An identification of the function $f(T)$ can be made possible by the use of some experimental data of the structure change.

JUMP CONDITIONS ON INTERFACE

Due to difference of materials behavior between the fiber and matrix composites, discontinuous phenomenon of thermomechanical fields on the interface of MMC materials during the quenching process will be presented. In order to describe the discontinuous phenomenon, some jump conditions can usually be used. If the interface of materials does not propagate within the domain, the conservation laws of mass, momentum and energy are respectively shown as[12]

$$[q] = 0 \quad ; \quad [\dot{\mathbf{u}} \cdot \mathbf{n}] = 0 \quad \text{and} \quad [\mathbf{t} \cdot \mathbf{n}] = 0 \quad , \quad (18)$$

where $\dot{\mathbf{u}}$ and \mathbf{t} indicate the displacement vector and stress vector on the interface surface. \mathbf{n} means the outward normal from the region (-) to the region (+) on the surface of the interface. The function $[\psi]$ represents the jump of a physical quantity ψ between the two domains over the interface, i.e.

$$[\psi] = \psi^+ - \psi^- \quad . \quad (19)$$

The discontinuity in the macroscopic sense take advantage from the phenomenological point of view when we deal with the thermo-mechanical behavior of structures involving imperfect interface.

ALGORITHM OF FINITE ELEMENT ANALYSIS

The formulated finite element equation system considering the coupling between increment of nodal displacement $\{\Delta u\}$ and temperature $\{T\}$ as well as volume fraction of structure ξ_I can be expressed as

$$[P]\{\dot{T}\} + [H]\{T\} = \{Q(\xi_I), \sigma_{ij}\} \quad (20)$$

and

$$[K(u_i)]\{\Delta u_i\} = \{\Delta F(T, \xi_I)\} \quad (21)$$

Here, matrices $[P]$, $[H]$ and $[K]$ represent the matrices of heat capacity, heat conduction and stiffness, respectively, and the vectors $\{Q\}$ and $\{\Delta F\}$ are heat flux, and increments of thermal load. These equations are strong nonlinear equation, which are derived by the use of the expression of stress increment vector as

$$\{d\sigma\} = [D] \left(\{d\varepsilon\} - \frac{3d\bar{\varepsilon}^c}{2\bar{\sigma}} \{s\} - \{\bar{\alpha}\} dT - \sum_{I=1}^N \{\bar{\beta}\} d\xi_I \right) + \frac{1}{S_0} \left(\frac{\partial \bar{\sigma}^2}{\partial T} dT + \sum_{I=1}^N \frac{\partial \bar{\sigma}^2}{\partial \xi_I} d\xi_I \right) \{s\}, \quad (22)$$

where $\bar{\varepsilon}^c$ and $\{s\}$ are equivalent creep strain and deviatoric stress vector. $[D]$ denote a elastic-plastic matrix based on Mises' type yield function. Here, the functions depending on temperature and phase transformation $\bar{\alpha}$ and $\bar{\beta}$ can be written as

$$\{\bar{\alpha}\} = \frac{\partial}{\partial T} ([D^e]^{-1} \{\sigma\}) + \sum_{I=1}^N (\alpha_I \xi_I \{1\} + \frac{\partial \alpha_I}{\partial T} \xi_I dT \{1\}), \quad (23)$$

and

$$\{\bar{\beta}\} = \frac{\partial}{\partial \xi_I} ([D^e]^{-1} \{\sigma\}) + \beta_I \{1\}, \quad (24)$$

α_I and β_I are the coefficients of thermal expansion and dilatation due to I-th phase transformation, respectively. $[D^e]$ denote the elastic matrix of materials.

In order to treat unsteady coupled equations depending on time, a time integration scheme 'step-by-step time integration method' is introduced in numerical calculation, while an incremental method[13] is used for deformation and stress analysis.

In order to treat the physical discontinuity, a penalty function method[14] or Lagrangian multiplier method was employed in this paper.

SIMULATED RESULTS

Model of Simulation

The material for simulation of quenching process was a metal matrix composite reinforced unidirectionally with continuous fibers. The matrix material was a Ti-Fe alloy (\bullet type) consisting of Ti-3.25Fe-2Cr-2Mo in weight percent. The reinforcing phase was continuous SiC-ZrO₂ fiber. The diameter of fibers is 300 μ m. It is assumed that the fiber is located periodically with the same interval and that each fiber is the same shape as shown in Fig.1(a). Then, the unit cell including a fiber depicted by broken line in Fig.1(a) is extracted from the bulk material. For the sake of simplification, a unit cell is considered as plane strain problem as indicated in Fig.1(b). In order to examine the effect of fiber size, three ratios of the radius of fiber to the width of matrix are considered with $r/a=1/3$ and $2/3$. The quenching process of the model is started from an initial temperature at 850 °C (temperature of oil 60 °C). The heat transfer coefficient to oil on the surface of the composites is chosen as $h=0.00235\text{cal}/(\text{mm}^2\cdot\text{s}\cdot^\circ\text{C})$. As for the finite element calculation of temperature and stress fields based on the obtained mixture rule of the phase transformations, the following material table are employed:

Table 1 Parameters for finite element analysis

	Matrix	Fiber
Heat conductivity [cal/mm s deg]	0.0361+0.0000193T	0.0289-0.0000128T
Density [g/cm ³]	7.84	3.18
Specific heat [cal/(g deg)]	0.286	0.219
Young's modulus [Gpa]	220.0+0.054T-0.00032T ²	398.4+0.039T-0.00028T ²
Poisson's ratio	0.32	0.19
Thermal expansion [1/deg]	0.518x10 ⁻⁵	0.31x10 ⁻⁵
Dilatation of phase transformation [%]	$\beta_M=-0.015; \beta_P=-0.011$	~
Yield stress [Mpa]	526.5-0.12T-0.00045T ²	780.0-0.16T-0.00049T ²
Hardening coefficient [Mpa]	238.2-0.225T	361.5-0.29T

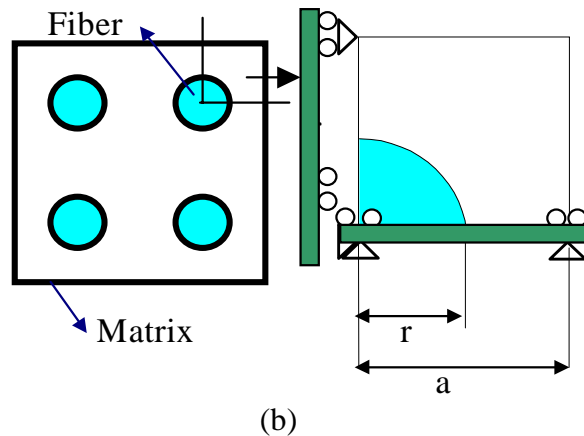
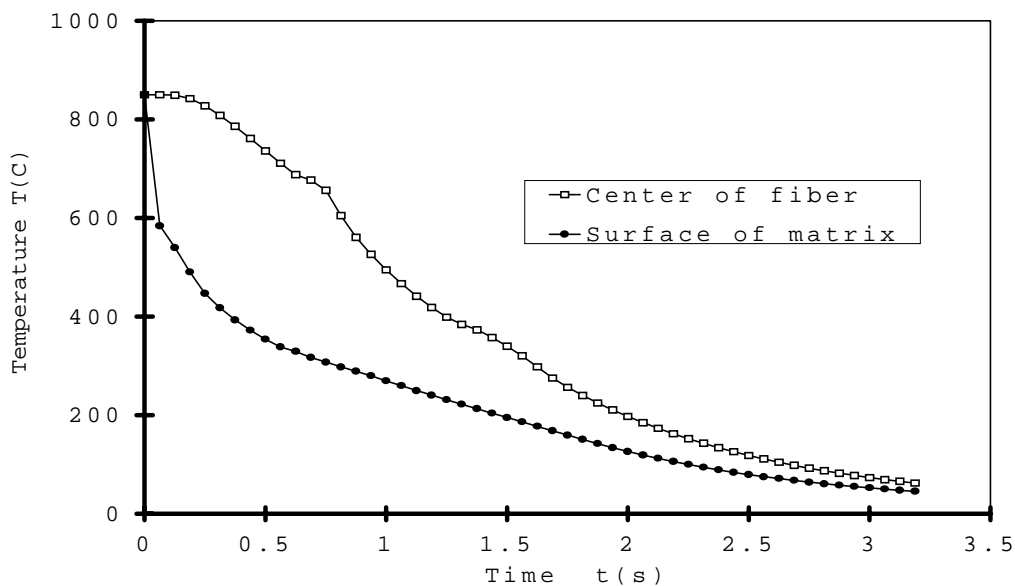


Fig. 1 Cross section of metal matrix composite and unit cell model.

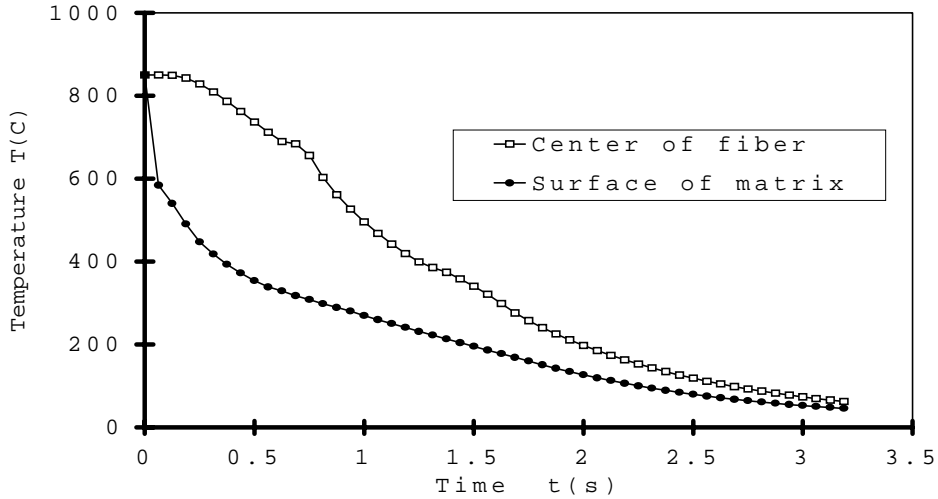
RESULTS OF SIMULATION

Figure 2(a) and (b) show the variation of temperature distribution on the center of the fiber and the surface of matrix corner. The volume fraction of martensite transformation at $t=0.125(\text{sec})$ for the two size ratio are shown in Fig.3. The equivalent stress at $t=0.125$ and $0.25(\text{sec})$ are shown in Fig.4 and Fig.5. Figure 6 shows the residual equivalent stress with different size ratio. From these results, we can observe that the temperature variation of composites of these two size ratio are nearly similar, but the distribution of martensite transformation near the interface has different form. When martensite transformation produced on the interface for the small size ratio ($r/a=1/3$), i.e. $t=0.125(\text{sec})$, distribution of the equivalent stress which is shown in Fig.4 exhibits jump phenomenon. However, jump behavior done not appear in the case of large size (ratio $r/a=2/3$). The jump of equivalent stress with small size ratio is remains until to finish of the quenching process.

On the interface region with small size ratio, the jump level of equivalent stress is also very small, but the rapid variation of equivalent stress appears in the finished domain of martensite. Due to high elastic modulus of the fibers and inelastic region in finished domain of martensite, a harmonious distribution of stress in fiber in the case of a small size ratio can be expected.

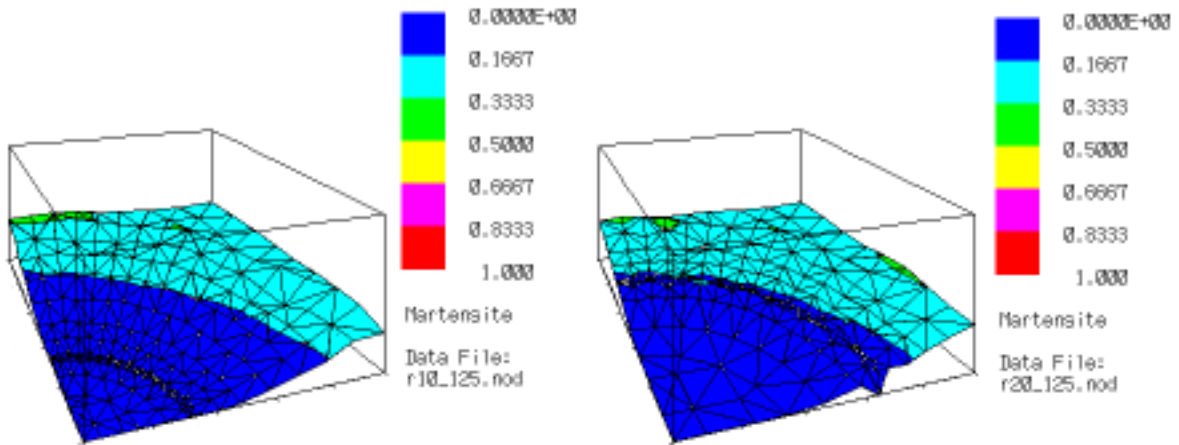


(a) $r/a = 1/3$



(b) $r/a = 2/3$

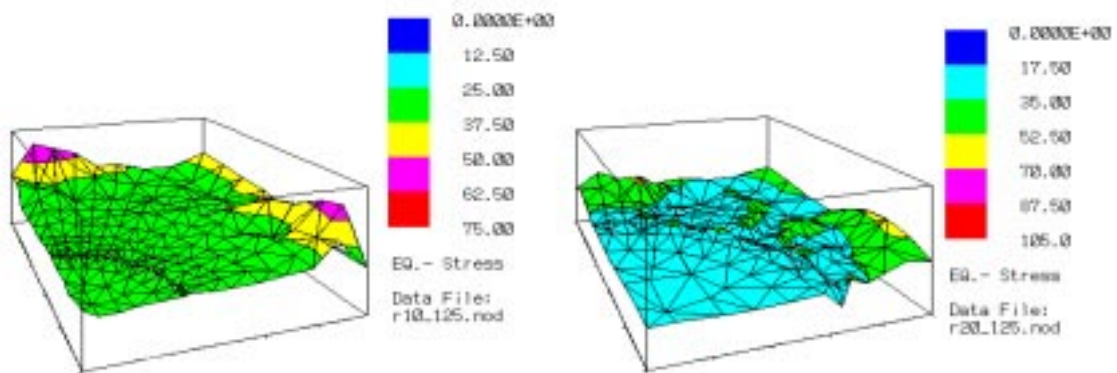
Fig.2 Temperature variation on center of fiber and surface of matrix corner.



(a) $r/a=1/3$

(b) $r/a=2/3$

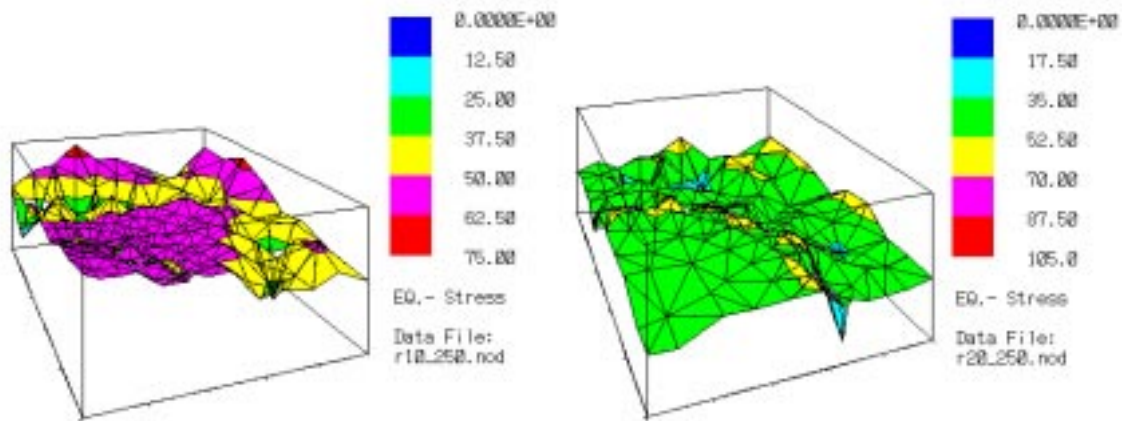
Fig.3 Distribution of martensite fraction at $t=0.125(\text{sec})$.



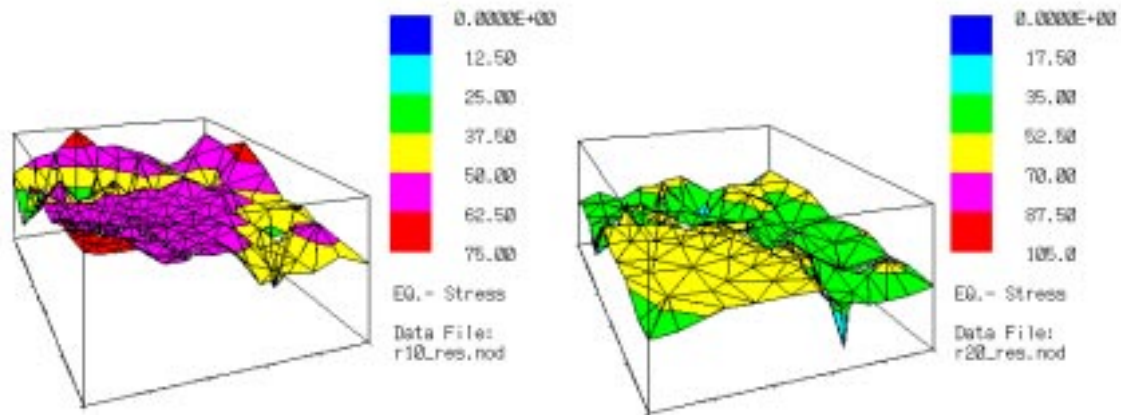
(a) $r/a = 1/3$

(b) $r/a = 2/3$

Fig.4 Distribution of equivalent stress at $t = 0.125(\text{sec})$.



(a) $r/a = 1/3$ (b) $r/a = 2/3$
 Fig.5 Distribution of equivalent stress at $t = 0.25$ (sec).



(a) $r/a = 1/3$ (b) $r/a = 2/3$
 Fig.6 Distribution of residual equivalent stress.

CONCLUDING REMARKS

Metallo-thermo-mechanical theory previously developed is extended to simulated the quenching process. By adopting this theory, finite element simulation of a unit cell of metal matrix composites is carried out, and some results of the calculated distribution of temperature and residual stress are discussed. From these results, we can obtain some useful conclusions:

- (1) Simulated results of temperature and stresses during and after quenching process based on coupled analysis present thermomechanical behavior on the interface of the MMC composites.
- (2) Micro-mechanism of quenching including structure change depending on temperature and inelastic effect on stress hardening due to martensite transformation is revealed to be reasonable.
- (3) Effect of size rate of fiber and matrix is presented and it is important to select the size ratio for a perfect design of MMC composites.

REFERENCE

- 1 Inoue, T. and Raniecki, B., "Determination of Thermal-hardening Stress in Steels by Use of Thermoplasticity", *Journal of Mech. Phys. Solids*, Vol.26, 1978, pp.87-212.
- 2 Inoue, T., Nagaki, S., Kishino T. and Monkawa, M., "Description of Transformation Kinetics, Heat Conduction and Elastic-Plastic Stress in the Course of Quenching and Temperature of Some Steels", *Ing.-Arch.*,50, 1981, pp.315-327.
- 3 Denis, S., Simon, A. and Beck, G., "Estimation of the Effect of Stress/Phase Transformation Interaction when Calculation Internal Stress During Martensitic Quenching of Steel", *Trans. ISIJ*, 22, 1982, pp.504-513.
- 4 Inoue, T., "Inelastic Constitutive Relationships and Applications to Some Thermomechanical Process Involving Phase Transformations", *Thermal Stresses*, 3, (R.B. Hetnarski, ed.), Elsevier Science Publishers, B.V., 1989, pp.192-278 .
- 5 Inoue, T. and Wang, Z.G., "Coupling between Stresses, Temperature and Metallic Structure During Process Involving Phase Transformation", *Material Science Technology*, 1, 1985, pp.845-850.
- 6 Inoue, T., Ju, D.Y. and Arimoto, K. "Metallo-Thermo-Mechanical Simulation of Quenching Process --- Theory and Implementation of Computer Code Hearts", *Proceeding of 1st International Conference on Quenching and Distortion Control*, Chicago, September, 1992, pp.205-212.
- 7 Ju, D.Y. Sahashi, M. Omori, T. and Inoue, T., "Residual Stresses and Distortion of a Ring in Quenching-Tempering Process Based on Metallo-Thermo-Mechanics", *Proceeding of 2nd International Conference on Quenching and Distortion Control*, Cleveland, November, 1996, pp.249-257.
- 8 Chawla, K.K., *Metal Matrix Composites, Materials Science and Technology*, (Chahn, R.W. Haasen, P. and Kramer, E.J. eds.), Volume 13, 1991, pp.122-179.
- 9 Bowen, R.M., "Continuum Physics", Vol.3, (A.C. Eringen ed.), Academic Press, New York, 1976, pp.2-129.
- 10 Magee, C.L., "Nucleation of Martensite", ASM, New York, 1968.
- 11 Johnson, W.A. and Mehl, R.F., "Reaction Kinetics in Processes of Nucleation and Growth", *Trans. AIME*, 135, 1939, pp.416-458.
- 12 Chadwick, P., *Continuum Mechanics*, George Allen & Unwin Ltd., London, 1976, p.114.
- 13 Bathe, K.J., "Finite Element Procedures in Engineering Analysis", Prentice-Hall, New Jersey, 1982.
- 14 Zienkiewicz, O.C., *The Finite Element Method*, McGraw-Hill Ltd., London, 1977, • p.284.

APPLICATIONS OF ADVANCED MATERIALS TO ROBOTIC DESIGN: THE FREEDOM-7 HAPTIC HAND CONTROLLER

John McDougall¹, Larry B. Lessard¹ and Vincent Hayward²

¹*Department of Mechanical Engineering - McGill University
817 Sherbrooke St. West, Montreal, Quebec, CANADA H3A 2K6*

²*Department of Electrical Engineering - McGill University
817 Sherbrooke St. West, Montreal, Quebec, CANADA H3A 2K6*

SUMMARY: Advanced composite materials have many potential benefits in a robotic design application. For the Freedom-7 haptic hand controller, two composite components are proposed. First, the stage 3 linkage is replaced by a small diameter commercially available carbon fiber tube with bonded metal inserts. Second, a composite box-beam structure is proposed to replace the existing aluminum effector arm. Finite element models are used to evaluate the proposed changes. The bond geometry parameters for the composite tube/aluminum insert interface is optimized for minimum weight. Comparisons are drawn between a proposed aluminum box-beam effector arm and a composite arm. Analysis shows an increase in lowest resonant natural frequency, an increase in stiffness and a decrease in overall weight of the composite arm over the aluminum arm. The result of this work is a lighter stiffer hand controller.

KEYWORDS: composite application to robotics, robotic design, finite element modeling, haptic control, force-feedback, bonding, modal vibration, optimization.

INTRODUCTION

Advanced robotic applications have two ever-present performance concerns: inertia reduction and increased stiffness. In most cases, these seem to be opposing criteria. To lower the manipulator inertia, robot links need to be light and slender. However, stiffness requirements ask for links to be heavy and robust. Often, an inadequate compromise has to be made between these two requirements when designers restrict themselves to traditional materials. Many robot designers try to circumvent the problems associated with traditional materials by enhancing the control structure of a manipulator. However, due to the inevitable trade-off between stiffness and inertia and the fundamental limits on what can be achieved by control, the field of robot design is being opened up to advanced composite materials. The high stiffness-to-weight ratio and the opportunity to precisely tailor properties such as stiffness, damping and thermal expansion obtainable with the advanced materials of today make them ideally suited to applications in the robot industry.

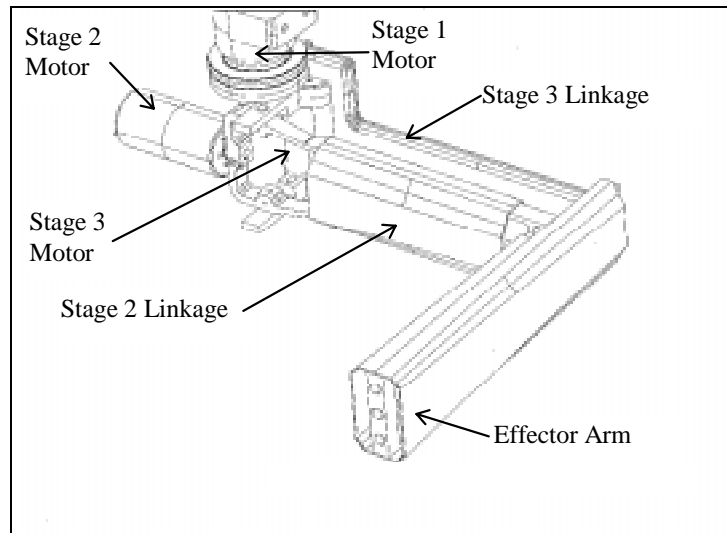


Figure 15: Translation Stage Schematic

Until recently, there have been few applications of advanced materials in the robotic industry due to a lack of adequate design tools and unfamiliarity of designers with the materials themselves. One major drawback to the application of these materials is the inevitable metal composite interfaces that arise at the joints of the manipulator. Composite materials do not easily accept bearing fittings or the attachment of drive assemblies.

The Freedom-7 consists of the development of a 7-DOF force feedback haptic hand controller for virtual and teleoperated environments. The hand controller consists of a 3-DOF translation stage (figure 1) and a 4-DOF rotational distal stage. Haptic devices, by their nature requiring interaction with the human hand's sense of touch, require high acceleration capability, which translates directly into the lowest possible link inertia for a given actuating capability [1]. Due to a user's limited ability to absolutely locate points in space, precision in displacement conditions on the end effector has little bearing on the effectiveness of a haptic device [1]. Therefore, the minimum allowable link stiffness is determined by the lowest structural resonant frequency.

The Freedom-7 has several design difficulties inherent in the original aluminum prototype. To reduce the inertia felt by the operator, the links have to be made very slender and light. A low modulus metal such as aluminum cannot provide the stiffness necessary to meet the frequency requirements. The lowest resonant natural frequency of the structure has to be above 200 Hz [2], for simulating contact with a rigid wall in a virtual environment.

Another consideration is that the distal stage is driven by a series of high modulus polymeric fiber bundles that run through a series of pulleys mounted on the translation stage to a fixed motor assembly. In the aluminum prototype, these strings were completely exposed. Such a configuration is clearly unacceptable for a production unit. A composite box-beam structure is proposed both as a structural member and as a protective cover for these strings. With proper choice of the layup material and fiber orientation, the superior stiffness and damping capabilities of composite materials can significantly increase the stiffness of this member while reducing its overall weight.

This paper will be divided into two sections. The first section deals with the incorporation of commercially available carbon-fiber tubes and metallic end fittings into the translation stage in the place of the stage 3 linkage (see figure 1). The second section deals with the design of

a carbon fiber box-section that will be used in the place of the effector arm as a structural member as well as a protective covering for the strings used to drive the distal stage.

CARBON FIBER TUBING IN STAGE 3 LINKAGE

There are several unique characteristics of the Freedom-7 that drive the design choices for the translation stage. For instance, the load cases on the individual links are three dimensional. All links must resist bending loads in two directions, as well as tensile and compressive axial loads. This type of loading suggests that the most efficient link cross section would be tubular. The link most open to exploitation of this design is the stage 3 linkage (see figure 1).

The main consideration for the incorporation of carbon fiber tubing into the design of the hand controller is the carbon/metal interface that occurs at the structure joints. The joints of the translation stage are articulated and so require bushing and/or bearing fittings. As such, machined metal inserts are required. The interface between metal and composite materials has been the subject of much research [3,4,5]. The preferred joining method for these two materials is an adhesive bond. The particular adhesives come in many forms with widely varying material properties, and many factors have to be weighed in order to choose the correct adhesive. Often, a more ductile adhesive will give a stronger bond than a stiffer, more brittle adhesive [3]. The geometry of the bond, including adhesive line thickness (l in figure 2), axial penetration length and adherend wall thickness (a in figure 2) are also of primary concern when designing a bonded interface [4].

The requirements for the Freedom-7 design are of an unusual nature. The two dimensional bending moments suggest that the optimal link cross-section be circular, however there is no torque applied axially to the shaft. Therefore design parameters that have been extensively studied for bonding of composite prop-shafts [4] do not apply. Another method for optimizing the bond geometry needs to be determined.

First, some choices had to be made about the general shape of the metal insert. Aesthetics and stiffness requirements would suggest that an internal plug type fitting would be the best solution but, due to the small inner diameter of the tubes in question, this is rather difficult to execute. A choice was made to use a cylindrical metal outer sleeve that could be machined out of a piece of stock material to the correct size to take the bearing fitting. The sleeve wall thickness, the adhesive line thickness and the sleeve machining are left to be determined.

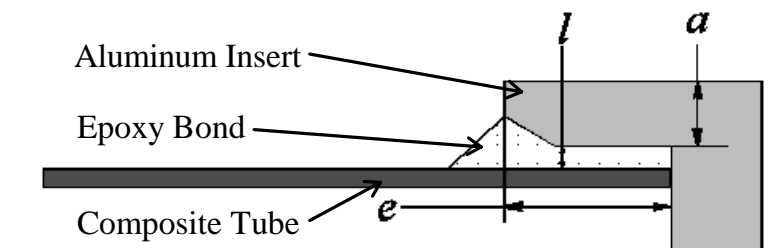


Figure 16: Bond Geometry Dimensions

As an initial attempt to identify the factors that weigh heaviest on the eventual joint strength, a series of finite element models were constructed with varying parameters. Twenty-four finite element tests were made, as summarized in table 1. The referenced dimensions are shown in figure 2, where e is the axial engagement of the composite tube, and a and l have already

been defined. The fillet at the end of the metal insert and the bond fillet are identical in each model, which is a generally accepted configuration for the reduction of peak stresses at the bond edges [5].

Each test was done to determine the maximum principal stress concentration in the overall bond and the stress distribution along the bottom (carbon fiber interface) for a simple tensile load case. The maximum principal and shear stress for each test is shown in table 2, with the referenced stress concentration locations shown in figure 3. Figures 4 to 6 compare the maximum principal stress distribution along the bottom surface of the bond for the variation of a , l , and e individually around the arbitrary median of 2 mm, 0.25 mm and 5 mm respectively.

Table 1 - Variation of Dimensions for Finite Element Tests

Test Number	a (mm)	l (mm)	e (mm)
Tests 1.1-1.4	2.0	0.25	5.0
Tests 2.1-2.4	0.5	0.25	5.0
Tests 3.1-3.4	4.0	0.25	5.0
Tests 4.1-4.4	2.0	1.0	5.0
Tests 5.1-5.4	2.0	0.05	5.0
Tests 6.1-6.4	2.0	0.25	10.0
Tests 7.1-7.4	2.0	0.25	3.0

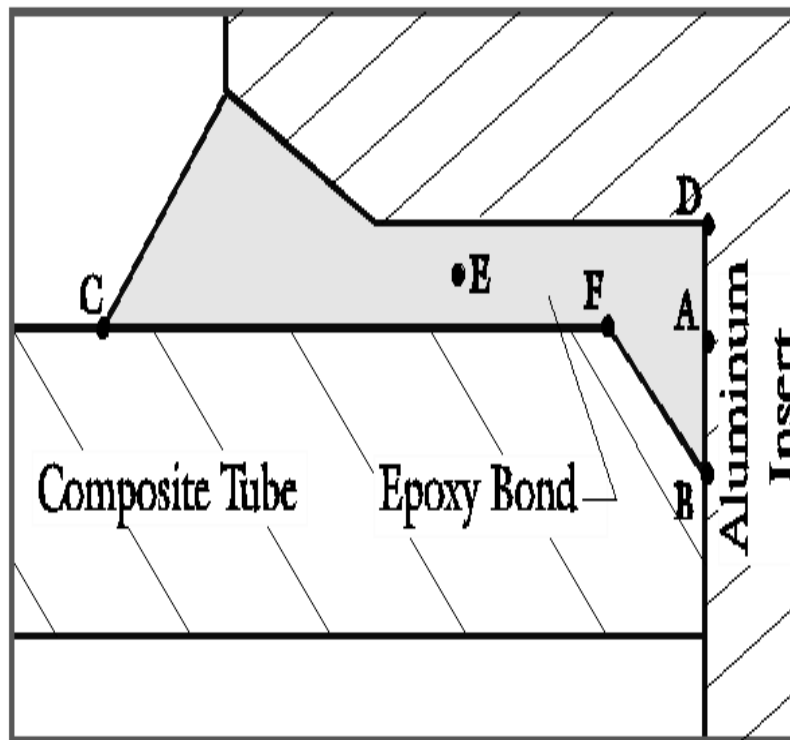


Figure 17: Stress Concentration Locations

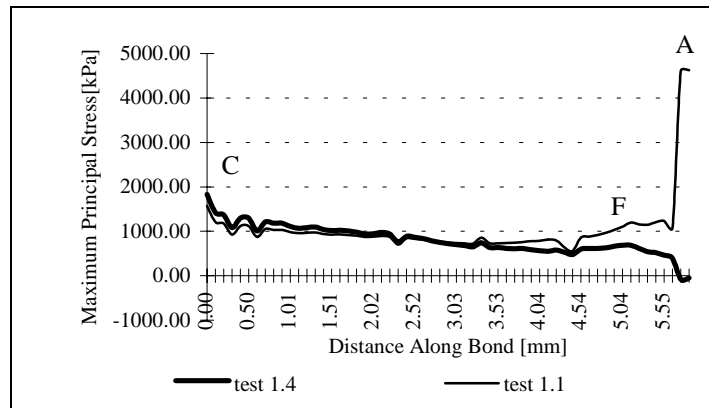


Figure 4: Variation of Maximum Principal Stress due to Bond Detachment

Table 2: Summary of Maximum Principal Stress Values

	Test 1.1	Test 1.2	Test 1.3	Test 1.4	Test 2.1	Test 2.2	Test 2.3
Max. Principal	1.50×10^4	1.16×10^4	1.22×10^3	1.34×10^3	1.67×10^4	1.18×10^4	1.46×10^3
Location	A	B	D	D	A	B	D
	Test 2.4	Test 3.1	Test 3.2	Test 3.3	Test 3.4	Test 4.1	Test 4.2
Max. Principal	1.67×10^3	3.96×10^3	4.34×10^3	9.96×10^2	1.16×10^3	3.29×10^3	2.37×10^3
Location	D	A	B	D	D	A	B&C
	Test 4.3	Test 4.4	Test 5.1	Test 5.2	Test 5.3	Test 5.4	Test 6.1
Max. Principal	1.89×10^3	1.89×10^3	9.87×10^3	6.96×10^3	1.23×10^3	2.06×10^3	1.08×10^4
Location	D&C	D&C	A	B	D&F	D	A
	Test 6.2	Test 6.3	Test 6.4	Test 7.1	Test 7.2	Test 7.3	Test 7.4
Max. Principal	1.84×10^3	6.69×10^2	7.55×10^2	1.11×10^4	8.45×10^3	1.39×10^3	1.64×10^3
Location	B	D	D	A	B	D	D

Each finite element test has similar configurations depending on the test number. For example, test 1.1 and test 1.4 are the same mesh exactly except that the bond has been broken away from the end of the aluminum insert (BD in fig.3). Tests 1.2 and 1.3 are similar to 1.1 and 1.4 in that the a , l , and e values remain constant but a chamfer has been introduced to the end of the carbon fiber tube (BF in fig.3). As well, test 1.2 has a complete bond with the aluminum insert while in test 1.3 it has once again been broken between the epoxy and the insert end. As we can see in figure 4, the effect of breaking the bond between the epoxy and the end of the tube removes the huge peak stress that can be observed at that interface (A) in test 1.1. The peak stress is transferred to point D (see figure 3) and, as noted in table 2, is reduced by an order of magnitude.

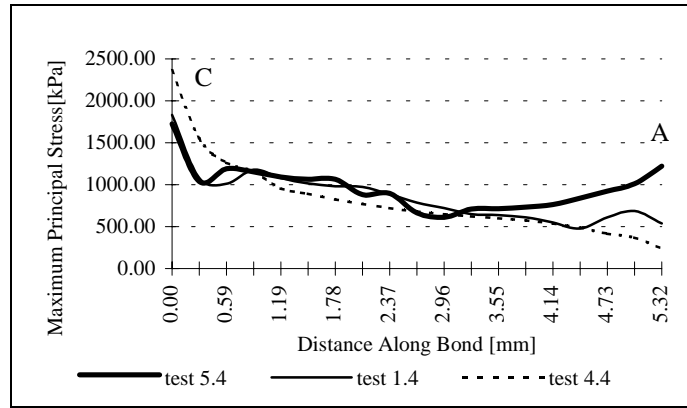


Figure 6: Variation of Maximum Principal Stress due to bond Line Thickness

Figure 5 shows the variation in the distribution of the maximum principal stress at the bottom of the bond due to a variation in a from 0.5 mm to 4.0 mm. The maximum principal stress is reduced along the whole length of the bond with increasing adherend thickness. However, the stresses are not very sensitive to this parameter.

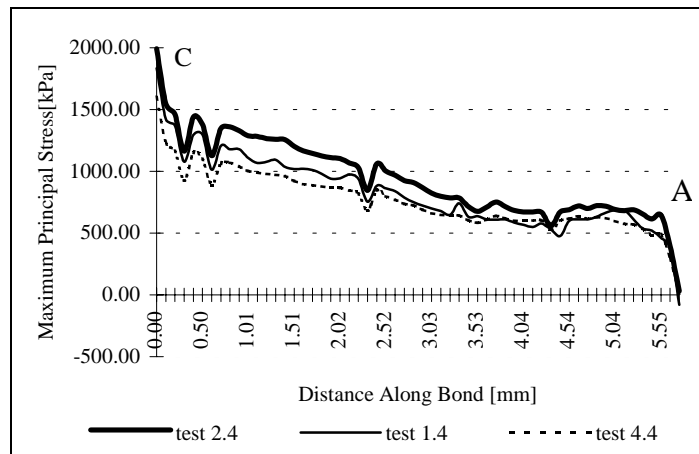


Figure 5: Variation of Maximum Principal Stress due to Adherend Thickness

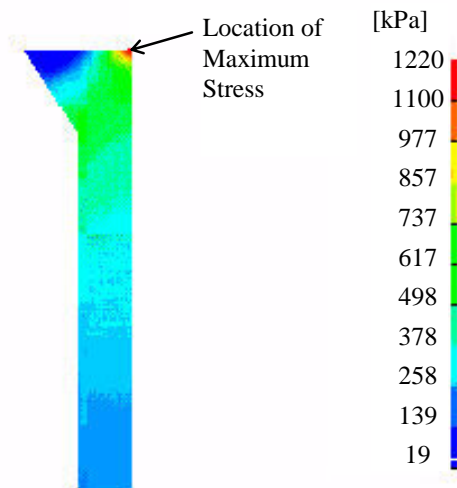


Figure 8: Max. Principal Stress Contour With Bond Fillet

Figure 6 shows the effect of increasing bond line thickness (l) from 0.05 mm to 1.0 mm. The magnitude of the stresses are more sensitive to this parameter, as seen in the changes of the principal stresses at points A and C.

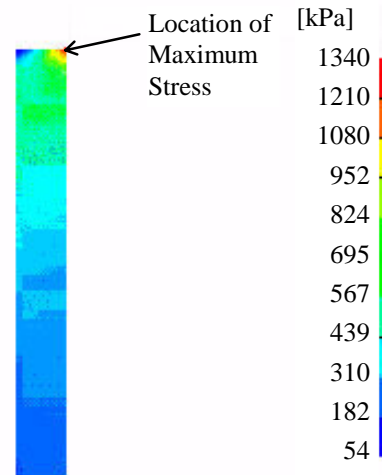


Figure 7: Max. Principal Stress Contour Without Bond Fillet

The axial engagement, e , is varied from 3.0 mm in tests 6.1-6.4 to 10 mm in tests 7.1-7.4. The maximum principal stress in the bond increases with the decreasing e [see Table 2]. For test 7.4, the maximum principal stress is 1.64 MPa, and decreases to 0.75 MPa in test 6.4 [Table 2].

Figures 7 and 8 compare the effect of adding a fillet to the end of the carbon fiber tube. Figure 7 shows the maximum principal stress contour in the bond near the end of the carbon tube. The contour shown in figure 8 shows the maximum principal stress contour in the same area with the addition of a bond fillet on the carbon tube (FB in Figure 3). The effect on the location of the peak principal stress is zero and the effect on the stress distribution is negligible. The same can be observed in the peak stress summaries given in table 2. The effect of introducing a fillet is negligible compared to the effect on the bond strength of breaking the contact with the end of the insert.

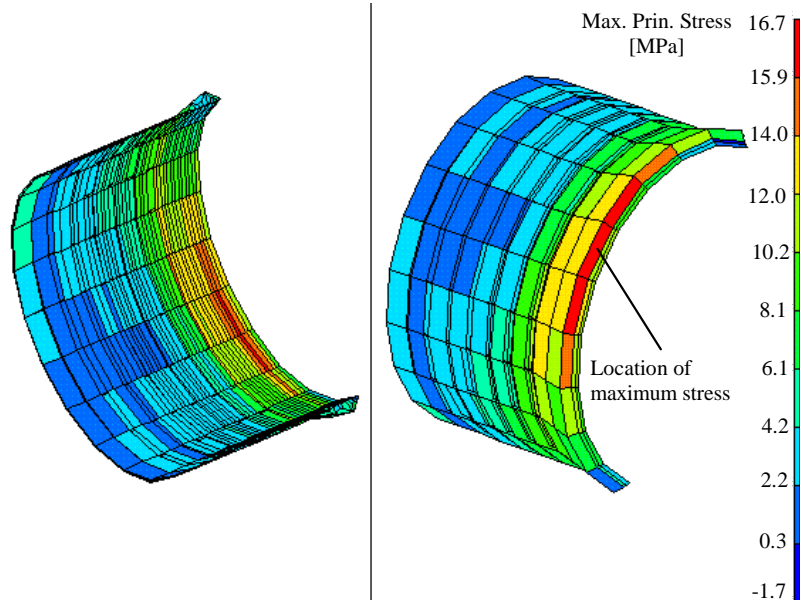


Figure 9: Maximum Principal Stress Distribution in Bond Material due to Bending Load

It is necessary to determine the factors that will contribute to optimizing the bond geometry while minimizing the total mass of the bond. The three main conclusions that can be drawn

from the parameter variation performed are: 1. maximum principal stress decreases with increase in bond length, 2. bond stress decreases with increase in adherend thickness, and 3. there is a peak in maximum principal stress with the decrease in bond line thickness somewhere between 0.25 and 0.05 mm. To minimize weight, an optimal bond geometry would have evenly distributed stresses with magnitudes as high as possible without failure. As a result, recommendations can be made for the final bond geometry. To minimize weight, ideally the bond length should be kept as short as possible, and the adherend wall thickness should be decreased, yet the bond line thickness must lie between 0.25 mm and 0.05 mm. However, a longer bond length is recommended in [6] for strength in bending so e is chosen to be 10.0 mm, a as 1.0 mm and l as 0.1 mm. These dimensions were used to construct a three-dimensional finite element model that was subjected to a bending load simulating an encounter with a limit stop. According to [7], the maximum load by one finger is approximately 40 N. The maximum load can be safely set at 80 N. The lever arm for the stage three linkage is 150 mm, and the offset for the limit stop is approximately 10 mm. The resultant maximum transverse load on the metallic end fitting is (for the purposes of a worst case scenario finite element analysis) 6×10^5 mN spread over seven nodes. The stress contours in the bond material are shown in figure 9. There is good distribution of the peak stress all along the edge of the bond, and the entire bond length is under stress. The ultimate strength of the epoxy is 20.3 MPa[8]. The maximum principal stress in the model is 16.7 MPa. The bond shows a design safety factor of 1.22. The design in this configuration is considered to be optimized.

CARBON FIBER BOX-BEAM IN EFFECTOR ARM

Tailoring of material properties in a box beam section has been the subject of many research papers [6,9-13]. The benefits of using a laminate box-beam for a robotic link are two-fold: first, weight reduction reduces actuator load and manipulator inertia and second, tailoring of material properties allows accurate control of stiffness and material damping, giving designers control over the natural frequency of the manipulator linkages [12,13].

The overall dimensions (inner, outer and length) of the box section that will be used for the effector arm (see figure 1) were defined by interference requirements with the distal stage workspace and the string rotations. Therefore, stiffness requirements for the link are obtainable by varying the material orientation only. The cross section dimensions of the box beam are 60 mm height by 30 mm width. The layup used is a combination of woven and unidirectional material, $[0 / (0/90)_3]^T$, of Advanced Composites Group LTM25 graphite-epoxy[14]. In this case, the (0/90) group represents one layer of woven material. The model will be used to verify the potential benefits in a prototype effector arm. As such, the layup was chosen to represent the materials on hand and the manufacturing concerns. The layup was determined by a finite element iterative method, progressively adding material in stiffer orientations until the required stiffness was reached.

Table 3: Summary of Comparison Between Box Beams

	Aluminum Arm	Composite Arm
Max. Deflection Vertically	1.50x10 ⁻² mm	1.37x10 ⁻² mm
Vertical Natural Freq.	552 Hz	728 Hz
Horizontal Natural Freq.	[186 Hz]	221 Hz
Total Weight	127 g	82 g

Initially, a hand lay-up around an internal removable mold was considered, but then rejected due to the poor quality external surface finish obtainable. For prototyping purposes an external split mold with an internal bag was used with a hand lay-up of cross plies to obtain the required stiffness and surface finish for the prototype. A single unidirectional ply is used on the outer surface of the box beam to create a smooth exterior surface finish, and to allow for easy layup procedure on the external mold. For more accurate tailoring of properties, including material damping, a filament wound part would be the ideal solution.

Finite element models of the composite arm (including the metal fittings required for attachment) and the proposed aluminum arm were constructed. The specifications for the motors show a maximum torque capability of 1 N·m. With the effector arm length of 200 mm, the maximum output force at the end effector is 5 N. For the purposes of comparison in the finite element model, we will use a maximum end load of 10 N. The maximum deflection of the end of the box-beam and the first natural frequency in bending is compared to the maximum deflection and lowest mode observed in the proposed aluminum arm in table 3. The composite arm showed an 8.67% decrease in the maximum deflection over the proposed aluminum arm in the vertical mode, with an overall weight decrease of 35.43%. The natural frequencies of the composite arm increased 31.88% and 18.82% in the vertical and horizontal modes respectively. Note that the aluminum arm failed to meet the frequency requirement of 200 Hz in the horizontal mode.

CONCLUSIONS

Upon examination of the original configuration of the aluminum prototype for the haptic hand controller, two areas were selected for exploitation of the benefits of advanced materials. First was the stage 3 linkage, which was redesigned as a circular cross-section composite tube bonded to two aluminum end fittings. Second was the effector arm, which was redesigned as a composite box section for the dual purpose of creating a structural entity and protecting the distal stage strings from user interference.

An optimum geometry was determined for the bonding of a circular cross-section composite tube to an aluminum cap end fitting, to be loaded in both tension and bending in two dimensions. The geometry was optimized for weight by reducing the material in the bonded entities to a minimum, while achieving a minimum factor of safety for the maximum principal stress in the epoxy.

A composite box-section beam was proposed as a stiffer, lighter alternative to a reinforced aluminum clad box section forearm. The composite box section showed a higher stiffness in both bending directions, an increase in the lowest resonant natural frequency, combined with a weight savings of 35.43%.

The result of this work is the foundation for the design of a lighter, stiffer translation stage for the 7 DOF haptic hand controller.

ACKNOWLEDGEMENTS

The authors would like to thank Dr. Ian Sinclair, Sander Boelen and Jean Poulin from MPB Technologies for their help with this project.

REFERENCES

- 1 Hayward, V., "Toward a seven axis haptic device", Proceedings IROS'95, Int. Workshop on Intelligent Robots and Systems, Vol.2, 1995, pp.133-139.
- 2 Verbal communication with Dr. Ian Sinclair, MPB Technologies Inc., Sep. 1996.
- 3 Lees, Dr. W. A., "Stress in Bonded Joints", Adhesion, Vol.12, 1988, pp.141-158.
- 4 Price, A. & Moulds, R. J., "Bonded Propshafts: design and assembly of composite tubes and metal end fittings", Materials Science and Technology, Vol.9, June 1993, pp.528-535.
- 5 Adams, R. D. & Harris, J. A., "Bonding of composites to metals", Adhesion, Vol.12, 1988, pp.193-204.
- 6 Lee, D. G. et al., "Development of the anthropomorphic robot with carbon fiber epoxy composite materials", Composite Structures, Vol.25, 1993, pp.313-324.
- 7 Massie, T.H., "So real I can almost touch it: the use of touch as an I/O device for graphics visualization", Course Notes for SIGGRAPH'96, Michael Bailey organizer, University of California at San Diego.
- 8 CIBA-GEIGY structural adhesives
- 9 Adams, R. D. & Bacon D., "The dynamic properties of unidirectional fiber reinforced composites in flexure and torsion", Journal of Composite Materials, Vol.7, Jan 1973, pp.53-67.
- 10 Ni, R. G. & Adams, R. D., "The damping and dynamic moduli of symmetric laminated composite beams - theoretical and experimental results", Journal of Composite Materials, Vol.18, Mar. 1984, pp.104-121.
- 11 Sung, C. K., & Thompson, B. S., "Methodology for synthesizing high-performance robots fabricated with optimally tailored composite materials", Transactions of the ASME, Vol.109, Mar. 1987, pp.74-86.
- 12 Sung, C. K. & Shyl S. S., "A Composite laminated box-section beam design for obtaining optimal elastodynamic responses of a flexible robot manipulator", International Journal of Mechanical Science, Vol.32, No.5, 1990, pp.391-403.
- 13 Gordaninejad, F. et al., "Nonlinear deformation of a shear deformable laminated composite-material flexible robot arm", Transactions of the ASME, Vol.114, Mar. 1992, pp.461-468.
- 14 The Advanced Composites Group, Tulsa, Oklahoma.

A CODE TO ANALYSE THE STRUCTURAL-TECHNOLOGICAL DESIGN OF FILAMENT WOUND PRESSURE VESSELS

G. Di Vita¹, M. Marchetti², M.Nappi²

¹C.I.R.A. - Italian Center for Aerospace Research, Via Maiorise, 81043 Capua, Italy

²Aerospace Department - University "La Sapienza" of Rome, Via Eudossiana 16, 00184 Rome, Italy

SUMMARY: Usually the alignment of successive circuits for the winding of a closed end vessel is not guaranteed, even when the winding process is set up by use of simulation. Often the alignment is obtained realising an additional hoop winding on one of the polar bosses, or by trials, varying slightly winding angle, band width or mandrel dimensions until the accomplishment of the objective. In order to establish a strategy for the solution of this problem, the influence of the technological variables - winding angle, band width, mandrel dimensions - on the technological parameters - dwell angle, slippage tendency, fiber tangency at the polar boss - was first investigated. Then a computer software, named "AL", was developed in order to automatically select the technological variables, able to give the alignment of the fibers without any additional winding on the polar bosses. The reliability of the code was experimentally tested applying the automatic optimisation method to the design and the successive manufacture of a scaled motor case.

KEYWORDS: filament winding, close end pressure vessel, winding circuits alignment

INTRODUCTION

The aircraft and aerospace industries are continuously investigating high strength to weight material systems. Fiber reinforced composites have established their value in the aerospace industry because they efforts to improve high strength to weight ratio, high temperature capability, resistance to aerospace environments and processing capability. One of the areas in which the advantages of composite materials can be widely applied to obtain the best results is that of the pressure vessels for aerospace applications.

The use of *filament winding* process to fabricate composite structures has become one of the main techniques in the composite industry. For certain closed shape composite structures, such as pressure vessels, it is probably the only technique used in production.

The primary advantages of filament winding are: lower cost for large number of components, due to relatively low material costs and to manpower reduction; the highly repetitive nature of fiber placement; the automation of the process. Disadvantages are: technological problems, such as inability to wind reverse curvature, possibility of slippage and misalignment of winding trajectory; need for mandrel; poor external surface.

One of the most important aerospace application of the filament winding technology is the solid propellant rocket motor cases manufacture. A typical motor case consists of two

isotensoid wounded domes and a cylindrical section. The pressure vessel is connected via an adapter skirt and flange to the rocket or satellite structure. The igniter and the nozzle are fixed at the polar opening interface fittings. The fibers, impregnated with a resin system, are wound by a numerically controlled high precision winding machine on a mandrel. After curing of the vessel an elastomer interlayer is prepared at the transition zone of the cylindrical part to the adapter skirt. Subsequently to a second curing cycle, the adapter flanges are machined and the complete motor case is ready for acceptance testing.

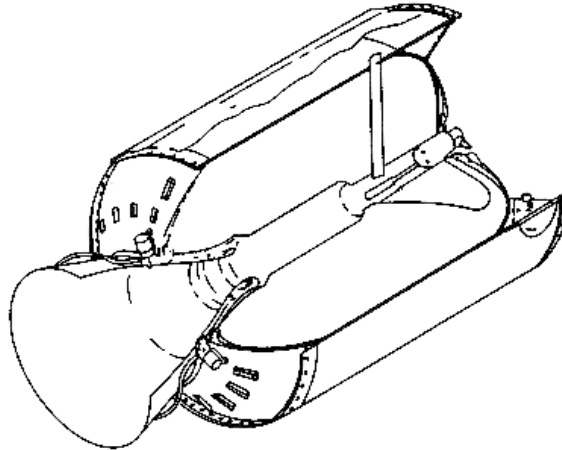


Fig. 1 : Solid rocket motor case section

The filament wound pressure vessel manufacture needs an integrated design procedure, due to the difficulty to satisfy both the structural and technological requirements. In order to make an automatic solution to the structural-technological design, a software system, named "ARIANNA", has been developed at the Materials and Technologies Department of CIRA. The software system ARIANNA allows to predict and, if the case, solve the technological problems of filament winding, such as inability to wind along certain trajectories with a specific winding angle, possibility of slippage and misalignment of winding trajectories, in respect of the structural requirements [1]. The system core, that gives the solution of structural-technological design of filament wound pressure vessels, consists of the following set of subsystems:

1. The Winding Trajectory Analysis module (FW). It optimises steady winding trajectory and calculates the thickness and fibers orientation of the wound composite [2]. Input data, as the geometry of the structure, the lamination sequence, the winding angle at user's defined control sections, the computing accuracy parameters, etc., can be easily varied giving the opportunity to optimise the complete winding with simulations.
2. The NASTRAN interface module (BULK). It gives the *bulk data* (geometrical configuration, lamination sequence, etc.) for the structural analysis, that currently can be performed making use of the NASTRAN FEM code.
3. The Machine Motion Analysis module (EY). It allows the generation of the path of motion for winding machines having 2, 3 or 4 degrees of freedom.
4. The CNC interface module. It allows the generation of the numerical control part program.

PROBLEM STATEMENT

The design of filament wound pressure vessels requires the following steps:

1. Preliminary design, realised using netting-analysis methods, with the aim to address the defined loads.
2. Material selection, dictated by both performance and environmental constraints.
3. Detailed stress analysis, obtained using the finite-element techniques.
4. Manufacturing reliability test, realised using a simulation code or winding proof.

The reliability test is a fundamental investigation to verify the manufacturing of the filament wound structure. Of course there is a remarkable difference between using a simulation code and a winding a proof. In case of abort of the proof, the manufacturing cost will increase considerably. Otherwise, the use of a consistent numerical simulation makes the proof useless and gives the possibility to adjust the design. This means that the designer needs a consistent simulation code, such as ARIANNA, to prevent a manufacture failure. A basis knowledge of technological problem is required to realise it.

A satisfactory technological design of filament wound pressure vessels needs to satisfy the following basic conditions:

1. filament stability during winding;
2. filament tangency at the polar boss;
3. winding trajectories alignment.

For this reason the two following technological parameters have been defined:

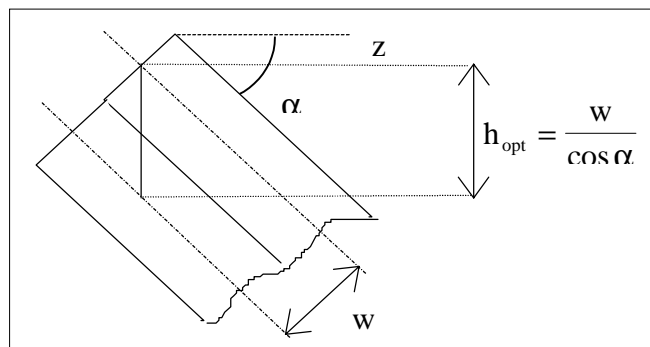
- the *slippage tendency*, whose value characterises the stability of winding [2].
- the *dwell angle*, that measures the angular distance between the axis of successive winding trajectories, and therefore the alignment of successive circuits, as shown in Fig. 4.

For the *filament tangency at the polar boss* the introduction of a new technological parameter is not necessary.

To optimise the technological parameters the designer could change mandrel geometry or lamination sequence, i.e. the value of technological variables. The winding trajectory will be optimised when the dwell angle reaches an optimal value $(dwell)_{opt}$:

$$(dwell)_{opt} = \frac{w}{R \cdot \cos \alpha} \quad (1)$$

This parameter depends on band width of roving and the internal radius of mandrel.



where w is the band width, R the internal radius and α the winding angle.

Fig. 2: Optimal dwell angle

The technological variables that can affect the technological parameters are:

- a) the *winding angle*, whose value modifies also the structural behaviour. The winding angle in the cylindrical section could be constant or variable. As shown in Fig. 3, two sections where the winding angle can be varied has been defined: one on the left basis and one on the right basis of the cylindrical section.
- b) the *polar boss radius*, whose value modifies both the mandrel geometry and the structural behaviour.
- c) the *internal radius* of the case, whose value modifies both the mandrel geometry and the structural behaviour.
- d) the *band width* of the roving (Fig. 3), whose value modifies neither structural behaviour nor mandrel geometry.

In order to set a strategy for the solution of the alignment problem, the influence of the technological variables on the technological parameters has to be investigated. This “knowledge basis” was obtained through a numerical simulation parameters analysis, using the FW module of ARIANNA. Two different geometry were taken into account:

1. a test mandrel (Fig. 3), whose geometry and lamination sequence are defined according to the current pressure vessel bibliography on the matter [3], [4].
2. an ASTM D2585 standard specimen mandrel (Fig. 4), whose geometry and lamination sequence are defined according to the standard norm [1].

The purpose of the simulations is to give an idea of parameters versus variables behaviour, i.e. the analytic law between the dwell angle and each of the variables. The results of the simulation performed [5] are shown in the graphs in Fig. 5 and Fig. 6.

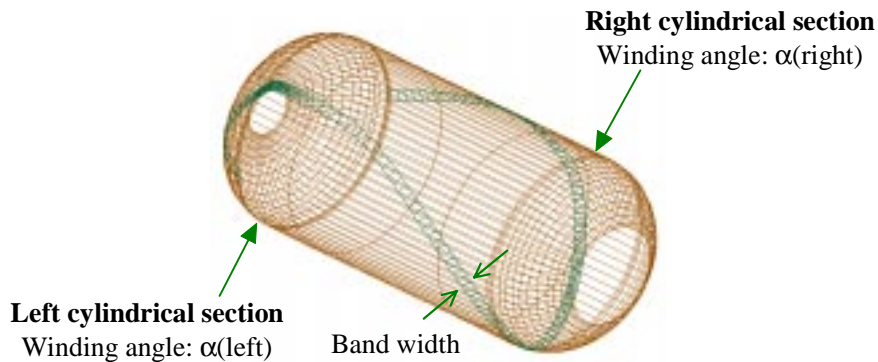


Fig. 3: Test mandrel winding simulation

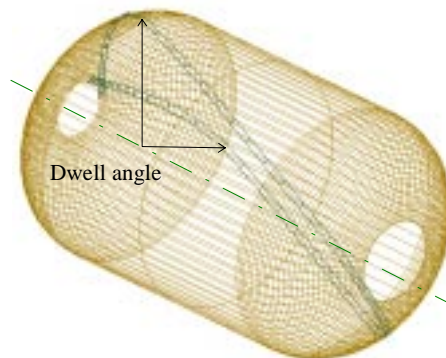
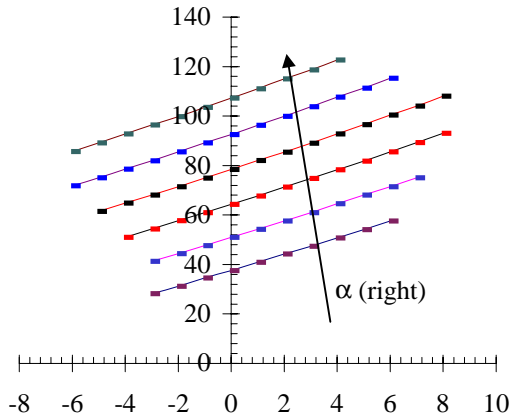
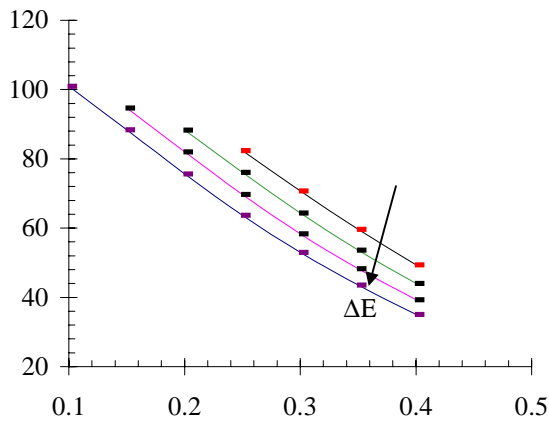


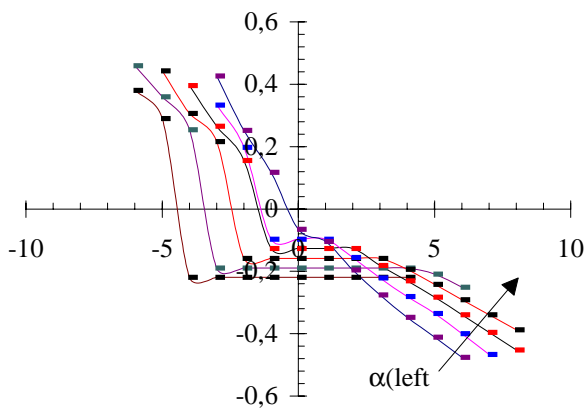
Fig. 4: ASTM D 2585 standard specimen mandrel winding simulation



Graph 1: [dwell angle - dwell optimal] Vs $[\alpha(\text{left})-\alpha(\text{right})]$

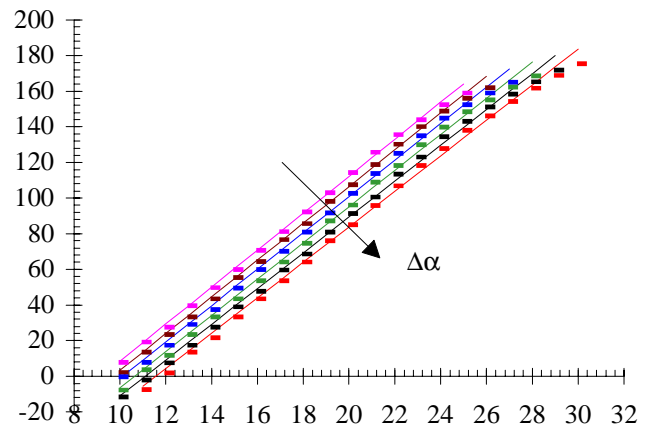


Graph 2: [dwell angle - dwell optimal] Vs $[R_p/R_0(\text{left})]$

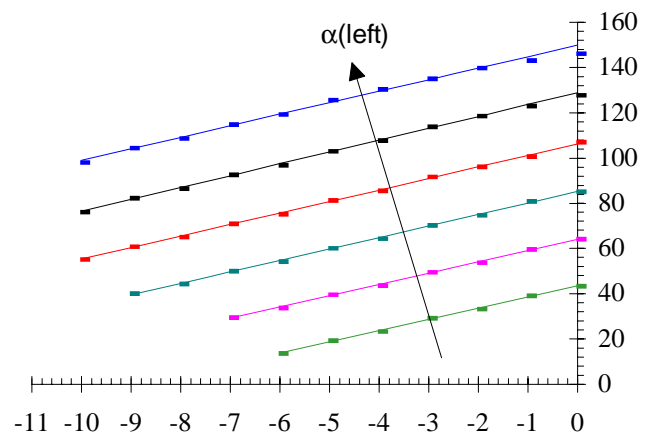


Graph 3: [max. slippage tendency] Vs $[\alpha(\text{left})-\alpha(\text{right})]$

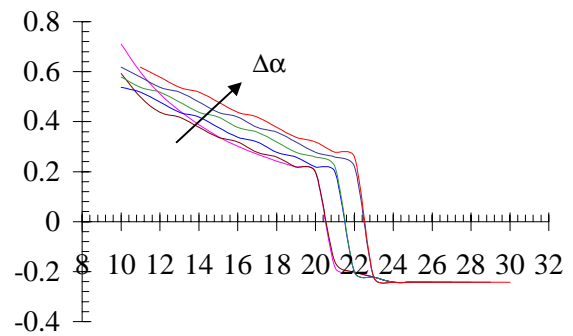
Fig. 5 : Test mandrel winding parameters



Graph 4: [dwell angle - dwell optimal] Vs $[\alpha(\text{left})]$



Graph 5: [dwell angle - dwell optimal] Vs $[\alpha(\text{left})-\alpha(\text{right})]$



Graph 6: [max. slippage tendency] Vs $[\alpha(\text{left})]$

Fig. 6 : ASTM specimen winding analysis parameters analysis

From the graphs shown in Fig. 5 and in Fig. 6 the following considerations can be summarised:

- a. The dwell angle increases when increasing the winding angle values in the left and in the right cylindrical section.
- b. The dwell angle decreases when increasing the polar openings, the internal radius and the roving band width.
- c. The dwell angle decreases when increasing the winding angles and the polar bosses difference between left and right cylindrical sections.
- d. It is not possible to predict the slippage tendency variation law as a function of winding angle.

THE AUTOMATIC ALIGNMENT "AL" CODE

General Description

A specific code, named "AL", has been written in order to automatically solve the alignment problem. Making use of an iterative procedure this code is able to reduce the dwell angle modifying the values of the technological variables.

The code is based on a simple algorithm that change the technological variables, rearranges the input data set and run a new simulation with the FW module of the ARIANNA code. From the output results the new values of *dwell angle* and *slippage tendency* can be evaluated. The "AL" code reiterates the procedure until the convergence condition has been satisfied, in respect of filament stability and polar bosses tangency. The convergence condition is defined in terms of overlap tolerance, i.e. in percent of band width overlap (*ovp*) between the first and the second winding trajectory, as shown in Fig. 7.

$$overlap\ tolerance = \left(\frac{ovp}{w} \right) \cdot 100 \tag{2}$$

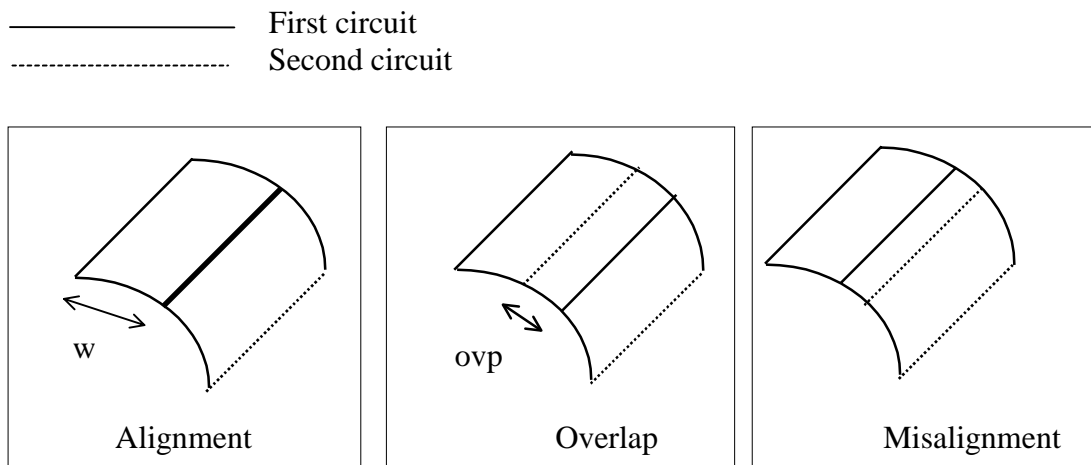


Fig. 7 Overlap definition for the convergence condition

Structure of the Code

As shown in the Fig. 8, the AL code algorithm provides to change the value of each variable, according to the knowledge basis and to the maximum allowable variation of the technological variables. The code is constituted by the following modules:

Knowledge Basis: with the aim to reach the convergence solution at the first step, the code performs two preliminary simulations and calculate the linear regression slope. The knowledge basis is updated step by step during the iterative procedure.

User's input: the user can define which of the variables are allowed to vary during the iterative process. The user can change both the mandrel geometry and the lamination sequence when the project is in the preliminary phase. Obviously, when the geometry is already defined and cannot be changed only the lamination sequence can be varied.

Variables change: the variables have been selected evaluating their influence on the lamination sequence and the mandrel geometry. There is a priority that guides the variables choice at each step. Initially the algorithm tries to change the winding law on the cylindrical part (move control section option). If the convergence condition is not satisfied, the algorithm provides to vary the lamination sequence, i.e. the band width of roving and the winding angle. Finally, the alignment can be determined changing the geometrical variables, i.e. the polar bosses radius and the internal radius.

Verify: at the end of each step the algorithm provides to verify the output of FW, i.e. the dwell angle, the slippage tendency and the filament trajectory co-ordinates.

AL starts a set of controls on this values. The controls are:

- *Slippage tendency and polar bosses tangency verification.* If slippage or no-tangency occurs, a special subroutine provides to search a satisfying solution, changing the technological variable and running again the FW module.
- *Convergence condition analysis.* When the overlap, measured in percent of band width, reaches the imposed tolerance limit, the user will be able to simulate the winding trajectory on the optimised mandrel with the optimised lamination sequence, and then to run the FEM analysis.

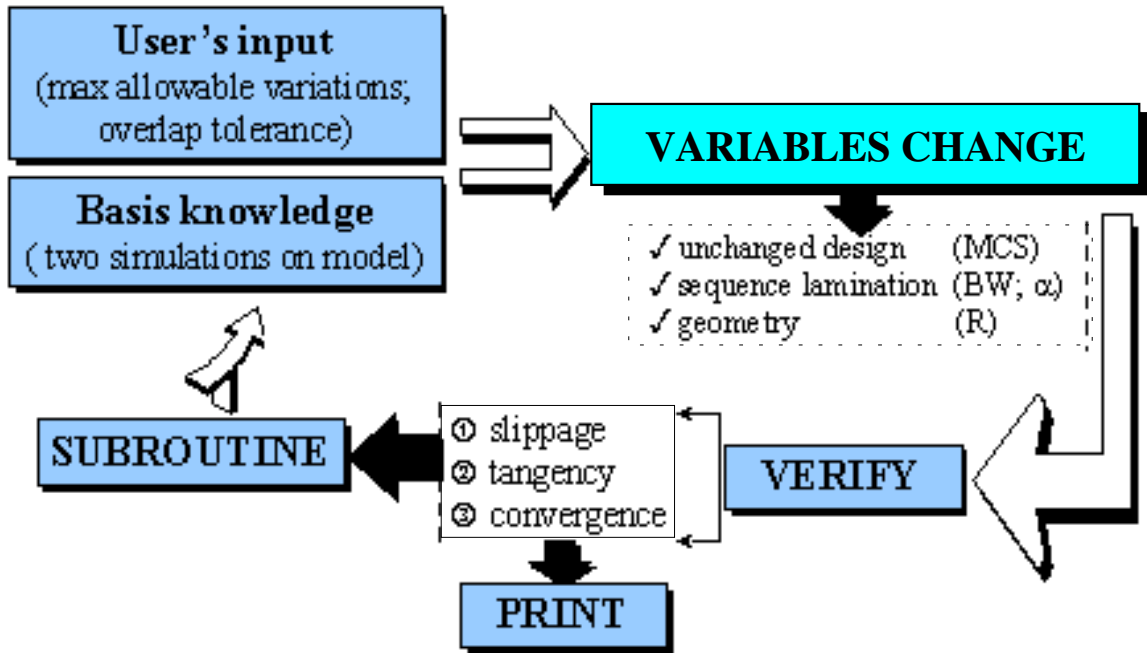


Fig. 8: the AL algorithm

SOME NUMERICAL RESULTS

A scaled mandrel, for the burst pressure proof of a motor case, named Zefiro and available at the BPD D&S production plant, has been used in order to test the AL code. The scale of the mandrel has been reduced by 1/5 compared to the size of the Zefiro motor case; the geometrical dimensions are the followings:

- polar boss radiuses respectively at the ignitor and at the nozzle side: 41.6 and 90.3 mm.
- internal radius at the cylindrical part: 188.3 mm.
- length of the cylindrical part: 905.5 mm.

The lamination sequence is made of nine plies, five helix winding plies and four hoop winding plies. In the sequence shown in Fig. 9, the ply thickness is 0.125 mm and the band width is 2.5 mm. The pressure vessel has been manufactured with CFRP prepreg.

The “AL” code has been tested to optimise the four helix winding plies of filament wound structure. Each ply had 23° and 26° nominal winding angle at the left and at the right cylindrical section respectively. The dwell angles for each layer have been calculated. They are summarised in Table 1 and requires the technological optimisation of the manufacture design.

Table 1: Dwell angle for various plies before the automatic alignment

Ply number	α (left)	α (right)	Δ (dwell angle)
1	23°	26°	-21,05°
3	23°	26°	-28,08°
5	23°	26°	-31,98°
7	23°	26°	-41,09

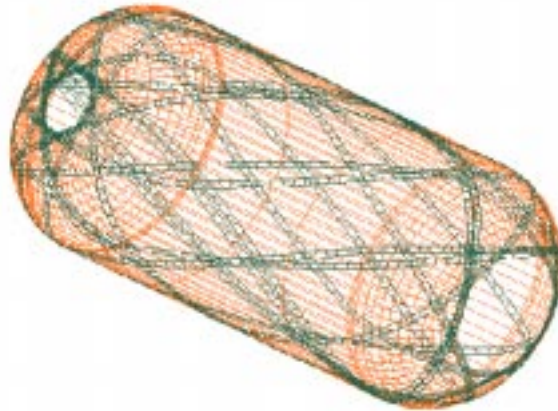


Fig. 9: Graphical simulation of the first ply before the optimisation

An optimal pattern 5 (a band is aligned to another one after 5 circuits) has been found for the Zefiro mandrel. In this situation the dwell angle is defined as the angular distance between the axis of the first and the 6th winding trajectory. For the optimisation procedure it has been supposed to change only the lamination sequence, i.e. the winding angle, and to have an overlap tolerance less than 10%. Moreover the left and right winding angles have been changed by the same amount. The result of this calculations is a new lamination sequence, with a small difference of winding angle, as summarised in Table 2. In Fig. 10 the resulting winding simulation for the first ply is shown.

Table 2: Winding angles at two sections after the automatic alignment

Ply number	α (left)	α (right)	Overlap Tolerance
1	23,4258°	26,4258°	7,03 %
3	23,5361°	26,5361°	4,125%
5	23,5733°	26,5733°	0,363%
7	23,6281°	26,6281°	2,538%

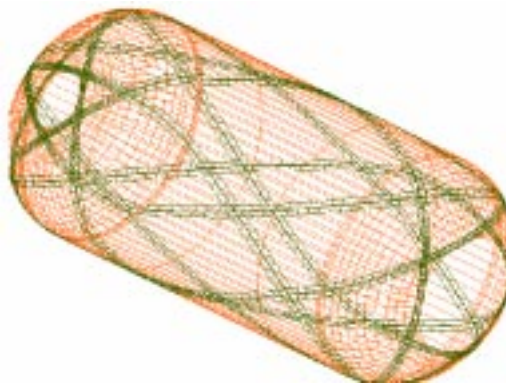


Fig. 10: Graphical simulation of the first ply after the optimisation

The NASTRAN input file has been obtained using the BULK task of ARIANNA. It includes the geometry, the local stacking sequences, the boundary conditions (in terms of constrains and loads) and the material of the Zefiro motor case. A structural analysis, that simulates the burst test, has been performed and the tensional field on each layer evaluated. Therefore, using the EY Machine Motion Analysis module and the CNC interface module of ARIANNA, the

numerical parameters required to control the winding machine movements have been calculated. The pressure vessel has been manufactured and, finally, loaded with an internal pressure up to burst.

EXPERIMENTAL VALIDATION

The software has been tested, with positive results at the BPD D&S laboratories and plants in Colleferro (Rome). One phase of the winding process for the Zefiro scaled motor is shown in Fig. 11 and can be compared with the simulation in Fig. 10. The experimental results agreed perfectly with the simulations confirming the reliability of the software.

CONCLUSIONS

The problem of the optimal alignment of successive circuits during winding of a closed end pressure vessel was studied. A software code, named "AL", was developed in order to automatically select the technological variables able to give the alignment of the fibers without any additional winding on the polar bosses. The alignment can be accomplished varying slightly, from their nominal value, some of the technological variables, such as winding angles, band width or dimensions of the mandrel, within the limits that the user can select for the specific case under consideration. The reliability of the code was experimentally tested applying the automatic optimisation method to the design and the successive manufacture of a scaled motor case with tangency of the fiber at the polar boss, alignment of the winding circuits and absence of slippage.



Fig. 11: Manufacturing of the Zefiro scaled mandrel

ACKNOWLEDGEMENTS

The contribution of BPD D&S to the present research, particularly for the experimental validation phase, is greatly appreciated and acknowledged.

REFERENCES

1. Di Benedetto C., Di Vita G., Moroni P., “An integrated software system for the structural-technological design and the process monitoring of generic non-axisymmetric filament wound composites”, *Computer Aided Design in Composite Material Technology V (CADCOMP '96)*, Udine, Italy, 1996, pp. 273-282.
2. Di Vita G., Perugini P., Marchetti M., “Non-geodesic winding path equations on non axisymmetric surface”, *Proceedings of the 8-th International Conference on Composite Materials*, Honolulu, USA, 1991.
3. Davey A.E., Curnow R.D., “Investigation of fibres and composites applicable to the design of high pressure vessels for satellites”, *NASA STAR Technical Report, Issue 13*, Rolls Royce (Composite Materials) Limited, 1972.
4. Chiao T.T., Hamstad M.A., Hanafee J.E., “Filament wound kevlar 49/epoxy pressure vessels”, *NASA STAR Technical Report, Issue 13*, 1973.
5. Nappi M., “Analisi comparata strutturale-tecnologica di un involucro motore a propellente solido per applicazioni Aerospaziali”, *MSc Thesis in Aeronautical Engineering (in Italian)*, University “La Sapienza”, Rome, Italy, 1996.

DESIGN CONSIDERATIONS FOR PLY DROPS IN COMPOSITE STRUCTURES

D.S. Cairns, J.F. Mandell, M.E. Scott and J.Z. Maccagnano

*Montana State University
DOE EPSCoR Wind Energy Cluster, Bozeman, Montana 59717*

SUMMARY: Thickness variations are required to optimize the design of modern laminated composite structures. These thickness variations are accomplished by dropping plies along the length to match varying in-plane and bending loads. In this study, we explore various factors for design of composite blades with ply drops. These factors include: thicknesses, ply stacking sequences, ply drop geometries, and manufacturing considerations. In addition, fatigue loading is considered with respect to delamination initiation and growth. All studies were conducted on a low-cost E-glass/polyester composite system. The results indicate that it will be difficult to completely suppress damage and delamination initiation in service. However, it was found that, in most cases, there is a threshold loading under which little growth after initiation is noted. Factors affecting this threshold are analyzed via the virtual crack closure method in Finite Element Analysis and verified experimentally. Design rules for ply dropping are presented on the basis of these results.

KEYWORDS: ply-drops, delamination, tapered, strain energy release rate, virtual crack closure method

Introduction

Ply drops in composite materials are a relevant design consideration in many structures, especially those with varying loads along the length. As an example, each ply in a composite laminate with no bending need to carry the same amount of strain when a ply is dropped. There is a reduction in area causing the thinner section to carry a higher stress, transitioning via shear lag. The ply drop introduces a stress concentration, causing a crack to form and propagate along the layer that forms the ply drop.

There are three possibilities for crack growth. Sometimes, the driving force is high enough where the crack will continue to propagate until the specimen fails. However, if the critical level is not reached, the delamination will start but will arrest at a certain length and remain constant length. The last case is where the stress is so low that delamination never begins within 500,000 cycles.

In this study, different configurations were tested that included both internal and external ply drops. In addition to this, a thicker material was constructed to represent material being used in industry. Finally, different methods of stopping and arresting delaminations were tried to see if they were practical solutions to stopping or slowing delaminations.

Description of specimens

In this experiment, all the specimens were made using resin transfer molding (RTM) equipment. The plies used in this experiment were made by Knytex in Texas. These plies are made from Owen/Corning E-Glass fibers. The zero degree layers were D155 material and the ± 45 layer were DB120. The matrix was a polyester resin manufactured by Interplastic Corporation in Minnesota that took approximately four to six hours to cure at room temperature. After the plates were made, 25.4 mm wide specimens were machined and the edges were polished to minimize edge effects from machining. The coupons were then post cured at 60 °C for two hours. Post-curing assures that the styrene in the polyester has cross-linked, giving the composite most of its strength.

The laminates in this diagram were not loaded until the entire specimen failed, but only until delamination took place. These strain energy release rates (G_{Ic}) were determined from the critical load (P_c) using the following strength of materials formula from Ramkumar [2]:

$$G_c = P_c^2 \frac{A_2 E_2 - A_1 E_1}{2w A_2 E_2 A_1 E_1} \quad (1)$$

The subscript 1 is for the thin section and 2 is for the thick part of each specimen. The A is the cross-sectional area and E is Young's modulus, respectively, for each part of the specimen. Also w in the above equation is the width of the coupon. A guide to all the laminates is found in Table 1, which lists the laminates tested and the properties of each laminate.

Fatigue Testing

Using the critical loads determined from the static tests, the fatigue load of each laminate could be approximated. All of the tests in this study were run at R=0.1 on an Instron 8501 machine.

In the ESA laminate, a single exterior ply was dropped and the initial maximum cyclic stress of 207 MPa in the thin section was chosen. The delamination initiated easily and grew rapidly as can be seen in Figure 1. It was not until the stress was lowered to 120 MPa that the delamination finally arrested after some growth, compared to the static strength of ESA of 452 MPa. The next laminate tested was the ESB laminate which consisted of a single internal ply drop.

From the static testing this laminate had approximately a 68.9 MPa higher stress level before delamination initiation than the ESA laminate. The internal ply has two shear surfaces to resist delamination and the geometry causes a less severe discontinuity. This was taken into account when calculating the strain energy release rate (G_c) value, with equation 1 being divided by two to account for the two crack fronts. The results for the ESB laminate show that the threshold stress for forming delamination (276 MPa) was more than twice as high as for the ESA

laminates. Results for the ESC laminate were similar to the ESB laminate, with only a slight gain in the maximum fatigue stress level. The ESC laminate differs from the ESB laminate in that the ply drop is in the center of the laminate rather than immediately under the surface, which reduced the additional bending stress.

To compare the different laminates on the same scale a graph of fatigue delamination growth rate vs. normalized energy release rate is given in Figure 2. This shows that although the strain energy release rate is higher for the ESB laminate, when normalized with their respective G_c the crack growth rate for both laminates correlate to a single relationship. However, it is noted that the normal analysis for G_c is based on a strength of materials approach. This may not be adequate for the complicated mixed mode problem. A non-linear finite element analysis as shown in Figure 3 is currently being used to investigate this problem. It was determined that a non-linear analysis was necessary as a consequence of the membrane/bending coupling in the surrounding plies. Errors as high as a factor of 2 in G_c calculations can result if the coupling is ignored. The virtual crack closure method was used for analysis [3].

Virtual Crack Closure method

Energy release rates were calculated using the virtual crack closure method. Using the virtual crack closure method, ESA, ESB, and ESC samples were examined for energy release rates from crack initiation and crack arrest using experimental data and loading. Using the accumulated data, it may be possible to predict crack arrest in complex composite structures under fatigue loading. However, it is necessary to first establish a relationship between the energy release rates and the loading before reasonable predictions can be made. Using the virtual crack closure method, Table 3 shows the percent of mode 1 and 2 responsible for extending the crack. This table shows the percentage of the each mode for the delamination extending into the thicker section (before the ply drop) with the percent displacement given for reference.

Non-linear runs at arrest crack lengths and loads into thicker section		
Laminate	Percent Mode1	Percent Mode2
ESA (0.46% disp)	40.7	59.3
ESB (1.06% disp)	---	100
ESC (1.07% disp)	---	100

Table 3: Percentage of strain energy release rates for crack growing into thicker section.

For this purpose, it is expedient to establish a larger database of energy release rates from the virtual crack closure method to compare to experimental data.

Laminates ESE, ESF, ESG and ESH

After the three initial laminates were studied, it was decided that other possibilities should also be considered. The ESE and ESF laminates were thicker laminates with a single ply drop. The ESE laminate had an exterior ply drop while the ESF laminate had an interior ply drop.

The ESE laminate had a lower delamination rate than the ESA laminate, which had a smaller overall cross-sectional area. The G_c for both the ESA and ESE laminates, along with the ESF laminate compared with the ESB

laminates were similar.

The ESG and ESH laminates were also thicker in cross-section, but, in an attempt to simulate a manufacturing situation, two plies were dropped instead of one. The ESG laminate contained two plies on the outside while the ESH laminate contained two plies on the interior. In both cases these configurations behaved poorly compared with their single ply drop counterparts. During testing of the ESH laminate, the resin rich area ahead of the ply drop was observed to crumble during the fatigue test. When the coupon was in the maximum stress part of the fatigue cycle a fracture in the resin pocket through the laminate's width was seen. No material was left ahead of the ply drop after the first initial cycles. This is illustrated in the Figure 4 below:

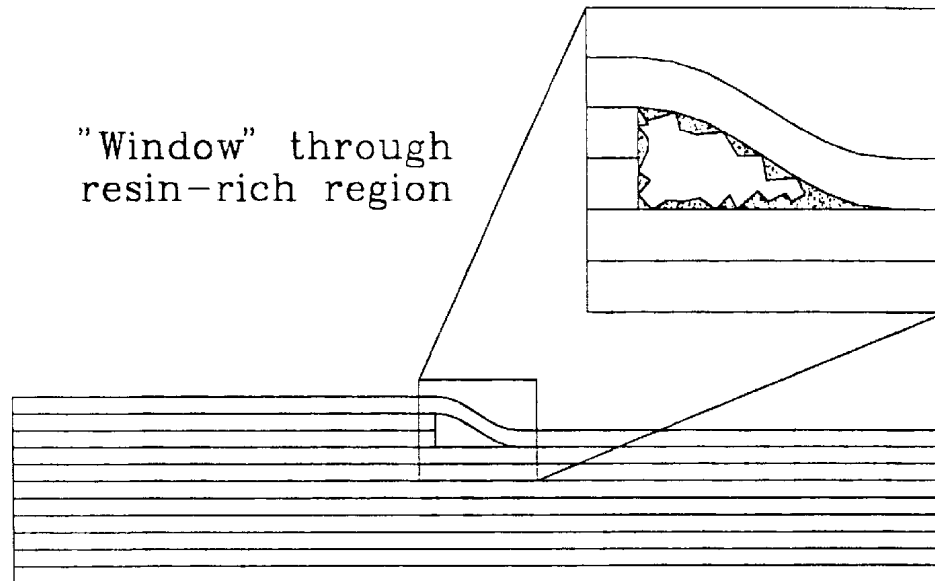


Fig 4: Sketch of resin rich region in ESH laminate.

The ESG laminate with a double external ply drop delaminated more easily than a single ply drop on the outside. One apparent reason for this is the higher strain energy release rate of the ESA laminate: the G_c of the ESG laminate was only 1.26 N/mm, while the G_c for the ESA laminate was 1.89 N/mm. Another reason for this was the increased bending moment created by the increased stiffness of having two layers creating the ply drop, as well as the larger dropped area. A comparison of laminates having internal ply drops is presented in Figure 5. As noted above, the ESH laminate with two interior ply drops had the highest delamination rate. The best configuration was the ESF laminate, which was a thicker laminate with a single internal ply drop.

Attempts to improve delamination resistance

After the original seven configurations were tested, methods of preventing delamination were studied. The first configuration used the ESA laminate as a basis for comparison, and a second configuration used the ESB laminate as a basis. First random mat fabric was included between the ply drop and the first continuous zero layer. Random mat was not used in the internal ply configuration case. A second modification is called "feathering." In this

case, alternating tows were pulled one half inch past the adjacent tows to provide a less defined delamination site (Figure 6).

In two other cases, the ESJ and ESK laminates, innovative methods were used to prevent delamination (Figure 6). In the ESJ laminate, "Z-Spiking" was used. "Z-Spiking" consisted of removing the scrim from the fabric and driving the fiber tows into the lower layers. Since the transverse strength properties are much lower than the longitudinal properties, providing fiber reinforcement in the thickness direction results in additional resistance to delamination. The ESK laminate used a one inch wide layer of Hysol EA 9309.2NA adhesive between the outer ply drop and the first continuous zero layer. This adhesive was applied, and was allowed to cure before the resin was injected into the mold. The theory behind this attempt was that by applying a thin, tough adhesive delamination initiation would be resisted. Also the adhesive layer enhances the process zone for fracture [4,5]. "Z-Spiking" and adding an adhesive region can also be applied to a hand lay-up process.

Results from the delamination prevention techniques

Since all of the delamination prevention techniques were applied to the same layer configuration as the ESA laminate, the ESA laminate was used as a standard by which the other laminates were judged. As can be seen from Figure 7, the feathered laminate provided a substantial decrease in the delamination rate. However, applying random mat to the lay-up had little effect, and possibly increased the delamination rate.

In Figure 8, the ESK laminate with the Hysol adhesive is compared with three other laminates. ESK shows a significant improvement over the other configurations tested. The delamination in the ESK laminate did not initiate until the other laminates had completely delaminated. The ESJ laminate with "Z-Spiking" is not shown on this graph because there was no delamination until more than 200,000 cycles. Both "Z-Spiking" and the Hysol adhesive delamination did not start like the other laminates. In both cases the delamination started at the specimen edges, although in both cases the edges of the specimens were carefully polished. Polishing mitigates, but does not preclude free-edge effects. The results for the ESJ laminate are in Figure 9, while those for the laminate based on the ESB laminate, but using feathered ply drops, are in Figure 10. From Figure 10 it can be clearly seen that the delamination started but stopped, while the ESB material with no feathering continued to grow at a slightly higher delamination rate. In Table 2, the delamination rate for various running stress levels and laminates ESA through ESK is presented. Running stress is defined as the ratio of maximum stress level to minimum stress level. In this table the ratio or R value equals 0.1.

Repairing samples tested previously

During testing the ESA laminate, which had an exterior ply drop, the outer layer peeled away from the rest of the laminate. We looked into whether it was possible to repair the delamination with two epoxy adhesives. The first adhesive was Hysol EA 9309.2NA, which is blue in color, while the second one was Hysol EA 9412, which is clear in color. The specimen was then retested at the same stress level and the delamination rate was compared to the original rate, which can be seen in Figure 11. From Figure 11, the two adhesives had a similar delamination rate and provided a significant reduction in delamination rate compared with the original laminate.

Conclusions and Design Recommendations

From the foregoing results, some general conclusions can be drawn about delamination and preventing delamination.

- For the same ply drops, thicker laminates are better in resisting delamination.
- Dropping more than one ply at the same location increases the delamination growth rate.
- Internal ply drops are more resistant to delamination than external ply drops.
- Repairing external plies using an adhesive is effective in preventing delamination from starting again.
- The use of “Z-Spiking” and adhesives in the manufacturing of parts initially substantially reduces the initial delamination rate.
- Using feathering at the ply drops reduces the delamination rate
- Random mat has a possible detrimental effect on delamination resistance.

Therefore, an optimum configuration of dropping plies may be to have an internal ply drop, with a combination of either “Z-Spiking,” an adhesive, or “feathering” used in the construction.

Further Study

The current analysis for ply drops is based on a strength of materials approach. It does not include details at the crack tip region. Further studies will include more detailed analysis, including the fracture mode type and mix. This may explain some of the differences in G_c for the various laminates.

In the future, determining the effect of spacing of ply drops should be considered. By doing this the number of plies that can be dropped over a given length can be determined. If the ply drops are too close together, then a resin rich area could possibly form, leading to failure (as in the ESH laminate). However, if the ply drops are too far apart, then tapering the thickness may be too gradual and therefore, inefficient.

References

1. Samborsky, D.D. and Mandell, J.F., “Fatigue Resistant Fiberglass Laminates For Wind Turbine Blades,” 1996 ASME Wind Symposium, Houston, TX.
2. Ramkumar, R.L. and Whitcomb, J.D., “Characterization of Mode I and Mixed-Mode Delamination Growth in T300/5208 Graphite/Epoxy,” in *Delamination and Debonding of Materials*, ASTM STP 876, W.S. Johnson, ED., ASTM, Phi., 1985.
3. Rybicki, E.F. and Kanninen, M.F., “A Finite Element Calculation of Stress-Intensity Factors by a Modified Crack Closure Integral.” *Engineering Fracture Mechanics*, 1977. 9:931-938.
4. Cairns, D.S., “Prediction of Fracture Toughness of Multi-Phase Materials”, Proceedings of the AIAA/ASME/ASCE/AHS/ASC 31st Structures, Structural Dynamics and Materials Conference, April, 1990.
5. Cairns, D.S., “Mixed-Mode Fracture and Toughening in Multi-Phase Materials”, Proceedings of the ASCE Engineering Mechanics Specialty Conference, May 20-22, 1991.

Delamination length vs. Cycles
 ESA Laminate, External Zero Dropped, R=0.1

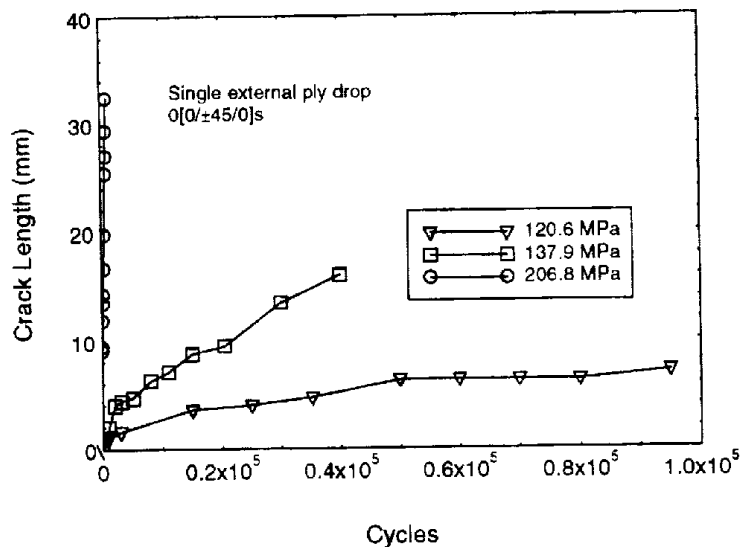


Figure 1

FATIGUE DELAMINATION GROWTH RATE VS.
 NORMALIZED ENERGY RELEASE RATE

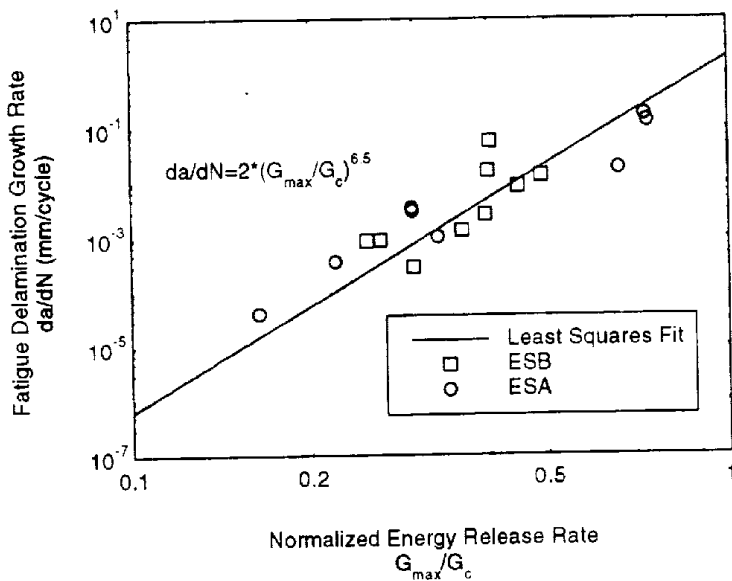


Figure 2

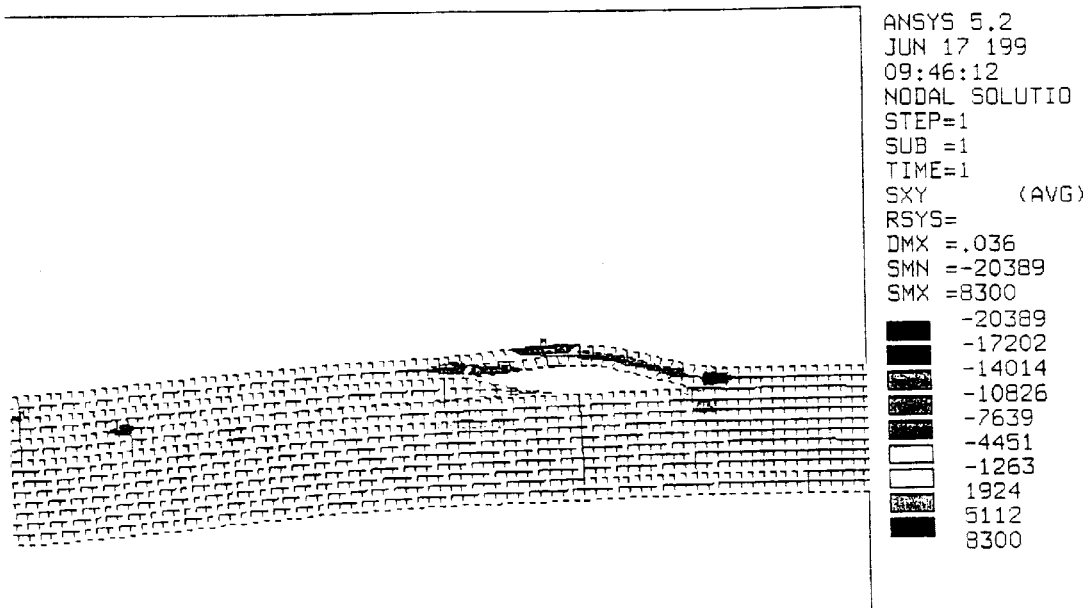


Figure 3

Delamination Length vs. Cycles
 Laminates ESB, ESH, ESF at 275 MPa, R=0.1

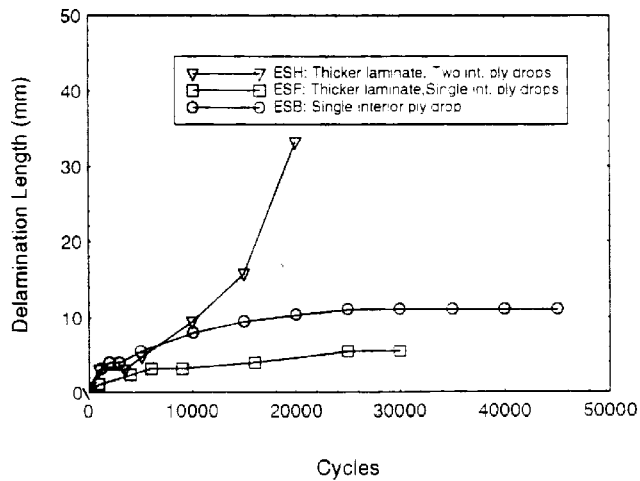


Figure 5

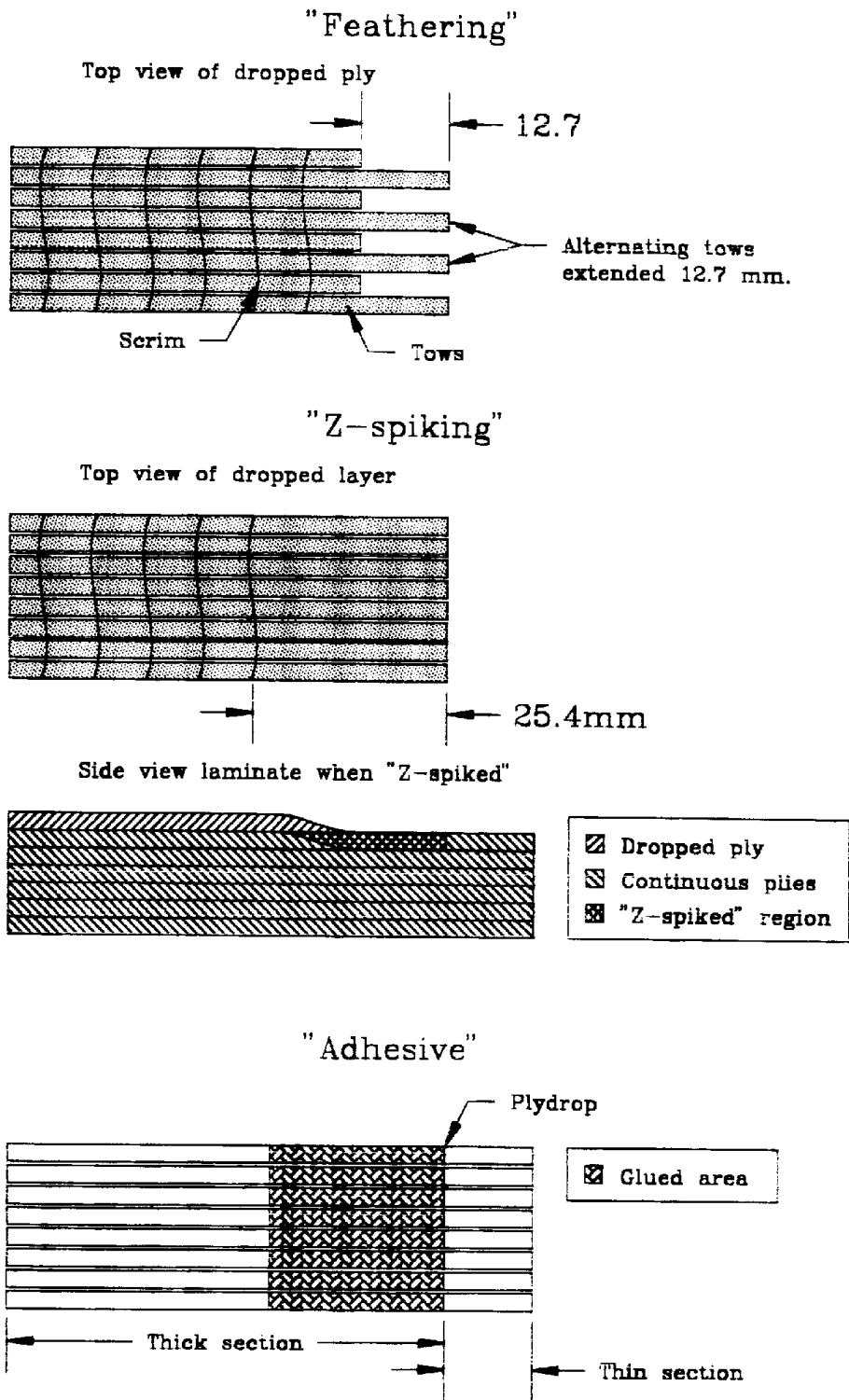


Figure 6

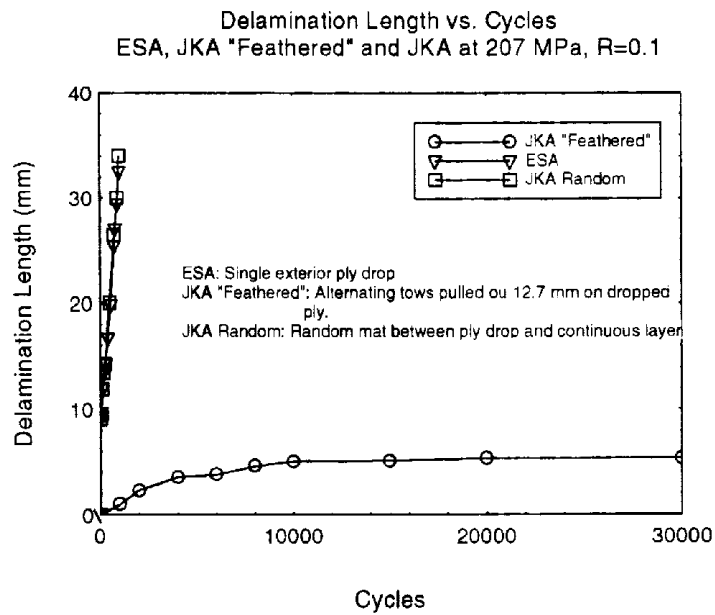


Figure 7

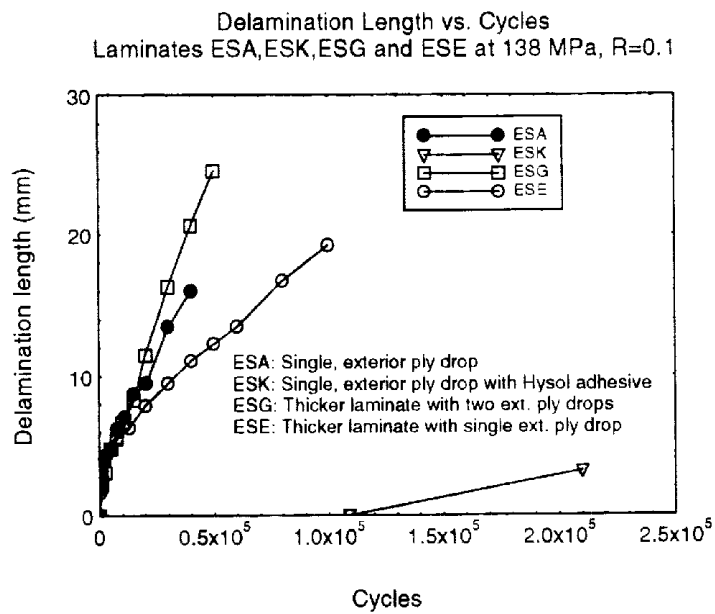


Figure 8

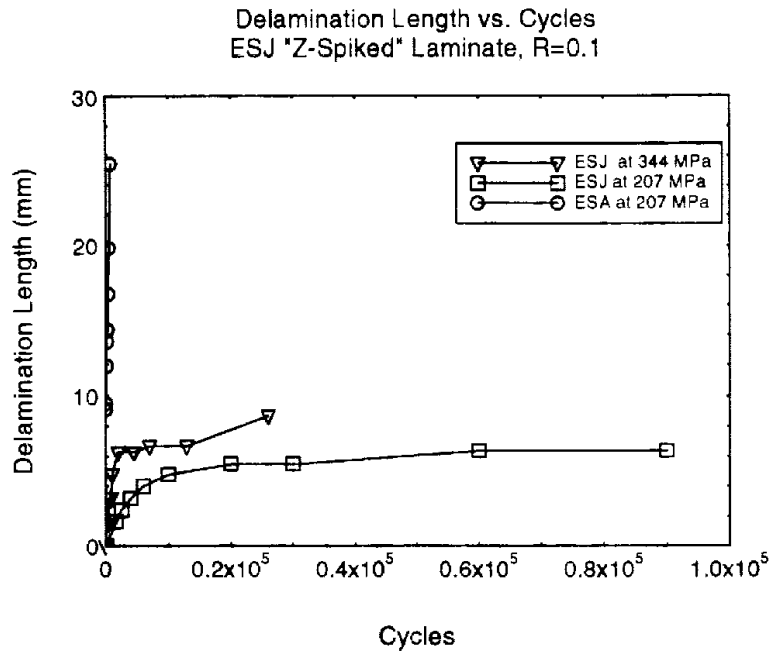


Figure 9

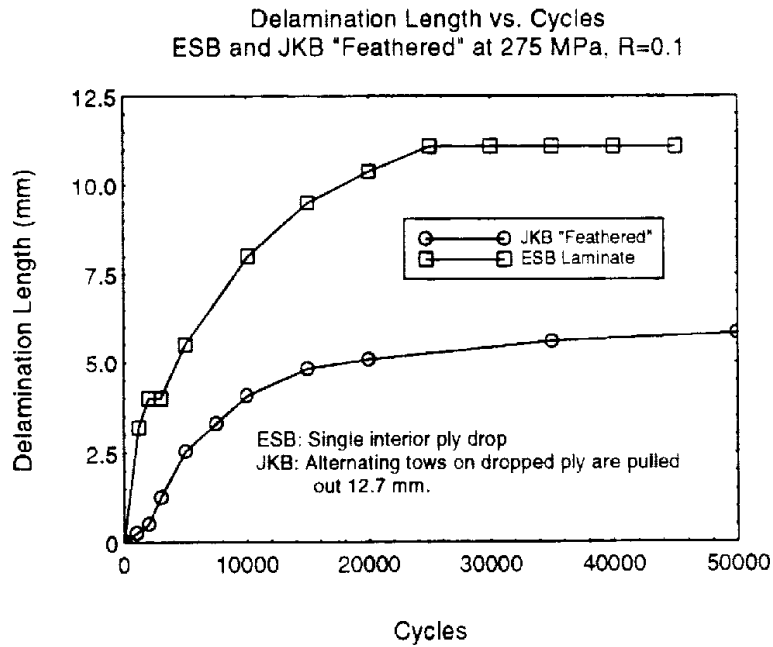


Figure 10

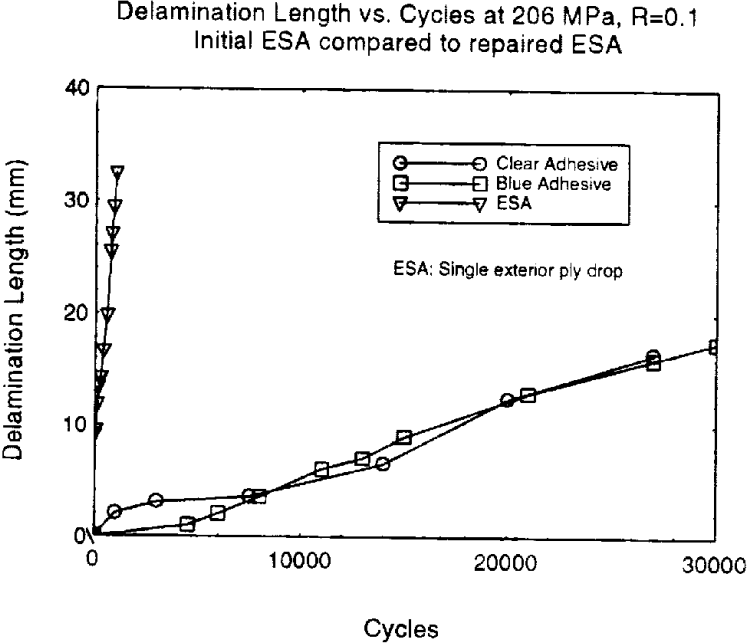


Figure 11

Table 1: Laminate configurations

Laminate Configurations and Specification					
Laminates	Lay-up	E ₁ (GPa)	V _r (%)	Avg. thick (mm) Thick/Thin	Comments
ESA	[0°/(0/±45/0),]	2.39	35.2	3.81/3.09	Single exterior ply drop
ESB	0[(0°/±45/0),]	2.48	35.1	3.70/3.00	Single interior ply drop
ESC	[0/±45/0/0°]	2.42	35.3	3.60/3.02	Single center ply drop
ESE	[0°(0/±45/0),]	3.05	39.7	4.52/3.81	Thicker laminate. Single ext. ply drop
ESF	[0°(0°/±45/0),]	3.33	39.7	4.70/4.06	Thicker laminate. Single int. ply drop
ESG	[0°/(0/±45/0),]	3.26	38.9	4.95/3.81	Thicker laminate. Two ext. ply drops
ESH	[0/0°(0°/±45/0),]	3.45	38.9	4.70/3.55	Thicker laminate. Two int. ply drops
ESJ	[0°/(0/±45/0),]	2.66	37.5	3.55/3.04	Single ext. ply drop w/ "Z-Spiking"
ESK	[0°/(0/±45/0),]	2.93	37.4	3.53/2.89	Single ext. ply drop w/ Hysol adhes

* Indicates the ply or plies dropped (not repeated or symmetrical, just the ply indicated).

** Reached the maximum capacity of the machine before delamination started.

Table 2

Delamination Rate (mm/cycle) for Various Running Stresses (Max. Stress/Min. Stress in MPa)					
	344/34.4	275/27.5	206/20.6	137/13.7	121/12.1
Laminate					
ESA			1.3e-1	3.0e-3	3.81e-4
ESB	1.37e-2	9.14e-4			
ESC	1.07e-3	2.9e-4			
ESE			3.05e-2	1.14e-3	
ESF			2.06e-3	4.83e-4	
ESG				8.64e-4	2.01e-4
ESH		1.38e-2	7.11e-5		
ESJ		4.42e-3	4.83e-4		
ESK			2.79e-3	1.50e-5	

INTEGRATED OPTIMUM DESIGN OF WING STRUCTURE WITH COMPOSITE SKINS

Xu Yang and Yining Zhang

Shenyang Aircraft Company, PO Box 725-204, SHEN YANG 110035, P.R. CHINA

SUMMARY: A minimum weight design procedure of wing structure with composite skins is described briefly, in which strength, frequency, displacement, divergence velocity, control-surface efficiency, flutter speed and thickness are considered as constraints. Main methods used in the procedure are also presented. New engineering requirements are imposed upon the integrated optimization design of composite structure. Method to meet these requirements are suggested and implemented in a newly developed Composite Structure Analysis and Optimum Design Program System (COMPASS). By using the automated design tool, the integrated optimization design for a delta wing structure with composite skins was performed. Under the constraints of unidirectional strains, total thickness limit, balanced-symmetrical limit and flutter speed, the optimum thickness of each ply orientation has been obtained. From the full-scale tests of the wing for strength, durability and damage tolerance, and the tests of ground resonance oscillation and flight of the airplane, it is indicated that tests values are in good compliance with the optimization design results and the integrated optimum design procedure and methods described in this paper can be used for practical optimization design of wing structure with composite skins

KEYWORDS: optimization, constraint, variable, integrate, structure design, composite skin

INTRODUCTION

Generally speaking, a weight saving of over 20% could be achieved when metallic skins of aircraft wing structure are replaced by advanced composite material skins. In addition, by using the characteristics of directional stiffness and the coupling effects of bending and twisting of composite, beneficial aeroelastic deformation (static or dynamic) of wing structure can be obtained. The integrated optimum design technique is a supporting technique to acquire minimum weight of aircraft structure and improve its aeroelastic performances. When composite materials are used on skins of wing structure, they bring new requirements to the technique. In this paper, a integrated optimization design procedure and methods used in the design of a delta wing structure with composite skins are described. New engineering requirements encountered during the optimization design procedure, such as how to find the maximum design point for composite laminate controlled by unidirectional strains, balanced-symmetrical limit and total thickness limit, are discussed. Methods to meet these requirements are also proposed. Test results indicate that the integrated optimum design procedure and methods used for the wing structure are very effective and efficient.

PROCEDURE AND METHODS

Procedure

The flow chart of the optimization design procedure for wing structures is shown in Fig 1.

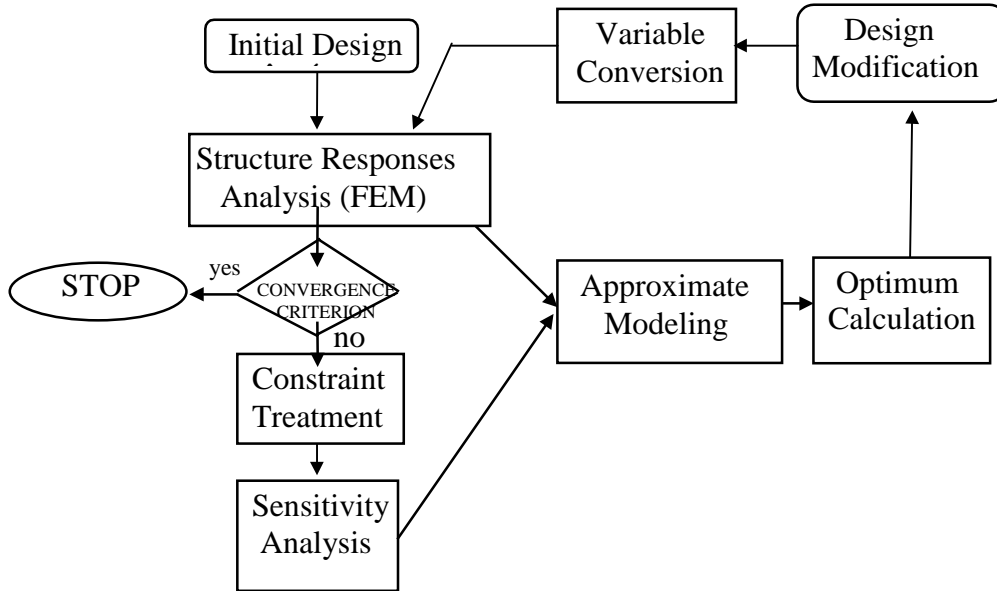


Fig. 1: Procedure of integrated optimum design for wing structures

Methods

Structure Response Analysis

The displacement methods are used to solve the force balance equation:

$$[k] \{u\} = \{F\} \quad (1)$$

where $[k]$ is the stiffness matrix, $\{u\}$ is the displacement vector and $\{F\}$ is the force vector.

Inherent characteristic problems can be reduced to solve the eigenvalues of the flowing equation:

$$[c] [M] \{q\} = (1 / \lambda) \{q\} \quad (2)$$

where $[c]$ is the damping matrix, $[M]$ is the generalized mass matrix, $\{q\}$ is the generalized mode shape and λ is the eigenvalue.

Flutter analysis includes the calculation of unsteady aerodynamic loads and the solving of flutter equation.

The Subsonic Doublet - Lattice Lifting Surface Method is used to calculate the unsteady aerodynamic loads and the v-g method used to calculate the flutter speed:

$$\lambda \{q\} = ([M_{mn}] + (1/k)[A_{mn}])^{-1} [\omega_m^2 M_{mn}] \{q\} \quad (3)$$

where λ is the eigenvalue, $\{q\}$ is the complex characteristic vector and $[M_{mn}]$ is the generalized mass matrix, ω_m is the frequency, $1/k$ is the reduced frequency and $[A_{mn}]$ is the matrix related to the structure^[4].

Static aeroelasticity analysis

Kernel Function Method is used to calculate the coefficients of aerodynamic loads, and the equations to calculate the divergence speed is:

$$V_D = \sqrt{\frac{2q_D}{\rho}} \quad (4)$$

where ρ is the air density and q_D is the eigenvalue of the following function

$$([K_{EE}] - q[R_{EE}])\{\xi_{EE}\} = \{0\} \quad (5)$$

where $[K_{EE}]$ is the generalized stiffness matrix and $[R_{EE}]$ is the generalized aerodynamic loads matrix.

Control-surface efficiency calculating equation is^[4]

$$m_{x^{\prime\prime}} = s^{-1} \ell^{-1} \left\{ \left[\bar{z} \right] \{q\} + q \left[\bar{z} \right]^B \phi \left(\bar{K} - q \bar{R} \right)^{-1} \phi \{q\}^T \right\} \quad (6)$$

Constraint Considerations

When designing a wing structure, the constraint conditions, such as dimension, stress, strain, displacement, vibration frequency, control-surface efficiency, divergence velocity and flutter speed, must be considered. To make the numerical value of constraint equation stable and speed up the convergence, constraint screening and norming techniques are used^[4].

Sensitivity Analysis

The sensitivity analysis take the longest time during the integrated optimum calculation. To reduce the computing time, the analytical derivative method is used as a primary method supported by the difference method. As the static aeroelastic analysis are based on the structure mode shapes, it is able to calculate the static aeroelastic sensitivity of large FEM.

Approximate Treatment

The goal of approximation treatment is to reduce structure re-analysis times and the dimension number of design variables and to increase the computing efficiency. The following approximation techniques are used:

Variable block, key element and variable linking method to reduce the variable numbers.

Temporal deletion of some constraints which can not become critical constraints when the variables are properly changed, to reduce constraint number during optimization calculation.

First-order Taylor-series expansion as explicit approximation expressions of the object and constraint functions, to reduce structure re-analysis times.

Limit the modified value of variables properly in every optimization step, to confirm the optimum searching in an adequate precision range and to improve the convergence performance.

Optimum Design Model

The structure weight, stress, strain, displacement, vibration frequency, control-surface efficiency, divergence velocity and flutter speed are defined as structure responses, one response or a combination of some response as the objective functions and the other repossess as the design constraints and the structural element sizes are selected as the design variables. For example, when we define weight as objective function, the optimum model can be reduced to the following mathematical programming problem:

$$\begin{aligned}
 & \text{find } = \{x_1, x_2, \dots, x_N\} \\
 & \text{min. } f(x) \\
 & \text{s.t. } \mathbf{g}_j(x) \leq 0 \quad j = 1, 2, \dots, M \\
 & \quad x_i^l \leq x_i \leq x_i^u \quad i = 1, 2, \dots, N
 \end{aligned} \tag{7}$$

where M is the number of constraints and N is the number of variables.

Optimization Design Algorithm

The Sequential Unconstrained Mathematical Techniques (SUMT) is used to obtain the minimum weight, in the following steps:

Conversion of the constrained problems to unconstrained minimization problems; solving the unconstrained problem with the Modified Newton Method;

Using Golden Section Method to solve one-dimension minimum search, and obtain the optimum step.

ENGINEERING REQUIREMENTS FOR THE INTEGRATED OPTIMUM DESIGN OF COMPOSITE STRUCTURES

Maximum Design Point

When composite materials are used on wing skins, the strength constraints are unidirectional strains required by durability and damage tolerance. Constraint space limited by the curved line (strength criterion of the curved line is often used by the academic environment) is different from that limited by the unidirectional constraints(Fig. 2). The requirement is how to find the maximum design point A for a composite laminate controlled by multi-unidirectional strains.

We apply the unidirectional constraints simultaneously to a composite key element controlled by static strength to find the optimum design point A.

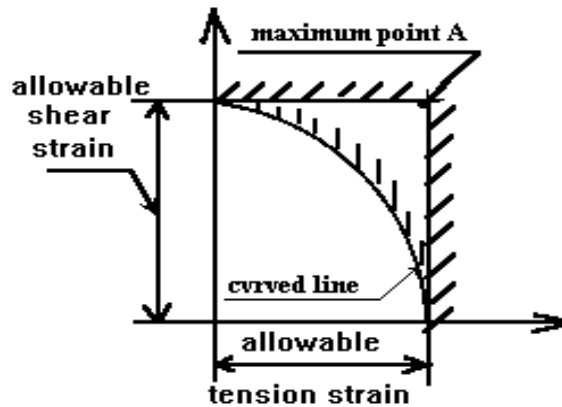


Fig. 2: Constraint space of composite kins controlled by strength

Balanced-Symmetrical Limit

Although the coupling characteristics of a laminate are needed for aeroelastic tailoring designs of composite wing structures, in some cases the balanced-symmetrical laminates are required to reduce deformation of the laminates during curing process, so the balanced - symmetrical design requirement is made.

We take the following steps to meet the balanced-symmetrical requirements adds the sensitivities of the variables which are required to be balanced or symmetrical

$$\partial \Pi / \partial D_{+\theta} + \partial \Pi / \partial D_{-\theta} = \partial \Pi / \partial D_{\pm\theta} \quad (8)$$

re-assigning their sensitivity values before iteration

$$\partial \Pi / \partial D_{+\theta} = \partial \Pi / \partial D_{-\theta} = \frac{1}{2} \partial \Pi / \partial D_{\pm\theta} \quad (9)$$

Total Thickness Limit

Consider a laminate composed of n ply orientations and the thickness of each ply orientation is taken as a variable(see Fig. 3). For some cases in practical designs, the total thickness dimension D is limited. Usually engineers choose D/n as the upper limit for each variable to meet the total thickness limit. As the weight sensitivity to the active constraint of each variable differ widely (because the orientation of each ply are different), such a case can probably happen that the variable having the maximum sensitivity reaches its upper limit and is limited, while the others do not reach their upper limits. If this occasion happens, the design results can not be a optimized one obviously. So a method to treat this special case is required.

$$d_i^u = \frac{\partial \Pi / w_i}{\sum_{i=1}^k \partial \Pi / \partial w_i} (D - \sum_{j=1}^{n-k} d_j^l) \quad (10)$$

where d_i^u is the upper limit of variable d_i , $\frac{\partial \Pi / \partial w_i}{\sum_{i=1}^k \partial \Pi / \partial w_i}$ is the weight sensitivity percentage of variable d_i , k is the number of variables which have positive sensitivities and $\sum_{j=1}^{n-k} d_j^l$ is the sum of the lower limit of variables which have negative sensitivities.

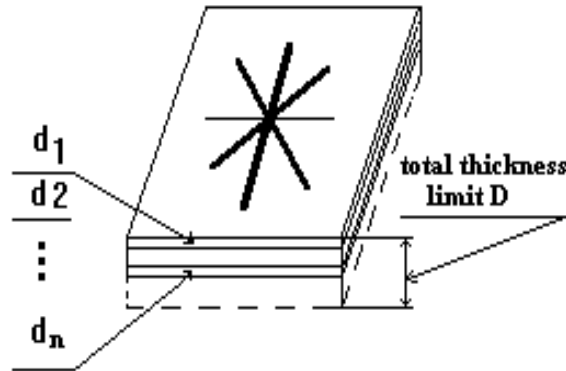


Fig. 3: Plot to explain the total thickness dimension limit

APPLICATION EXAMPLE

Using the integrated optimum design computer program (COMPASS) based on the procedure and methods mentioned above, the integrated optimum design for the composite skins of a delta wing structure carrying a external tank was performed. This wing structure has metallic ribs and beams, its FEM is shown in Fig. 4 and the location of composite skins are shown in Fig. 5. The composite skins were partitioned into 12 variable blocks, 12 key elements and 48 variables (thickness) and two cases of critical load are taken into consideration. The design goals are to obtain the minimum structure weight and an increased flutter speed. The constraints are shown in table 1.

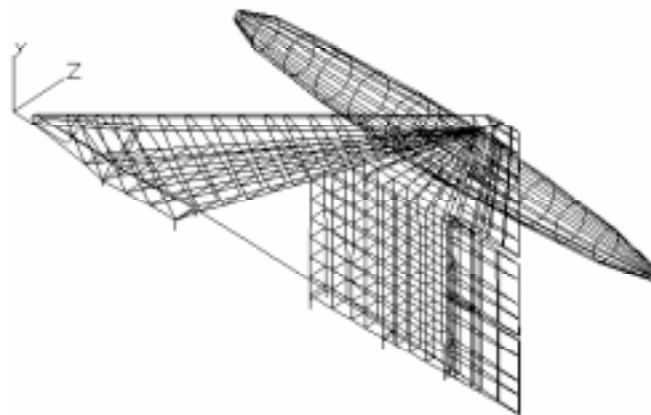


Fig. 4 FEM of the wing structure carrying a external tank

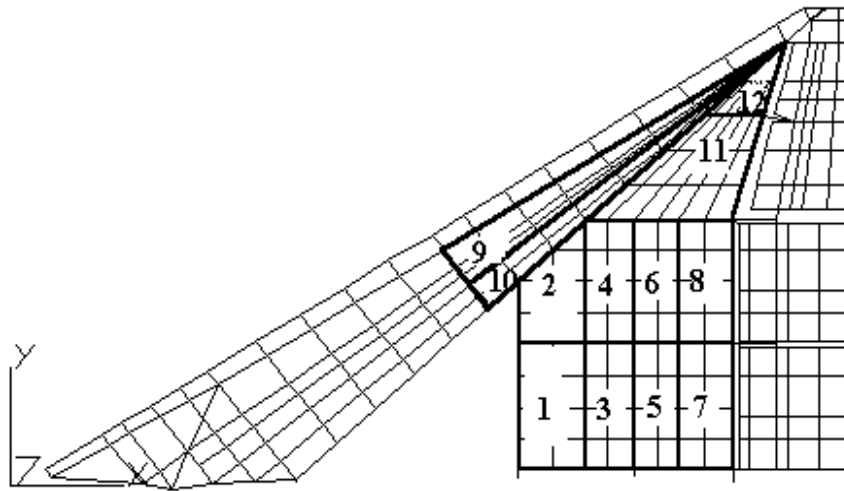


Fig. 5 The location of composite skins and variable blocks

Table 1: Integrated optimum design constraints

Items	Constraints
Allowable Tension Strain (a.t.s)	3500 ($\mu\epsilon$)
Allowable Compression Strain(a.c.s)	2700 ($\mu\epsilon$)
Allowable Shear Strain (a.s.s)	5300 ($\mu\epsilon$)
Balanced and Symmetrical	Thickness at $+45^0$ equals to that at -45^0
Total Thickness	Total thickness D less than 5(mm) for block 11, and less than 6(mm) for the other blocks
Flutter Speed	276.00 (m/s)

After 6 iteration steps, the optimization calculation was converged and all constraints were satisfied. Fig. 6 shows the strain ratios of tension and shear of a key element controlled by static strength and indicate that two unidirectional strain ratios converge toward the optimum value 1. Fig. 7 shows the iteration process of variable thickness, in which the $+45^0$ -ply thickness is equal to the 45^0 -ply and the balanced-symmetrical constraint satisfied. Fig. 8 shows the flutter speed versus incremental structure weight, in which the average sensitivity criterion is applied to line 1. The technique makes the upper limit of a variable higher if it's sensitivity is higher. As the thickness distribution to each ply orientation in the laminate is more reasonable under the constraint of the total thickness, the structure weight efficiency is increased.

The convergence tendency of flutter and structure weight is typical (Fig. 9 and Fig. 10). As a large external tank is taken into account, the coupling between the store pitch and the first wing bending results in a slow flutter type. The flutter v-g plot is shown in Fig. 11. Table 2 is the results of the integrated optimum design.

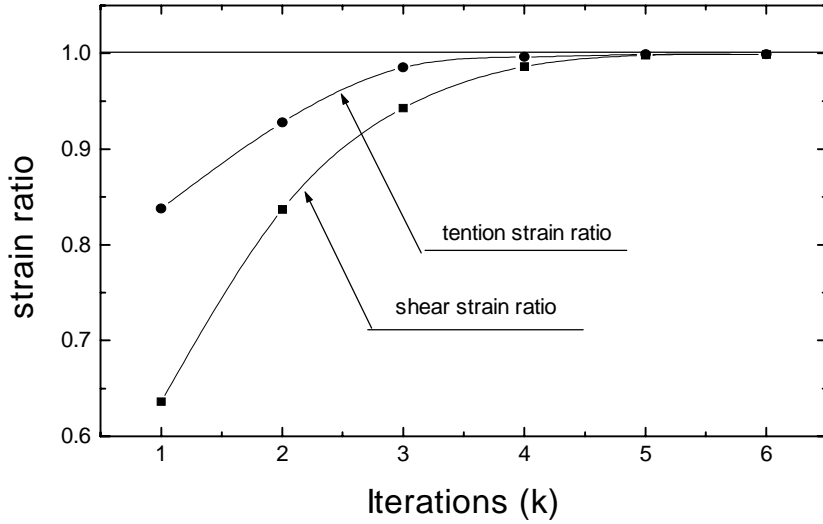


Fig. 6: Strain ratios of tension and shear

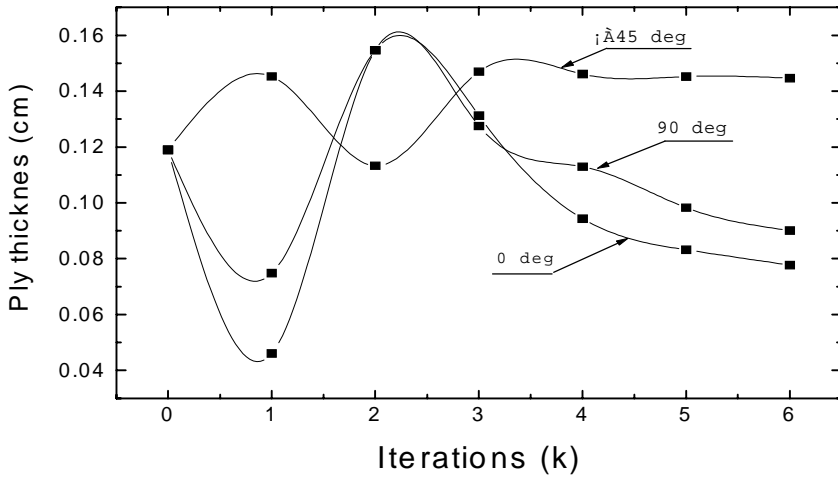


Fig. 7: Variable thickness history of iteration

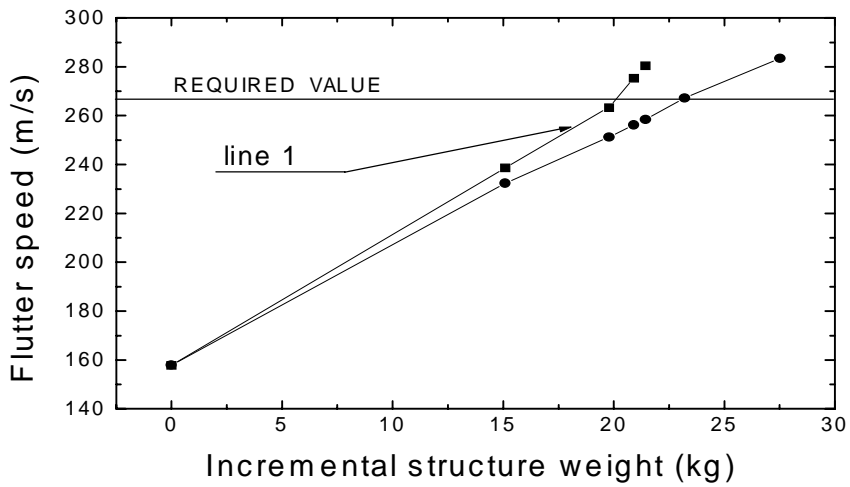


Fig. 8: Flutter speed vs. incremental structure weight

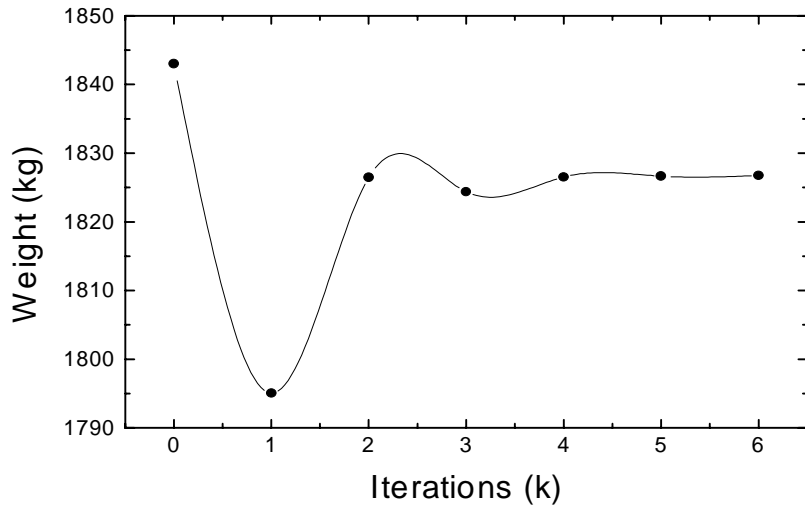


Fig. 9 Structure weight history of iteration

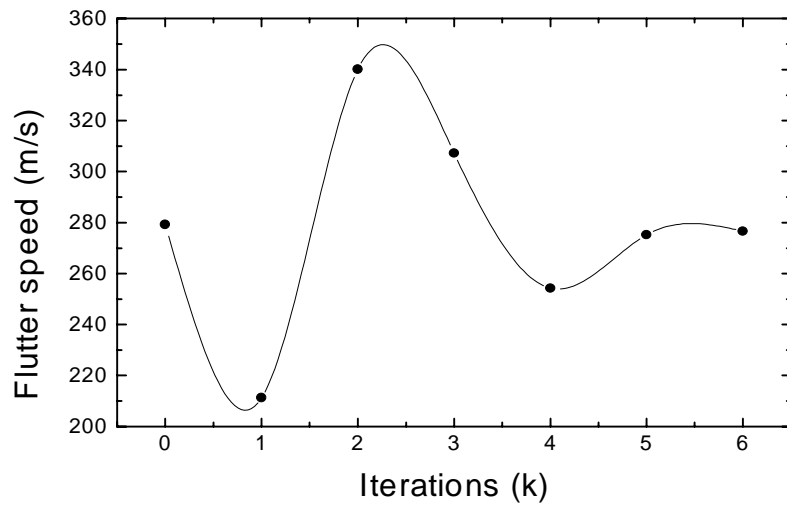


Fig. 10: The flutter speed history of iteration

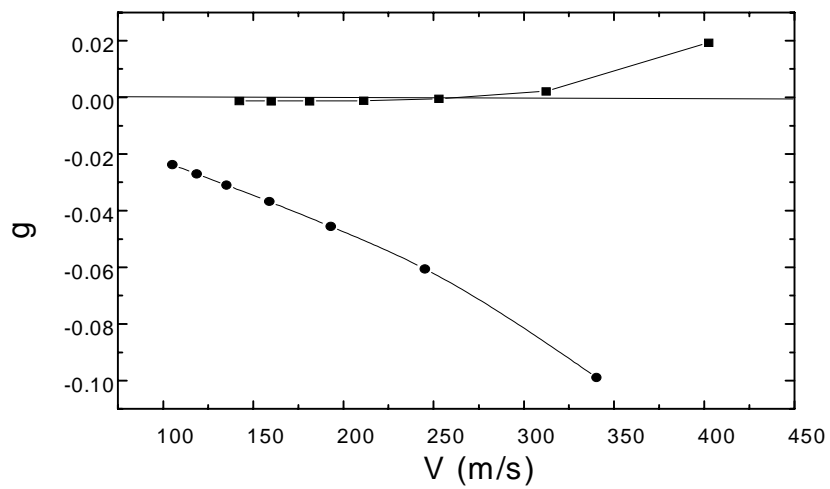


Fig. 11 Plot of v-g

Table 2: Results of integrated optimum design

Block No	Ply layout (angle _{ply number})	Active Constraint Type	Block No	Ply layout (angle _{ply number})	Active Constraint Type
1	0 ₈ /±45 ₂₈ /90 ₃	strength	7	0 ₈ /±45 ₁₆ /90 ₃	strength
2	0 ₈ /±45 ₂₄ /90 ₃	strength	8	0 ₈ /±45 ₂₄ /90 ₃	flutter
3	0 ₈ /±45 ₁₆ /90 ₅	strength	9	0 ₈ /±45 ₁₂ /90 ₂	strength
4	0 ₁₂ /±45 ₂₈ /90 ₃	flutter	10	0 ₁₀ /±45 ₁₂ /90 ₄	strength
5	0 ₈ /±45 ₂₄ /90 ₃	strength	11	0 ₁₁ /±45 ₂₈ /90 ₄	flutter
6	0 ₁₀ /±45 ₃₆ /90 ₅	flutter	12	0 ₇ /±45 ₁₂ /90 ₂	flutter
1. The total weight saving of composite skins is 20%.					
2. The flutter speed of the composite wing with an 1400(L) external tank is increased by 23% compared with the metallic wing.					

TEST RESULTS AND CONCLUSION

To verify the integrated optimum design results of Table 2, three full-scale wing structures with composite skins are fabricated, one for static strength, durability and damage tolerance tests, the other two for ground resonance oscillation and flight tests. The results indicate that the test values are in good compliance with the optimization design results of Table 2^[2].

CONCLUSION

The integrated optimum design procedure and methods described in this paper can be used for the practical optimization design of wing structures with composite skins, the engineering requirements can be satisfied and the design results are verified by a lot of different types of tests.

REFERENCES

- [1]. Xu Yang, 'Research of Integrated Optimum design for Composite wing structure', Technical Report of Shenyang Aircraft Company, 1993.5.
- [2]. Yining Zhang, 'Research and Manufacturing Summarization of Composite Wing Structure with Integrated Full Tanks', Technical Report of Shenyang Aircraft Company, 1995.11.
- [3]. Yining Zhang, 'Theoretical Manual of SAFDOP', Technical Report of Shenyang Aircraft Company, 1985.10.
- [4]. Huiliang Ding, 'Theoretical Manual of COMPASS', Technical Report of Airplane Strength Research Institute, P.R. China , 1989.3.
- [5]. D.J.Neill, 'ASTPOS-A Multidisciplinary Automated Structural Design Tool', N89-25174.
- [6]. CLINTON V.ECKSTROM, CHARLES V., 'Design Considerations And Experiences in The Use of Composite Material For An Aeroelastic Research Wing', NASA Technical Memorandum 83291.
- [7]. Michael H.shirk, Terrence J.Hertz, 'Aeroelastic Tailoring - Theory, Practice,-and Promise', J.AIRCRAFT, Vol.23, No.1.
- [8]. Warner L, Edwin Lerner, 'Application of Structural Optimization for Strength and Aeroelastic Design Requirements', AGARD R-664.
- [9]. V.B.Venkayya, 'Recent Developments in Large-Scale Structural Optimization', N89-25231.
- [10]. K.B.Bowman, 'Optimum Structural Design With Static Aeroelastic Constraints', N89-25171.
- [11]. Philip Mason, 'Applications of Integrated Design /Analysis Systems in Aerospace Structural Design', N89-25147.

THE OPTIMUM DESIGN OF FUNCTIONAL COMPOSITE MATERIALS FOR ELECTRICAL BRUSHES IN DC MACHINES

Yuying Wu, Weijie Tang and Guoding Zhang and Qing Hong

*Institute of Composite Materials, Shanghai Jiao Tong University,
Shanghai, 200030, P.R.China*

SUMMARY: The designability of composite materials is a big advantage over other even structured materials. In this work, a CAD program had been developed to design Carbon fiber/Graphite composite brushes to take advantages of both of the designability of composite materials and the commutation equations of DC machines for the best commutation performance. The electrical properties of both the carbon fiber and the graphite had been measured and the commutation curve under different fiber distribution had been calculated. The design scheme of the composite brush which meet the best commutation performance was given by the program and also several factors which had effects on the commutation had been discussed according to the results of computer simulation. The results given by the computer meet the real application and theoretical analysis quite well.

KEYWORDS: optimum design, brush, DC machines, carbon fiber

INTRODUCTION

The bad commutation performance of DC machines is one of the key factors that hindered machines' development. So, how to improve the commutation performance had always been the hot topic among people who are engaged in the design and use of DC machines.

Electrical brush is the main part used for current transmission in DC machines, its performance has a direct effect on the commutation. According to the commutation principle of DC machines, the existence of the commutation current makes the current distribution uneven on the contact face between brush and commutator. In other words, during the commutation period, the current flowing through the different parts of brush's working face is different. So it is apparently that the even structure of the conventional brush can not meet the need of current variation during the commutation period.

Carbon fiber/Graphite composite brush is an uneven structure brush made from carbon fiber and graphite matrix. The big advantage of the composite brush is that the amount and the distribution of the fiber can be varied on the brush surface to meet the need of the electrical machine to achieve the best performance. Fig.1 is the draft of such composite brush.

The purpose of this work is to complete a CAD program, with the specified properties of the DC machine, the carbon fiber and the graphite matrix, a design scheme of the distribution of the carbon fiber on graphite matrix will be given to meet the best commutation performance of the DC machine.

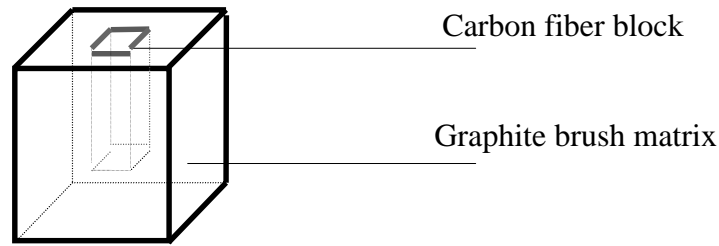


Fig.1 Draft of Carbon Fiber/Graphite Brush

DESIGN PRINCIPLE

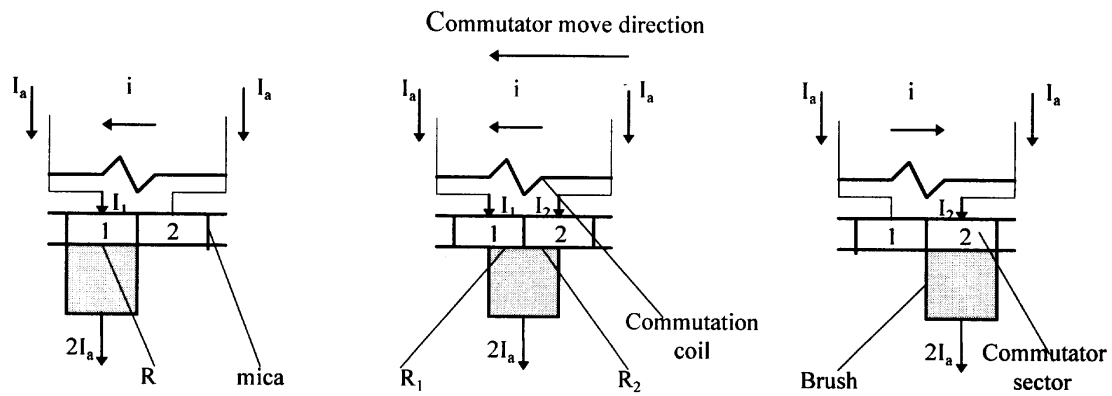


Fig. 2 Illustration of commutation

Commutation procedure is such a period that during a short time interval, the current in commutation coil reversed. As shown in Fig.2, the current in commutation coil (bold line) reversed when brush had moved from position 1 to position 2. According to the commutation principle of DC machines, we got the following equations.[1][2]

$$\begin{aligned}
 \Delta U_1 - \Delta U_2 &= \Sigma e \\
 \Delta U_1 &= I_1 R_1 \\
 \Delta U_2 &= I_2 R_2 \\
 I_1 &= I_a + i \\
 I_2 &= I_a - i
 \end{aligned}
 \tag{1}$$

- $\Delta U_1, \Delta U_2$ — Contact voltage drops between brush and sector 1, brush and sector 2.
- I_1, I_2 — Current flowing through sector 1 or sector 2.
- R_1, R_2 — Contact resistance between brush and sector 1, brush and sector 2.
- I_a — Current in normal coil.
- i — Commutation current.

If it is assumed that the contact resistance is inversely proportional to the contact area between the brush and the sector, from Eqn 1, the commutation current i at time t .

$$i_t = i_a \left(1 - \frac{2t}{T_k}\right) + \frac{\Sigma e}{R} \tag{2}$$

t — commutation time, Σe — composed e.m.f.(electromotive force)
 T_k — commutation period, R — contact resistance between brush and commutator sector.

Eqn 2 is discussed as shown in Fig.3.

When $\Sigma e = 0$, i is linear with t , it is called linear resistance commutation.

When $\Sigma e < 0$, commutation current changes earlier than that of the resistance commutation, it is so called over commutation.

When $\Sigma e > 0$, commutation current changes later than that of the resistance commutation, it is so called under commutation.

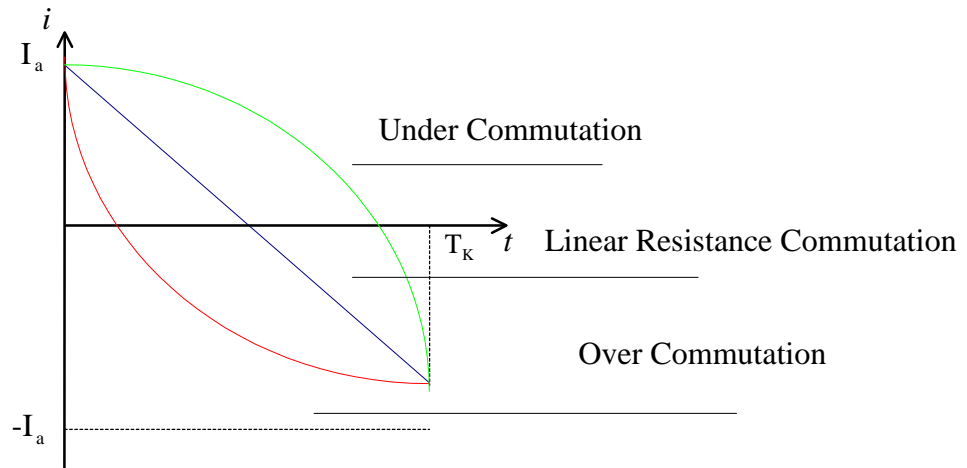


Fig. 3 Illustration of three commutation models

The most serious problem during commutation is commutation sparking which will seriously affect the normal operation of DC machines. Linear resistance commutation, which is the perfect commutation, has no sparking, while serious over and under commutation will lead to sparking. The physical cause for sparking is that at the end of the commutation, the current in commutation coil does not reach the value in other normal coil. As shown in Fig.4, the remaining current difference i_k will lead to the energy releasing(sparking) to complete the commutation. The reason of the existence of remaining current difference is as following. During practical commutation, the actual contact between brush and commutator sectors occurs only at relatively few discrete points, the remaining areas is separated by gaps of the order of 0.5×10^{-6} m. Passage of current through limited points develops high intensity electric field between the non-contact areas. Such electric field initiates field emission, which makes the contact resistance not increase with the decrease of the contact area during the end period of commutation[3][4]. It means the assumption of “contact resistance is inversely proportional to the contact area between the brush and the sector” can not be taken as we discussed in Fig.3. The low resistance at the end of commutation causes the finishing

commutation current in brush different than that in normal coil, thus leads to the energy releasing of the sparking.

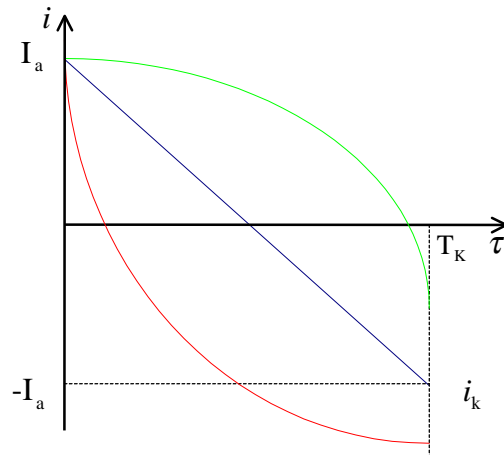


Fig.4 Practical Commutation Curve

As discussed above, there will be two ways to prevent the bad commutation sparking. One is to modify the contact performance of the brush and commutator, prevent the field emission which will leads to resistance decrease. The other is to modify the commutation current, makes it change smoothly to prevent the energy release due to sudden change of the current. As proved in real practice, the linear resistance commutation is the perfect commutation with no sparking.

The use of Carbon fiber/Graphite composite brush can meet the above two requirements. First, the excellent contact and conductivity performance of carbon fibers greatly improves the contact performance between brush and commutator, reduces the possibility of field emission. Second, the designability of the composite materials makes it possible to change the distribution of the fibers on graphite brush surface to modify the commutation curve to be closed to the linear commutation.

DESIGN PROCEDURE

From Eqn 1, commutation current

$$i = \frac{\Sigma e - I_a R_1 + I_a R_2}{R_1 + R_2} \quad (3)$$

To a specified DC machine, Σe and I_a are constant. So the commutation current i is changed with the change of R_1 and R_2 . Thus, to design the commutation current variation with the requirement is just to design a proper variation of the contact resistance between brush and commutator. For composite brushes, such design requirement is technically realized by varying the amount and the distribution of carbon fibers on the surface of the graphite brush matrix. So it is necessary to know the electrical contact properties of both the graphite and the fiber.

Electrical Contact Properties of the Components

Fig.5 is the V-A property of the D172 graphite which is used as brush matrix.

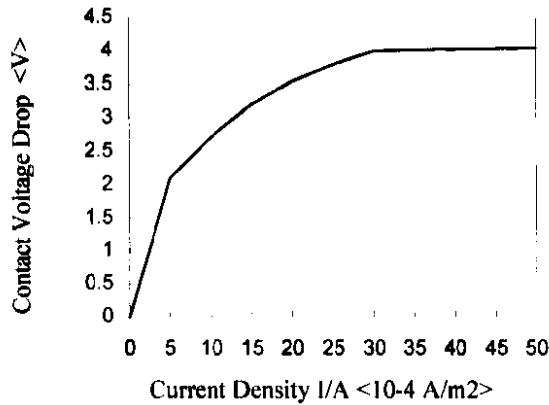


Fig.5 V-A curve of the D172 graphite

Fig.5 is regressed to get the V-A equation of the D172 graphite,

$$\Delta U_G = a_G \left(\frac{I_G}{S_G}\right)^3 + b_G \left(\frac{I_G}{S_G}\right)^2 + c_G \left(\frac{I_G}{S_G}\right) + d_G \tag{4}$$

ΔU_G — Contact voltage drop of the graphite

I_G — The current flowing through the graphite,

S_G — The contact area of the graphite,

$a_G = 4.67 \times 10^{-17}$,

$b_G = -5.62 \times 10^{-11}$,

$c_G = 2.25 \times 10^{-5}$,

$d_G = 1.05$

Use the same method, the V-A equation of the carbon fiber used in composite brush is,

$$\Delta U_F = a_F \left(\frac{I_F}{S_F}\right)^3 + b_F \left(\frac{I_F}{S_F}\right)^2 + c_F \left(\frac{I_F}{S_F}\right) + d_F \tag{5}$$

ΔU_F — Contact voltage drop of the carbon fiber

I_F — The current flowing through the fiber, S_F — The contact area of the fiber,

$a_F = 2.36 \times 10^{-19}$,

$b_F = -8.89 \times 10^{-13}$,

$c_G = 1.28 \times 10^{-6}$,

$d_G = 1.81$

Find the Result of the Commutation Current

In a same contact face of the brush and the commutator, the contact voltage drop of the fiber part is equal to that of the graphite part, so

$$\Delta U_F = \Delta U_G \tag{6}$$

From Eqn 1, 4, 5, 6, we got

$$\begin{aligned}
 a_G \left(\frac{I_{1G}}{S_{1G}}\right)^3 + b_G \left(\frac{I_{1G}}{S_{1G}}\right)^2 + c_G \left(\frac{I_{1G}}{S_{1G}}\right) + d_G &= a_F \left(\frac{I_{1F}}{S_{1F}}\right)^3 + b_F \left(\frac{I_{1F}}{S_{1F}}\right)^2 + c_F \left(\frac{I_{1F}}{S_{1F}}\right) + d_F \\
 I_{1G} + I_{1F} = I_1, I_1 = I_a + i_t & \\
 a_G \left(\frac{I_{2G}}{S_{2G}}\right)^3 + b_G \left(\frac{I_{2G}}{S_{2G}}\right)^2 + c_G \left(\frac{I_{2G}}{S_{2G}}\right) + d_G &= a_F \left(\frac{I_{2F}}{S_{2F}}\right)^3 + b_F \left(\frac{I_{2F}}{S_{2F}}\right)^2 + c_F \left(\frac{I_{2F}}{S_{2F}}\right) + d_F \\
 I_{2G} + I_{2F} = I_2, I_2 = I_a - i_t &
 \end{aligned} \tag{7}$$

S_{1G}, S_{1F} — The contact area between sector 1 and graphite, sector 1 and fiber.
 S_{2G}, S_{2F} — The contact area between sector 2 and graphite, sector 2 and fiber.
 I_{1G}, I_{1F} — Current flowing through sector 1 and graphite, sector 1 and fiber.
 I_{2G}, I_{2F} — Current flowing through sector 2 and graphite, sector 2 and fiber.
 i_t — Commutation current at time t .

The Newton method is used to find the result of the commutation current i . An assumed value of commutation current i' is assigned to i_t . From Eqn 7, we got the result of

$$I_{1G}, I_{2G}, I_{1F}, I_{2F}$$

Use them in Eqn 4,5, we got the result of

$$\Delta U_{1G}, \Delta U_{2G}, \Delta U_{1F}, \Delta U_{2F}$$

From the equation $R=\Delta U/I$, we got the value of

$$R_{1G}, R_{2G}, R_{1F}, R_{2F}$$

From the parallel connection law of the resistance, we got the value of

$$R_1, R_2,$$

Use them in Eqn 3, we got the commutation current i .

A threshold ξ is assigned, when $|i - i'| < \xi$, value i' can be taken as the solution of the commutation current i . Otherwise, $i_t = (i + i')/2$ is taken and the above procedure is repeated. Since practically, i_t should have a solution, so this equation should be restraint.

Realization of the Optimization

Different distributions of fibers on brush surface will result in different commutation curves. Since the linear resistance commutation is the best one, the difference to the linear one is chosen as the criterion to find the best commutation. The computer realization is as following. The commutation period is divided into k time interval. At moment t , the current on linear commutation curve is i_{0t} , the current on real commutation curve is i_t , the mean square of the errors for totally k moments is

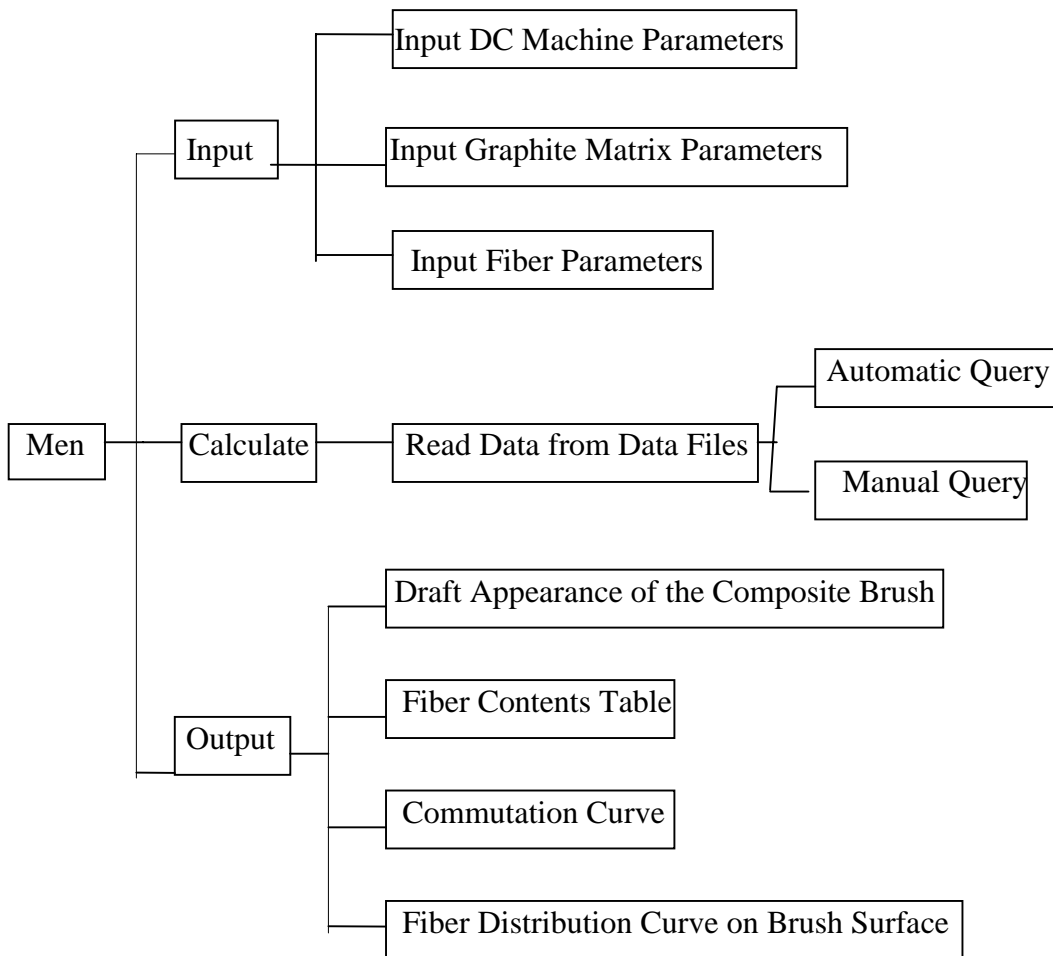
$$W = \sum_{t=1}^k (i_t - i_{0t})^2$$

Virtually, the surface of the brush is divided into n even parts, the proportions of the fibers on each part can be varied from $1/m$, $2/m$ to m/m . The value of n and m can be assigned by the user. So there is totally m^n different distributions for a specified composite brush. The commutation curve of each fiber distribution is calculated and the one with the minimized W is chosen as the best commutation, the corresponding fiber distribution is also given out.

INTRODUCTION TO THE CAD PROGRAM

The program is developed with C language on IBM PC platform.

Program Module



Program Explanation

Four types of parameters should be input to complete the design. They are parameters of electrical machines, graphite brush matrix, carbon fibers and parameters used for calculation. Automatic query and manual query are used in this program. In automatic query, the commutation curve of every different fiber distribution on graphite matrix are calculated and the one which is most close to the perfect liner commutation will be found out, also the design

scheme of such composite brush will be given. In manual query, the commutation curve will be given by the program with the fiber distribution input by user.

The Characteristic of the CAD Program.

Good Modular Structure and User Interface

Every module is independent to each other which makes the further modification and maintenance easy. The large amount of parameters of DC machines, graphite matrices and carbon fibers, once input, they will be stored in the computer with different names and ready for use in the further calculation. Also, each design scheme is stored in the computer and can be read when needed. Meanwhile, the friendly user interface is specially designed to those customers without computer background. It is easy to learn and use.

Double Functions on Both Design and Simulation

This CAD program, not only can be used to give out the optimum design scheme according to different DC machines, also, it can simulate the commutation curve with different brush materials, different brush current densities and different commutation conditions. It gives us big flexibility during brush design.

THE RESULTS OF THE COMPUTER DESIGN

Required Parameters

The parameters of the DC machine used in design is shown in Table 1.

Table 1: DC machine parameters

I_a (A)	Σe (V)	Mica width(m)	Sector width(m)	Commutator speed(m/s)	Winding	Number of the sectors one brush covers
288	7	0.004	0.016	30.4	Single lap	1

The graphite matrix used in composite brush is D172, its electrical property is given by Eqn 4. The electrical property of the carbon fiber used in composite brush is given by Eqn 5. During calculation, we choose the virtually brush division $n=4$, the number of the different fiber distribution in one part $m=4$, the number of the time interval in one commutation period $k=15$.

Design Result

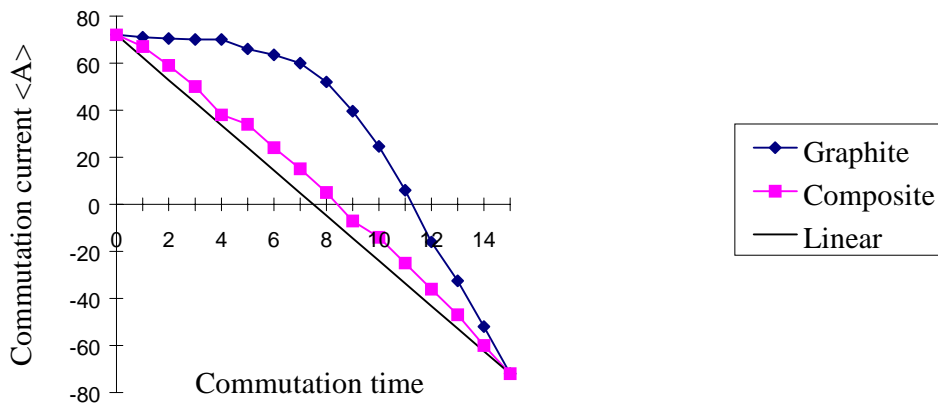


Fig.6 Comparison between theoretical perfect liner commutation, computer designed composite brush commutation and graphite brush commutation

Fig.6 shows the comparison between the commutation curve of the optimum designed composite brush and that of the pure graphite brush. The brush current density is $0.36\text{MA}/\text{m}^2$. It is apparently that the use of computer designed composite brush significantly improved the commutation performance compared to the use of pure graphite brush. The design scheme can be given by several ways. Fig.7 shows the draft of the composite brush with the best commutation performance. Table 2 gives the design scheme by the fiber distribution value.

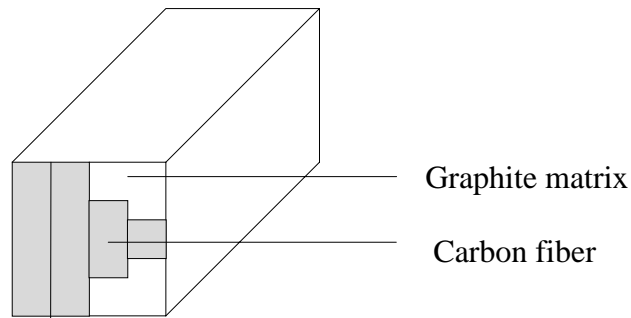


Fig.7 Draft of the optimal designed composite brush

Table 2 *The fiber distribution of the optimal designed composite brush*

Block	1	2	3	4
Fiber contents	100%	100%	50%	25%

DISCUSSION ON THE SIMULATION RESULTS

Factors Affect the Commutation

Brush Current Density

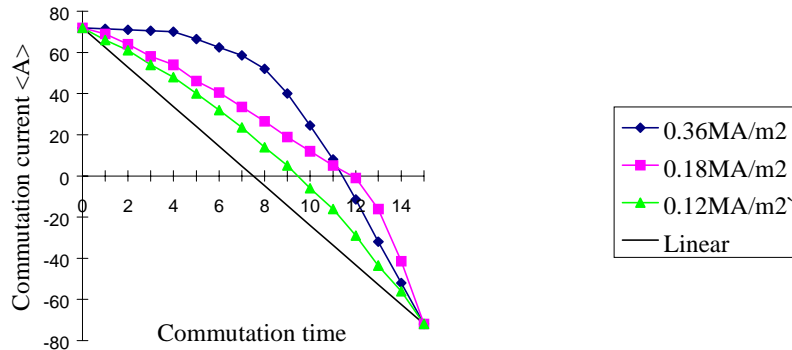


Fig.8 Commutation curves under different brush current densities

Fig.8 shows the simulation result of the commutation curves for a same graphite brush under different current densities. It is apparently that with the decrease of the current density, the curve is going close to the linear commutation. The simulation results can be explained physically that under high current density, the field emission in the contact face of the brush and the commutator is quite serious and results in sparking. While if the current density is low, such field emission will not be activated and the commutation performance will be better. So, reduce the brush current density is good to commutation.

Contact Resistance

Fig.9 shows the simulation result of the commutation curves of two graphite brush with different contact resistance. The brush with high contact resistance has a better commutation. Theoretically, it can be explained that high contact resistance is good to reduce the commutation current, thus good to commutation. While the increment of the contact resistance will also result in the increment of the contact voltage drop, and this will lead to the loss of the DC machine's output power. So, although increase the contact resistance is good to commutation, it will reduce the output power.

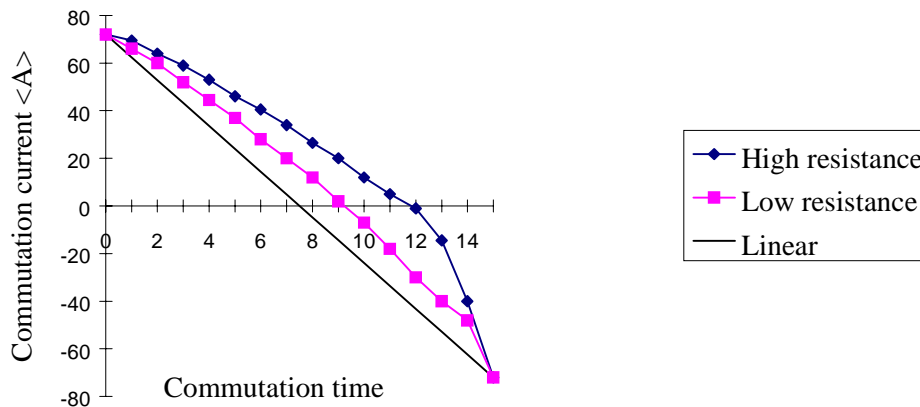


Fig.9 Commutation curves under different contact resistance

Composed e.m.f.

Fig.10 shows the simulation result of the commutation curves of two DC machines with different composed e.m.f. The brush in use is same. The composed e.m.f. of one machine is 7 times higher than that of another machine. It is apparently that reduce the composed e.m.f. is good to commutation, in practical use, reduce the e.m.f. is done by add a pair of commutation poles.

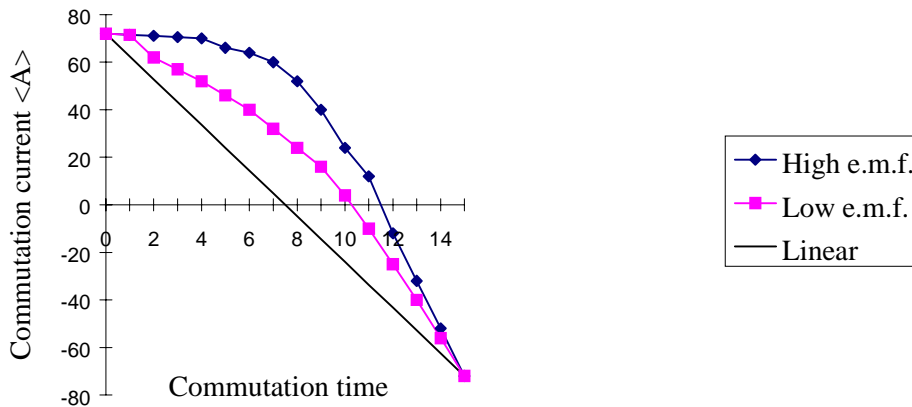


Fig.10 Commutation curves of the DC machines with different composed e.m.f.

Comparison between the Simulation Results and the Practical Use

Brush Current Density

From Fig.8, we got the commutation curves of the D172 graphite brush under different current densities. When the current density is 0.18MA/m^2 or 0.36MA/m^2 , the simulated curve is far from the linear commutation. In real application, graphite brushes working under such high current density results in serious sparking. When current density is 0.12MA/m^2 , the simulated commutation curve is close to the linear commutation. And actually, 0.12MA/m^2 is just the normal working current density for D172 graphite brush.

The Composite Brush Real In Use

Fig.11 shows the simulation result of the commutation curves of the real in use composite brush, computer designed composite brush and the graphite brush. Although the commutation curve of the real in use composite brush is worse than that of the computer designed one, it is still better than that of the conventional graphite brush. And in real application, the use of our current available composite brush significantly improved the DC machine's commutation performance. Brush current carrying capacity increased by 3-4 times, the wearing resistance improved by 20%-50%, and the no-sparking zone (a strong indicator of commutation performance) enlarged by 5-7 times.

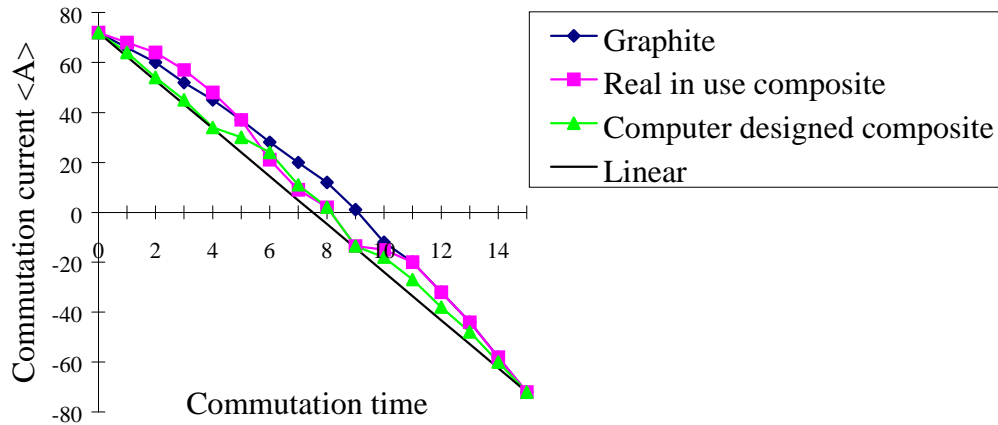


Fig.11 Commutation curves of the real in use composite brush and computer designed brush

CONCLUSION

According to the discussion of the above sections, we found that reduce the brush current density, increase the contact resistance and reduce the composed e.m.f. are good to improve the commutation performance of DC machines. Once the proper physical models and mathematical methods were chosen, the optimum design of the composite brush can be realized by the computer program with the different DC machines, brush matrices and carbon fibers. The use of such composite brush will result in the best commutation performance.

REFERENCE

1. Shen, Guaqiu, *Direct Current Machines*, Shanxi Science and Technology Publishing, China, 1979
2. Li, Fahai, *Electrical Machines*, The Second Edition, Science Publishing, China, 1991
3. Say, M.G. and Taylor, E.O., *Direct Current Machines*, Pitman Publishing Limited, London, 1980.
4. Holm, R., *Electrical Contact Handbook*, Springer Berlin, 1958

SUBJECT INDEX

3D failure analysis	671	columns	88
ageing aircraft	1	commercial transport aircraft	178
aging	402, 467	composite application to robotics	806
air-turbo-ram-jet engine	283	composite applications	257
analysis	528	composite design methodologies	600
analysis methods	52	composite failure criteria	52
and composite manufacturing	535	composite fan blade	200
angle components	719	composite fasteners	426
application of composite materials	789	composite flanges	709
artificial leg shell	477	composite horizontal stabilizer	302
asphalt-reinforcement	336	composite laminate strengths	52
Automated Layup	583	composite laminates	719
automotive composites	275	composite manufacturing	257
automotive composites consortium	275	composite materials	436
automotive polymer composites	275	composite piping	402
		composite plates	365
		composite skin	840
barely visible impact damage	302	composite structural testing	535
belt structure	781	composite structure	178
bending	652	composites	88, 134
bending properties	218	composites affordability	257
bicycle bridge	330	composites development requirements	257, 275
bicycle frame	419	compressed natural gas	393
bike tubes	266	compression strength after impact	748
bioactive	496	computer aided design and manufacture	640
biocompatibility	496	computer simulation materials design	134
biodegradation	509	computer-aided design	652
biomaterial	488	Concorde	383
biomaterials	496	concrete columns	320
bonded repairs	1	constituent properties	200
bonding	806	constraint	840
boron-epoxy doublers	563	continuous fibre laminates	621
box-beam	652	corrosion fatigue	344
braids	218	cost	621
brake disk	671	cost estimation	630, 640
breast implants	467	crack	552
bridge	330	crack bridging	159
brush	851	cricket bat	365
buckling	552, 611, 689	cylindrical shell	611
C130 flap	528	damage	552
CAD/CAE/CAM	590	damage tolerance	178, 302, 552
CAD/CAM/CAPPS	583	damping	355, 738
cantilever	738	DC machines	851
carbon fiber	851	decks	88
carbon/carbon (C/C) composite	283	deflection	652
carbon/carbon brake disk	295	deformation	448
carbon-carbon	671	delamination	25, 159, 302, 552, 827
carbon-fiber reinforced plastic	178	design	330, 528, 640
centrifugal rotor	436	design for manufacture (DFM)	583
certification	1, 178, 528	design methodology	590
CF/PEEK	509	design rules	402
CFRP	355	design-for-manufacturing	257
civil Infrastructure	88	development	528
close end pressure vessel	816	direct flame processing head	419
coefficient of restitution	365	dorsal fin design and development	772

dove tail joint	283	high-speed research program	383
durability	88, 467	honeycomb	383
dynamic test	302	HSCT	383
dynamic torque test	295	HSR	383
		hull mounted sonar dome	426
elastomers	458	hydrostatic extrusion	488
electric motor	419	hydroxyapatite	488, 518
element	552		
energy absorption mechanism	218	I-beam	218
engine certification	200	impact	365, 552
environmental degradation	679	impact damage	748
environmental test chamber	344	impact damage tolerance design	748
evolutionary algorithms	611	impact performance	200
		impact resistance	748
FAA certification	535	impact test	218
fairing band	426	inelastic constitutive equation	797
fatigue	178	inertia dynamometer	295
feasibility study automotive structural		initiation	552
components	574	in-plane shear modulus	748
FEM analysis	393	in-plane stress concentration	748
fiber volume fraction	393	inspection interval	302
fiberglass reinforced plastics in automotive		integrate	840
applications	275	integrated design and manufacturing	
fibre failures	52	methodology	574
fibre reinforced plastics	574	integrated product team	528
fibre viscoelasticity	448	interface behavior	797
filament winding	411, 419, 816	interlaminar stresses	709
filament wound composite shells	730	interlayer	738
finite difference method	730	internal pressure	393
finite element analysis	320, 355, 699, 797	intervertebral disc prosthesis	458
finite element model	781	IrO ₂ coatings	518
finite element modeling	806	isoelastic implants	518
first-ply-failure	689		
flow analysis	477	jump conditions	797
foam-cored sandwich structures	699		
force-feedback	806	knitted fabrics	108
fracture	159, 552	knowledge-based economy	543
FRP	330, 611		
fully potted inserts	661	laminated shell theory	709
functionally graded	496	layered beam	738
		layerwise analysis	590
genetic algorithms	611, 689	leaf spring	738
geogrid	336	lightweight structures	509, 679
glass fibre	218	liner	411
glass fibre composite	320	load introduction	661
glass mat thermoplastic	365		
glass reinforced plastics (GRP)	426	main wing design optimization	355, 375
glass/PP	411	mandrel extractor	266
golf club	355	manufacturability	762
golf shafts	266	manufacturing	88, 528, 630, 719
graphite/epoxy	344	manufacturing and processing	134
		material	552
haptic control	806	material gradient	738
high density polyethylene	393	material selection and qualification	535
high energy particle physics	679	matrix failures	52
high hydrostatic pressure	344	mechanical performance	621
high modulus carbon fiber	355	mechanical properties	25, 108
high performance composites	679	mechanical stability	679
high-order theory	661, 670	mechanics	448, 552
high-speed civil transport	383	mechanistic considerations	52

medical applications	509	resin transfer moulding	310, 719
metal matrix composites	797	resorbable polyesters	509
metallo-thermo-mechanical theory	797	robotic design	806
micromechanics	159	Robotics	583
MIL-W-5013	295	rods	159
modal vibration	806	rotational moulding	458
mode I and mode II fracture toughness	25	RTM process	477
mode shape function	365	rubber	781
model analysis by VPI	355		
modelling	25, 108, 552, 590	safety-related applications	402
multi-functional structures	134	sandwich	383
		sandwich plates	661
natural frequencies	365	seawater	344
NDI	563	seismic retrofit	88
NDT	402	selection of materials	402
near-net-shape forming	509	semi-rigid fixation	509
notched composites	600	shell structure	590
numerical analysis	611	side member	218
		silicone elastomers	467
object-oriented database management system	630	SKUA high-speed target drone	355, 375
optimization	611, 689, 762, 806, 840	smart patches	1
optimization by viscosity characterization	477	smart structures	134
optimum design	283, 436, 851	sol-gel	518
orthotropic laminates	611	solid mechanics	134
osteosynthesis implants	509	SPATE	699
		spring-in	719
patching	302	SST	383
pedestrian bridge	330	stacking sequences	611
phenolic panel	247	static and fatigue behaviour	789
plates	689	static test	302
ply stresses	709	stealth airframe design methodology	772
plydrop	762	stiffness	652, 771
ply-drops	827	stiffness couplings	781
poly (l-lactide)	509	stitching	25, 159
polyethylene	488	strain energy release rate	827
polymer composites for automotive applications	275	strength	178, 762
polymer matrix composite	200	stringers	310
polyoxymethylene fibers	336	structural analysis and design	781
porous sintering	518	structural optimization	738
power plants	402	structural qualification	355, 375
precision detector	679	structural testing	178
pre-preg material	719	structure design	840
pressure vessel	411, 419	structures	134, 488
process development	355, 375	surface structure	524
process optimization	477		
progressive crushing	218	table rolling	266
properties	488, 552	tailored fibre placement,	600
prostheses	448	taper, sublaminare	762
prototype bat	365	tapered	827
		technology transfer	543
quenching process	797	technology transfer mechanism	574
		tee-joints	699
radar absorbing composite structures	772	test	310
radar cross section reduction	772	testing	528, 789
rail car floors	247	textile composites	108, 458
recreation tubes	266	textile reinforcement architectures	200
reference standards	563	textiles	159
renewal	88	theory	159
research organizations	543	theory of elasticity	709
residual stresses	719	thermoelastic analysis	671

thermoelastic stress analysis	699	treated plywood	247
thermoelasticity	730	trends in composites development	257
thermography	563	tube rolling	266
thermoplastic	411, 419	twisted cord	781
through-thickness reinforcement	25		
TiB ₂	518	validation	563
ti-composites	518	variable	840
TiN	518	vibration	355
tip	552	virtual crack closure method	827
titanium matrix	496		
tool mold manufacturing	590	weaving	159
tooling	310	winding circuits alignment	816
tooling techniques	355, 375	wing	310
transverse core flexibility	661	wrapping technique	320
transverse shear effects	689		
transverse shear strain	730	z-reinforcement	159